



# Acoustic and Aero-Mixing Experimental Results for Fluid Shield Scale Model Nozzles

M. Salikuddin, V.G. Mengle, H.W. Shin, and R.K. Majjigi  
General Electric Aircraft Engines, Cincinnati, Ohio

## The NASA STI Program Office . . . in Profile

Since its founding, NASA has been dedicated to the advancement of aeronautics and space science. The NASA Scientific and Technical Information (STI) Program Office plays a key part in helping NASA maintain this important role.

The NASA STI Program Office is operated by Langley Research Center, the Lead Center for NASA's scientific and technical information. The NASA STI Program Office provides access to the NASA STI Database, the largest collection of aeronautical and space science STI in the world. The Program Office is also NASA's institutional mechanism for disseminating the results of its research and development activities. These results are published by NASA in the NASA STI Report Series, which includes the following report types:

- **TECHNICAL PUBLICATION.** Reports of completed research or a major significant phase of research that present the results of NASA programs and include extensive data or theoretical analysis. Includes compilations of significant scientific and technical data and information deemed to be of continuing reference value. NASA's counterpart of peer-reviewed formal professional papers but has less stringent limitations on manuscript length and extent of graphic presentations.
- **TECHNICAL MEMORANDUM.** Scientific and technical findings that are preliminary or of specialized interest, e.g., quick release reports, working papers, and bibliographies that contain minimal annotation. Does not contain extensive analysis.
- **CONTRACTOR REPORT.** Scientific and technical findings by NASA-sponsored contractors and grantees.

- **CONFERENCE PUBLICATION.** Collected papers from scientific and technical conferences, symposia, seminars, or other meetings sponsored or cosponsored by NASA.
- **SPECIAL PUBLICATION.** Scientific, technical, or historical information from NASA programs, projects, and missions, often concerned with subjects having substantial public interest.
- **TECHNICAL TRANSLATION.** English-language translations of foreign scientific and technical material pertinent to NASA's mission.

Specialized services that complement the STI Program Office's diverse offerings include creating custom thesauri, building customized databases, organizing and publishing research results . . . even providing videos.

For more information about the NASA STI Program Office, see the following:

- Access the NASA STI Program Home Page at <http://www.sti.nasa.gov>
- E-mail your question via the Internet to [help@sti.nasa.gov](mailto:help@sti.nasa.gov)
- Fax your question to the NASA Access Help Desk at 301-621-0134
- Telephone the NASA Access Help Desk at 301-621-0390
- Write to:  
NASA Access Help Desk  
NASA Center for Aerospace Information  
7121 Standard Drive  
Hanover, MD 21076





# Acoustic and Aero-Mixing Experimental Results for Fluid Shield Scale Model Nozzles

M. Salikuddin, V.G. Mengle, H.W. Shin, and R.K. Majjigi  
General Electric Aircraft Engines, Cincinnati, Ohio

Prepared under Contract NAS3-25951

National Aeronautics and  
Space Administration

Glenn Research Center

## Acknowledgments

The authors are thankful to Mr. J. Brausch for his contribution in designing and acquiring the acoustic hardware and helping the installation of the hardware in GEAE's Cell 41 for testing and Mr. J. Askew for his contribution in designing and acquiring the hardware for aerodynamic tests. The authors are also thankful to Mr. W.E.

Niehoff and Mr. J. Hencheck for running the test facility, Mr. D. Lewis and Mr. W. Brown for helping in data analysis, Dr. C.E. Whitfield and Mr. S. Wisler for covering the aerodynamic tests in GEAE's Aerodynamic Research Laboratory. The authors are particularly thankful to Mr. R. Lee for his useful suggestions and discussions during the course of this work.

## Document History

This research was originally published internally as HSR024 in January 1996.

Note that at the time of writing, the NASA Lewis Research Center was undergoing a name change to the NASA John H. Glenn Research Center at Lewis Field. Both names may appear in this report.

Available from

NASA Center for Aerospace Information  
7121 Standard Drive  
Hanover, MD 21076

National Technical Information Service  
5285 Port Royal Road  
Springfield, VA 22100

Available electronically at <http://gltrs.grc.nasa.gov>

## FOREWORD

This report is prepared by GE Aircraft Engines, Cincinnati, Ohio for NASA-Lewis Research Center, Cleveland, Ohio under Contract NAS3-25951, Task Order 9, entitled "APT Fluid-Shield Nozzle Scale-Model Development." Mr. Doug Harrington was the Project Manager for NASA-Lewis Research Center and Mr. Fred Krause was the Project Manager for GEAE. GEAE Program Manager was Dr. R. K. Majjigi.



## SUMMARY

The principle objectives of this investigation are to evaluate the acoustic and aerodynamic characteristics of fluid shield nozzle concept and to assess Far 36, Stage 3 potential for fluid shield nozzle with Flade Cycle. Acoustic data for nine scale model nozzle configurations are obtained. The effects of simulated flight and geometric and aerothermodynamic flow variables on the acoustic behavior of the fluid shield are determined. The acoustic tests are aimed at studying the effect of (1) shield thickness, (2) wrap angle, (3) mass flow and velocity ratios between shield and core streams at constant cycle specific thrust (i.e., mixed velocity), (4) porous plug, and (5) subsonic shield. Shadowgraphs of six nozzle configurations are obtained to understand the plume flowfield features. Static pressure data on suppressor chutes in the core stream (shielded and unshielded) sides, and on plug surface are acquired to determine the impact of fluid shield on base drag of the 36-chute suppressor nozzle and the thrust augmentation due to the plug, respectively.

The significant influence of fluid shield on acoustics of the nozzle concept are : (a) mid and high frequency noise reduction, more dominantly in the rear arc, due to shielding and jet source strength reduction due to mean shear modification and (b) low frequency noise amplification due to an elongation of jet plume.

Slight noise reduction is achieved due to the porous plug. However, the amount of benefit is much less than what was expected of porous plugs. Suppressions of about 8 EPNdB is achieved by the 36-chute suppressor alone configuration with porous plug at takeoff and cutback cycle conditions.

For the takeoff thrust of about 67 to 69 klbs, with flight simulation, while noise suppression of about 8 EPNdB is achieved by the suppressor alone configuration, additional benefit of about 4 to 8 EPNdB are obtained due to fluid shields of different thicknesses compared to the suppressor alone configuration. Similar noise benefits due to suppressor alone configuration and due to fluid shields are also obtained with respect to core stream velocity. At takeoff condition (i.e., at core velocity of 2475 ft/sec), noise benefit of as high as 8 EPNdB with flight simulation is observed for 0.75" and 1.0" thick shields with respect to the suppressor alone configuration. With respect to FAR 36 Stage 3 noise requirement the best of fluid shield configuration falls short of about 3.5 EPNdB at takeoff with an ideal gross thrust of about 68 klbs. Noise suppression increases with increasing shield thickness until it reaches an optimum

value. The trend is reversed by further increase in shield thickness. For the present study 0.75"-thick shield (i.e., about 5.25" for full scale nozzle) seems to be the optimum.

Noise level decreases with increasing velocity ratio,  $V_r$  (i.e., fluid shield velocity/primary stream velocity) and/or mass flow ratio,  $W_r$  (i.e., fluid shield mass flow rate/primary stream mass flow rate). With respect to shield thickness, minimum  $V_r$  and  $W_r$  for a fixed noise level correspond to the 0.75"-thick shield with 220° wrap. The noise characteristics with respect to  $V_r$  and  $W_r$  are of opposing behavior to the  $(\Delta C_{fg})_t$  (i.e., correction factor to the gross thrust coefficient,  $C_{fg}$ , in % due to the drag or thrust contributions by the relative pressure distributions on plug and chute surfaces) characteristics, that a lower negative  $(\Delta C_{fg})_t$ , which is desirable for takeoff thrust from performance considerations, occurs at lower velocity and mass flow ratios. A compromise between acoustic and  $(\Delta C_{fg})_t$  needs to be considered for the application of fluid shield in real engines.

Azimuthal variation of farfield noise is relatively less dominant for the fluid shield nozzles. Azimuthal noise variation is insignificant with subsonic shield flow. With flight simulation azimuthal noise variation increases compared to the static case.

The plume shock structures on the unshielded side are distinctly different from those on the shielded side, as observed in shadowgraphs. Porous plug was not effective in reducing shock strength (from shadowgraphs), since the high aspect ratio primary chute passages resulted in oblong shock structures which did not "sense" the porous plug.

Based on the static pressure distribution on the plug and chutes, the plug contributes additional thrust due to pressure recovery. However, the chute base drag increases due to the fluid shield, since the shields reduce ventilation of the chutes. For the suppressor alone configuration, the combined correction to  $C_{fg}$  is close to zero for static case, but negative with flight simulation. However, with increasing nozzle pressure ratio  $(\Delta C_{fg})_t$  increases and is closer to zero for higher nozzle pressure ratio. The  $(\Delta C_{fg})_t$  is about 0 % and -1.5 % at takeoff for static and with flight simulation, respectively. The corresponding values at cutback are -0.5 % and -2 % respectively.

The  $(\Delta C_{fg})_t$  for 0.5"-thick fluid shield nozzle is about 2 to 3 % lower compared to the suppressor alone configuration. With increasing thickness small reduction of  $(\Delta C_{fg})_t$  is noticed. With flight simulation plug and chute pressure contributions to nozzle gross thrust coefficient ( $C_{fg}$ ) is about 4 to 5 % thrust loss over most of the cycle conditions.

## CONTENTS

	Page
FOREWORD	iii
SUMMARY	v
1.0 INTRODUCTION	1
2.0 TESTS IN ACOUSTIC ANECHOIC CHAMBER FOR THREE DIMENSIONAL FLUID SHIELD SCALE MODEL NOZZLES	5
2.1 TEST FACILITY DESCRIPTION AND DATA ACQUISITION PROCEDURES	7
2.1.1 Anechoic Free-Jet Jet Noise Facility	7
2.1.2 Data Acquisition Systems	10
2.2 CONFIGURATION DESCRIPTION AND SCOPE OF TESTING	13
2.2.1 Description of Test Nozzle Configurations	13
2.2.2 Instrumentation Layout for Static Pressure Measurement	21
2.2.3 Test Procedure	27
2.2.4 Scope of Testing	31
2.3 SHADOWGRAPH RESULTS	43
2.3.1 Flow Structures on the Unshielded Side	45
2.3.2 Flow Structures on the Shielded Side	51
2.3.3 Suppressor Alone Configurations	55
2.3.4 Fluid-Shield Nozzle Configurations	58
2.4 STATIC PRESSURE RESULTS	67
2.4.1 Static Pressure Data Analysis	67
2.4.2 Static Pressure Distribution on Plug Surface	68
Suppressor Alone Configuration	68

	Fluid-Shield Nozzle Configurations	73
2.4.3	Base Pressure Distribution on Chutes	87
	Suppressor Alone Configuration	87
	Fluid-Shield Nozzle Configurations	87
2.4.4	Contribution of Plug Static Pressure and Chute Base Drag to Specific Gross Thrust Coefficient ( $\Delta C_{fg}$ )	97
	Suppressor Alone Configuration with Rigid Plug	97
	Fluid-Shield Nozzle Configurations	99
2.5	ACOUSTIC DATA NOMENCLATURE, NORMALIZATION AND ACCURACY	115
2.5.1	Acoustic Data Nomenclature and Normalization	115
2.5.2	Acoustic Data Accuracy	121
	Tower Versus Fixed Microphone Data	121
	Online Versus IDR Data	122
	Freejet Background Noise	125
	Flight Effect on Jet Noise and Shock Noise	132
	Measured Versus SAE Prediction Comparisons	136
	Measured Versus MS Prediction Comparisons	144
	Old Versus Present Conical Nozzle Noise Data	149
2.6	EFFECT OF POROUS PLUG ON NOISE	183
2.6.1	Suppressor Alone Configurations	183
2.6.2	Fluid Shield Nozzle Configurations with 0.5"-Thick Shield of 220° Wrap	192
2.7	ACOUSTIC CHARACTERISTICS OF THE 36-CHUTE SUPPRESSOR COMPARED TO AN EQUIVALENT CONICAL NOZZLE	197
2.7.1	Acoustic Characteristics of the 36-Chute Suppressor Compared to an Equivalent Conical Nozzle	197
2.7.2	Acoustic Characteristics of the 36-Chute Suppressor Compared to Other Multi-Chute Suppressors	212



2.7.3	Conclusions	226
2.8	ACOUSTIC CHARACTERISTICS OF FLUID SHIELD NOZZLES -227	
	EFFECT OF FLUID SHIELD THICKNESS	
2.8.1	Noise Suppression Due to Fluid Shield as a Function of Ideal Gross Thrust	235
2.8.2	Noise Suppression Due to Fluid Shield Nozzles on an Equal Area Basis	257
2.8.3	Noise Suppression Due to Fluid Shield Nozzles With Respect to Core Stream Velocity ( $V_{j,p}$ )	277
2.8.4	Comparison of Acoustic Results between Fluid shield and Thermal Shield Configurations	286
2.8.5	Comparison of Acoustic Results between Fluid shield and Mixer Ejector Configurations	300
2.8.6	Conclusions	327
2.9	ACOUSTIC CHARACTERISTICS OF FLUID SHIELD NOZZLES 329	
	DUE TO PARAMETRIC VARIATIONS OF AEROTHERMODYNAMIC CONDITIONS	
2.9.1	Static Data	330
	Effect of Velocity Ratio $V_r$ and Mass Flow Ratio $W_r$	330
	Effect of Fluid Shield Nozzle Pressure Ratio $P_{r,s}$	354
	Effect of Fluid Shield Nozzle Total Temperature $T_{t,s}$	354
	Effect of Primary Nozzle Pressure Ratio $P_{r,p}$	357
	Effect of Primary Nozzle Total Temperature $T_{t,p}$	372
2.9.2	Flight Data	372
	Effect of Velocity Ratio $V_r$ and Mass Flow Ratio $W_r$	381
	Effect of Fluid Shield Nozzle Pressure Ratio $P_{r,s}$	381
	Effect of Fluid Shield Nozzle Total Temperature $T_{t,s}$	390
	Effect of Primary Nozzle Pressure Ratio $P_{r,p}$	390
	Effect of Primary Nozzle Total Temperature $T_{t,p}$	396

2.10 AZIMUTHAL VARIATION OF ACOUSTIC CHARACTERISTICS OF FLUID SHIELD NOZZLES	401
2.10.1 Azimuthal Noise Variation for 0.5"-Thick Fluid Shield Nozzle with Porous Plug	403
Ambient Temperature Results	403
Results at $V_{mix} = 1811$ ft/sec	403
Results at $V_{mix} = 2030$ ft/sec	414
2.10.2 Effect of Shield Thickness on Azimuthal Noise Variation for Fluid Shield Nozzles with Porous Plug	414
Results at $V_{j,p} = 1345$ ft/sec	414
Results at $V_{j,p} = 2198$ ft/sec	414
Results at $V_{j,p} = 2475$ ft/sec	425
2.10.3 Noise Variation Between Sideline and Community Points for Fluid Shield Nozzles with Porous Plug	425
Static Data	425
Flight Simulation Data	449
2.11 EFFECT OF FLIGHT SIMULATION ON ACOUSTIC CHARACTERISTICS OF FLUID SHIELD NOZZLE CONFIGURATIONS	461
2.11.1 Single Stream Jets for Convergent Conical and 36-Chute Suppressor Nozzles	461
Conical Nozzle Results	461
36-Chute Suppressor Nozzle with Porous Plug	466
2.11.2 Dual Stream Fluid Shield Nozzle Configurations with Porous Plug	479
2.12 CONCLUSIONS AND RECOMMENDATIONS	491

3.0	AERO-MIXING TESTS IN AERODYNAMIC RESEARCH LABORATORY FOR TWO DIMENSIONAL FLUID SHIELD SCALE MODEL NOZZLES	495
3.1	TEST FACILITY AND DATA ACQUISITION SYSTEMS	497
3.1.1	Wind-Tunnel Facility for Aero-Mixing Tests	497
3.1.2	Aerodynamic Data Acquisition System	502
3.1.3	Shadowgraph System	502
3.1.4	Laser Velocimetry (LV) System	502
3.1.5	Planar Laser Sheet System	508
3.2	SCALE MODEL NOZZLE DESCRIPTION AND SCOPE OF TESTING	511
3.2.1	Description of Test Nozzle Configurations	511
3.2.2	Scope of Testing	522
3.3	EXPERIMENTAL RESULTS AND ANALYSIS	525
3.3.1	Shadowgraph Data	525
3.3.2	Laser Velocimetry Results & Interpretation	538
	Shallow-Chute Configuration	543
	Baseline Configuration	564
	Effect of CD-Core Flow Passages	577
	Effect of SAR	579
3.3.3	Planar Laser Sheet Results	582
3.4	CONCLUSIONS AND RECOMMENDATIONS	587
3.4.1	Flow-Field Insights	587
3.4.2	Recommendations	588
APPENDIX A	LIST OF SYMBOL	589
APPENDIX B	TABULATED ACOUSTIC DATA	593
REFERENCES		613



## 1.0 INTRODUCTION

Environmental acceptability and economic viability are crucial issues in the development of the next generation HSCT (High Speed Civil Transport). Low noise exhaust nozzle technology has significant impact on both these issues. The exhaust system design that meets FAR 36 Stage 3 takeoff acoustic requirements and provides high levels of cruise and transonic performance and adequate takeoff performance at an acceptable weight is essential to the success of any HSCT program.

One concept that appears to be promising in reducing takeoff noise is the use of high flow approach to reduce the jet exhaust velocity. Further noise reduction to meet Far 36 Stage 3 takeoff requirement can be met by using an efficient multi-chute suppressor to reduce low-frequency noise and a fluid shield to attenuate high-frequency noise emanating from the exhaust-nozzle jet.

Major components of a fluid shield nozzle, as illustrated in the conceptual fladed variable cycle engine (see Figure 1.0-1), are a multi-chute single stream suppressor, a plug, and a fluid shield partially surrounding the core flow. While the suppressor reduces low-frequency noise, the fluid shield attenuates high-frequency noise due to mean shear reduction similar to conventional high bypass ratio nozzles.

To demonstrate the potential acoustic benefit and to develop an understanding of the aerodynamic mixing of an unheated or moderately heated fluid shield with an improved mechanical suppressor, acoustic fluid shield scale model nozzles, designed and fabricated under Contract NAS3-25951 (APT), Task Order 4, were tested under the present task order. The concept selection procedure, the design and fabrication of fluid shield scale models, and the development of test plan are described in a design report (Ref. 1). Acoustic, static pressure measurement on model surface, and flow visualization tests using shadowgraph technique were conducted in GEAE's Anechoic Free-Jet Facility (Cell 41) for 3-dimensional scale models of full-up fluid shield nozzles under APT Task Order 9. Also under APT Task Order 9, static pressure measurement on model surface, flow visualization tests using shadowgraph technique, and detailed aerodynamic measurements using laser velocimeter were conducted in GEAE's Aerodynamic Research Laboratory (ARL) wind tunnel for two-dimensional sectors of fluid shield nozzles.

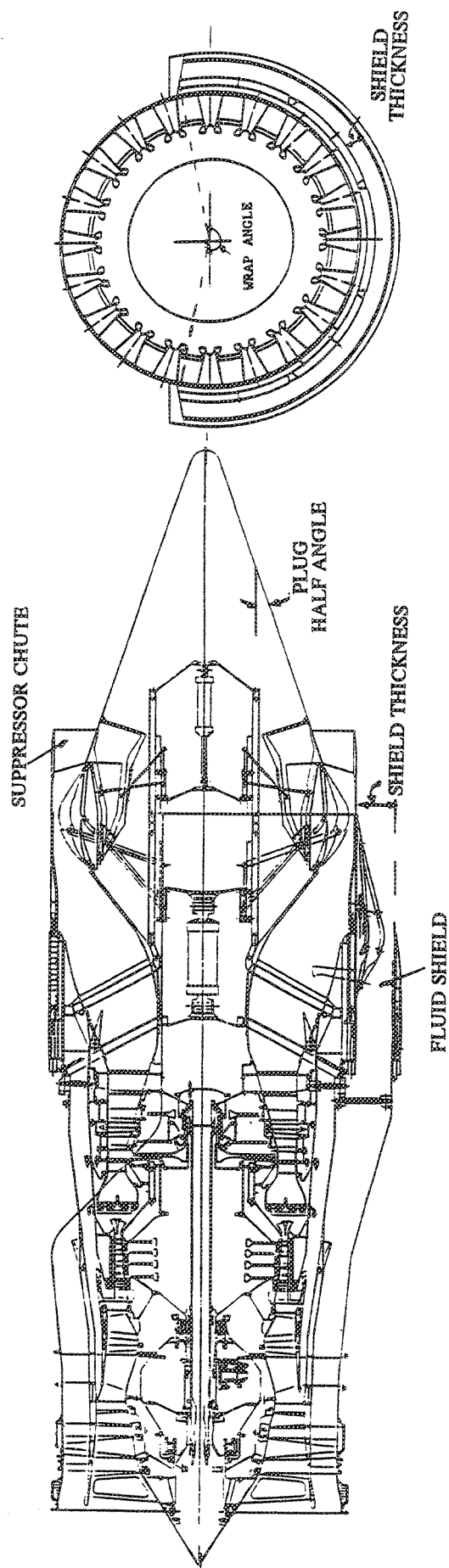


Figure 1.0-1. Schematic of a conceptual flared variable cycle engine (VCE) with multi-chute suppressor exhaust nozzle partially surrounded by a fluid shield.

The core stream suppressor nozzle is designed for lower specific thrust core engine cycles with jet velocities in the range of about 2400 ft/sec at takeoff. The design of these scale models permitted parametric variations of select suppressor geometry and fluid shield parameters to determine their effect on aerodynamic mixing and acoustic characteristics of the exhaust jet.

Test results of anechoic chamber, containing static pressure data, shadowgraph observations, and acoustic data, are presented in section 2. The static pressure data, the shadowgraph observations, and the LV results, acquired from aeromixing tests in ARL facility are presented in section 3.





## 2.0 TESTS IN ACOUSTIC ANECHOIC CHAMBER

Acoustic fluid shield scale model nozzles designed and fabricated under APT Task Order 4 (Contract NAS3-25951) were tested in the GEAE Cell 41, which is an anechoic free-jet jet noise facility. This facility is equipped with acoustic test instruments as well as laser velocimeter and shadowgraph equipment for flow field diagnostics. The two hot-flow system of the facility is surrounded by a tertiary duct with necessary airflow to simulate forward flight up to a Mach number of about 0.4. The inner stream is used for the core and the outer flow is used for fluid shield. Tests were also conducted using a conical nozzle to assess noise reduction obtained by the fluid shield nozzle system. These tests provide the experimental data to assess potential for fluid shield nozzle for the flade cycle to meet FAR-36 Stage 3 noise levels.

The principle objectives of these tests are to evaluate the acoustic and aerodynamic characteristics of fluid shield nozzle concept and to assess Far 36, Stage 3 potential for fluid shield nozzle with Flade Cycle. In addition, the acoustic tests are aimed at studying the effect of (1) shield thickness, (2) wrap angle, (3) mass flow and velocity ratios between secondary and primary streams at fixed mixed velocities, (4) porous plug, and (5) subsonic shield. Limited amount of acoustic data are tabulated in the Appendix B in a summary form.



## 2.1 TEST FACILITY DESCRIPTION AND DATA ACQUISITION PROCEDURES

All of the acoustic and shadowgraph tests for the acoustic model scale nozzles are conducted in the General Electric Anechoic Free-Jet Facility, known as Cell 41, located in Evendale, Ohio. Brief description of the facility and data acquisition procedures are included in this section.

### 2.1.1 Anechoic Free-Jet Jet Noise Facility

The GEAE anechoic free-jet jet noise facility, shown in Figure 2.1-1, is a cylindrical chamber 43' (13.1 meters) in diameter and 72' (21.95 meters) tall. The inner surfaces of the chamber are lined with anechoic wedges made of fiberglass wool to render the facility anechoic above 220 Hz. The facility can accommodate model configurations up to 5.3" (13.5 cm) and 5.5" (14.0 cm) equivalent flow diameter in the inner and outer flow streams, respectively. The corresponding throat areas for these streams are 22 and 24 square inches. The streams of heated air for the dual flow arrangement, produced by two separate natural gas burners, flow through silencers and plenum chambers before entering the test nozzle. The operating domain of the facility in terms of total temperature, pressure ratio, mass flow rate, and jet velocity is indicated in Figure 2.1-2 for single- and dual-flow operation and for static and simulated flight operation. Each stream can be heated to a maximum of 1960°R with nozzle pressure ratios as high as 5.5, resulting in a maximum jet velocity of 3000 feet/second.

The tertiary air stream system, which is used to simulate external flow, consists of a 250,000 scfm (at 50" of water column static pressure) fan and a 3,500 horsepower electric motor. The transition duct work and silencer route the air from the fan discharge through the 48" (1.2 meter) diameter free-jet exhaust. The silencer reduces the fan noise by 30 dB to 50 dB. Tertiary flow at its maximum permits simulation up to a Mach number of about 0.4. Mach number variation is achieved by adjusting the fan inlet vanes. The combined model and free-jet airflow is exhausted through a "T" stack silencer directly over the models in the ceiling of the chamber. The "T" stack is acoustically treated to prevent high levels of noise to the surrounding community.

The facility is equipped with two systems of microphone arrays to measure the acoustic characteristics of the test models in the farfield, a fixed array of microphones and an

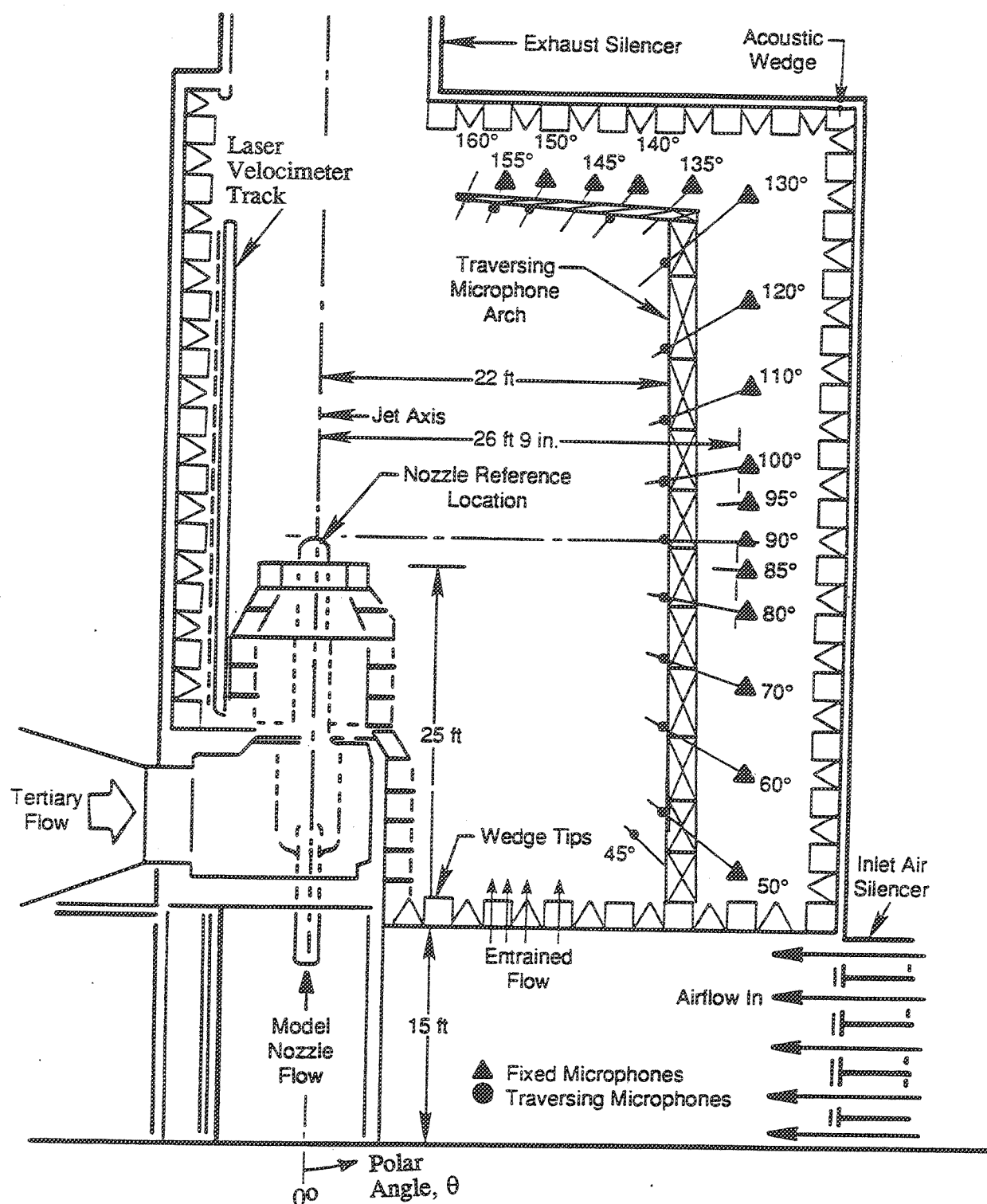


Figure 2.1-1. Side view of Cell 41 Anechoic Free Jet Facility in the azimuthal plane of  $\phi = 45^\circ$ .

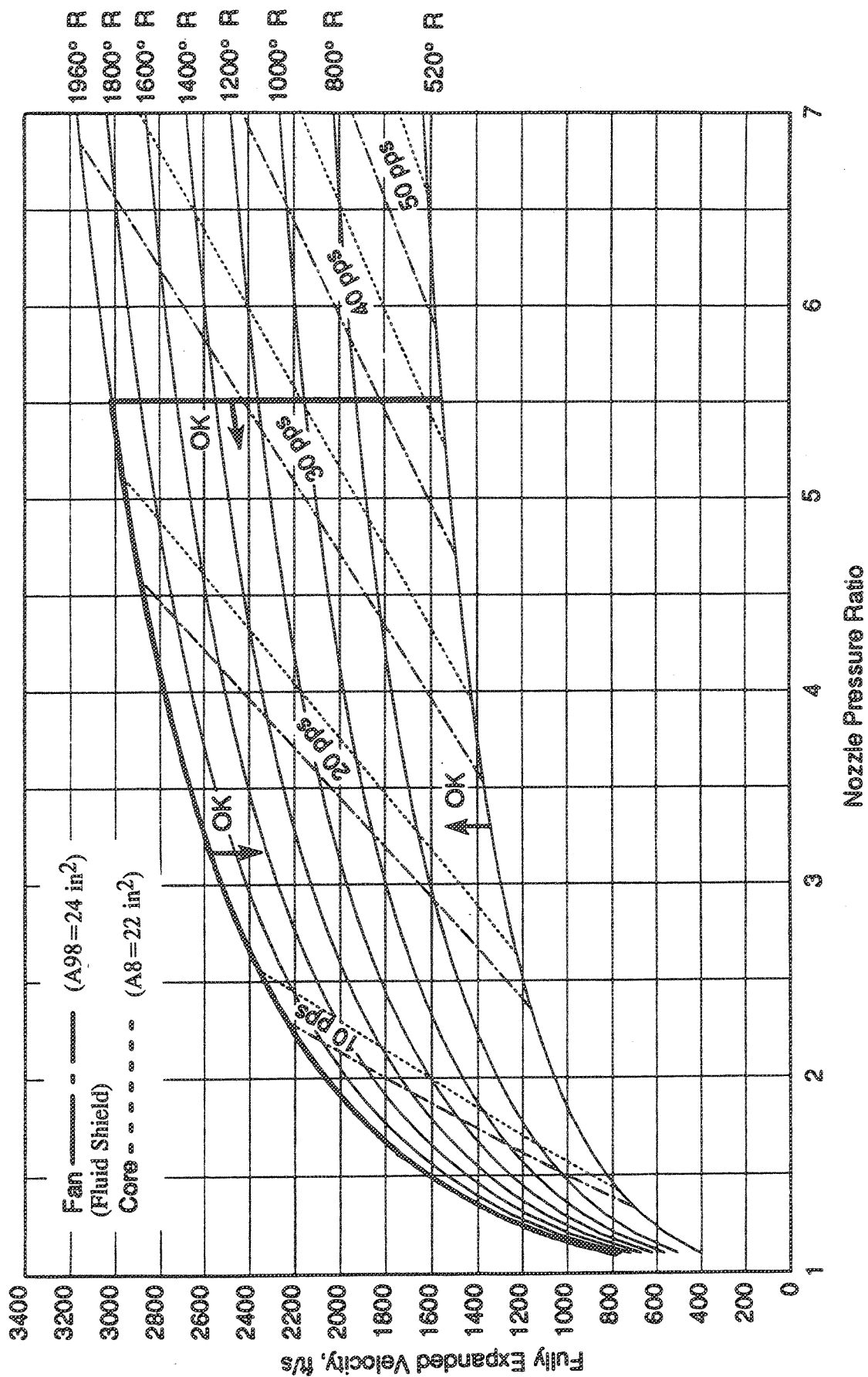


Figure 2.1-2. Operating domain of the Cell 41 Anechoic Free Jet Facility.

array on a traversing tower. The fixed array has 17 microphones mounted from the false floor, the wall, and the ceiling of the test cell, which provides measurements at a minimum distance of 26.75' (8.15 meter) from the nozzle reference location covering the polar angle ( $\theta$ ) range from  $50^{\circ}$  to  $155^{\circ}$ . The traversing tower contains 13 microphones, mounted at polar angles  $\theta$  ranging from  $45^{\circ}$  to  $155^{\circ}$ , and provides measurements at a distance of 22' (6.7 meter) from the nozzle reference location. The traversing tower can be positioned at any azimuthal angle  $\phi$  between  $+55^{\circ}$  to  $-55^{\circ}$  with respect to the fixed microphone array (or  $\phi = -10^{\circ}$  to  $100^{\circ}$ ) as shown in Figure 2.1-3.

The facility is also equipped with a laser velocimeter (LV) system and a shadowgraph system for jet flowfield measurement and flow visualization, respectively. LV tests were not conducted in Cell 41 for acoustic models and, therefore, the LV system is not described in this section. The shadowgraph system, illustrated in Figure 2.1-4, was employed in the anechoic chamber to acquire flow visualization data. This system includes a mounting in close proximity to the free jet nozzle, a steady-state light system, a 10" diameter mirror system to collimate the light through the test volume, a backdrop screen of sufficient size to encompass the total test volume, and a mounting platform for the light source, mirror, and camera system so as to control remotely and record the position of shadowgraph system for an approximate 6-foot vertical plume definition.

### 2.1.2 Data Acquisition Systems

Cell 41 is supported by well-calibrated acoustic and aerodynamic data acquisition systems. Acoustic data measured by both the microphone arrays is analyzed by an on-line system, which computes 1/3-octave band data for model scale at a 40' arc corrected to standard day conditions (i.e.,  $59^{\circ}\text{F}$  and 70 % humidity) and narrowband data as measured. In addition, this data is recorded on magnetic tapes for post processing. All static and total pressures including model surface pressures are measured using an aerodynamic data acquisition system consisting of multiport scanivalve contained pressure transducers, signal conditioner, and analog/digital converters. The pressure signals are supplied to a Micro VAX computer system where it can be analyzed or down-loaded to GE's mainframe computer system. Concurrently, a front-end computer with touch-screen application is used for signal and facility control and for real time data monitoring. Temperature data (thermocouple signals) are fed directly to the front-end computer.

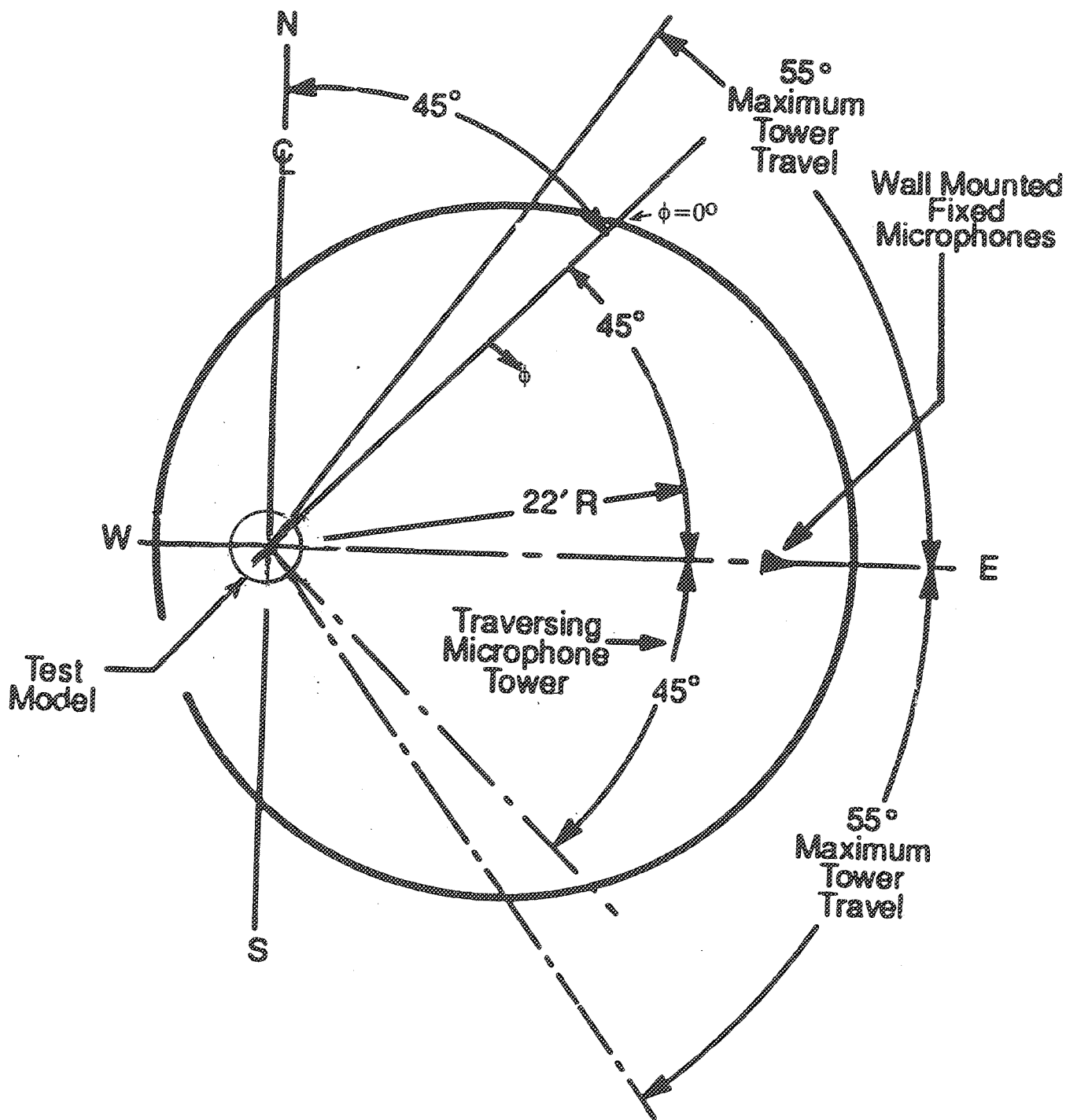


Figure 2.1-3. Plane view of Cell 41 Anechoic Free Jet Facility.

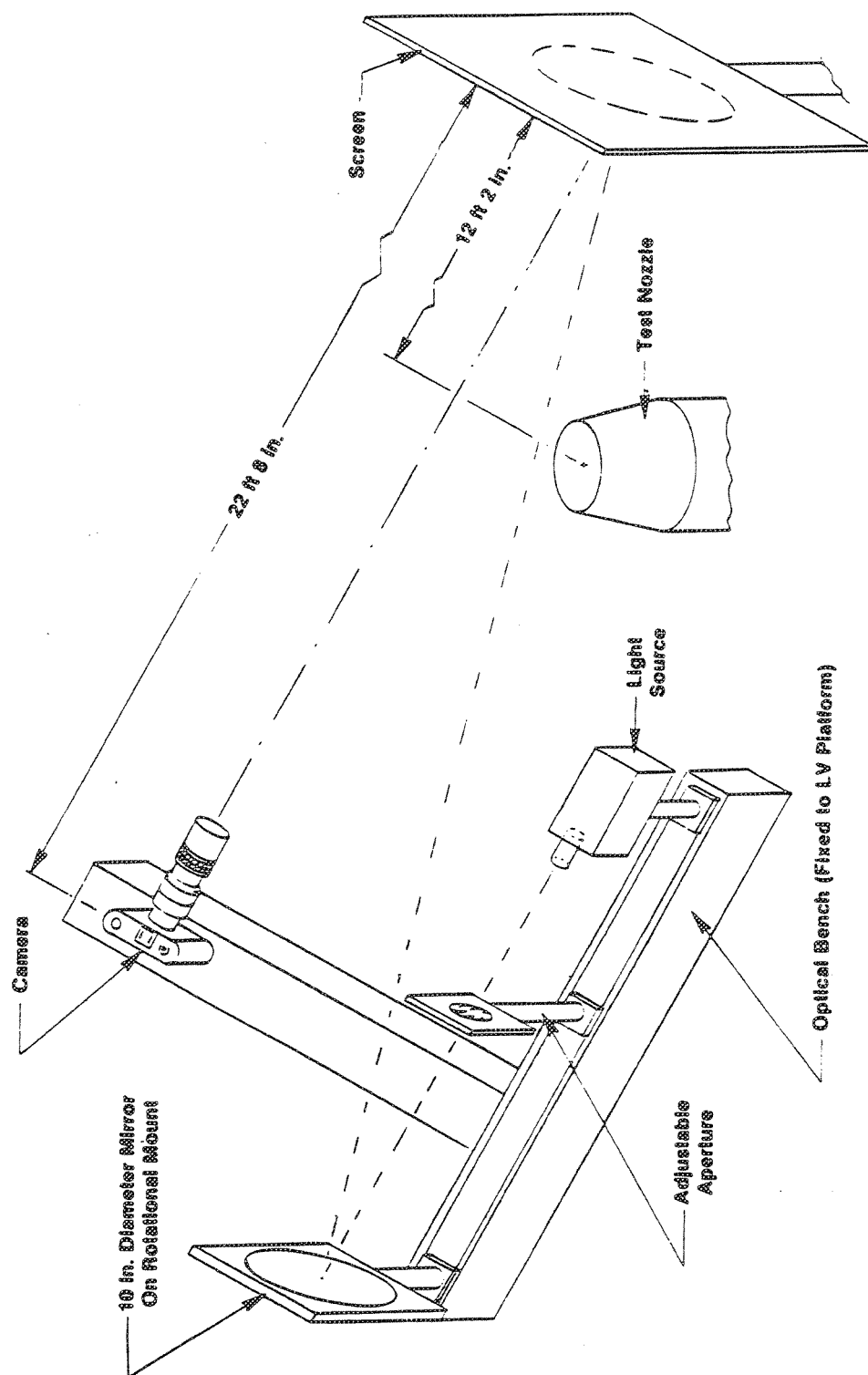


Figure 2.1-4. Schematic of the shadowgraph setup in the Anechoic Free Jet Facility.



## 2.2 CONFIGURATION DESCRIPTION AND SCOPE OF TESTING

Acoustic fluid shield scale model nozzles designed and fabricated (Ref. 1) under APT Task Order 4 (Contract NAS3-25951) were tested in the GEAE Cell 41. In addition, an existing conical nozzle is also tested for comparison purposes. The test matrices were designed (Ref. 1) to cover typical aero thermodynamic conditions of the Flade cycle, along with limited parametric variations. Shadowgraph measurements were performed for a limited number of test conditions for select configurations. Nozzle configurations tested in Cell 41 and the scope of these tests are briefly described in this section.

### 2.2.1 Description of Test Nozzle Configurations

**Conical Nozzle :** An existing conical nozzle was tested first, which is a dual stream coplanar nozzle of inner and outer stream diameters of 2.89" and 5.1", respectively (see Figure 2.2-1). The inner stream of the nozzle was used as a single stream conical nozzle. During static tests, the outer nozzle was removed. However, with flight simulation, the outer nozzle was mounted to achieve proper closure for the tertiary flow. In this situation, the nozzle outer stream and the tertiary stream were both operated at the same flight simulation velocity. Since the lip thickness of the outer nozzle is small (i.e., 0.06") its effect on the acoustic data may be small. This approach was taken as there was no other reference conic nozzle hardware available at the time of testing.

**Fluid Shield Nozzle Configurations :** A linear scale factor for the fluid shield acoustic models with respect to the preliminary full-scale design was selected to be 7.377, which is based on a simplified model layout for Cell 41 tests. A linear scale factor in the vicinity of 8 is normally selected since acoustic data can be reliably measured up to 80 kHz, which is necessary for acoustic data projection up to 10 kHz required for full scale EPNL projections. This linear scale factor also yields reasonable values of metal thicknesses for chutes. A smaller scale model results in relatively unproportionately larger base region due to metal thicknesses. A smaller scale model also introduces additional uncertainties in atmospheric absorption vagaries at higher frequencies (32 kHz and higher) and proportionately larger portion of measured spectra. Based on the scale factor of 7.337 the physical parameters for the model scale nozzle components are listed below.

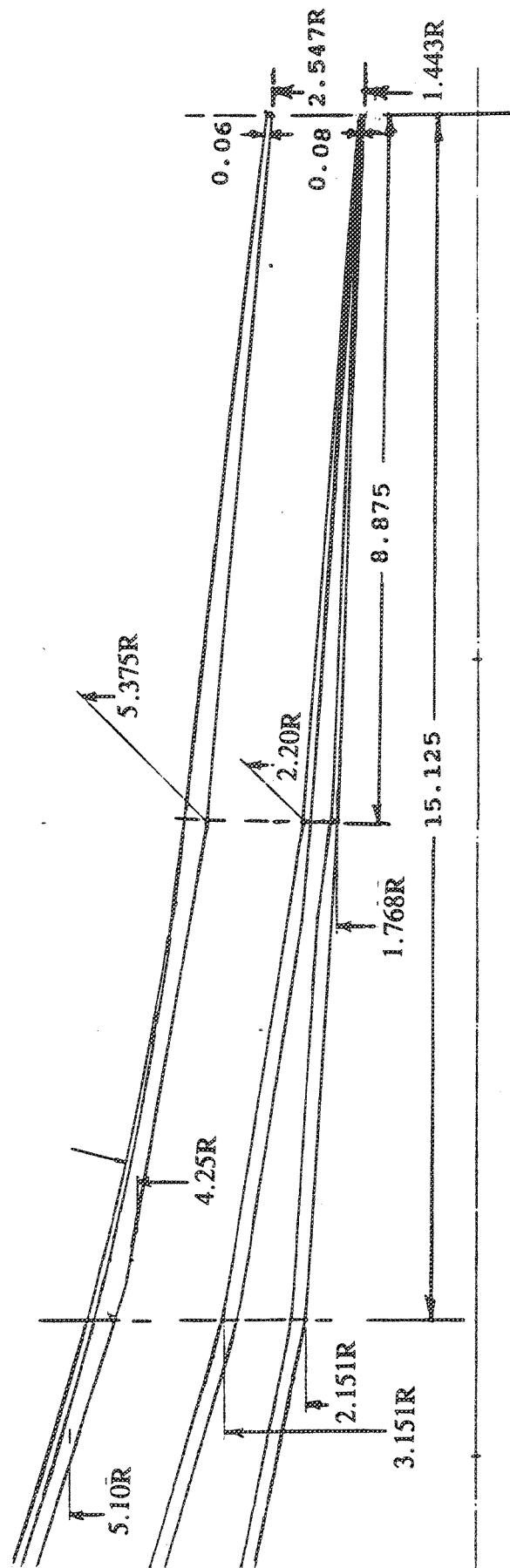


Figure 2.2-1. The coannular conical nozzle used as single stream nozzle (all dimensions are in inches).

**Suppressor :** Based on the concept selection process (Ref. 1) a 36-chute suppressor with convergent flow path, parallel sided core elements, and with conical plug was designed and fabricated. The relevant physical parameters are listed below:

Radius ratio,  $R_{Ci}/R_{Co} = 0.7$   
Suppressor area ratio,  $SAR = 2.5$   
Cant Angle =  $0^{\circ}$   
Chute Leading Edge Inclination =  $35^{\circ}$   
Throat area (A8) =  $21.5913 \text{ in}^2$   
Suppressor outer radius ( $R_{Co}$ ) =  $5.804''$   
Suppressor inner radius ( $R_{Ci}$ ) =  $4.063''$   
Mass flow rate for takeoff cycle =  $11.944 \text{ pps}$

The design details of the 36 chute suppressor with  $SAR = 2.5$  is illustrated in Figure 2.2-2. Radially tapering chutes with constant hot flow widths of the suppressor correctly simulate the stowable chutes of the preliminary design. One hardwalled plug and one porous plug with 10% porosity were designed and fabricated. The plug base radius is the same as the suppressor inner radius of  $4.063''$ . Based on  $15^{\circ}$  plug half angle the length of the plug up to the cone apex becomes  $15.163''$ . However, this length is slightly reduced due to the plug tip rounding (see Figure 2.2-3). The 10% porous plug, as shown in Figure 2.2-3, has axially equispaced holes of  $0.063''$  nominal diameter on the first  $9.62''$  slant length. The rest of the plug is not porous. Staggered hole pattern is adopted on the plug surface in circumferential direction (see Figure 2.2-3)

**Fluid Shield :** Fluid shield nozzle configurations are built by installing a shield of constant thickness partially around the 36-chute suppressor (described above). Based on the nominal mass flow split for the preliminary full scale flade cycle (i.e.,  $650/400 \text{ pps}$ ), and the core outer wall thickness at shield lip (i.e.,  $0.19''$ ) the following are the physical parameters for fluid shield nozzles:

Fluid shield throat area for takeoff cycle (A98) =  $11.734 \text{ in}^2$   
Fluid shield inner radius =  $5.994''$   
Mass flow rate for takeoff cycle =  $7.35 \text{ pps}$

For the takeoff cycle condition two fluid shield nozzles with different wraps, but with the same throat area of  $11.734 \text{ in}^2$  were fabricated. The wrap angles and the corresponding shield thicknesses are as follows:

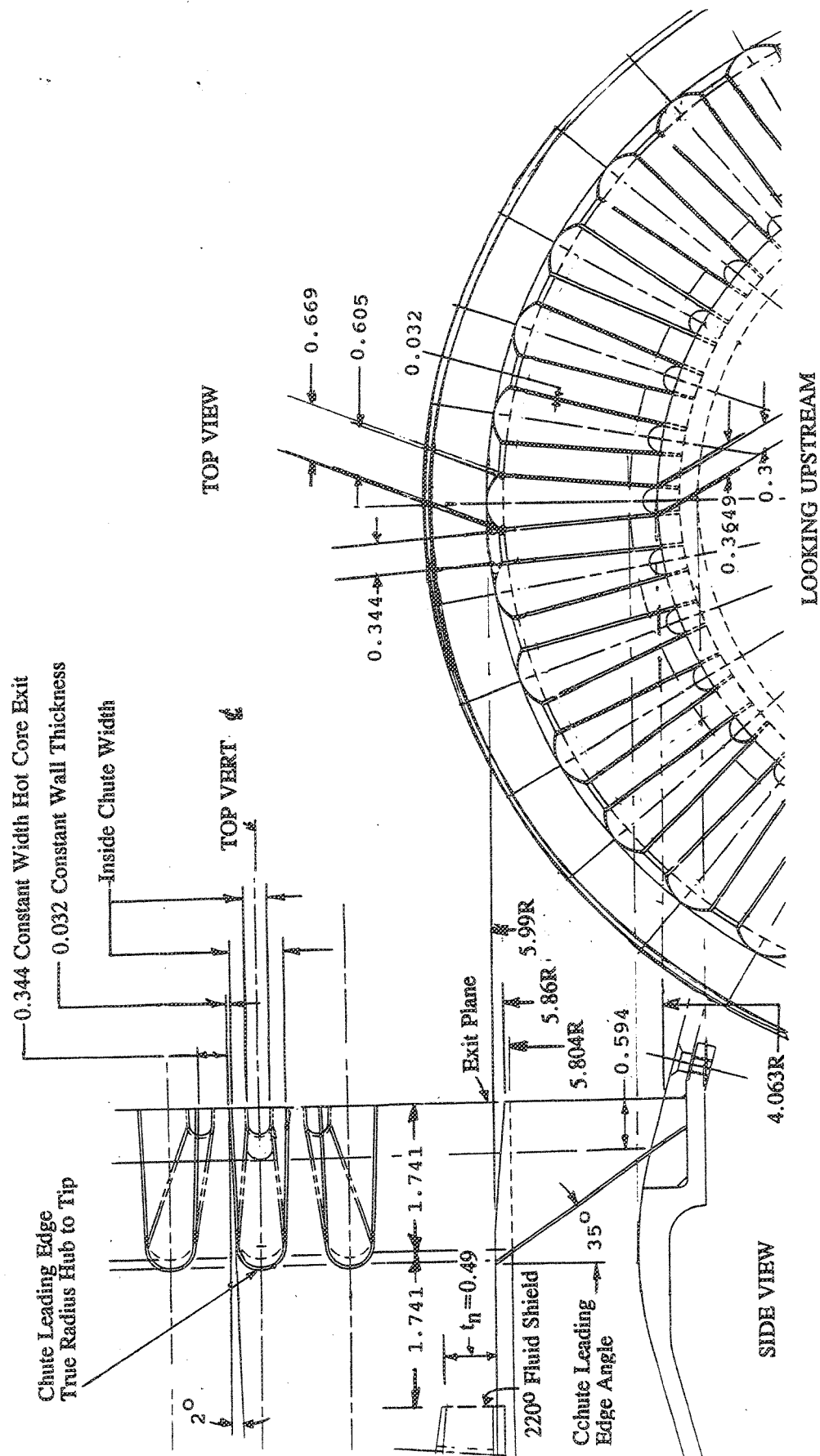


Figure 2.2-2. Design details of the 36 chute suppressor for the fluid shield nozzle (All dimensions are in inches).

Wrap Angle  $\phi_s$ 

180°

220°

Shield Thickness  $t_n$ 

0.59" (Nominally 0.6")

0.49" (Nominally 0.5")

To study the effect of shield thickness and the mass flow ratio on noise suppression two more 220° wrap fluid shield nozzles with different shield thicknesses were fabricated. The parameters pertaining to these cases are substantially different from the flade cycle. This shield thickness study is exploratory and is intended to establish effect of shield thickness and mass flow ratio on the noise suppression. The list below shows the various parameters based on the shield thicknesses for 220° wrap.

<u>Shield Thickness <math>t_n</math></u>	<u>Flade Area <math>A_{98}</math></u>	<u>Mass Flow Rate <math>W_s</math></u>
0.4898"	11.734 in <sup>2</sup>	7.350 pps (Design Case)
0.7500"	18.200 in <sup>2</sup>	11.788 pps
1.0000"	24.800 in <sup>2</sup>	16.060 pps

The range of shield thickness for the present fluid shield nozzles coincides approximately with the prior thermal shield test program (Ref. 2). Layout of the scale model fluid shield nozzle for 220° wrap is shown in Figures 2.2-2 and 2.2-3. Various components for fluid shield nozzles are shown in Figure 2.2-4.

Using one of the four fluid shield nozzles with the 36-chute suppressors four basic fluid shield configurations can be obtained. Accounting for the conical nozzle and suppressor alone configuration, the following six configurations (see Figure 2.2-5) were tested in Cell 41, in this test program:

1.	Conical Nozzle, $A_8 = 20.43 \text{ in}^2$	Diameter = 5.1"
2.	36 Chute Suppressor, $A_8 = 21.59 \text{ in}^2$	Equivalent Diameter = 5.243"
3.	36 Chute Suppressor with 0.5" Thick Fluid shield (Baseline Configuration)	Wrap Angle = 220° Shield Area = 11.734 in <sup>2</sup>
4.	36 Chute Suppressor with 0.75" Thick Fluid Shield	Wrap Angle = 220° Shield Area = 18.2 in <sup>2</sup>
5.	36 Chute Suppressor with 1.0" Thick Fluid Shield	Wrap Angle = 220° Shield Area = 24.8 in <sup>2</sup>
6.	36 Chute Suppressor with 0.6" Thick Fluid Shield	Wrap Angle = 180° Shield Area = 11.734 in <sup>2</sup>

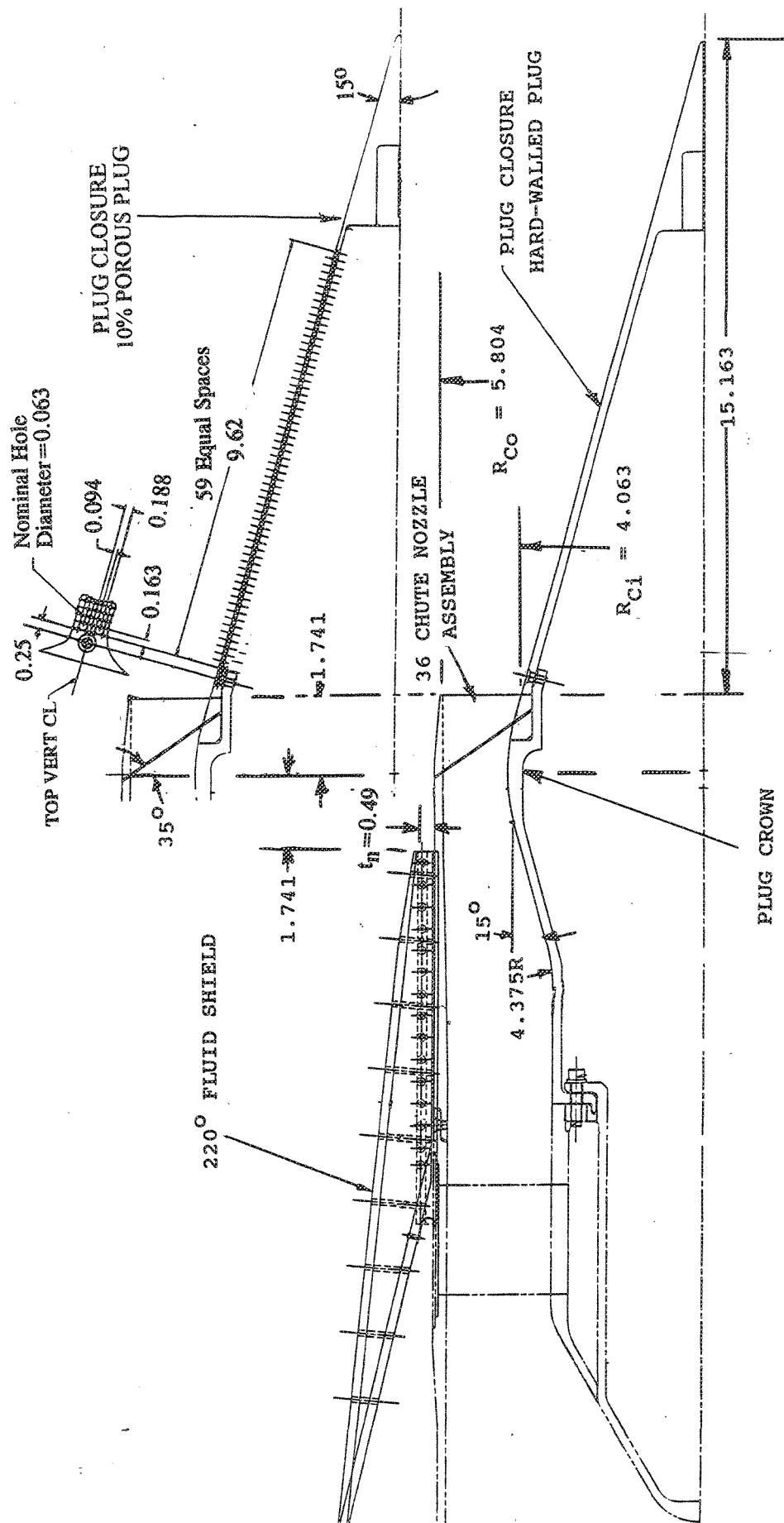


Figure 2.2-3. Layout of the fluid shield nozzle with 220° wrap for acoustic tests (All dimensions are in inches).

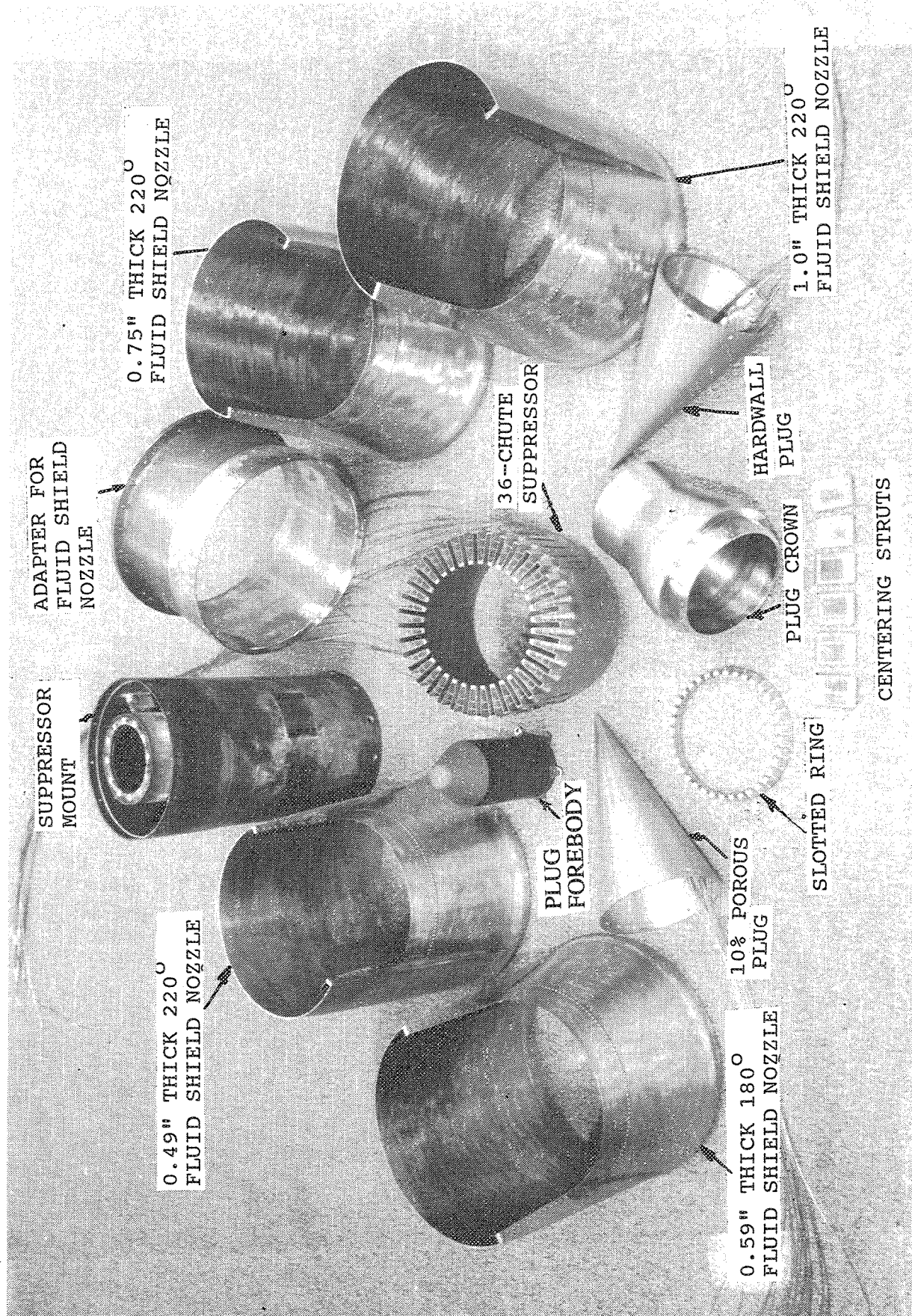


Figure 2.2-4. Various components for fluid shield nozzles for acoustic test.

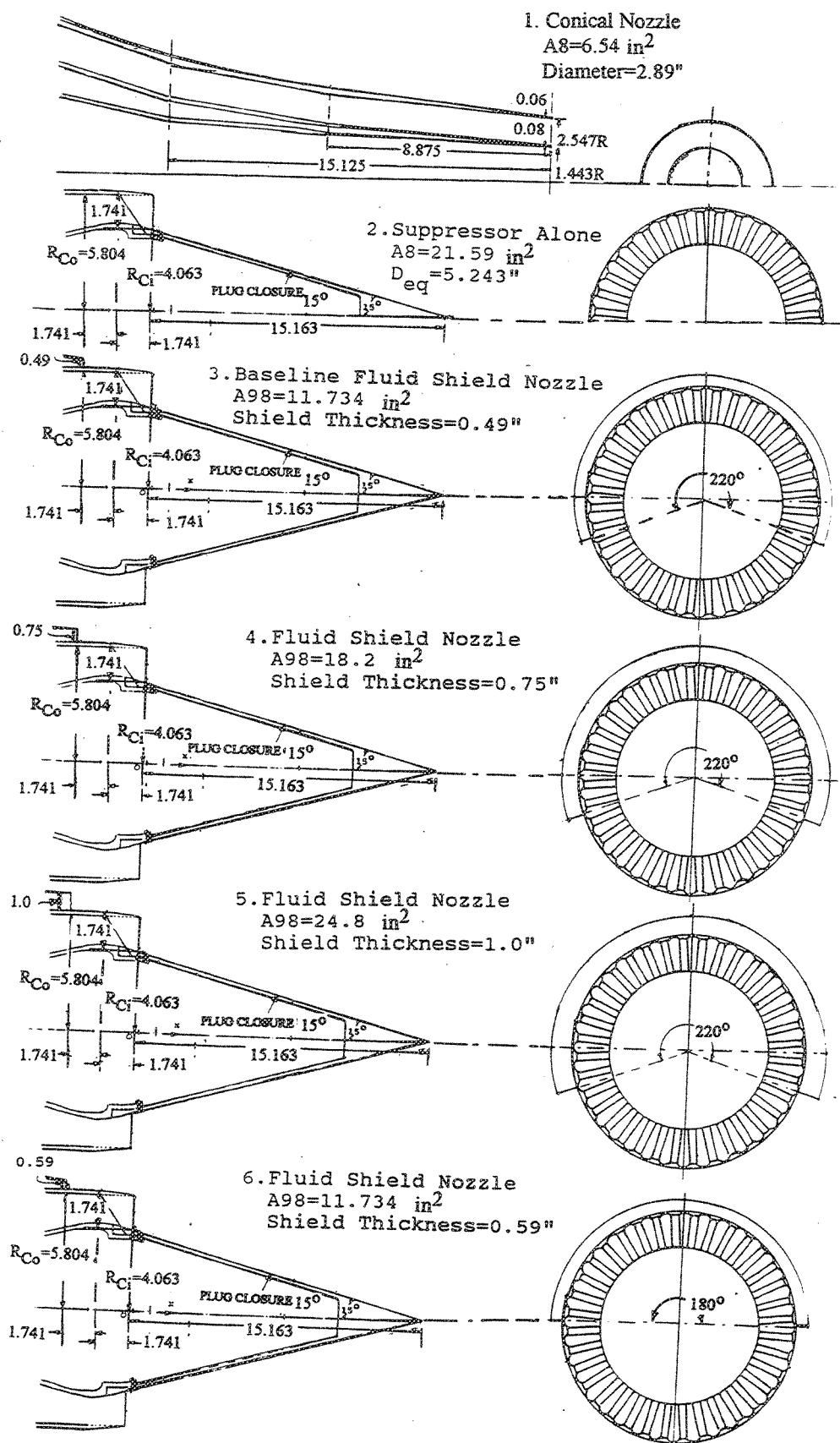


Figure 2.2-5. Model configurations tested in the Anechoic Free Jet Facility  
 (all dimensions are in inches).



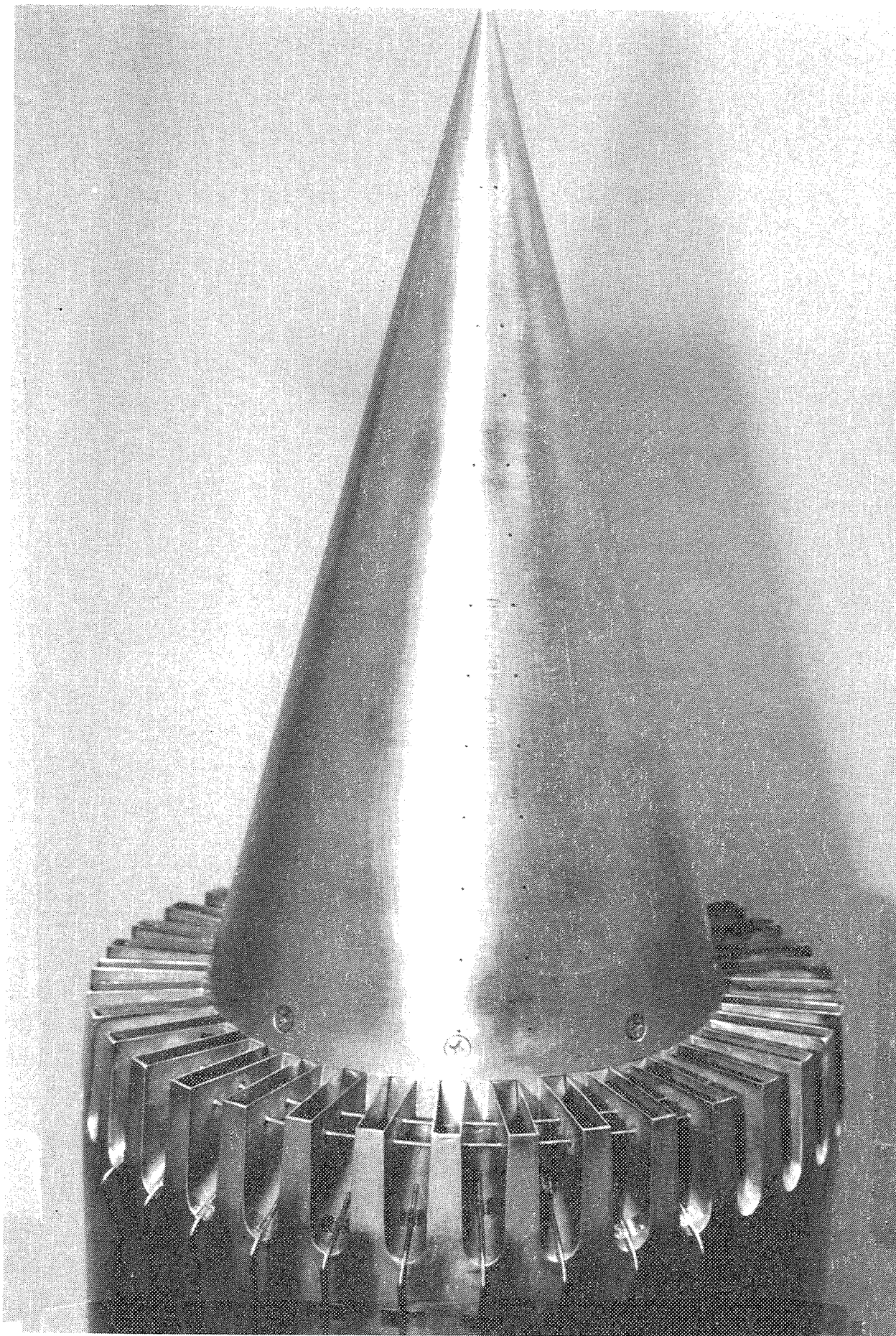
All five configurations, 2 through 6, are tested with the 10% porous plug. The suppressor alone and the baseline fluid shield configurations are tested with the hard walled plug also. Suppressor alone configurations, with hard walled and porous plugs, are shown in Figures 2.2-6 and 2.2-7. A fluid shield nozzle configuration with porous plug is shown in Figure 2.2-8.

### 2.2.2 Instrumentation Layout for Static Pressure Measurement :

Instrumentation layouts for fluid shield nozzles are shown in Figures 2.2-9 and 2.2-10. Static pressure taps are the major part of this layout. Two rows of static pressure taps, 22 in total, marked P1, P2, P3, etc., are mounted on the plug surface distributed axially from the base (i.e.,  $X/L=0$ ,  $X$  being the axial distance from plug root and  $L$  being the plug length) to the plug tip (i.e.,  $X/L=1$ ). The first 12 taps are aligned with the hot core flow path and the remaining 10 taps are aligned with the chute centerline of the suppressor.

Sixteen pressure taps, marked P23 through P38, are placed on the base region of the chute (see Figure 2.2-9). The first eight of the taps are placed on chutes exposed to the region under the fluid shield when the fluid shield nozzle is mounted. The other 8 are mounted on chutes, which remain unshielded for fluid shield nozzle configurations. Each of these eight tap sets covers the chutes radially from inner (i.e.,  $R_{Ci}/R_{Co}=0.7$ ,  $R_{Ci}$  and  $R_{Co}$  being the radial location of the tap and outer radius of the suppressor, respectively) to the outer radii (i.e.,  $R_{Ci}/R_{Co}=1$ ), to measure radial variation of chute base pressure for an assessment of chute base drag. To avoid crowding of and subsequent influence of leads on static pressure measurement (as the taps are surface mounted and routed), only one tap is placed in each chute. The radial location of these taps are on centers of equal projected areas on the exit plane. The radial location of the taps, the tap number, and the corresponding chute number (marked as C1, C2, etc.) are listed in Figure 2.2-9.

Three pressure taps, P39, P40, and P41, are mounted on the suppressor outer surface, upstream of the exit, where the fluid shield nozzle is mounted. These taps indicate the circumferential flow variation for fluid shield nozzles. The angular locations  $\psi$  of these taps are shown in Figure 2.2-9. Four thermocouples are mounted on the chutes to monitor the skin temperature. Two of these thermocouples are mounted on C36 and the other two are mounted on C18 and C19. These are located at different radial locations.



NASA/CR-2005-213213 Figure 2.2-6. 36-chute suppressor model assembly with the hardwalled plug.

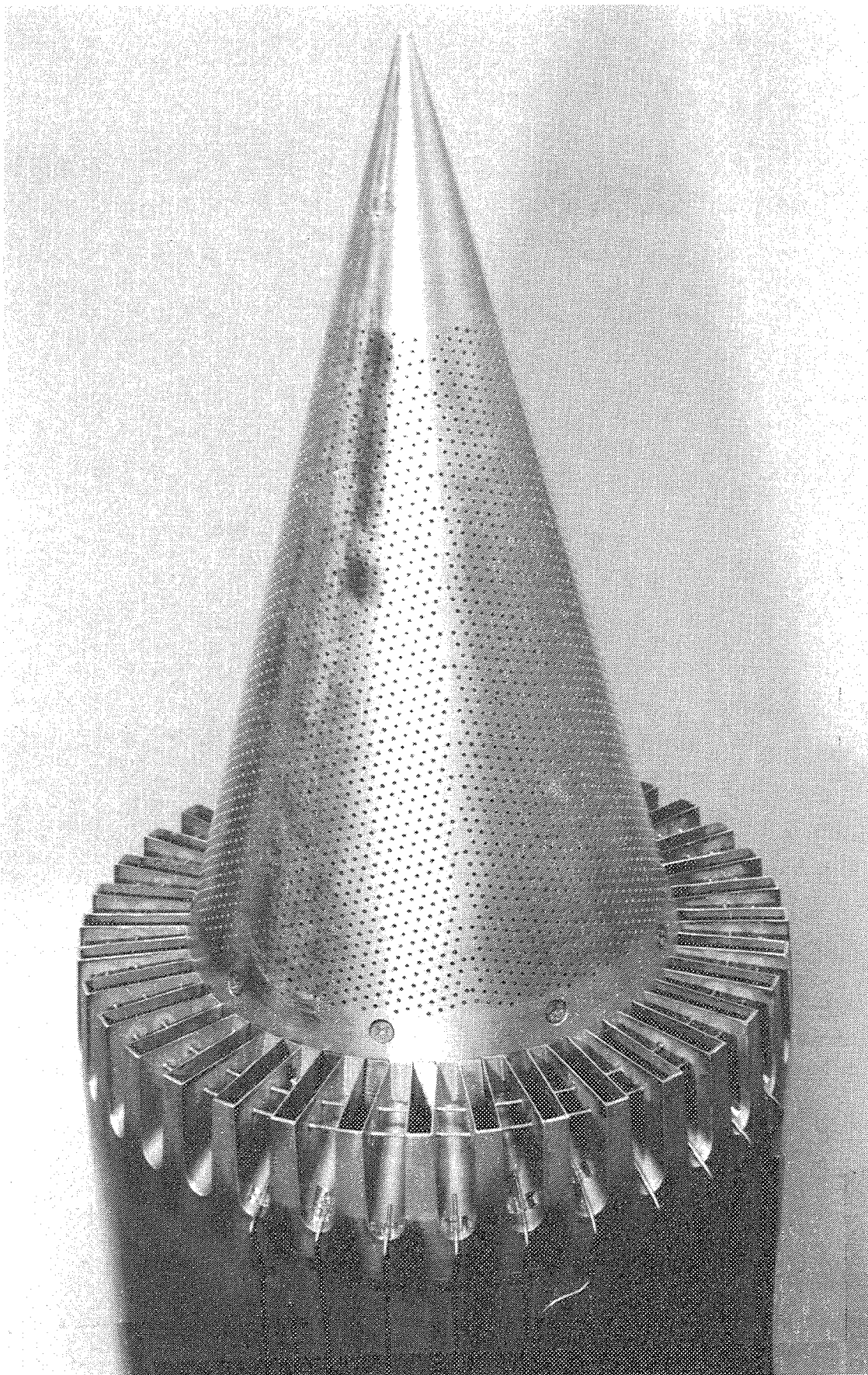


Figure 2.2-7. 36-chute suppressor model assembly with the 10% porous plug.



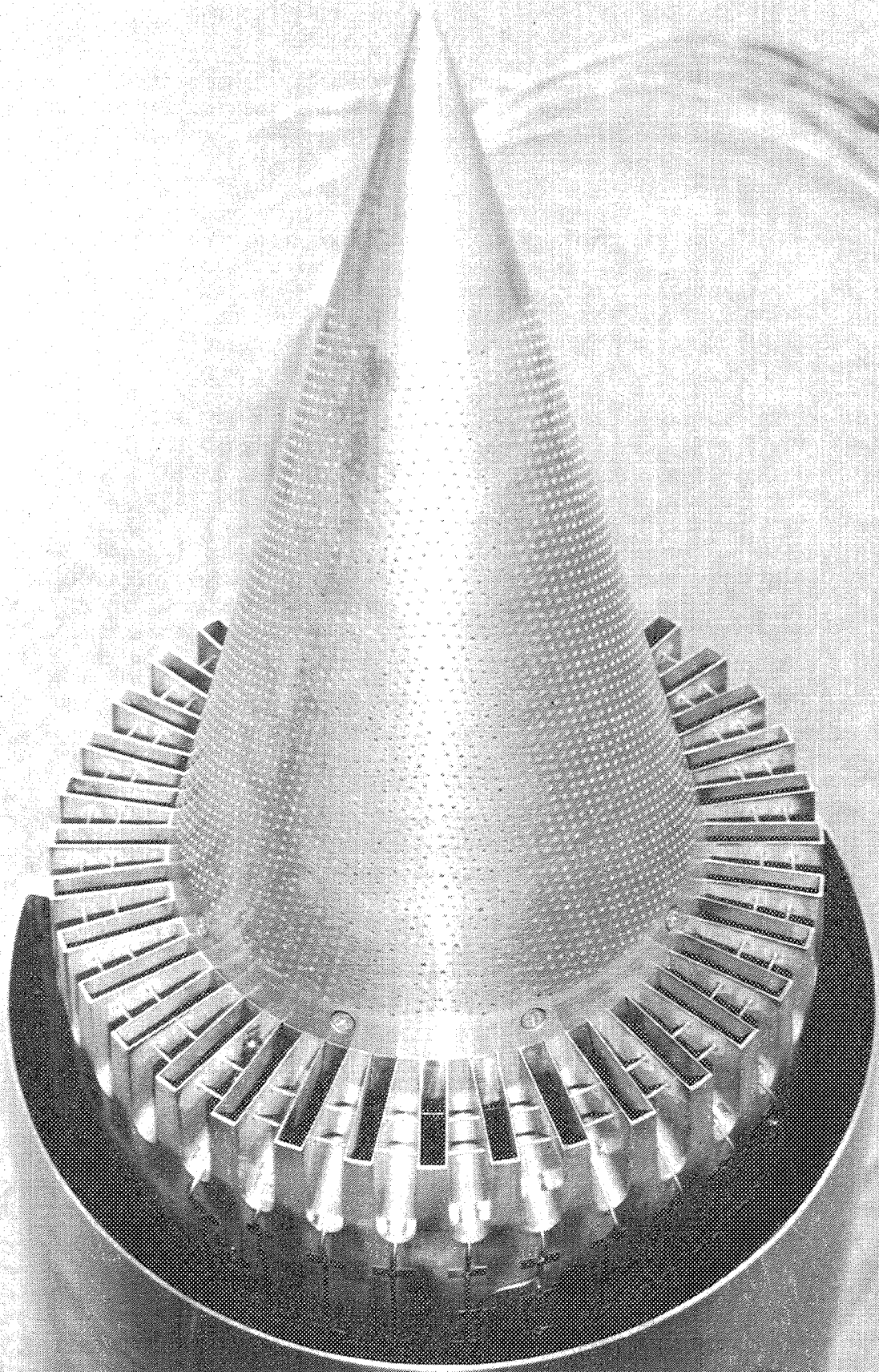


Figure 2.2-8. Fluid shield nozzle assembly with 10% porous plug; fluid shield thickness = 0.5", wrap angle =  $220^{\circ}$ .

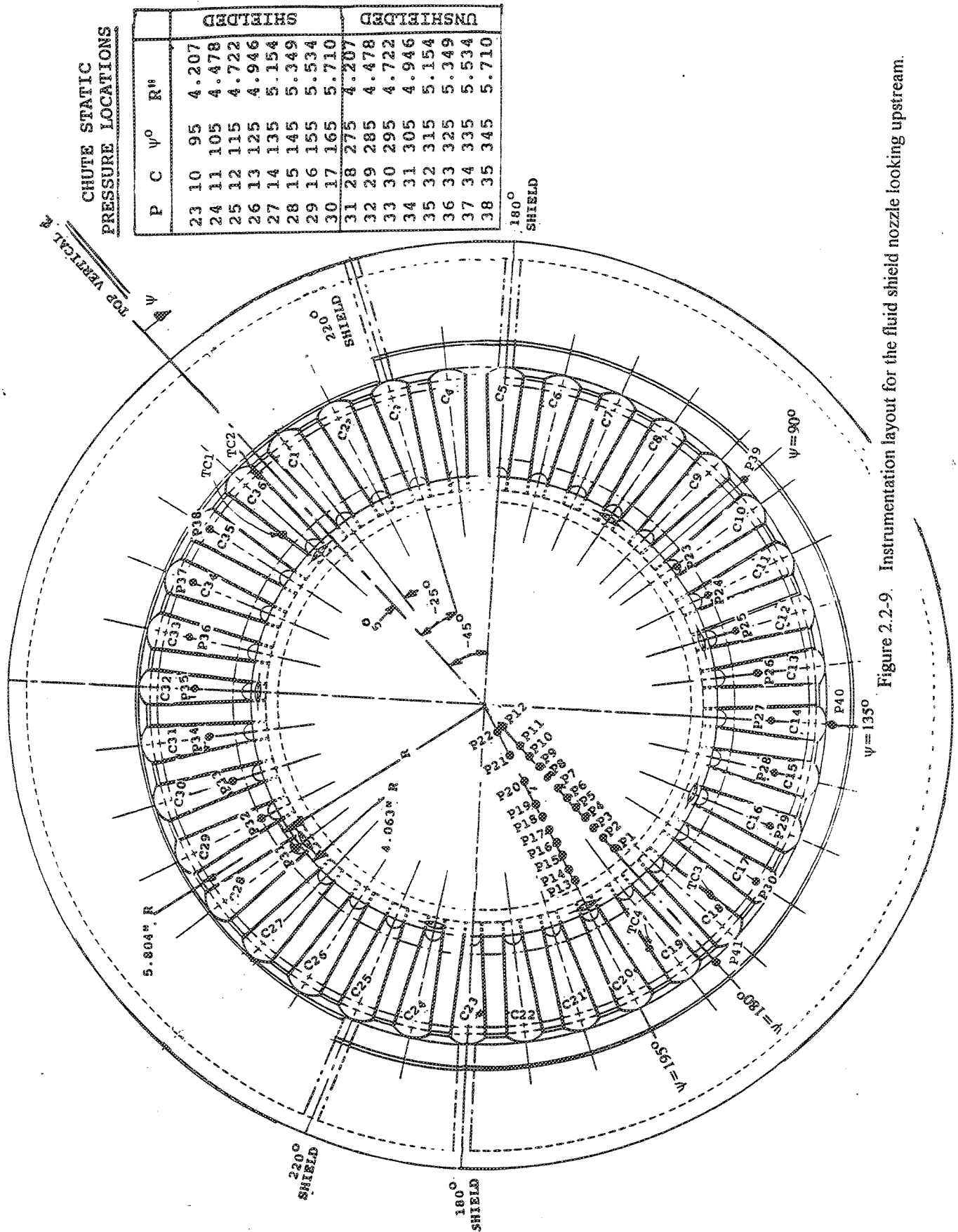


Figure 2.2-9. Instrumentation layout for the fluid shield nozzle looking upstream.

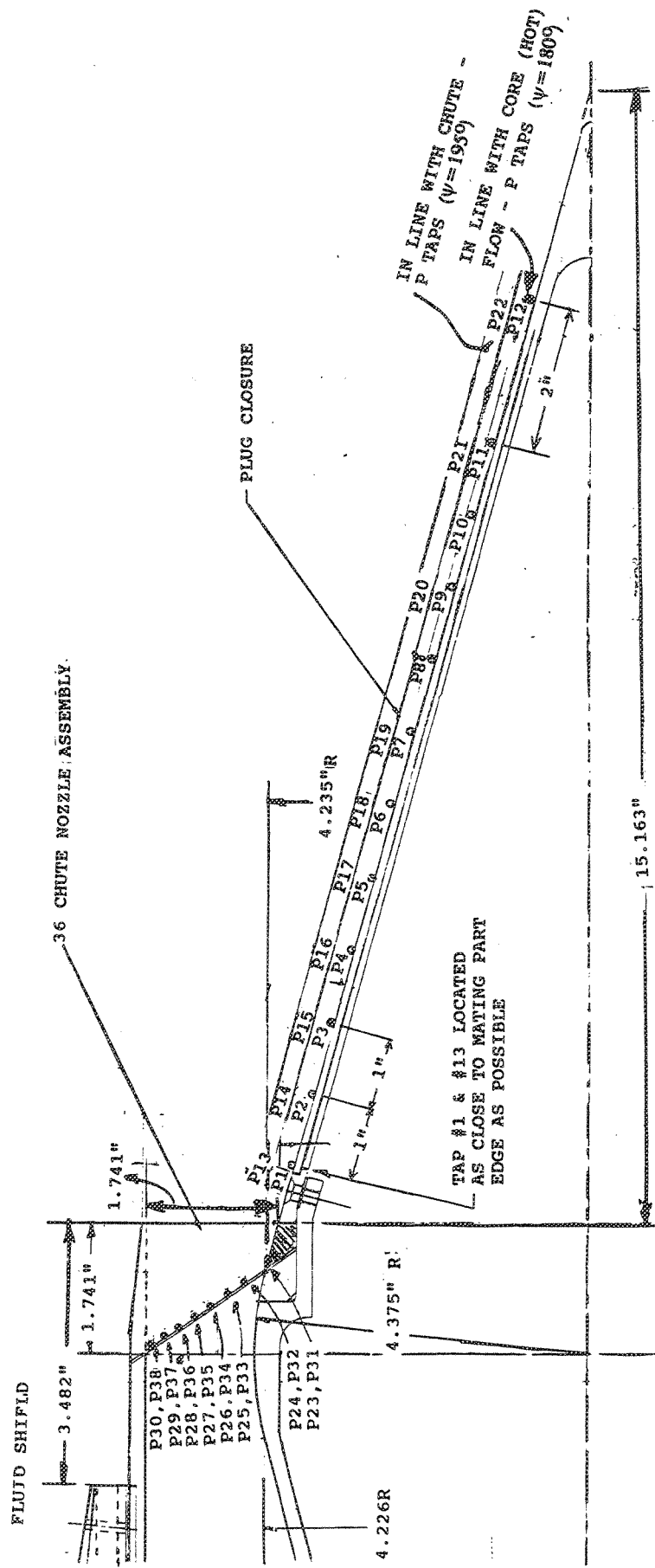


Figure 2.2-10. Side view of the static pressure instrumentation layout for the fluid shield nozzle.

### 2.2.3 Test Procedure

During the acoustic tests the LV and shadowgraph setups are removed from the test chamber to avoid any possible acoustic interference. During a test, the acoustic signal is measured by the microphone arrays, which is analyzed by an on-line system and simultaneously recorded on magnetic tapes for post processing. Surface static pressures are measured and stored simultaneously by an aerodynamic data system. Acoustic data is not acquired during shadowgraph tests. However, the surface static pressures are measured by the aerodynamic data system during these tests.

For the conical nozzle and suppressor nozzle tests, measurements were made by tower microphones, tower at  $\phi = 10^\circ$  and by fixed microphones for all the test conditions. Fixed microphone array is located at  $\phi = 45^\circ$  position. Additional measurements were made by tower microphones at  $\phi = 45^\circ$  and  $\phi = 75^\circ$  for a few test conditions. Orientations of the conical nozzle and the suppressor nozzle in Cell 41 are shown in Figures 2.2-11 and 2.2-12, respectively. The azimuthal locations at  $10^\circ$  and  $75^\circ$  represent the sideline and community locations, respectively. The sideline angle location is based on Boeing's trajectory studies which indicate the altitude of the aircraft is about 689' at which the sideline peaks at the 1476' sideline noise monitor. This translates the angle of  $25^\circ$  relative to horizon, which corresponds to  $\phi = 10^\circ$ . There is no anticipated azimuthal variation of noise field for the axisymmetric conical and suppressor alone nozzles. Measurements at different azimuthal locations for these configurations were made to assess the azimuthal uniformity of acoustic field of these configurations.

A plan view of Cell 41 with a typical fluid shield nozzle configuration is shown in Figure 2.2-13. The nozzle in Cell 41 was oriented such that the side line and community points lie at azimuthal locations of  $\phi = 10^\circ$  and  $\phi = 75^\circ$ , respectively. Measurements were made by tower microphones, with the tower at  $\phi = 10^\circ$  and  $75^\circ$  and by fixed microphones for all the test conditions. Additional measurements were made by tower microphones at  $\phi = 4^\circ$ ,  $25^\circ$ , and  $60^\circ$  for a few test conditions to study the azimuthal directivity.

To obtain a full  $360^\circ$  azimuthal directivity of fluid shield noise the unshielded side of the 0.5" thick  $220^\circ$  fluid shield nozzle was mounted on the suppressor with an offset of  $120^\circ$  compared to its nominal configuration. It should be noted that a complete  $180^\circ$

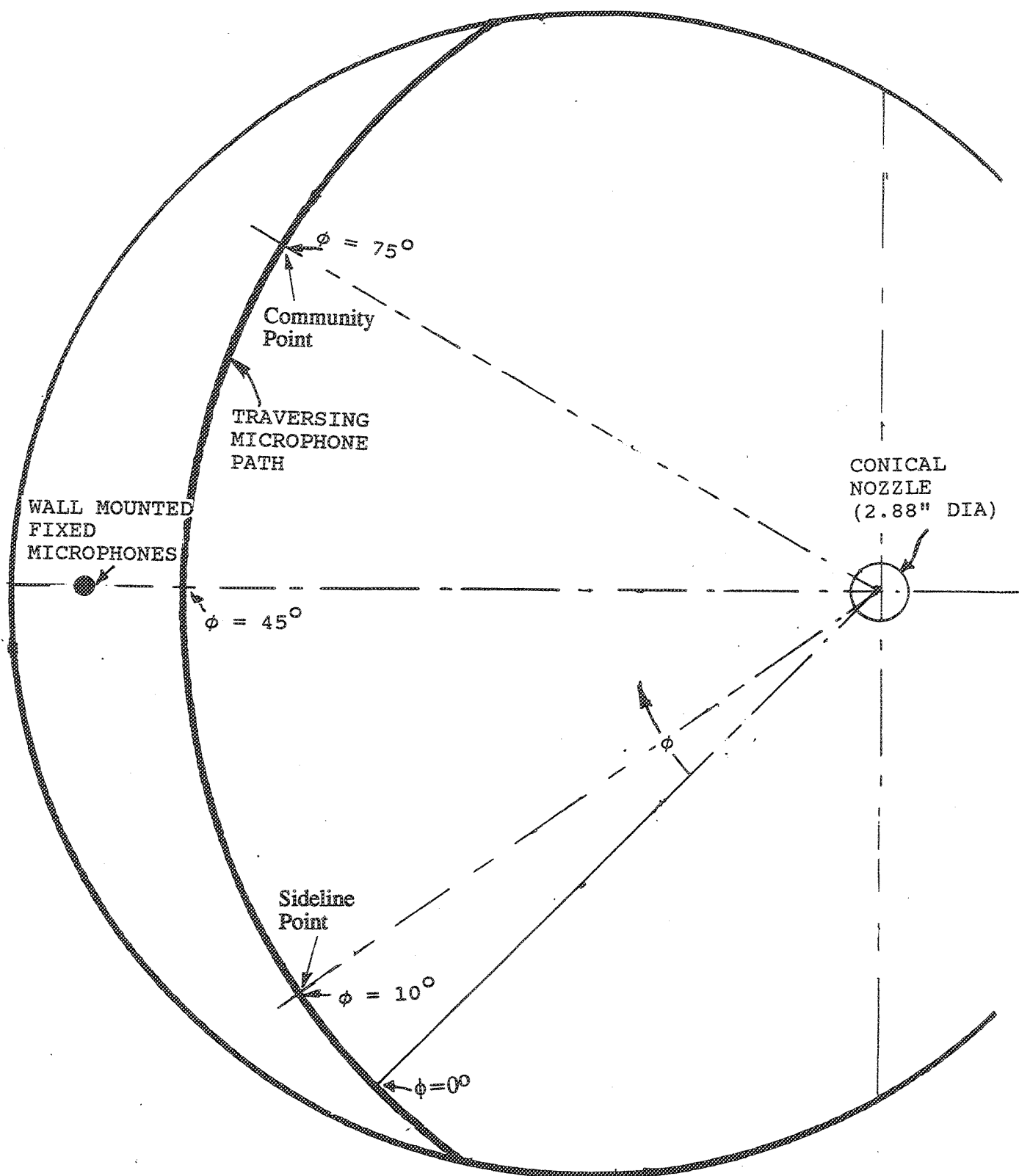


Figure 2.2-11. Plan view of Cell 41 showing the 2.88" diameter conical nozzle and the azimuthal locations ( $\phi$ ) for traversing microphone tower (not to scale).



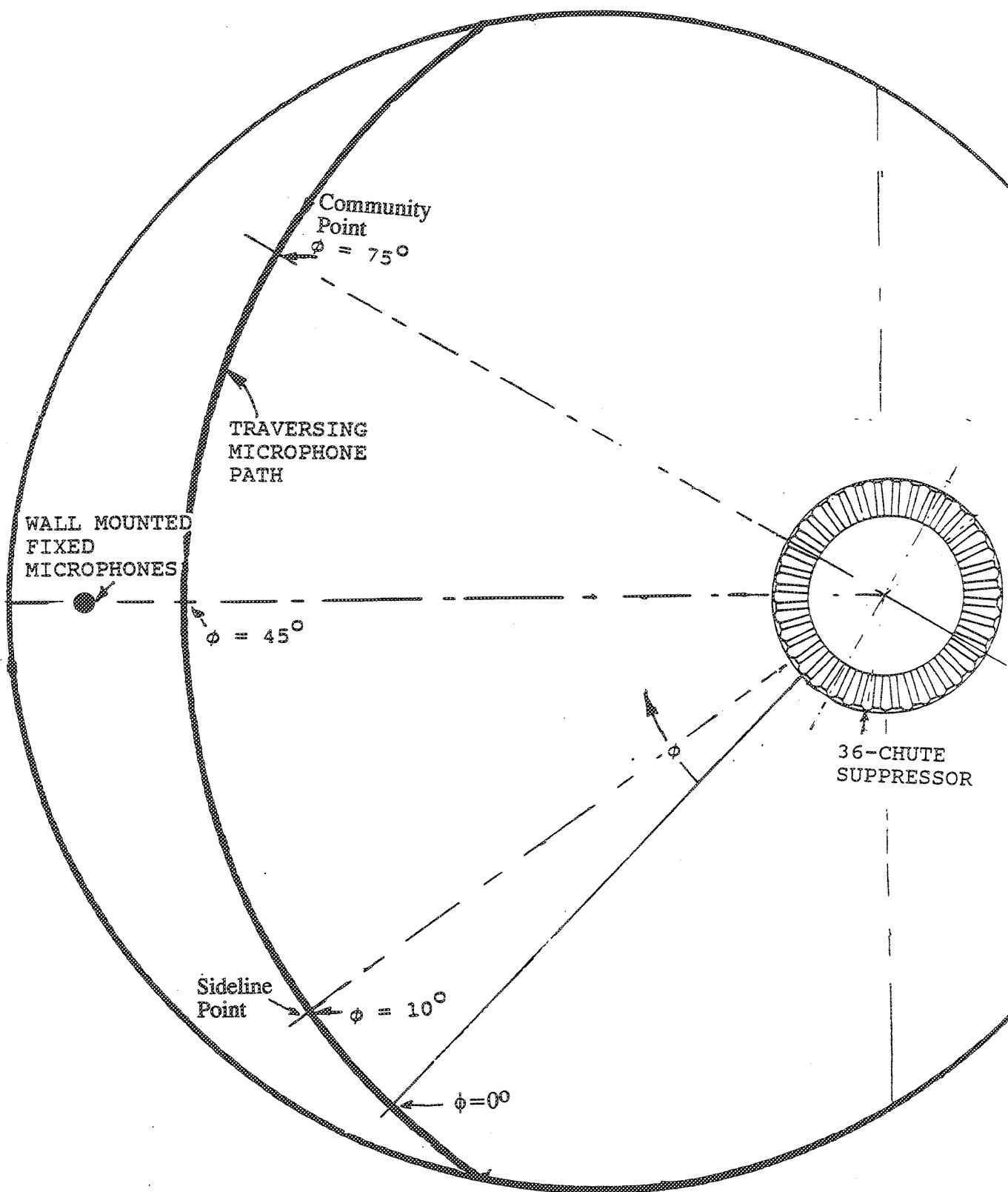


Figure 2.2-12. Plan view of Cell 41 showing the 36-chute suppressor and the azimuthal locations ( $\phi$ ) for traversing microphone tower (not to scale).

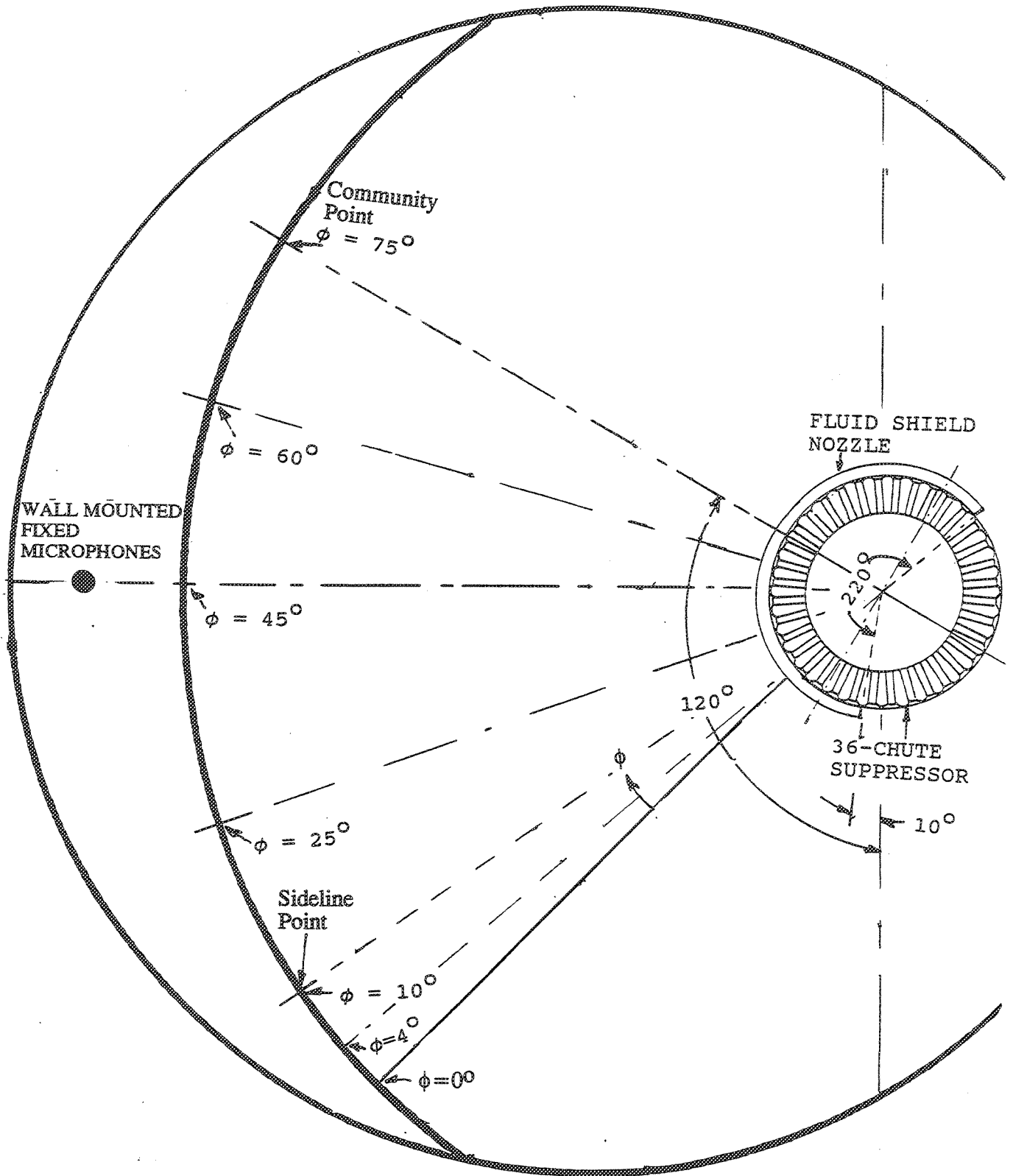


Figure 2.2-13. Fluid shield nozzle orientation in Cell 41 for nominal configuration (not to scale).

orientation change for fluid shield was not possible due to hardware limitations. In this orientation, shown in Figure 2.2-14, the mid point of the unshielded portion of the suppressor was aligned with  $\phi = 15^\circ$  azimuthal plane. The 10% porous plug was used in this study. Measurements were made for a few test conditions by tower microphones only, with the tower at  $\phi = 15^\circ, 30^\circ, 45^\circ, 65^\circ, 85^\circ$ , and  $100^\circ$  for all the test conditions.

**Shadowgraph Tests :** Shadowgraph tests in Cell 41 were conducted for six configurations including suppressor alone and fluid shield nozzle configurations. Photographs of the shadowgraphs were taken up to 4-5 equivalent diameters (based on flow area of suppressor only) downstream from the suppressor exit plane. For suppressor alone configuration shadowgraphs were acquired at three axial locations covering one half of the plume (due to symmetry) as defined in Figure 2.2-15. For fluid shield nozzles the shadowgraphs were acquired at six axial locations covering shielded and unshielded sides at the plane of symmetry, as defined in Figure 2.2-16. Coordinates for these photographs are listed in the figures. While the shadowgraph photographs were taken at specific locations at steady aero thermodynamic conditions, video pictures of the shadowgraph were made in real time, even during the adjustment process of aero thermodynamic conditions. Tests were conducted for a selected number of test conditions with flight simulation.

#### 2.2.4 Scope of Testing

The fluid shield scale model design and the selection of test conditions are based on the GEAE's M=2.4 Flade Cycle B1 and the preliminary design concept of the fluid shield nozzles. This cycle employs a nominal split of 650/400 pps in the core and flade stream at takeoff. The aero thermodynamic cycle conditions and select full scale Flade cycle parameters at the takeoff flight Mach number of  $M_F = 0.32$  are shown in Figures 2.2-17 and 2.2-18. While the secondary stream (fluid shield) total temperature and nozzle pressure ratio remain more or less constant throughout the throttle variation, they vary considerably for the core stream. The core area at the exit plane (A8) is maintained constant throughout the throttle variation reflecting the geometric constraint imposed by the deployed core stream suppressor. Whereas, the fluid shield exit plane area (A98) is changed throughout the throttle variation. This is an important difference between the scale model nozzle and the full scale preliminary design, in that the fluid shield area at the exit plane remains constant for the models.

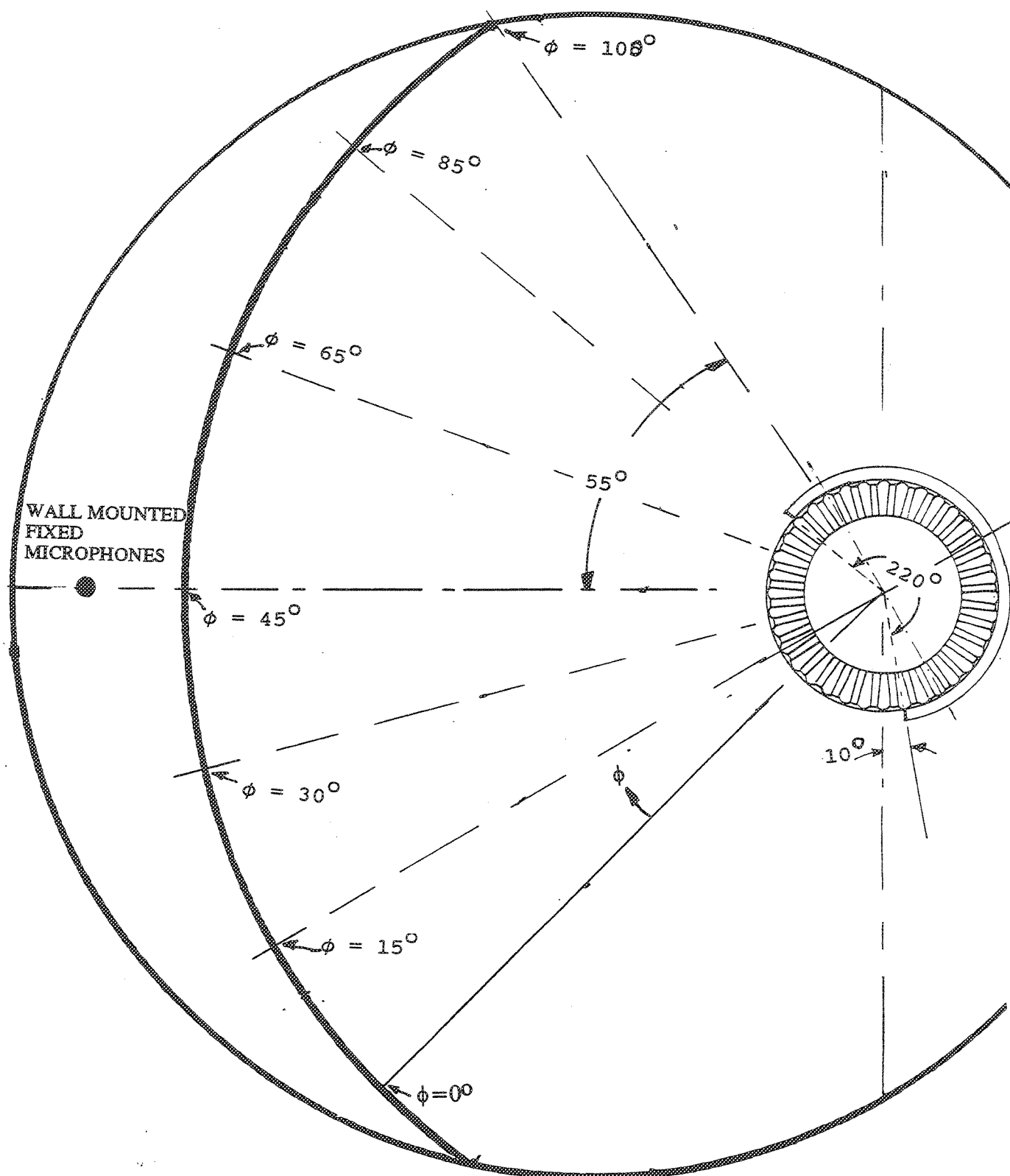


Figure 2.2-14. Fluid shield nozzle orientation in Cell 41 for azimuthal directivity study. 220° wrap, 0.5" thick (not to scale).



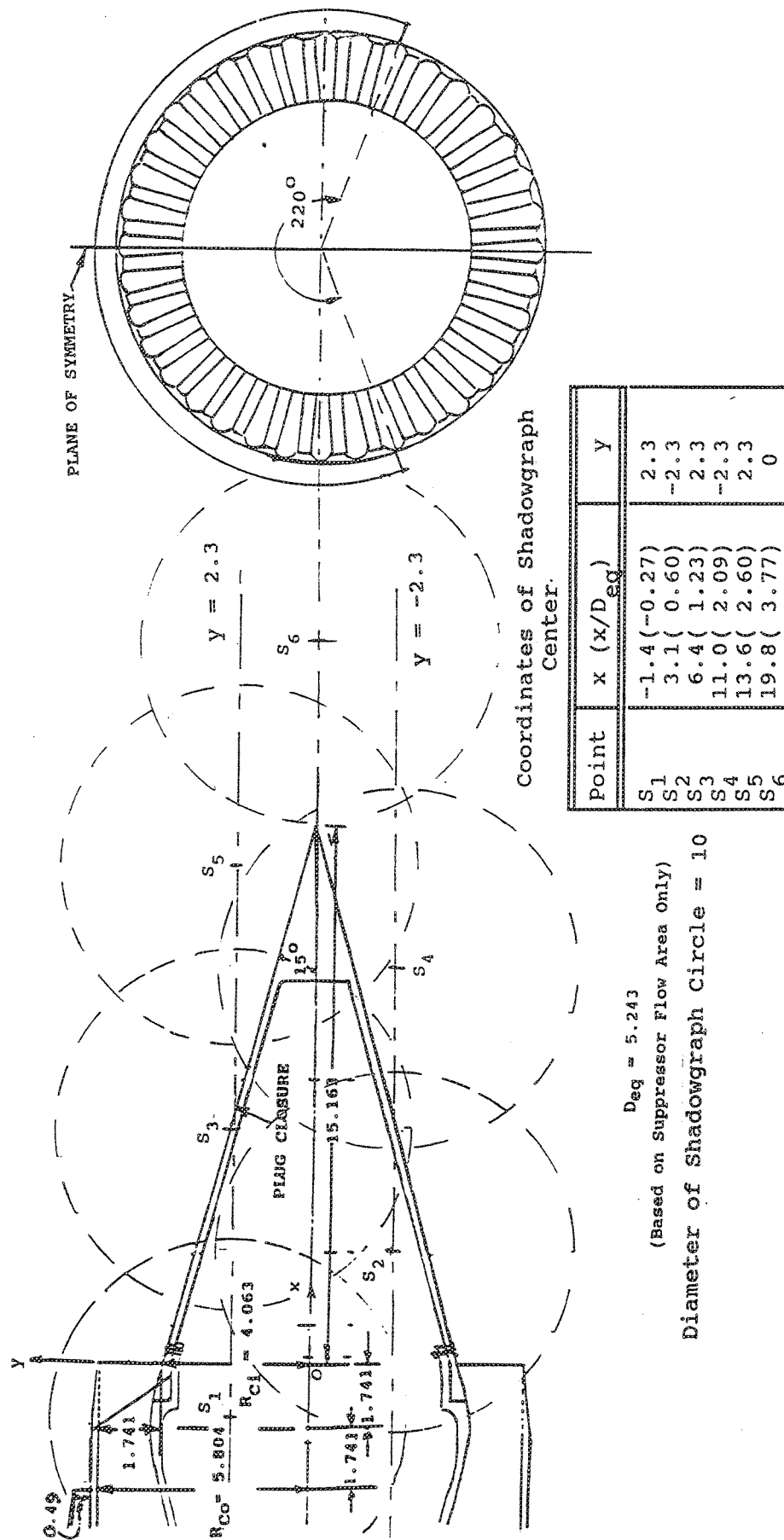


Figure 2.2-16. Shadowgraph measurement locations on the plane of symmetry for the fluid shield nozzle configuration (all dimensions are in inches).

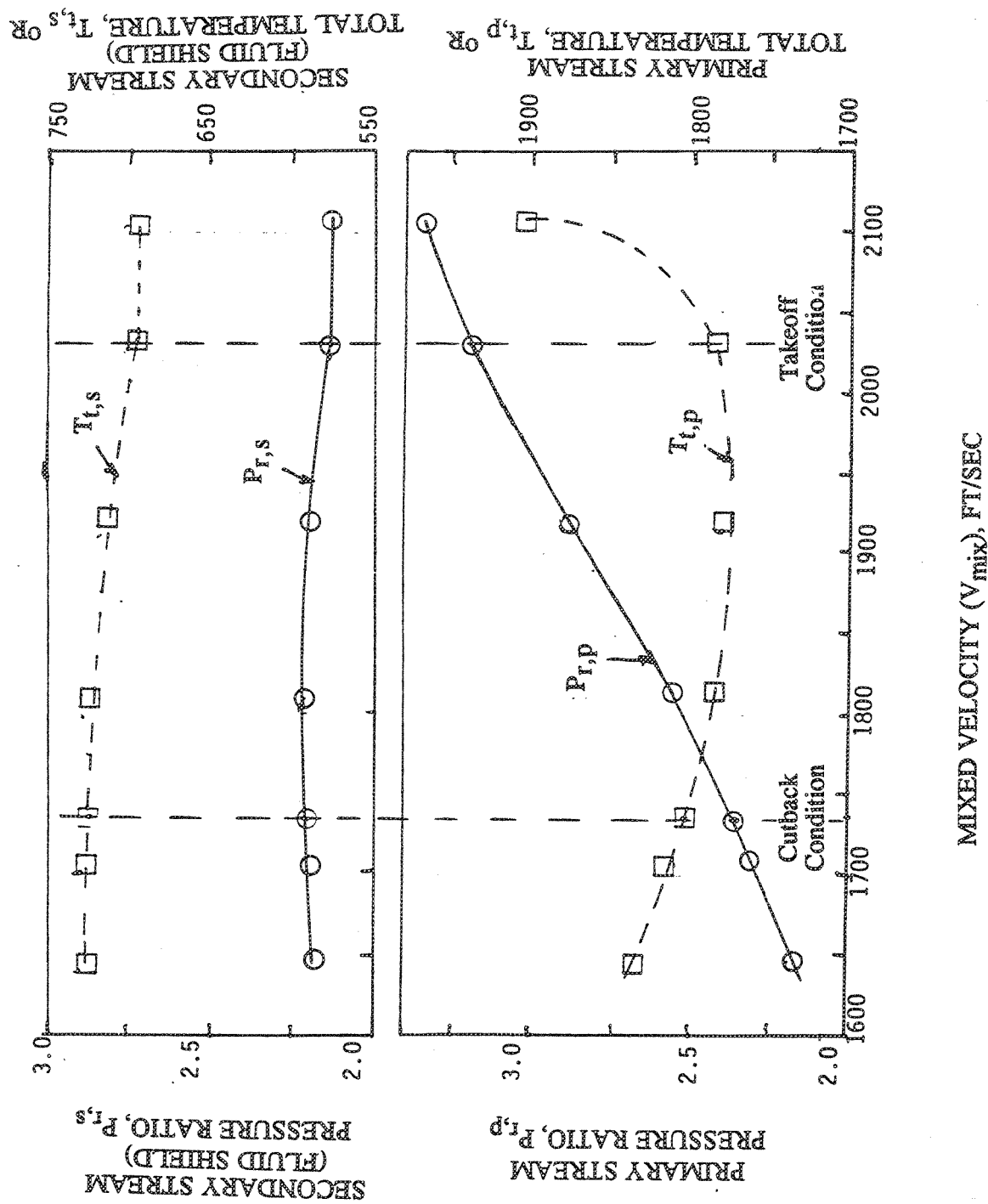


Figure 2.2-17. M2.4 Fiade cycle conditions with respect to  $V_{mix}$ ,  $M_F = 0.32$  (GE21/FLA - Study B1).

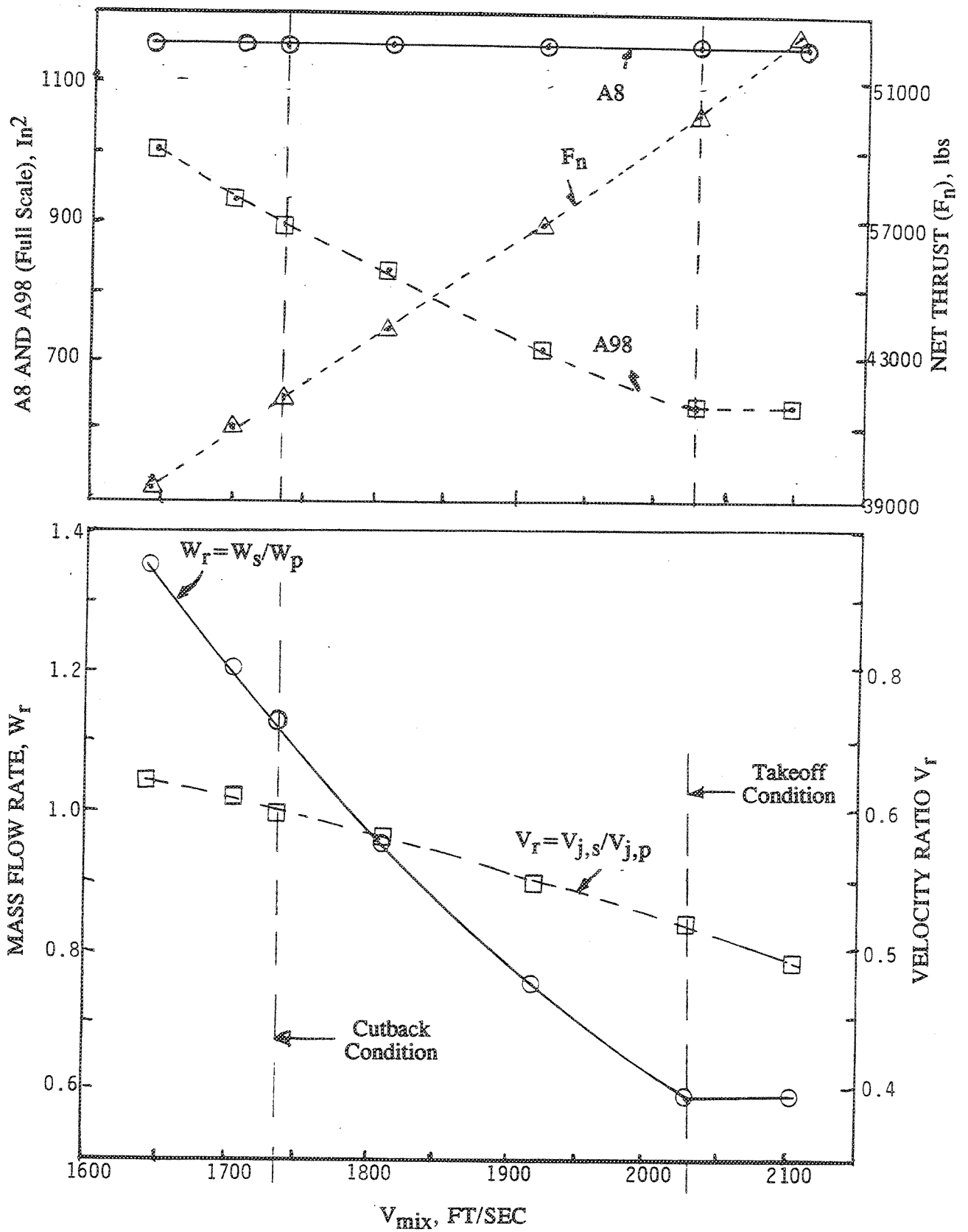


Figure 2.2-18. Full scale cycle parameters with respect to  $V_{mix}$ ,  $M_F = 0.32$  (GE21/FLA - Study B1).



**Test Conditions for Fluid Shield Nozzles :** To assess the effect of A98 (i.e., secondary stream or fluid shield stream throat area) variation the three fluid shield nozzles with different A98 were tested, such that, the baseline shield ( $A98=11.734 \text{ in}^2$ ) matches with full scale Flade cycle at higher power codes close to takeoff condition, whereas, the shield with a higher A98 (i.e.,  $A98=18.2 \text{ in}^2$ ) matches with the full scale Flade cycle at lower power codes close to cutback conditions. The third shield with much higher A98 (i.e.,  $A98=24.8 \text{ in}^2$ ) was built to explore the effect of shield for a much larger weight flow ratio.

The test conditions for each of the three fluid shield nozzles of different throat areas (i.e., A98 of  $11.734 \text{ in}^2$ ,  $18.2 \text{ in}^2$  and  $24.8 \text{ in}^2$ ) include the aero-thermodynamic conditions (i.e.,  $P_{r,p}$ ,  $T_{t,p}$ ,  $P_{r,s}$ , and  $T_{t,s}$ ), defined below, to coincide with those of the Flade Cycle (i.e., GE21/FLA - Study B1) and additional aero-thermodynamic conditions for parametric study.

$P_{r,p}$  = Primary or core stream nozzle pressure ratio

$T_{t,p}$  = Primary or core stream nozzle total temperature in degree R

$P_{r,s}$  = Secondary or fluid shield stream nozzle pressure ratio

$T_{t,s}$  = Secondary or fluid shield stream nozzle total temperature in degree R

The Flade Cycle aero-thermodynamic variables are identical for all three nozzles, but the fluid shield jet velocities and the mixed velocities are different due to the different shield areas. These variables are plotted in Figure 2.2-19.

Parametric study of aero-thermodynamic variables ( $P_{r,p}$ ,  $T_{t,p}$ ,  $P_{r,s}$ , and  $T_{t,s}$ ) were carried out in two ways. First, these variables for both the streams were varied keeping  $V_{\text{mix}}$  fixed at 2030 ft/sec and 1811 ft/sec, which are the design takeoff and cutback cycle velocities, respectively. This allows the parametric variation of weight flow ratios and velocity ratios at fixed mixed velocities. Several sets of aero-thermodynamic conditions were selected to generate these fixed  $V_{\text{mix}}$  values for all the three fluid shield areas. These conditions are plotted in Figure 2.2-20. Second, limited number of tests were conducted for all three fluid shield nozzles, in which, one of the four aero-thermodynamic parameters, namely,  $T_{t,p}$ ,  $P_{r,p}$ ,  $T_{t,s}$ , and  $P_{r,s}$ , was varied keeping the other three parameters fixed. Figure 2.2-20 indicates very little variation of  $P_{r,p}$  with respect to  $P_{r,s}$  for fixed  $V_{\text{mix}}$ . Hence, these test points are used to study the

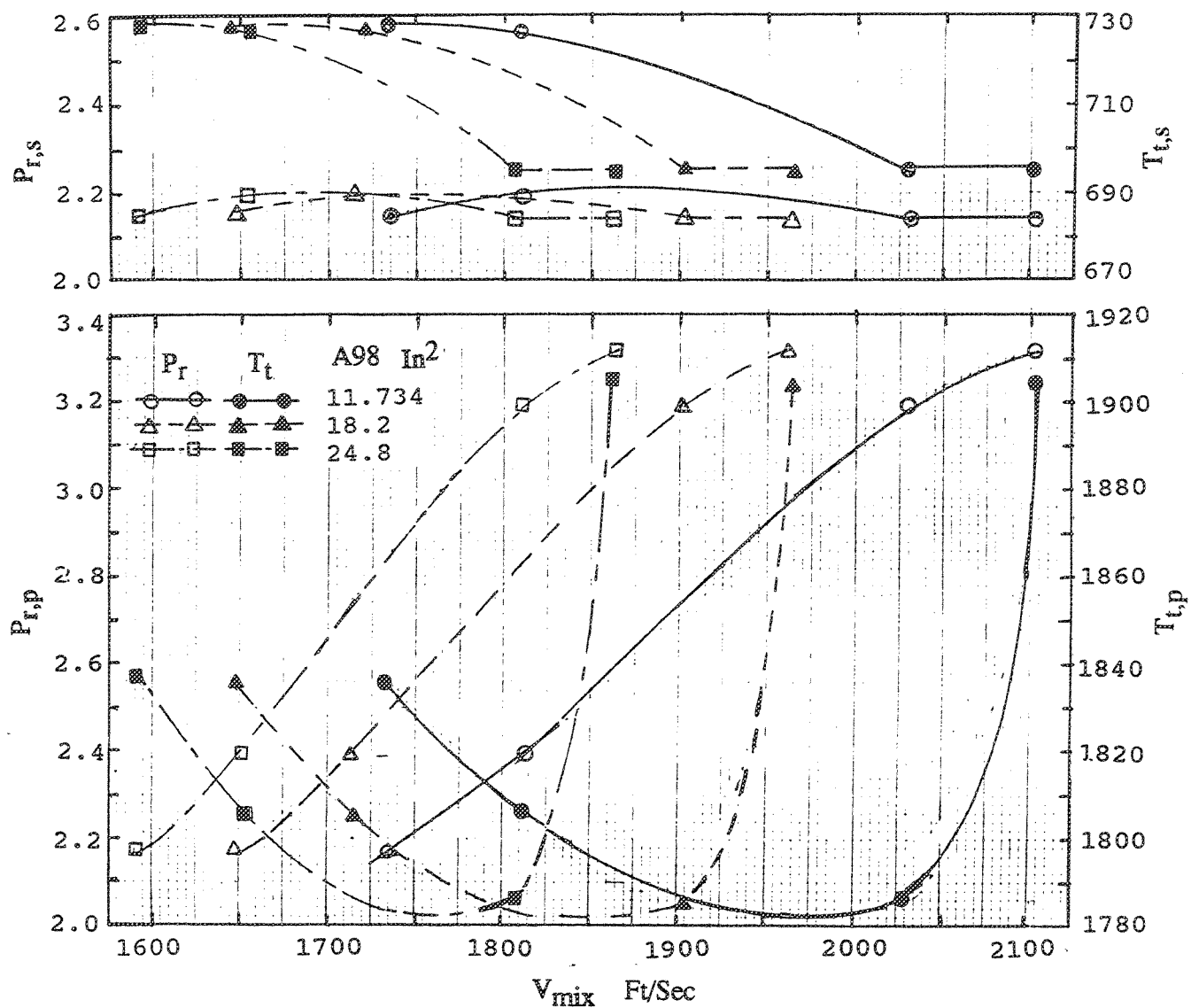


Figure 2.2-19. Aerothermodynamic test conditions for fluid shield nozzles of different throat areas (A98),  $A_8=21.59 \text{ in}^2$ .

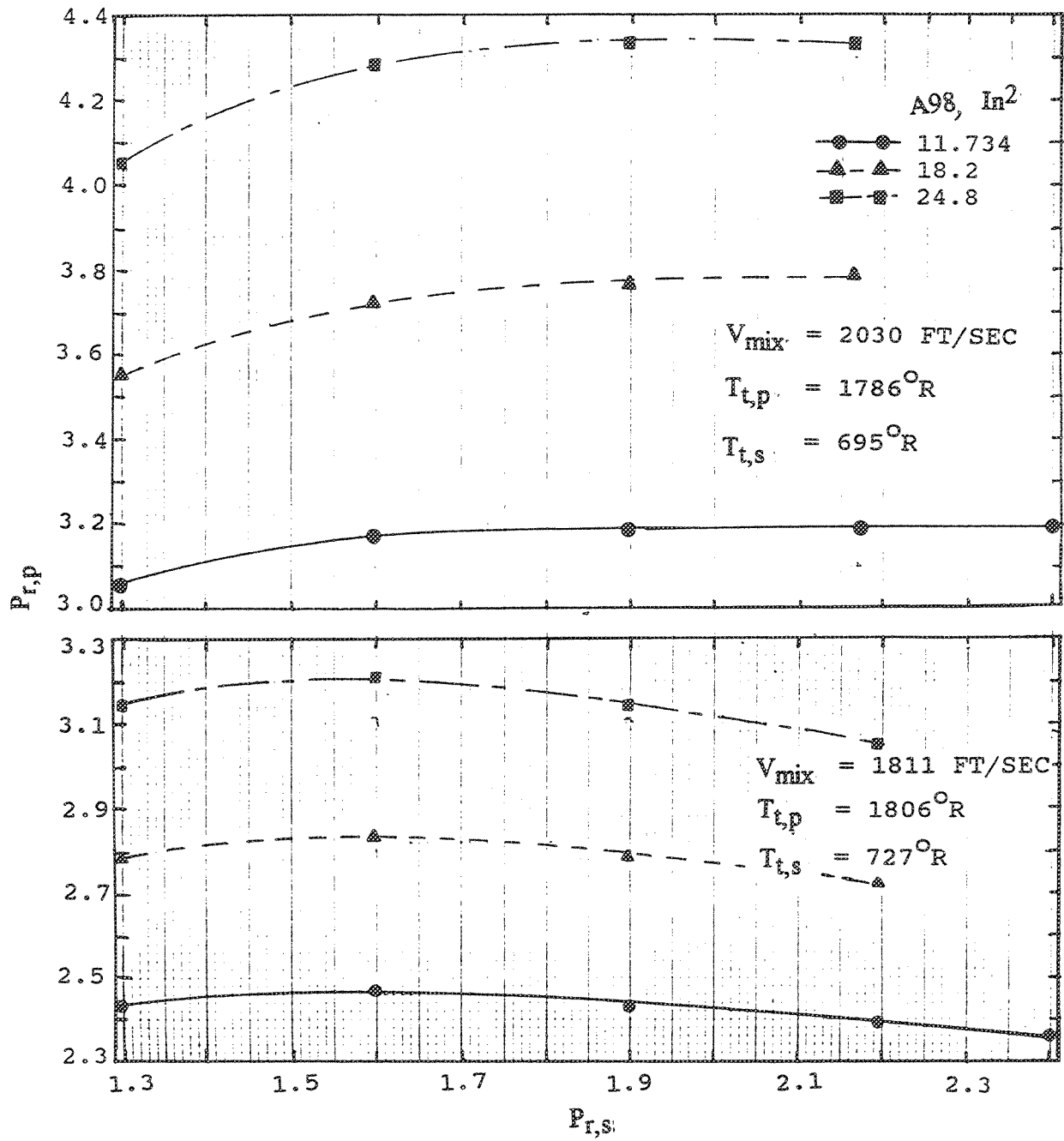


Figure 2.2-20. Aerothermodynamic test conditions to generate fixed  $V_{mix}$  values for fluid shield nozzles of different throat areas ( $A_{98}$ ),  $A_8=21.59 \text{ in}^2$ .

parametric variation of  $P_{r,s}$ . The test conditions for variations in  $T_{t,p}$ ,  $P_{r,p}$ , and  $T_{t,s}$  are illustrated in Figure 2.2-21.

**Test Conditions for the Conical Nozzle and the Suppressor Alone Operation :** The test conditions for the suppressor alone were selected to cover the primary jet velocity range of the throttle line for the Flade cycle. In order to compare the suppressor alone characteristics with those with the fluid shield configurations it is preferable to select the aero thermodynamic conditions, which would yield the jet velocities ( $V_{j,p}$ ) same as the  $V_{mix}$  values corresponding to the three fluid shield areas at cutback and takeoff condition. This would permit acoustic comparison of nozzles with and without shield at the same specific thrust during FAR-36 Stage 3 noise assessment. Engine companies tend to compare dual flow nozzles on a specific thrust basis, since aircraft thrust requirements change during conceptual and preliminary design studies significantly. Noise characteristics established on a specific thrust basis, could be easily modified for required thrust levels once they are better established. An alternate way is to compare the configurations with and without the fluid shield at the same core jet velocities and making adjustments for thrust differences.

The resulting mixed conditions (mass averaged) were selected for the conical nozzle and the suppressor alone operation. The conditions corresponding to the takeoff and cutback for the core by itself were also included. In addition, the takeoff cycle condition corresponding to a high specific thrust cycle such as VCE was also included, for the sake of comparison with the 2D-CD suppressor-ejector being tested under Contract NAS3-25415. The test conditions for conical nozzle and suppressor alone are plotted in Figure 2.2-22. A few additional test points with subsonic flow conditions and with ambient temperature conditions were added to the conditions described above. For the conical nozzle and the suppressor alone configurations the aero thermodynamic conditions,  $P_{r,p}$ ,  $T_{t,p}$ , and  $V_{mix}$ , are also represented by  $P_R$ ,  $T_T$ , and  $V_J$ , respectively.

Limited number of shadowgraph tests were conducted for six configurations, namely, the suppressor alone and the 0.5"-thick base line fluid shield nozzle configurations with hardwalled and porous plugs, and 0.75"-thick and 1.0"-thick fluid shield nozzle configurations with porous plug only.

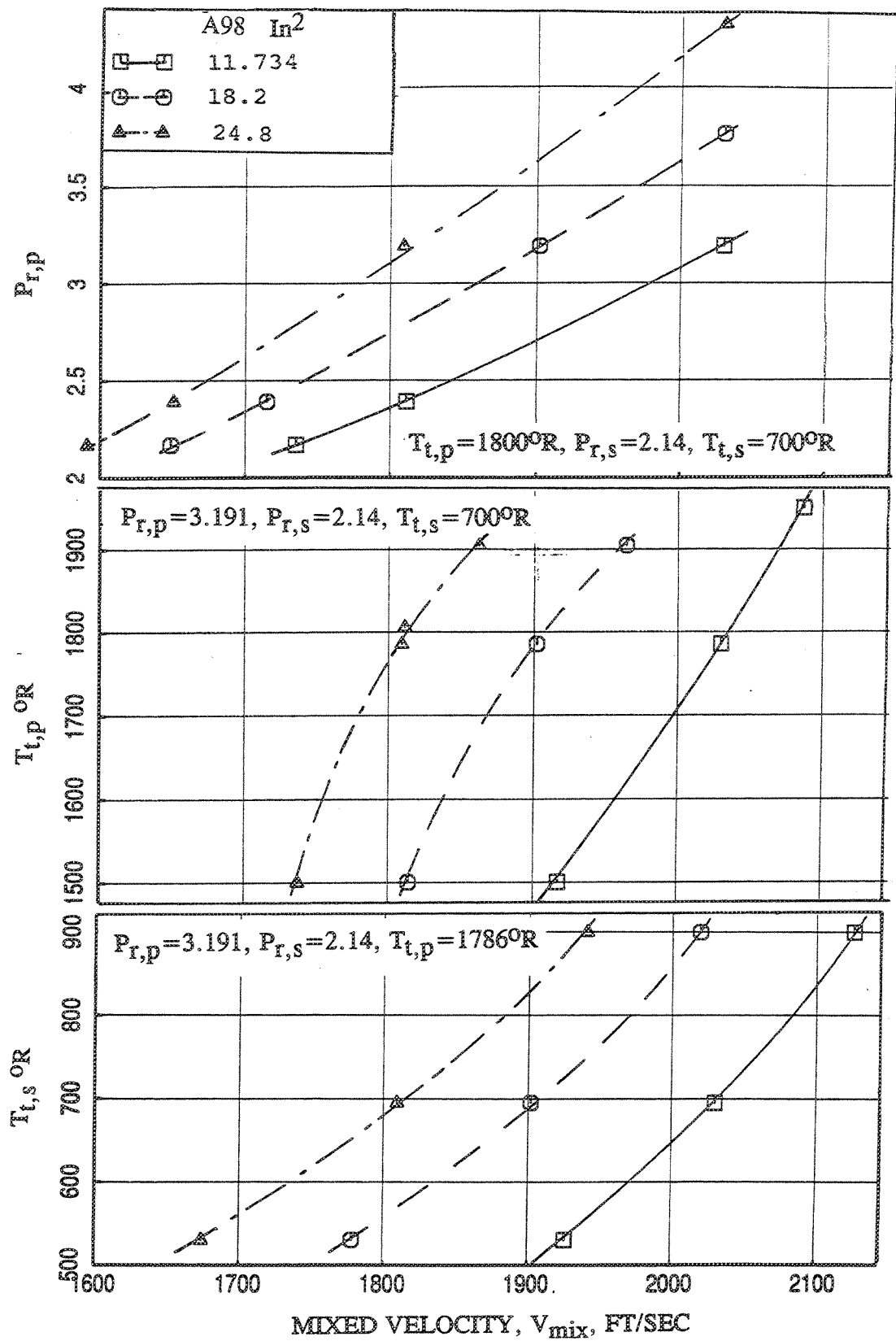


Figure 2.2-21. Parametric variation of aero thermodynamic test conditions for fluid shield nozzles of different throat areas ( $A_{98}$ ),  $A_8 = 21.59$  in<sup>2</sup>.

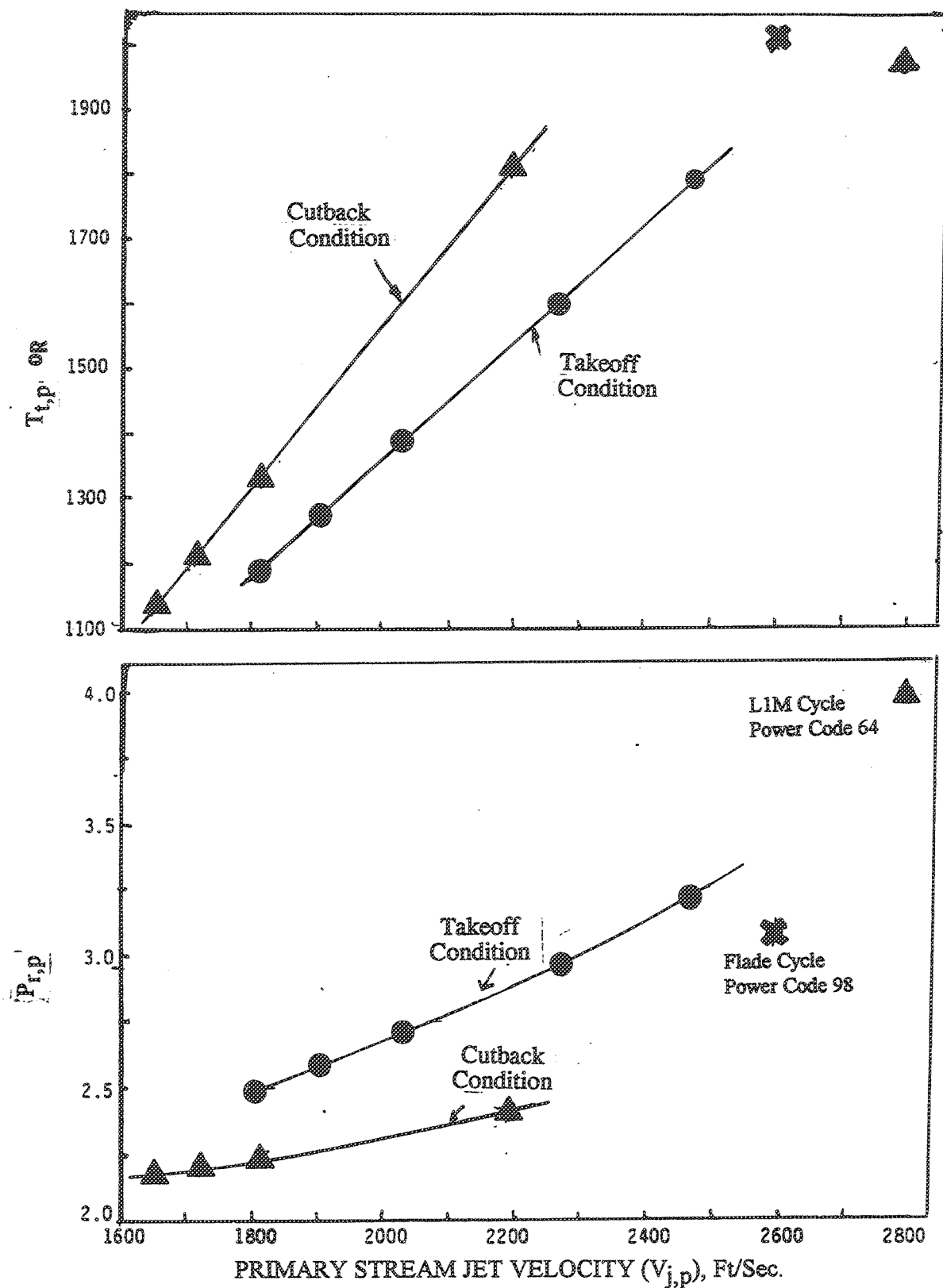


Figure 2.2-22. Variation of total temperature ( $T_{t,p}$ ) and nozzle pressure ratio ( $P_{r,p}$ ) with respect to jet velocity for suppressor alone configurations and conical nozzle.

### 2.3 SHADOWGRAPH RESULTS

Shadowgraph tests in Cell 41 were conducted for the suppressor alone and for three fluid shield nozzles with 220° wrap for a selected number of test conditions. Photographs of the shadowgraphs were taken up to 4-5 equivalent diameters (based on flow area of suppressor only) downstream from the suppressor exit plane. For suppressor alone configuration shadowgraphs were acquired at three axial locations covering one half of the plume (due to symmetry) as defined in Figure 2.2-15. For fluid shield nozzles the shadowgraphs were acquired at six axial locations covering shielded and unshielded sides at the plane of symmetry, as defined in Figure 2.2-16.

The shadowgraph photographs are analyzed to determine the effect of plug porosity, fluid-shield, flight simulation, and aero thermodynamic conditions on the plume shock structures. Shadowgraphs capture variations in the density gradients in the flow through which the light beam passes (Ref. 3). Such density gradients and their variations are caused mainly due to shock surfaces and expansion waves. Shock-surfaces appear as black lines followed by white lines, whereas, expansion waves, although smeared, appear as white-and-then grayish. However, flow gradients caused by vortex sheets or slip surfaces and shear layers will also be captured.

We will first discuss the observed shadowgraph features for a typical shielded-flow nozzle configuration, then postulate the possible mechanisms which produce these typical observed features and, finally, summarize the parametric effects on these observed structures.

A typical shadowgraph picture for a fluid shield nozzle configuration with 1"-thick shield and with porous plug is shown in Figure 2.3-1. In this case the nozzle pressure ratios for both the streams, primary and secondary, are supersonic, so that the flowfield in the nozzle plumes would contain shocks. As observed in this figure the plume shock structures on the unshielded side are distinctly different from those on the shielded side. On the unshielded side the plume shows vertical and horizontal bright lines, whereas, in the shielded plume, which begins at the shield exit plane, triangular lines are seen on the nozzle surface upstream of the suppressor exit. Close to the suppressor exit plane complex structures are seen compared to rectangular structures of unshielded side. Following this the structures become somewhat rectangular in shape further downstream of the suppressor exit plane.

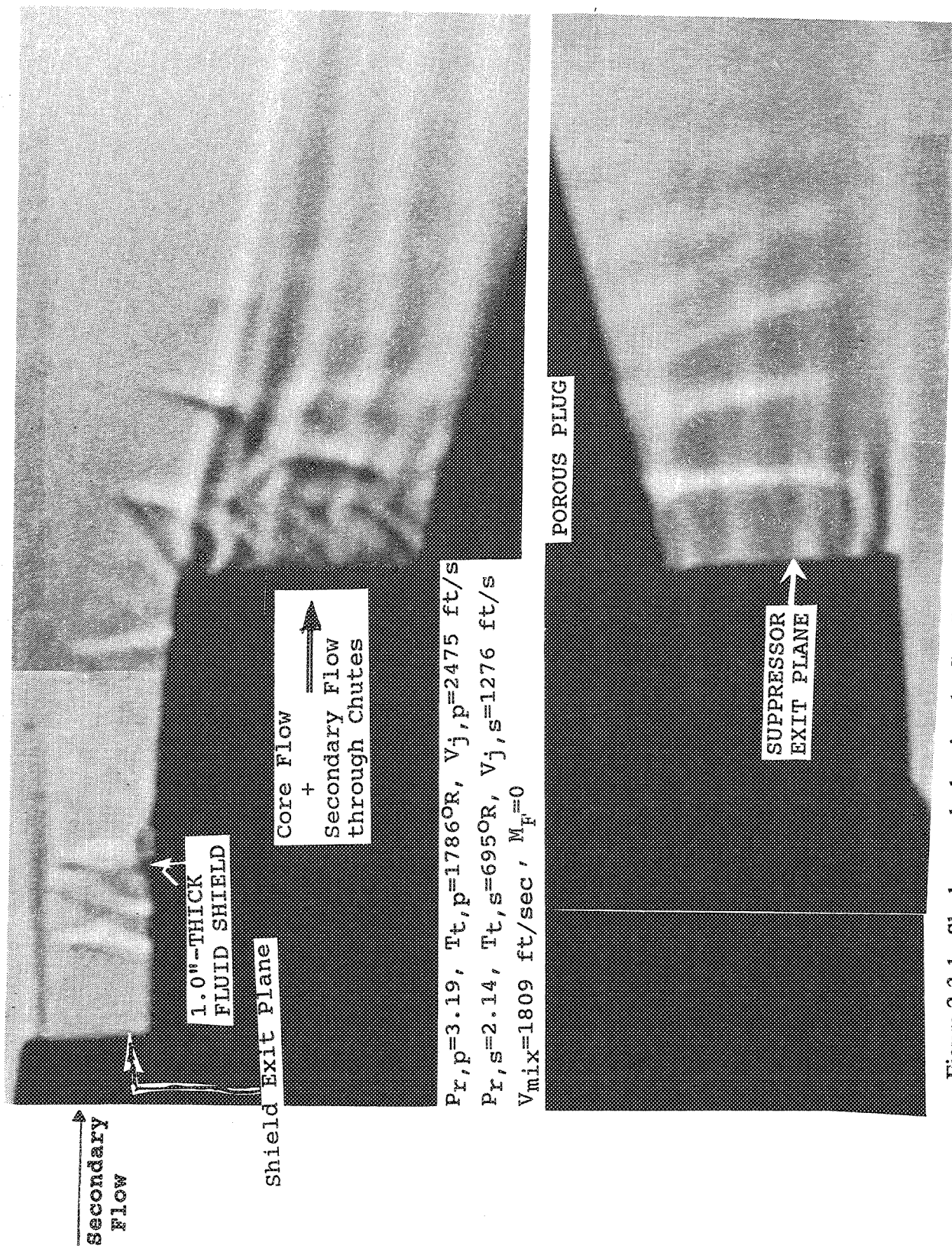


Figure 2.3-1. Shadowgraph showing the flowfield on shielded and unshielded sides of a fluid-shield nozzle of 1.0"-thick and 220° wrap shield with porous plug.



To explain the observed structures in the plume it is essential to be clear about the flowfield which is portrayed in the shadowgraph. The suppressor includes 36 hot flow cores and 36 chutes placed one after the other around an axisymmetric plug. The flowfield observed from the side, as is the case in shadowgraph pictures (see Figure 2.3-2), is the superposition of the flow from several chutes and cores. Due to the axisymmetric geometry of the suppressor the flowfields of different cores and chutes projected on the vertical plane (i.e., same as the shadowgraph field of view), are at different heights. As shown in Figure 2.3-2 the flowfield due to several cores and chutes, which lie below the line A-A are photographed on unshielded side. On the shielded side the flowfield above the line B-B is photographed, which is the combined flowfield of core-chute flow (i.e., similar to the unshielded side flowfield) and shield flow.

### 2.3.1 Flow Structures on the Unshielded Side

First, let us analyze for simplicity, the bottom unshielded side in Figure 2.3-1. The bottom most horizontal dark/bright streak is most likely due to the shear-layers leaving the lips of the surfaces covering the bottom-most core-flows. The other four dark/bright horizontal streaks then must be due to similar shear-layers exiting the remaining lips at lower projected radial distances (as explained earlier using Figure 2.3-2). The largely-vertical bright streaks, however, appear to be due to the waves emanating from the sides of the chutes and need further explanation as given below.

Due to the high nozzle pressure ratio (i.e.,  $P_{r,p} = P_{t,p}/P_{amb}$ ) of 3.19 for the convergent core flow, which is a supercritical pressure ratio, the static pressure at the exit becomes critical i.e.,  $P_{ex} = P_{crit}$  ( $P_{crit}$  is the static pressure corresponding to unit Mach number at the exit and is given by  $(2/(\gamma+1))^{\gamma/(\gamma-1)} P_{t,p}$ ), assuming 1-D isentropic flow, as mentioned before, and the flow is underexpanded i.e.,  $P_{ex} > P_{amb}$ . Although one dimensional analysis predicts a sonic surface right at the exit plane, three-dimensional effects for a convergent nozzle curve the sonic surface slightly outwards (Ref. 4) such that close to the edge there exists sonic/supersonic flow and close to the core or centerline there is subsonic flow which, however, quickly accelerates downstream to supersonic flow. Since the induced ambient flow in the unshielded chutes is most likely subsonic, the static pressure in it close to the core-exit plane is near ambient and, hence, less than  $P_{ex}$  too.

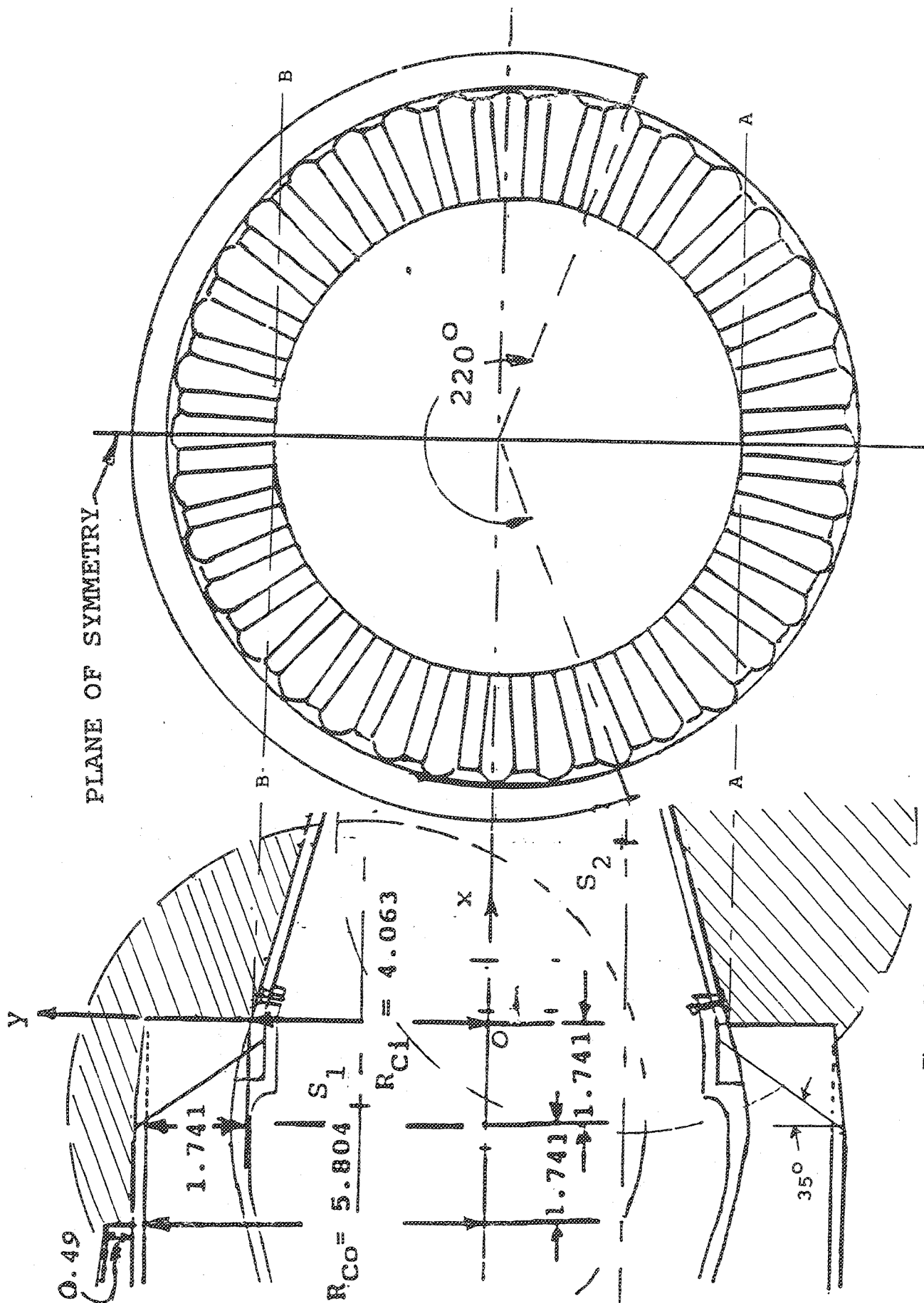


Figure 2.3-2. Schematic showing various elements contributing to the shadowgraph flowfield for fluid-shield nozzle configuration.

With near supersonic flow at core-exit edges and exit pressure more than the surrounding ambient flow we should, hence, have Prandtl-Meyer expansion fans starting from at least the three edges surrounding the core flow. Indirect evidence of such expansion waves from the bottom lips is seen from the outward bulging of the bottom-most lip shear layers. Such bulging is, indeed, predicted by local two-dimensional analysis of supersonic flow at the lip, as shown in Figure 2.3-3.

In order to see the spatial evolution of the expansion waves emitted from the sides of the suppressors, it is convenient to first know the simplified flow picture for an underexpanded 2D nozzle. The core nozzles here are indeed of high aspect ratios (height/width  $\cong 4.7$ ) and their widths are much smaller than the plug radius at the chute exit plane. Also, although, the flow within the core-nozzle is not completely uniform, as mentioned earlier, and the secondary flow in the chutes is inclined towards the nozzle axis, the core flow at, say, mid-height of the chute should locally resemble that for a 2D underexpanded flow. Such a flow for an inviscid fluid is shown schematically in Figure 2.3-4. It should be noted that there is also the possibility of a Mach-disk when two shock-waves interact but is not shown in Figure 2.3-4.

With this picture in mind, it is now slightly easier to picture the 3D wave-surfaces coming out of the chutes. However, the inclination of the plug-surface at the bottom will complicate the flow picture further. Hence, as a next step towards the real flow, we show schematically in Figure 2.3-5 a physically possible structure of the 3D waves from an underexpanded core flow over a non-porous cylindrical plug with zero ramp angle. The alternate expansion cells and shock-cells are formed if we assume the following:

$$P_1 < P_a < P_{ex} \quad \text{Expansion Cell}$$

$$P_1 < P_a < P_2 \quad \text{Shock Cell}$$

$$P_3 < P_a < P_2 \quad \text{Expansion Cell, and so on.}$$

Other possibilities for the evolution of the wave emanating from the lip may also arise. If, e.g.,  $P_1 > P_a$ , then it can be shown that the jet border keeps on deflecting away from the jet axis - a feature not observed in this or any other shadowgraph. The wave-structures shown in Figure 2.3-5 can be thought of as those corresponding to an

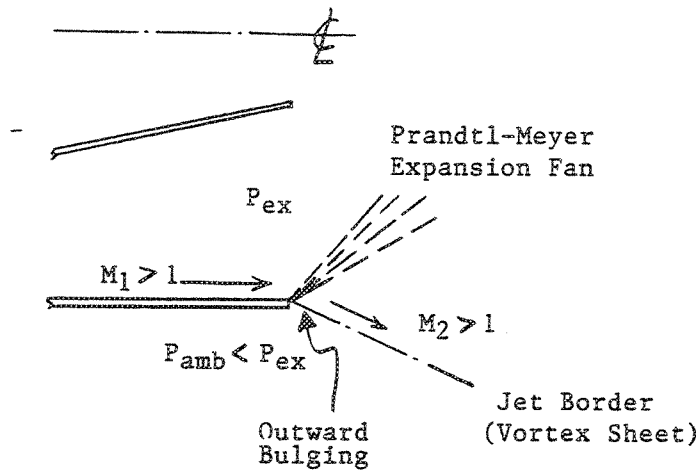


Figure 2.3-3. Two-dimensional underexpanded supersonic flow at the edge of a nozzle showing outward bulging of the jet border.

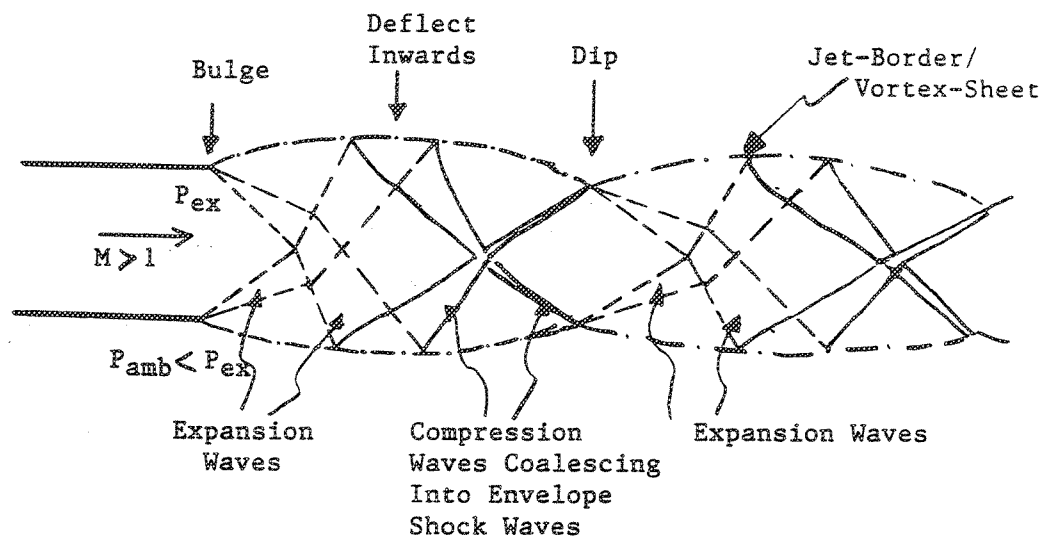


Figure 2.3-4. Two-dimensional underexpanded nozzle plume structure with uniform supersonic exit flow.

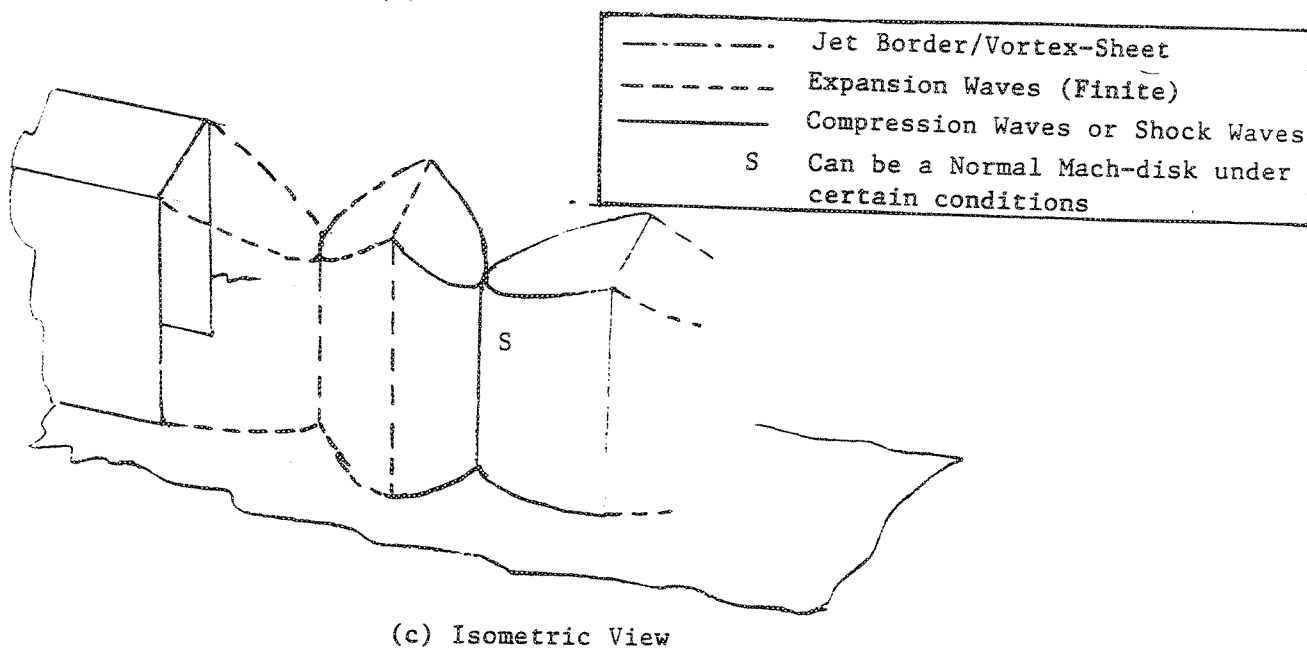
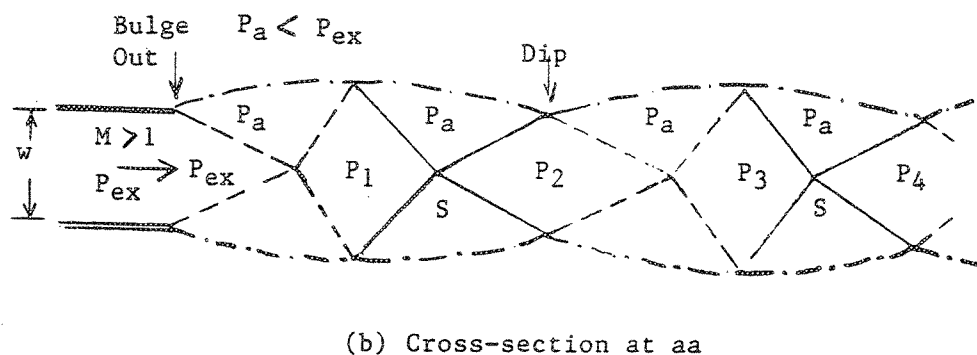
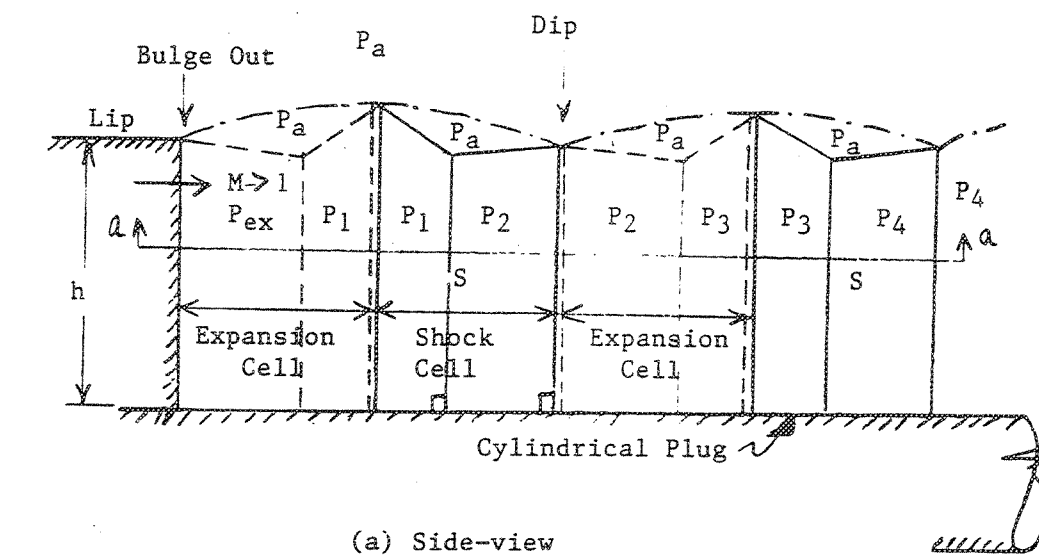


Figure 2.3-5. Schematic of a possible structure of 3D shock-cells from an underexpanded choked nozzle with a non-porous cylindrical plug.

underexpanded flow from a convergent conical nozzle which has been topologically squashed to a rectangular nozzle, with a wall in the axial direction on one side.

Notice that since the ambient pressure surrounding the core flow at the three edges is approximately same, the angles of the leading and near-most Mach-lines from these edges are the same; however, since the width of the core,  $w$ , is much smaller than its height,  $h$ , such Mach-lines from the side-edges interact with each other before allowing the direct interaction of the lip-wave with the plug surface. The wave from the lip, thus, simply keeps on reflecting from the top "edges" of the waves emitted from the chute sides and the lip shear-layer never "sees" the plug surface. Further the waves from the sides of the chutes are orthogonal to the plug surface. These two properties have important repercussions on the noise produced when the plug surface is porous and will be discussed later.

The inclination of the plug-surface (which here is  $15^\circ$ ) would make the vertical waves from the chute sides relatively oblique for the flow near the plug surface, if it is not already separated. This would mean that there will be some complicated reflections (regular, irregular, etc.) of the vertical wave-surfaces discussed above (see, Ref. 5 for all possible types of shock reflections). For example, the shock-surfaces may have a Mach stem at the bottom which is normal to the plug or the whole Mach-disk, if any, can be so inclined as to be normal to the plug, etc. Although the inner core flow path is converging between the two sides of the chutes, it is diverging in the radial plane, especially, along the plug surface. Such radial divergence for supersonic flow can lead to the possibility of  $\lambda$ -shocks on the plug surface slightly downstream of the chute exit plane, as in transonic flow in channels or over airfoils. At this stage it is not completely clear as to the nature of these waves very close to the inclined plug-surface.

Further in the actual model, the inner core flow path on the conical plug just upstream of the chute exit plane is simply a continuation of the conical surface without any abrupt expansion corners. Thus, we do not expect an expansion fan from the core bottom as is seen from the top lip.

Viscosity of the fluid changes the above picture in two respects. All the vortex-sheets on the three sides become thick shear layers and it introduces a boundary-layer on the plug surface. All of these layers grow as they flow downstream. This, in turn, will reduce the shock cell height, width and their spacing as we go downstream. Further, in

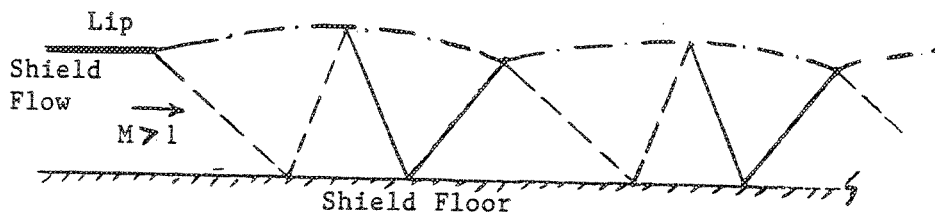
multi-core flows, as we have here, the neighboring jets will also merge at some distance downstream on the plug. However, it appears that the shock-patterns exist in this and other shadowgraphs before such merging of jets occurs.

Going back to the shadowgraph of Figure 2.3-1 we observe that the first white vertical strip has a dip in the shear-layer/vortex-sheet. Such a dip occurs usually when a shock-wave reflects off of a shear-layer/vortex-sheet as an expansion wave (as shown in Figures 2.3-5(a) and 2.3-5(b)). Such dips, although not as clear in the particular shadowgraph, are seen much clearly in other shadowgraphs for no-shield cases (to be shown later). Thus, we believe that these white largely vertical-stripes in Figure 2.3-1 demarcate the different shock-cells (compare Figure 2.3-5(a)).

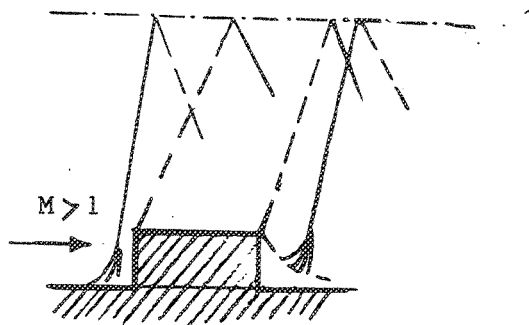
### 2.3.2 Flow Structures on the Shielded Side

The top side in Figure 2.3-1 shows shielded flow with shield nozzle pressure ratio of  $P_{r,s} = 2.14$ , which too is supersonic like the core flow discussed above. However, the shield-flow itself exhausts through an annular passage without chutes making its shadowgraph simpler and more comprehensible. With an underexpanded convergent annular nozzle for the supersonic shield flow we expect the evolution of an expansion wave from the top-lip depicted in Figure 2.3-6 (a). Of course, the progression of the waves downstream will change once the supersonic flow "sees" the chute entrance. However, we notice in Figure 2.3-1 a bunch of prominent  $\Lambda$ -shaped wave-structures just before the chute entrance, where there also exists a semi-circular object on the bottom of the shield-flow. Now the plane of the shadowgraph is parallel to the plane of shield-symmetry, shown in Figure 2.3-2, and closer examination of the pressure tubes on that surface (see Figure 2.3-7) convinces us that the semi-circular curved object is simply the shadow of the bent pressure tube. Figure 2.3-7 also shows that there can be other disturbances triggered in this supersonic shield flow, for example, by the circumferentially bent Pressure tube (diameter = 62 mils) near the plane of symmetry or from the thin tacks (thickness 3 mils) used to hold down the pressure tubes. The inverted-V type wave-structures created by such disturbances is schematically shown in Figure 2.3-6 (b) and seem to bear close resemblance to their type and location in Figure 2.3-1.

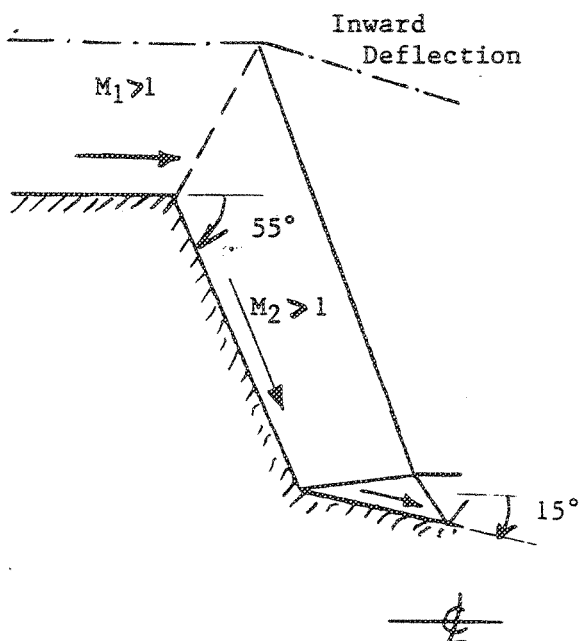
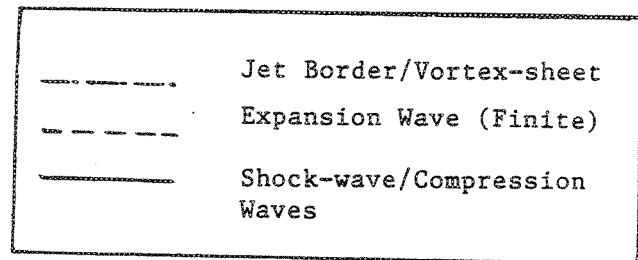
Slightly downstream in the shield-flow, but upstream of the chute exit plane we also see a shock-wave being reflected from the free shear-layer. This ought to be in the



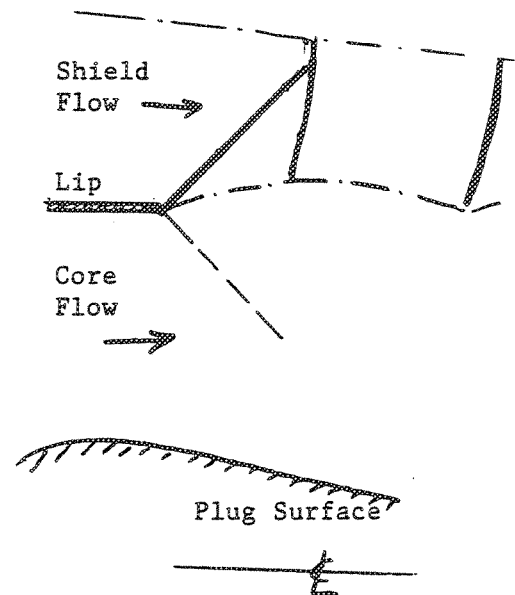
(a) Disturbance from the lip for an annular underexpanded nozzle with a "wall" on one side (wall-jet).



(b) Disturbance from an obstruction in supersonic shield flow.



(c) Disturbance at the chute entrance and supersonic flow inside the chute



(d) Disturbance at the lip in the Primary/Core Radial Plane.

Figure 2.3-6. Disturbances in supersonic shield flow.



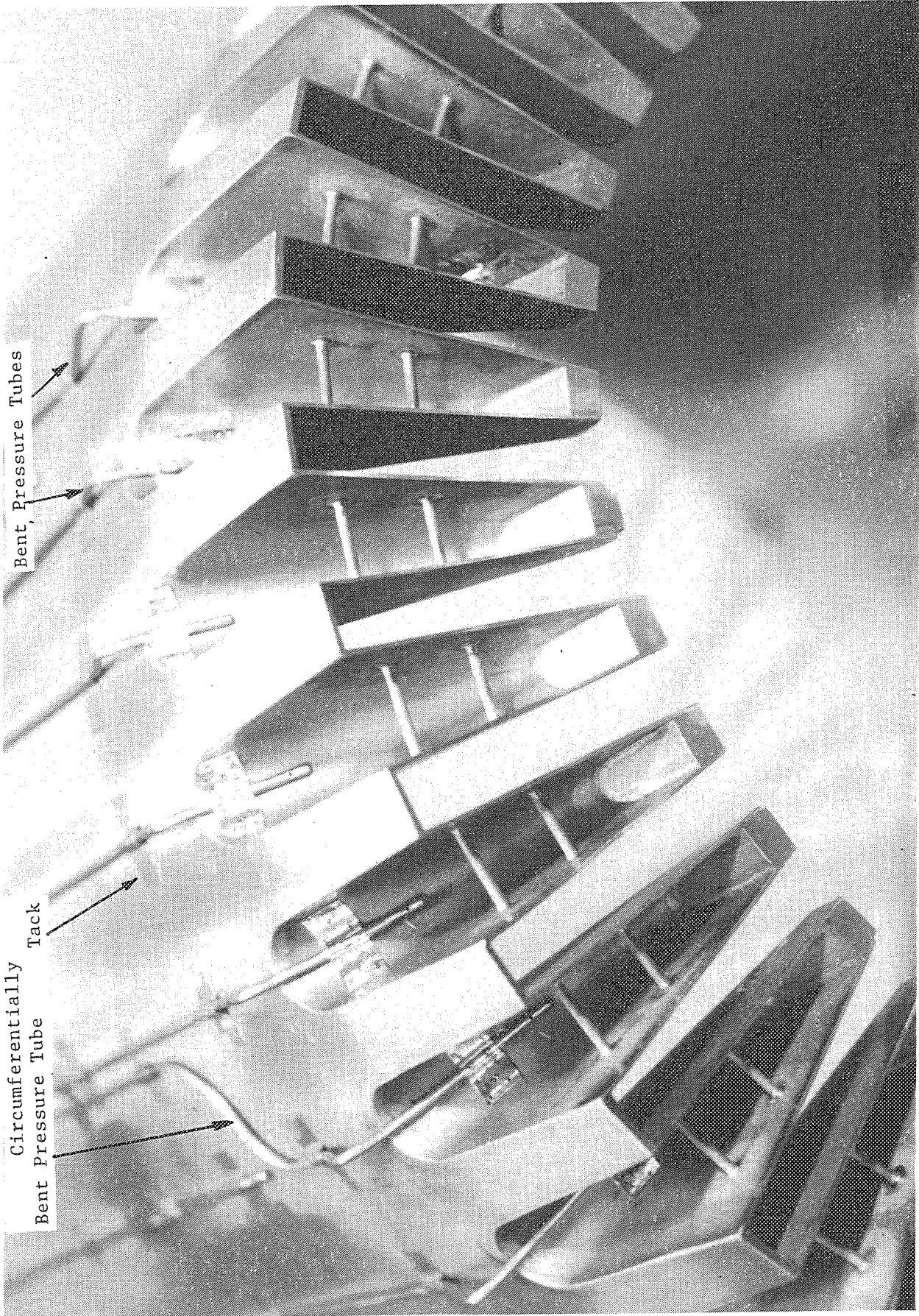


Figure 2.3-7. A close-up of the pressure tubes and their tacks placed in the shield flow.

radial plane between the chutes, that is, above the core flow and not in the radial plane inside the top chute for reasons explained further. The supersonic shield flow in the radial plane inside a chute, sees a sudden drop of the bottom surface (at the chute entrance it is  $55^\circ$ ) resulting in an expansion-fan at the chute entrance. This wave, and the other preceding waves, reflect from the top shear layer entering the chute only to be further reflected from either the chute slant leading surface or the internal chute shock which must be created to re-deflect the chute flow parallel to the plug surface (see Figure 2.3-6(c)). Also note the inward deflection of the shield jet border (which has been more clearly seen in other shadowgraphs) which an incident expansion wave would create. This is, of course, an idealized view; the shape of the chute entrance will rather create a "lampshade" type envelope of expansion waves from its edge to be reflected down the chute as a compression wave which has enough height to coalesce into a shock surface. The point is that the reflection of these waves from inside the chute, for the given slant angle of  $55^\circ$ , gives less probability of them exiting again through the top chute entrance; rather, they will exit through the chute exit plane. At higher temperatures these waves will be very weak, if the shield flow is still supersonic.

Finally, the last structure that we discuss in the shield flow is the wave created in it at the lip above the core-flow just downstream of the chute exit plane (see Figure 2.3-1). The angle appears such that it cannot be a reflection of waves from within the chute, but is rather a wave formed at the lip in the radial plane between two chutes. In this radial plane the outer border of the shield-flow appears deflected towards the plug-surface and its inner border is deflected outwards creating a contraction and an almost normal shock wave there before the lip wave is reflected off the top jet border (see schematic in Figure 2.3-6(d)). In any case, these two dominant waves in the shield flow coming off from other neighboring chute lips when projected on the shadowgraph plane appear to complicate the picture very near the chute exit plane. The second normal shock wave like structure in the shield flow and projections of similar waves from the neighboring lips appear to form another black-and-white strip further downstream. Since there are no more waves seen downstream of it either the shield flow has become subsonic or the viscous shear-layers have consumed the potential annular core of the shield flow after that point.

Amidst the complex features created in this shadowgraph by the round supersonic shield flow, there still exists a dominant shock-wave structure in the shadowgraph of

Figure 2.3-1 between the two almost vertical stripes discussed earlier. It is certainly not due to any projection effects from the wave structures in outer shield flow because it is not seen in the radial-plane of symmetry of the top most shield flow region. Hence, it must be in the core flow between two chutes or secondary shield flow within one chute, if supersonic.

However, at present, we can only speculate about its origin. It could be similar to the vertical stripes seen on the unshielded side and whose structure was explained earlier as some distortion of the series of shock expansion cells shown in Figure 2.3-5. Since all the lines defining this structure are black upstream and white downstream they all must be shock-surfaces, rather than expansion waves. If that is the case, then in shock-structure, the middle stem is most likely due to the interaction of two side shocks or a Mach-shock, S (see Figure 2.3-5), the top V shocks are from the lip-wave and the bottom inverted-V is the foot modification of S to adapt to the inclination of the plug-angle of  $150^\circ$ . The distortion of waves shown in Figure 2.3-5 seems to be in the shrinking of expansion-cell and the lengthening of shock-cell region. Another interaction distortion can come from the shock surfaces in the secondary shield flow exiting the chutes (see Figure 2.3-6(c)), however, this should be weak.

The shock cell spacing in the shielded side also appears larger than on the unshielded side. This is similar to the stretching of shock cells in flight conditions as opposed to static conditions at same ambient pressure. This can be explained, as in Ref. 6, by the decreased spreading rate of the shear-layer when in flight, which is itself due to decreased rate of growth of instability waves in the weakened shear layer.

Another possible mechanism is that the static pressure in the shield-flow, which is supersonic near the core exit plane is less than the ambient, thus, effectively increasing the pressure ratio  $P_{ex}/P_{surrounding}$  shield flow. Increase in this ratio spreads the expansion fan Mach-lines and the shock-cell length.

### 2.3.3. Suppressor Alone Configurations

Figure 2.3-8 shows the effect of core nozzle pressure ratio on the shock structures for the suppressor alone configurations with hard-wall as well as porous plugs. A general observation is the increasing axial shock-cell spacing with increasing nozzle pressure ratio. When nozzle pressure ratio (NPR) is increased, we essentially change the total


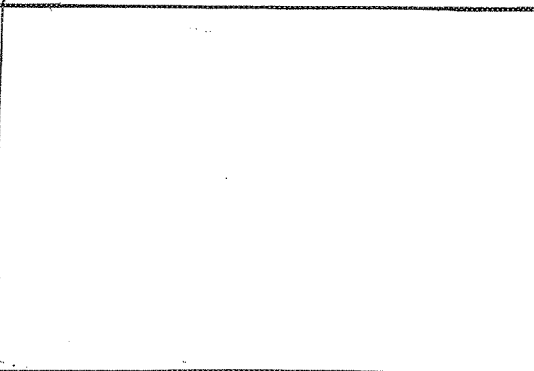



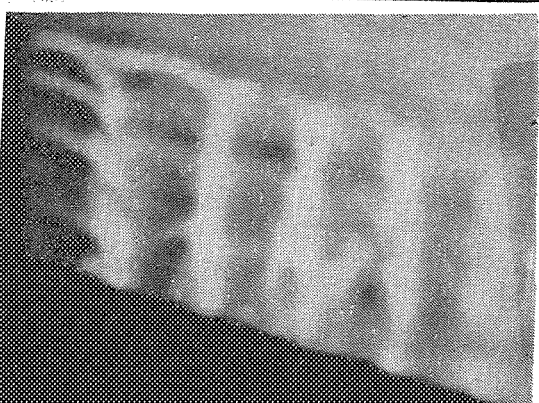
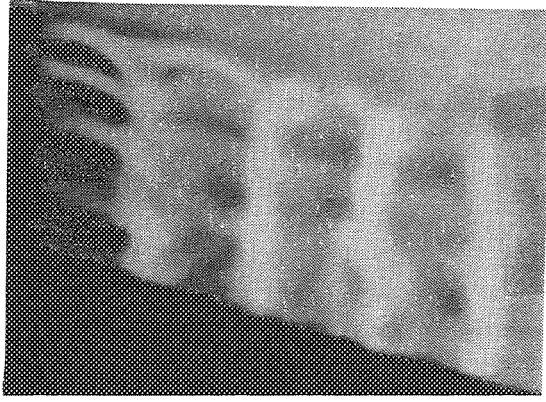

$P_{r,p}$	Hard-Walled Plug	Porous Plug
2.5		
3.0		
3.5		
4.0		

Figure 2.3-8. Effect of nozzle pressure ratio ( $P_{r,p}$ ) and plug porosity on shock structure for the 36-chute suppressor configuration at ambient temperature.



pressure inside the nozzle with the ambient pressure effectively remaining the same. Thus the  $P_{ex}/P_{amb}$  ratio is higher when NPR is higher. With higher NPR there exists a stronger and more spread-out Prandtl-Meyer expansion fan at the beginning with a shallower rear Mach-line, consequently giving rise to shallower coalescing shock-waves. This increases the length of the shock-cells.

Effectiveness of the porous plug in reducing shock strength is not evident from these qualitative pictures, even though, a small benefit is observed acoustically (reported later in this report). It is known that porosity of the plug helps decrease noise (Refs. 7-10) to the order of 5 dB in OASPL in the forward quadrant (Ref. 10) in high radius ratio annular plug nozzles without suppressor chutes. Hence, it is important to know why plug-porosity failed to decrease noise by such a large amount in these chuted nozzles. An explanation follows first for the cylindrical plug (with zero ramp-angle) whose simpler 3D shock cell structure is discussed earlier using Figure 2.3-5.

Shock associated noise, which is dominant in the front quadrant, is known to be dominantly produced by the interaction of turbulence structures/eddies in the shear layer with the shock surfaces in the jet and its amplitude is proportional to the shock strengths. In underexpanded annular nozzles without chutes, the expansion wave from the lip is incident on the plug surface which if porous allows a weaker reflected expansion wave (similar to that shown in Figure 2.3-6(a)). This in turn gives a weaker shock wave reflected from the shear layer than in the non-porous plug case. All further reflections thus give weaker shocks and, hence, less shock-associated noise.

In underexpanded nozzles with chutes, however, such is not the case. (see Figures 2.3-5 (a) & (c)). The wave from the lip, as explained earlier, never "sees" the plug surface. Moreover, the shocks from the sides of the chutes are orthogonal to the cylindrical plug and their strengths are largely governed by the effective nozzle pressure ratio at the core exit plane and not so much by the porosity of the plug. Thus, neither is the strength of the lip shock decreased nor is that of the side shocks decreased due to the porosity in the plug. Hence, the shock associated noise component should not change much if the plug was made porous.

This same argument can be extended to conical porous plugs, however, with some reservations due to the possibly more complicated shock structures near the plug-surface, mentioned earlier. In any case, the lip wave again does not see the conical

plug surface and the shadowgraphs show hardly any change in the locations or density of vertical stripes when a porous-plug is used. Whatever change that the flow in and out from the pores causes must be local and does not affect much the global strength of the side shocks and hence does not decrease much the shock associated noise component in the front quadrant.

Figure 2.3-9 compares the effect of nozzle total temperature on plug shock structures for both hardwalled and porous plugs at the same  $P_{r,p}$  of 4.0. It is noted that with increase in temperature, the shock structures seem more diffused and not clearly defined particularly after the first shock structure. In the case of ambient temperature, possible atmospheric condensation may be contributing to noticeable density gradients, not evident for hot flow cases. Again the effect of porous plug compared to the hard-walled plug is not evident from these shadowgraph pictures.

Figure 2.3-10 shows the flight effect for porous plugs at two nozzle pressure ratios. With flight, a very small increase, if at all, is observed in the distance between the two vertical stripes which as explained earlier supposedly demarcate the shock-cells. Increase in the shock-cell spacing with flight is a well-known effect for round nozzles without chutes (Ref. 6). Such an increase is also seen when the nozzle pressure ratio is increased, as mentioned earlier (see Figure 2.3-8), and is also seen by examining any horizontal row in Figure 2.3-10.

In simulated flight by a freejet, the strength of this viscous shear layer surrounding the jet decreases, the spatial growth rate of the instability waves in it is lower than in the static case leading to a lower spreading angle. With the leading and the rear Mach lines of the lip expansion fan at the same locations as in the static case (due to the same NPR), a decrease in the spreading angle of the shear layer will then imply a slight increase in the axial distance where the reflected shock-waves intersect the shear layer. This means a slight increase in the shock-cell spacing.

#### 2.3.4 Fluid-Shield Nozzle Configurations

Figures 2.3-1, 2.3-11, and 2.3-12 are the shadowgraph photographs of three fluid-shield nozzle configurations with decreasing fluid-shield thickness and with the same porous plug, operated at the same aero thermodynamic conditions. The unshielded side of these figures do not show any noticeable difference, since the flowfield in this side is

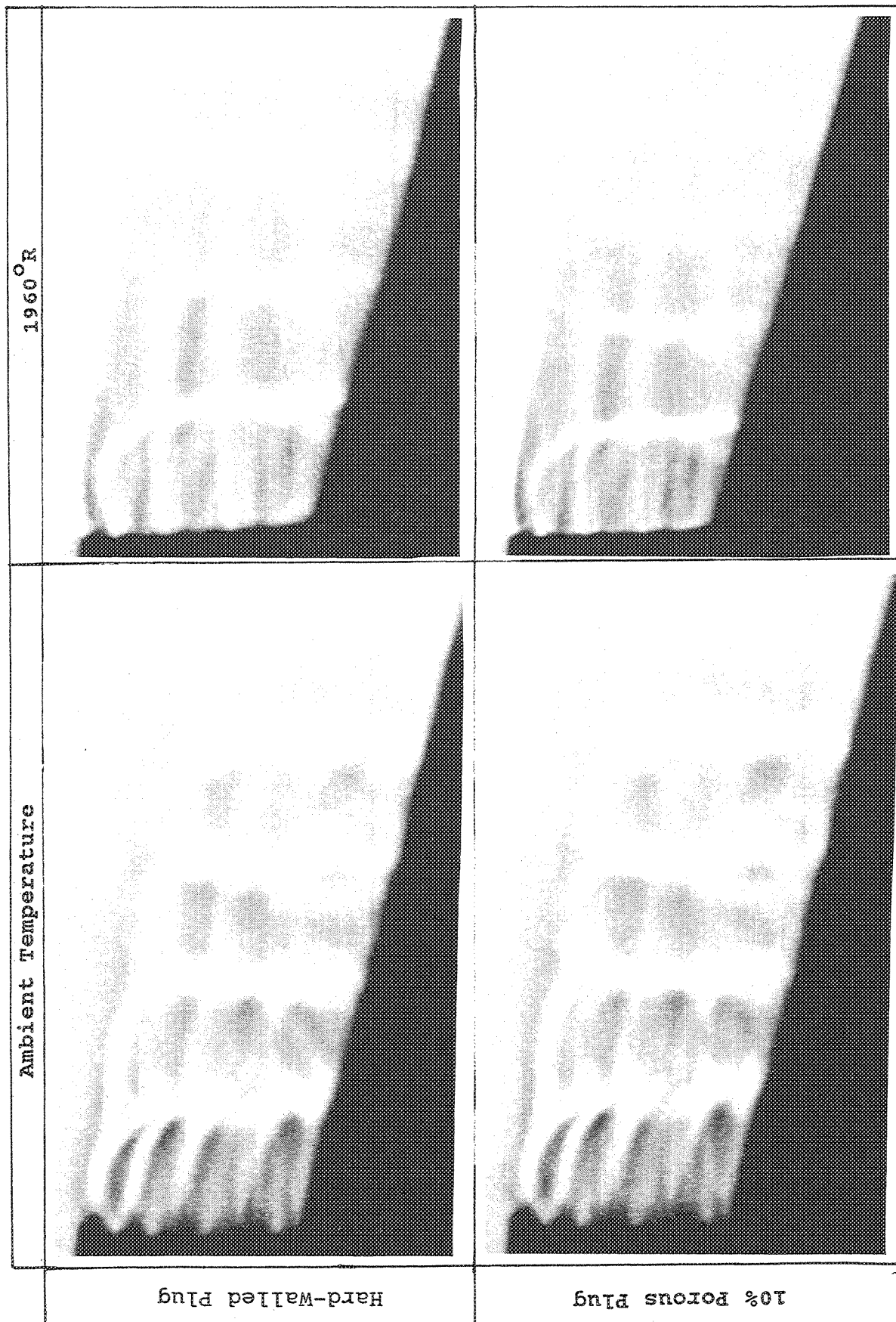


Figure 2.3-9. Effect of nozzle total temperature ( $T_{t,p}$ ) and plug porosity on shock structure for the 36-chute suppressor configuration at nozzle pressure ratio  $P_{t,p}=4$ .

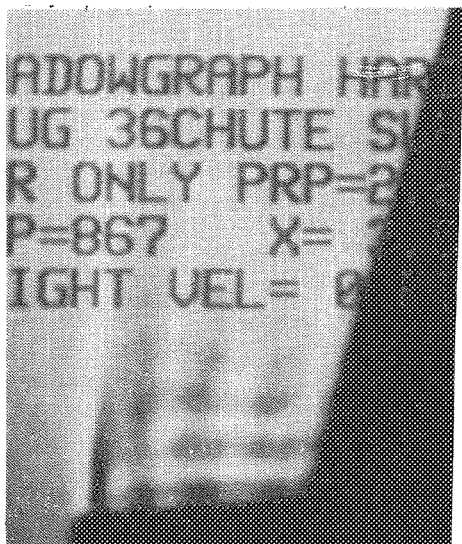
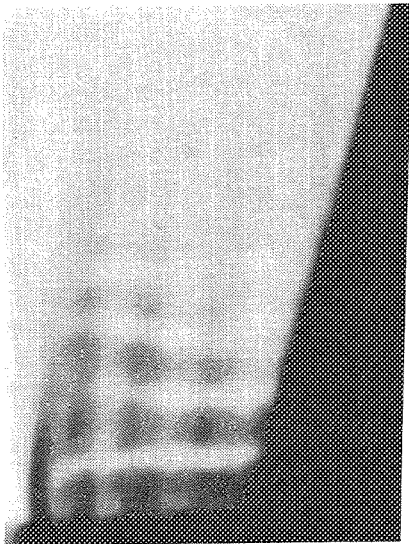
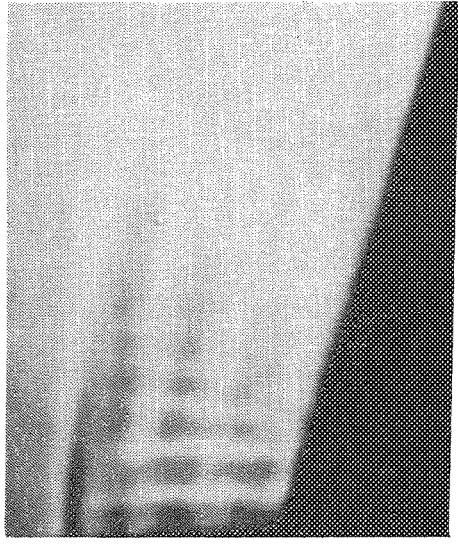
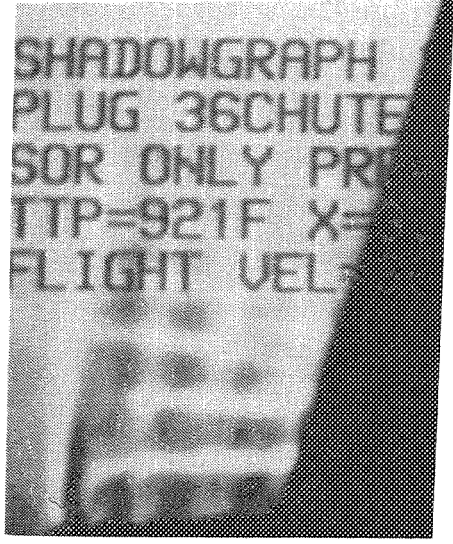
Static, $M_F=0$	$P_{r,p}=2.23$ , $T_{t,p}=1327^{\circ}\text{R}$ , $V_{j,p}=1811$ ft/s 	$P_{r,p}=2.7$ , $T_{t,p}=1381^{\circ}\text{R}$ , $V_{j,p}=2030$ ft/s 
With Flight Simulation, $M_F=0.32$		

Figure 2.3-10. Effect of flight simulation on shock structure for the 36-chute suppressor configuration with porous plug.



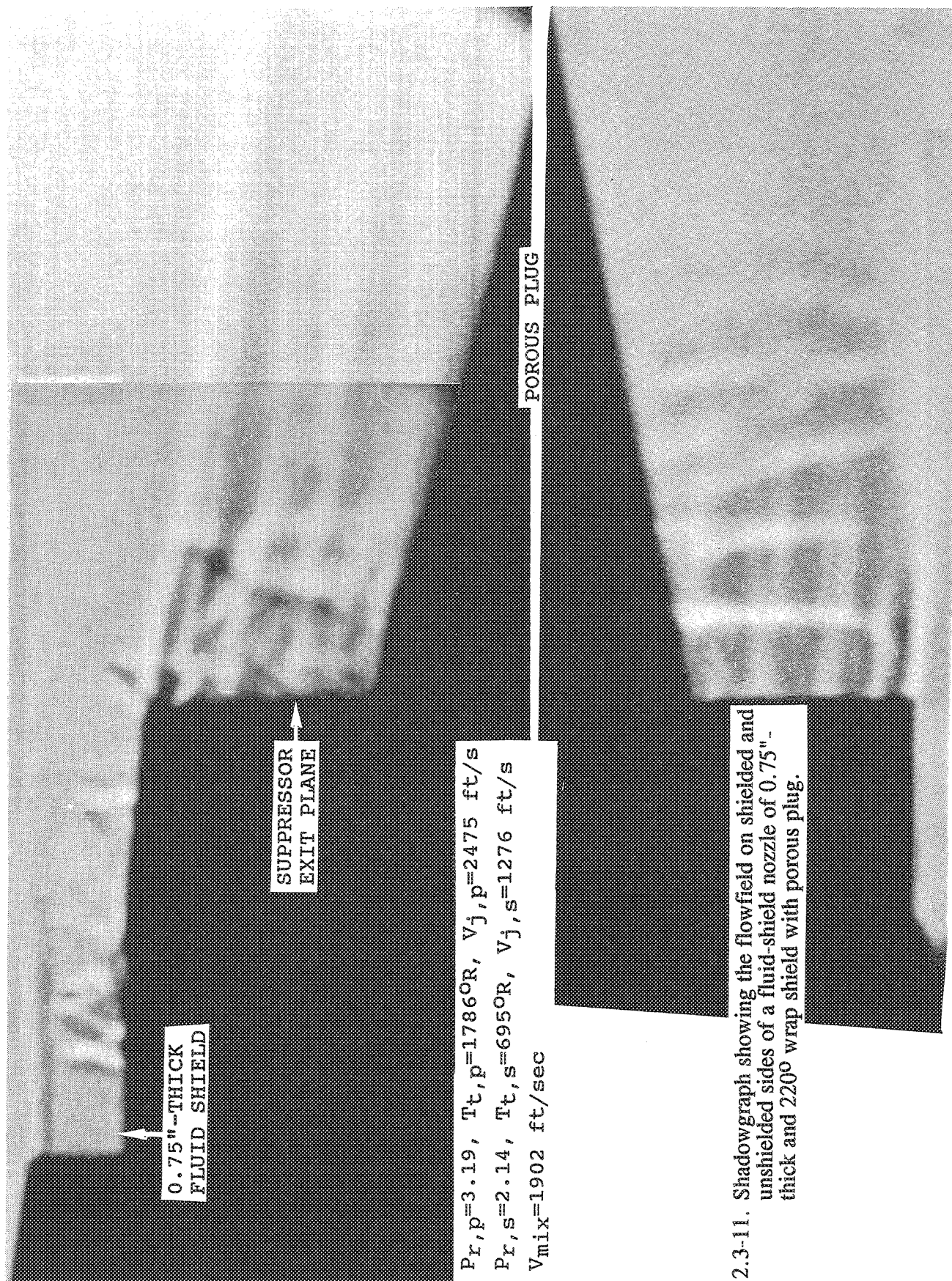


Figure 2.3-11. Shadowgraph showing the flowfield on shielded and unshielded sides of a fluid-shield nozzle of 0.75" - thick and 220° wrap shield with porous plug.

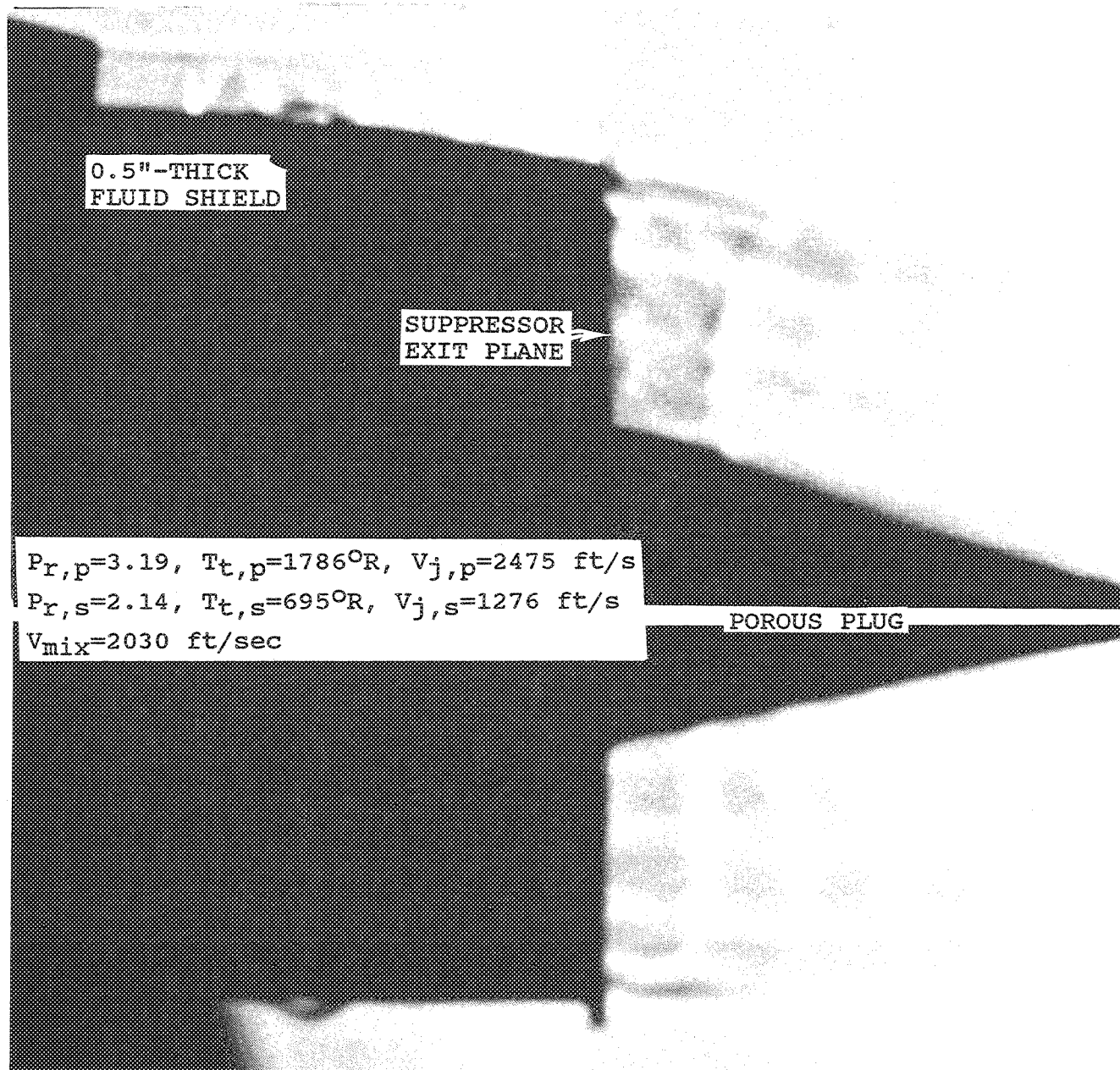


Figure 2.3-12. Shadowgraph showing the flowfield on shielded and unshielded sides of a fluid-shield nozzle of 0.5"-thick and 220° wrap shield with porous plug.

expected to be identical in each case. On the shielded side the thicker shield exhibits stronger interaction of core and chute flows with the shield flow.

The complexities observed on the shielded side are caused by the supercritical shield flows. This is identified by comparing the supercritical shield flow (see Figure 2.3-1) with subsonic shield flow (see Figure 2.3-13). Compared to Figure 2.3-1 the shielded side shock structure in Figure 2.3-13 is quite different. However, unshielded flow streams are similar. The axial shock spacing on shielded side seems to be higher than that of unshielded side for subsonic shield, which could be explained due to reduced mean shear by the subsonic shield, similar to flight effect by freejet. These effects are further illustrated in Figures 2.3-14 and 2.3-15 for the 0.5"-thick fluid-shield nozzle with hard-walled plug at two different mix velocity conditions.

Previous experimental studies which compared acoustic characteristics of suppressor nozzles with convergent and C-D chutes showed relatively minor noise reduction (about 2 PNdB @  $\theta_1=60^\circ$ ) by C-D chutes over convergent chutes at design condition (Ref. 11) indicating that the contribution of shock noise to total noise for a suppressor is not as large as in the case of unsuppressed plug nozzles. MGB predictions for suppressor nozzles gave reasonable agreement with data when shock noise was not included (Ref. 12). Hence, it is not unreasonable to expect minor noise benefit by shock noise reduction due to porous plug. It seems, that a C-D chute design may yield more noise reduction than porous plug at design NPR. A combination of C-D chute and plug porosity may be needed to increase shock noise reduction at design and slightly off design conditions.

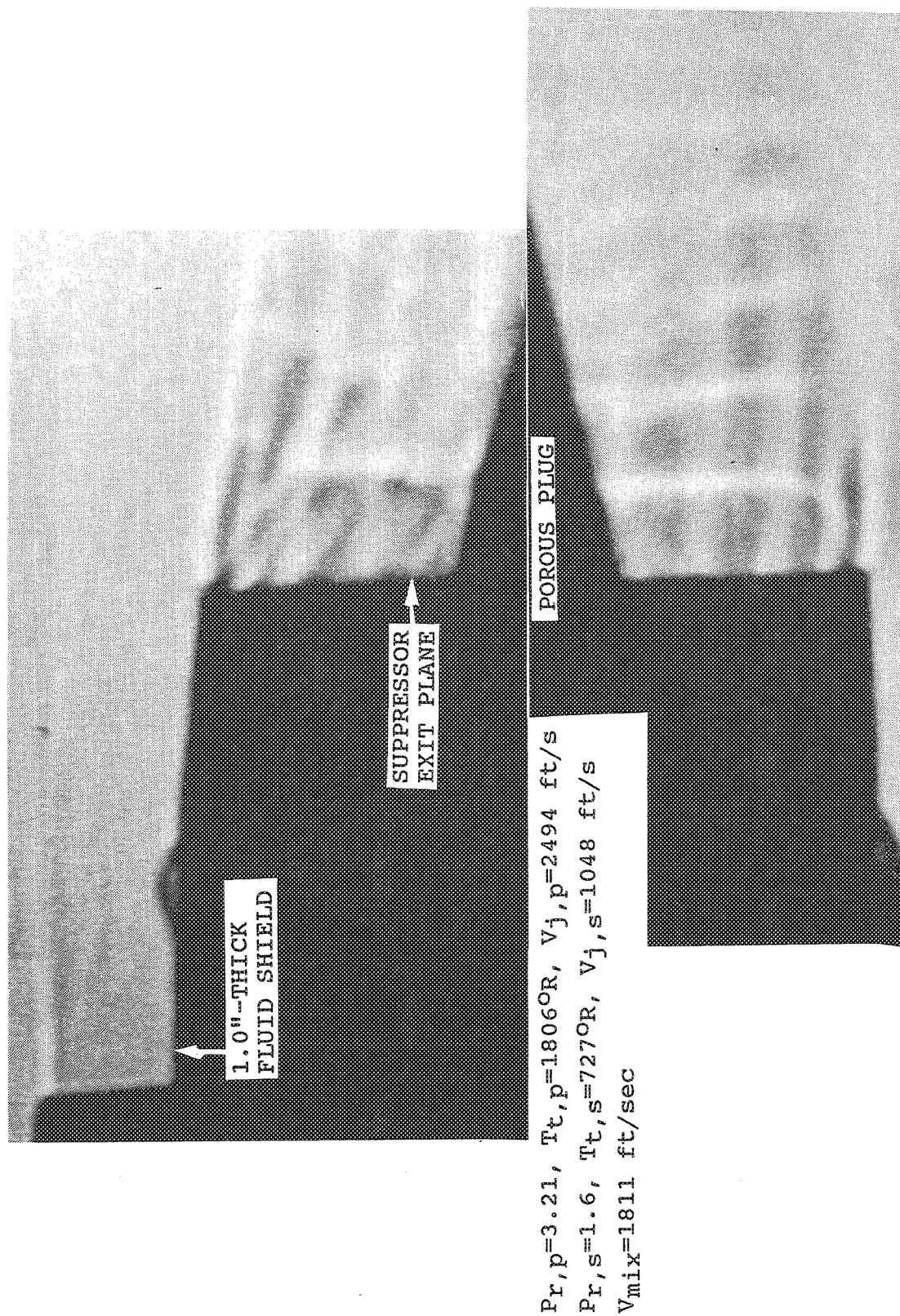


Figure 2.3-13. Shadowgraph showing the flowfield on shielded and unshielded sides of a fluid-shield nozzle of 1.0" -thick and 220° wrap shield with porous plug.



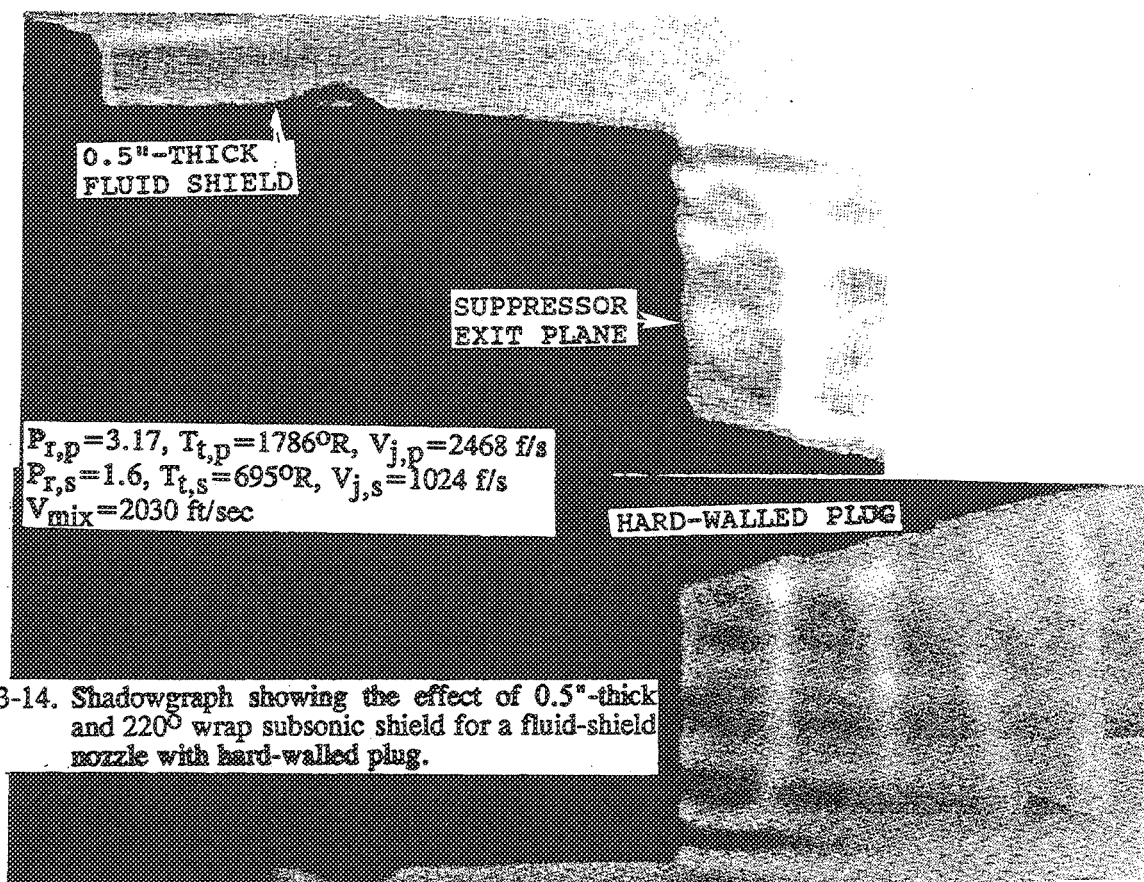
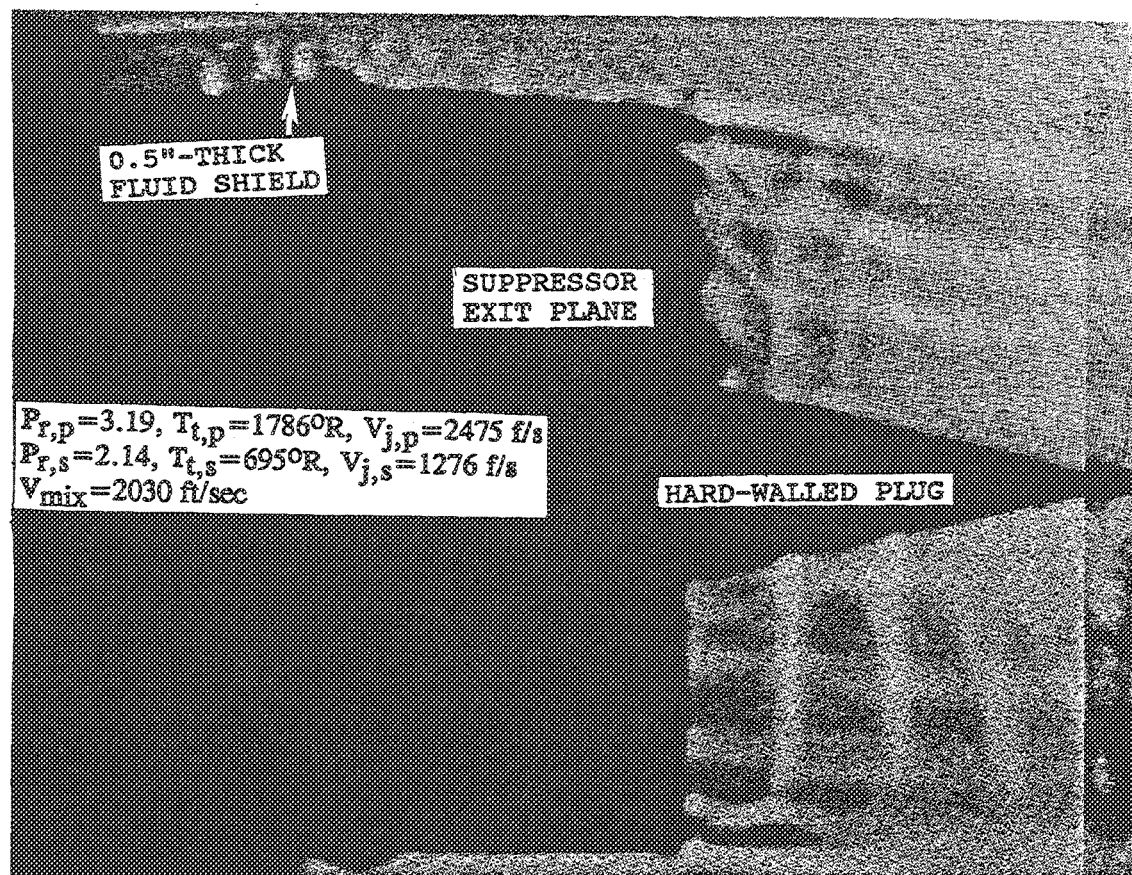


Figure 2.3-14. Shadowgraph showing the effect of 0.5"-thick and 220° wrap subsonic shield for a fluid-shield nozzle with hard-walled plug.

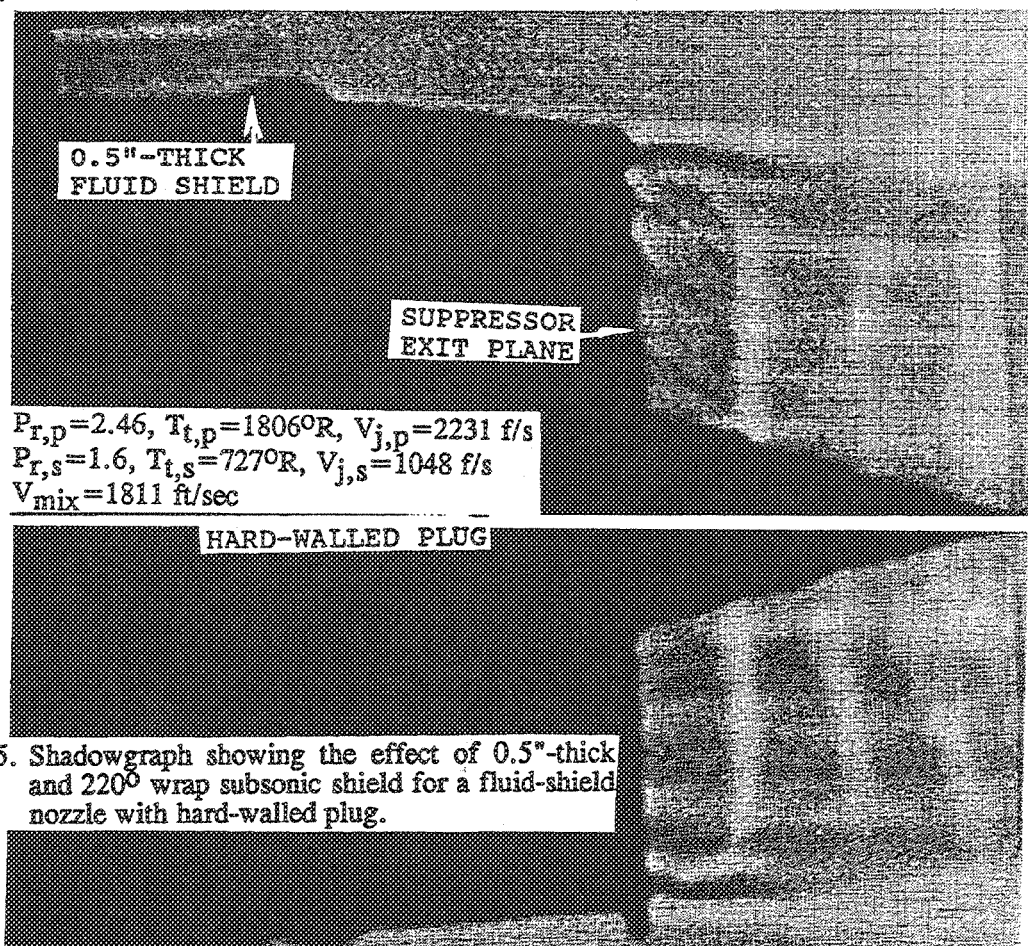
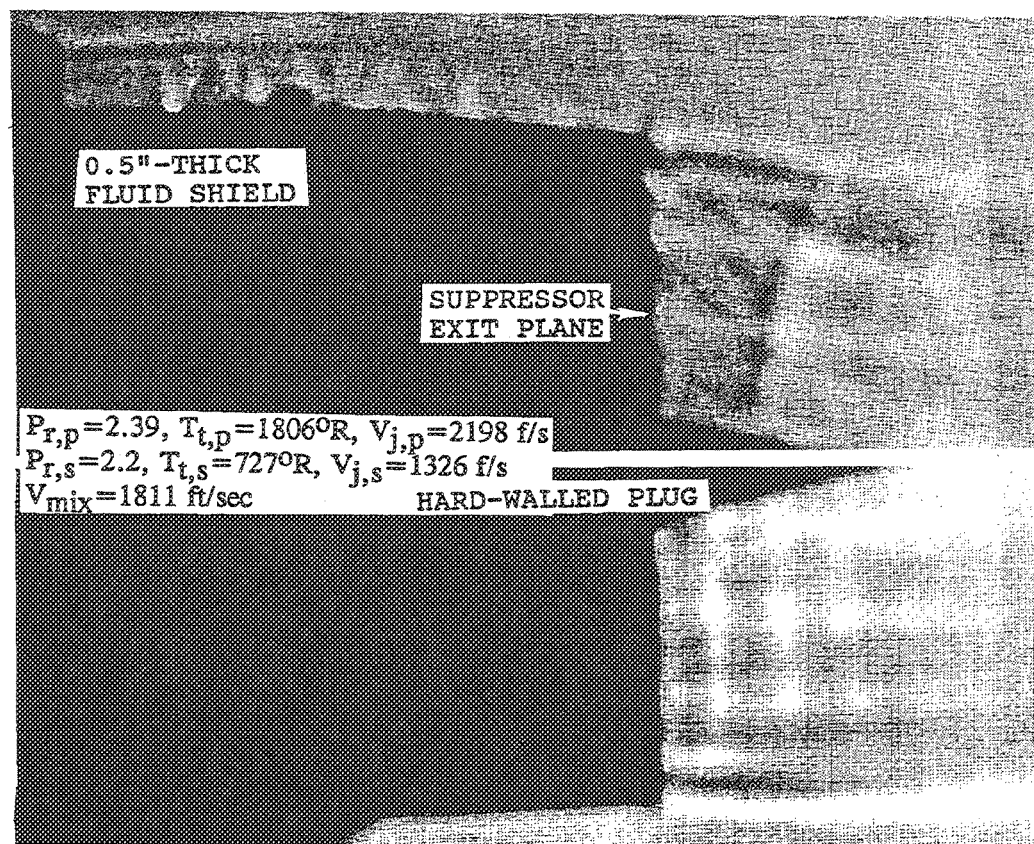


Figure 2.3-15. Shadowgraph showing the effect of 0.5"-thick and 220° wrap subsonic shield for a fluid-shield nozzle with hard-walled plug.

## 2.4 STATIC PRESSURE RESULTS

One of the significant considerations in employing a shield flow on a mechanical suppressor nozzle with chutes is the increase in base drag of the suppressor due to the presence of a shield flow over the chutes. The presence of a flow over the chutes reduce ventilation in the base region of the chutes, leading to a reduction in base pressure and consequent increase in the base drag. In order to evaluate the influence of fluid shield on the chutes and plug, static pressure measurements were made in the chute base region and on plug surface. The static pressure distributions on the plug and the suppressor chutes relative to ambient pressure contribute force either in the direction of drag or in the direction of thrust.

### 2.4.1 Static Pressure Data Analysis

As per the instrumentation layouts ( see Figures 2.2-9 and 2.2-10) two rows of static pressure taps were mounted on the plug surface distributed axially from the base (i.e.,  $X/L=0$ ,  $X$  and  $L$  being the axial distances from the plug root and the plug length, respectively) to the plug tip (i.e.,  $X/L=1$ ), one row along the hot core flow of the suppressor and the other along the chute carrying ambient cold air. In addition, two rows of static pressure taps were mounted on suppressor chutes distributed radially on an equal area basis from the root (i.e.,  $R/R_{CO}=0.7$ ,  $R$  and  $R_{CO}$  being the radial location of pressure tap and outer radius of the suppressor, respectively) to the tip (i.e.,  $R/R_{CO}=1$ ), one row on the unshielded side and the other on the shielded side of the suppressor.

Static pressure distributions on the plug and the chutes are presented as ratios of measured pressures with respect to ambient pressure (i.e.,  $PS/P_{amb}$ ,  $PS$  and  $P_{amb}$  being the measured static pressure at a tap location and ambient pressure, respectively). For the suppressor alone configuration, since there is no fluid shield nozzle, static pressure distributions on chutes, measured by both the rows of taps are very close to each other. Therefore, in the present analysis average of these two sets of taps are employed for suppressor alone configuration.

The drag or thrust contributions due to the relative static pressure distributions on plug and chutes is expressed in terms of a correction factor to the gross thrust coefficient ( $\Delta C_{fg}$ ) in % of ideal gross thrust and is expressed as follows :

$$\Delta C_{fg} = \sum[(PS_i - P_{amb}) A_i] 100 / (FG)_i$$

Where,

$PS_i$  = static pressure measured by the  $i$ th tap

$A_i$  = elemental projected area in axial direction for the static pressure  $PS_i$  in  $in^2$

$(FG)_i$  = ideal gross thrust in lbs

Following are the various  $\Delta C_{fg}$  associated with plug and chutes :

$(\Delta C_{fg})_{ph} = \Delta C_{fg}$  for the plug evaluated by hot flow row data

$(\Delta C_{fg})_{pc} = \Delta C_{fg}$  for the plug evaluated by cold flow row data

$(\Delta C_{fg})_{pa} =$  average  $\Delta C_{fg}$  for the plug

$(\Delta C_{fg})_{cs} = \Delta C_{fg}$  for the shielded chutes

$(\Delta C_{fg})_{cu} = \Delta C_{fg}$  for the unshielded chutes

$(\Delta C_{fg})_{ca} =$  average  $\Delta C_{fg}$  for the chutes

$$= [\phi (\Delta C_{fg})_{cs} + (360 - \phi) (\Delta C_{fg})_{cu}] / 360$$

where,  $\phi$  is the shield wrap angle in degrees.

$(\Delta C_{fg})_t =$  total  $\Delta C_{fg}$  for the plug and chutes

$$= (\Delta C_{fg})_{pa} + (\Delta C_{fg})_{ca}$$

$(\Delta C_{fg})_{f-s} =$  relative  $\Delta C_{fg}$  due to flight simulation

$$= [(\Delta C_{fg})_t]_{flight} - [(\Delta C_{fg})_t]_{static}$$

These correction factors to gross thrust coefficient are computed using the appropriate plug and chute projected axial areas.

#### 2.4.2 Static Pressure Distribution on Plug Surface

**Suppressor Alone Configuration :** Figures 2.4-1 and 2.4-2 illustrate the comparison of axial static pressure distributions on the hard-walled plug between the hot flow row and cold flow row with and without flight simulation. Figure 2.4-1 includes the comparisons for heated core flow with nozzle pressure ratios of 1.6 to 3.1. In this range of  $P_{r,p}$  there is no appreciable difference in plug static pressure distributions between hot and cold flow rows. As the flow exits from the suppressor, in most cases (i.e., for higher  $P_{r,p}$  and  $T_{t,p}$ ), it accelerates, which results in lower than ambient pressure near the plug crown. The pressure distributions exhibit a constant value at the



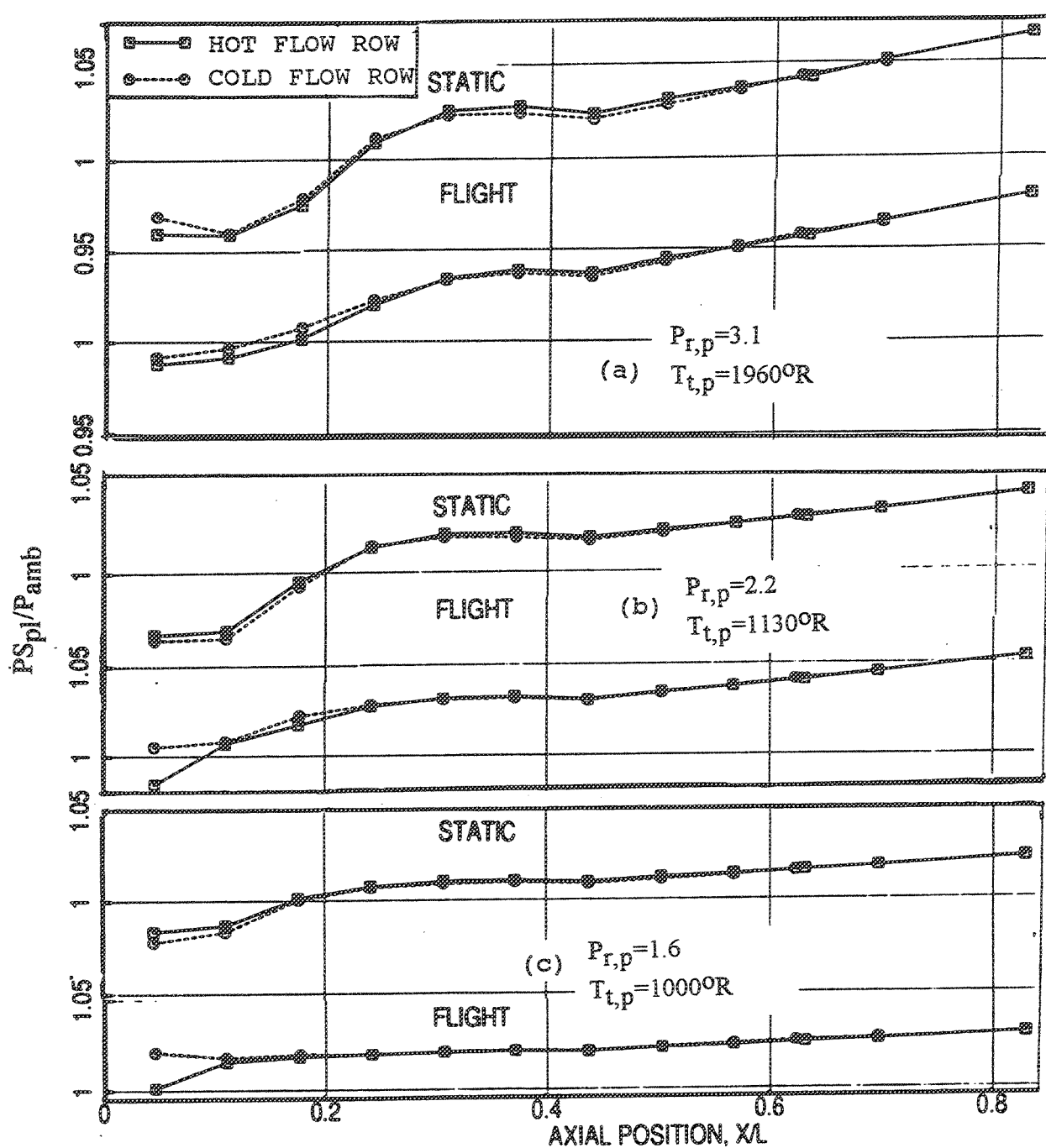


Figure 2.4-1. Comparison of axial static pressure distributions along the hot flow row with those along the cold flow row on the hard-walled plug attached to the 36-chute suppressor with ( $M_F=0.32$ ) and without flight simulation.

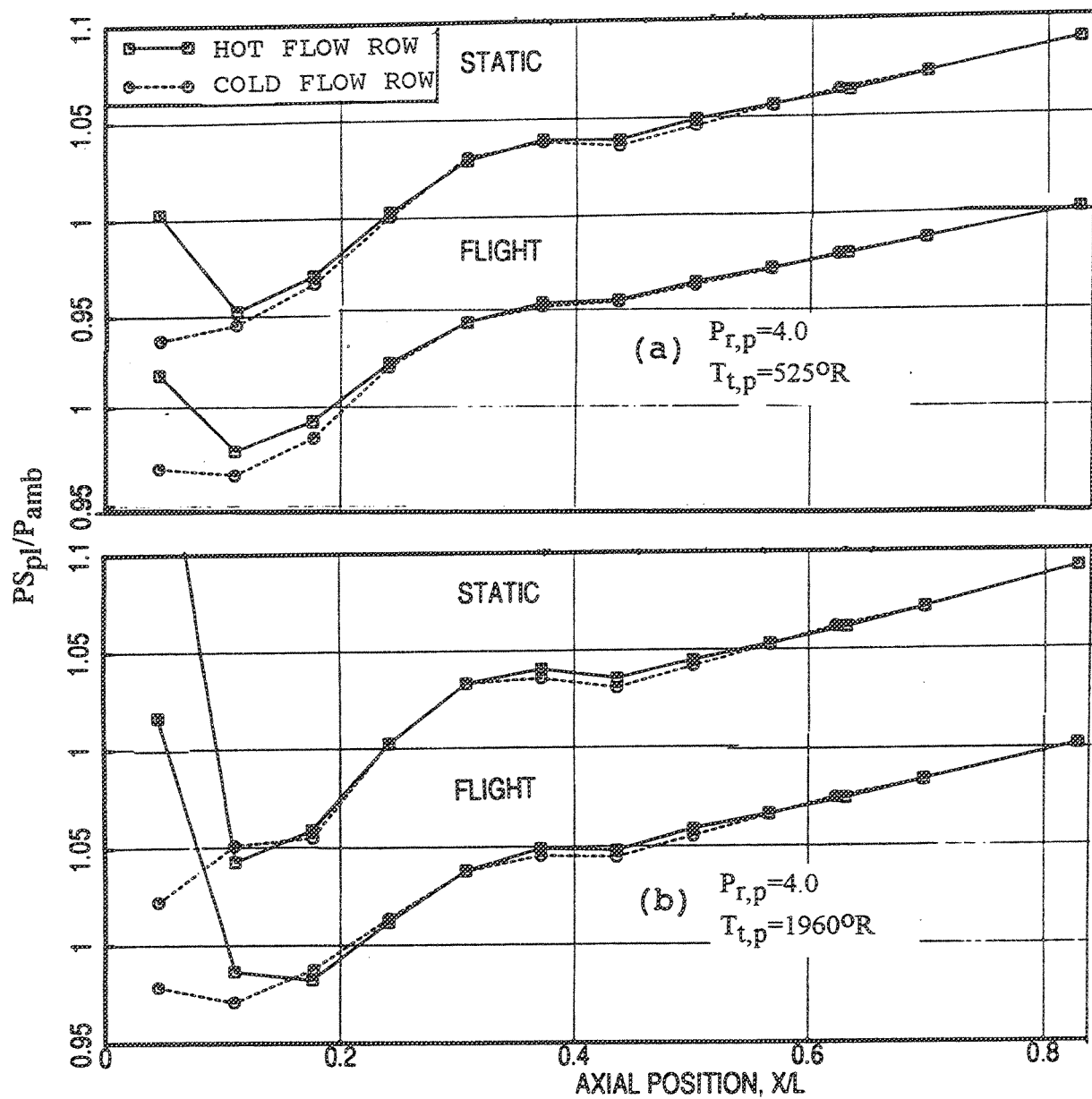


Figure 2.4-2. Comparison of axial static pressure distributions along the hot flow row with those along the cold flow row on the hard-walled plug attached to the 36-chute suppressor with ( $M_F=0.32$ ) and without flight simulation,  $P_{r,p}=4.0$ .

crown of the plug and as the flow develops further downstream (especially for higher  $P_{r,p}$  values), the plug is pressurized with axial distance (i.e.,  $X/L$ ), due to a recompression of the flow after the initial acceleration.

Figure 2.4-2 shows the plug static pressure distributions for hot and cold flow rows for a higher  $P_{r,p}$  of 4 at ambient temperature and at 1960°R core flow temperatures. The plug static pressure distributions between hot and cold flow rows differ near the plug crown and then are identical for rest of the plug surface. The hot core flow seems to overexpand more than the ambient core flow as it turns the plug crown due to Prandtl-Meyer expansion and then a pressure rise is observed due to a recompression. Stronger Prandtl-Meyer expansion occurs for higher nozzle pressure ratios for the same turning angle. This is observed in the shadowgraph pictures (see Figures 2.3-8 and 2.3-9) and is explained in section 2.3 that the shock spacing increases with increasing nozzle pressure ratio due to stronger and more spread-out Prandtl-Meyer expansion fan.

The pressure distribution along the hot flow row is somewhat influenced at the plug crown by core flow temperature at this high nozzle pressure ratio (see Figure 2.4-2). Measured static pressures on the plug hot flow row indicate a higher static pressure at the plug base for heated case compared to the cold flow case. One reason for this is the lower specific heat ratio at higher temperature (at a total temperature of 1960°R and  $P_{r,p}=4.0$ ,  $\gamma$  the specific heat ratio at the throat is 1.34), which elevates the static pressure relative to the ambient temperature case for which  $\gamma$  is 1.4. For the present case assuming unity Mach number at the nozzle exit plane the static pressure at this point becomes  $0.528 P_T$  for cold flow and  $0.539 P_T$  for hot flow due to different specific heat ratios,  $P_T$  being the total pressure. Another probable reason for the static pressure difference between hot and ambient core flows can be attributed to some thermal growth of the chutes under heated conditions, and the resulting flow path differences.

Further downstream on the plug surface, for all conditions (see Figures 2.4-1 and 2.4-2), the flow seems to develop on the plug surface uniformly resulting in some amount of pressure recovery.

Figure 2.4-3 compares axial static pressure distributions on the porous plug along hot and cold flow rows for static case. These distributions are very similar to what is observed for hard-walled plug, except for pressure ratio 4. In this case, the difference

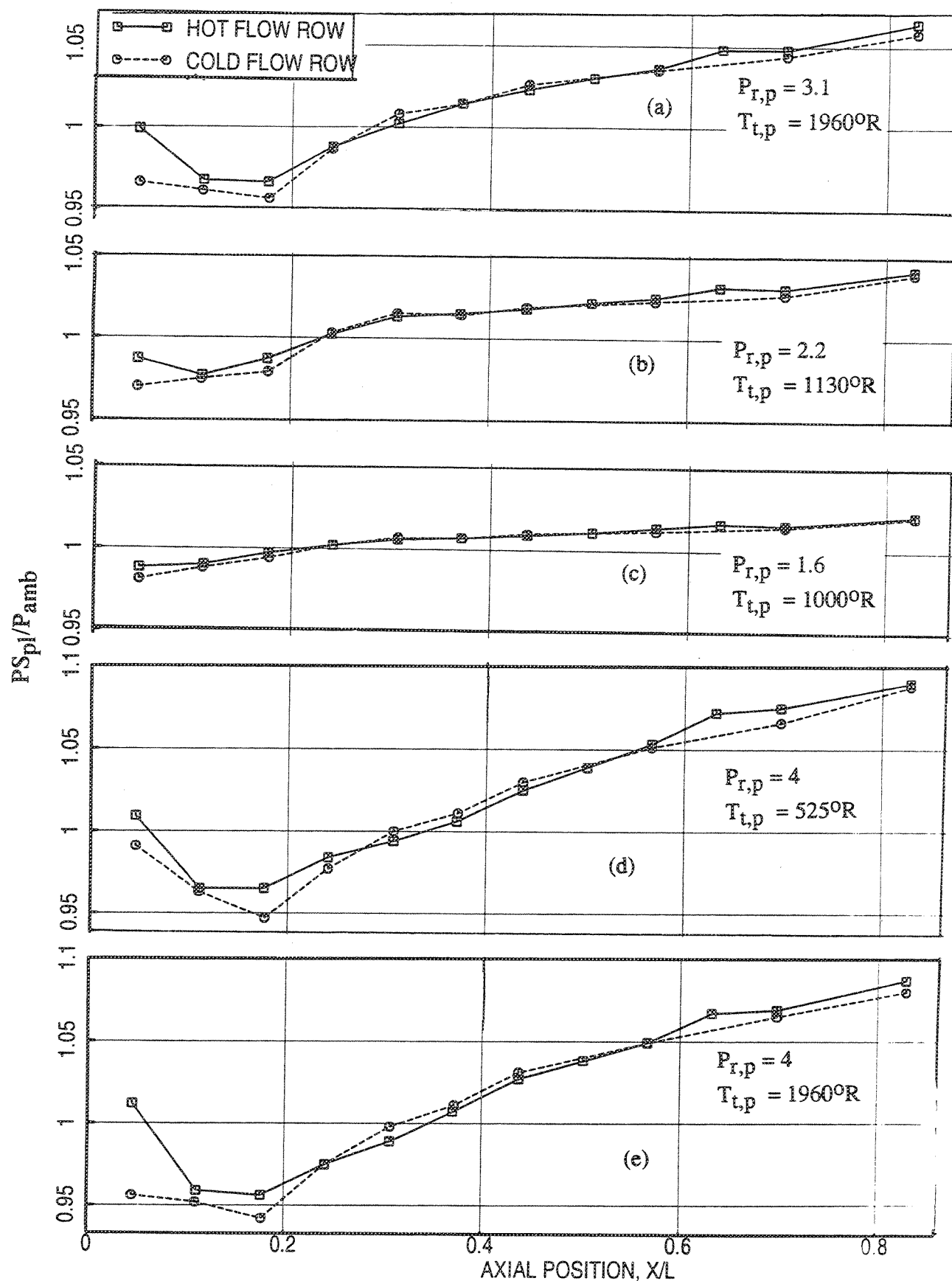


Figure 2.4-3. Comparison of axial static pressure distributions along the hot flow row with those along the cold flow row on the porous plug attached to the 36-chute suppressor at static condition.

between hot and cold flow rows are much less compared to hardwalled plug. The influence of porous plug is further demonstrated in Figure 2.4-4 by comparing the pressure distributions between hardwalled and porous plugs for both hot and cold flow rows. The pressure rise on hardwalled plug is steeper close to  $X/L=0.2$ , indicating the presence of moderately stronger shock compared to porous plug. However, the shadowgraph photographs (see Figures 2.3-8 and 2.3-9) show minimal differences in the shock structures between porous and hardwalled plugs. Hence, although  $PS_{pl}$  (i.e., static pressure on plug surface) distributions on porous plug show some differences compared to hardwalled plug distributions, it is not sufficient to show up in a shadowgraph picture, which is more qualitative in nature.

Considering the limited difference between hot and cold flow row static pressure distributions, an average value of these two (i.e.,  $(PS_{pl}/P_{amb})_{avr}$ ) is used for computing axial plug thrust component. Effect of temperature on the plug axial pressure distribution, shown in Figure 2.4-5, has minimal effect at low nozzle pressure ratios. At higher nozzle pressure ratios, the static pressure increases due to temperature at and near the plug crown. The reasons for these effects are the same as those described earlier. For the rest of the plug small reduction of static pressure is observed due to temperature rise. The effect is similar with and without flight simulation.

Increasing nozzle pressure ratio (shown in Figure 2.4-6) results in an over-acceleration of the flow around the plug crown and hence lower static pressure and subsequent higher levels of the recovery pressures on the plug surface. In general, similar effect is observed due to increasing jet velocity shown in Figure 2.4-7. However, the nozzle pressure ratio, not the jet velocity, is primarily responsible for this effect. This can be observed from Figure 2.4-7, in that the increase in the static pressure is insignificant between the jet velocities of 1651 ft/sec and 1811 ft/sec, since the nozzle pressure ratios are very close for these cases.

The effect of flight, demonstrated in Figure 2.4-8, is to increase the static pressure levels on the plug compared to static cases. This results in a small increase in axial plug thrust contribution.

**Fluid Shield Nozzle Configurations :** Figure 2.4-9 compares axial static pressure distributions on the hard-walled and porous plugs between the hot and cold flow rows for 0.5"-thick fluid shield nozzle at the shielded side. Figure 2.4-9 includes the comparisons for two flow conditions. There is no appreciable difference in plug static

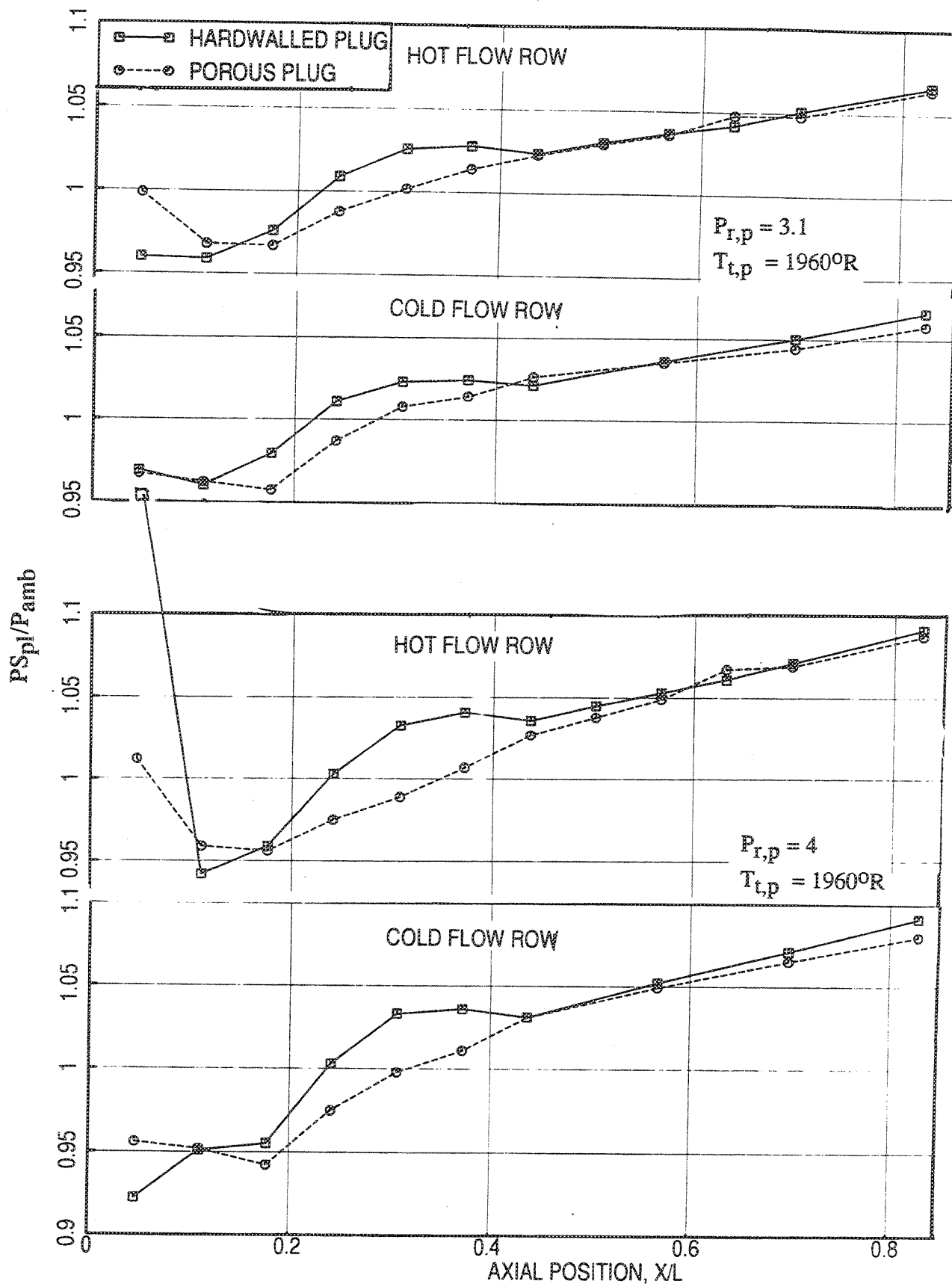


Figure 2.4-4. Effect of porous plug compared to hardwalled plug on plug axial static pressure distributions for the suppressor alone configurations at static condition.

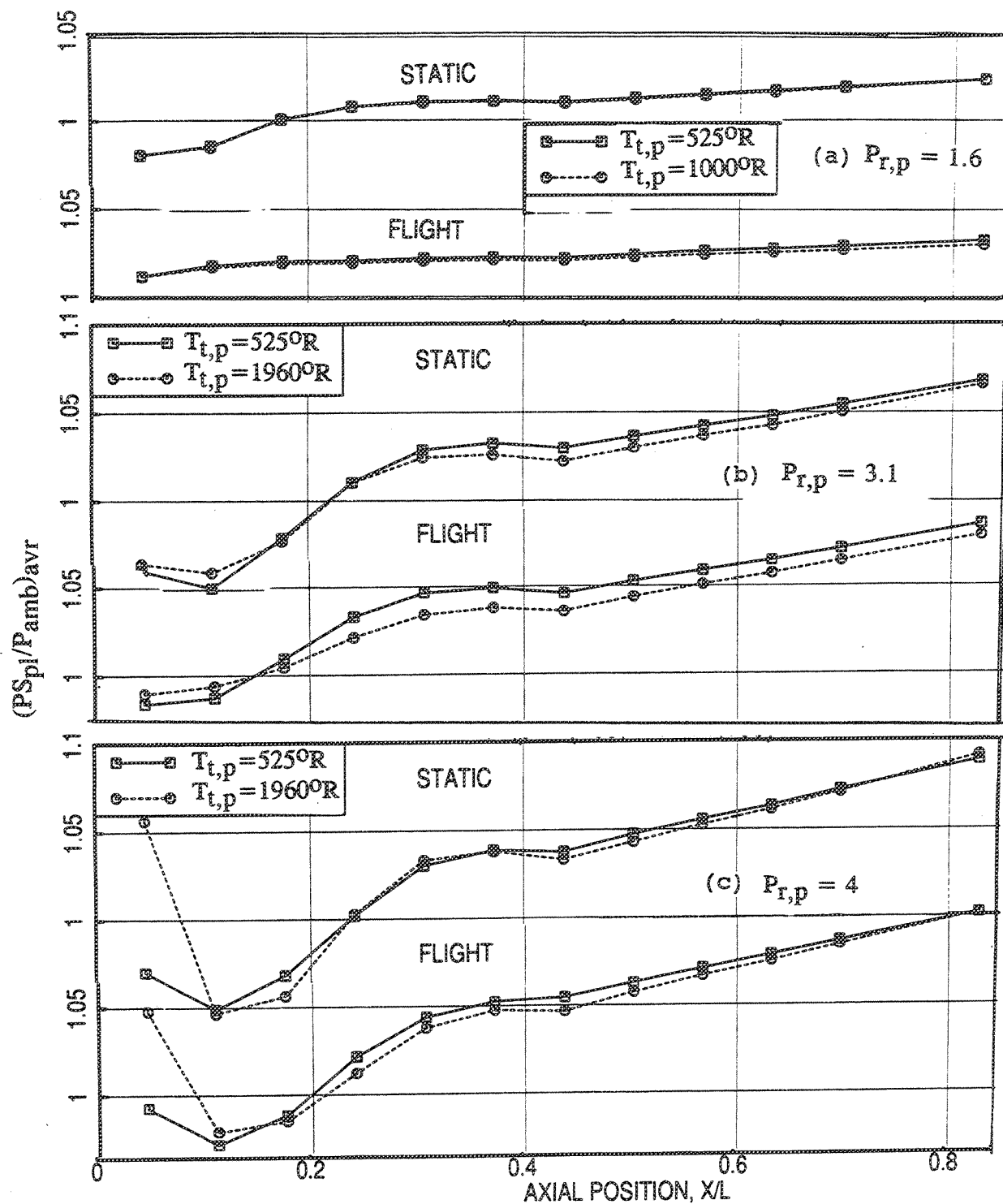


Figure 2.4-5. Effect of nozzle total temperature on axial average static pressure distribution on the hard-walled plug attached to the 36-chute suppressor with ( $M_F=0.32$ ) and without flight simulation.

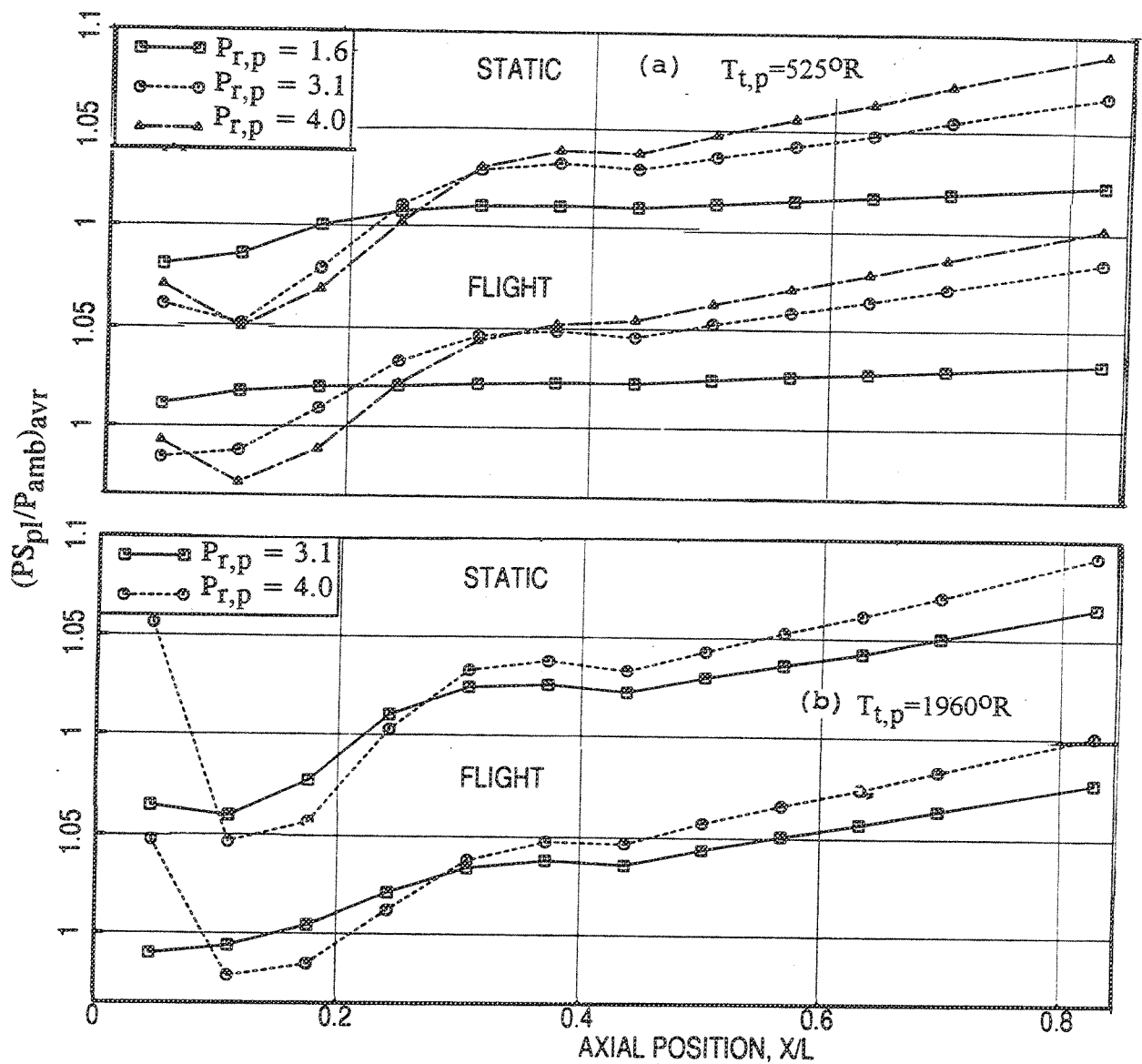


Figure 2.4-6. Effect of nozzle pressure ratio on axial average static pressure distribution on the hard-walled plug attached to the 36-chute suppressor with ( $M_F=0.32$ ) and without flight simulation.



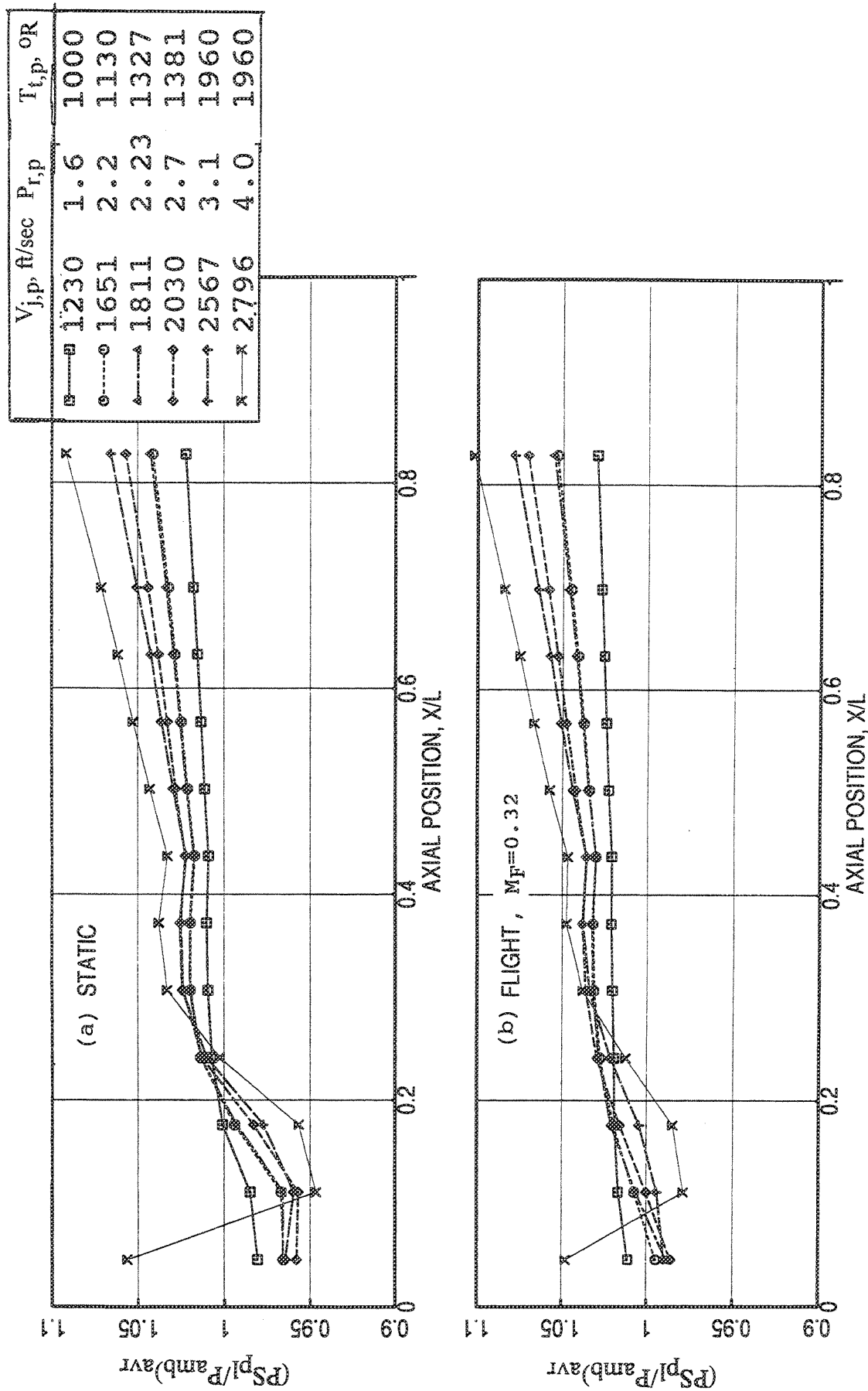


Figure 2.4-7. Effect of jet velocity on axial average static pressure distribution on the hard-walled plug attached to the 36-chute suppressor with ( $M_F=0.32$ ) and without flight simulation.

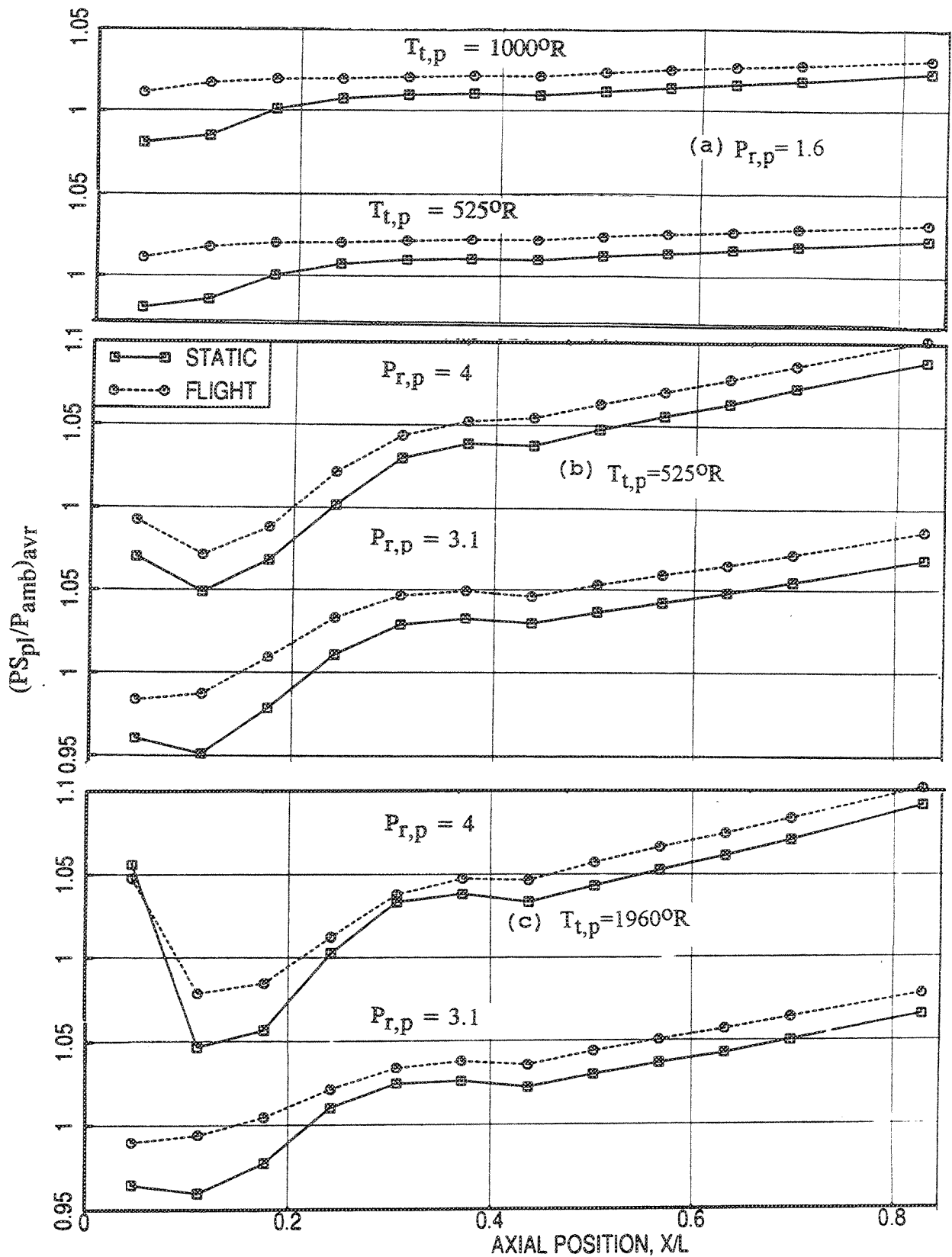


Figure 2.4-8. Effect of simulated flight ( $M_F=0.32$ ) on axial average static pressure distribution on the hard-walled plug attached to the 36-chute suppressor.

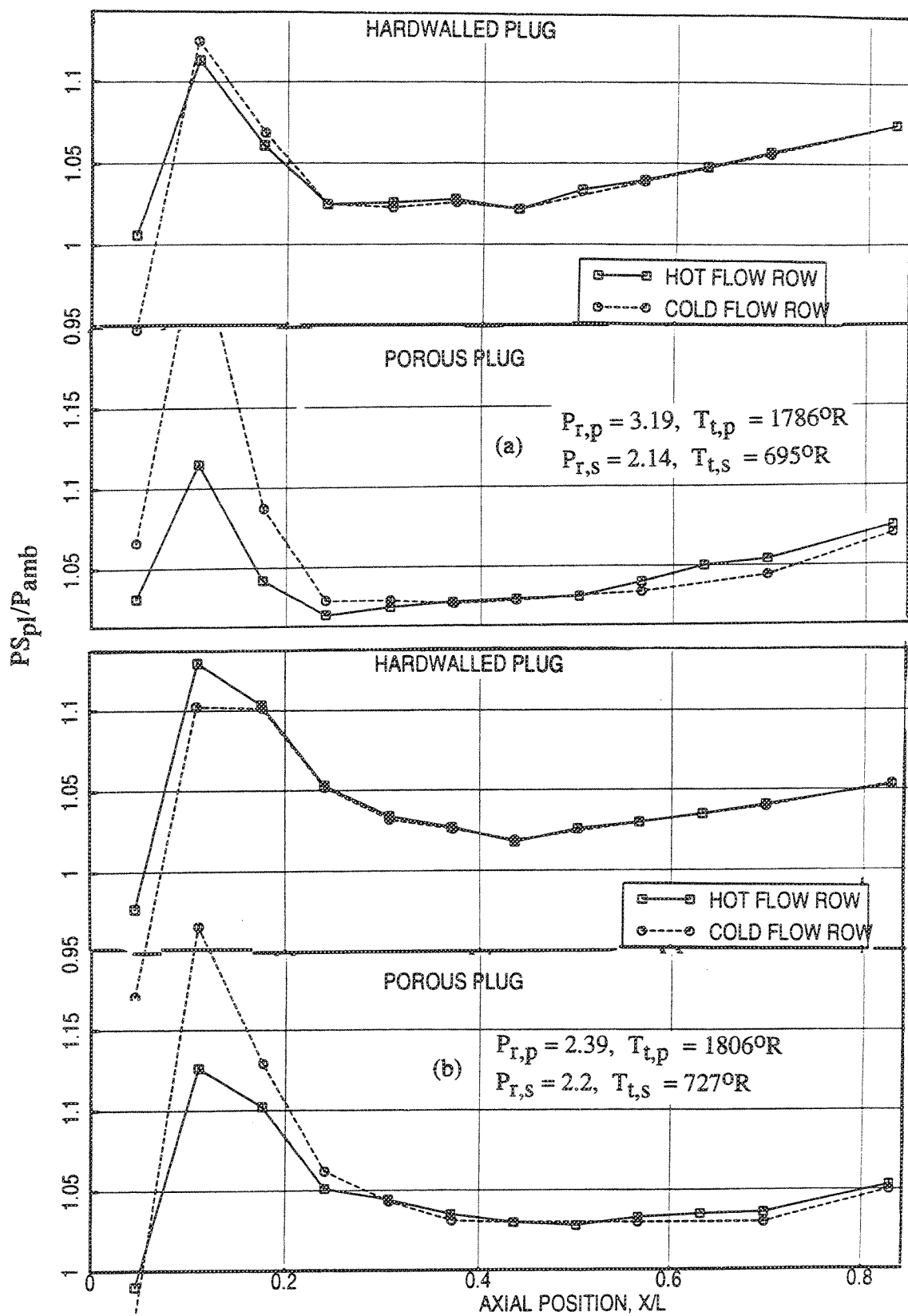


Figure 2.4-9. Comparison of axial static pressure distributions along the hot flow row with those along the cold flow row on the porous plug attached to the 0.5"-thick, 220° wrap fluid shield nozzle at static condition.

pressure distributions between hot and cold flow rows for hardwalled plug, however, a significant difference is observed for porous plug close to the suppressor exit. The difference in the axial plug pressure distributions between suppressor alone and fluid shield nozzle is observed close to the nozzle exit (see Figures 2.4-3 and 2.4-9). While the static pressure drops initially and then increases along the plug surface for the suppressor, the trend is reversed in the presence of fluid shield.

The influence of porous plug is demonstrated in Figure 2.4-10 by comparing the pressure distributions between hardwalled and porous plugs for both hot and cold flow rows. There is very little difference in plug pressure distribution in the hot flow row between hardwalled and porous plugs. Higher static pressure levels occur for porous plug close to the nozzle exit plane along cold flow row. There is no difference in plug pressure distributions beyond  $X/L=0.2$ .

Effect of fluid shield thickness on plug pressure distribution is shown in Figure 2.4-11 for different aero thermodynamic conditions. Static pressure seems to decrease slightly with shield thickness close to the exit plane. However, the trend is reversed beyond  $X/L=0.15$ , that the static pressure increases with shield thickness and finally becomes the same for all thicknesses at the plug tip.

*Effect of Parametric Variations:* Effect of velocity and mass flow ratios (i.e.,  $V_r$  and  $W_r$ ) on plug static pressure distributions, shown in Figure 2.4-12 for 0.5"-thick shield, indicates pressure increase with these ratios for fixed  $V_{mix}$  for most of the plug length. The velocity and mass flow ratios are derived by varying the primary and secondary stream nozzle pressure ratios. While the  $P_{r,s}$  is varied considerably the magnitude of  $P_{r,p}$  for a fixed  $V_{mix}$  is almost constant. Hence, the plug pressure variation observed in this figure is also the effect of secondary flow nozzle pressure ratio. Similar results are obtained for 0.75"- and 1.0"-thick fluid shield nozzles.

Effect of other aero thermodynamic parameters, namely, secondary stream total temperature  $T_{t,s}$ , primary stream nozzle pressure ratio  $P_{r,p}$  and total temperature  $T_{t,p}$ , on plug pressure distribution are shown in Figures 2.4-13 through 2.4-15, respectively. Slight increase in static pressure is observed due to increasing  $T_{t,s}$ . The effect of  $P_{r,p}$  (see Figure 2.4-14) is relatively significant due to higher acceleration and subsequent recompression. The static pressure increases with  $P_{r,p}$  close to the plug crown and

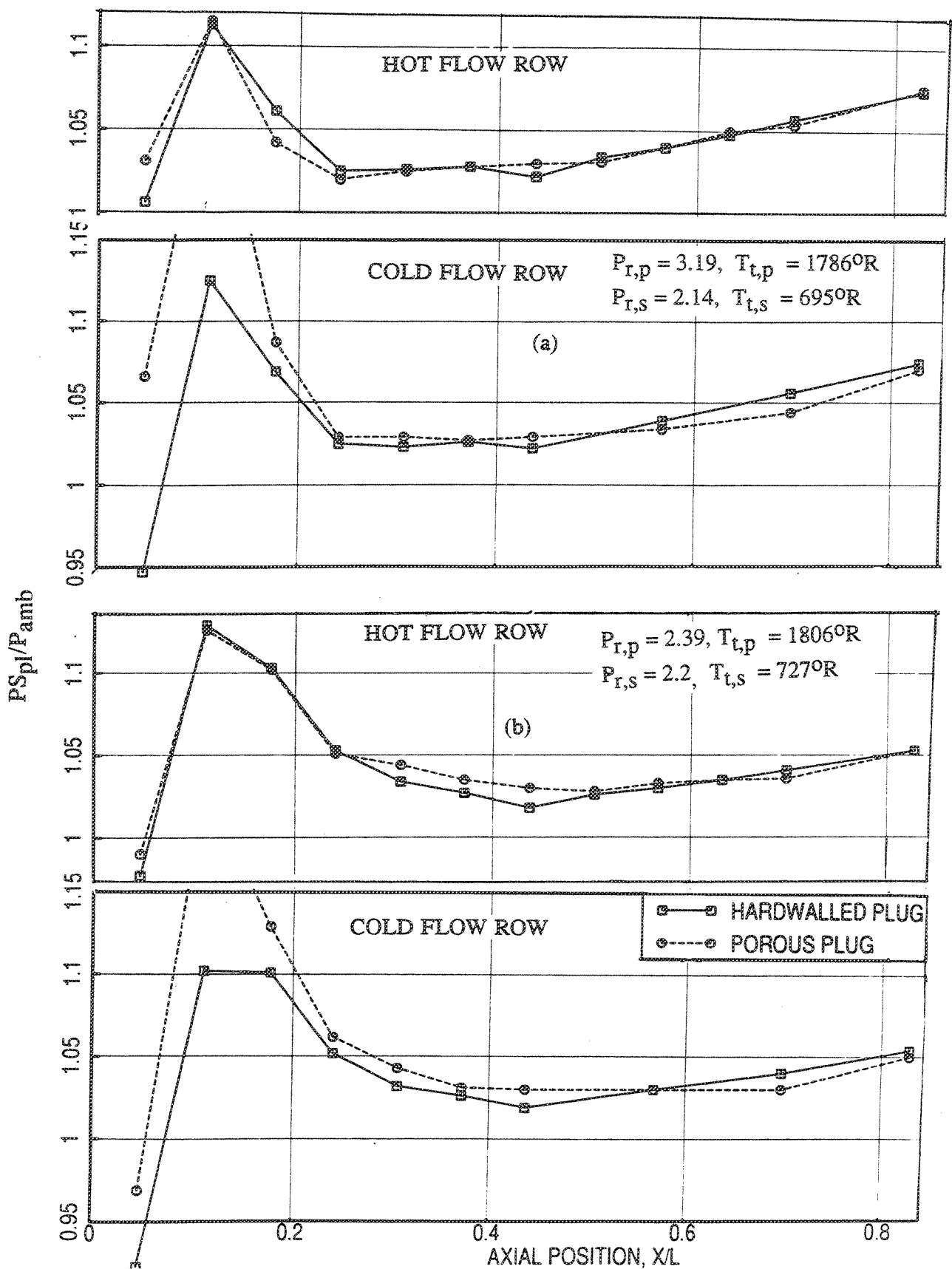


Figure 2.4-10. Effect of porous plug compared to hardwalled plug on plug axial static pressure distributions for 0.5"-thick, 220° wrap fluid shield nozzle configurations at static condition.

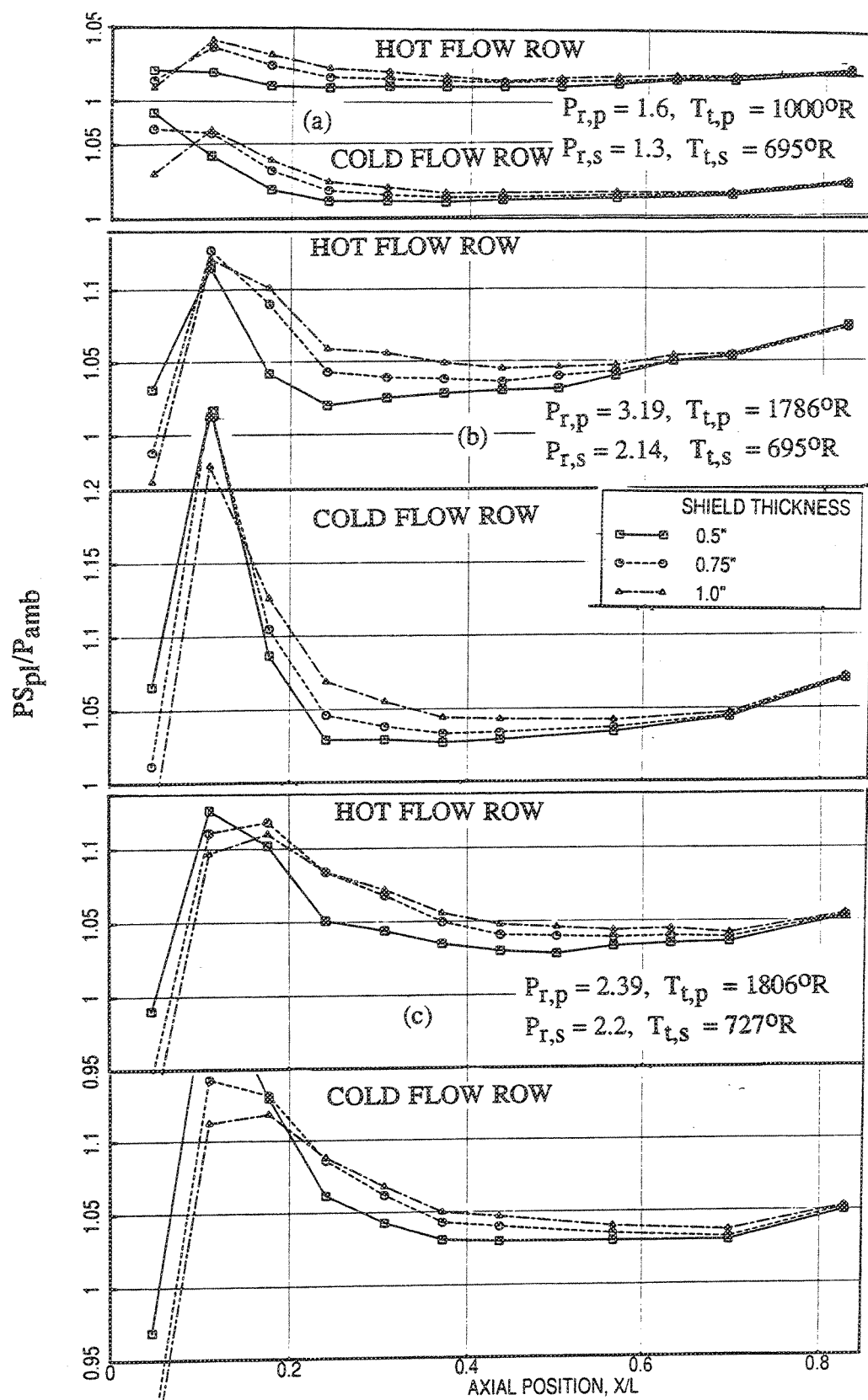


Figure 2.4-11. Effect of shield thickness on plug axial static pressure distributions for 2200 wrap fluid shield nozzle configurations with porous plug at static condition.

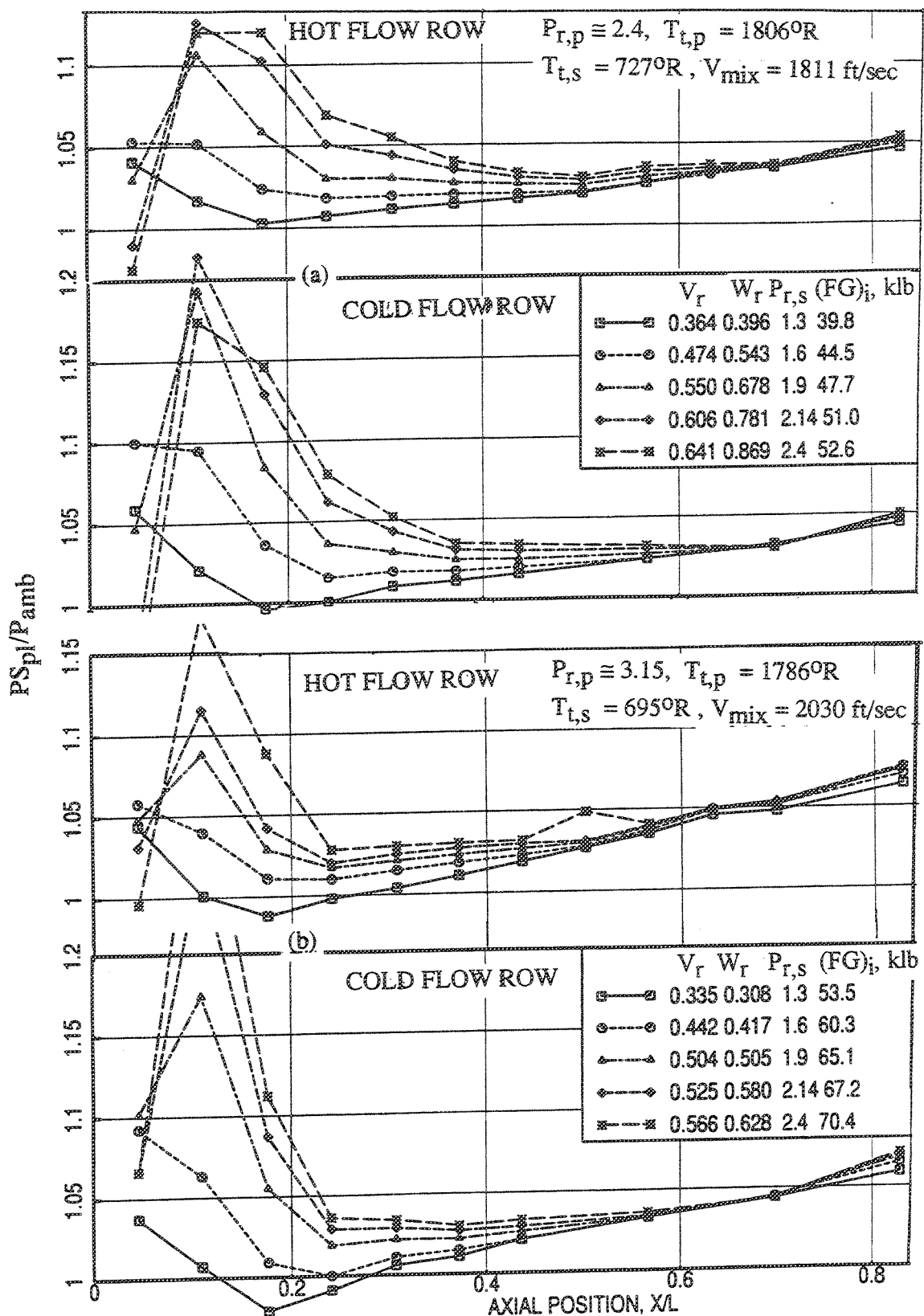


Figure 2.4-12. Effect of velocity ratio (or mass flow ratio) on plug axial static pressure distributions for 0.5"-thick, 220° wrap fluid shield nozzle with porous plug at static condition.

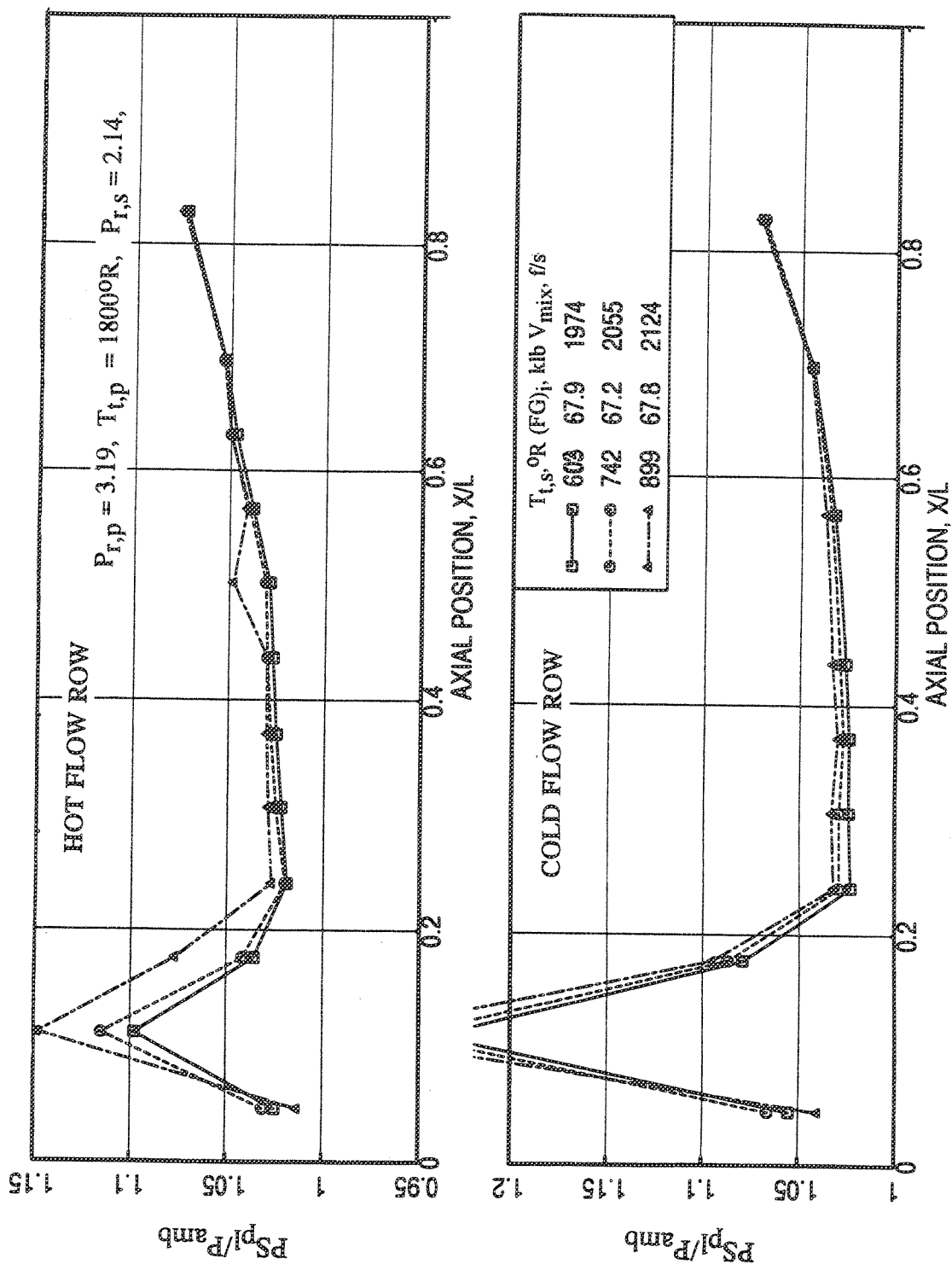


Figure 2.4-13. Effect of flade stream total temperature ( $T_{t,s}$ ) on plug axial static pressure distributions for 0.5"-thick, 220° wrap fluid shield nozzle with porous plug at static condition.



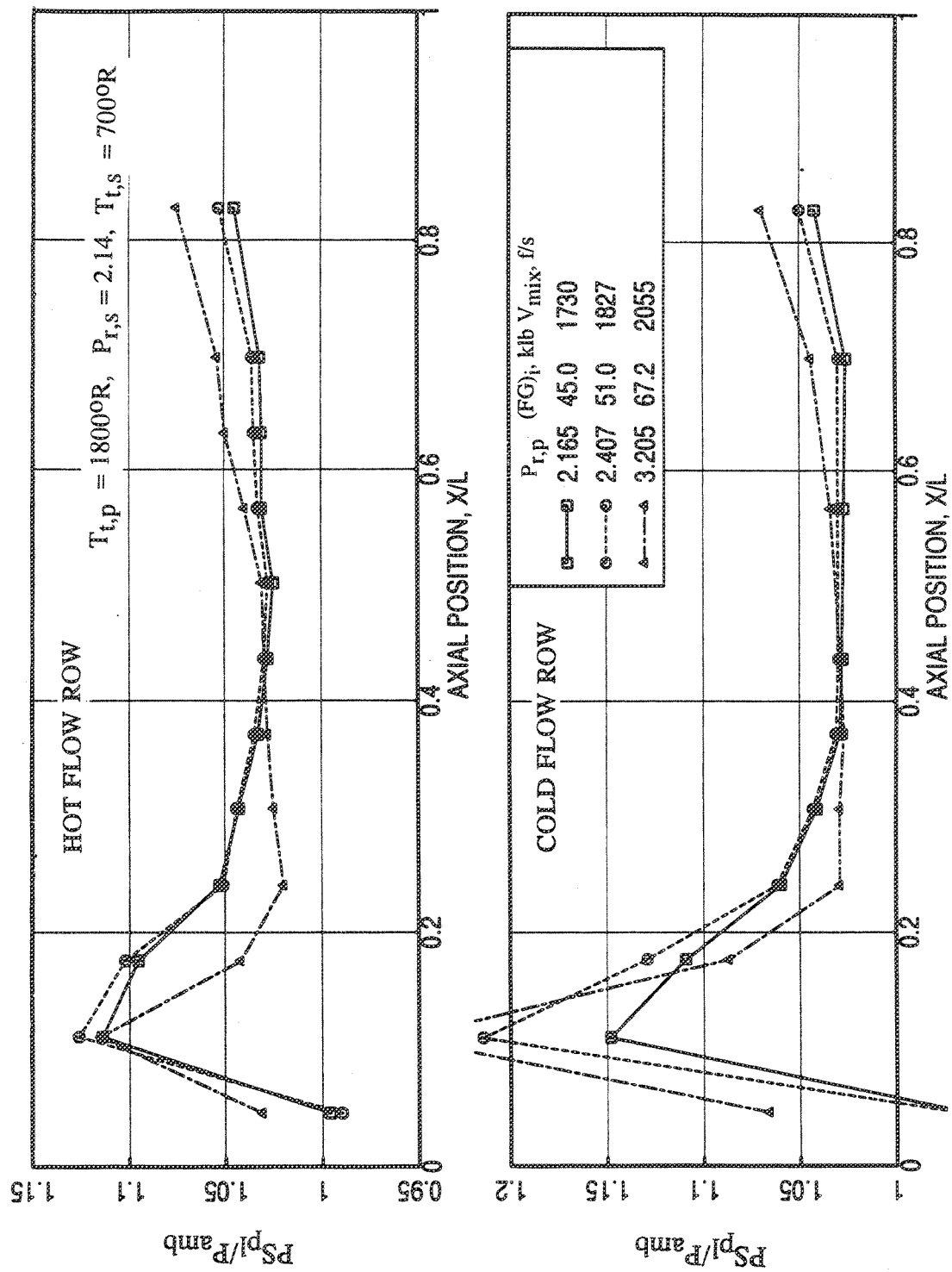


Figure 2.4-14. Effect of core stream pressure ratio ( $P_{r,p}$ ) on plug axial static pressure distributions for 0.5"-thick, 2200 wrap fluid shield nozzle with porous plug at static condition.

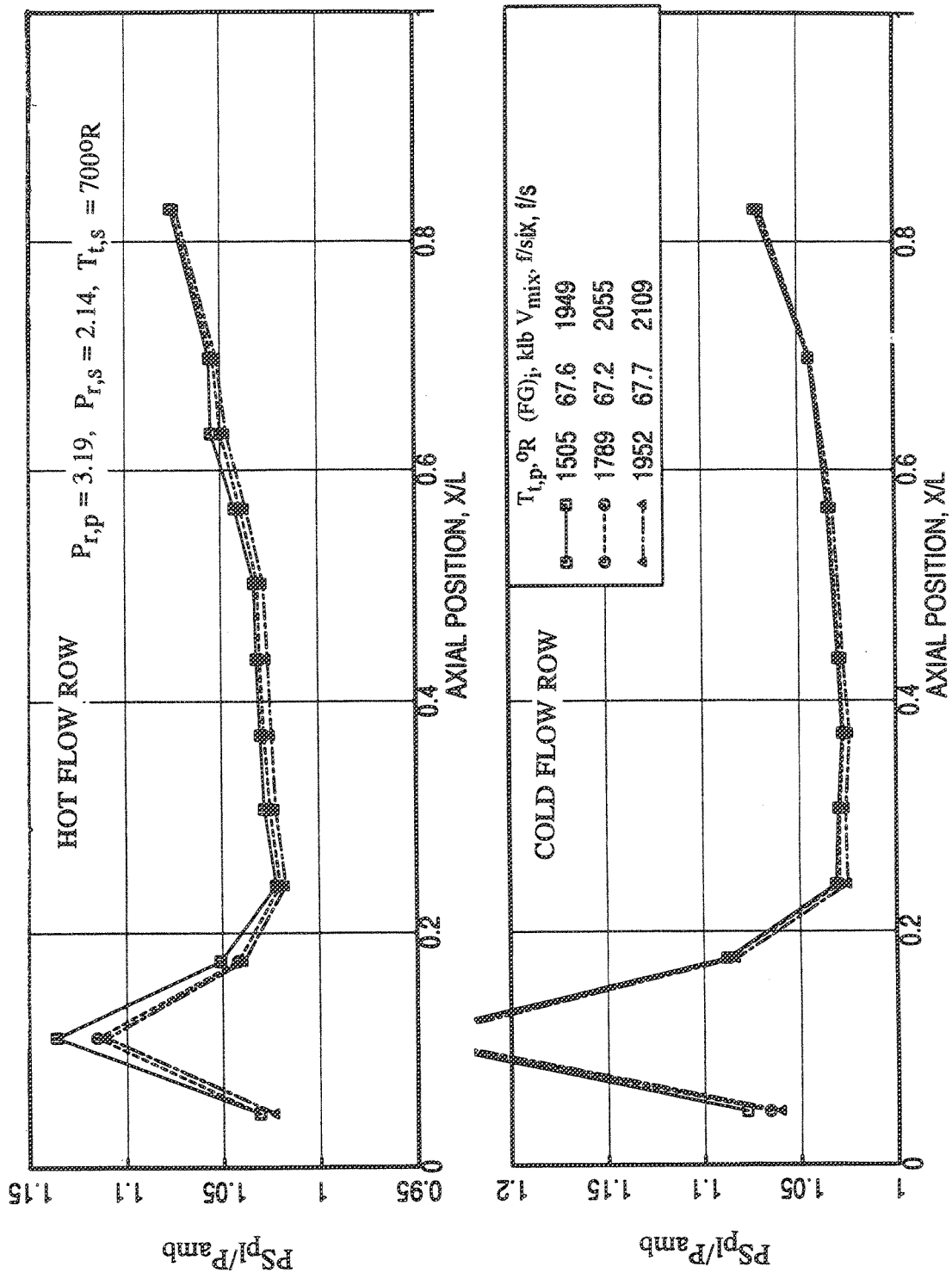


Figure 2.4-15. Effect of core stream total temperature ( $T_{t,p}$ ) on plug axial static pressure distributions for 0.5"-thick, 220° wrap fluid shield nozzle with porous plug at static condition.

towards the tip (i.e., for  $X/L > 0.4$ ). The trend is reversed in the middle. The effect of  $T_{t,p}$  is small and that the pressure decreases with increasing  $T_{t,p}$ .

The effect of flight is similar to what is observed for suppressor alone configuration, in that the static pressure levels are higher on the plug with flight simulation compared to static cases.

### 2.4.3 Base Pressure Distribution on Chutes

**Suppressor Alone Configuration :** For suppressor alone configurations an average of shielded and unshielded side chute-base static pressure distributions,  $PS_{ch}/P_{amb})_{avr}$  is utilized, since there was no fluid shield for these configurations. The chute base pressure increases slightly for the static case with flow temperature for the upper half of the chutes (i.e., between  $R/R_{CO}=0.85$  and  $R/R_{CO}=1$ ), as shown in Figure 2.4-16. Close to hub the effect of temperature on chute base pressure does not show any definite trend. The temperature effect is more prominent with flight simulation. The static pressure levels decrease with increasing nozzle pressure ratio for entire chute surface (see Figure 2.4-17). For higher nozzle pressure ratios the core flow accelerates more at the chute exit and, therefore, potentially entrains more ambient air through the chutes. Increased ambient flow increases the velocity and reduces the static pressure.

As shown in Figure 2.4-18, the static pressure levels decrease with increasing jet velocity for entire chute radial surface. However, with flight simulation the trend seems to be reversed close to chute root. Dominant static pressure reduction is observed (see Figure 2.4-19) due to flight simulation on entire chute surface for all test conditions. Flight simulation prevents entrainment of ambient air in to the chutes. This creates a partial vacuum in the chutes (i.e., lower base pressure), more dominantly at the hub, and therefore, considerable pressure drop is experienced on the chute surfaces. The geometry of chute leading edge is such that the freejet needs to negotiate a sharp turn of  $55^\circ$  (since chute leading edge angle is  $35^\circ$  to the vertical) to fill the chutes. Hence, in all likelihood, freejet stream separates as it flows over the chutes, which results in lower chute base pressure. This has been explained in section 2.3 utilizing shadowgraph results also.

**Fluid Shield Nozzle Configurations :** A typical example of the effect of shield flow on the chute pressure distribution is shown in Figure 2.4-20. Comparison of static pressure distributions between shielded and unshielded chute demonstrates dominant

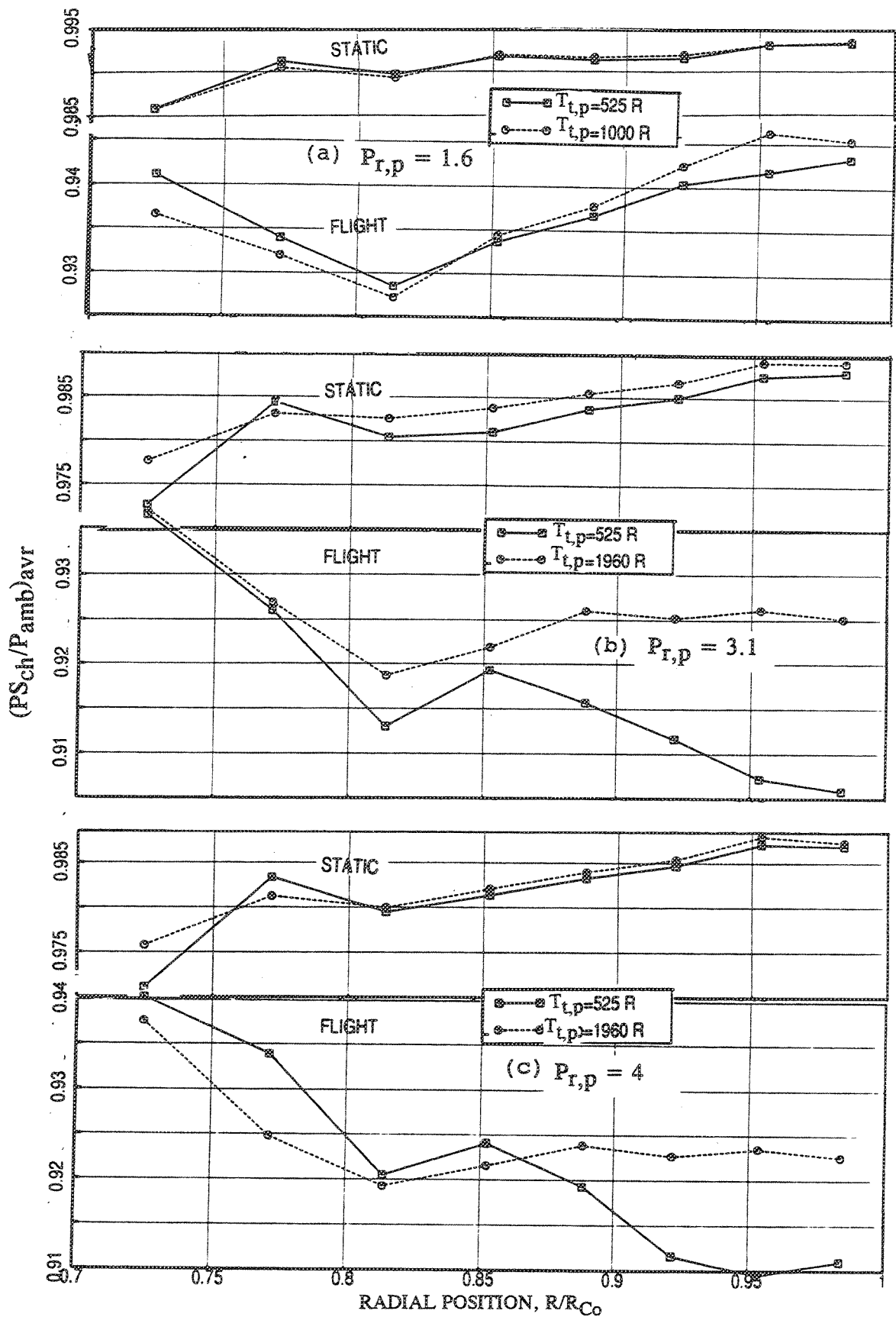


Figure 2.4-16. Effect of nozzle total temperature on radial static pressure distribution on suppressor chute for the 36-chute suppressor with hard-walled plug configuration, with ( $M_F=0.32$ ) and without flight simulation.

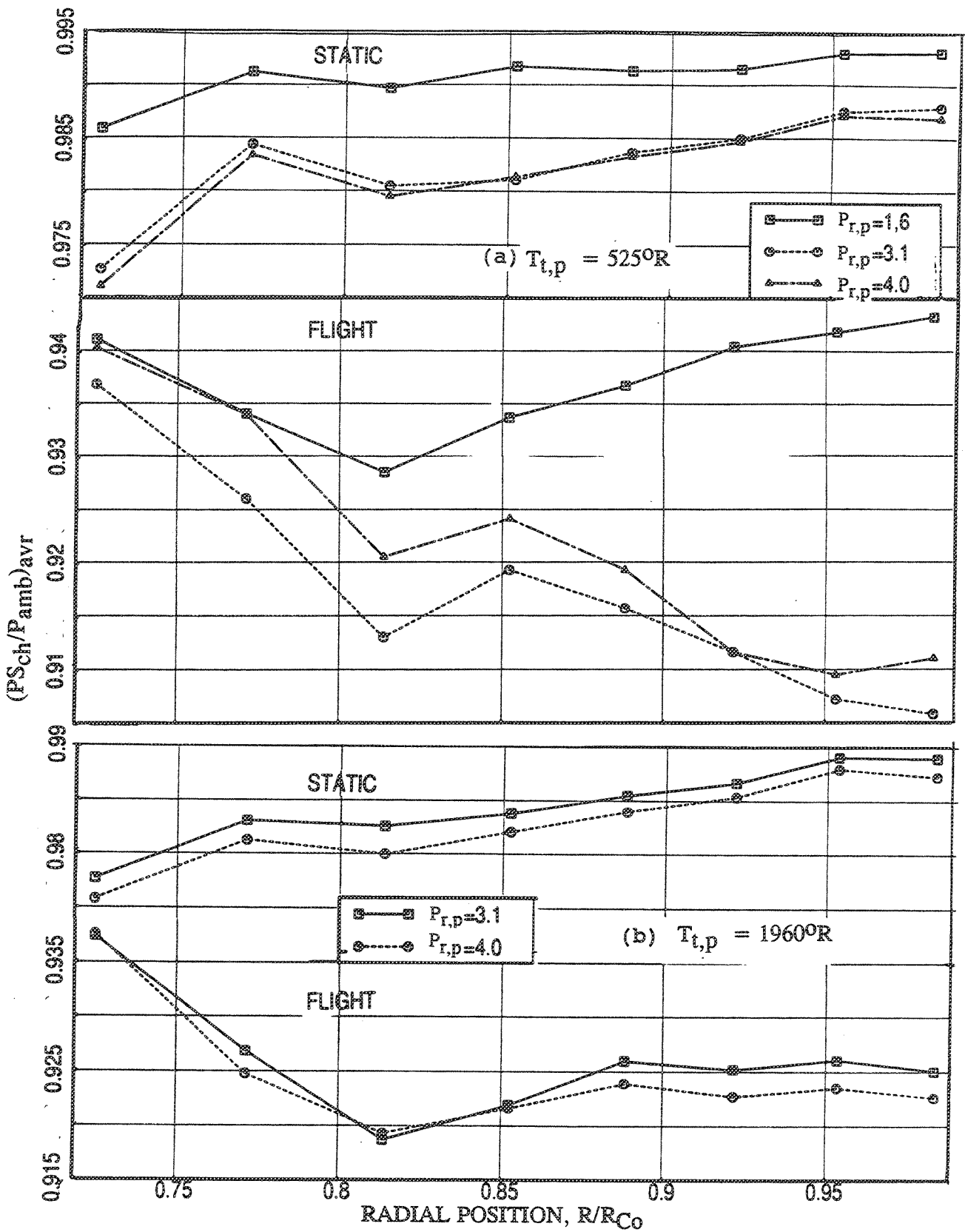


Figure 2.4-17. Effect of nozzle pressure ratio on radial static pressure distribution on suppressor chute for the 36-chute suppressor with hard-walled plug configuration, with ( $M_F=0.32$ ) and without flight simulation.

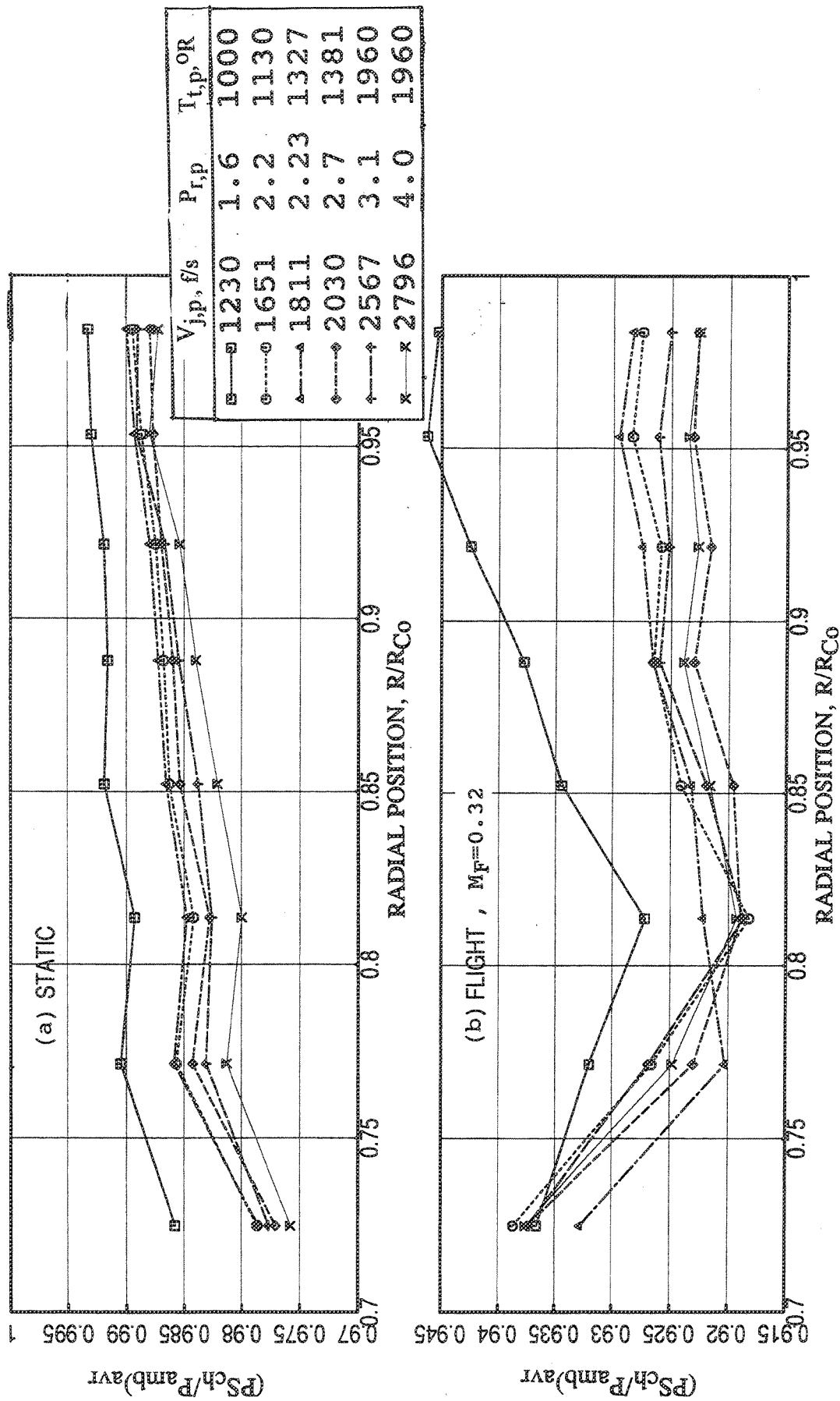


Figure 2.4-18. Effect of jet velocity on radial static pressure distribution on suppressor chute for the 36-chute suppressor with hard-walled plug configuration, with ( $M_F=0.32$ ) and without flight simulation.

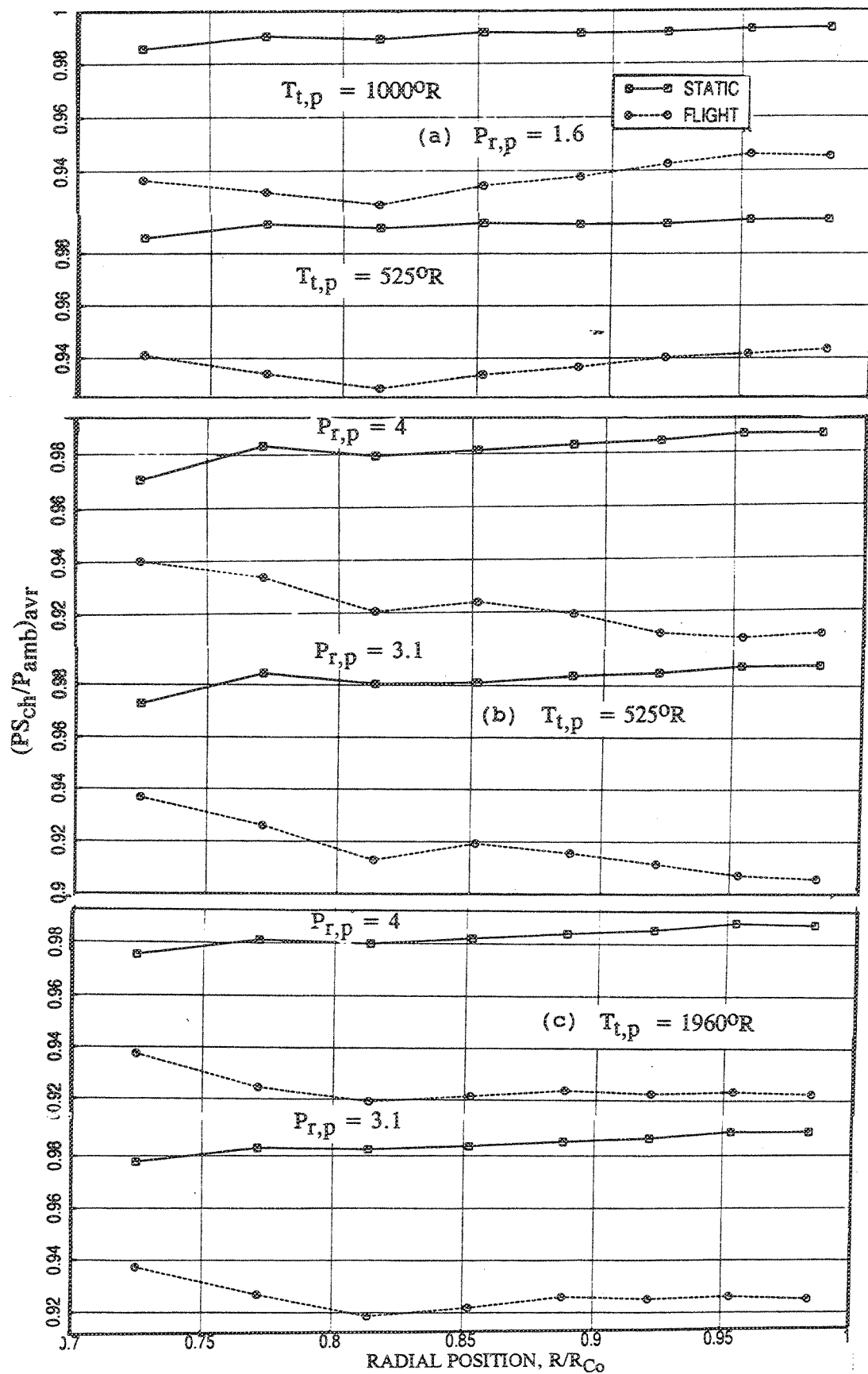


Figure 2.4-19. Effect of simulated flight ( $M_F=0.32$ ) on radial static pressure distribution on suppressor chute for the 36-chute suppressor with hard-walled plug configuration.

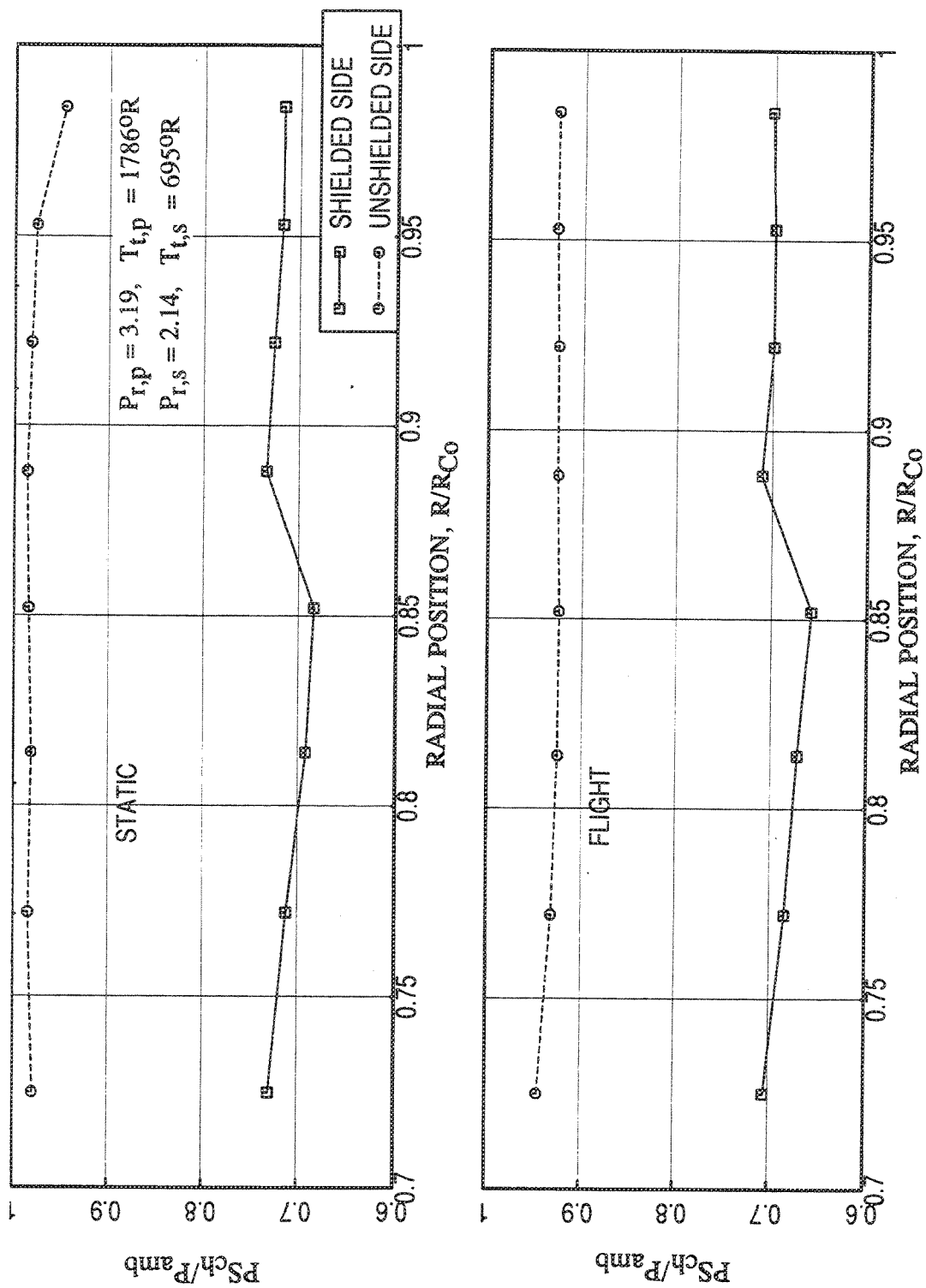


Figure 2.4-20. Effect of fluid shield on radial static pressure distribution on suppressor chutes for 0.5"-thick, 220° wrap fluid shield nozzle with porous plug.



static pressure drop due to shield flow from hub to tip. Shield flow prevents entrainment of ambient air in to the chutes in a manner similar to the freejet, may be more so, which creates a partial vacuum in the chutes (i.e., lower base pressure), and therefore, considerable pressure drop is experienced on the chute surfaces. The effect of flight simulation, as demonstrated in Figure 2.4-20, is to reduce the static pressure further more. The effect of freejet in reducing chute base pressure is more evident on the unshielded case compared to the shielded case, since the fluid shield "insulates" the chutes from "seeing" the freejet on the shielded case, to some extent.

The effect of fluid shield thickness on the chute static pressure is examined in Figure 2.4-21. The radial static pressure distributions on the shielded and unshielded chutes are plotted in this figure for different aero thermodynamic conditions. Static pressure reduces with increasing shield thickness for all cases on shielded chutes. As expected, the effect of shield thickness is virtually absent on the unshielded chutes, except near the tip.

*Effect of Parametric Variations:* Effect of velocity and mass flow ratios (i.e.,  $V_r$  and  $W_r$ ) on chute static pressure distributions, shown in Figure 2.4-22 for 0.5"-thick shield, indicates decreasing pressure with increasing  $V_r$  (or  $W_r$ ) for fixed  $V_{mix}$  on shielded chutes. Pressure distribution on unshielded chutes are unaffected by velocity or mass flow ratios. Since the secondary stream pressure ratio varies with velocity and mass flow ratios, the chute pressure variations observed in Figure 2.4-22 are principally influenced by the shield nozzle pressure ratio. Similar results are obtained for 0.75"- and 1.0"-thick fluid shield nozzles.

Effect of other aero thermodynamic parameters, namely, secondary stream total temperature  $T_{t,s}$ , primary stream nozzle pressure ratio  $P_{r,p}$  and total temperature  $T_{t,p}$ , on chute pressure distribution are shown in Figure 2.4-23. Slight decrease in static pressure on shielded chutes and no effect on unshielded chutes are observed due to increasing  $T_{t,s}$ . The effect of  $P_{r,p}$  is relatively significant on shielded chutes in that the static pressure decreases with  $P_{r,p}$  probably due to overexpansion of the primary flow into secondary flow passage downstream of the chute exit, thereby hindering entrainment of secondary stream. There is no effect of primary nozzle pressure ratio on unshielded chutes. The effect of  $T_{t,p}$  is small on shielded chutes and that the pressure increases with increasing  $T_{t,p}$ . However, the static pressure on unshielded chutes are unaffected by  $T_{t,p}$ .

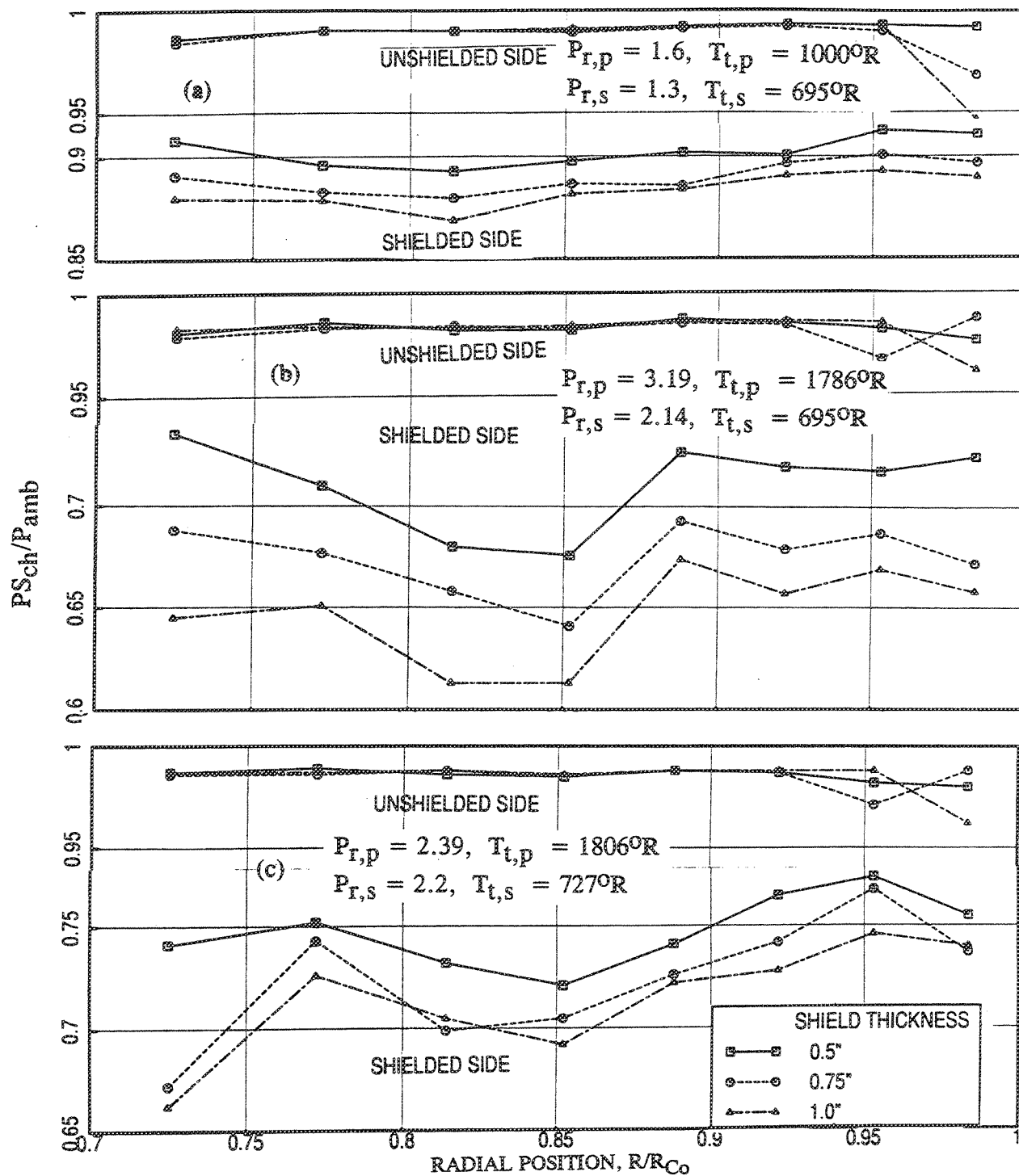


Figure 2.4-21. Effect of shield thickness on chute radial static pressure distributions for 220° wrap fluid shield nozzle configurations with porous plug at static condition.

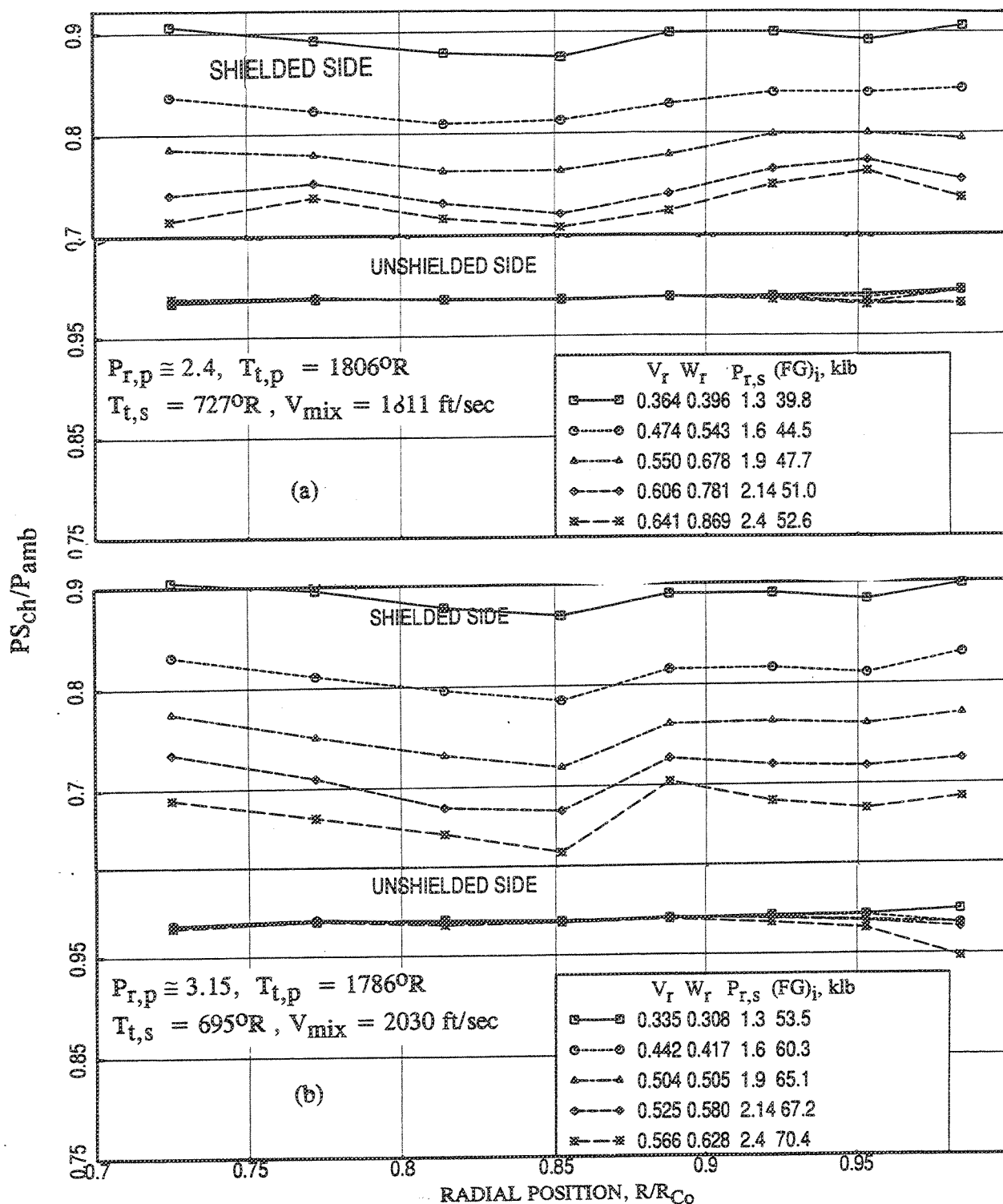


Figure 2.4-22. Effect of velocity ratio (or mass flow ratio) on chute radial static pressure distributions for 0.5"-thick, 220° wrap fluid shield nozzle with porous plug at static condition.

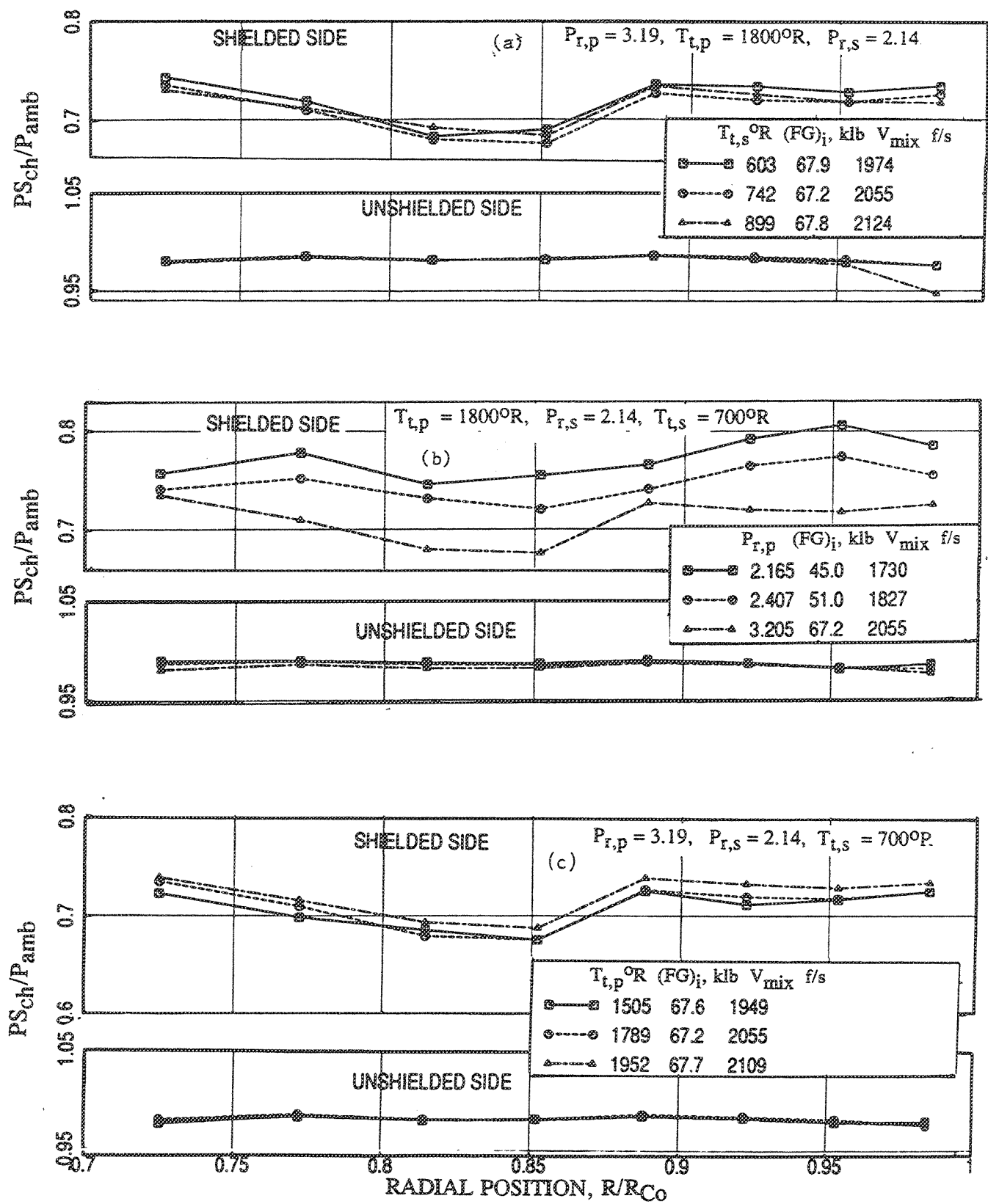


Figure 2.4-23. Effect of (a) flade stream total temperature ( $T_{t,s}$ ), (b) core stream pressure ratio ( $P_{r,p}$ ), and (c) core stream total temperature ( $T_{t,p}$ ) on chute radial static pressure distributions for 0.5"-thick, 220° wrap fluid shield nozzle with porous plug at static condition.

#### 2.4.4 Contribution of Plug Static Pressure and Chute Base Drag to Specific Gross Thrust Coefficient ( $\Delta C_{fg}$ )

Since force balance data is not available in Cell 41, chute base pressures and plug static pressure distributions are utilized to compute their contributions to axial drag/thrust by area integration and these forces are normalized by ideal gross thrust to yield a  $\Delta C_{fg}$  as % of ideal gross thrust. The static pressure distributions on the plug and the suppressor chutes relative to ambient pressure contribute force either in the direction of drag or in the direction of thrust. This contribution, as described earlier, is expressed in terms of a correction factor to the gross thrust coefficient ( $\Delta C_{fg}$ ) in % of ideal gross thrust. These  $\Delta C_{fg}$  factors are plotted as functions of primary nozzle pressure ratio for the suppressor alone configuration and mixed pressure ratio ( $P_{r,mix}$ ) for fluid shield nozzle configurations for cycle conditions, which seem to be the most influencing parameter on static pressure distributions on the plug and chute surfaces. For parametric study the  $\Delta C_{fg}$  is plotted with respect to the individual aero thermodynamic parameters.

**Suppressor Alone Configuration with Hardwalled Plug :** Figure 2.4-24 shows the variation of different components of  $\Delta C_{fg}$  with respect to nozzle pressure ratio with and without flight simulation. As observed earlier the pressure difference between hot and cold rows on the plug is very small, which resulted in insignificant difference on  $\Delta C_{fg}$  of the plug on hot and cold flow region basis. Effect of nozzle pressure ratio on  $\Delta C_{fg}$  is very little for static cases, however, is significant with flight simulation. In this situation ( $\Delta C_{fg}$ )<sub>pa</sub> (i.e., for the plug) decreases and ( $\Delta C_{fg}$ )<sub>ca</sub> (i.e., for the chutes) increases with respect to nozzle pressure ratio.

The reason why the absolute value of  $\Delta C_{fg}$  (i.e., plug thrust or chute base drag) decreases with nozzle pressure ratio is as follows: Although the chute base pressure and plug static pressure distributions change somewhat with nozzle pressure ratio, total value of plug thrust and chute base drag change slowly compared to the increase in gross ideal thrust level  $((FG)_i)$  with nozzle pressure ratio. The noted trend of  $\Delta C_{fg}$  with nozzle pressure ratio is thus explained, since the denominator (i.e.,  $(FG)_i$ ) is increasing rapidly compared to the numerator (i.e., chute base drag or plug thrust) with respect to nozzle pressure ratio.

The ( $\Delta C_{fg}$ )<sub>pa</sub> (i.e., for plug) is positive for all nozzle pressure ratio with and without flight simulation. The chute force contribution is always negative and is higher in

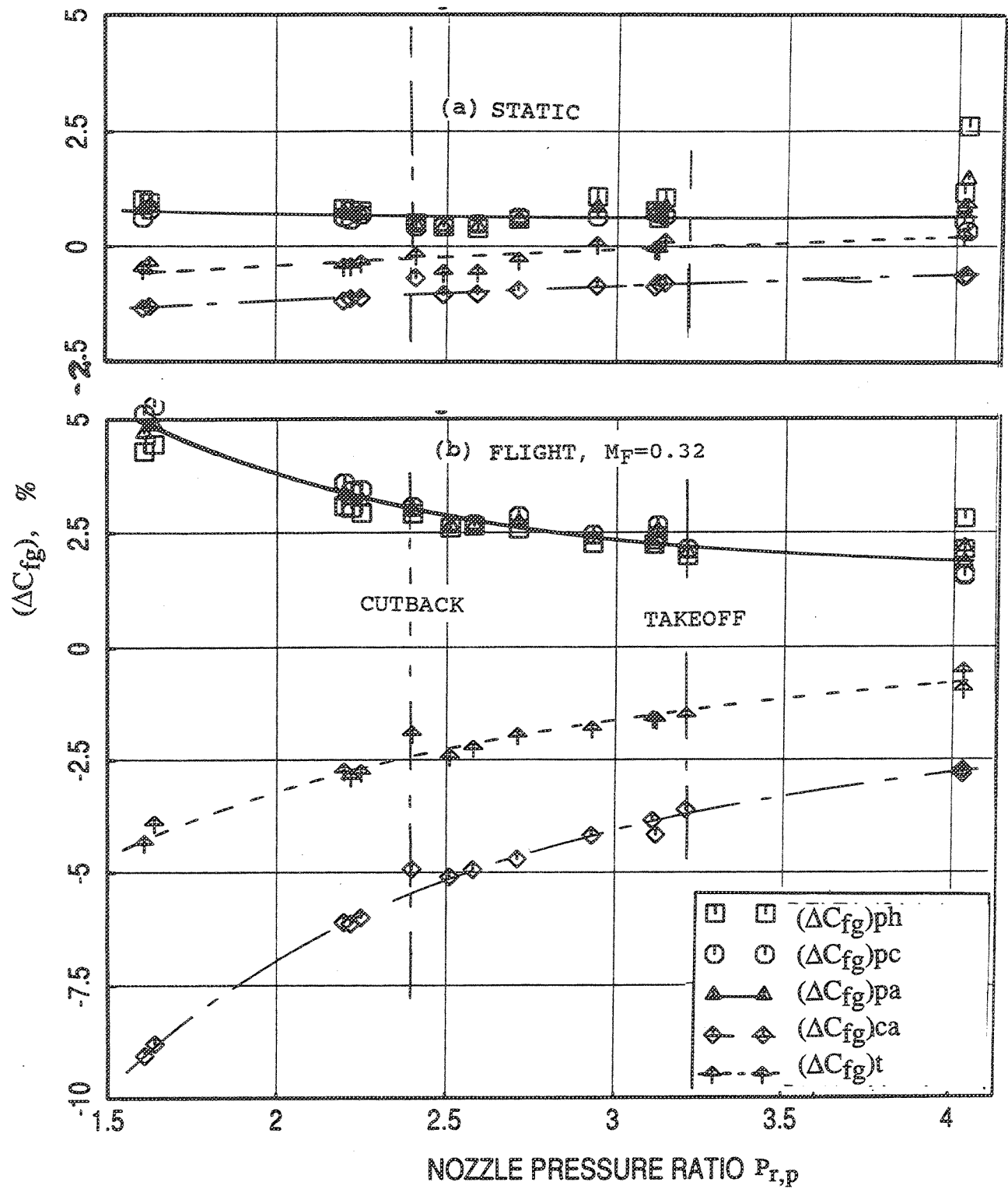


Figure 2.4-24. Correction to gross thrust coefficient ( $\Delta C_{fg}$ ) as a function of nozzle pressure ratio due to hard-walled plug and suppressor chutes for suppressor alone configuration.

magnitude for most cases. The combined correction to  $C_{fg}$  is close to zero for static case, but negative with flight simulation. However, with increasing nozzle pressure ratio  $(\Delta C_{fg})_t$  increases and is closer to zero for higher nozzle pressure ratio. As indicated in Figure 2.4-24 the  $(\Delta C_{fg})_t$  is about 0 % and -1.5 % at takeoff for static and with flight simulation, respectively. The corresponding values at cutback are -0.5 % and -2 % respectively.

Effect of flight simulation on  $\Delta C_{fg}$  is demonstrated in Figure 2.4-25. This  $\Delta C_{fg}$  factor increases for the plug and decreases for the chutes with flight simulation. The relative correction factor  $(\Delta C_{fg})_{f-s}$  is negative and increases with nozzle pressure ratio.

In conclusion, the hardwalled plug behaves favorably with respect to gross thrust coefficient, whereas, the chutes contribute adversely to  $C_{fg}$ . Flight simulation deteriorates the  $C_{fg}$  value. Higher nozzle pressure ratio is favorable to combined plug-chute thrust contribution.

Effect of porous plug on  $\Delta C_{fg}$  is demonstrated in Figure 2.4-26. For static condition  $\Delta C_{fg}$  is lower for porous plug compared to the hardwalled plug for entire range of nozzle pressure ratio. However, with flight simulation the difference of  $\Delta C_{fg}$  between hardwalled and porous plugs is very small and the  $\Delta C_{fg}$  for porous plug is slightly lower compared to hardwalled plug at higher nozzle pressure ratios. The trend is reversed at lower (i.e., below 2.75) nozzle pressure ratios.

**Fluid Shield Nozzle Configurations :** Effect of porous plug on  $\Delta C_{fg}$  for the 0.5"-thick fluid shield nozzle is depicted in Figure 2.4-27. For static condition  $\Delta C_{fg}$  is higher for porous plug compared to the hardwalled plug for entire range of mixed nozzle pressure ratio, which is opposite to the trend observed for the suppressor alone configuration. However, with flight simulation the difference of  $\Delta C_{fg}$  between hardwalled and porous plugs is reduced considerably and the trend is reversed, that the  $\Delta C_{fg}$  for porous plug is slightly lower compared to hardwalled plug.

The  $\Delta C_{fg}$  study for fluid shield nozzles discussed below are only for porous plug configurations. Figure 2.4-28 demonstrates the effect of shield thickness on  $\Delta C_{fg}$  for static condition. As per the plug contribution, the  $(\Delta C_{fg})_{pa}$  for 0.5"-thick fluid shield nozzle is much higher compared to the suppressor alone configuration. However, small decrease in  $(\Delta C_{fg})_{pa}$  is noticed with increasing shield thickness. The trend is

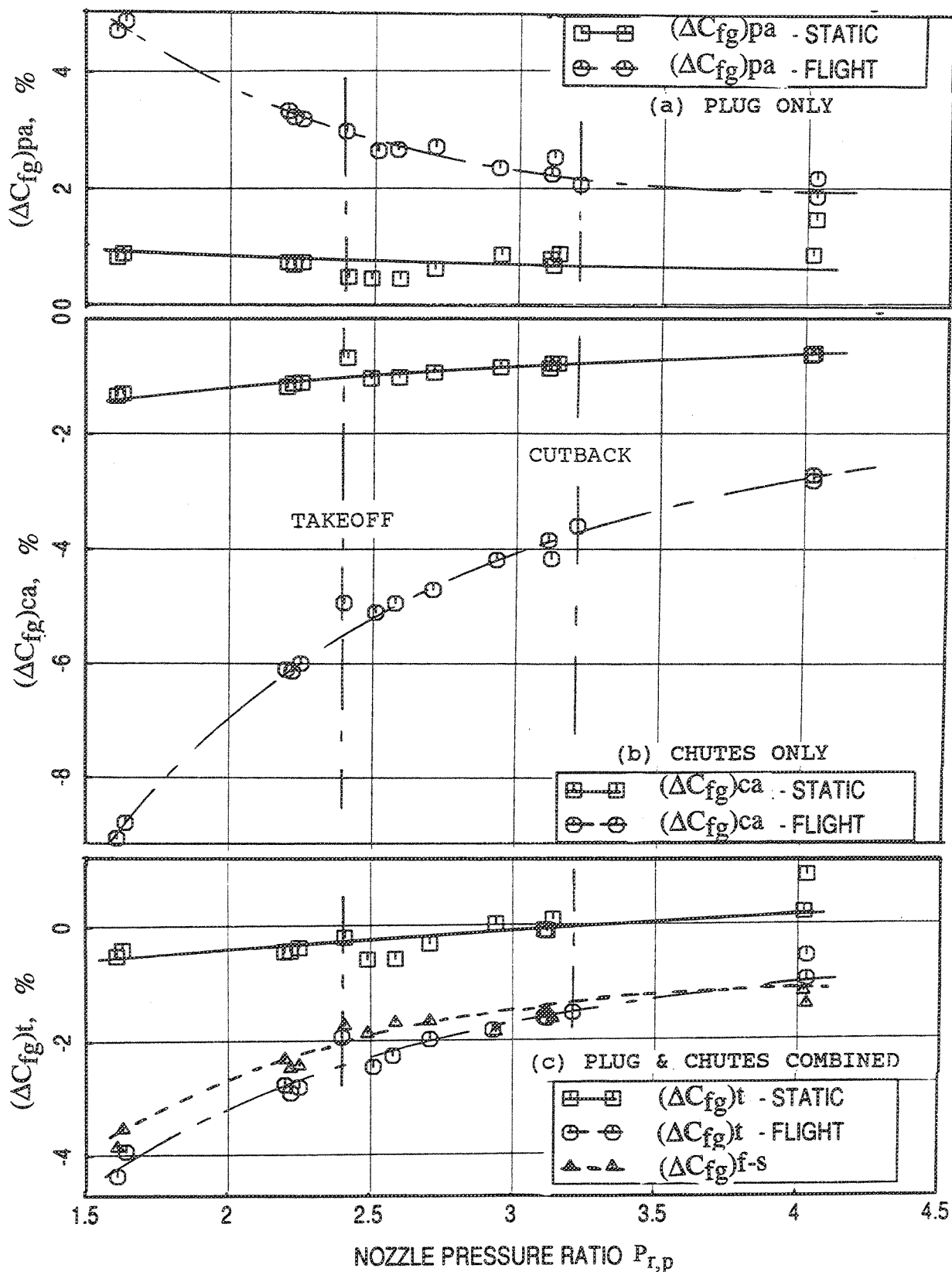


Figure 2.4-25. Effect of simulated flight ( $M_F=0.32$ ) on correction to gross thrust coefficient ( $\Delta C_{fg}$ ) as a function of nozzle pressure ratio due to hard-walled plug and suppressor chutes for suppressor alone configuration.



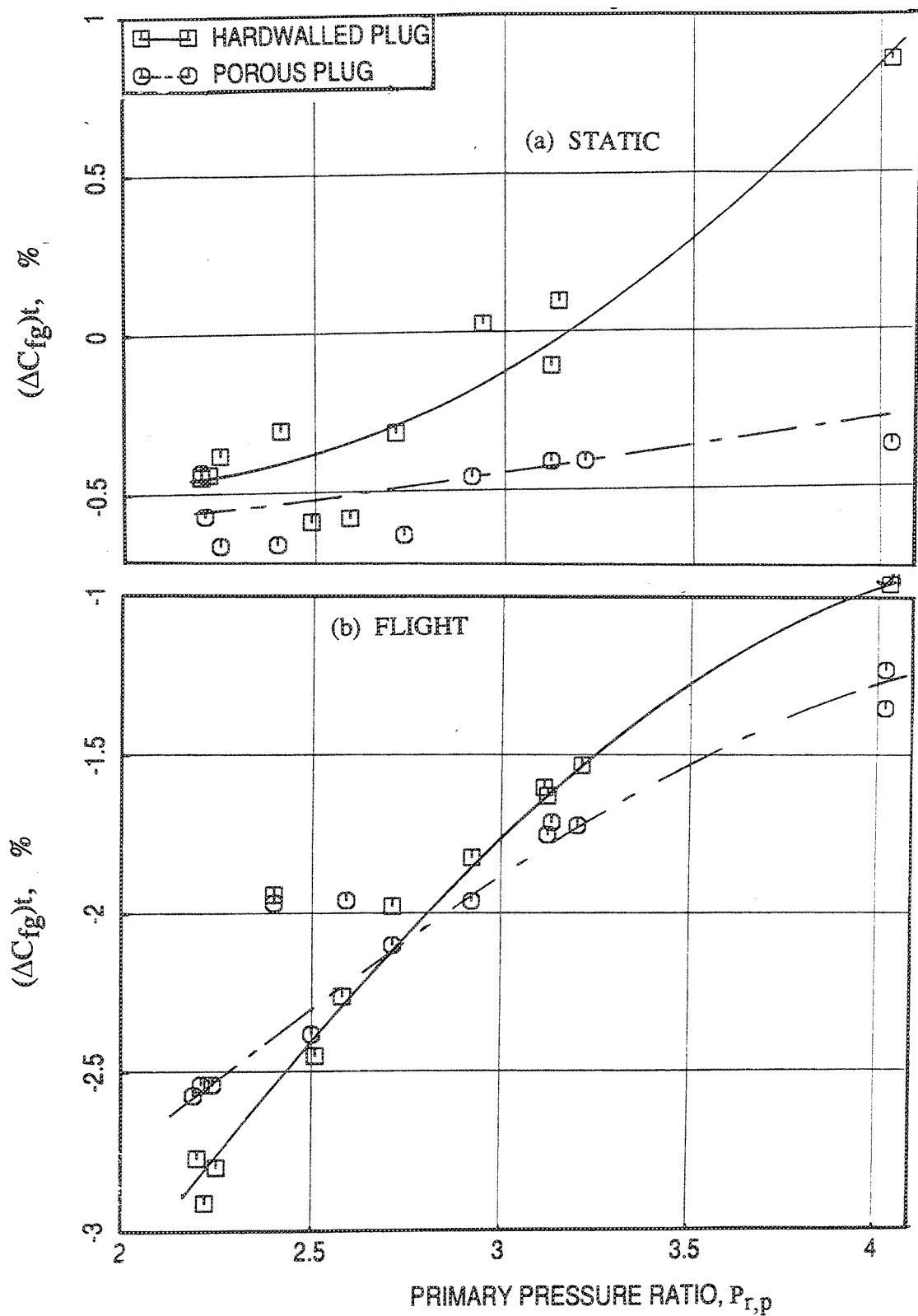


Figure 2.4-26. Effect of porous plug compared to hard-walled plug on  $(\Delta C_{fg})t$  as a function of nozzle pressure ratio for suppressor alone configurations.

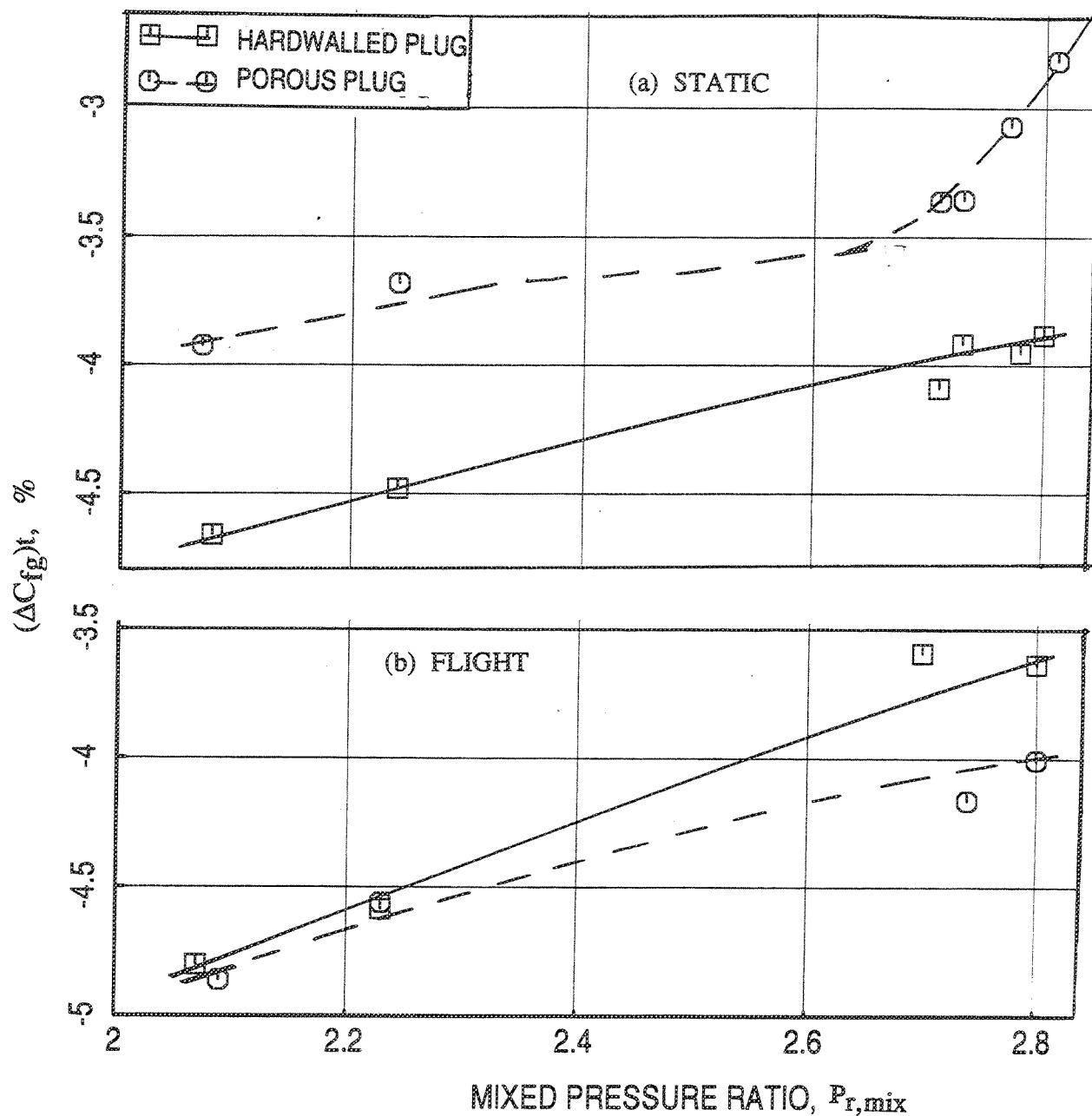


Figure 2.4-27. Effect of porous plug compared to hard-walled plug on  $(\Delta C_{fg})t$  as a function of mixed nozzle pressure ratio for 0.5"-thick, 220° wrap fluid shield nozzle configurations.

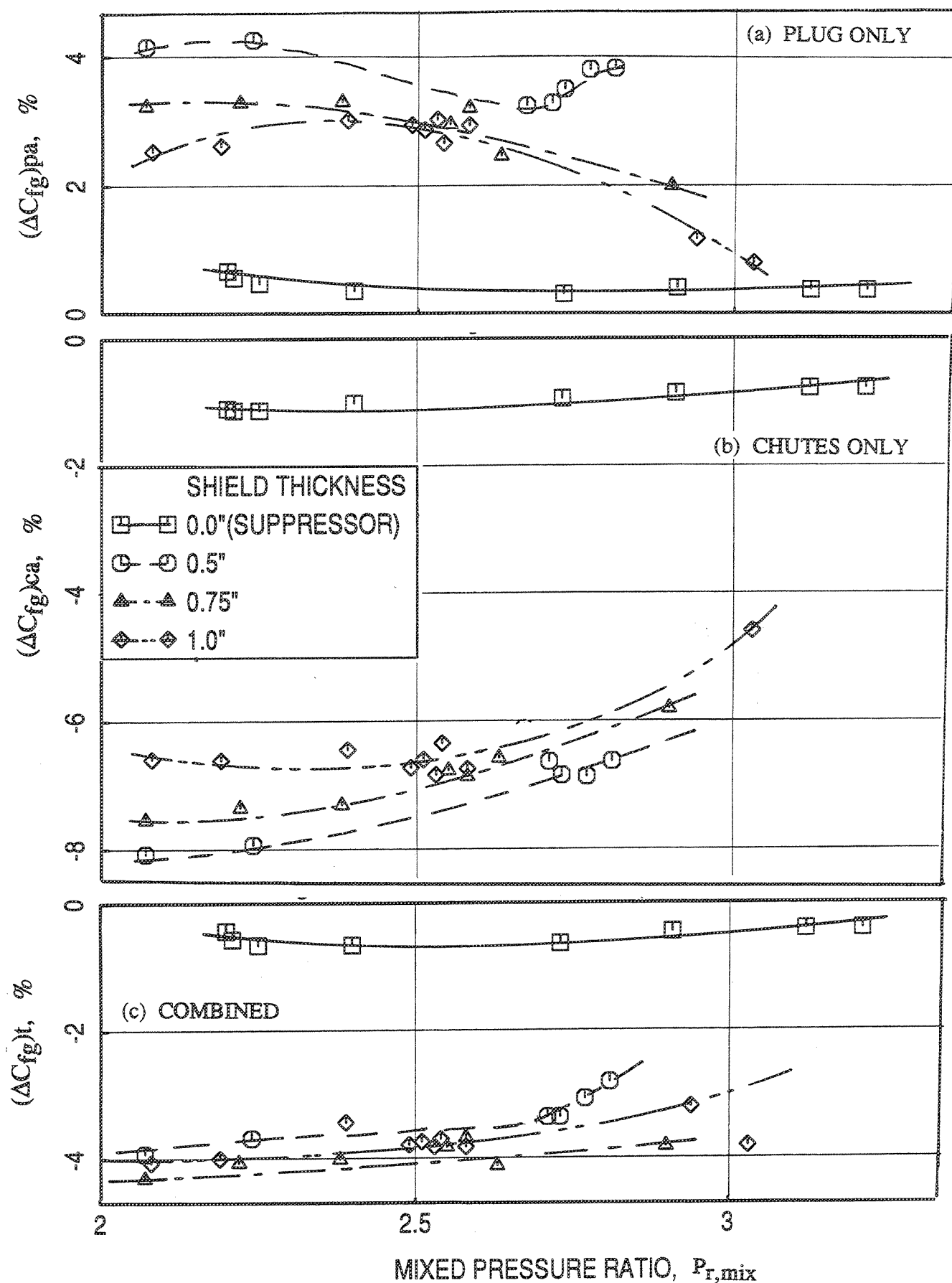


Figure 2.4-28. Effect of shield thickness on  $\Delta C_{fg}$  as a function of mixed nozzle pressure ratio for 220° wrap fluid shield nozzle configurations with porous plug at static condition.

completely reversed for chute contribution,  $(\Delta C_{fg})_{ca}$ , in that the levels drop drastically for 0.5"-thick fluid shield nozzle and slight improvement is observed with increasing shield thickness. The combined values (i.e.,  $(\Delta C_{fg})_t$ ) indicate that the  $(\Delta C_{fg})_t$  for 0.5"-thick fluid shield nozzle is about 2 to 3 % lower compared to the suppressor alone configuration. With increasing thickness small reduction of  $(\Delta C_{fg})_t$  is noticed. Similar results with flight simulation are presented in Figure 2.4-29. Thus the plug and chute pressure contributions to nozzle  $C_{fg}$  is about 4 to 5 % thrust loss over most of the cycle conditions for flight simulated cases. This is a significant disadvantage of this shielded-chute combination.

*Effect of Parametric Variations:* Several additional tests were conducted by varying the secondary flow (i.e., flade flow) pressure ratio to achieve a wide range of velocity and mass flow ratio (i.e.,  $V_r$  and  $W_r$ ) for the fluid shield nozzles. Figures 2.4-30 and 2.4-31 show the effect of fluid shield thickness on  $(\Delta C_{fg})_t$  with respect to  $V_r$  and  $W_r$  for fixed  $V_{mix}$  values. With respect to  $V_r$   $(\Delta C_{fg})_t$  decreases with shield thickness and the trend is reversed when plotted with respect to  $W_r$ . To derive a meaningful conclusion contours of constant  $(\Delta C_{fg})_t$  with respect to  $V_r$  and  $W_r$  are plotted for fixed  $V_{mix}$  values in Figure 2.4-32. It can be observed that a lower negative  $(\Delta C_{fg})_t$ , which is desirable for takeoff thrust from performance considerations, occurs at lower velocity and mass flow ratios. While lower  $V_r$  and  $W_r$  levels are desirable from performance consideration, it will be shown later in this report that the reverse is true from noise reduction considerations.

Effect of aero thermodynamic parameters, namely, fluid shield nozzle pressure ratio  $P_{r,s}$  and total temperature  $T_{t,s}$ , and primary stream nozzle pressure ratio  $P_{r,p}$  and total temperature  $T_{t,p}$ , on  $(\Delta C_{fg})_t$  are shown in Figures 2.4-33 through 2.4-36, respectively. As illustrated in Figure 2.4-33,  $(\Delta C_{fg})_{pa}$  for the plug increases with  $P_{r,s}$ , and the levels decrease with increasing shield thickness. The variation of chute  $(\Delta C_{fg})_{ca}$  with respect to  $P_{r,s}$  as well as with respect to shield thickness is reversed compared to  $(\Delta C_{fg})_{pa}$ . The combined  $(\Delta C_{fg})_t$ , however, decreases with  $P_{r,s}$  and the effect of shield thickness seems to be small. Similar results are also obtained for a higher  $V_{mix}$  (i.e., with a higher  $P_{r,p}$  value of about 4.3). Based on these observations, a lower  $P_{r,s}$  is desirable from performance considerations.

Effect of primary nozzle pressure ratio is quite significant when considered individually for the plug and chutes (see Figure 2.4-34). The  $(\Delta C_{fg})_{pa}$  increases a little and then

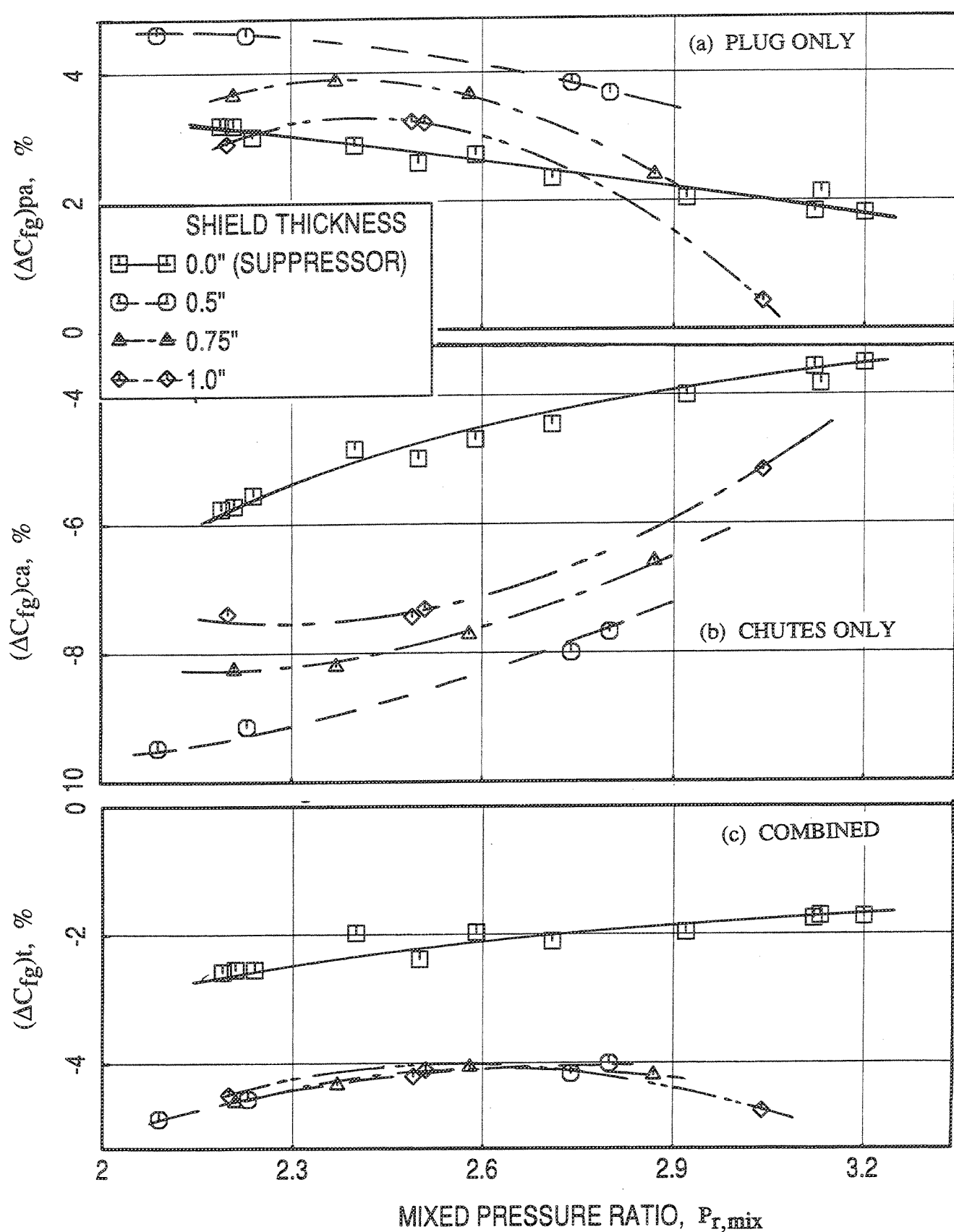


Figure 2.4-29. Effect of shield thickness on  $\Delta C_{fg}$  as a function of mixed nozzle pressure ratio for 220° wrap fluid shield nozzle configurations with porous plug with flight simulation.

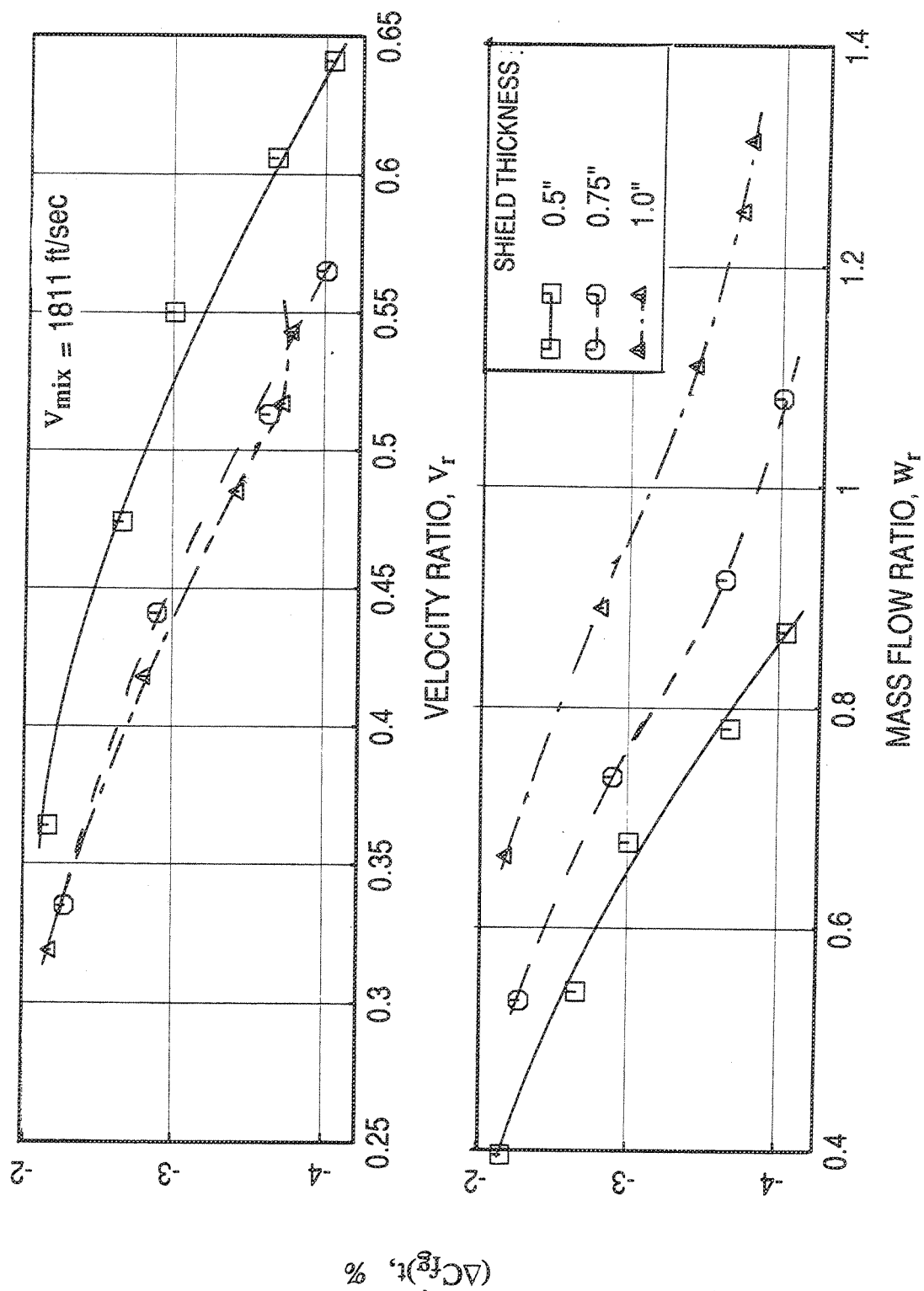


Figure 2.4-30. Effect of shield thickness on  $\Delta C_{fg}$  with respect to velocity ratio and mass flow ratio for 220° wrap fluid shield nozzle configurations with porous plug at static condition.

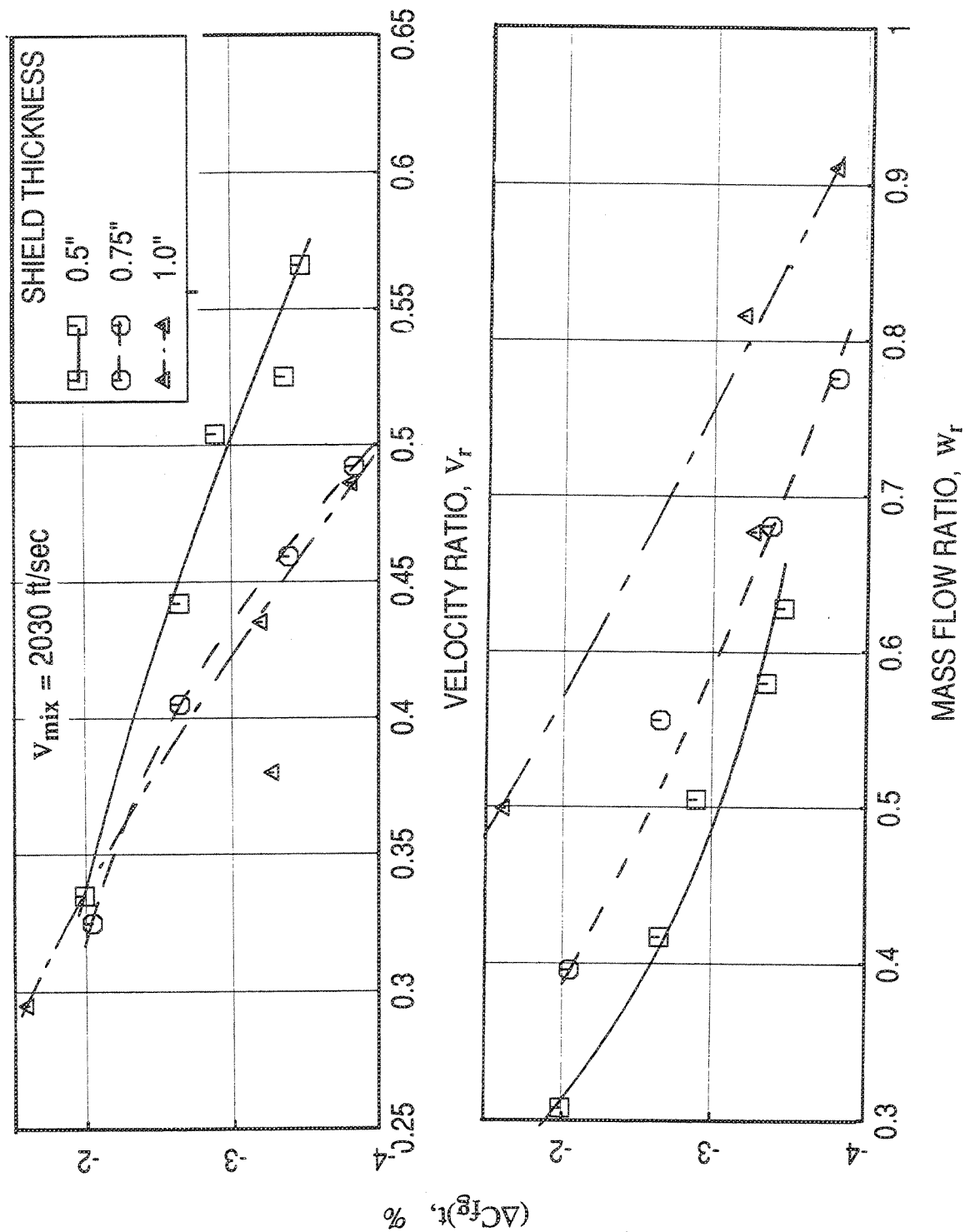


Figure 2.4-31. Effect of shield thickness on  $\Delta C_{fg}$  with respect to velocity ratio and mass flow ratio for 220° wrap fluid shield nozzle configurations with porous plug with flight simulation.

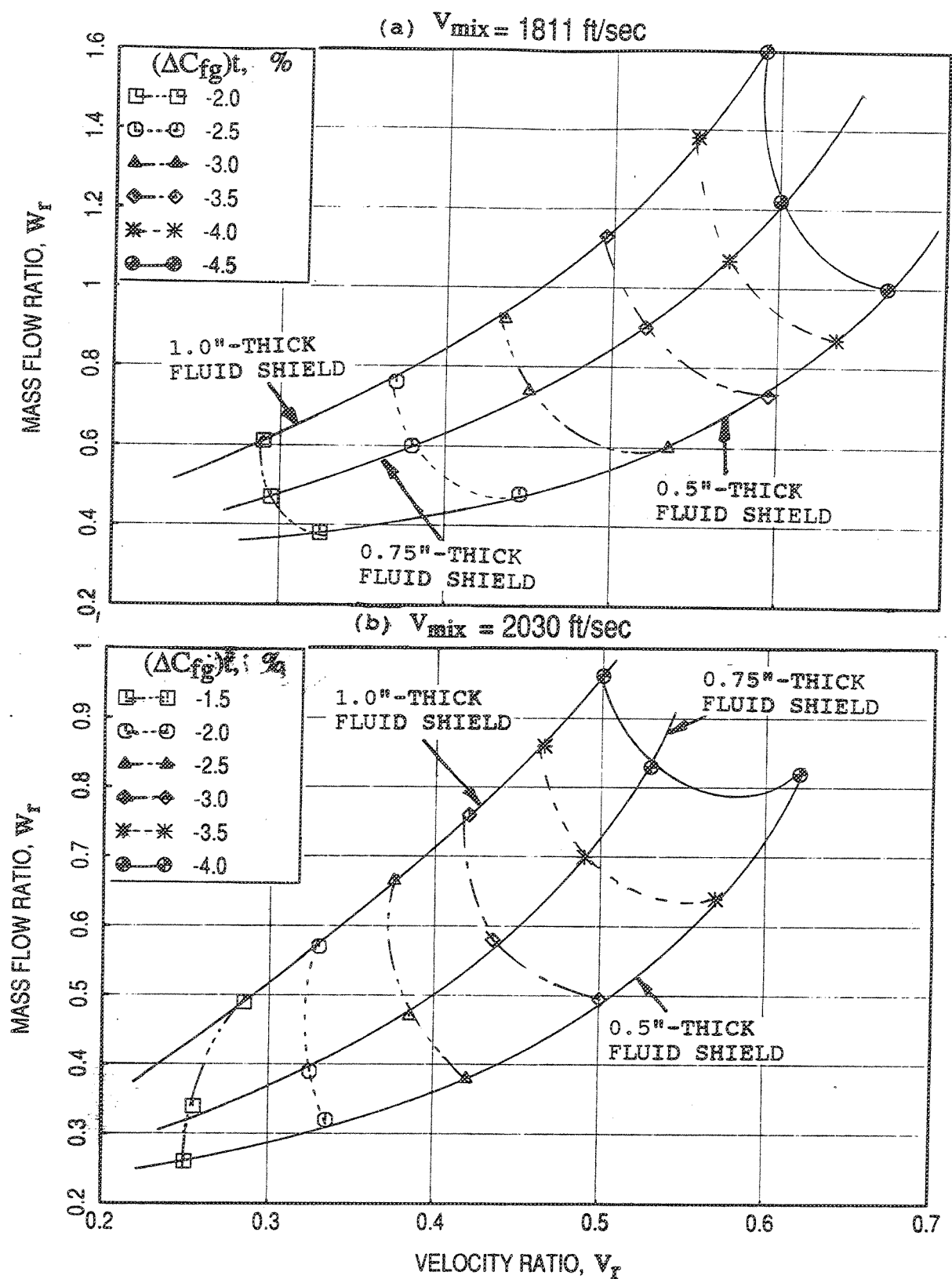


Figure 2.4-32. Contours of constant  $\Delta C_{fg}$  as a function of velocity ( $V_r$ ) and mass flow ( $W_r$ ) ratios for  $220^\circ$  wrap fluid shield nozzles with porous plug at static condition.



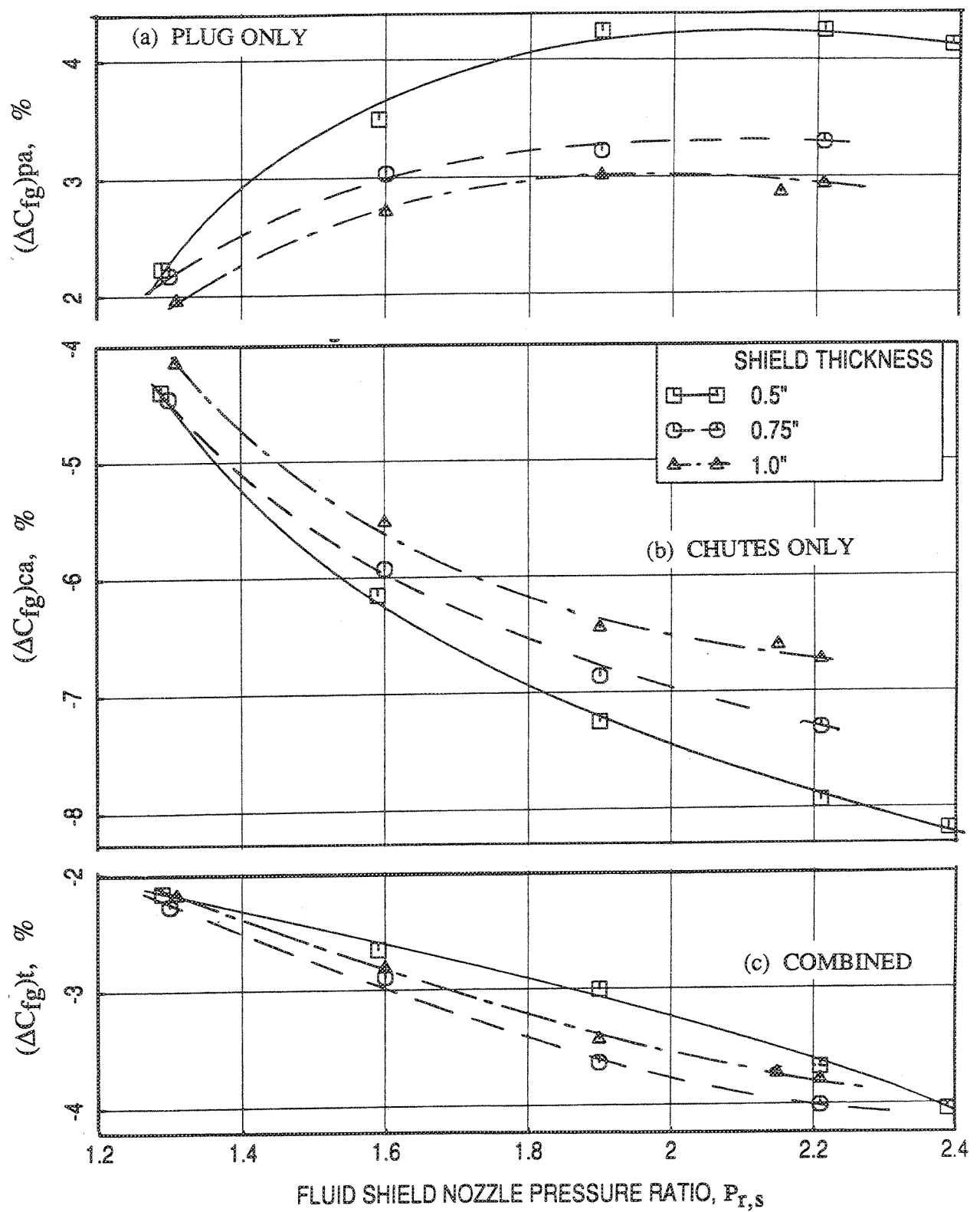


Figure 2.4-33. Effect of flade stream pressure ratio ( $P_{r,s}$ ) on  $\Delta C_{fg}$  for 220° wrap fluid shield nozzle configurations with porous plug at static condition.

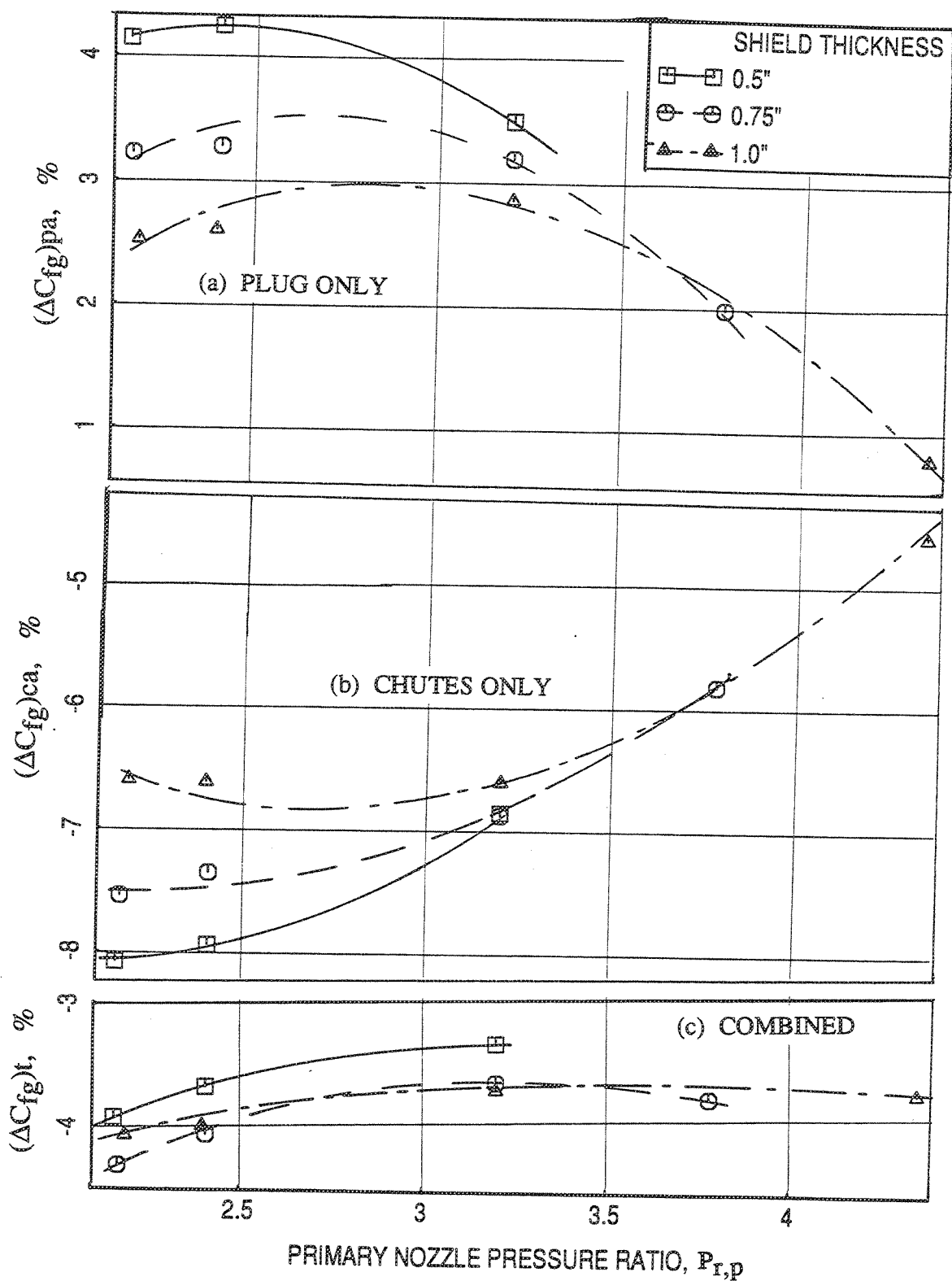


Figure 2.4-34. Effect of core stream pressure ratio ( $P_{r,p}$ ) on  $\Delta C_{fg}$  for 220° wrap fluid shield nozzle configurations with porous plug at static condition.

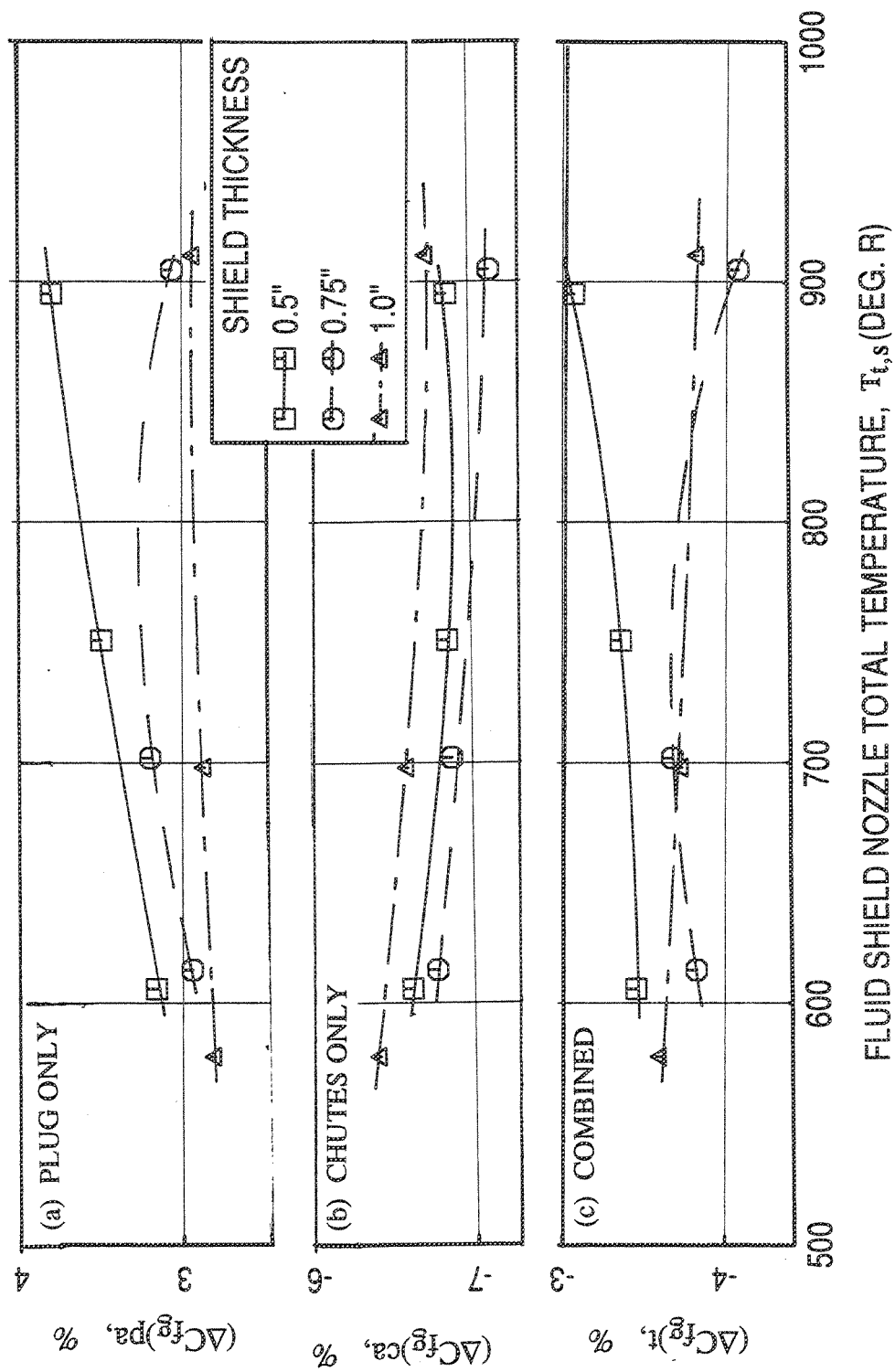


Figure 2.4-35. Effect of flade stream total temperature ( $T_{t,s}$ ) on  $\Delta C_{f_g}$  for 2200 wrap fluid shield nozzle configurations with porous plug at static condition.

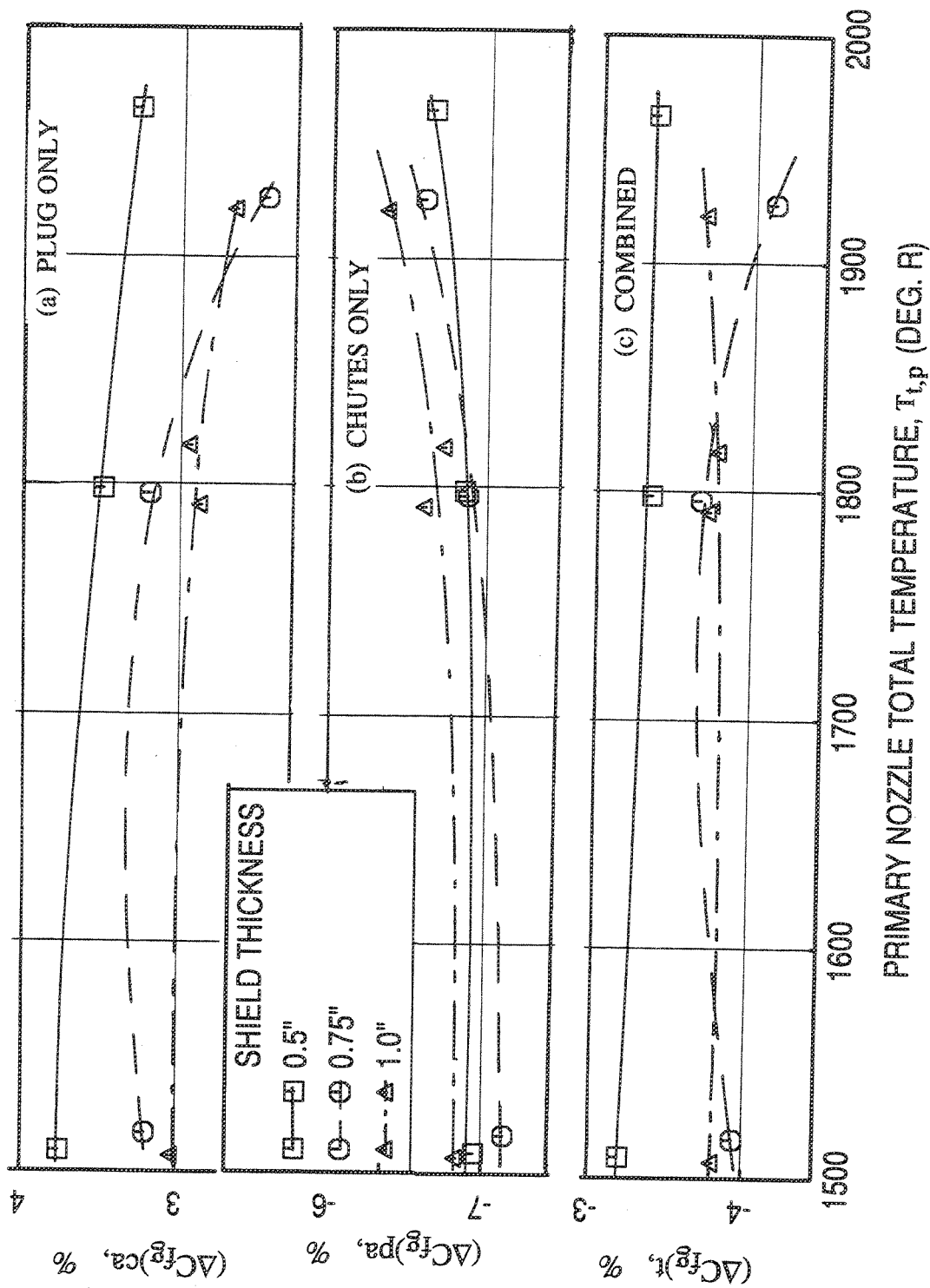


Figure 2.4-36. Effect of core stream total temperature ( $T_{t,p}$ ) on  $\Delta C_{f,g}$  for 2200° wrap fluid shield nozzle configurations with porous plug at static condition.

decreases with  $P_{r,p}$  and the levels decrease with shield thickness for lower  $P_{r,p}$  values. The trend is completely opposite for chute  $(\Delta C_{fg})_{ca}$ . The combined  $(\Delta C_{fg})_t$  is insensitive to  $P_{r,p}$ . Again, the 0.5"-thick fluid shield seems to perform better. Effect of fluid shield nozzle total temperature on  $\Delta C_{fg}$ , as shown in Figure 2.4-35, is relatively small. The 0.5"-thick fluid shield seems to be more favorable. Variation of  $\Delta C_{fg}$  with respect to  $T_{t,p}$ , as shown in Figure 2.4-36, is similar to  $T_{t,s}$  and is very little. Again, 0.5"-thick fluid shield seems to be better compared to the 0.75"- and 1.0"-thick shields.



## 2.5 ACOUSTIC DATA NOMENCLATURE, NORMALIZATION AND ACCURACY

The principal objective of this investigation is to evaluate the acoustic characteristics of a mechanically suppressed nozzle with fluid shields of different thickness and wrap angle. Tests were conducted for a 2.9" diameter conical nozzle (see Figure 2.2-1), a 36-chute mechanical suppressor (see Figures 2.2-6 and 2.2-7), and the 36-chute suppressor with various fluid shield nozzles (see Figure 2.2-8). Select configurations, mounted in Cell 41 for acoustic tests, are shown in Figures 2.5-1 through 2.5-4. Before discussing the acoustic results of this investigation, acoustic data nomenclature, normalization, and accuracy are described in this section. In addition, the accuracy and the validity of measured data are discussed in this section.

### 2.5.1 Acoustic Data Nomenclature and Normalization

The farfield data measured by an array of microphones at an azimuthal location  $\phi$  are analyzed to generate various acoustic parameters. These parameters include Sound Pressure Level (SPL), Sound Power Level (PWL), Overall Sound Pressure level (OASPL), Perceived Noise Level (PNL), Tone corrected Perceived Noise Level (PNLT), and Effective Tone corrected Perceived Noise Level (EPNLT) which are presented as functions of Mixed Jet Velocity ( $V_{mix}$ ), Jet Velocity Parameter ( $V_{par}$ ), Ideal Gross Thrust ( $FG)_i$ , Frequency ( $f$ ), Angle to Inlet or Polar Angle ( $\theta$ ), Shock Strength Parameter ( $SH_{par}$ ), where,

$$V_{mix} = (V_{j,p} \cdot W_p + V_{j,s} \cdot W_s) / (W_p + W_s)$$

$$V_{j,p} = \text{Ideal Nozzle Exhaust Velocity for primary (core) stream ft/sec}$$

$$V_{j,s} = \text{Ideal Nozzle Exhaust Velocity for secondary (flade) stream ft/sec}$$

$$W_p = \text{Mass Flow Rate for primary stream lbs/sec}$$

$$W_s = \text{Mass Flow Rate for secondary stream lbs/sec}$$

$$V_{par} = 10 \text{ LOG}_{10}[V_{mix}/a_0]$$

$$SH_{par} = 10 \text{ LOG}_{10}[\beta]$$

$$a_0 = \text{Ambient Speed of Sound ft/sec}$$

$$\beta = [M_{mix}^2 - 1]^{1/2}$$

$$M_{mix} = V_{mix}/a_0$$

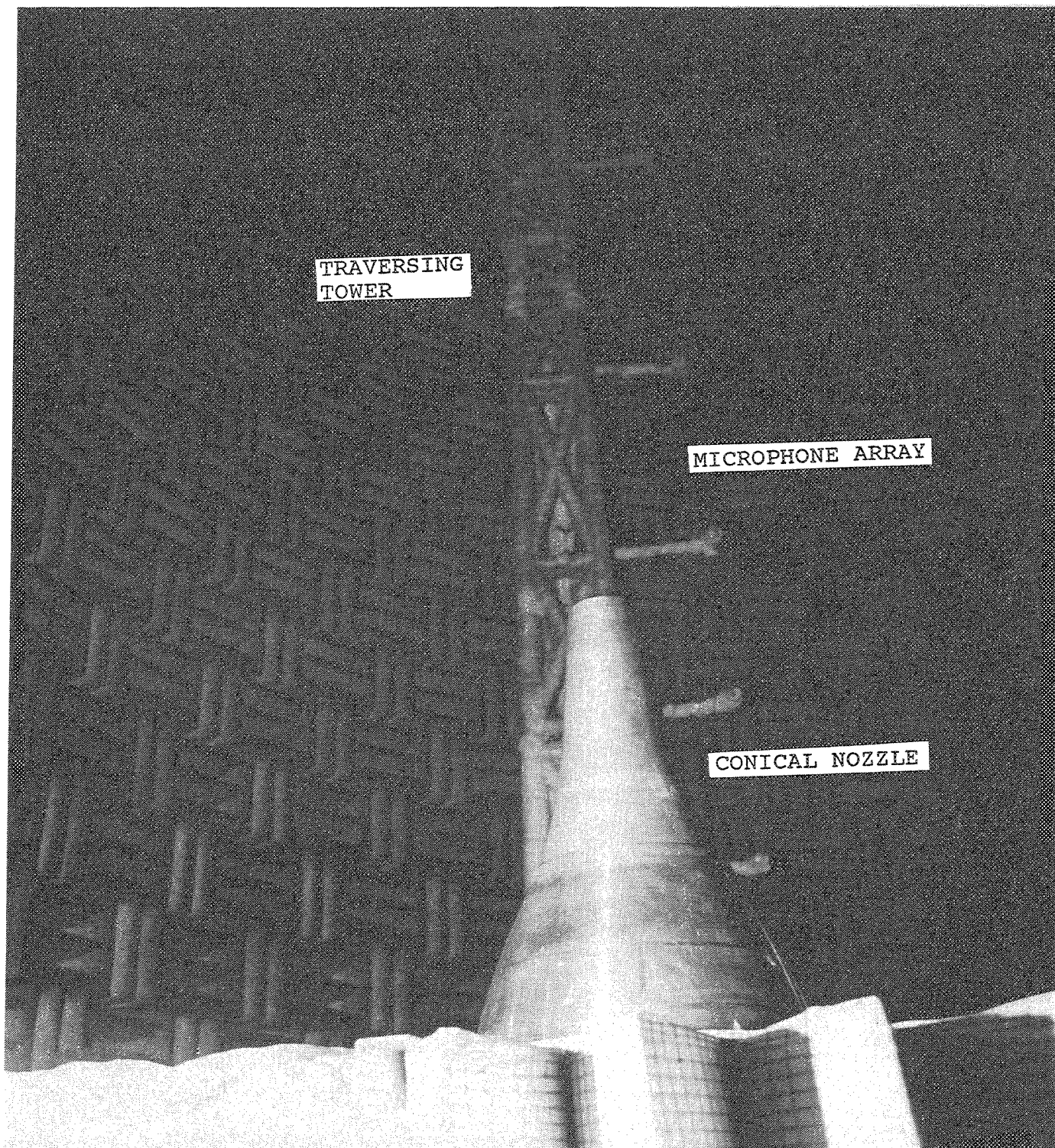


Figure 2.5-1. Conical nozzle mounted in Cell 41 for and the traversing tower with an array of microphone for acoustic measurement.



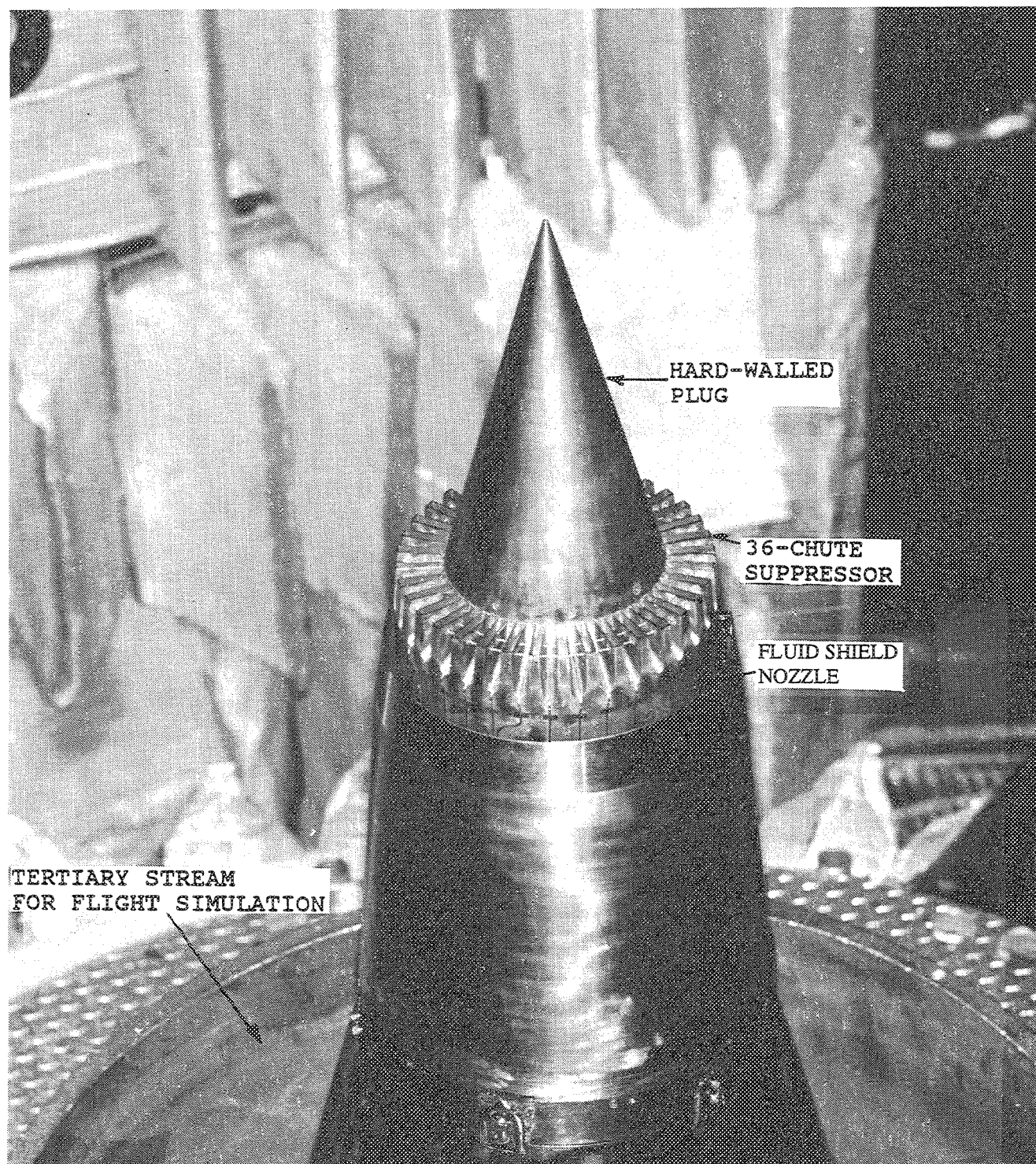


Figure 2.5-2. 0.5"-thick fluid shield nozzle in Cell 41, wrapped around the 36-chute suppressor with hard-walled plug by 220°.

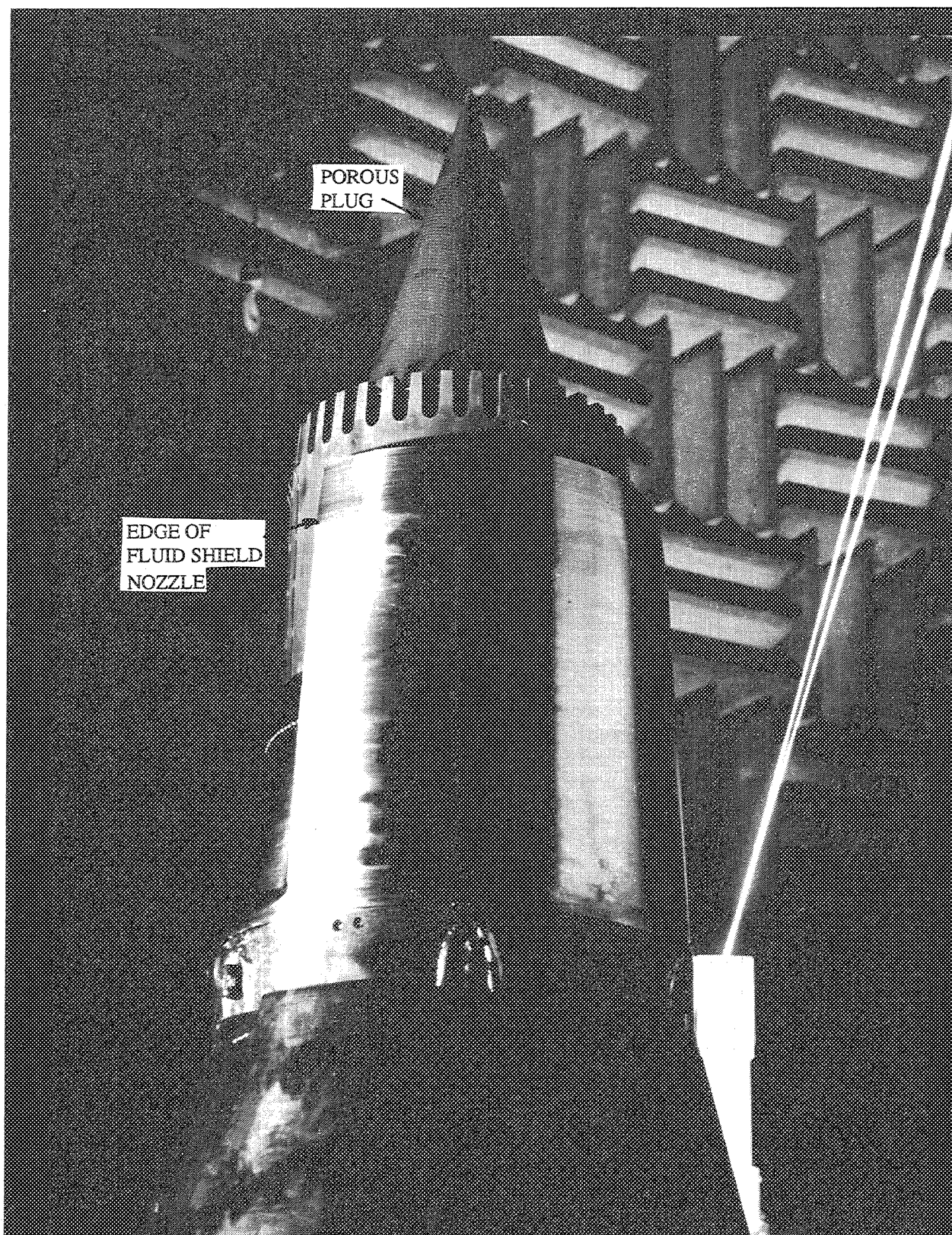


Figure 2.5-3. 0.5"-thick fluid shield nozzle in Cell 41, wrapped around the 36-chute suppressor with porous plug by 220°.



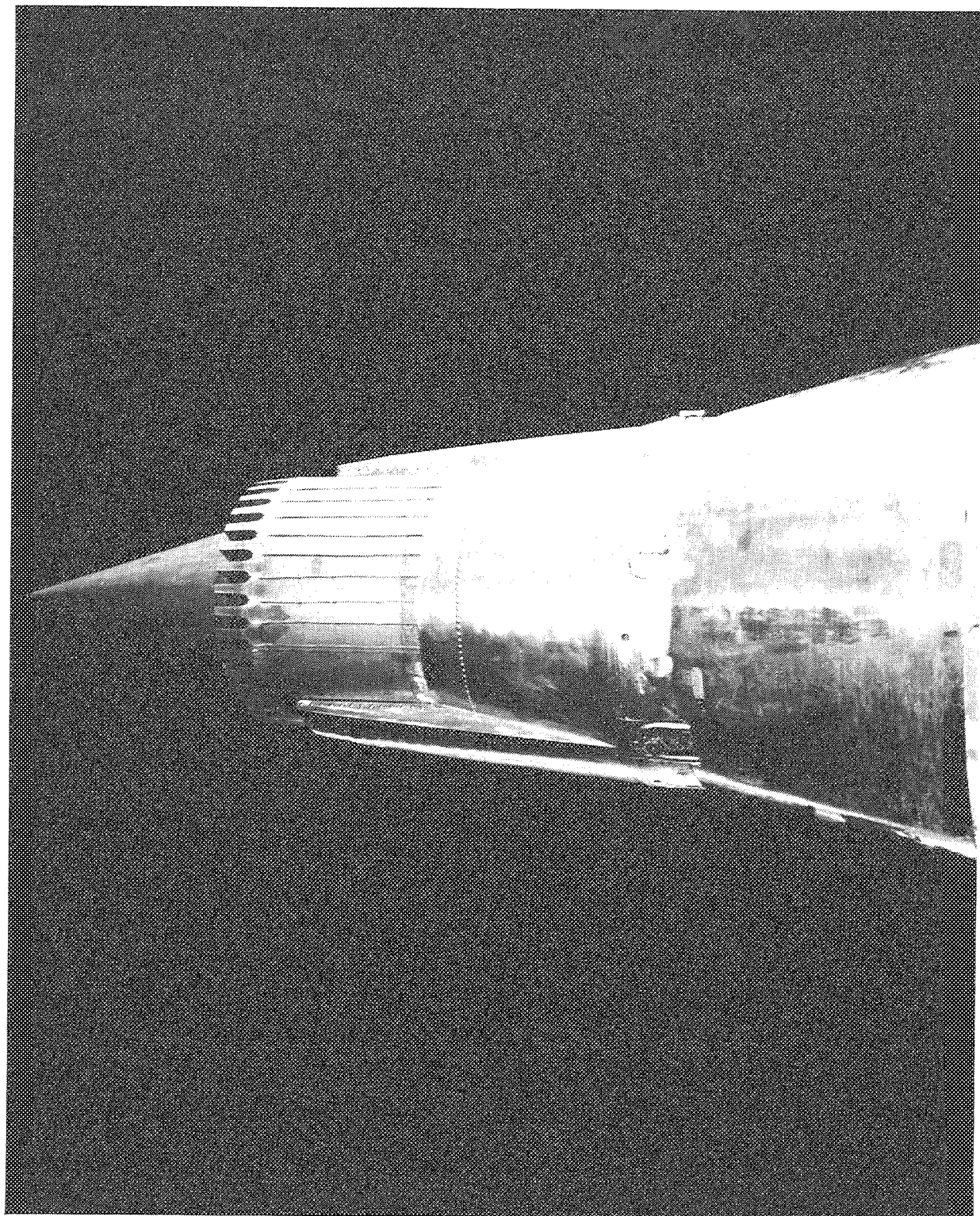


Figure 2.5-4. The unshielded side of the fluid shield nozzle configuration in Cell 41.

EPNLT for static condition is computed using the PNL T values assuming a flight velocity of 360 ft/sec (i.e.,  $M_F=0.32$ ) and is termed as Pseudo EPNLT. For single stream nozzles, like the conical nozzle and the suppressor nozzle alone configurations,  $V_{mix}$  reduces to  $V_{j,p}$  (or  $V_J$ ), the ideal exhaust jet velocity. For some cases, the noise level parameters are also presented with respect to velocity ratio  $V_r$ , mass flow ratio  $W_r$ , and aero thermodynamic parameters (i.e.,  $P_{r,p}$ ,  $P_{r,s}$ ,  $T_{t,p}$ , and  $T_{t,s}$ ), where,

$$\begin{aligned} V_r &= V_{j,s} / V_{j,p} \\ W_r &= W_s / W_p \end{aligned}$$

Often the noise level parameters are normalized with respect to a reference thrust  $F_{ref}$  or with respect to the reference thrust  $F_{ref}$  and jet density. These normalization arose out of establishing velocity dependence of jet noise, using Lighthill's scaling laws as follows:

$$I \propto \rho^\omega A_J V_J^n \quad (1)$$

Where,  $I$  = Noise source intensity

$\rho$  = Jet density

$A_J$  = Cross-sectional area of the jet

$V_J$  = Jet velocity

$\omega$  = Density exponent, 2 for high velocities (Ref. 13)

$n$  = Jet velocity exponent

Equation (1) may be regrouped as

$$I \propto (\rho A_J V_J^2) \rho^{(\omega-1)} V_J^{(n-2)} \quad (2)$$

$$\text{or } I \propto (FG)_i \rho^{(\omega-1)} V_J^{(n-2)}$$

Where,  $(FG)_i = (\rho A_J V_J^2)$ , ideal gross thrust.

Hence, source intensity dependence on jet velocity on a constant thrust basis may be extracted if source intensity is normalized for a reference thrust and density as;

$$I = \frac{I}{(F_{\text{ref}} \rho_o^{(\omega-1)})}$$

or

$$\bar{I} = \left[ \frac{(FG)_i}{F_{\text{ref}}} \right] \left[ \frac{\rho}{\rho_o} \right]^{(\omega-1)} V_j^{(n-2)} \quad (3)$$

$$\text{Hence, } 10 \log(\bar{I}) = 10 \log(I) + NF \propto 10 \log[V_j^{(n-2)}] \quad (4)$$

$NF_{\text{th}}$  = Normalization factor with respect to thrust

$$= -10 \text{ Log } ((FG)_i / F_{\text{ref}}), \text{ dB}$$

$NF$  = Total normalization factor with respect to thrust and density

$$= -10 \text{ Log } ((FG)_i / F_{\text{ref}}) (\rho / \rho_o)^{\omega-1}, \text{ dB}$$

where,

$F_{\text{ref}}$  = Reference Gross Thrust, 60000 lbs

$\rho_o$  = Ambient Density of Air

Note that a new value of  $F_{\text{ref}} = 60,000$  lbs is chosen for these studies, which reflects the full scale engine thrust at takeoff for an HSCT with a TOGW (i.e., takeoff gross weight) of about 700,000 lbs. Thus, the noise levels, if normalized for 60,000 lbs gross thrust, will be more representative of anticipated full scale engine noise levels.

### 2.5.2 Acoustic Data Accuracy

Acoustic data accuracy discussion deals with the issues of freejet background noise levels, the tower array microphone data compared to fixed array microphone data, the azimuthal symmetry with respect to tower microphone array, on-line data compared to post processed data, and present conical nozzle results compared to prior test data and predictions.

**Tower Versus Fixed Microphone Data :** As described earlier, while the fixed microphone array is placed at a sideline distance of about 26 feet the tower microphone array is at a distance of about 21 feet from the nozzle exit plane. To assess whether the tower microphones are in the farfield or not, acoustic data measured by tower microphones at different azimuthal locations ( $\phi$ ) for axisymmetric nozzles (i.e., conic and suppressor alone configurations) are compared with data measured by the fixed microphone arrays, which, based on past test experience at Cell 41, are in the far field (Ref. 14). This comparison is also essential to establish the accuracy of traversing

microphone measurement, since the community point and the sideline point noise levels are different for nonaxisymmetric fluid shield nozzles and are measured by positioning the tower microphone array at different azimuthal planes. For conical nozzle and 36-chute suppressor alone configurations measurements were made by tower microphone as well as fixed microphone arrays by positioning the tower at three azimuthal locations (i.e.,  $10^\circ$ ,  $45^\circ$ , and  $75^\circ$ ) for a few test conditions (see Figures 2.2-11 and 2.2-12).

Figures 2.5-5 and 2.5-6 show the comparisons of tower microphone data, acquired at three azimuthal locations, with fixed microphone data, positioning the tower at  $10^\circ$  and  $75^\circ$ , for the conical nozzle with  $P_{r,p} = 1.6$  and  $T_{t,p} = 1000^\circ\text{R}$  and without flight simulation. Fixed microphone data, when tower is positioned at  $\phi = 45^\circ$ , is not included in these comparisons, since the influence of tower is significant when parked in front of the fixed microphone array at  $\phi = 45^\circ$ . Comparison of overall sound pressure directivities, shown in Figure 2.5-5, shows very good agreement with each other, except for the lowest polar angle of  $45^\circ$ . This is due to the influence of the chamber floor, which is not perfectly uniform in terms of acoustic insulation due to the track arrangement installed for the tower microphone system. The effect of tower on fixed microphone data is negligible when the tower is parked at  $10^\circ$  or at  $75^\circ$ . The agreement between the tower data measured at different azimuthal angles and with fixed microphone data are further illustrated in Figure 2.5-6 by comparing the SPL spectra at a number of polar angles ( $\theta$ ). These comparisons and similar results for other test conditions and configuration indicate that the tower microphone data are within one dB compared to the fixed microphone data for most polar locations and frequencies. Hence, the tower microphone data is commensurate with fixed microphone data which has been shown to be in the acoustic far field for conic and other nozzles. Hence, the tower microphone system is considered acceptable for acoustic measurements for this program.

**On-line Versus IDR Data :** Acoustic data measured by both the microphone arrays is analyzed by an on-line system and also is recorded on magnetic tapes for post processing by Instrumentation Data Room (IDR) analysis system. The on-line system computes 1/3-octave band data for model scale at a  $40'$  arc up to 80 kHz corrected to standard day conditions (i.e.,  $59^\circ\text{F}$  and 70 % humidity) and narrowband data as measured, by utilizing analog data from two microphone channels at a time. Hence, the on-line output from all the microphone channels is essentially not acquired from the same time segment of the test. If measurable fluctuation exists in the data, one may

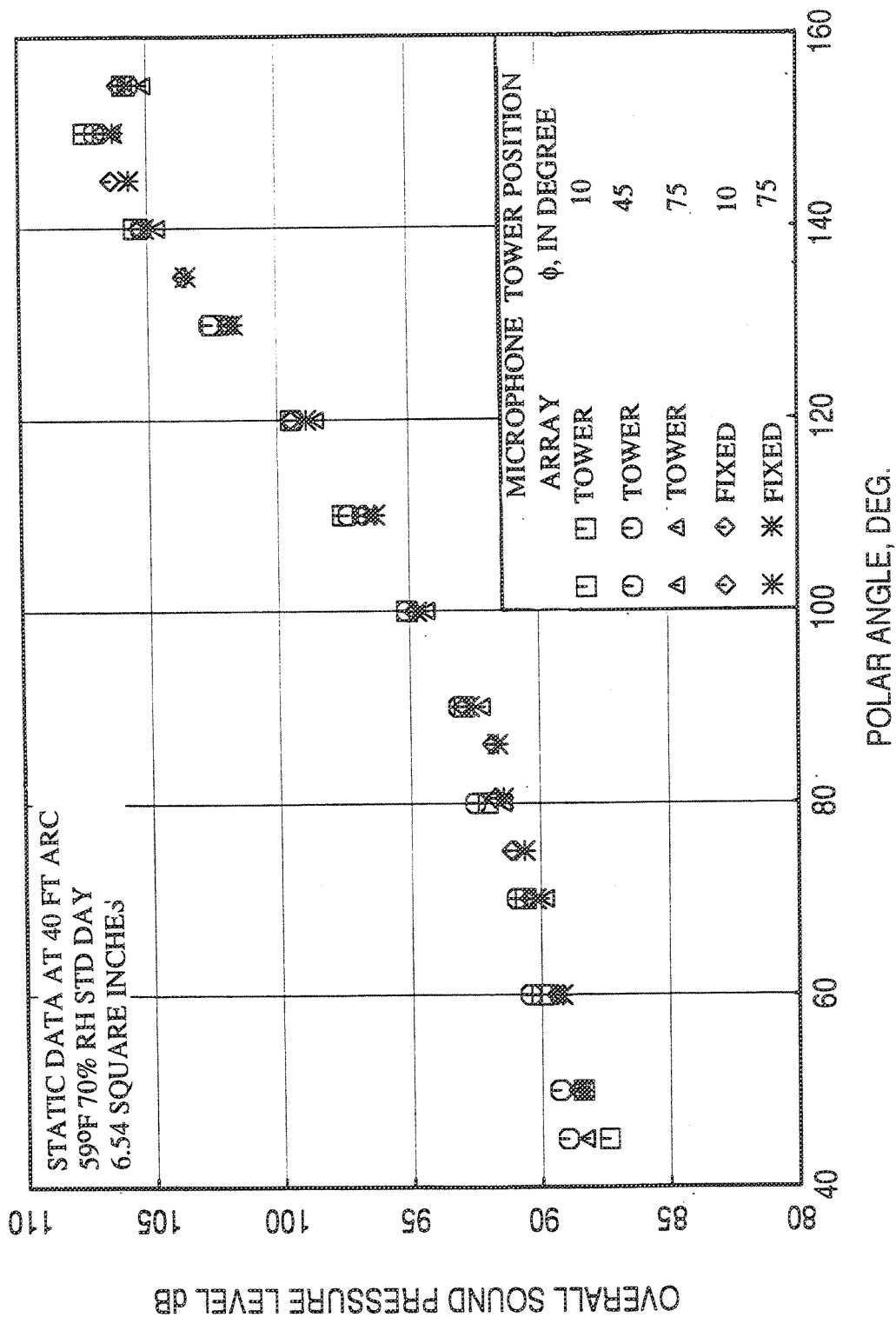


Figure 2.5-5. Comparison of OASPL directivities for the 6.54 in<sup>2</sup> conical nozzle measured by the tower and fixed microphone arrays by positioning the tower at different azimuthal ( $\phi$ ) locations;  $P_R=1.6$ ,  $T_T=1000^\circ R$ ,  $V_J=1230$  ft/sec.

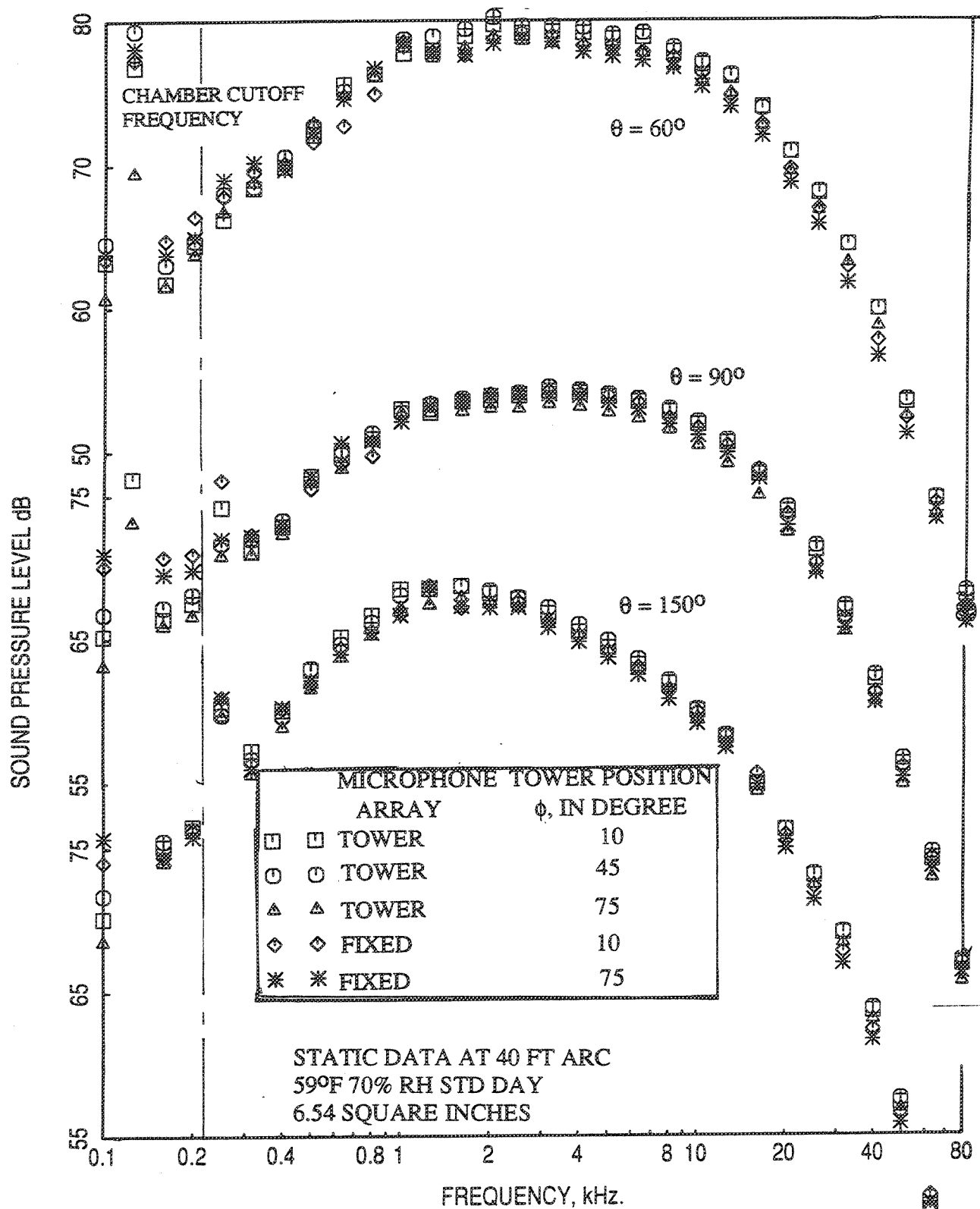


Figure 2.5-6. Comparison of SPL spectra for the 6.54 in<sup>2</sup> conical nozzle measured by the tower and fixed microphone arrays by positioning the tower at different azimuthal ( $\phi$ ) locations;  $P_R=1.6$ ,  $T_T=1000^\circ R$ ,  $V_J=1230$  ft/sec.



find discrepancy in on-line output between different pairs of channels. The IDR analysis system utilizes the data from a particular test segment for all the channels to compute the 1/3-octave band data and narrowband data. In addition, a pre-emphasis is applied to the data recorded for IDR analysis at higher frequency range (i.e., above 20 kHz) for microphones in the rear arc (i.e., above 110°) to avoid any signal to noise problem due to lower tape recorder dynamic range. To establish that the on-line output is as good as IDR data, comparisons are made between on-line and IDR outputs for different test configurations with different test conditions. The comparisons include data on conical nozzle, the suppressor alone configuration, and fluid shield configurations. Typical results are shown here.

Figures 2.5-7 and 2.5-8 show the spectral comparison of IDR data with on-line data for fixed microphone array for the 6.54 in<sup>2</sup> conical nozzle at two test conditions. The agreement is very good for all the polar locations in the frequency range of interest (i.e., 250 Hz - 80 kHz). Some amount of disagreement is observed for 50°. This is due to the data contamination during the recording of analog signal on a particular channel of the tape corresponding to 50° angle, which was used by IDR for analysis. At 120° the agreement between these two sets of data is poor at mid frequency range. This is due to a faulty microphone at 120° position, which was working intermittently.

Figure 2.5-9 shows the spectral comparison of IDR data with on-line data for tower microphone array for the suppressor alone configuration with hard-wall plug. The agreement between on-line and IDR data is very good for all the angles between 200 Hz and 20 kHz. At higher frequencies the IDR levels are slightly higher (i.e., about 1 dB) compared to on-line data. Comparison of OASPL and PNLT directivities for the same configuration, shown in Figure 2.5-10, indicates good agreement between on-line and IDR data. Similar comparisons are shown in Figures 2.5-11 and 2.5-12 for the fluid shield nozzle configuration with 1"-thick shield and with hard-wall plug. The agreement between on-line and IDR data is very good. Based on these comparisons, on-line data is considered to be acceptable and will be used in this program.

**Freejet Background Noise :** Freejet background noise is examined to establish the range of test conditions not influenced by the freejet background noise for flight simulation tests. The background noise is acquired by operating the freejet tunnel and both the streams of the coannular conical nozzle (see Figure 2.2-1) at the same velocity of 360 ft/sec (i.e.,  $M_F=0.32$ ) at ambient temperature. These background noise levels

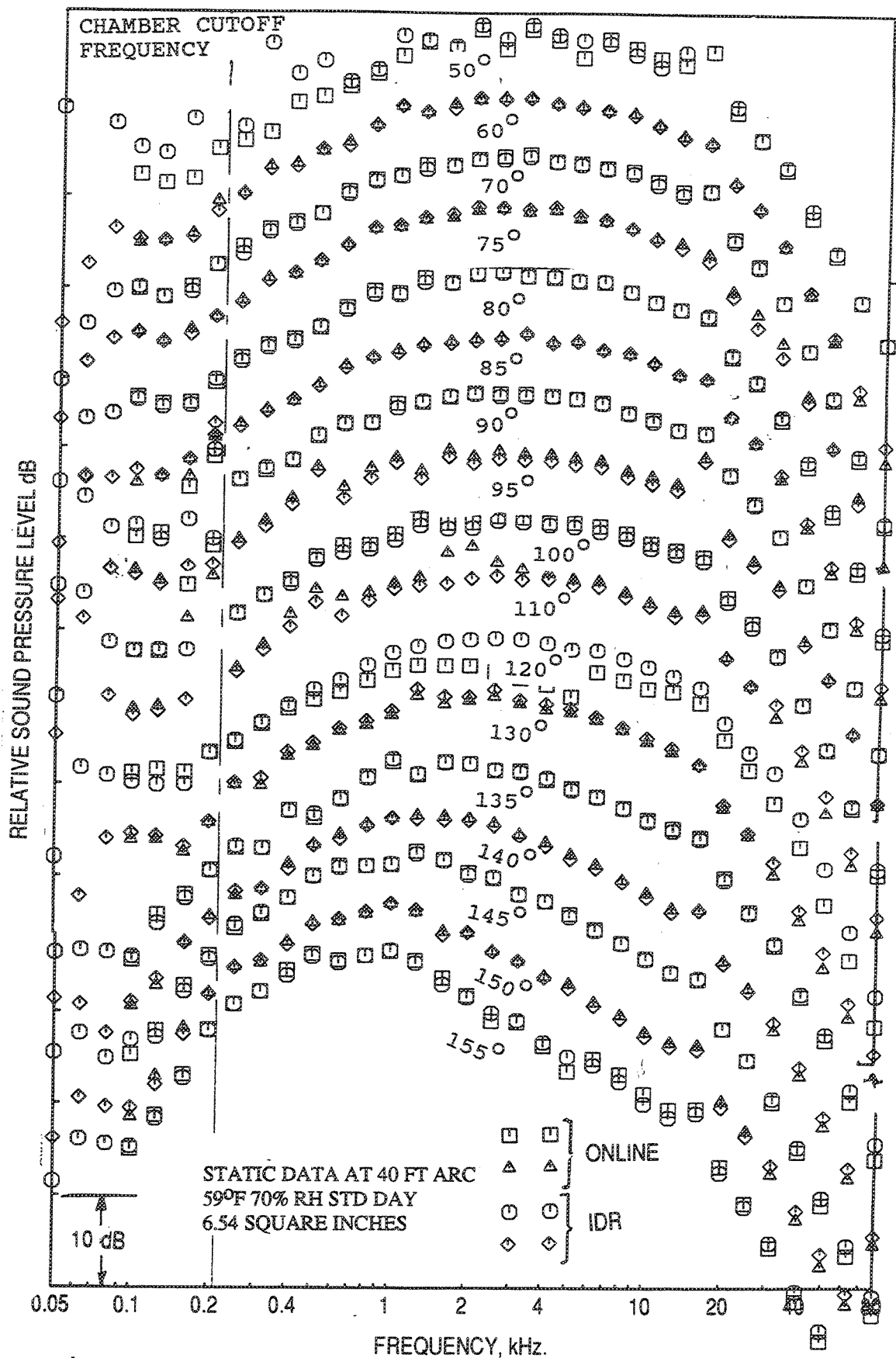


Figure 2.5-7. Comparison of SPL spectra for the 6.54 in<sup>2</sup> conical nozzle of on-line analysis with IDR analysis at all the polar angles ( $\theta$ ) measured by the fixed microphones;  $P_R=1.6$ ,  $T_T=520^\circ\text{R}$ ,  $V_J=900$  ft/sec.

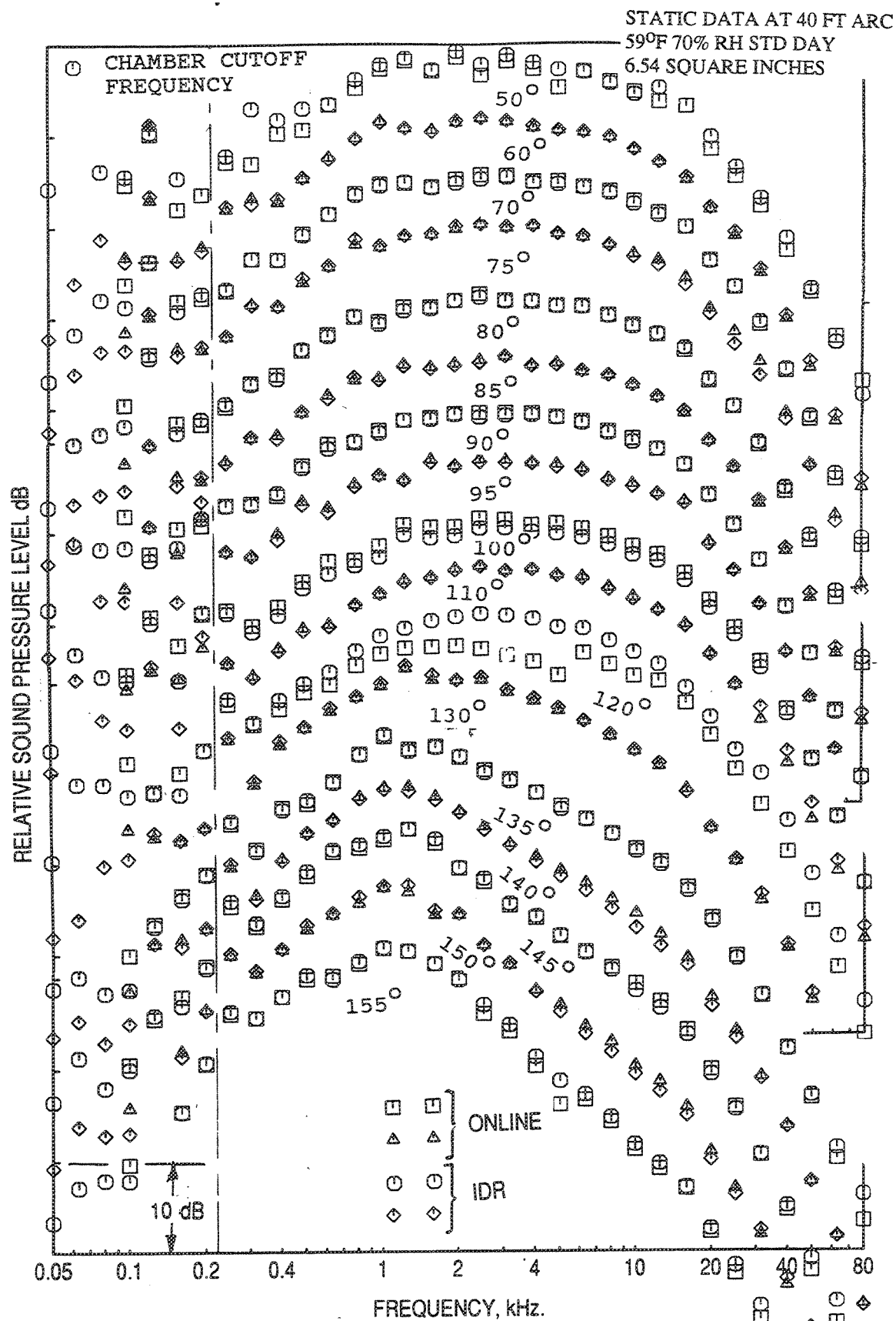


Figure 2.5-8. Comparison of SPL spectra for the 6.54 in<sup>2</sup> conical nozzle of on-line analysis with IDR analysis at all the polar angles ( $\theta$ ) measured by the fixed microphones;  $P_R=1.6$ ,  $T_T=1000^\circ R$ ,  $V_J=1230$  ft/sec.

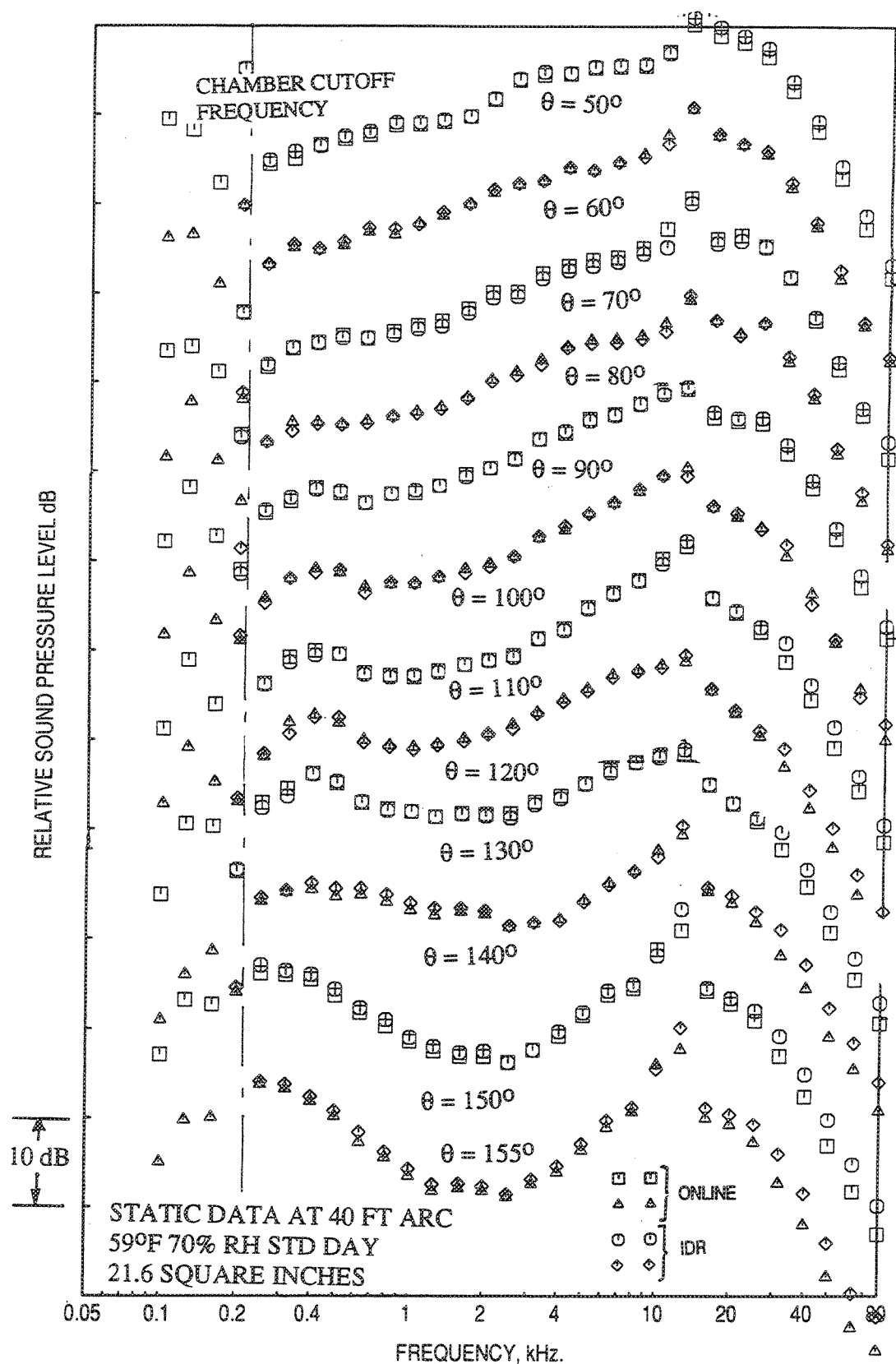


Figure 2.5-9. Comparison of SPL spectra for the 36-chute suppressor with hard-walled plug of on-line analysis with IDR analysis at all the polar angles ( $\theta$ ) measured by the tower microphones;  $P_R=2.7$ ,  $T_T=1381^\circ\text{R}$ ,  $V_J=2030$  ft/sec.

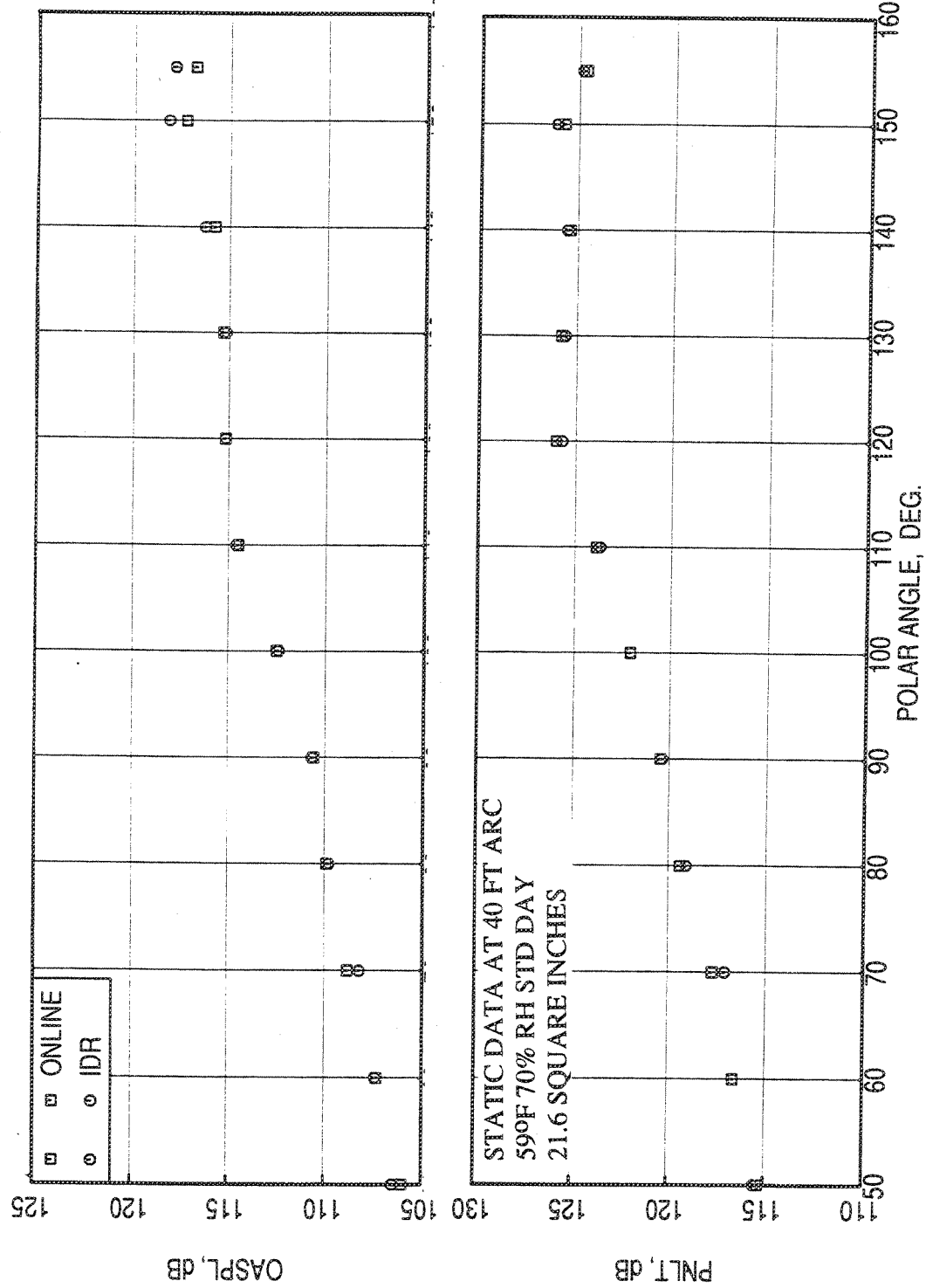


Figure 2.5-10. Comparison of OASPL and PNLT directivities for the 36-chute suppressor with hard-walled plug of on-line analysis with IDR analysis measured by the tower microphones;  $PR=2.7$ ,  $T_T=1381^\circ R$ ,  $V_J=2030$  ft/sec.

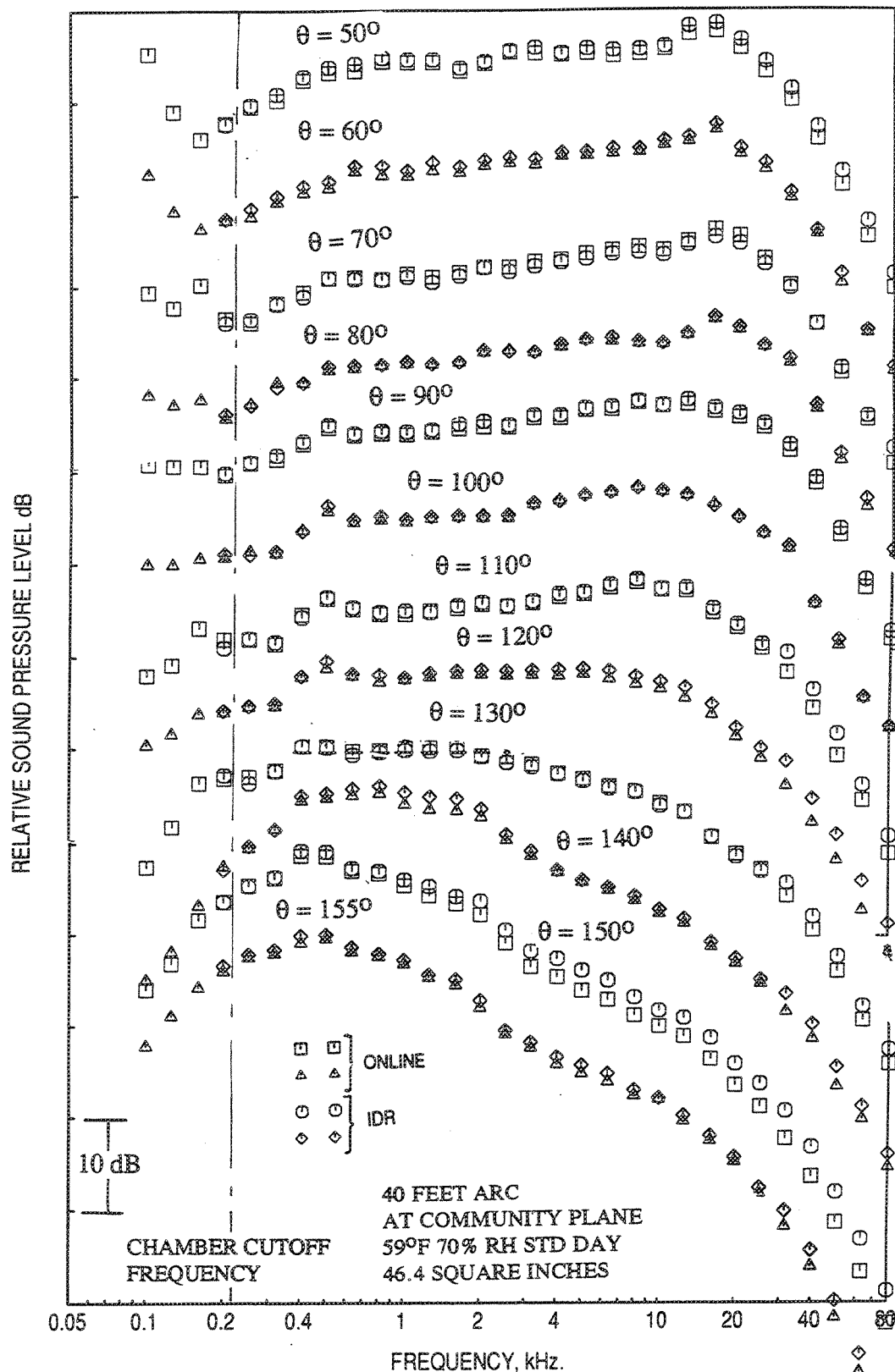


Figure 2.5-11. Comparison of SPL spectra for the suppressor with 1"-thick, 2200 wrap fluid shield and with hard-walled plug of on-line analysis with IDR analysis at all the polar angles ( $\theta$ ) measured by the tower microphones;  $P_{r,p}=3.19$ ,  $P_{r,s}=2.14$ ,  $T_{t,p}=1786^\circ\text{R}$ ,  $T_{t,s}=695^\circ\text{R}$ ,  $V_{\text{mix}}=1809$  ft/sec at static condition.

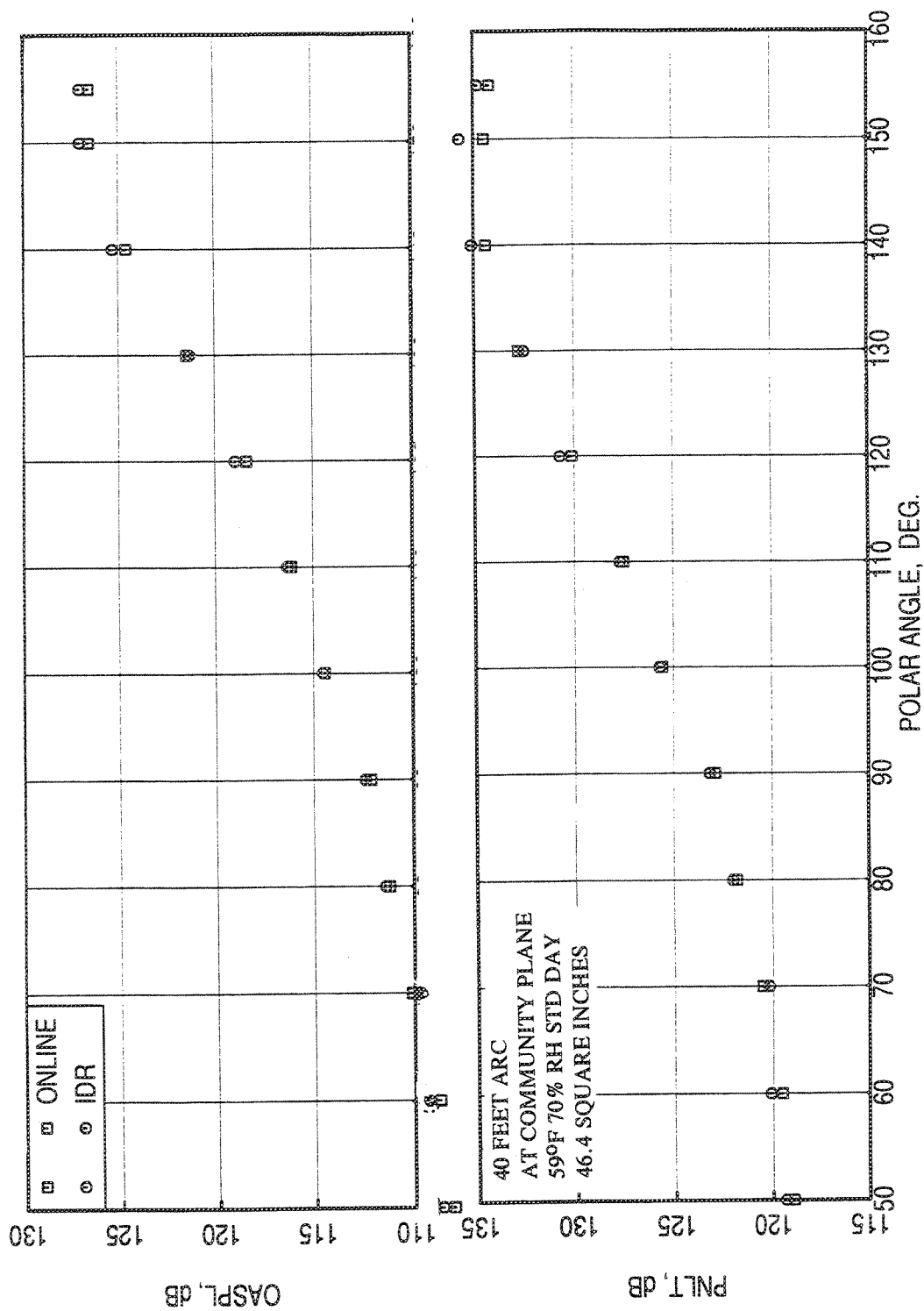


Figure 2.5-12. Comparison of OASPL and PNLT directivities for the suppressor with 1"-thick, 2200 wrap fluid shield and with hard-walled plug of on-line analysis with IDR analysis at all the polar angles ( $\theta$ ) measured by the tower microphones;  $P_{r,p} = 3.19$ ,  $P_{r,s} = 2.14$ ,  $T_{t,p} = 1786^\circ R$ ,  $T_{t,s} = 695^\circ R$ ,  $V_{mix} = 1809$  ft/sec at static condition.

are compared with the 6.54 in<sup>2</sup> conical nozzle noise data at various jet velocities. Figure 2.5-13 shows the comparison of free jet background OASPL directivity at  $M_F=0.32$  with those for the 6.54 in<sup>2</sup> conical nozzle at different jet velocities under static conditions. Freejet background OASPL levels are considerably lower compared to the conic nozzle OASPL levels, especially for  $V_J = 1215$  ft/sec and higher. Figures 2.5-14 and 2.5-15 show spectral comparisons of PWL and SPL, respectively, for the background and conic nozzle data. The noise levels for the present test conditions are considerably higher than the freejet background noise. A criterion of 10 dB signal-to-noise ratio is usually considered to be acceptable for minimal interference of noise floor with the signal to be measured. On that basis for  $V_J > 1200$  ft/sec freejet noise background level for freejet Mach number of 0.32 adequately meet the general criterion. Freejet background noise is not considered a problem for suppressor and suppressor with fluid shield nozzles due to relatively low levels of freejet noise as such nozzles' flow to be noisier than conic at low jet velocities.

**Flight Effect on Jet Noise and Shock Noise:** It is well known that the noise generated by a jet is considerably effected by forward flight. Full-scale flight testing is a direct method for obtaining the required levels without using any theory or intermediate steps. However, full-scale flight testing is very expensive and has other problems associated with measurement techniques. Hence, flight simulation on the ground for scale-model nozzle is an attractive alternative to assess the effect of flight on jet noise. When a free-jet is used as a wind tunnel to simulate the effects of flight on model noise sources, with microphones placed outside the free-jet in an anechoic environment, it is necessary to utilize analytical and/or experimental methods to correct the influence of the free-jet shear layer on the radiated sound, since the shear layer is absent in the true flight case. A number of methods have been reported in the published literature to convert flight simulation data measured in a free-jet facility to the corresponding wind-tunnel data and, finally to the true flight case.

GEAE's flight transformation method for jet noise (i.e., jet-mixing and shock noise combined) corrects for freejet shear layer refraction effects and synthesizes a mixture of monopole, dipole and quadrupole sources from the deduced static directivity and applies analytically derived dynamic amplification factors for these sources. This method is described in detail in Reference 15 along with data-theory comparisons of this technique using Bertin-Aerotraine moving frame experiments. Turbulence absorption corrections due to the propagation of noise through the free-jet flow is



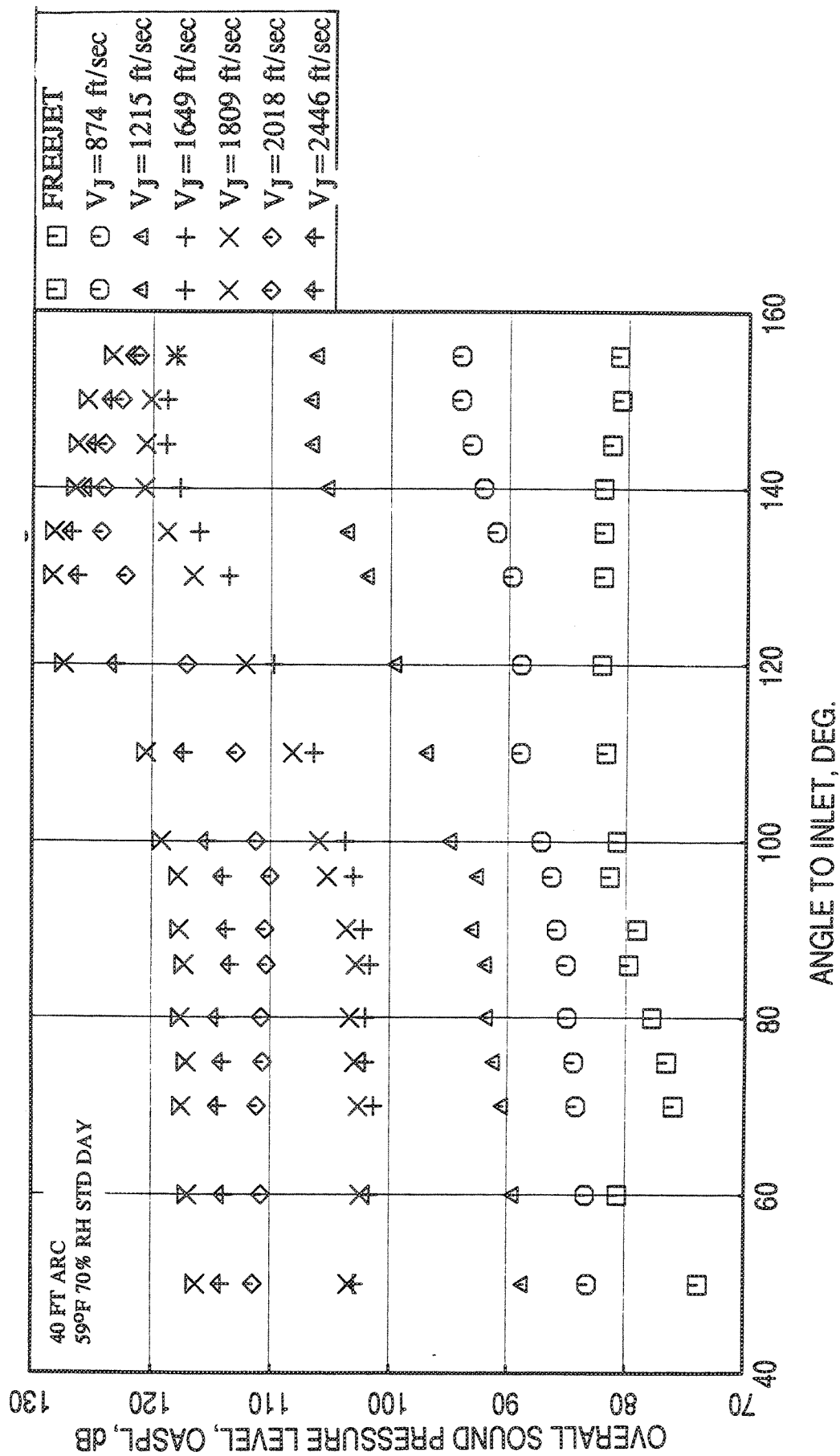


Figure 2.5-13. Comparison of freejet OASPL at free jet Mach number,  $M_F=0.32$  with OASPL of a conical nozzle of  $6.54 \text{ in}^2$  at different jet velocities ( $V_J$ ), at static conditions.

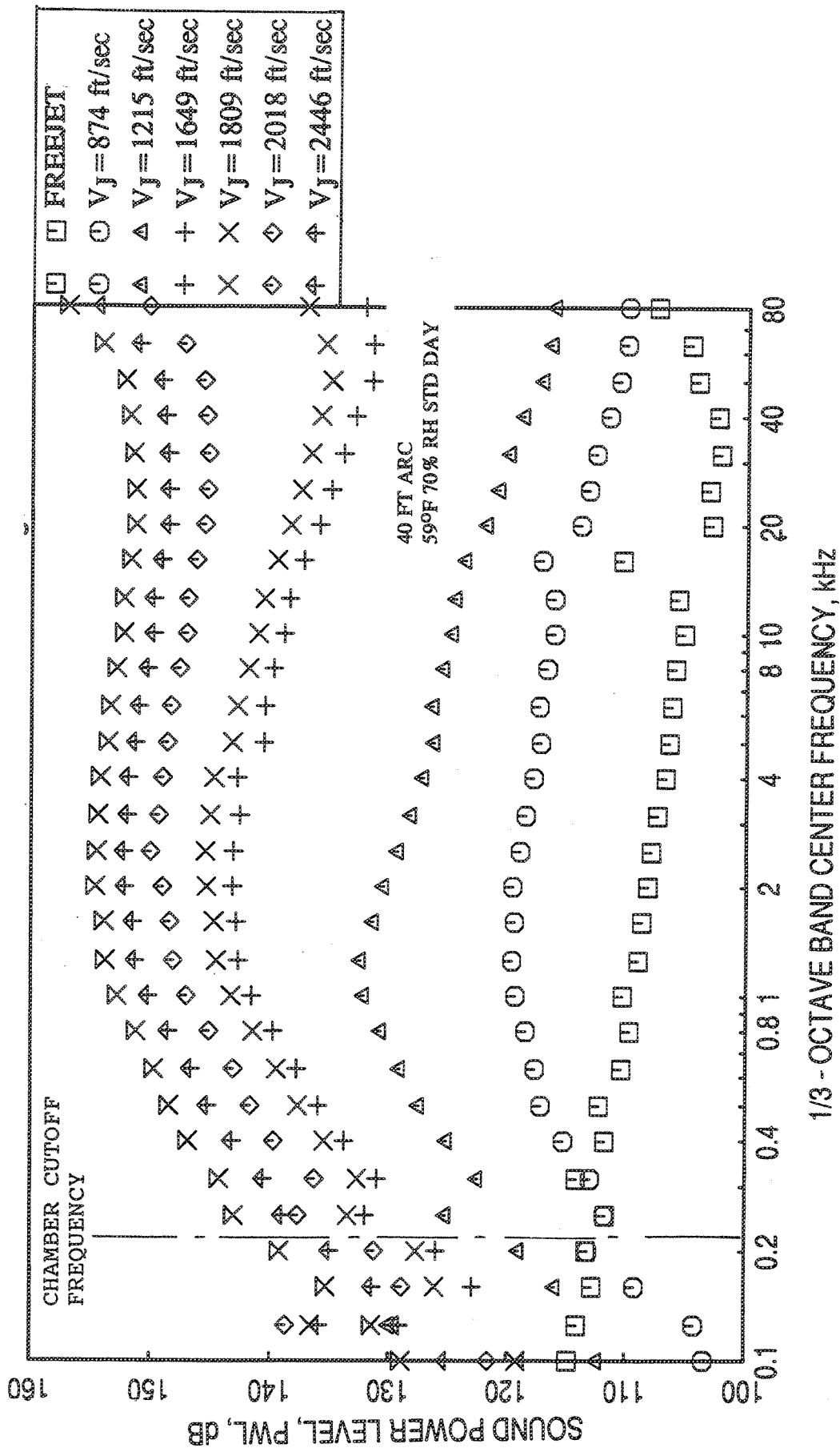


Figure 2.5-14. Comparison of freejet PWL spectrum at free jet Mach number,  $M_F = 0.32$  with PWL spectra of a conical nozzle of  $6.54 \text{ in}^2$  at different jet velocities ( $V_j$ ), at static conditions.

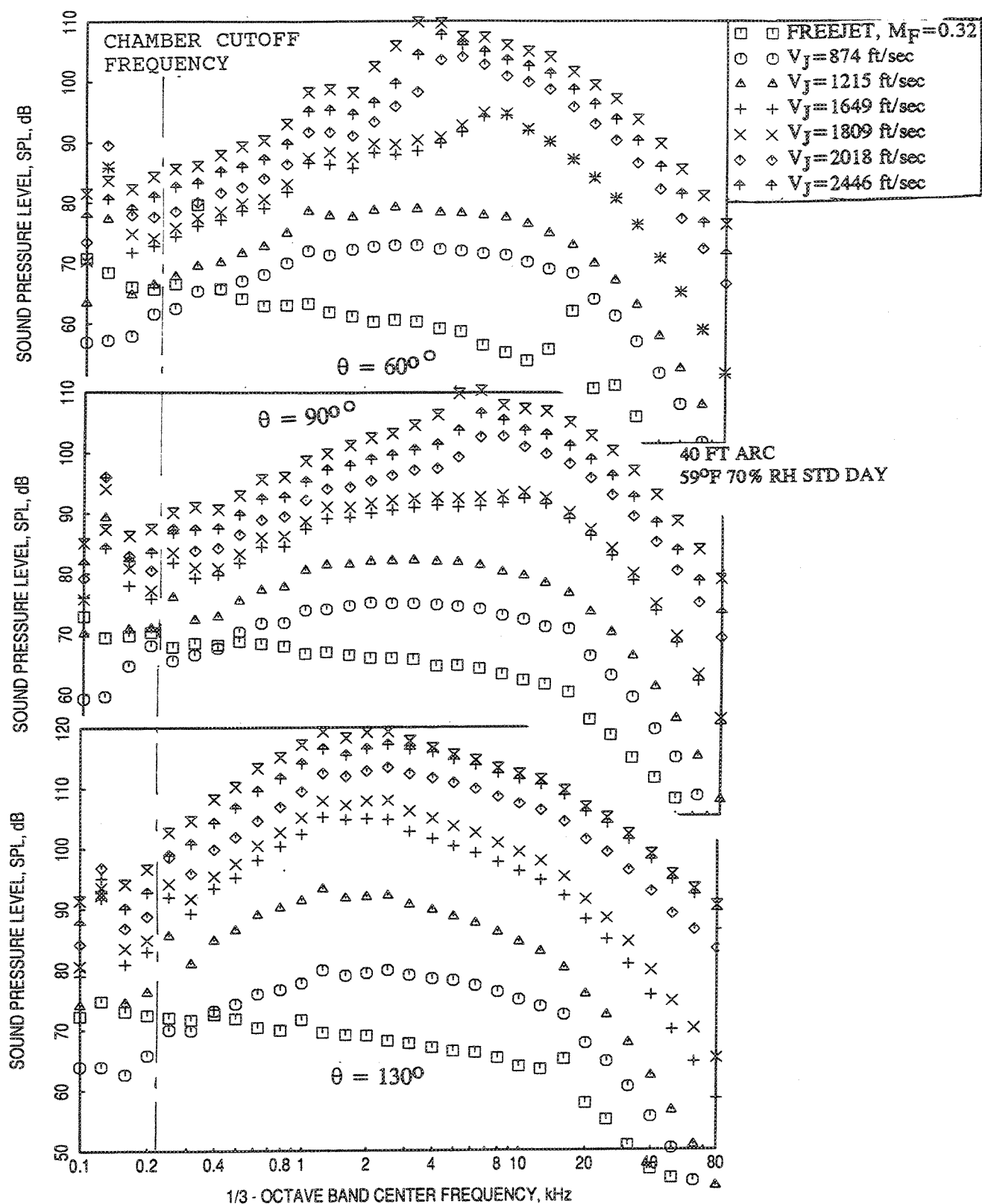


Figure 2.5-15. Comparison of freejet SPL spectrum at free jet Mach number,  $M_F=0.32$  with SPL spectra of a conical nozzle of  $6.54 \text{ in}^2$  at different jet velocities ( $V_J$ ), at static conditions.

modeled in this method. However, the user has the option to include or not to include the turbulence correction during data analysis.

Lockheed-Georgia (Ref. 16) did extensive experimental and analytical investigation of freejet simulation technique for flight effects and extended Amiet's method (Ref. 17 and 18) of angle and amplitude corrections for axially distributed sources, as one would expect for jets. In this investigation, careful analysis of experimental data indicated that as acoustic waves are refracted and scattered by the freejet shear layer as they propagate to far field, there is no or nominal absorption of acoustic energy by the turbulence in the freejet shear layer. GEAE's flight transformation procedure includes an ad hoc "turbulence absorption correction" to enable simulated flight data from freejet simulation to agree with moving train experiments. There are some technical concerns about lack of sufficient accuracy in the Bertin-Aerotraine experiments. However, Lockheed-Georgia's investigations indicated that such an absorption of acoustic energy by freejet shear layer turbulence does not occur. Hence, in all of the data that is processed, GEAE has selected to use no turbulence absorption correction option.

**Measured Versus SAE Prediction Comparisons :** Farfield noise levels are predicted by SAE method (Ref. 19) and are compared with the measured data for the 6.54 in<sup>2</sup> conical nozzle at 40 ft arc. Measured sound pressure level spectra at different polar angle  $\theta$  for a number of test conditions, with and without flight simulation, are compared with the SAE prediction. Each comparison contains the fixed as well as tower microphone data.

*Static case:* Results, without flight simulation, for three different conditions with different jet velocities are presented here in Figures 2.5-16 through 2.5-18. For a relatively lower jet velocity of  $V_J = 1716$  ft/sec (i.e., for  $P_R = 2.2$ ,  $T_T = 1216^\circ\text{R}$ ) the agreement between data and prediction is reasonably good for all angles (see Figure 2.5-16).

Similar plots for and  $V_J = 2475$  ft/sec (i.e., for  $P_R = 3.2$ ,  $T_T = 1786^\circ\text{R}$ ) are shown in Figures 2.5-17 and 2.5-18, respectively. For these cases the agreement between prediction and data seems to be good at lower frequencies. Some disagreement is observed at higher frequencies. It is our understanding that SAE method used extrapolations at large jet velocities, as the data base did not extend to high jet

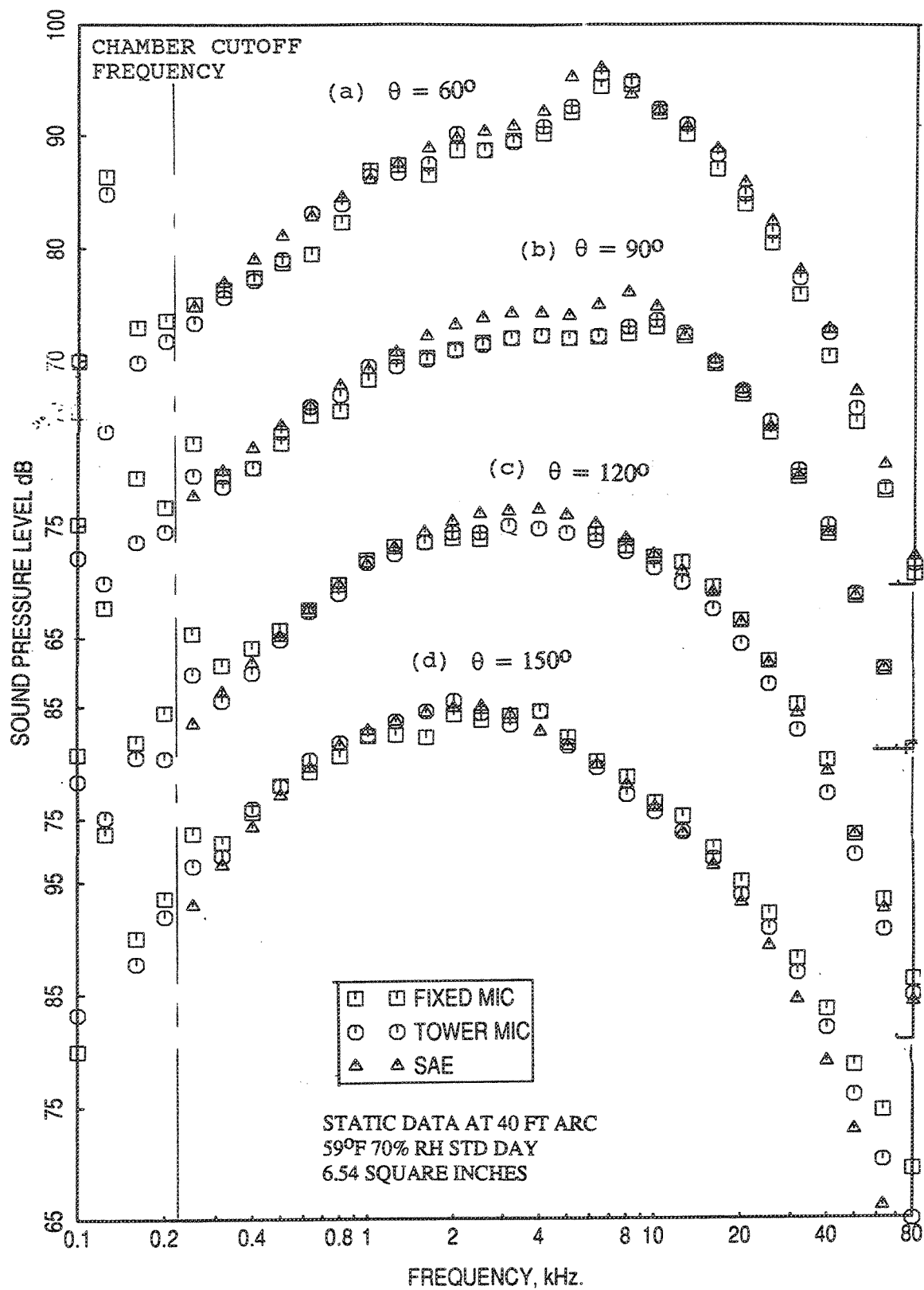


Figure 2.5-16. Comparison of SPL spectra between data and SAE prediction for a 6.54 in<sup>2</sup> conical nozzle;  $P_R=2.2$ ,  $T_T=1209^\circ\text{R}$ ,  $V_J=1716$  ft/sec.

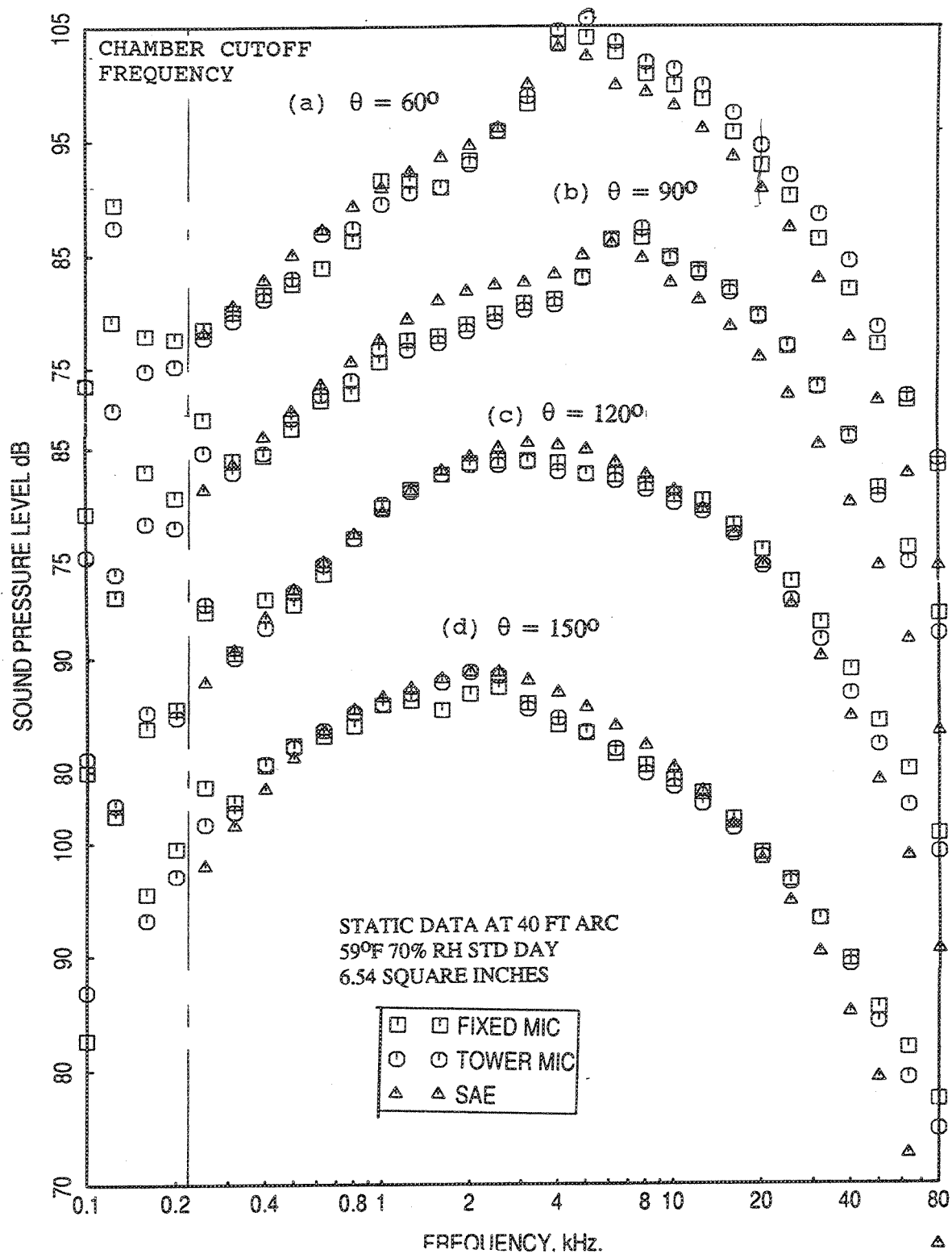


Figure 2.5-17. Comparison of SPL spectra between data and SAE prediction for a 6.54 in<sup>2</sup> conical nozzle;  $P_R=2.7$ ,  $T_T=1381^\circ R$ ,  $V_J=2030$  ft/sec.

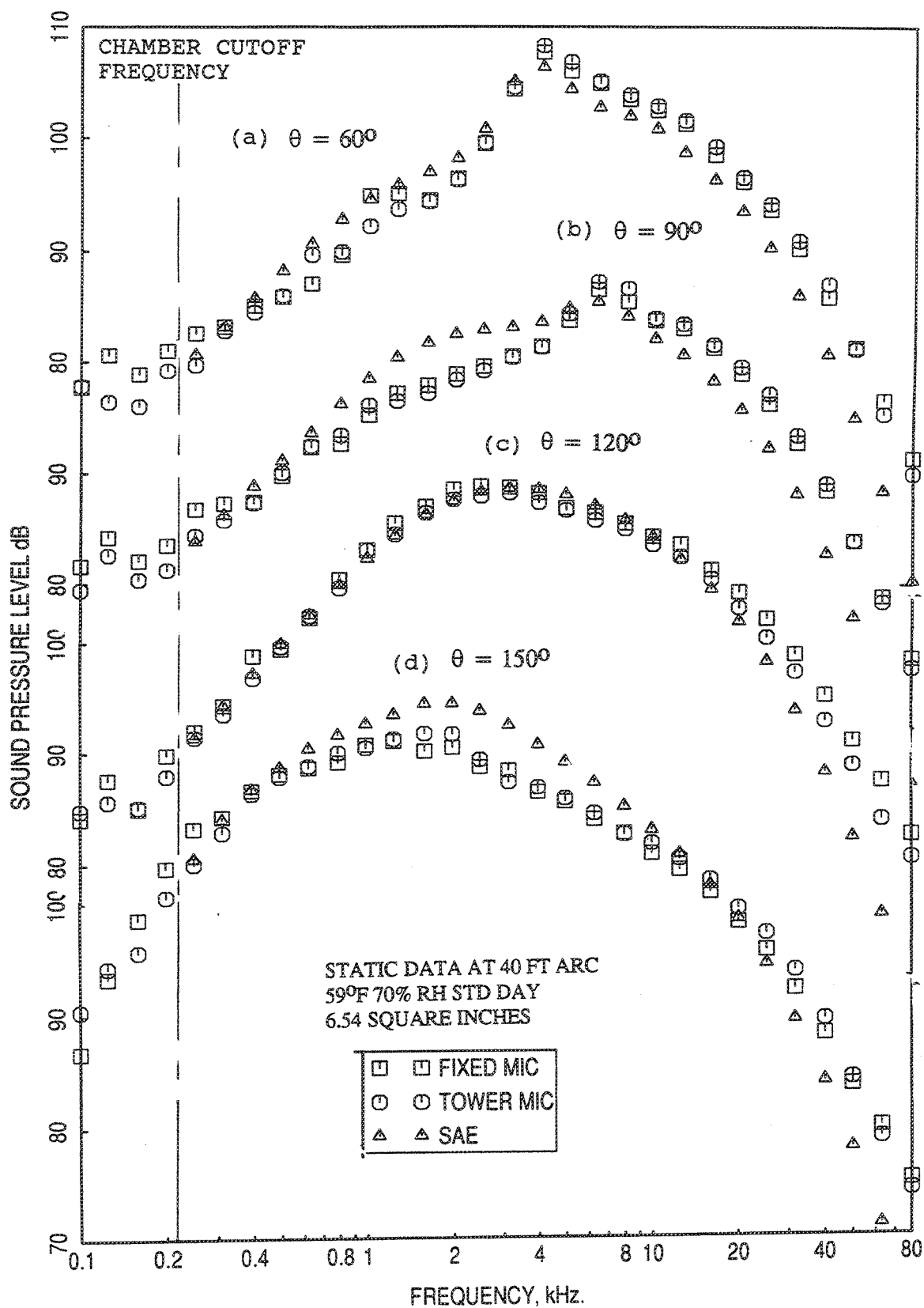


Figure 2.2-18. Comparison of SPL spectra between data and SAE prediction for a 6.54 in<sup>2</sup> conical nozzle;  $P_R=3.2$ ,  $T_T=1786^\circ\text{R}$ ,  $V_J=2475$  ft/sec.

velocities such as 2800 fps. Hence, some disagreement with SAE method is probably understandable.

Comparisons between prediction and measurements for the 6.54 in<sup>2</sup> conical nozzle with simulated flight are made in the same way as those described above for static cases. Figure 2.5-19 shows the spectral comparisons of SPL for a jet velocity of  $V_J = 1716$  ft/sec (i.e., for  $P_R = 2.2$ ,  $T_T = 1216^\circ\text{R}$ ) and the agreement between data and prediction is reasonably good for higher angles (see Figure 2.5-19). For lower angles the disagreement seems to be significant at lower frequencies. Comparisons for  $V_J = 2030$  ft/sec (i.e., for  $P_R = 2.7$ ,  $T_T = 1381^\circ\text{R}$ ) and  $V_J = 2475$  ft/sec (i.e., for  $P_R = 3.2$ ,  $T_T = 1786^\circ\text{R}$ ), as shown in Figures 2.5-20 and 2.5-21, respectively, show significant disagreement between data and prediction for all angles and frequencies. However, predicted and measured shock noise peak frequencies and corresponding amplitude are in good agreement. SAE predictions tend to be higher than data at low frequencies and vice-a-versa at higher frequencies. However, at  $150^\circ$ , the differences between data and prediction seem to be relatively small for entire frequency range.

Possible reasons for the noted difference between SAE predictions and data are given below:

1. SAE method utilizes a "flight exponent (m) method" to project to flight using static jet mixing noise spectra. It utilizes the simple and widely used monopole dynamic amplification factor for shock noise. GEAE's flight transformation method corrects for freejet shear layer refraction effects and synthesizes a mixture of monopole, dipole and quadrupole sources from the measured spectra and applies appropriate dynamic amplification factors for these sources. This method is described in detail in Reference 15 along with data-theory comparisons of this technique using Bertin-Aerotraine moving frame experiments. The relatively large differences at low frequencies at very small angles to the jet axis are possibly attributable to the differences in the "relative velocity effect" on jet mixing noise between the two methods.

2. During the flight simulation tests an annular nozzle was mounted around the core conical nozzle, which was operated at the same velocity as that of the tertiary flow (i.e., flight simulation velocity of 360 feet/sec.). Even though the velocity in this secondary stream was 360 feet/sec the temperature was relatively higher compared to



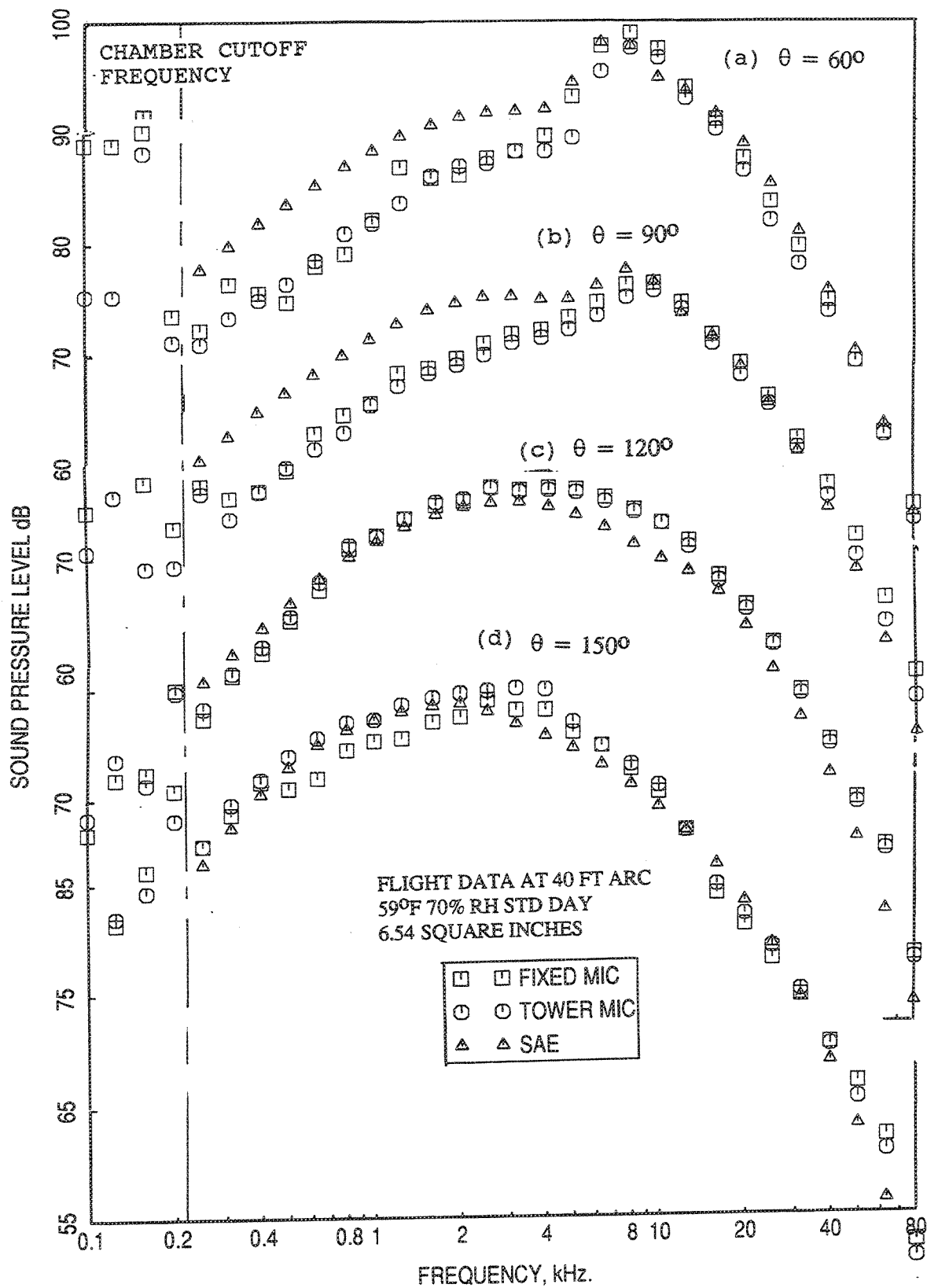


Figure 2.5-19. Comparison of SPL spectra between data and SAE prediction with flight simulation for a 6.54 in<sup>2</sup> conical nozzle;  $M_F=0.32$ ,  $P_R=2.7$ ,  $T_T=1381^\circ R$ ,  $V_J=2030$  ft/sec.

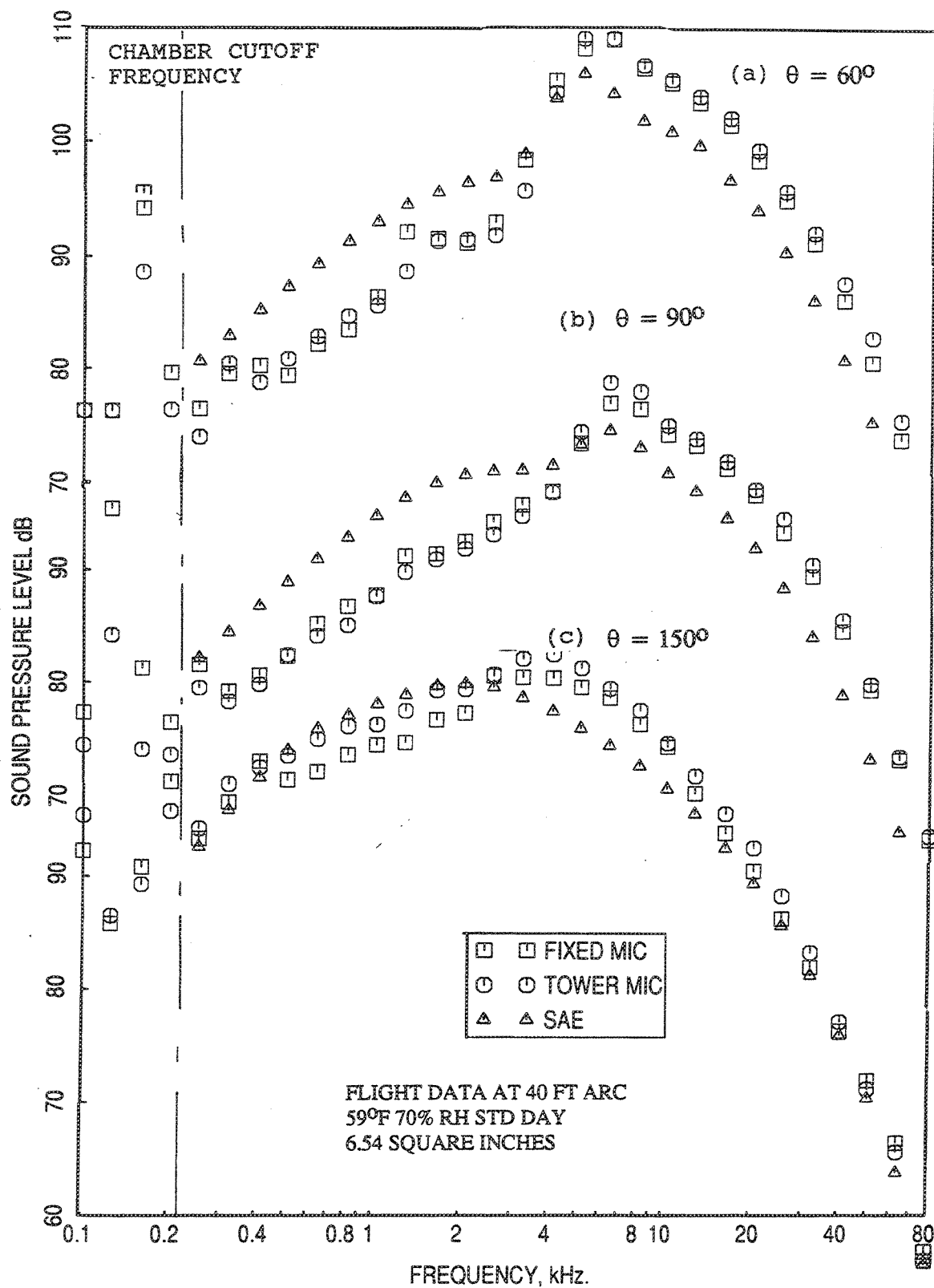


Figure 2.5-20. Comparison of SPL spectra between data and SAE prediction with flight simulation for a 6.54 in<sup>2</sup> conical nozzle;  $M_F=0.32$ ,  $P_R=3.2$ .  $T_T=1786^\circ R$ ,  $V_J=2475$  ft/sec.

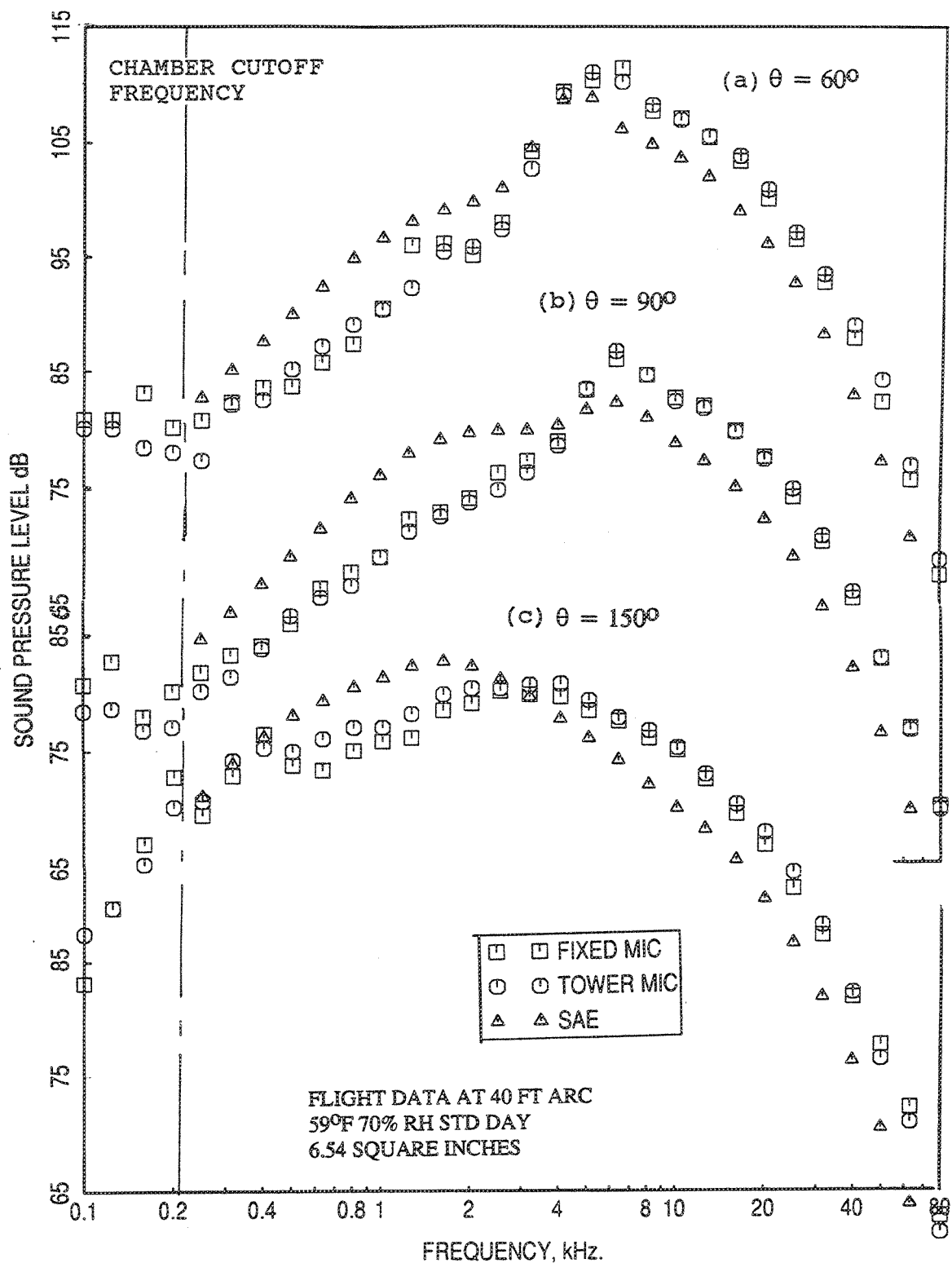


Figure 2.5-21. Comparison of SPL spectra between data and SAE prediction with flight simulation for a 6.54 in<sup>2</sup> conical nozzle;  $M_F=0.32$ ,  $P_R=4.0$ ,  $T_T=1960^\circ R$ ,  $V_J=2796$  ft/sec.

the tertiary flow due to the heat transfer from heated core flow. This might have created an additional shear layer.

It should be noted that the agreement between the fixed microphone data and traversing microphone data is very good for most of the angular locations in the above results.

**Measured Versus MS Prediction Comparisons :** The MS method (Ref. 20) to predict farfield noise for a single conical nozzle jet is similar to the SAE method, except the jet noise correlations are slightly modified by utilizing additional test data. Farfield noise levels are predicted by MS method and are compared with the measured data for the 6.54 in<sup>2</sup> conical nozzle, extrapolated to a sideline distance of 1629 ft and scaled to a size of 1175 in<sup>2</sup>. In these comparisons, only the tower microphone data are used.

*Static case:* Figure 2.5-22 shows the comparison between data and prediction of pseudo EPNLT and PNLT at various polar angles  $\theta$  with respect to jet velocity  $V_J$ . Reasonable agreement is achieved in these comparisons, except the measured PNLT values are relatively higher for higher jet velocities at lower polar angles. These disagreements are mainly due to the dominant screech and shock associated noise in the measurement, not accurately predicted by MS method. There are two distinct lines, showing the variation of PNLT with respect to  $V_J$ , especially at lower polar angles. This is due to the two different aero thermodynamic lines, namely, takeoff flade cycle and cutback flade cycle (see Figure 2.2-22), used for testing and prediction. Takeoff cycle covers higher nozzle pressure ratio with lower temperatures and the cutback cycle covers relatively lower nozzle pressure ratio with higher temperatures. Even with the normalized PNLT, the dominant shock associated noise due to higher nozzle pressure ratio of takeoff cycle does not collapse with that of a case with the same jet velocity for cutback cycle.

Measured PNLT and OASPL directivities and sound pressure level spectra at different polar angle  $\theta$  for three test conditions are compared with the MS prediction in Figures 2.5-23 through 2.5-25. For a relatively lower jet velocity of  $V_J = 1651$  ft/sec (i.e., for  $P_R = 2.188$ ,  $T_T = 1129^\circ\text{R}$ , a cutback cycle point) with less shock associated noise the predicted PNLT and OASPL values agree well with the data at lower and higher polar angles, as shown in Figure 2.5-23. The spectral agreement of SPL is very good at  $60^\circ$ . At higher angles the predicted SPLs are relatively higher at lower frequencies compared to data. For higher velocities due to takeoff cycle the PNLT and OASPL

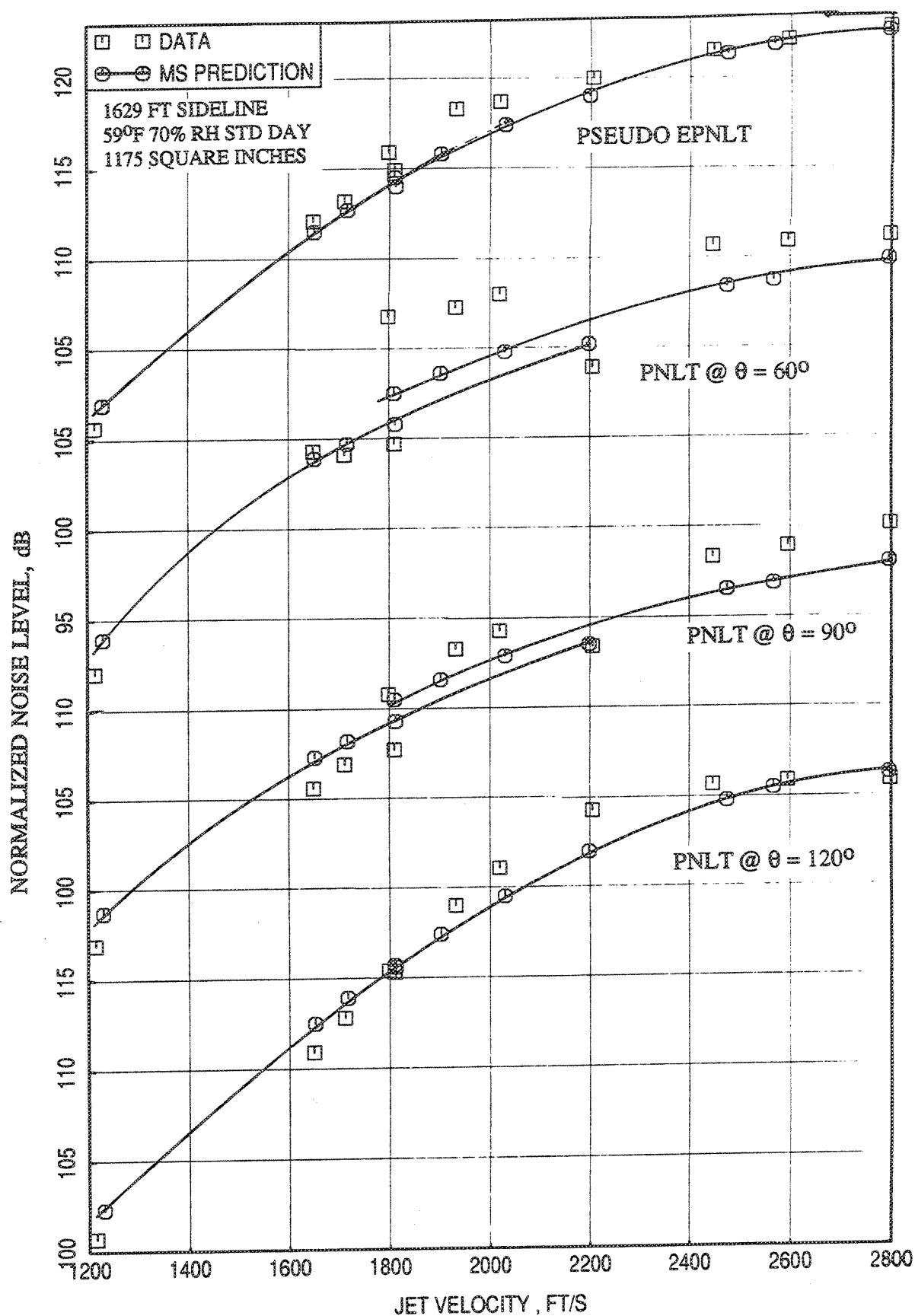


Figure 2.5-22. Comparison of pseudo EPNLT and PNLT at different polar angles  $\theta$  between data and MS prediction with respect to jet velocity  $V_J$  for a 6.54 in<sup>2</sup> conical nozzle.

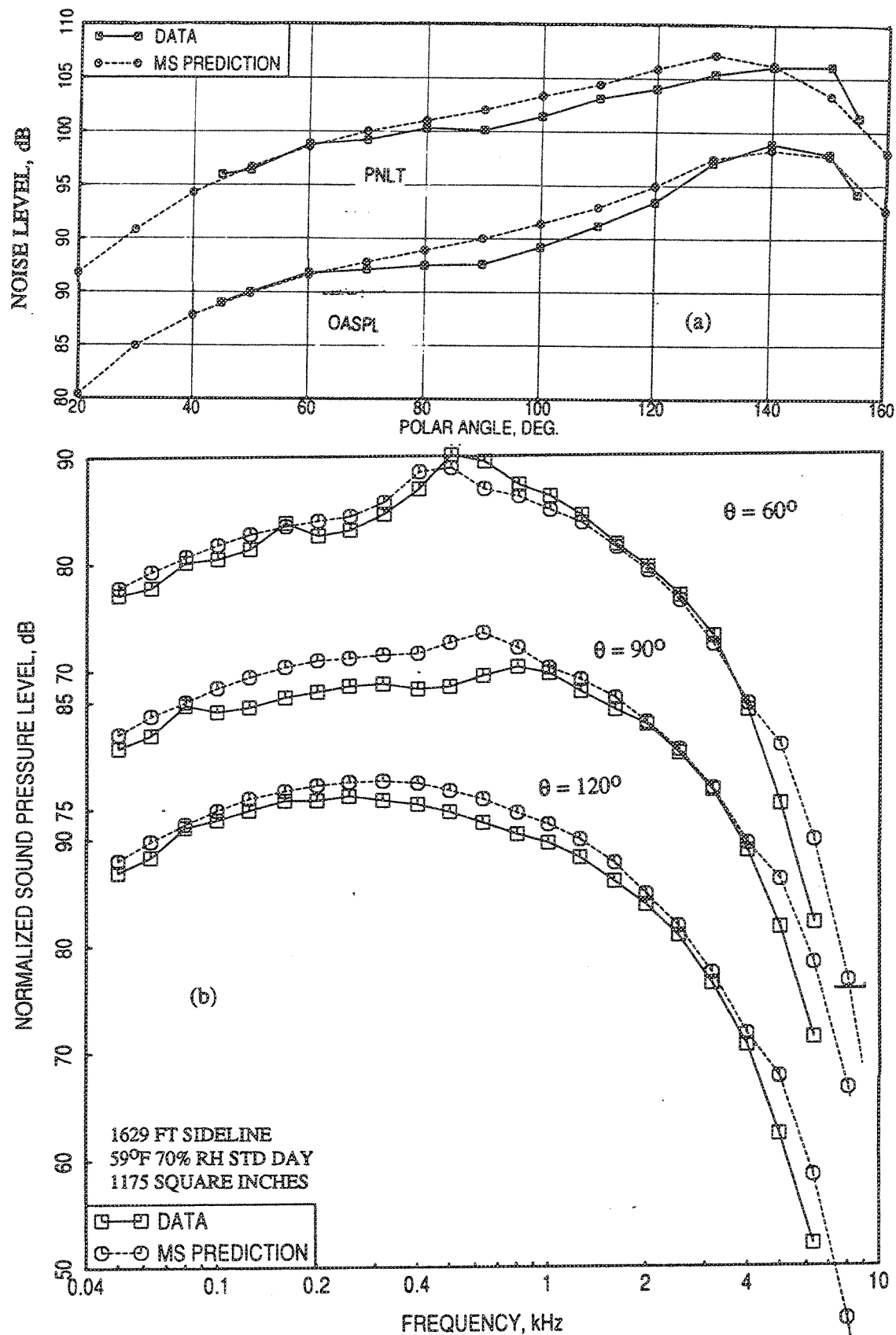


Figure 2.5-23. Comparison of (a) PNLT and OASPL directivities and (b) SPL spectra between data and MS prediction for a 6.54 in<sup>2</sup> conical nozzle;  $P_R=2.188$ ,  $T_T=1129^\circ\text{R}$ ,  $V_J=1651$  ft/sec.

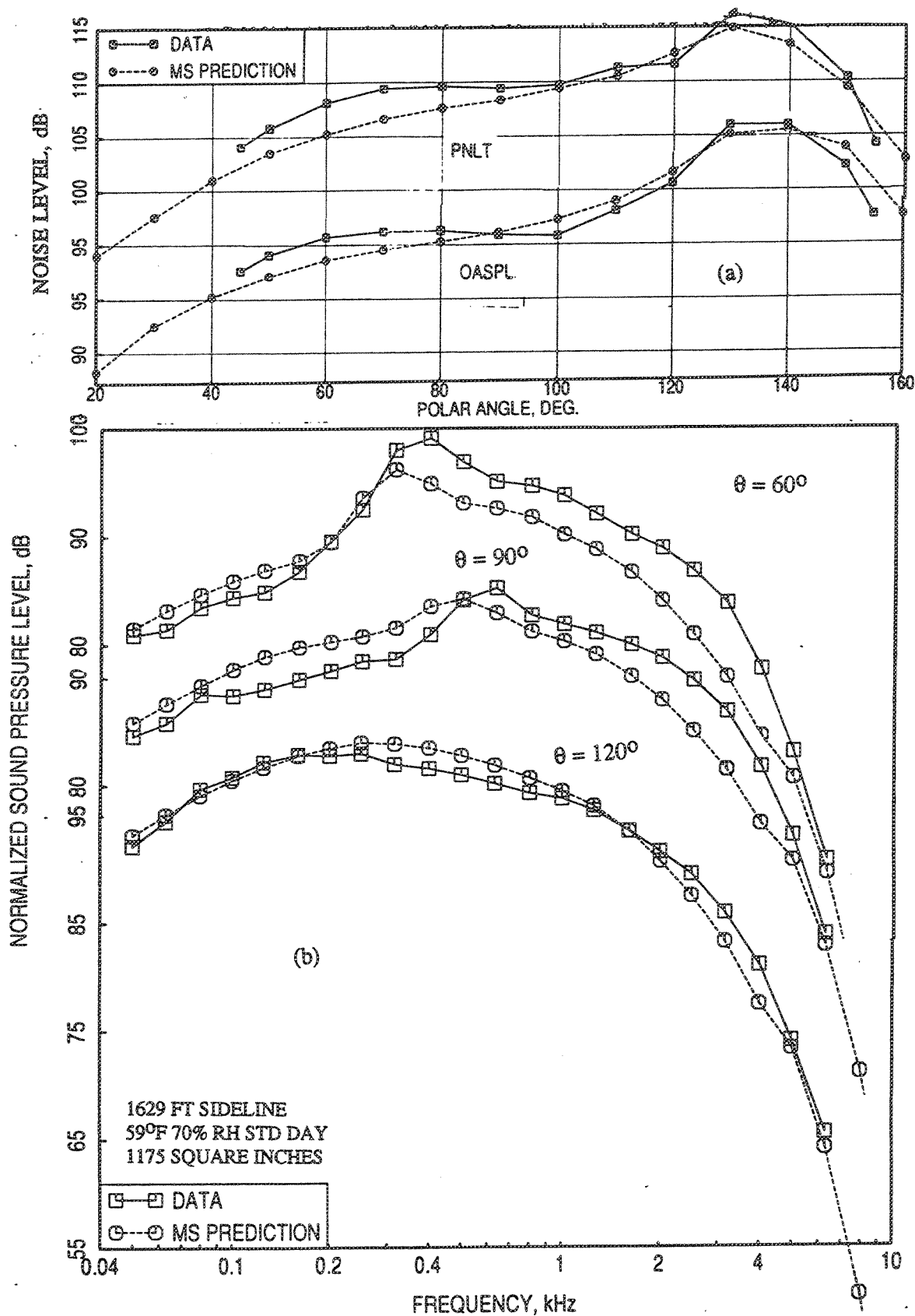


Figure 2.5-24. Comparison of (a) PNLT and OASPL directivities and (b) SPL spectra between data and MS prediction for a 6.54 in<sup>2</sup> conical nozzle;  $P_R=2.7$ ,  $T_T=1381^\circ\text{R}$ ,  $V_J=2030$  ft/sec.

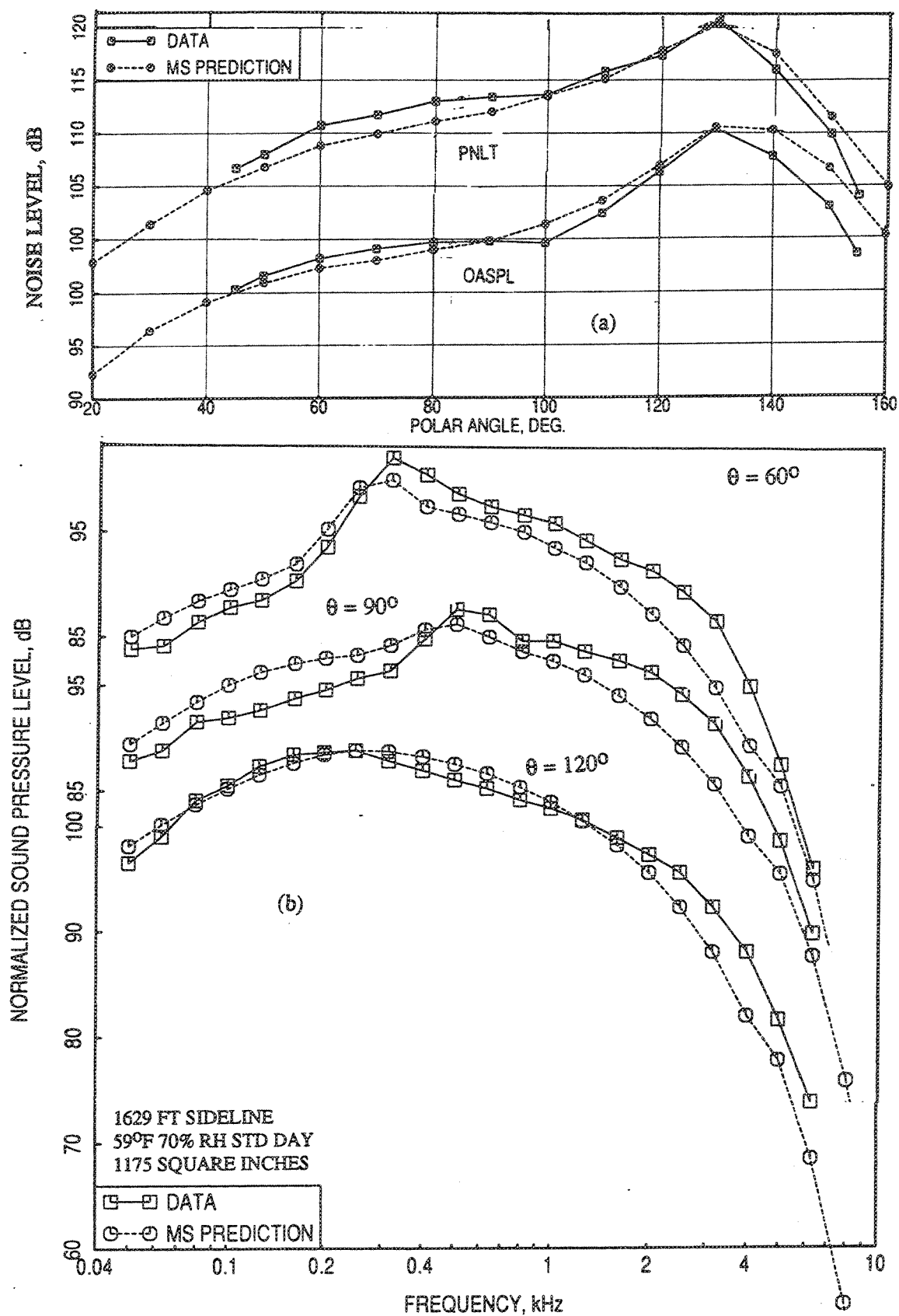


Figure 2.5-25. Comparison of (a) PNLT and OASPL directivities and (b) SPL spectra between data and MS prediction for a 6.54 in<sup>2</sup> conical nozzle;  $P_R=3.2$ ,  $T_T=1786^\circ\text{R}$ ,  $V_J=2475$  ft/sec.



directivities show disagreement between data and prediction at lower polar angles, which is due to dominant shock noise in the measurement (see Figures 2.5-24 and 2.5-25). This is clearly observed in the corresponding SPL spectra, where the measured SPL levels are higher compared to prediction at lower angles.

*Flight case:* For flight simulated case the predicted results are compared with the measured data processed without turbulence absorption. Figure 2.5-26 shows the comparison between data and prediction of EPNLT and PNLT at various polar angles  $\theta$  with respect to jet velocity  $V_J$ . Reasonable agreement is achieved in these comparisons between prediction and data for takeoff cycle. The significant disagreement between prediction and data at lower velocities are most likely due to the reasons described earlier under SAE comparison, that the flight simulation corrections are not adequately modeled in the prediction and that the tested nozzle was not strictly a single stream nozzle.

To examine the comparisons of PNLT and OASPL directivities and sound pressure level spectra at different polar angle  $\theta$ , three test conditions are chosen, which show reasonable agreement of EPNLT and PNLT between the data and prediction with respect to  $V_J$  (see Figures 2.5-27 through 2.5-29). For a relatively lower jet velocity of  $V_J = 1809$  ft/sec (i.e., for  $P_R = 2.5$ ,  $T_T = 1180^\circ\text{R}$ ) the predicted PNLT and OASPL values agree well with the data at higher polar angles, as shown in Figure 2.5-27. The spectral comparison of SPL indicates over prediction in lower frequency range and under prediction in the higher frequencies. The similar trends are also observed at higher jet velocities of 2030 ft/sec and 2475 ft/sec as shown in Figures 2.5-28 and 2.5-29.

**Old Versus Present Conical Nozzle Noise Data :** Acoustic data from previous NASA sponsored test efforts on conical nozzles within the General Electric Anechoic Free-jet Facility (Ref. 21-23) and a full scale conical nozzle engine test (Ref. 24) are summarized in Reference 25 in a systematic manner to establish a baseline for conical nozzle noise data. These results include Sound Power Level (PWL), Overall Sound Pressure level (OASPL), Perceived Noise Level (PNL), and Sound Pressure Level (SPL) presented as functions of Jet Velocity Parameter ( $V_{\text{par}}$ ), Frequency ( $f$ ), Angle to Inlet ( $\theta$ ), Shock Strength Parameter ( $SH_{\text{par}}$ ). In an attempt to validate the present measured data for the 6.54 in<sup>2</sup> conical nozzle, some of these data are compared with the old results.

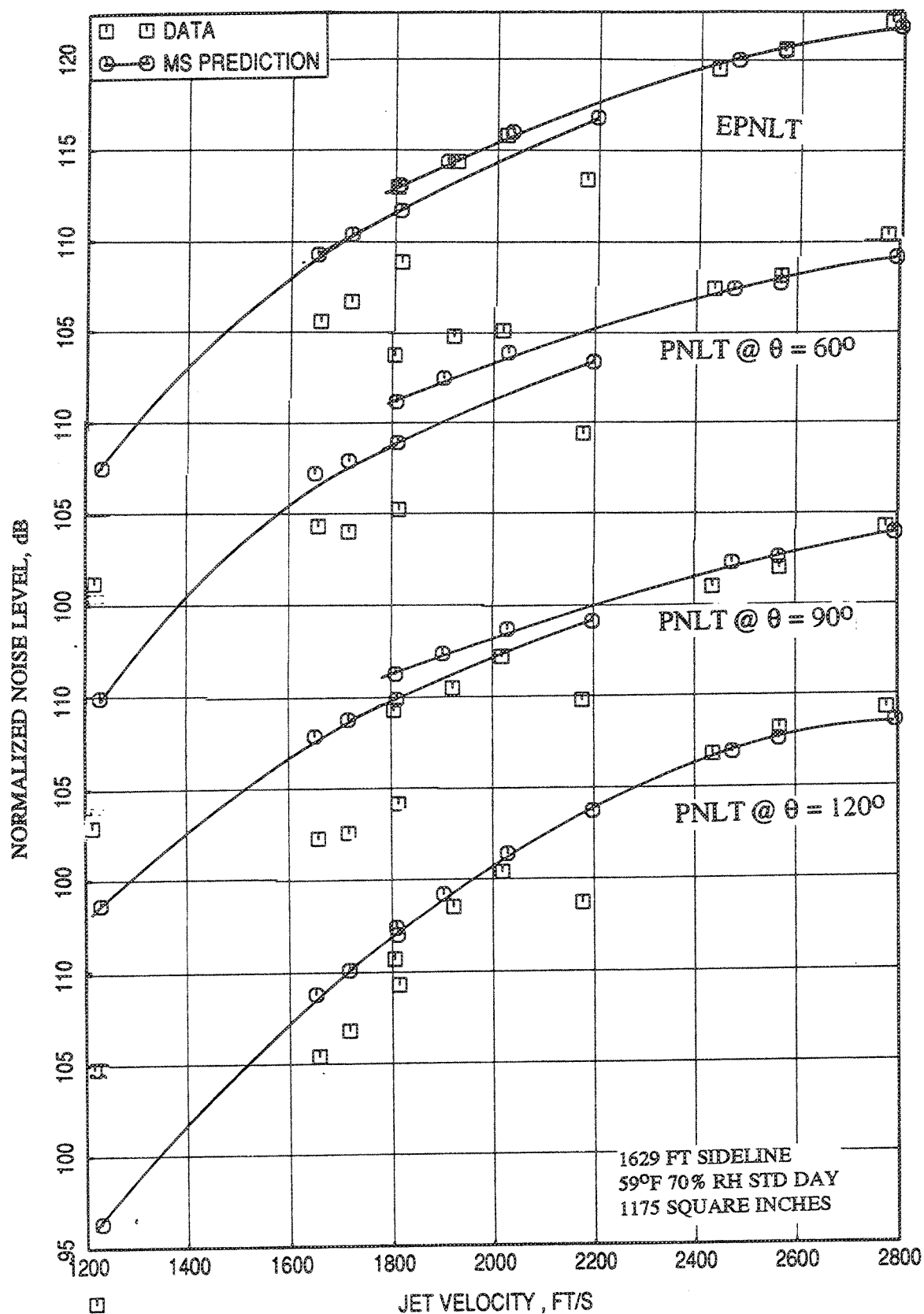


Figure 2.5-26. Comparison of EPNLT and PNLT at different polar angles  $\theta$  between data and MS prediction with respect to jet velocity  $V_J$  for a  $6.54 \text{ in}^2$  conical nozzle with flight simulation;  $M_F=0.32$ .

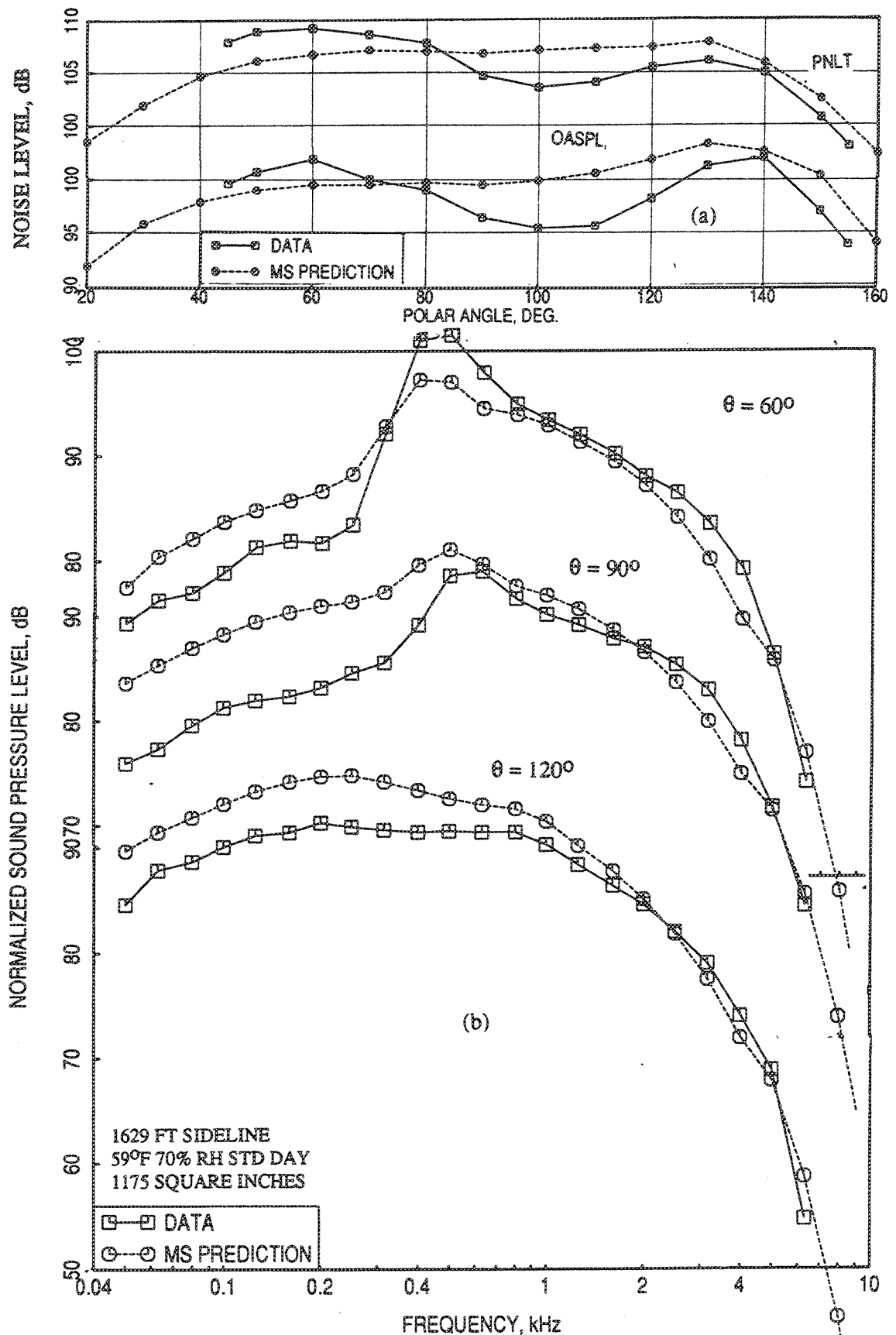


Figure 2.5-27. Comparison of (a) PNLT and OASPL directivities and (b) SPL spectra between data and MS prediction with flight simulation for a 6.54 in<sup>2</sup> conical nozzle;  $M_F=0.32$ ,  $P_R=2.5$ ,  $T_T=1180^\circ\text{R}$ ,  $V_J=1809$  ft/sec.

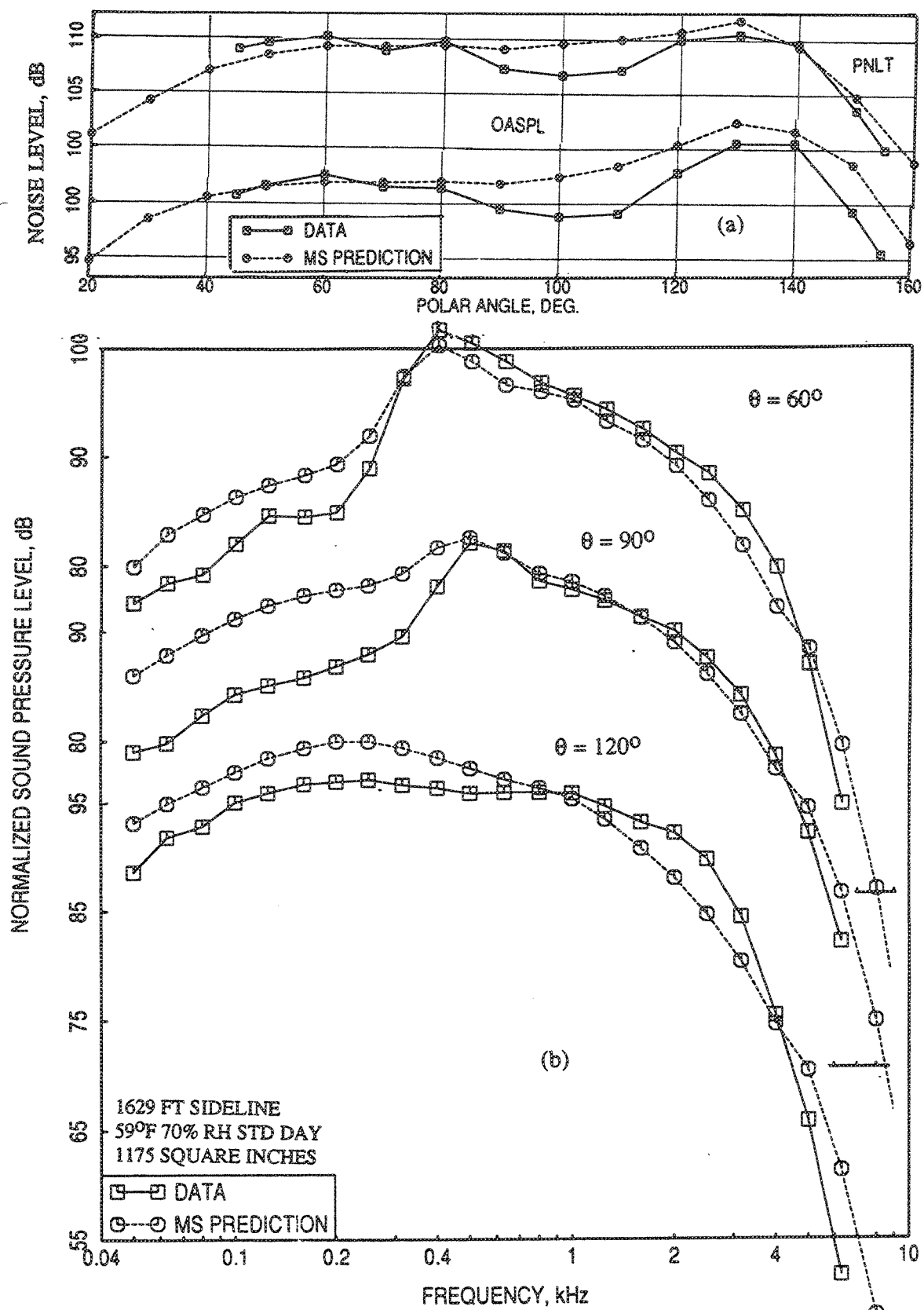


Figure 2.5-28. Comparison of (a) PNLT and OASPL directivities and (b) SPL spectra between data and MS prediction with flight simulation for a 6.54 in<sup>2</sup> conical nozzle;  $M_F=0.32$ ,  $P_R=2.7$ ,  $T_T=1381^\circ R$ ,  $V_J=2030$  ft/sec.

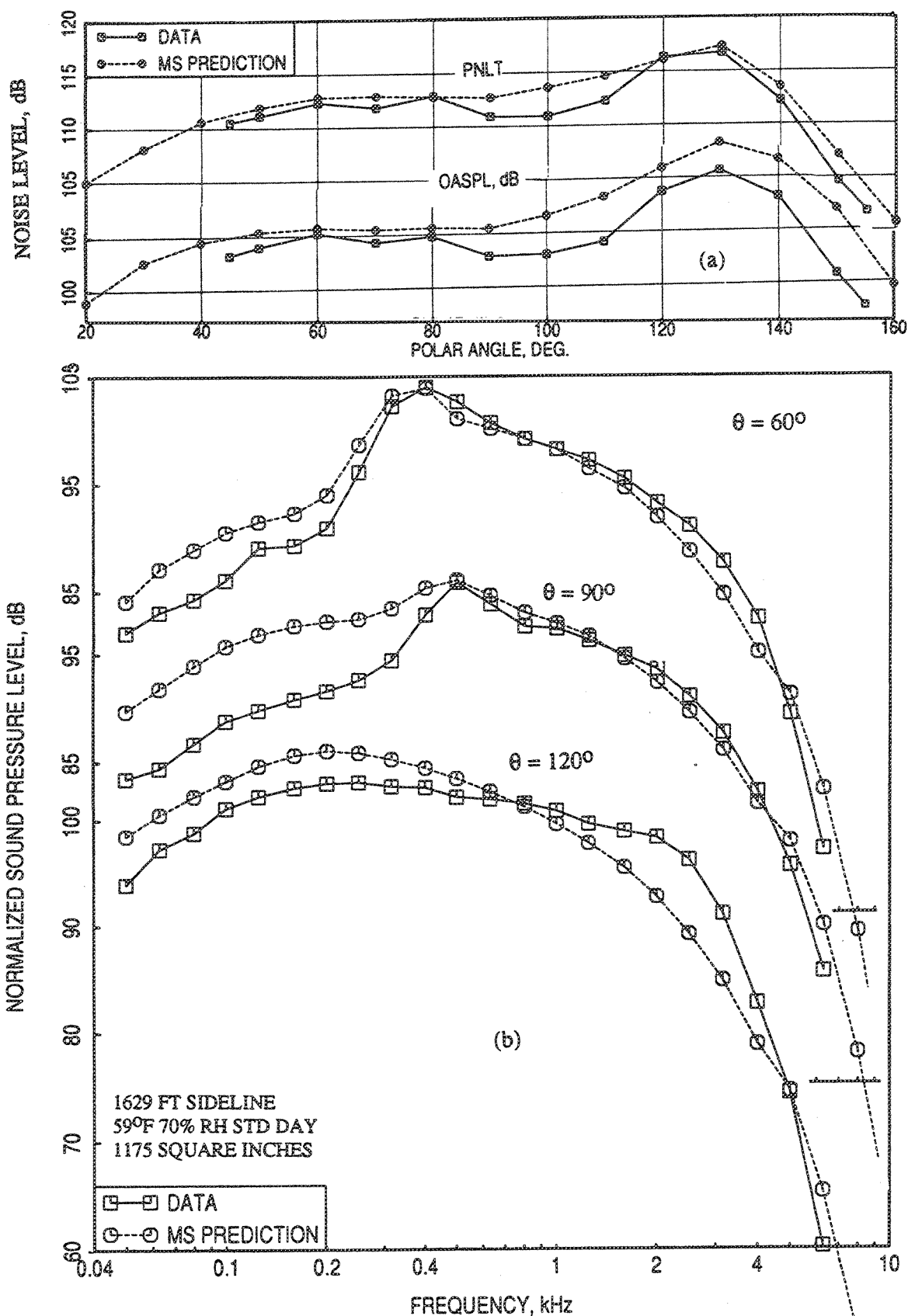


Figure 2.5-29. Comparison of (a) PNLT and OASPL directivities and (b) SPL spectra between data and MS prediction with flight simulation for a 6.54 in<sup>2</sup> conical nozzle;  $M_F=0.32$ ,  $P_R=3.2$ ,  $T_T=1786^\circ R$ ,  $V_J=2475$  ft/sec.

Comparison of old and present data are illustrated in this section, first for static condition and then with flight simulation. In all these comparisons the present data acquired by the tower microphones at  $\phi=10^\circ$  position and by the fixed microphones at  $\phi=45^\circ$  position are plotted against the old data. All the data, old and present, are scaled to 1400 in<sup>2</sup> nozzle exit area, extrapolated to 2400 feet sideline, and corrected to standard day conditions of 59°F and 70% relative humidity. Turbulence absorption correction is applied to these results and a reference thrust,  $F_{\text{ref}} = 5130$  lbs, is used for normalization process to be consistent with the old data. Limited amount of narrowband data are presented to illustrate certain shock and screech phenomena. These data are also scaled to 1400 in<sup>2</sup> nozzle exit area and extrapolated to 2400 feet sideline. Standard day corrections, atmospheric absorption during extrapolation process, and microphone head and line corrections are not applied to the narrowband data. Since all the narrowband comparisons are made for the same microphone position, these corrections are not crucial for diagnostic studies.

*Static Data :* Figure 2.5-30 shows the comparison of Normalized Overall Sound Power Level (OAPWLN) and Normalized Overall Sound Pressure Level (OASPLN) and Figure 2.5-31 shows the comparison of Normalized Perceived Noise Level (PNLN) between old and present data as functions of jet velocity parameter. The agreement between old and present OAPWLN data is excellent for entire velocity range. For OASPLN and PNLN, the agreement is very good except in the forward arc for jet velocity parameters between 2.0 and 2.6. In addition, points at 1.7 and 1.9 are slightly off at  $60^\circ$  position. Figures 2.5-32 and 2.5-33 show the comparison of old OASPL and PNL data as functions of shock strength parameter with the present data. The agreement is very good except in the forward arc for shock strength parameter between -1.6 and -1.0, which corresponds to the same data points not agreeing with old results in normalized form, shown in Figures 2.5-30 and 2.5-31.

The jet noise spectra of model nozzles operating at supercritical pressure ratios, similar to the present study, contain discrete tones. These intense discrete tones, known as screech, are generated from a feedback mechanism. Screech is an unsteady phenomenon which may not occur for every nozzle or for each supercritical conditions. The occurrence of this noise is more probable for small scale nozzles, since smaller nozzles have thinner lips which is known to induce screech more readily. Screech is dominant in the forward arc.

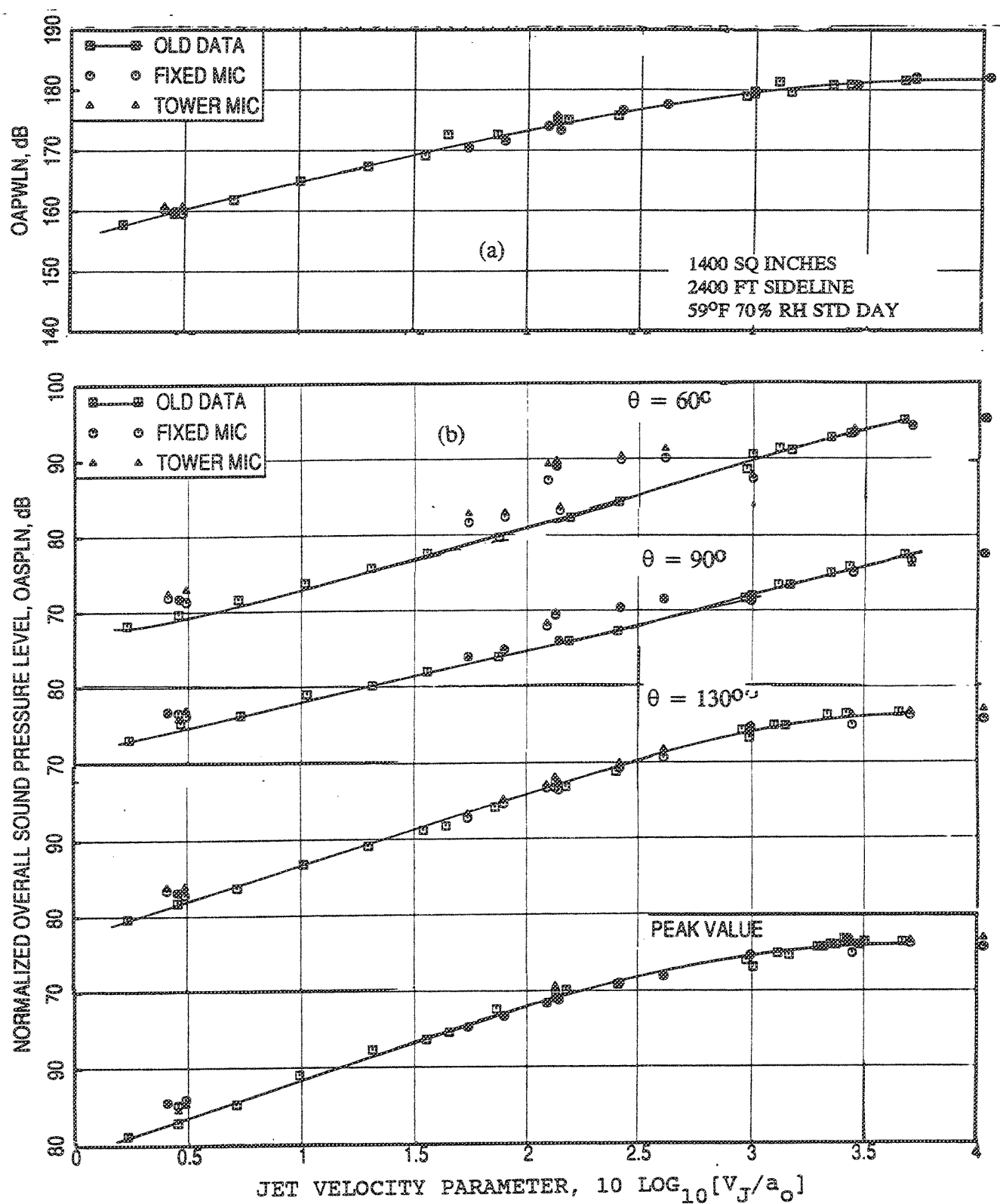


Figure 2.5-30. Comparison of old normalized (a) OAPWL and (b) OASPL data as a function of jet velocity parameter with the present data acquired using a 6.54 in<sup>2</sup> conical nozzle at static condition.

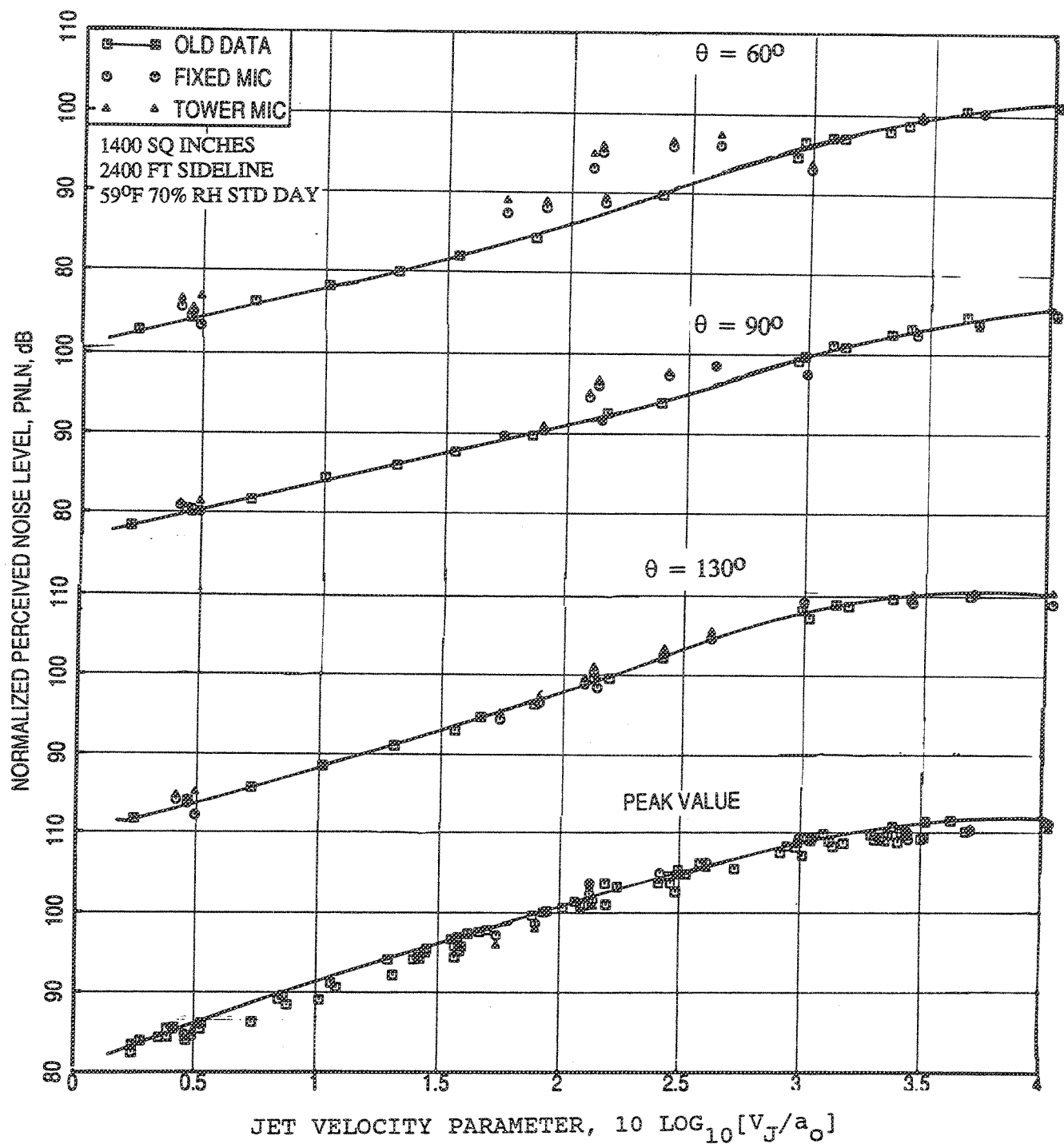


Figure 2.5-31. Comparison of old normalized PNL data as a function of jet velocity parameter with the present data acquired using a 6.54 in<sup>2</sup> conical nozzle at static condition.



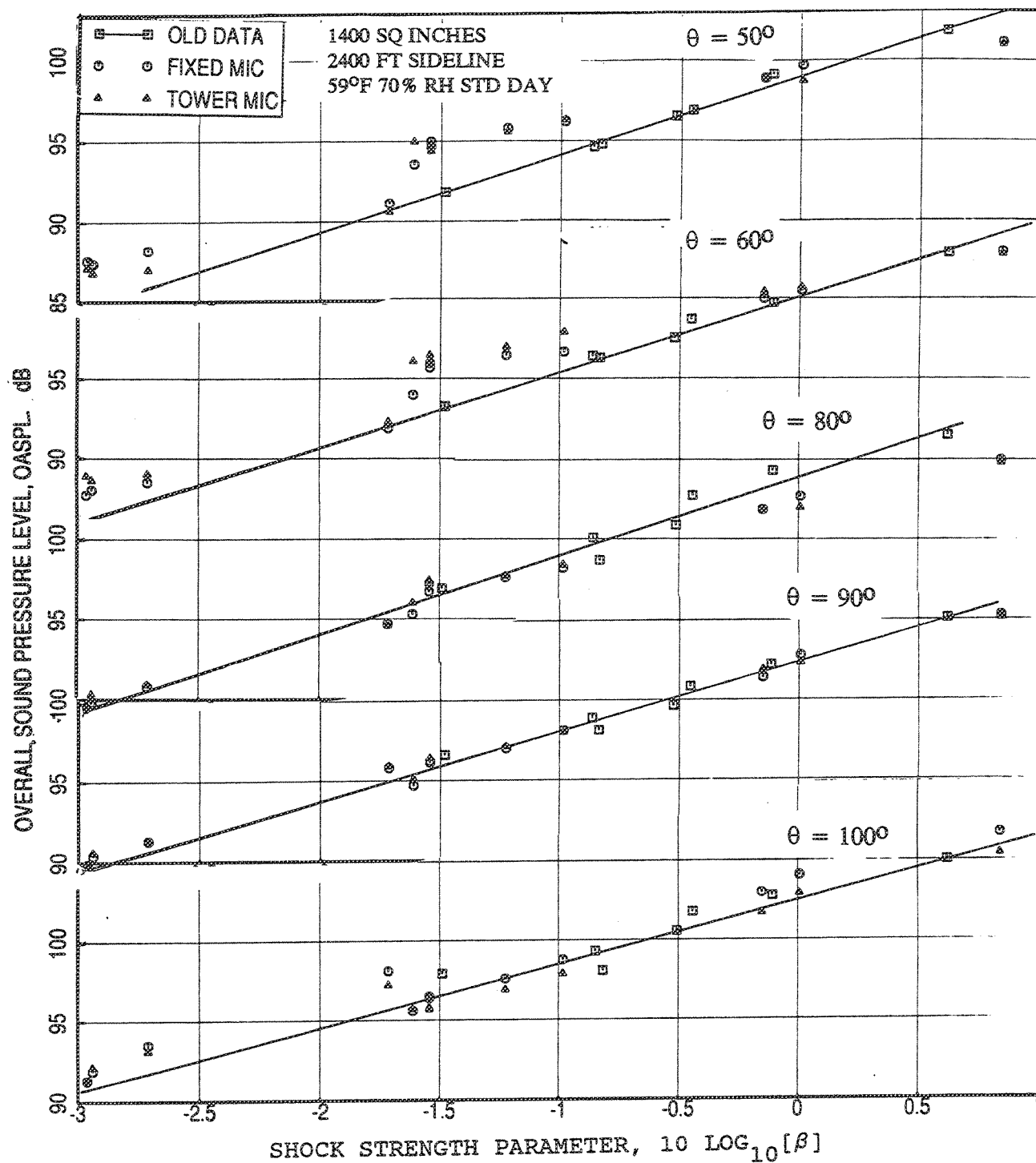


Figure 2.5-32. Comparison of old OASPL data as a function of shock strength parameter with the present data acquired using a 6.54 in<sup>2</sup> conical nozzle at static condition.

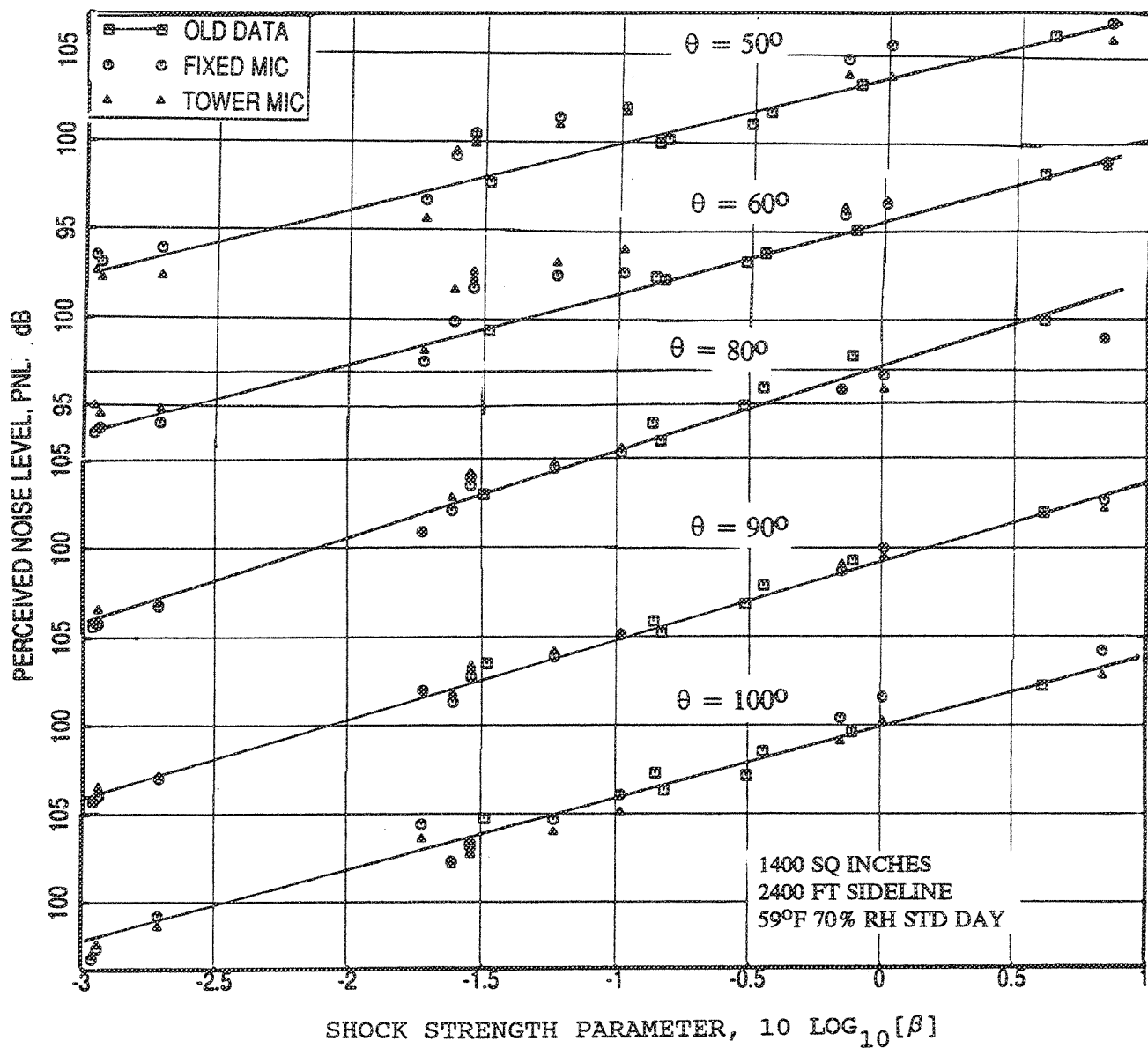


Figure 2.5-33. Comparison of old PNL data as a function of shock strength parameter with the present data acquired using a 6.54 in<sup>2</sup> conical nozzle at static condition.

The plume shock structure and strength are sensitive to the presence of screech and depend on the aero thermodynamic conditions (such as, pressure ratio and total temperature). Therefore, the shock associated broadband noise can be different for a nozzle at same  $V_J$  but different combinations of nozzle pressure and temperature. In addition, two different nozzles with same aero thermodynamic conditions, one with screech and the other without screech, will generate different noise spectra. Similar to screech the shock associated broadband noise is also dominant in the forward arc.

Based on the observed disagreement between the present and old data in the forward arc it is worthwhile to examine some of the present data to identify if the screech and the shock associated broadband noise are the causes of such disagreement. The aero thermodynamic conditions ( $P_R$  and  $T_T$ ), jet velocity ( $V_J$ ), ideal gross thrust  $(FG)_i$ , jet Mach number ( $M_J$ ), velocity parameter ( $V_{par}$ ), shock strength parameter ( $SH_{par}$ ), total correction factor (NF), and normalized OAPWL, OASPLs, and PNLs for all the test cases are listed in Table 2.5-1. Test points 9 and 10 are the repeat runs of point 8. OASPLN and PNLN values for these points corresponding to a  $V_{par}$  value of 2.1 do not agree with old data (at  $\theta=60^\circ$ ) as well as with the present data of test point 7 with the same  $V_{par}$ . The aero thermodynamic conditions and the noise levels for test points 7 and 8 are examined in detail. The nozzle pressure ratio and total temperature for point 8 are 2.46 and 1182°R compared to 2.21 and 1337°R for point 7. Based on the relationship of shock associated noise due to the nozzle pressure difference (i.e., shock associated noise is proportional to  $10 \text{ LOG}_{10}[\beta^4]$ ) an increase of about 4 dB is expected in the forward arc for test point 8 compared to 7. As shown in Figure 2.5-34(a), increase of 5.6 dB and 5.7 dB are observed for the normalized OASPL and PNL at  $\theta = 60^\circ$  at the same jet velocity of about 1800 ft/sec (i.e.,  $V_{par}$  of 2.1), which suggests the presence of higher shock associated noise for test point 8 compared to test point 7.

It is to be noted from Figure 2.5-34(a) that the agreement between the two sets of data in the aft quadrant is excellent, which is dominated by jet mixing noise. Since jet mixing noise is principally dependent on  $V_J$  and since  $V_J$  values are matched well for these two test cases (i.e., test points 7 and 8 of Table 2.5-1), aft quadrant data are in good agreement. Narrowband SPLs are compared in Figure 2.5-34(b) for  $\theta = 60^\circ$ ,  $90^\circ$ , and  $130^\circ$ . Presence of screech as well as strong shock associated noise in test point 8 is evident from these figures. The fundamental frequency of screech can be computed using the following expression (Ref. 26):

Table 2.5-1. Aerothermodynamic conditions, related parameters, and some acoustic noise levels for the conical nozzle at static condition.

TEST NO	P <sub>r</sub>	T <sub>t</sub> OR T <sub>0</sub>	V <sub>0</sub>	ft/s	(FG) 1	lbs	M <sub>0</sub>	V <sub>par</sub>	SH <sub>par</sub>	NF	CASPWLIN dB	OASPLN dB				PNLIN dB					
												60°	90°	130°	max ang	max level	60°	90°	130°	max ang	max level
1	1.580	518.6	873.7	20167.8			0.836	-1.019	-	-4.99	149.3	65.5	68.3	70.9	140	70.9	69.0	72.1	72.9	110	74.0
2	1.590	988.0	1214.5	20437.5			0.844	0.411	-	-3.68	161.4	72.5	76.8	84.0	140	85.5	76.3	81.0	84.8	120	85.1
3	1.600	1012.0	1237.0	20729.6			0.851	0.491	-	-3.64	161.3	73.0	77.1	84.1	140	85.4	76.6	81.3	85.2	130	85.1
4	1.600	997.0	1227.8	20731.5			0.851	0.458	-	-3.71	160.4	71.8	75.9	83.2	140	84.5	75.2	79.8	84.3	130	84.2
5	2.180	1131.0	1649.2	36317.5			1.121	1.740	-2.962	-5.97	170.8	82.9	83.8	93.4	140	95.3	89.0	89.6	95.2	140	95.9
6	2.180	1216.0	1710.7	36290.2			1.122	1.899	-2.939	-5.64	172.1	83.1	85.0	95.4	140	96.8	88.9	90.9	97.1	140	97.9
7	2.210	1337.0	1809.0	37035.3			1.134	2.141	-2.710	-5.32	173.9	83.8	86.1	97.5	140	98.8	89.5	91.8	99.7	140	100.8
8	2.460	1182.0	1797.5	43662.6			1.215	2.088	-1.611	-6.77	174.3	89.3	88.3	97.2	140	98.2	94.9	95.0	99.6	140	100.2
9	2.480	1182.0	1804.5	43291.2			1.221	2.126	-1.543	-6.70	175.7	89.4	89.7	98.0	140	100.3	95.6	96.7	100.9	140	103.2
10	2.480	1182.0	1804.5	43291.2			1.221	2.126	-1.543	-6.70	175.9	89.8	89.7	98.1	140	100.6	96.0	96.5	101.0	140	103.6
11	2.580	1302.0	1930.8	45834.9			1.253	2.420	-1.225	-6.57	176.7	90.4	90.6	100.1	140	101.1	96.6	97.6	103.4	140	104.0
12	2.670	1379.0	2018.9	48140.4			1.279	2.614	-0.982	-6.56	177.8	91.3	91.5	101.7	130	101.7	97.4	98.6	105.5	130	105.5
13	2.400	1809.0	2204.7	41015.6			1.206	2.996	-1.715	-4.51	179.3	87.8	91.4	104.7	130	104.7	93.7	97.5	108.9	130	108.9
14	3.090	1787.0	2446.2	58966.3			1.391	3.447	-0.149	-6.45	181.1	94.0	95.5	106.2	130	106.2	100.0	102.7	110.2	130	110.2
15	3.190	1960.0	2595.5	61550.0			1.415	3.705	0.007	-6.25	181.7	94.4	96.2	106.6	130	106.6	100.4	103.3	110.4	130	110.4
16	4.010	1960.0	2797.6	83396.5			1.572	4.030	0.837	-7.84	182.3	95.1	97.4	107.0	130	107.0	100.8	104.4	110.4	130	110.3

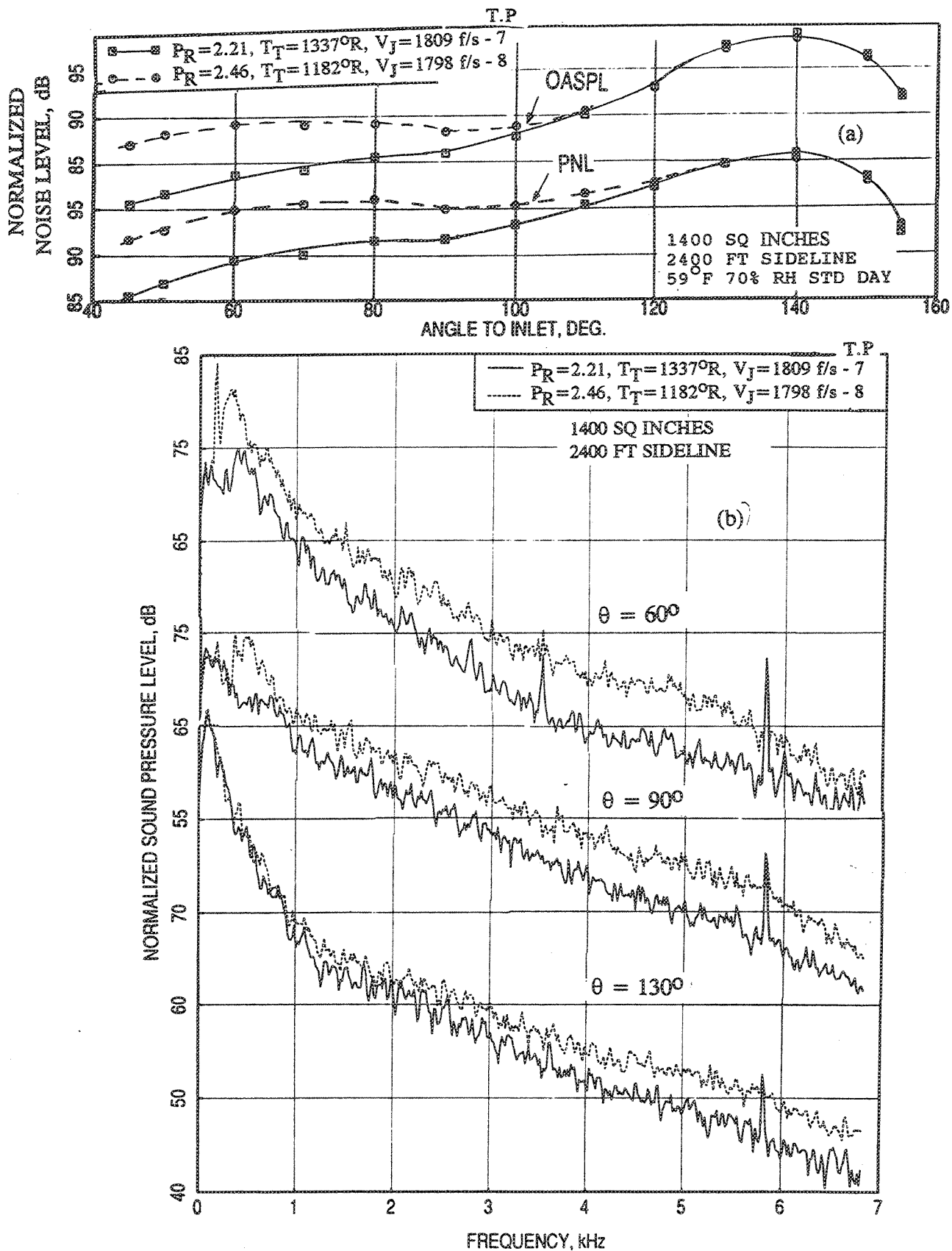


Figure 2.5-34. Comparison of (a) normalized PNL and OASPL directivities and (b) narrowband SPL spectra between two test points of present study acquired using a 6.54 in<sup>2</sup> conical nozzle at static condition for a nominal jet velocity of 1800 ft/sec.

$$f = a_0/[3d(P_R-1.89)^{1/2}]$$

where,  $d$  is the nozzle exit diameter, which is 42.22" for 1400 in<sup>2</sup> nozzle. The screech frequency is independent of observer angle for the case of no relative motion between nozzle and observer.

The shock associated noise exhibits a peak value at a frequency, which can be calculated using the following expression (Ref. 27) :

$$f = U_c/[1.1 d \beta (1+M_c \cos\theta)]$$

where,  $U_c$  is the convection velocity, which is about  $0.7 V_J$  and  $M_c = V_J/a_0$ . A more accurate expression for screech frequency, derived using the above expression with  $\theta = 0$ , is as follows :

$$f = U_c/[1.1 d \beta (1+M_c)]$$

The calculated fundamental screech frequency for test point 8 is about 180 Hz compared to the observed value of about 172 Hz (see Figure 2.5-34(b)). Based on the expression for the frequency of shock associated noise peak, it is computed as 260 Hz at  $\theta=60^\circ$  and 471 Hz at  $\theta=90^\circ$  for test point 8 compared to 336 Hz and 610 Hz for test point 7. Figure 2.5-34 shows such peaks occurring at frequencies very close to the computed values.

It is quite clear that the disagreement at  $V_{par}=2.1$  (see Figures 2.5-30 and 2.5-31) between old and present data of test point 8 and that between the test points 7 and 8 are due to the difference of aero thermodynamic conditions, which resulted in screech and higher shock associated noise for test point 8. Data from a few more test points also deviate from the old results as shown in Figures 2.5-30 and 2.5-31. Results of test points 5, 6, 11, and 12 deviate from old data, whereas the rest of the present data agree well with old data, even at  $\theta=60^\circ$ . The disagreement could be due to the same reason of what is observed for test point 8. To confirm the cause, narrowband spectra of test points 5, 12 (data of these points deviate from old results), and 13 (data of this point agree well with old results) are plotted in Figure 2.5-35. At  $\theta=60^\circ$  a substantially strong shock associated noise peak is observed around 400 Hz for test point 5 even though the jet velocity is much smaller ( $V_J = 1649$  ft/sec). It should be noted that the

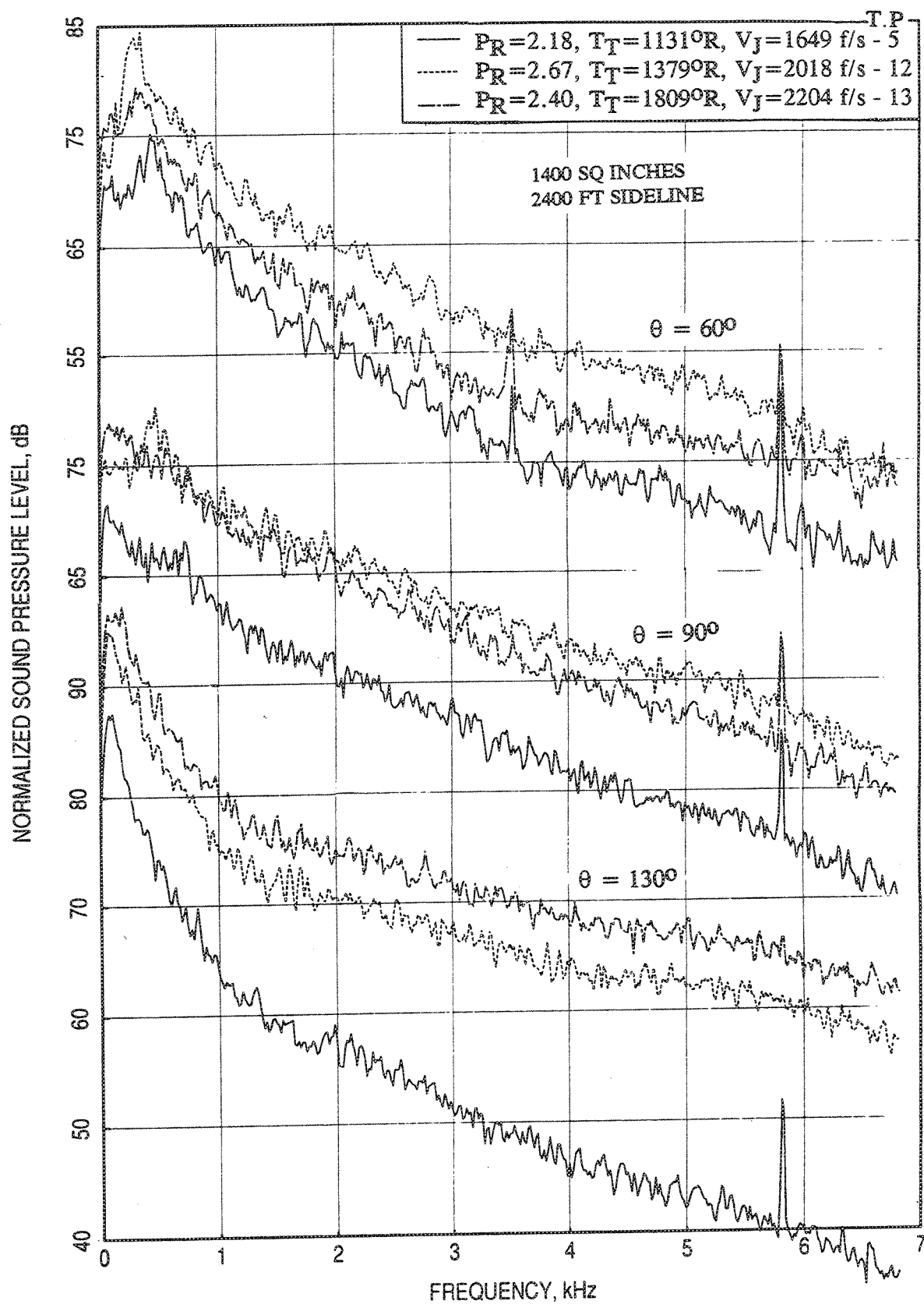


Figure 2.5-35. Narrowband SPL spectra of three test points of present study acquired using a 6.54 in<sup>2</sup> conical nozzle at static condition.

peak for test point 5 is not higher than those for test points 12 and 13, since  $V_J$  for test point 5 is much lower compared to  $V_J$  values for 12 and 13. Between test points 12 and 13, 12 shows a stronger shock associated noise peak even though the jet velocity is about 2018 ft/sec compared to 2204 ft/sec for test point 13. The higher shock noise is due to the nozzle pressure ratio of 2.67 for point 12 compared to 2.4 for point 13. Directivities of normalized OASPL and PNL for these three points are plotted in Figure 2.5-36, which indicates higher levels in the forward arc for test point 12 compared to 13.

Spikes at 3500 Hz and 5800 Hz are observed in the narrowband spectra, when the broadband noise levels are relatively lower. These spikes correspond to the actual measured frequencies of 51000 Hz and 85000 Hz for the model scale nozzle. These are the low level electronic signals generated in the narrowband FFT analyzer and do not effect the 1/3-octave noise levels obtained from different analyzer.

Figure 2.5-37 shows the spectral comparison of normalized SPL at different polar angles and the PNLN and OASPLN directivity comparisons between old and present data (test point 7 of Table 2.5-1) for a nominal jet velocity of 1800 ft/sec. The test conditions between the old and the present cases are slightly different. The jet velocity for old data is slightly higher due to its higher total temperature. On this basis the present data is expected to be lower (about 1 dB using  $50 \log V_R$ ) in levels compared to the old data. Figure 2.5-37(a) shows slightly lower SPLN levels for the present data at higher frequencies. For the same reason the PNLN and OASPLN levels are slightly lower for old data in the aft arc as shown in Figure 2.5-37(b).

Similar comparisons are made for another case with a higher jet velocity (i.e., nominal jet velocity of 2400 ft/sec). The test conditions between the old and present case (test point 14 of Table 2.5-1) are again somewhat different. The jet velocity for old data is lower due to its lower total temperature and nozzle pressure ratio. On this basis the present data is expected to be  $\sim 1.1$  dB (using  $50 \log V_R$ ) higher in sound pressure levels compared to the old data. Figure 2.5-38(a) shows the spectral comparison of SPLN at different polar angles between old and present data and the SPLN levels for the present case are slightly higher than the old data. The corresponding PNLN and OASPLN directivity comparisons, shown in Figure 2.5-38(b), indicate lower levels for old data in the forward arc.



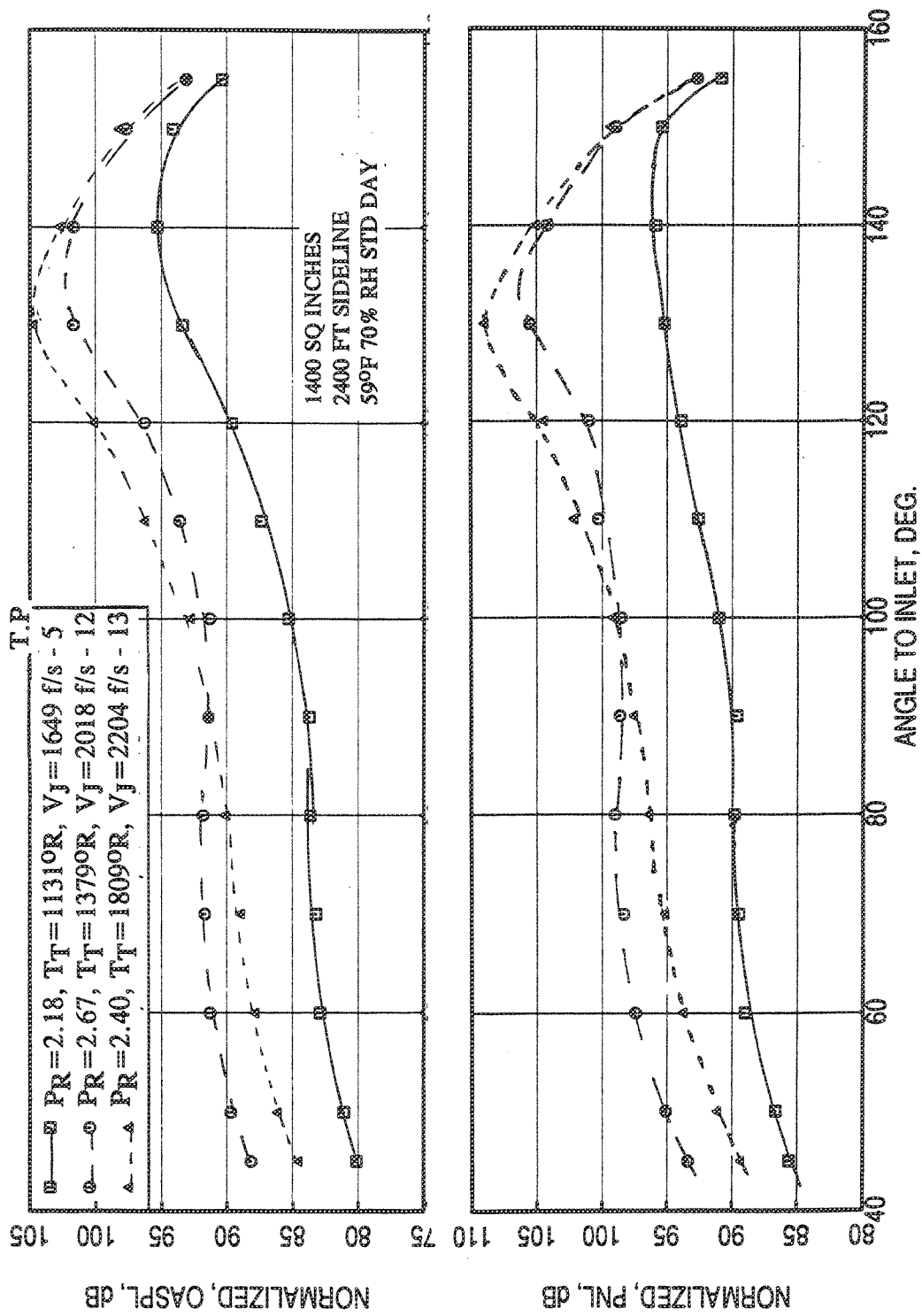


Figure 2.5-36. Normalized PNL and OASPL directivities of three test points of present study at acquired using a 6.54 in<sup>2</sup> conical nozzle static condition.

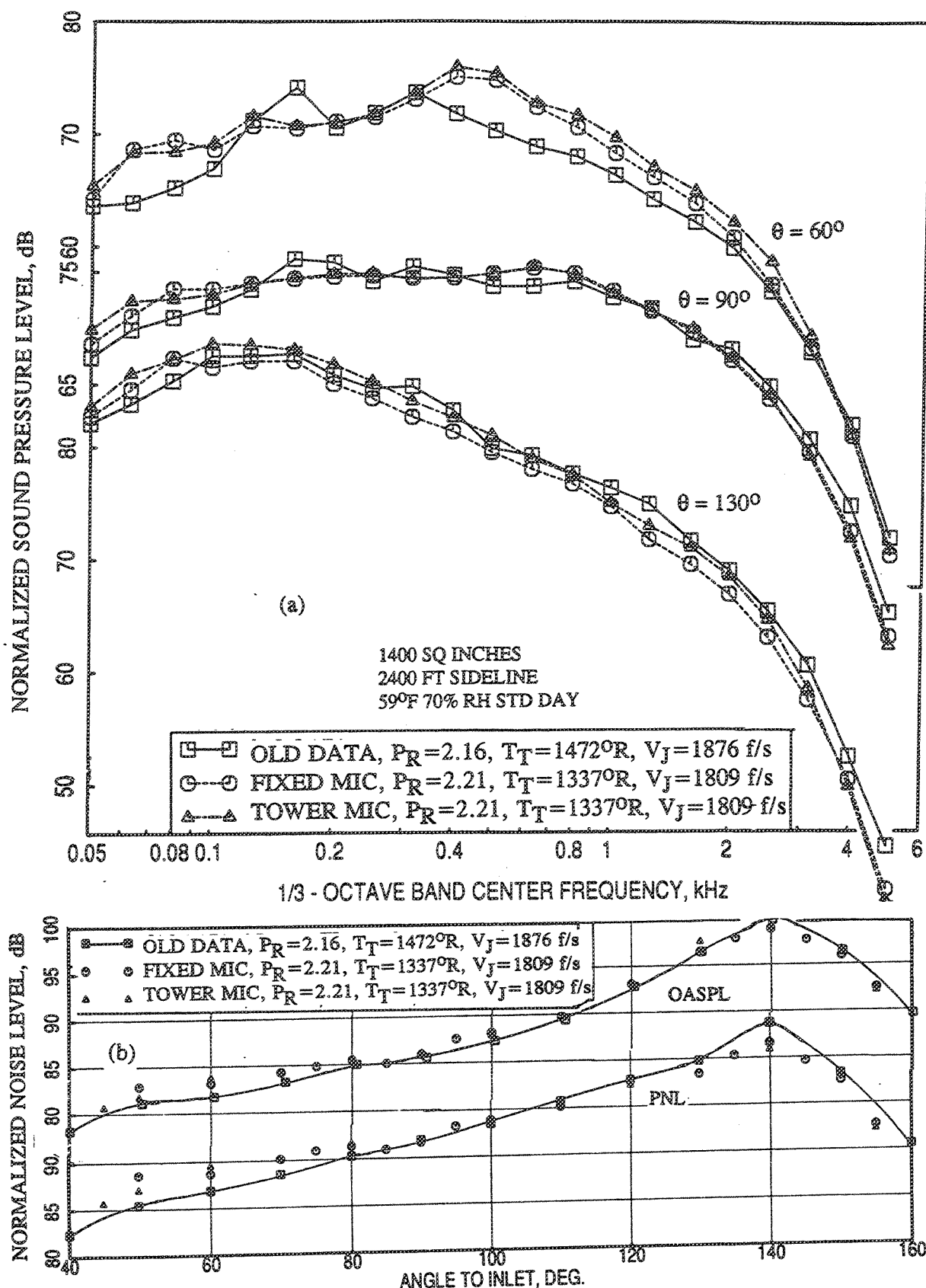


Figure 2.5-37. Comparison of old normalized (a) SPL spectra and (b) PNL and OASPL directivities with the present data acquired using a 6.54 in<sup>2</sup> conical nozzle at static condition for a nominal jet velocity of 1800 ft/sec.

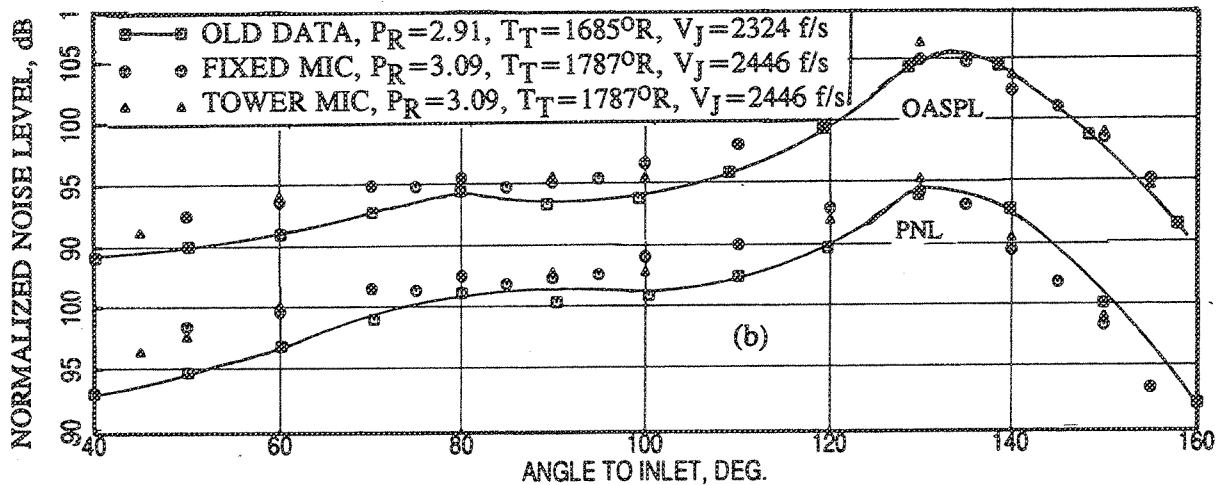
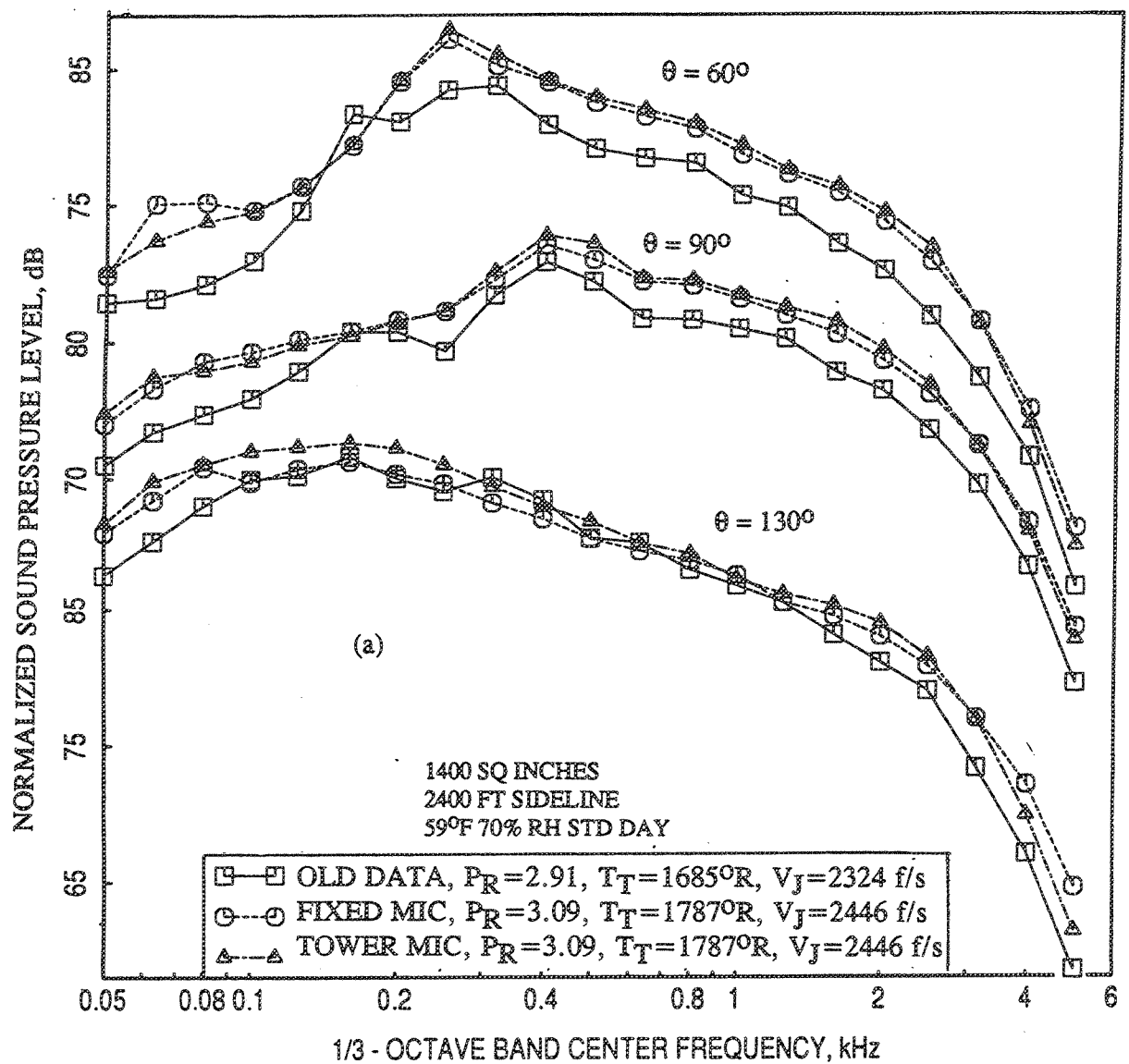


Figure 2.5-38. Comparison of old normalized (a) SPL spectra and (b) PNL and OASPL directivities with the present data acquired using a 6.54 in<sup>2</sup> conical nozzle at static condition for a nominal jet velocity of 2400 ft/sec.

*Flight Simulation Data* : Data with flight simulation at  $M_F=0.32$  are compared in this section. Figure 2.5-39 shows the comparison of Normalized Overall Sound Power Level (OAPWLN) and Normalized Overall Sound Pressure Level (OASPLN) and Figure 2.5-40 shows the comparison of Normalized Effective Perceived Noise Level (EPNLN) and Normalized Perceived Noise Level (PNLN) between old and present data as functions of jet velocity parameter. Agreement of OAPWLN and EPNLN between old and present data is reasonably good, except for EPNLN levels for jet velocity parameter between 1.7 and 2.7. In the forward arc for jet velocity parameter between 1.7 and 2.7 the present OASPLN and PNLN values are higher compared to the old data. The agreement between old and present data is very good in the rear arc. Figures 2.5-41 and 2.5-42 show the comparison of old OASPL and PNL data as functions of shock strength parameter with the present data. The agreement is good except in the forward arc for the test points correspond to the same data points not agreeing with old results in normalized form, shown in Figures 2.5-39 and 2.5-40.

The disagreement between old and new data in the forward arc is mostly due to the difference in shock associated noise caused by the differences in aero thermodynamic conditions and screech caused by differences in nozzle size and geometry. This can be explained in the same manner as those described for static cases, since the test conditions for static and flight simulation are identical.

The aero thermodynamic conditions ( $P_R$  and  $T_T$ ), jet velocity ( $V_J$ ), ideal gross thrust  $(FG)_i$ , jet Mach number ( $M_J$ ), velocity parameter ( $V_{par}$ ), shock strength parameter ( $SH_{par}$ ), total correction factor (NF), and normalized OAPWL, OASPLs, and PNLs for all the test cases with flight simulation are listed in Table 2.5-2.

OASPLN and PNLN values for test point 5 of Table 2.5-2 corresponding to a  $V_{par}$  value of 2.1 do not agree with old data (at  $\theta=60^\circ$ ) as well as with the present data of test point 4 of same  $V_{par}$ . The aero thermodynamic conditions and the noise levels for test points 4 and 5 are examined in detail. The nozzle pressure ratio and total temperature for point 5 are 2.5 and 1174°R compared to 2.23 and 1331°R for point 4. Based on the relationship of shock associated noise due to the nozzle pressure difference (i.e., shock associated noise is proportional to  $10 \text{ LOG}_{10}[B^4]$ ) an increase of about 4 dB is expected in the forward arc for test point 5 compared to 4. About 4 to 5 dB increase is observed between the normalized OASPL and PNL directivities of test points 4 and 5 in the forward arc, with the same jet velocity of about 1800 ft/sec (i.e.,

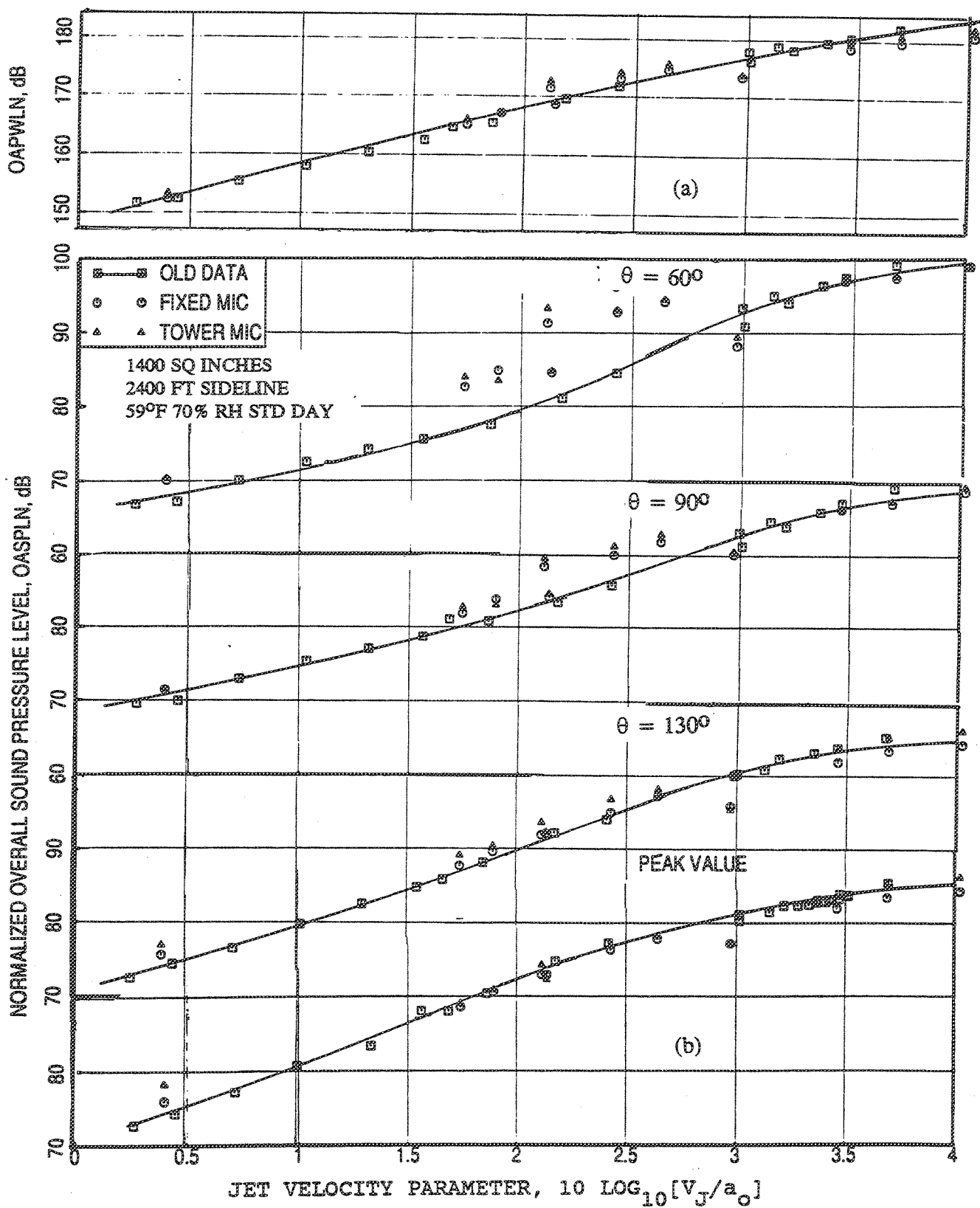


Figure 2.5-39. Comparison of old normalized (a) OAPWL and (b) OASPL data as a function of jet velocity parameter with the present data acquired using a 6.54 in<sup>2</sup> conical nozzle with flight simulation,  $M_F=0.32$ .

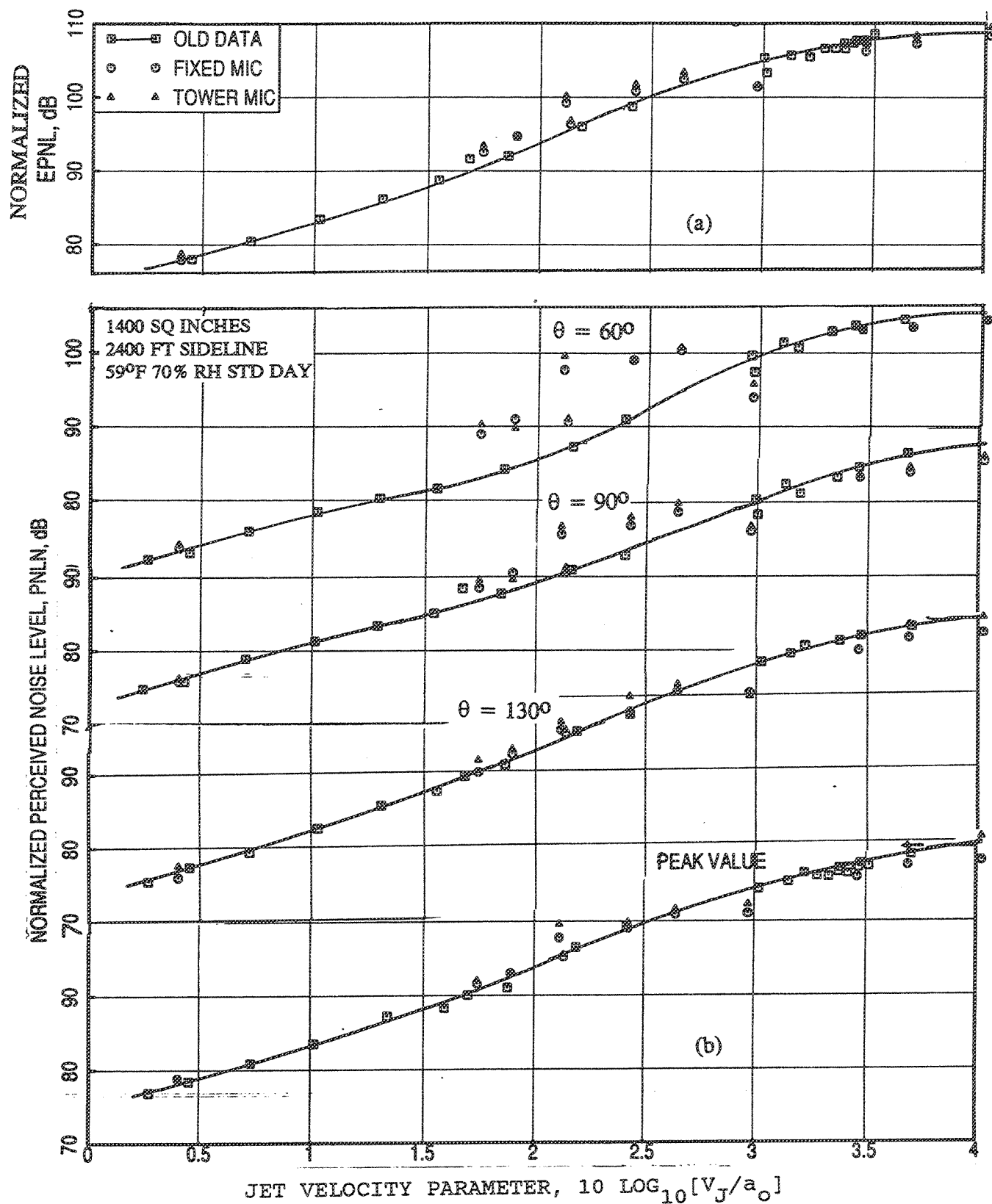


Figure 2.5-40. Comparison of old normalized (a) EPNL and (b) PNL data as a function of jet velocity parameter with the present data acquired using a 6.54 in<sup>2</sup> conical nozzle with flight simulation,  $M_F=0.32$ .

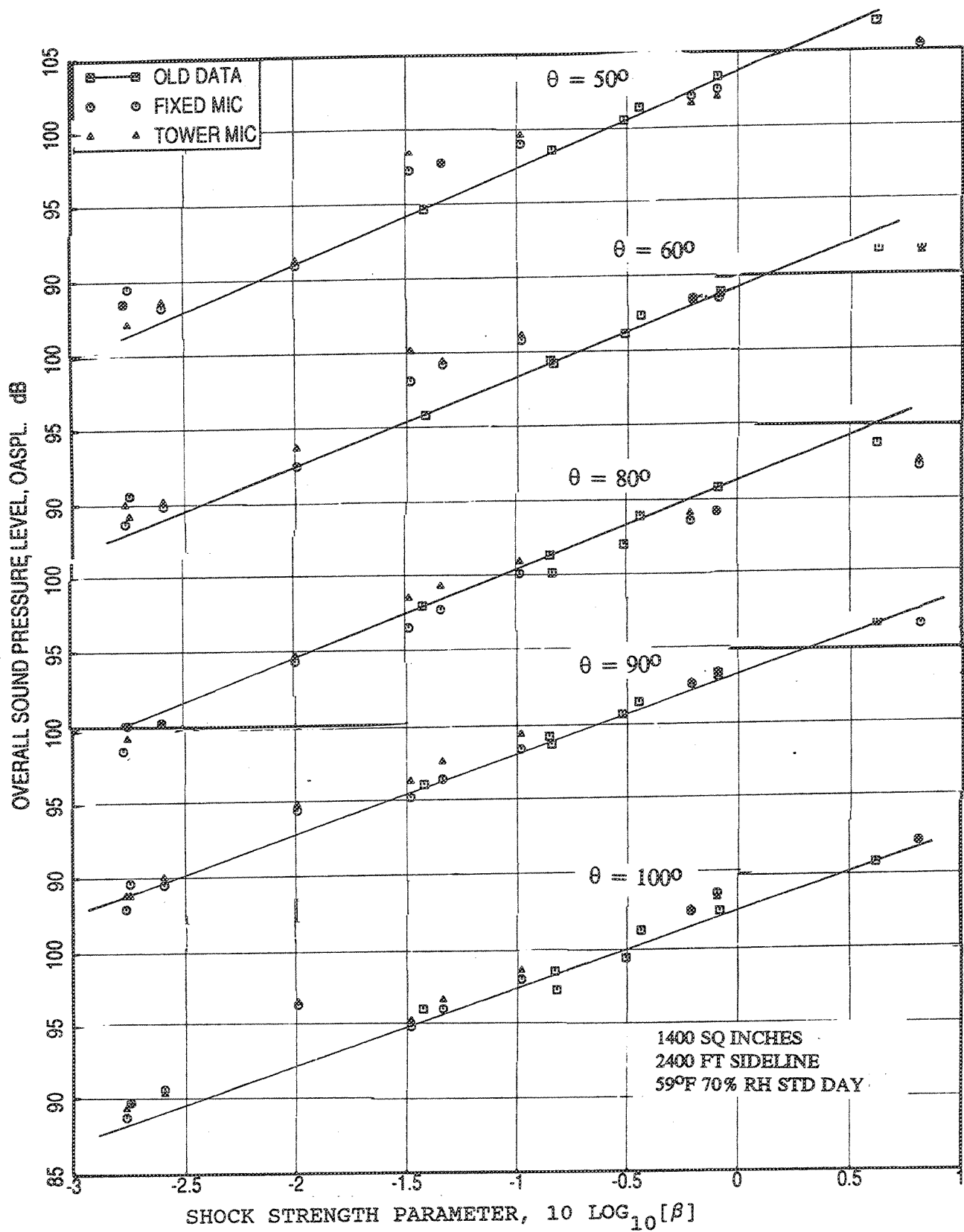


Figure 2.5-41. Comparison of old OASPL data as a function of shock strength parameter with the present data acquired using a 6.54 in<sup>2</sup> conical nozzle with flight simulation,  $M_F=0.32$ .

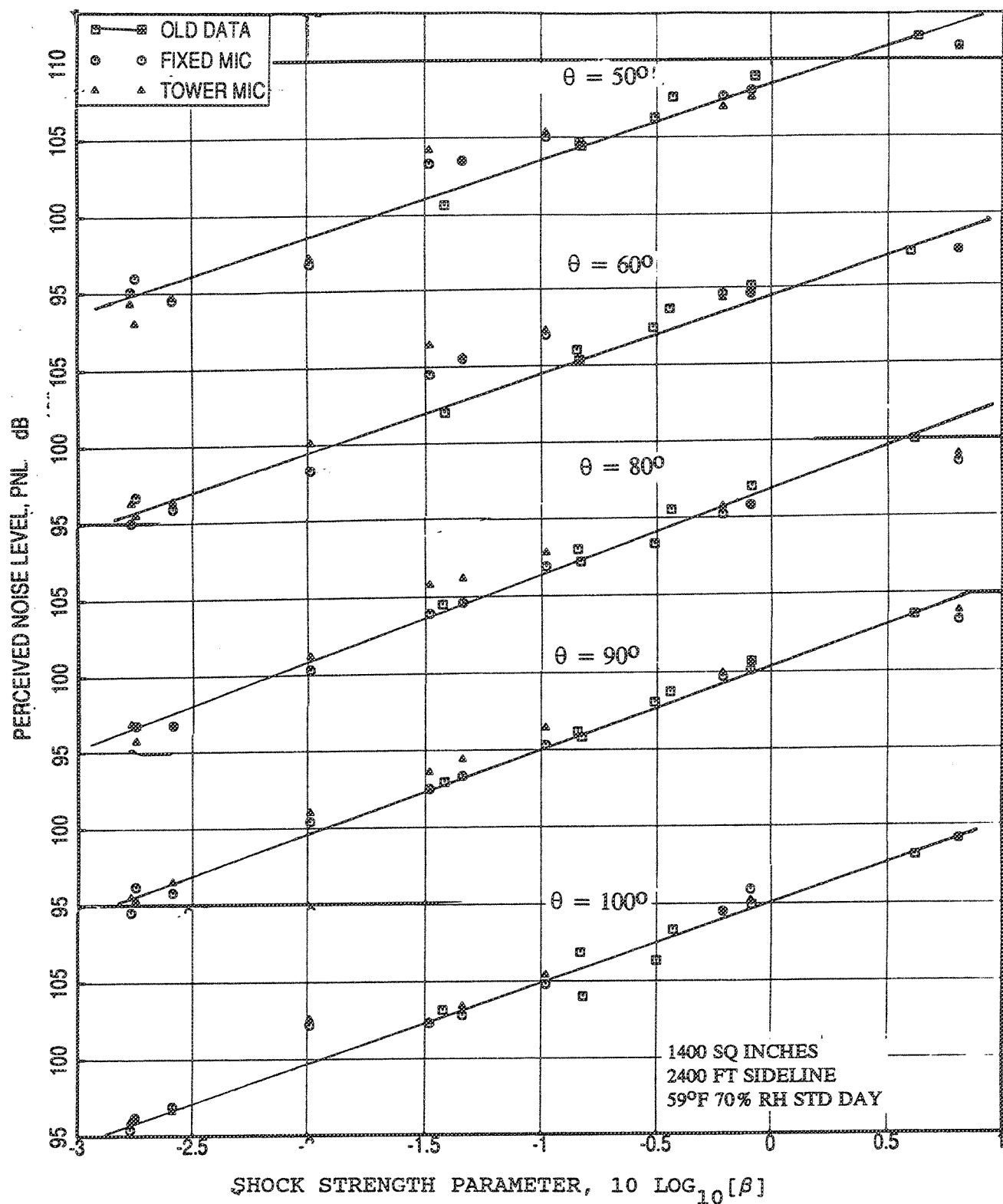


Figure 2.5-42. Comparison of old PNL data as a function of shock strength parameter with the present data acquired using a 6.54 in<sup>2</sup> conical nozzle with flight simulation,  $M_F=0.32$ .



Table 2.5-2. Aerothermodynamic conditions, related parameters, and some acoustic noise levels for the conical nozzle with flight simulation ( $M_F=0.32$ ).

TEST NO	P <sub>R</sub>	T <sub>T</sub> OR	V <sub>J</sub>	ft/s	(FG) ↓	lbs	M <sub>J</sub>	V <sub>par</sub>	SH <sub>par</sub>	NF	OASPMWLN dB	OASPLN dB					PNLN dB				
												60°	90°	130°	max ang	max level	60°	90°	130°	max ang	max level
1	1.580	1004.0	1216.5	19674.6	0.839	0.401	-	-3.47	152.3	70.3	71.5	76.9	140	78.2	74.0	76.3	77.5	120	78.7		
2	2.210	1125.0	1657.6	36249.8	1.131	1.744	-2.765	-6.03	165.2	84.0	82.8	89.1	130	89.1	90.3	89.5	91.5	120	92.0		
3	2.210	1205.0	1716.1	36224.5	1.132	1.895	-2.746	-5.73	167.2	83.5	83.1	90.4	140	90.9	89.8	89.6	93.0	130	93.0		
4	2.230	1331.0	1814.0	36694.9	1.141	2.136	-2.593	-5.35	168.7	84.8	84.7	92.3	140	92.3	91.1	91.2	95.5	130	95.5		
5	2.500	1174.0	1805.3	43690.4	1.227	2.115	-1.480	-6.81	171.5	93.3	89.5	93.6	140	94.3	99.6	96.8	96.6	130	99.6		
6	2.540	1308.0	1921.3	45571.7	1.241	2.429	-1.338	-6.44	173.1	93.0	91.2	96.8	140	96.9	99.2	98.0	99.9	130	99.8		
7	2.670	1379.0	2018.9	48973.9	1.279	2.644	-0.982	-6.58	174.7	94.5	92.8	98.2	130	98.2	100.7	99.8	101.5	120	101.6		
8	2.330	1819.0	2177.4	39892.3	1.183	2.972	-1.990	-4.27	173.5	89.4	90.5	95.4	120	97.2	95.8	96.7	99.8	120	102.2		
9	3.050	1790.0	2436.2	58917.5	1.381	3.460	-0.209	-6.36	178.6	96.9	96.4	103.6	120	103.6	102.9	103.5	107.8	120	107.8		
10	3.120	1952.0	2568.8	60743.0	1.400	3.690	-0.091	-6.12	179.7	97.6	97.5	105.2	130	105.2	103.6	104.6	109.3	130	110.0		
11	3.980	1942.0	2778.1	83165.6	1.567	4.026	0.813	-7.81	180.9	98.7	99.4	106.2	130	106.2	104.5	106.1	110.2	130	111.3		

$V_{\text{par}}$  of 2.1) for both the cases (see Figure 2.5-43), which suggests the presence of strong shock associated noise for test point 5.

Comparing the directivity plots of Figures 2.5-34(a) and 2.5-43(a), corresponding to static and flight cases of same test conditions, it can be observed that the noise amplification due to flight in the forward arc is much higher for the case with higher shock associated noise. This amplification is so high that the PNL peak location is moved from rear arc to forward arc. This phenomenon has significant influence on the EPNL values.

Narrowband SPLs are compared in Figure 2.5-43(b) for  $\theta = 60^\circ$ ,  $90^\circ$ , and  $130^\circ$ . Presence of strong shock associated noise in test point 5 is evident from these figures. The computed and observed frequencies of shock associated noise peaks at  $\theta=60^\circ$  and  $\theta=90^\circ$  are very close to each other.

Similar to the static case, data from a few more test points also deviate from the old results as shown in Figures 2.5-39 and 2.5-40. Results of test points 2, 3, 6, and 7 of Table 2.5-2 deviate from old data, whereas the rest of the present data agree well in the forward arc. The disagreement could be due to the same reason as for test point 5. To confirm the cause, narrowband spectra of test points 2, 7 (data of these points deviate from old results), and 8 (data of this point agree well with old results) are plotted in Figure 2.5-44. At  $\theta=60^\circ$  a substantially strong shock associated noise peak is observed around 400 Hz for test point 2 even though the jet velocity is much smaller ( $V_J = 1658$  ft/sec). Between test points 7 and 8, 7 shows a stronger shock associated noise peak even though the jet velocity is about 2019 ft/sec compared to 2177 ft/sec for test point 8. The higher shock noise is due to the nozzle pressure ratio of 2.67 for point 7 compared to 2.33 for point 8. Directivities of normalized OASPL and PNL for these three points are plotted in Figure 2.5-45, which indicates higher levels in the forward arc for test point 7 compared to 8. Shock associated noise amplification due to flight simulation can be observed comparing Figures 2.5-36 and 2.5-45.

Similar to the static cases spectral comparisons of SPLN and directivity comparisons of PNLN and OASPLN are made between old and present data (test points 4 and 9 of Table 2.5-2) with flight simulation at two nominal jet velocities of 1800 ft/sec and 2400 ft/sec in Figures 2.5-46 and 2.5-47, respectively. For 1800 ft/sec case, reasonable agreement is seen between old and present SPLN data, except for a higher peak at  $\theta$

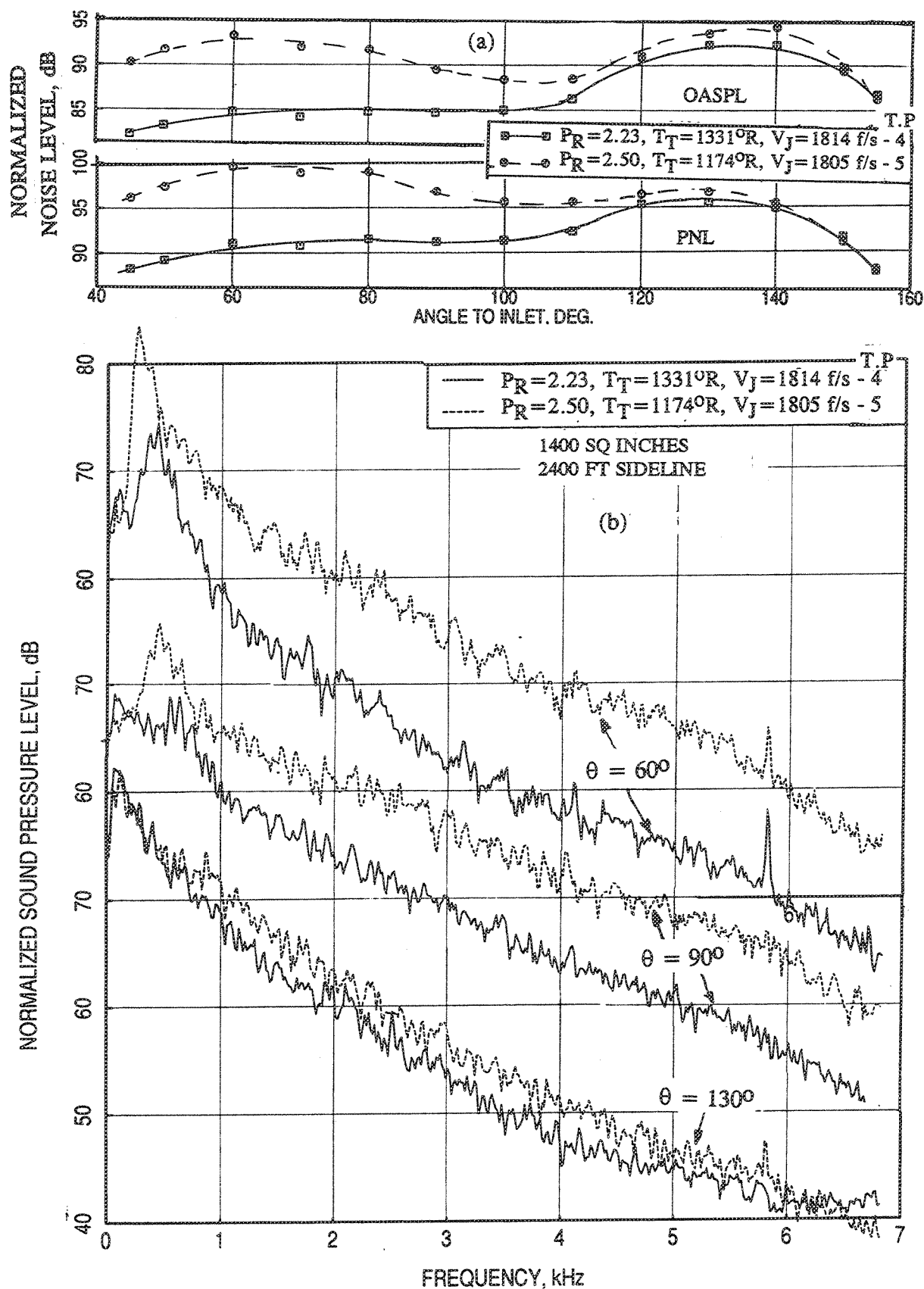


Figure 2.5-43. Comparison of (a) normalized PNL and OASPL directivities and (b) narrowband SPL spectra between two test points of present study acquired using a 6.54 in<sup>2</sup> conical nozzle with flight simulation,  $M_F=0.32$ , for a nominal jet velocity of 1800 ft/sec.

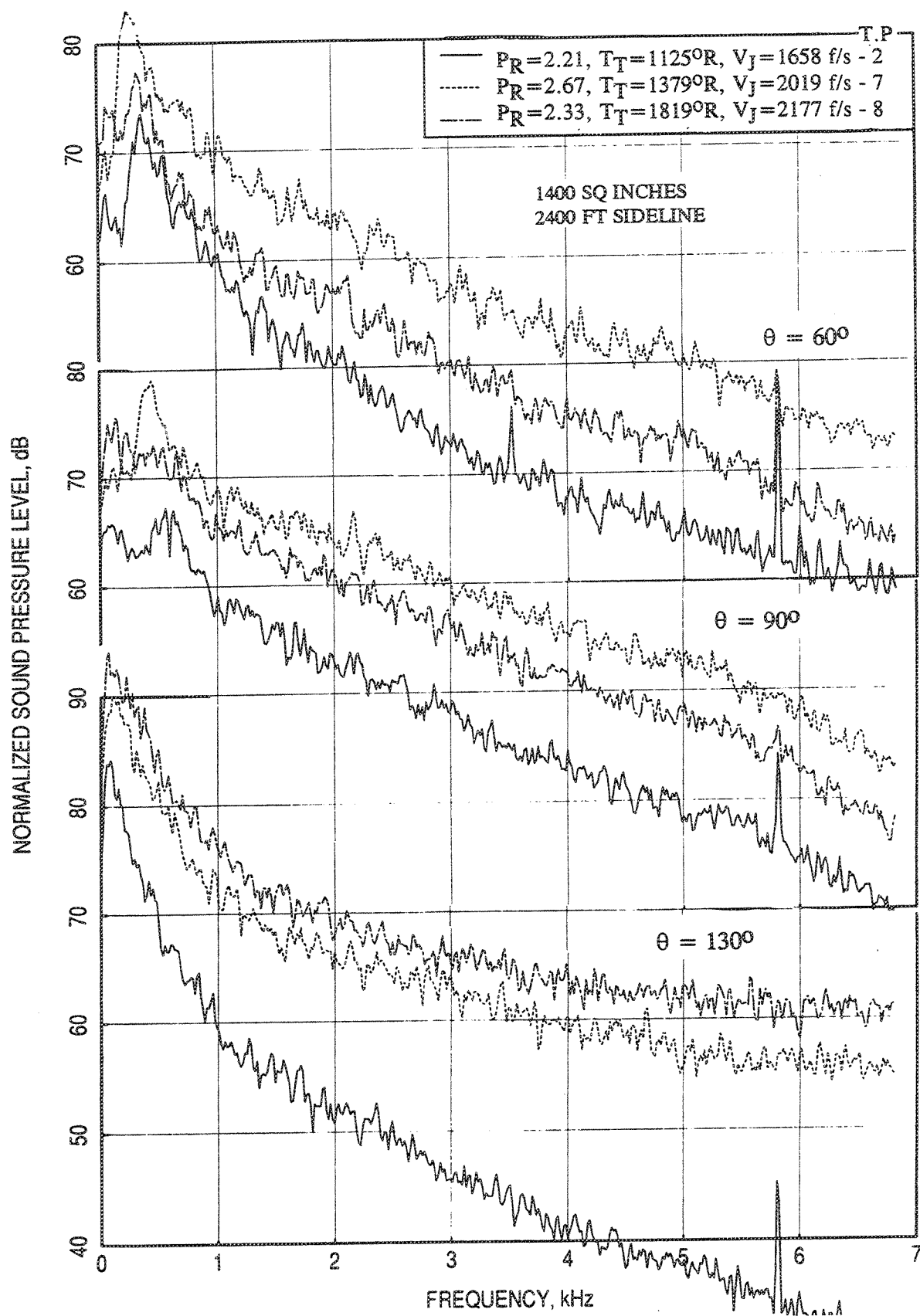


Figure 2.5-44. Narrowband SPL spectra of three test points of present study acquired using a  $6.54 \text{ in}^2$  conical nozzle with flight simulation,  $M_F=0.32$ .

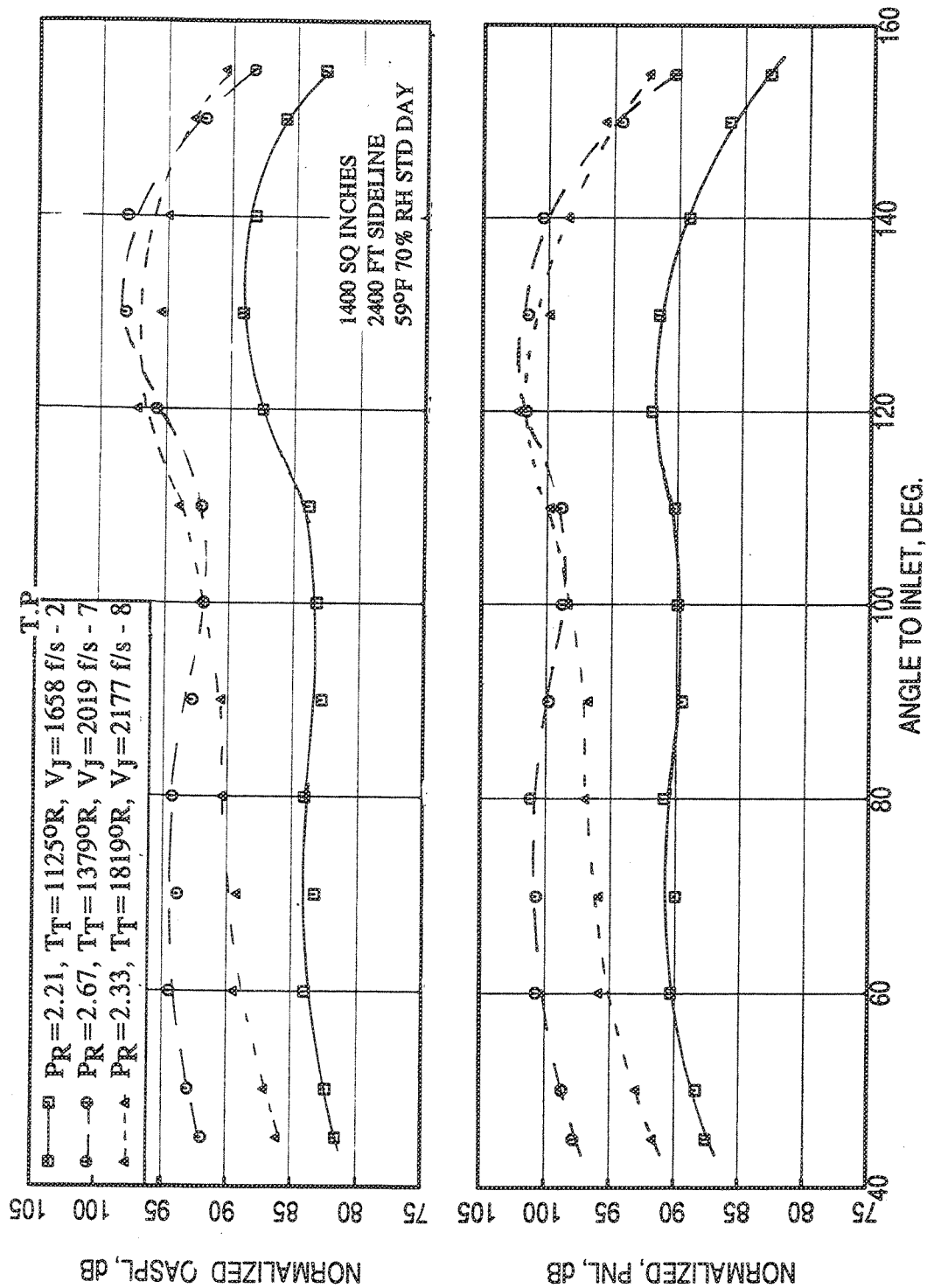


Figure 2.5-45. Normalized PNL and OASPL directivities of three test points of present study acquired using a 6.54 in<sup>2</sup> conical nozzle with flight simulation,  $M_F=0.32$ .

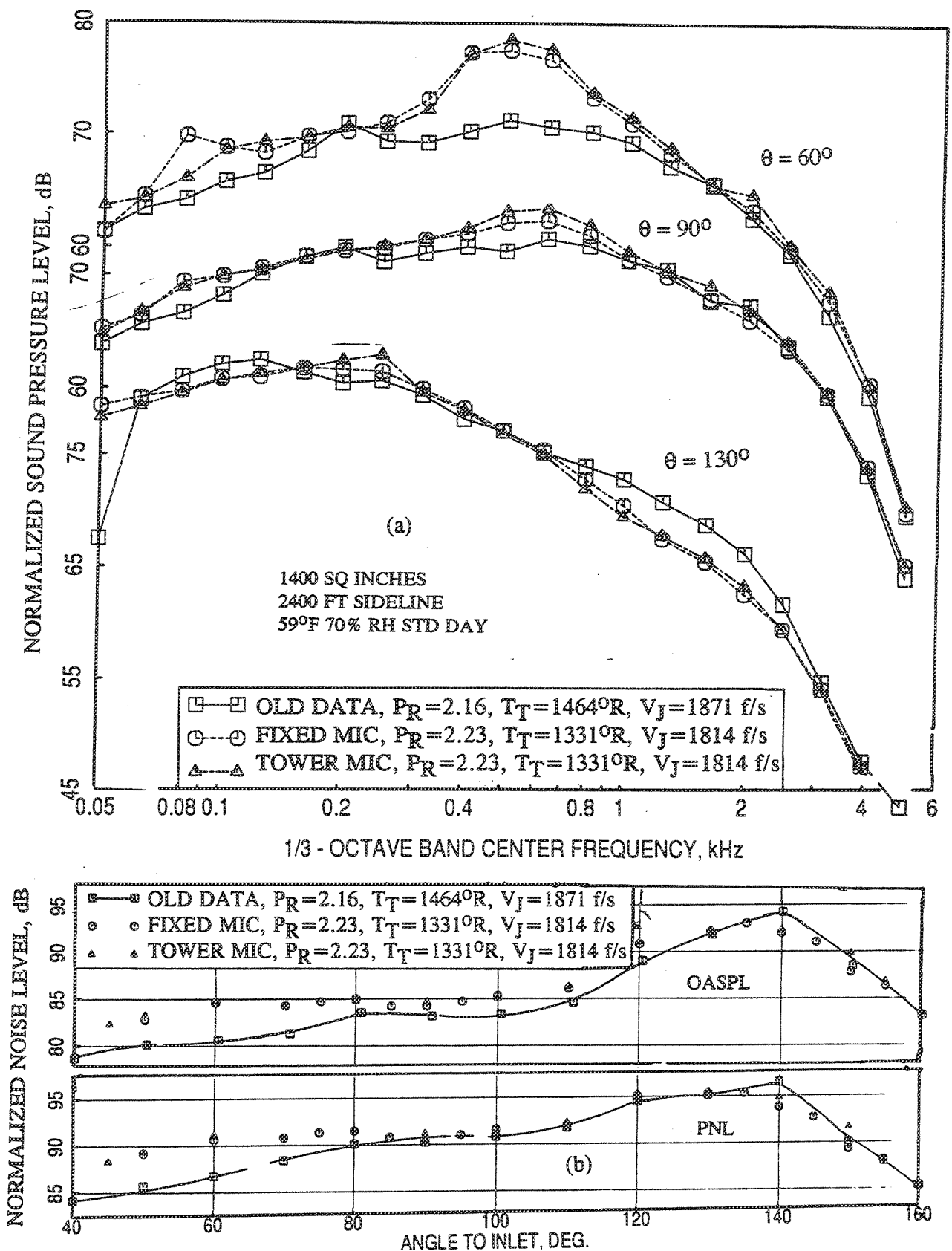


Figure 2.5-46. Comparison of old normalized (a) SPL spectra and (b) PNL and OASPL directivities with the present data acquired using a 6.54 in<sup>2</sup> conical nozzle with flight simulation ( $M_F=0.32$ ) for a nominal jet velocity of 1800 ft/sec.

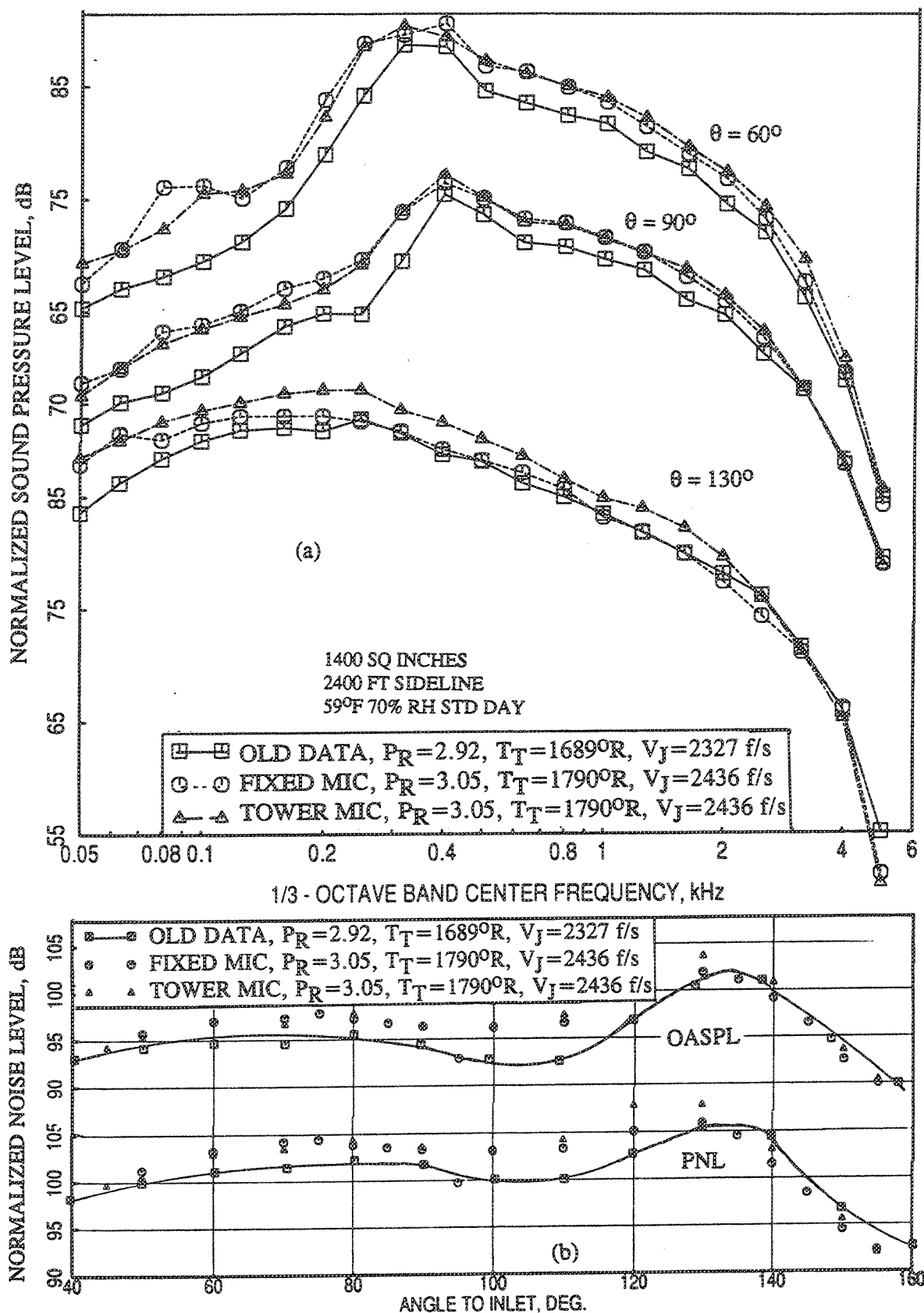


Figure 2.5-47. Comparison of old normalized (a) SPL spectra and (b) PNL and OASPL directivities with the present data acquired using a 6.54 in<sup>2</sup> conical nozzle with flight simulation ( $M_F=0.32$ ) for a nominal jet velocity of 2400 ft/sec.

$=60^\circ$  at about 500 Hz, and relatively lower level at  $\theta=130^\circ$  between 700 Hz to 2500 Hz, for the present case compared to the old data. As examined in Figure 2.5-43(b), a strong shock associated noise peak is present in the forward arc for this condition. The corresponding PNLN and OASPLN directivity comparisons of Figure 2.5-46(b) indicate higher levels in the forward arc and reasonable agreement in the rear arc for the present data compared to old data.

For 2400 ft/sec case, the SPLN values for present case, shown in Figure 2.5-47(a), are relatively higher in the frequency range below 2000 Hz compared to old data. The corresponding PNLN and OASPLN directivity comparisons, shown in Figure 2.5-47(b) indicate higher levels in the forward arc and reasonable agreement in the rear arc for the present data compared to old data.

It is to be noted in all the above comparisons, agreement between tower and fixed microphones is excellent. Comparison between old and present data shows good agreement in most cases, especially for static condition, establishing the validity of the upgraded Cell 41 test facility and data acquisition processes. Possible reasons for the noted differences between old and present data particularly for the flight simulation case are as follows :

1. The strength and generation of screech is very sensitive to nozzle configuration (i.e., nozzle size, convergent angle, lip thickness, etc.) and upstream flow conditioning. The shock structure and its strength are dependent on the screech. Slight mismatch in nozzle geometry can alter the screech levels including the broadband noise amplification. Bigger nozzles (A8 for the model scale nozzles tested in Cell 41 are 20.38 and 16.91 sq. inch.) were used in the previously acquired data compared to the present nozzle of 6.54 in<sup>2</sup> and the other physical parameters, such as, convergence angle, lip thickness, etc., are also different between the nozzles used in the past and the present one. These factors might have contributed to the observed discrepancies in agreement between old and present data.

2. Shock associated noise is very sensitive to aero thermodynamic conditions. A small mismatch in these conditions can contribute appreciable amount to the shock associated noise. For comparison purpose exact simulation of aero thermodynamic conditions is essential.



3. During the present flight simulation tests an annular nozzle was mounted around the core conical nozzle, which was operated at the same velocity as that of the tertiary flow (i.e., flight simulation velocity of 360 feet/sec.). Boundary layer growth on the inside of annular nozzle passage creates an additional shear layer in the core jet evolution which was not there in "old" tests. This additional shear layer is expected to alter mixing of the jet downstream and hence jet mixing noise. Static pressure mismatch between inner jet and annular jet simulating freejet could have additional effect on shock structure and associated differences in shock noise features.

4. The old flight simulated data were acquired at free jet velocity of about 400 ft/sec, whereas, the present tests were conducted with a free jet velocity of 360 ft/sec. This difference might have contributed to the observed disagreement in flight data.

Based on the results and the discussions presented in this section it is concluded that the facility and the acoustic data acquisition and processing methods are suitable for obtaining accurate noise data for the present program.



## 2.6 EFFECT OF POROUS PLUG ON NOISE

The objective of using a porous plug, for the suppressor alone and suppressor with fluid shield configurations, is to reduce the shock-associated broadband noise for super critical nozzle pressure ratios. The porous surface of the plug reduces shock strength and thereby, reduces the shock-associated broadband noise (Refs. 7-10). Tests are conducted for the suppressor alone and the baseline fluid shield nozzle (i.e., with 0.5"-thick fluid shield) configurations with hardwalled plug and with a 10% porous plug to evaluate the effectiveness of the porous plug in reducing the noise level and the results are examined in this section. The farfield data measured by the tower microphones at  $\phi = 10^\circ$  are analyzed in terms of Sound Power Level (PWL), Overall Sound Pressure level (OASPL), Perceived Noise Level (PNLT), Effective Perceived Noise Level (EPNLT), and Sound Pressure Level (SPL), which are presented as functions of Jet Velocity ( $V_J$ ), Frequency ( $f$ ), Angle to Inlet ( $\theta$ ).

### 2.6.1 Suppressor Alone Configurations:

The 36-chute suppressor was tested with hard-walled plug and with 10% porous plug at static condition and with flight simulation. The farfield noise data are corrected to the standard day conditions of 59° F and 70% relative humidity, extrapolated to 1629' distance, and scaled to 1175 in<sup>2</sup> area (full scale suppressor area of Flade Cycle).

**Static Data :** As an overview the Normalized Effective Perceived Noise Levels of the suppressor with hard-walled plug and the suppressor with porous plug (EPNLT), Peak PNL, Overall Sound Power Levels (OAPWL), and Peak OASPL as functions of jet velocity are compared in Figure 2.6-1. In these comparisons the noise levels for the suppressor with porous plug seems to be slightly lower (about 1 to 2 dB) compared to those for the suppressor with hard-walled plug for most of the test cases.

To examine the effect of porous plug in detail PNL and OASPL directivities and SPL spectra for three different test points with different  $V_J$  are examined. The nominal velocities, cycle condition definitions, and the corresponding aerothermodynamic conditions (i.e., Nozzle Pressure Ratio  $P_{r,p}$  and Total Temperature,  $T_{t,p}$ ) for these three cases are listed below :

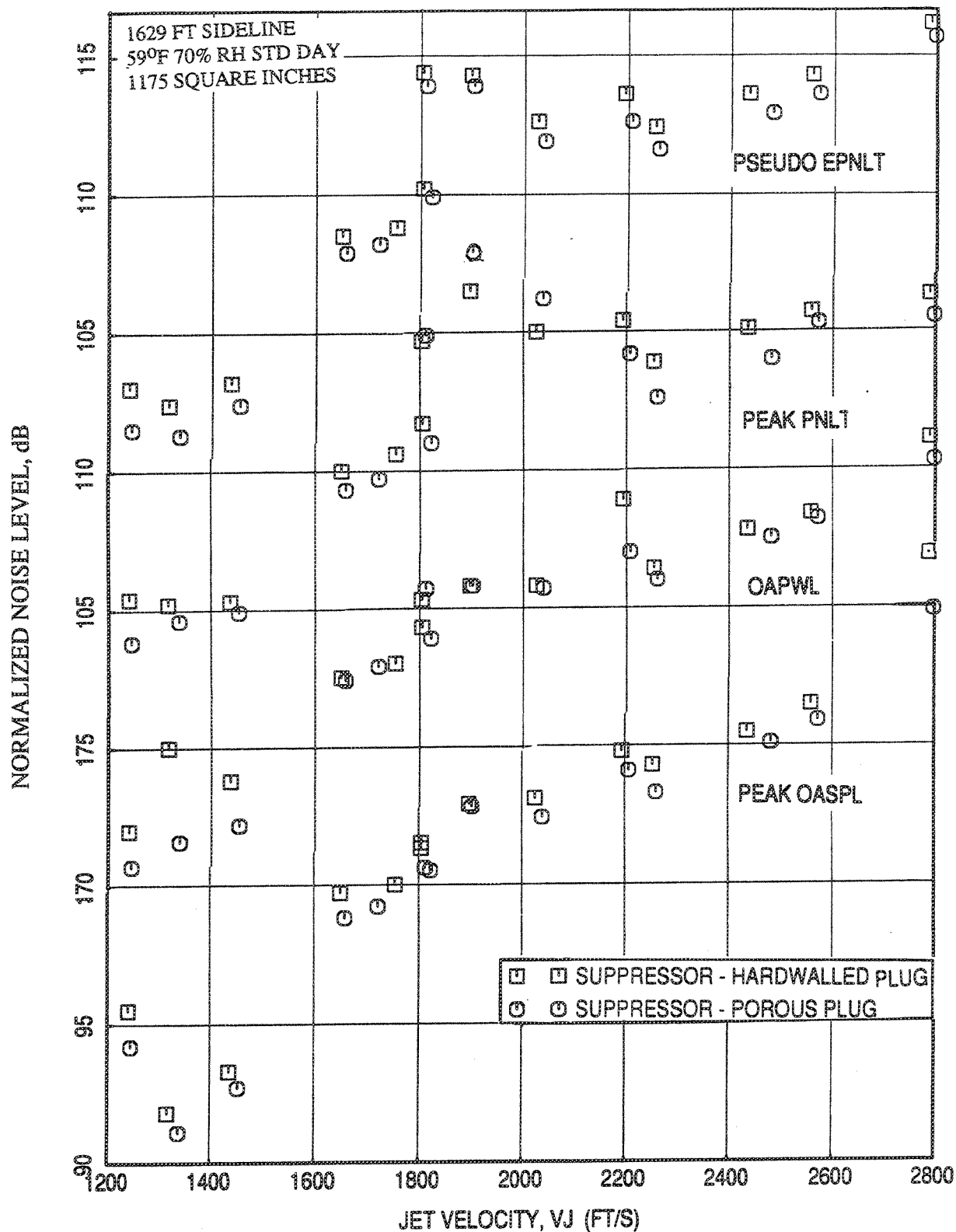


Figure 2.6-1. Effect of porous plug compared to hard-walled plug on normalized EPNLT, peak PNLT, OAPWL and peak OASPL data as functions of jet velocity for the 36-chute suppressor at static condition.

1. 2030 ft/sec: Flade Cycle mass averaged takeoff velocity,  $P_{r,p}=2.7$ ,  $T_{t,p}=1381^{\circ}\text{R}$  (Figure 2.6-2).
2. 2796 ft/sec: core velocity at LIM Cycle takeoff condition,  $P_{r,p}=4.0$ ,  $T_{t,p}=1960^{\circ}\text{R}$  (Figure 2.6-3).
3. 1452 ft/sec: at ambient temperature,  $P_{r,p} = 4.0$ ,  $T_{t,p} = 537^{\circ}\text{R}$  (Figure 2.6-4).

For all these cases some amount of OASPL reduction is observed for all angles. For ambient temperature case the OASPL reduction is confined to the forward arc. PNLT reduction is relatively lower compared to OASPL reduction. For 2030 ft/sec case PNLT levels with porous plug is relatively higher compared to hard wall case at some angles. This is due to the tone corrections for possible screech or shock noise spikes. Spectral results indicate modest SPL reductions at mid to low frequencies and predominantly in the forward quadrant due to porous plug. Amount of noise suppression seems to be higher in the forward arc.

**Flight Data :** Similar to the static case, Normalized Effective Perceived Noise Levels of the suppressor with hard-walled plug and the suppressor with porous plug (EPNLT), Peak PNLT, Overall Sound Power Levels (OAPWL), and Peak OASPL as functions of jet velocity are compared in Figure 2.6-5 with flight simulation ( $M_F=0.32$ ). In all these comparisons the noise levels for the suppressor with porous plug seems to be lower by about 1 to 2 dB compared to those for the suppressor with hard-walled plug for most of the test cases.

To examine the effect of porous plug in detail PNLT and OASPL directivities and SPL and PWL spectra for two different test points with different  $V_J$  are examined. The nominal velocities, cycle condition definitions, and the corresponding aerothermodynamic conditions (i.e., Nozzle Pressure Ratio  $P_{r,p}$  and Total Temperature,  $T_{t,p}$ ) for these cases are listed below :

1. 2030 ft/sec: Flade Cycle mass averaged takeoff velocity,  $P_{r,p}=2.7$ ,  $T_{t,p}=1381^{\circ}\text{R}$  (Figure 2.6-6).
2. 2475 ft/sec: core velocity at Flade Cycle takeoff condition,  $P_{r,p}=3.19$ ,  $T_{t,p}=1786^{\circ}\text{R}$  (Figure 2.6-7).

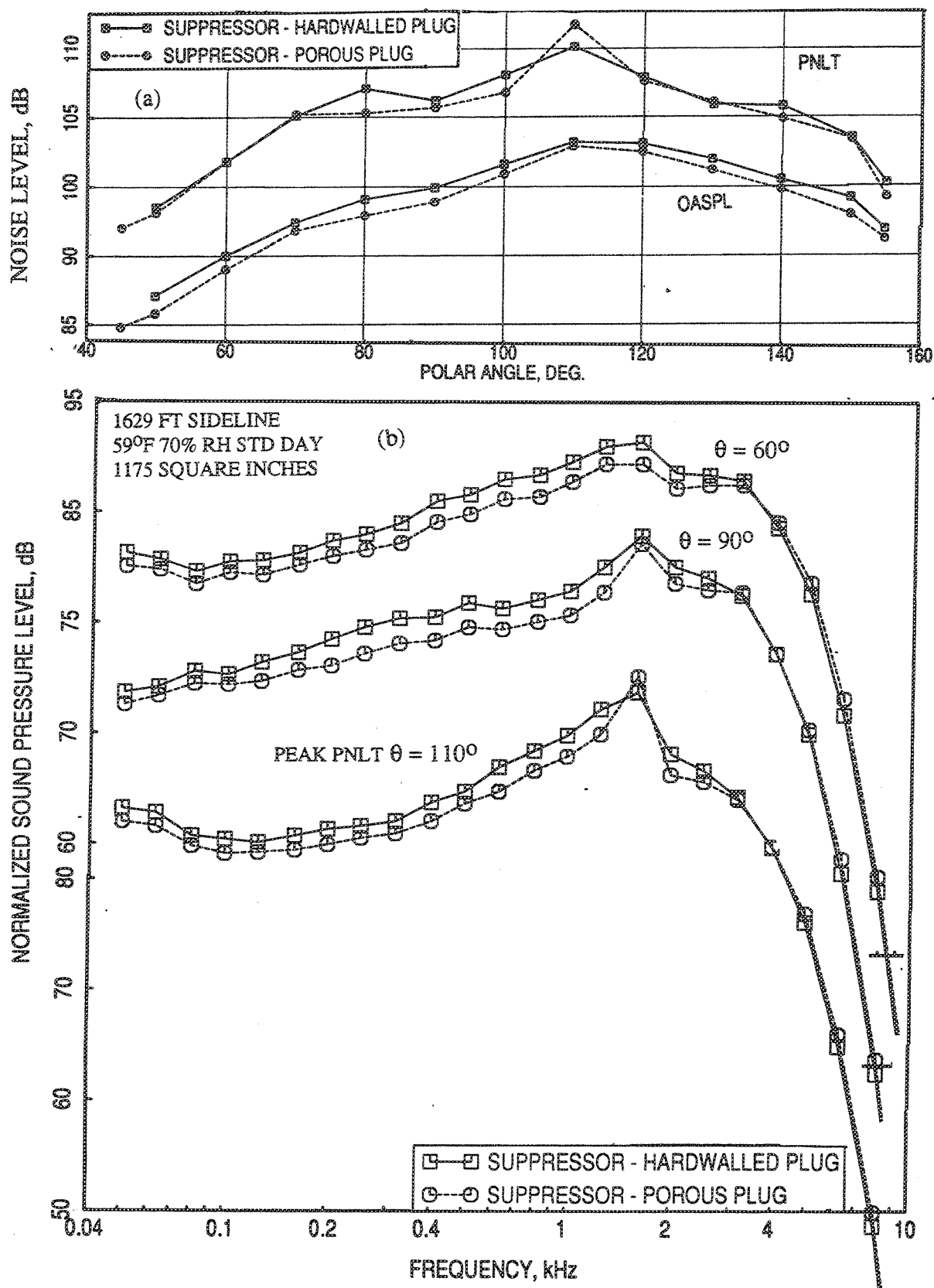


Figure 2.6-2. Effect of porous plug compared to hard-walled plug on (a) PNLT and OASPL directivities and (b) SPL spectra for the 36-chute suppressor at static condition, Nominal Values:  $P_{r,p}=2.7$ ,  $T_{t,p}=1381^\circ R$ ,  $V_{j,p}=2030$  ft/sec.

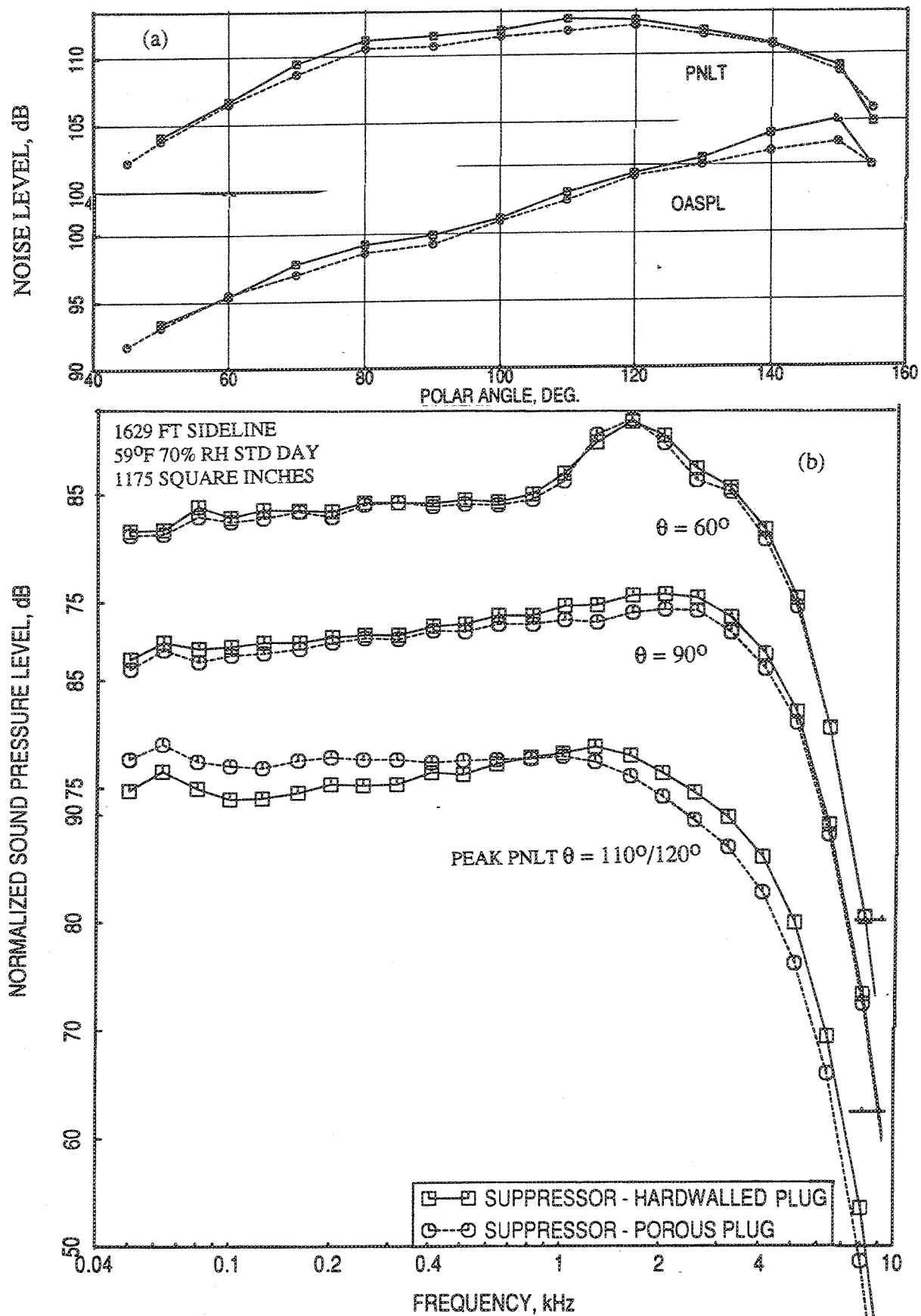


Figure 2.6-3. Effect of porous plug compared to hard-walled plug on (a) PNLT and OASPL directivities and (b) SPL spectra for the 36-chute suppressor at static condition, Nominal Values:  $P_{r,p}=4.0$ ,  $T_{t,p}=1960^\circ R$ ,  $V_{j,p}=2796$  ft/sec.

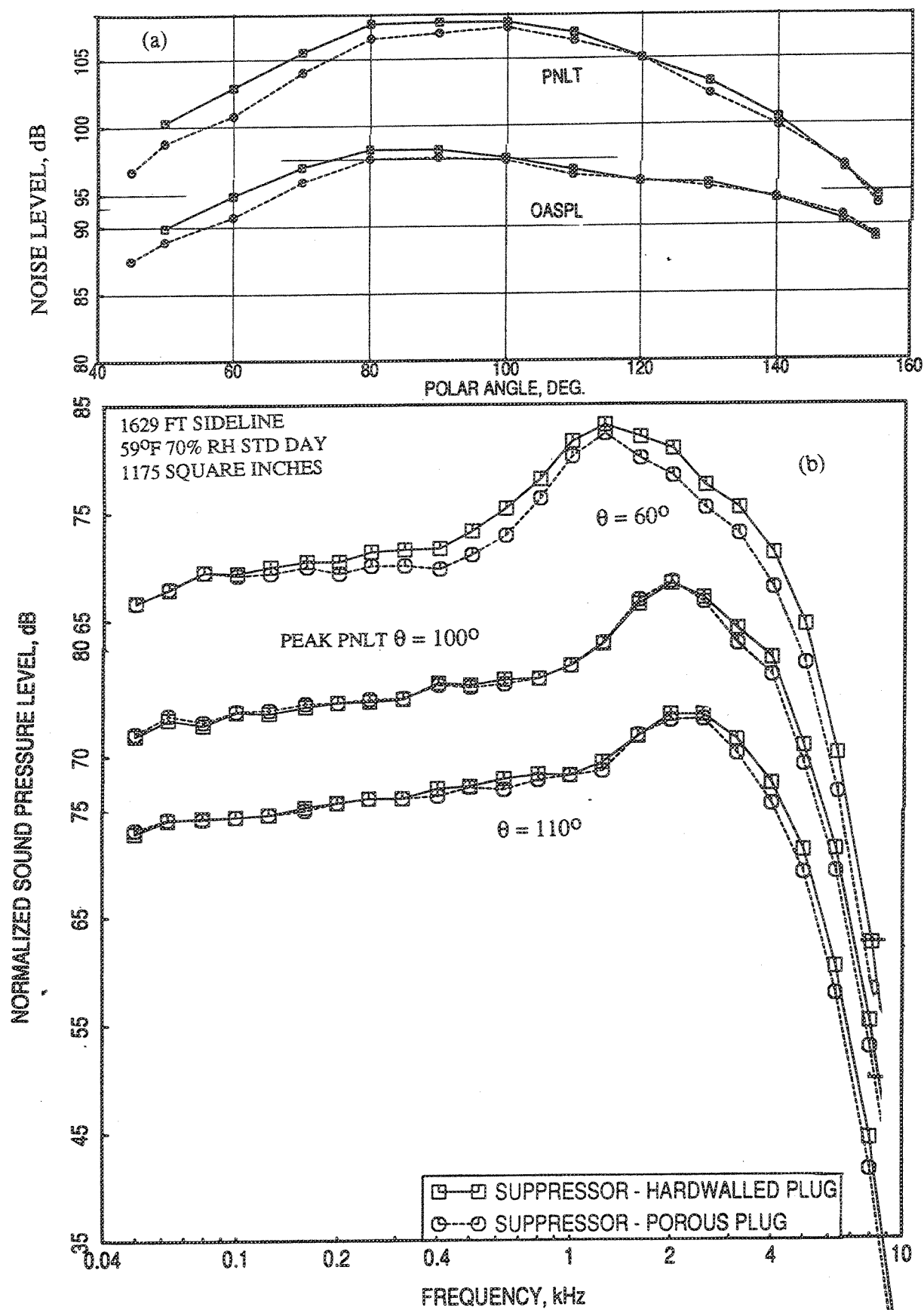


Figure 2.6-4. Effect of porous plug compared to hard-walled plug on (a) PNLT and OASPL directivities and (b) SPL spectra for the 36-chute suppressor at static condition, Nominal Values:  $P_{r,p}=4.0$ ,  $T_{t,p}=537^\circ R$ ,  $V_{j,p}=1452$  ft/sec.



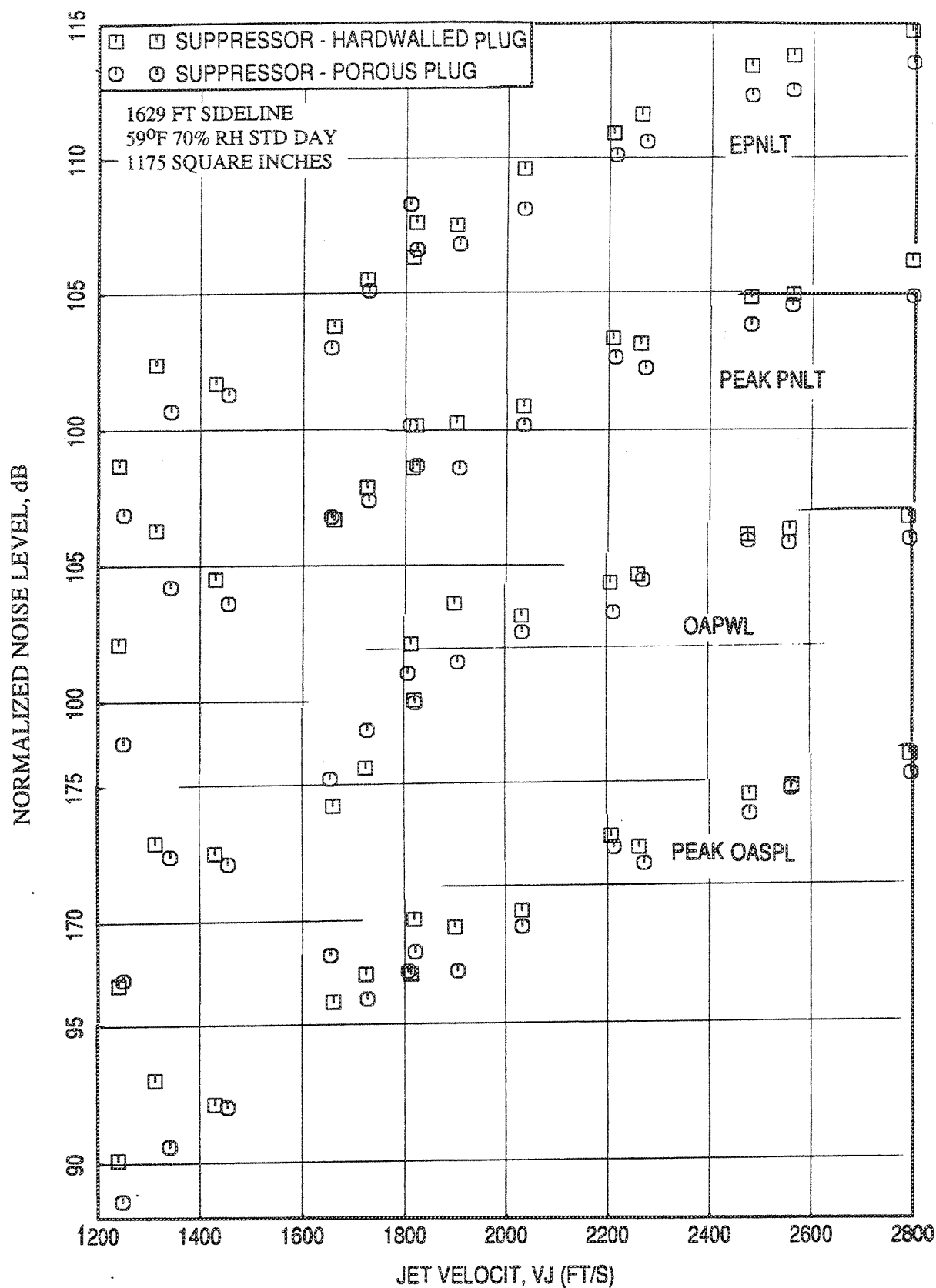


Figure 2.6-5. Effect of porous plug compared to hard-walled plug on normalized EPNLT, peak PNLT, OAPWL and peak OASPL data as functions of jet velocity for the 36-chute suppressor with flight simulation ( $M_F=0.32$ ).

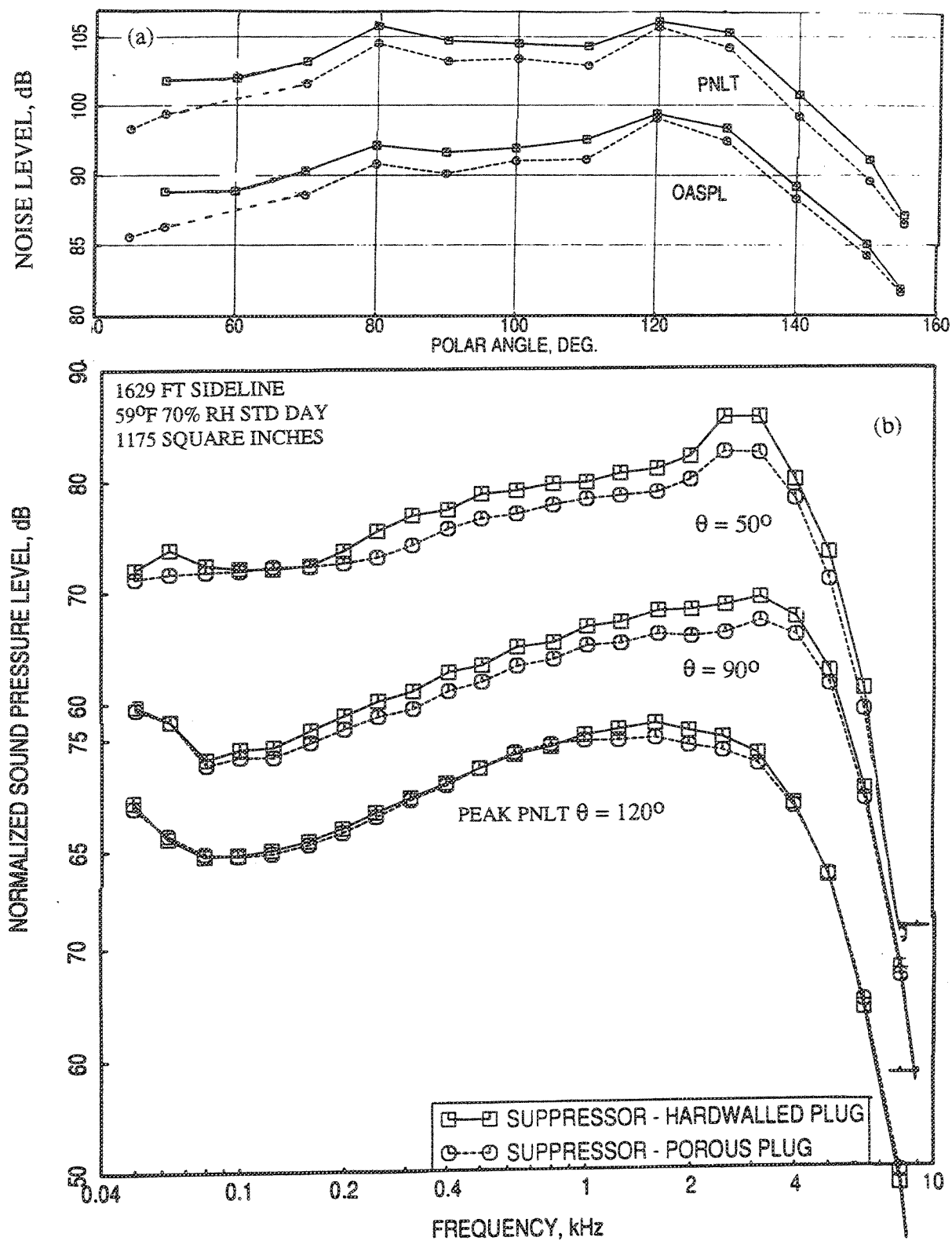


Figure 2.6-6. Effect of porous plug compared to hard-walled plug on (a) PNLT and OASPL directivities and (b) SPL spectra for the 36-chute suppressor with flight simulation ( $M_F=0.32$ ). Nominal Values:  $P_{r,p}=2.7$ ,  $T_{t,p}=1381^\circ\text{R}$ ,  $V_{j,p}=2030$  ft/sec.

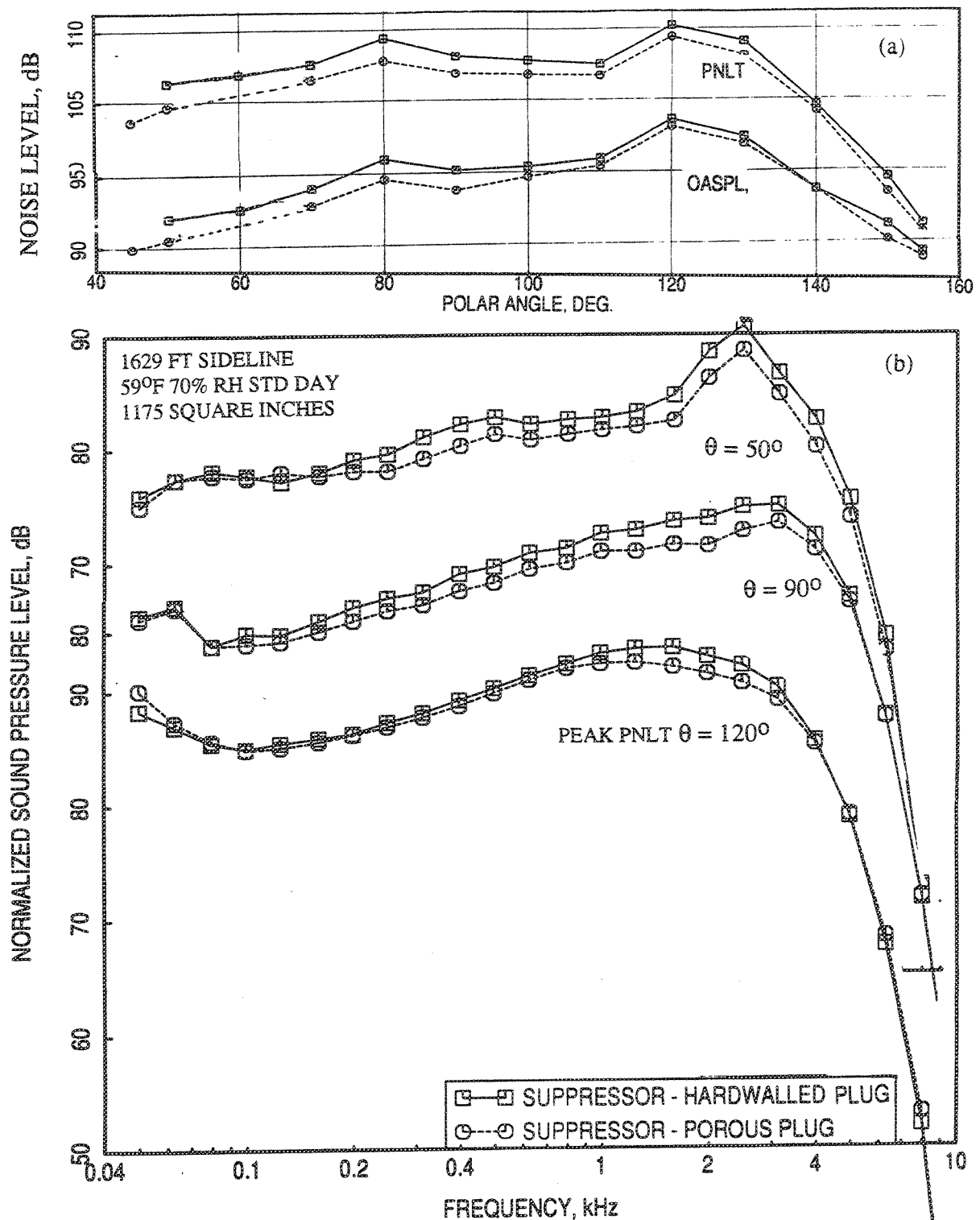


Figure 2.6-7. Effect of porous plug compared to hard-walled plug on (a) PNLT and OASPL directivities and (b) SPL spectra for the 36-chute suppressor with flight simulation ( $M_F=0.32$ ), Nominal Values:  $P_{r,p}=3.2$ ,  $T_{t,p}=1786^\circ\text{R}$ ,  $V_{j,p}=2475$  ft/sec.

For all these cases some amount of OASPL as well as PNLT reduction is observed for all angles. Spectral results indicate SPL reductions at all frequency and at all angles due to porous plug. Amount of noise suppression seems to be higher in the forward arc relative to the static case. Potential weakening of shock structure due to porous plug and corresponding reduction in shock noise is more evident in flight than static due to predominance of shock noise in the forward quadrant and amplification of shock noise due to flight.

### 2.6.2 Fluid Shield Nozzle Configurations with 0.5"-Thick Shield of 220° Wrap:

Similar to the suppressor alone case the results for the fluid shield configurations are examined with and without flight simulation to evaluate the effect of porous plug. Since the observations are qualitatively similar between static and flight simulated cases, only simulated flight results are presented here.

**Flight Simulated Data :** Figure 2.6-8. shows the comparison of Normalized EPNLT, peak PNLT, and peak OASPL as functions of mixed jet velocity ( $V_{mix}$ ) for the 0.5"-thick fluid shield nozzle, between hard wall and porous plug configurations, with flight simulation (flight simulation Mach number,  $M_F=0.32$ ). In this plot the results for porous and hard wall plugs for the same test condition are not exactly appearing at the same  $V_{mix}$ . This is due to the difference in temperature levels in the streams compared to the desired temperatures between hard wall and porous plug tests. It was difficult to maintain the desired temperature in the secondary stream (flade stream), since secondary flow temperatures were much lower compared to the primary stream. Thus, the corresponding points are indicated by arrows in Figure 2.6-8 and the results show some amount of acoustic benefit due to porous plug for almost all test cases.

Detailed examination of OASPL and PNLT directivities and SPL spectra are carried out for two select test points. The nominal velocities, cycle condition definitions, and the corresponding aerothermodynamic conditions (i.e., Nozzle Pressure Ratios  $P_{r,p}$  and  $P_{r,s}$  and Total Temperatures,  $T_{t,p}$  and  $T_{t,s}$ ) for these cases are listed below :

1. 2030 ft/sec: Flade Cycle mass averaged takeoff velocity with supercritical fluid shield flow,  $P_{r,p} = 3.2$ ,  $T_{t,p} = 1786^\circ R$ ,  $P_{r,s} = 2.14$ ,  $T_{t,s} = 695^\circ R$  (Figure 2.6-9).

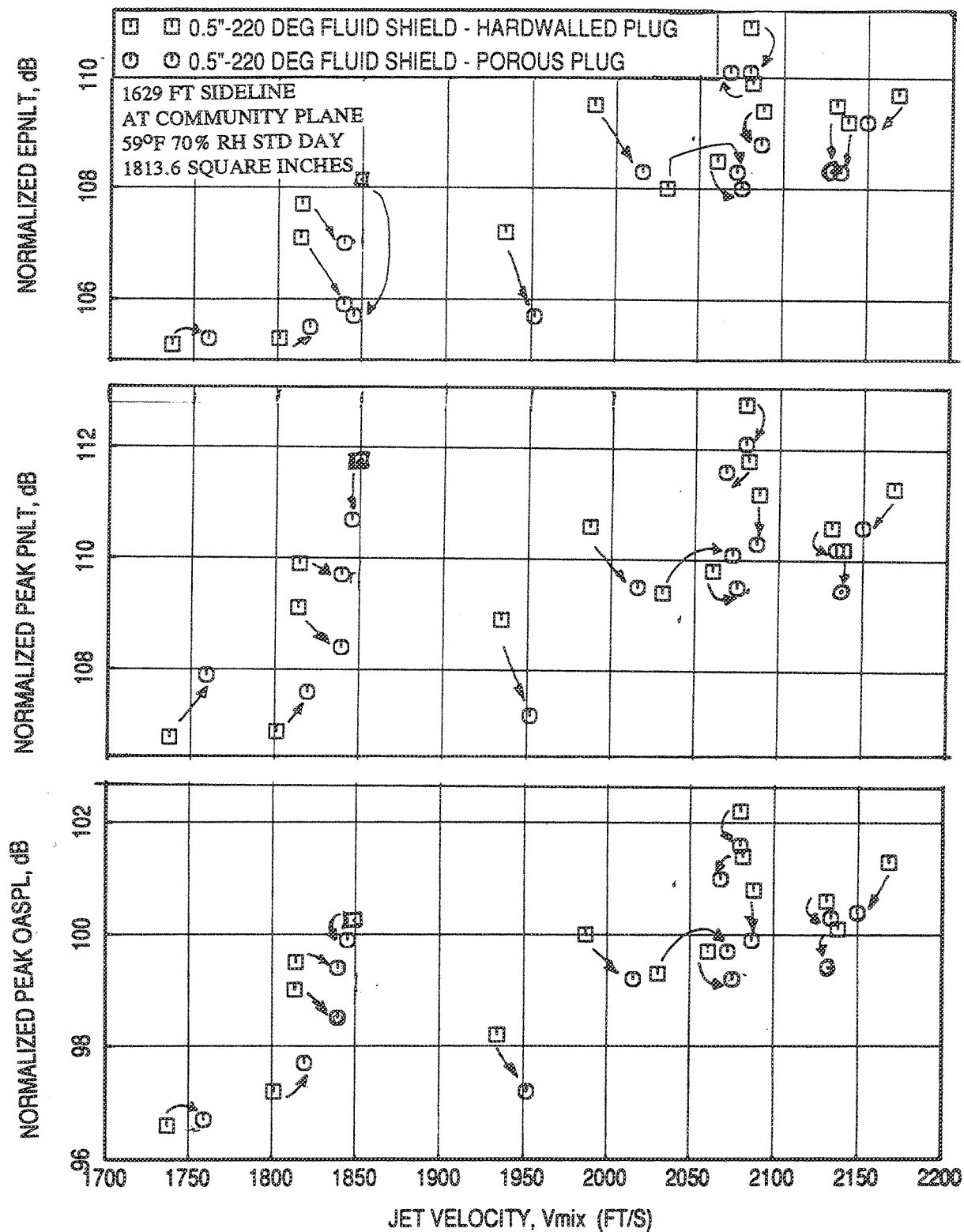


Figure 2.6-8. Effect of porous plug compared to hard-walled plug on normalized EPNLT, peak PNL, and peak OASPL data as functions of jet velocity for the 0.5"-thick, 220° wrap fluid shield nozzle with flight simulation ( $M_F=0.32$ ).

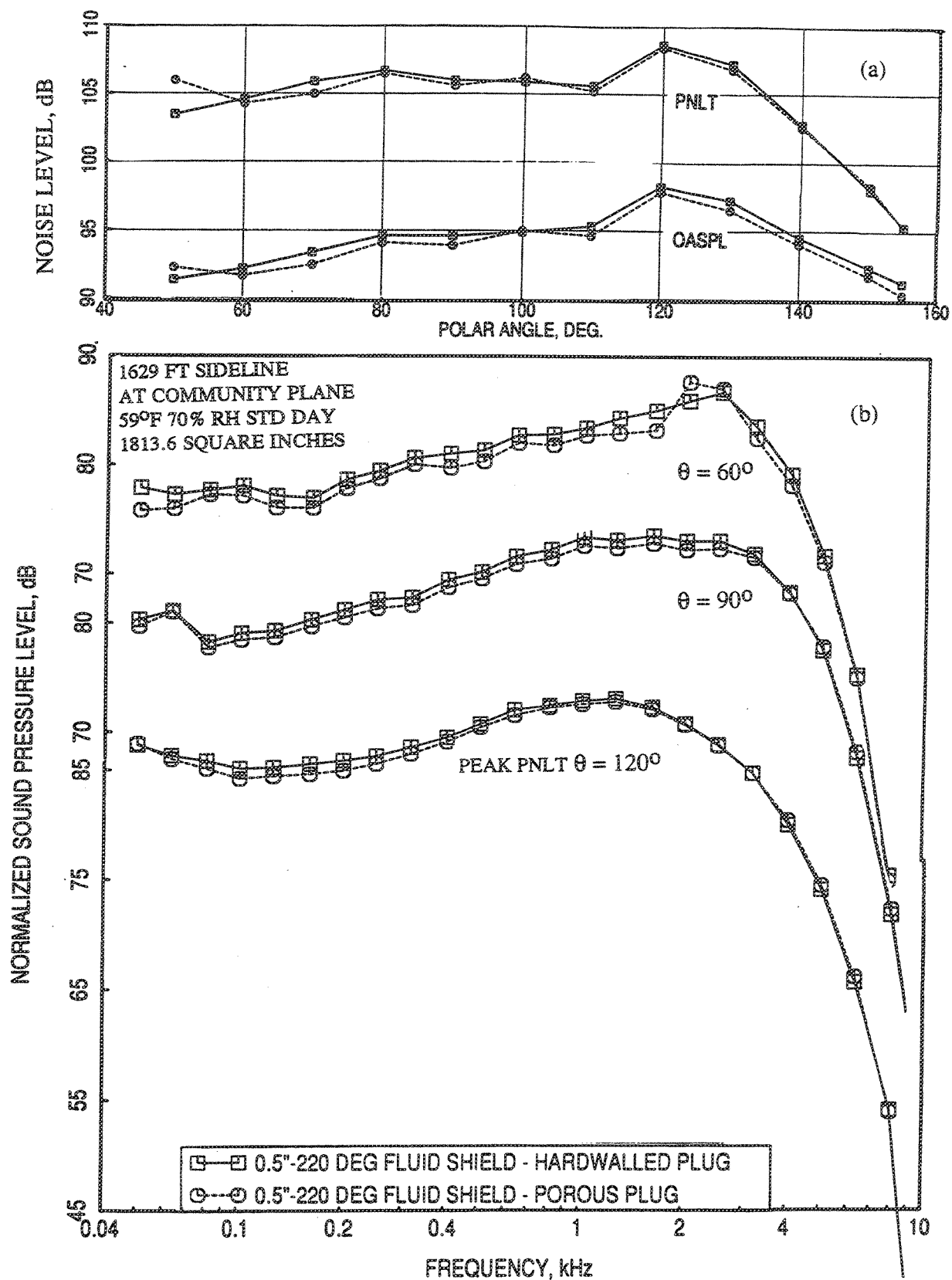


Figure 2.6-9. Effect of porous plug compared to hard-walled plug on (a) PNLT and OASPL directivities and (b) SPL spectra for the 0.5"-thick, 220° wrap fluid shield nozzle with flight simulation ( $M_F=0.32$ ), Nominal Values:  $P_{r,p}=3.17$ ,  $T_{t,p}=1786^\circ\text{R}$ ,  $P_{r,s}=1.6$ ,  $T_{t,s}=695^\circ\text{R}$ ,  $V_{\text{mix}}=2030$  ft/sec.

2. 1251 ft/sec: at ambient temperature,  $P_{r,p} = 3.17$ ,  $T_{t,p} = 537^{\circ}\text{R}$ ,  $P_{r,s} = 1.6$ ,  $T_{t,s} = 537^{\circ}\text{R}$  (Figure 2.6-10).

For  $V_{\text{mix}} = 2030$  ft/sec very little effect of porous plug is observed in OASPL, PNLT, and SPL levels for supercritical fluid shield. For ambient temperature condition the acoustic benefit of the porous plug is significant as indicated in Figure 2.6-10, as the relative contribution to total noise by shock broadband noise is higher at lower temperatures and the effectivity of porous plug is more evident when shock noise dominates the spectrum.

Based on the acoustic results, slight noise reduction is achieved due to the porous plug. However, the amount of benefit is much less than what was noted by other research works of porous plugs. Shadowgraph results of suppressor indicate insignificant difference in the shock structures between hard wall plug and porous plug configurations (see Figures 2.3-8 and 2.3-9). In addition, while the static pressure distributions on plug for suppressor alone configuration indicate some difference between hard wall and porous plugs (see Figure 2.4-4), similar results for a 0.5"-thick fluid shield nozzle configuration show even smaller differences between the two plugs (see Figure 2.4-10). A physical interpretation of the shock structures of the chuted suppressor with high aspect ratio chutes on the basis of shadowgraph photographs (see Figures 2.3-3 through 2.3-6) is elaborated in section 2.3 of this report.

The aspect ratio of individual chutes is such that plug porosity is "felt" by the narrow side of the complex 3-D shock structure of the chutes as envisaged and explained in section 2.2, using shadowgraph photographs. Significant shock dimension is in the direction normal to the porous plug which is not effectively modified by the plug porosity. Previous experimental studies in plug porosity were conducted with simple high radius ratio plugs which had a much smaller annulus height. Hence, it is plausible that very large levels of shock noise suppression were noted in those cases. A combined C-D flowpath for chutes and limited plug porosity may be necessary to eliminate most of the shock noise for these complex multi-element suppressor nozzles. On the basis of acoustic results it may be still beneficial to use porous plug compared to a hard-walled plug if the aerodynamic performance is not severely degraded compared to hard-walled plug.

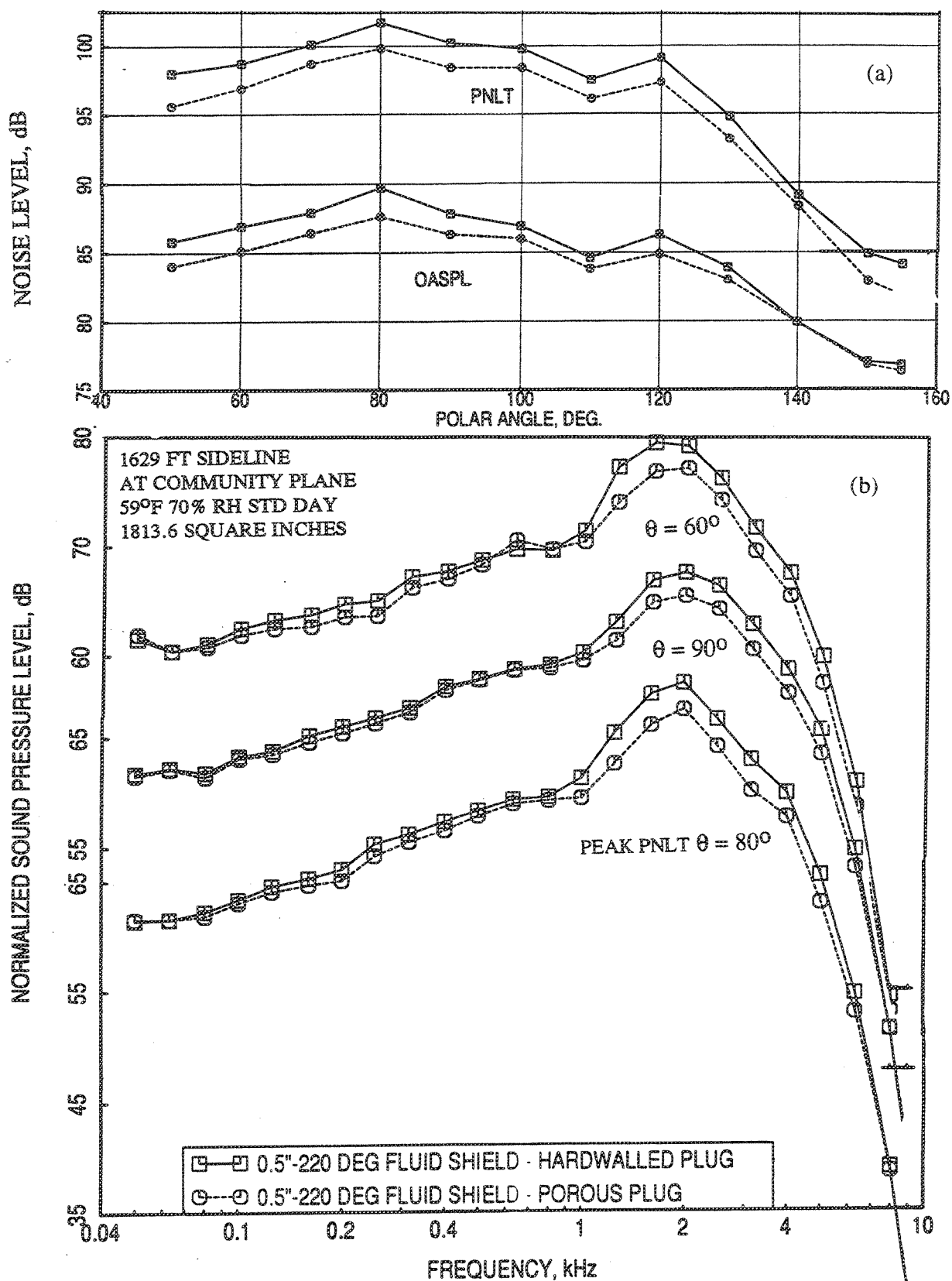


Figure 2.6-10. Effect of porous plug compared to hard-walled plug on (a) PNLT and OASPL directivities and (b) SPL spectra for the 0.5"-thick, 220° wrapfluid shield nozzle with flight simulation ( $M_F=0.32$ ), Nominal Values:  $P_{r,p}=3.17$ ,  $T_{t,p}=537^\circ\text{R}$ ,  $P_{r,s}=1.6$ ,  $T_{t,s}=537^\circ\text{R}$ ,  $V_{\text{mix}}=1251$  ft/sec.



## 2.7 ACOUSTIC CHARACTERISTICS OF THE 36-CHUTE SUPPRESSOR COMPARED TO AN EQUIVALENT CONICAL NOZZLE

The objective of this section is to analyze the noise suppression capability of the suppressor alone configurations with respect to an equivalent conical nozzle and with respect to other multi-chute suppressors with different designs.

### 2.7.1 Acoustic Characteristics of the 36-Chute Suppressor Compared to an Equivalent Conical Nozzle:

The farfield data measured by the tower microphones at  $\phi=10^\circ$  and the fixed microphones at  $\phi=45^\circ$  for the 6.54 in<sup>2</sup> conical nozzle and the 21.59 in<sup>2</sup> 36-chute suppressor with hard-walled plug and porous plug were analyzed to study the acoustic characteristics of the suppressor. The acoustic characteristics of the suppressor with the porous plug are examined in this section, since it has been illustrated in section 2.6, that the porous plug configuration is slightly quieter than the hard wall plug configuration.

All the acoustic variables are corrected to the standard day conditions of 59° F and 70% relative humidity, extrapolated to 1629' distance, and scaled to 1175 in<sup>2</sup> area (full scale suppressor area of Flade Cycle). The distance of 1629' corresponds to the hypotenuse formed by a sideline distance of 1467' for FAR-36 Stage 3 and a typical aircraft altitude of 689', at which the sideline noise has been shown to peak by airframer studies. The results derived from tower microphone data agree very well with those derived from fixed microphone measurements for axisymmetric nozzles. For brevity, only the tower microphone results are presented in this section.

**Static Data :** As an overview the Normalized Overall Sound Power Levels (OAPWLN) and Overall Sound Pressure levels (OASPLN) at different polar angles, as functions of jet velocity are compared between the suppressor and the conic nozzle in Figure 2.7-1. In these comparisons the noise levels for the suppressor are lower compared to those for conic nozzle and the difference between them increases with the velocity. Suppressor results at velocities of about 1320 ft/sec and 1430 ft/sec deviate from the trend for the rest of the data points. These two points are derived from the test conditions with a jet temperature of about 525°R compared to the heated flow for the rest of the points. This introduces a large density difference and a significantly different

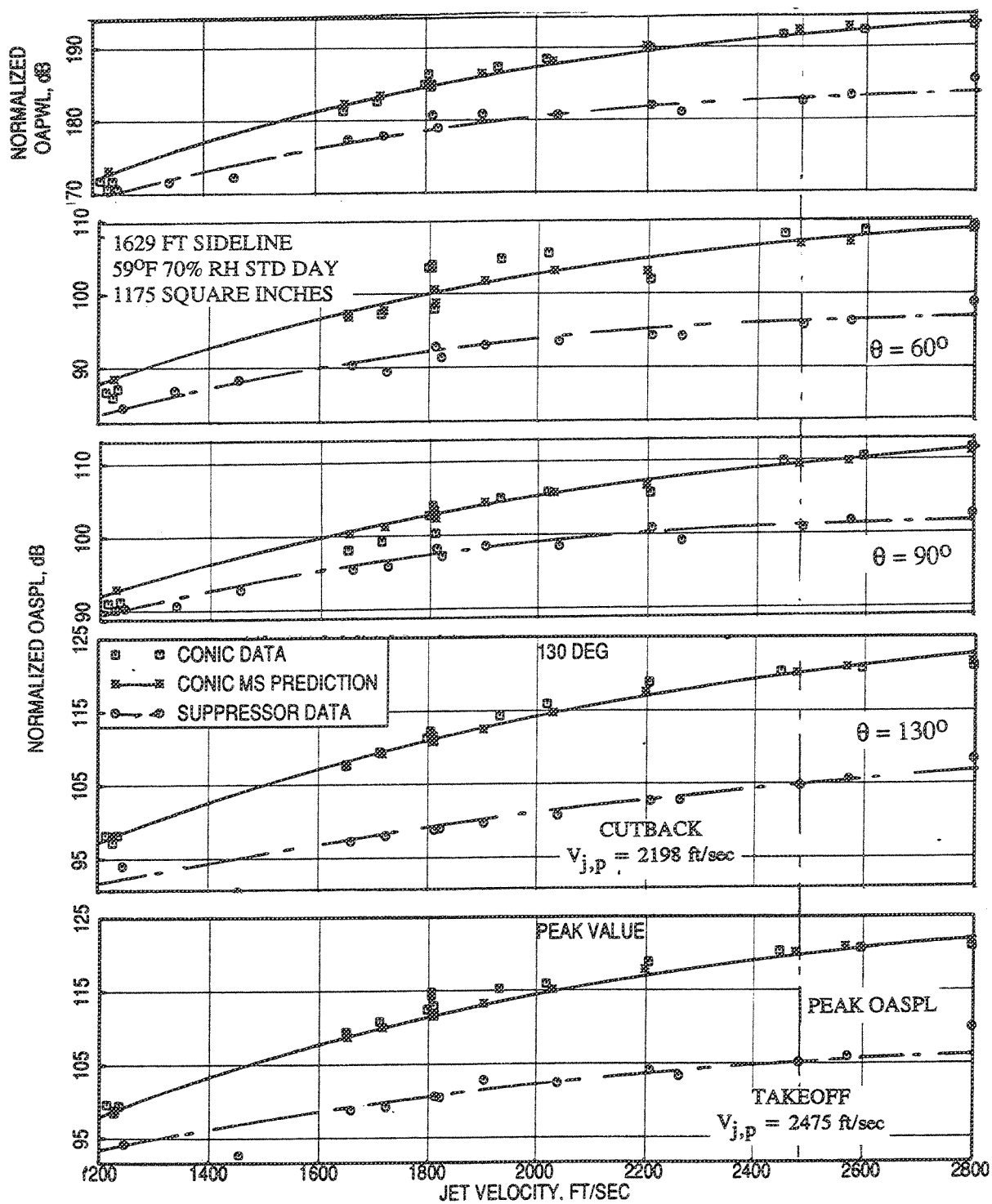


Figure 2.7-1. Comparison of normalized OAPWL and OASPL data as a function of jet velocity for the 36-chute suppressor with porous plug with those of a 6.54 in<sup>2</sup> conical nozzle at static condition.

composition of shock and jet mixing noise, which is not entirely accounted for by the normalization for jet density and gross thrust. On OAPWLN basis acoustic suppressions of about 8 dB and 5.5 dB are observed at takeoff (i.e.,  $V_J=2030$  ft/sec) and cutback (i.e.,  $V_J=1811$  ft/sec) conditions. Normalized Overall Sound Pressure Levels (OASPLN) at various polar angles and their peak level comparisons indicate noise reductions of about 13 and 11.5 peak OASPL dBs at takeoff and cutback conditions due to the suppressor compared to conic nozzle.

Similar results for Normalized EPNLT and Normalized PNLT are shown in Figure 2.7-2. Suppressions of about 6 to 7 EPNL dB is observed at takeoff and cutback conditions. Corresponding peak PNLT suppressions are about 9 to 10 dB.

To evaluate the acoustic characteristics of the suppressor in detail, PWL spectra, PNLT and OASPL directivities, and SPL spectra for four different  $V_J$  are examined. The nominal velocities and cycle condition definitions are as follows:

1.  $V_J=1811$  ft/sec: Flade Cycle mass averaged cutback velocity;  $P_R = 2.23$ ,  $T_T = 1327^\circ\text{R}$ .
2.  $V_J = 2030$  ft/sec: Flade Cycle mass averaged takeoff velocity;  $P_R = 2.7$ ,  $T_T = 1381^\circ\text{R}$ .
3.  $V_J = 2475$  ft/sec: core velocity at Flade Cycle takeoff condition;  $P_R = 3.2$ ,  $T_T = 1786^\circ\text{R}$ .
4.  $V_J = 2796$  ft/sec: core velocity at LIM Cycle takeoff condition;  $P_R = 4.0$ ,  $T_T = 1960^\circ\text{R}$ .

Comparison of normalized PWL spectra between the conic nozzle and the suppressor with porous plug for the above four conditions are shown in Figure 2.7-3. Maximum PWL spectral suppressions of about 20 dB is observed for  $V_J = 1811$  ft/sec and 2030 ft/sec at about 160 Hz. For higher velocity conditions the PWL suppressions are relatively lower and are about 18 and 13 dB for  $V_J = 2475$  ft/sec and 2796 ft/sec, respectively. The amount of PWL suppression increases first and then decreases with increasing frequency after reaching a maximum level. The relative dominance of low frequency content over the high frequency of the suppressor increases due to the

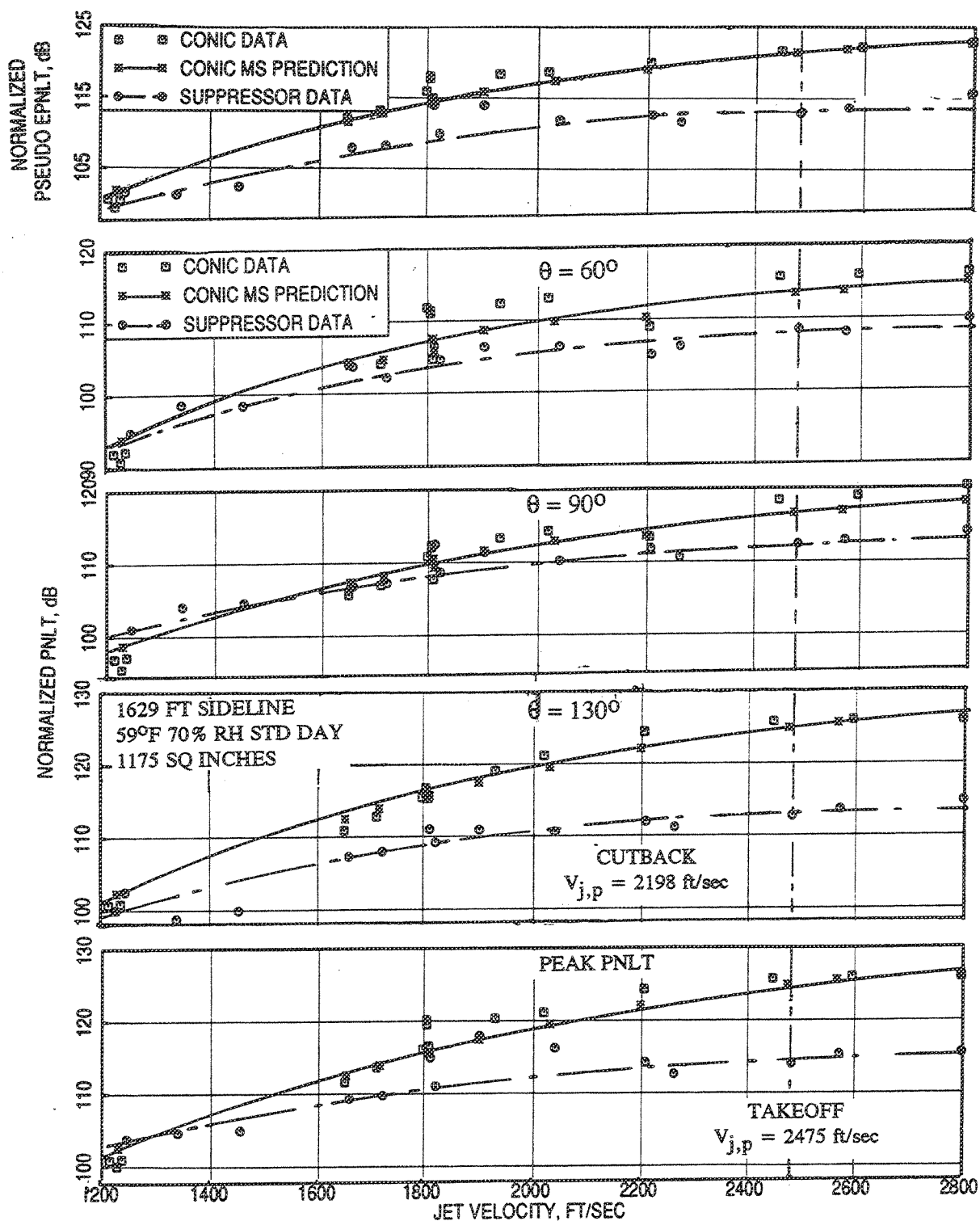


Figure 2.7-2. Comparison of normalized pseudo EPNLT and PNLT data as a function of jet velocity for the 36-chute suppressor with porous plug with those of a  $6.54 \text{ in}^2$  conical nozzle at static condition.

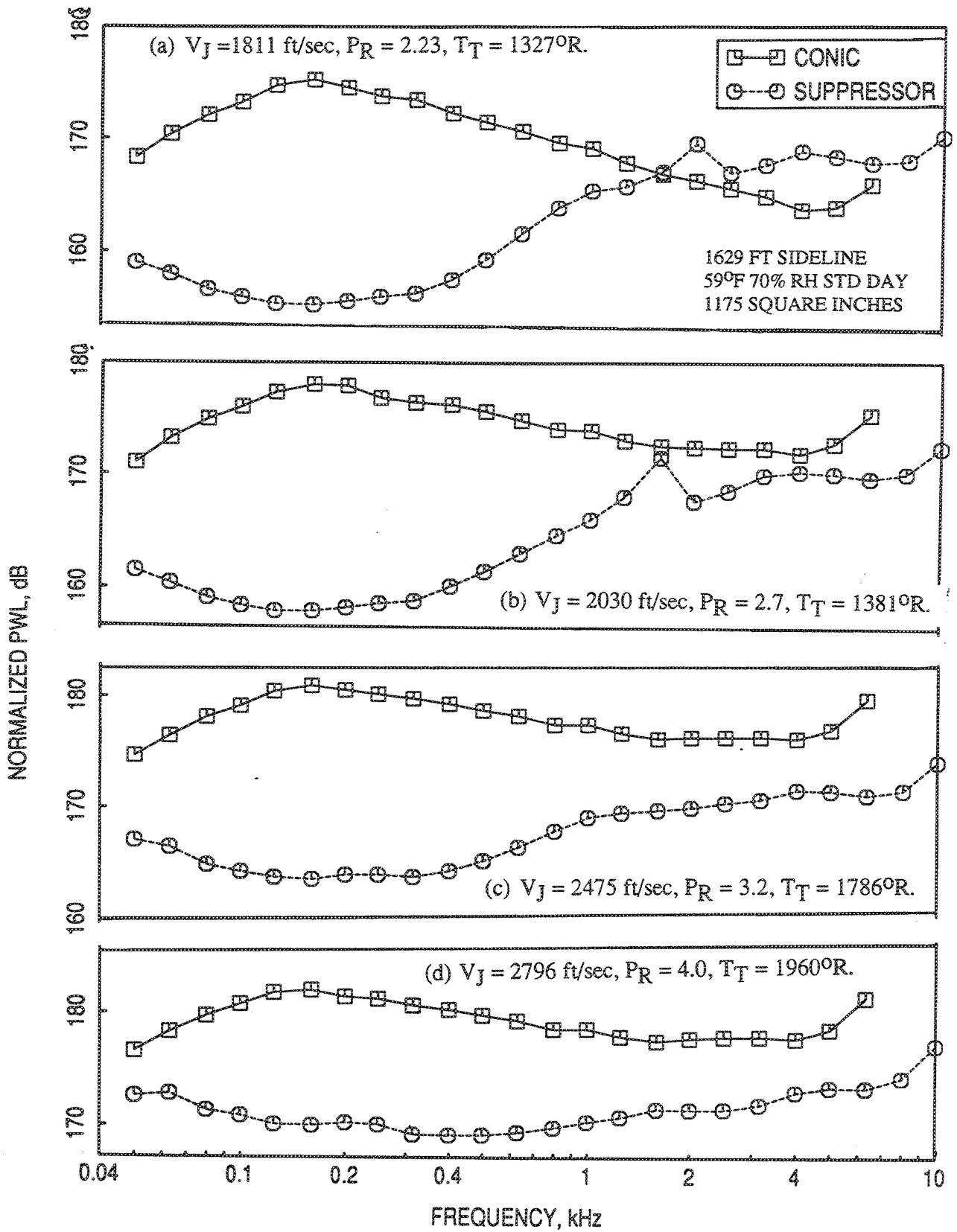


Figure 2.7-3. Comparison of PWL spectra for the 36-chute suppressor with porous plug with those of a  $6.54 \text{ in}^2$  conical nozzle for four different jet velocities at static condition.

reduced mixing effectiveness at higher jet velocities. Low frequency noise is very effectively suppressed by the use of the multi-chute suppressor, due to the increased mixing with the ambient air.

Figure 2.7-4(a) shows the directivity comparisons for PNLT and OASPL between the conical nozzle and the suppressor for a nominal  $V_J$  of 1811 ft/sec. Suppression levels as high as 8 PNLT dB and 16 OASPL dB are observed in the rear arc at the same angular locations of  $\theta = 140^\circ$ . SPL spectral plots for the same condition are shown in Figure 2.7-4(b). At the peak PNL angle, spectral suppression as high as 23 dB is noted at a frequency of about 160 Hz. The suppressor has very effectively suppressed low frequency noise due to rapid plume decay.

It should be noted that the OASPL levels for the suppressor are significantly lower compared to those for conic nozzle at all polar angles. This is due to the large amount of low frequency noise reductions and the equal weighting of all frequency components in computing OASPL. The large low frequency noise reduction are correspondingly achieved by only modest reduction in mid to high frequencies which have significant impact on PNLT and hence PNLT reductions are not as large as OASPL. In some instances, the PNLT (i.e., tone corrected PNL) levels for the suppressor at a number of angles, specially in the forward arc, are higher than those for the conic nozzle at  $V_J=1811$  ft/sec (see Figure 2.7-4). This is due to the excessive tone corrections due to the presence of screech (and shock noise) in suppressor data at around 2 kHz (i.e., about 15 kHz for the model scale). The SPL spectrum at  $70^\circ$  shows a strong peak, which resulted in a much higher PNLT level as shown in Figure 2.7-4(a).

Similar results for  $V_J=2030$  ft/sec are shown in Figure 2.7-5. Suppressions of about 10 PNLT dB and 16 OASPL dB at  $\theta = 130^\circ$ , and 24 SPL dB at about 160 Hz (at peak PNLT angle) are observed. Suppressions at  $V_J=2476$  ft/sec case, as shown in Figure 2.7-6, are about 10 PNLT dB and 15 OASPL dB at  $\theta = 130^\circ$ , and 23 SPL dB at about 160 Hz (at peak PNLT angle). Results for  $V_J=2796$  ft/sec, shown in Figure 2.7-7, indicate suppressions of about 11 PNLT dB and 13 OASPL dB at  $\theta = 130^\circ$ , and 20 SPL dB at about 160 Hz (at peak PNL angle).

**Flight Simulated Data :** Flight simulation tests were conducted with a free jet flow Mach number  $M_F=0.32$ . As an overview the Normalized Overall Sound Power Levels (OAPWLN) and Overall Sound Pressure levels (OASPLN) at different polar angles, as

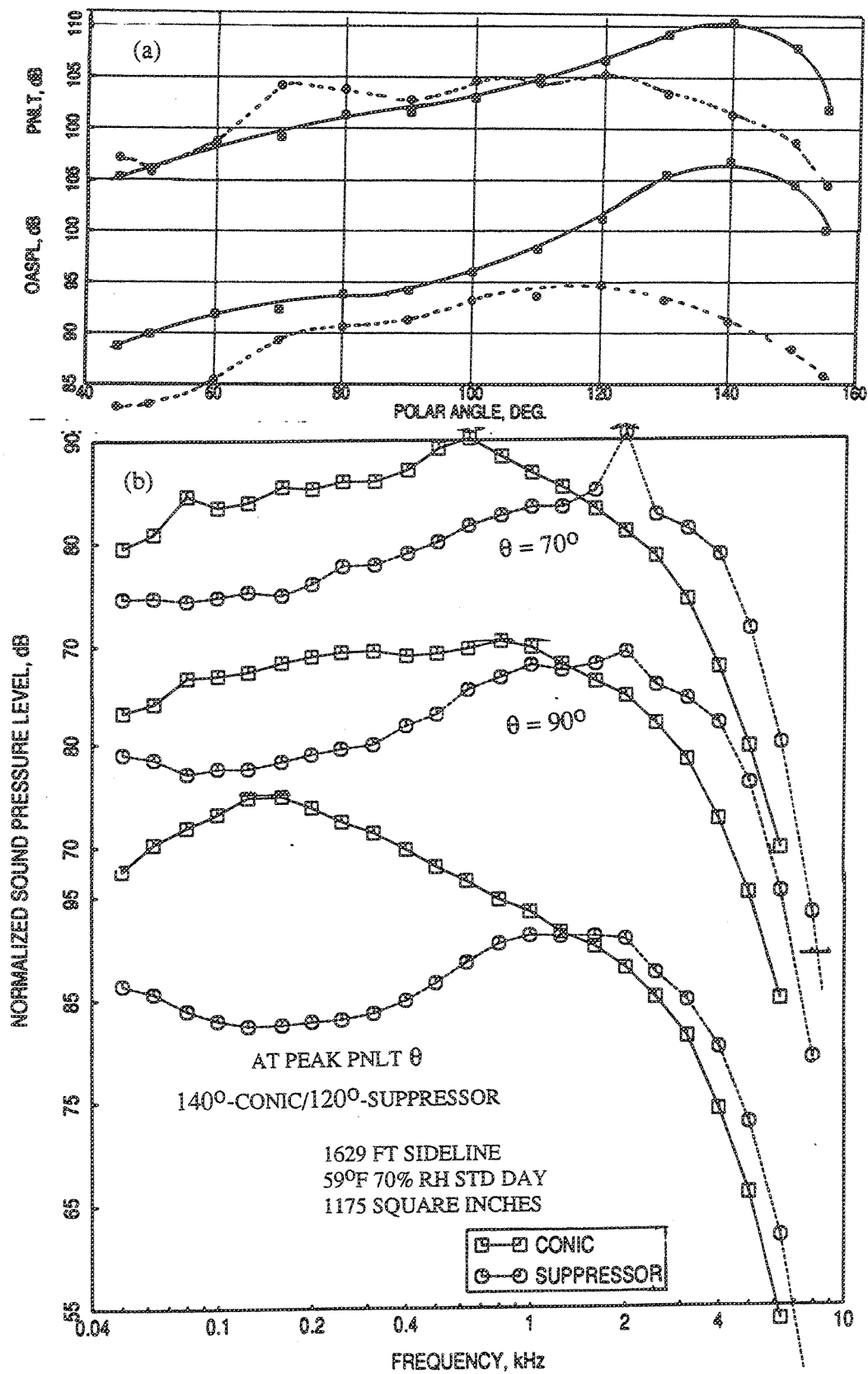


Figure 2.7-4. Comparison of (a) PNLT and OASPL directivities and (b) SPL spectra for the 36-chute suppressor with porous plug with those of a 6.54 in<sup>2</sup> conical nozzle at static condition,  $P_{r,p}=2.23$ ,  $T_{t,p}=1327^\circ\text{R}$ ,  $V_{j,p}=1811$  ft/sec.

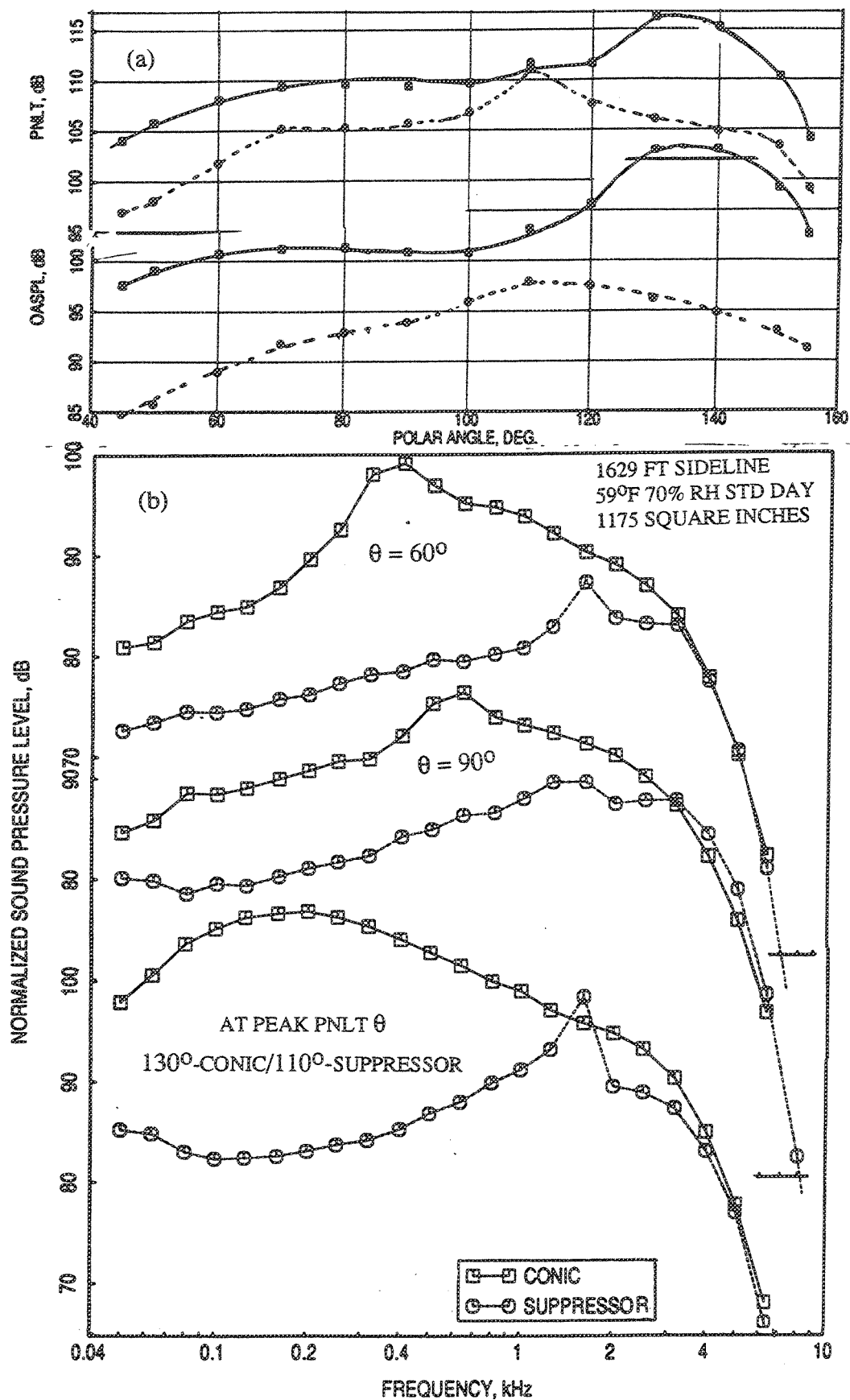


Figure 2.7-5. Comparison of (a) PNLT and OASPL directivities and (b) SPL spectra for the 36-chute suppressor with porous plug with those of a 6.54 in<sup>2</sup> conical nozzle at static condition,  $P_{r,p}=2.7$ ,  $T_{t,p}=1381^\circ\text{R}$ ,  $V_{j,p}=2030$  ft/sec.



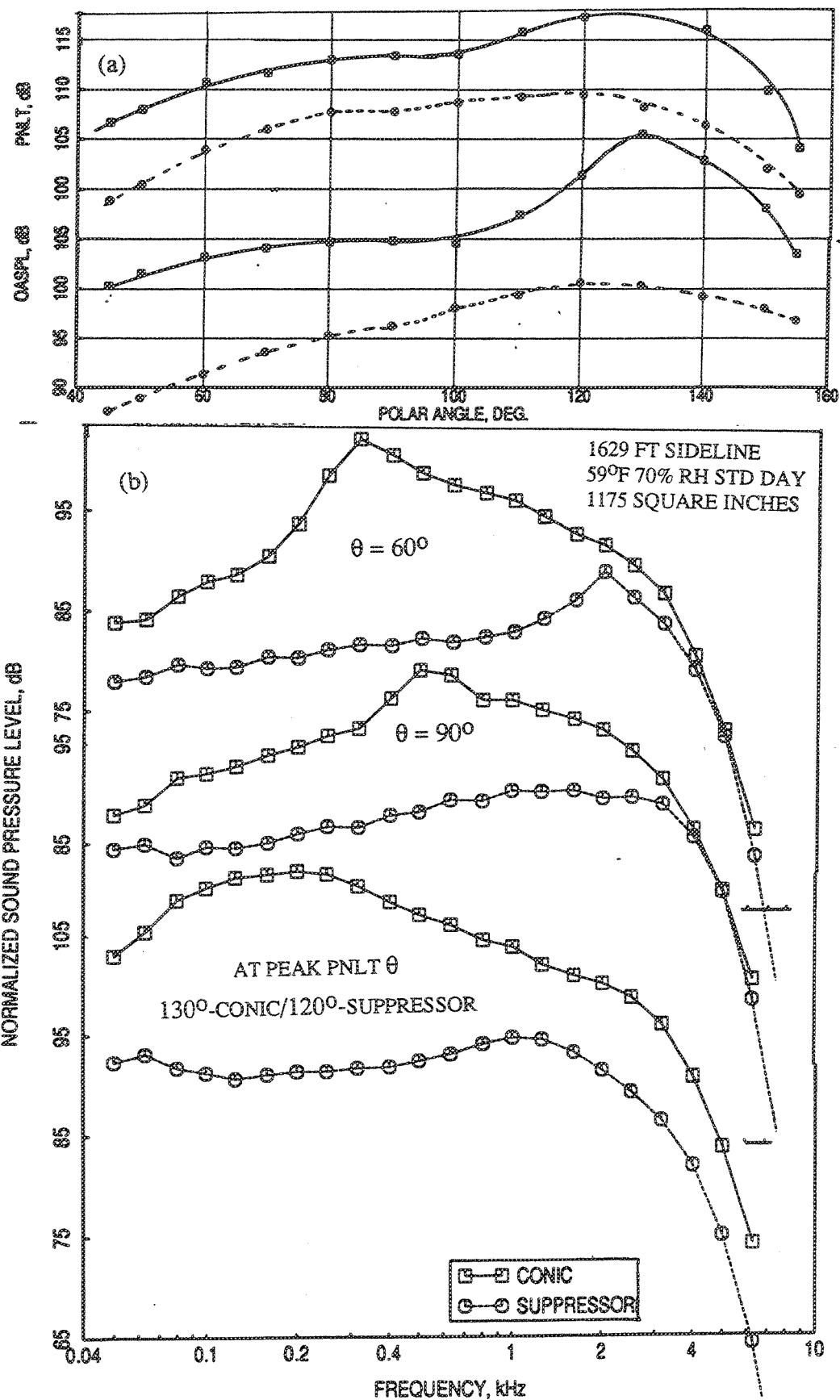


Figure 2.7-6. Comparison of (a) PNLT and OASPL directivities and (b) SPL spectra for the 36-chute suppressor with porous plug with those of a 6.54 in<sup>2</sup> conical nozzle at static condition,  $P_{r,p}=3.2$ ,  $T_{t,p}=1786^\circ\text{R}$ ,  $V_{j,p}=2476$  ft/sec.

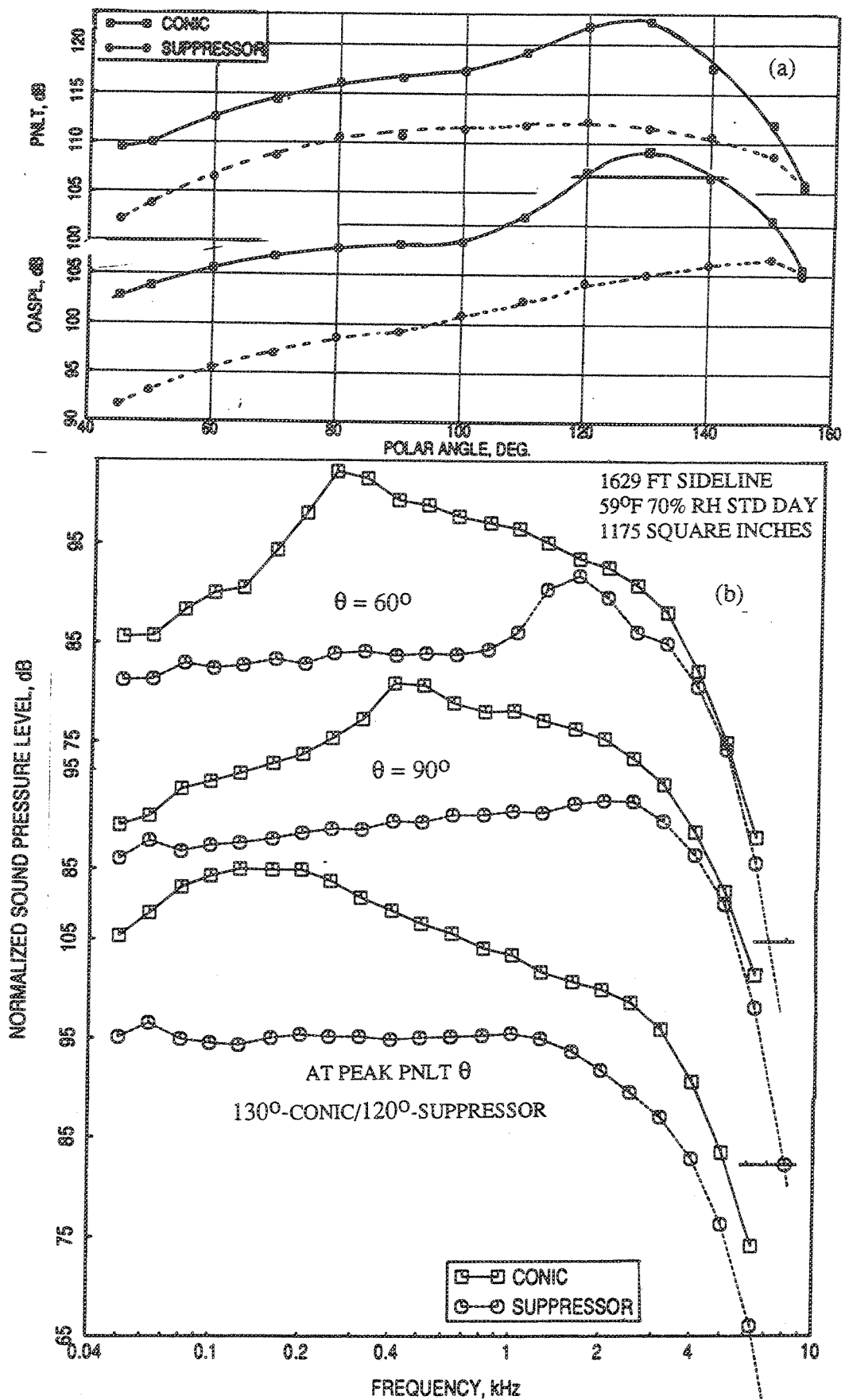


Figure 2.7-7. Comparison of (a) PNLT and OASPL directivities and (b) SPL spectra for the 36-chute suppressor with porous plug with those of a 6.54 in<sup>2</sup> conical nozzle at static condition,  $P_{t,p}=4.0$ ,  $T_{t,p}=1960^\circ\text{R}$ ,  $V_{j,p}=2796$  ft/sec.

functions of jet velocity are compared between the suppressor and the conic nozzle in Figure 2.7-8. Similar to static condition, the noise levels for the suppressor are lower compared to those for conic nozzle and the difference between them increases with the velocity. Suppressor results at velocities of about 1320 ft/sec and 1430 ft/sec deviate from the trend for the rest of the data points, since they are derived from the test conditions of ambient temperature. Acoustic suppressions observed in this figure are similar to those obtained with static condition.

Similar results for Normalized EPNLT and Normalized PNLT are shown in Figure 2.7-9. Suppressions of about 8 EPNL dB is observed at takeoff and cutback conditions. Corresponding peak PNLT suppressions are about 5 to 6 dB, which are relatively lower compared to static condition.

It should be noted that the conic nozzle noise levels (i.e., OAPWL, OASPL, EPNLT, and PNLT) with flight simulation for the test conditions with lower nozzle pressure ratios (i.e., mixed conditions corresponding to flade cycle cutback points, see Figure 2.2-22) are much lower compared to the predictions. This is due to the use of a coannular nozzle, instead of a single stream conic nozzle, as described in section 2.5.

PWL spectra, PNLT and OASPL directivities, and SPL spectra for four different  $V_j$ , same as those of static conditions, are examined. Comparison of normalized PWL spectra between the conic nozzle and the suppressor with porous plug for the four velocity conditions are shown in Figure 2.7-10. Maximum spectral PWL suppressions of about 19 dB, 21 dB, 19 dB, and 17 dB are observed for  $V_j = 1811$  ft/sec, 2030 ft/sec, 2475 ft/sec, and 2796 ft/sec, respectively at about 160 to 200 Hz. The amount of PWL suppression increases first and then decreases with increasing frequency after reaching a maximum level. In fact, the PWL for the suppressor becomes higher than that for the conic nozzle at higher frequencies. The cross over frequency increases with velocity. In general, the low frequency noise is effectively reduced by the suppressor.

Figure 2.7-11(a) shows the directivity comparisons for PNLT and OASPL between the conical nozzle and the suppressor for a nominal  $V_j$  of 1811 ft/sec. Suppressions of as high as 8 PNLT dB and 16 OASPL dB are observed in the rear arc at the same angular locations of  $\theta = 150^\circ$ . SPL spectral plots for the same condition are shown in Figure 2.7-11(b). Corresponding to peak PNLT angle, spectral suppression as high as 21 dB is noted at a frequency of about 160 Hz.

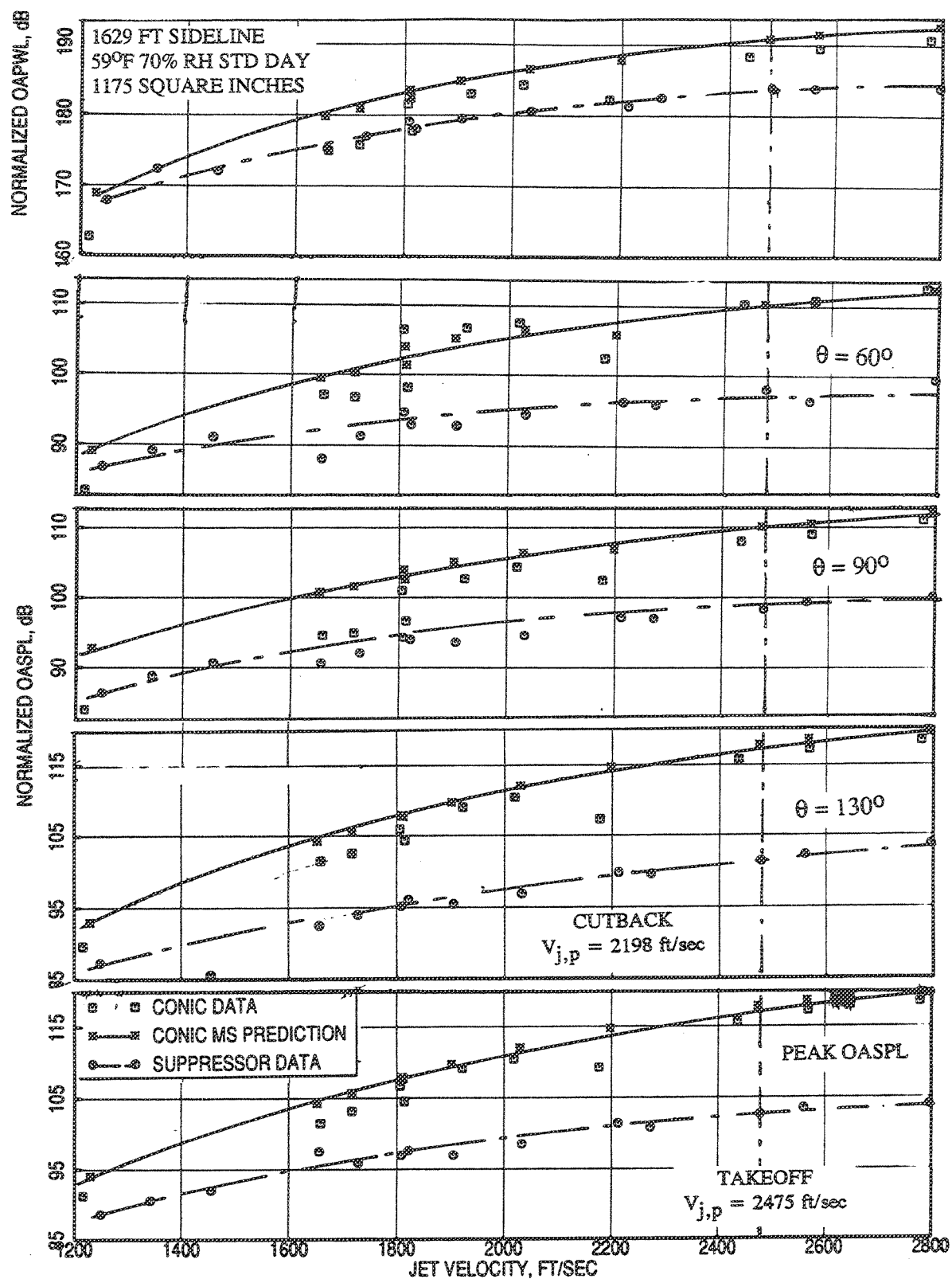


Figure 2.7-8. Comparison of normalized OAPWL and OASPL data as a function of jet velocity for the 36-chute suppressor with porous plug with those of a 6.54 in<sup>2</sup> conical nozzle with flight simulation ( $M_F=0.32$ ).

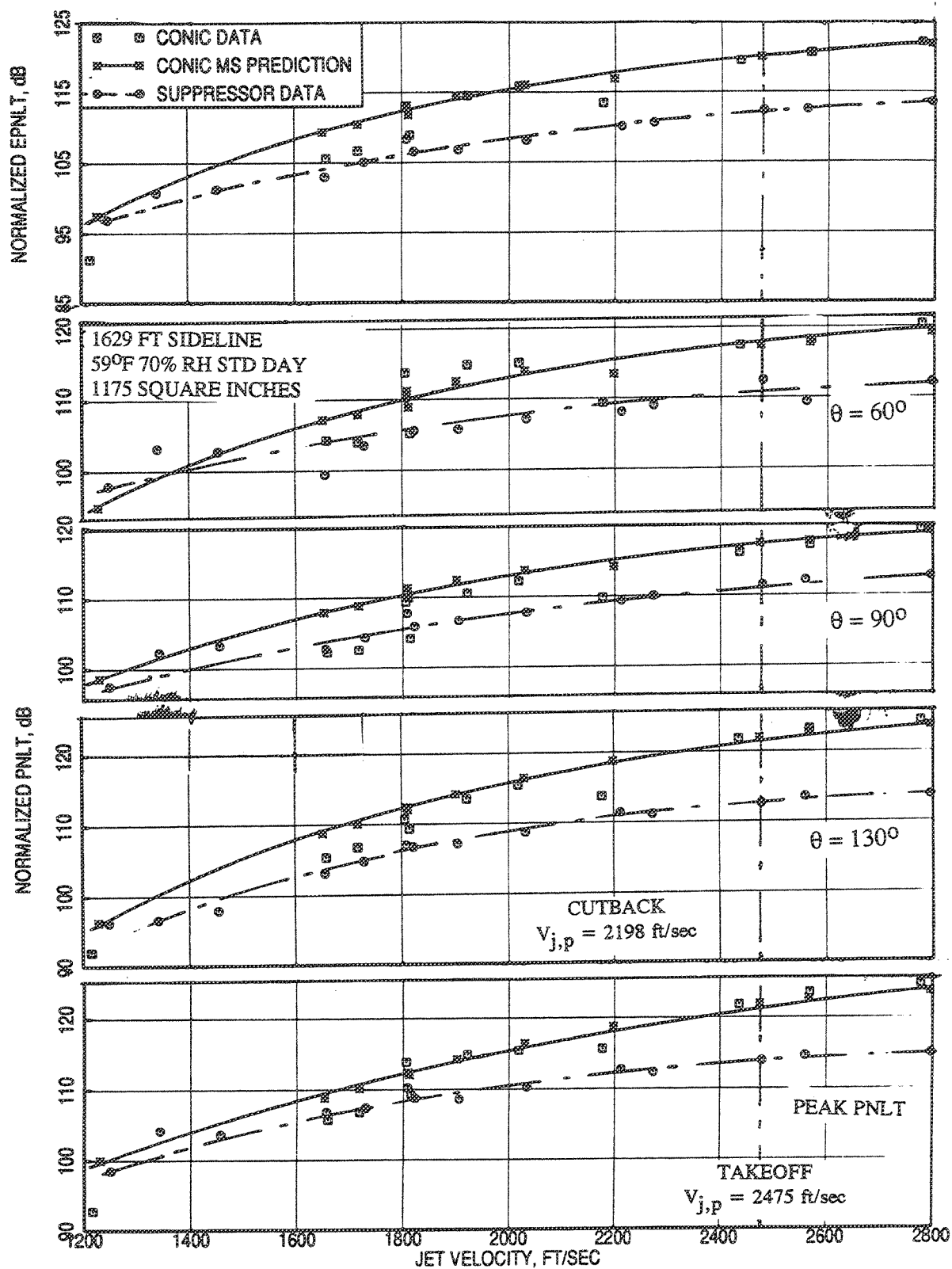


Figure 2.7-9. Comparison of normalized EPNLT and PNLT data as a function of jet velocity for the 36-chute suppressor with porous plug with those of a 6.54 in<sup>2</sup> conical nozzle with flight simulation ( $M_F=0.32$ ).

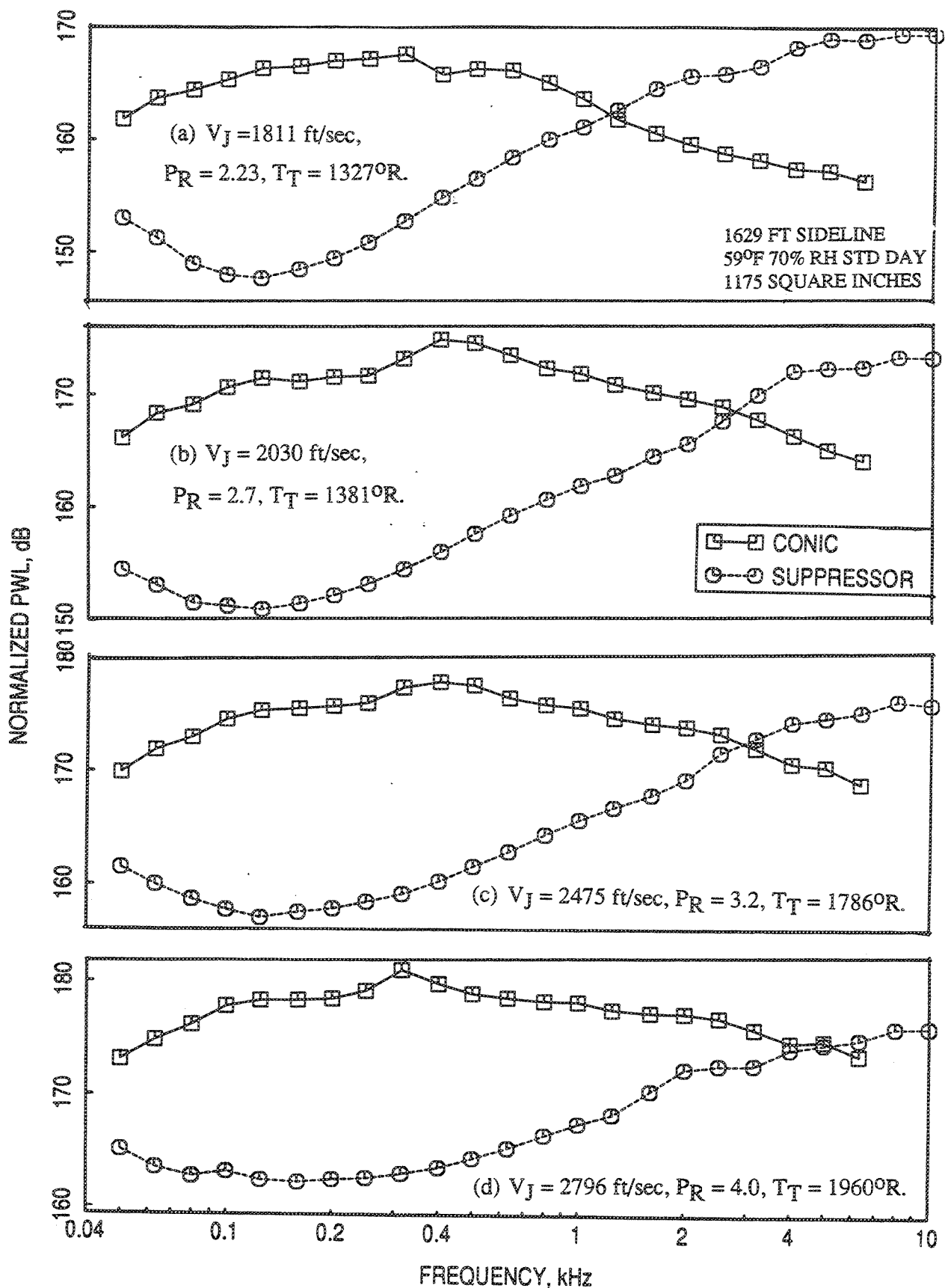


Figure 2.7-10. Comparison of PWL spectra for the 36-chute suppressor with porous plug with those of a 6.54 in<sup>2</sup> conical nozzle at four different jet velocities with flight simulation ( $M_F = 0.32$ ).

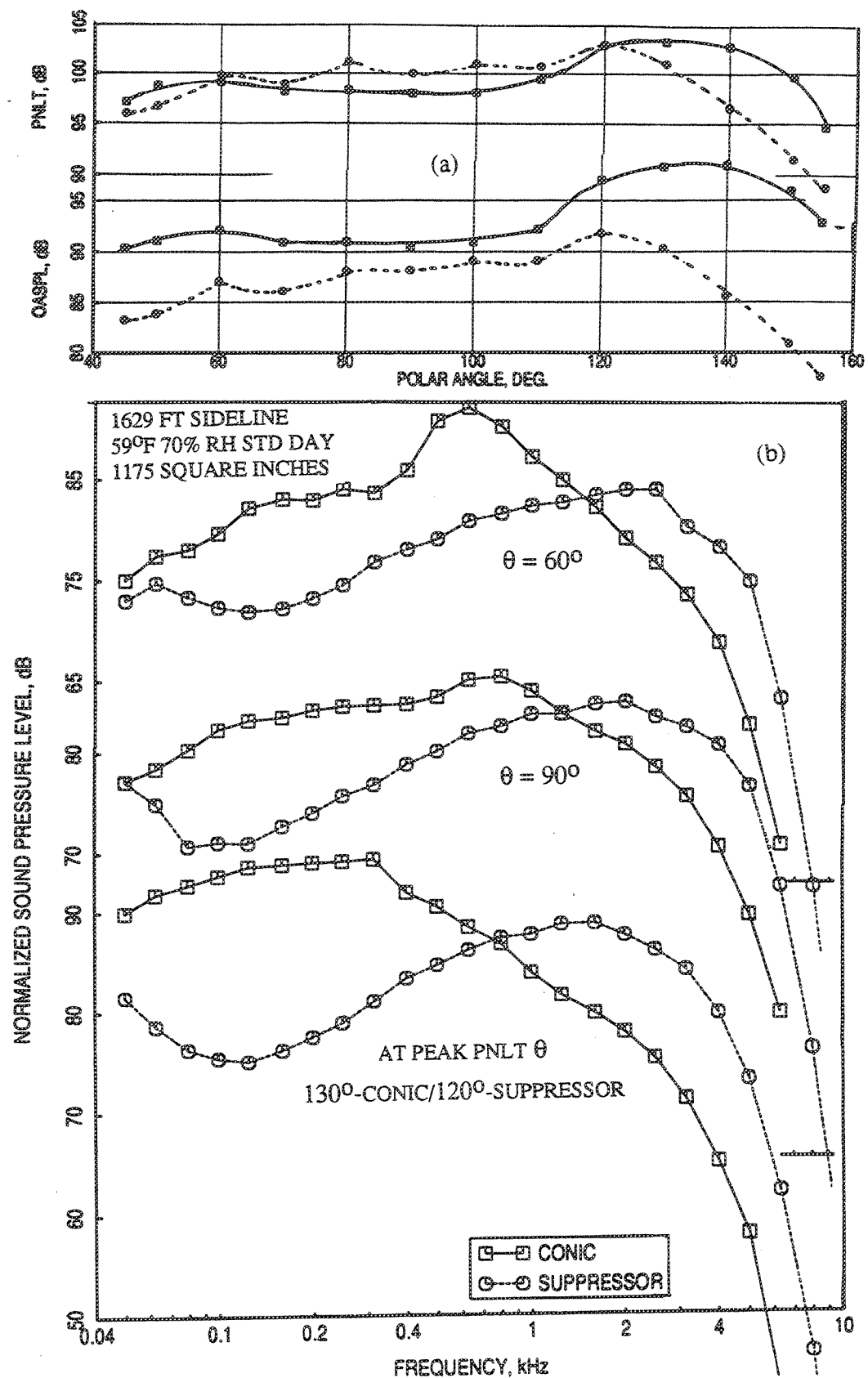


Figure 2.7-11. Comparison of (a) PNLT and OASPL directivities and (b) SPL spectra for the 36-chute suppressor with porous plug with those of a 6.54 in<sup>2</sup> conical nozzle with flight simulation ( $M_F=0.32$ ),  $P_{r,p}=2.23$ ,  $T_{t,p}=1327^\circ R$ ,  $V_{j,p}=1811$  ft/sec

It should be noted that the OASPL levels for the suppressor are significantly lower compared to those for conic nozzle at all polar angles. However, the PNLT (i.e., tone corrected PNL) levels for the suppressor at a number of angles, specially in the forward arc, are higher than those for the conic nozzle. This is due to the tone corrections due to the presence shock noise in suppressor data at around 2 kHz (i.e., about 15 kHz for the model scale).

Similar results for  $V_J=2030$  ft/sec are shown in Figure 2.7-12. Suppressions of about 10 PNLT dB and 17 OASPL dB at  $\theta = 50^\circ$  and  $140^\circ$ , and 24 SPL dB at about 160 Hz (at peak PNLT angle) are observed. Suppressions at  $V_J=2476$  ft/sec case, as shown in Figure 2.7-13, are about 10 PNLT dB and 15 OASPL dB at  $\theta = 130^\circ$ , and 23 SPL dB at about 160 Hz (at peak PNLT angle). Results for  $V_J=2796$  ft/sec, shown in Figure 2.7-14, indicate suppressions of about 11 PNLT dB and 15 OASPL dB at  $\theta = 130^\circ$ , and 25 SPL dB at about 160 Hz (at peak PNLT angle).

Note that the PNLT levels for the suppressor are lower at all polar angles compared to conical nozzle at higher velocity points. At these velocities, the jet mixing noise is more dominant compared to shock noise for suppressor nozzles, where as conic nozzle has significant amount of shock noise in the forward quadrant.

### 2.7.2 Acoustic Characteristics of the 36-Chute Suppressor Compared to Other Multi-Chute Suppressors:

The acoustic characteristics of the 36-chute suppressor with porous plug, used for the present fluid shield test program, are compared with similar results of two other multi-chute plug suppressor configurations. One of them is the 32-chute suppressor with hard wall plug (see Figure 2.7-15), utilized to develop a technology base for thermal acoustic shield (THSL) concept as a noise suppression device (Ref. 2). Relevant dimensions of this suppressor and the contoured hardwalled plug are shown in Figure 2.7-15. The thermal acoustic shield suppressor was consisted of convergent flow path and parallel sided core flow elements. The throat area of the suppressor was 26.15 square inches and the equivalent diameter on the basis of throat area was 5.77". The suppressor area ratio (SAR) was 2.1.

The second one was a 24-chute suppressor with porous plug (see Figure 2.7-16), utilized for a series of axisymmetric mixer-ejector nozzle (AMEN) tests to enhance the



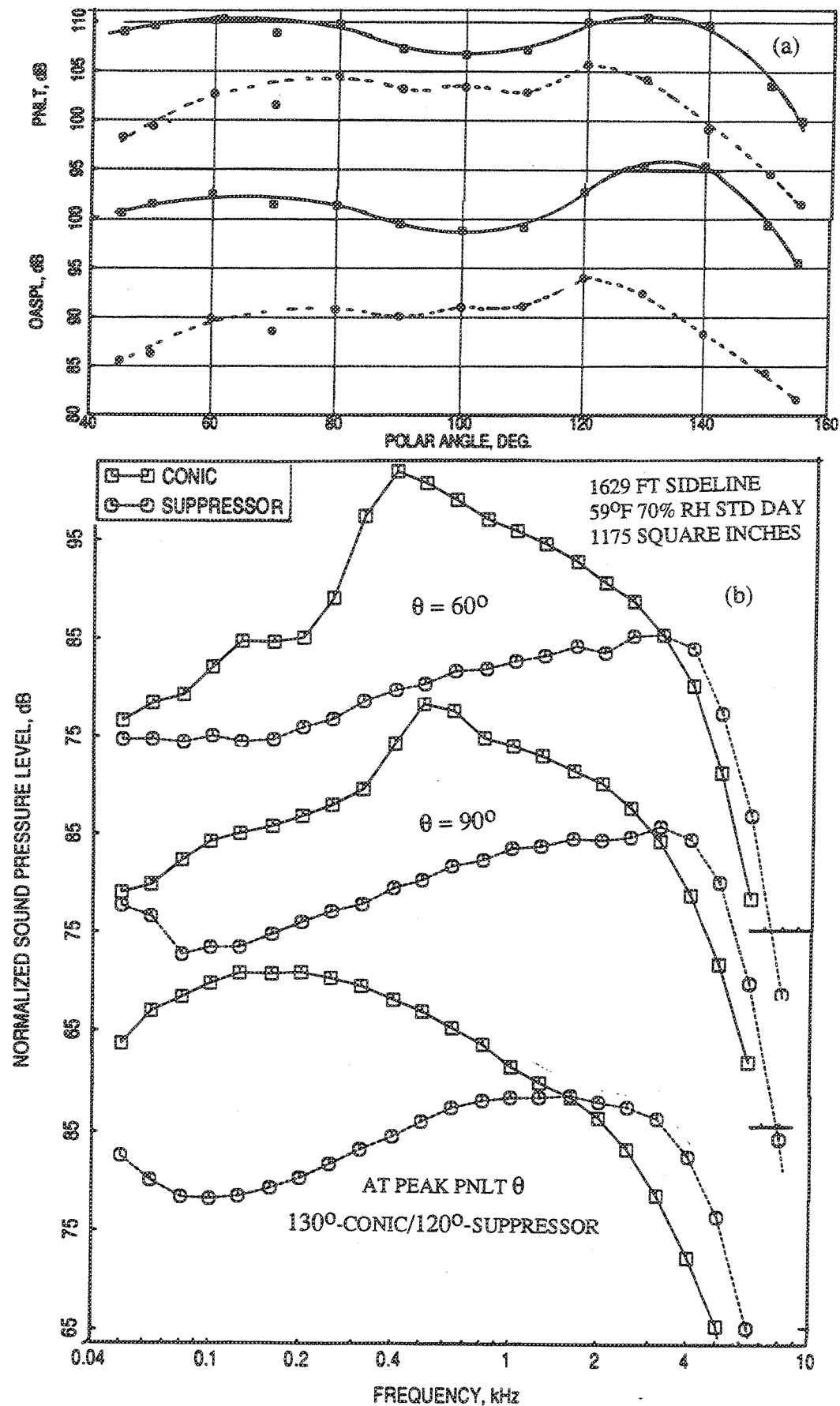


Figure 2.7-12. Comparison of (a) PNLT and OASPL directivities and (b) SPL spectra for the 36-chute suppressor with porous plug with those of a 6.54 in<sup>2</sup> conical nozzle with flight simulation ( $M_{F,P}=0.32$ ),  $P_{r,p}=2.7$ ,  $T_{t,p}=1381^\circ\text{R}$ ,  $V_{j,p}=2030$  ft/sec.

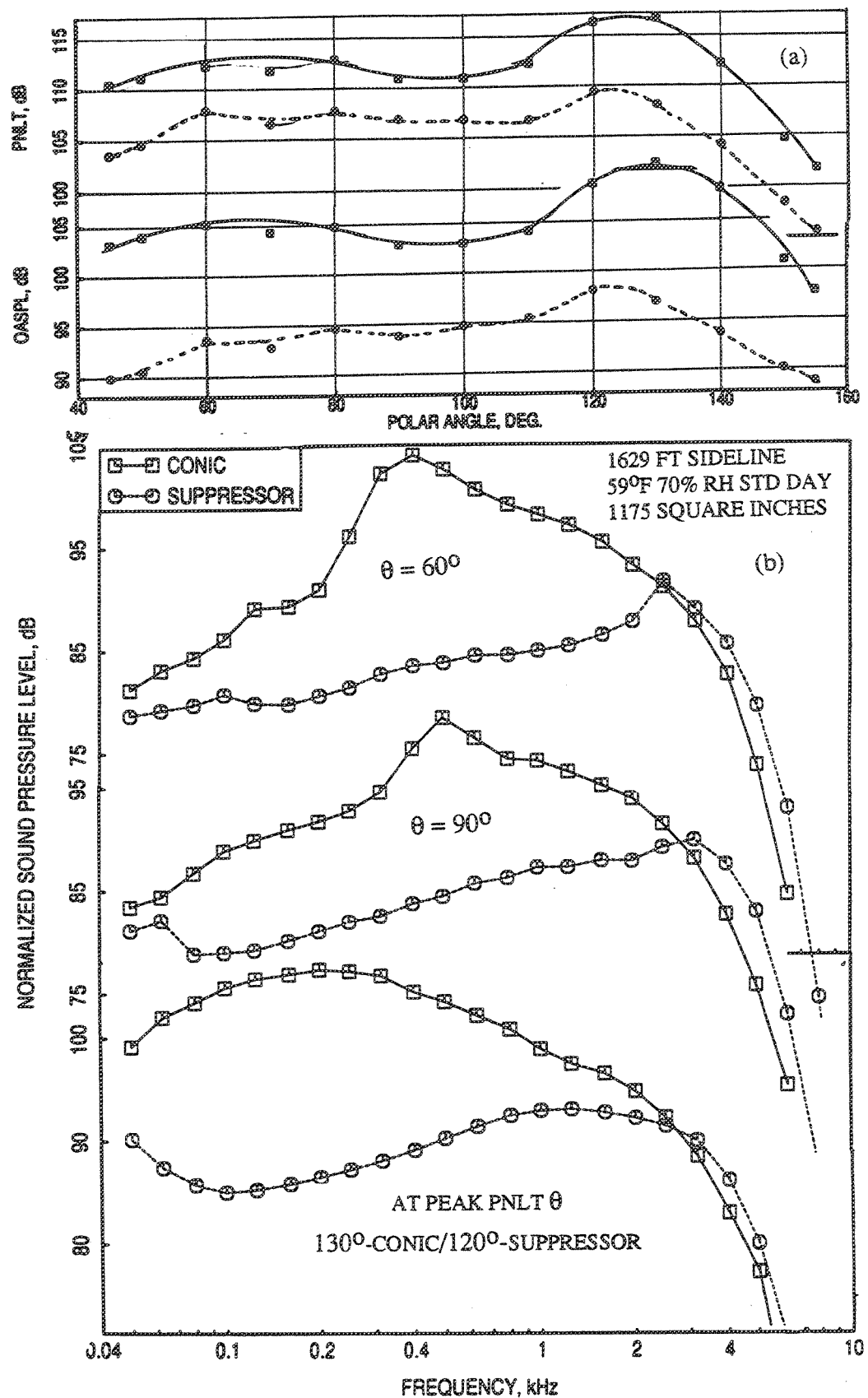


Figure 2.7-13. Comparison of (a) PNLT and OASPL directivities and (b) SPL spectra for the 36-chute suppressor with porous plug with those of a 6.54 in<sup>2</sup> conical nozzle with flight simulation ( $M_F=0.32$ ),  $P_{r,p}=3.2$ ,  $T_{t,p}=1786^\circ\text{R}$ ,  $V_{j,p}=2476$  ft/sec.

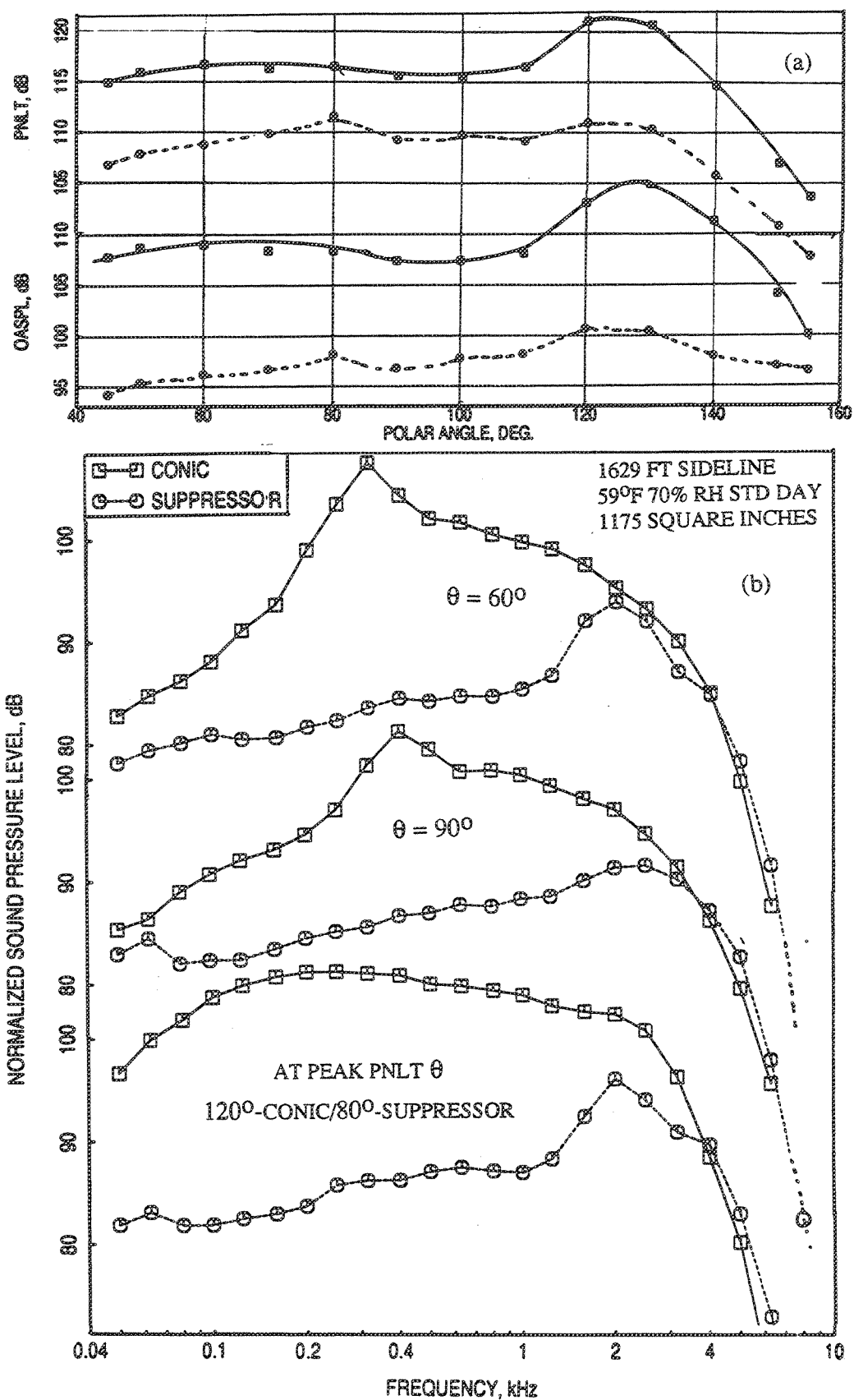


Figure 2.7-14. Comparison of (a) PNLT and OASPL directivities and (b) SPL spectra for the 36-chute suppressor with porous plug with those of a 6.54 in<sup>2</sup> conical nozzle with flight simulation ( $M_F=0.32$ ),  $P_{r,p}=4.0$ ,  $T_{t,p}=1960^\circ\text{R}$ ,  $V_{j,p}=2796$  ft/sec

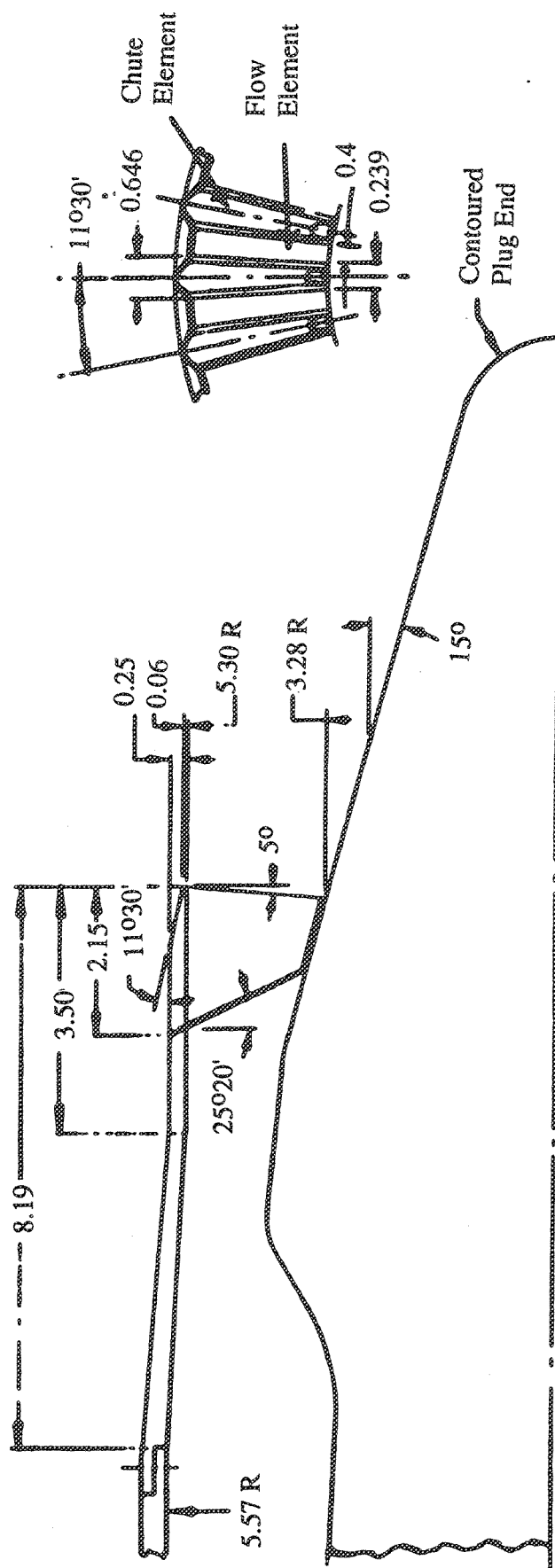


Figure 2.7-15. Side view of a 32-Chute annular plug suppressor nozzle used for thermal acoustic shield configurations (Ref. 2), SAR=2.1.

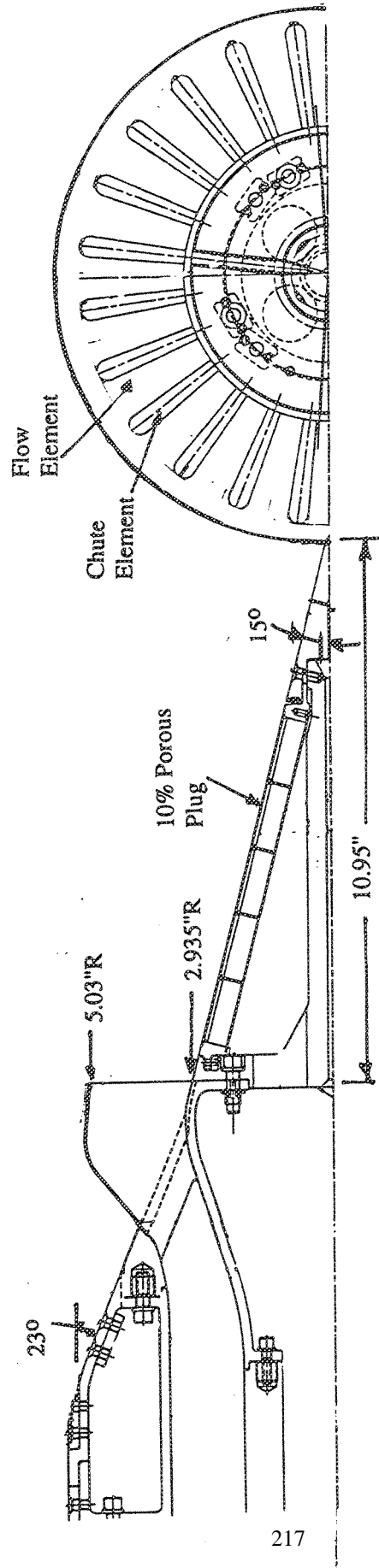


Figure 2.7-16. Side view of a 24 CD-chute axisymmetric suppressor with porous plug used for axisymmetric mixer ejector nozzle (AMEN) configurations (Ref, 28) SAR=3.7.

mixing by providing more shear area between the engine flow and entrained air (Ref. 28). The AMEN suppressor, shown in Figure 2.7-16, had 24 CD chutes with chute expansion ratio of 1.25, designed for  $\text{NPR}=4.0$  with respect to an ambient pressure of 14.7 psia. The throat area of the suppressor ( $A_8$ ) was 13.2 square inches (i.e., equivalent diameter=4.1") and the suppressor area ratio (SAR) was 3.7. Results for the 24-chute suppressor alone with a 10% porous plug configuration are used for comparison.

The thermal acoustic shield (THSL) suppressor results are processed for a full scale area of 1400 square inch and extrapolated to 2400 feet sideline distance. To obtain proper comparison between the acoustic results for all three suppressors, the acoustic data for the fluid shield suppressor (FLSH) and the ejector suppressor (AMEN) are also processed for the same full scale area of 1400 square inch and extrapolated to the same sideline distance of 2400 feet. All the acoustic variables are corrected to the standard day conditions of 59° F and 70% relative humidity. While, the aerothermodynamic conditions of the tests between 24-chute suppressor (AMEN) and 36-chute suppressor (FLSH), compared under this study are identical, those for the 32-chute suppressor (THSH) are not so. Thermodynamic conditions for the tests for this suppressor are selected to match the ideal jet velocity for the three suppressors as close as possible. Normalized results are utilized for the comparison to account for any deviation of conditions from their nominal values. Comparisons are made for static condition only.

Normalized levels of OASPL and PNL directivities and SPL spectra between the three suppressors are compared at six different velocities, the nominal values being 1660, 1820, 2040, 2200, 2480, and 2600 ft/sec, in Figures 2.7-17 through 2.7-22, respectively.

The OASPL levels increase with decreasing chute numbers for polar angles less than 120°. At higher polar angles the 32-chute thermal shield suppressor exhibits the highest OASPL levels. With respect to PNL directivities, the levels increase with decreasing chute numbers for all angles. With respect to SPL spectra the increasing trend with chute number is also observed at all angles at higher frequencies above 400 Hz. At lower frequencies, the 32-chute suppressor exhibits higher SPL compared to the other two suppressors. The low frequency sound pressure level dominance for the 32-chute suppressor is more drastic at higher polar angles. As a typical example, Figure 2.7-23 shows the SPL spectra for the 32-chute suppressor at a number of polar angles for a jet

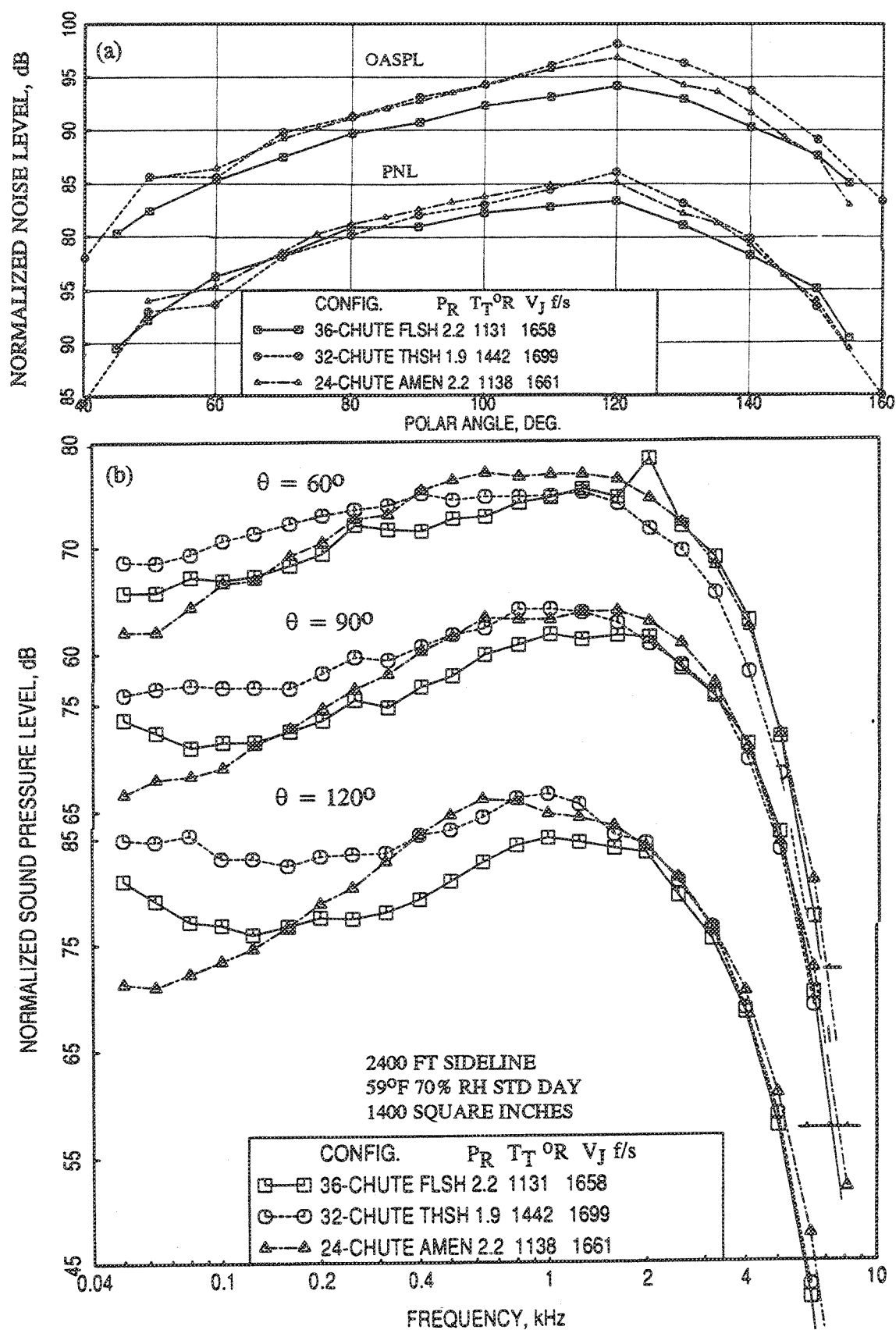


Figure 2.7-17. Comparison of (a) PNL and OASPL directivities and (b) SPL spectra for three suppressors with different chute numbers at a nominal  $V_J = 1660$  ft/sec at static condition.

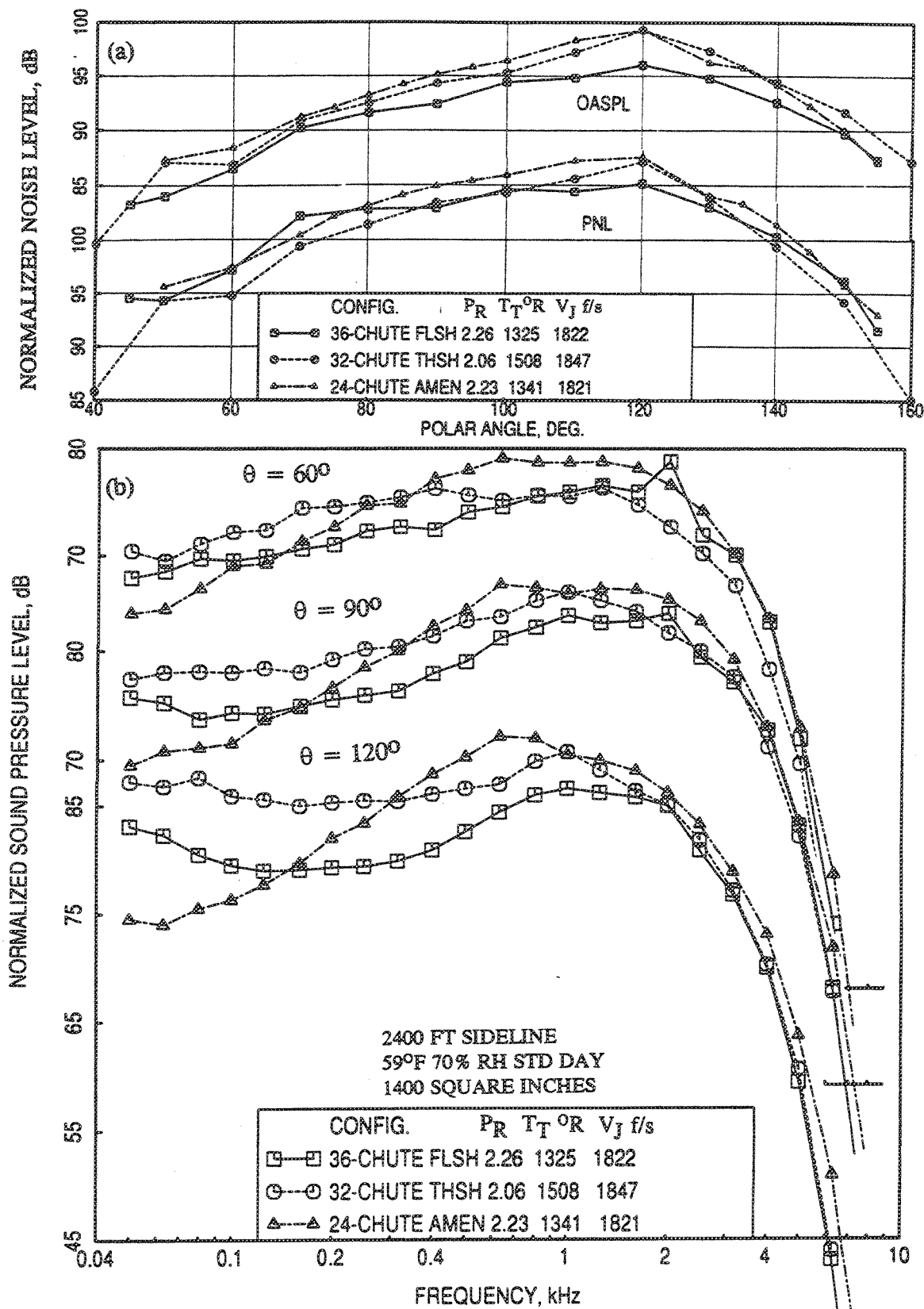


Figure 2.7-18. Comparison of (a) PNL and OASPL directivities and (b) SPL spectra for three suppressors with different chute numbers at a nominal  $V_J = 1820$  ft/sec at static condition.



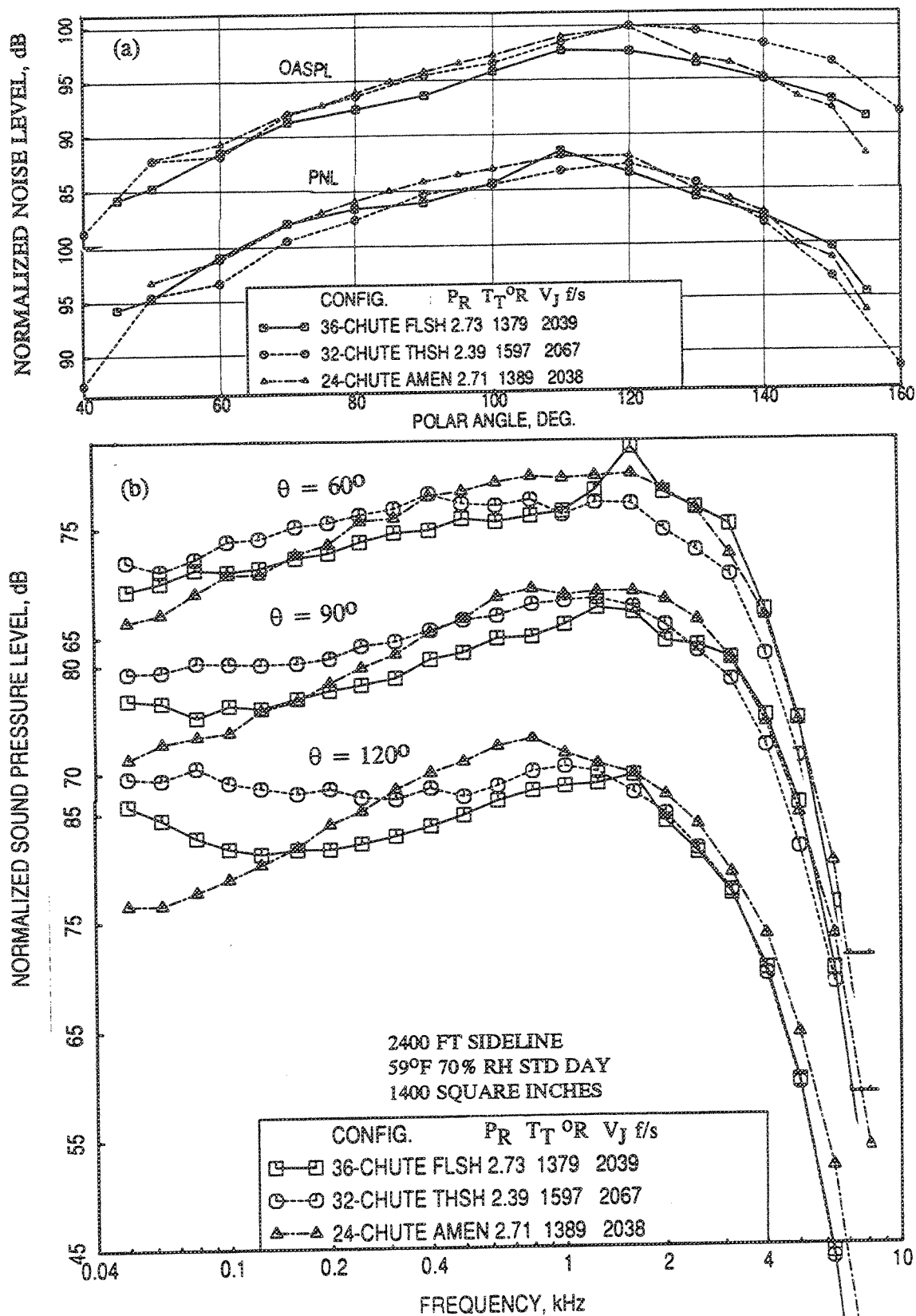


Figure 2.7-19. Comparison of (a) PNL and OASPL directivities and (b) SPL spectra for three suppressors with different chute numbers at a nominal  $V_J = 2040$  ft/sec at static condition.

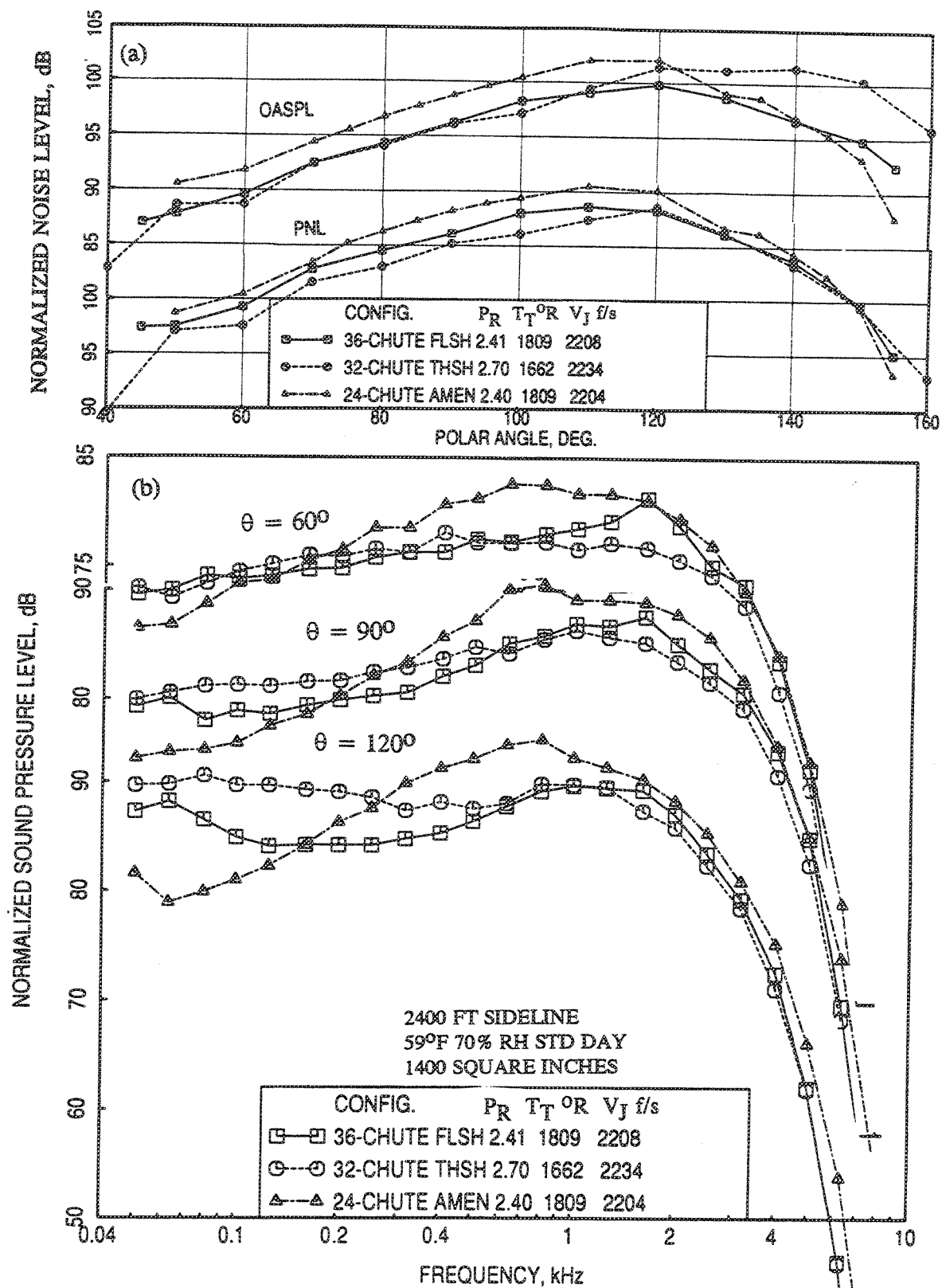


Figure 2.7-20. Comparison of (a) PNL and OASPL directivities and (b) SPL spectra for three suppressors with different chute numbers at a nominal  $V_J = 2200$  ft/sec at static condition.

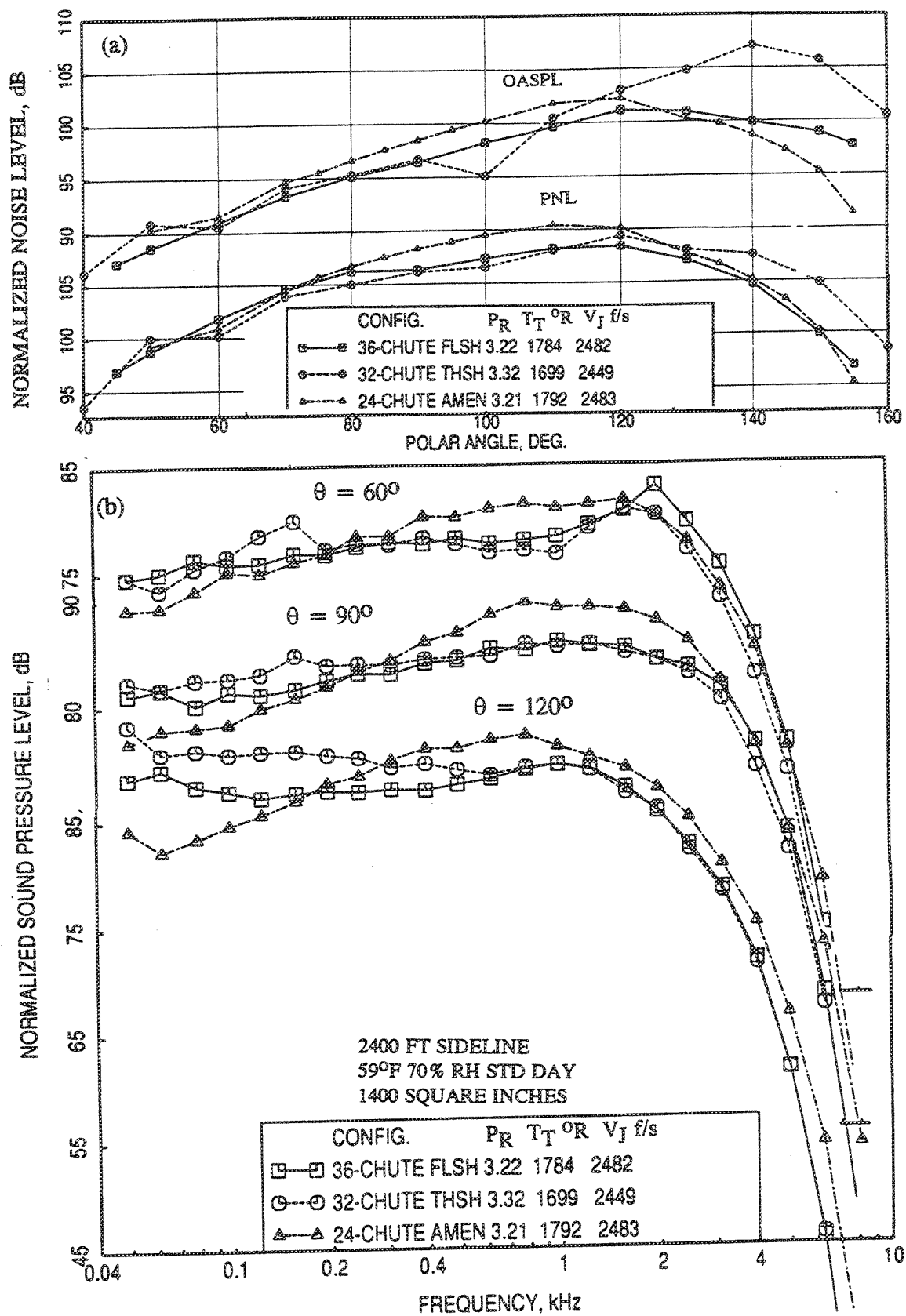


Figure 2.7-21. Comparison of (a) PNL and OASPL directivities and (b) SPL spectra for three suppressors with different chute numbers at a nominal  $V_j = 2480$  ft/sec at static condition.

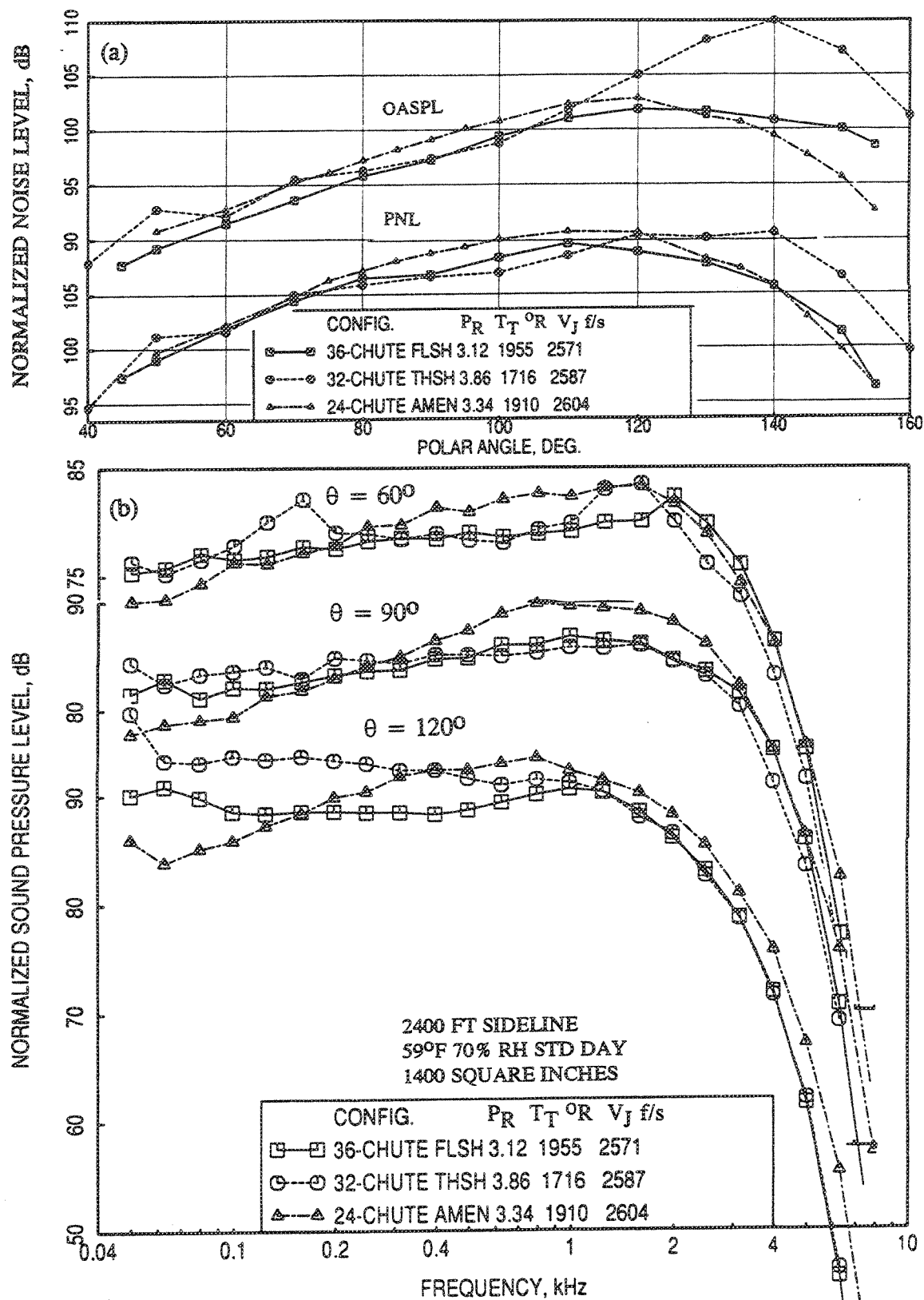


Figure 2.7-22. Comparison of (a) PNL and OASPL directivities and (b) SPL spectra for three suppressors with different chute numbers at a nominal  $V_j = 2600$  ft/sec at static condition.

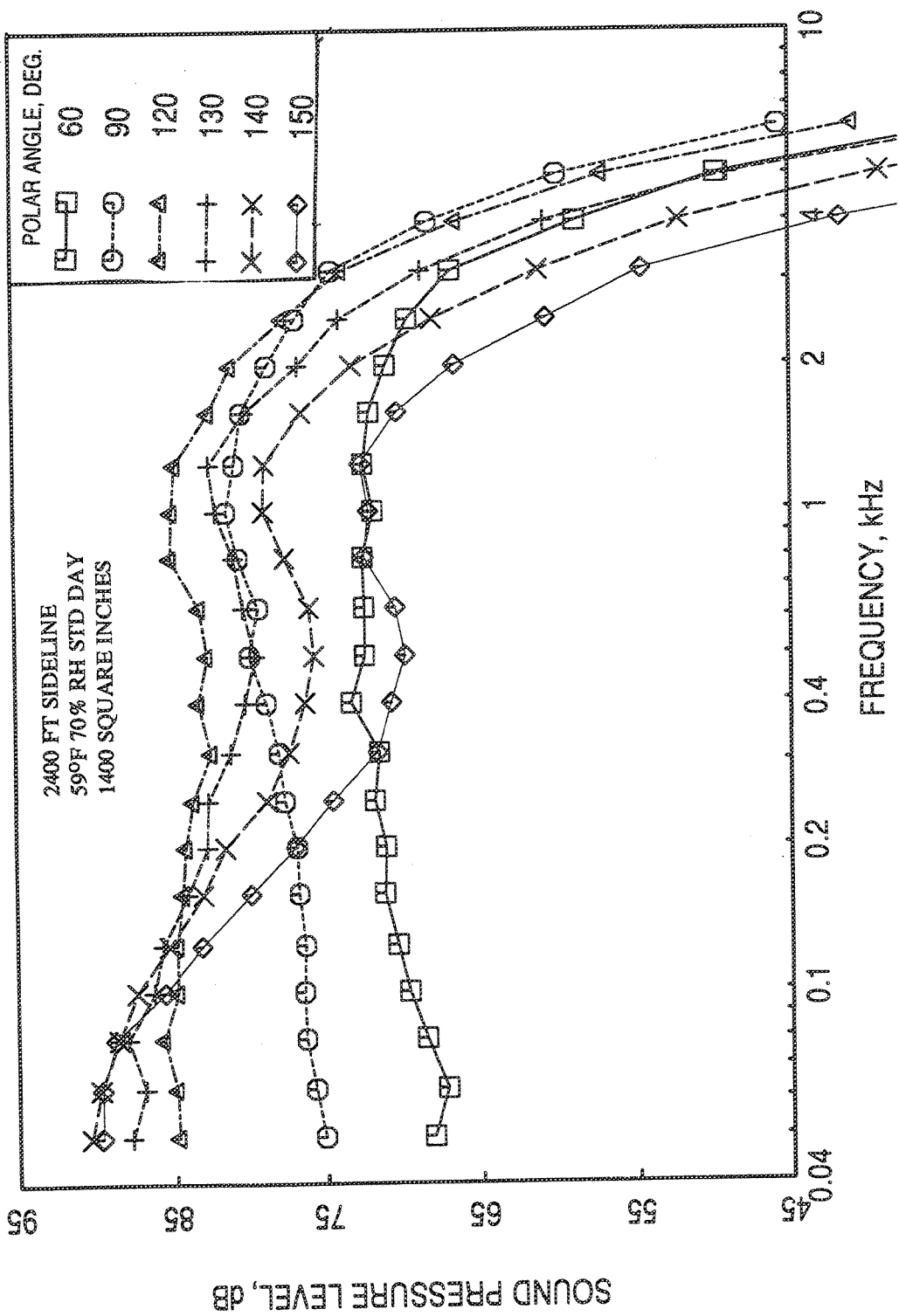


Figure 2.7-23. Sound pressure level spectra at different polar angles for the 32-chute suppressor with hardwall plug at static condition,  $P_{r,p}=2.7$ ,  $T_{t,p}=1662^{\circ}\text{R}$ ,  $V_{j,p}=2234$  ft/sec.

velocity of 2234 ft/sec. The SPLs at lower frequency are much lower in the forward arc compared to rear arc. At these angles the OASPL is basically influenced by the low frequency levels and that is the reason why the 32-chute suppressor OASPL levels are higher compared to other two suppressors at angles above  $120^\circ$ . While the low frequency levels are the dominant contributors for OASPL, their contributions are minimal for PNL due to the lower NOY factors at these frequencies. This is the reason for such difference in trends between OASPL and PNL directivities at higher polar angles, described earlier. The exceptional low frequency performance of AMEN suppressor is most likely due to the higher flow entrainment and the favorable aerodynamic flow path. In addition, the CD design of the chutes might have reduced some amount of shock-associated noise.

In general, the 36-chute suppressor seems to be the quietest among all three suppressors. The noise levels decrease with increasing chute number due to the decreasing chute sizes. At lower frequencies (less than 400 Hz) the 24-chute suppressor has the lowest noise level. This is most probably due to the shallow flow path in the chutes (i.e.,  $25^\circ$  inclination compared to  $55^\circ$  for fluid shield suppressor), for which the flow might have remained attached and generated less low frequency noise. For the fluid shield suppressor a shallower flow angle through the chutes may be useful for better noise suppression.

### 2.7.3 Conclusions

Suppressions of about 8 EPNdB is achieved by the fluid shield suppressor with porous plug configuration at takeoff and cutback cycle conditions. While, these noise suppressions are reasonable, higher suppressions would have been helpful in meeting the Noise requirement goals. The measured farfield noise due to the suppressor contains some amount of shock associated noise as evident from acoustic, static pressure, and shadowgraph data. This noise could be reduced by using CD chute designs for takeoff condition. In addition, the chute flow path for this suppressor has relatively higher slope, due to stability constraint, which might have caused flow separation in the secondary flow and caused noise increase. Improvement on chute suppressor design by optimizing SAR, chute leading edge angle, and chute flow path may contribute some more noise reduction.

## 2.8 ACOUSTIC CHARACTERISTICS OF FLUID SHIELD NOZZLES - EFFECT OF FLUID SHIELD THICKNESS

Influence of fluid shield thickness on the suppressor with porous plug in reducing the farfield noise is analyzed in this section with respect to shield thickness with fixed wrap angle. The acoustic data measured at  $\phi=75^\circ$  (i.e., at community plane) for the three fluid shield configurations of shield thicknesses of 0.5", 0.75", and 1.0" with the same wrap angle of  $220^\circ$  and with porous plug are analyzed for static and flight conditions. These results are compared (1) with the acoustic data for the conical nozzle and the suppressor alone with porous plug configuration, (2) with thermal shield results tested earlier at GEAE (Ref. 2), and (3) with mixer-ejector results tested at GEAE under other HSCT programs. For the first set of data comparison, the conical nozzle and suppressor data are scaled to the full scale core nozzle size of 1175 square inches. Keeping the same linear scale factor the 0.5", 0.75" and 1.0" thick fluid shield nozzles are scaled to 1813.6, 2165.5, and 2524.7 square inches, respectively. All the data are extrapolated to a sideline distance of 1629 feet and are corrected for standard day conditions of  $59^\circ\text{F}$  and 70% humidity. Same fluid shield is used for mixer-ejector comparison. However, for thermal shield data comparison, all the fluid shield data are scaled to 1400 square inches and are extrapolated to a sideline distance of 2400 feet to be consistent with the thermal shield processed data..

Normalized acoustic data (OASPL, PNLT, EPNLT, etc.) are obtained (i.e., normalized with respect to thrust and density using the factor NF, see section 2.5.1) to extract velocity dependence and also to account for minor differences in thrust and jet density during experimental test conditions. An identical normalization procedure was employed by GEAE for dual flow nozzles during the conduct of coannular flow studies for inverted and conventional velocity profiles (Refs.: 20-22). For two flows, the jet velocity employed was the mass-averaged velocity,  $V_{\text{mix}}$ , as defined earlier (also called as specific thrust, i.e., thrust per unit flow rate).

Comparison of acoustic data at the same specific thrust for the same total thrust was deemed to be the appropriate way to extract any benefit of inverted velocity profile compared to conventional profile. Similar approach was adopted by other researchers, notably Syracuse university and Lockheed Georgia Company. From an engine cycle point of view, noise comparisons on the basis of specific thrust are meaningful. Such comparisons indicate what combination of flow split and velocity ratio between the two streams gives lowest noise for a given pound of air flow producing the same thrust. Also comparing at same  $V_{\text{mix}}$  separates the "noise reduction" obtained due to nozzle design from "noise reduction" due to bypass ratio effects.

On the basis of above explanation the fluid shield nozzles seem to fall in the category of dual flow nozzles and hence, the acoustic data could be presented in normalized form with respect to  $V_{mix}$ . As an example, the normalized pseudo EPNLTs (for static condition) and EPNLTs (with flight simulation) for the three fluid shield nozzles are compared with those for the conical nozzle and the suppressor alone configuration in Figure 2.8-1 with respect to mass averaged jet velocity ( $V_{mix}$ ). It should be noted that the predicted data for the conical nozzle is also plotted in this figure. Since the data is normalized for a reference thrust of 60 klbs the normalized EPNLT levels at a jet velocity represent the relative levels for different configurations at a fixed thrust. While the EPNLTs for the suppressor alone configuration show substantial noise reduction compared to the reference conical nozzle, the fluid shield configurations do not indicate any noticeable noise reduction compared to the suppressor alone configuration on a  $V_{mix}$  basis. Specially, at takeoff condition (i.e., at mixed velocity of 2030 ft/s) we do not see much advantage of the fluid shield.

However, the unnormalized EPNLTs at a fixed thrust of 60 klbs indicate substantial noise benefit due to fluid shields compared to suppressor alone configuration. The normalization process, which was fine for dual flow IVP/CVP nozzles may not be applicable for the fluid shield nozzle configurations due to the differences between the coannular nozzles and the fluid shield nozzles due to differences in noise generation/reduction mechanisms, flow field features as well as geometries.

Geometrically, while both the streams of a coannular nozzle are axisymmetric, the outer stream of the fluid shield nozzle only partially surrounds the primary stream. Hence, noise generated in this situation may not follow the same "scaling" relationship of a coannular nozzle. In addition, the primary nozzle remains the same for all the fluid shield nozzle configurations, while the outer stream cross-sectional area is varied considerably from model to model. Hence, the ideal gross thrust generated at a fixed  $V_{mix}$  is widely varied from one model to another based on the total nozzle exit area. Thrust normalization, which is effective for slight thrust variation between one configuration to other at a fixed  $V_{mix}$ , may not be appropriate in this case.

The aerothermodynamic conditions of the individual streams differ considerably from one fluid shield nozzle to another to generate a fixed  $V_{mix}$  due to the variation in the primary to secondary area ratio among the nozzles. Normalization of noise level due to flow density may not be uniformly applicable in this situation using a mass-averaged jet density.



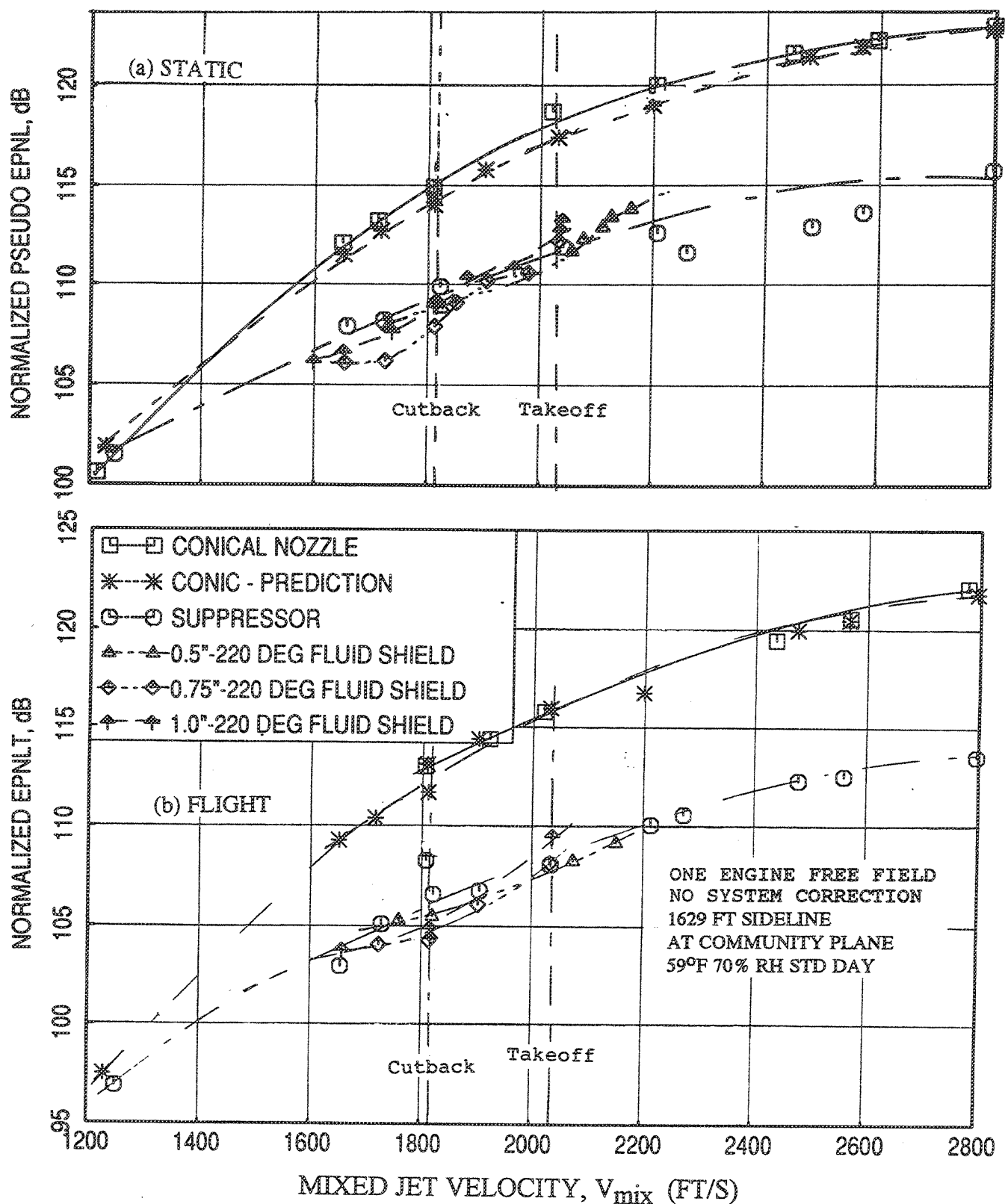


Figure 2.8-1. Noise suppression due to fluid shield nozzles in terms of normalized EPNL data as a function of jet velocity (a) at static condition and (b) with flight simulation ( $M_F=0.32$ ).

Finally, the scaling law used for the normalization process may not fully account for the noise reduction mechanism of fluid shield due to shear reduction. Simple normalization on the basis of thrust (i.e., area scaling for fixed flow conditions) probably does not scale this component of noise reduction, which is dependent on thickness of shield, velocity ratio and mass flow ratio between the two streams.

Based on the wide variation of aerothermodynamic conditions between the shields and the core flows, an attempt is made to normalize the data only with respect to thrust and not for density variation. Pseudo EPNLTs (for static condition) and EPNLTs (with flight simulation) normalized with respect to thrust for the three fluid shield nozzles are compared with those for the conical nozzle and the suppressor alone configuration in Figure 2.8-2 for different jet velocities ( $V_{mix}$ ). Again, the fluid shield configurations do not indicate significant additional noise reduction compared to the suppressor alone configuration.

Based on the concerns expressed above, in terms of applicability of comparison on a  $V_{mix}$  basis for fluid shield nozzle configurations, an alternate way is to present the unnormalized noise levels with respect to ideal gross thrust,  $(FG)_i$ . This will show the noise benefit at a fixed thrust. However, the  $V_{mix}$  (or  $V_J$ ) associated with the thrust is not evident from this type of data presentation. Therefore, it is possible to show noise benefit at a given thrust, which is due to higher total engine flow and may not necessarily be due to nozzle design. This problem can be avoided by keeping track of the  $V_{mix}$  associated with the thrust level of interest. Hence, the unnormalized noise data are plotted with respect to ideal gross thrust for the fluid shield nozzles.

Pseudo EPNLTs and EPNLTs at static condition and with flight simulation are plotted in Figures 2.8-3 and 2.8-4, respectively, with respect to ideal gross thrust  $((FG)_i)$  for all five configurations similar to Figure 2.8-1. Noise reductions due to fluid shields compared to the suppressor alone configuration are quite apparent at fixed ideal gross thrust. The correspondence between the  $V_{mix}$  and  $(FG)_i$  are determined in Figure 2.8-5 by plotting the ideal gross thrust with respect to jet velocity for the said five configurations. For the takeoff thrust of about 67 to 69 klbs additional noise suppression of about 2 to 7 EPNdB statically and 4 to 8 EPNdB with flight simulation are observed due to fluid shields compared to the suppressor alone configuration. For this thrust level the jet velocities for each configuration are different (i.e., 2800 ft/sec for conical nozzle and suppressor and for fluid shield nozzles of thicknesses 0.5, 0.75,

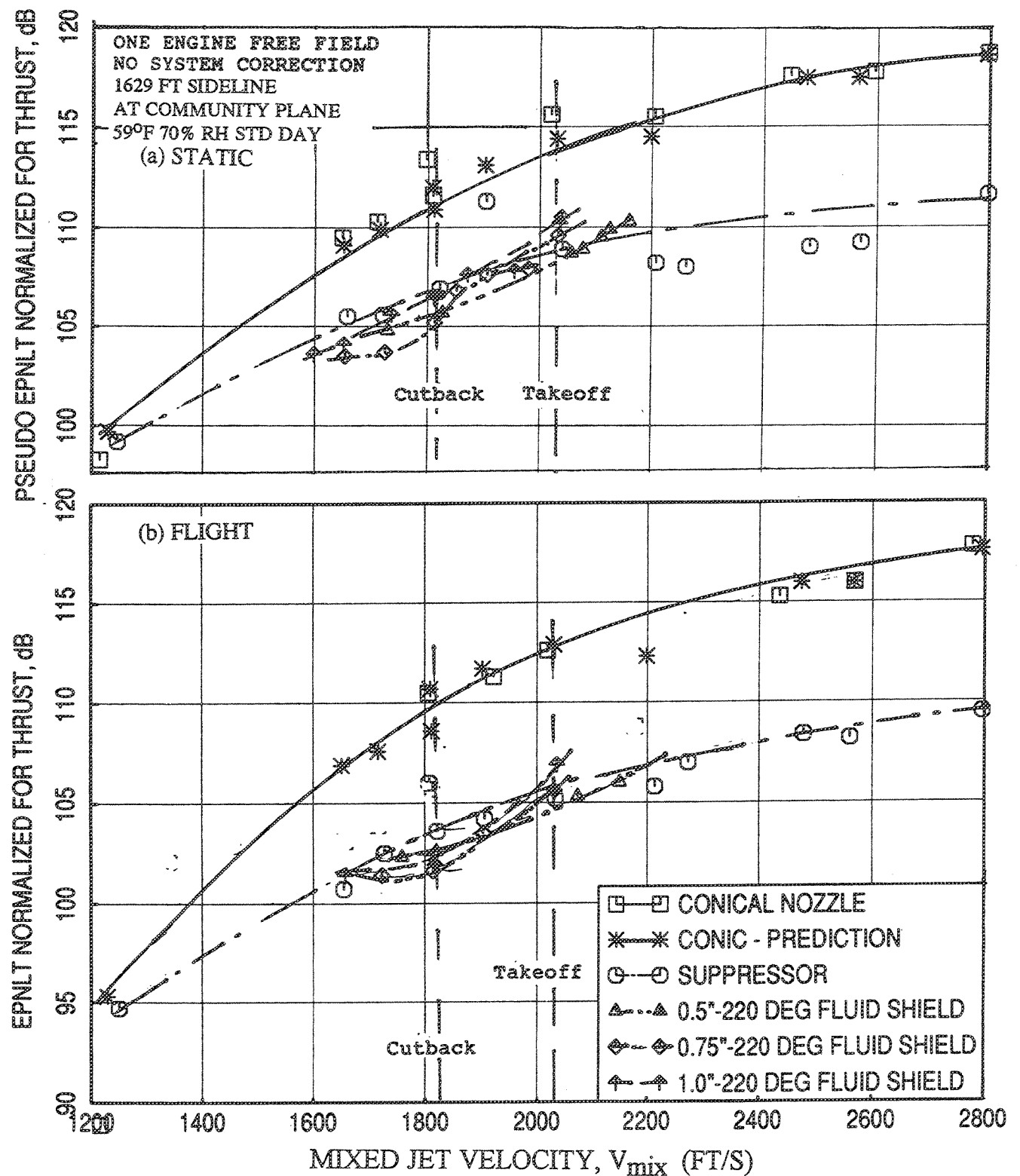


Figure 2.8-2. Noise suppression due to fluid shield nozzles in terms of EPNLT data, normalized with respect to thrust only, as a function of jet velocity (a) at static condition and (b) with flight simulation ( $M_F=0.32$ ).

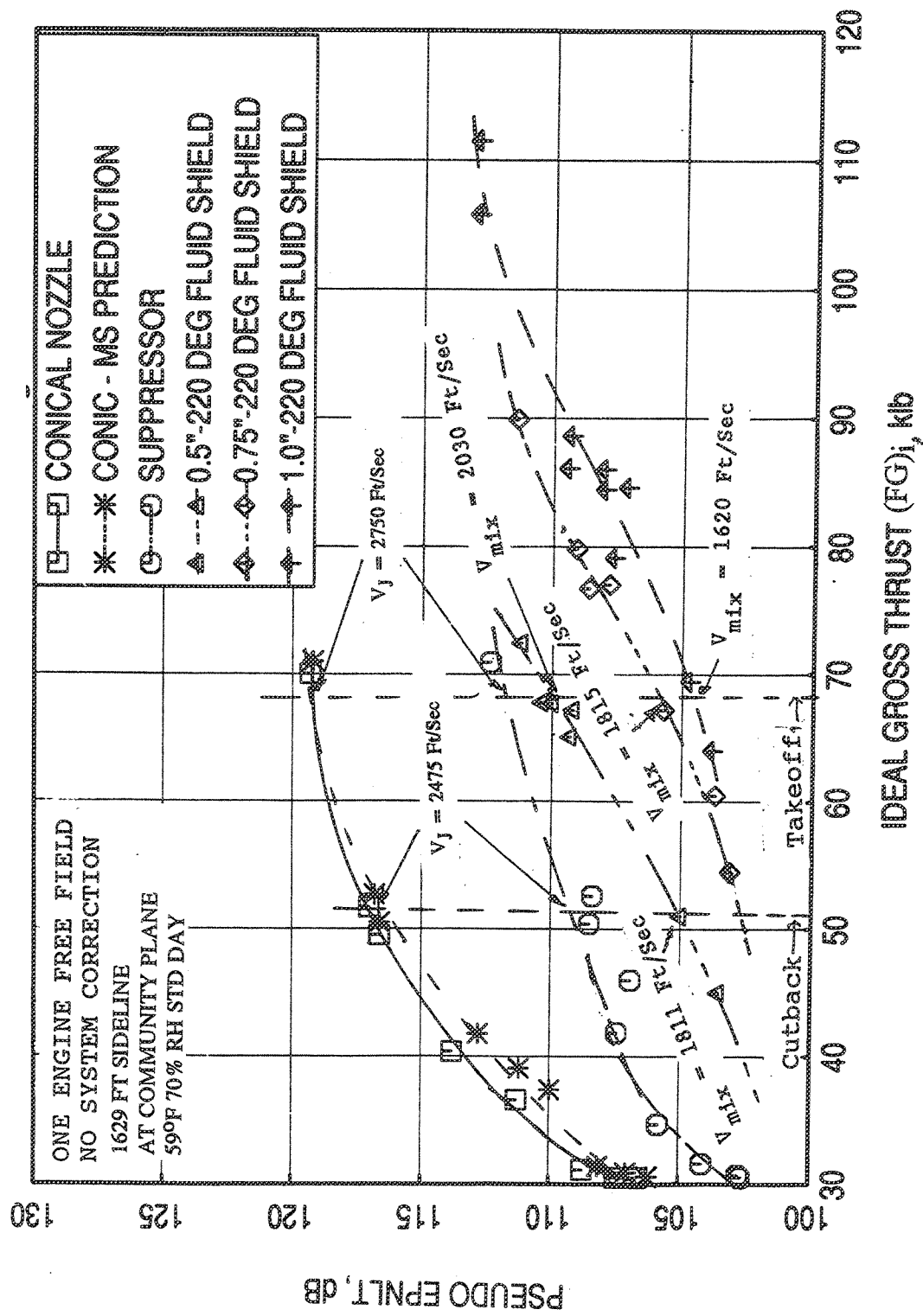


Figure 2.8-3. Noise suppression due to fluid shield nozzles in terms of EPNLT data as a function of ideal gross thrust at static condition.

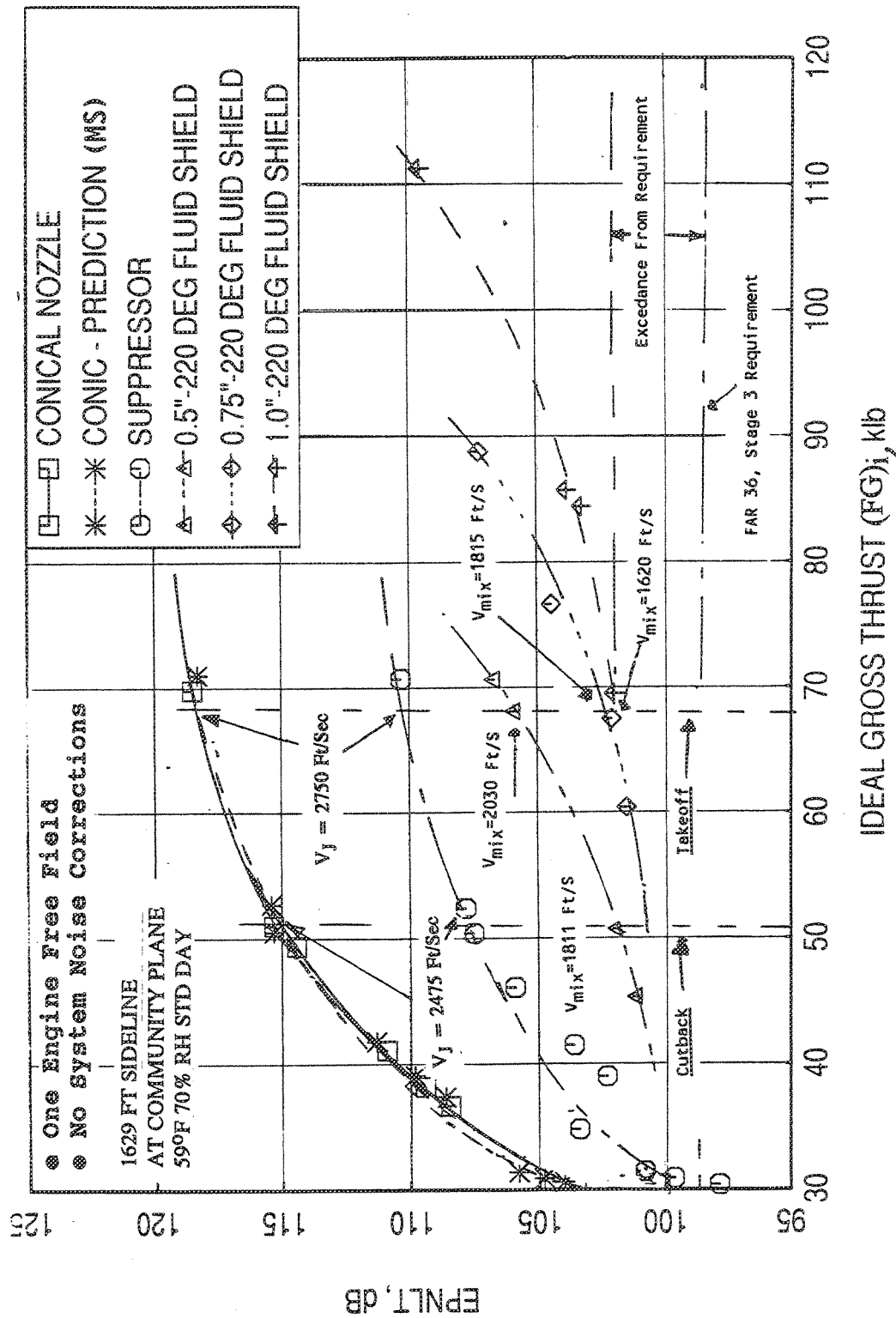


Figure 2.8-4. Noise suppression due to fluid shield nozzles in terms of EPNLT data as a function of ideal gross thrust with flight simulation ( $M_F=0.32$ ).

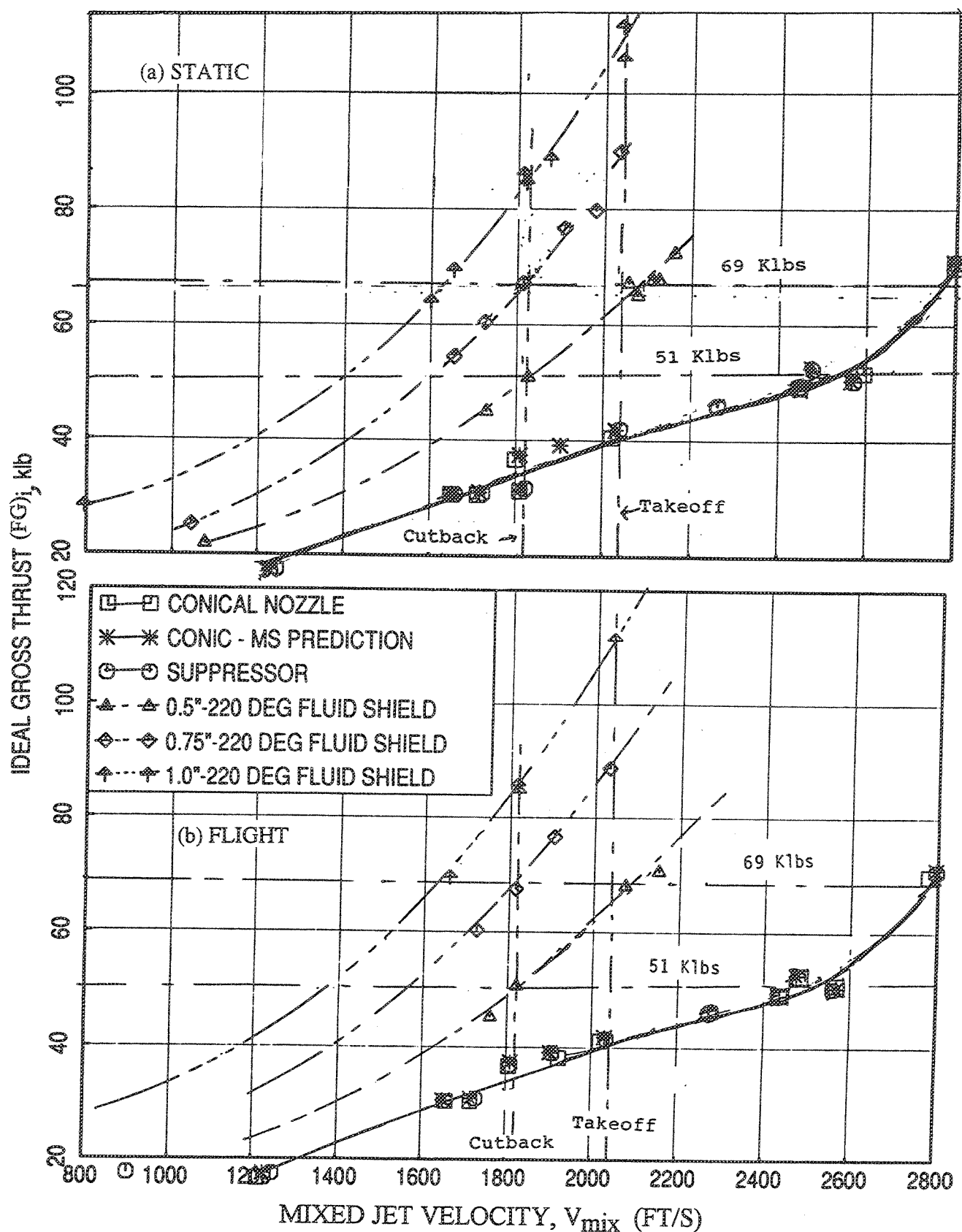


Figure 2.8-5. Variation of ideal gross thrust with respect to jet velocity for the reference conical nozzle, the suppressor alone configuration, and the three fluid shield configurations (a) at static condition and (b) with flight simulation ( $M_F=0.32$ ).

and 1.0 inches these velocities are 2030, 1815, and 1620 ft/sec, respectively). Similar advantage is observed for cutback ideal gross thrust requirement of about 51 klbs.

#### **2.8.1 Noise Suppression Due to Fluid Shield as a Function of Ideal Gross Thrust :**

##### **EPNLT and PNLT Vs Ideal Gross Thrust:**

**Static Data:** Figure 2.8-3 shows the EPNdB suppressions due to the fluid shields for static condition. At the takeoff condition, the 1.0-inch thick shield yields highest suppression of about 7 to 8 EPNdB compared to the suppressor alone configuration. At cutback the 0.75"-thick shield gives an additional suppression of about 7 EPNdB compared to the suppressor alone configuration. A total suppression of about 15 EPNdB is achieved due to suppressor-fluid shield configuration compared to the reference conical nozzle for takeoff as well as for cutback conditions. Peak PNLT values are plotted in Figure 2.8-6, which indicates noise suppressions of about 7 and 4 dB due to fluid shield at takeoff and cutback, respectively. PNLTs at three polar angles are plotted in Figure 2.8-7. Higher noise suppressions are achieved in the rear arc.

**Flight Data :** Figure 2.8-4 shows the EPNdB suppressions due to the fluid shields with flight simulation. At the takeoff condition, the 0.75"-thick and 1.0"-thick shields yield highest suppression of about 8 to 9 EPNdB compared to the suppressor alone configuration. At cutback the 0.75"-thick shield seems to yield an additional suppression of about 7 EPNdB compared to the suppressor alone configuration. A total suppression of about 15 to 17 EPNdB is achieved due to suppressor-fluid shield configuration compared to the reference conical nozzle for takeoff as well as for cutback conditions. Peak PNLT values, plotted in Figure 2.8-8, indicate noise suppressions of about 9 and 6 PNdBs due to fluid shield at takeoff and cutback, respectively. PNLTs at three polar angles are plotted in Figure 2.8-9. Higher noise suppressions are achieved in the rear arc.

##### **PNLT Directivities and SPL Spectra :**

To examine the effect of fluid shields in detail PNLT directivities and SPL spectra for all five configurations are compared at two fixed mixed jet velocity (i.e.,  $V_{mix}$ ) and at two fixed ideal gross thrust (i.e.,  $(FG)_j$ ) conditions. The two fixed mixed jet velocities considered here are about 2030 ft/sec and 1811 ft/sec, which correspond to the takeoff and cutback velocities of the flade cycle with 0.5"-thick fluid shield configuration.

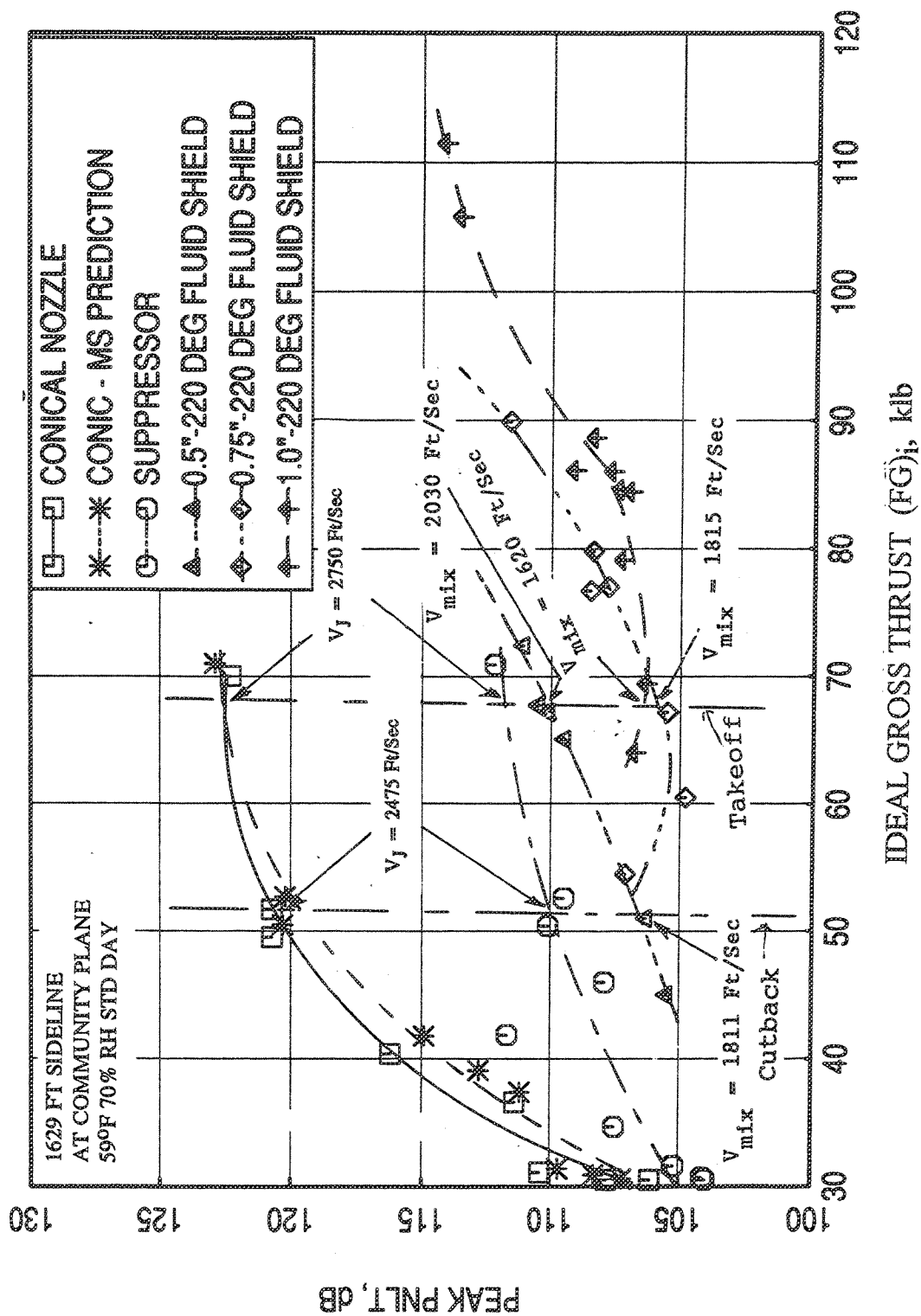


Figure 2.8-6. Noise suppression due to fluid shield nozzles in terms of peak PNLT data as a function of ideal gross thrust at static condition.



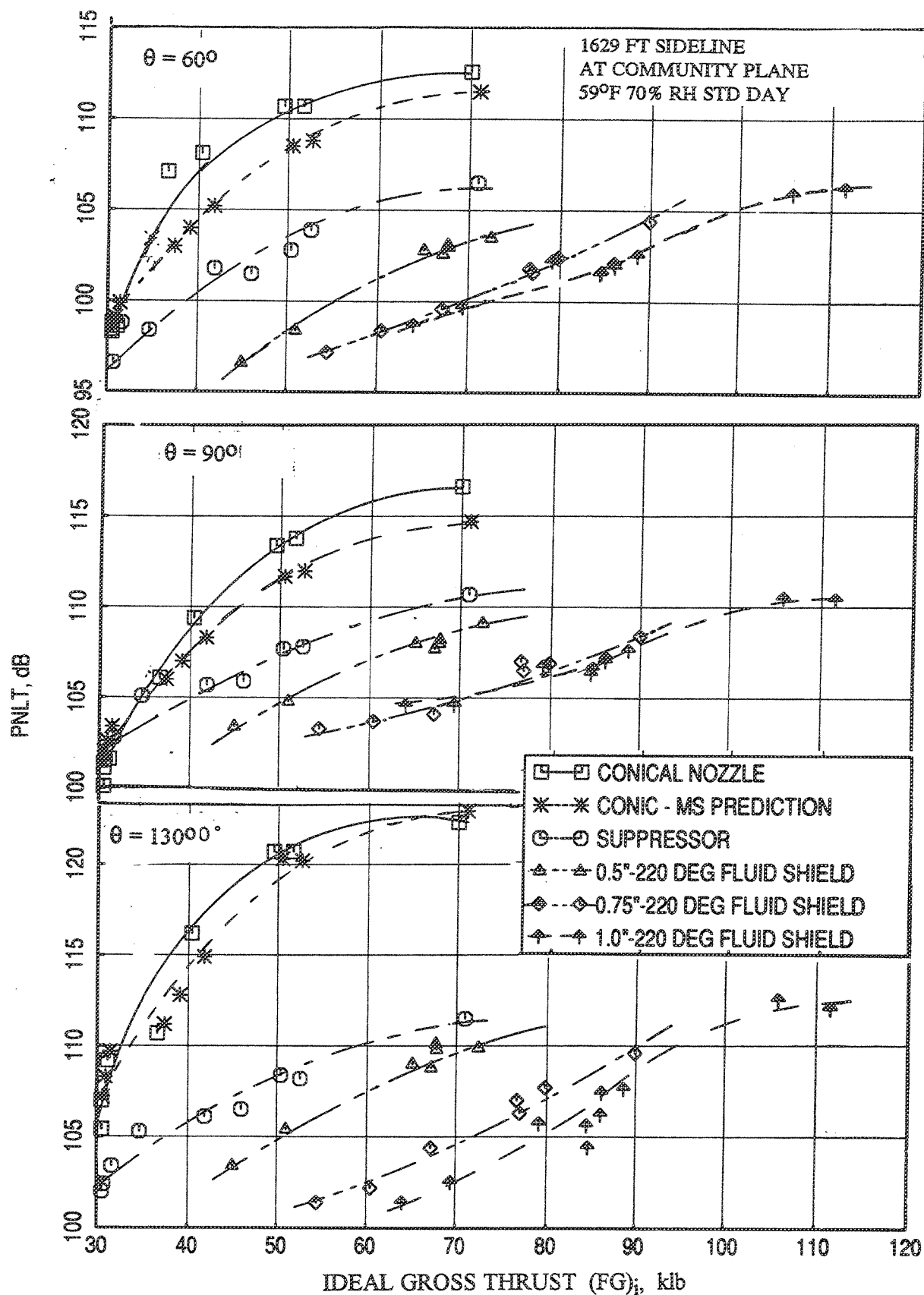


Figure 2.8-7. Noise suppression due to fluid shield nozzles in terms of PNLT data at different polar angles ( $\theta$ ) as a function of ideal gross thrust at static condition.

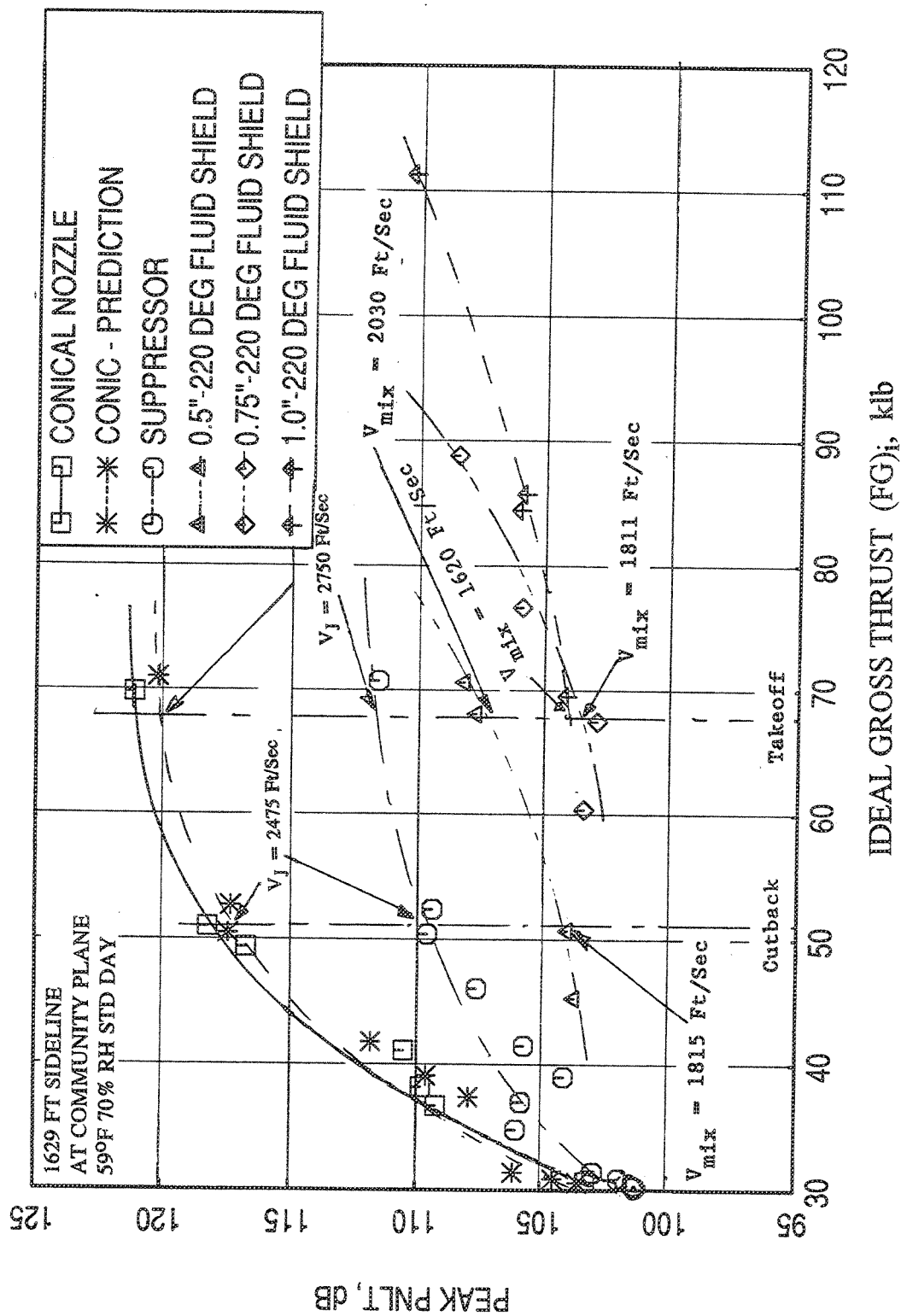


Figure 2.8-8. Noise suppression due to fluid shield nozzles in terms of peak PNLT data as a function of ideal gross thrust with flight simulation ( $M_F=0.32$ ).

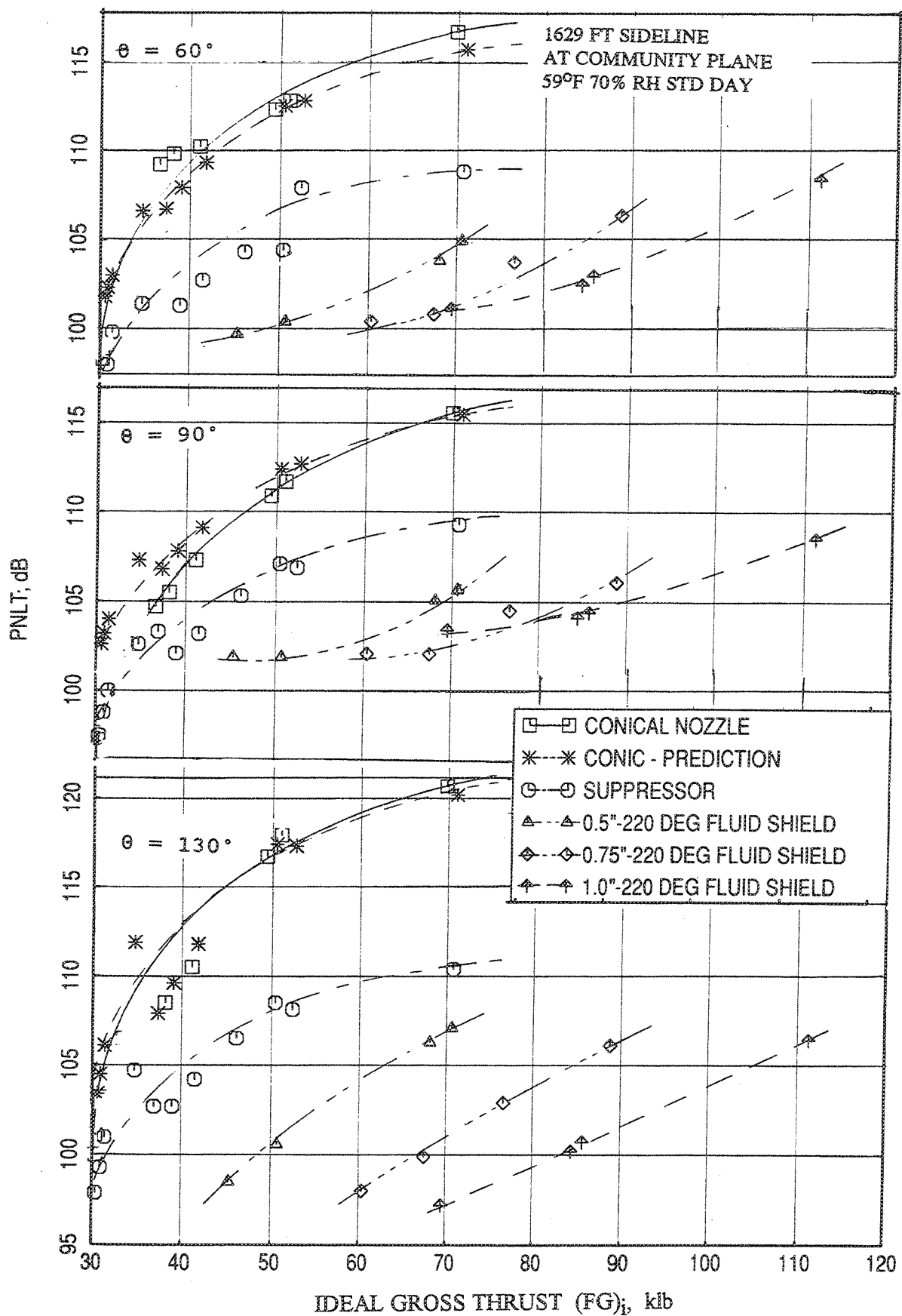


Figure 2.8-9. Noise suppression due to fluid shield nozzles in terms of PNLT data at different polar angles ( $\theta$ ) as a function of ideal gross thrust with flight simulation ( $M_F=0.32$ ).

While, 0.5"-thick fluid shield configuration yields about 68 klbs and 51 klbs ideal gross thrust at takeoff and cutback conditions, respectively (see Figure 2.8-5), the other two shield configurations yield much higher thrusts and the reference conical nozzle and suppressor alone configuration yield lesser thrust at the corresponding velocities. Alternately, at fixed thrust conditions of 68 klbs and 51 klbs, while the  $V_{mix}$  for 0.5"-thick fluid shield are 2030 ft/sec and 1811 ft/sec, the  $V_{mix}$  for other two shields are much lower in magnitudes.

Static Data : Results at Fixed  $V_{mix}$  : Normalized PNLT directivities are shown in Figure 2.8-10 at a fixed mixed jet velocity of about 2030 ft/sec, which is the takeoff velocity for the reference flade cycle. Relatively small benefit in terms of PNdB suppression due to shield is observed. Normalized SPL spectra at a number of polar angles are plotted in Figure 2.8-11. Sound pressure levels increase at low frequencies and decrease at higher frequencies due to fluid shields compared to suppressor alone configuration, which is a direct consequence of the mean shear reduction by the fluid shield stream.

Normalized PNLT directivities are plotted in Figure 2.8-12 at a fixed mixed jet velocity of about 1811 ft/sec, which is the cutback velocity for the 0.5"-thick fluid shield. The 0.75"-thick fluid shield shows the highest amount of PNdB suppression at all polar angles. Normalized SPL spectra at a number of polar angles are plotted in Figure 2.8-13. Again, sound pressure levels increase at low frequencies and decrease at higher frequencies due to fluid shields compared to suppressor alone configuration. The high frequency suppression is much higher compared to low frequency SPL increase, which resulted in a PNLT reduction for all polar angles due to fluid shields.

Results at Fixed (FG)i : Unnormalized PNLTs are plotted in Figure 2.8-14 with respect to polar angle for a fixed (FG)i of about 67 to 69 klbs, which is the required ideal gross thrust for takeoff condition. Substantial benefit in terms of PNdB suppression due to shield is observed. At this condition the fluid shields of 0.75"-thick and 1.0"-thick give more or less same amount of noise suppression. Unnormalized SPL spectra at a number of polar angles are plotted in Figure 2.8-15 for the same condition. Substantial sound pressure level decrease is achieved due to fluid shields compared to suppressor alone configuration for entire frequency range, which is a combined effect of generating the required thrust of a larger total engine flow as well as mean shear reduction of fluid shield.

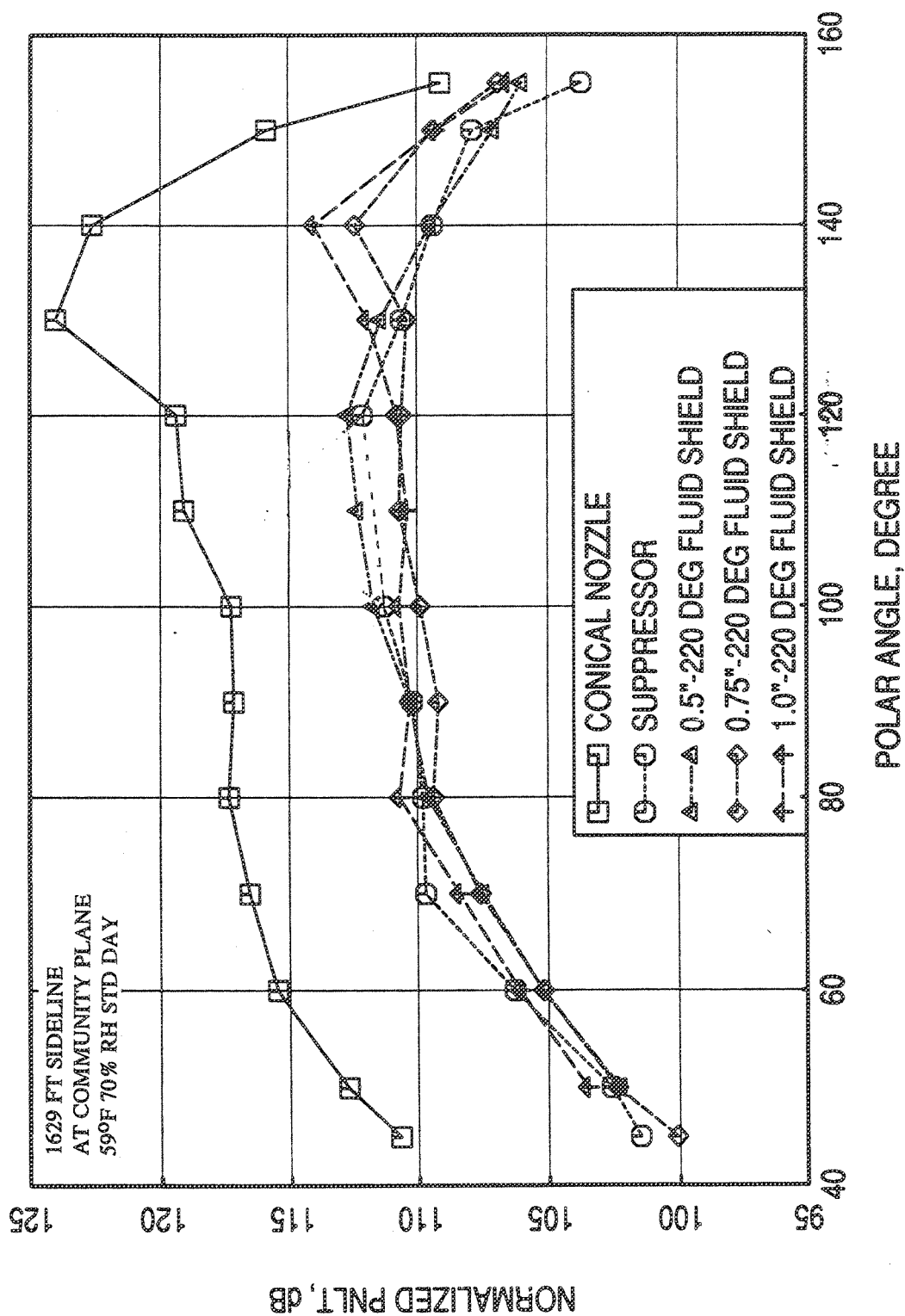


Figure 2.8-10. Noise suppression due to fluid shield nozzles in terms of normalized PNLT directivities for a fixed nominal mixed jet velocity of 2030 ft/sec at static condition.

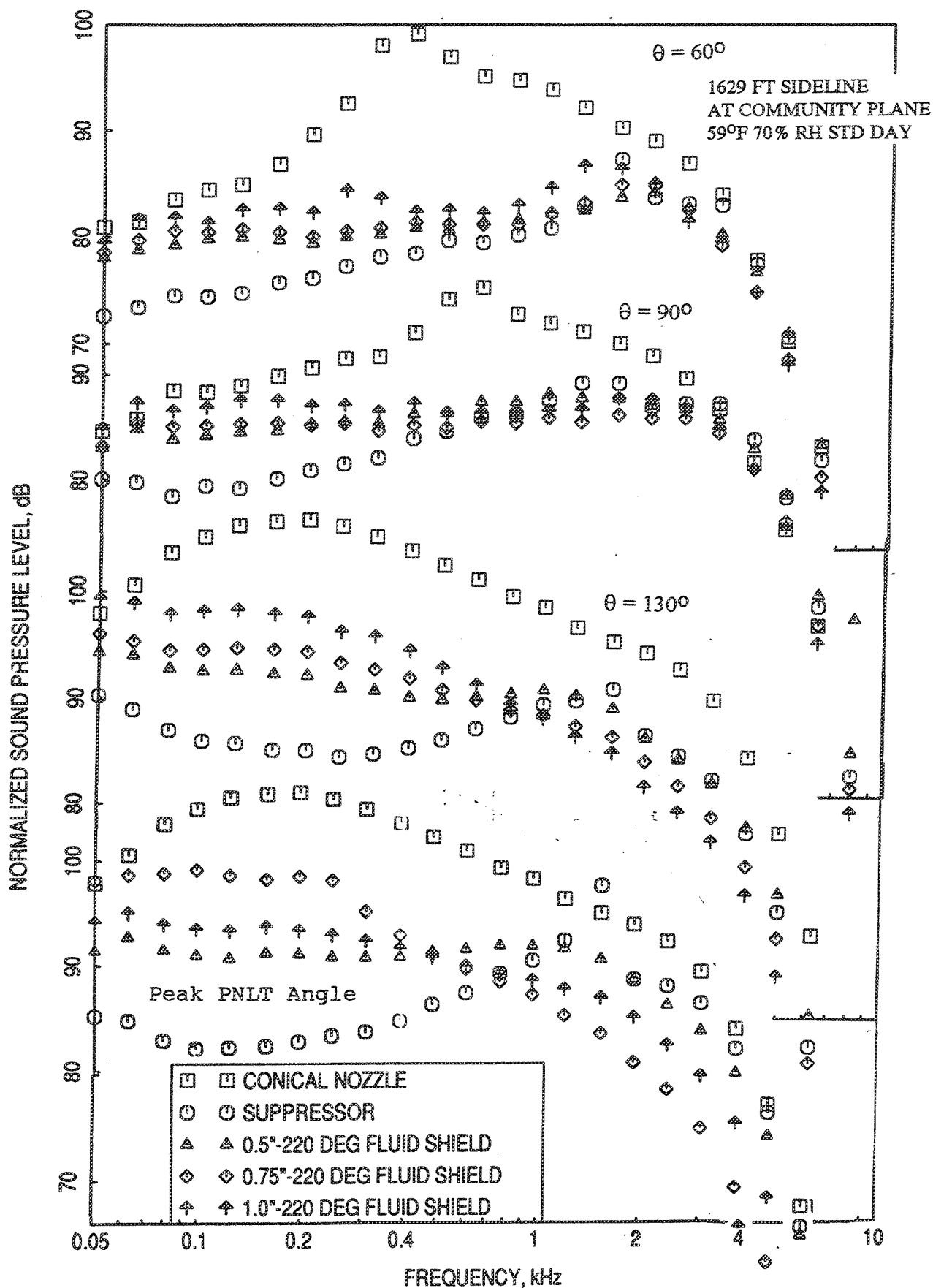


Figure 2.8-11. Noise suppression due to fluid shield nozzles in terms of normalized SPL spectra at different polar angles ( $\theta$ ) for a fixed nominal mixed jet velocity of 2030 ft/sec at static condition.

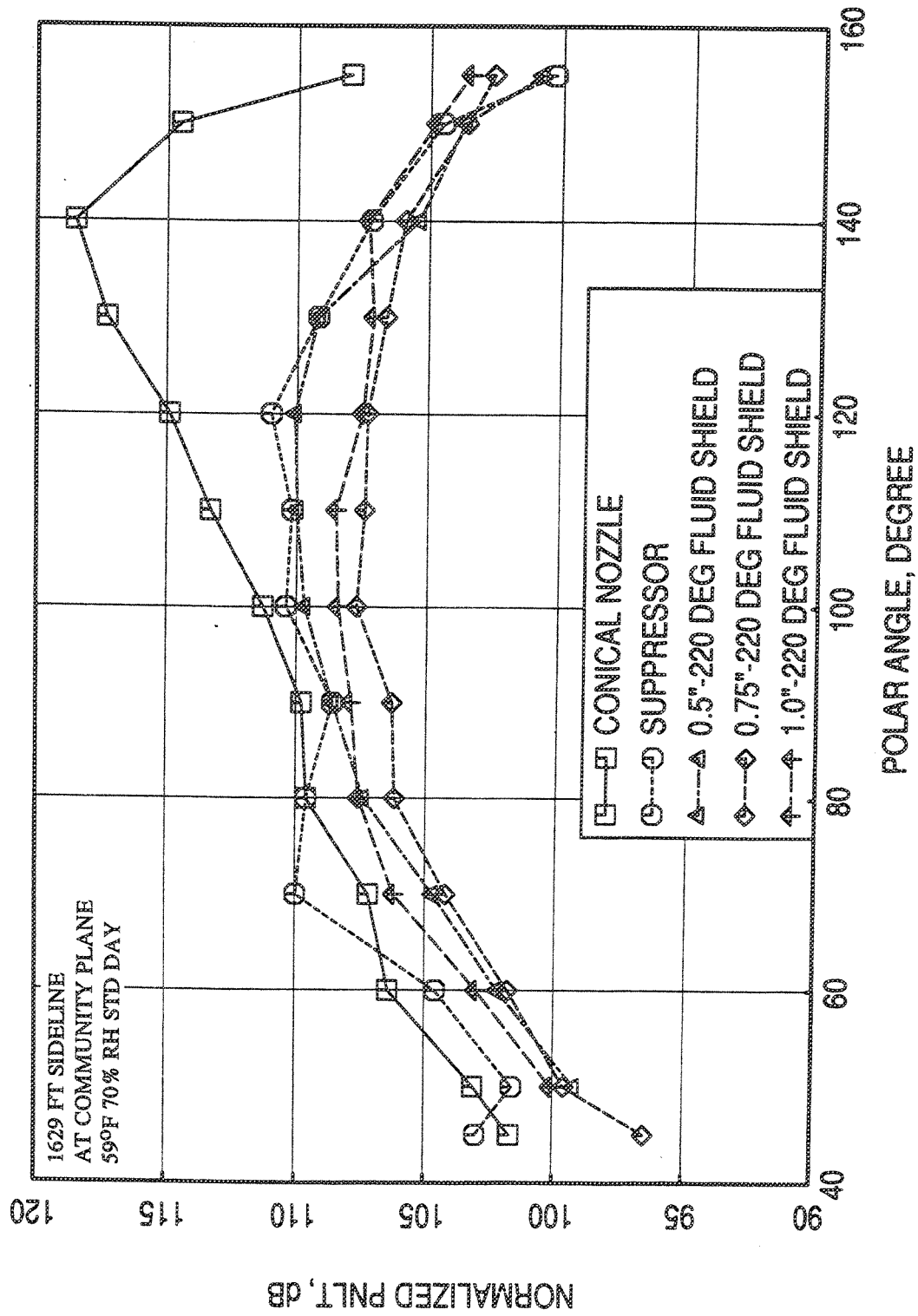


Figure 2.8-12. Noise suppression due to fluid shield nozzles in terms of normalized PNLT directivities for a fixed nominal mixed jet velocity of 1811 ft/sec at static condition.

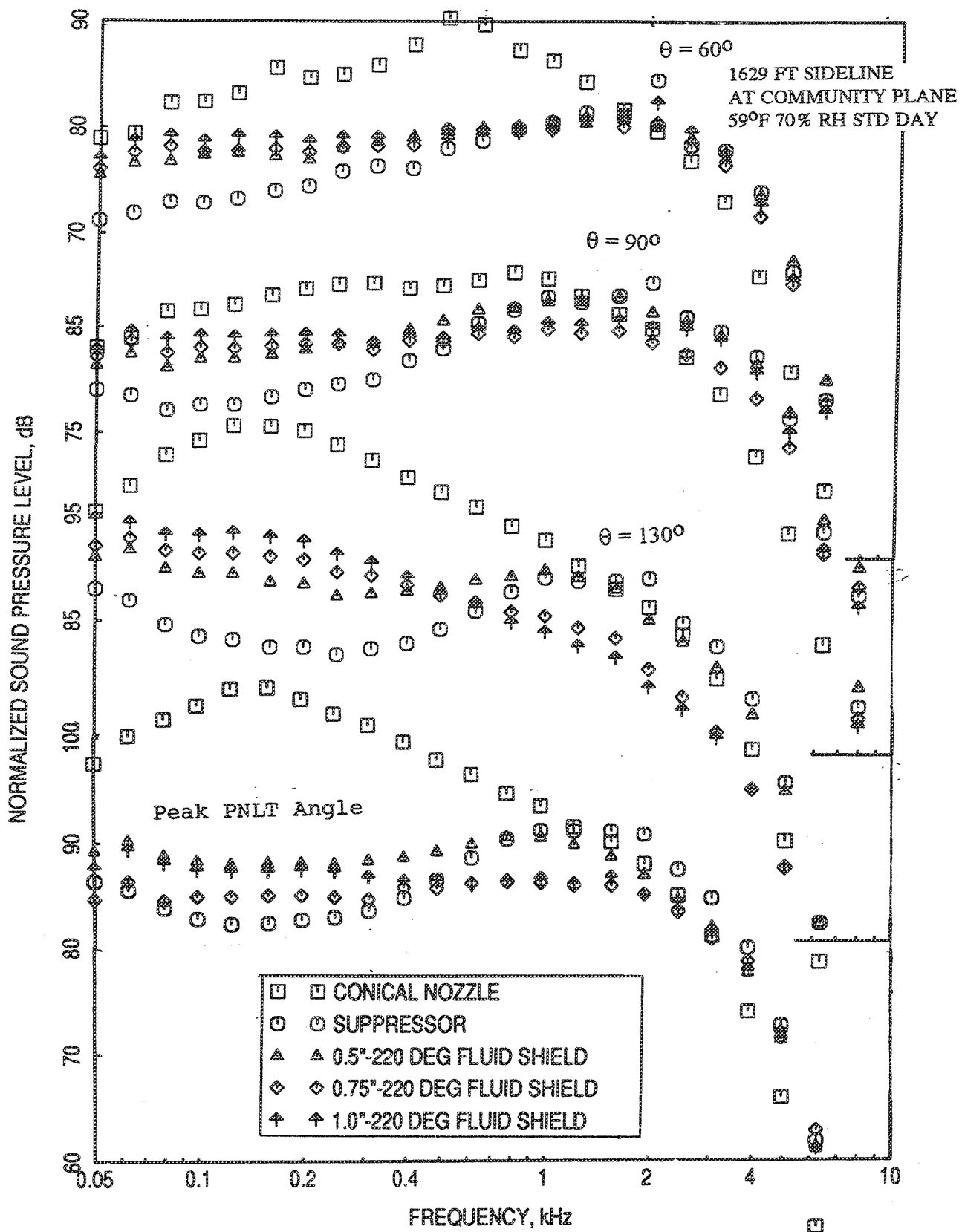


Figure 2.8-13. Noise suppression due to fluid shield nozzles in terms of normalized SPL spectra at different polar angles ( $\theta$ ) for a fixed nominal mixed jet velocity of 1811 ft/sec at static condition.



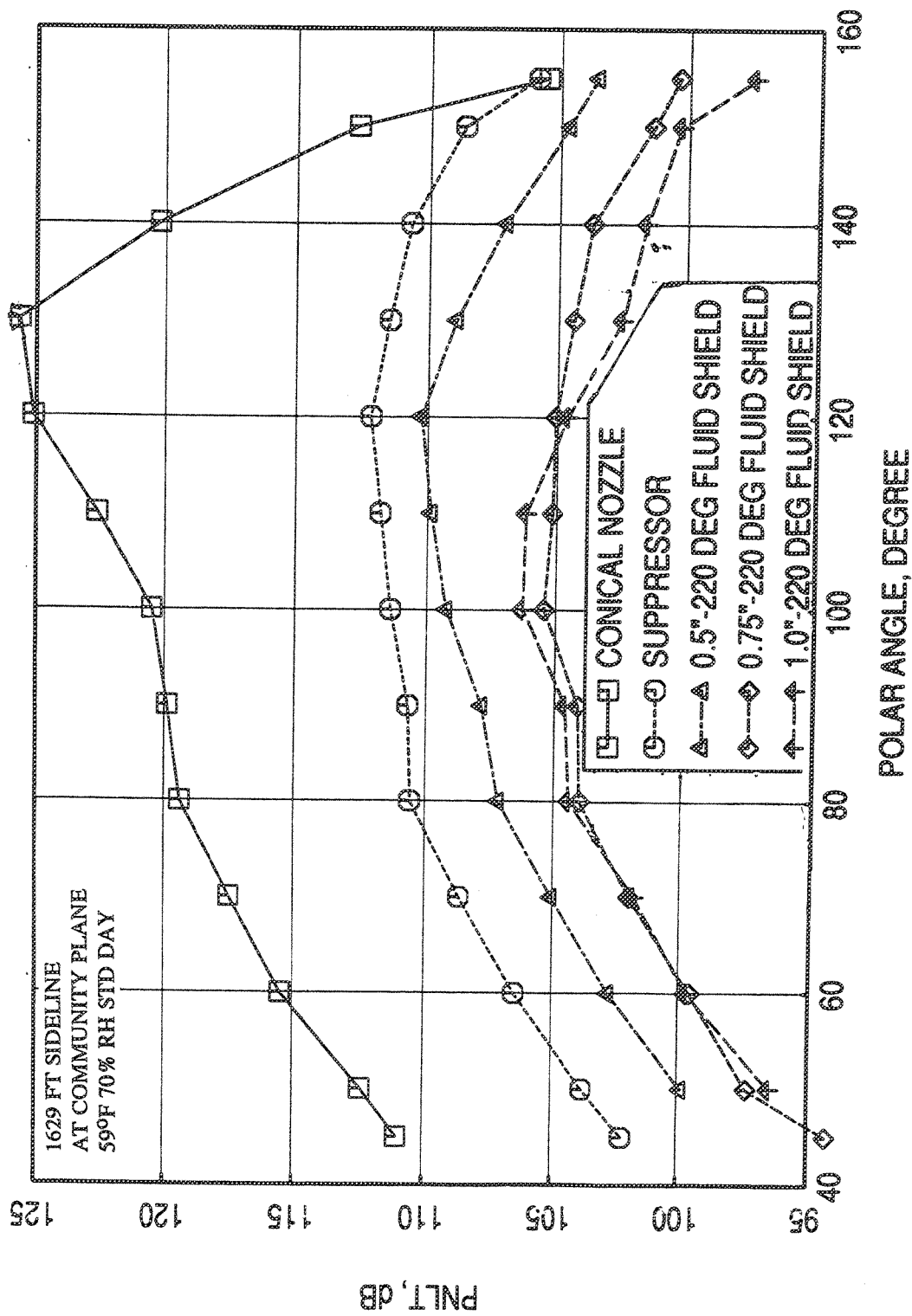


Figure 2.8-14. Noise suppression due to fluid shield nozzles in terms of PNL T directivities for a fixed nominal ideal gross thrust of 68 kbs at static condition.

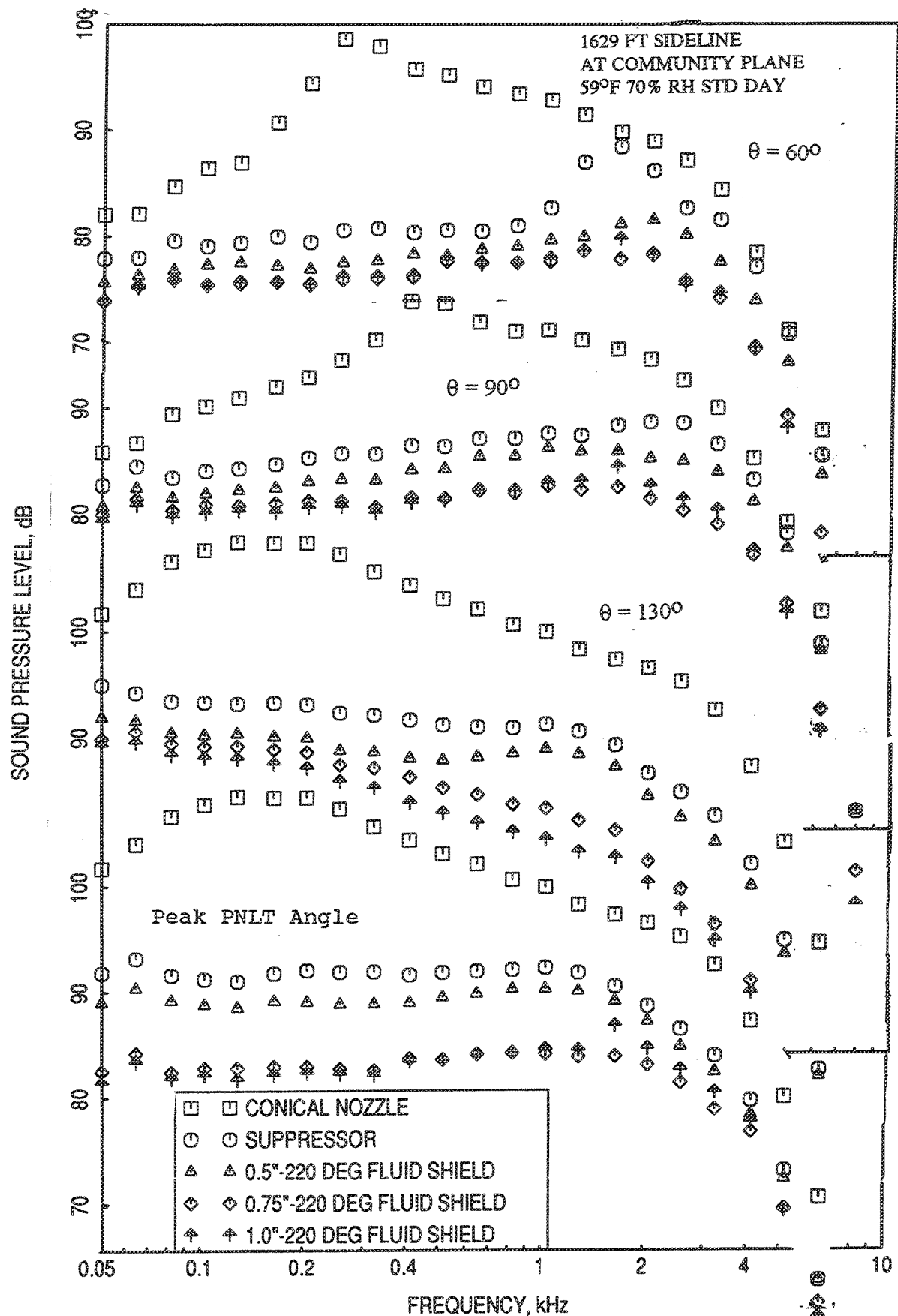


Figure 2.8-15. Noise suppression due to fluid shield nozzles in terms of SPL spectra at different polar angles ( $\theta$ ) for a fixed nominal ideal gross thrust of 68 klbs at static condition.

Unnormalized PNLT directivities are plotted in Figure 2.8-16 for a fixed  $(FG)_i$  of about 51 klbs, which is the required ideal gross thrust for cutback condition. One inch thick shield results are not shown in this figure, since this configuration was not tested at this low thrust condition. Substantial benefit in terms of PNdB suppression due to shield is observed. Unnormalized SPL spectra at a number of polar angles are plotted in Figure 2.8-17 for the same condition. Substantial sound pressure level decrease is achieved due to fluid shields compared to suppressor alone configuration for entire frequency range.

Flight Data : Results at Fixed  $V_{mix}$  : Normalized PNLT directivities are shown in Figure 2.8-18 at a fixed mixed jet velocity of about 2030 ft/sec, which is the takeoff velocity for the nominal flade cycle. Relatively small benefit in terms of PNdB suppression due to shield is observed. Normalized SPL spectra at a number of polar angles are plotted in Figure 2.8-19. Sound pressure levels increase at lower frequencies and decrease at higher frequencies due to fluid shields compared to suppressor alone configuration.

Normalized PNLT directivities are plotted in Figure 2.8-20 at a fixed mixed jet velocity of about 1811 ft/sec, which is the cutback velocity for the 0.5"-thick fluid shield. The 0.75"-thick fluid shield shows the highest amount of PNdB suppression at all polar angles. Normalized SPL spectra at a number of polar angles are plotted in Figure 2.8-21. Again, sound pressure levels increase at lower frequencies and decrease at higher frequencies due to fluid shields compared to suppressor alone configuration. The high frequency suppression is much higher compared to low frequency SPL increase, which resulted in PNLT reduction for all polar angles due to fluid shields.

Results at Fixed  $(FG)_i$  : Unnormalized PNLTs are plotted in Figure 2.8-22 with respect to polar angle for a fixed  $(FG)_i$  of about 67 to 69 klbs, which is the required ideal gross thrust for takeoff condition. Substantial benefit in terms of PNdB suppression due to fluid shield is observed. At this condition the fluid shields of 0.75"-thick and 1.0"-thick give more or less same amount of noise suppression. Unnormalized SPL spectra at a number of polar angles are plotted in Figure 2.8-23 for the same condition. Substantial sound pressure level decrease is achieved due to fluid shields compared to suppressor alone configuration for entire frequency range.

Unnormalized PNLT directivities are plotted in Figure 2.8-24 for a fixed  $(FG)_i$  of about 51 klbs, which is the required ideal gross thrust for cutback condition. One inch

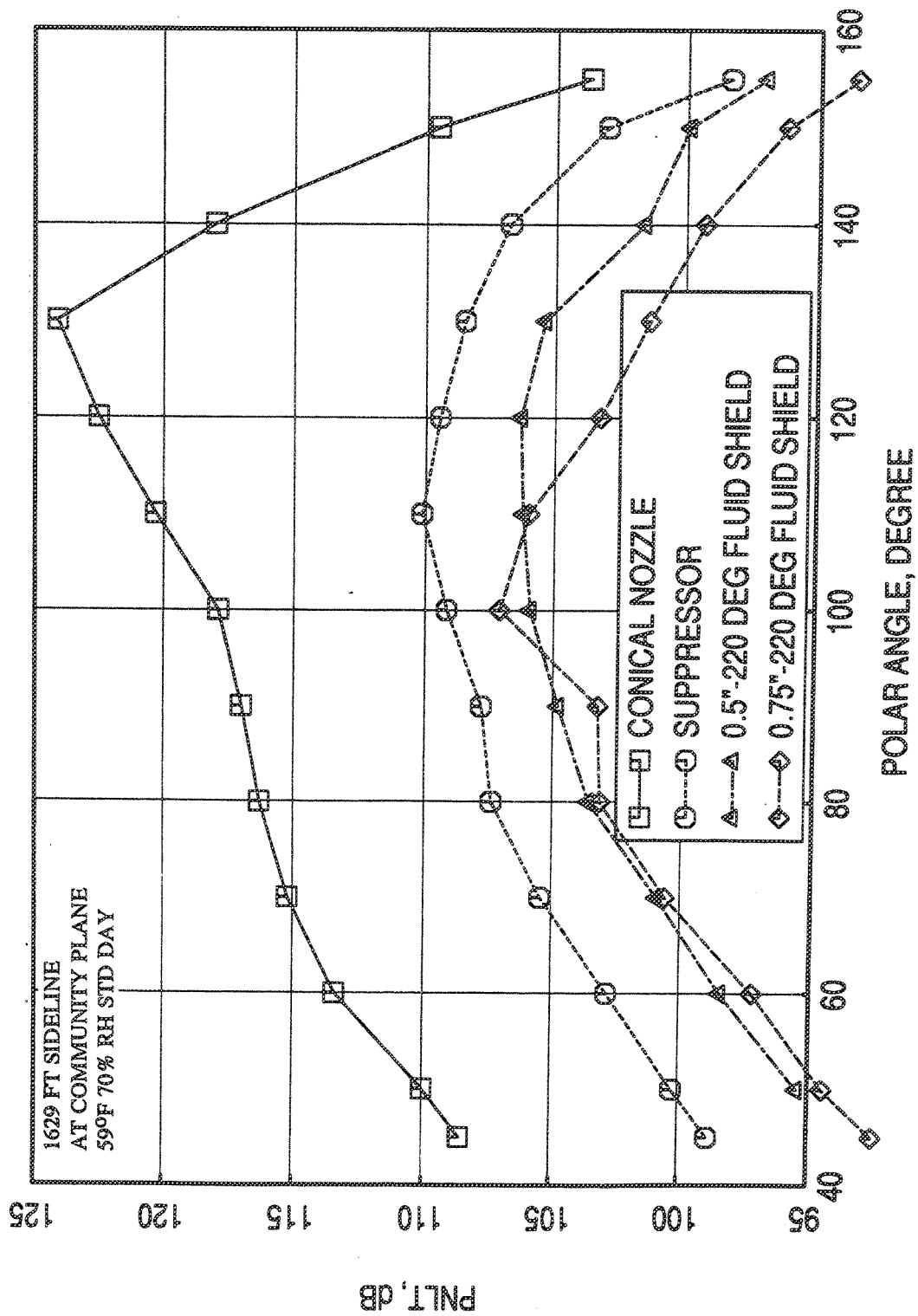


Figure 2.8-16. Noise suppression due to fluid shield nozzles in terms of PNL T directivities for a fixed nominal ideal gross thrust of 51 klbs at static condition.

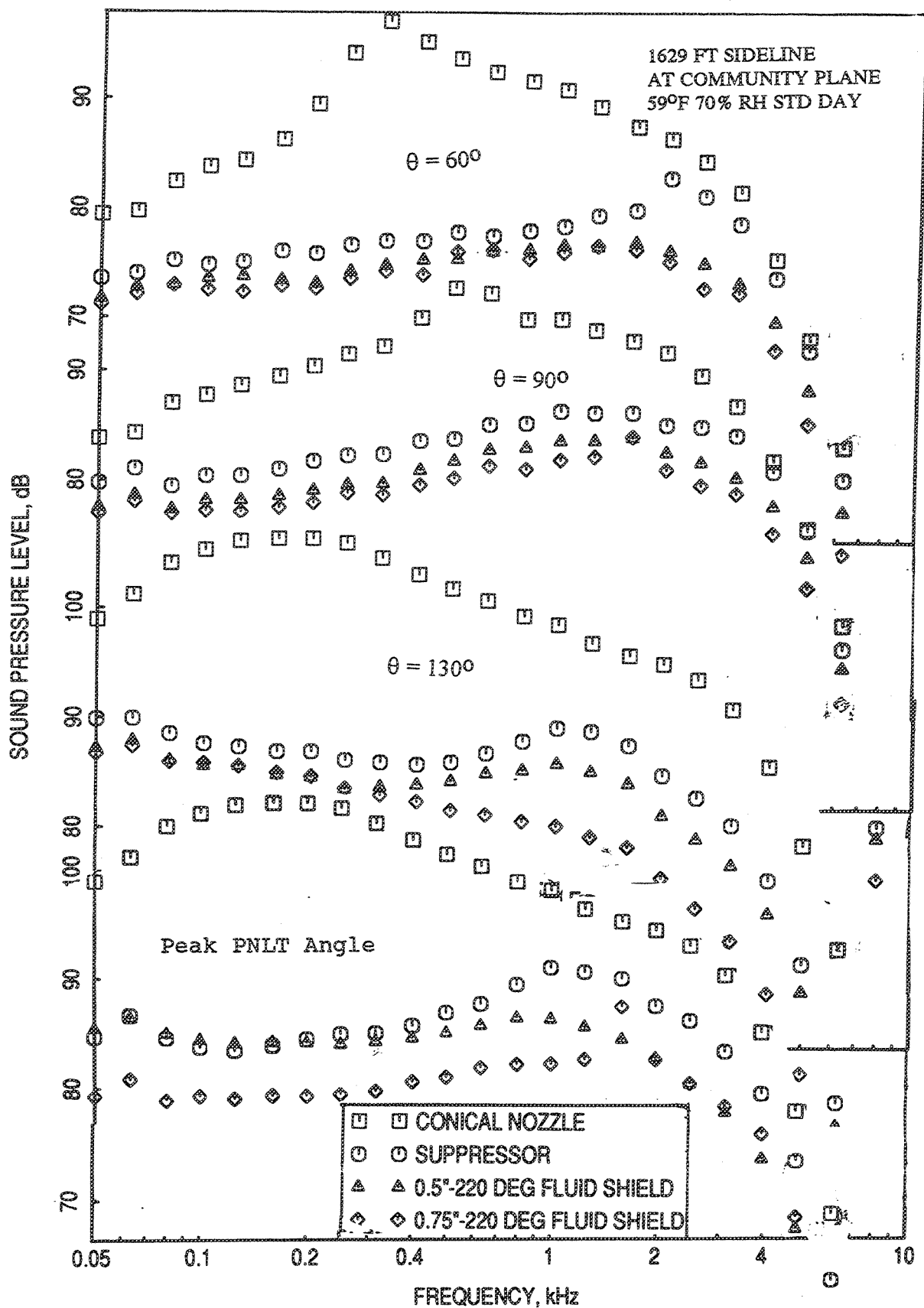


Figure 2.8-17. Noise suppression due to fluid shield nozzles in terms of SPL spectra at different polar angles ( $\theta$ ) for a fixed nominal ideal gross thrust of 51 klbs at static condition.

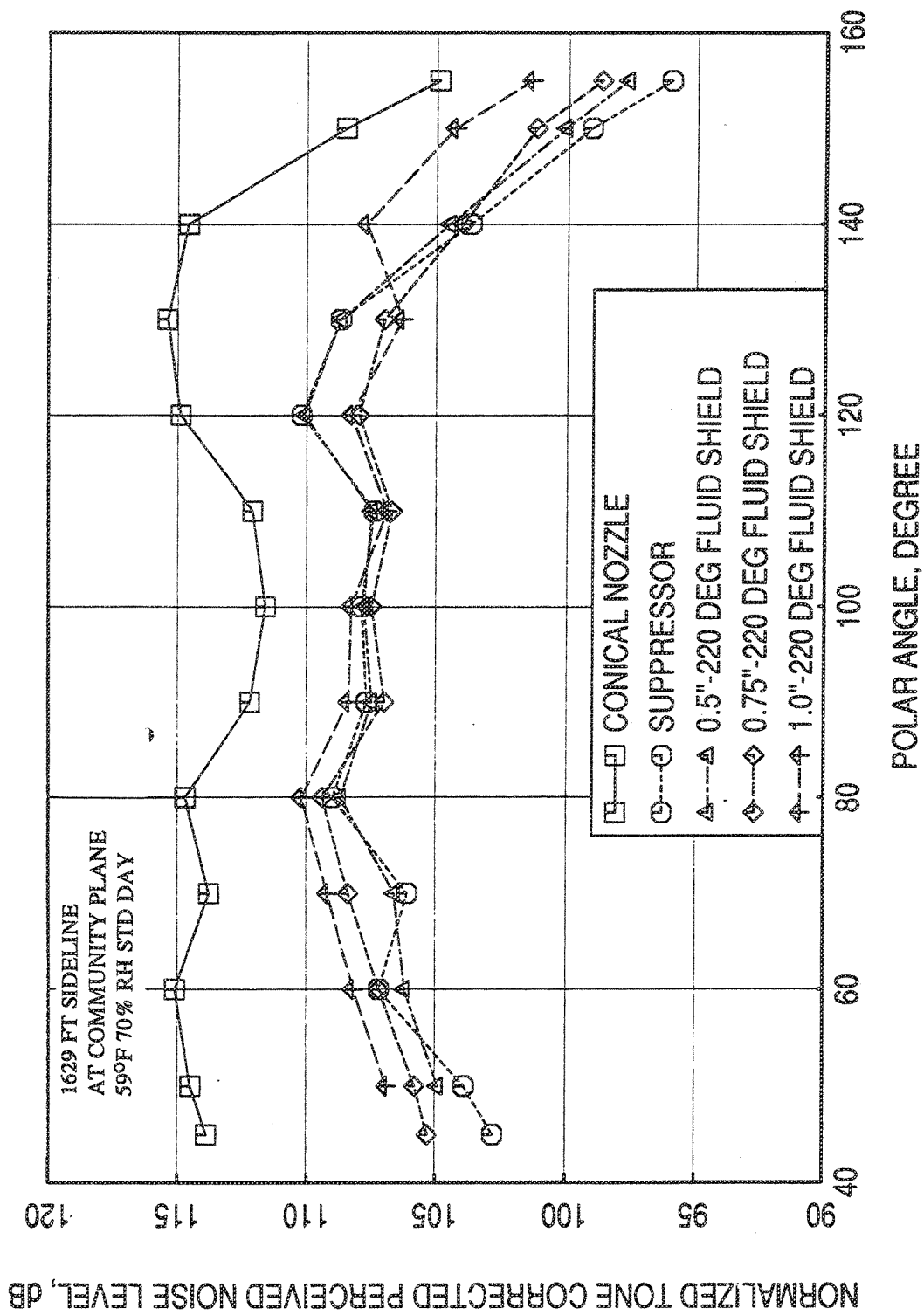


Figure 2.8-18. Noise suppression due to fluid shield nozzles in terms of normalized PNLT directivities for a fixed nominal mixed jet velocity of 2030 ft/sec with flight simulation ( $M_F=0.32$ ).

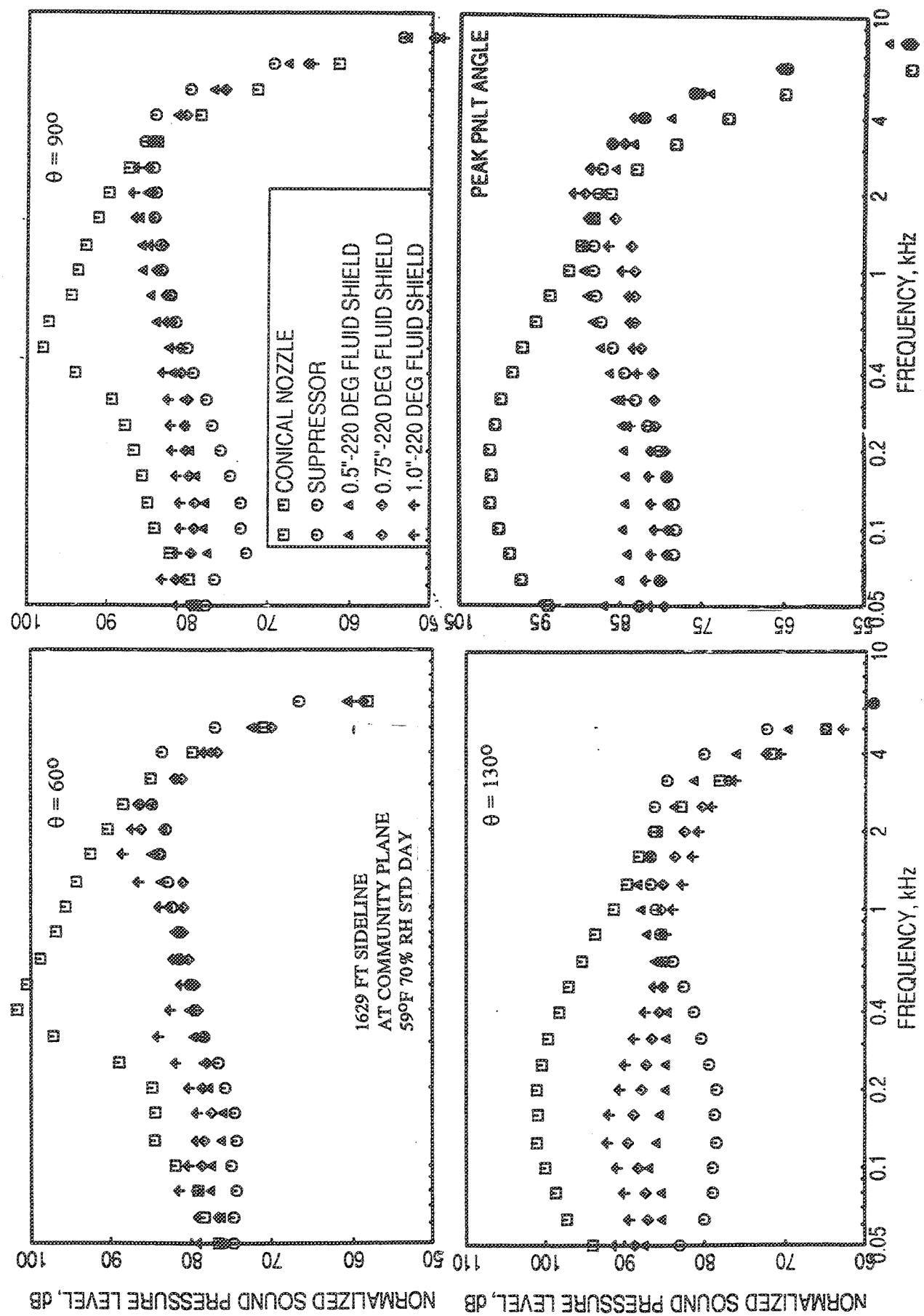


Figure 2.8-19. Noise suppression due to fluid shield nozzles in terms of normalized SPL spectra at different polar angles ( $\theta$ ) for a fixed nominal mixed jet velocity of 2030 ft/sec with flight simulation ( $M_F=0.32$ ).

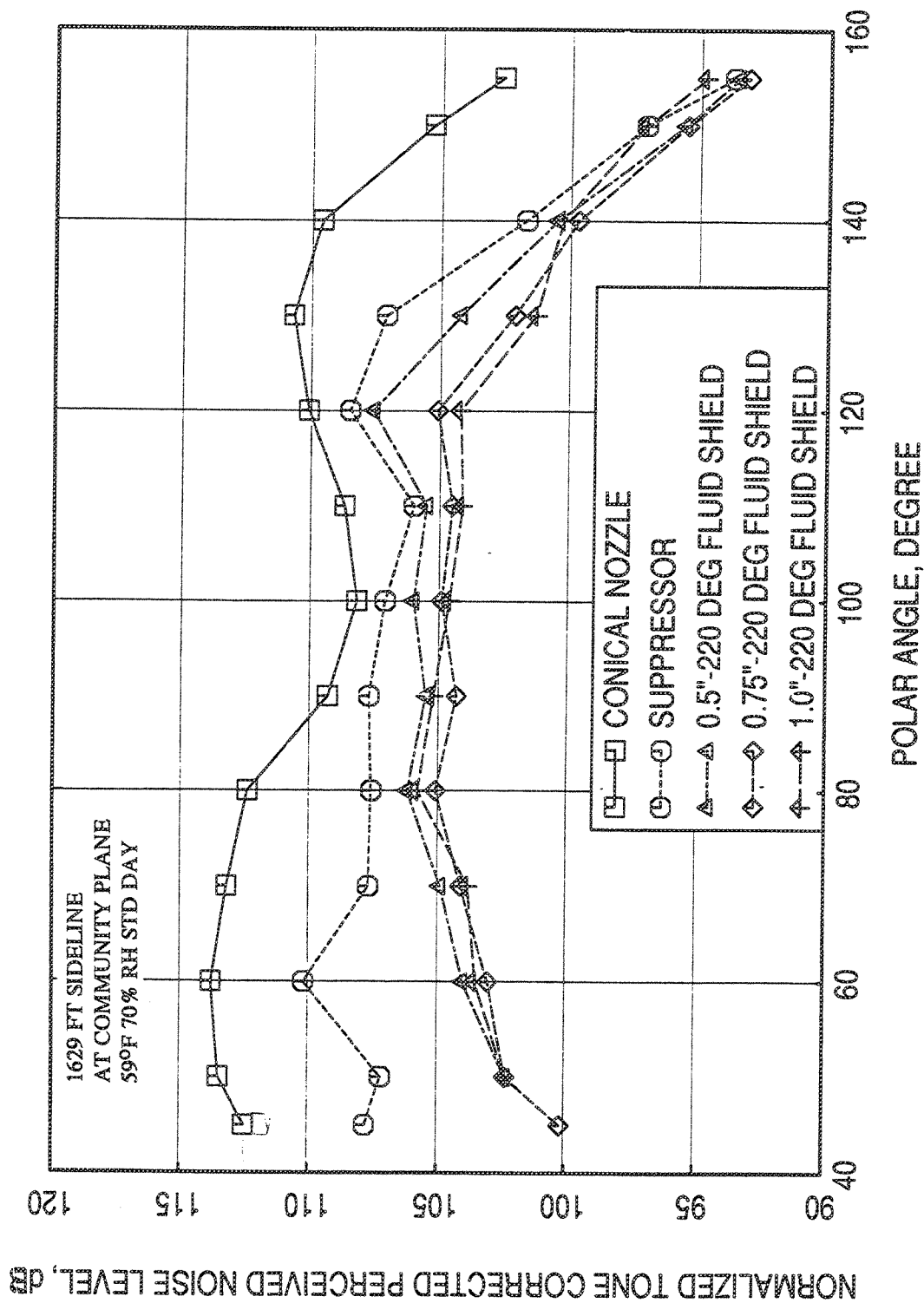


Figure 2.8-20. Noise suppression due to fluid shield nozzles in terms of normalized PNLT directivities for a fixed nominal mixed jet velocity of 1811 ft/sec with flight simulation ( $M_F=0.32$ ).



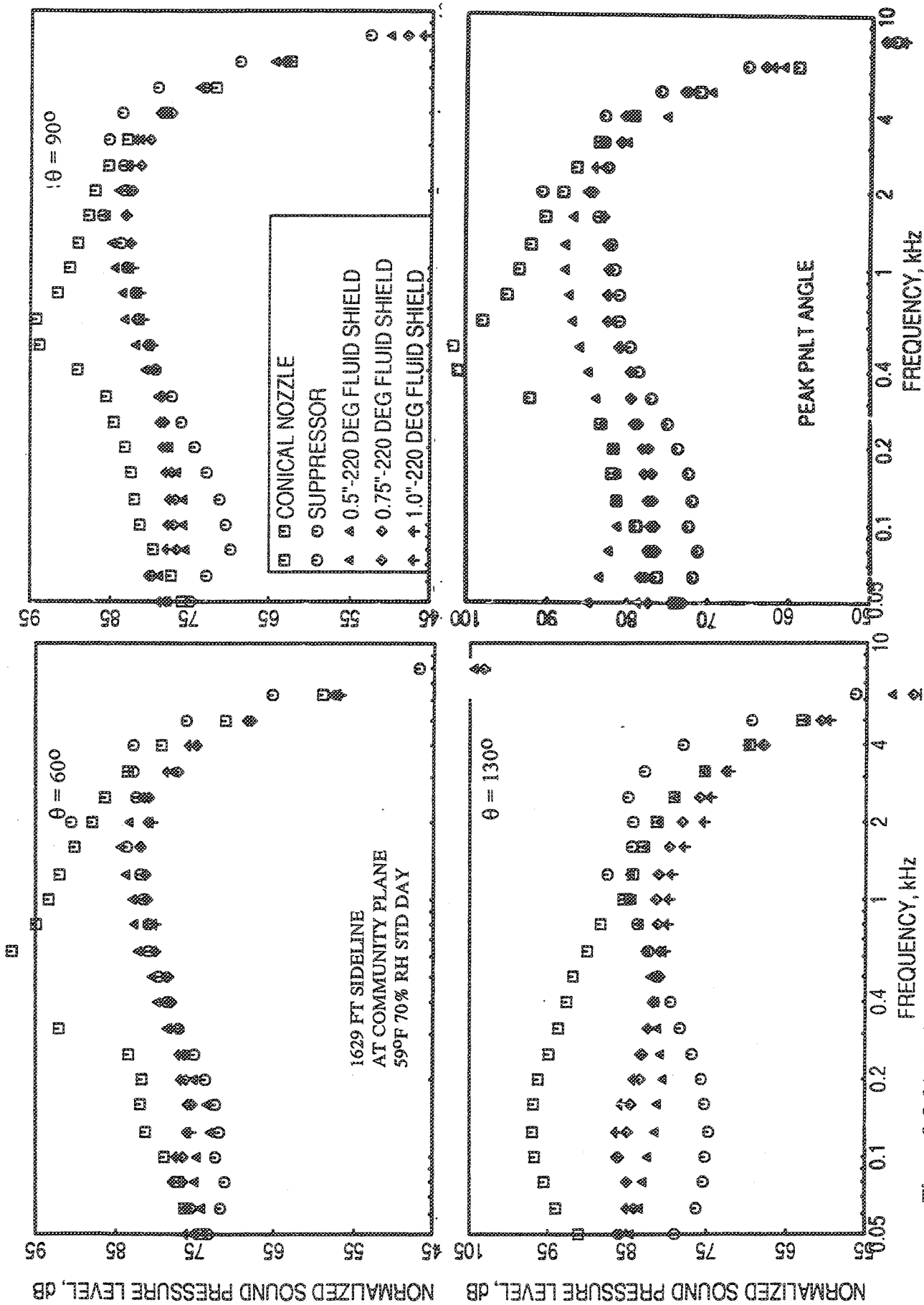


Figure 2.8-21. Noise suppression due to fluid shield nozzles in terms of normalized SPL spectra at different polar angles ( $\theta$ ) for a fixed nominal mixed jet velocity of 1811 ft/sec with flight simulation ( $M_F=0.32$ ).

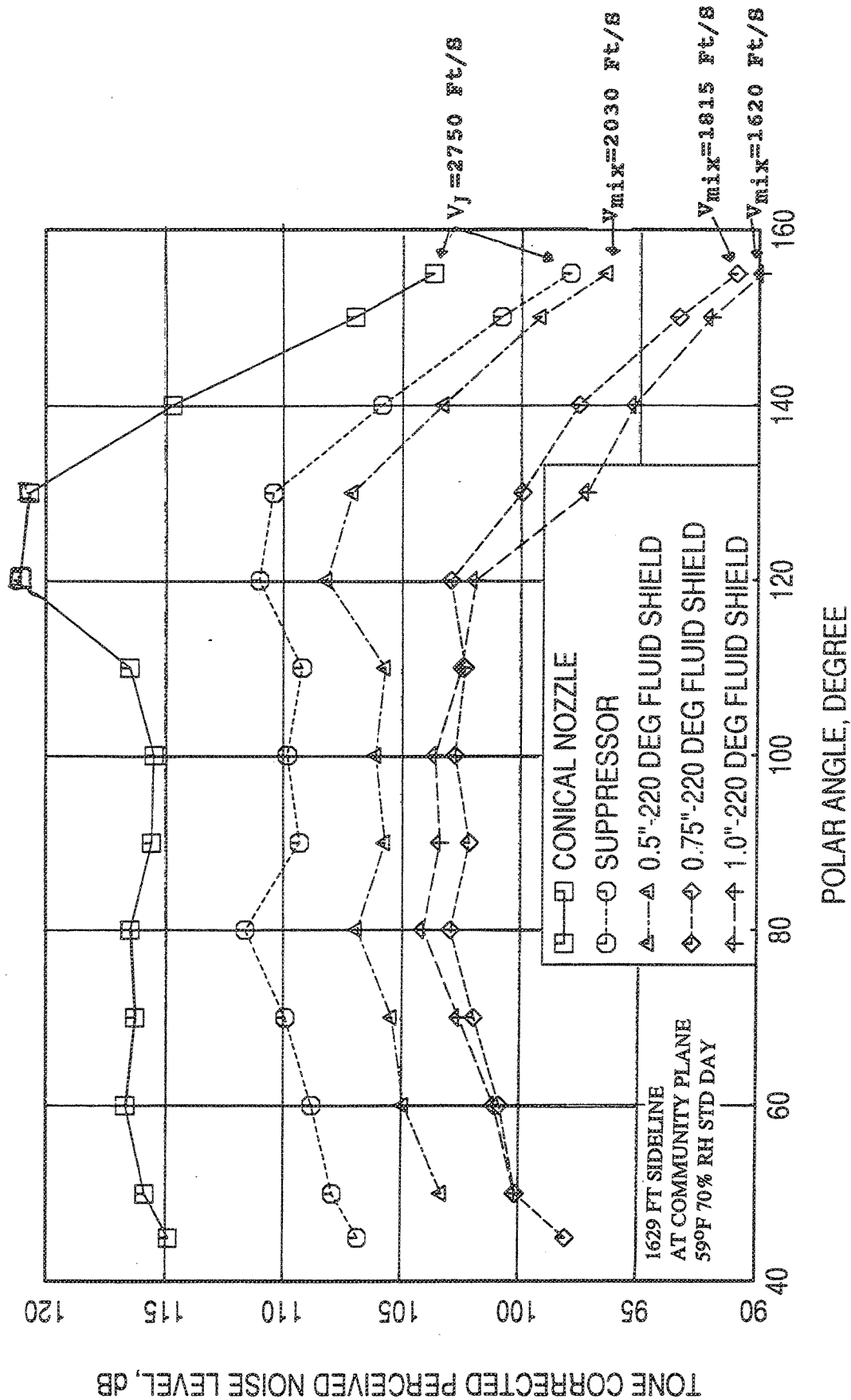


Figure 2.8-22. Noise suppression due to fluid shield nozzles in terms of PNL T directivities for a fixed nominal ideal gross thrust of 68 kibs with flight simulation ( $M_F=0.32$ ).

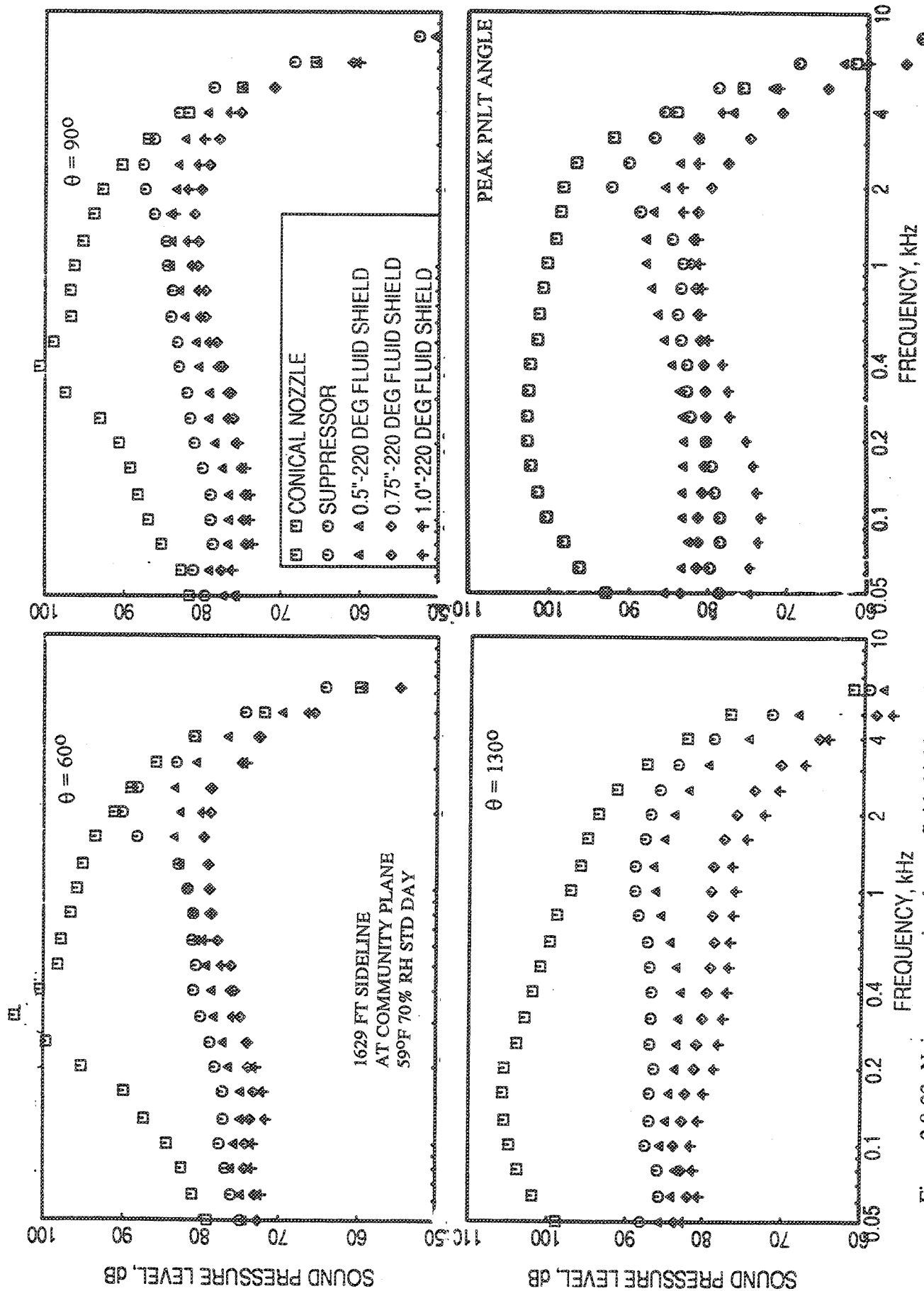


Figure 2.8-23. Noise suppression due to fluid shield nozzles in terms of SPL spectra at different polar angles ( $\theta$ ) for a fixed nominal ideal gross thrust of 68 klbs with flight simulation ( $M_F=0.32$ ).

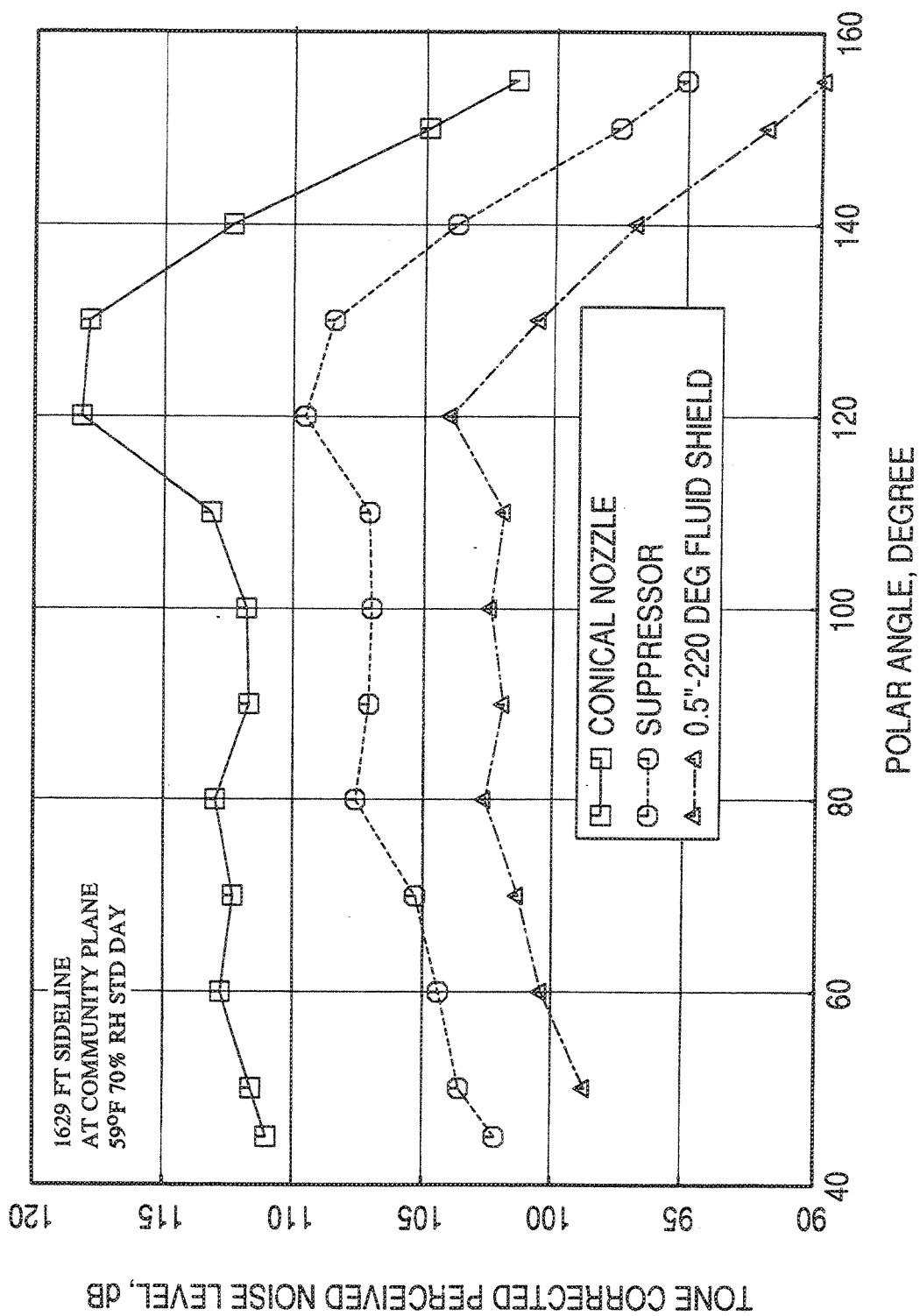


Figure 2.8-24. Noise suppression due to fluid shield nozzles in terms of PNL T directivities for a fixed nominal ideal gross thrust of 51 klbs with flight simulation ( $M_F=0.32$ ).

thick shield results are not shown in this figure, since this configuration was not tested at this low thrust condition. Substantial benefit in terms of PNdB suppression due to the fluid shield is observed. Unnormalized SPL spectra at a number of polar angles are plotted in Figure 2.8-25 for the same condition. Substantial sound pressure level decrease is achieved due to the fluid shield compared to suppressor alone configuration for the entire frequency range.

### 2.8.2 Noise Suppression Due to Fluid Shield Nozzles on an Equal Area Basis :

In the previous section, the significantly large noise benefit due to the fluid shield compared to the suppressor alone configuration is noted when compared on a constant thrust basis. However, at a fixed thrust condition the jet velocity of the suppressor alone configuration is much higher compared to a fluid shield configuration, since the throat area of the suppressor is smaller compared to the entire shield nozzle. Therefore, the question arises whether the benefit observed is really due to the fluid shield mechanism or the same amount of noise benefit can be obtained by oversizing the suppressor to have the same area as the total A8 of both core and fluid shield streams. In other words, is there a noise benefit to a single flow suppressor nozzle without a fluid shield relative to a suppressor with fluid shield nozzle generating the "same" amount of thrust Scaled up suppressor nozzle and fluid shield nozzle provide same ideal gross thrust at approximately same total flow rate and hence are being compared at same specific thrust,  $V_{mix}$ . To resolve this issue the acoustic data for the reference conical nozzle and the suppressor alone configuration are scaled to the areas 1813.6, 2165.5, and 2524.7 square inches, which correspond to the full scale total exit areas of 0.5", 0.75", and 1.0" thick fluid shields, respectively. These results for each area are compared with the corresponding fluid shield data in a fixed thrust basis.

As described in section 2.2 that the conical nozzle was tested for a few aerothermodynamic conditions corresponding to two mixed flow conditions of each fluid shield nozzles. Due to the scatter in the conical nozzle test results (reasons discussed in section 2.5) predictions are made at the same conditions and are used in the previous presentation along with the test data. Since the results in this subsection will be studied on equal area basis, noise levels for conical nozzle at the same full scale area of each fluid shield configurations are predicted at the corresponding mixed aerothermodynamic conditions. The mixed aerothermodynamic conditions for the three fluid shield nozzles are shown in Figure 2.8- 26 Superimposed are the conditions at

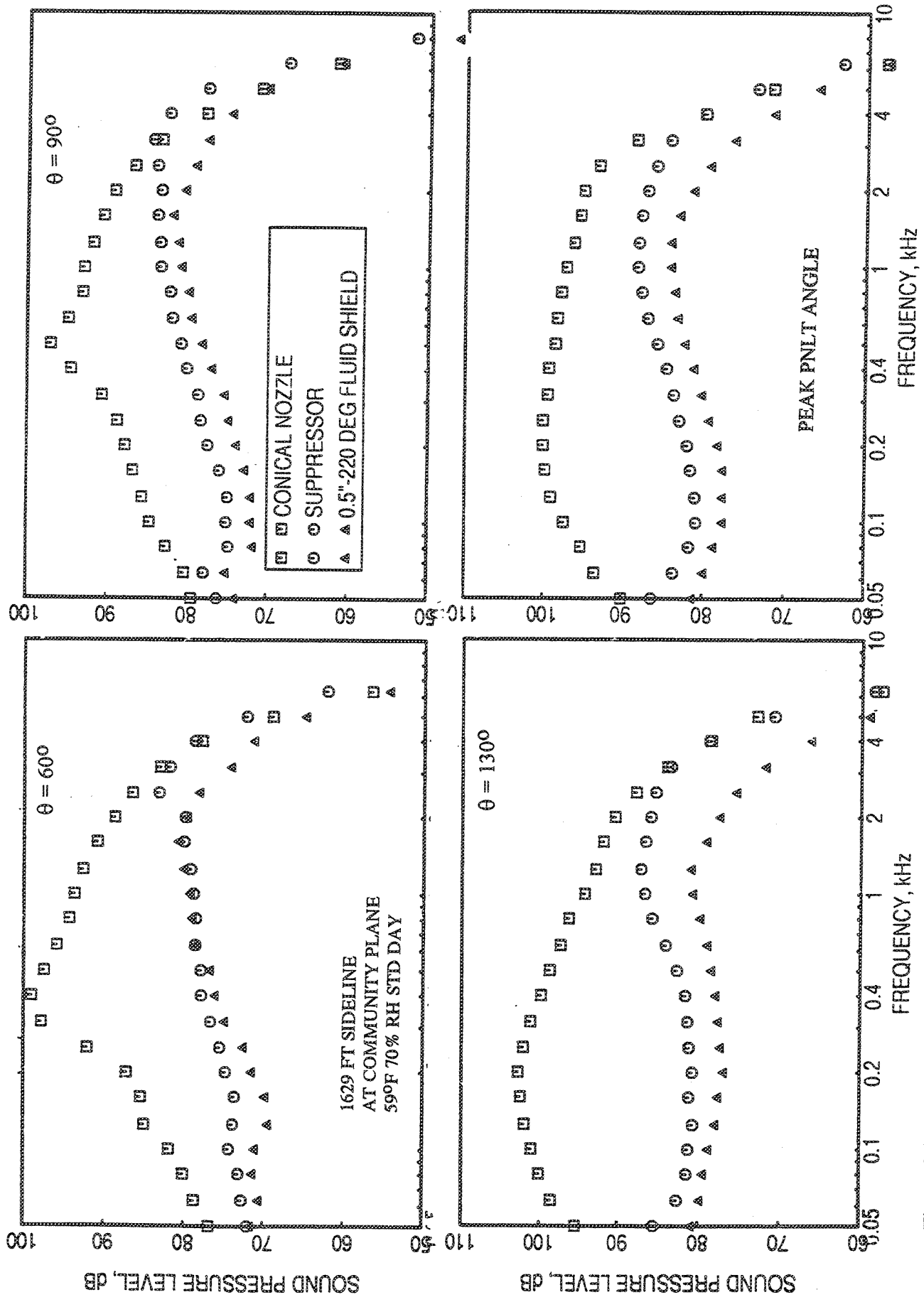


Figure 2.8-25. Noise suppression due to fluid shield nozzles in terms of SPL spectra at different polar angles ( $\theta$ ) for a fixed nominal ideal gross thrust of 51 klbs with flight simulation ( $M_F=0.32$ ).

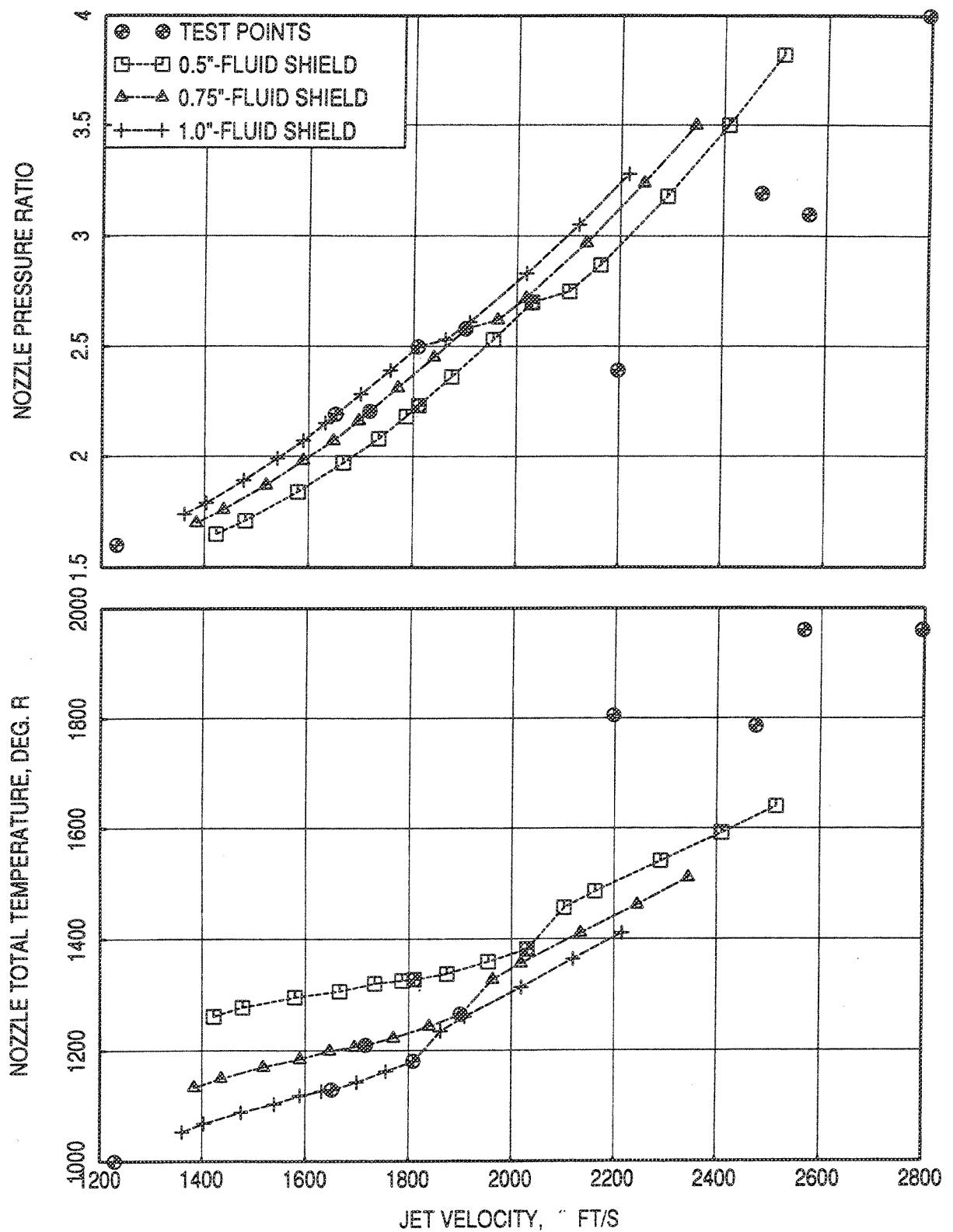


Figure 2.8-26. Mixed aerothermodynamic conditions derived using dual stream fluid shield conditions.

which the conical nozzle was tested and for which the predictions were made earlier. The predicted and measured results for conical nozzle are shown in Figures 2.8-27 and 2.8-28, respectively for static and flight conditions. The predicted results in terms of normalized levels vary slightly with respect to the A8 value, especially at higher jet velocities. Deviation of test data from prediction is discussed in section 2.5. Measured and predicted results of appropriate fluid shield will be utilized in our subsequent presentation.

**Static Data :** Figure 2.8-29 illustrates the noise benefits in terms of EPNdB and peak PNLTdB realized by the 0.75"-thick fluid shield nozzle compared to the conical nozzle and the suppressor alone configuration, all being scaled to 2165.5 square inch, the full scale area for the 0.75"-thick shield configuration. Suppression of about 3 to 4 EPNdB compared to the suppressor alone configuration of the same total area is obtained in the range of 60 to 70 klbs ideal gross thrust. These suppressions illustrate the noise reduction benefit of splitting the total engine flow (core+flade) into two stream nozzle, with the core stream being a multi-element nozzle and flade stream partially surrounding it as compared to exhausting the total engine flow through a single stream multi-element suppressor. PNLTs at three polar angles are plotted with respect to ideal gross thrust in Figure 2.8-30 for the 0.75"-thick fluid shield on equal area basis. The advantage of the fluid shield is clearly demonstrated in these results.

Similar results for the 0.5"-thick shield, where, all configurations are scaled to an area of 1813.6 square inch, are plotted in Figures 2.8-31 and 2.8-32. Again, we see the benefit of the shield. It should be noted that the 0.5"-thick shield is effective in the range of 50 to 65 klbs ideal gross thrust and the amount of suppressions are relatively smaller compared to the 0.75"-thick shield.

For 1.0"-thick shield, similar exercise is carried out by scaling all the configurations to 2524.7 square inch and the results are shown in Figures 2.8-33 and 2.8-34. Again, we see the benefit of the fluid shield and is effective in the thrust range of 65 to 90 klbs.

**Flight Data :** Figure 2.8-35 illustrates the noise benefits, in terms of EPNLT and peak PNLT, realized by the 0.75"-thick fluid shield nozzle compared to the conical nozzle and the suppressor alone configuration, all being scaled to 2165.5 square inch, the full scale area for the 0.75"-thick shield configuration. Additional EPNdB suppression (about 4 to 5 EPNdB) compared to the suppressor alone configuration of same total



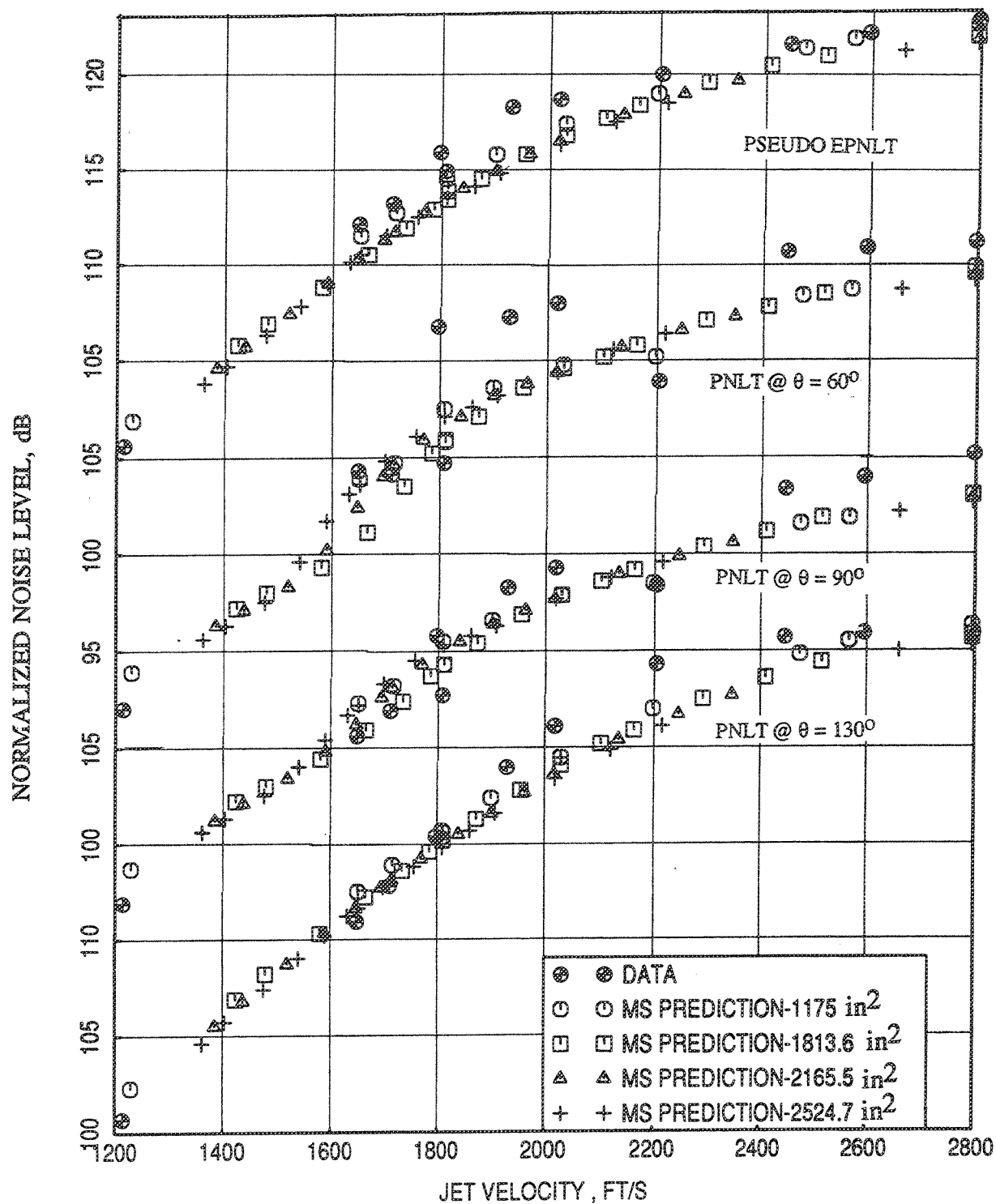


Figure 2.8-27. Predicted and measured normalized pseudo EPNLT and PNLT at different polar angles ( $\theta$ ) for conical nozzles with equivalent full size fluid shield areas at mixed aerothermodynamic conditions of Figure 2.28-26 at static condition.

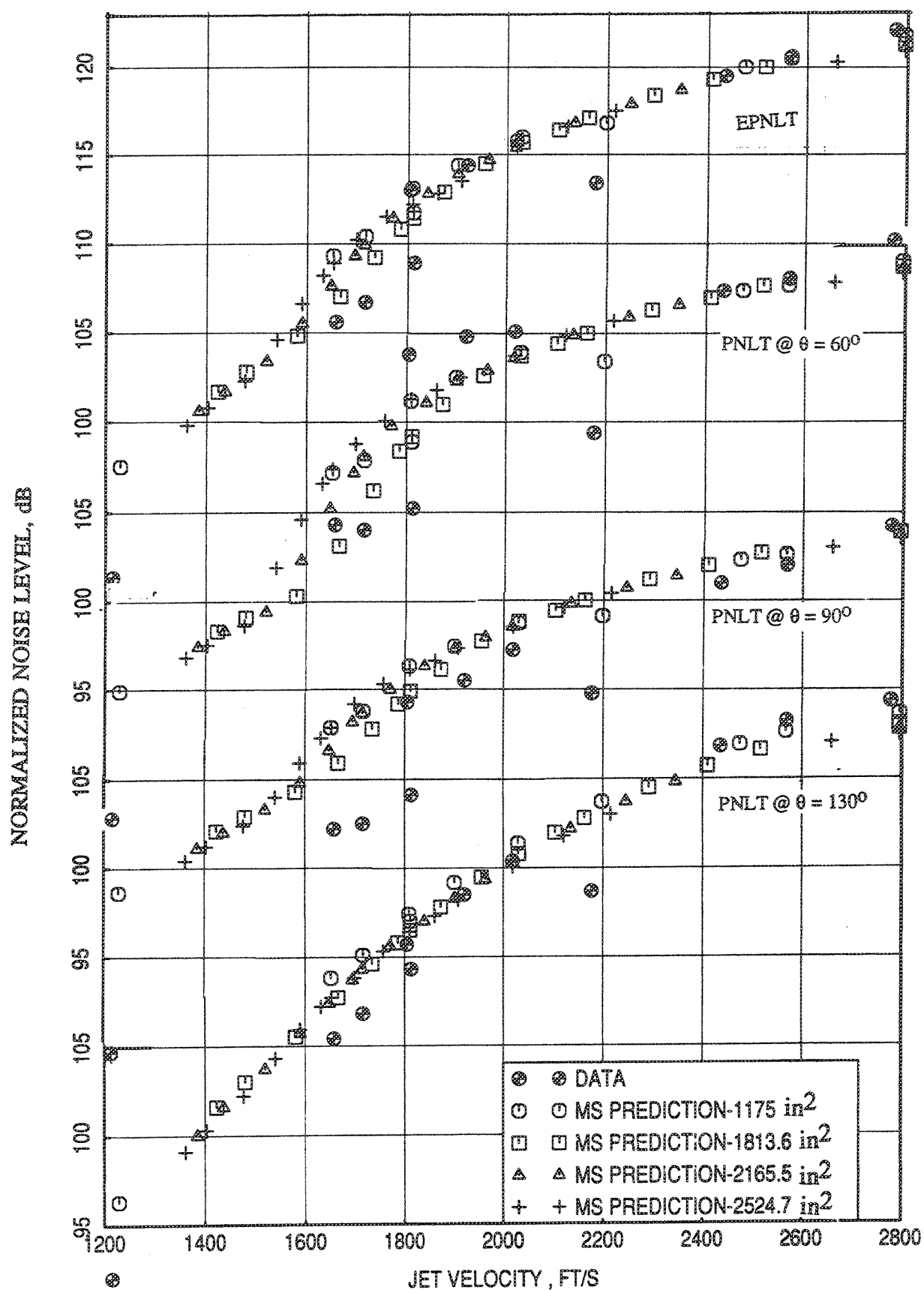


Figure 2.8-28. Predicted and measured normalized EPNLT and PNLT at different polar angles ( $\theta$ ) for conical nozzles with equivalent full size fluid shield areas at mixed aerothermodynamic conditions of Figure 2.28-26 with flight simulation ( $M_F=0.32$ ).

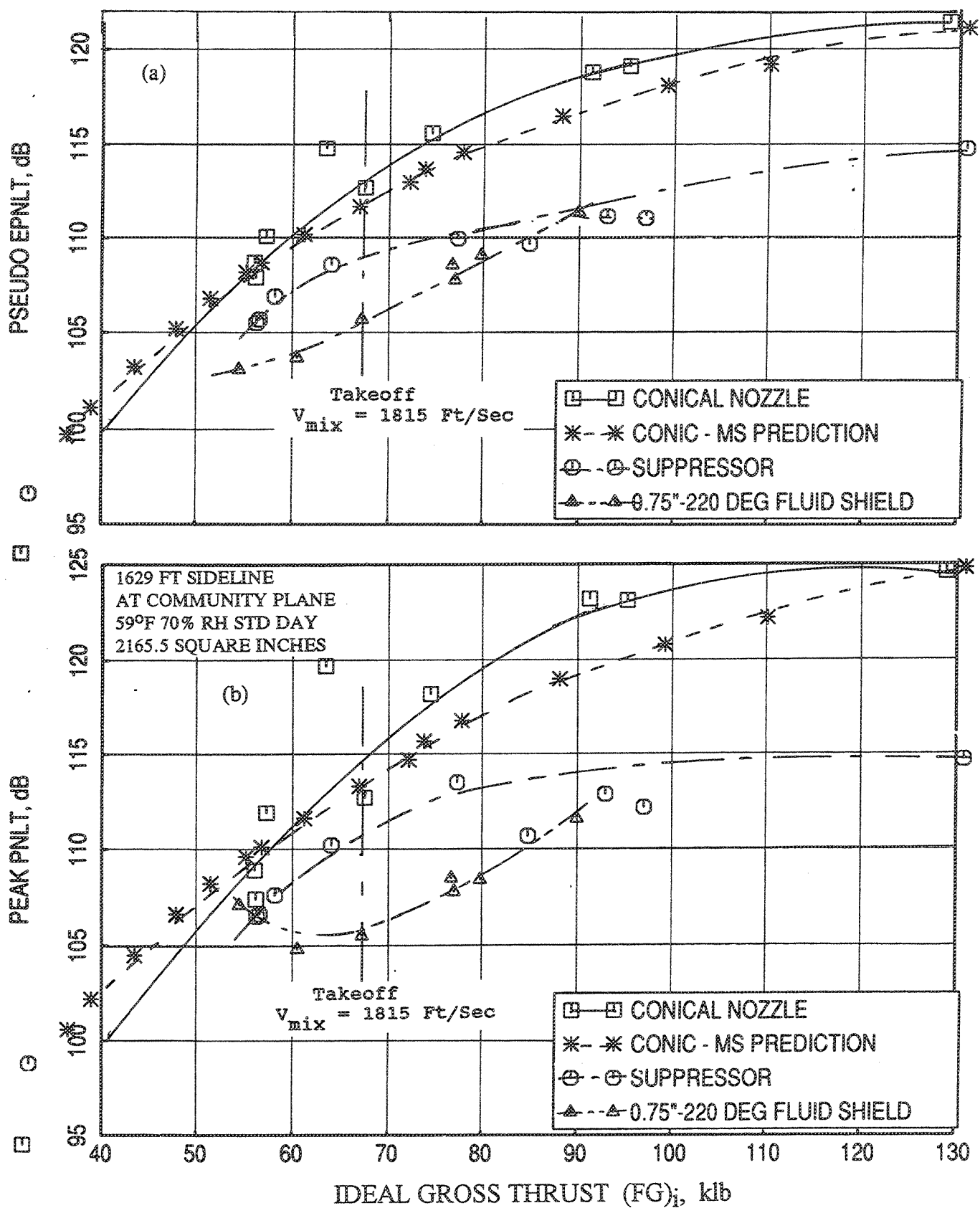


Figure 2.8-29. Noise suppression due to 0.75"-thick fluid shield nozzle in terms of (a) EPNLT and (b) peak PNL data as a function of ideal gross thrust at static condition in an equal area basis of 2165.5 square inches.

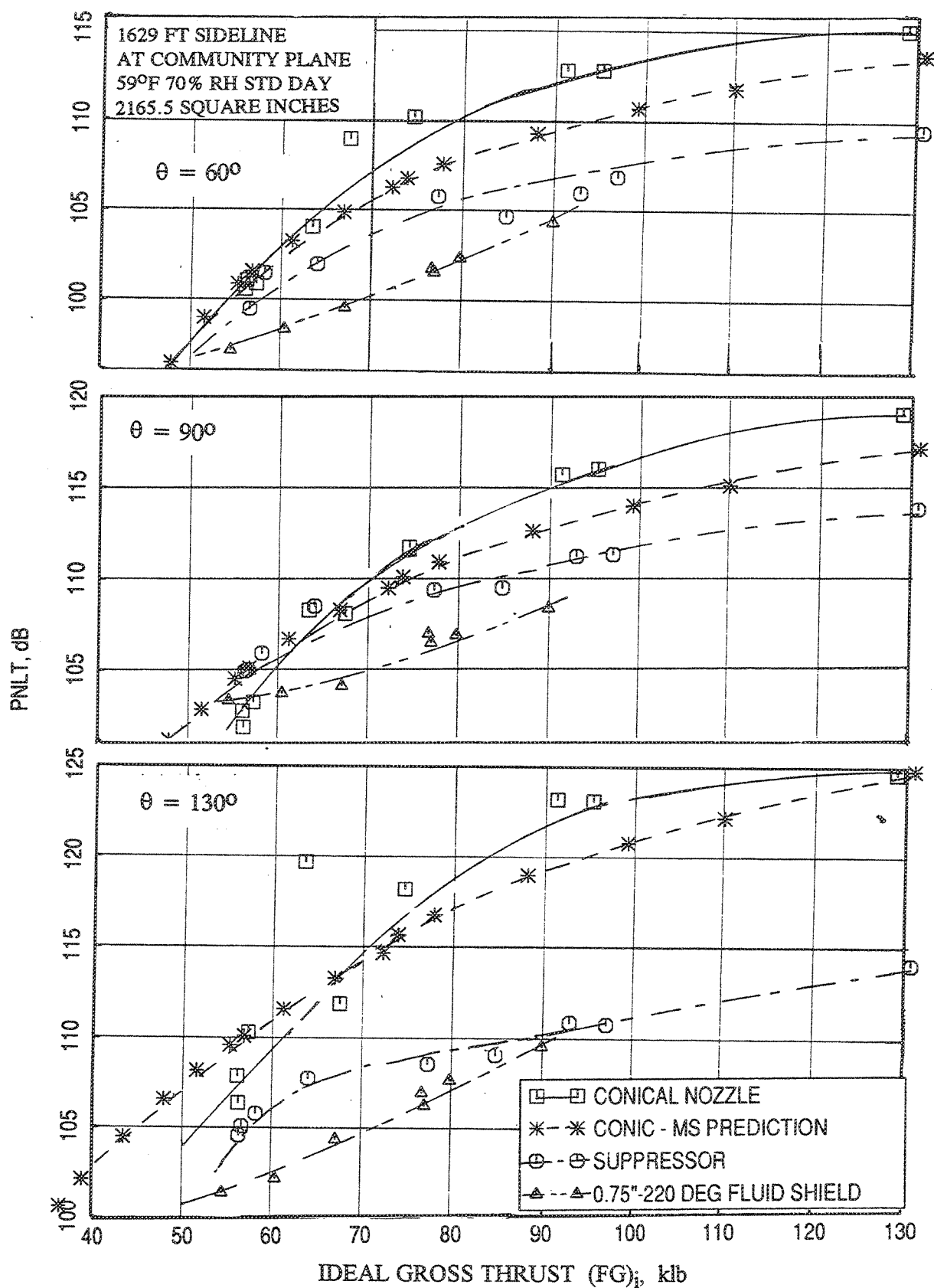


Figure 2.8-30. Noise suppression due to 0.75"-thick fluid shield nozzle in terms of PNL T data at different polar angles ( $\theta$ ) as a function of ideal gross thrust at static condition in an equal area basis of 2165.5 square inches.

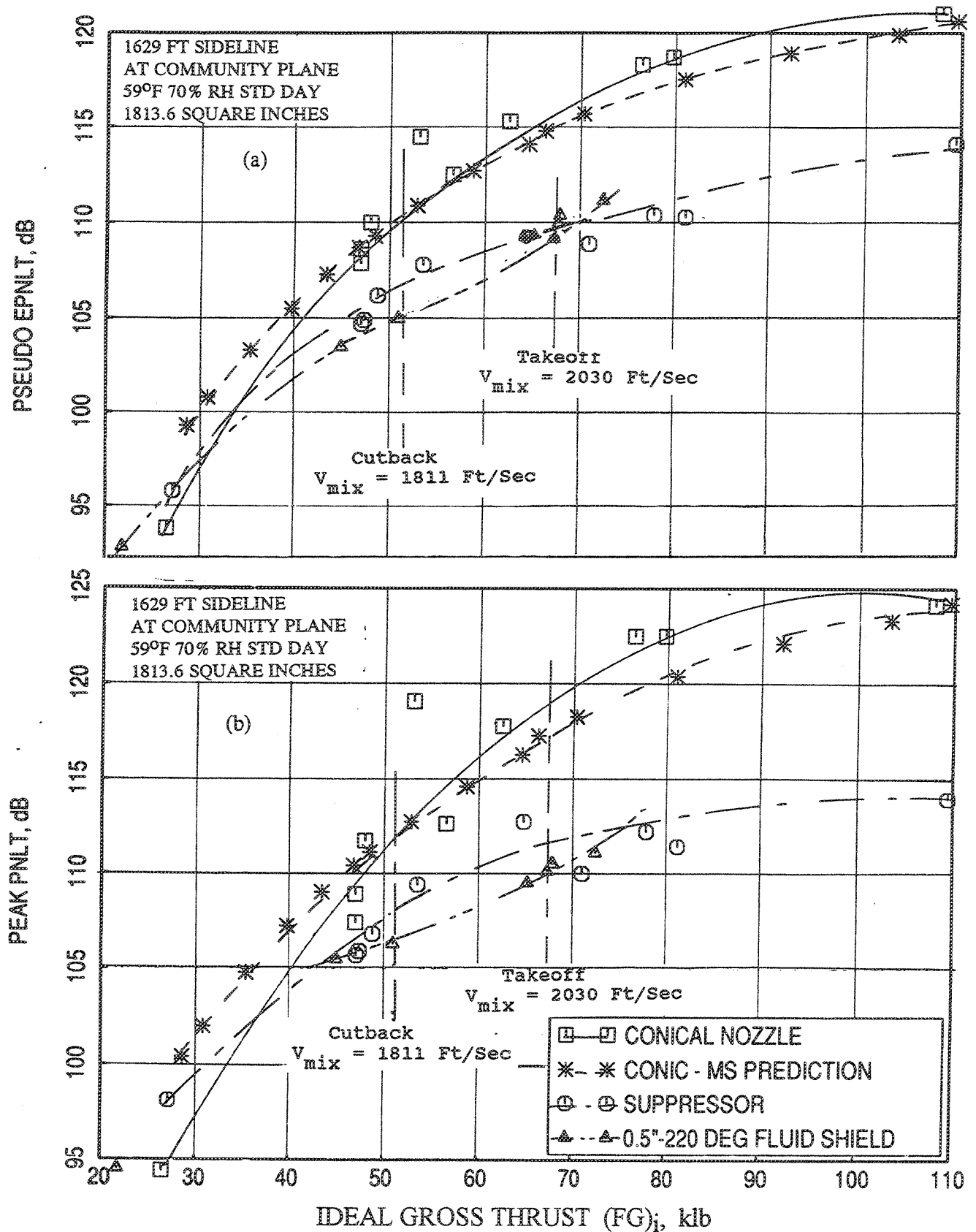


Figure 2.8-31. Noise suppression due to 0.5"-thick fluid shield nozzle in terms of (a) EPNLT and (b) peak PNL data as a function of ideal gross thrust at static condition in an equal area basis of 1823.6 square inches.

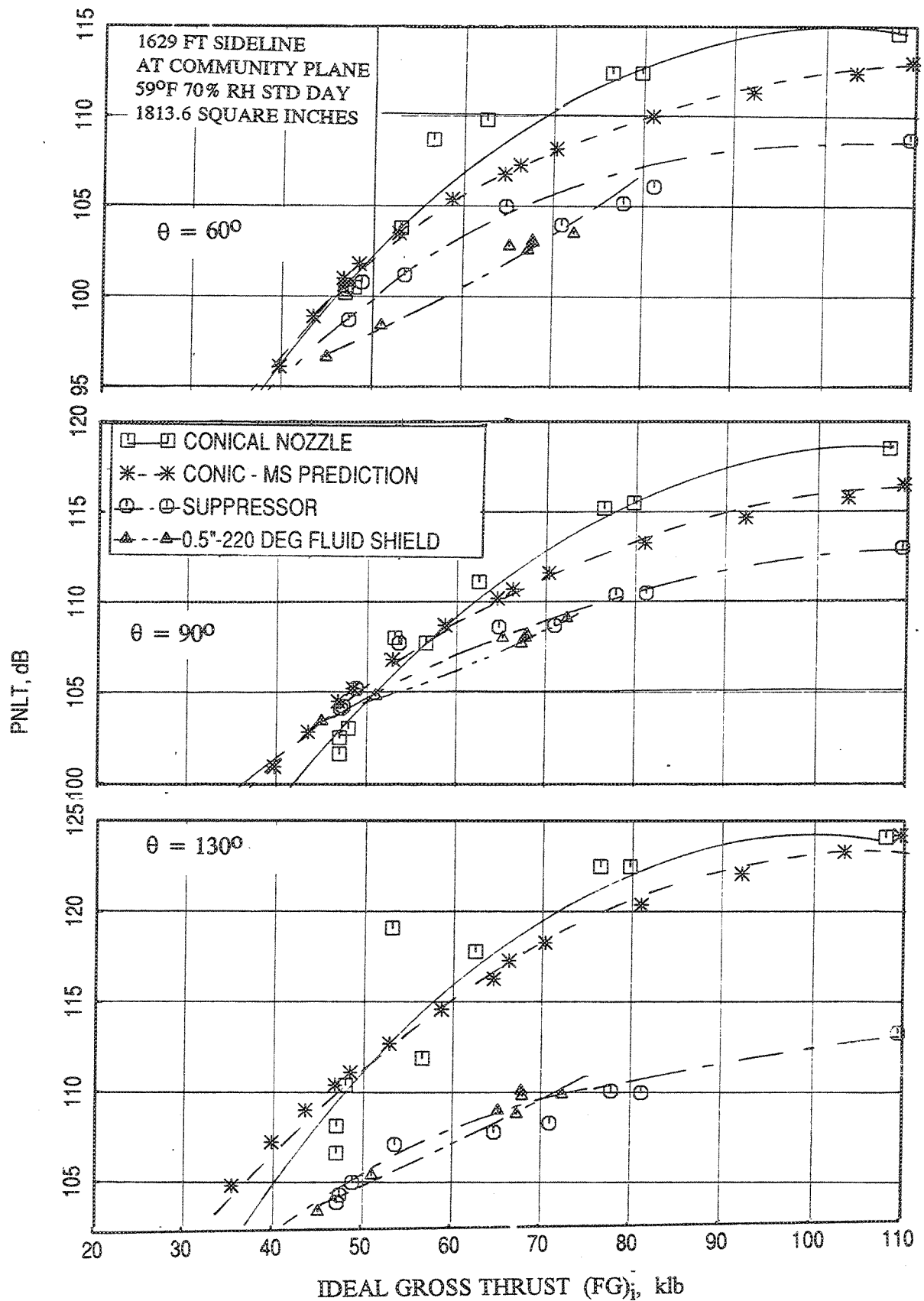


Figure 2.8-32. Noise suppression due to 0.5"-thick fluid shield nozzle in terms of PNLT data at different polar angles ( $\theta$ ) as a function of ideal gross thrust at static condition in an equal area basis of 1813.6 square inches.

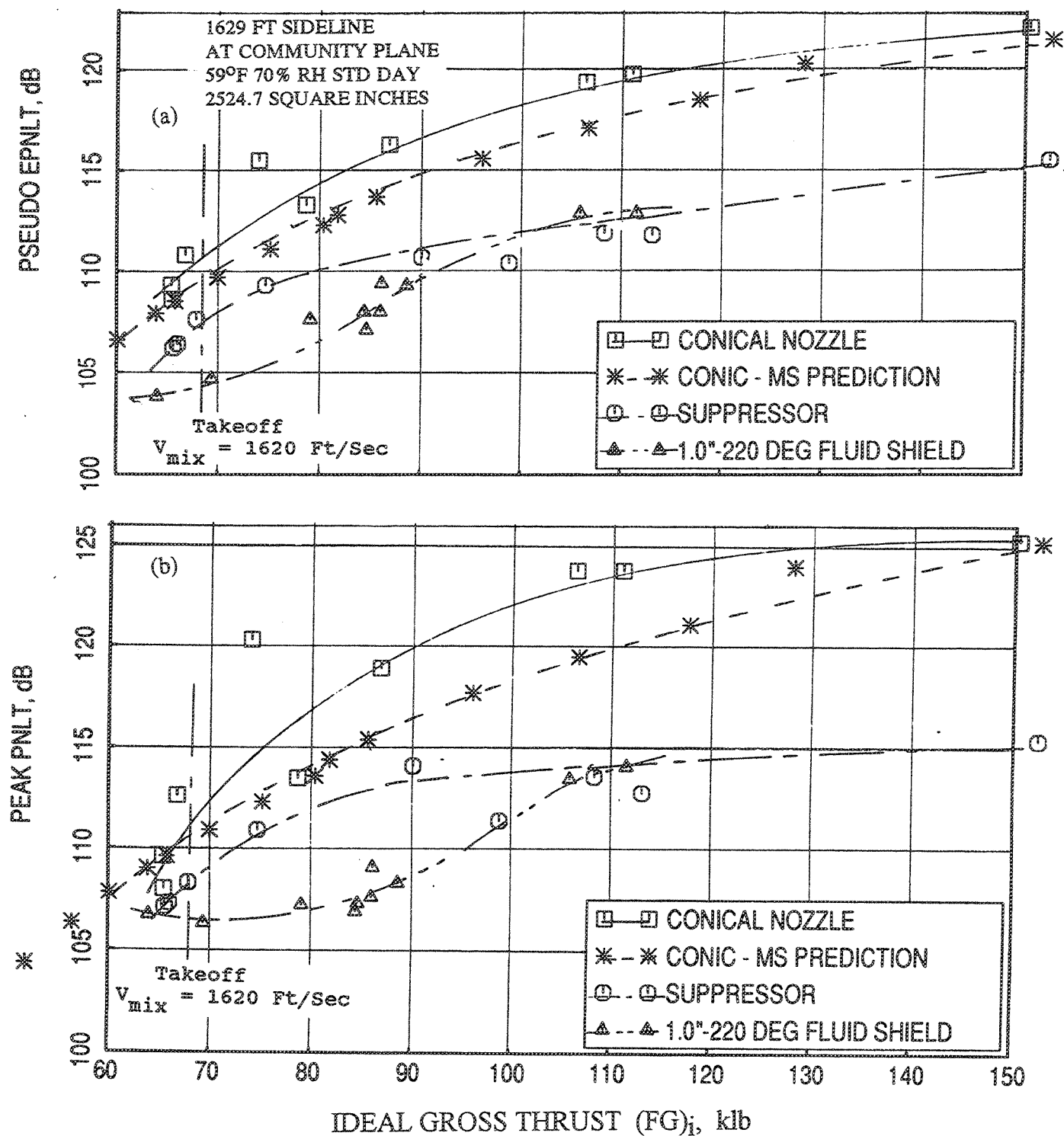


Figure 2.8-33. Noise suppression due to 1.0"-thick fluid shield nozzle in terms of (a) EPNLT and (b) PNLT data as a function of ideal gross thrust at static condition in an equal area basis of 2524.7 square inches.

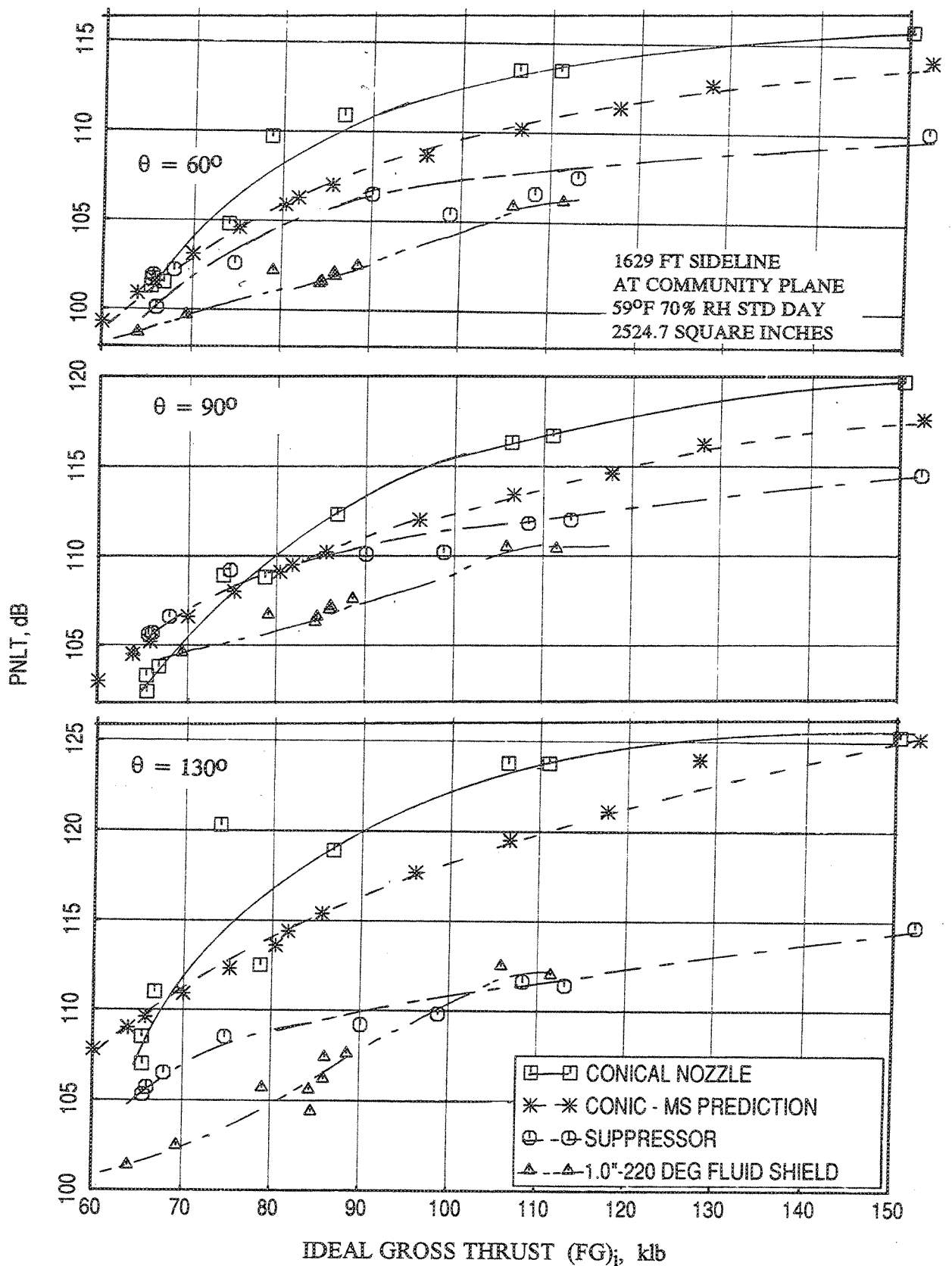


Figure 2.8-34. Noise suppression due to 1.0"-thick fluid shield nozzle in terms of PNL T data at different polar angles ( $\theta$ ) as a function of ideal gross thrust at static condition in an equal area basis of 2524.7 square inches.



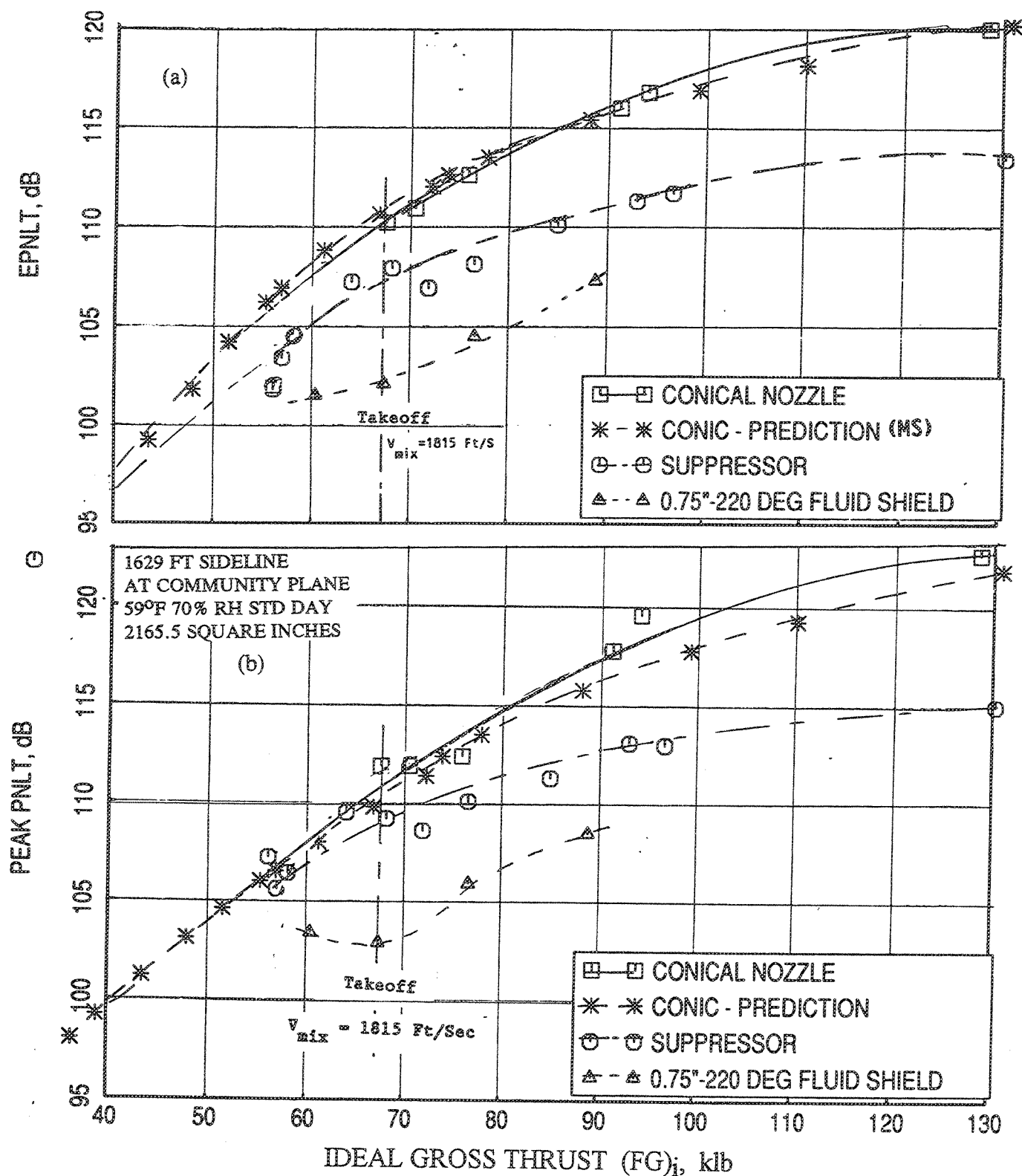


Figure 2.8-35. Noise suppression due to 0.75"-thick fluid shield nozzle in terms of (a) EPNLT and (b) peak PNLT data as a function of ideal gross thrust with flight simulation ( $M_F=0.32$ ) in an equal area basis of 2165.5 square inches.

area is obtained in the range of 55 to 90 klbs ideal gross thrust. A total EPNL reduction of about 8 dB is noted relative to the reference conic nozzle at the required takeoff thrust by this shield nozzle configuration at a  $V_{\text{mix}}$  of 1815 ft/sec. On a single engine free field basis, FAR 36 Stage 3 sideline noise requirement is about 98.5 EPNdB. EPNL achieved is about 102 dB. Thus, the best of shield configurations still misses FAR 36 Stage 3 requirement by about 3.5 EPNdB without accounting for any other noise components such as turbomachinery etc. These suppressions illustrate the noise reduction benefit of splitting the total engine flow (core+flame) into two stream nozzle, with the core stream being a multi-element nozzle and flame stream partially surrounding it as compared to exhausting the total engine flow through a single stream multi-element suppressor. PNLTs at three polar angles are plotted with respect to ideal gross thrust in Figure 2.8-36 for the 0.75"-thick fluid shield on equal area basis. The advantage of the fluid shield is clearly demonstrated in these results.

Similar results for the 0.5"-thick shield, where, all configurations are scaled to an area of 1813.6 square inch, are plotted in Figures 2.8-37 and 2.8-38. Again, we see the benefit of the shield. It should be noted that the 0.5"-thick shield is effective in the range of 50 to 75 klbs ideal gross thrust.

For 1.0"-thick shield, similar exercise is carried out by scaling all the configurations to 2524.7 square inch and the results are shown in Figures 2.8-39 and 2.8-40. Again, we see the benefit of the fluid shield and is effective in the thrust range of 65 to 115 klbs.

Flight simulation results indicate lower noise levels and relatively more noise suppression due to the fluid shields compared to static results. In equal area basis if the aerothermodynamic conditions for the suppressor and conic nozzle match with the mixed conditions of the fluid shield configurations, then, each configuration would generate the same amount of thrust with the same mixed velocity. For such cases, acoustic suppression with respect to  $V_{\text{mix}}$  would be similar to those observed with respect to gross thrust. This is illustrated in Figure 2.8-41 by plotting the unnormalized EPNLT and peak PNLT with respect to  $V_{\text{mix}}$  for 0.75"-thick fluid shield on an equal area basis of 2165.5 square inches. At  $V_{\text{mix}} = 1815$  the noise suppressions, both in EPNdB and peak PNdB are identical to those observed in Figure 2.8-35, where the same data are plotted with respect to gross thrust. At this velocity point the conic nozzle and the suppressor alone configuration were tested at aerothermodynamic conditions identical to the mixed conditions of the fluid shield nozzle. For most other

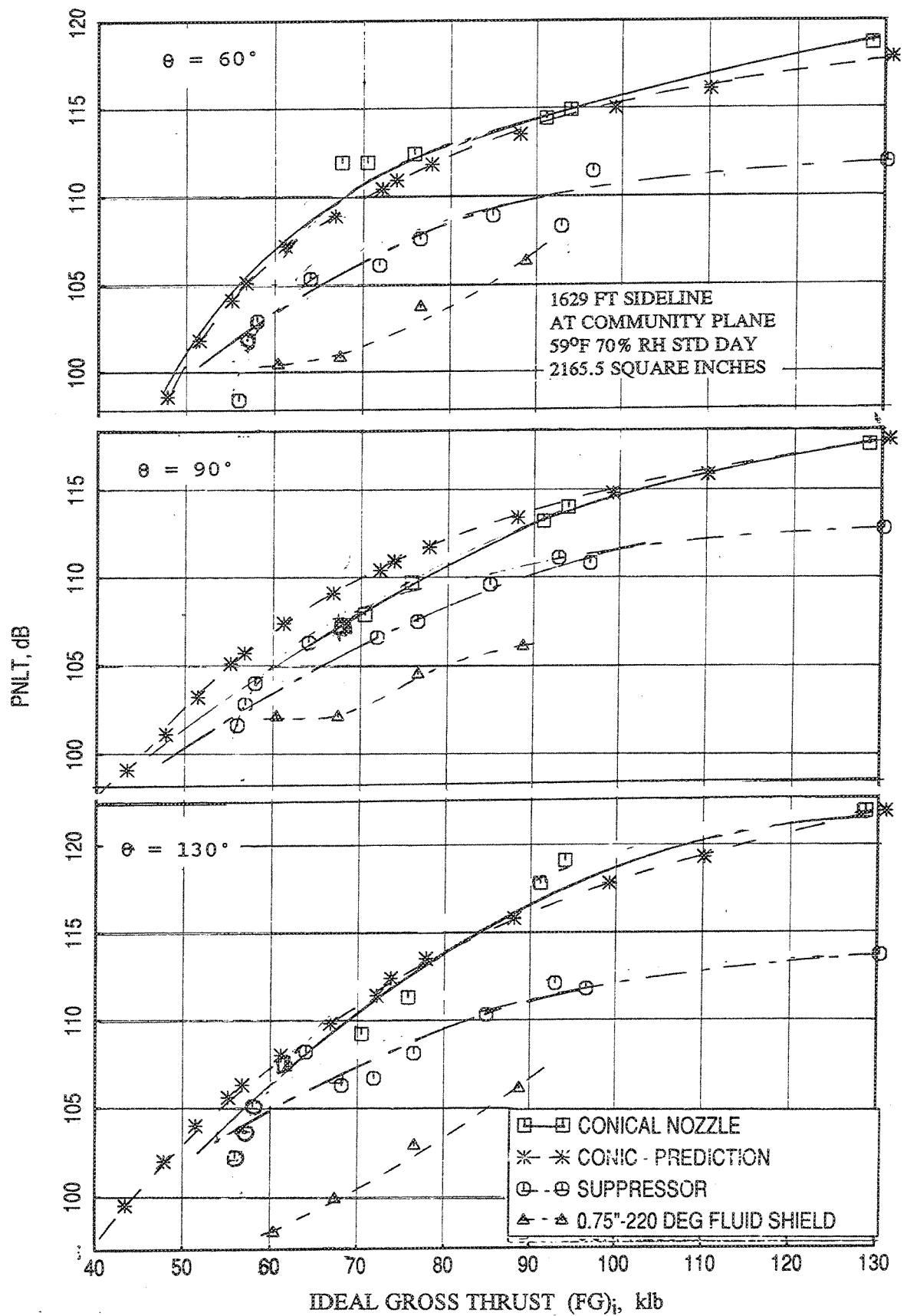


Figure 2.8-36. Noise suppression due to 0.75"-thick fluid shield nozzle in terms of PNLT data at different polar angles ( $\theta$ ) as a function of ideal gross thrust with flight simulation ( $M_F=0.32$ ) in an equal area basis of 2165.5 square inches.

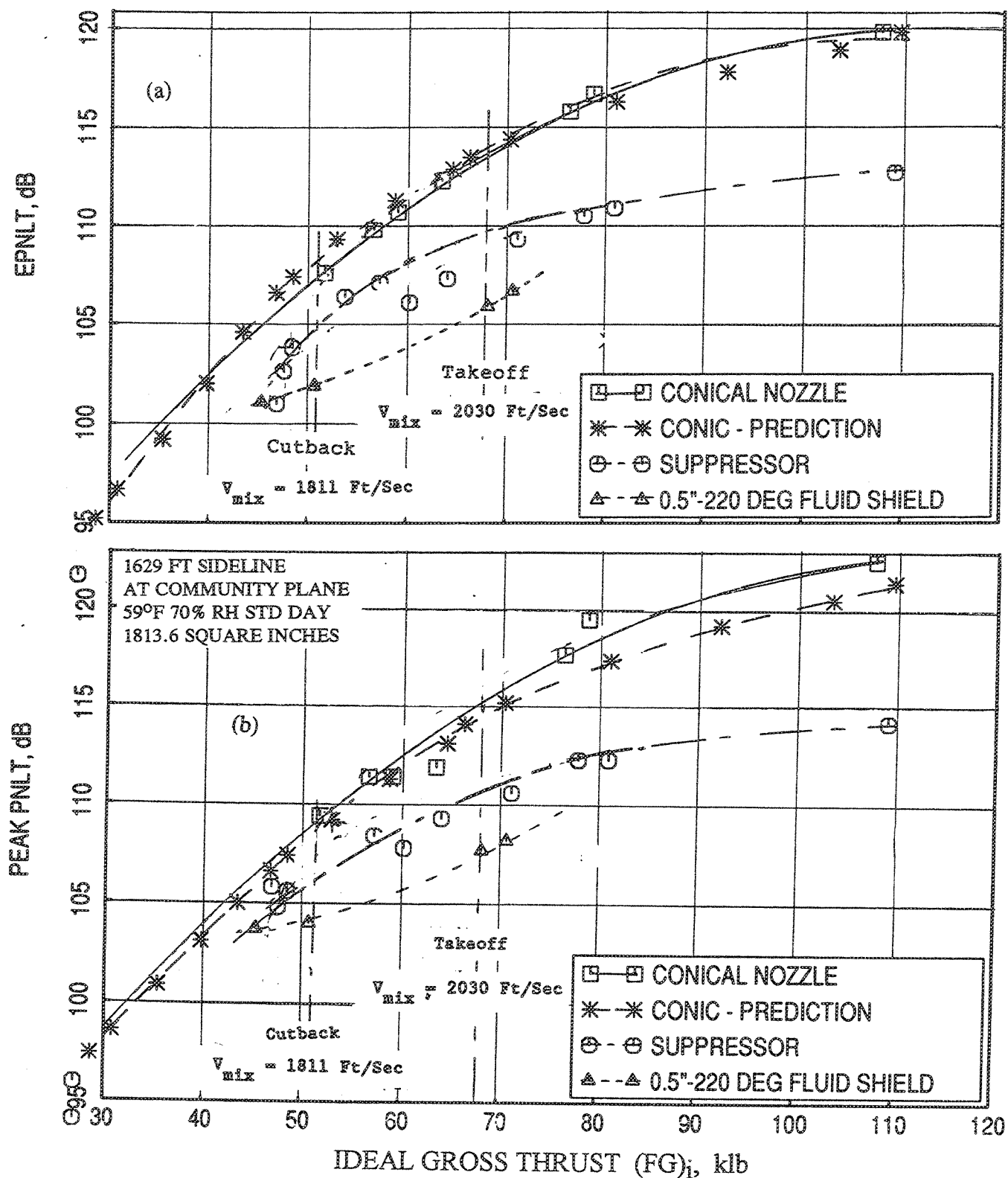


Figure 2.8-37. Noise suppression due to 0.5"-thick fluid shield nozzle in terms of (a) EPNLT and (b) peak PNLT data as a function of ideal gross thrust with flight simulation ( $M_F=0.32$ ) in an equal area basis of 1823.6 square inches.

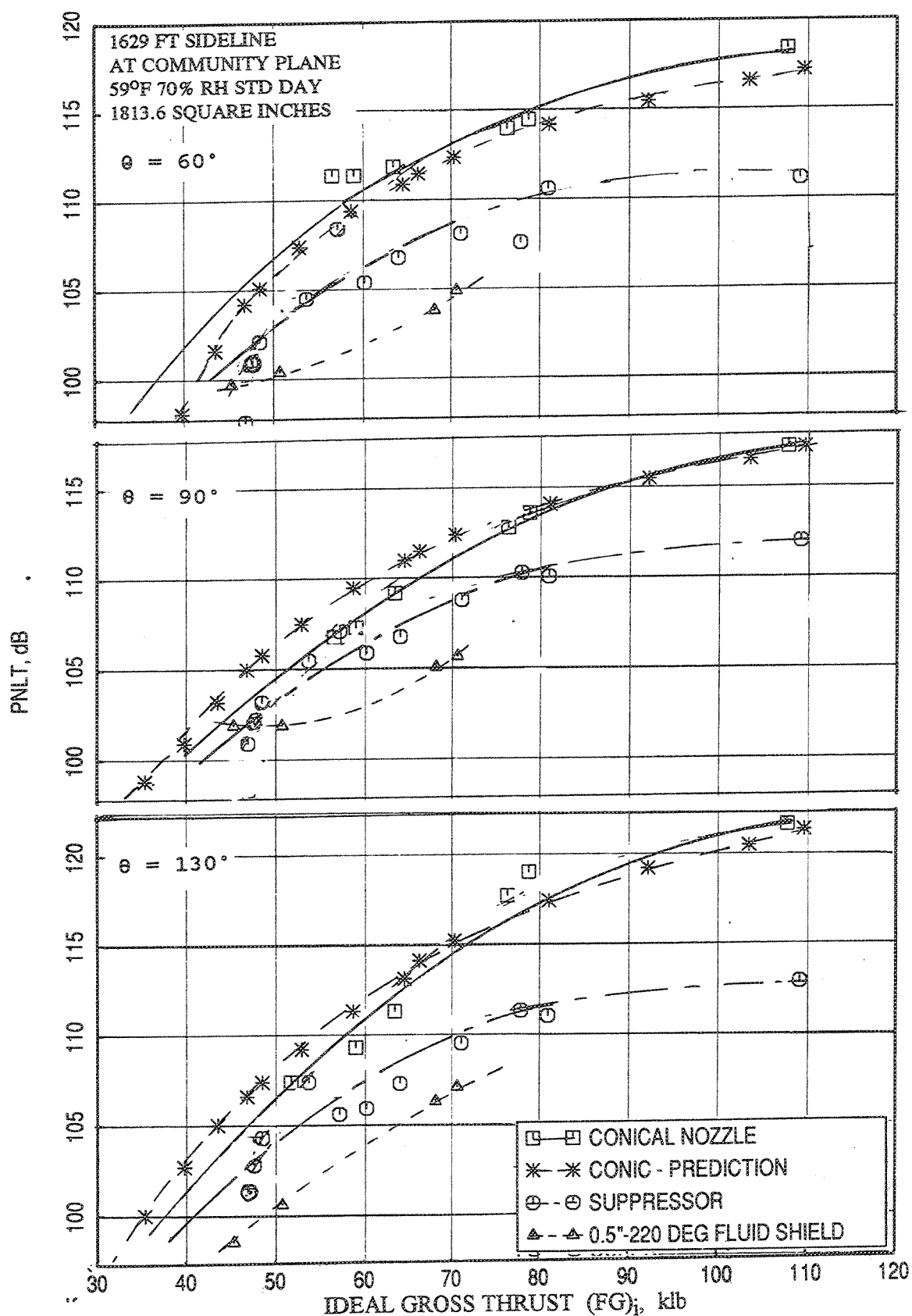


Figure 2.8-38. Noise suppression due to 0.5"-thick fluid shield nozzle in terms of PNL T data at different polar angles ( $\theta$ ) as a function of ideal gross thrust with flight simulation ( $M_F=0.32$ ) in an equal area basis of 1813.6 square inches.

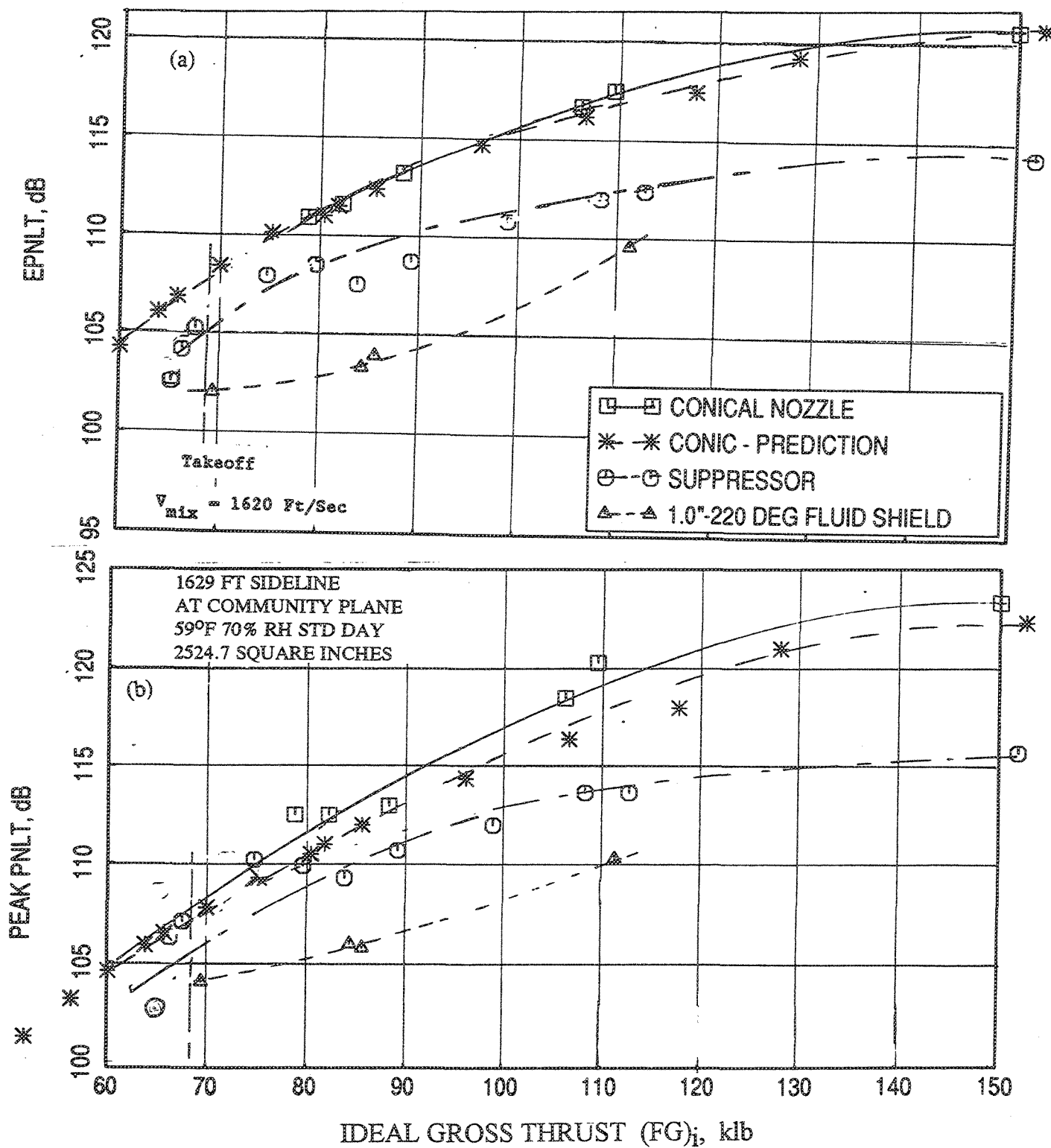


Figure 2.8-39. Noise suppression due to 1.0"-thick fluid shield nozzle in terms of (a) EPNLT and (b) PNLT data as a function of ideal gross thrust with flight simulation ( $M_F=0.32$ ) in an equal area basis of 2524.7 square inches.

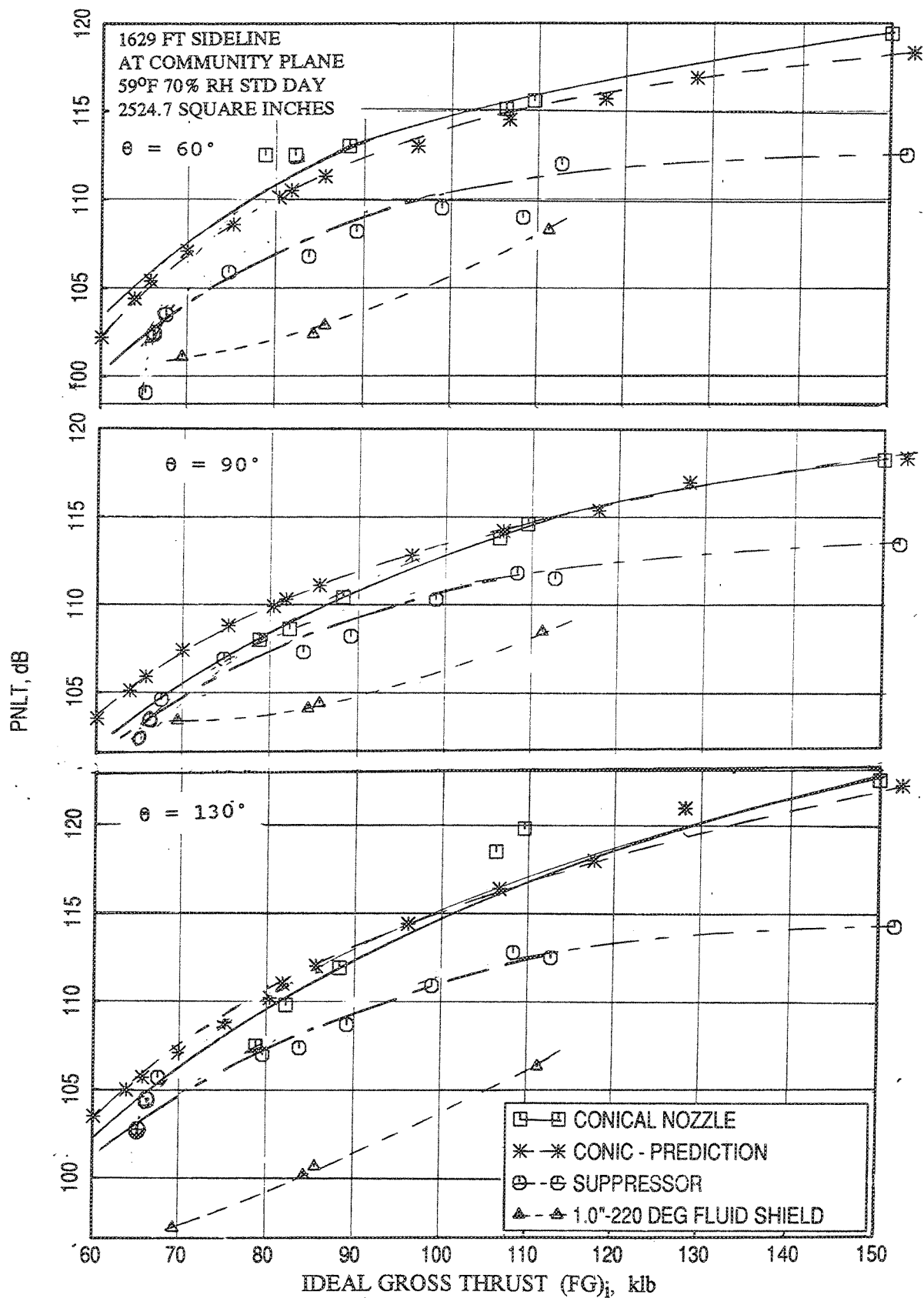


Figure 2.8-40. Noise suppression due to 1.0"-thick fluid shield nozzle in terms of PNL T data at different polar angles ( $\theta$ ) as a function of ideal gross thrust with flight simulation ( $M_F=0.32$ ) in an equal area basis of 2524.7 square inches.

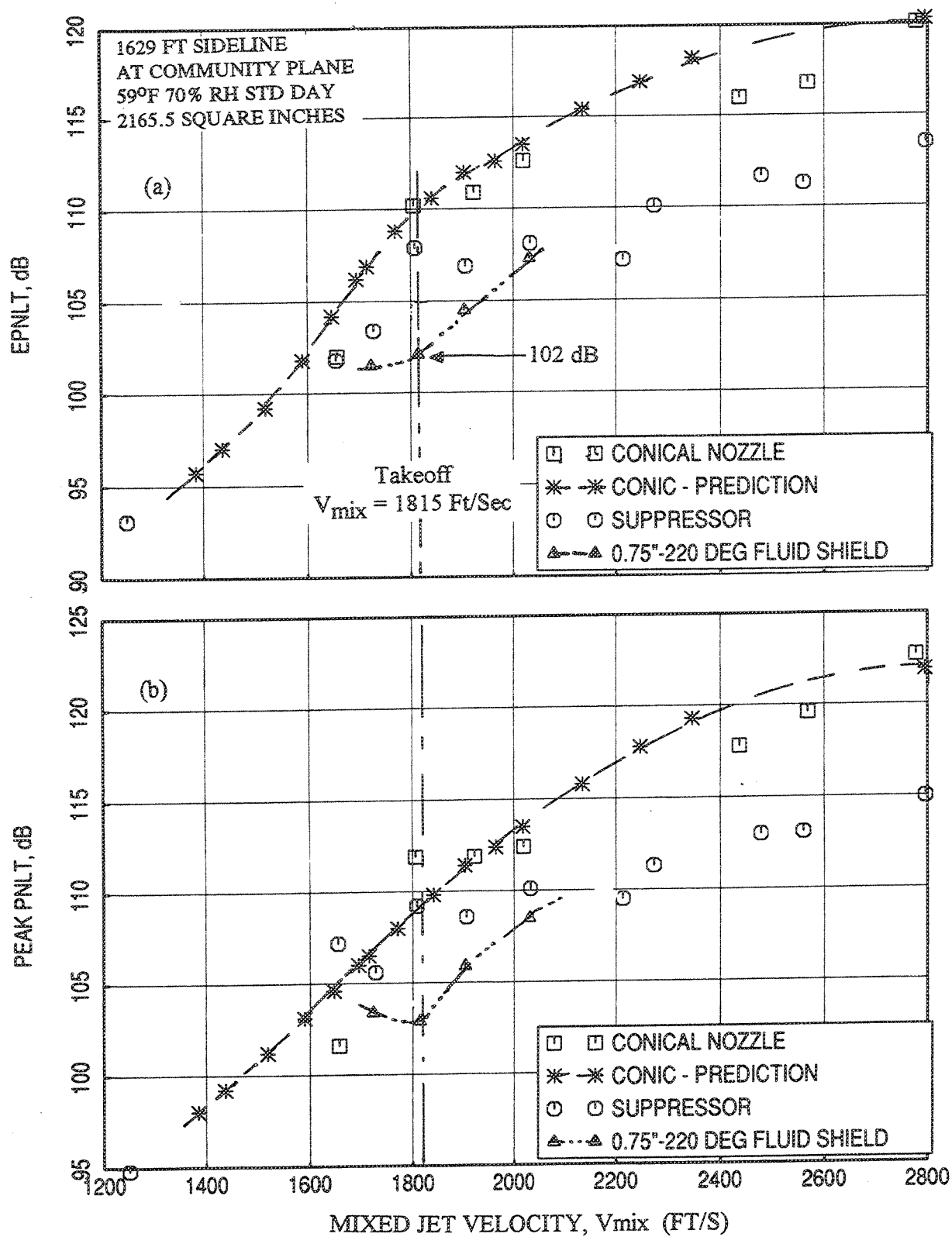


Figure 2.8-41. Noise suppression due to 0.75"-thick fluid shield nozzle in terms of (a) EPNLT and (b) peak PNL data as a function of mixed jet velocity  $V_{mix}$  with flight simulation ( $M_F=0.32$ ) in an equal area basis of 2165.5 square inches.



velocity points the aerothermodynamic conditions for the suppressor alone and the conic nozzle were not the same as the fluid shield mixed conditions. Hence, the acoustic suppression with respect to  $V_{mix}$  are not identical to the corresponding points shown with respect to gross thrust (see Figure 2.8-35) and hence, the data at these points need to be normalized for small differences in thrust and density between the single stream configurations and fluid shield configuration for  $V_{mix}$  basis. Figure 2.8-42 shows the acoustic suppressions in terms of normalized EPNLT for the three fluid shield nozzles of different thicknesses with respect to  $V_{mix}$  on equal area basis.

### 2.8.3 Noise Suppression Due to Fluid Shield Nozzles With Respect to Core Stream Velocity ( $V_{j,p}$ ):

Another way to examine the noise benefit of fluid shield is to compare the results with respect to the core stream velocity,  $V_{j,p}$ . The normalized noise levels due to different fluid shields surrounding the suppressor compared to the suppressor alone configuration, at a fixed  $V_{j,p}$ , which would indicate the noise benefit of adding the fluid shield to the suppressor system. In this situation, the noise comparison becomes more meaningful, since the primary stream (i.e., the suppressor) conditions remain the same for all the configurations. Hence, the additional noise suppression due to fluid shield is clearly identified. This is comparable with the noise suppression due to an ejector attached to a multichute mixer, where, the noise benefit is examined with respect to ideal core stream velocity.

**Static Data :** Figure 2.8-43 shows the noise suppression due to fluid shields of different thicknesses in terms of pseudo EPNLT and peak PNLT. Noise suppression increases with increasing shield thickness. Noise benefit of as high as 7 EPNdB is observed for 0.75" and 1.0" thick shields with respect to the suppressor alone configuration. The effectiveness of the shield diminishes with increasing  $V_{j,p}$ . Normalized EPNLTs at different polar angles, plotted with respect to  $V_{j,p}$  in Figure 2.8-44, show substantial noise benefits in terms of PNdB.

In these figures, at a fixed x-coordinate, which is the core stream velocity of all the fluid shield configurations, the mixed velocities are different for each configuration and are lower compared to the core stream velocity. Hence, if one tries to compare the noise benefits with respect to mixed velocity, the shield results in Figures 2.8-43 and 2.8-44 would move to the left based on the mixed velocity. Hence, a lower noise

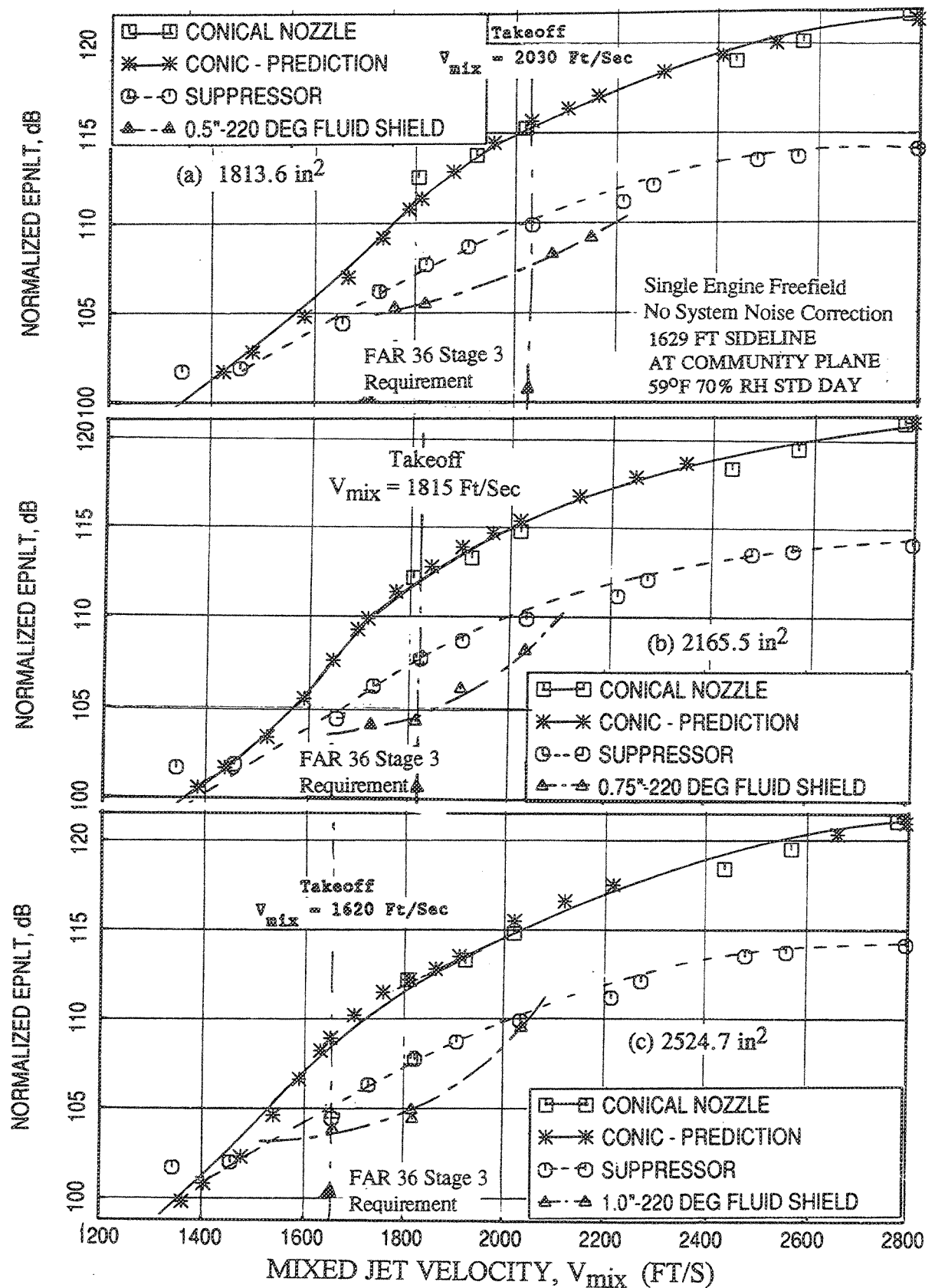


Figure 2.8-42. Noise suppression due to (a) 0.5"-thick, (b) 0.75"-thick, and (c) 1.0"-thick fluid shield nozzles in terms of EPNLT data as a function of mixed jet velocity with flight simulation ( $M_F=0.32$ ) in an equal area basis.

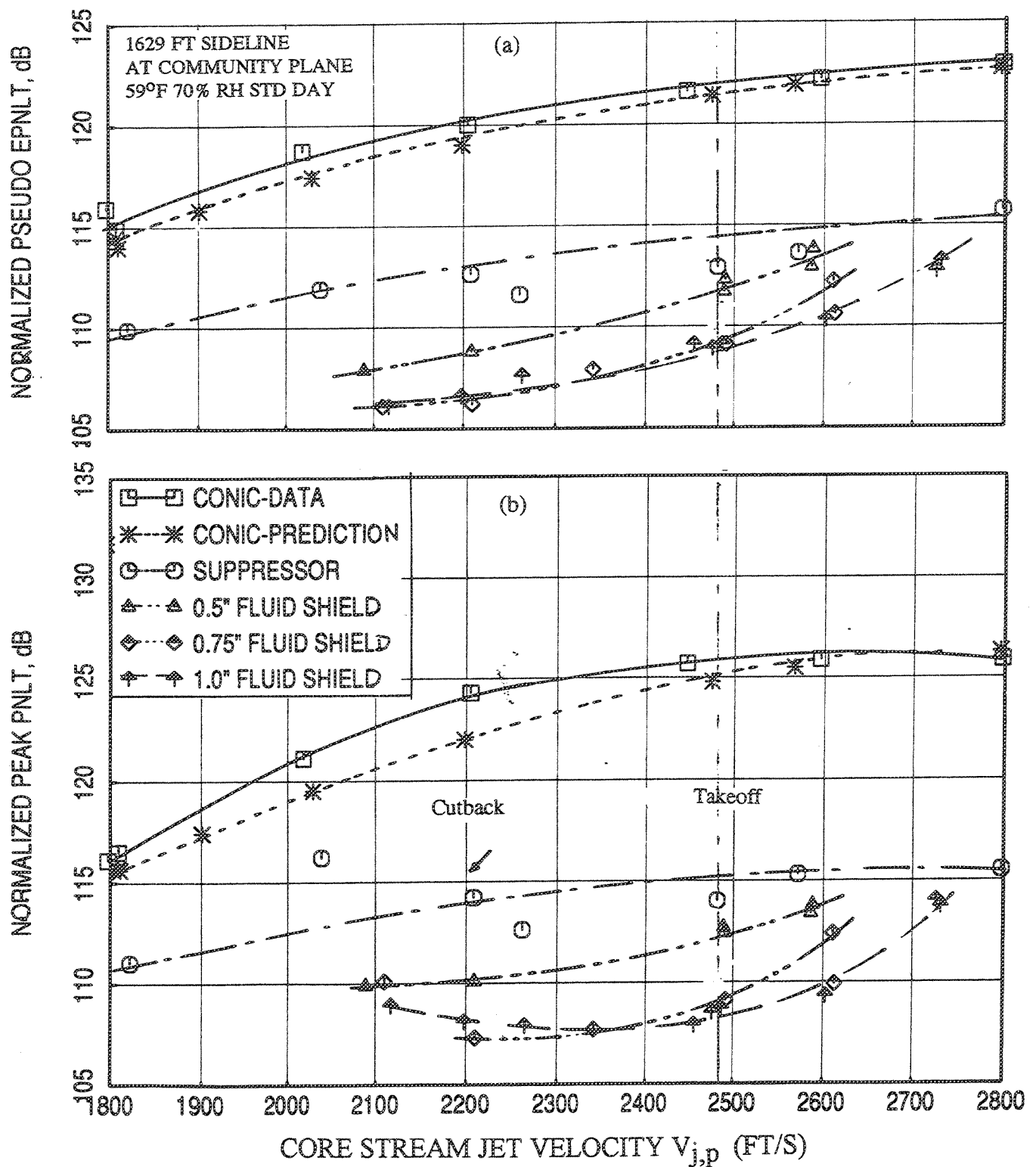


Figure 2.8-43. Noise suppression due to fluid shield nozzles in terms of normalized (a) pseudo EPNLT and (b) peak PNLT as functions of corestream jet velocity at static condition.

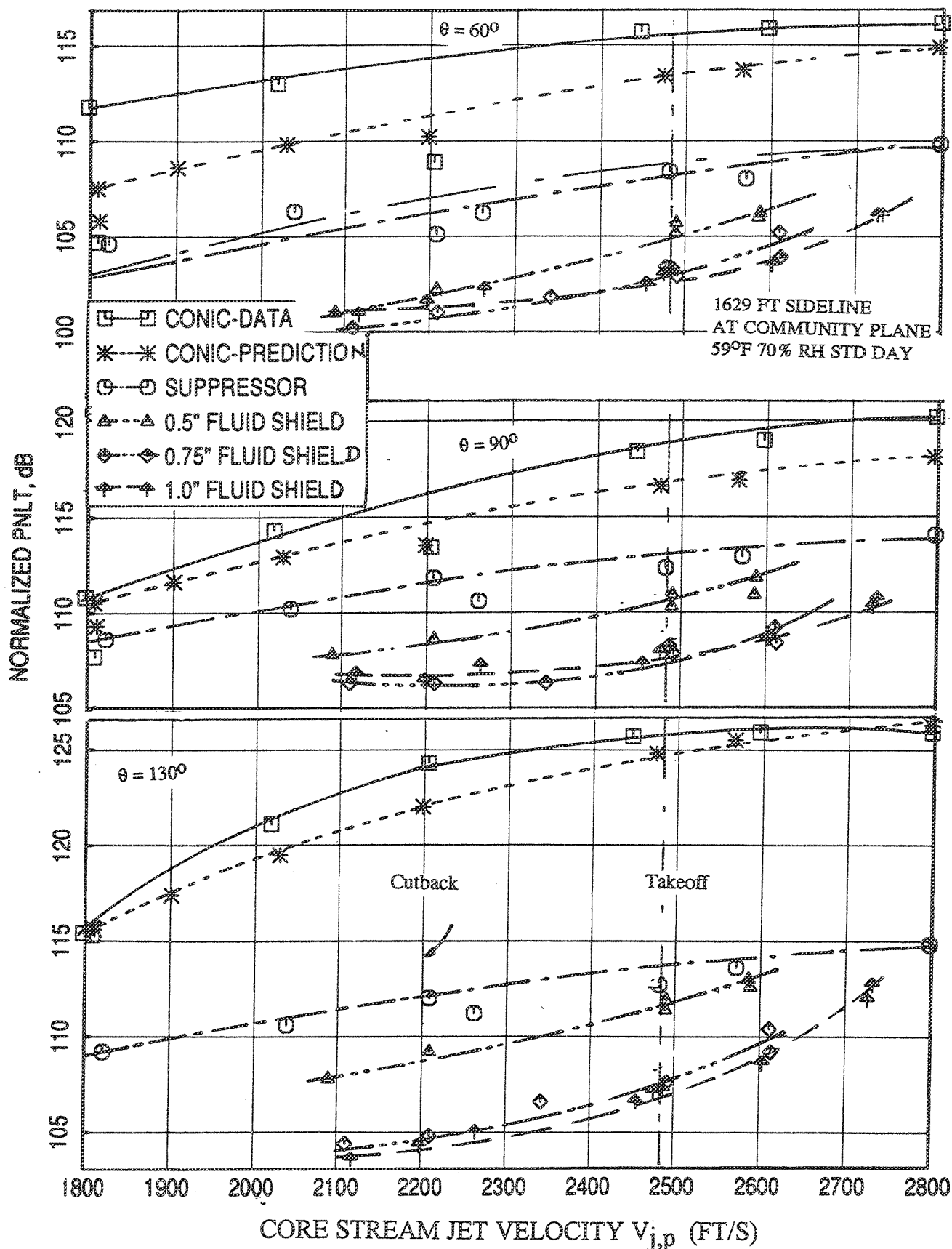


Figure 2.8-44. Noise suppression due to fluid shield nozzles in terms of normalized PNLT at different polar angles ( $\theta$ ) as functions of corestream jet velocity at static condition.

benefit will be observed at a mixed velocity point. This is the reason, why we observed small noise benefits for fluid shields with respect to mixed velocity comparisons.

To examine the effect of fluid shields in detail PNLT directivities, PWL and SPL spectra for the fluid shield configurations are compared with the conic nozzle and suppressor alone configuration at two fixed core stream jet velocities (i.e.,  $V_{j,p}$ ). The two fixed velocities considered here are about 2198 ft/sec and 2475 ft/sec, which correspond to the cutback and takeoff core stream velocities of the nominal flade cycle.

Results at Fixed  $V_{j,p} = 2198$  ft/sec: Normalized PNLT directivities and PWL spectra are shown in Figure 2.8-45 at a fixed core stream jet velocity of about 2198 ft/sec, which is the cutback condition for the nominal flade cycle. It should be noted that the PWL values for the fluid shield configurations are not the "real" PWL, since these nozzles are not axisymmetric. However, due to small azimuthal noise variation of these nozzles (will be shown later in this report) the PWLs evaluated on the basis of axisymmetry are expected to be reasonably close to the "real" values. Significant benefit in terms of PNdB suppression due to shield is observed. The amount of noise suppression is increased with shield thickness, especially between 0.5" and 0.75" thick shields. No significant additional noise reductions are noted in going from 0.75" to 1.0" thick shields indicating, 0.75" thick shield may be close to optimum. In terms of PWL, noise benefit is observed at higher frequencies above 315 Hz. Again, the benefit increases with increasing shield thickness. At lower frequencies, below 400 Hz, the PWL levels for the shields are higher compared to the suppressor alone configuration and the levels increase with increasing shield thickness. Normalized SPL spectra at a number of polar angles are plotted in Figure 2.8-46. Sound pressure levels decrease considerably at higher frequencies due to fluid shields compared to suppressor alone configuration and the benefit is higher with thicker fluid shield. The noise benefits with respect to shield thickness is not significant between 0.75" and 1.0" thick shields at this velocity condition.

Results at Fixed  $V_{j,p} = 2475$  ft/sec: Normalized PNLT directivities and PWL spectra are shown in Figure 2.8-47 at a fixed core stream jet velocity of about 2475 ft/sec, which is the takeoff condition for the flade cycle. Normalized SPL spectra at a number of polar angles are plotted in Figure 2.8-48. Again, the noise benefit increases with increasing shield thickness. The amount of noise suppression is increased with shield thickness. In terms of PWL and SPL, noise benefit is observed at higher frequencies

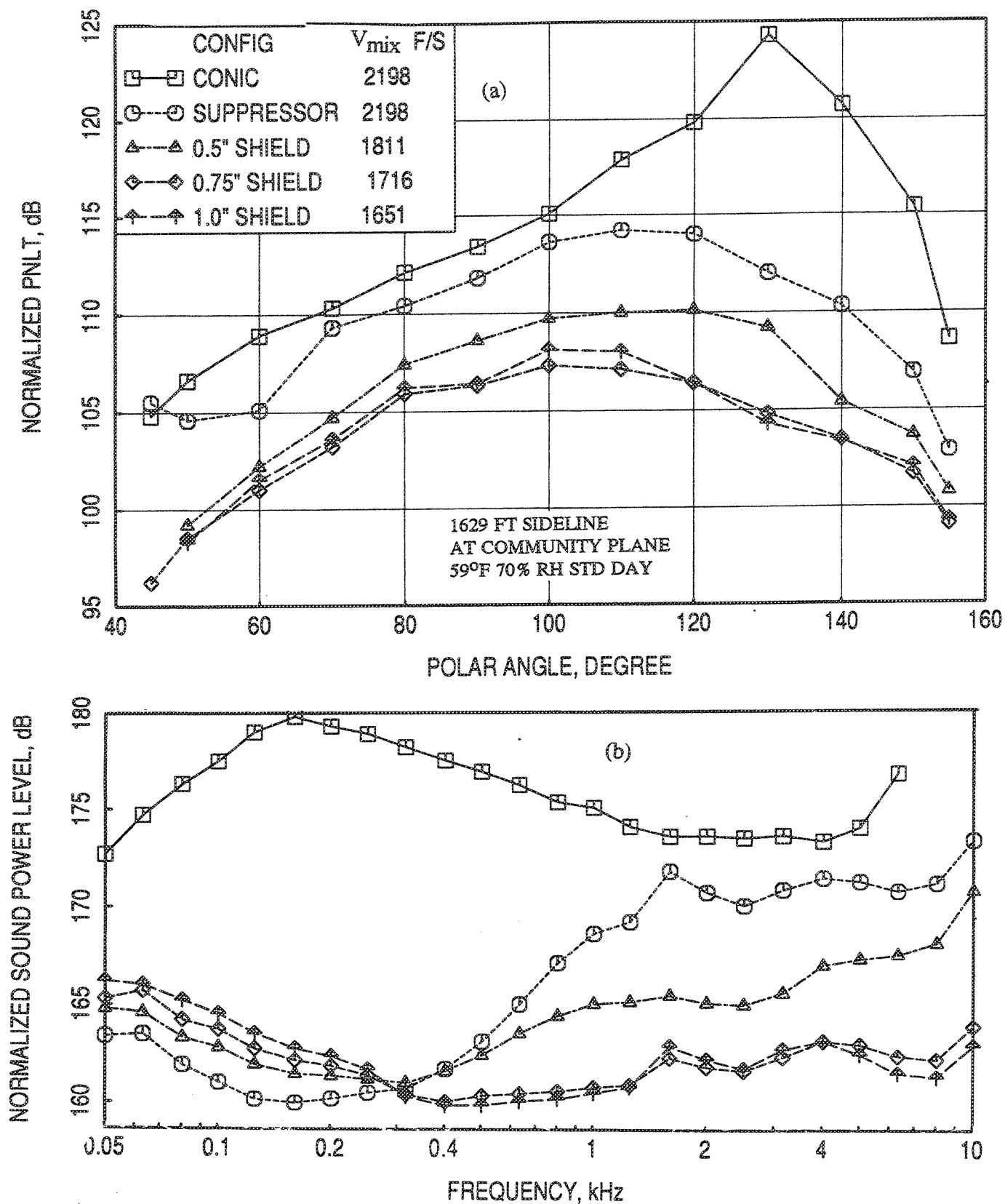


Figure 2.8-45. Noise suppression due to fluid shield nozzles in terms of normalized (a) PNLT directivities and (b) pseudo PWL spectra for a fixed nominal corestream jet velocity of 2198 ft/sec at static condition.

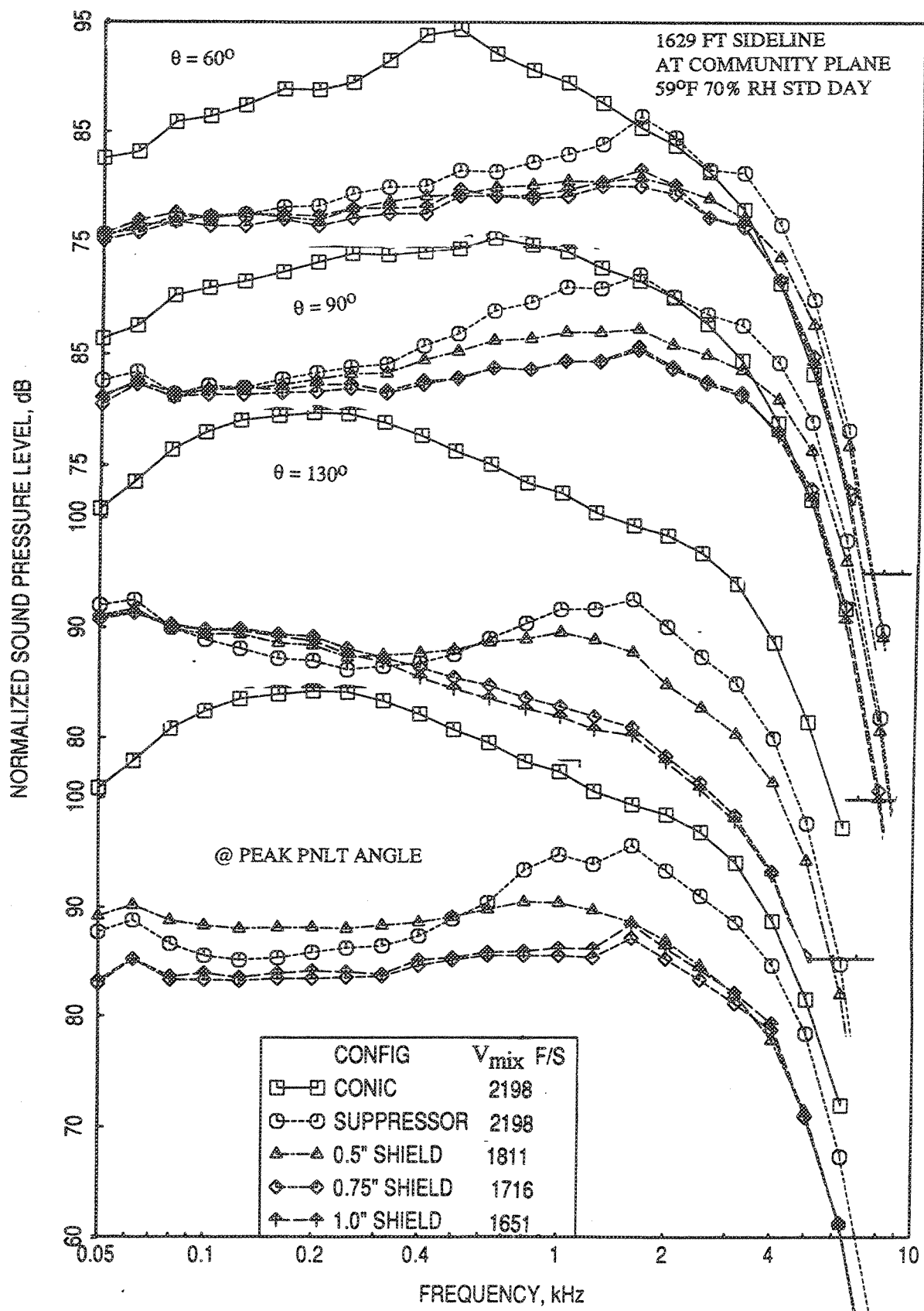


Figure 2.8-46. Noise suppression due to fluid shield nozzles in terms of normalized SPL spectra at different polar angles ( $\theta$ ) for a fixed nominal corestream jet velocity of 2198 ft/sec at static condition

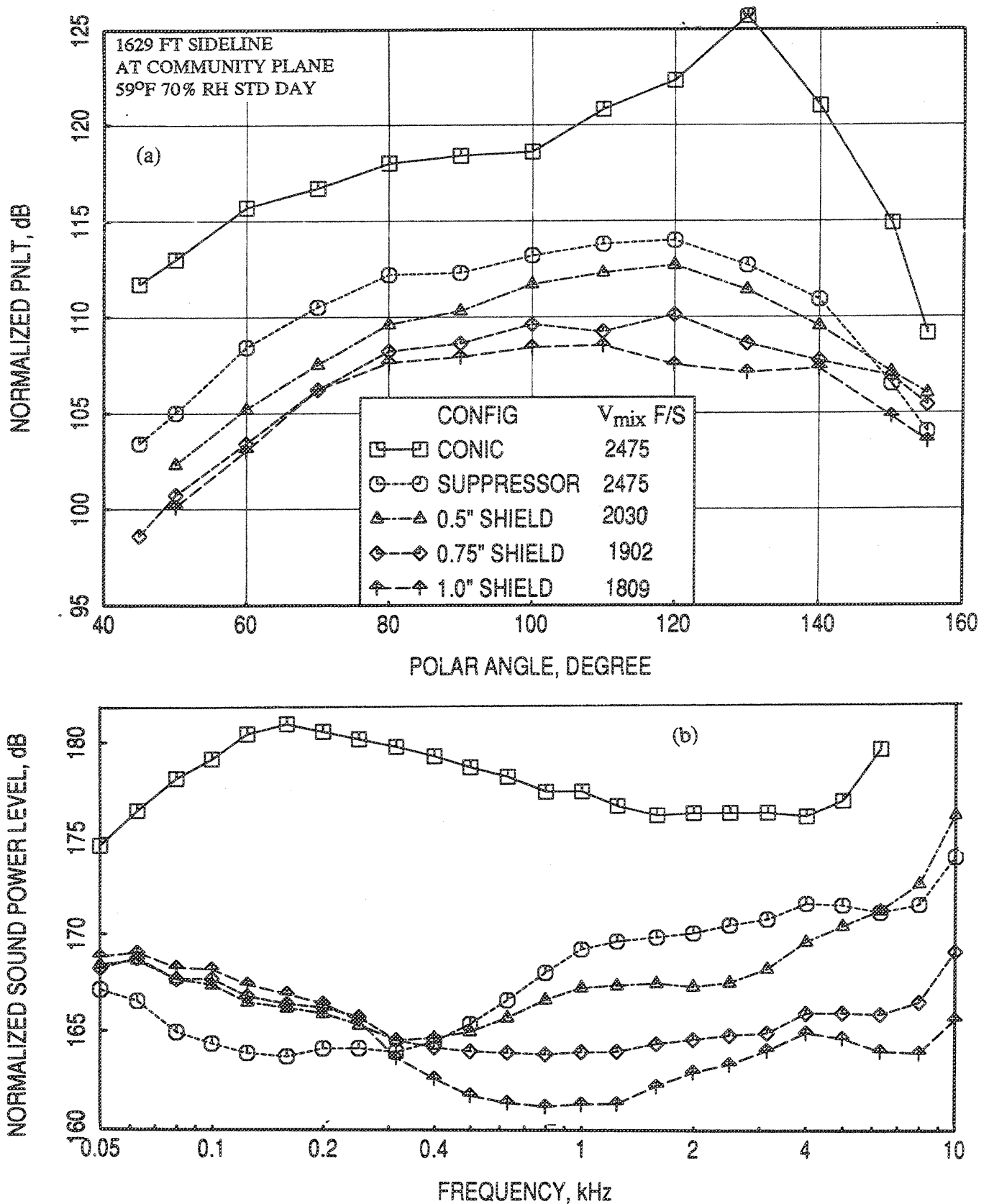


Figure 2.8-47. Noise suppression due to fluid shield nozzles in terms of normalized (a) PNLT directivities and (b) pseudo PWL spectra for a fixed nominal corestream jet velocity of 2475 ft/sec at static condition.



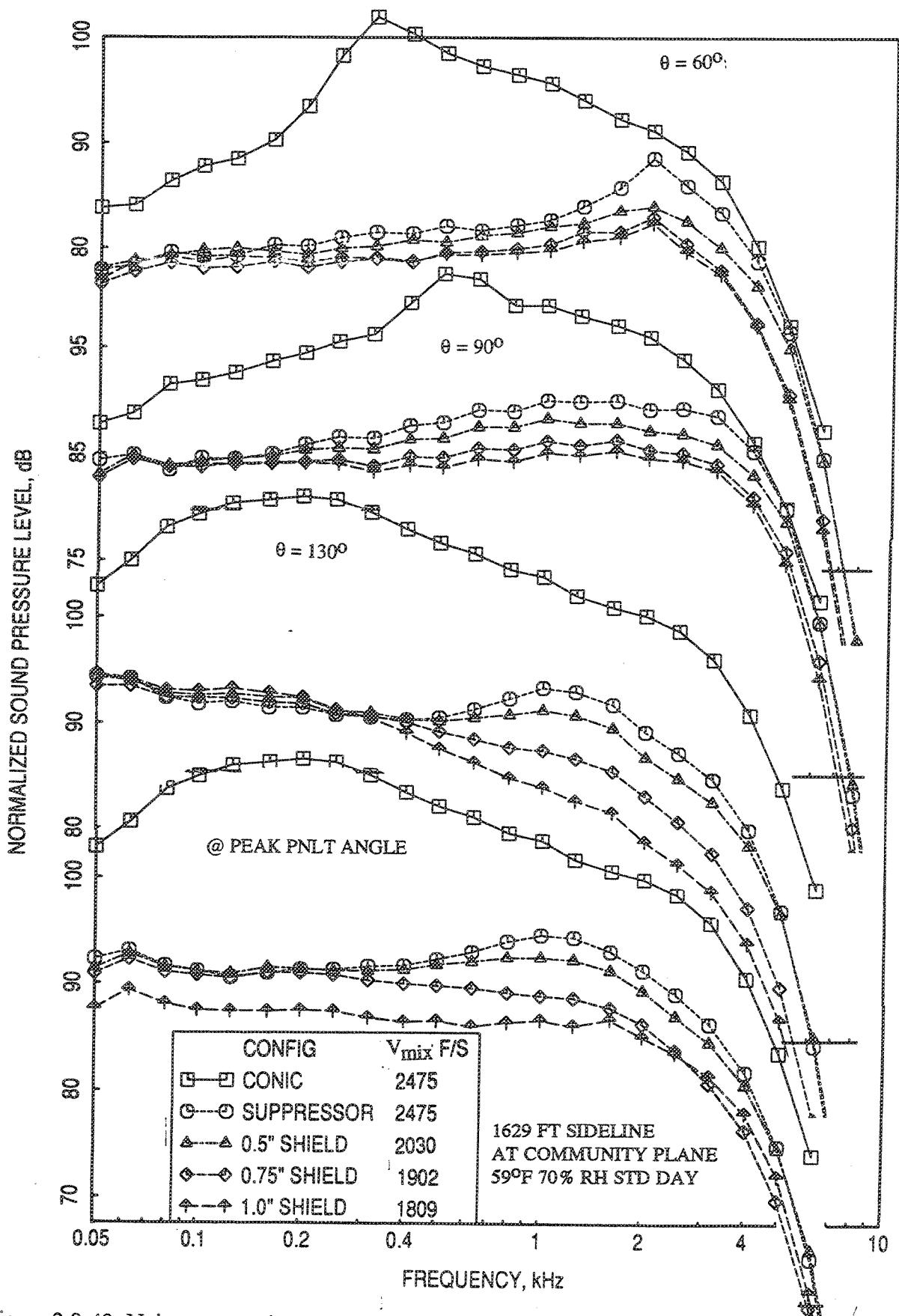


Figure 2.8-48. Noise suppression due to fluid shield nozzles in terms of normalized SPL spectra at different polar angles ( $\theta$ ) for a fixed nominal corestream jet velocity of 2475 ft/sec at static condition

above 315 Hz and the benefit increases with increasing shield thickness. At lower frequencies, below 400 Hz, the PWL levels for the shields are higher compared to the suppressor alone configuration and the levels increase with increasing shield thickness. Noise suppression in terms of SPL is higher in the rear arc compared to the forward arc. Unlike the cutback point, the noise benefit increases uniformly with respect to shield thickness, including the 1.0"-thick configuration.

**Flight Data :** Figure 2.8-49 shows the noise suppression due to fluid shields of different thicknesses in terms of EPNLT and peak PNLT with flight simulation ( $M_F=0.32$ ). Similar to static data, noise suppression increases with increasing shield thickness. Noise benefit of as high as 8 EPNdB is observed for 0.75" and 1.0" thick shields with respect to the suppressor alone configuration. The effectiveness of the shield diminishes with increasing  $V_{j,p}$ . Normalized EPNLTs at different polar angles, plotted with respect to  $V_{j,p}$  in Figure 2.8-50, show substantial noise benefits in terms of PNdB with flight simulation.

Results at Fixed  $V_{j,p}$  : Similar to the static case, normalized PNLT directivities, PWL and SPL spectra are shown in Figures 2.8-51 through 2.8-54 at two fixed core stream jet velocities of about 2198 ft/sec and 2475 ft/sec, which are the cutback and takeoff conditions for the flade cycle. The noise benefits observed in these figures are qualitatively similar to those observed for static condition, especially, that the noise suppressions in terms of PNLT, PWL, and SPL increase with increasing shield thickness. A major difference between static and flight cases is that the PWL and SPL levels are relatively lower, especially in the rear quadrant, with flight simulation.

#### 2.8.4 Comparison of Acoustic Results between Fluid Shield and Thermal Shield Configurations:

Several acoustic thermal shield (THSH) configurations using a 32-chute suppressor with hardwalled plug were tested at GEAE under a NASA contract (Ref. 2). Two of the configurations with thermal shield thickness of 0.48" and 0.97" are closely comparable with the current fluid shield (FLSH) configurations with 0.49" and 1.0" thick shields. Hence, the acoustic results for these configurations are compared in this section, addressing these thicknesses nominally as 0.5" and 1.0", respectively. Figure 2.8-55 shows the side views of the two thermal shield configurations. The 32-chute suppressor with hardwalled plug, used for thermal shield configurations are described

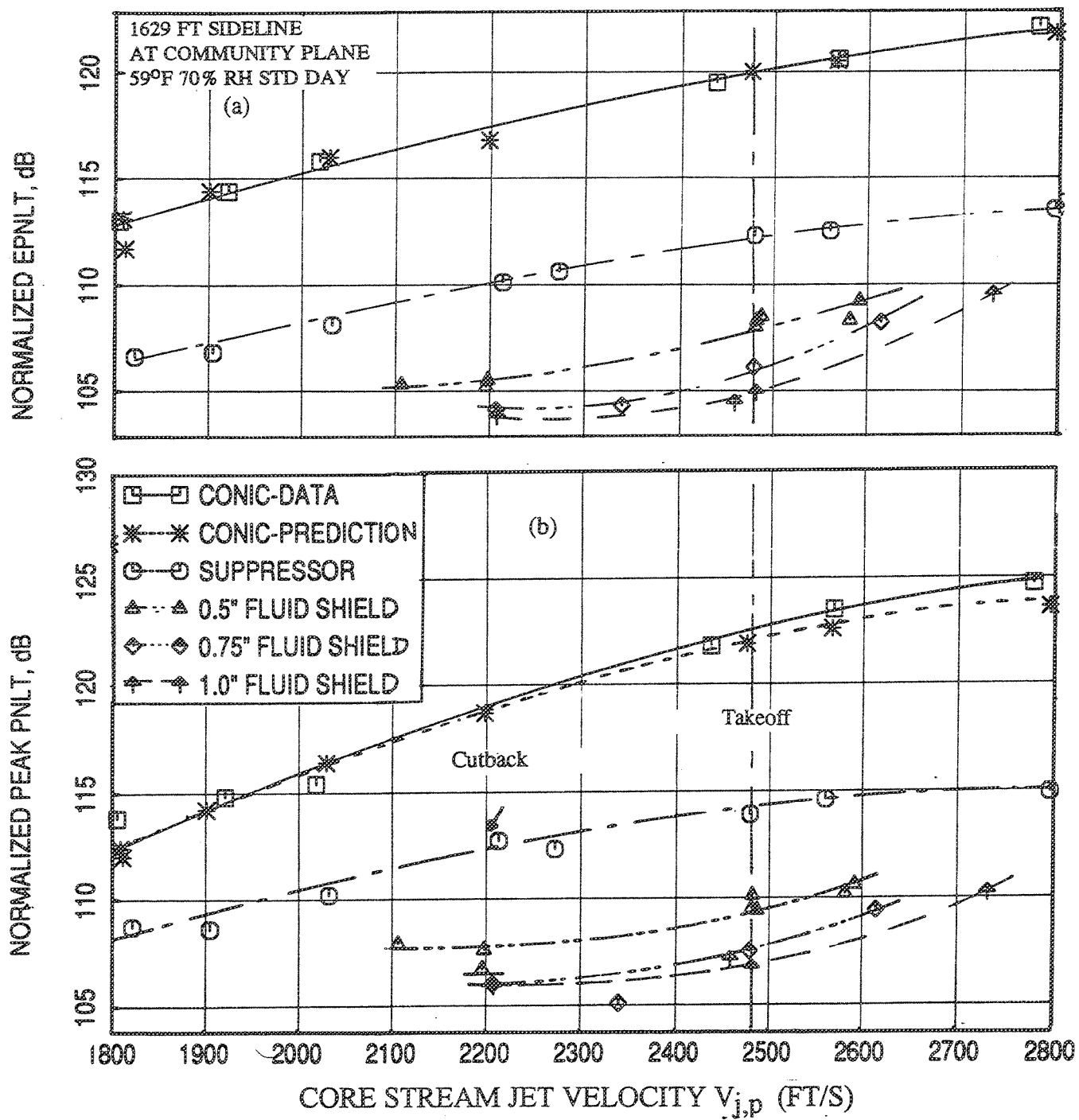


Figure 2.8-49. Noise suppression due to fluid shield nozzles in terms of normalized (a) EPNLT and (b) peak PNLT as functions of corestream jet velocity with flight simulation ( $M_F=0.32$ ).

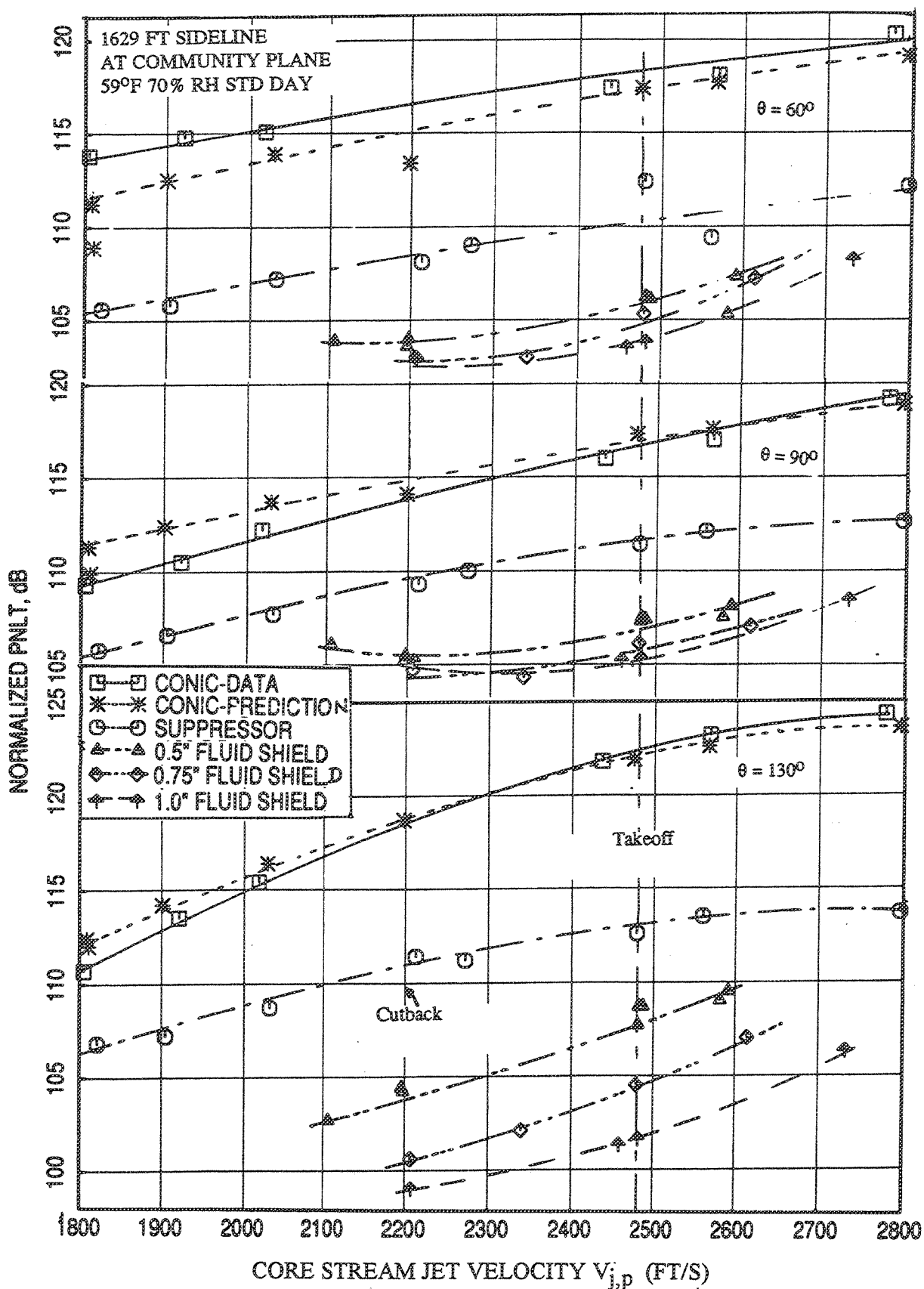


Figure 2.8-50. Noise suppression due to fluid shield nozzles in terms of normalized PNLT at different polar angles ( $\theta$ ) as functions of corestream jet velocity with flight simulation ( $M_F=0.32$ ).

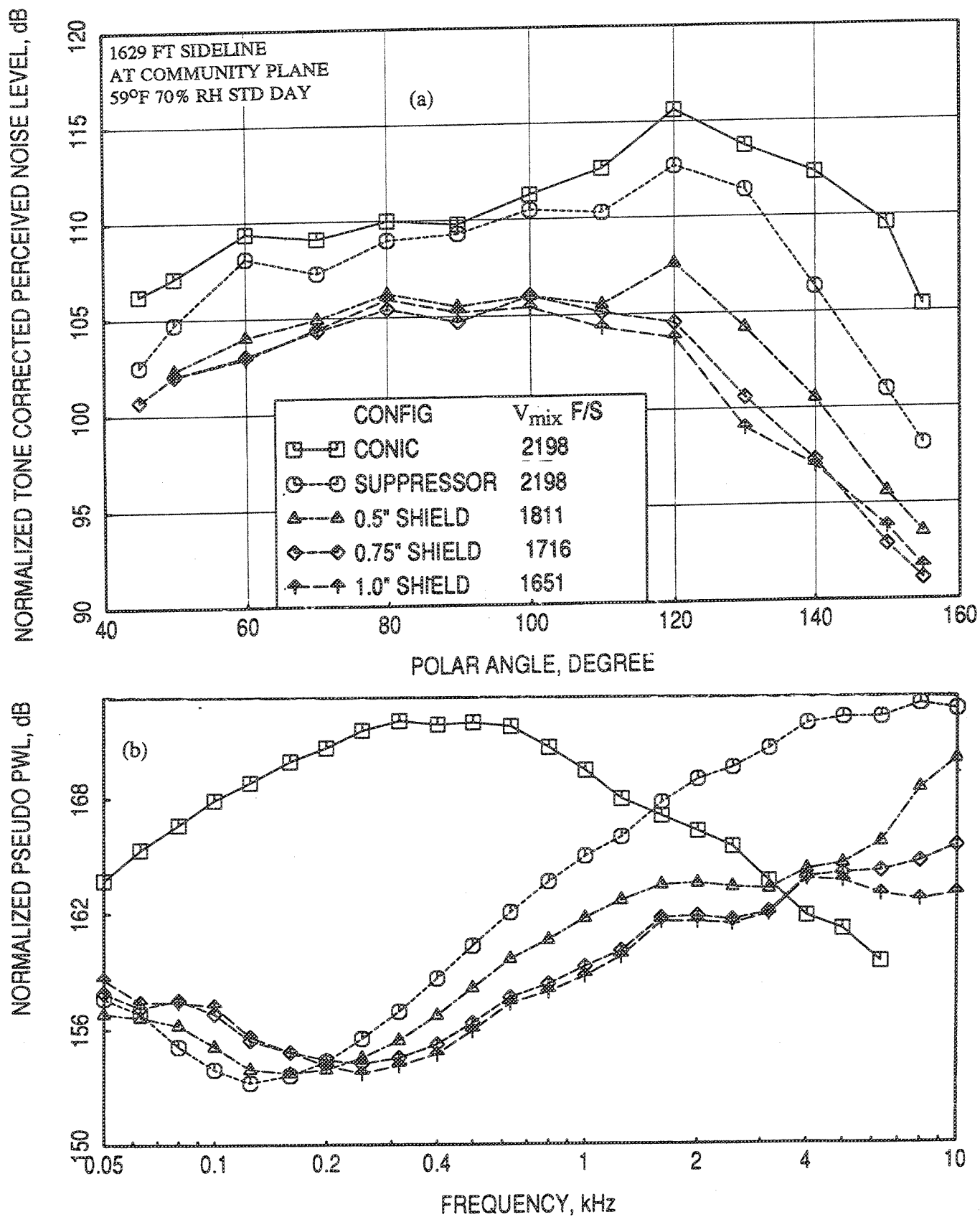


Figure 2.8-51. Noise suppression due to fluid shield nozzles in terms of normalized (a) PNLT directivities and (b) pseudo PWL spectra for a fixed nominal corestream jet velocity of 2198 ft/sec with flight simulation ( $M_F=0.32$ ).

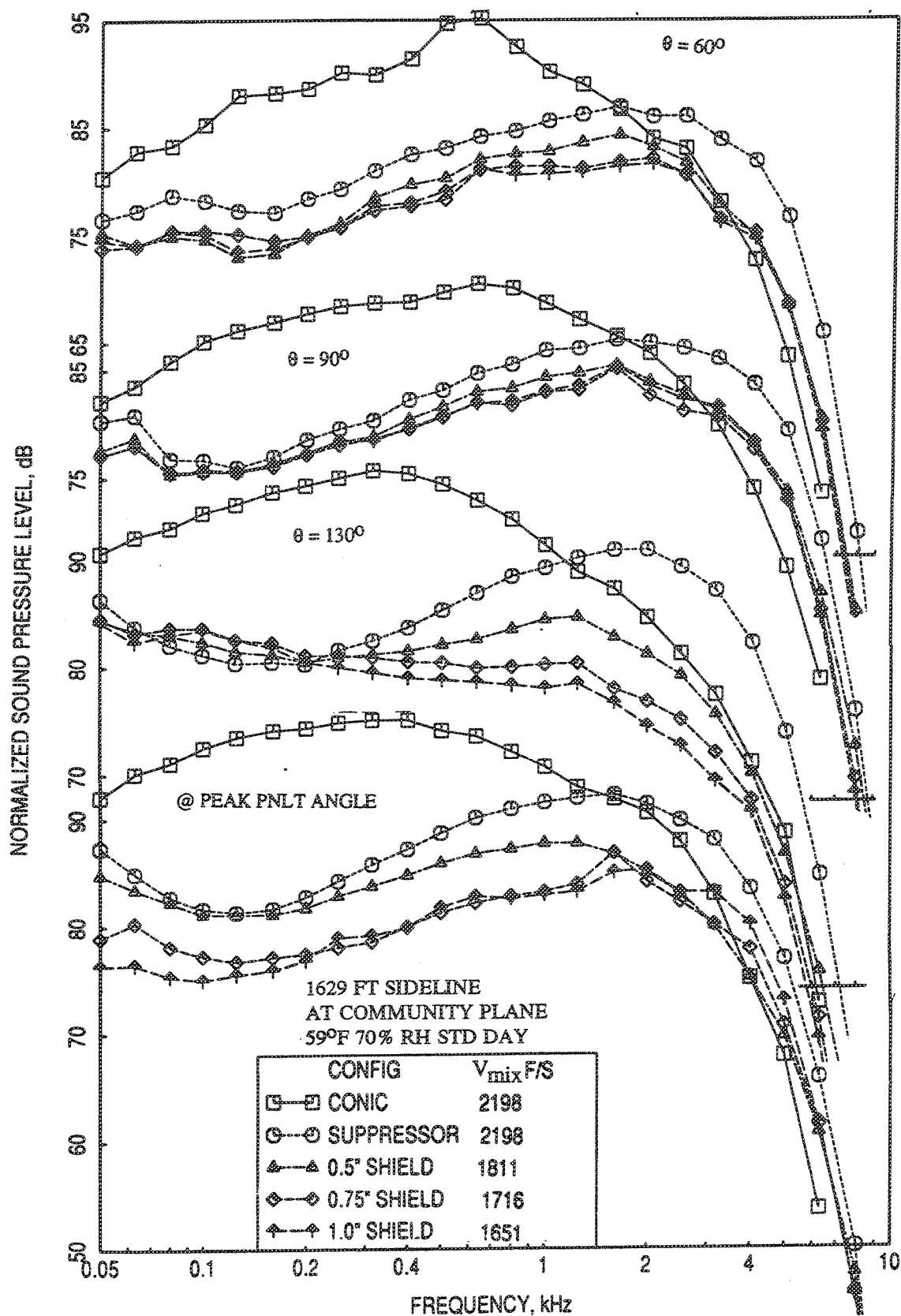


Figure 2.8-52. Noise suppression due to fluid shield nozzles in terms of normalized SPL spectra at different polar angles ( $\theta$ ) for a fixed nominal corestream jet velocity of 2198 ft/sec with flight simulation ( $M_F=0.32$ ).

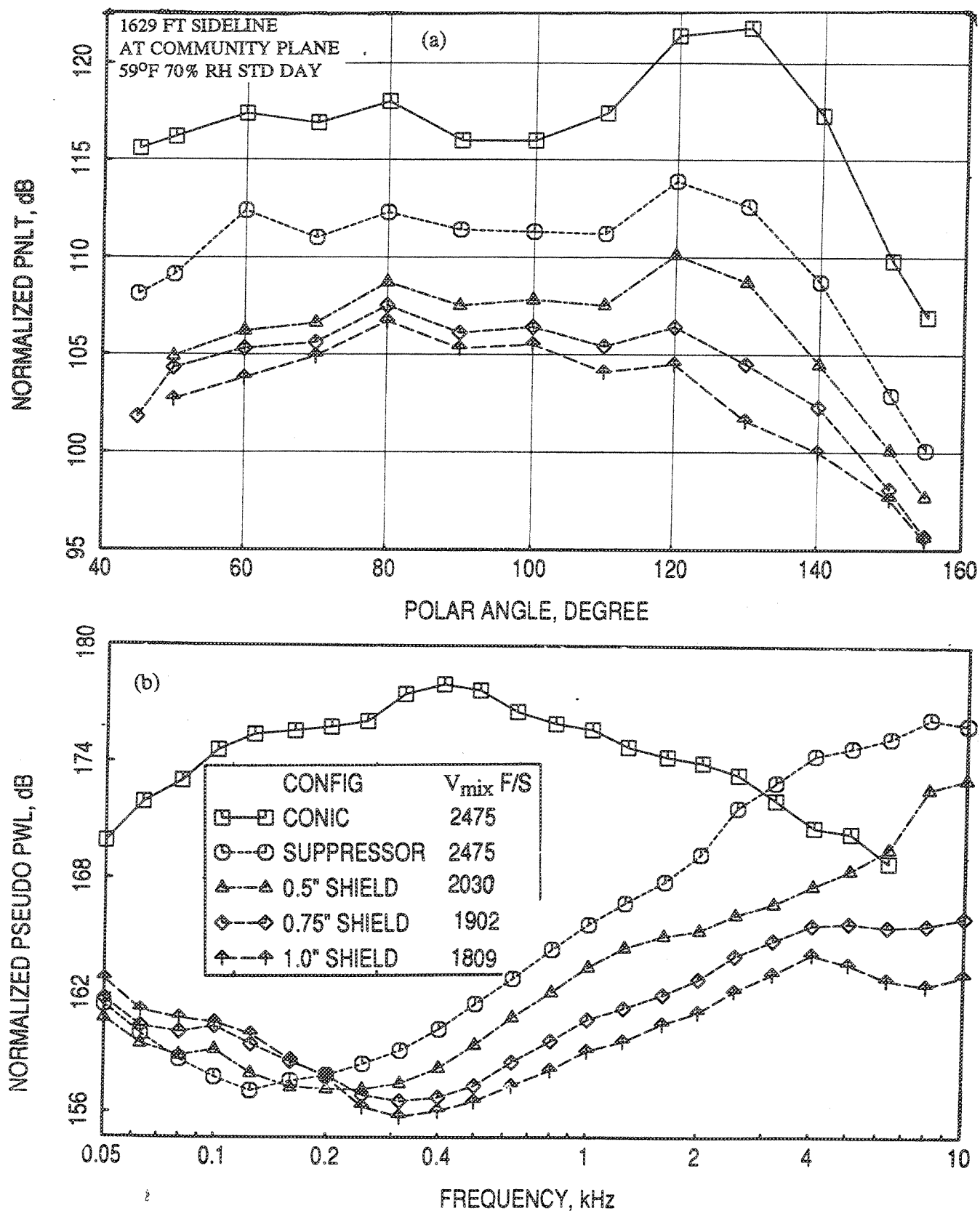


Figure 2.8-53. Noise suppression due to fluid shield nozzles in terms of normalized (a) PNLT directivities and (b) pseudo PWL spectra for a fixed nominal corestream jet velocity of 2475 ft/sec with flight simulation ( $M_F=0.32$ ).

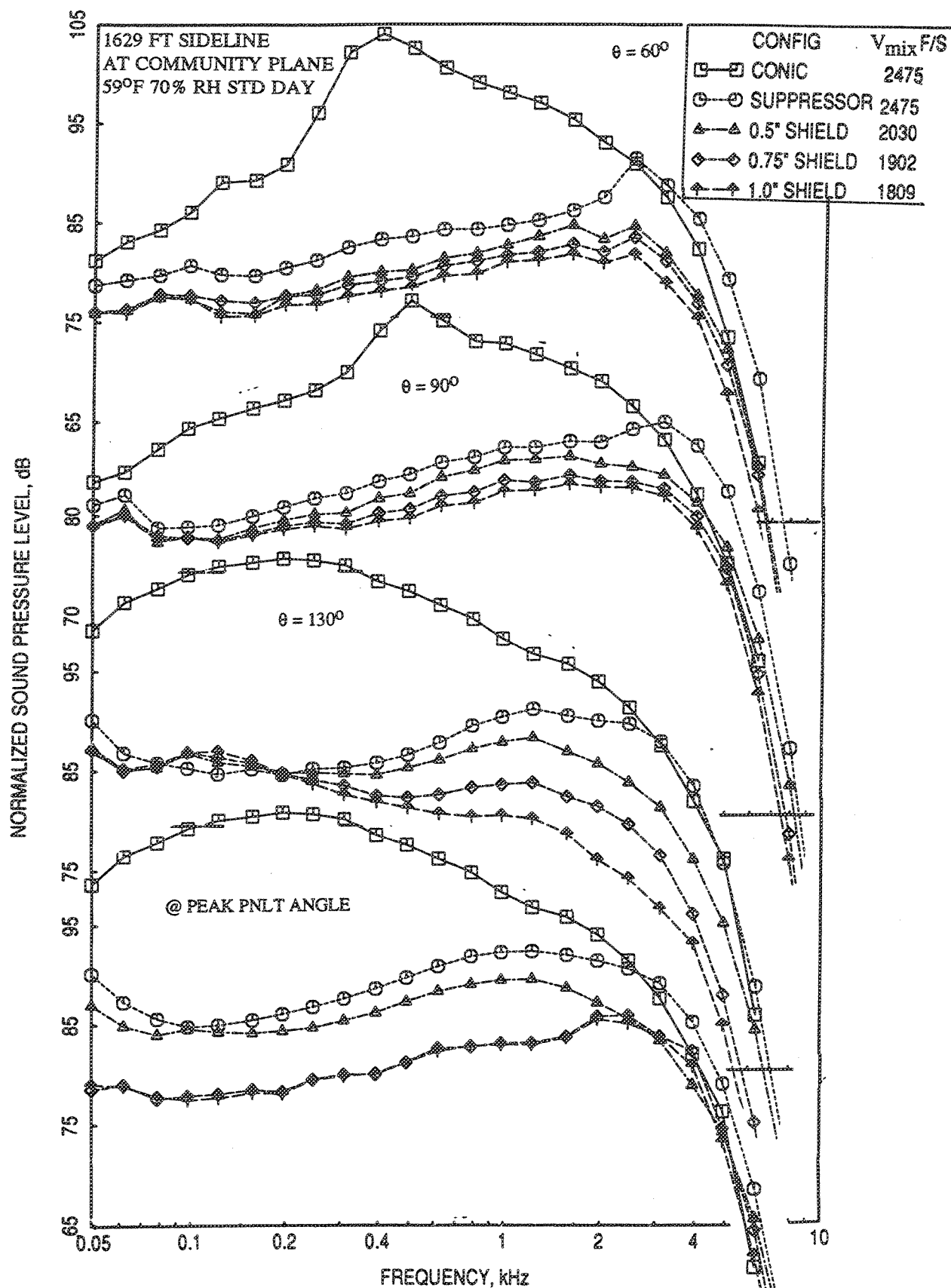


Figure 2.8-54. Noise suppression due to fluid shield nozzles in terms of normalized SPL spectra at different polar angles ( $\theta$ ) for a fixed nominal corestream jet velocity of 2475 ft/sec with flight simulation ( $M_F=0.32$ ).



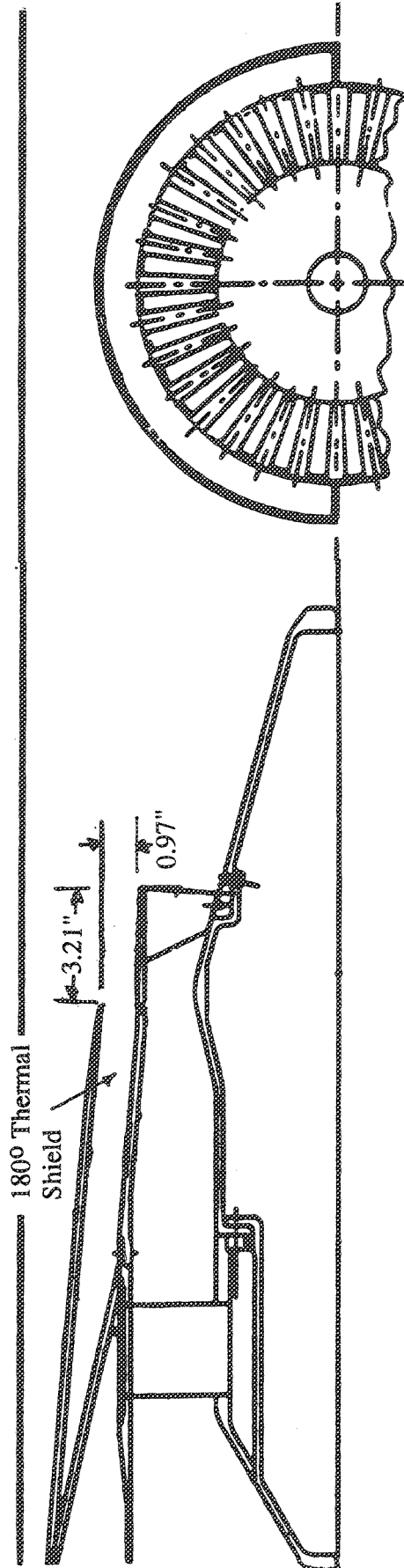
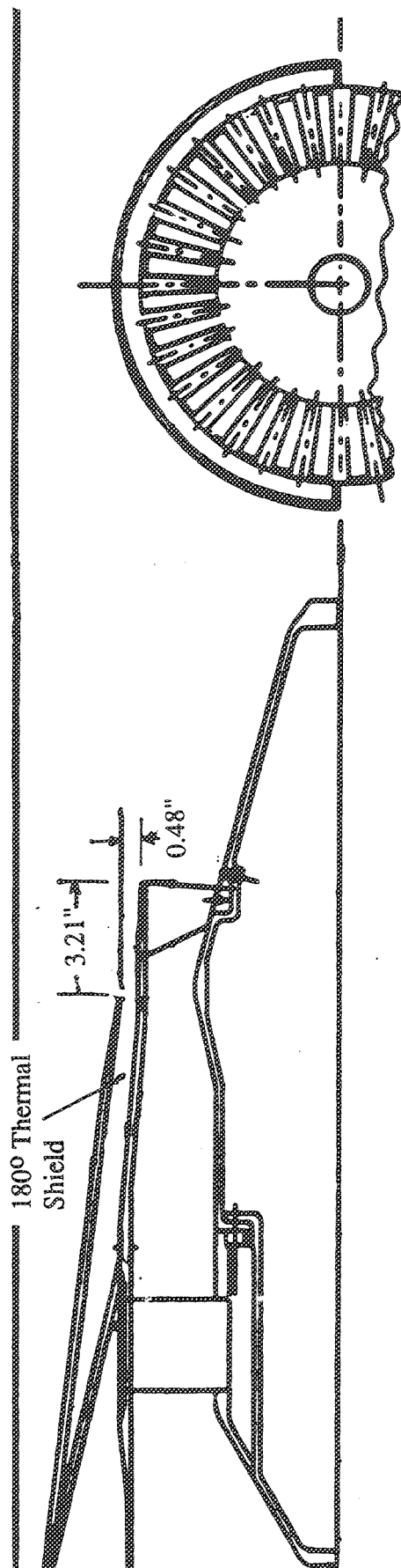


Figure 2.8-55 Side view of 32-Chute annular plug suppressor nozzles with 180° thermal acoustic shield of (a) 0.48" and (b) 0.97" thicknesses (Ref. 2).

in section 2.6. The thermal shields for the configurations are wrapped around the suppressor, as shown in Figure 2.8-55, by  $180^\circ$ , compared to a  $220^\circ$  wrap for the similar fluid shield configurations. Since, the wrap angles for thermal and fluid shield configurations are not the same, the data are compared at the community point only, which corresponds to the mid point of the shields. The thermal shield data with flight simulation were processed including the turbulence absorption. Therefore, the current fluid shield data are also processed in the same manner for consistency. The results are normalized for thrust and density.

The comparison of acoustic results between fluid and thermal shields are made with respect to PNL as function of mixed jet velocity ( $V_{mix}$ ) at a number of polar angles, OASPL and PNL directivities and SPL spectra at a number of polar angles at the same nominal mixed jet velocities. Even though, the mixed velocities, in a comparison, are close between the two shield configurations, their aerothermodynamic conditions are not the same. For thermal shield configurations the secondary stream temperature was much higher compared to fluid shield configurations. Hence, for the same mixed velocity the primary stream temperature and the pressure ratios for both streams of the fluid shield configurations are usually higher compared to those for thermal shield configurations.

**0.5" -Thick Shield Data:** Figure 2.8-56 shows the comparison of PNL as a function of mixed jet velocity ( $V_{mix}$ ) at a number of polar angles. Statically the PNLs for fluid shield are slightly higher at  $60^\circ$  and the trend reverses for the other angles. With flight simulation, the PNLs for fluid shield agree well at  $60^\circ$  and are lower for other angles compared to thermal shield results.

OASPL and PNL directivities and SPL spectra at a number of polar angles at four nominal mixed jet velocities, 1735, 1811, 2030, and 2087 ft/sec, are compared between 0.5"-thick thermal and fluid shield configurations for static as well as with flight simulation ( $M_F=0.32$ ).

*Static Data :* Figures 2.8-57 through 2.8-60 show the comparison of OASPL and PNL directivities and SPL spectra between fluid and thermal shield configurations at fixed nominal mixed velocities at static condition. The actual aerothermodynamic conditions of the flow are indicated in the individual figures. The general indication is that the fluid shield configuration is quieter compared to thermal shield with respect to OASPL, PNL, and SPL for all the velocity conditions.

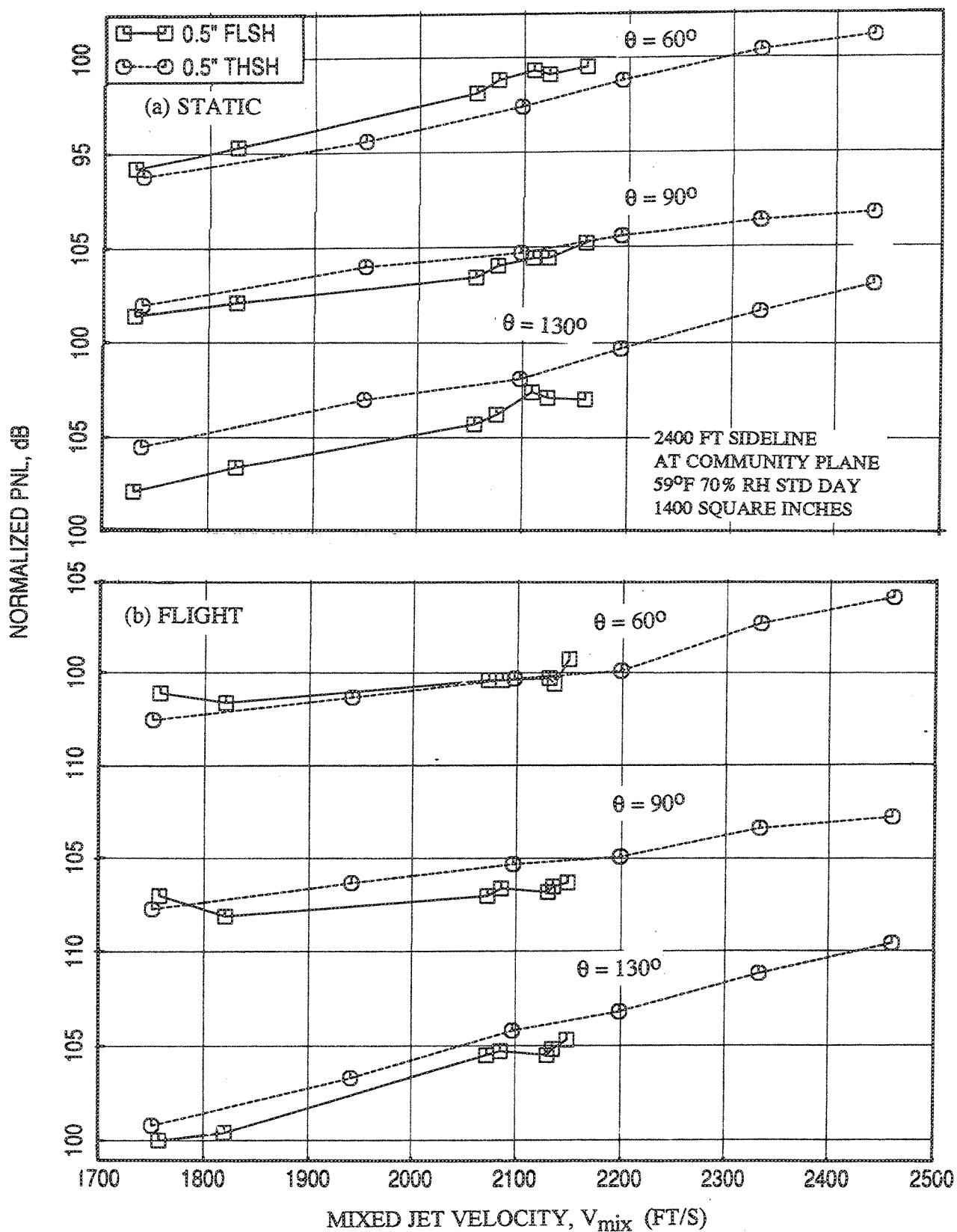


Figure 2.8-56. Comparison of normalized PNL data at a number of polar angles ( $\theta$ ) as a function of mixed jet velocity (a) at static condition and (b) with flight simulation ( $M_F=0.32$ ) between 0.5"-thick acoustic fluid shield and thermal acoustic shield configurations.

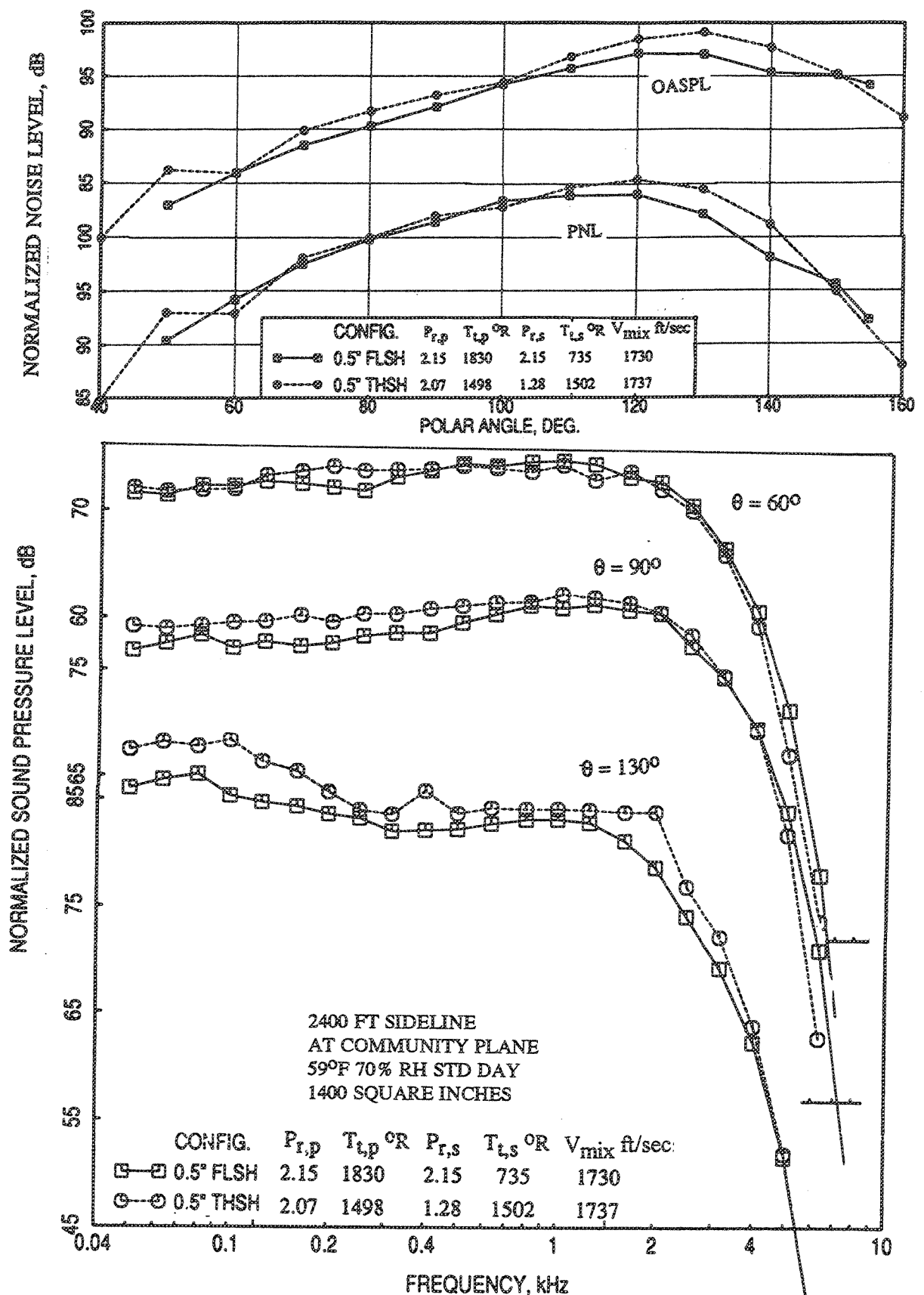


Figure 2.8-57. Comparison of (a) PNL and OASPL directivities and (b) SPL spectra between 0.5"-thick acoustic fluid shield and thermal acoustic shield configurations at a nominal  $V_{mix}=1735$  ft/sec at static condition.

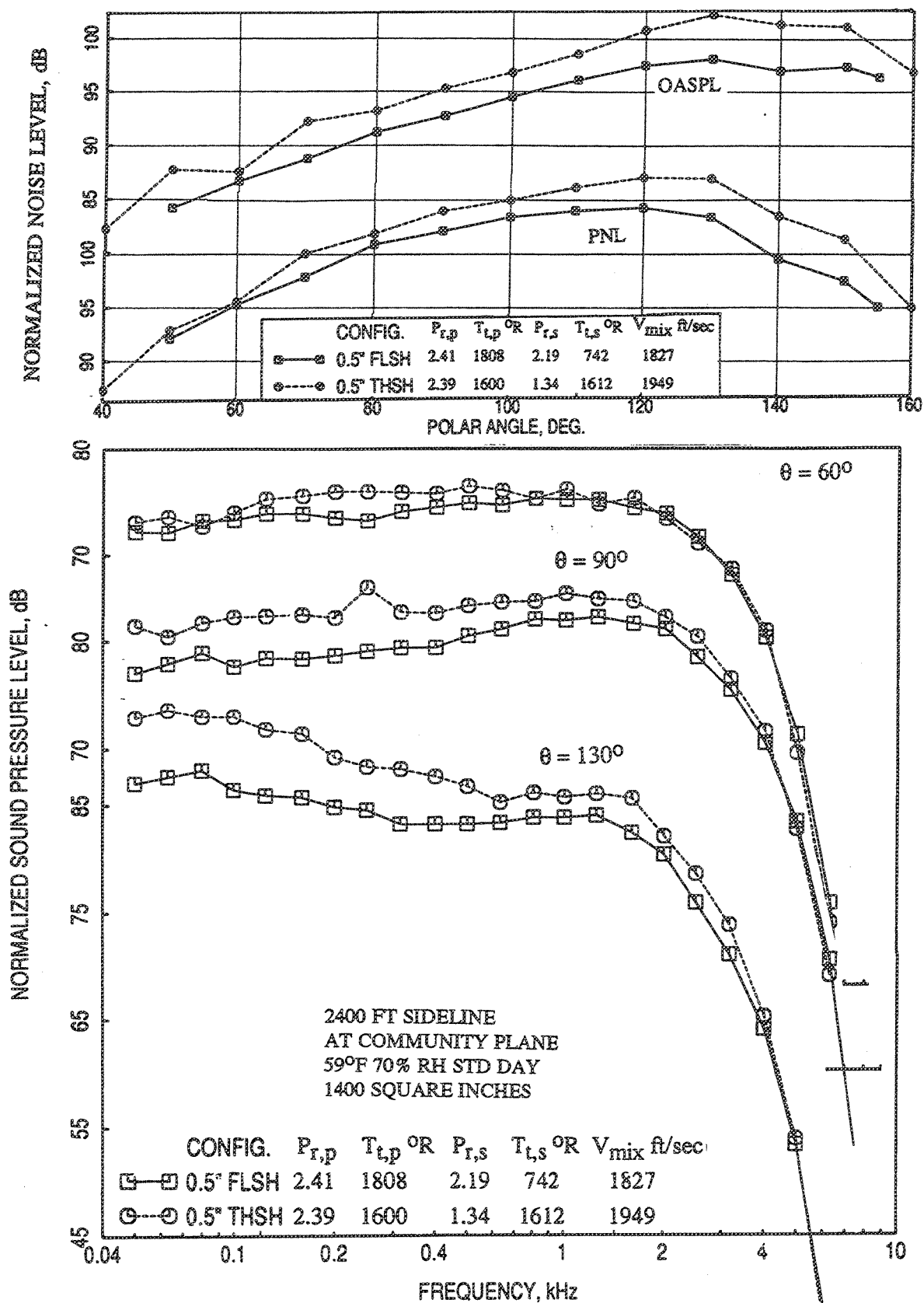


Figure 2.8-58. Comparison of (a) PNL and OASPL directivities and (b) SPL spectra between 0.5"-thick acoustic fluid shield and thermal acoustic shield configurations at a nominal  $V_{mix}=1811$  ft/sec at static condition.

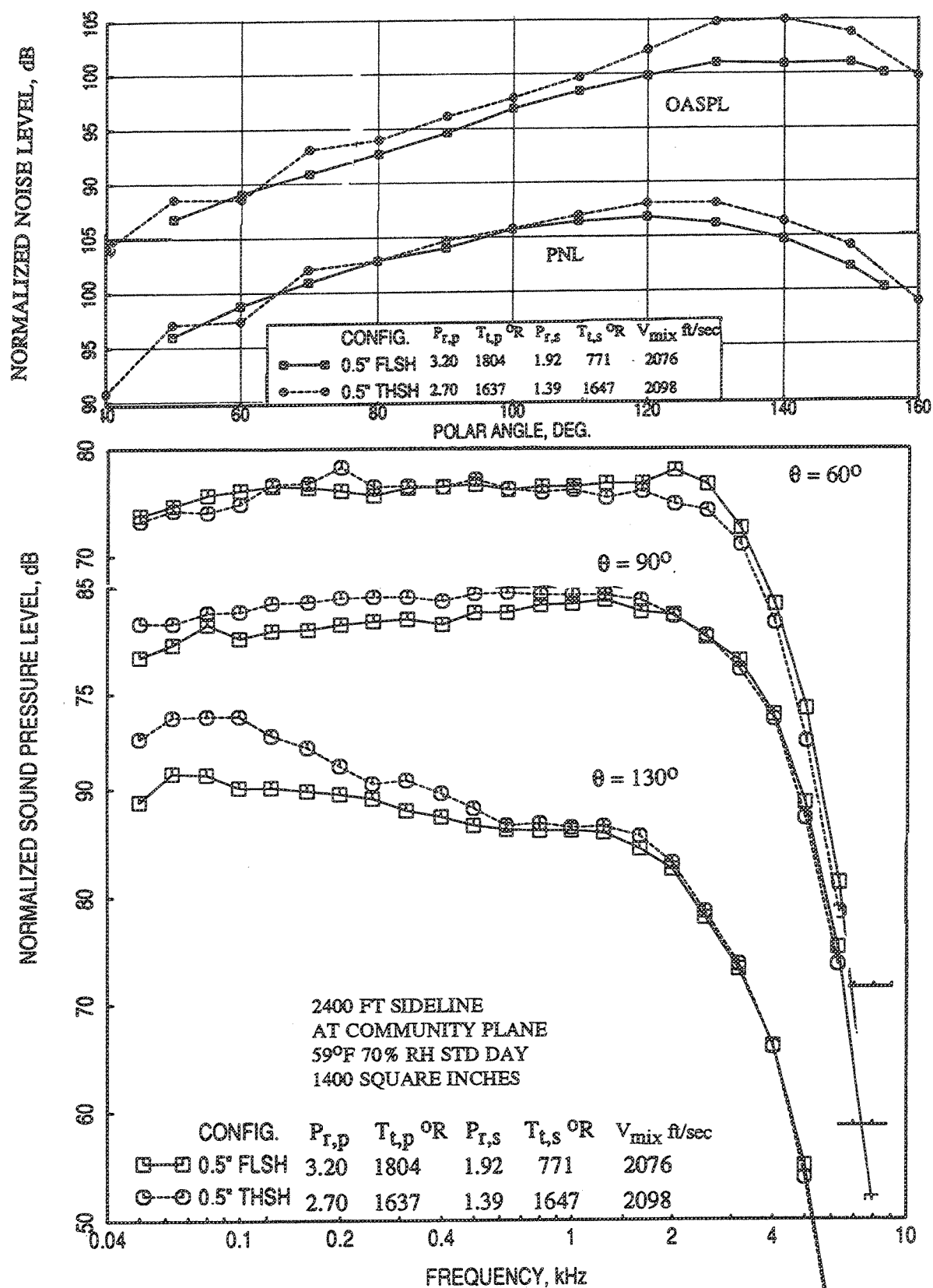


Figure 2.8-59. Comparison of (a) PNL and OASPL directivities and (b) SPL spectra between 0.5"-thick acoustic fluid shield and thermal acoustic shield configurations at a nominal  $V_{mix}=2030$  ft/sec at static condition.

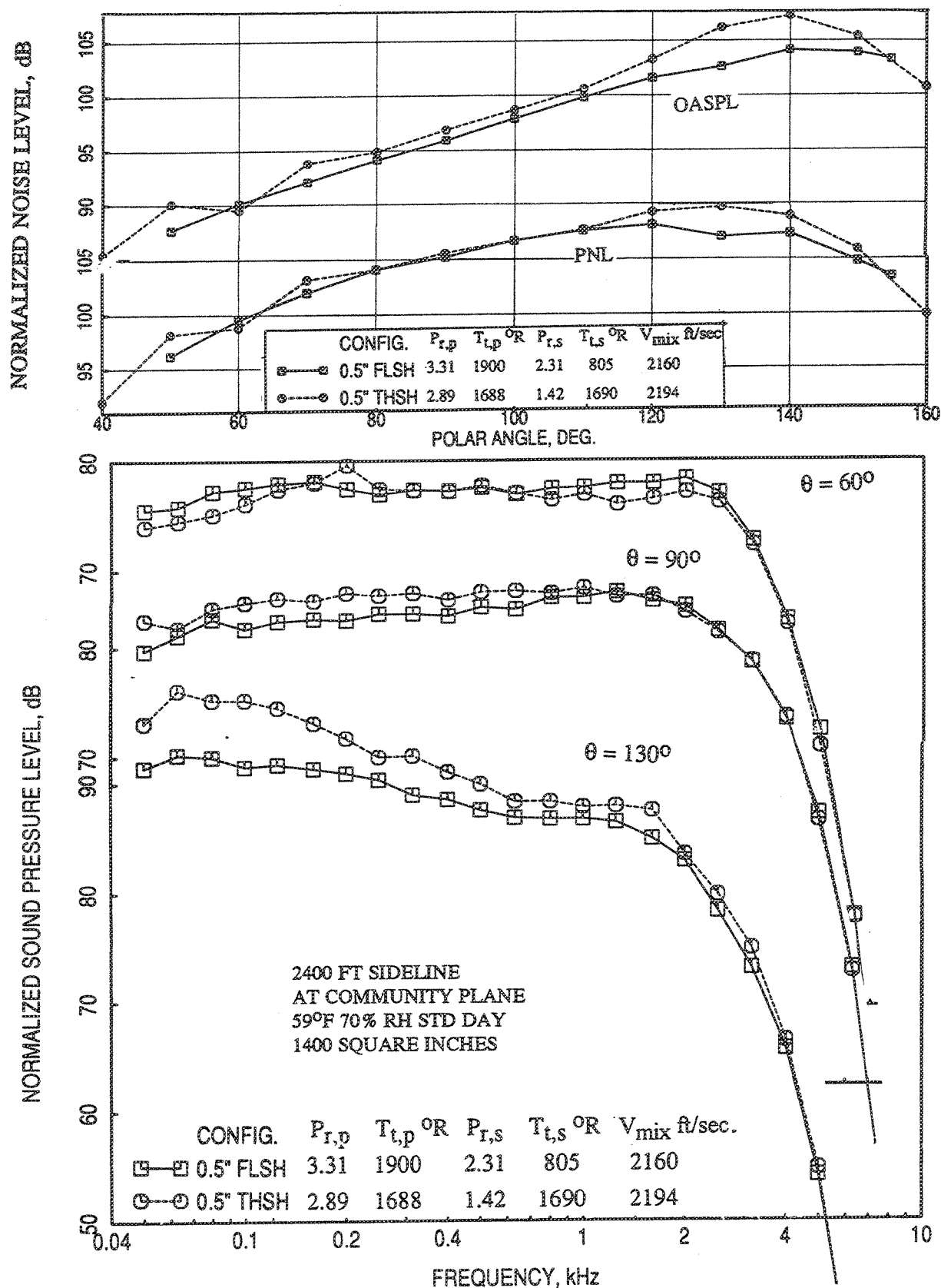


Figure 2.8-60. Comparison of (a) PNL and OASPL directivities and (b) SPL spectra between 0.5"-thick acoustic fluid shield and thermal acoustic shield configurations at a nominal  $V_{mix}=2087$  ft/sec at static condition.

*Flight Data :* Figures 2.8-61 through 2.8-64 show the comparison of OASPL and PNL directivities and SPL spectra between fluid and thermal shield configurations at fixed nominal mixed velocities with flight simulation. Again, similar to static data, the fluid shield configuration is quieter compared to thermal shield with respect to OASPL, PNL, and SPL for all the velocity conditions.

**1.0" -Thick Shield Data:** Figure 2.8-65 shows the comparison of PNL as a function of mixed jet velocity ( $V_{mix}$ ) at a number of polar angles. Statically and with flight simulation the PNLs for the fluid shield configuration are slightly higher at  $60^\circ$  and are of the same magnitude for other polar angles.

OASPL and PNL directivities and SPL spectra at a number of polar angles at a number of nominal mixed jet velocities are compared between 1.0"-thick thermal and fluid shield configurations for static as well as with flight simulation ( $M_F=0.32$ ).

*Static Data :* Figures 2.8-66 through 2.8-69 show the comparison of OASPL and PNL directivities and SPL spectra between fluid and thermal shield configurations at four fixed nominal mixed velocities, 1651, 1811, 1940, and 2030 ft/sec, at static condition. On OASPL basis the fluid shield seems to be quieter compared to thermal shield. However, on the basis of PNLs, both configurations are equally noisier. On SPL basis, the 1.0"-thick fluid shield seems to be noisier at higher frequencies.

*Flight Data :* Figures 2.8-70 through 2.8-72 show the comparison of OASPL and PNL directivities and SPL spectra between fluid and thermal shield configurations at three fixed nominal mixed velocities, 1651, 1811, and 2030 ft/sec, with flight simulation. In general, both configurations exhibit similar noise characteristics with flight simulation.

#### **2.8.5 Comparison of Acoustic Results between Fluid Shield and Mixer Ejector Configurations:**

Along with the fluid shield concept mixer ejector concept was also pursued for HSCT exhaust system. Two mixer ejector concepts, an axisymmetric and a two dimensional, were designed and tested for their acoustic performance. Typical results of these two exhaust nozzles are compared with the fluid shield results in this section. Figure 2.8-73 shows the side view of an axisymmetric mixer ejector nozzle (AMEN) with a 24-CD



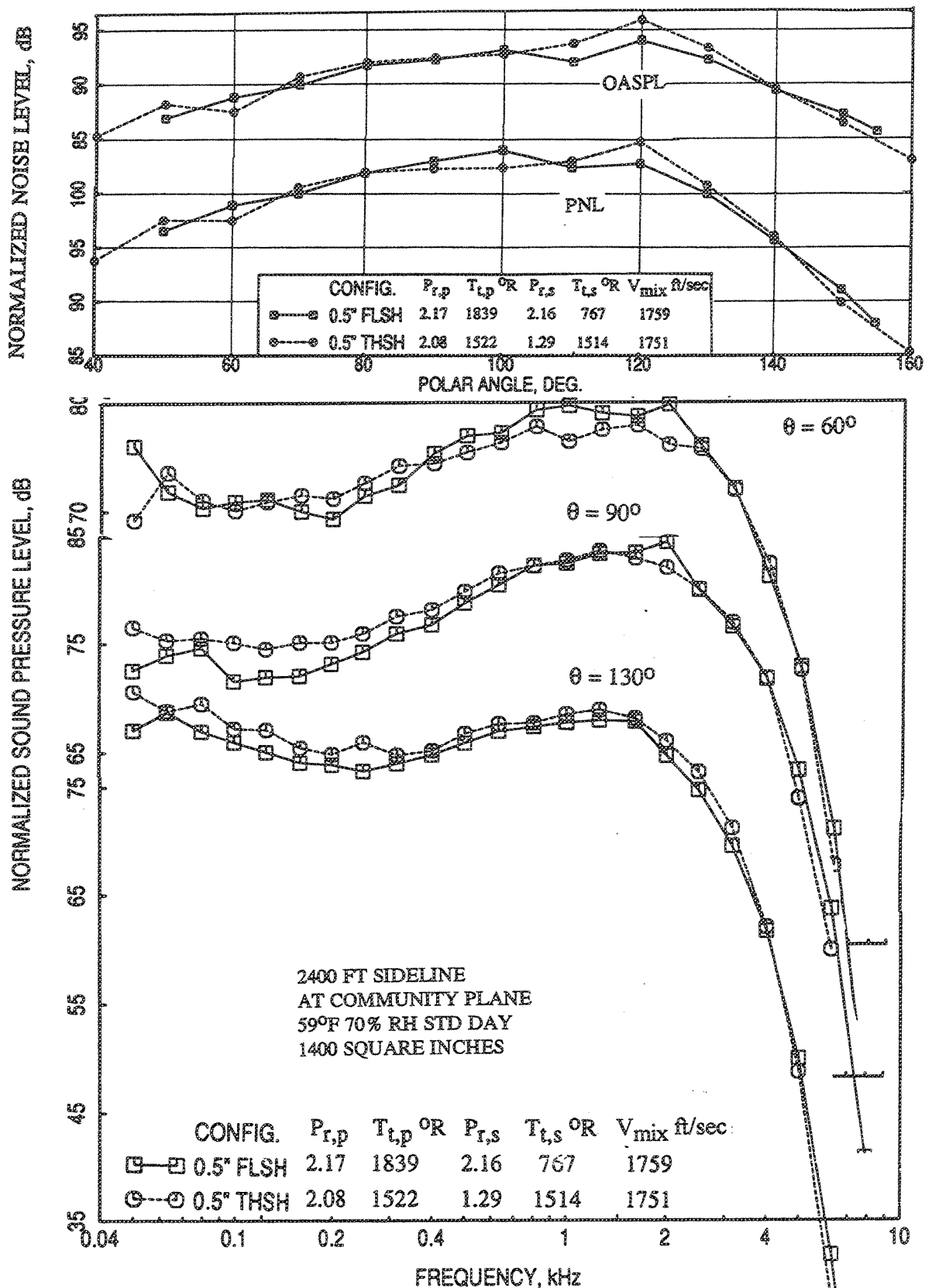


Figure 2.8-61. Comparison of (a) PNL and OASPL directivities and (b) SPL spectra between 0.5"-thick acoustic fluid shield and thermal acoustic shield configurations at a nominal  $V_{mix}=1735$  ft/sec with flight simulation ( $M_F=0.32$ ).

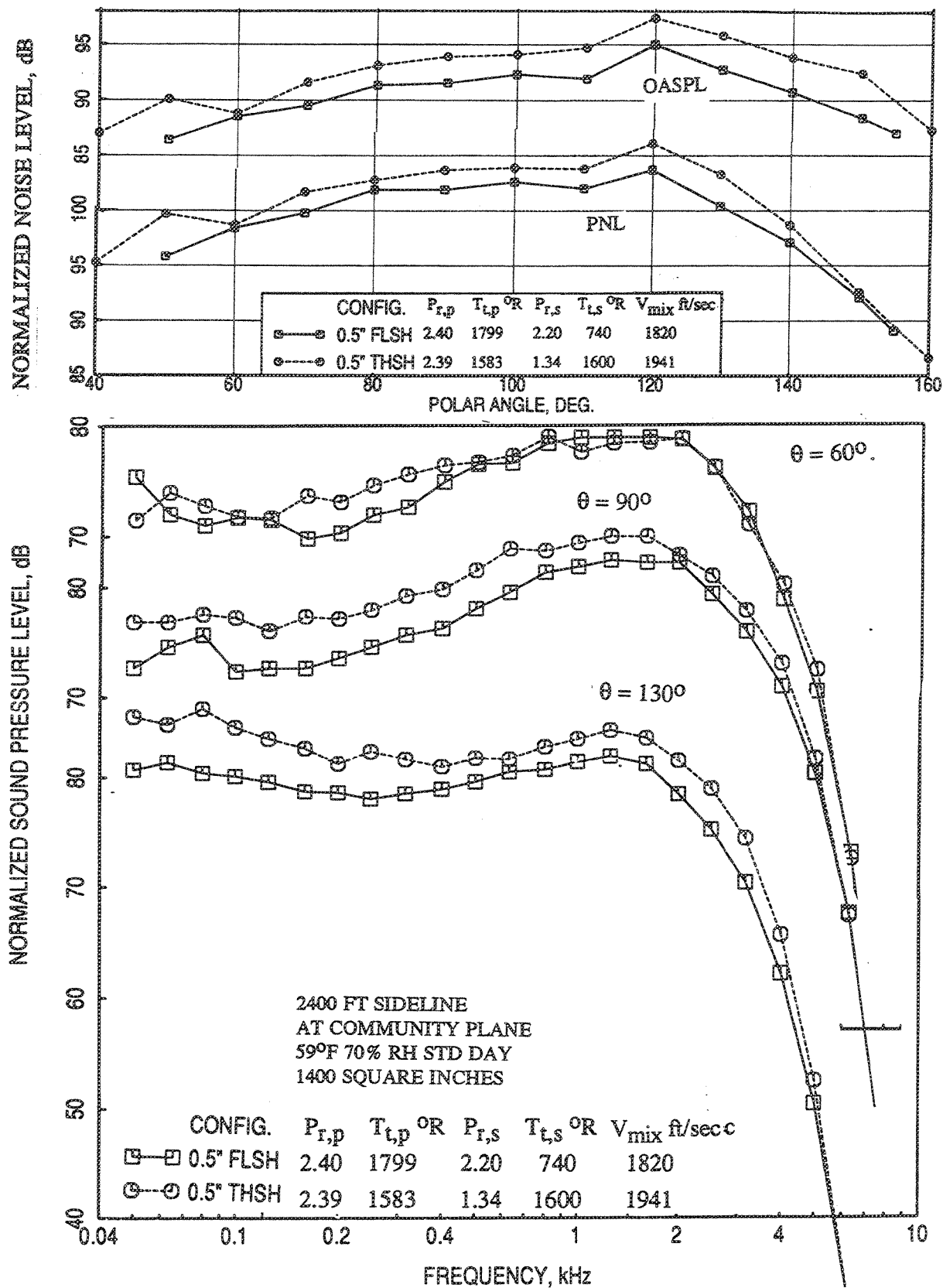


Figure 2.8-62. Comparison of (a) PNL and OASPL directivities and (b) SPL spectra between 0.5"-thick acoustic fluid shield and thermal acoustic shield configurations at a nominal  $V_{mix}=1811$  ft/sec with flight simulation ( $M_F=0.32$ ).

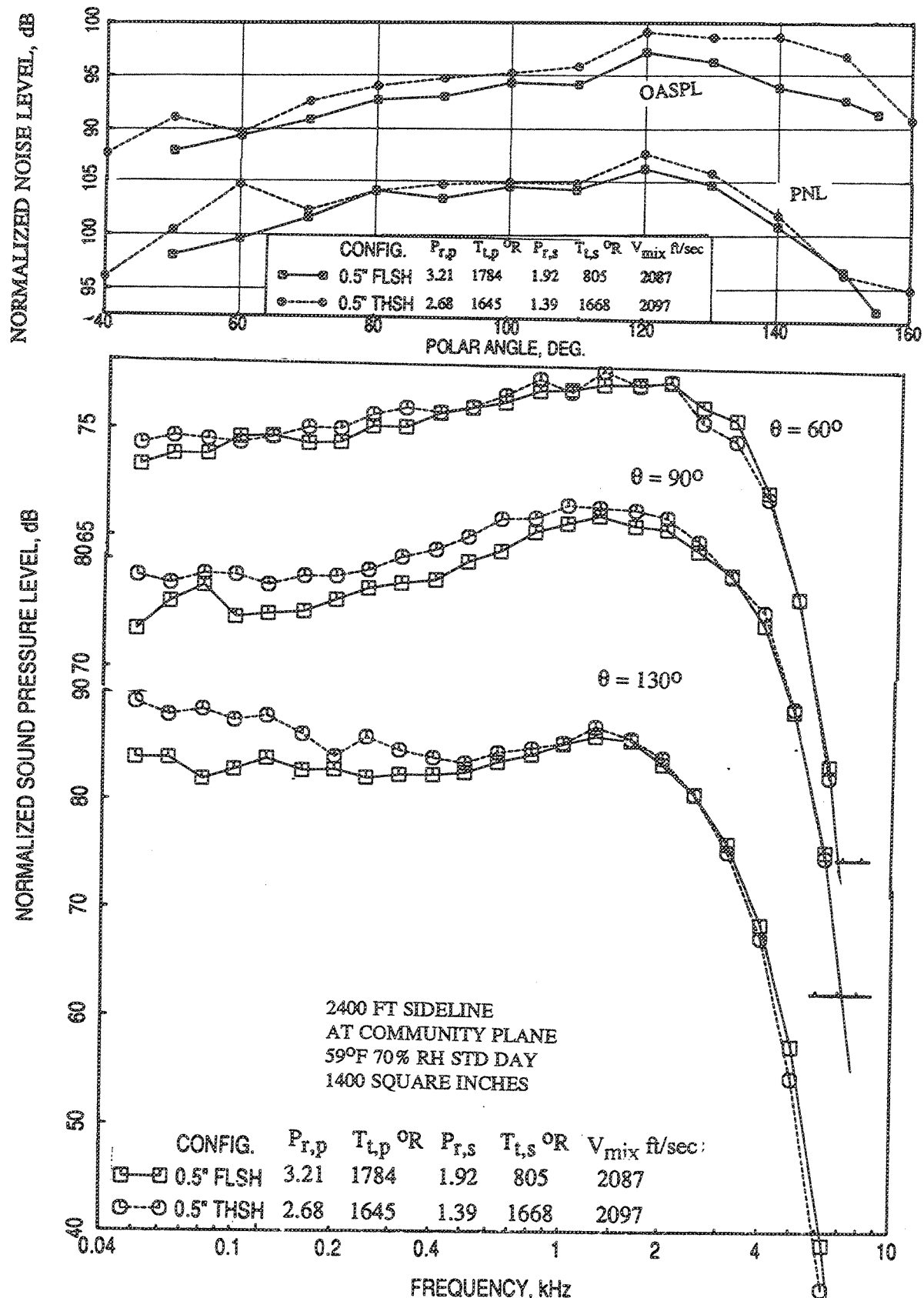


Figure 2.8-63. Comparison of (a) PNL and OASPL directivities and (b) SPL spectra between 0.5"-thick acoustic fluid shield and thermal acoustic shield configurations at a nominal  $V_{mix}=2030$  ft/sec with flight simulation ( $M_F=0.32$ ).

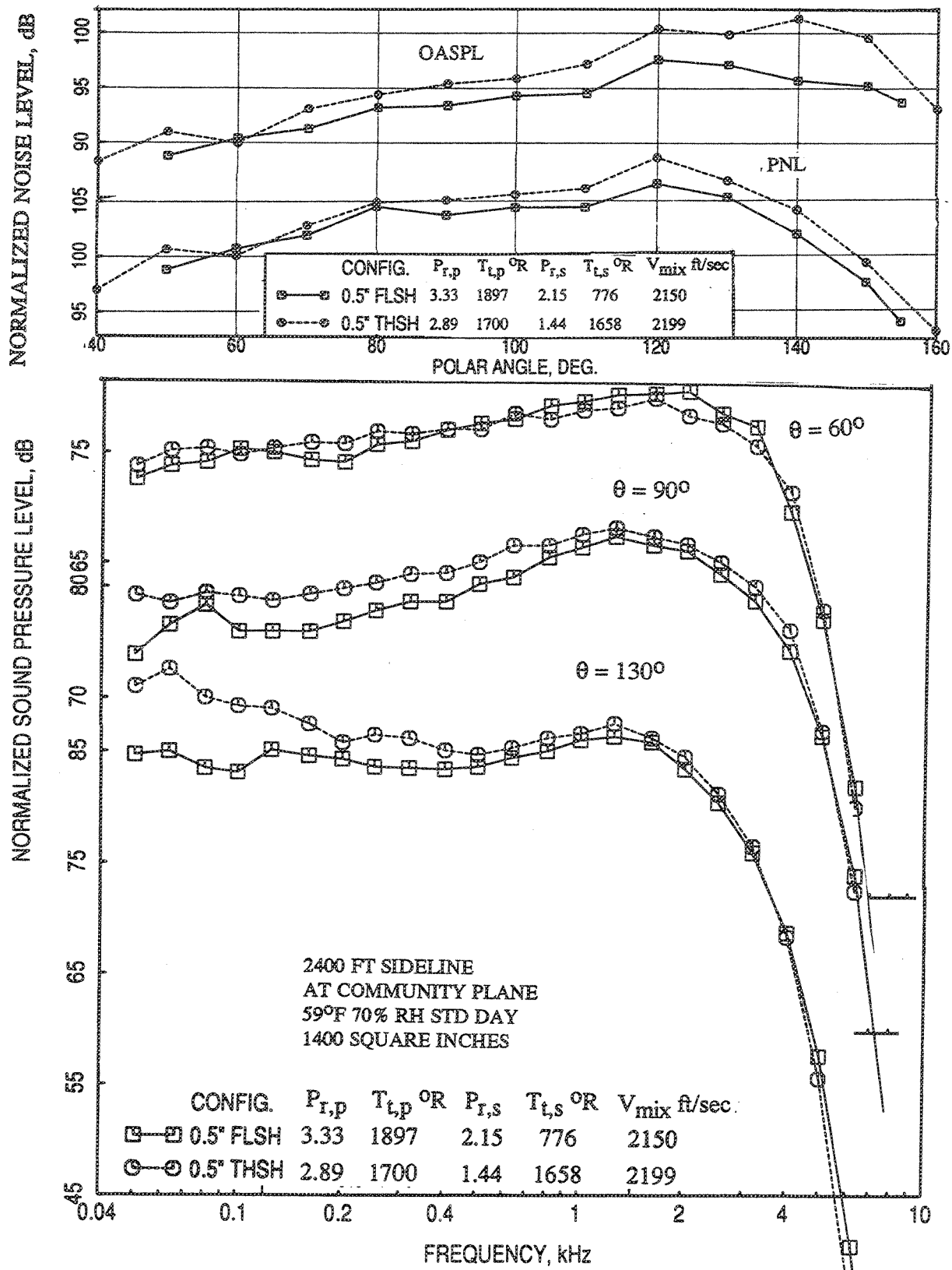


Figure 2.8-64. Comparison of (a) PNL and OASPL directivities and (b) SPL spectra between 0.5"-thick acoustic fluid shield and thermal acoustic shield configurations at a nominal  $V_{mix}=2087$  ft/sec with flight simulation ( $M_F=0.32$ ).

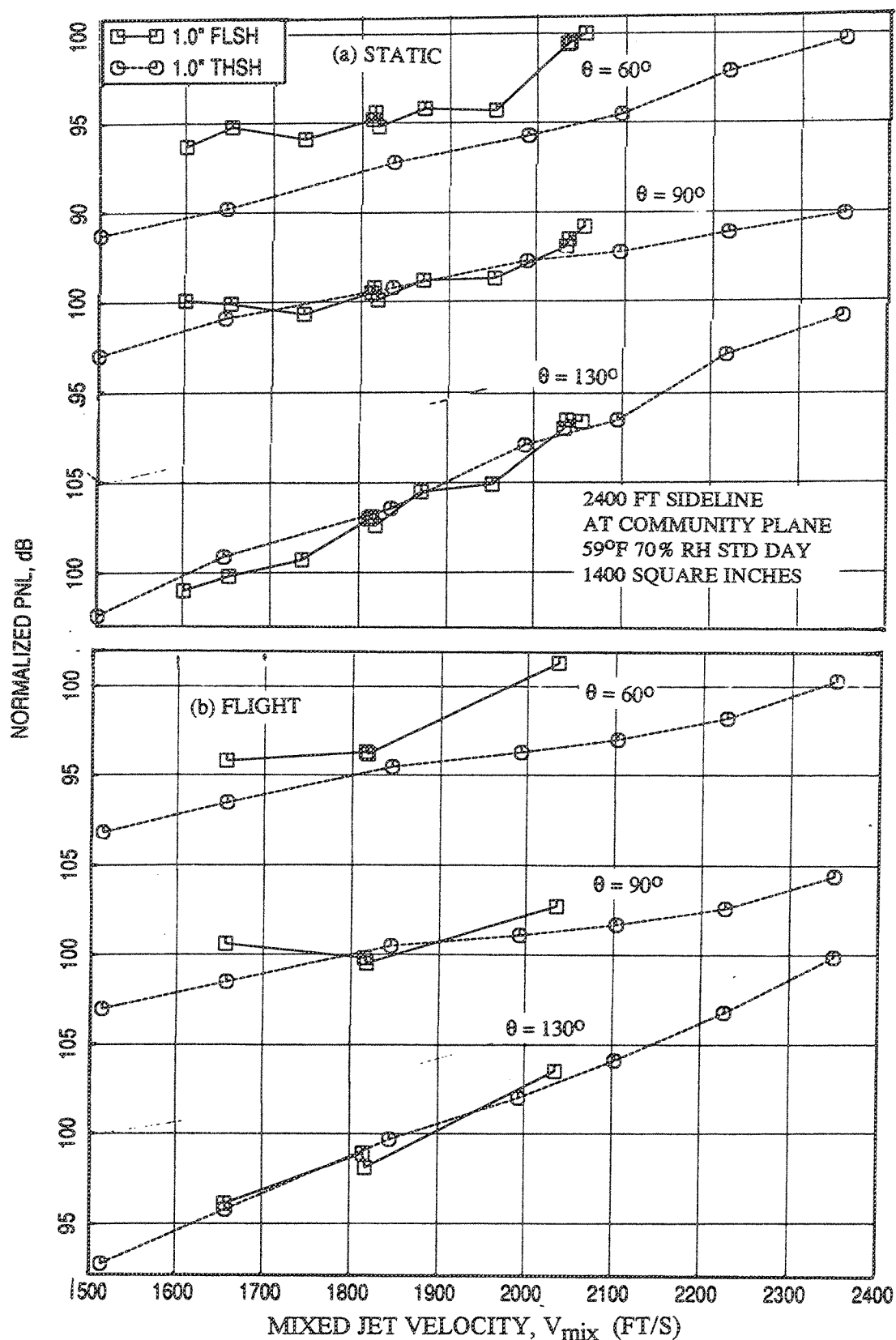


Figure 2.8-65. Comparison of normalized PNL data at a number of polar angles ( $\theta$ ) as a function of mixed jet velocity (a) at static condition and (b) with flight simulation ( $M_F=0.32$ ) between 1.0"-thick acoustic fluid shield and thermal acoustic shield configurations.

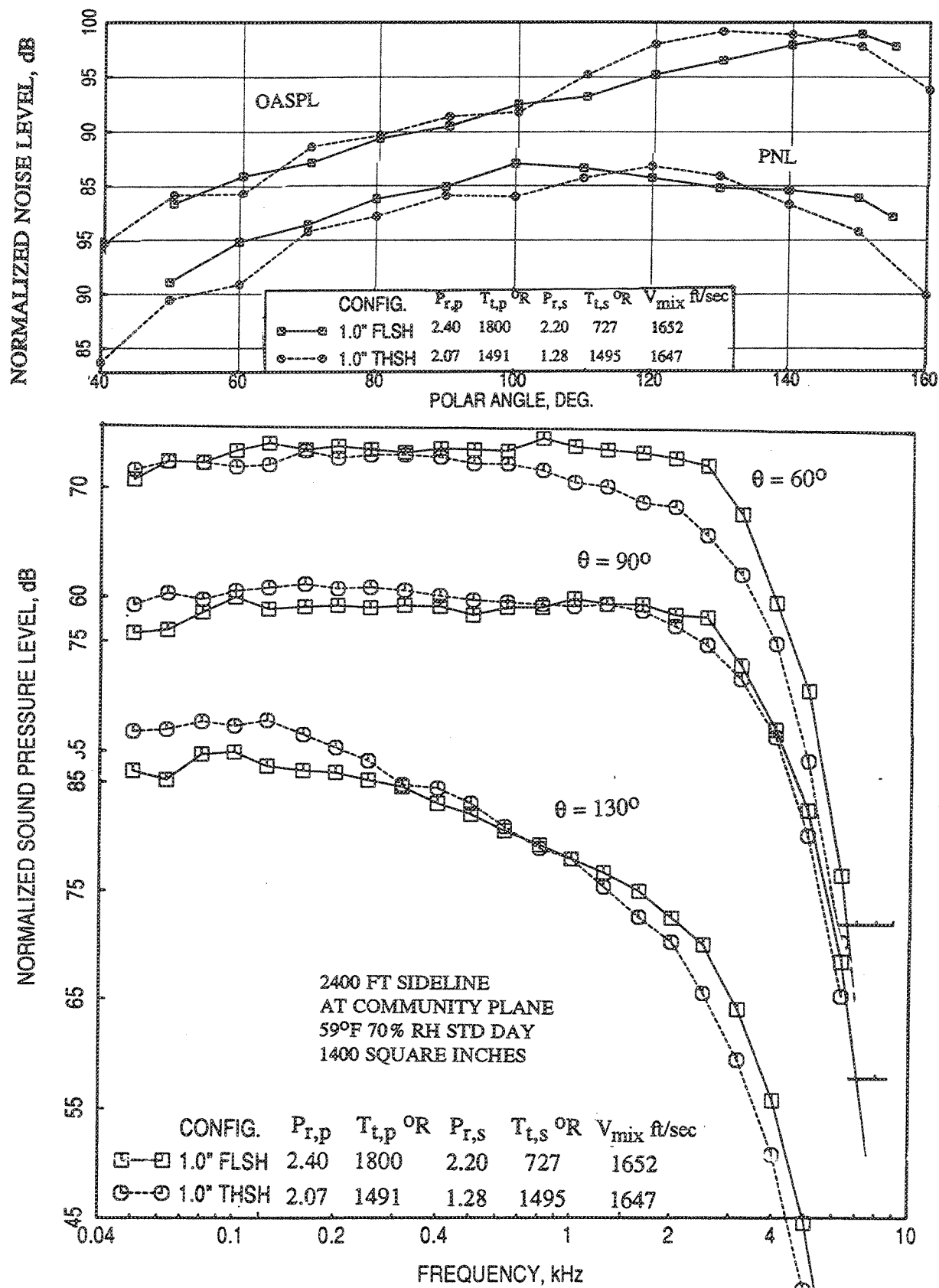


Figure 2.8-66. Comparison of (a) PNL and OASPL directivities and (b) SPL spectra between 1.0"-thick acoustic fluid shield and thermal acoustic shield configurations at a nominal  $V_{mix}=1651$  ft/sec at static condition.

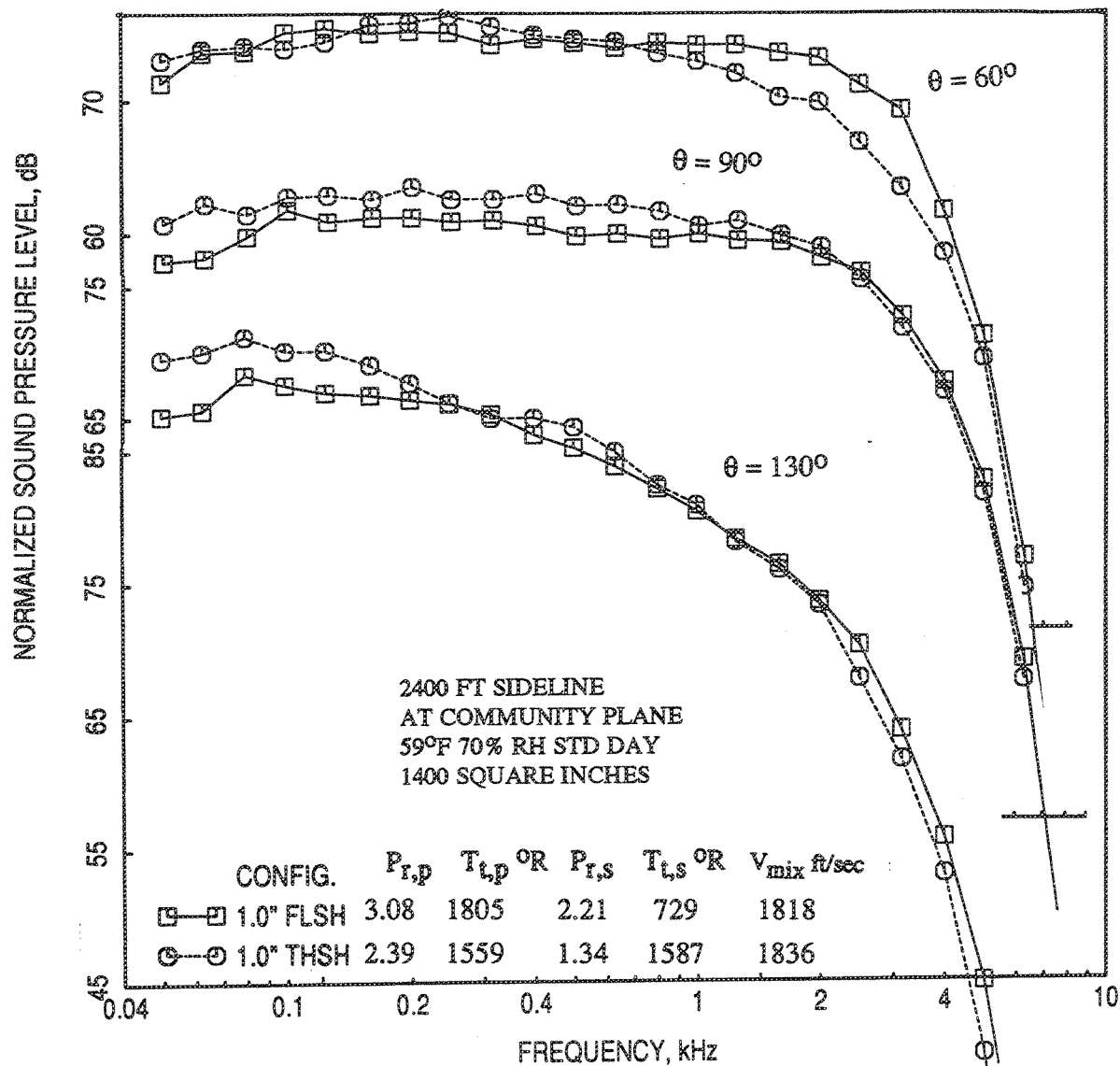
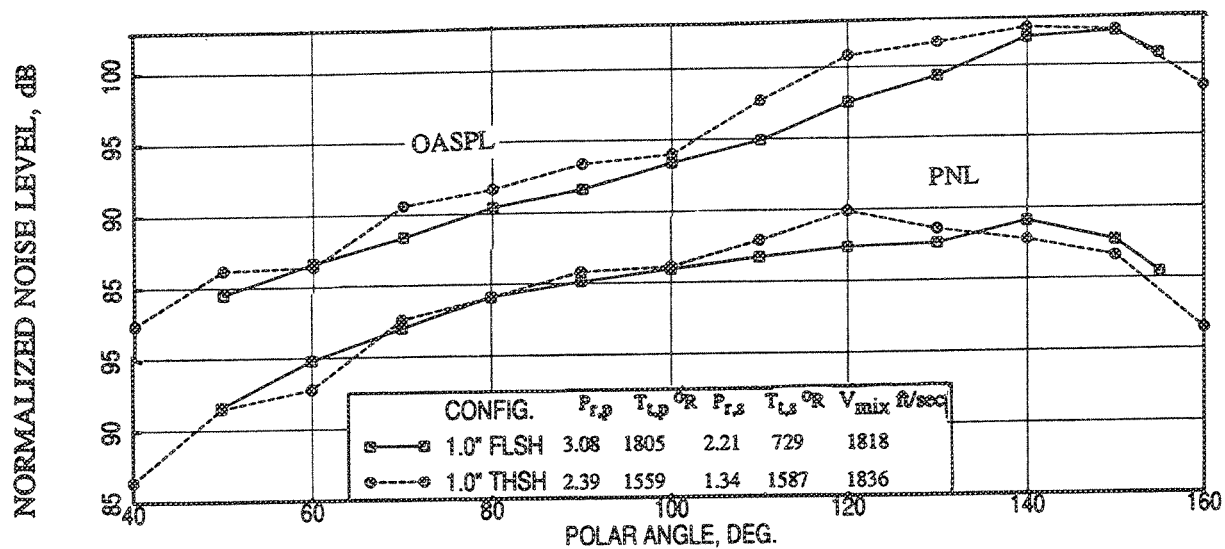


Figure 2.8-67. Comparison of (a) PNL and OASPL directivities and (b) SPL spectra between 1.0"-thick acoustic fluid shield and thermal acoustic shield configurations at a nominal  $V_{mix}=1811$  ft/sec at static condition.

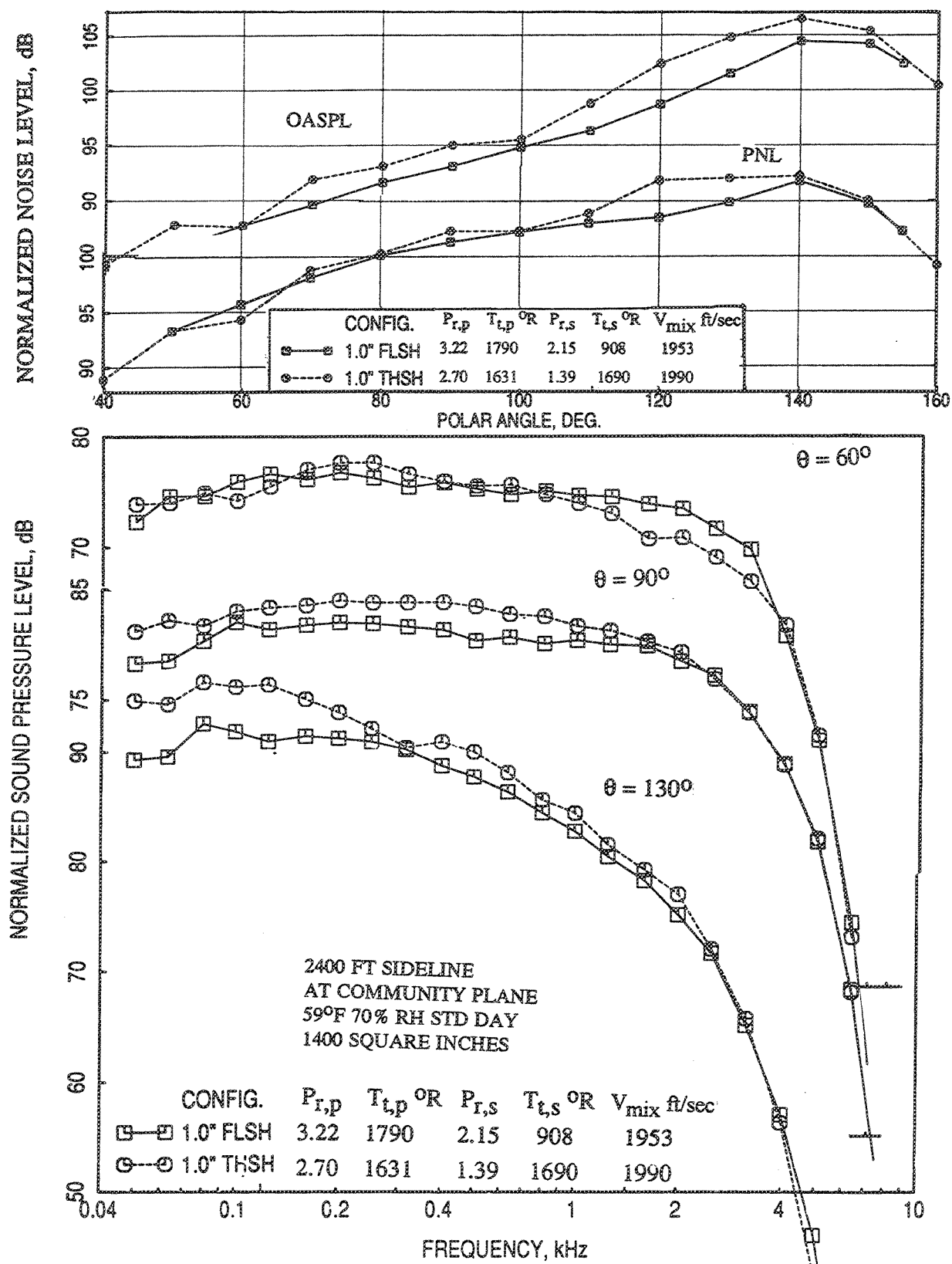


Figure 2.8-68. Comparison of (a) PNL and OASPL directivities and (b) SPL spectra between 1.0"-thick acoustic fluid shield and thermal acoustic shield configurations at a nominal  $V_{mix}=1940$  ft/sec at static condition.



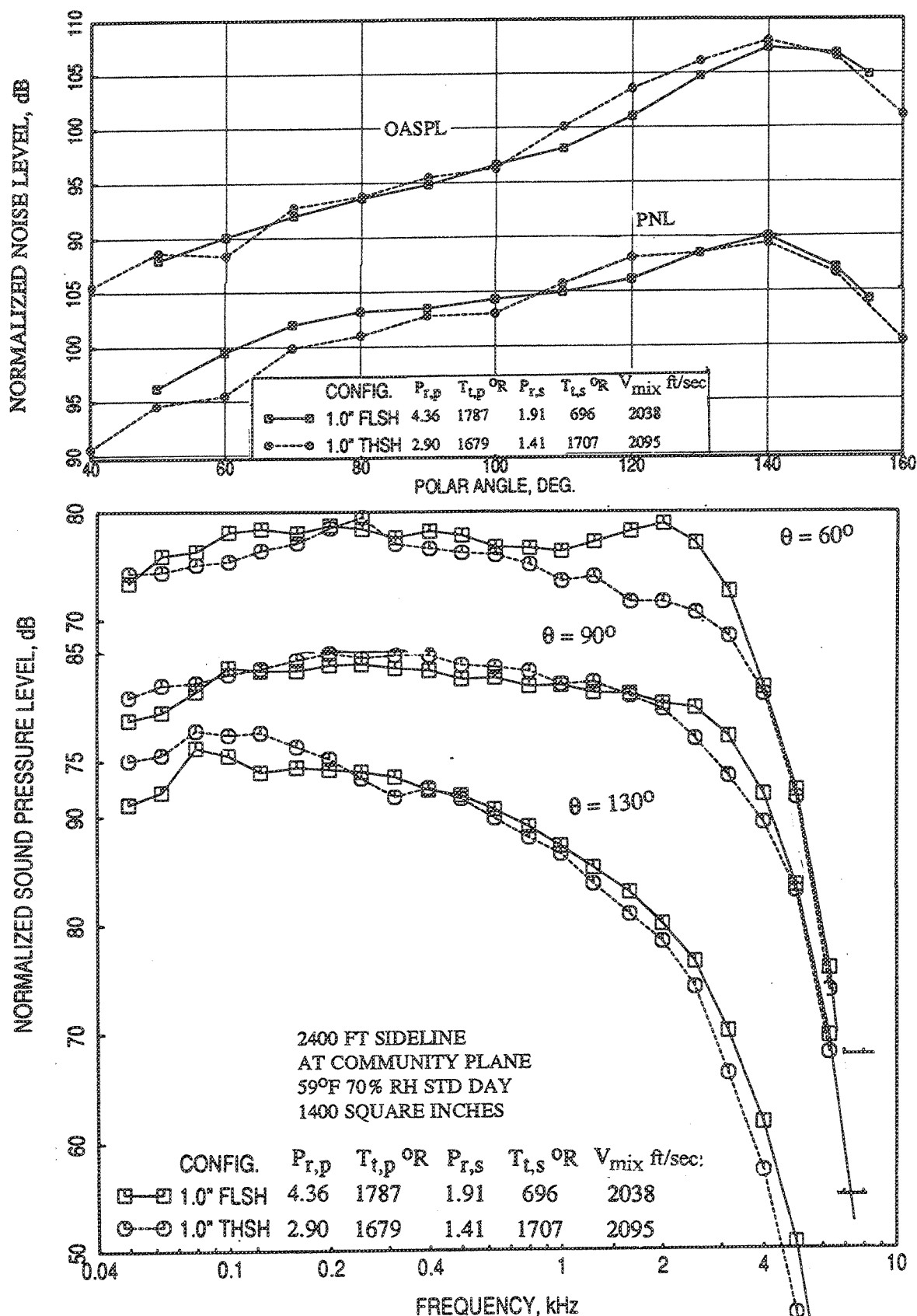


Figure 2.8-69. Comparison of (a) PNL and OASPL directivities and (b) SPL spectra between 1.0-inch-thick acoustic fluid shield and thermal acoustic shield configurations at a nominal  $V_{mix}=2030$  ft/sec at static condition.

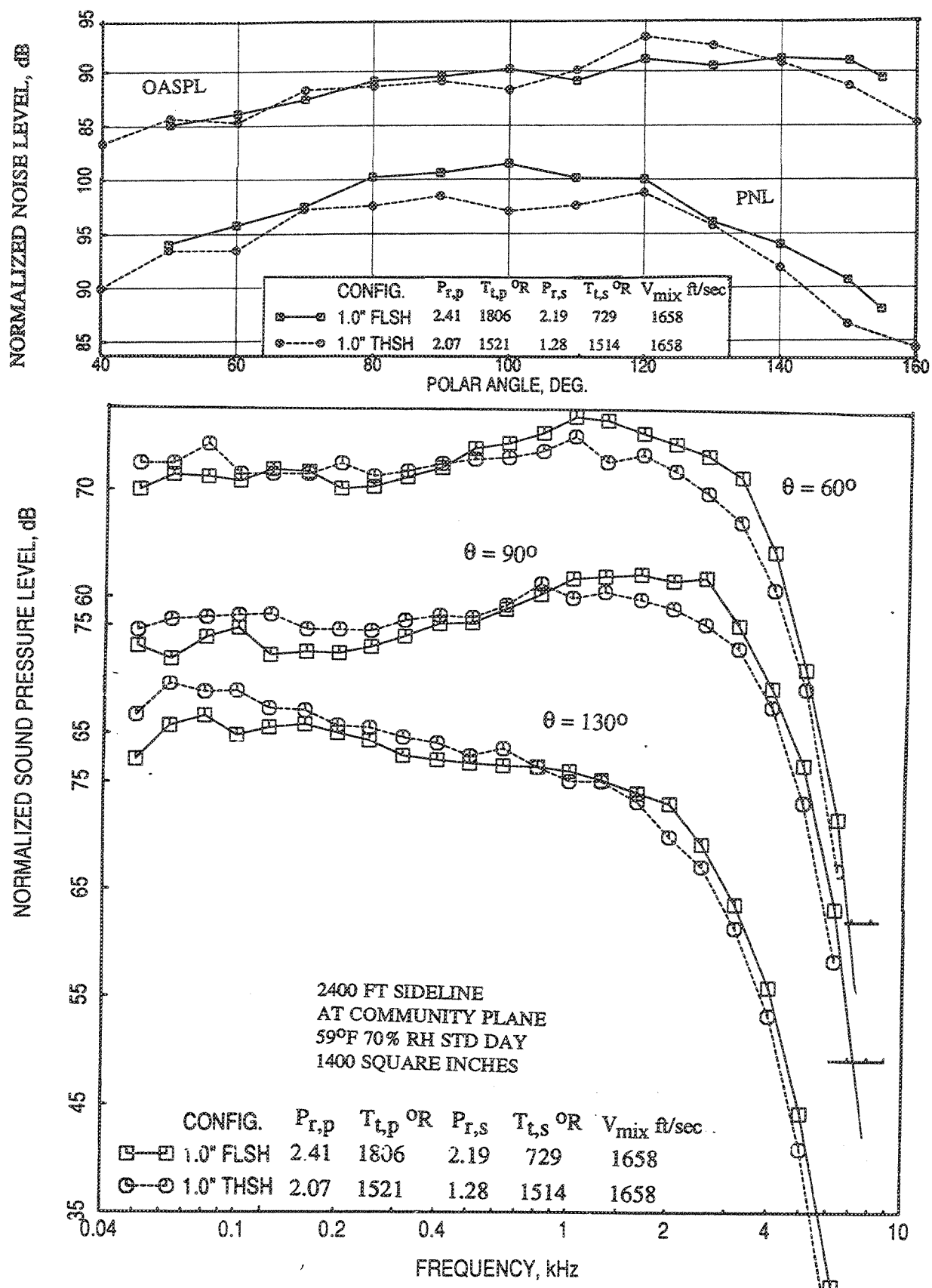


Figure 2.8-70. Comparison of (a) PNL and OASPL directivities and (b) SPL spectra between 1.0"-thick acoustic fluid shield and thermal acoustic shield configurations at a nominal  $V_{mix}=1651$  ft/sec with flight simulation ( $M_F=0.32$ ).

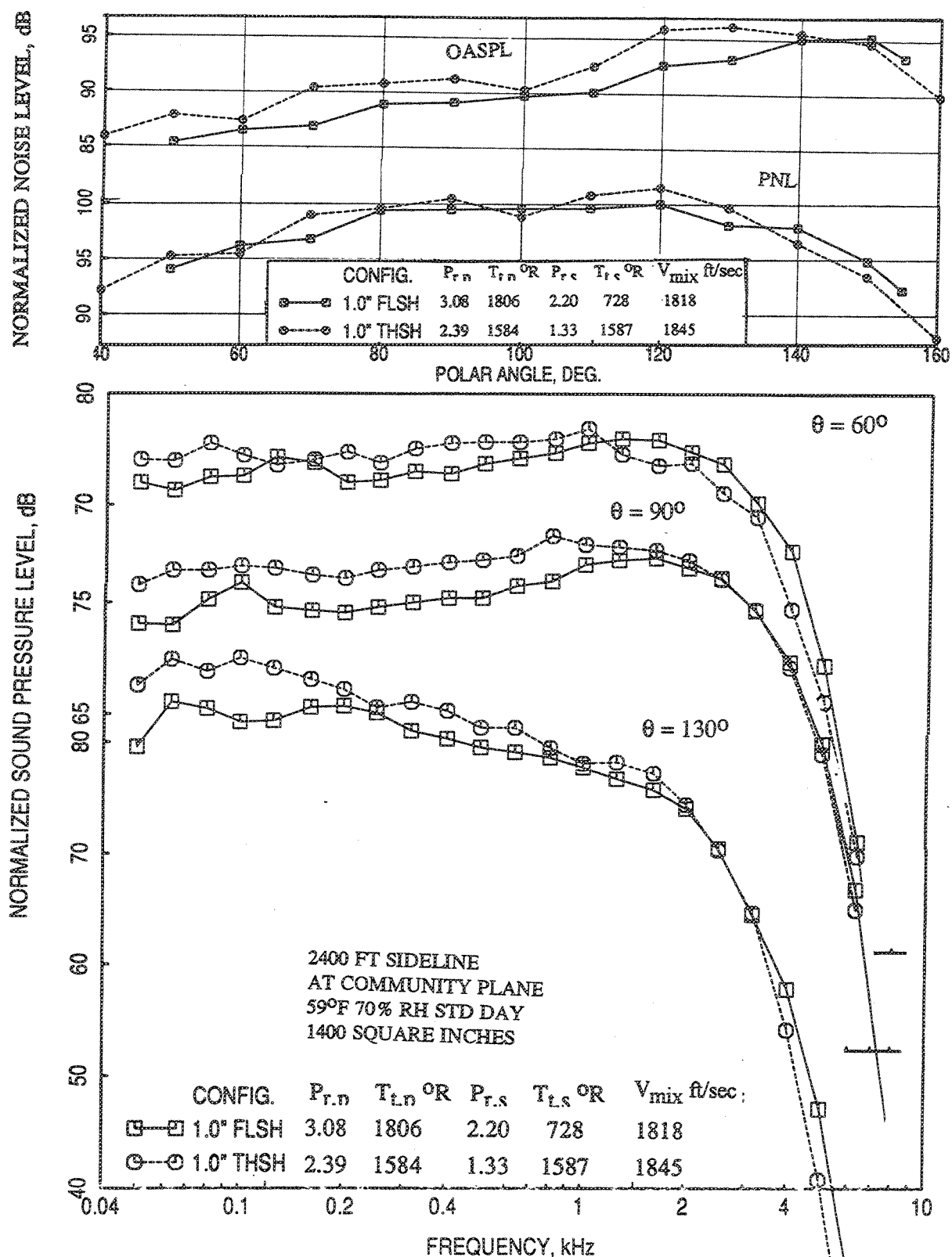


Figure 2.8-71. Comparison of (a) PNL and OASPL directivities and (b) SPL spectra between 1.0"-thick acoustic fluid shield and thermal acoustic shield configurations at a nominal  $V_{mix}=1811$  ft/sec with flight simulation ( $M_F=0.32$ ).

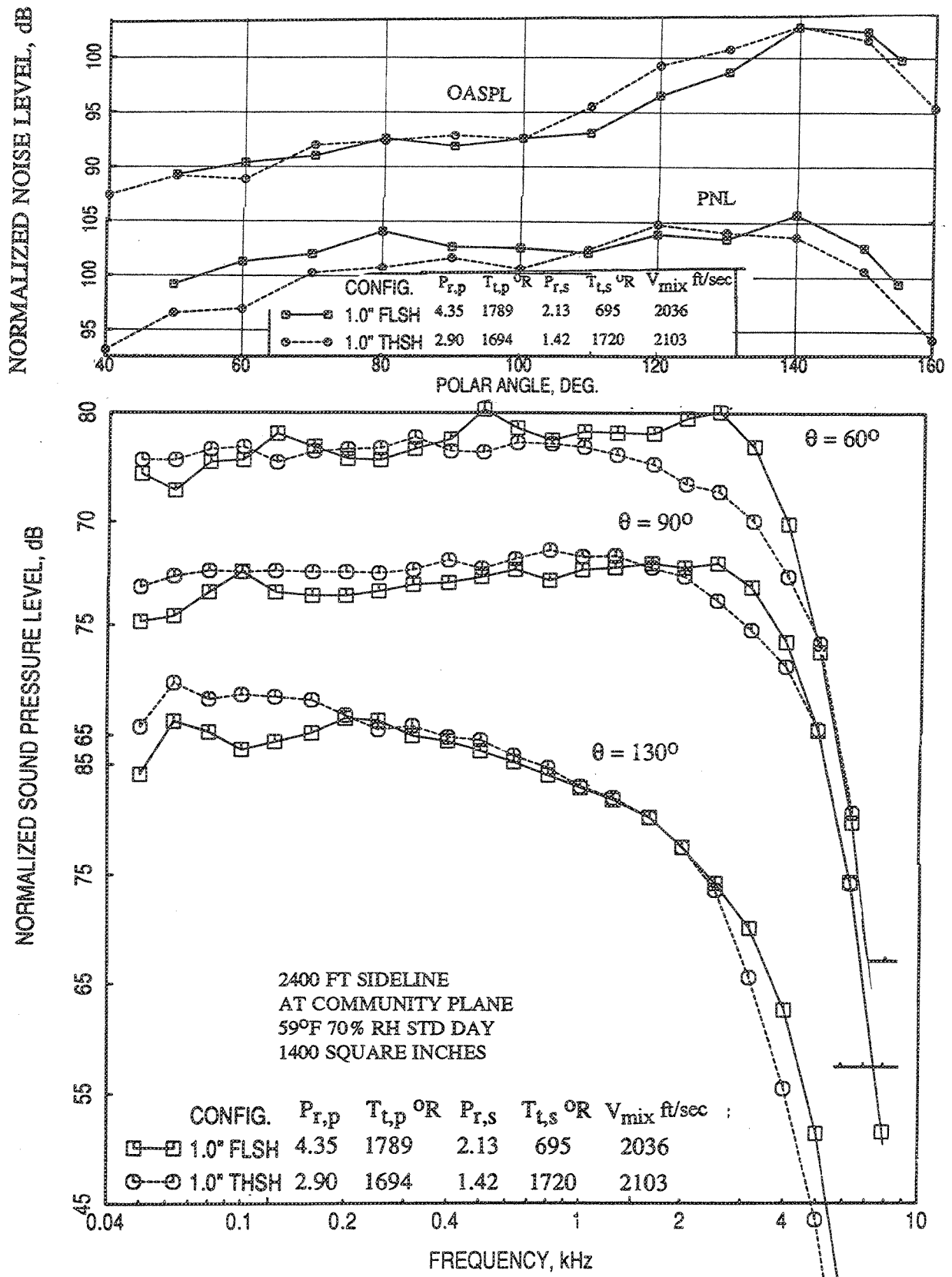


Figure 2.8-72. Comparison of (a) PNL and OASPL directivities and (b) SPL spectra between 1.0"-thick acoustic fluid shield and thermal acoustic shield configurations at a nominal  $V_{mix}=2030$  ft/sec with flight simulation ( $M_F=0.32$ ).

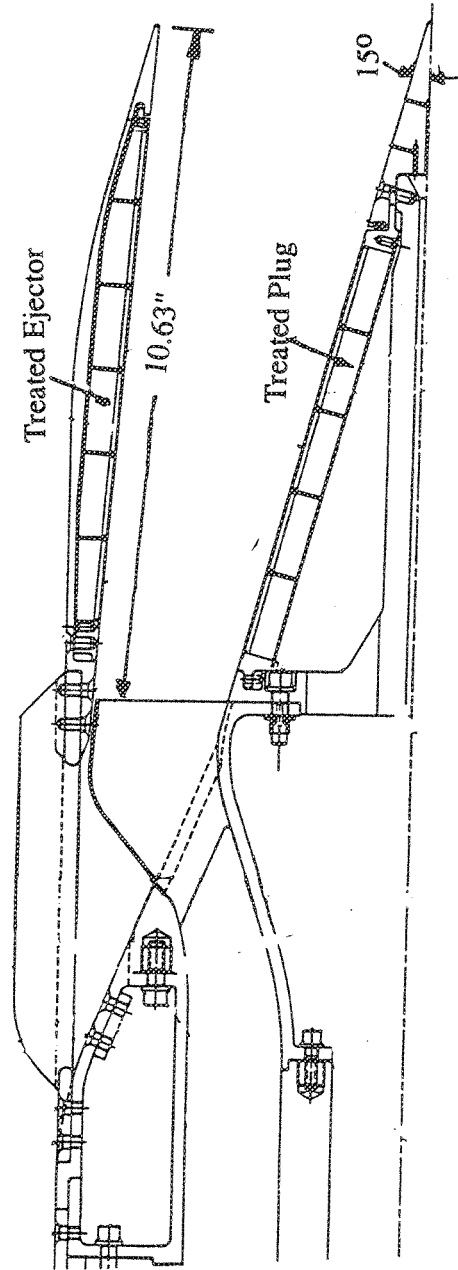


Figure 2.8-73. Side view of a 24 CD-chute axisymmetric mixer ejector nozzle (AMEN) with flush inlet and treated ejector and plug, SAR=3.7.

chute suppressor ( $SAR=3.7$ ) and treated plug and ejector with mixing area ratio,  $MAR$ , of 1.2 (Ref. 28). The throat area of the suppressor was 13.2 square inches.

The 2D mixer-ejector (termed as NRA), shown in Figure 2.8-74, consisted of a 20 aligned CD chute mixer with  $SAR=2.8$  and a 16.055" long treated ejector with  $MAR=0.95$ . Based on the throat area ( $A_8$ ) of the mixer of 22.16 square inches and the chute expansion ratio ( $CER$ ) of 1.43, the mixer exit area is 32.69 square inches and the equivalent mixer diameter at the throat becomes 5.31". The flaps and sidewalls were fully treated with astroquartz of 1 lb/ft<sup>3</sup> with a 37% porous faceplate.

The results presented in this section show comparisons of acoustic performance of three fluid shield nozzles of 0.5", 0.75", and 1.0" thick with the same wrap angle of 220°, the axisymmetric mixer ejector nozzle (AMEN), and the 2D mixer ejector nozzle. The results are scaled to an area of 1175 square inches, extrapolated to a distance of 1629' in the community point, and normalized with respect to thrust only.

*Static Data :* Figure 2.8-75 shows the comparison of EPNLT and PNLT at a number of polar angles between the three fluid shield nozzles and the two mixer ejector nozzles as functions of core (primary) stream jet velocity at static condition. EPNLT levels are comparable between AMEN and two fluid shield nozzles with 0.75" and 1.0" thick shields for entire velocity range. The 0.5"-thick fluid shield is relatively noisier. At lower velocities, below 2300 ft/sec, the 2D mixer ejector is quieter compared to other configurations. However, the trend is reversed at higher velocities. In the forward arc the PNLTs for ejector mixer configurations are lower compared to fluid shield nozzles. The trend is reversed in the rear arc.

PNLT and OASPL directivities for fluid shield and ejector mixer nozzles are compared at three nominal primary stream jet velocities, 2200, 2400, and 2600 ft/sec, in Figure 2.8-76. At lower velocities the mixer ejector nozzles exhibit lower PNLT and OASPLs in the forward arc. The 0.75" and 1.0" shield nozzles are of comparable PNLT and OASPLs with respect to mixer ejector nozzles in the rear arc. At higher velocity of 2600 ft/sec, the 0.75" and 1.0" fluid shield nozzle exhibit lower PNLT and OASPLs for all polar angles, except that the levels at angles higher than 120° for AMEN nozzle are considerably lower.

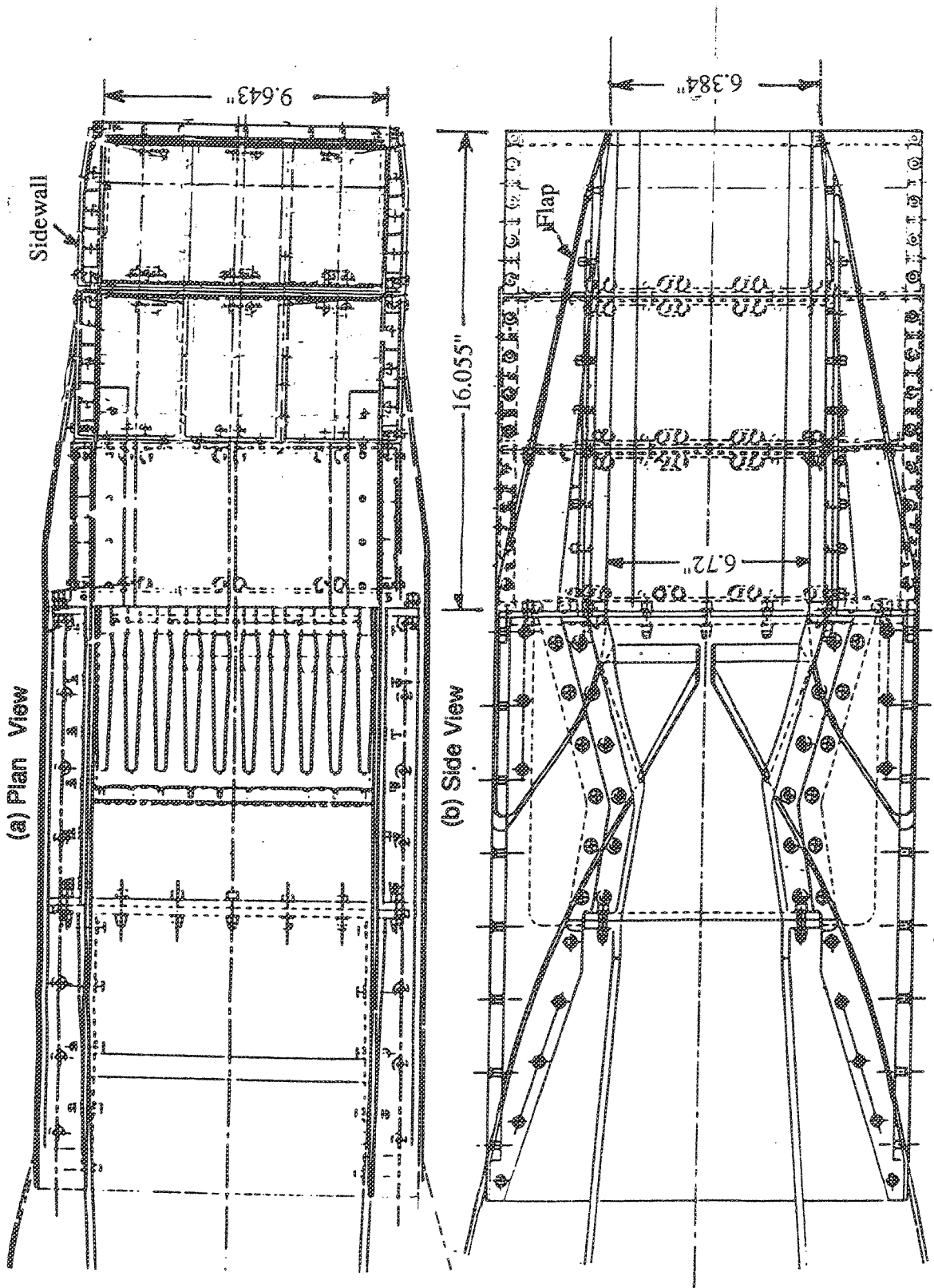


Figure 2.8-74. Plan and side vies of a 20 CD-chute 2D suppressor ejector nozzle with treated long shroud, SAR=2.8, MAR=0.95.

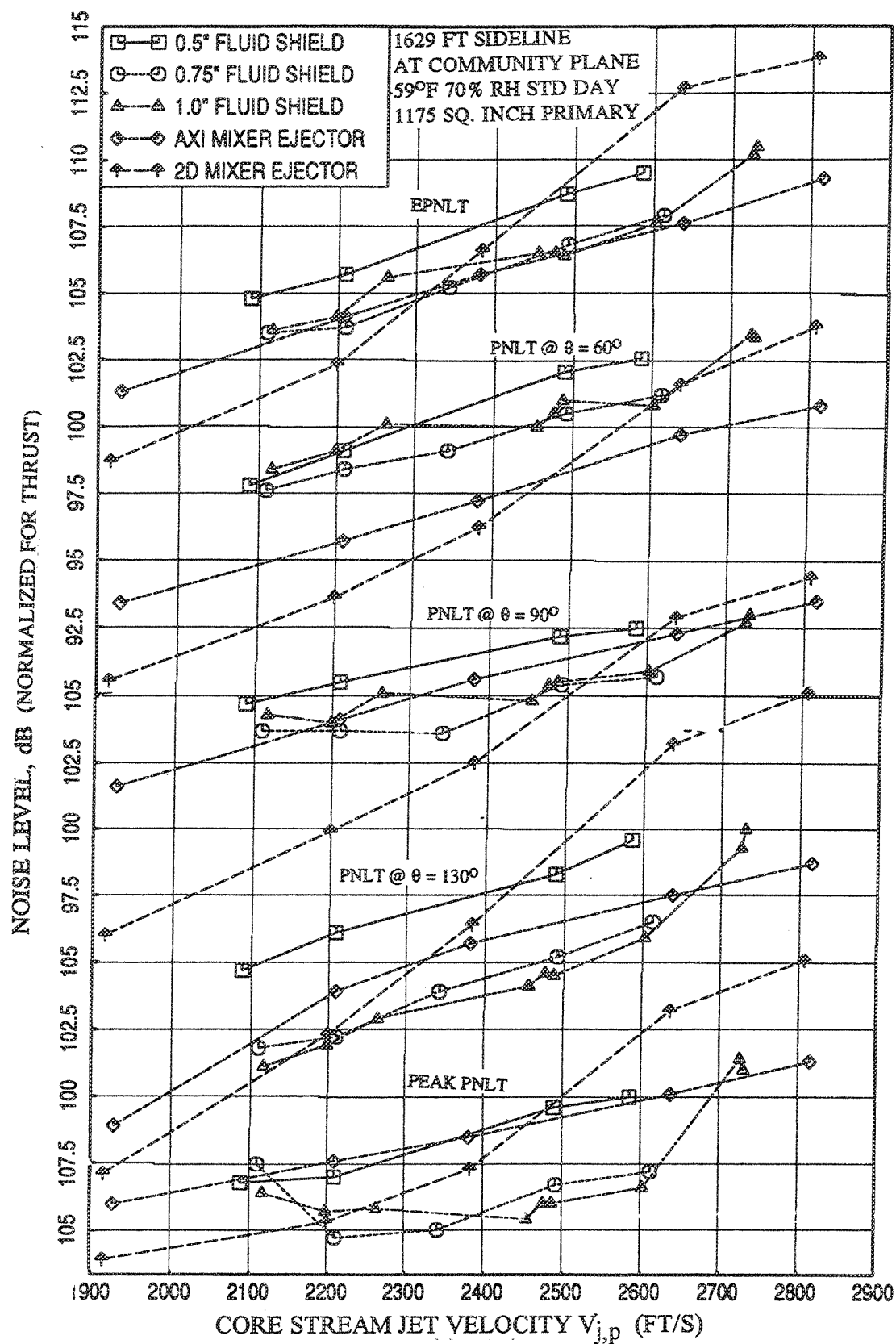


Figure 2.8-75. Comparison of EPNLT and PNLT data at a number of polar angles ( $\theta$ ), normalized for thrust only, as a function of primary jet velocity at static condition between the three fluid shield nozzles, AMEN, and 2D mixer-ejector nozzle.



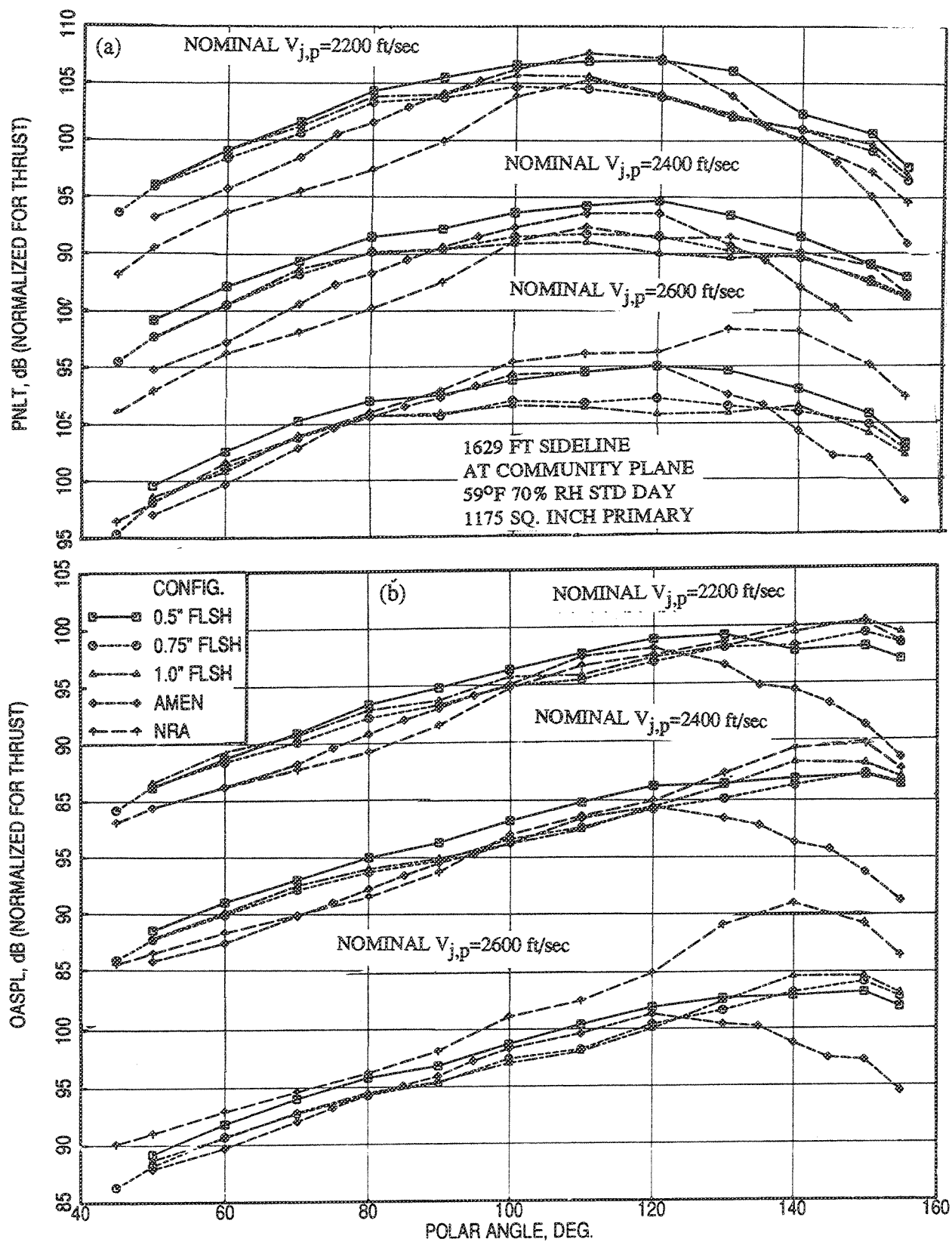


Figure 2.8-76. Comparison of (a) PNLT and (b) OASPL directivities, normalized for thrust only, for a number of primary jet velocities at static condition between the three fluid shield nozzles, AMEN, and 2D mixer-ejector nozzle.

Spectral comparison of sound pressure levels for the fluid shield and mixer-ejector nozzles at a number of polar angles are shown in Figures 2.8-77 through 2.8-79 for nominal primary stream velocities of 2200, 2400, and 2600 ft/sec, respectively. SPL levels are lowest for the AMEN nozzle at frequencies lower than 200 Hz for all angles and velocities. For frequencies above 200 Hz, the 2D ejector seems to be quieter at 2200 and 2400 ft/sec cases in the forward arc. In the rear arc, sound pressure levels for 0.75" and 1.0" fluid shield and 2D mixer-ejector nozzles are comparable and relatively lower than AMEN and 0.5"-thick fluid shield nozzles. At 2600 ft/sec, the sound pressure levels for the 0.75" and 1.0" thick fluid shield nozzles are lower compared to other configurations for all the polar angles above 400 Hz. The SPLs are much higher for the 2D mixer-ejector nozzle at this velocity.

*Flight Data* : Figure 2.8-80 shows the comparison of EPNLT and PNLT at a number of polar angles between the three fluid shield nozzles and the two mixer ejector nozzles as functions of core (primary) stream jet velocity with flight simulation ( $M_F=0.32$ ). EPNLT levels are comparable between AMEN and two fluid shield nozzles with 0.75" and 1.0" thick shields for lower velocities (i.e., below 2400 ft/sec). The 0.5"-thick fluid shield is relatively noisier. At lower velocities, below 2400 ft/sec, the 2D mixer ejector is quieter compared to other configurations. However, the trend is reversed at higher velocities. AMEN nozzle seems to be quieter in terms of EPNdB at velocities above 2600 ft/sec. In the forward arc the PNLTs for ejector mixer configurations are lower compared to fluid shield nozzles. The trend changes in the rear arc.

PNLT and OASPL directivities for fluid shield and ejector mixer nozzles are compared at three nominal primary stream jet velocities, 2200, 2400, and 2600 ft/sec, in Figure 2.8-81. At lower velocities the 2D mixer ejector nozzle exhibits lowest PNLT and OASPLs in the forward arc. The 0.75" and 1.0" shield nozzles are of comparable PNLT and OASPLs with respect to mixer ejector nozzles in the rear arc. At higher velocity of 2600 ft/sec, the 0.75" fluid shield nozzle exhibits lowest PNLT and OASPLs for all polar angles, except that the levels at angles higher than  $120^\circ$  are considerably lower for AMEN nozzle. Data for 1.0" fluid shield at this velocity was not acquired.

Spectral comparison of sound pressure levels for the fluid shield and mixer-ejector nozzles at a number of polar angles are shown in Figures 2.8-82 through 2.8-84 for nominal primary stream velocities of 2200, 2400, and 2600 ft/sec, respectively. SPL

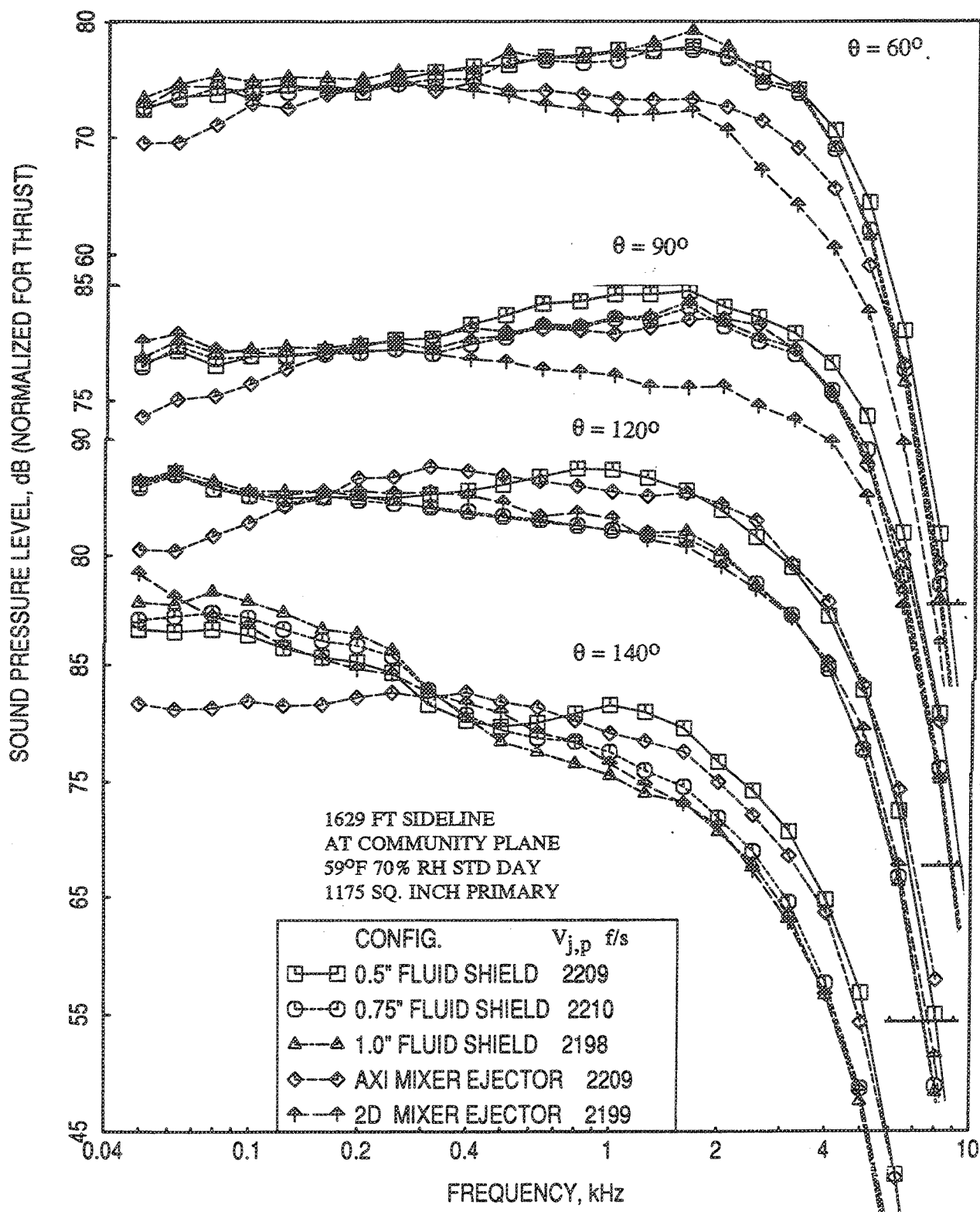


Figure 2.8-77. Comparison of SPL spectra, normalized for thrust only, between the three fluid shield nozzles, AMEN, and 2D mixer-ejector nozzle at a nominal  $V_{j,p} = 2200$  ft/sec at static condition.

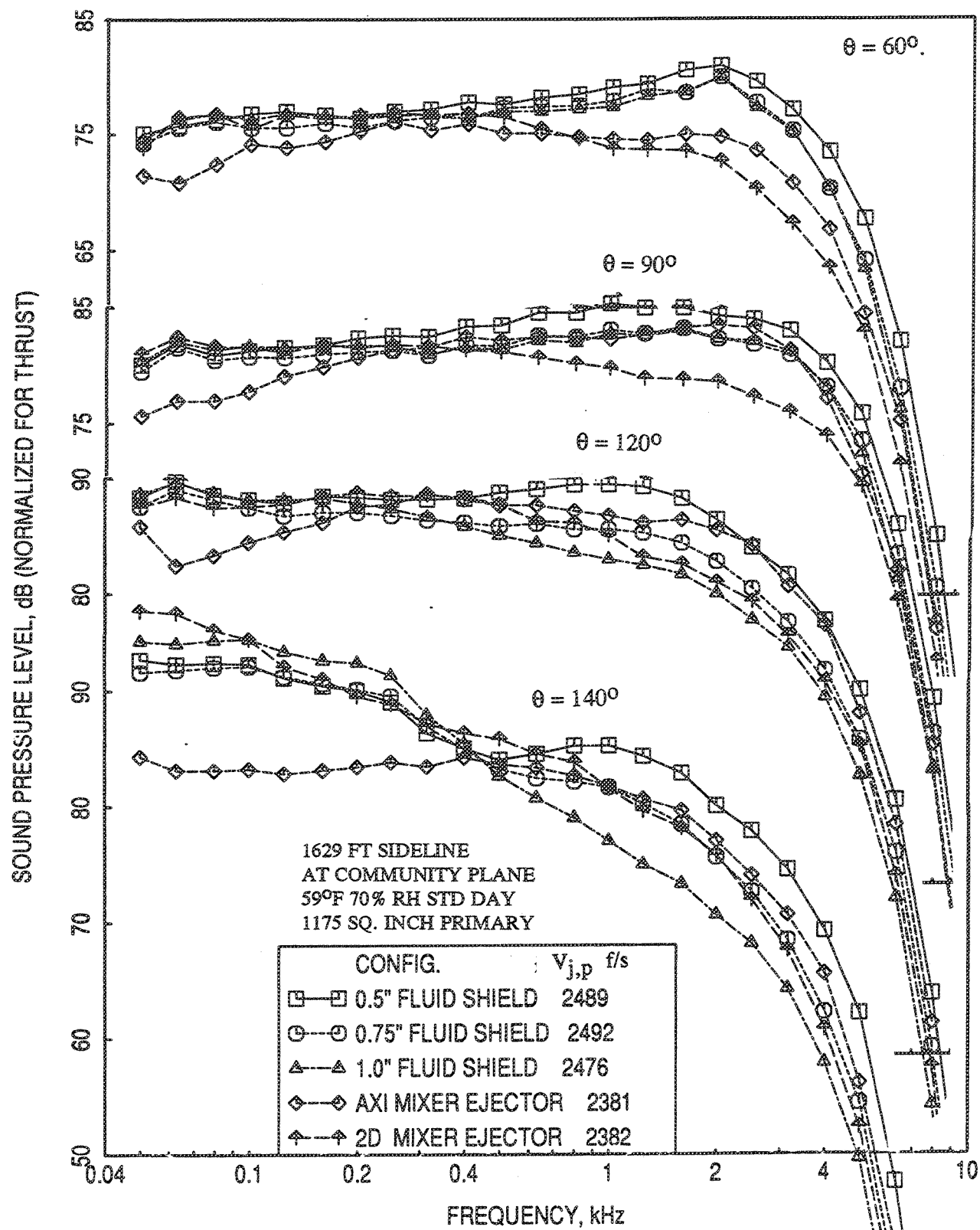


Figure 2.8-78. Comparison of SPL spectra, normalized for thrust only, between the three fluid shield nozzles, AMEN, and 2D mixer-ejector nozzle at a nominal  $V_{j,p}=2400$  ft/sec at static condition.

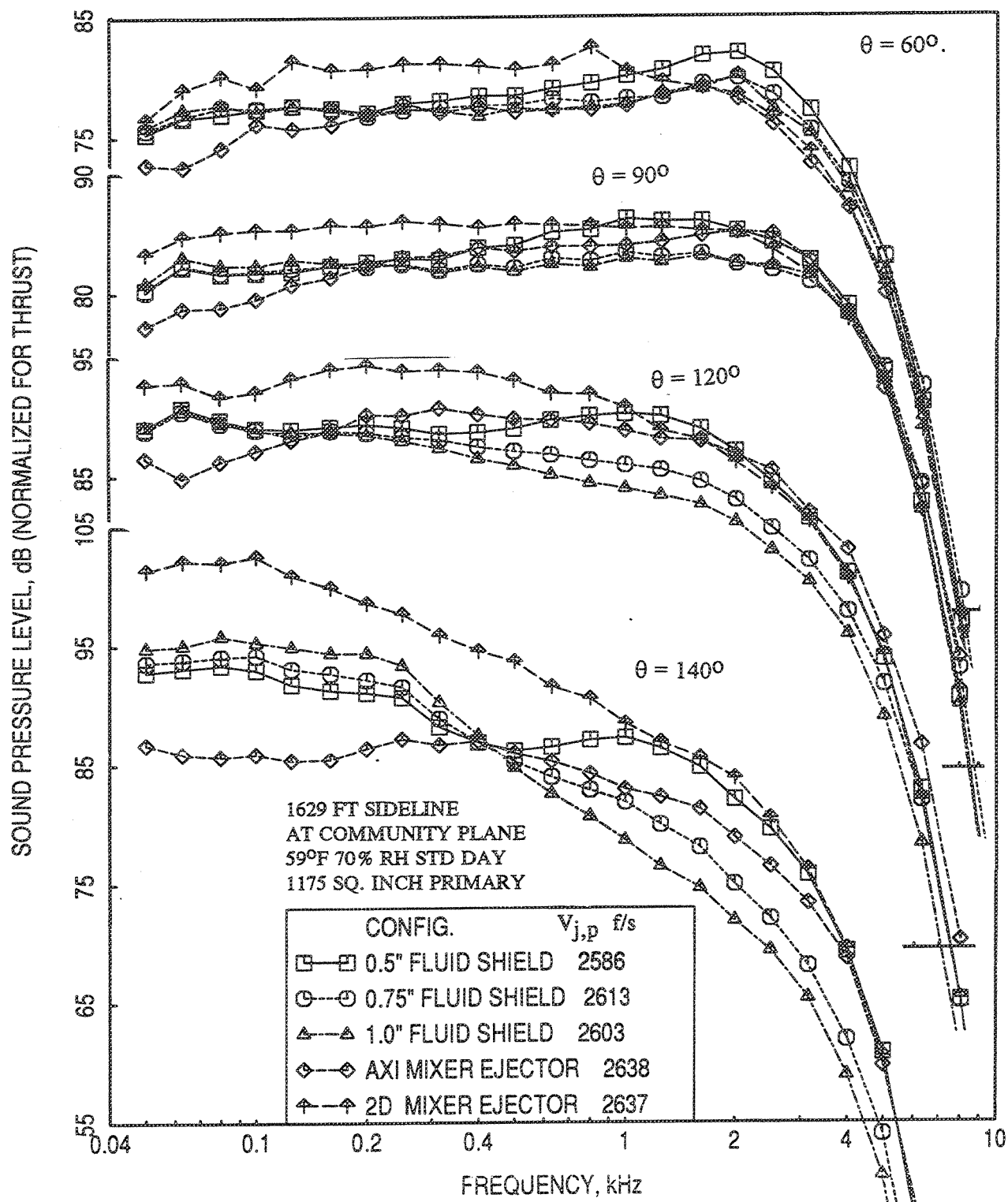


Figure 2.8-79. Comparison of SPL spectra, normalized for thrust only, between the three fluid shield nozzles, AMEN, and 2D mixer-ejector nozzle at a nominal  $V_{j,p} = 2600$  ft/sec at static condition.

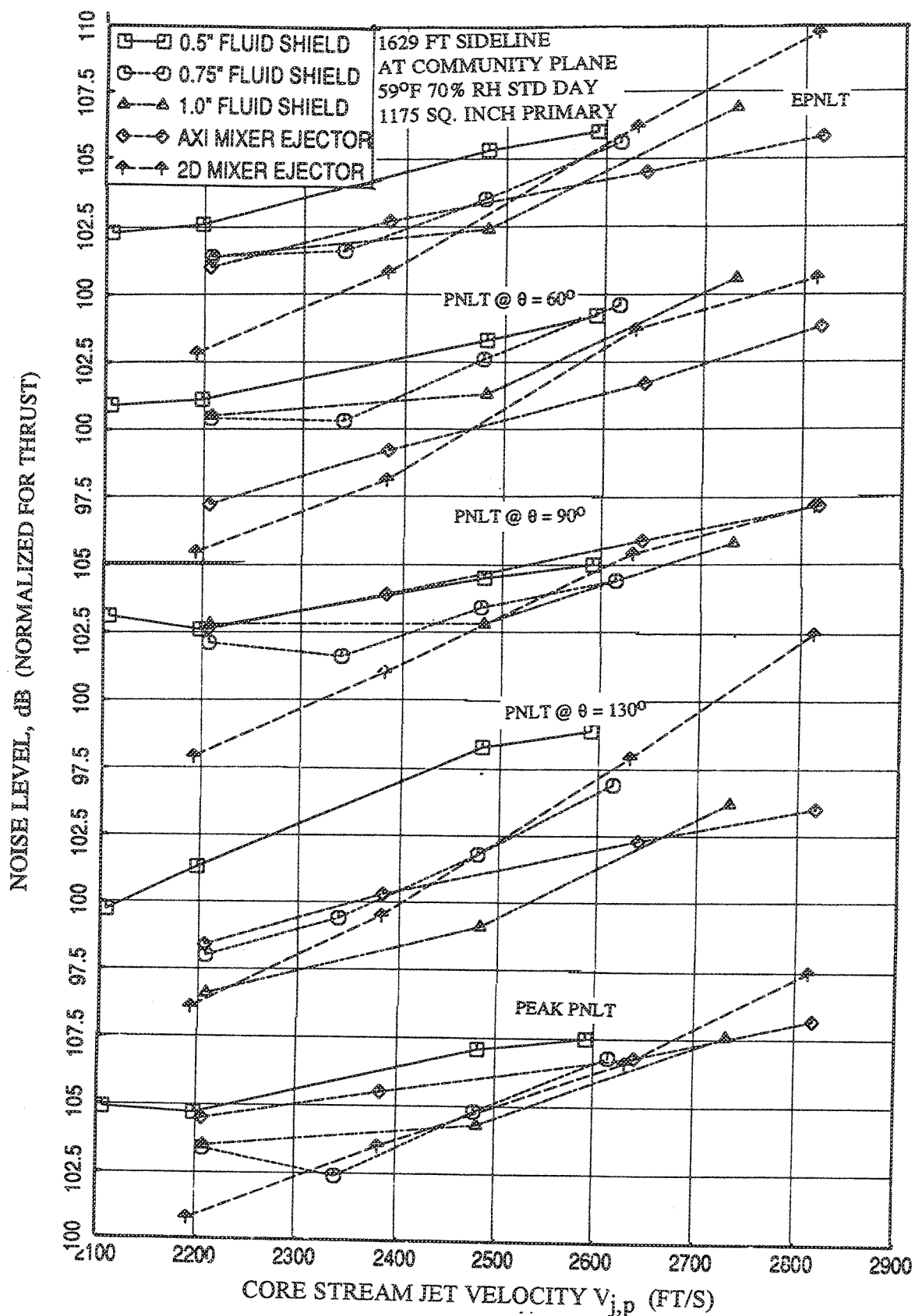


Figure 2.8-80. Comparison of EPNLT and PNLT data at a number of polar angles ( $\theta$ ), normalized for thrust only, as a function of primary jet velocity (a) at static condition and (b) with flight simulation ( $M_F=0.32$ ) between the three fluid shield nozzles, AMEN, and 2D mixer-ejector nozzle.

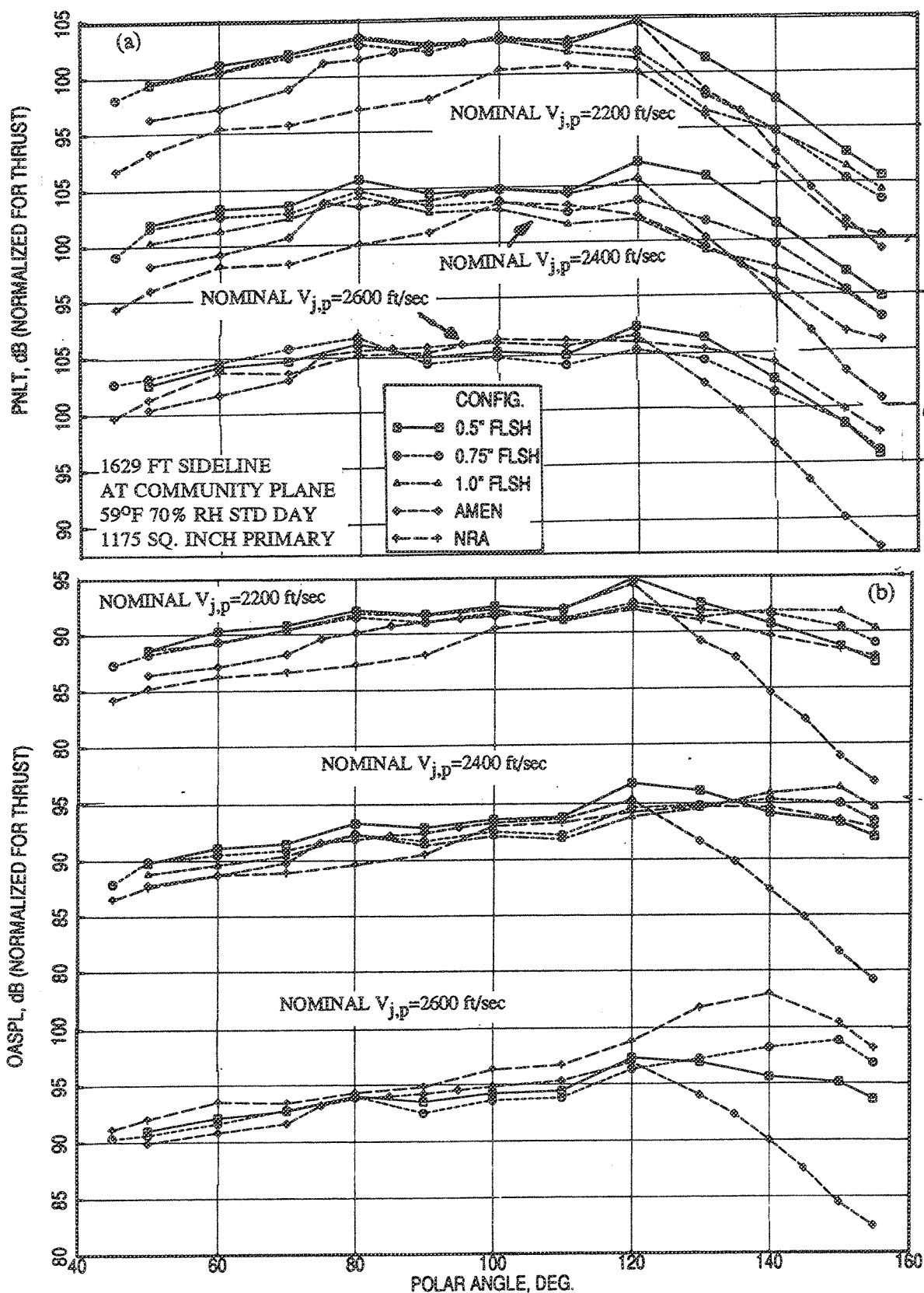


Figure 2.8-81. Comparison of (a) PNLT and (b) OASPL directivities, normalized for thrust only, for a number of primary jet velocities with flight simulation ( $M_F=0.32$ ) between the three fluid shield nozzles, AMEN, and 2D mixer-ejector nozzle.

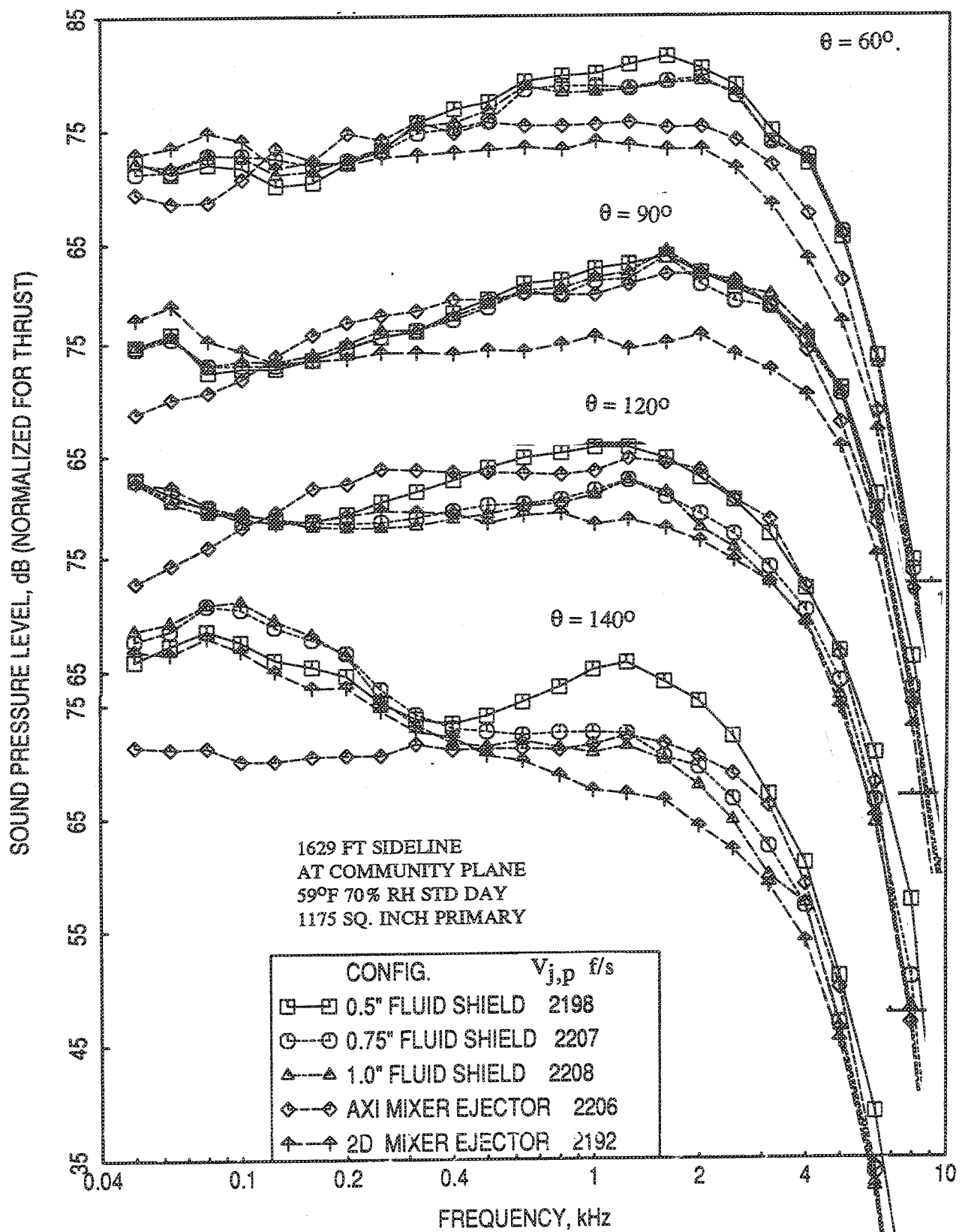


Figure 2.8-82. Comparison of SPL spectra, normalized for thrust only, between the three fluid shield nozzles, AMEN, and 2D mixer-ejector nozzle at a nominal  $V_{j,p}=2200$  ft/sec with flight simulation ( $M_F=0.32$ ).



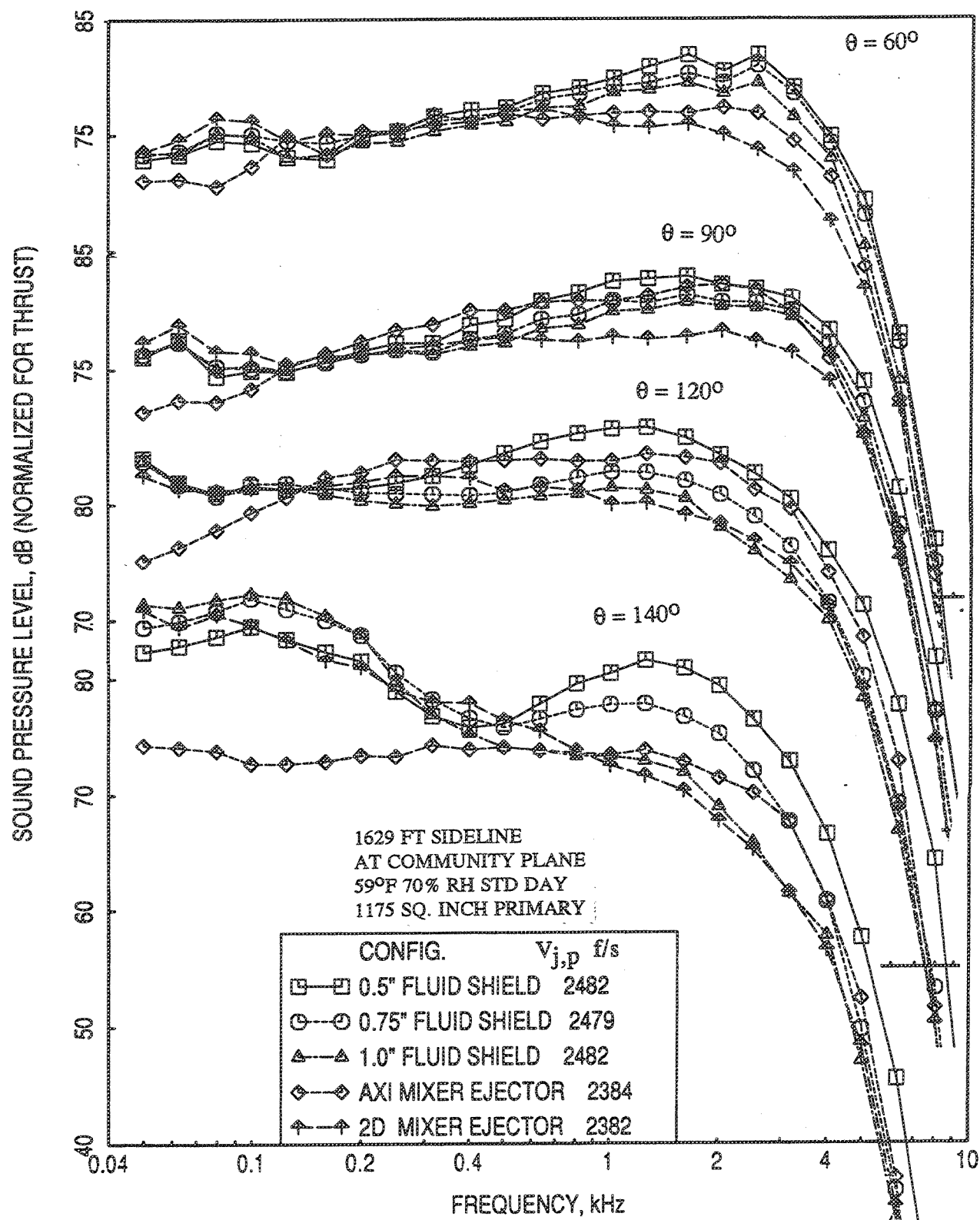


Figure 2.8-83. Comparison of SPL spectra, normalized for thrust only, between the three fluid shield nozzles, AMEN, and 2D mixer-ejector nozzle at a nominal  $V_{j,p}$ =2400 ft/sec with flight simulation ( $M_F$ =0.32).

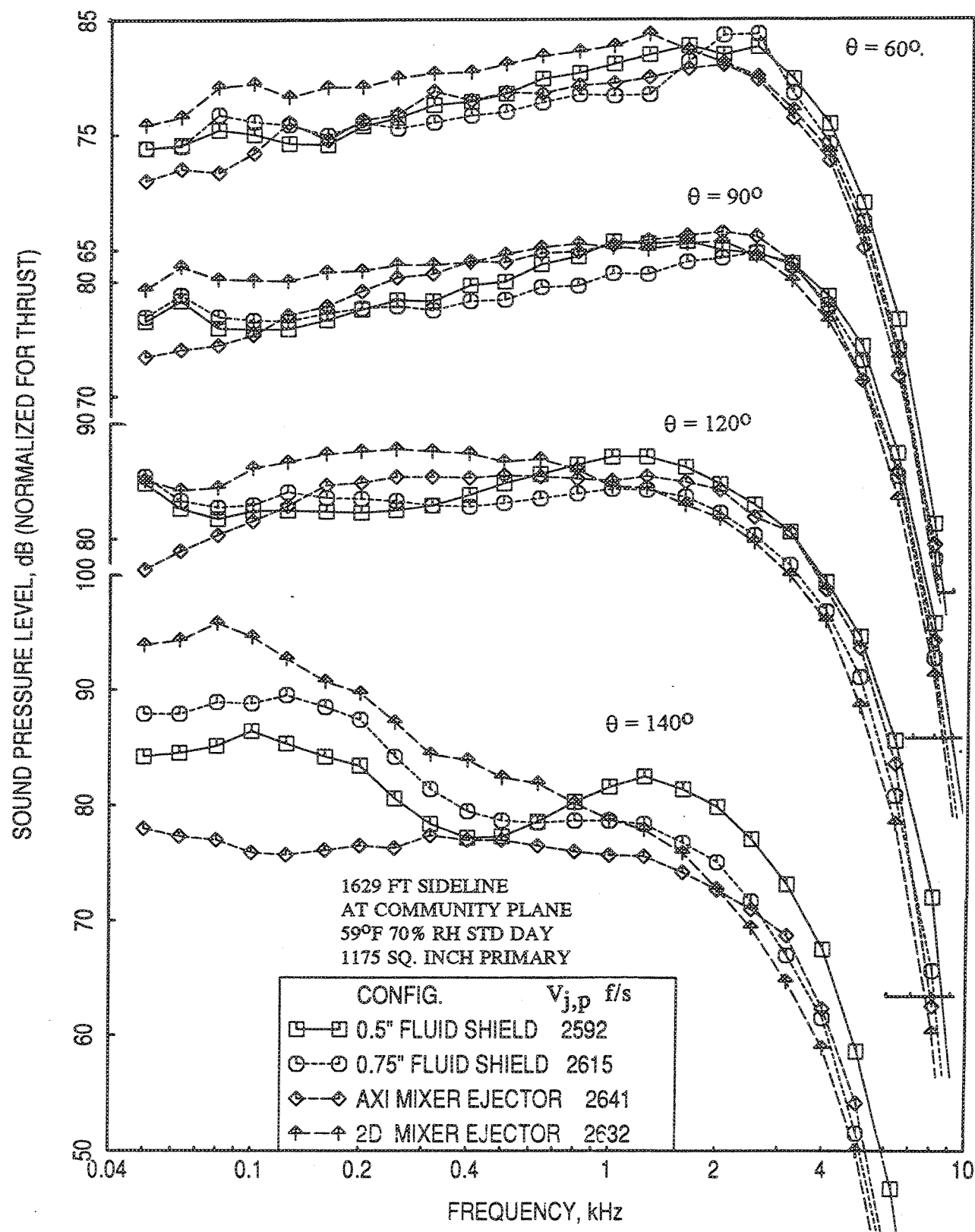


Figure 2.8-84. Comparison of SPL spectra, normalized for thrust only, between the three fluid shield nozzles, AMEN, and 2D mixer-ejector nozzle at a nominal  $V_{j,p}=2600$  ft/sec with flight simulation ( $M_F=0.32$ ).

levels are lowest for the AMEN nozzle at very low frequencies for all angles and velocities. For higher frequencies the 2D ejector seems to be quieter at 2200 and 2400 ft/sec cases. In the rear arc, sound pressure levels for 0.75" and 1.0" fluid shield and 2D mixer-ejector nozzles are comparable and relatively lower than AMEN and 0.5"-thick fluid shield nozzles. At 2600 ft/sec, the sound pressure levels for the 0.75" thick fluid shield nozzle are lower compared to other configurations for most polar angles above 400 Hz.

#### 2.8.6 Conclusions

1. While the EPNLTs for the suppressor alone configuration show substantial noise reduction compared to the reference conical nozzle, the fluid shield configurations do not indicate any noticeable noise reduction compared to the suppressor alone configuration on a  $V_{mix}$  basis. Specially, at takeoff condition (i.e., at mixed velocity of 2030 ft/s) we do not see much advantage of the fluid shield. However, the unnormalized EPNLTs at fixed thrust indicate substantial noise benefit due to fluid shields compared to suppressor alone configuration. For the takeoff thrust of about 67 to 69 klbs additional noise suppression of about 2 to 7 EPNdB statically and 4 to 8 EPNdB with flight simulation are observed due to fluid shields compared to the suppressor alone configuration.
2. On an equal area basis significant noise benefit is observed due to fluid shields compared to suppressor alone configuration. For 0.75"-thick shield noise suppression of about 3 to 4 EPNdB at static condition and about 4 to 8 EPNdB with flight simulation are obtained compared to the suppressor alone configuration of the same total area in the range of 60 to 70 klbs ideal gross thrust.
3. Significant noise suppression due to fluid shield is obtained at fixed core stream velocities. Noise benefit of as high as 7 EPNdB at static condition and 8 EPNdB with flight simulation is observed for 0.75" and 1.0" thick shields with respect to the suppressor alone configuration. The effectiveness of the shield diminishes with increasing core stream velocity.
4. Results of previously tested acoustic thermal shield configurations are compared with the data obtained for the present acoustic fluid shield configurations. For 0.5" thick shields the fluid shield configuration is quieter compared to the thermal shield

with respect to OASPL, PNL, and SPL for all the velocity conditions. For 1.0" thick shields both configurations exhibit similar noise characteristics.

5. Typical acoustic results of two mixer ejector nozzles, namely an axisymmetric (AMEN) and a 2D, designed, fabricated, and tested for HSCT exhaust system, are compared with the fluid shield nozzle results. EPNLT levels are comparable between AMEN and two fluid shield nozzles with 0.75" and 1.0" thick shields for core stream velocity range of 2100 to 2600 ft/sec. At lower velocities, the 2D mixer ejector is quieter compared to other configurations. However, the trend is reversed at higher velocities.

6. With respect to FAR 36 Stage 3 noise requirement the best of fluid shield configuration falls short of about 3.5 EPNdB at takeoff with an ideal gross thrust of about 68 klbs.

## 2.9 ACOUSTIC CHARACTERISTICS OF FLUID SHIELD NOZZLES DUE TO PARAMETRIC VARIATIONS OF AEROTHERMODYNAMIC CONDITIONS

Parametric studies due to aerothermodynamic conditions are conducted in two ways. First, the aerothermodynamic variables, namely, the total temperatures and the nozzle pressure ratios, of both the streams are varied to generate a fixed  $V_{\text{mix}}$ , which gives velocity ratio  $V_r$  and mass flow ratio  $W_r$  variation. For the present study two  $V_{\text{mix}}$  values, corresponding to the baseline fluid shield model (i.e., 0.5"-thick fluid shield nozzle) at takeoff and cutback cycle conditions (i.e., 2030 ft/sec and 1811 ft/sec, respectively) are chosen. Tests were conducted at several sets of aerothermodynamic conditions to generate these fixed  $V_{\text{mix}}$  values for all the fluid shield nozzles, which resulted in a wide variation of  $W_r$  with respect to  $V_r$ . In these tests only the nozzle pressure ratios were varied. The total temperatures of both the streams were maintained constant at the cycle condition values (i.e., 1786°R and 695°R for  $V_{\text{mix}}=2030$  ft/sec, and 1806°R and 727°R for  $V_{\text{mix}}=1811$  ft/sec, in primary and fluid shield nozzle streams, respectively). These tests include several subsonic shield flow conditions (i.e., outer stream).  $V_r$  and  $W_r$  values are increased with increasing fluid shield nozzle pressure ratio with very little change of primary nozzle pressure ratio for fixed  $V_{\text{mix}}$ . These test conditions are described in section 2.2 and illustrated in Figure 2.2-20.

Second, one of the four aerothermodynamic parameters, namely,  $P_{r,p}$ ,  $T_{t,p}$ ,  $P_{r,s}$ , and  $T_{t,s}$ , was varied keeping the other three parameters fixed, which illustrated the influence of each of these parameters on the noise characteristics of fluid shield nozzles. These test conditions are described in section 2.2 and illustrated in Figure 2.2-21.

Normalized pseudo EPNLT, PNLT, and SPL values are calculated for the three fluid shield nozzles of thicknesses 0.5", 0.75", and 1.0" with fixed wrap of 220° and 0.6"-thick fluid shield nozzle with 180° wrap using the acoustic data measured at  $\phi=75^\circ$  (i.e., at community plane). All configurations were tested with porous plug. Keeping the same linear scale factor the 0.5", 0.75", and 1.0" fluid shield nozzles are scaled to 1813.6, 2165.5, and 2524.7 square inches, respectively. Since the 0.6"-thick fluid shield has the same model scale area (i.e.,  $A_8=11.734 \text{ in}^2$ ) of that of 0.5"-thick, this configuration is also scaled to 1813.6 square inches. All the data are extrapolated to a sideline distance of 1629 feet and are corrected for standard day conditions. Most of the studies are made utilizing the data for the three fluid shield nozzles with the same wrap angle of 220°.

### 2.9.1 Static Data

Effect of Velocity ratio  $V_r$  and Mass Flow Ratio  $W_r$  :

At  $V_{mix} = 1811$  ft/sec :

Normalized PNLTs are plotted with respect to  $V_r$  in Figure 2.9-1 at different polar angles ( $\theta$ ) for the three fluid shield nozzles for  $V_{mix}$  of 1811 ft/sec. Normalized PNLT decreases with  $V_r$ . Figure 2.9-2 illustrates the variation of normalized peak PNLT and pseudo EPNLT with  $V_r$ . The general trend is similar to PNLT variation, except for 1.0"-thick shield, for which, the pseudo EPNLT decreases with  $V_r$  and then increases, resulting at a minimum level. For other configurations, such noise minima might exist at  $V_r$  larger than what were tested.

Variation of PNLT and pseudo EPNLT with respect to  $W_r$  are shown in Figures 2.9-3 and 2.9-4. The general trends are similar to those observed in Figures 2.9-1 and 2.9-2 with respect to  $V_r$  for individual configurations. In a comparative basis, noise levels decrease with increasing shield thickness (bypass ratio) at fixed  $V_r$  and the trend is reversed with fixed  $W_r$ . Velocity ratio ( $V_r$ ) depends on the aerothermodynamic conditions of the flow streams, whereas, at the same aerothermodynamic conditions the mass flow ratio ( $W_r$ ) increases with increasing shield thickness. Due to this the noise curves with respect to  $V_r$  move to the right with increasing fluid shield thickness when plotted with respect to  $W_r$ . Since, the noise levels decrease with increasing  $V_r$  (or  $W_r$ ), a reversal in trend is observed between  $V_r$  and  $W_r$  distributions.

Normalized PNLT directivities for 0.5"-thick shield are plotted in Figure 2.9-5 for different  $V_r$  and  $W_r$ . PNLT at all angles decreases with increasing  $V_r$  (or  $W_r$ ), whereas, ideal gross thrust increases with  $V_r$ . As mentioned earlier, further increase in  $V_r$  may reverse the trend for PNLT, and an optimum  $V_r$  may be established. Corresponding normalized SPL spectra are plotted in Figure 2.9-6, which also indicates the similar trend at all frequencies.

Normalized PNLT directivities and normalized SPL spectra for the other two fluid shield configurations with 0.75"-thick and 1.0"-thick shields are shown in Figures 2.9-7 through 2.9-10. Similar trends with respect to  $V_r$  (or  $W_r$ ) are also observed for these configurations.

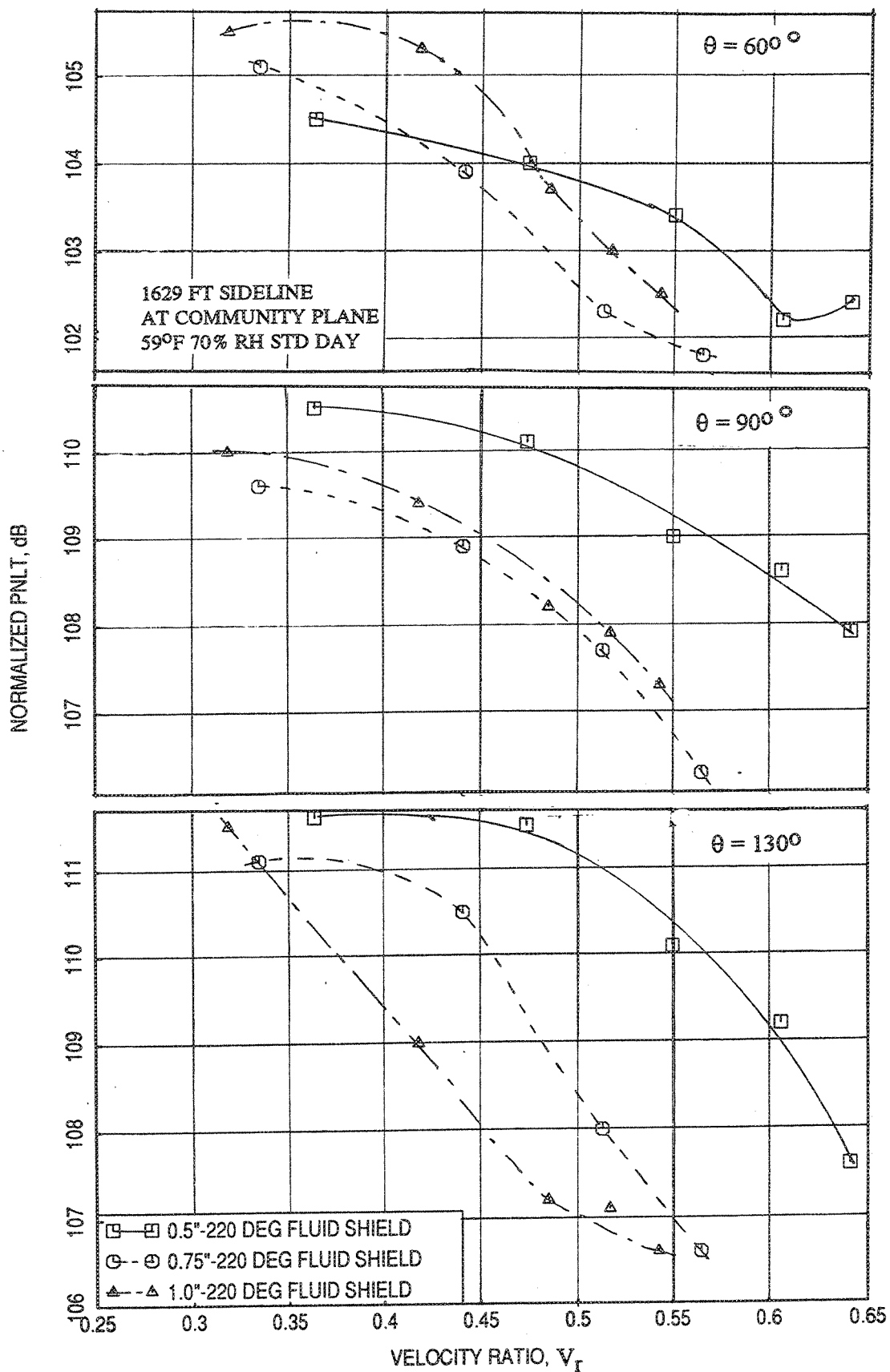


Figure 2.9-1. Effect of velocity ratio  $V_r$  on normalized PNLT data at different polar angles ( $\theta$ ) for fluid shield nozzles for a fixed jet velocity,  $V_{mix}$ , of 1811 ft/sec at static condition.

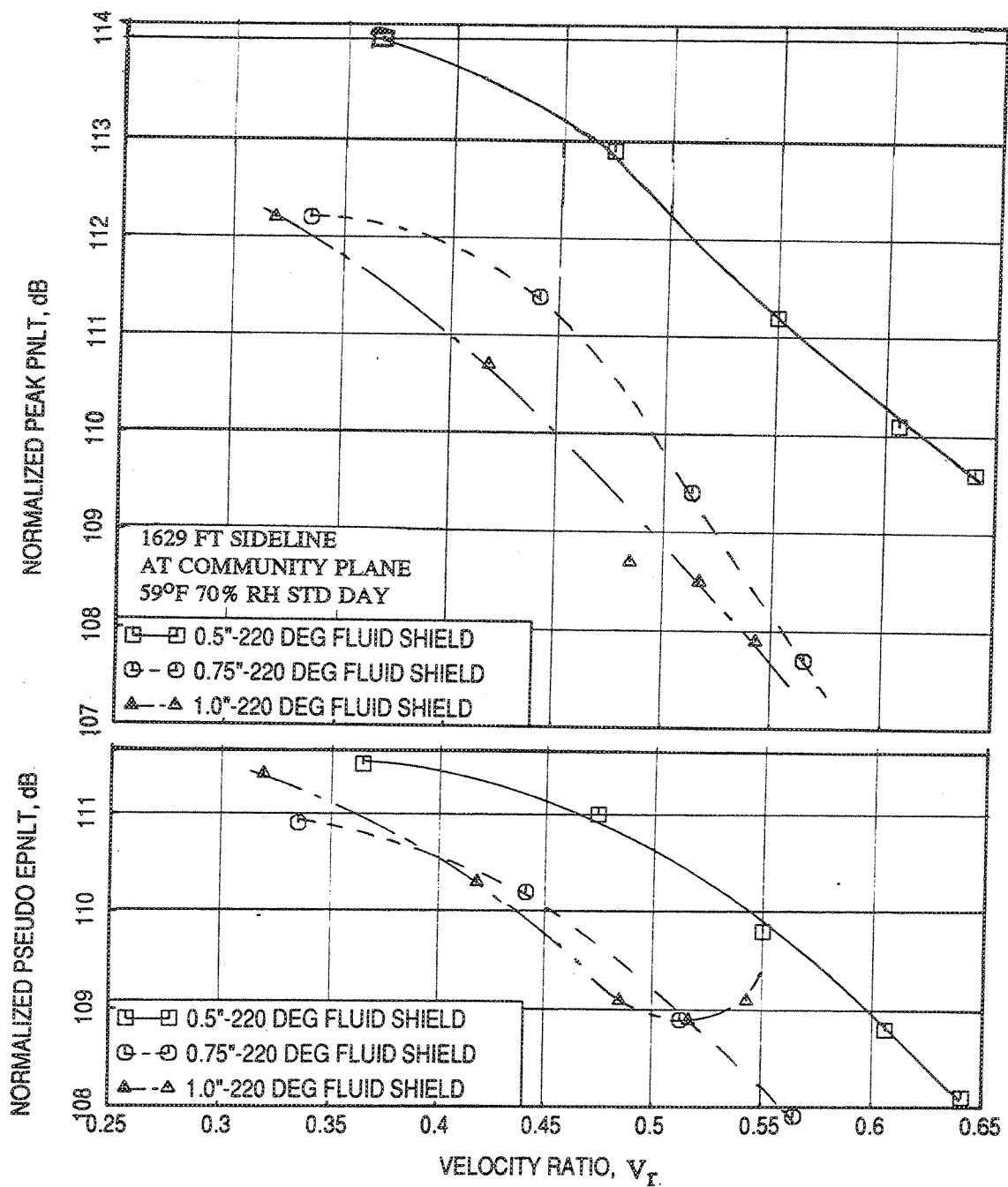


Figure 2.9-2. Effect of velocity ratio  $V_r$  on normalized peak PNLT and normalized pseudo EPNLT data for fluid shield nozzles for a fixed jet velocity,  $V_{mix}$ , of 1811 ft/sec at static condition.



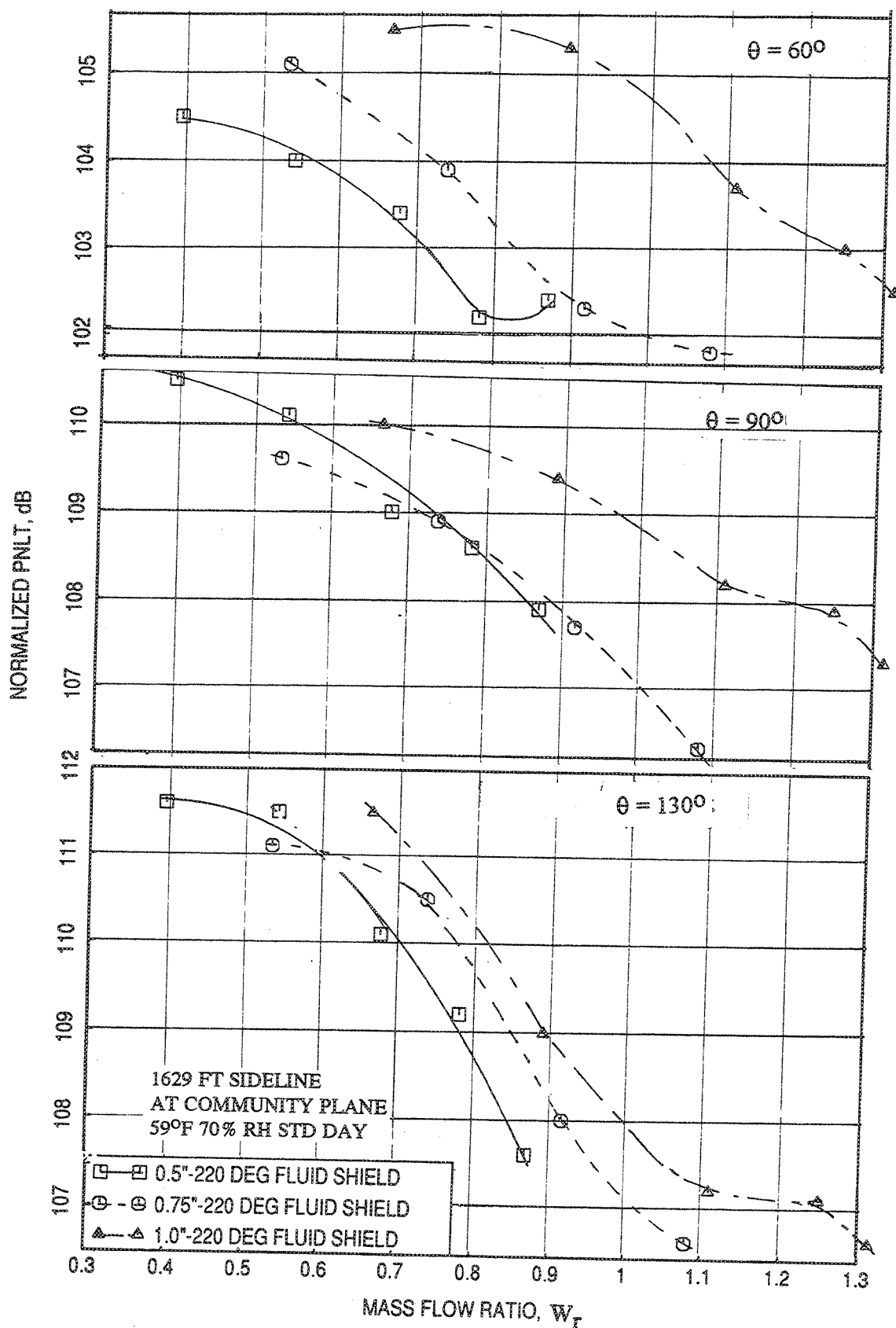


Figure 2.9-3. Effect of mass flow ratio  $W_r$  on normalized PNLT data at different polar angles ( $\theta$ ) for fluid shield nozzles for a fixed jet velocity,  $V_{mix}$ , of 1811 ft/sec at static condition.

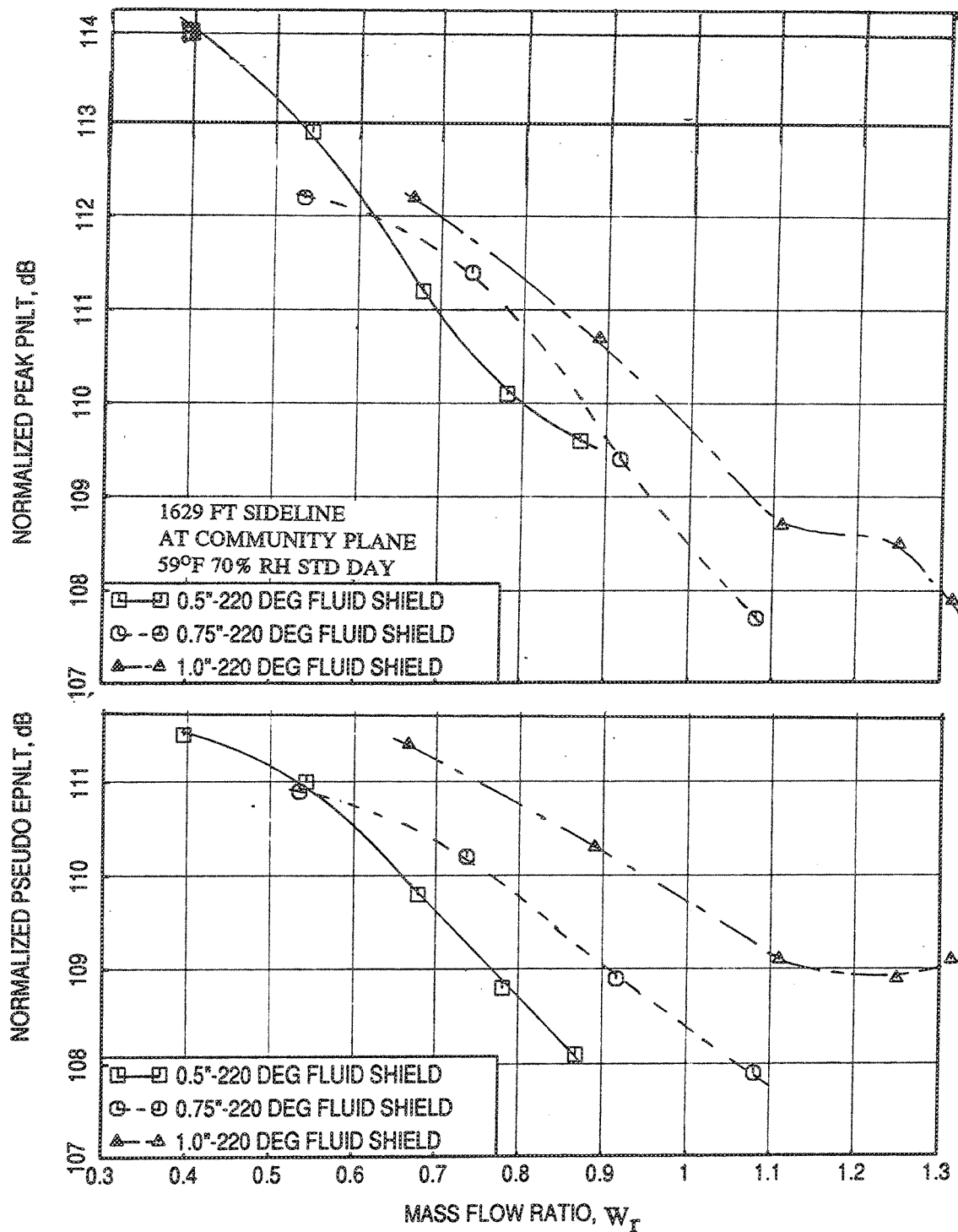


Figure 2.9-4. Effect of mass flow ratio  $W_r$  on normalized peak PNLT and normalized pseudo EPNLT data for fluid shield nozzles for a fixed jet velocity,  $V_{mix}$ , of 1811 ft/sec at static condition.

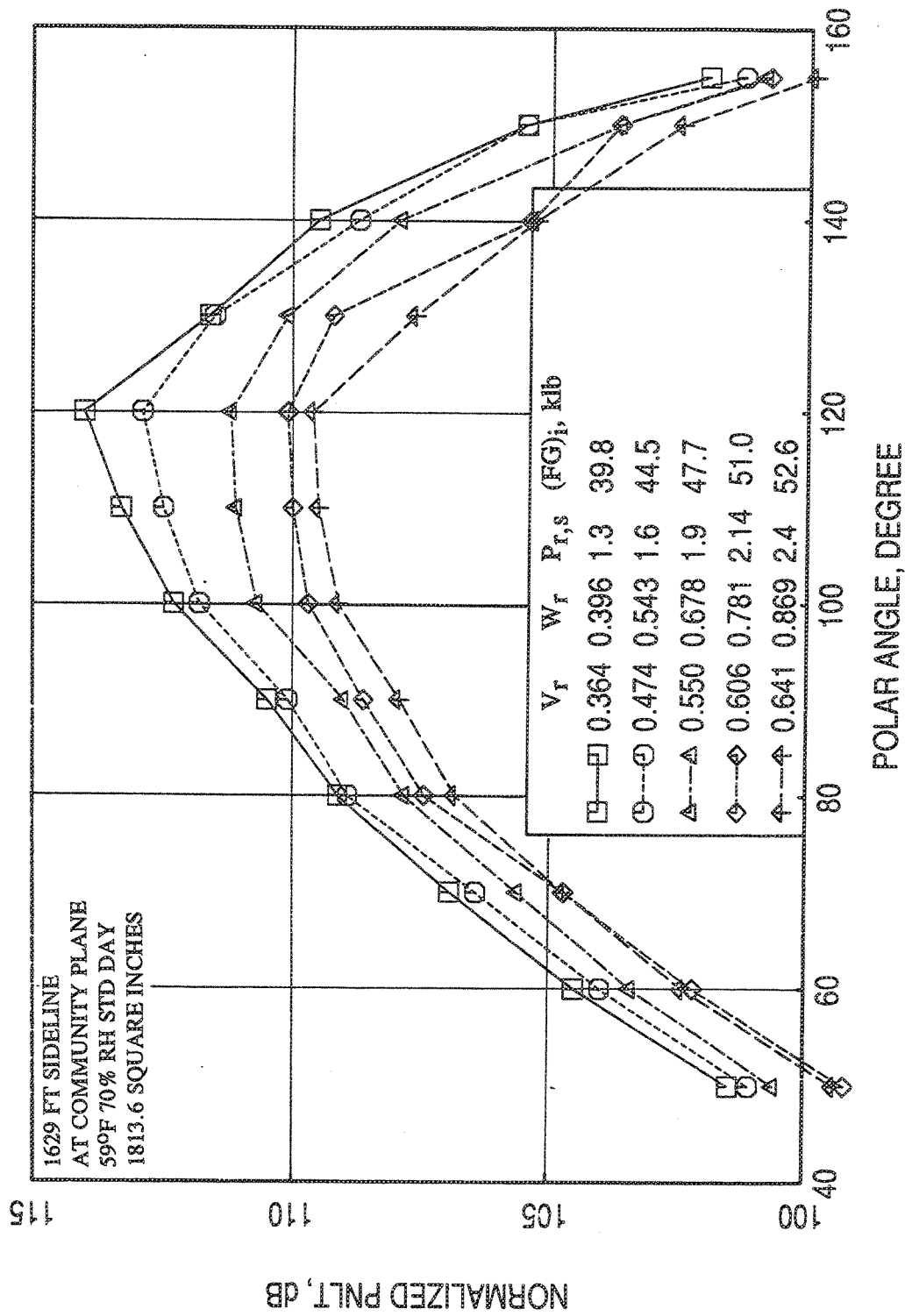


Figure 2.9-5. Normalized PNLT directivities for the 0.5"-thick fluid shield nozzle at different  $V_r$  (and  $W_r$ ) for a fixed jet velocity,  $V_{mix}$ , of 1811 ft/sec at static condition.

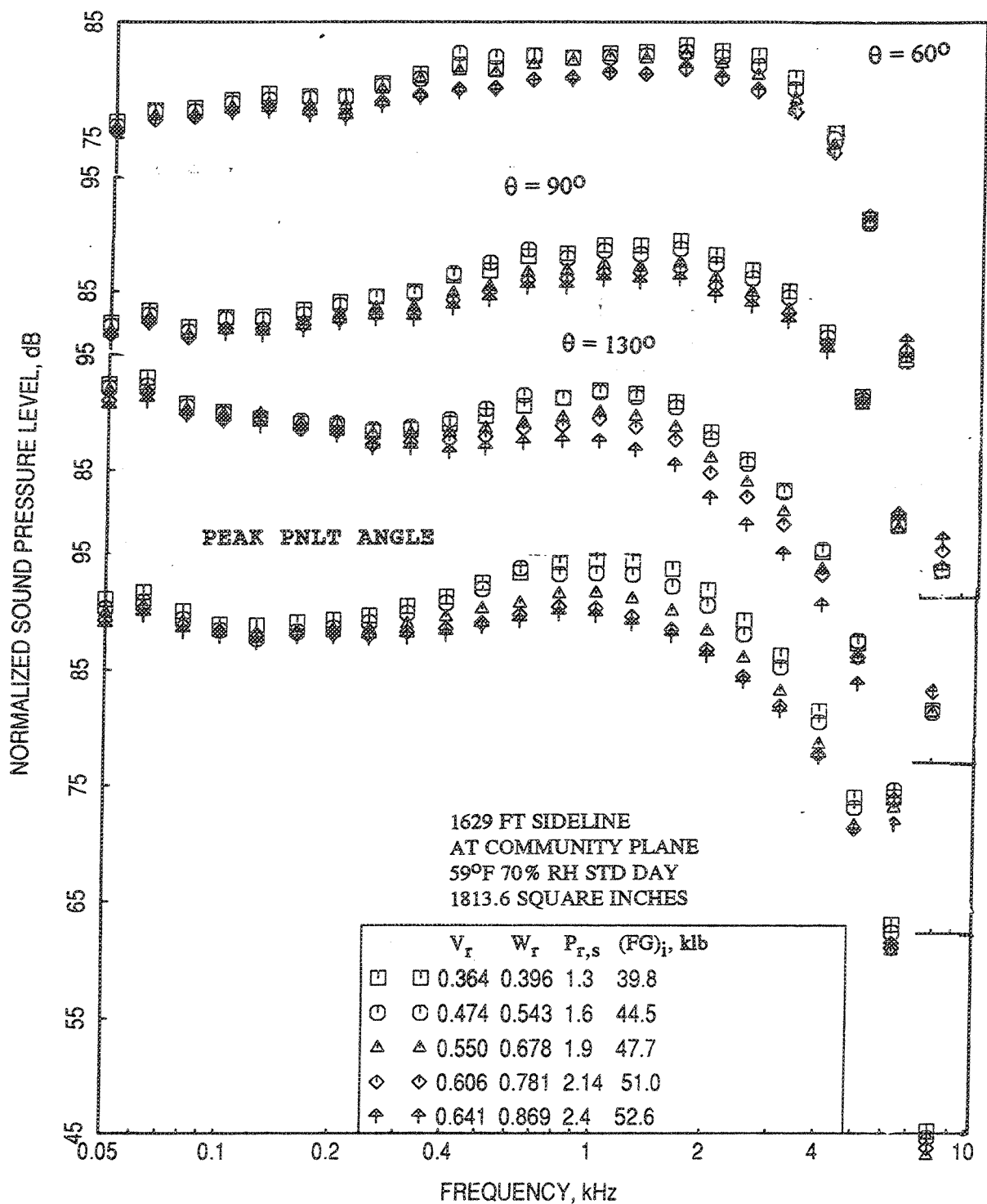


Figure 2.9-6. Normalized SPL spectra at different polar angles ( $\theta$ ) for the 0.5"-thick fluid shield nozzle at different  $V_r$  (and  $W_r$ ) for a fixed jet velocity,  $V_{mix}$ , of 1811 ft/sec at static condition.

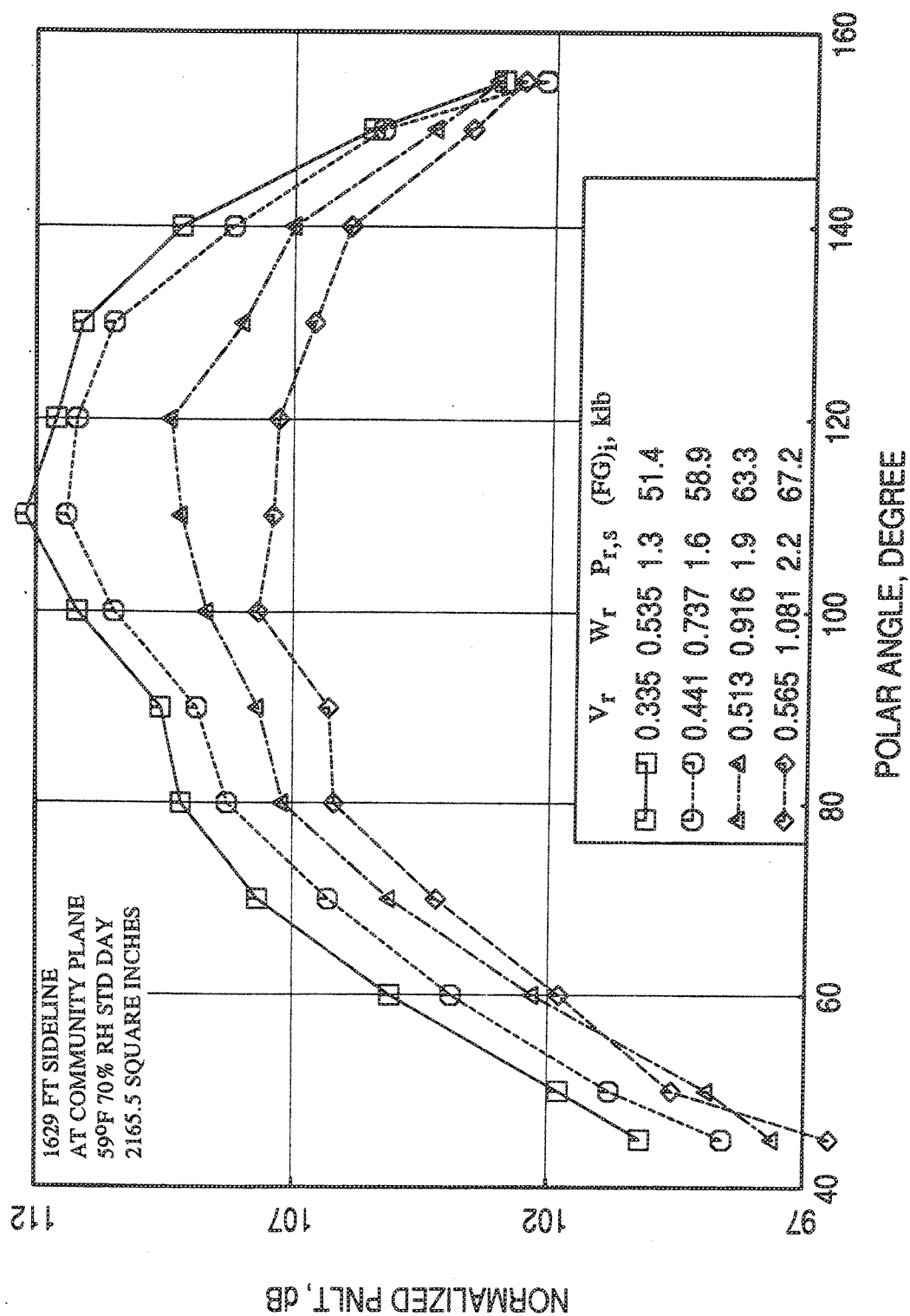


Figure 2.9-7. Normalized PNL T directivities for the 0.75"-thick fluid shield nozzle at different  $V_r$  (and  $W_r$ ) for a fixed jet velocity,  $V_{mix}$ , of 1811 ft/sec at static condition.

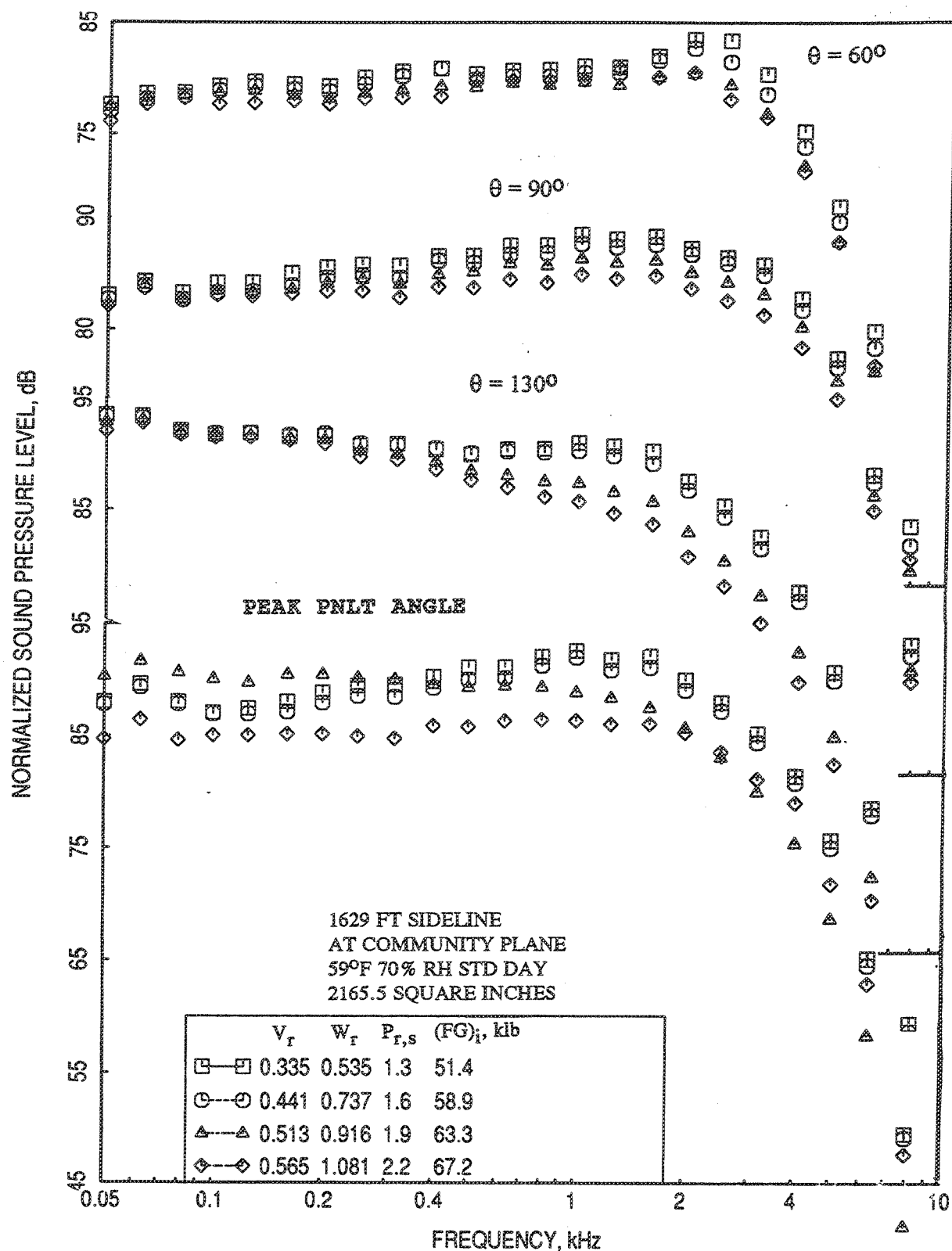


Figure 2.9-8. Normalized SPL spectra at different polar angles ( $\theta$ ) for the 0.75"-thick fluid shield nozzle at different  $V_r$  (and  $W_r$ ) for a fixed jet velocity,  $V_{mix}$ , of 1811 ft/sec at static condition.

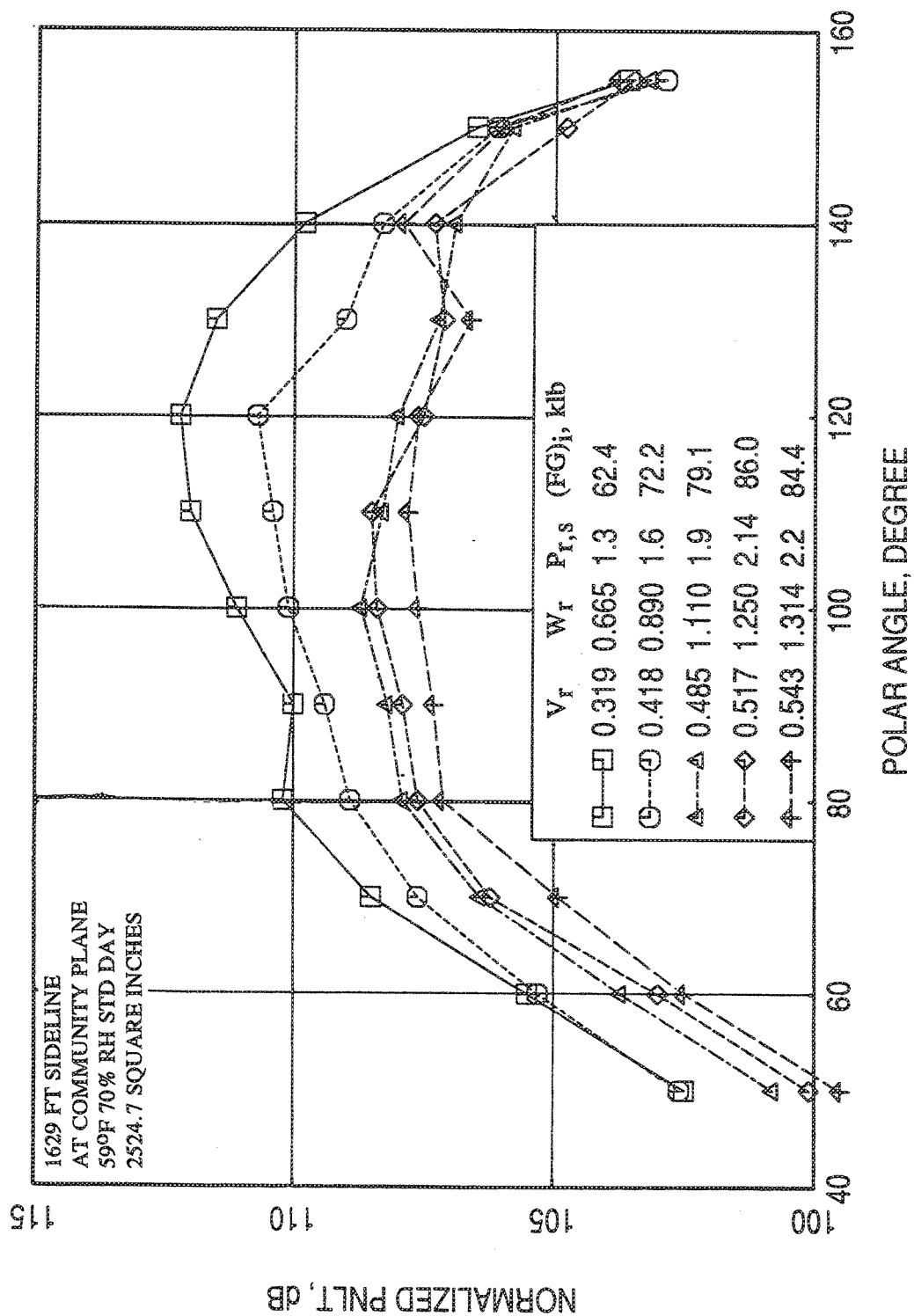


Figure 2.9-9. Normalized PNLT directivities for the 1.0"-thick fluid shield nozzle at different  $V_r$  (and  $W_r$ ) for a fixed jet velocity,  $V_{mix}$ , of 1811 ft/sec at static condition.

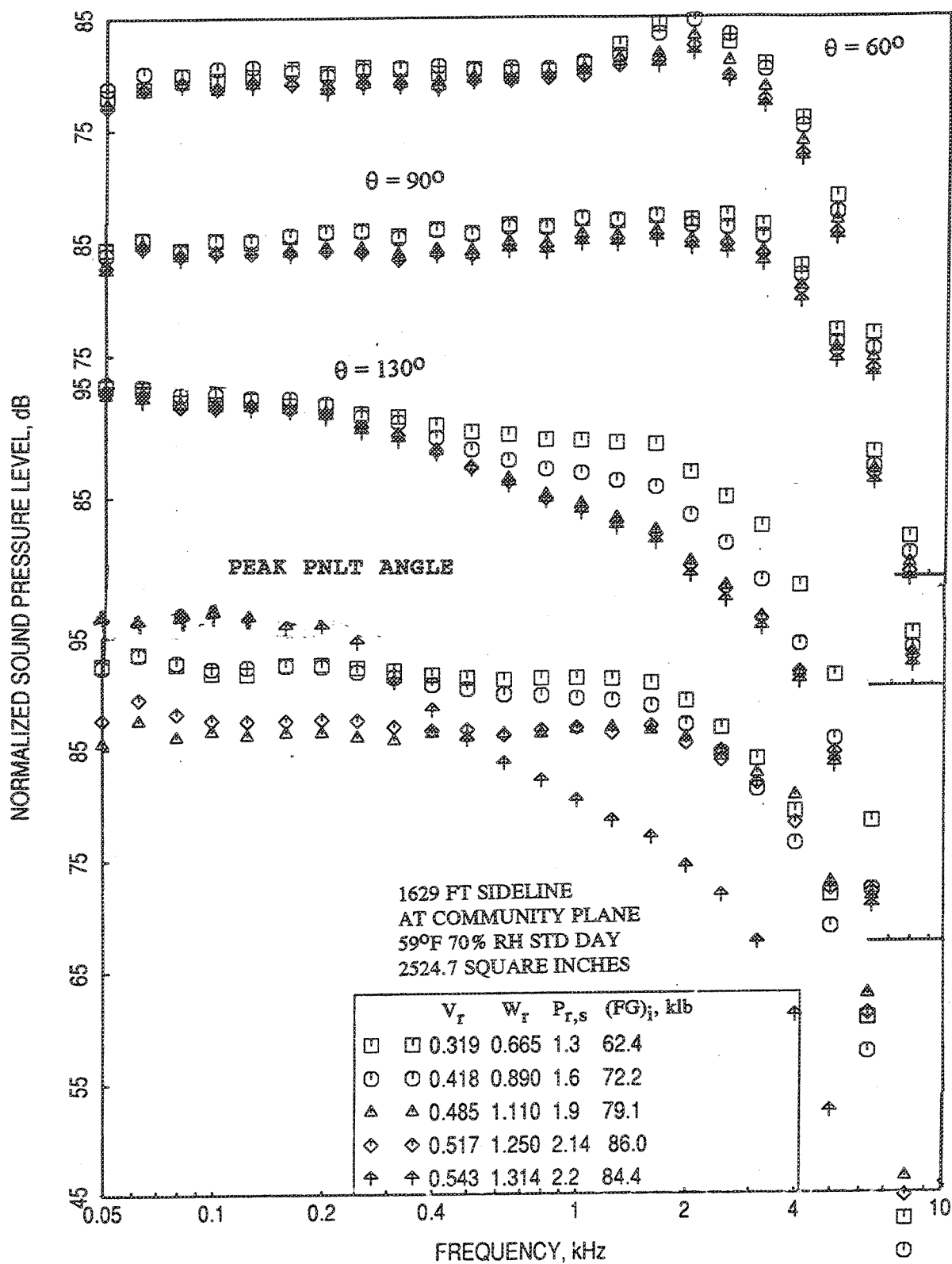


Figure 2.9-10. Normalized SPL spectra at different polar angles ( $\theta$ ) for the 1.0"-thick fluid shield nozzle at different  $V_r$  (and  $W_r$ ) for a fixed jet velocity,  $V_{mix}$ , of 1811 ft/sec at static condition.



At  $V_{\text{mix}} = 2030$  ft/sec :

Normalized PNLTs at different polar angles ( $\theta$ ), peak PNLTs, and pseudo EPNLTs are plotted with respect to  $V_T$  in Figure 2.9-11 for the three fluid shield nozzles for  $V_{\text{mix}}$  of 2030 ft/sec. Normalized PNLTs and pseudo EPNLTs decrease with  $V_T$ . For 0.5"-thick fluid shield a minimum level is observed, after which the PNLT and pseudo EPNLT start increasing with  $V_T$ . Similar results plotted with respect to  $W_T$  are shown in Figure 2.9-12. The general trends are similar to those observed in Figure 2.9-11 with respect to  $V_T$  for individual configurations.

Normalized PNLT directivities for 0.5"-thick shield are plotted in Figure 2.9-13 for different  $V_T$  and  $W_T$ . PNLT at all angles decreases with increasing  $V_T$  (or  $W_T$ ) up to  $V_T=0.525$  (corresponding  $W_T=0.580$ ) and then the trend is reversed. Whereas, ideal gross thrust increases with  $V_T$  monotonically. Corresponding normalized SPL spectra are plotted in Figure 2.9-14, which also indicates the similar trend at all frequencies.

Normalized PNLT directivities and normalized SPL spectra for the other two fluid shield configurations with 0.75"-thick and 1.0"-thick shields are shown in Figures 2.9-15 through 2.9-18. Unlike 0.5"-thick shield configuration, PNLT at all angles decreases with increasing  $V_T$  (or  $W_T$ ). Further increase in  $V_T$  may reverse the trend for PNLT, and an optimum  $V_T$  may be established for these configurations. Corresponding normalized SPL spectra also indicate the similar trend at all frequencies.

Carpet Plot to Illustrate Effects of  $V_T$  and  $W_T$  Simultaneously :

Carpet plots are generated between  $V_T$  and  $W_T$  for fixed EPNLT levels. In these plots data for all four fluid shield nozzles of different thicknesses are utilized. The EPNLTs are normalized only with respect to thrust. Figure 2.9-19 shows the Normalized EPNdB plots with respect to  $V_T$  and  $W_T$  for fluid shield nozzles of different thicknesses at  $V_{\text{mix}}=1811$  ft/sec. These results are utilized to generate the contour plot of EPNdB in Figure 2.9-20 with respect to  $V_T$  and  $W_T$ . Noise levels for fluid shields of constant thicknesses are shown in this figure. Noise level seems to decrease with increasing  $V_T$  and/or  $W_T$ . With respect to shield thickness, minimum  $V_T$  and  $W_T$  for a fixed noise level correspond to the 0.75"-thick shield. Similar results for  $V_{\text{mix}}=2030$  ft/sec are generated and shown in Figures 2.9-21 and 2.9-22. The noise characteristics of the fluid shield nozzles are similar to what is observed for  $V_{\text{mix}}=1811$  ft/sec case.

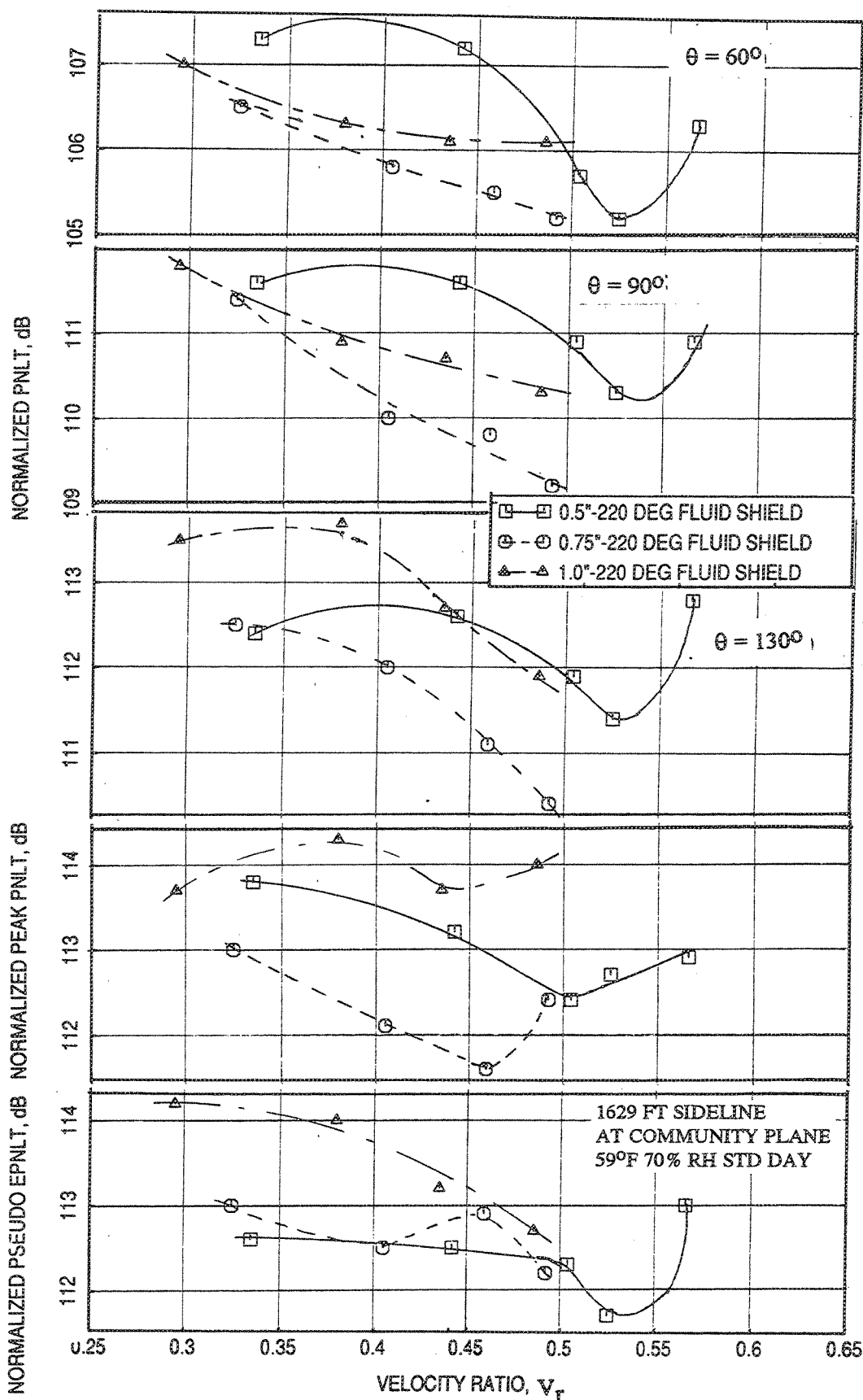


Figure 2.9-11. Effect of velocity ratio  $V_r$  on normalized PNLT at different polar angles ( $\theta$ ), peak PNLT, and pseudo EPNLT for fluid shield nozzles for a fixed jet velocity,  $V_{mix}$ , of 2030 ft/sec at static condition.



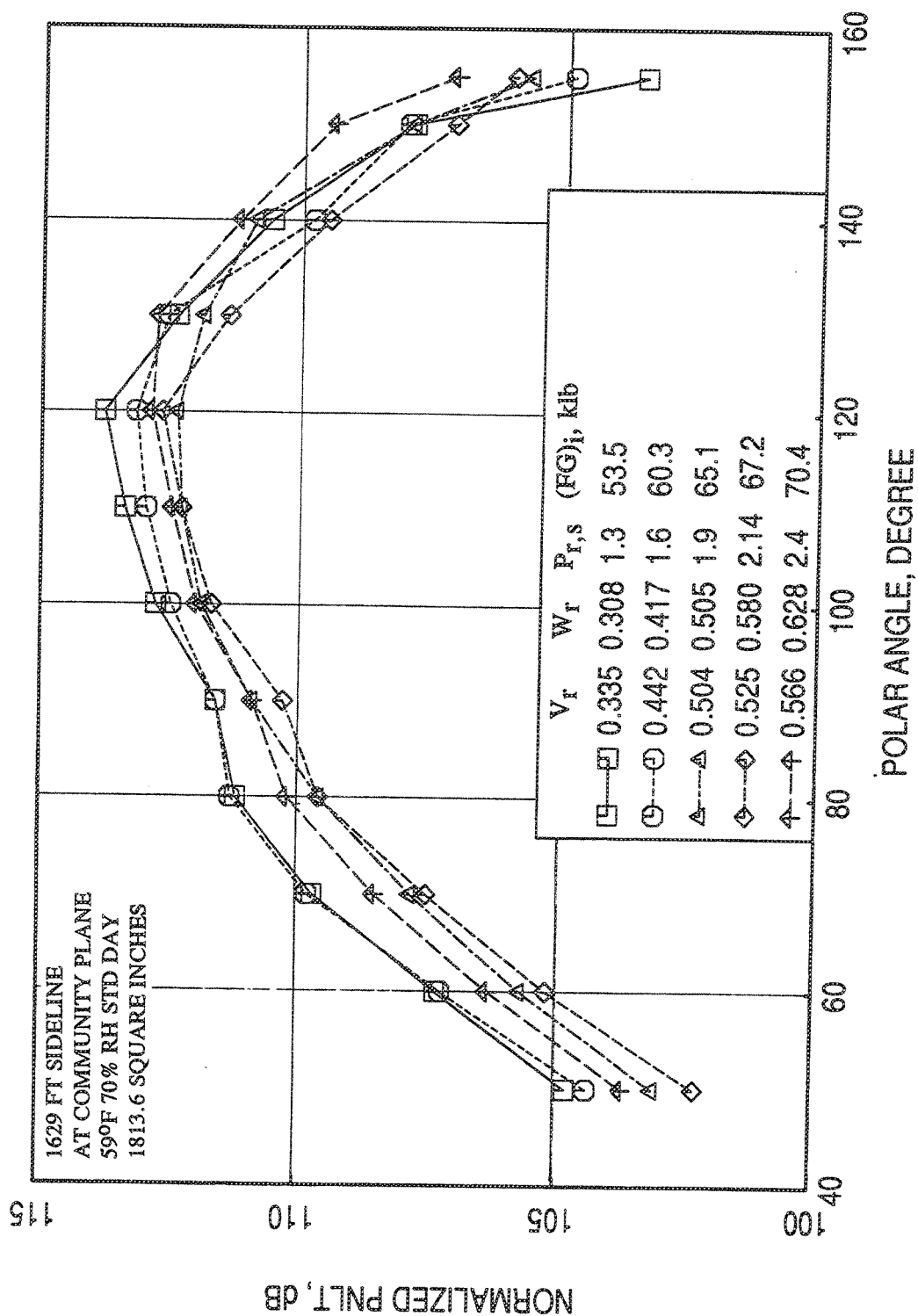


Figure 2.9-13. Normalized PNL T directivities for the 0.5"-thick fluid shield nozzle at different  $V_r$  (and  $W_r$ ) for a fixed jet velocity,  $V_{mix}$ , of 2030 ft/sec at static condition.

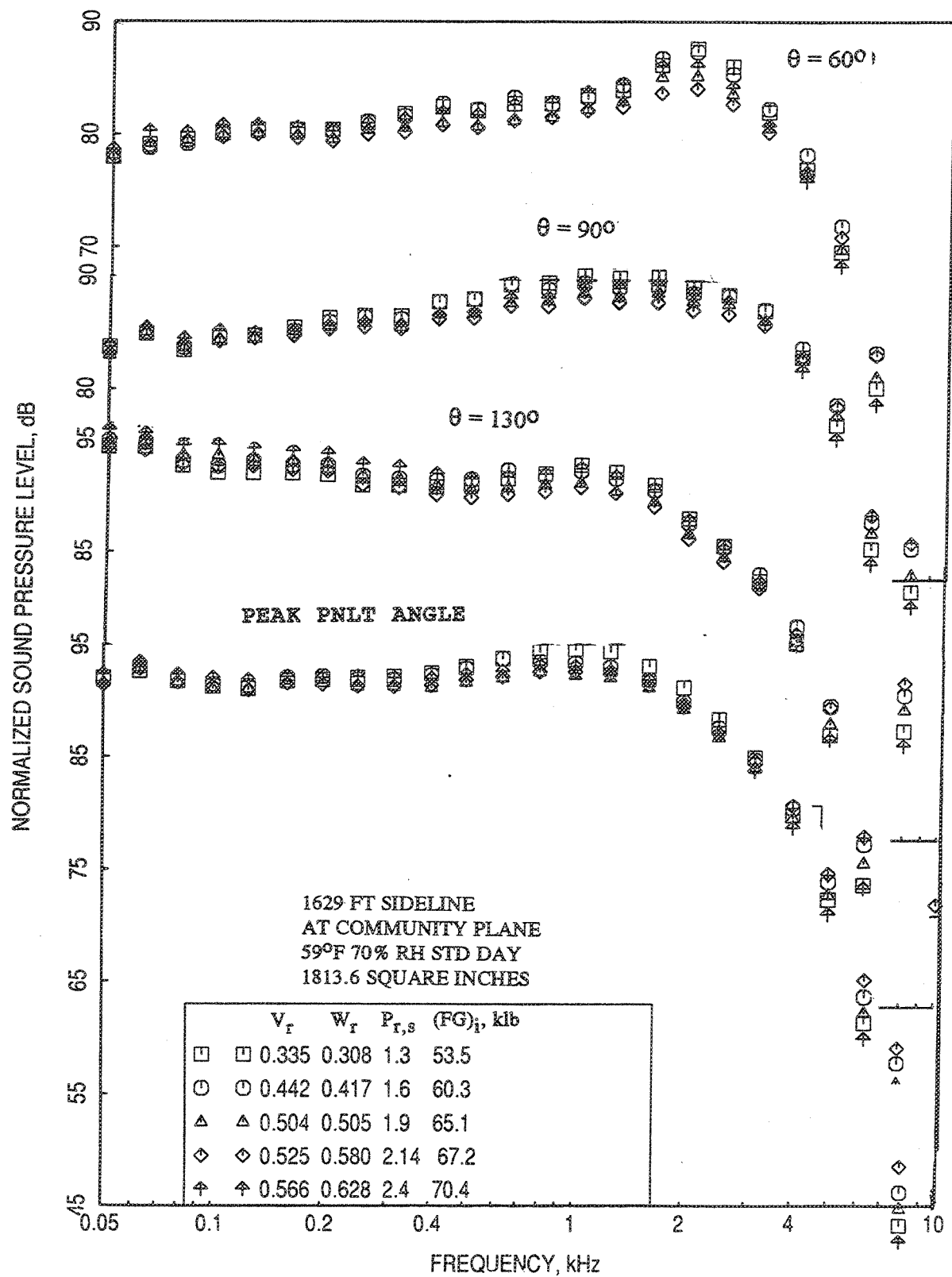


Figure 2.9-14. Normalized SPL spectra at different polar angles ( $\theta$ ) for the 0.5"-thick fluid shield nozzle at different  $V_r$  (and  $W_r$ ) for a fixed jet velocity,  $V_{mix}$ , of 2030 ft/sec at static condition.

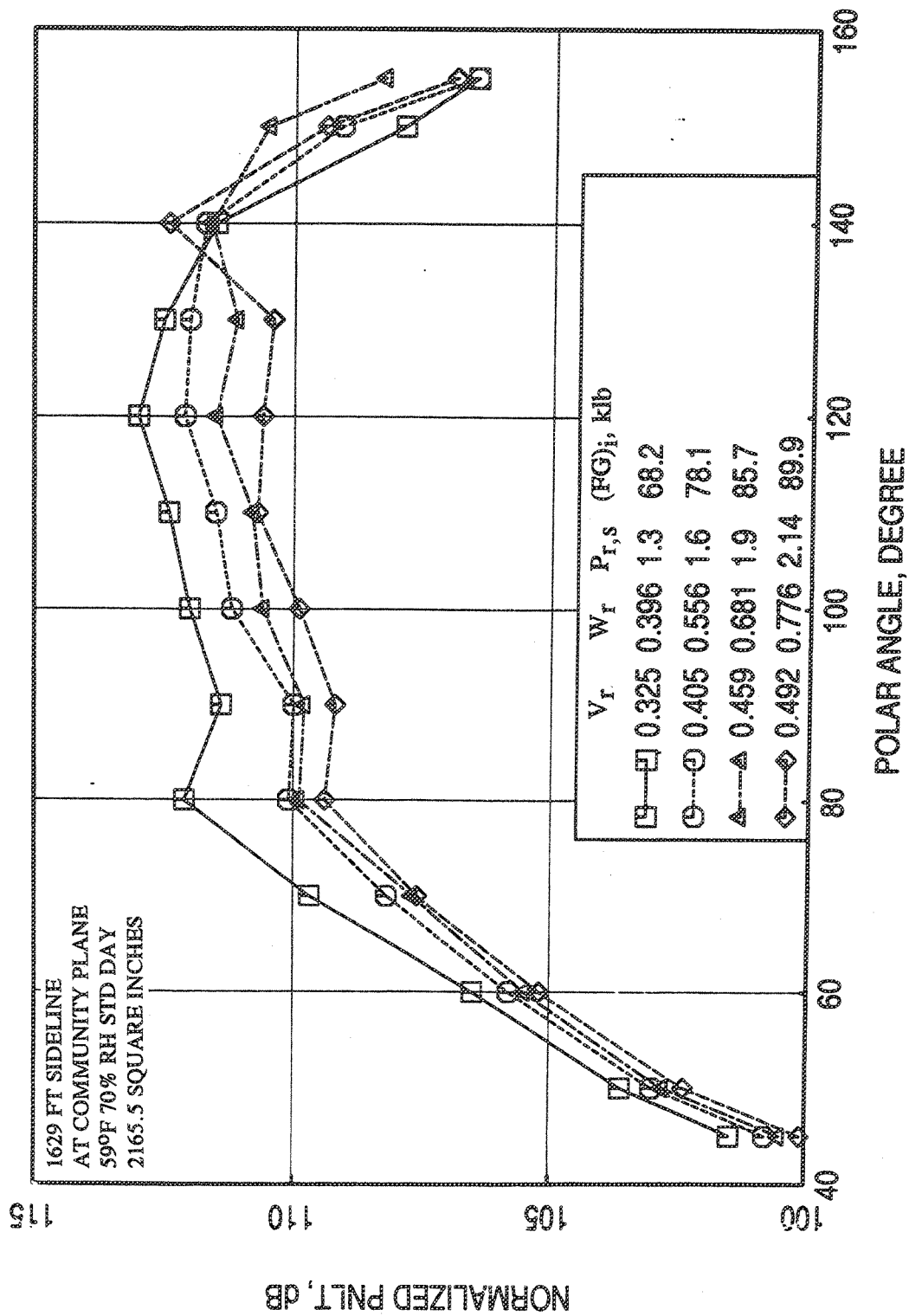


Figure 2.9-15. Normalized PNL T directivities for the 0.75"-thick fluid shield nozzle at different  $V_r$  (and  $W_r$ ) for a fixed jet velocity,  $V_{mix}$ , of 2030 ft/sec at static condition.

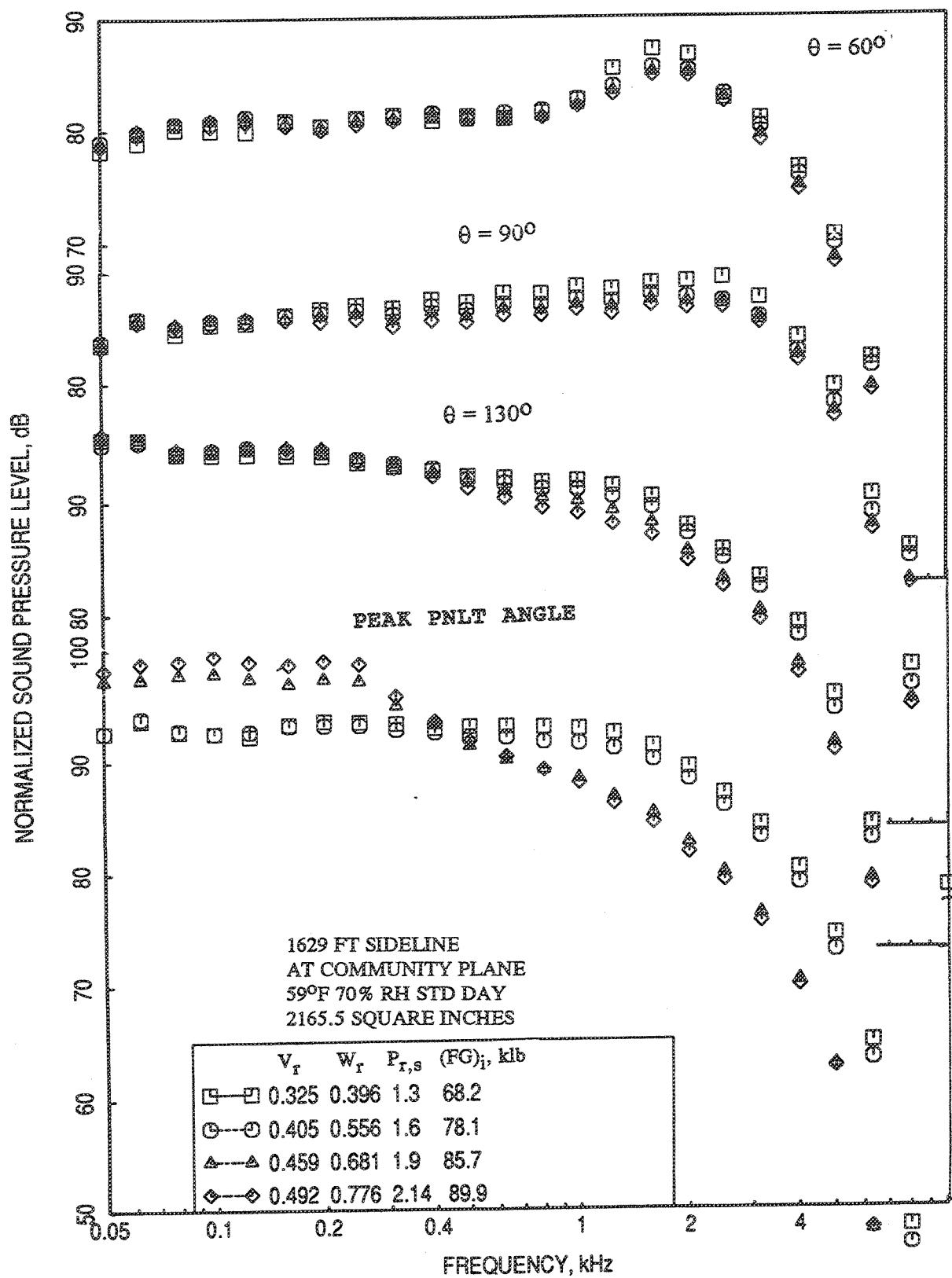


Figure 2.9-16. Normalized SPL spectra at different polar angles ( $\theta$ ) for the 0.75"-thick fluid shield nozzle at different  $V_T$  (and  $W_T$ ) for a fixed jet velocity,  $V_{max}$ , of 2030 ft/sec at static condition.

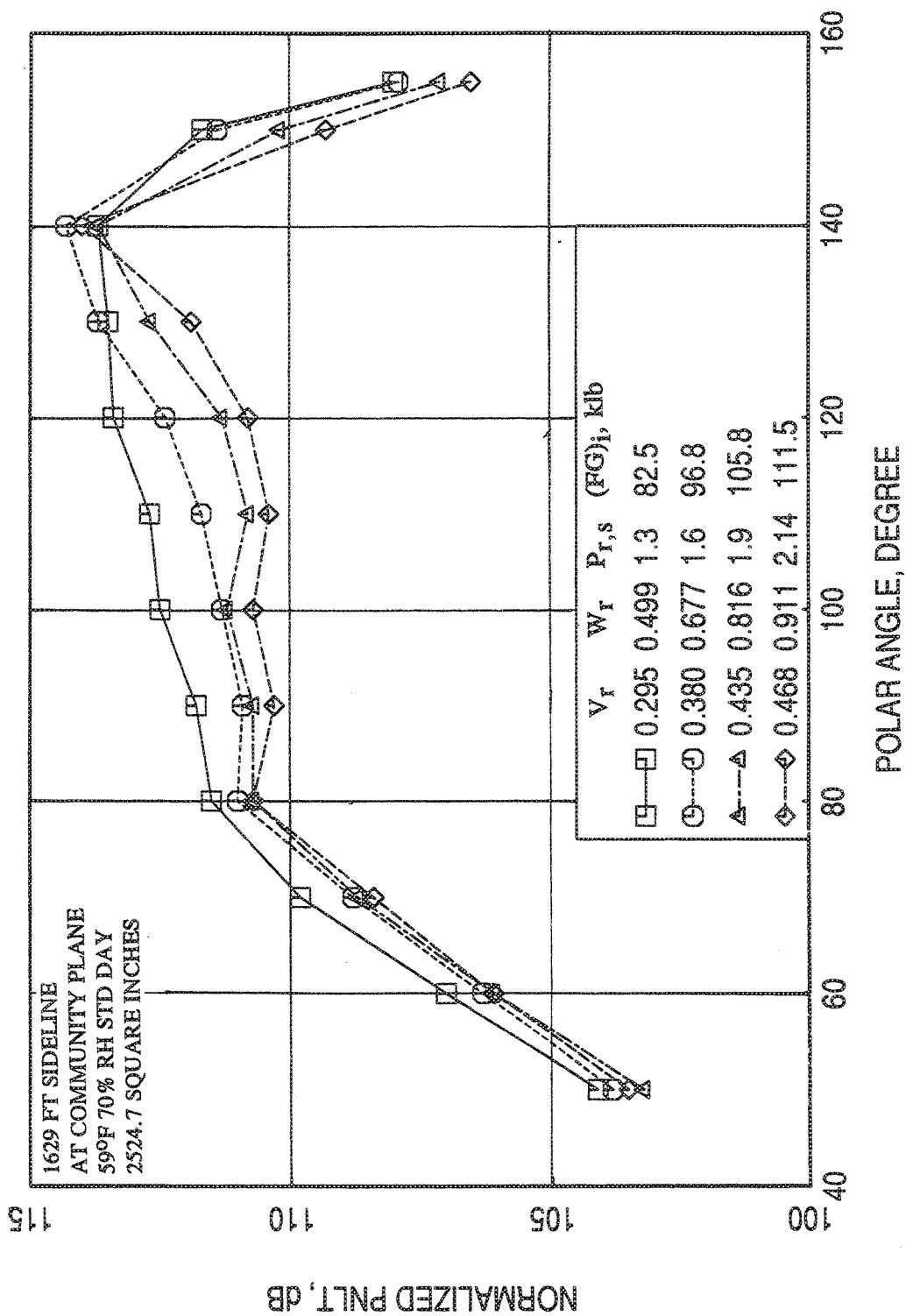


Figure 2.9-17. Normalized PNL T directivities for the 1.0"-thick fluid shield nozzle at different  $V_r$  (and  $W_r$ ) for a fixed jet velocity,  $V_{mix}$ , of 2030 ft/sec at static condition.



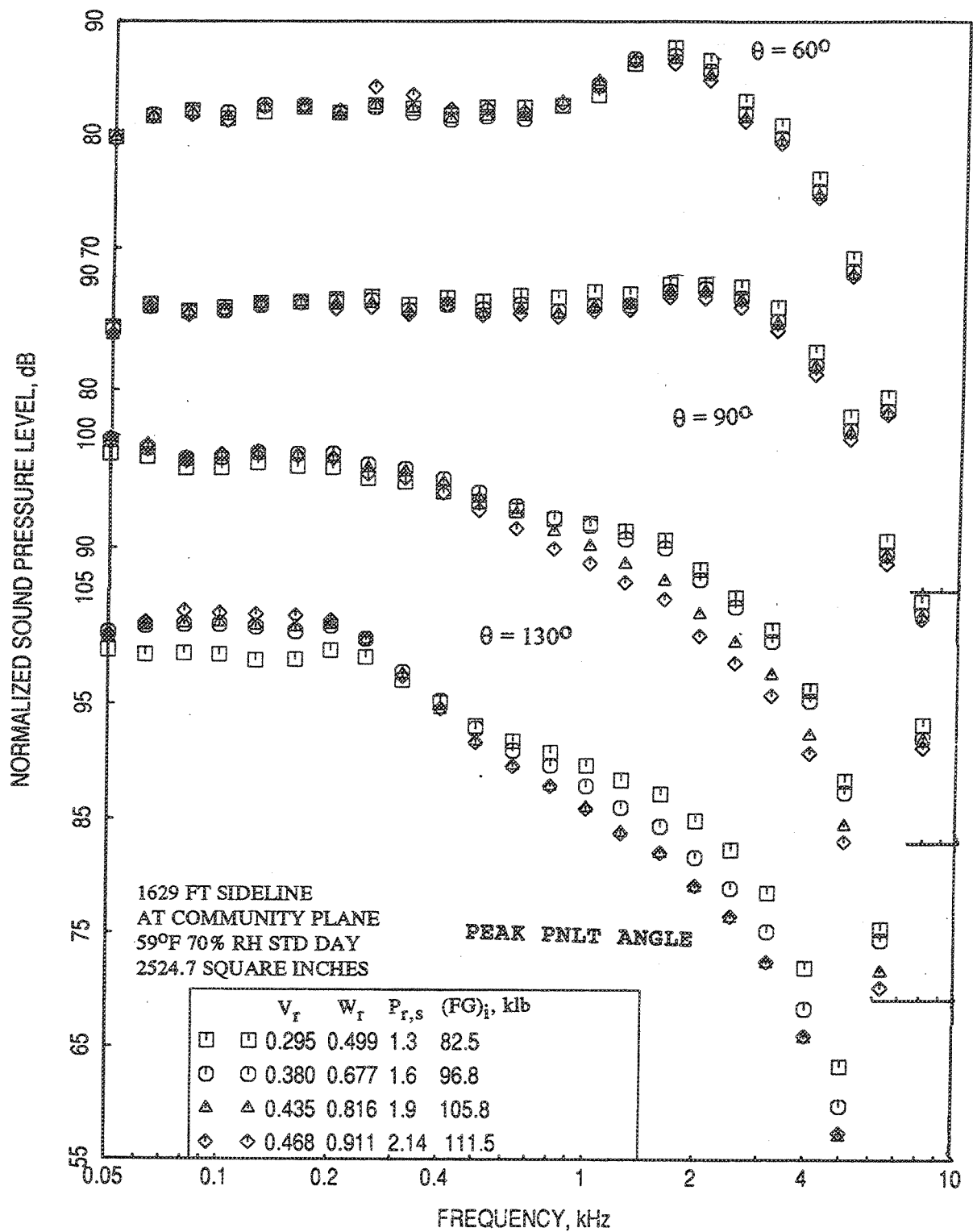


Figure 2.9-18. Normalized SPL spectra at different polar angles ( $\theta$ ) for the 1.0"-thick fluid shield nozzle at different  $V_r$  (and  $W_r$ ) for a fixed jet velocity,  $V_{mix}$ , of 2030 ft/sec at static condition.

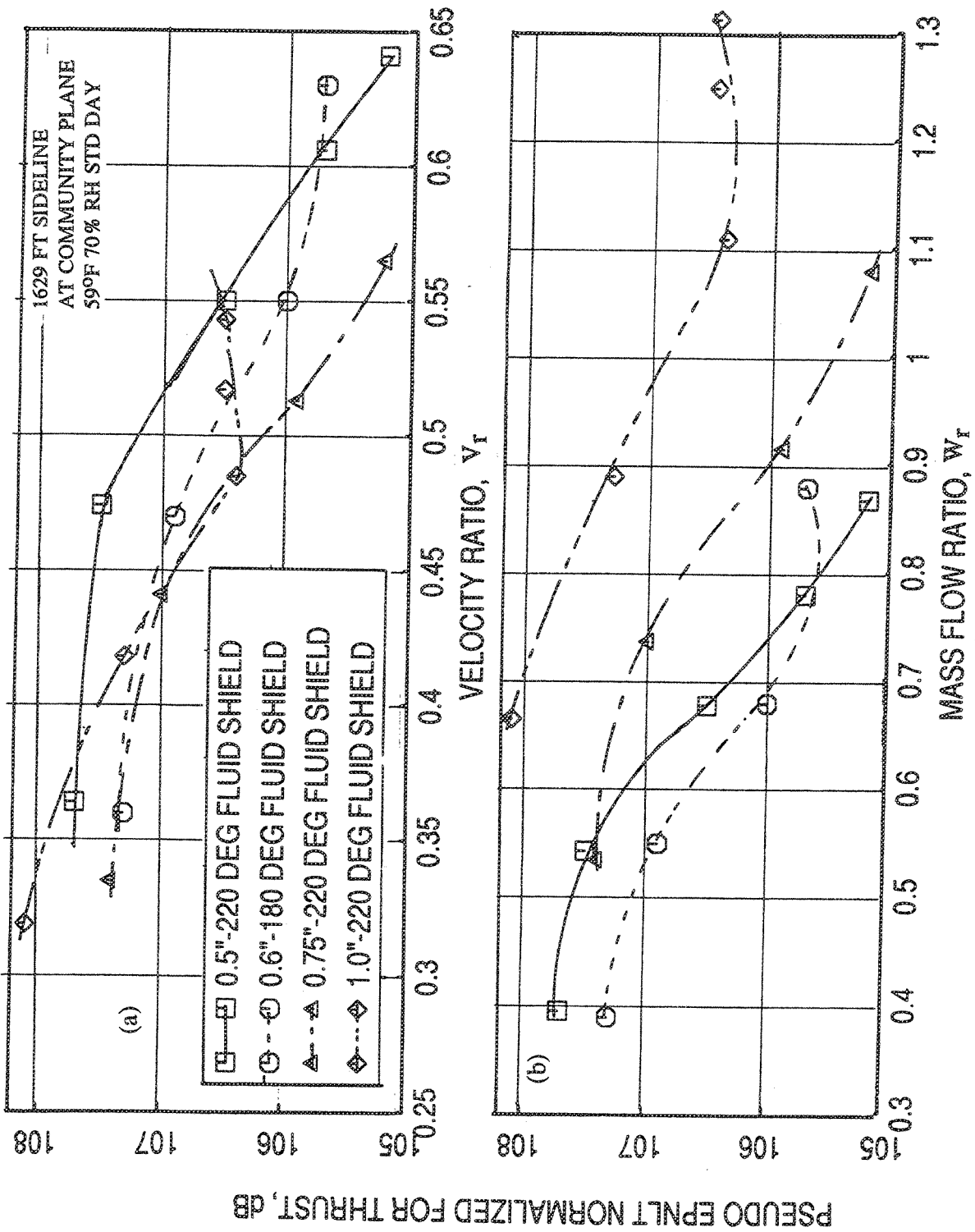


Figure 2.9-19. Effect of (a) velocity ratio  $V_r$  and (b) mass flow ratio  $W_r$  on normalized pseudo EPNLT data for fluid shield nozzles at a fixed jet velocity,  $V_{mix}$ , of 1811 ft/sec at static condition.

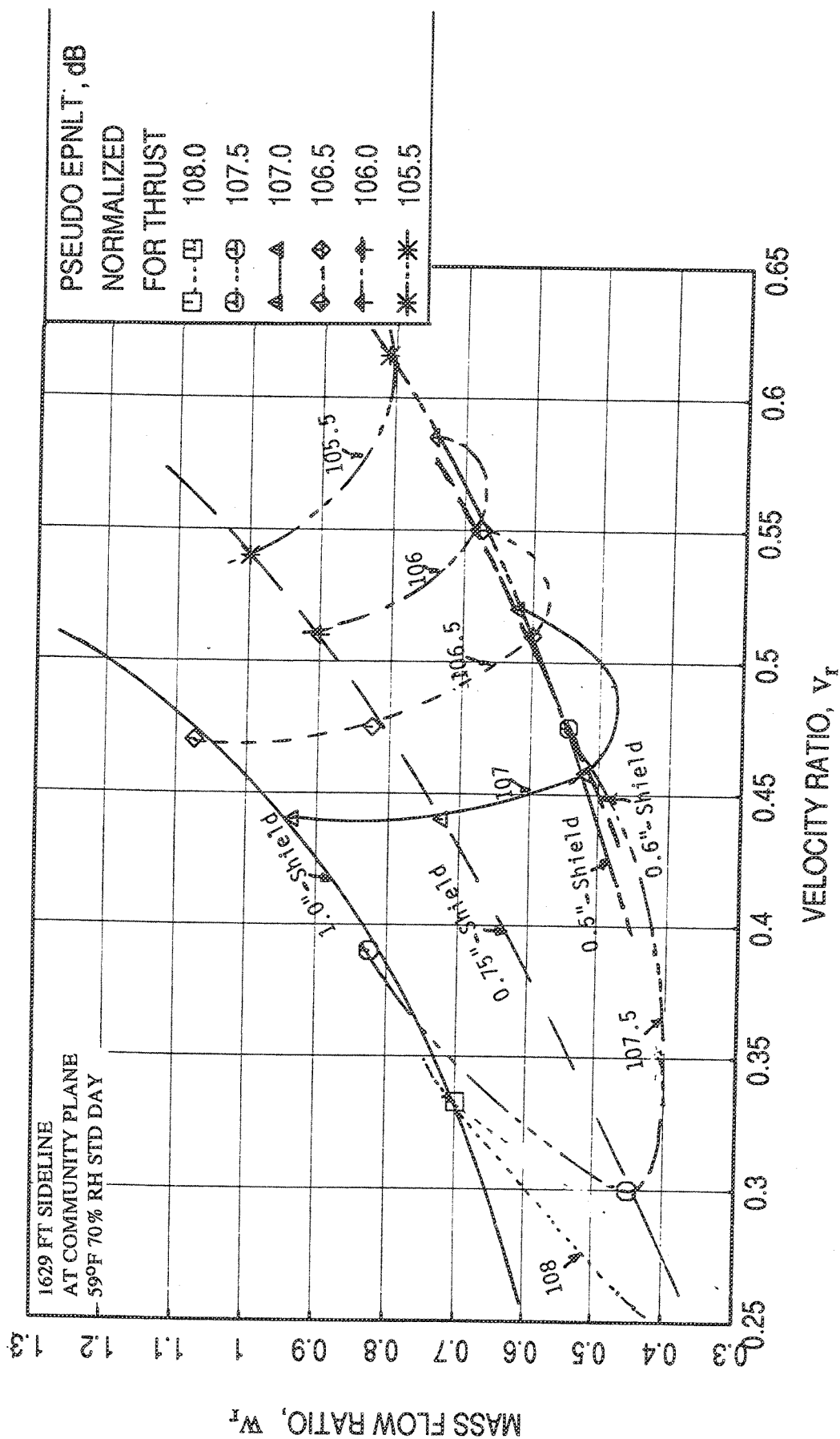


Figure 2.9-20. Normalized pseudo EPNLT contours with respect to velocity ratio  $V_r$  and mass flow ratio  $W_r$  for fluid shield nozzles at a fixed jet velocity,  $V_{mix}$ , of 1811 ft/sec at static condition.

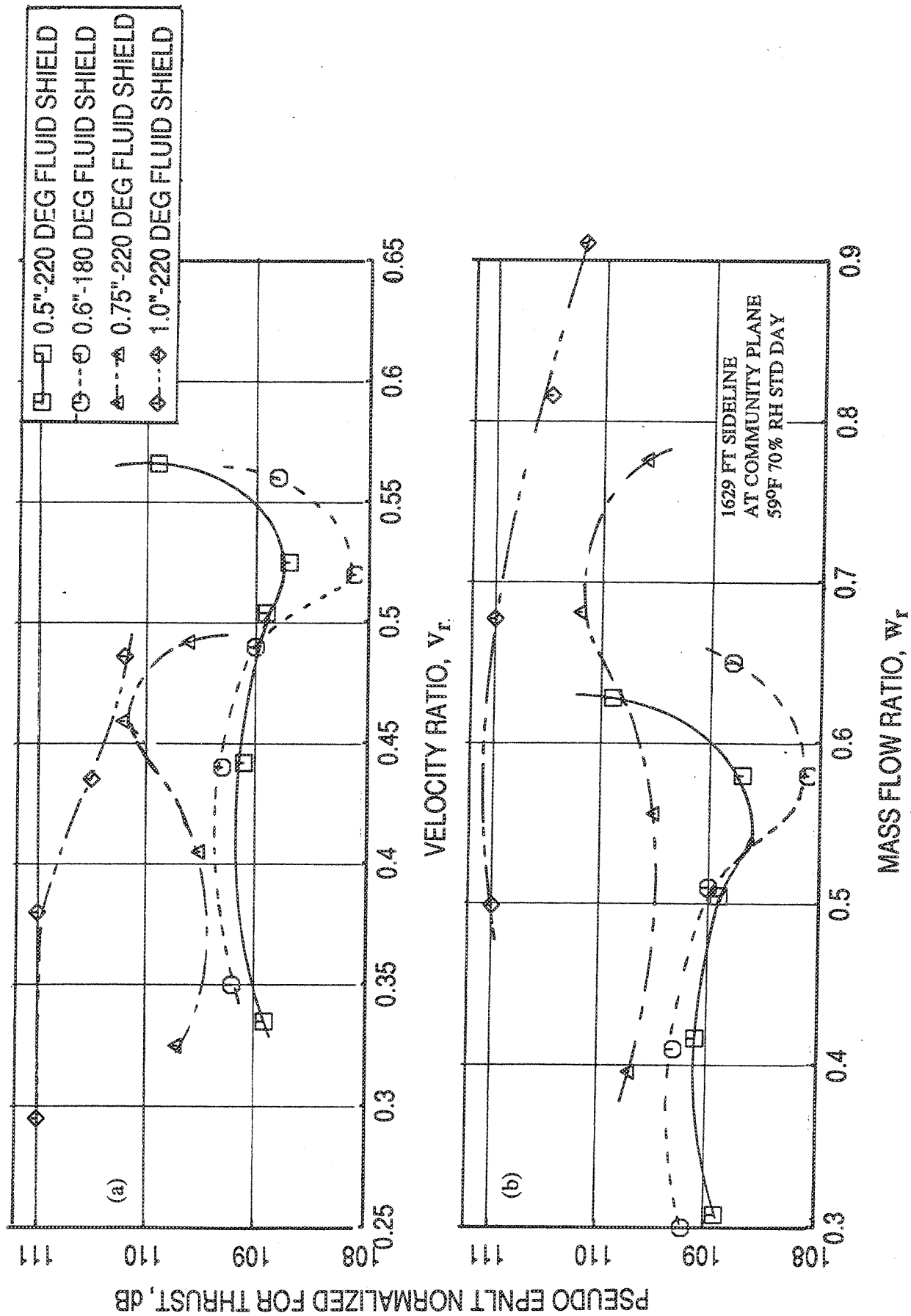


Figure 2.9-21. Effect of (a) velocity ratio  $V_r$  and (b) mass flow ratio  $W_r$  on normalized pseudo EPNLT data for fluid shield nozzles at a fixed jet velocity,  $V_{mix}$ , of 2030 ft/sec at static condition.

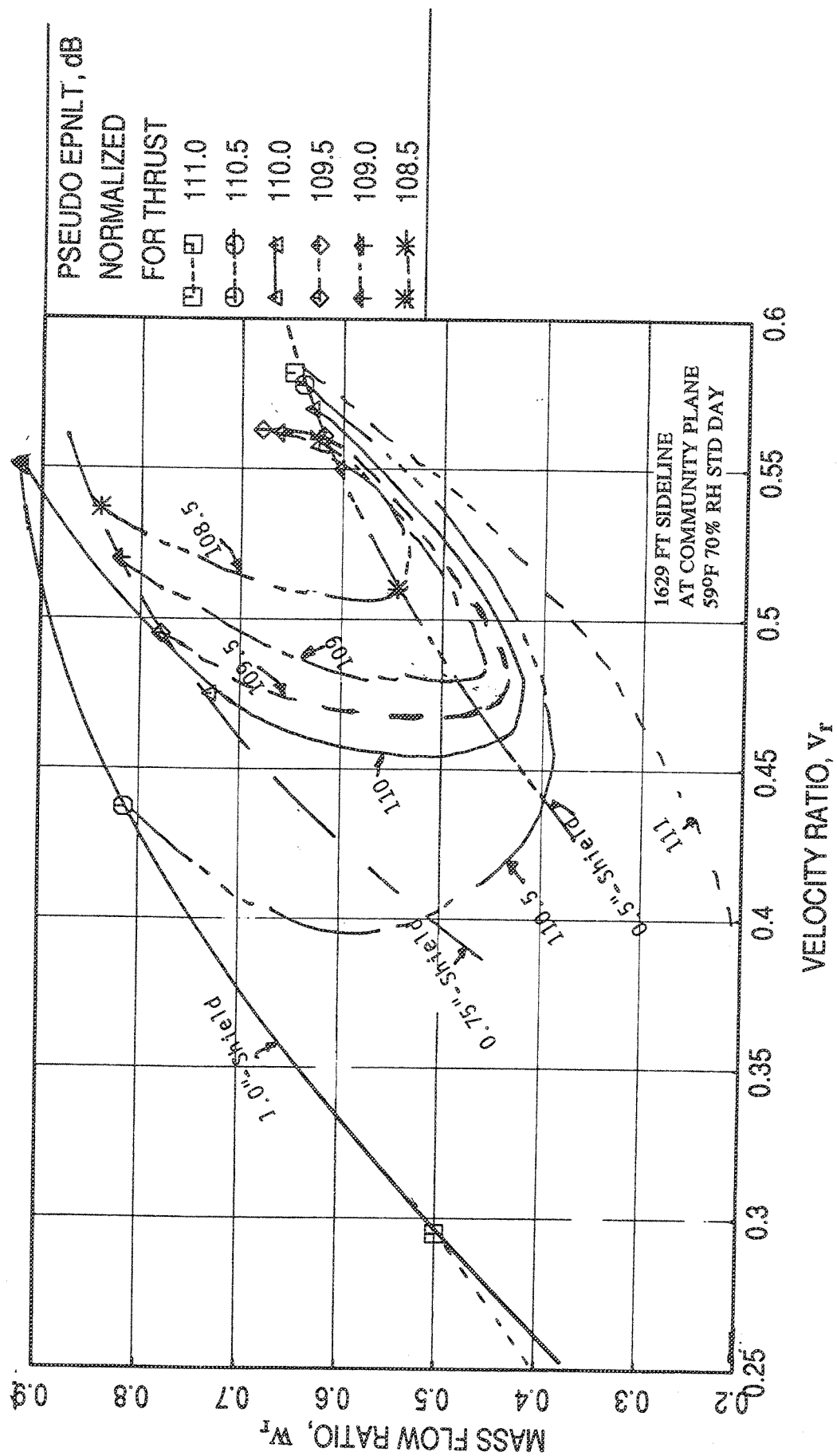


Figure 2.9-22. Normalized pseudo EPNLT contours with respect to velocity ratio  $V_r$  and mass flow ratio  $W_r$  for fluid shield nozzles at a fixed jet velocity,  $V_{mix}$ , of 2030 ft/sec at static condition.

The noise characteristics with respect to  $V_r$  and  $W_r$  are of opposing behavior to the  $\Delta C_{fg}$  characteristics, as shown in Figure 2.4-32. A compromise between acoustic and  $\Delta C_{fg}$  needs to be considered for the application of fluid shield in real engines.

#### Effect of Fluid Shield Nozzle Pressure Ratio, $P_{r,s}$ :

In the tests performed for a fixed  $V_{mix}$  the variation of  $V_r$  and  $W_r$  was achieved by varying the fluid shield nozzle pressure ratio without changing the primary nozzle pressure ratios significantly. For example, while  $P_{r,s}$  is varied between 1.3 to 2.2 for the 1"-thick fluid shield, the  $P_{r,p}$  varied from 3.06 to 3.2 for  $V_{mix}=1811$  ft/sec and from 4.06 to 4.32 for  $V_{mix}=2030$  ft/sec. One may assume average  $P_{r,p}$  of 3.15 and 4.2 for  $V_{mix}$  of 1811 ft/sec and 2030 ft/sec as fixed values to study the effect of  $P_{r,s}$  on 1"-thick fluid shield nozzle noise characteristics. Similar  $P_{r,p}$  values for 0.5"-thick and 0.75"-thick fluid shield nozzle configurations are 2.4 and 2.8 at  $V_{mix}=1811$  ft/sec and 3.2 and 3.7 at  $V_{mix}=2030$  ft/sec, respectively. The implication of this is favorable on the Flade engine, since it would be relatively easy to control pressure ratio of flade stream by appropriate design of flade-tip and associated flade system, rather than varying other parameters. Hence, the tests simulated possible scenario on Flade Engine. Hence the effect of  $P_{r,s}$  can be determined from results of  $V_r$  and  $W_r$  studies, presented in Figures 2.9-1 through 2.9-18.

Since  $V_r$  (or  $W_r$ ) increases with increasing  $P_{r,s}$ , the variation of normalized PNLT and pseudo EPNLT with respect to  $P_{r,s}$  will be similar to what is illustrated in Figures 2.9-1 through 2.9-18, that the noise levels decrease with respect to  $P_{r,s}$ , except for a few cases, where a reverse trend is observed due to further increase in  $V_r$  or  $W_r$  values corresponding to a higher  $P_{r,s}$  of 2.4.

#### Effect of Fluid Shield Nozzle Total Temperature, $T_{t,s}$ :

Tests were conducted for fluid shield nozzle configurations by varying  $T_{t,s}$  with fixed  $P_{r,p}=3.2$ ,  $T_{t,p}=1800^\circ\text{R}$ , and  $P_{r,s}=2.14$ . Variation of  $T_{t,s}$  includes the nominal cycle condition of  $695^\circ\text{R}$  at the middle of the range (see Figure 2.2-21). Normalized PNLTs are plotted with respect to  $T_{t,s}$  in Figure 2.9-23 at different polar angles ( $\theta$ ) for the three fluid shield nozzles. Normalized PNLT increases with  $T_{t,s}$ . Figure 2.9-24 illustrates the variation of normalized peak PNLT and pseudo EPNLT with  $T_{t,s}$ . PNLT and pseudo EPNLT increase with  $T_{t,s}$  for each configuration. Obtaining a variation in

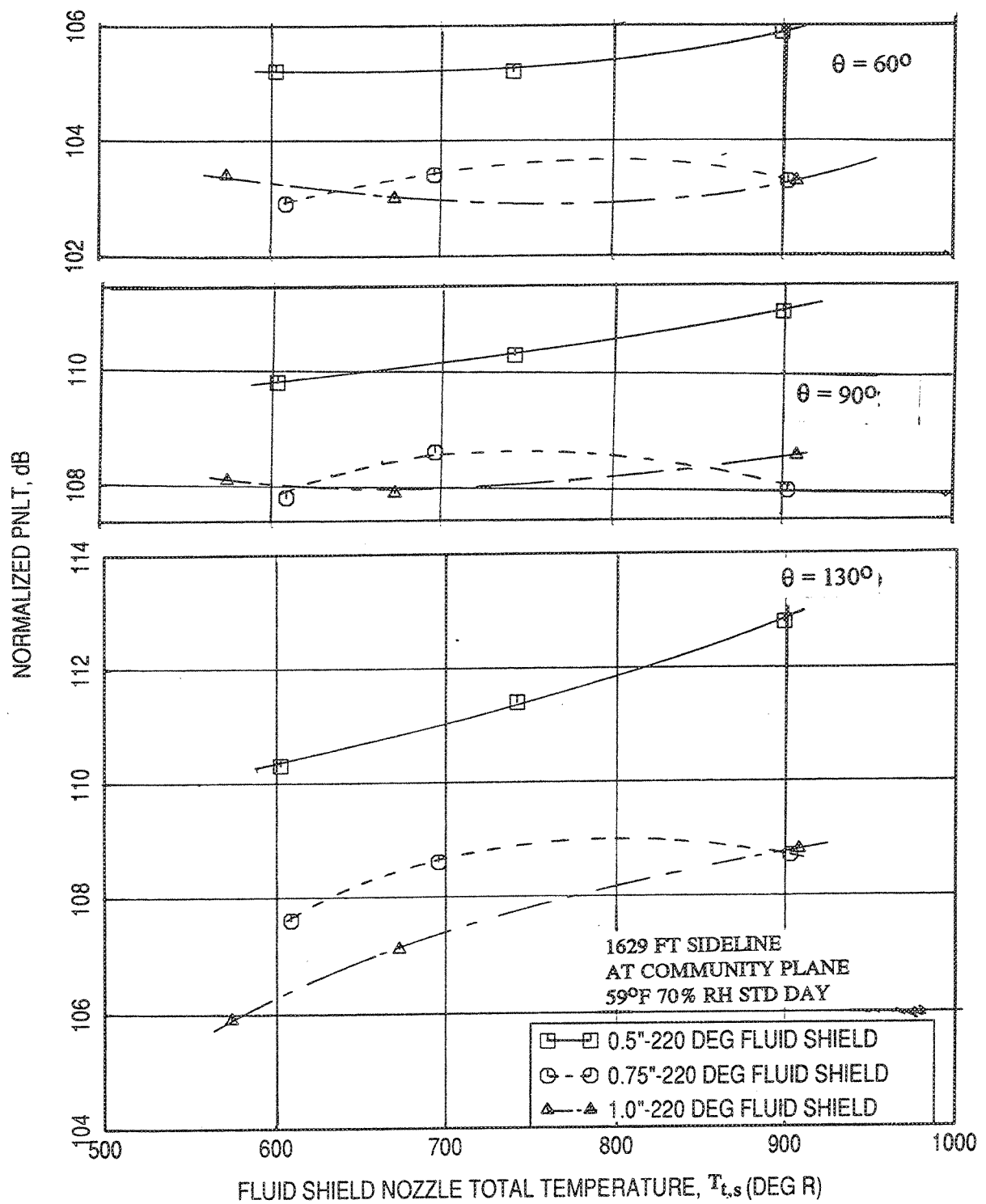


Figure 2.9-23. Effect of fluid shield nozzle total temperature,  $T_{t,s}$ , on normalized PNLT data at different polar angles ( $\theta$ ) for fluid shield nozzles for fixed  $P_{r,p}=3.2$ ,  $T_{t,p}=1800^\circ\text{R}$ , and  $P_{r,s}=2.14$  at static condition.

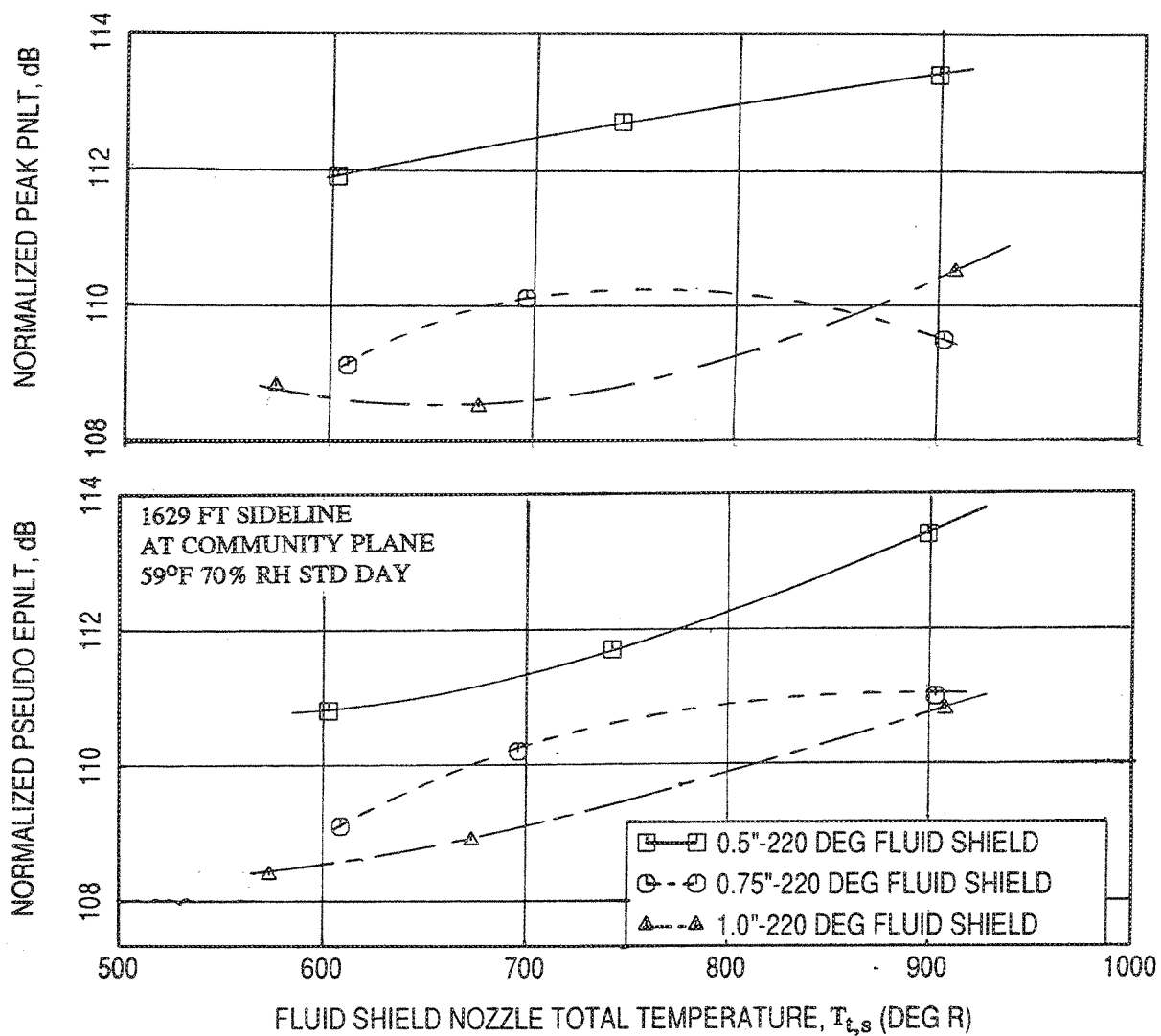


Figure 2.9-24. Effect of fluid shield nozzle total temperature,  $T_{t,s}$ , on normalized peak PNL and normalized pseudo EPNL data for fluid shield nozzles for fixed  $P_{r,p}=3.2$ ,  $T_{t,p}=1800^{\circ}\text{R}$ , and  $P_{r,s}=2.14$  at static condition.



$T_{t,s}$  on the flade engine is relatively more difficult. This test series was conducted to see if there is an potential benefit for varying  $T_{t,s}$ .

Normalized PNLT directivities for 0.5"-thick shield are plotted in Figure 2.9-25 for different  $T_{t,s}$ . PNLT at all angles increases with  $T_{t,s}$  whereas, ideal gross thrust remains more or less same for all the cases. Corresponding normalized SPL spectra are plotted in Figure 2.9-26, which also indicates the similar trend at all frequency. It seems beneficial from noise consideration to operate the fluid shield at lower temperature.

Normalized PNLT directivities and normalized SPL spectra for the other two fluid shield configurations with 0.75"-thick and 1.0"-thick shields are shown in Figures 2.9-27 through 2.9-30. Similar to 0.5"-thick shield configuration, PNLT at all angles decreases with decreasing  $T_{t,s}$ . Corresponding normalized SPL spectra also indicate the similar trend at all frequencies. Observed variation could be due to changes in  $V_{mix}$ .

#### Effect of Primary Nozzle Pressure Ratio, $P_{r,p}$ :

Acoustic results for a set of tests are selected for fluid shield nozzle configurations to study the effect of  $P_{r,p}$ . In these tests  $P_{r,p}$  is varied from 2.0 to 4.5, while the other aerothermodynamic parameters are kept fixed (i.e.,  $T_{t,p}=1800^{\circ}\text{R}$ ,  $P_{r,s}=2.14$ , and  $T_{t,s}=700^{\circ}\text{R}$ ). Normalized PNLTs are plotted with respect to  $P_{r,p}$  in Figure 2.9-31 at different polar angles ( $\theta$ ) for the three fluid shield nozzles. Normalized PNLT increases with  $P_{r,p}$ . Figure 2.9-32 illustrates the variation of normalized peak PNLT and pseudo EPNLT with  $P_{r,p}$ . Pseudo EPNLT increase with  $P_{r,p}$  for each configuration.

Normalized PNLT directivities for 0.5"-thick shield are plotted in Figure 2.9-33 for different  $P_{r,p}$ . PNLT at all angles increases with  $P_{r,p}$ . Corresponding normalized SPL spectra are plotted in Figure 2.9-34, which also indicates the similar trend at all frequency. It should be noted that the ideal gross thrust increases significantly with increasing  $P_{r,p}$ .

Normalized PNLT directivities and normalized SPL spectra for the other two fluid shield configurations with 0.75"-thick and 1.0"-thick shields are shown in Figures 2.9-35 through 2.9-38. Similar to 0.5"-thick shield configuration, PNLT at all angles

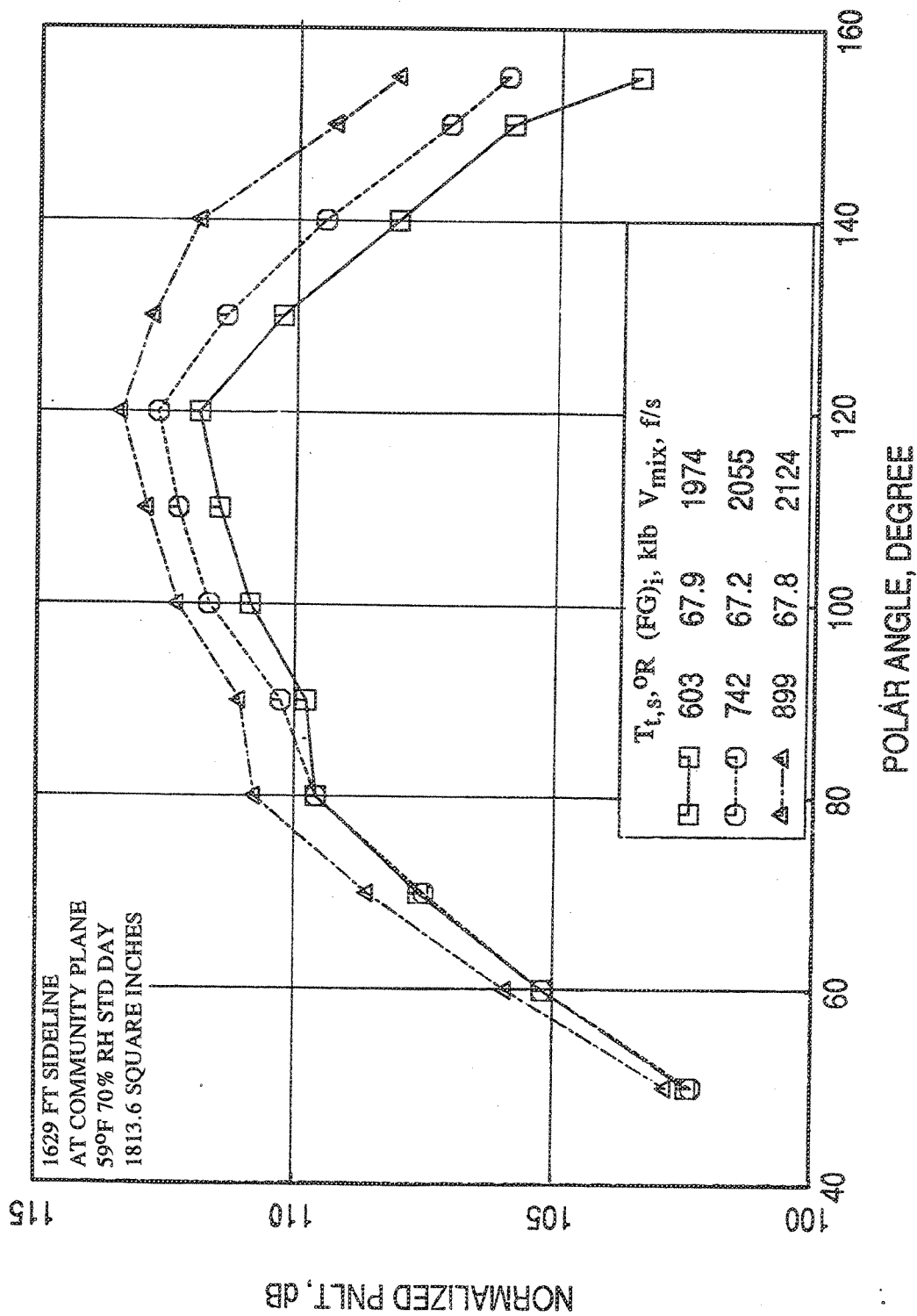


Figure 2.9-25. Normalized PNLT directivities for the 0.5"-thick fluid shield nozzle at different  $T_{t,s}$  for fixed  $P_{r,p}=3.2$ ,  $T_{t,p}=1800^{\circ}R$ , and  $P_{r,s}=2.14$  at static condition.

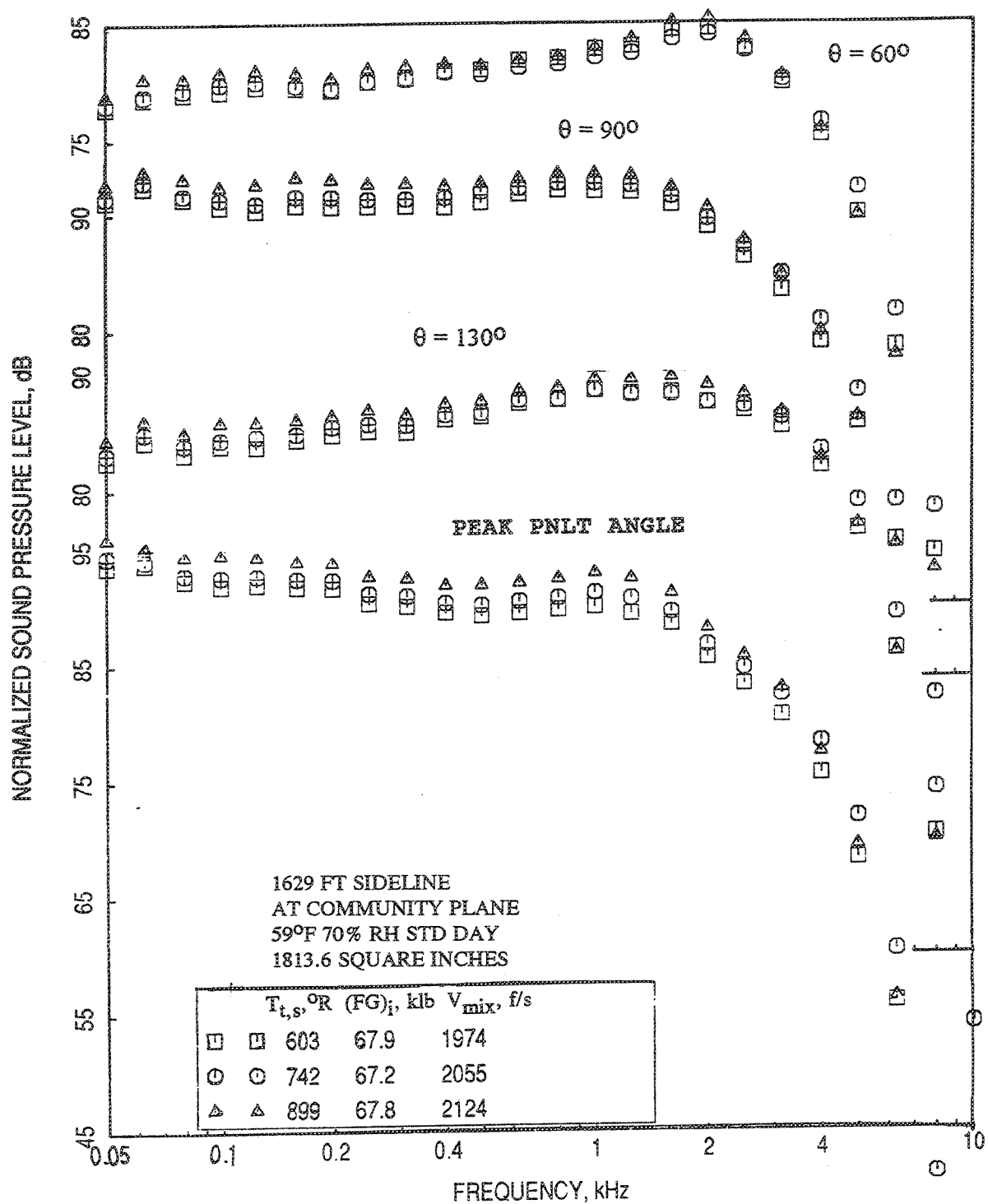


Figure 2.9-26. Normalized SPL spectra at different polar angles ( $\theta$ ) for the 0.5"-thick fluid shield nozzle at different  $T_{t,s}$  for fixed  $P_{r,p}=3.2$ ,  $T_{t,p}=1800^{\circ}\text{R}$ , and  $P_{r,s}=2.14$  at static condition.

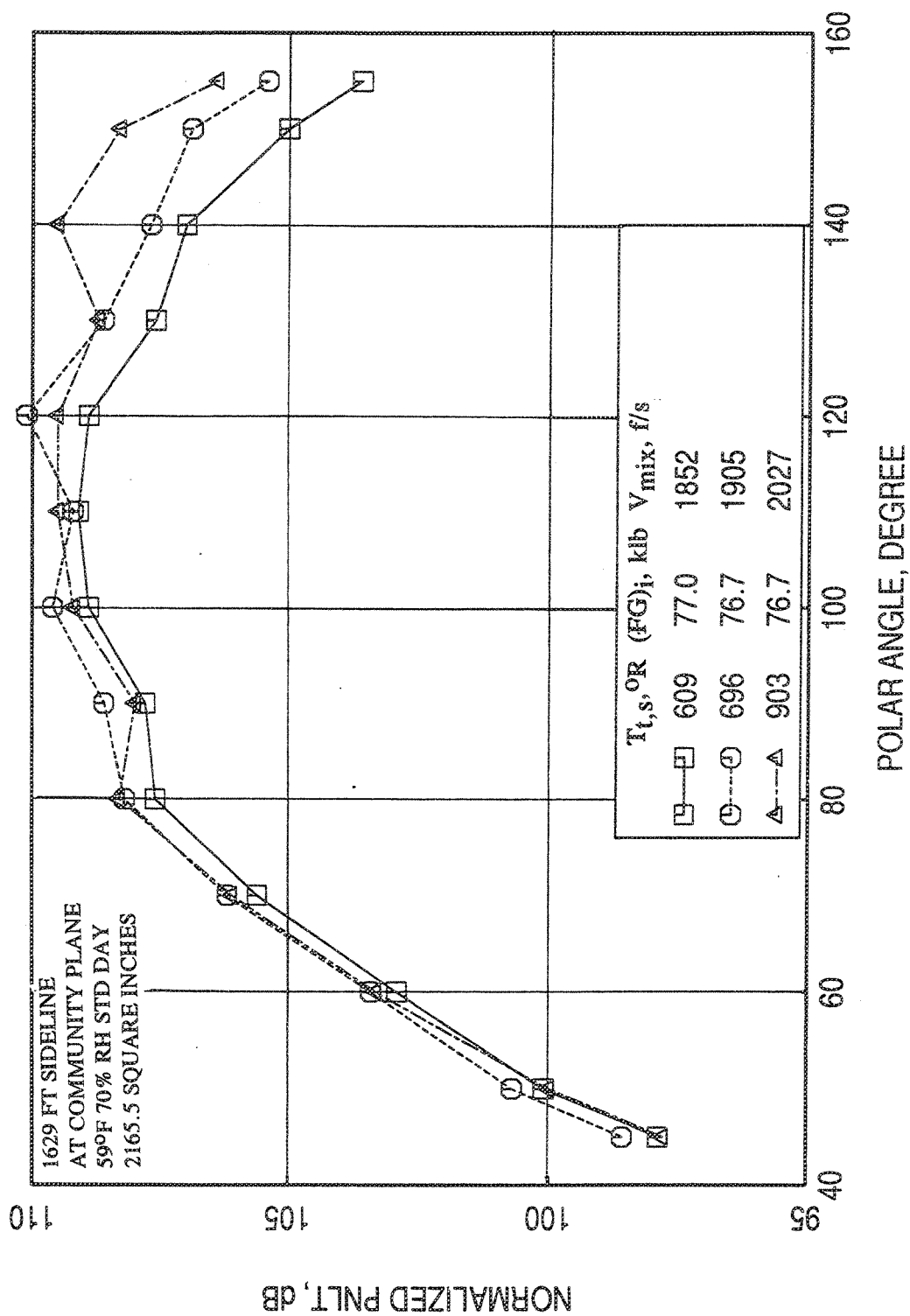


Figure 2.9-27. Normalized PNLT directivities for the 0.75"-thick fluid shield nozzle at different  $T_{t,s}$  for fixed  $P_{r,p}=3.2$ ,  $T_{t,p}=1800^\circ R$ , and  $P_{r,s}=2.14$  at static condition.

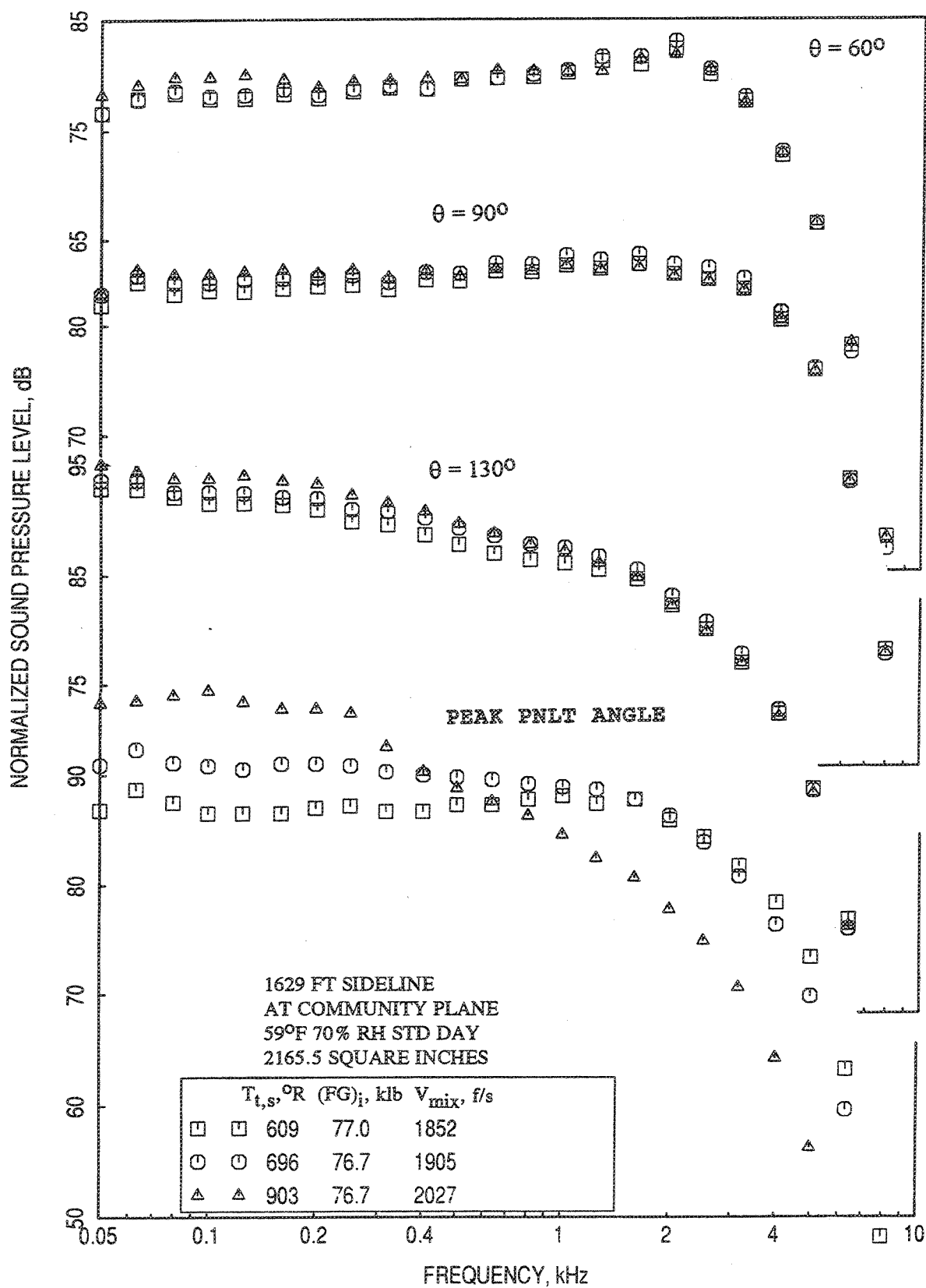


Figure 2.9-28. Normalized SPL spectra at different polar angles ( $\theta$ ) for the 0.75"-thick fluid shield nozzle at different  $T_{t,s}$  for fixed  $P_{r,p}=3.2$ ,  $T_{t,p}=1800^\circ R$ , and  $P_{r,s}=2.14$  at static condition.

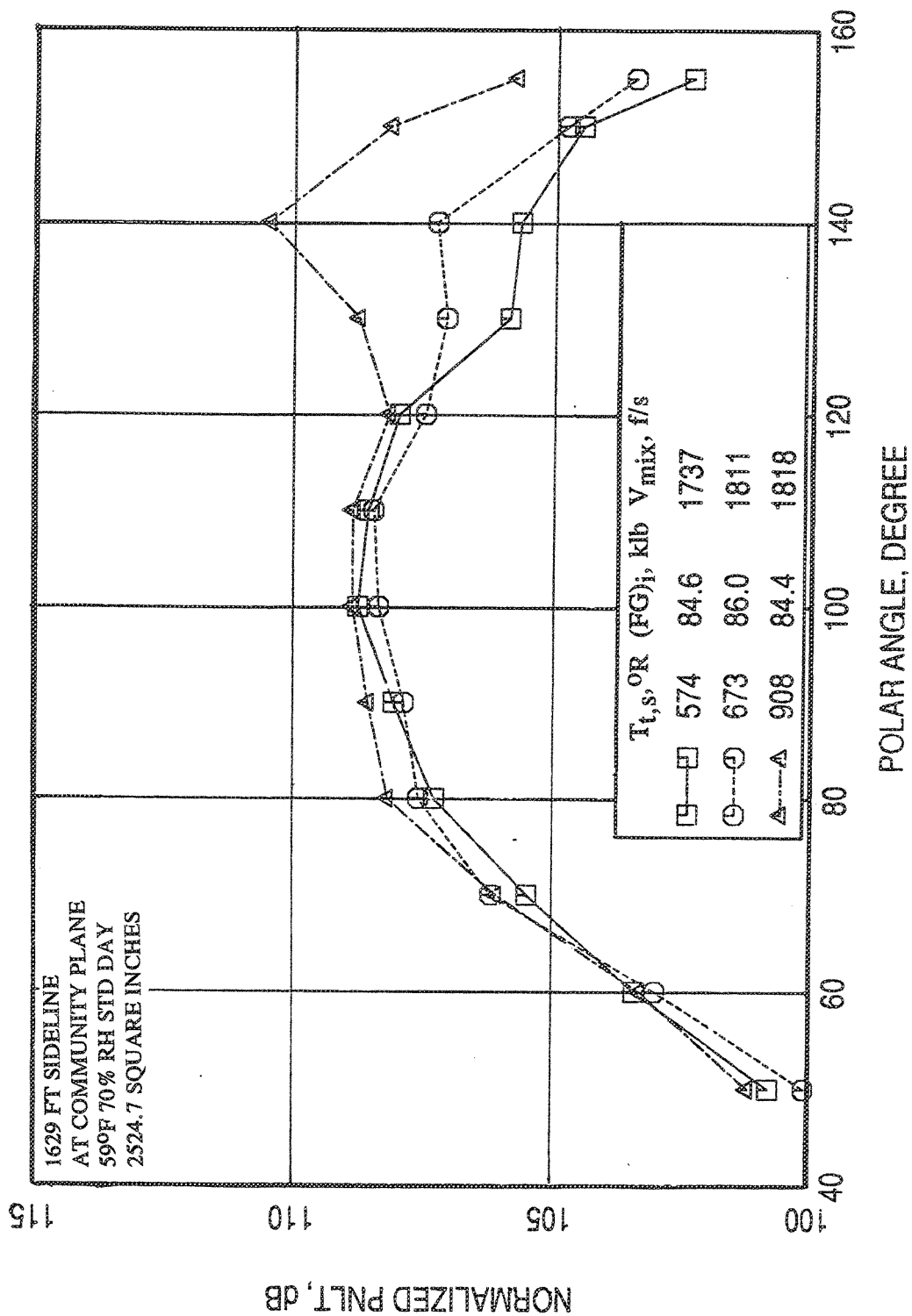


Figure 2.9-29. Normalized PNLT directivities for the 1.0"-thick fluid shield nozzle at different  $T_{t,s}$  for fixed  $P_{r,p}=3.2$ ,  $T_{t,p}=1800^\circ R$ , and  $P_{r,s}=2.14$  at static condition.

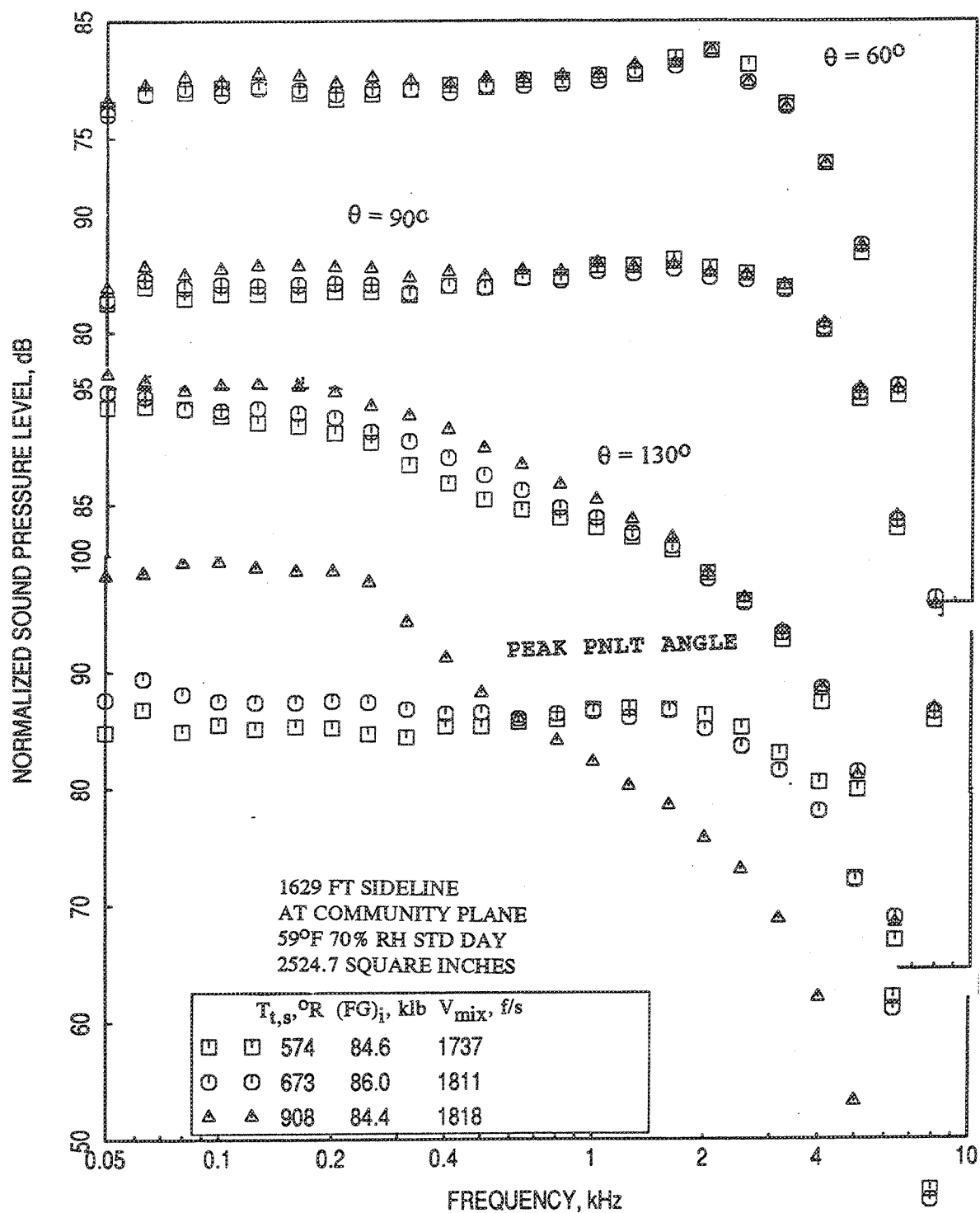


Figure 2.9-30. Normalized SPL spectra at different polar angles ( $\theta$ ) for the 1.0"-thick fluid shield nozzle at different  $T_{ts}$  for fixed  $P_{r,p}=3.2$ ,  $T_{t,p}=1800^\circ R$ , and  $P_{r,s}=2.14$  at static condition.

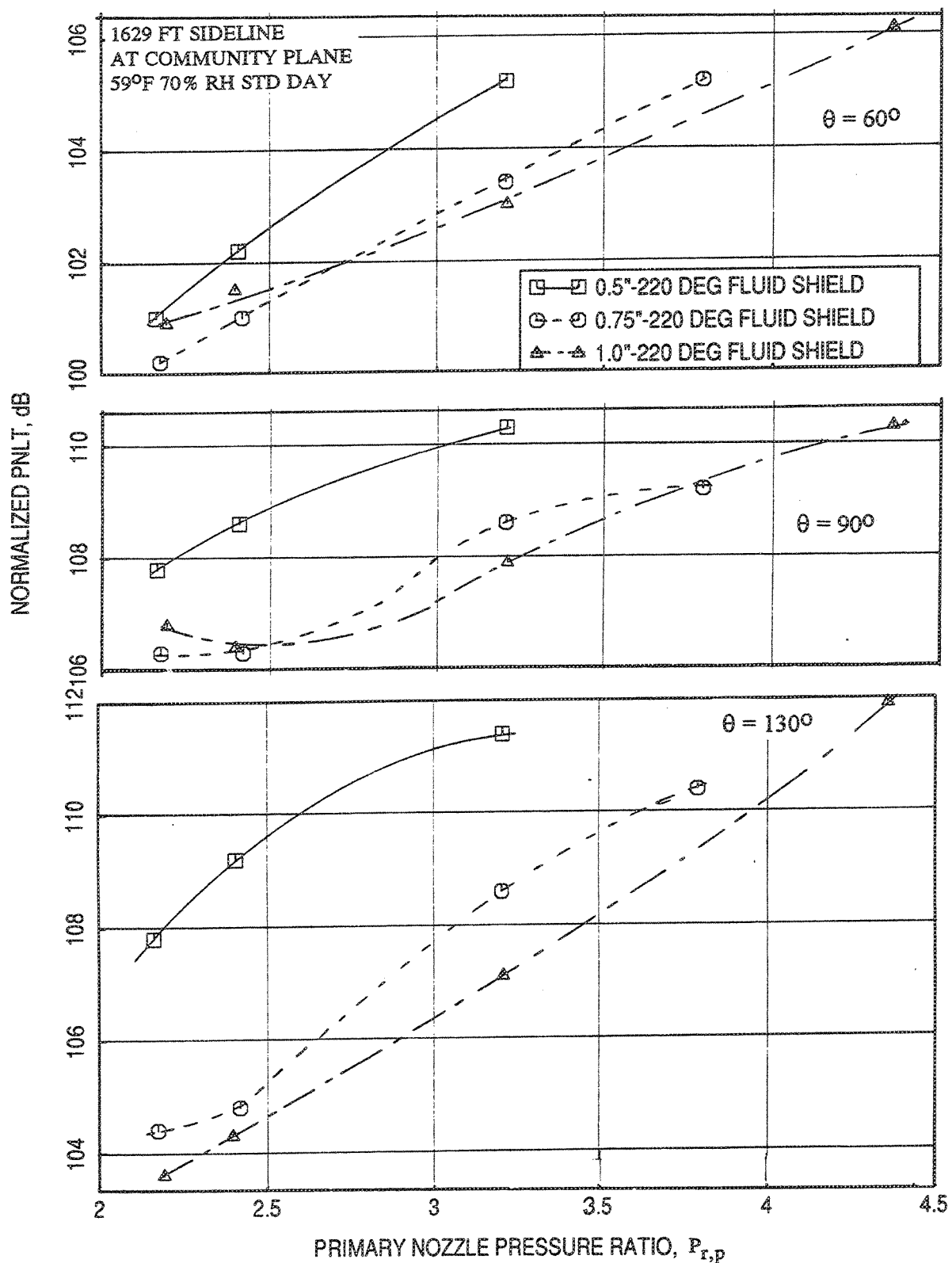


Figure 2.9-31. Effect of primary nozzle pressure ratio,  $P_{r,p}$ , on normalized PNLT data at different polar angles ( $\theta$ ) for fluid shield nozzles for fixed  $T_{t,p}=1800^\circ\text{R}$ ,  $P_{r,s}=2.14$ , and  $T_{t,s}=700^\circ\text{R}$  at static condition.



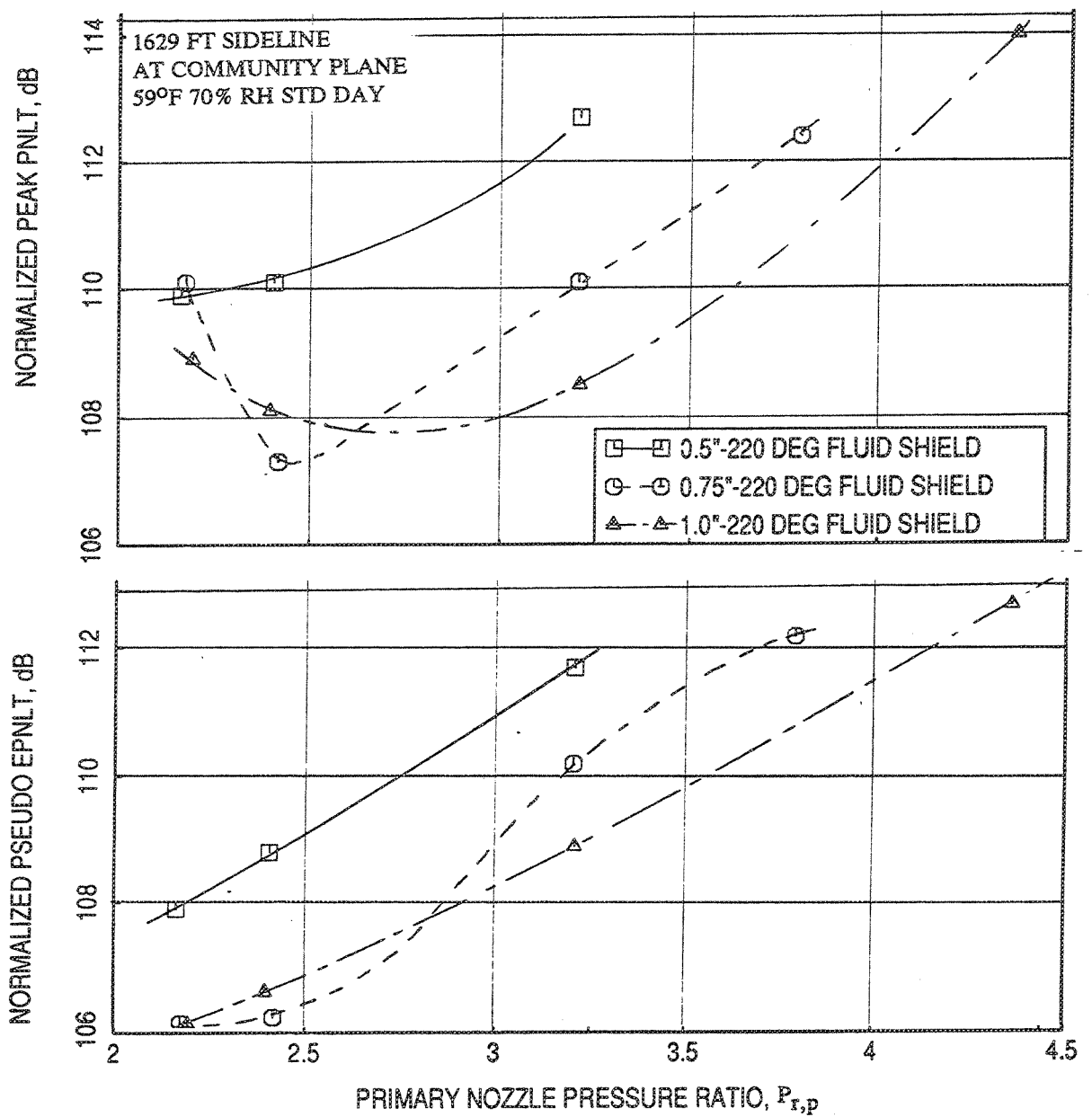


Figure 2.9-32. Effect of primary nozzle pressure ratio,  $P_{r,p}$ , on normalized peak PNLT and normalized pseudo EPNLT data for fluid shield nozzles for fixed  $T_{t,p}=1800^{\circ}\text{R}$ ,  $P_{r,s}=2.14$ , and  $T_{t,s}=700^{\circ}\text{R}$  at static condition.

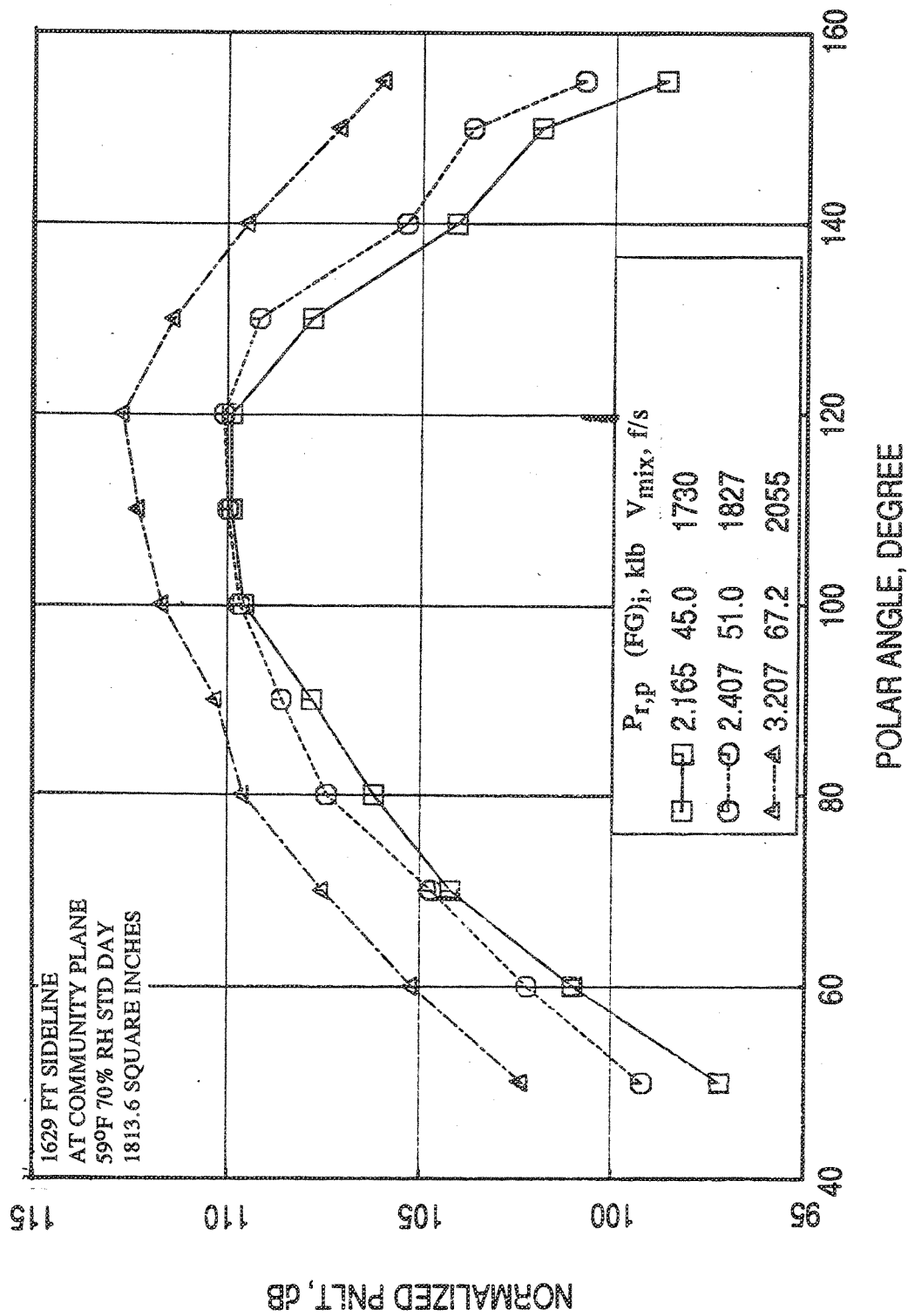


Figure 2.9-33. Normalized PNLT directivities for the 0.5"-thick fluid shield nozzle at different  $P_{r,p}$  for fixed  $T_{t,p}=1800^{\circ}R$ ,  $P_{r,s}=2.14$ , and  $T_{t,s}=700^{\circ}R$  at static condition.

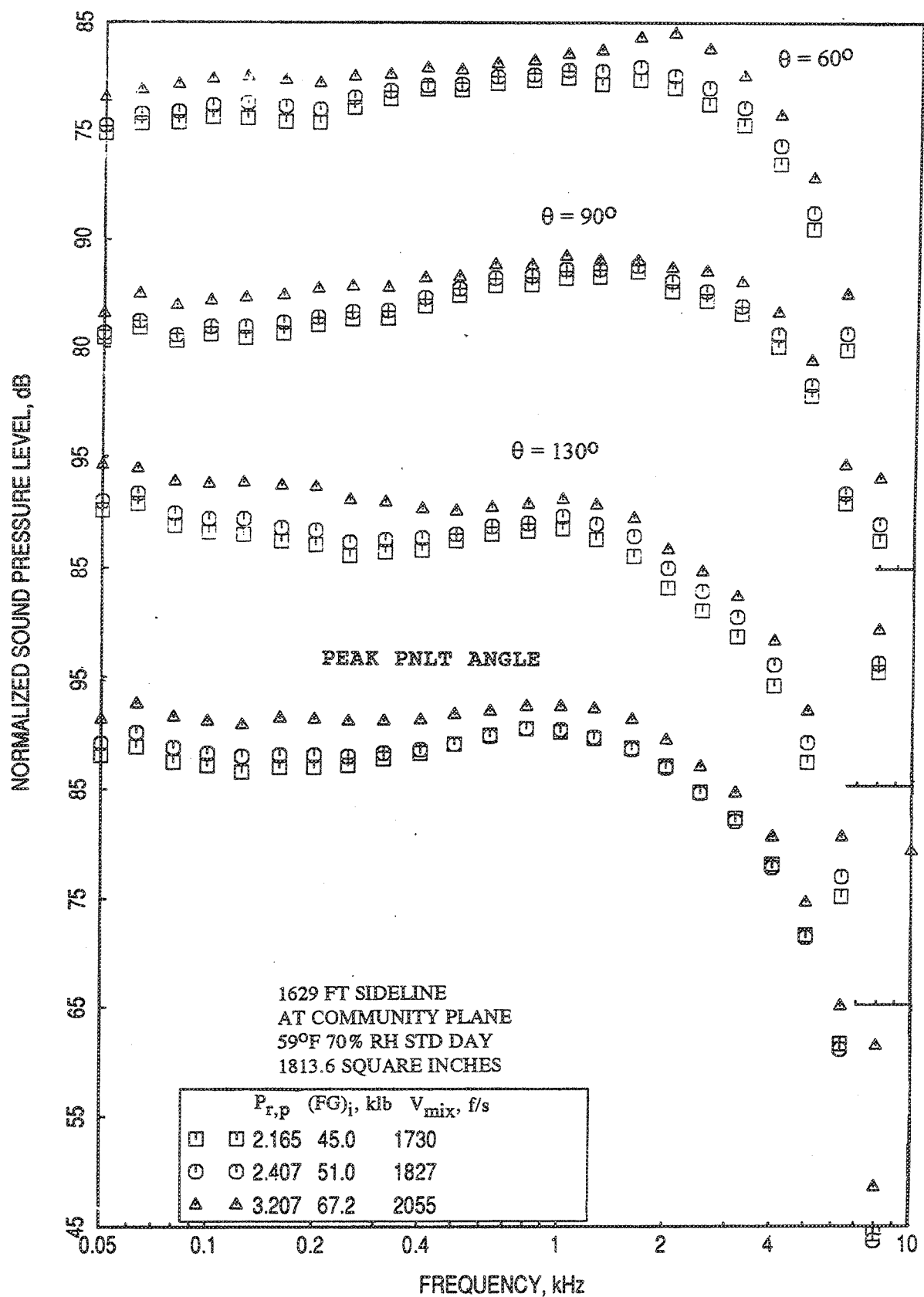


Figure 2.9-34. Normalized SPL spectra at different polar angles ( $\theta$ ) for the 0.5"-thick fluid shield nozzle at different  $P_{r,p}$  for fixed  $T_{t,p}=1800^\circ\text{R}$ ,  $P_{r,s}=2.14$ , and  $T_{t,s}=700^\circ\text{R}$  at static condition.

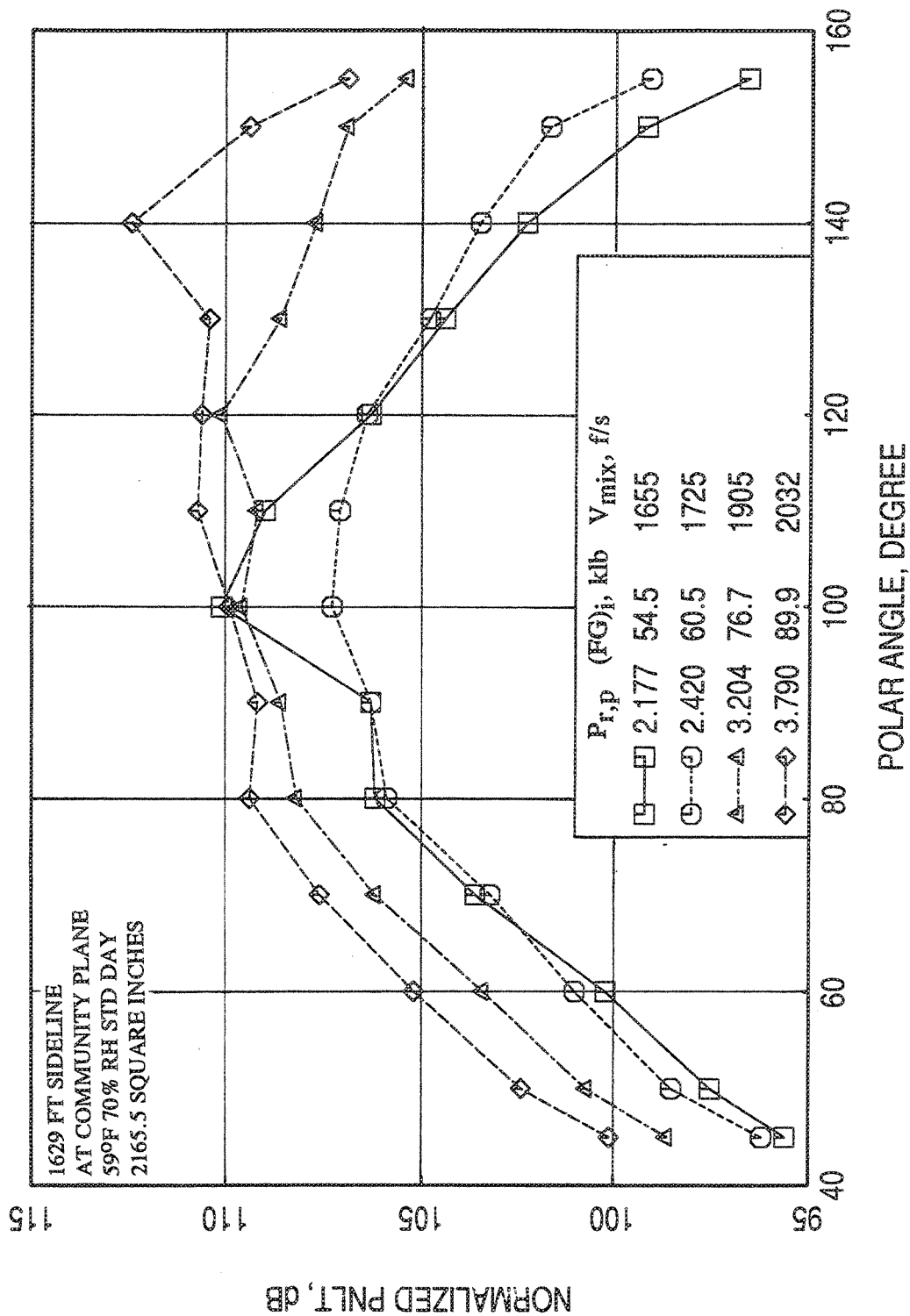


Figure 2.9-35. Normalized PNLT directivities for the 0.75" -thick fluid shield nozzle at different  $P_{r,p}$  for fixed  $T_{t,p}=1800^{\circ}\text{R}$ ,  $P_{r,s}=2.14$ , and  $T_{t,s}=7000^{\circ}\text{R}$  at static condition.

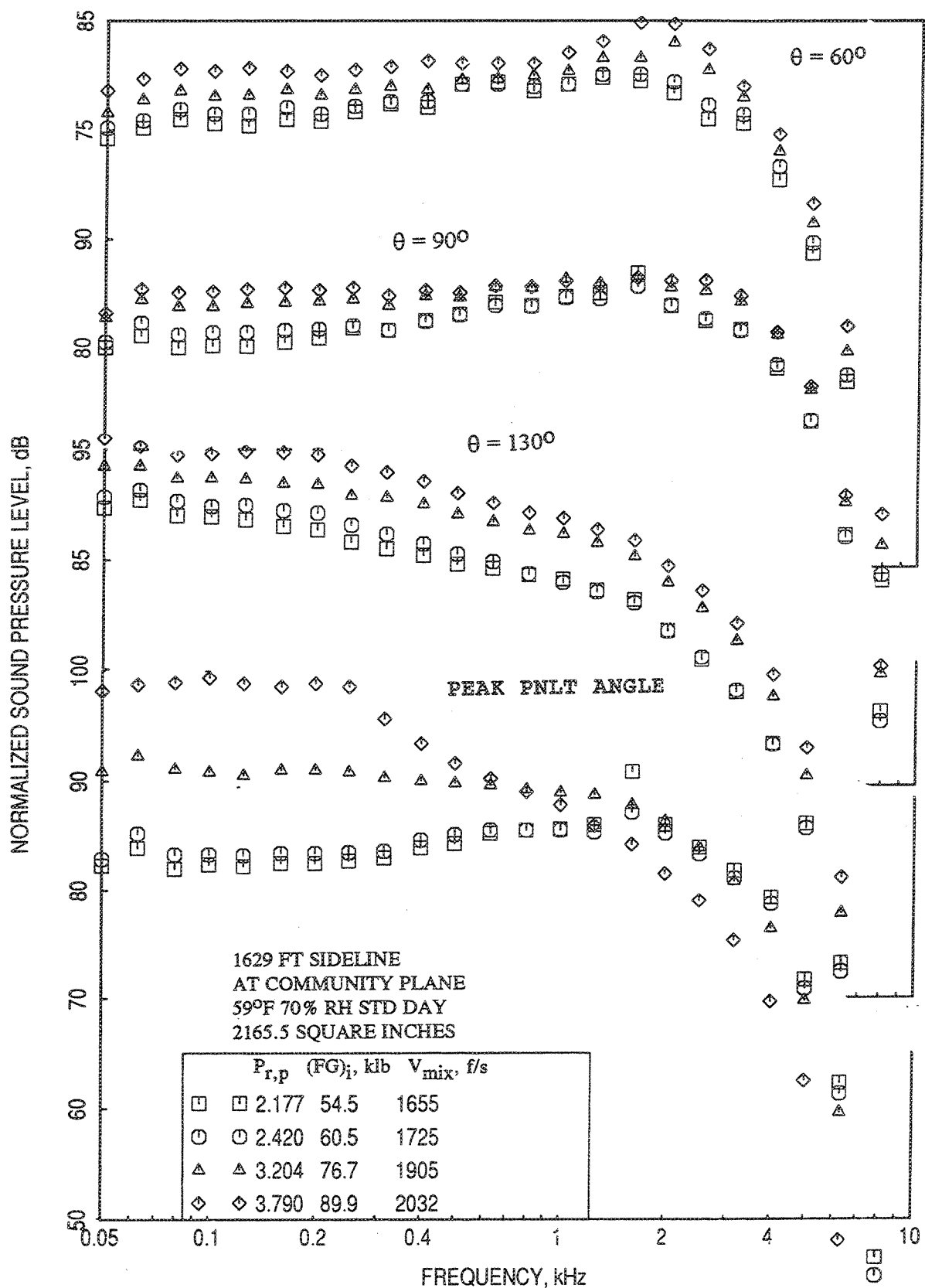


Figure 2.9-36. Normalized SPL spectra at different polar angles ( $\theta$ ) for the 0.75"-thick fluid shield nozzle at different  $P_{r,p}$  for fixed  $T_{t,p}=1800^\circ\text{R}$ ,  $P_{r,s}=2.14$ , and  $T_{t,s}=700^\circ\text{R}$  at static condition.

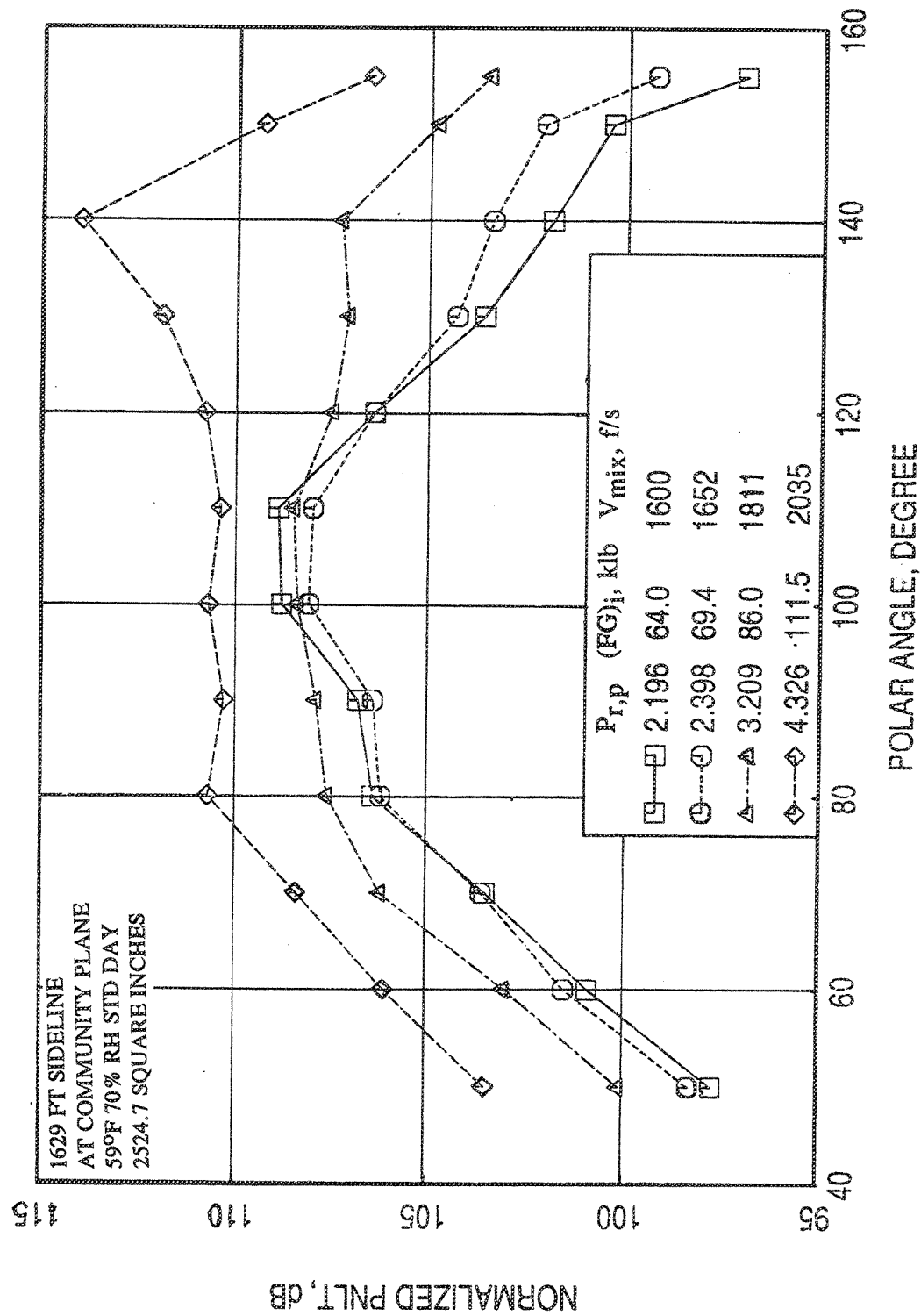


Figure 2.9-37. Normalized PNLT directivities for the 1.0"-thick fluid shield nozzle at different  $P_{r,p}$  for fixed  $T_{t,p}=1800^{\circ}\text{R}$ ,  $P_{r,s}=2.14$ , and  $T_{t,s}=700^{\circ}\text{R}$  at static condition.

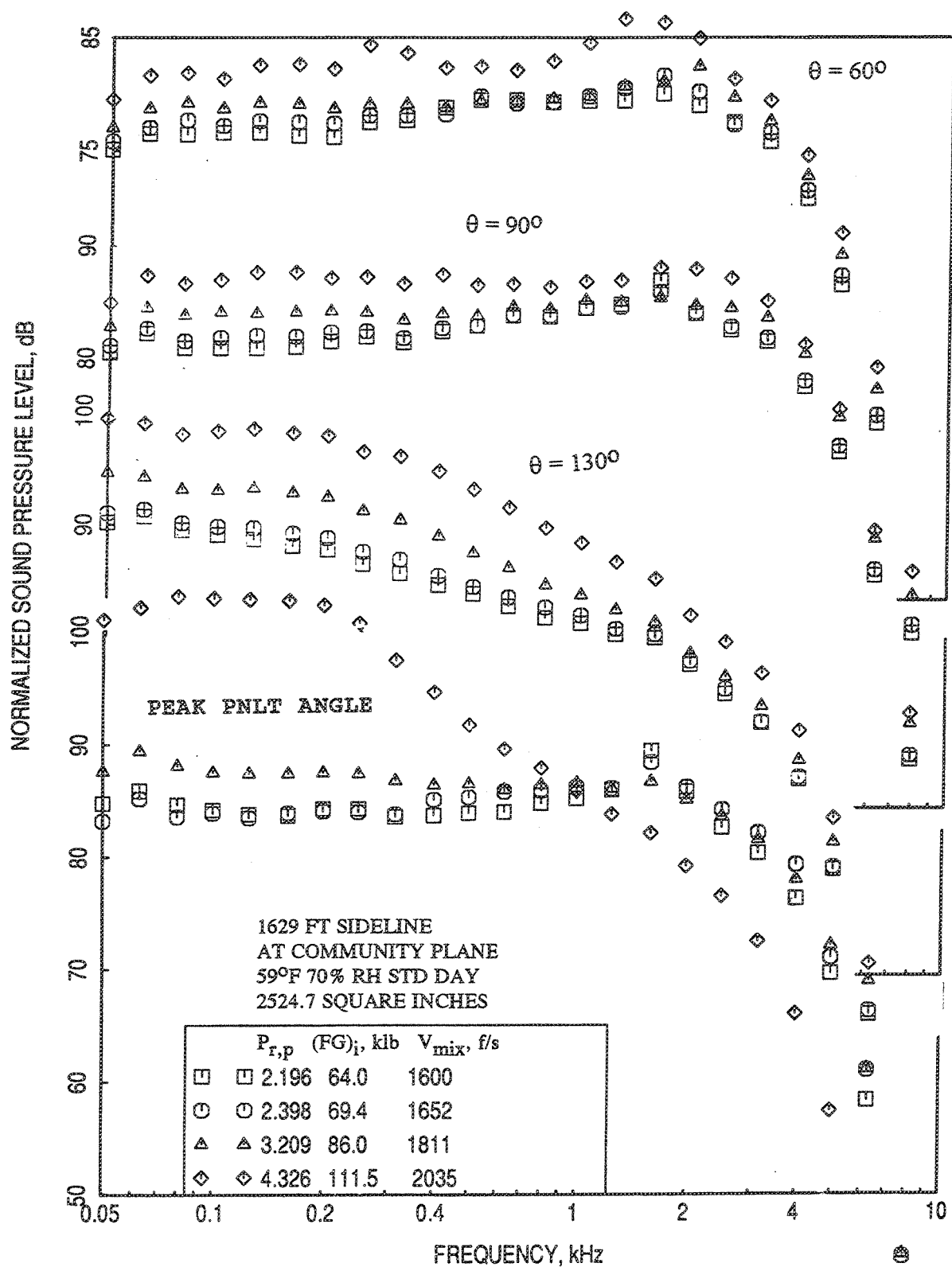


Figure 2.9-38. Normalized SPL spectra at different polar angles ( $\theta$ ) for the 1.0"-thick fluid shield nozzle at different  $P_{r,p}$  for fixed  $T_{t,p}=1800^\circ\text{R}$ ,  $P_{r,s}=2.14$ , and  $T_{t,s}=700^\circ\text{R}$  at static condition.

increases with increasing  $P_{r,p}$ . Corresponding normalized SPL spectra also indicate the similar trend at all frequencies.

#### Effect of Primary Nozzle Total Temperature, $T_{t,p}$ :

Several tests were conducted for fluid shield nozzle configurations by varying  $T_{t,p}$  with fixed  $P_{r,p}=3.2$ ,  $P_{r,s}=2.14$ , and  $T_{t,s}=7000^{\circ}\text{R}$  (see Figure 2.2-21). Normalized PNLTs are plotted with respect to  $T_{t,p}$  in Figure 2.9-39 at different polar angles ( $\theta$ ) for the three fluid shield nozzles. Normalized PNLT increases with  $T_{t,p}$ . Figure 2.9-40 illustrates the variation of normalized peak PNLT and pseudo EPNLT with  $T_{t,s}$ . PNLT and pseudo EPNLT increase with  $T_{t,p}$  for each configuration.

Normalized PNLT directivities for 0.5"-thick shield are plotted in Figure 2.9-41 for different  $T_{t,p}$ . PNLT at all angles increases with  $T_{t,p}$  whereas, the ideal gross thrust remains more or less same for all the cases. Corresponding normalized SPL spectra are plotted in Figure 2.9-42, which also indicates the similar trend at all frequency. It seems beneficial from noise consideration to operate the primary nozzle at lower temperature.

Normalized PNLT directivities and normalized SPL spectra for the other two fluid shield configurations with 0.75"-thick and 1.0"-thick shields are shown in Figures 2.9-43 through 2.9-46. Similar to 0.5"-thick shield configuration, PNLT at all angles increases with  $T_{t,p}$ . Corresponding normalized SPL spectra also indicate the similar trend at all frequencies.

#### 2.9.2 Flight Data

Acoustic tests with parametric variation of aerothermodynamic conditions, as per Figures 2.2-20 and 2.2-21, with flight simulation (i.e.,  $M_F=0.32$ ) were conducted only for the 0.5"-thick fluid shield nozzle. Hence, all the data with flight simulation are for 0.5"-thick fluid shield nozzle configuration.



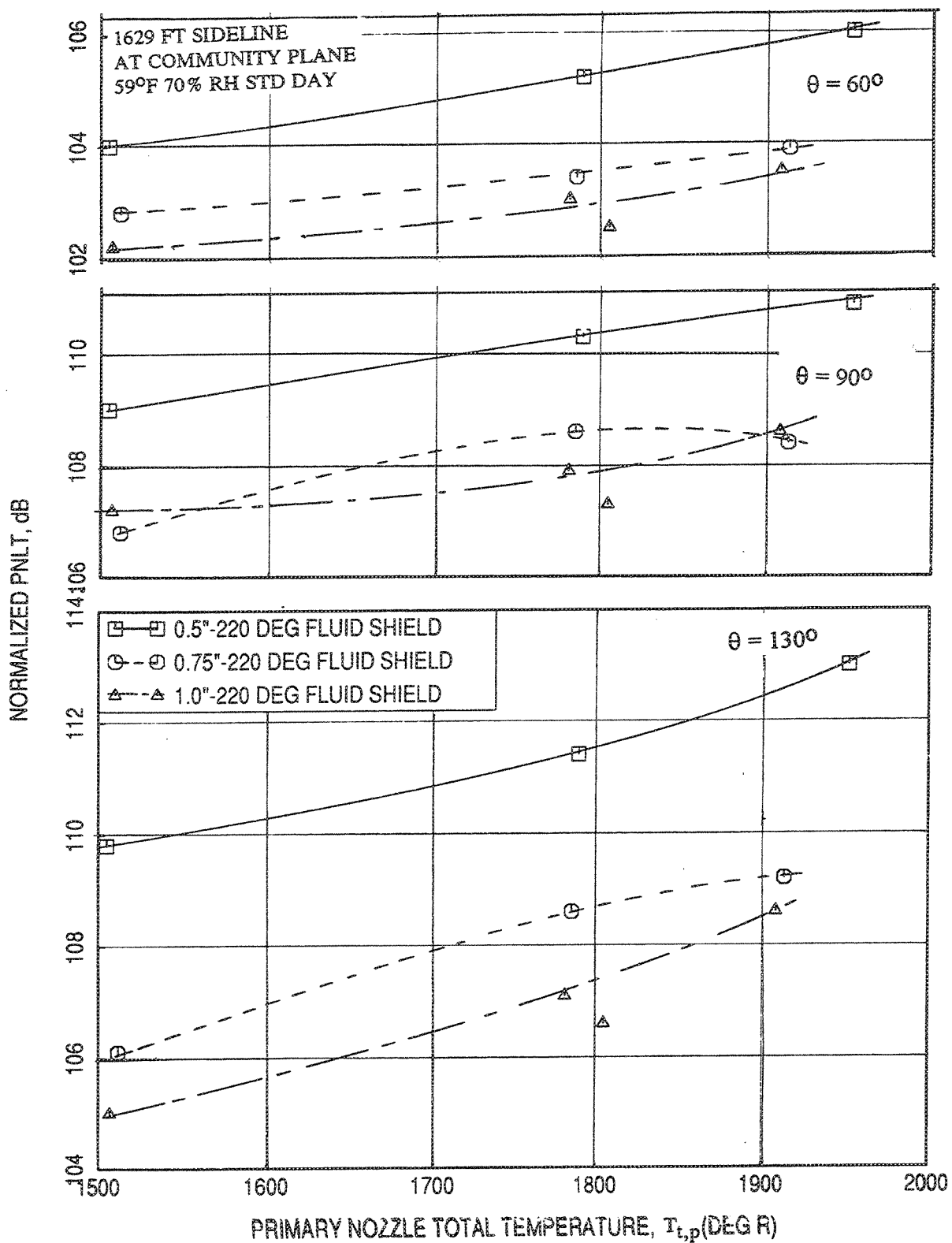


Figure 2.9-39. Effect of primary nozzle total temperature,  $T_{t,p}$ , on normalized PNLT data at different polar angles ( $\theta$ ) for fluid shield nozzles for fixed  $P_{r,p}=3.2$ ,  $P_{r,s}=2.14$ , and  $T_{t,s}=700^\circ\text{R}$  at static condition.

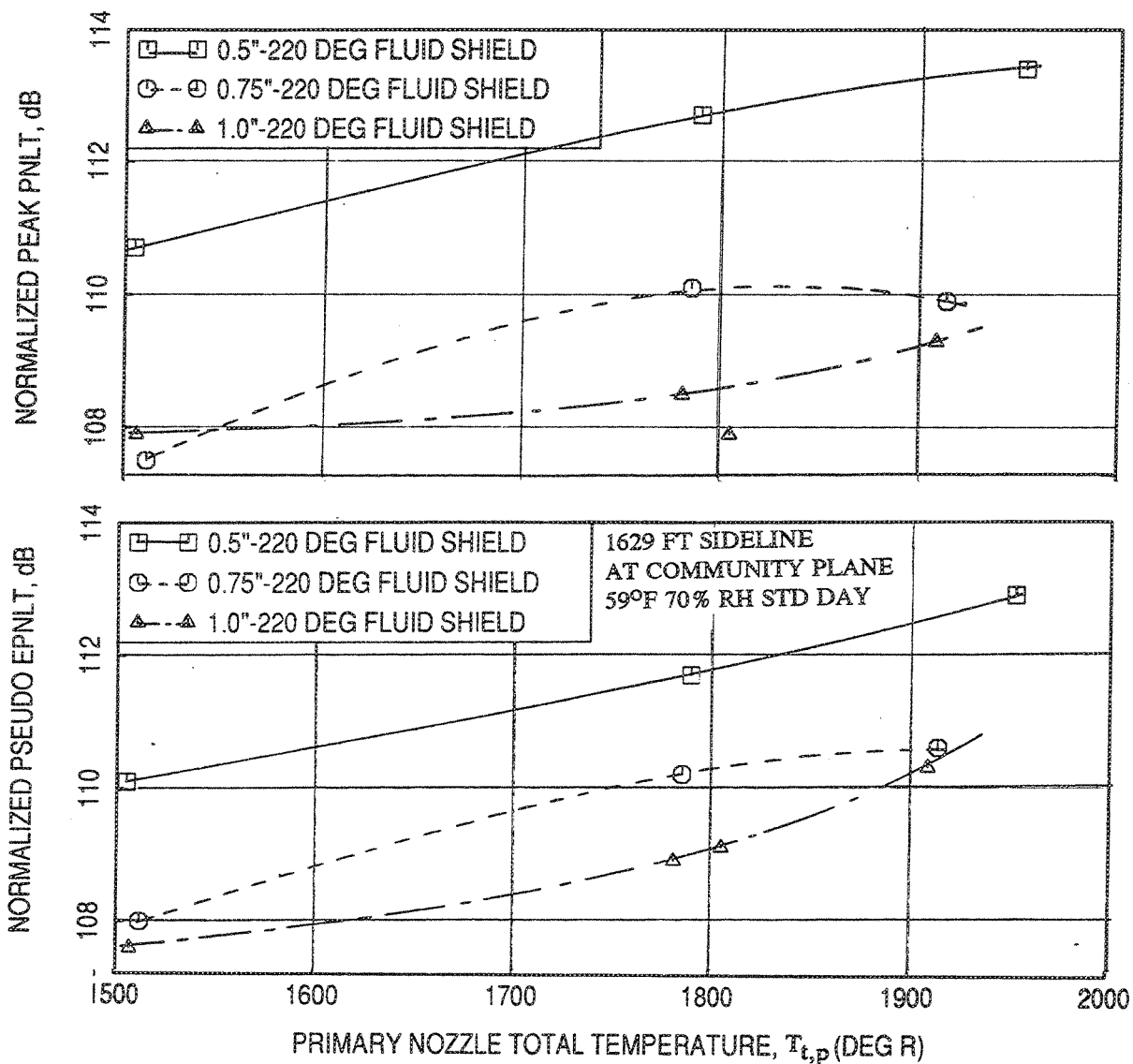


Figure 2.9-40. Effect of primary nozzle total temperature,  $T_{t,p}$ , on normalized peak PNLT and normalized pseudo EPNLT data for fluid shield nozzles for fixed  $P_{r,p}=3.2$ ,  $P_{r,s}=2.14$ , and  $T_{t,s}=7000^{\circ}\text{R}$  at static condition.

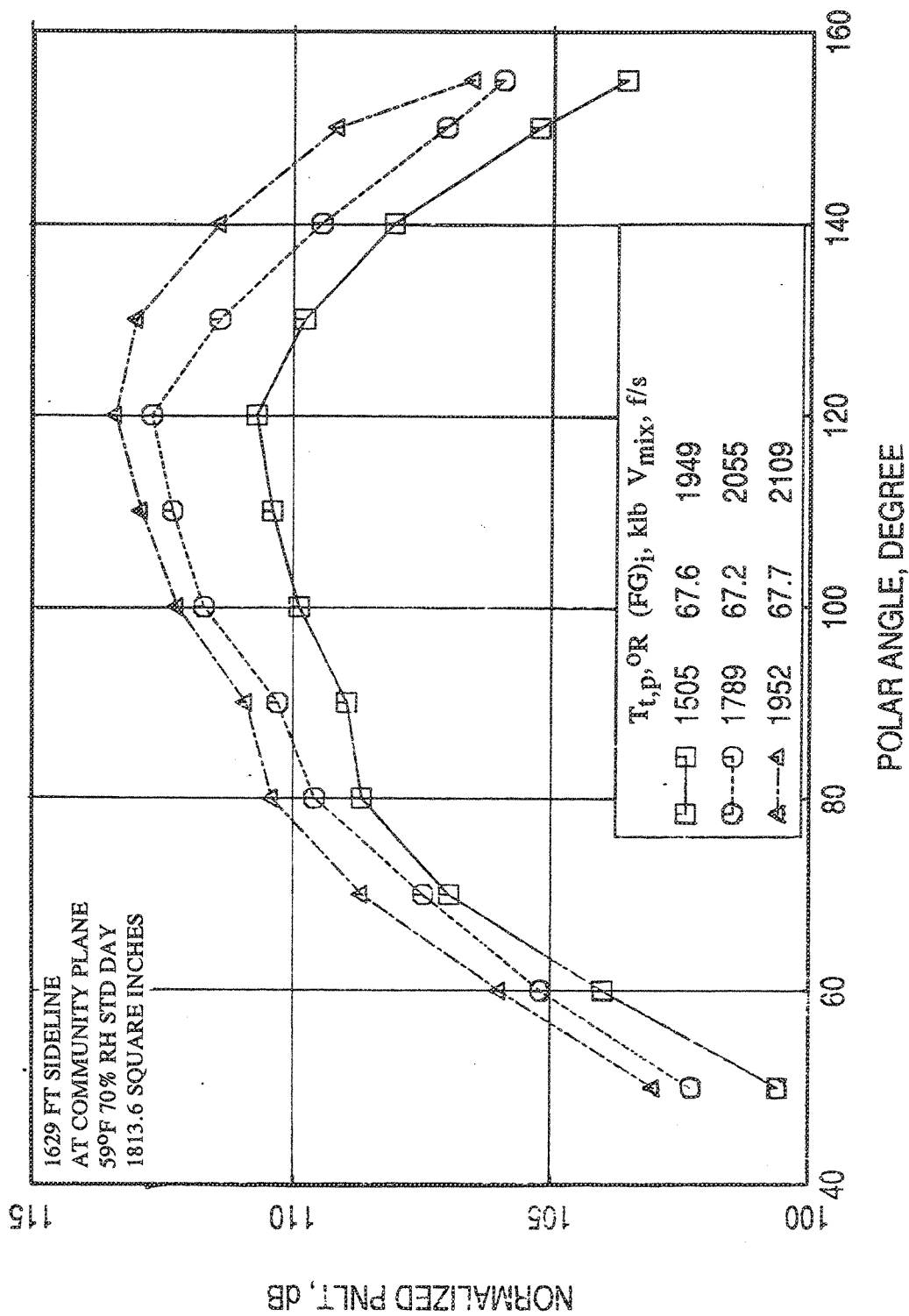


Figure 2.9-41. Normalized PNL T directivities for the 0.5"-thick fluid shield nozzle at different  $T_{t,p}$  for fixed  $P_{r,p}=3.2$ ,  $P_{r,s}=2.14$ , and  $T_{t,s}=700^\circ R$  at static condition.

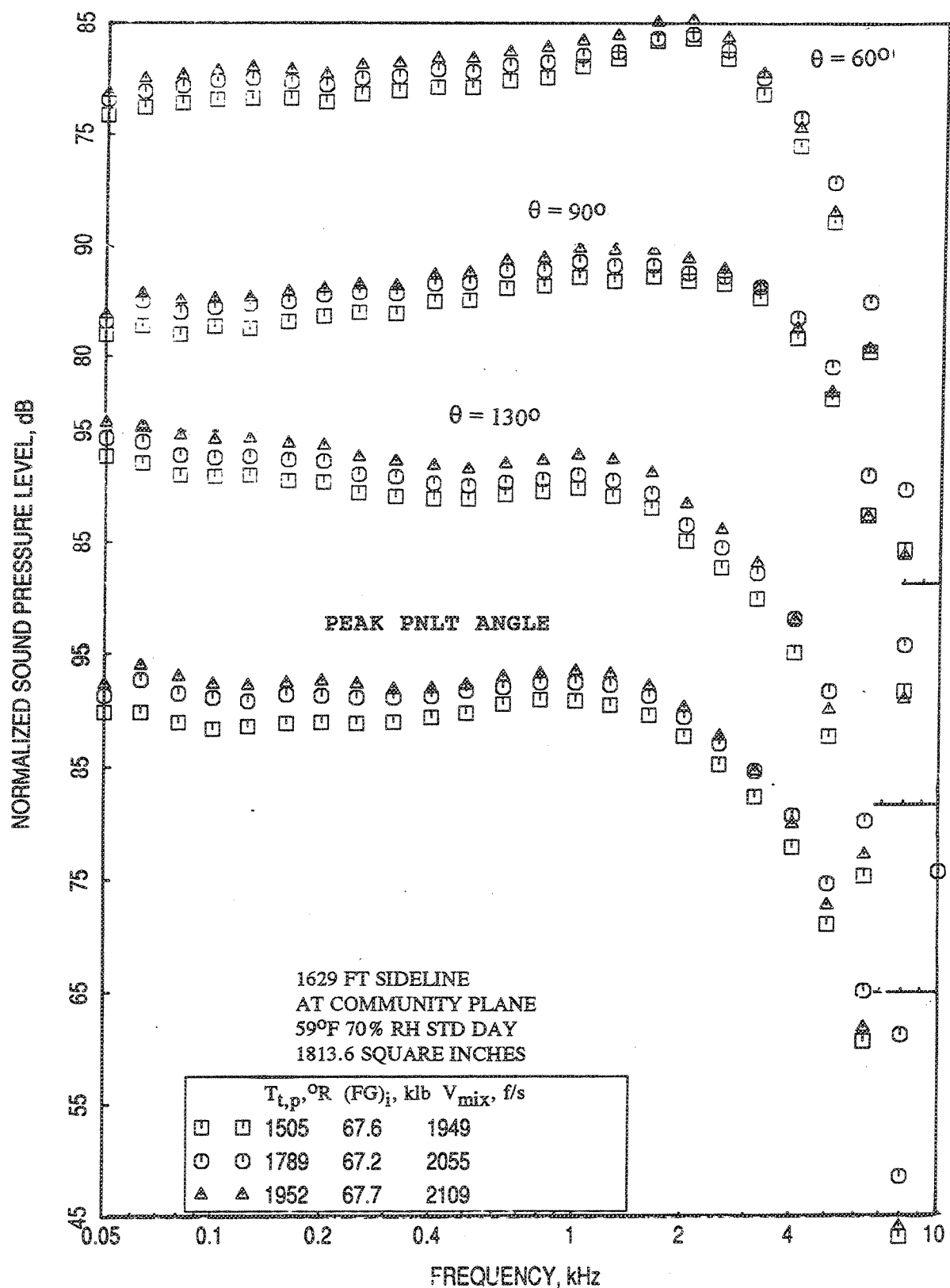


Figure 2.9-42. Normalized SPL spectra at different polar angles ( $\theta$ ) for the 0.5"-thick fluid shield nozzle at different  $T_{t,p}$  for fixed  $P_{r,p}=3.2$ ,  $P_{r,s}=2.14$ , and  $T_{t,s}=700^\circ\text{R}$  at static condition.

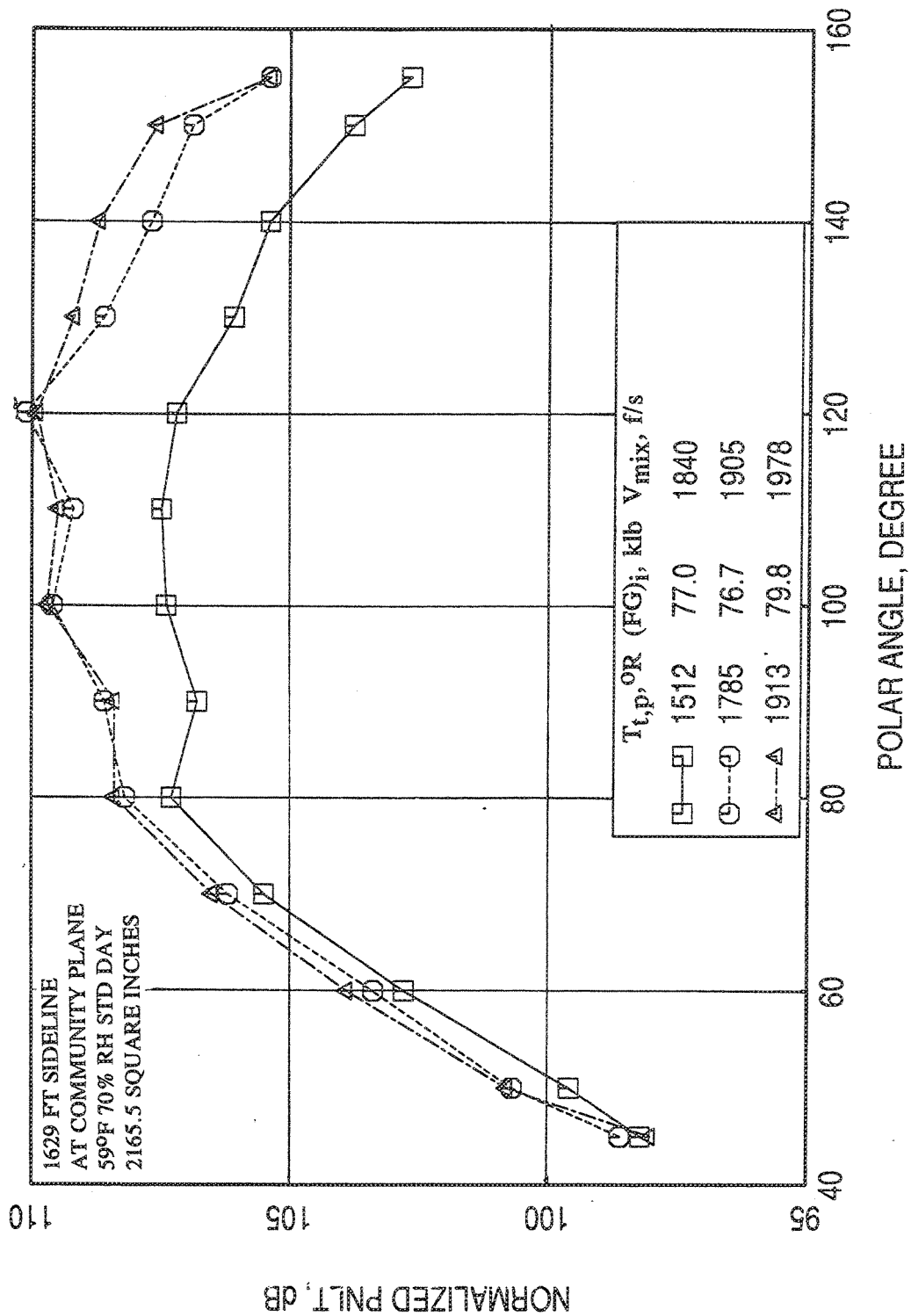


Figure 2.9-43. Normalized PNL T directivities for the 0.75"-thick fluid shield nozzle at different  $T_{t,p}$  for fixed  $P_{r,p}=3.2$ ,  $P_{r,s}=2.14$ , and  $T_{t,s}=700^\circ R$  at static condition.

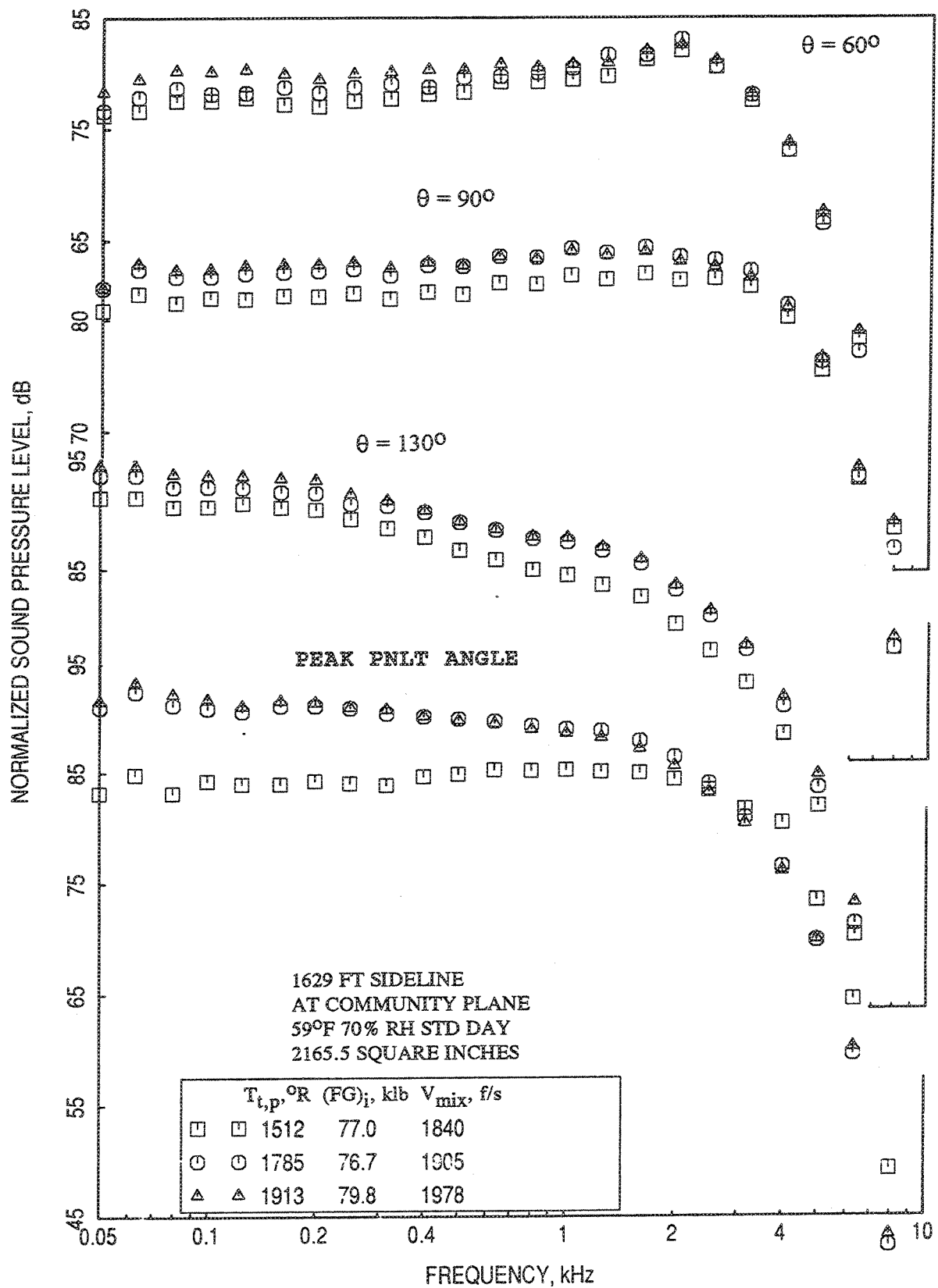


Figure 2.9-44. Normalized SPL spectra at different polar angles ( $\theta$ ) for the 0.75"-thick fluid shield nozzle at different  $T_{t,p}$  for fixed  $P_{r,p}=3.2$ ,  $P_{r,s}=2.14$ , and  $T_{t,s}=700^\circ R$  at static condition.

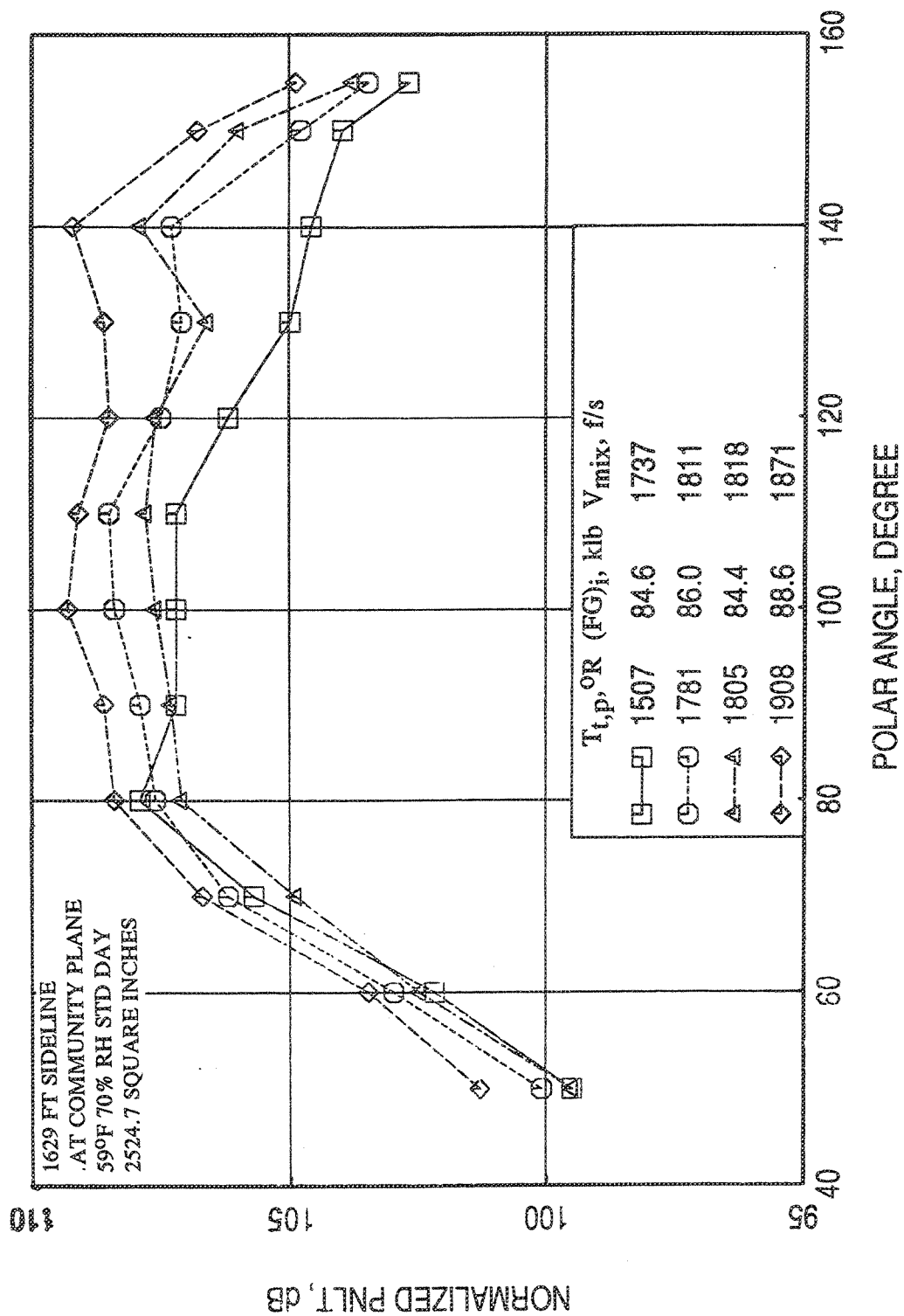


Figure 2.9-45. Normalized PNLT directivities for the 1.0"-thick fluid shield nozzle at different  $T_{t,p}$  for fixed  $P_{r,p}=3.2$ ,  $P_{r,s}=2.14$ , and  $T_{t,s}=700^\circ R$  at static condition.

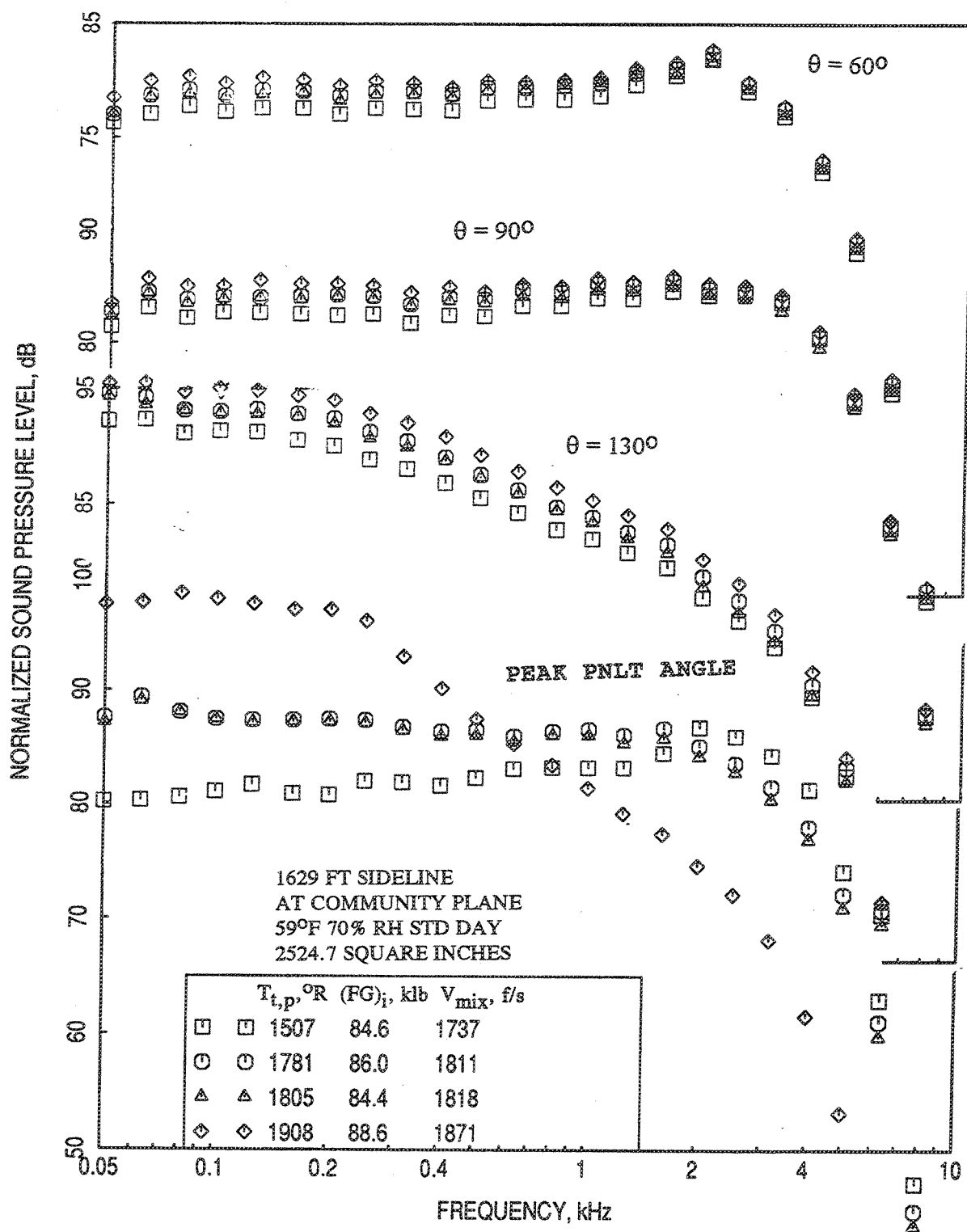


Figure 2.9-46. Normalized SPL spectra at different polar angles ( $\theta$ ) for the 1.0"-thick fluid shield nozzle at different  $T_{t,p}$  for fixed  $P_{r,p}=3.2$ ,  $P_{r,s}=2.14$ , and  $T_{t,s}=700^\circ R$  at static condition.



### Effect of Velocity ratio $V_T$ and Mass Flow Ratio $W_T$ :

At  $V_{mix} = 1811$  ft/sec :

Normalized PNLTs at different polar angles ( $\theta$ ) and EPNLTs are plotted with respect to  $V_T$  in Figure 2.9-47 for  $V_{mix}$  of 1811 ft/sec. Normalized PNLT as well as EPNLT decrease with  $V_T$ , except at  $\theta = 60^\circ$ , where PNLT decreases and then increases with  $V_T$ . Variation of PNLT and pseudo EPNLT with respect to  $W_T$  are shown in Figure 2.9-48. The general trends are similar to those observed in Figure 2.9-47.

Normalized PNLT directivities are plotted in Figure 2.9-49 for different  $V_T$  and  $W_T$ . PNLT at all angles decreases with increasing  $V_T$  (or  $W_T$ ), whereas, ideal gross thrust increases with  $V_T$ . As mentioned earlier, further increase in  $V_T$  may reverse the trend for PNLT, and an optimum  $V_T$  may be established. Corresponding normalized SPL spectra are plotted in Figure 2.9-50, which also indicates the similar trend at all frequencies.

At  $V_{mix} = 2030$  ft/sec :

Normalized PNLTs at different polar angles ( $\theta$ ), peak PNLTs, and EPNLTs are plotted with respect to  $V_T$  in Figure 2.9-49 for  $V_{mix}$  of 2030 ft/sec. Normalized PNLTs and pseudo EPNLTs decrease with  $V_T$ . A minimum EPNLT is observed, after which the level starts increasing with  $V_T$ . Similar results plotted with respect to  $W_T$  are shown in Figure 2.9-52. The general trends are similar to those observed in Figure 2.9-51 with respect to  $V_T$ .

Normalized PNLT directivities for 0.5"-thick shield are plotted in Figure 2.9-53 for different  $V_T$  and  $W_T$ . PNLT at all angles decreases with increasing  $V_T$  (or  $W_T$ ). Whereas, ideal gross thrust increases with  $V_T$ . Corresponding normalized SPL spectra are plotted in Figure 2.9-54, which also indicates the similar trend at all frequencies.

### Effect of Fluid Shield Nozzle Pressure Ratio, $P_{r,s}$ :

In the tests performed for a fixed  $V_{mix}$  the variation of  $V_T$  and  $W_T$  was achieved by varying the fluid shield nozzle pressure ratio without changing the primary nozzle pressure ratios significantly. For example, while  $P_{r,s}$  is varied between 1.3 to 2.4 for

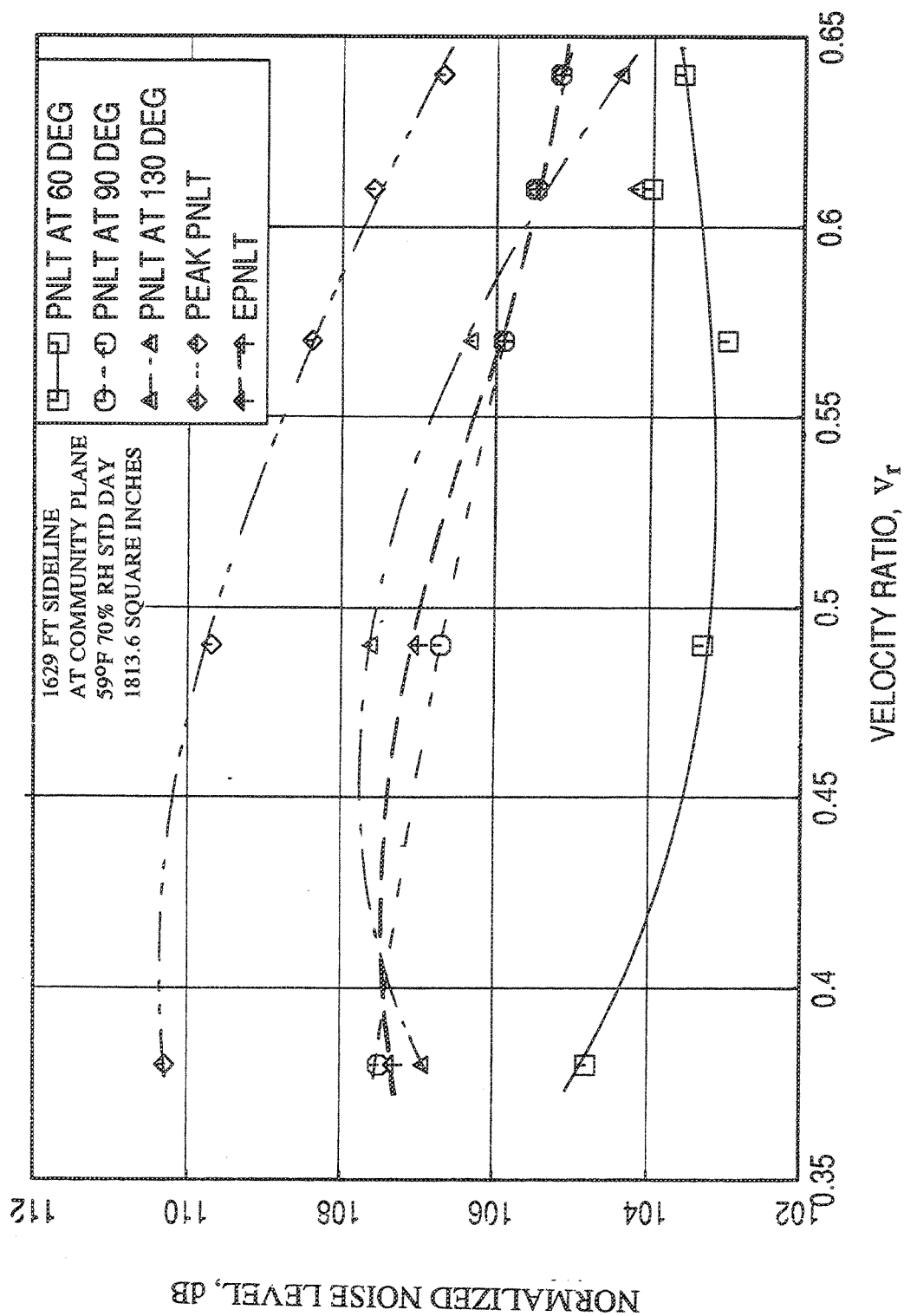


Figure 2.9-47. Effect of velocity ratio  $V_r$  on normalized PNL T data at different polar angles ( $\theta$ ) and EPNL T for the 0.5"-thick fluid shield nozzle for a fixed jet velocity,  $V_{mix}$ , of 1811 ft/sec with flight simulation ( $M_F=0.32$ ).

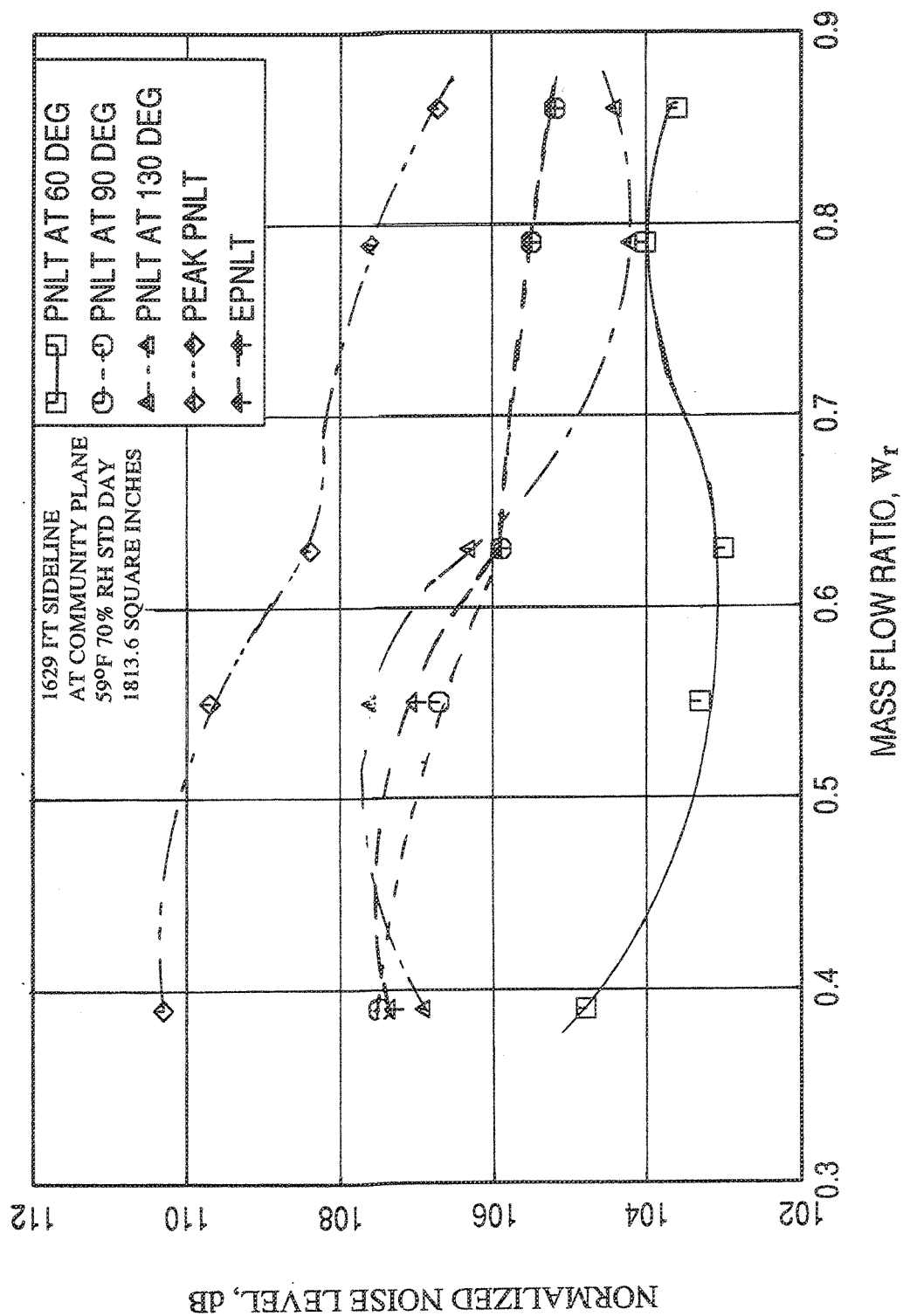


Figure 2.9-48. Effect of mass flow ratio  $W_t$  on normalized PNL.T data at different polar angles ( $\theta$ ) and EPNL.T for the 0.5"-thick fluid shield nozzle for a fixed jet velocity,  $V_{mix}$ , or 1811 ft/sec with flight simulation ( $M_F=0.32$ ).

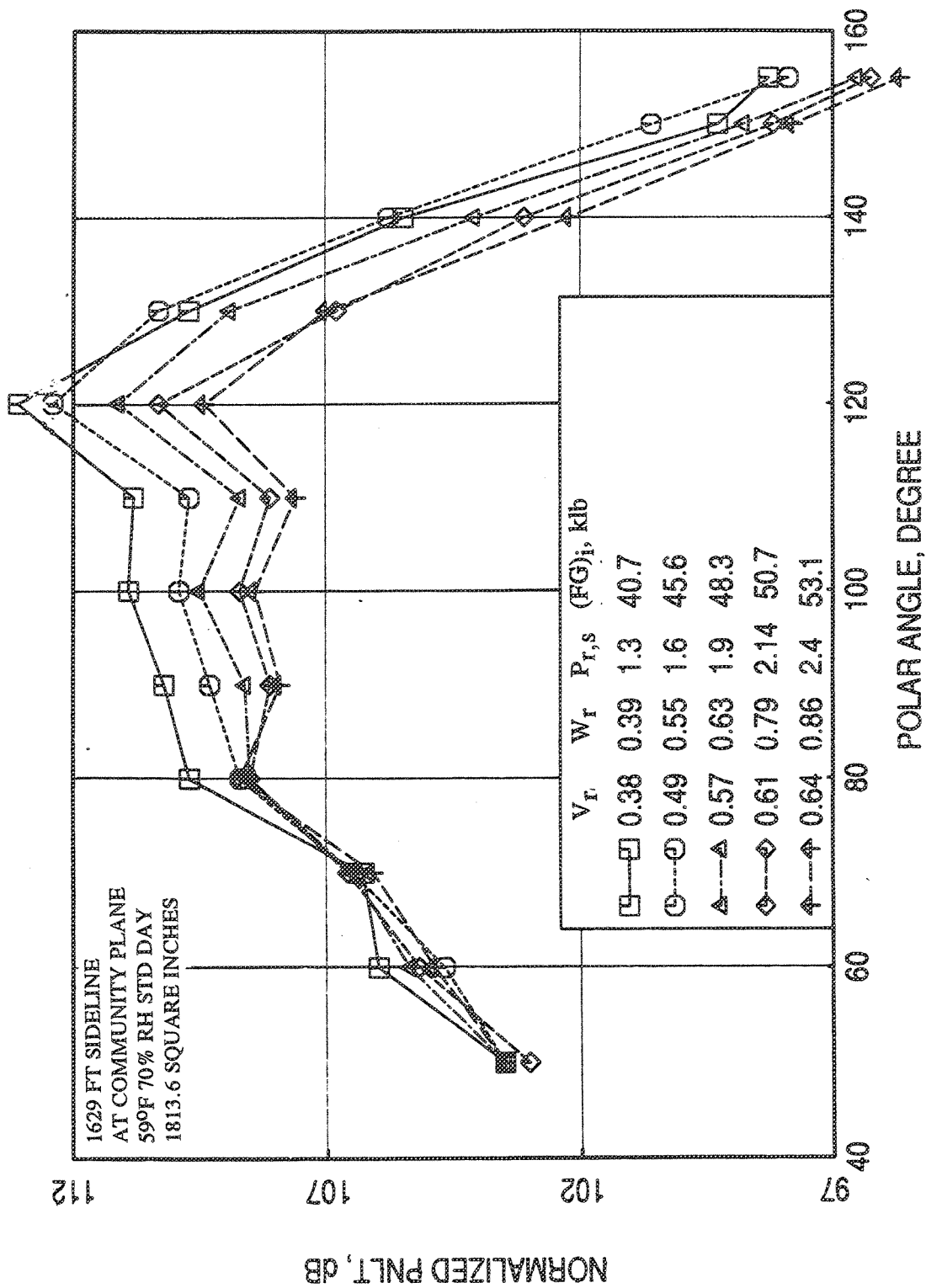


Figure 2.9-49. Normalized PNLT directivities for the 0.5"-thick fluid shield nozzle at different  $V_r$  (and  $W_r$ ) for a fixed jet velocity,  $V_{mix}$ , of 1811 ft/sec with flight simulation ( $M_F=0.32$ ).

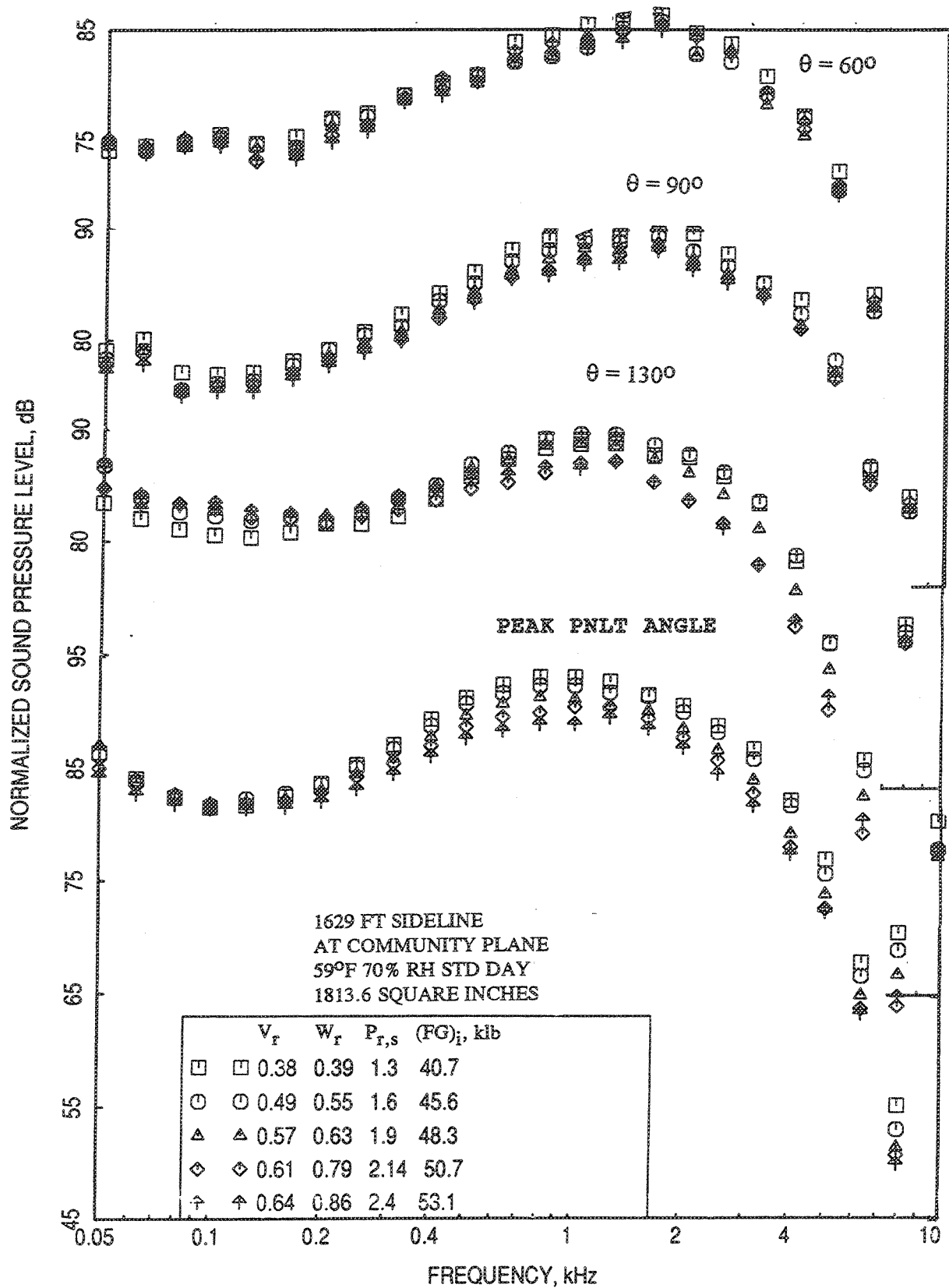


Figure 2.9-50. Normalized SPL spectra at different polar angles ( $\theta$ ) for the 0.5"-thick fluid shield nozzle at different  $V_r$  (and  $W_r$ ) for a fixed jet velocity,  $V_{mix}$ , of 1811 ft/sec with flight simulation ( $M_F=0.32$ ).

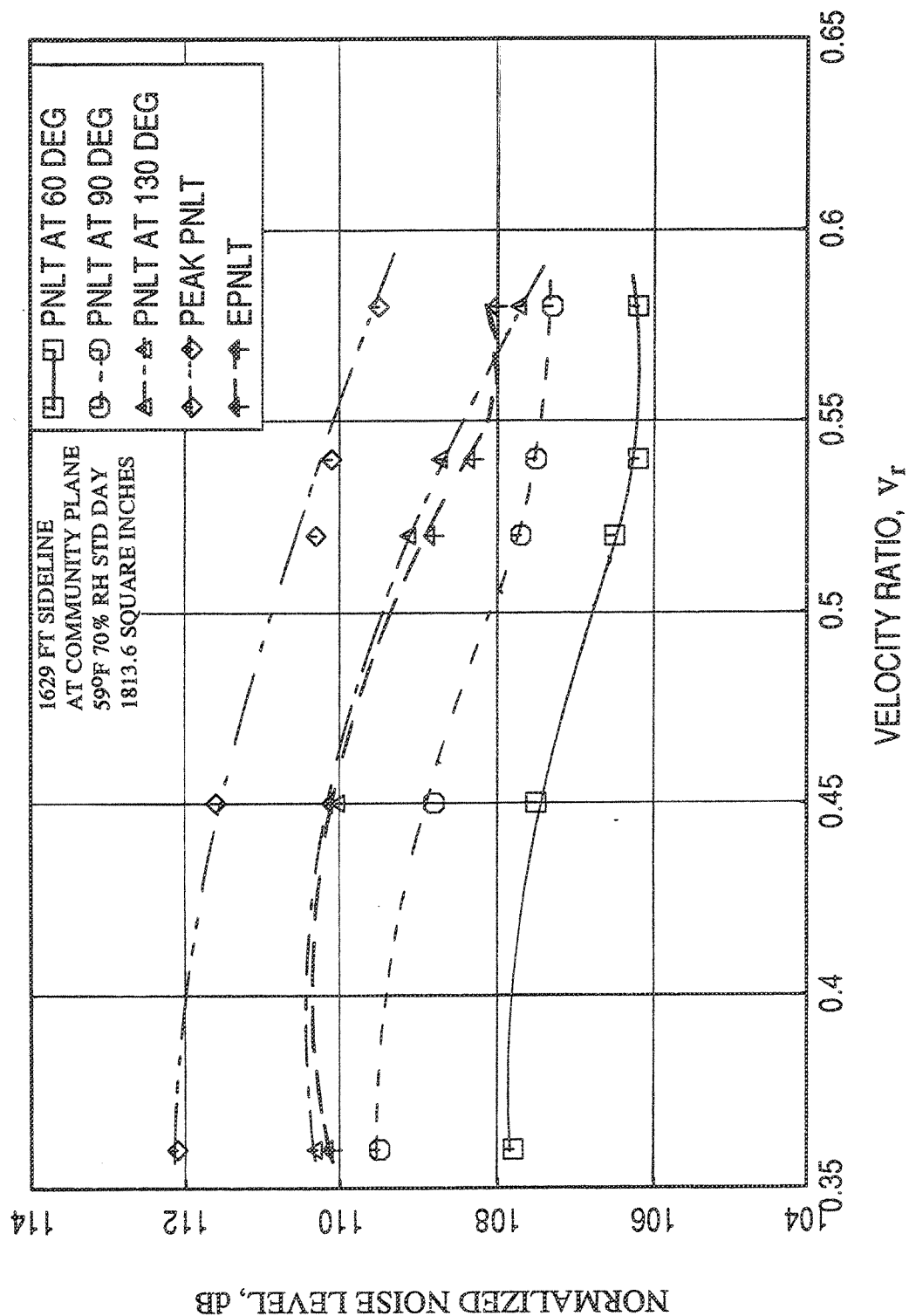


Figure 2.9-51. Effect of velocity ratio  $V_r$  on normalized PNL/T data at different polar angles ( $\theta$ ) and EPNL/T for the 0.5"-thick fluid shield nozzle for a fixed jet velocity,  $V_{mix}$ , of 2030 ft/sec with flight simulation ( $M_F=0.32$ ).

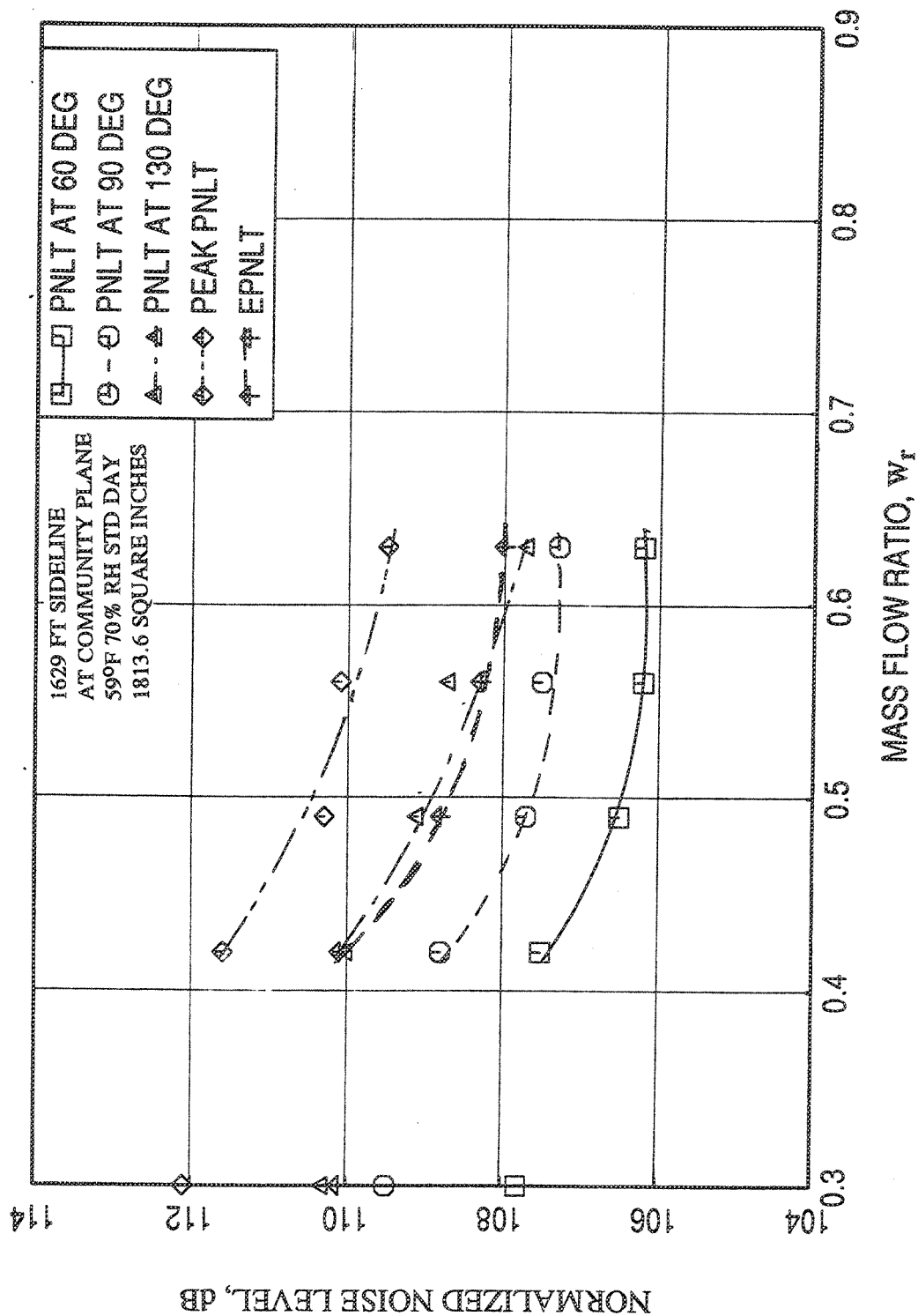


Figure 2.9-52. Effect of mass flow ratio  $w_r$  on normalized PNLT data at different polar angles ( $\theta$ ) and EPNLT for the 0.5"-thick fluid shield nozzle for a fixed jet velocity,  $V_{mix}$ , of 2030 ft/sec with flight simulation ( $M_F=0.32$ ).

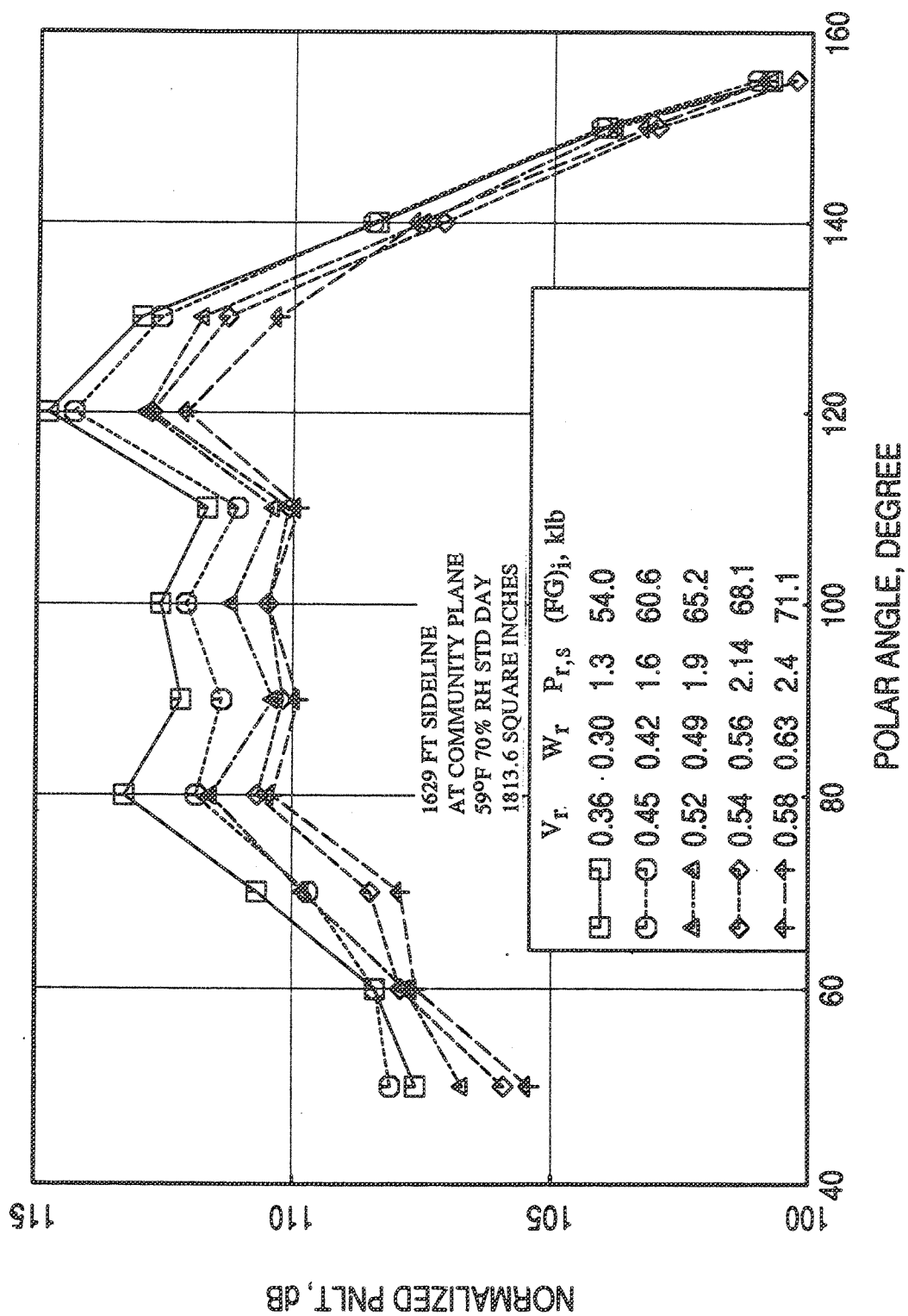


Figure 2.9-53. Normalized PNL T directivities for the 0.5"-thick fluid shield nozzle at different  $V_r$  (and  $W_r$ ) for a fixed jet velocity,  $V_{mix}$ , of 2030 ft/sec with flight simulation ( $M_F=0.32$ ).



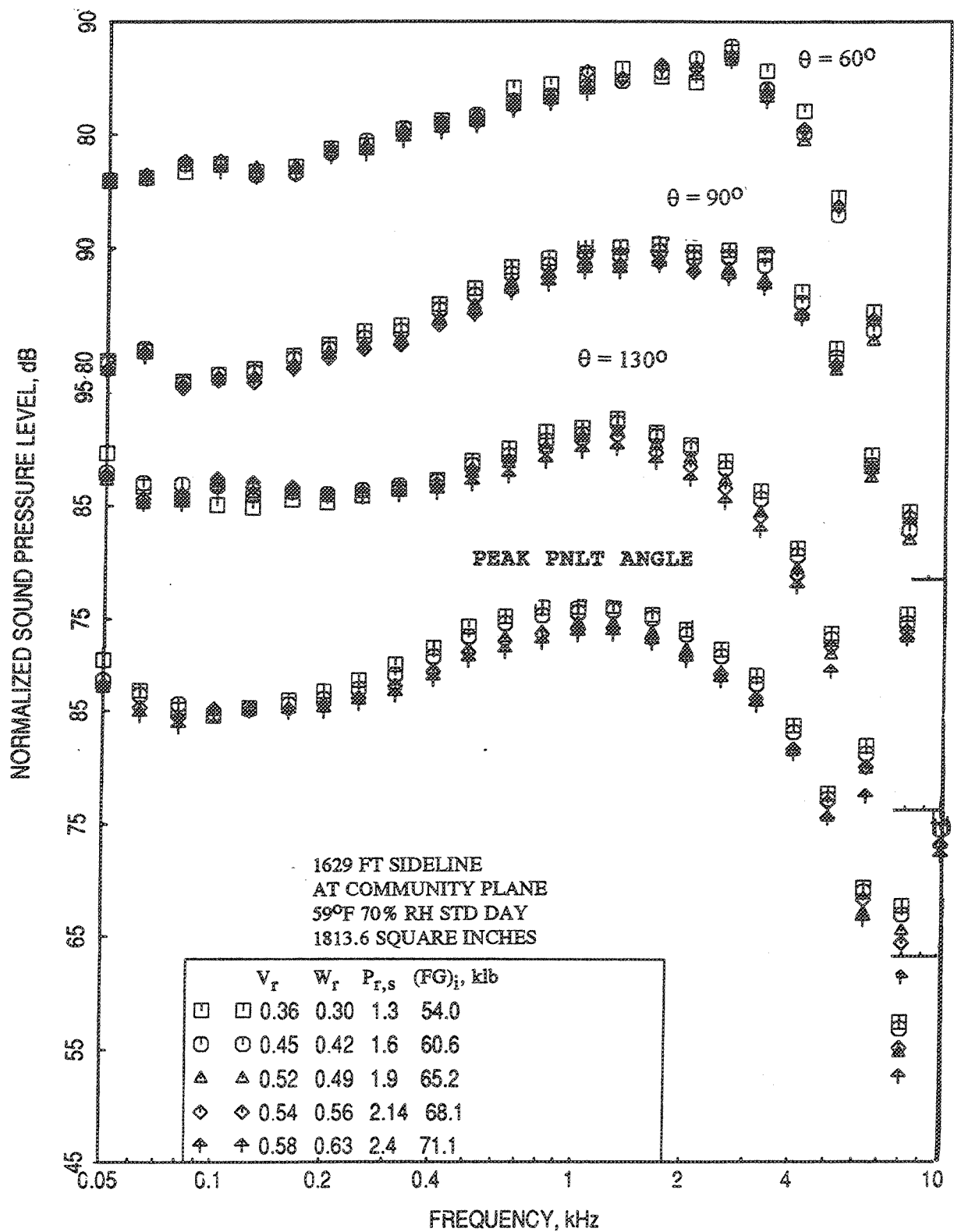


Figure 2.9-54. Normalized SPL spectra at different polar angles ( $\theta$ ) for the 0.5"-thick fluid shield nozzle at different  $V_r$  (and  $W_r$ ) for a fixed jet velocity,  $V_{mix}$ , of 2030 ft/sec with flight simulation ( $M_F=0.32$ ).

the 0.5"-thick fluid shield, the  $P_{r,p}$  varied from 2.43 to 2.36 for  $V_{mix}=1811$  ft/sec and from 3.06 to 3.19 for  $V_{mix}=2030$  ft/sec. One may assume average  $P_{r,p}$  of 2.45 and 3.2 for  $V_{mix}$  of 1811 ft/sec and 2030 ft/sec, respectively, as fixed values to study the effect of  $P_{r,s}$  on 0.5"-thick fluid shield nozzle noise characteristics. As mentioned earlier, the implication of this is favorable on the Flade engine, since it would be relatively easy to control pressure ratio of flade stream by appropriate design of flade-tip and associated flade system, rather than varying other parameters. Hence, the tests simulated possible scenario on Flade Engine. Hence the effect of  $P_{r,s}$  can be determined from results of  $V_r$  and  $W_r$  studies, presented in Figures 2.9-47 through 2.9-54.

Since  $V_r$  (or  $W_r$ ) increases with increasing  $P_{r,s}$ , the variation of normalized PNLT and pseudo EPNLT with respect to  $P_{r,s}$  will be similar to what is illustrated in Figures 2.9-47 through 2.9-54, that the noise levels decrease with respect to  $P_{r,s}$ .

#### Effect of Fluid Shield Nozzle Total Temperature, $T_{t,s}$ :

Tests were conducted by varying  $T_{t,s}$  with fixed  $P_{r,p}=3.2$ ,  $T_{t,p}=1800^\circ\text{R}$ , and  $P_{r,s}=2.14$ . Variation of  $T_{t,s}$  includes the nominal cycle condition of  $695^\circ\text{R}$  at the middle of the range (see Figure 2.2-21). Normalized PNLTs are plotted with respect to  $T_{t,s}$  in Figure 2.9-55 at different polar angles ( $\theta$ ). Unlike the static test results, where normalized PNLT and pseudo EPNLT increase with  $T_{t,s}$ , the effect of  $T_{t,s}$  is insignificant with flight simulation. Normalized PNLT directivities and normalized SPL spectra for 0.5"-thick shield are plotted in Figures 2.9-56 and 2.9-57, respectively, for different  $T_{t,s}$ . Again, the effect of  $T_{t,s}$  seems to be minimal.

#### Effect of Primary Nozzle Pressure Ratio, $P_{r,p}$ :

Acoustic results for a set of tests are selected for fluid shield nozzle configurations to study the effect of  $P_{r,p}$ . In these tests  $P_{r,p}$  is varied from 2.0 to 3.2 (see Figure 2.2-21), while the other aerothermodynamic parameters are kept fixed (i.e.,  $T_{t,p}=1800^\circ\text{R}$ ,  $P_{r,s}=2.14$ , and  $T_{t,s}=700^\circ\text{R}$ ). Normalized PNLTs at different polar angles ( $\theta$ ) and EPNLTs are plotted with respect to  $P_{r,p}$  in Figure 2.9-58. Normalized PNLT and EPNLT increase with  $P_{r,p}$ . Normalized PNLT directivities for 0.5"-thick shield are plotted in Figure 2.9-59 for different  $P_{r,p}$ . PNLT at all angles increases with  $P_{r,p}$ . Corresponding normalized SPL spectra are plotted in Figure 60, which also indicates

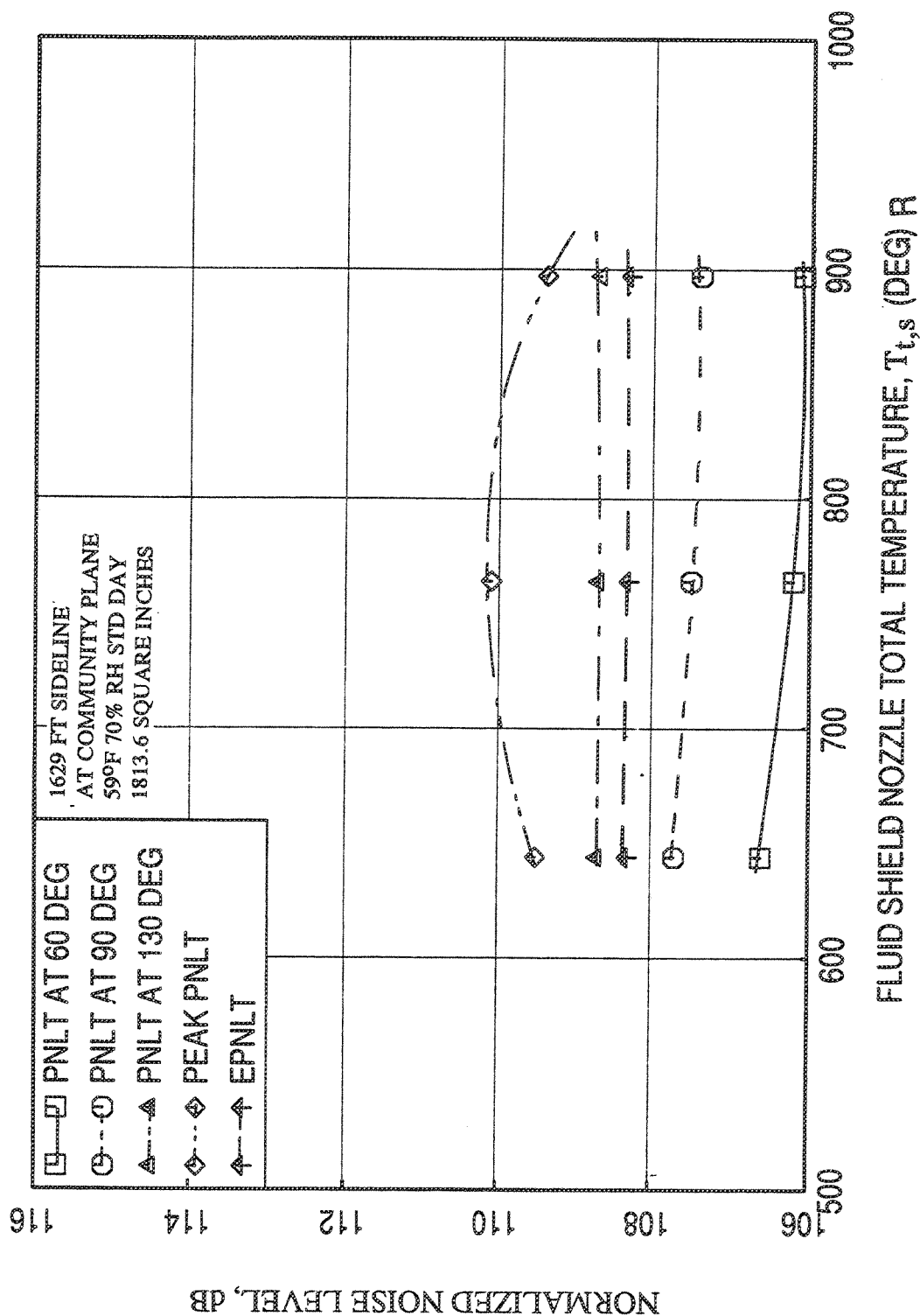


Figure 2.9-55. Effect of fluid shield nozzle total temperature,  $T_{t,s}$ , on normalized PNLt data at different polar angles ( $\theta$ ) and EPNLt for the 0.5"-thick fluid shield nozzle for fixed  $P_{r,p}=3.2$ ,  $T_{t,p}=1800^\circ\text{R}$ , and  $P_{r,s}=2.14$  with flight simulation ( $M_F=0.32$ ).

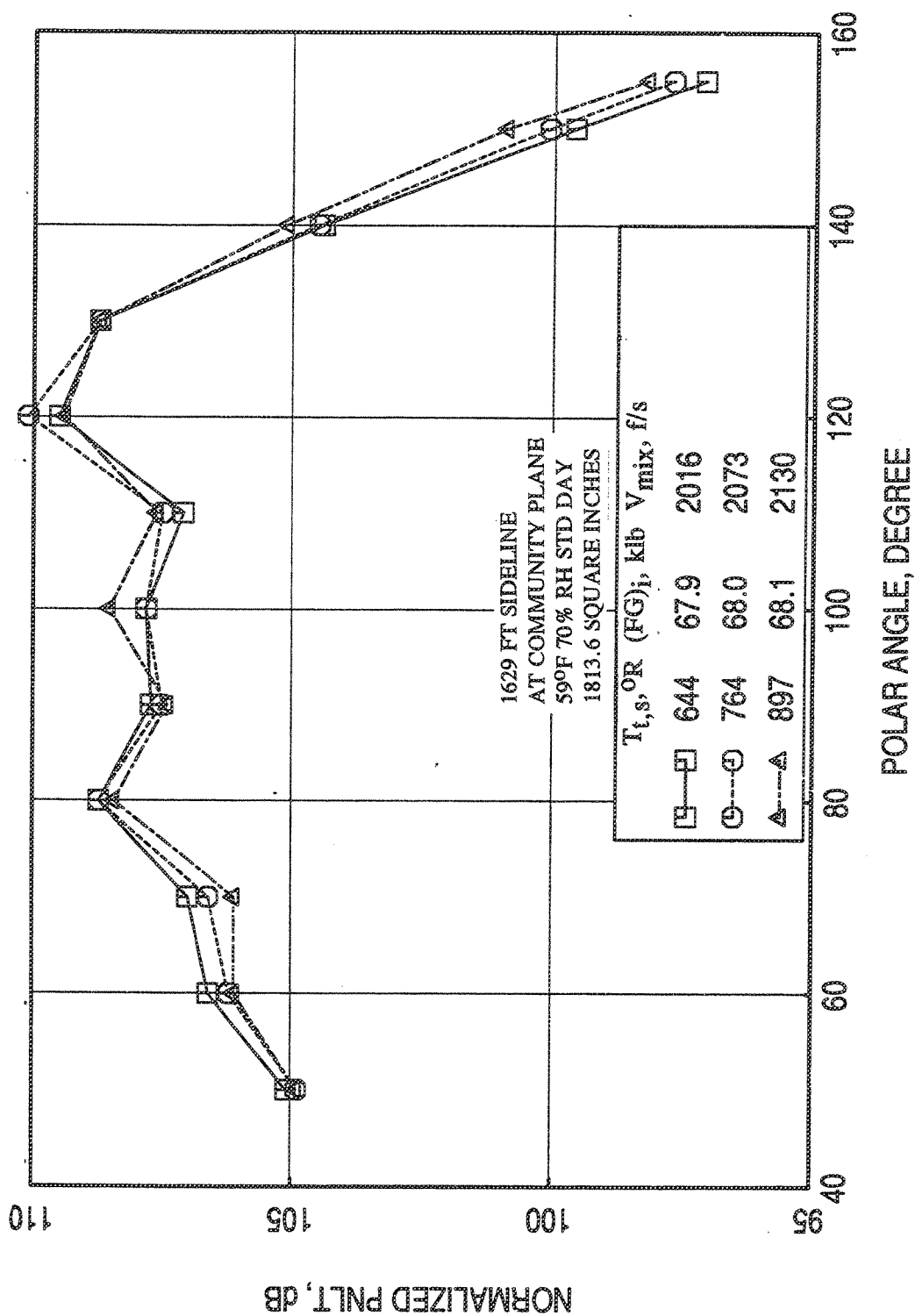


Figure 2.9-56. Normalized PNLT directivities for the 0.5"-thick fluid shield nozzle at different  $T_{t,s}$  for fixed  $P_{r,p}=3.2$ ,  $T_{t,p}=1800^{\circ}\text{R}$ , and  $P_{r,s}=2.14$  with flight simulation ( $M_F=0.32$ ).

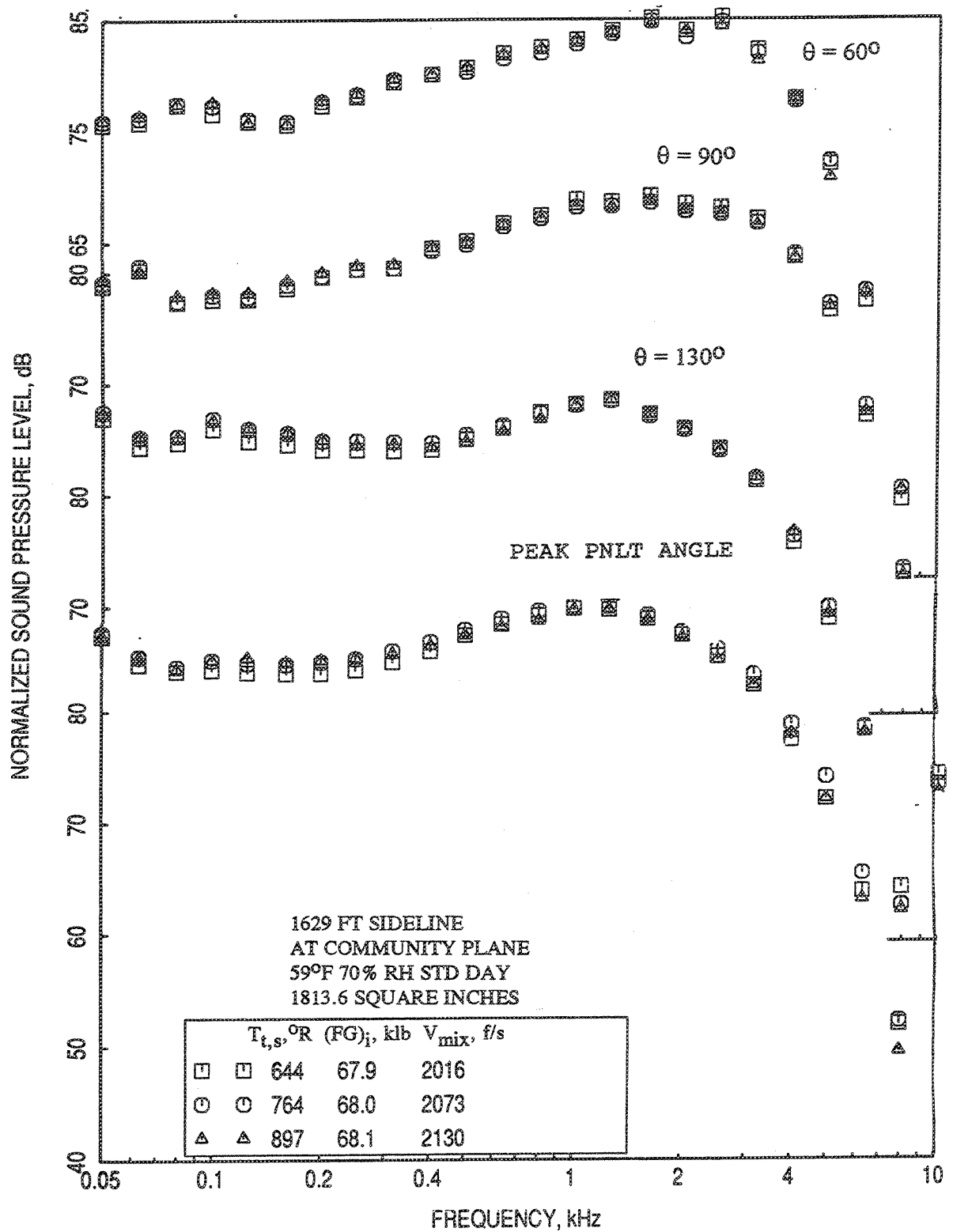


Figure 2.9-57. Normalized SPL spectra at different polar angles ( $\theta$ ) for the 0.5"-thick fluid shield nozzle at different  $T_{t,s}$  for fixed  $P_{r,p}=3.2$ ,  $T_{t,p}=1800^\circ R$ , and  $P_{r,s}=2.14$  with flight simulation ( $M_F=0.32$ ).

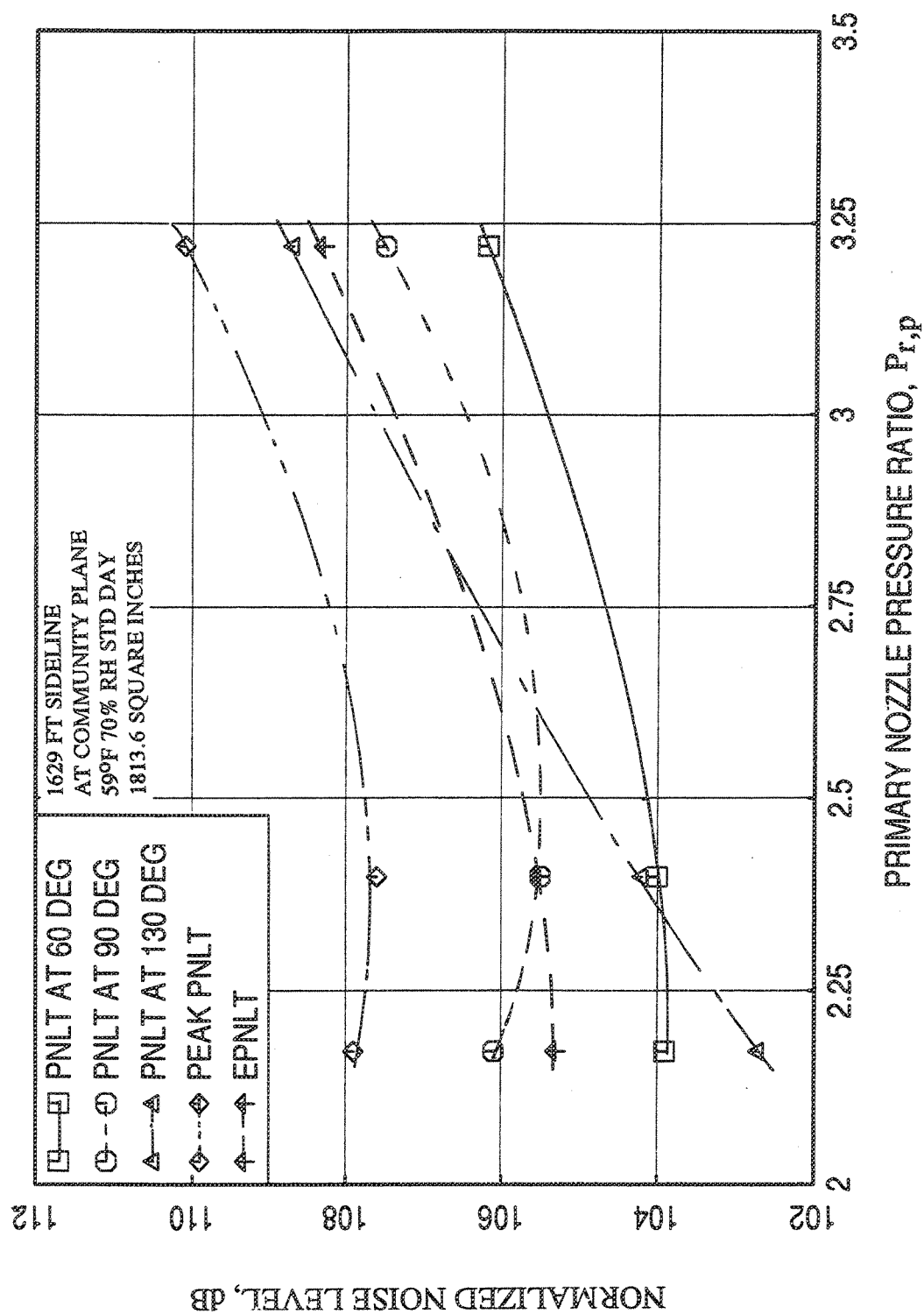


Figure 2.9-58. Effect of primary nozzle pressure ratio,  $P_{r,p}$ , on normalized PNL T at different polar angles ( $\theta$ ) and EPNLT for the 0.5-inch thick fluid shield nozzle for fixed  $T_{t,p}=1800^{\circ}\text{R}$ ,  $P_{r,s}=2.14$ , and  $T_{t,s}=700^{\circ}\text{R}$  with flight simulation ( $M_F=0.32$ ).

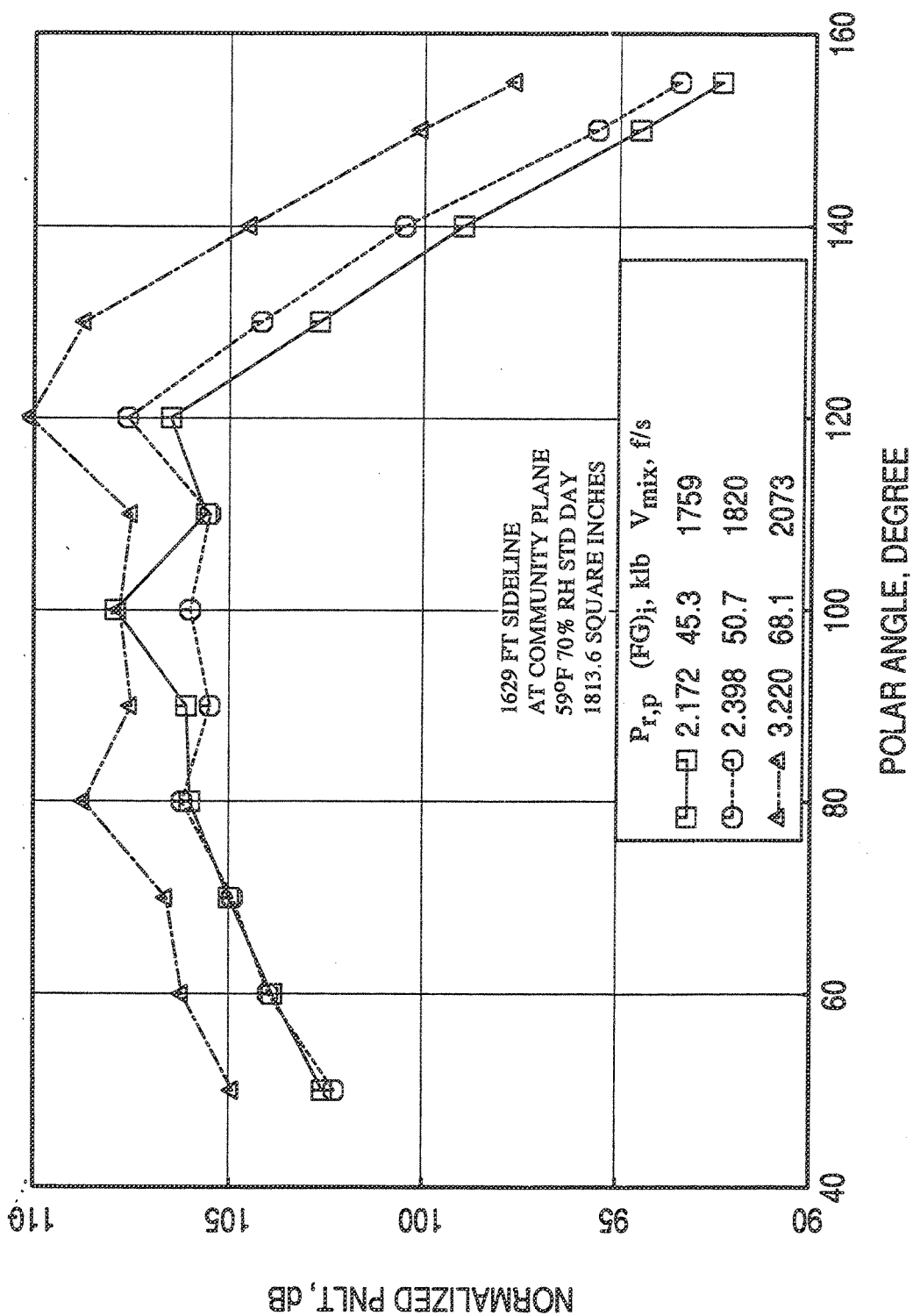


Figure 2.9-59. Normalized PNLT directivities for the 0.5"-thick fluid shield nozzle at different  $P_{r,p}$  for fixed  $T_{t,p}=1800^{\circ}\text{R}$ ,  $P_{r,s}=2.14$ , and  $T_{t,s}=700^{\circ}\text{R}$  with flight simulation ( $M_F=0.32$ ).

the similar trend at all frequency. It should be noted that the ideal gross thrust increases significantly with increasing  $P_{r,p}$ .

#### Effect of Primary Nozzle Total Temperature, $T_{t,p}$ :

Several tests were conducted for the 0.5"-thick fluid shield nozzle configuration by varying  $T_{t,p}$  with fixed  $P_{r,p}=3.2$ ,  $P_{r,s}=2.14$ , and  $T_{t,s}=700^{\circ}\text{R}$  (see Figure 2.2-21). Normalized PNLTs at different polar angles ( $\theta$ ) and EPNLTs are plotted with respect to  $T_{t,p}$  in Figure 2.9-61. Except for  $\theta = 60^{\circ}$ , normalized PNLT increases with  $T_{t,p}$ . Normalized EPNLT also increases with  $T_{t,p}$ . Normalized PNLT directivities for 0.5"-thick shield are plotted in Figure 2.9-62 for different  $T_{t,p}$ . PNLT at all angles increases with  $T_{t,p}$ , except, very little difference is observed for  $T_{t,s}=1785^{\circ}\text{R}$  and  $T_{t,s}=1929^{\circ}\text{R}$ . Whereas, the ideal gross thrust remains more or less same for all the cases. Corresponding normalized SPL spectra are plotted in Figure 2.9-63, which also indicates the similar trend at all frequency. It seems beneficial from noise consideration to operate the primary nozzle at lower temperature.



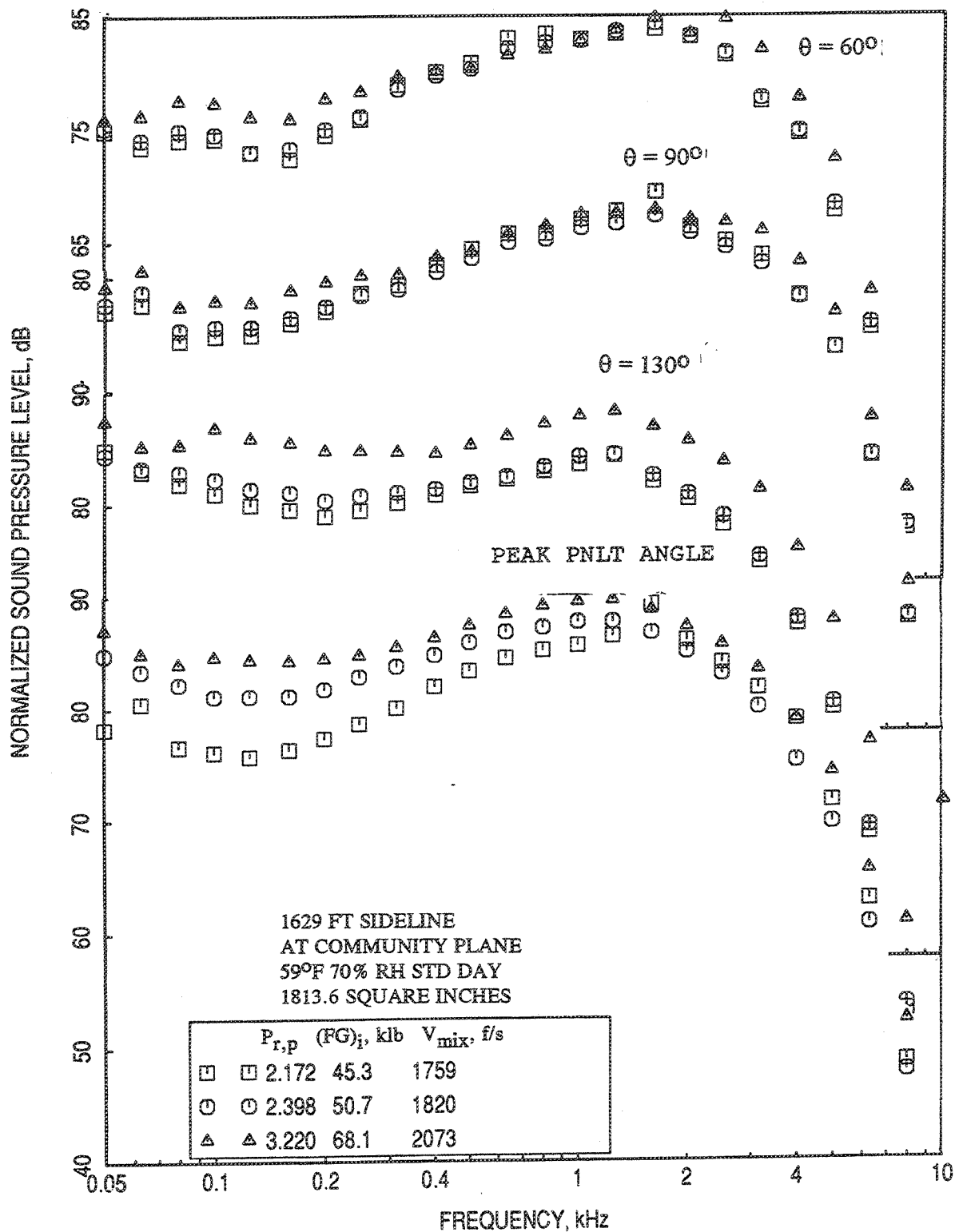


Figure 2.9-60. Normalized SPL spectra at different polar angles ( $\theta$ ) for the 0.5"-thick fluid shield nozzle at different  $P_{r,p}$  for fixed  $T_{t,p}=1800^\circ\text{R}$ ,  $P_{r,s}=2.14$ , and  $T_{t,s}=700^\circ\text{R}$  with flight simulation ( $M_F=0.32$ ).

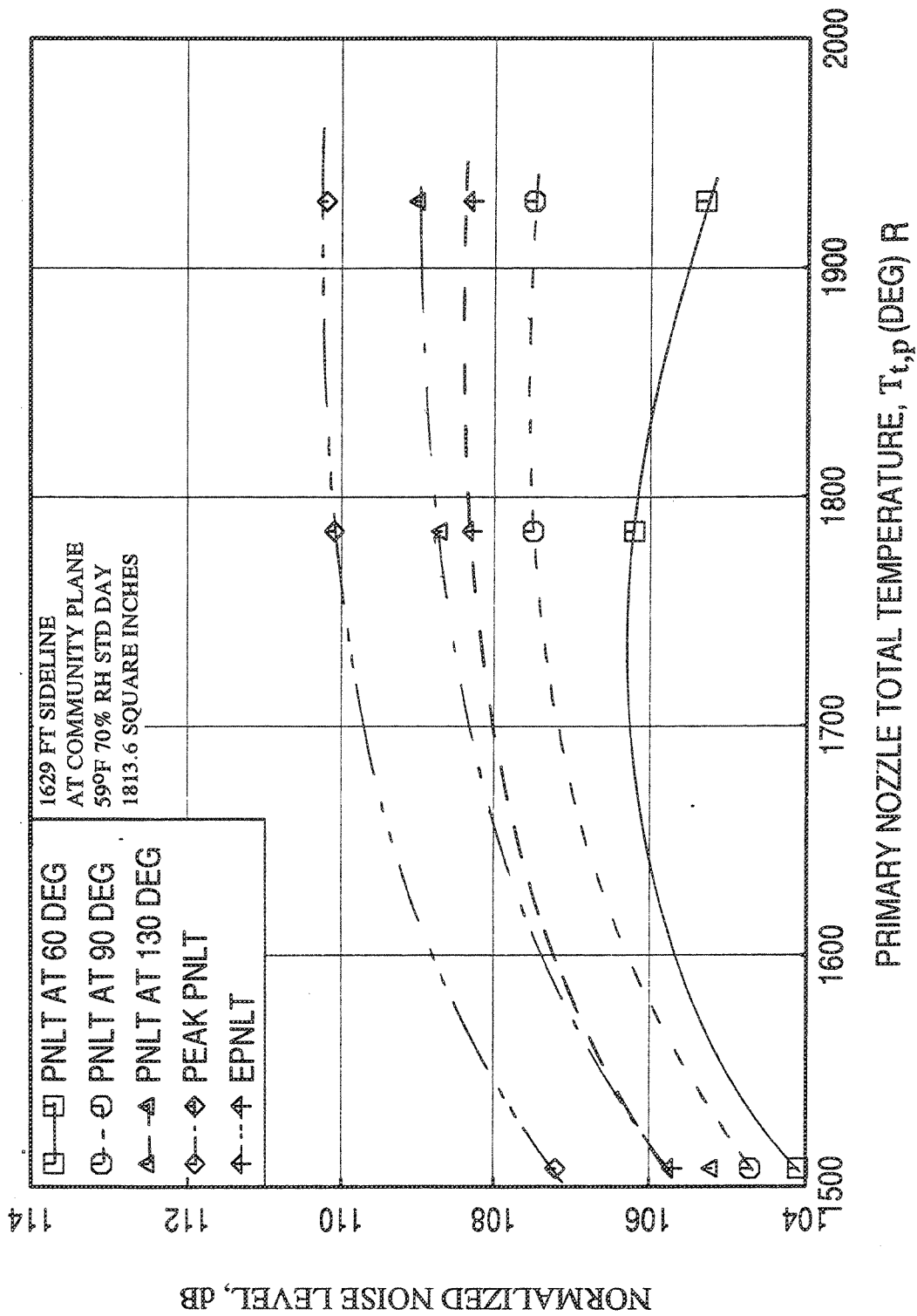


Figure 2.9-61. Effect of primary nozzle total temperature,  $T_{t,p}$ , on normalized PNL at different polar angles ( $\theta$ ) and EPNL for the 0.5"-thick fluid shield nozzle for fixed  $P_{r,p}=3.2$ ,  $P_{r,s}=2.14$ , and  $T_{t,s}=7000^{\circ}\text{R}$  with flight simulation ( $M_F=0.32$ ).

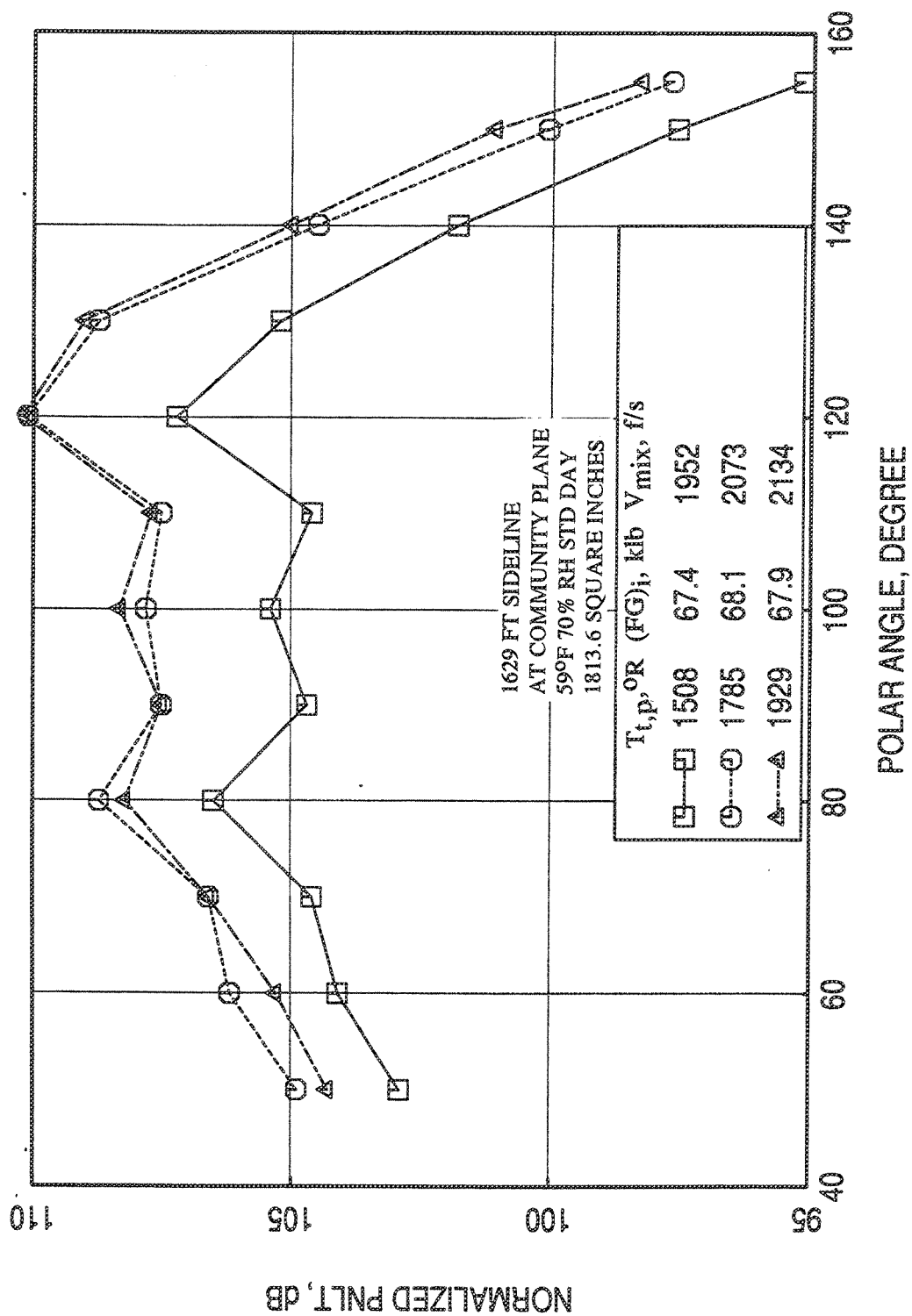


Figure 2.9-62. Normalized PNLT directivities for the 0.5"-thick fluid shield nozzle at different  $T_{t,p}$  for fixed  $P_{r,p}=3.2$ ,  $P_{r,s}=2.14$ , and  $T_{t,s}=700^\circ R$  with flight simulation ( $M_F=0.32$ ).

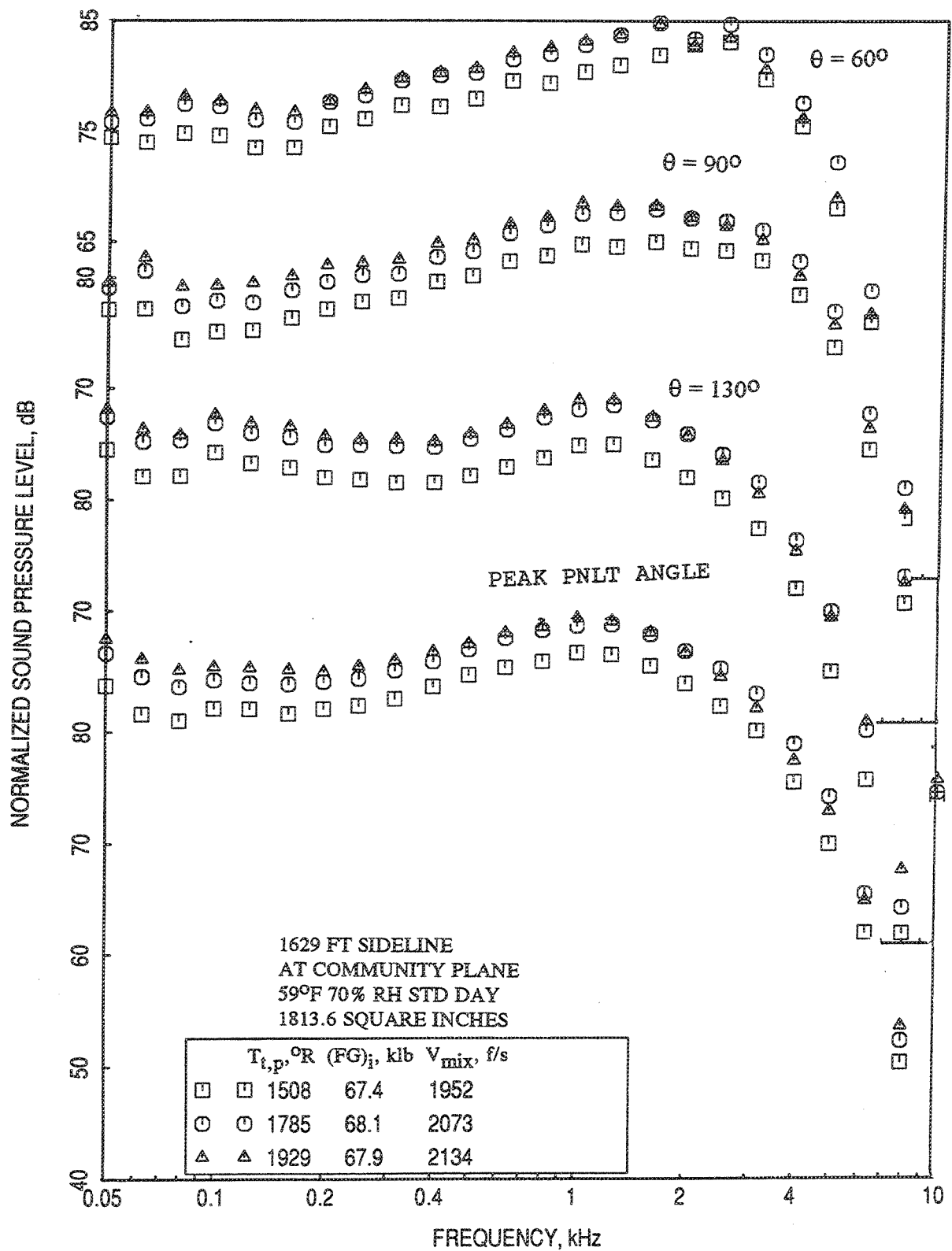


Figure 2.9-63. Normalized SPL spectra at different polar angles ( $\theta$ ) for the 0.5"-thick fluid shield nozzle at different  $T_{t,p}$  for fixed  $P_{r,p}=3.2$ ,  $P_{r,s}=2.14$ , and  $T_{t,s}=7000^\circ R$  with flight simulation ( $M_F=0.32$ ).

## 2.10 AZIMUTHAL VARIATION OF ACOUSTIC CHARACTERISTICS OF FLUID SHIELD NOZZLES

The acoustic characteristics for fluid shield nozzle configurations are expected to depend on azimuthal direction, since these nozzles are non-axisymmetric due to the presence of partial wrap of fluid shield around the core suppressor. Some tests were conducted to evaluate the azimuthal variation of noise field for these nozzles. All the fluid shield nozzles in Cell 41 were oriented (standard orientation) such that the side line and community points lie at azimuthal locations of  $\phi = 10^\circ$  and  $\phi = 75^\circ$ , respectively, with respect to the cell (Figure 2.2-13). Measurements were made by tower microphones, tower at  $\phi = 10^\circ$  and  $75^\circ$  and by fixed microphones at  $\phi = 45^\circ$  for all the test conditions. Additional measurements were made by tower microphones at  $\phi = 4^\circ$ ,  $25^\circ$ , and  $60^\circ$  for a few test conditions to study the azimuthal directivity.

To obtain a full  $360^\circ$  azimuthal directivity of fluid shield noise the unshielded side of the 0.5" thick 220° fluid shield nozzle was mounted on the suppressor with an offset of  $120^\circ$  (indexed orientation) compared to its nominal configuration. It should be noted that a complete  $180^\circ$  orientation change for fluid shield was not possible due to hardware limitations. In this orientation, shown in Figure 2.2-14, the mid point of the unshielded portion of the suppressor was aligned with  $\phi = 15^\circ$  azimuthal plane. The 10% porous plug was used in this study. Measurements were made for a few test conditions by tower microphones only, tower at  $\phi = 15^\circ$ ,  $30^\circ$ ,  $45^\circ$ ,  $65^\circ$ ,  $85^\circ$ , and  $100^\circ$  for all the test conditions.

The azimuthal direction for a fluid shield nozzle is shown in Figure 2.10-1. Based on this figure, the measurement locations of  $4^\circ$ ,  $10^\circ$ ,  $25^\circ$ ,  $45^\circ$ ,  $60^\circ$ , and  $75^\circ$  with respect to the cell for standard orientation give the noise characteristics at nozzle azimuthal angles ( $\phi_N$ ) of  $19^\circ$ ,  $25^\circ$ ,  $40^\circ$ ,  $60^\circ$ ,  $75^\circ$ , and  $90^\circ$ , respectively. The measurement locations of  $15^\circ$ ,  $30^\circ$ ,  $45^\circ$ ,  $65^\circ$ ,  $85^\circ$ , and  $100^\circ$  with respect to the cell for indexed orientation coincide with the nozzle azimuthal angles ( $\phi_N$ ) of  $-90^\circ$ ,  $-75^\circ$ ,  $-60^\circ$ ,  $-40^\circ$ ,  $-20^\circ$ , and  $-5^\circ$ , respectively. Hence, a complete azimuthal variation between  $\phi_N$  of  $-90^\circ$  and  $90^\circ$  is obtained from the measurements for both orientations of a nozzle configuration. Keeping the same linear scale factor the 0.5", 0.75" and 1.0" thick fluid shield nozzles are scaled to 1813.6, 2165.5, and 2524.7 square inches, respectively. All the data are extrapolated to a sideline distance of 1629 feet and are corrected for

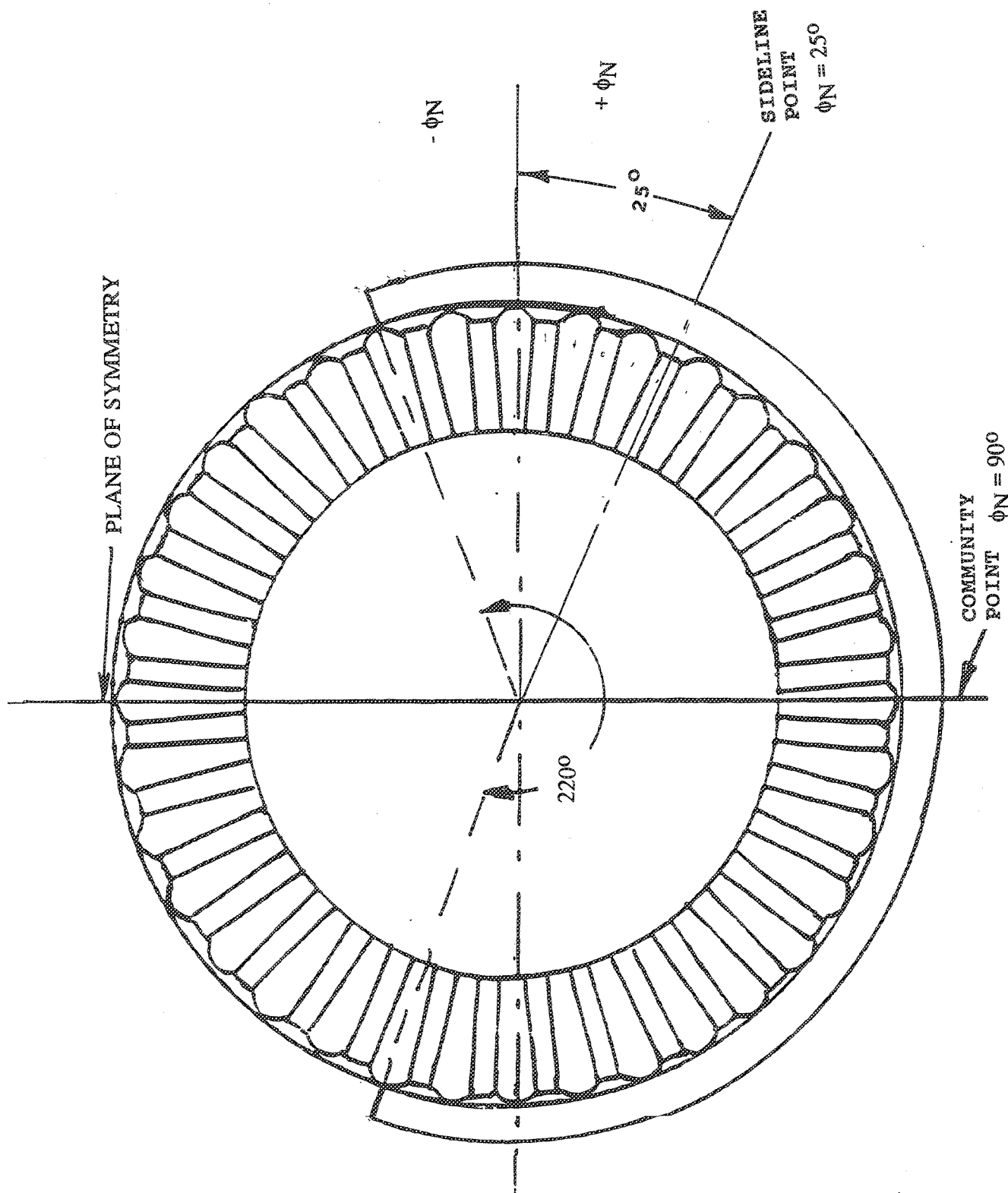


Figure 2.10-1. Plan view of a fluid shield nozzle indicating the azimuthal direction, including sideline and community points for noise measurement.

standard day conditions of 59°F and 70% humidity. All the data presented in this section are normalized for thrust only.

**2.10.1 Azimuthal Noise Variation For 0.5"-Thick Fluid Shield Nozzle With Porous Plug :** Tests were conducted for 0.5"-thick fluid shield nozzle with porous plug at a few test conditions for both orientations to evaluate azimuthal noise characteristics in the farfield.

*Ambient Temperature Results :* Tests were conducted by keeping both streams at ambient temperature to examine the impact of dominant shock noise. Figure 2.10-2a shows the azimuthal variation of PNLT at different polar angles, peak PNLT, and pseudo EPNLT at static condition. While the PNLT at  $\theta=60^\circ$  shows an azimuthal variation of about 2 to 3 dB, the variations at other polar angles are very small. The azimuthal variation for EPNLT is insignificant. The PNLT directivities at various azimuthal angles are shown in Figure 2.10-2b. While a variation of about 3 dB is observed in the forward arc, very little azimuthal variation is seen in the rear quadrant. The forward arc noise levels are mostly due to shock-associated noise and hence the shock-associated noise shows measurable azimuthal variation. This is further apparent from the spectral SPL plots of Figure 2.10-3, where the dominant shock noise appears at the forward angles. In general, the noise levels are lower at and close to the center of the shield (i.e.,  $\phi_N=90^\circ$ ). Similar results with flight simulation are shown in Figures 2.10-4 and 2.10-5. The azimuthal variation of PNLT and EPNLT changes with flight simulation. Relatively more azimuthal variation of PNLT and EPNLT are observed compared to the static condition.

*Results At  $V_{mix} = 1811$  ft/sec:* Tests were conducted to generate  $V_{mix}=1811$  ft/sec with two different fluid shield conditions, namely supersonic shield (i.e.,  $P_{r,s}=2.2$ ) and subsonic shield (i.e.,  $P_{r,s}=1.6$ ), at static condition. While, Figures 2.10-6 and 2.10-7 show the results for supersonic shield, the subsonic shield results are presented in Figures 2.10-8 and 2.10-9. The azimuthal variations in terms of PNLT, EPNLT, and SPL are relatively small and uniform with respect to azimuthal angle; and are observed at all polar angles for both the shield flows. The basic difference between supersonic and subsonic shields is that the noise levels are decreased due to supersonic shield on the shielded side and the trend is reversed for subsonic shield. With flight simulation the noise levels are further decreased on the shielded side due to supersonic shield as shown in Figures 2.10-10 and 2.10-11.

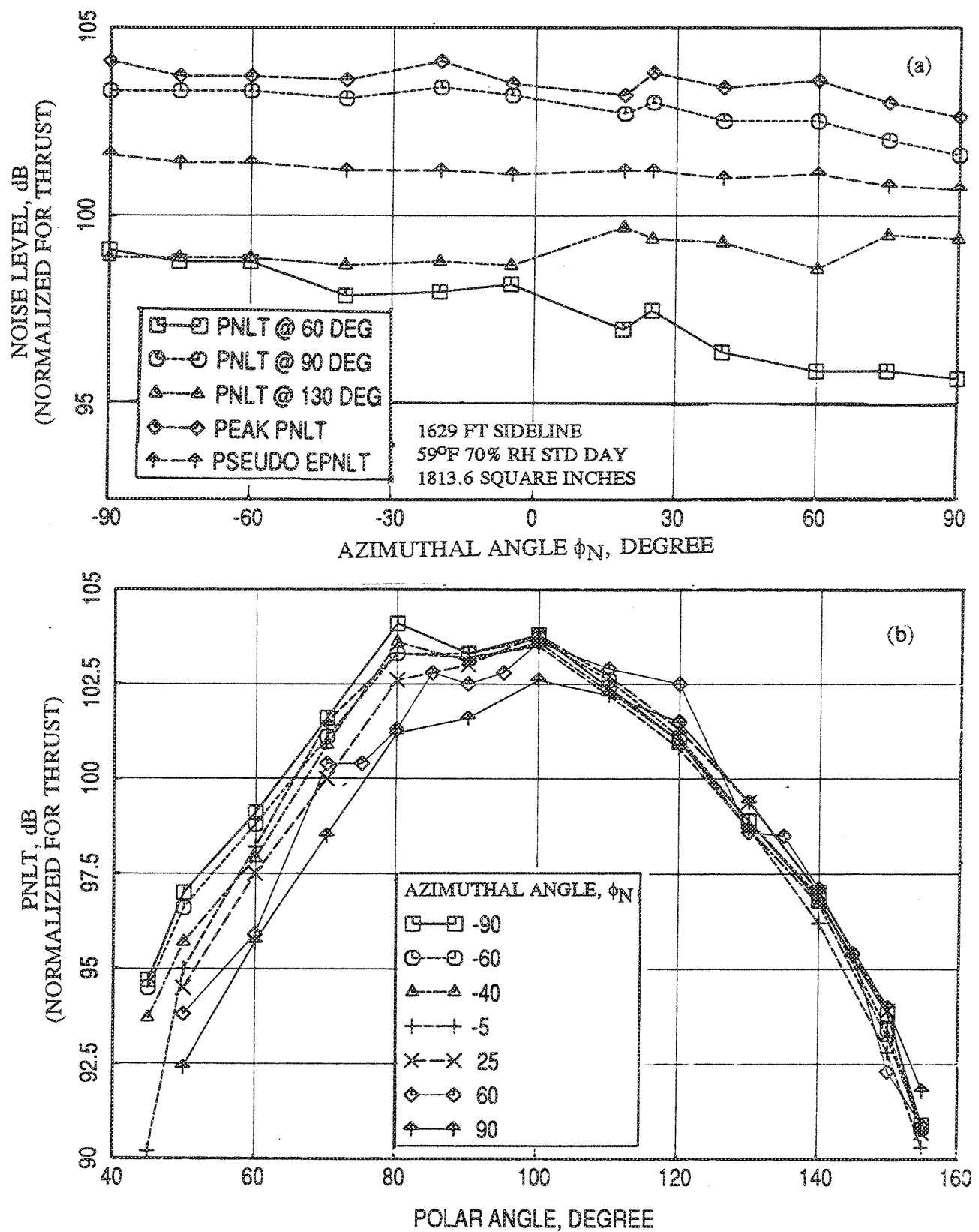


Figure 2.10-2. (a) Azimuthal variation of PNLTs at different polar angles ( $\theta$ ), peak PNLT, and pseudo EPNLT and (b) comparison of PNLT directivities between azimuthal angles for 0.5"-thick fluid shield nozzle at static condition at a jet velocity,  $V_{mix} = 1251$  ft/sec;  $P_{r,p} = 3.17$ ,  $P_{r,s} = 1.6$ , both streams being of ambient temperature.



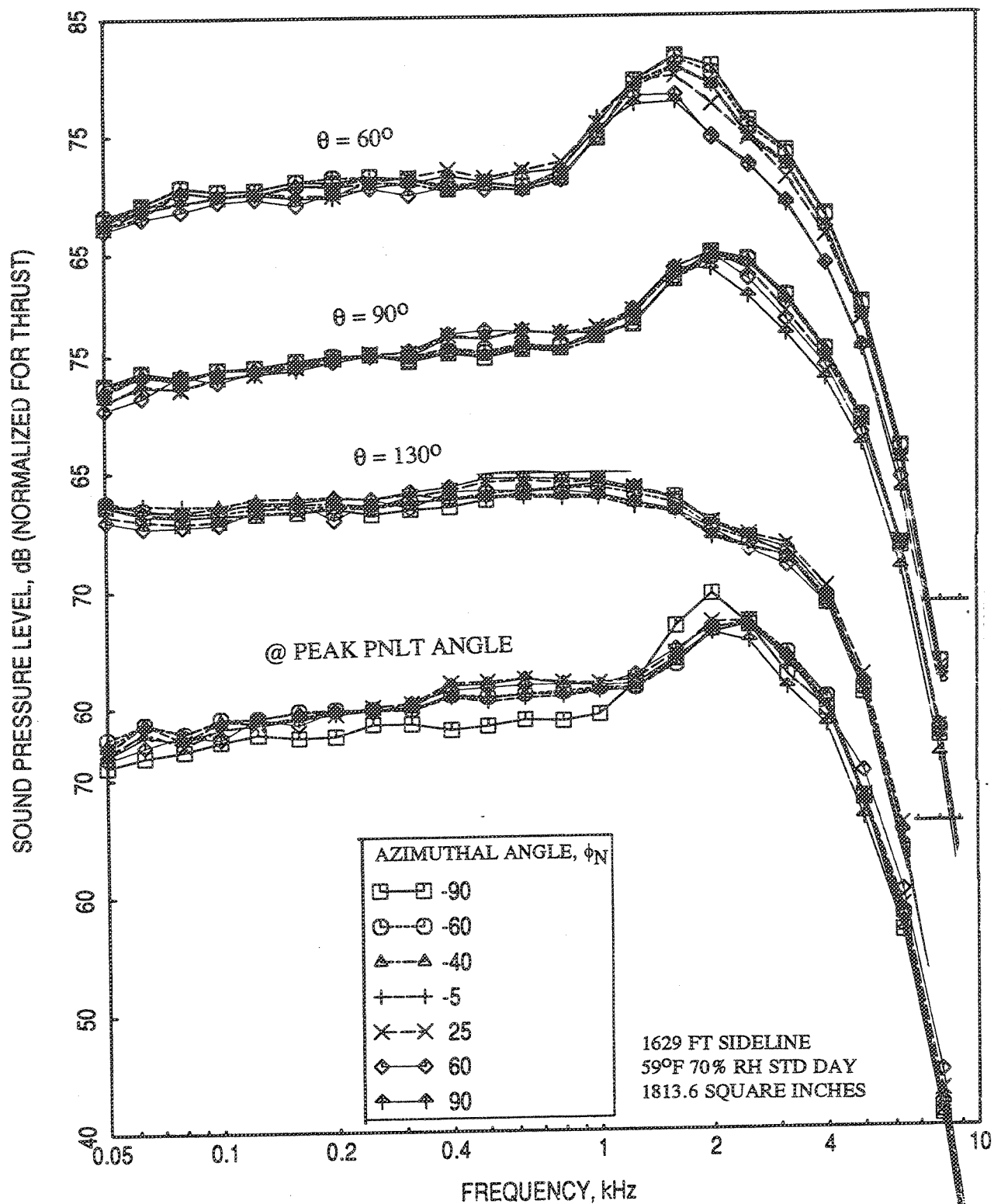


Figure 2.10-3. Comparison of SPL spectra at different polar angles ( $\theta$ ), between azimuthal angles, for 0.5"-thick fluid shield nozzle at static condition at a jet velocity,  $V_{\text{mix}} = 1251$  ft/sec;  $P_{r,p} = 3.17$ ,  $P_{r,s} = 1.6$ , both streams being of ambient temperature.

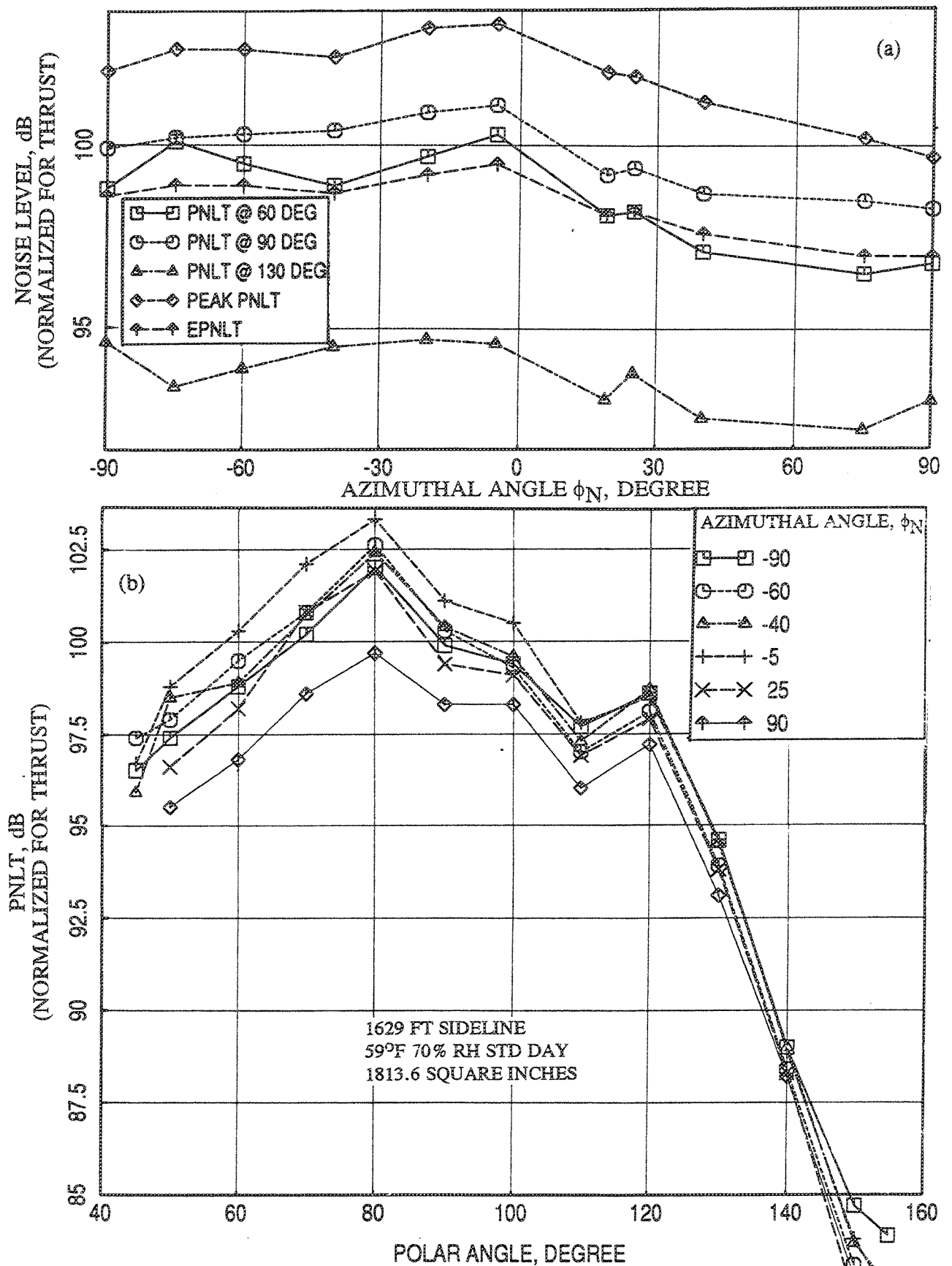


Figure 2.10-4. (a) Azimuthal variation of PNLTs at different polar angles ( $\theta$ ), peak PNLT, and EPNLT and (b) comparison of PNLT directivities between azimuthal angles for 0.5"-thick fluid shield nozzle with flight simulation ( $M_F=0.32$ ) at a jet velocity,  $V_{mix} = 1251$  ft/sec;  $P_{r,p}=3.17$ ,  $P_{r,s}=1.6$ , both streams being ambient..

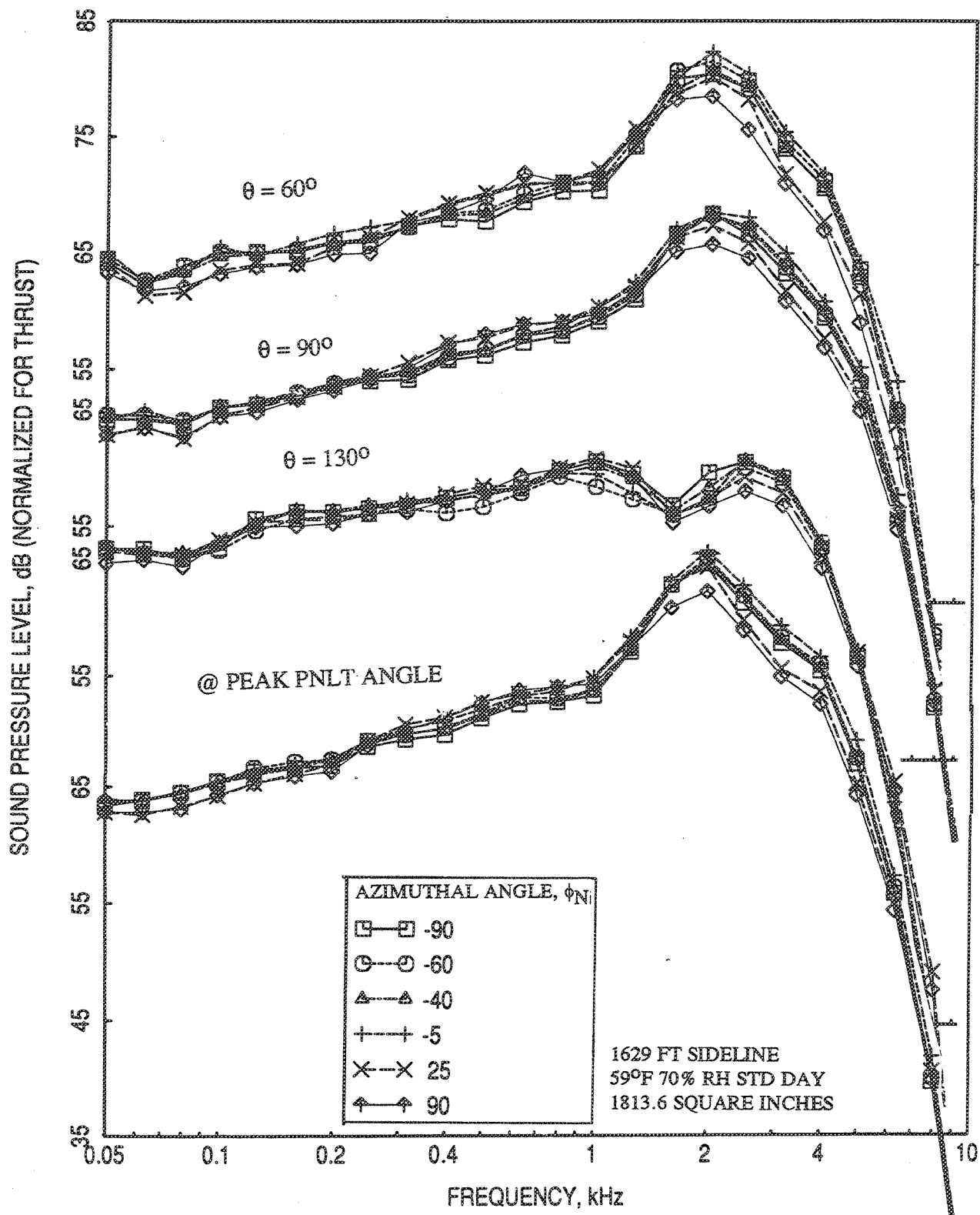


Figure 2.10-5. Comparison of SPL spectra at different polar angles ( $\theta$ ), between azimuthal angles, for 0.5"-thick fluid shield nozzle with flight simulation ( $M_F=0.32$ ) at a jet velocity,  $V_{mix}=1251$  ft/sec;  $P_{r,p}=3.17$ ,  $P_{r,s}=1.6$ , both streams being of ambient temperature.

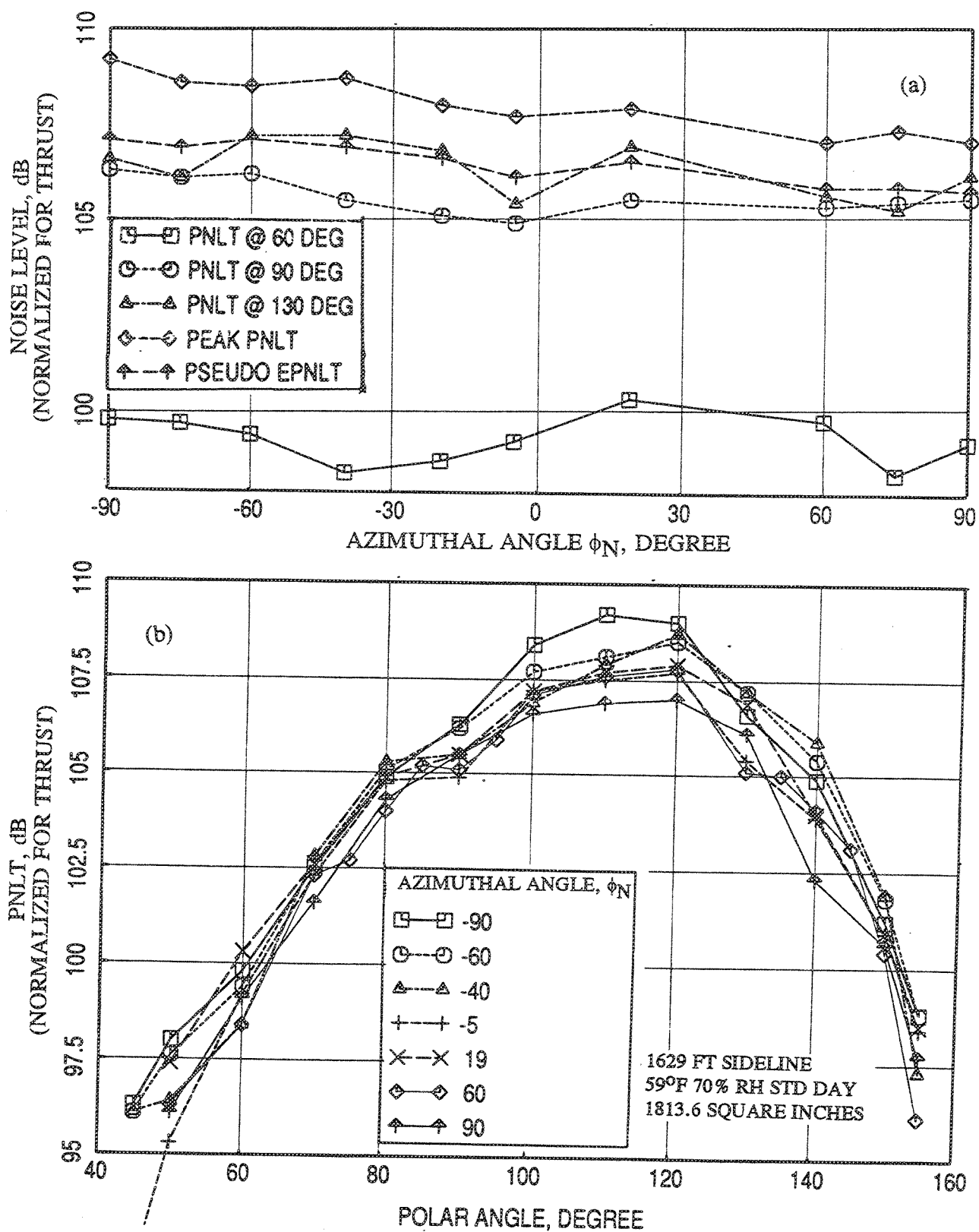


Figure 2.10-6. (a) Azimuthal variation of PNLTs at different polar angles ( $\theta$ ), peak PNLT, and pseudo EPNLT and (b) comparison of PNLT directivities between azimuthal angles for 0.5"-thick fluid shield nozzle at static condition at a jet velocity,  $V_{mix} = 1811$  ft/sec;  $P_{r,p} = 2.39$ ,  $P_{r,s} = 2.2$ ,  $T_{t,p} = 1806^\circ R$ ,  $T_{t,s} = 727^\circ R$ .

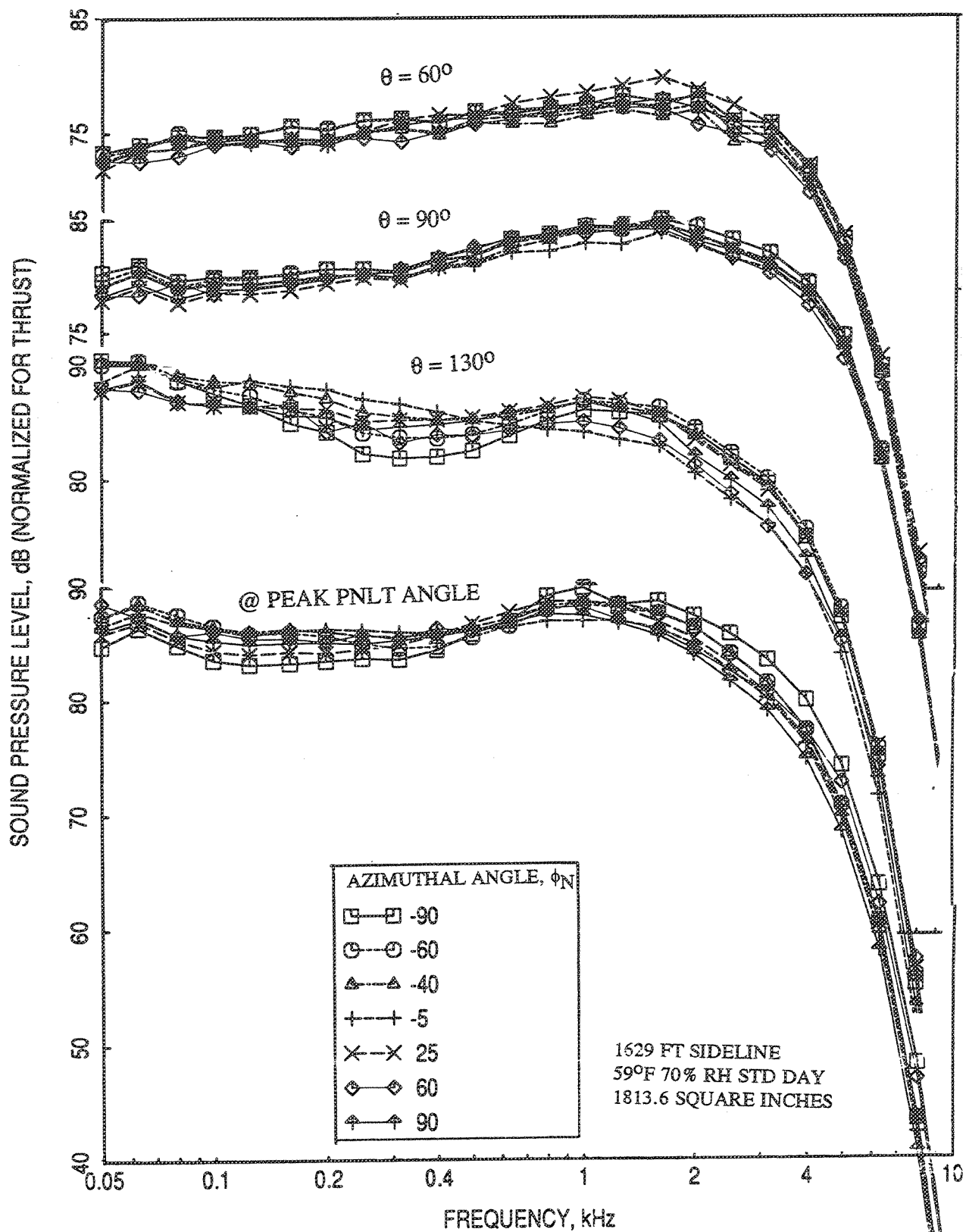


Figure 2.10-7. Comparison of SPL spectra at different polar angles ( $\theta$ ), between azimuthal angles, for 0.5"-thick fluid shield nozzle at static condition at a jet velocity,  $V_{\text{mix}} = 1811$  ft/sec;  $P_{r,p} = 2.39$ ,  $P_{r,s} = 2.2$ ,  $T_{t,p} = 1806^\circ\text{R}$ ,  $T_{t,s} = 727^\circ\text{R}$ .

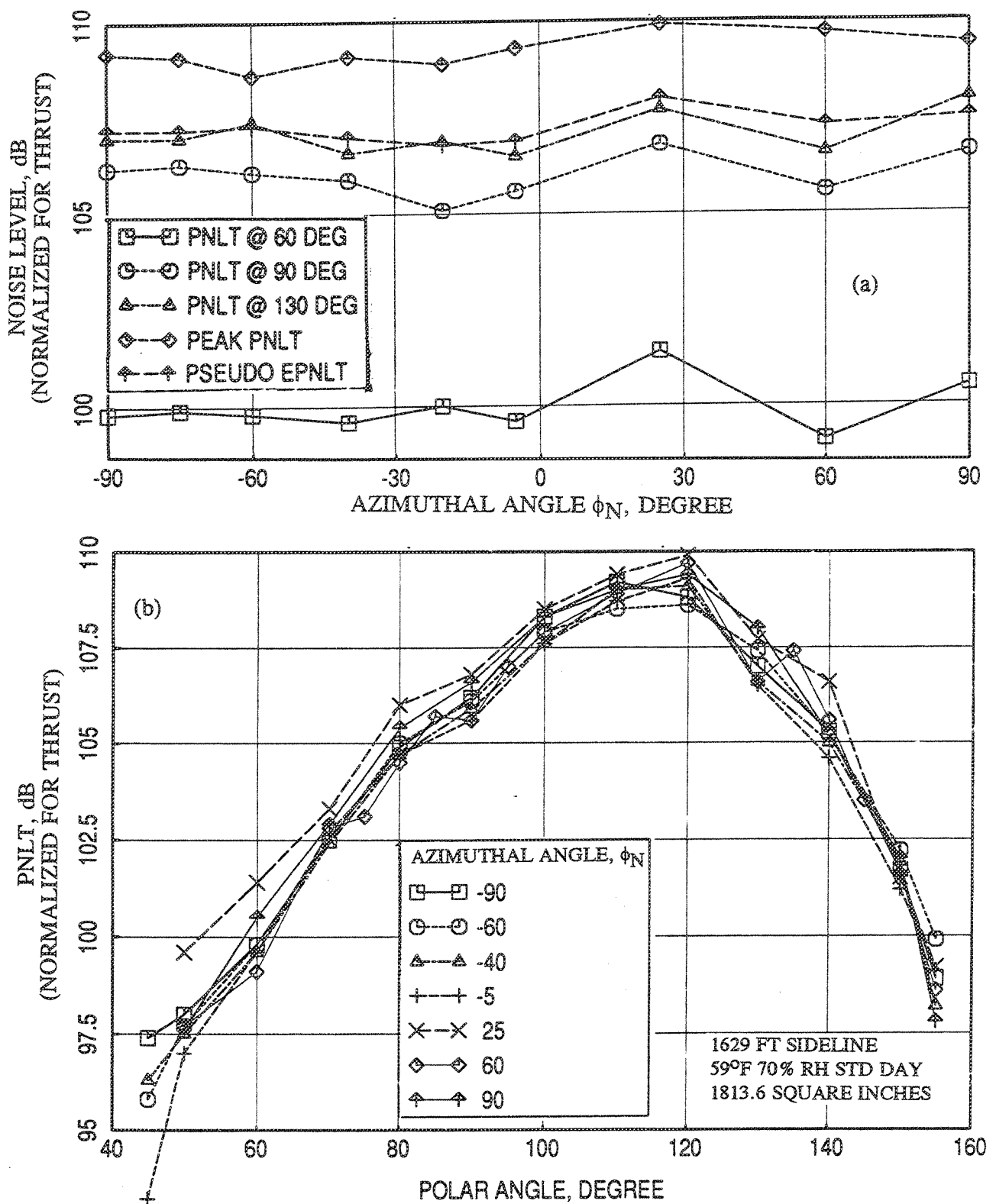


Figure 2.10-8. (a) Azimuthal variation of PNLTs at different polar angles ( $\theta$ ), peak PNLT, and pseudo EPNLT and (b) comparison of PNLT directivities between azimuthal angles for 0.5"-thick fluid shield nozzle at static condition at a jet velocity,  $V_{mix} = 1811$  ft/sec;  $P_{r,p} = 2.46$ ,  $P_{r,s} = 1.6$ ,  $T_{t,p} = 1806^\circ R$ ,  $T_{t,s} = 727^\circ R$ .

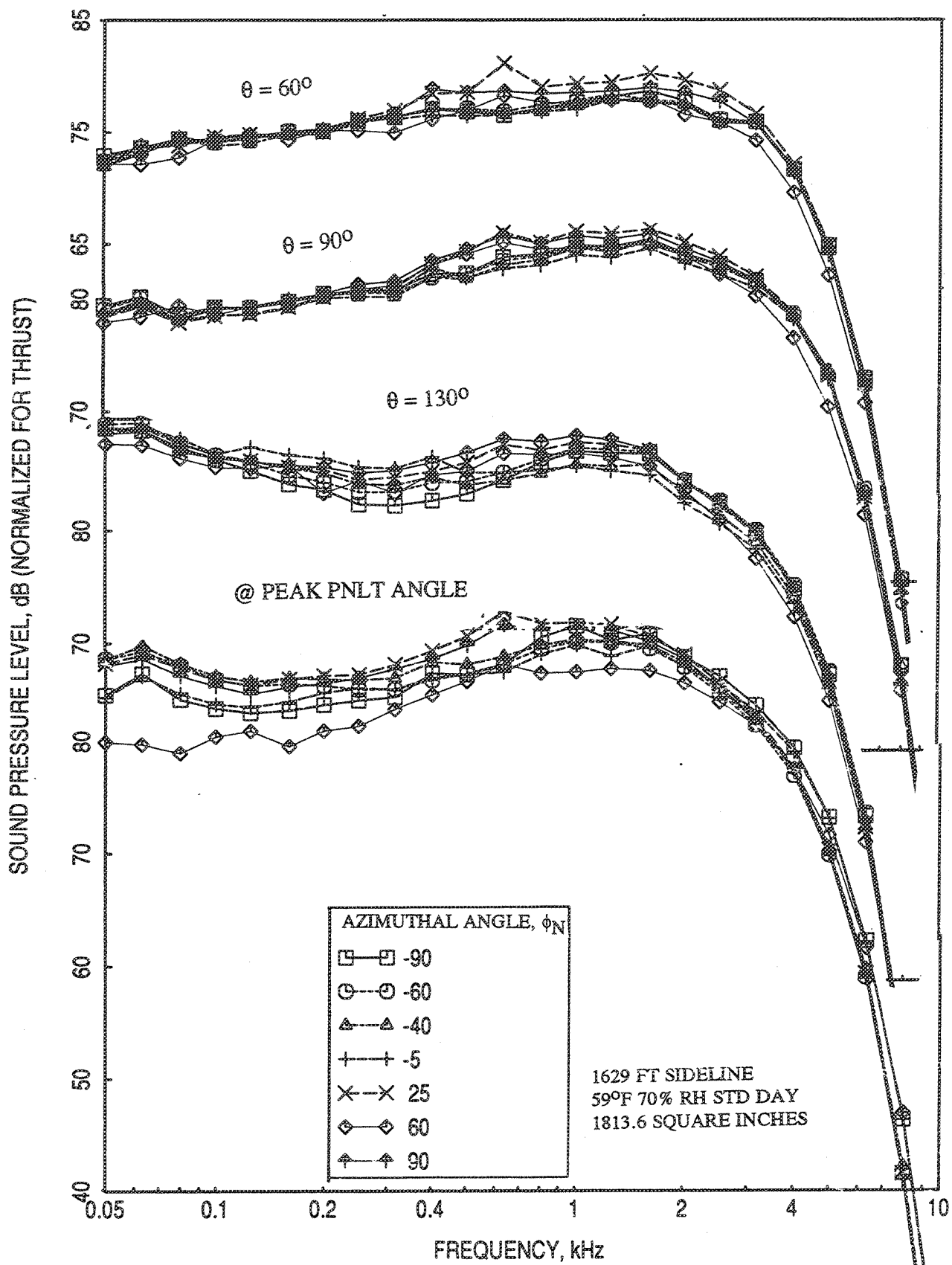


Figure 2.10-9. Comparison of SPL spectra at different polar angles ( $\theta$ ), between azimuthal angles, for 0.5"-thick fluid shield nozzle at static condition at a jet velocity,  $V_{\text{mix}} = 1811 \text{ ft/sec}$ ;  $P_{r,p} = 2.4.6$ ,  $P_{r,s} = 1.6$ ,  $T_{t,p} = 1806^\circ\text{R}$ ,  $T_{t,s} = 727^\circ\text{R}$ .

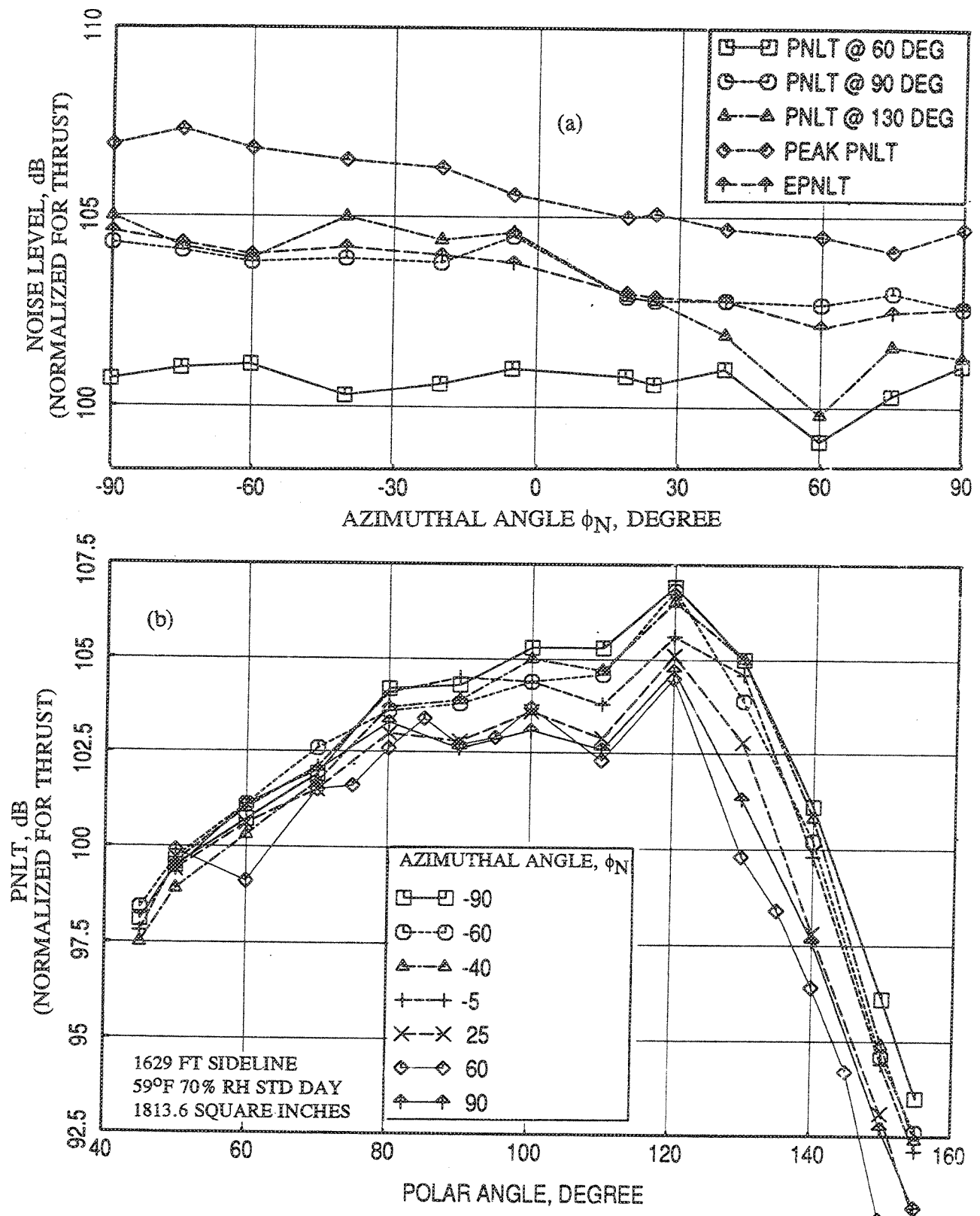


Figure 2.10-10. (a) Azimuthal variation of PNLTs at different polar angles ( $\theta$ ), peak PNLT, and EPNLT and (b) comparison of PNLT directivities between azimuthal angles for 0.5"-thick fluid shield nozzle with flight simulation ( $M_F=0.32$ ) at a jet velocity,  $V_{mix} = 1811$  ft/sec;  $P_{r,p}=2.39$ ,  $P_{r,s}=2.2$ ,  $T_{t,p}=1806^\circ R$ ,  $T_{t,s}=727^\circ R$ .



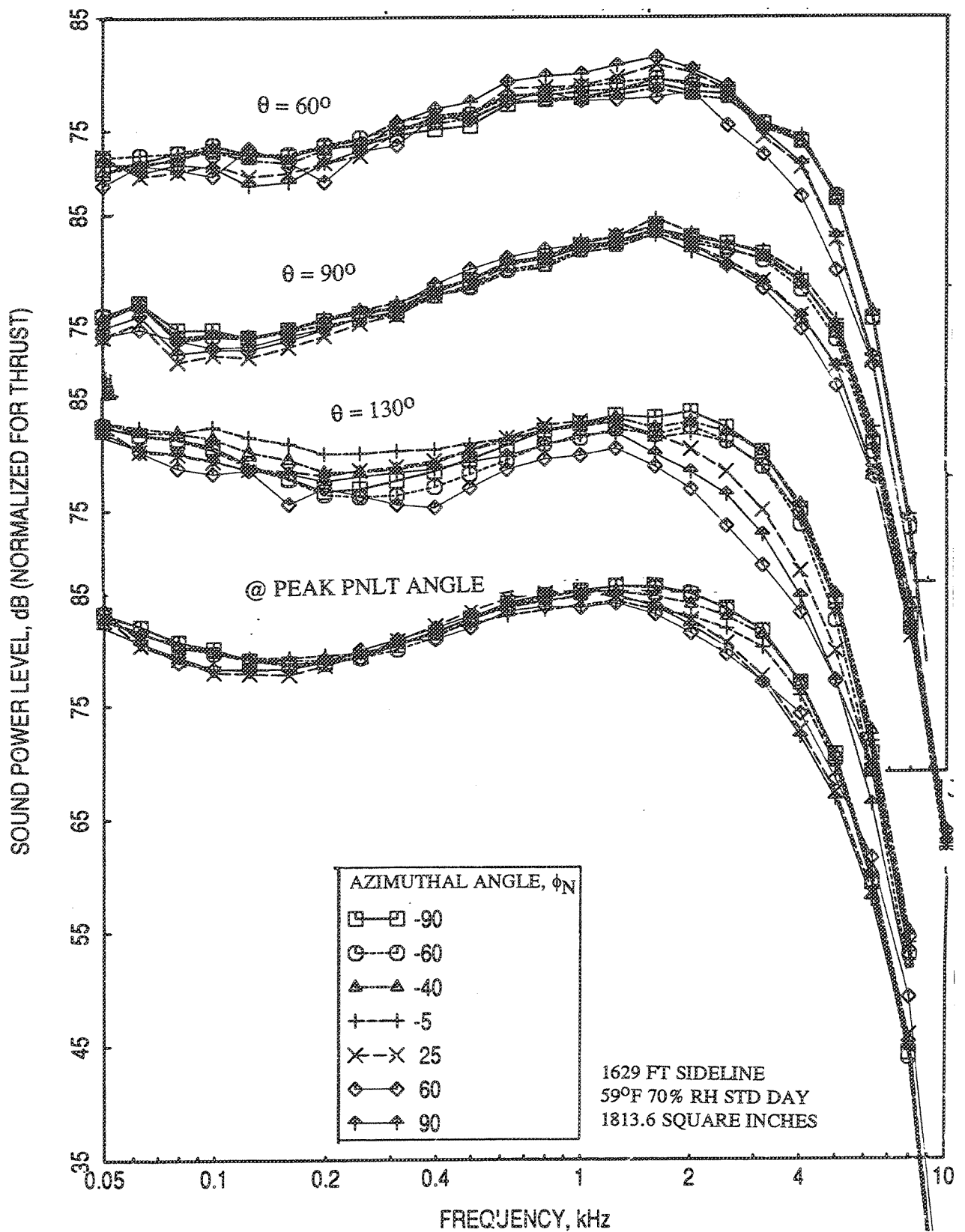


Figure 2.10-11. Comparison of SPL spectra at different polar angles ( $\theta$ ), between azimuthal angles, for 0.5"-thick fluid shield nozzle with flight simulation ( $M_F=0.32$ ) at a jet velocity,  $V_{\text{mix}} = 1811 \text{ ft/sec}$ ;  $P_{r,p}=2.39$ ,  $P_{r,s}=2.2$ ,  $T_{t,p}=1806^\circ\text{R}$ ,  $T_{t,s}=727^\circ\text{R}$ .

**Results At  $V_{mix} = 2030$  ft/sec:** Similar to  $V_{mix}=1811$  ft/sec case tests were conducted to generate  $V_{mix}=2030$  ft/sec with two different fluid shield conditions, namely supersonic shield (i.e.,  $P_{r,s}=2.14$ ) and subsonic shield (i.e.,  $P_{r,s}=1.6$ ), at static condition. The azimuthal variations in terms of PNLT, EPNLT, and SPL are relatively small compared to  $V_{mix}=1811$  ft/sec case (see Figures 2.10-12 and 2.10-13). Again, very little effect is observed in azimuthal noise variation for subsonic shield also (see Figures 2.10-14 and 2.10-15). With flight simulation the noise levels are slightly decreased on the shielded side for to supersonic shield as shown in Figures 2.10-16 and 2.10-17.

**2.10.2 Effect of Shield Thickness on Azimuthal Noise Variation For Fluid Shield Nozzles With Porous Plug :** Fluid shield nozzles with 0.75" and 1.0" thick shields were not tested with indexed orientation. Hence, the azimuthal noise variation for these nozzles are only derived for standard orientation cases for  $\phi_N$  between  $190^\circ$  and  $90^\circ$ . Thus, the effect of shield thickness on azimuthal noise variation is examined with in the azimuthal angles of  $190^\circ$  and  $90^\circ$ . In this section, the comparisons between different nozzles are made for fixed primary stream velocity.

**Results At  $V_{j,p} = 1345$  ft/sec with Ambient Temperature Conditions:** Figure 2.10-18 shows the azimuthal variation of PNLT at different polar angles, peak PNLT, and pseudo EPNLT at static condition for fluid shield nozzles of different thicknesses. In general, the 1.0"-thick shield shows more noise reduction under the shielded region. The PNLT directivities at various azimuthal angles are shown in Figure 2.10-19. Relatively larger noise variation between  $190^\circ$  and  $90^\circ$  is observed for 1"-thick fluid shield, among the three nozzle configurations. The spectral SPL plots at  $\theta = 120^\circ$  and  $90^\circ$  are shown in Figure 2.10-20. Very little SPL difference is observed with respect to azimuthal angle as well as shield thickness at  $\theta = 90^\circ$ . However, at  $\theta = 120^\circ$  the spectral SPL level decreases with the azimuthal angle, more prominently for 1.0"-thick shield.

**Results At  $V_{j,p} = 2198$  ft/sec :** This is the cutback cycle condition for the Flade cycle. The corresponding mixed velocities for the three fluid shield nozzles of 0.5", 0.75", and 1.0" shield thicknesses are 1811, 1751, and 1651 ft/sec, respectively. Figure 2.10-21 shows the azimuthal variation of PNLT at different polar angles, peak PNLT, and pseudo EPNLT at static condition for fluid shield nozzles of different thicknesses. The

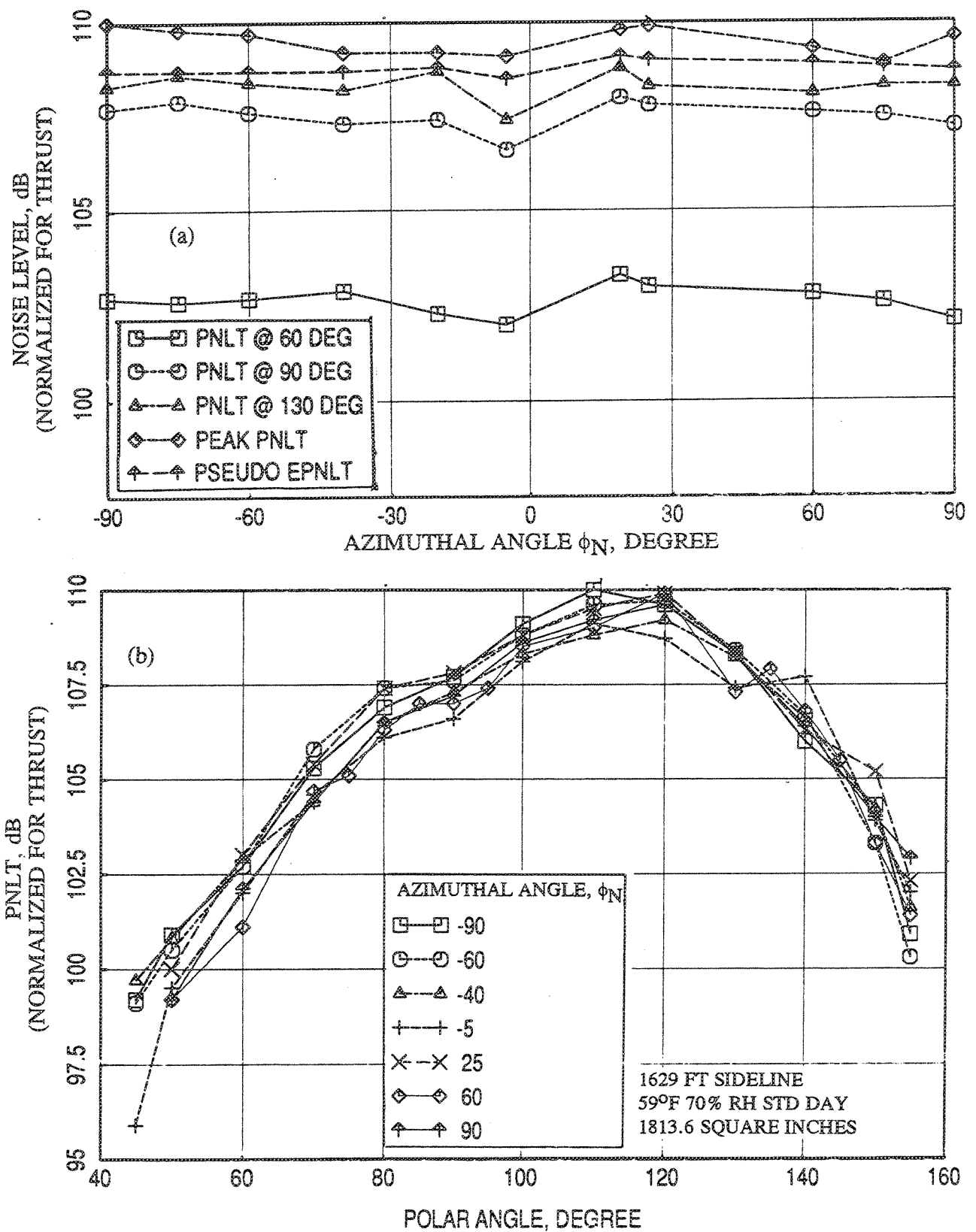


Figure 2.10-12. (a) Azimuthal variation of PNLTs at different polar angles ( $\theta$ ), peak PNLT, and pseudo EPNLT and (b) comparison of PNLT directivities between azimuthal angles for 0.5"-thick fluid shield nozzle at static condition at a jet velocity,  $V_{mix} = 2030$  ft/sec;  $P_{r,p} = 3.19$ ,  $P_{r,s} = 2.1.4$ ,  $T_{t,p} = 1786^\circ R$ ,  $T_{t,s} = 695^\circ R$ .

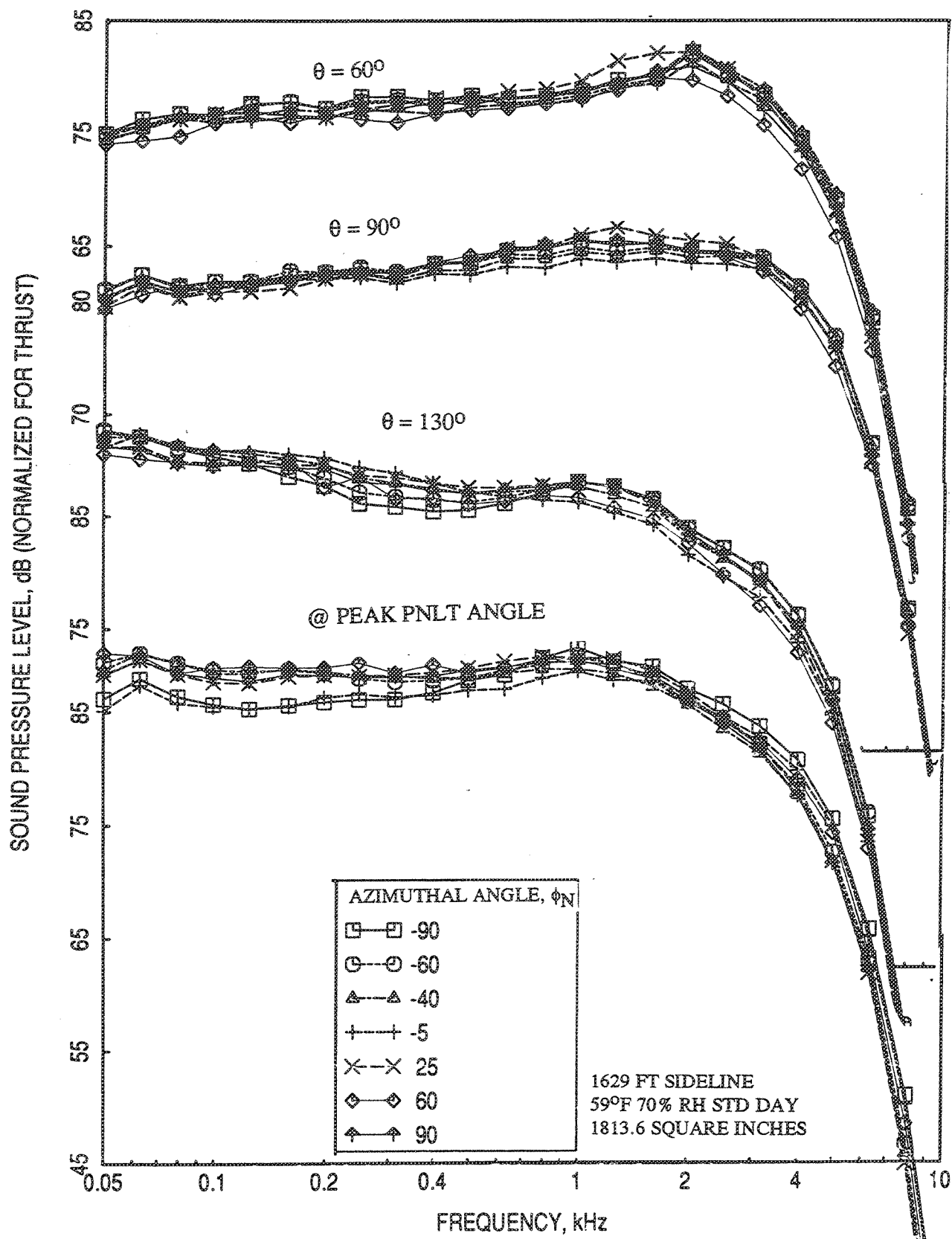


Figure 2.10-13. Comparison of SPL spectra at different polar angles ( $\theta$ ), between azimuthal angles, for 0.5"-thick fluid shield nozzle at static condition at a jet velocity,  $V_{mix} = 2030$  ft/sec;  $P_{r,p} = 3.19$ ,  $P_{r,s} = 2.1.4$ ,  $T_{t,p} = 1786^\circ R$ ,  $T_{t,s} = 695^\circ R$ .

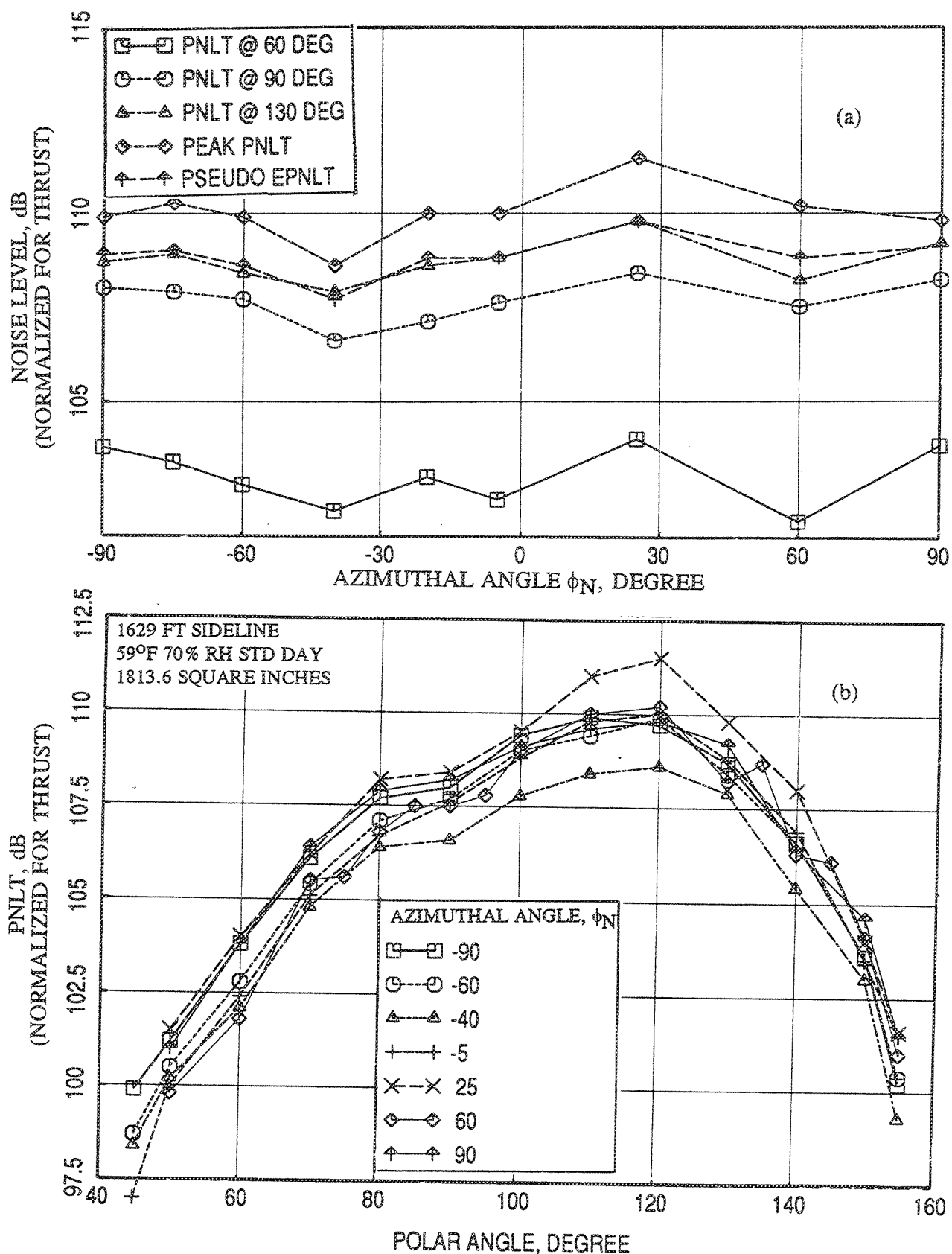


Figure 2.10-14. (a) Azimuthal variation of PNLTs at different polar angles ( $\theta$ ), peak PNLT, and pseudo EPNLT and (b) comparison of PNLT directivities between azimuthal angles for 0.5"-thick fluid shield nozzle at static condition at a jet velocity,  $V_{mix} = 2030$  ft/sec;  $P_{r,p} = 3.17$ ,  $P_{r,s} = 1.6$ ,  $T_{t,p} = 1786^\circ R$ ,  $T_{t,s} = 695^\circ R$ .

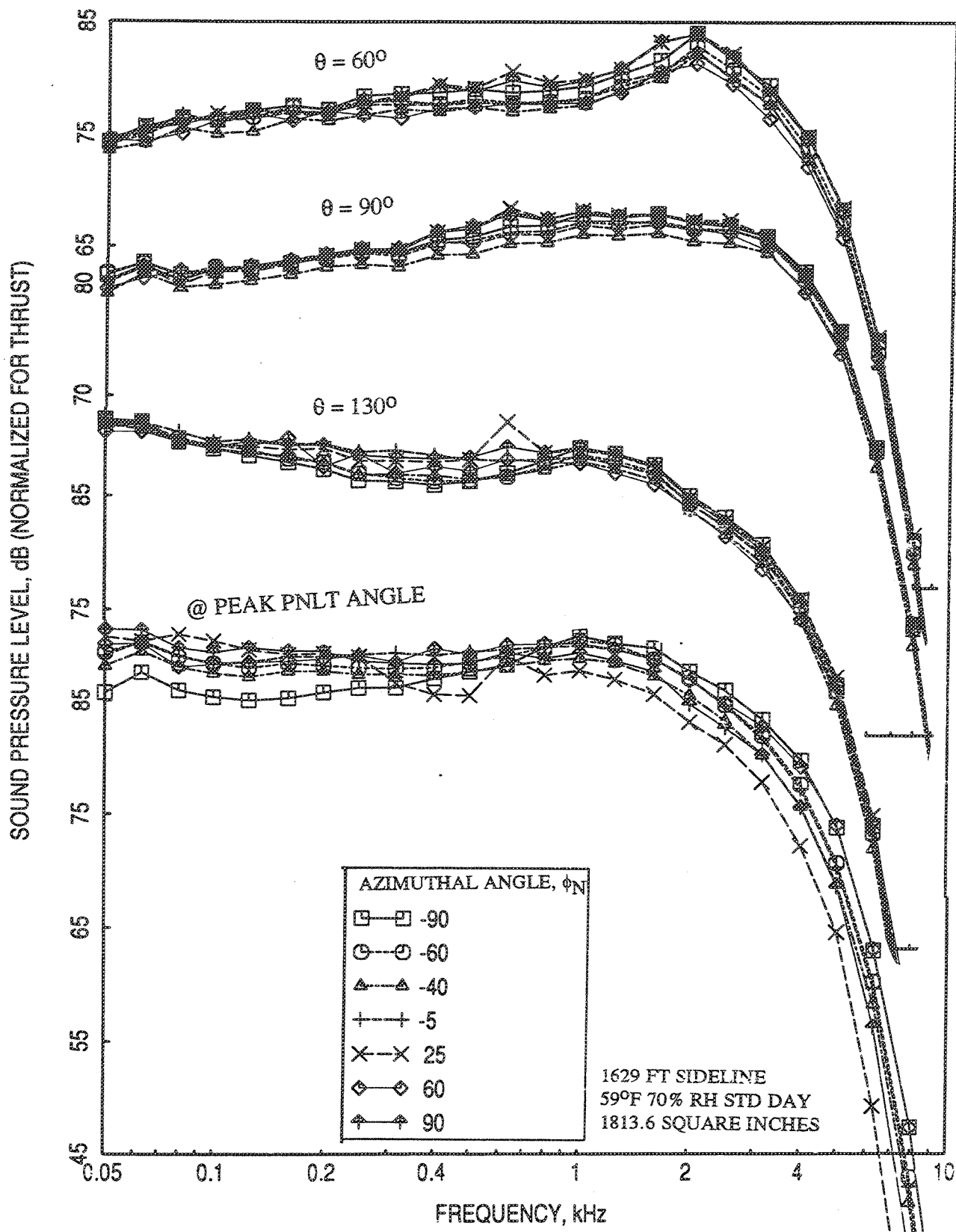


Figure 2.10-15. Comparison of SPL spectra at different polar angles ( $\theta$ ), between azimuthal angles, for 0.5"-thick fluid shield nozzle at static condition at a jet velocity,  $V_{\text{mix}} = 2030$  ft/sec;  $P_{r,p} = 3.17$ ,  $P_{r,s} = 1.6$ ,  $T_{t,p} = 1786^\circ\text{R}$ ,  $T_{t,s} = 695^\circ\text{R}$

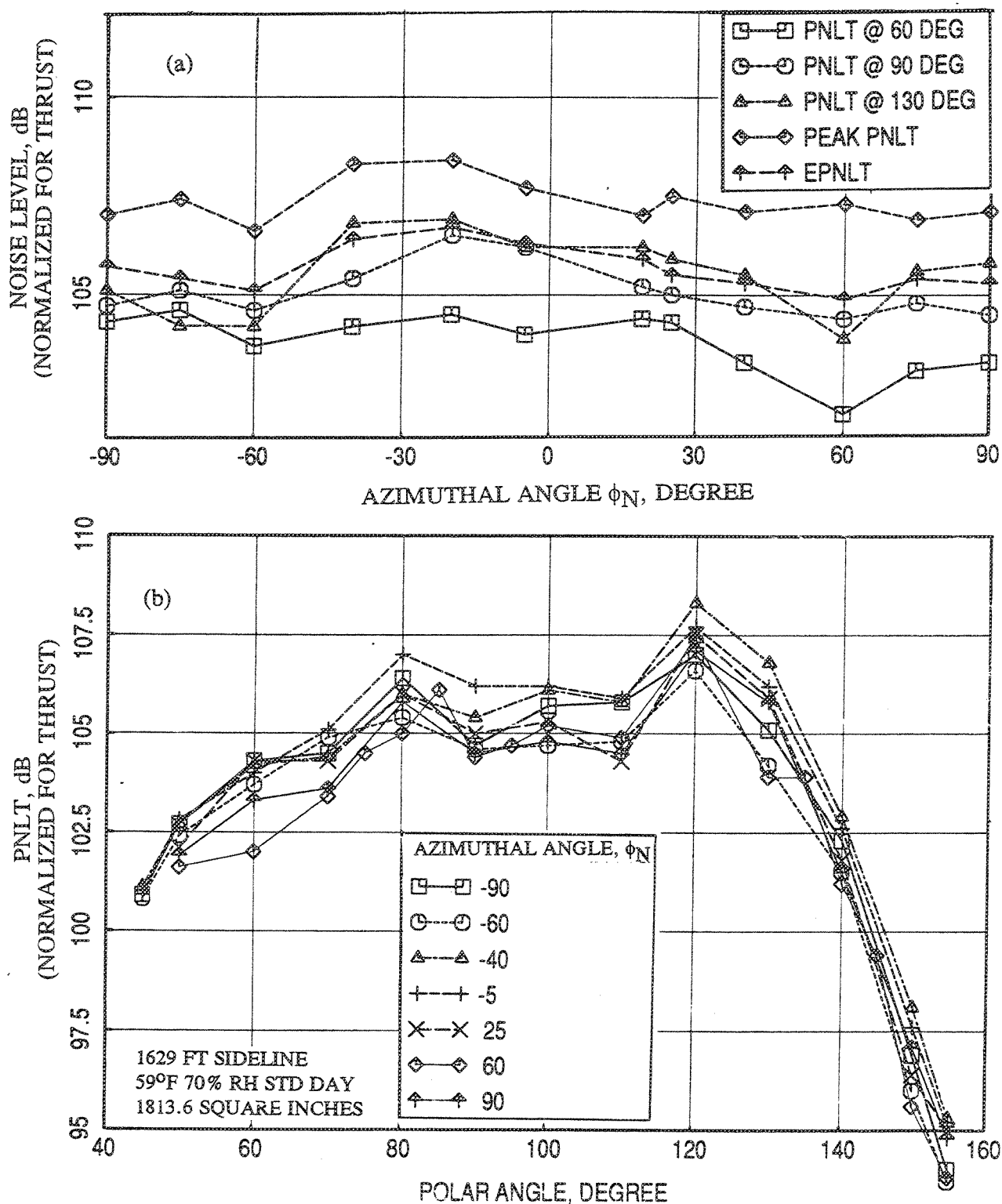


Figure 2.10-16. (a) Azimuthal variation of PNLTs at different polar angles ( $\theta$ ), peak PNLT, and EPNLT and (b) comparison of PNLT directivities between azimuthal angles, for 0.5"-thick fluid shield nozzle with flight simulation ( $M_F=0.32$ ) at a jet velocity,  $V_{mix} = 2030$  ft/sec;  $P_{r,p}=3.19$ ,  $P_{r,s}=2.1.4$ ,  $T_{t,p}=1786^\circ R$ ,  $T_{t,s}=695^\circ R$ .

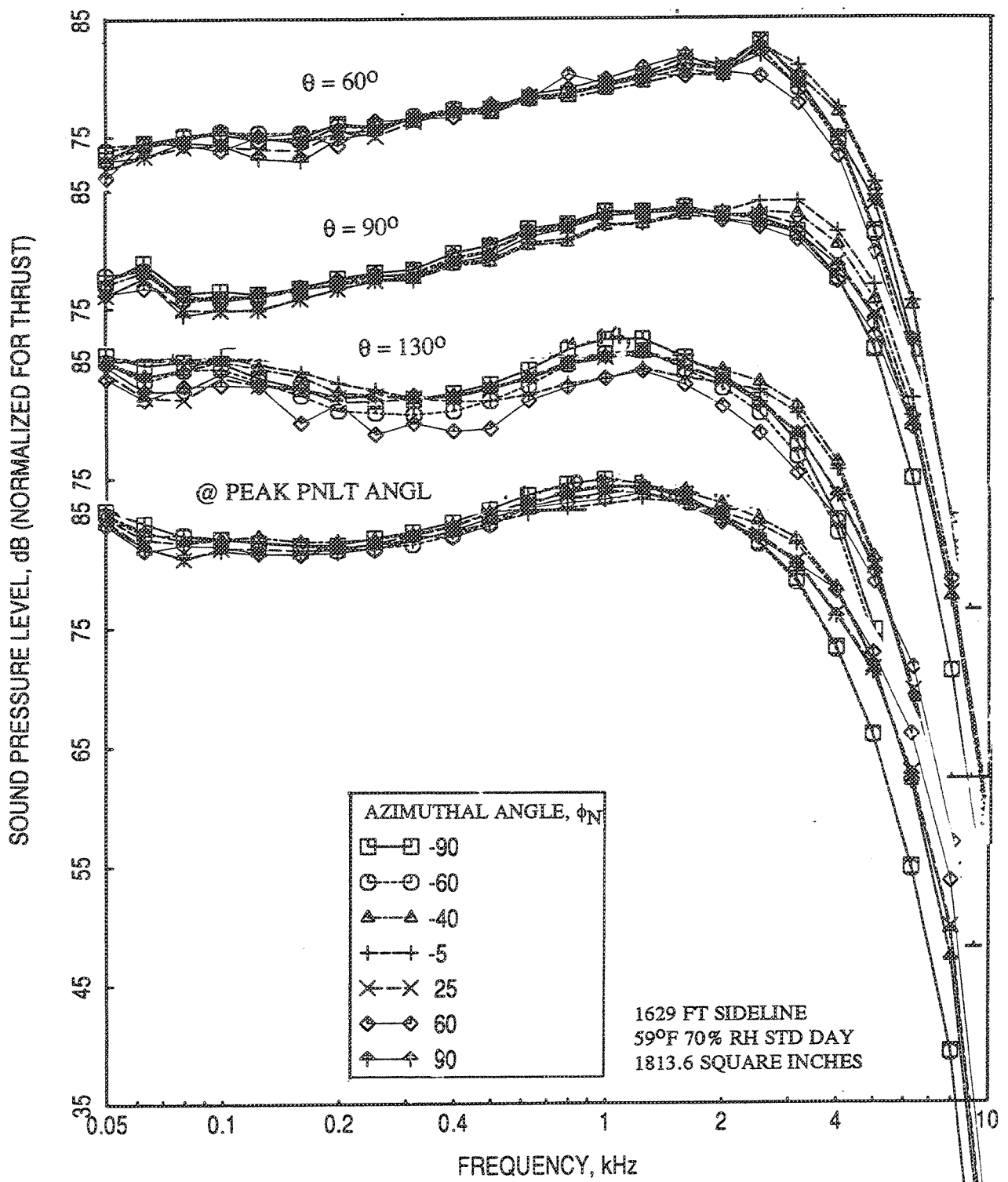


Figure 2.10-17. Comparison of SPL spectra at different polar angles ( $\theta$ ), between azimuthal angles, for 0.5"-thick fluid shield nozzle with flight simulation ( $M_F=0.32$ ) at a jet velocity,  $V_{mix}=2030$  ft/sec;  $P_{r,p}=3.19$ ,  $P_{r,s}=2.1.4$ ,  $T_{t,p}=1786^\circ R$ ,  $T_{t,s}=695^\circ R$ .



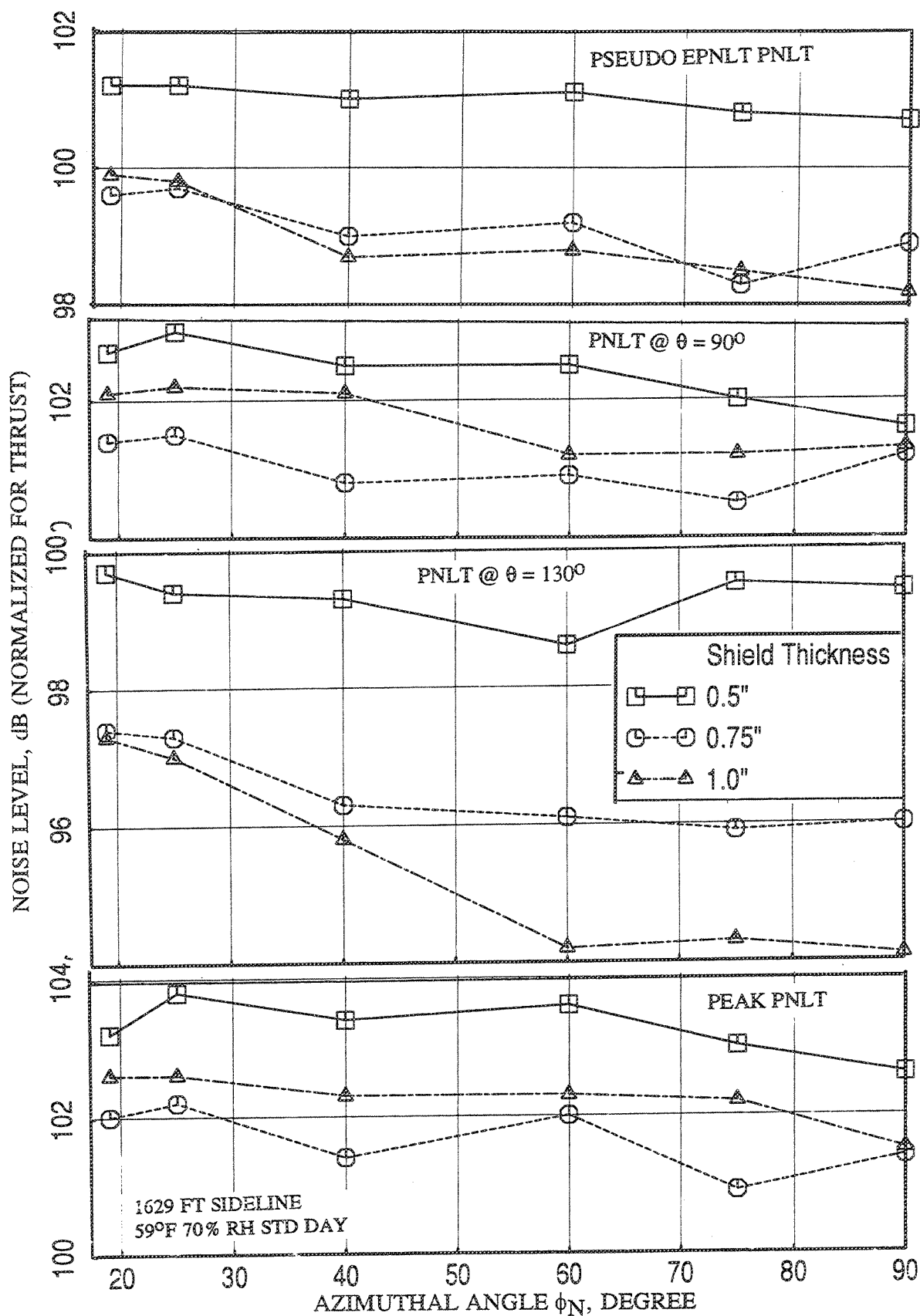


Figure 2.10-18. Comparison of pseudo EPNLT, PNLTs at different polar angles ( $\theta$ ), and peak PNLT between the fluid shield nozzles with different shield thicknesses with respect to azimuthal angle at static condition at a core jet velocity,  $V_{j,p}=1345$  ft/sec;  $P_{r,p}=3.17$ ,  $P_{r,s}=1.6$ , both streams being of ambient temperature.

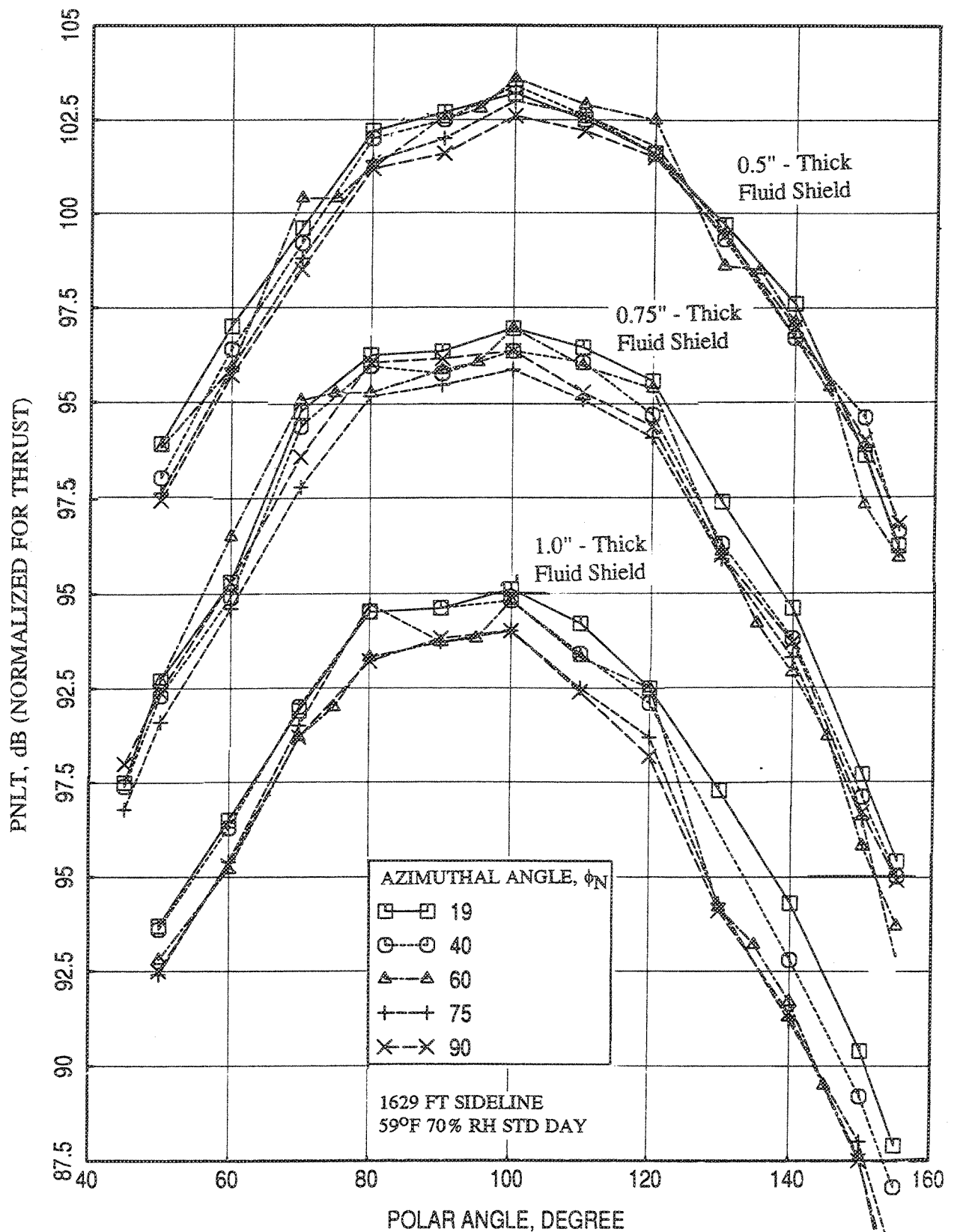


Figure 2.10-19. Comparison of PNLT directivities between azimuthal angles for fluid shield nozzles with different shield thicknesses at static condition at a core jet velocity,  $V_{j,p}=1345$  ft/sec;  $P_{r,p}=3.17$ ,  $P_{r,s}=1.6$ , both streams being of ambient temperature.

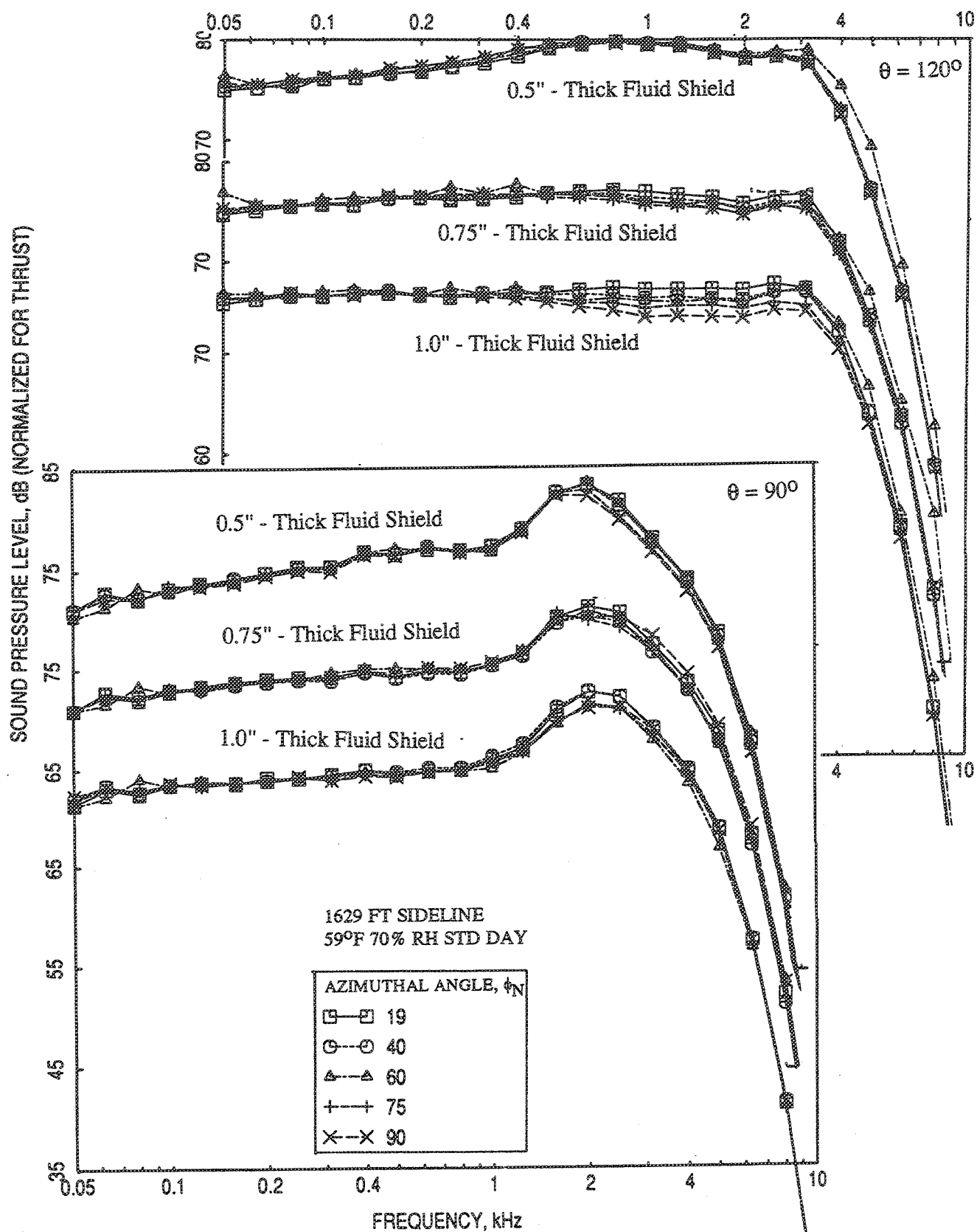


Figure 2.10-20. Comparison of SPL spectra at two polar angles ( $\theta$ ), between azimuthal angles, for fluid shield nozzles with different shield thicknesses at static condition at a core jet velocity,  $V_{j,p}=1345$ ;  $P_{r,p}=3.17$ ,  $P_{r,s}=1.6$ , both streams being of ambient temperature.

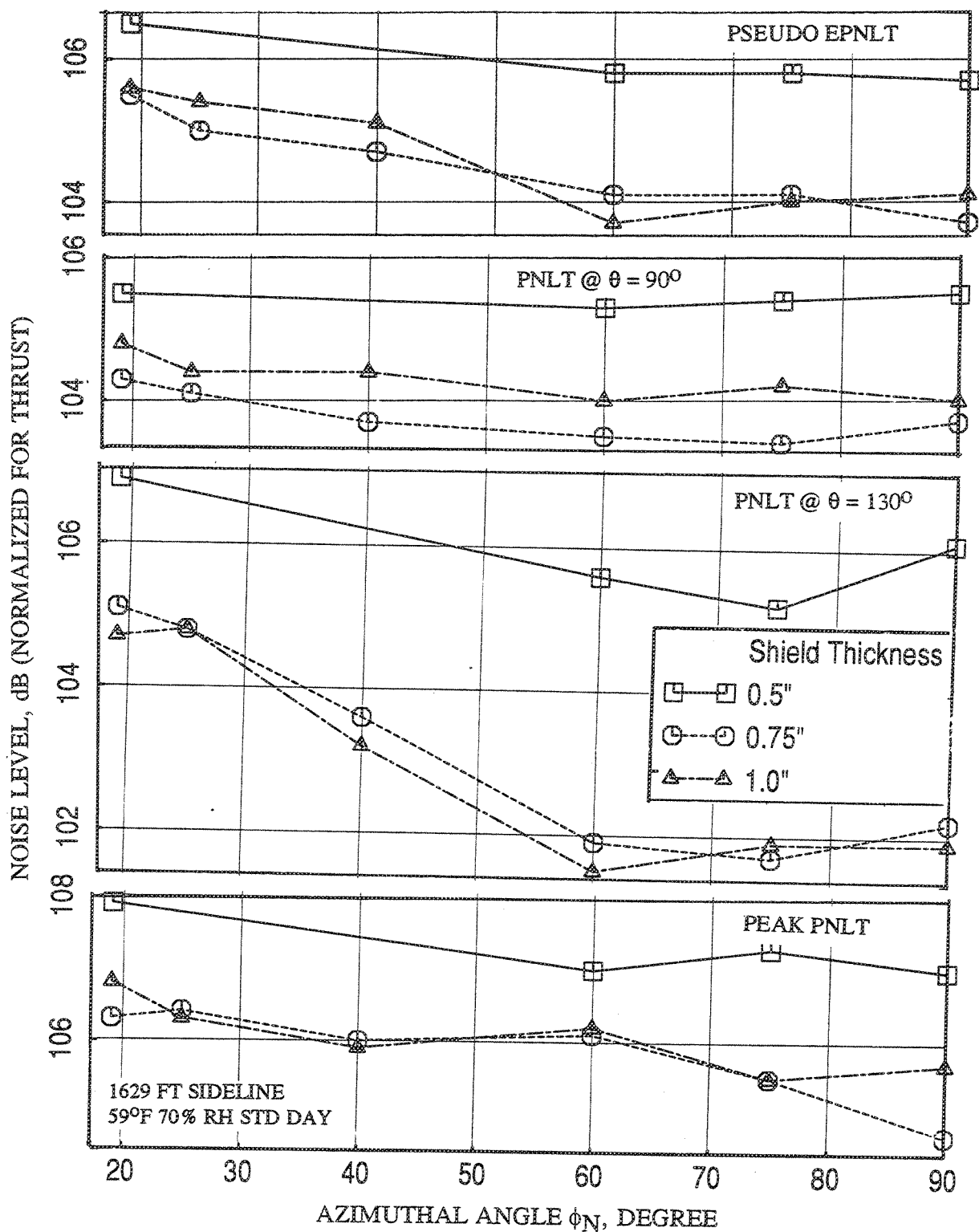


Figure 2.10-21. Comparison of pseudo EPNLT, PNLTs at different polar angles ( $\theta$ ), and peak PNLT between the fluid shield nozzles with different shield thicknesses with respect to azimuthal angle at static condition at a core jet velocity,  $V_{j,p}=2198$  ft/sec;  $P_{r,p}=2.39$ ,  $P_{r,s}=2.2$ ,  $T_{t,p}=1806^\circ\text{R}$ ,  $T_{t,s}=727^\circ\text{R}$ .

0.75" and 1.0"-thick shields show more noise reduction under the shielded region compared to 0.5" shield. The PNLT directivities at various azimuthal angles are shown in Figure 2.10-22. Relatively larger noise variation between  $190^\circ$  and  $90^\circ$  is observed for 0.75" and 1"-thick fluid shields, among the three nozzle configurations. The spectral SPL plots at  $\theta = 120^\circ$  and  $90^\circ$  are shown in Figure 2.10-23. Very little SPL difference is observed with respect to azimuthal angle as well as shield thickness at  $\theta = 90^\circ$ . However, at  $\theta = 120^\circ$  the spectral SPL level decreases with the azimuthal angle, more prominently for 0.75" and 1.0"-thick shields. Similar results with flight simulation are shown in Figures 2.10-24 through 2.10-26.

**Results At  $V_{j,p} = 2475 \text{ ft/sec}$  :** This is the takeoff condition for the Flade cycle. The corresponding mixed velocities for the three fluid shield nozzles of 0.5", 0.75", and 1.0" shield thicknesses are 1030, 1902, and 1809 ft/sec, respectively. Figure 2.10-27 shows the azimuthal variation of PNLT at different polar angles, peak PNLT, and pseudo EPNLT at static condition for fluid shield nozzles of different thicknesses. The 1.0"-thick shield shows more noise reduction under the shielded region compared to 0.5" and 0.75" shields. The PNLT directivities at various azimuthal angles are shown in Figure 2.10-28. Relatively larger noise variation between  $190^\circ$  and  $90^\circ$  is observed for 1"-thick fluid shield, among the three nozzle configurations. The spectral SPL plots at  $\theta = 120^\circ$  and  $90^\circ$  are shown in Figure 2.10-29. Small amount of SPL difference is observed with respect to azimuthal angle as well as shield thickness at  $\theta = 90^\circ$ . However, at  $\theta = 120^\circ$  the spectral SPL level decreases with the azimuthal angle, more prominently for 1.0"-thick shield. Similar results with flight simulation are shown in Figures 2.10-30 through 2.10-32, exhibiting characteristics similar to those at static condition.

**2.10.3 Noise Variation Between Sideline and Community Points For Fluid Shield Nozzles With Porous Plug :** Acoustic data for fluid shield nozzles were acquired at community point as well as at sideline point. In this section the acoustic data for fluid shield nozzles at community point are compared with those at sideline location to indicate azimuthal difference between these two points.

**Static Data :**

**PNLT and Pseudo EPNLT with respect to Jet Velocity,  $V_{\text{mix}}$  :** Figure 2.10-33 shows the comparison of PNLTs at different polar angles, peak PNLT, and pseudo

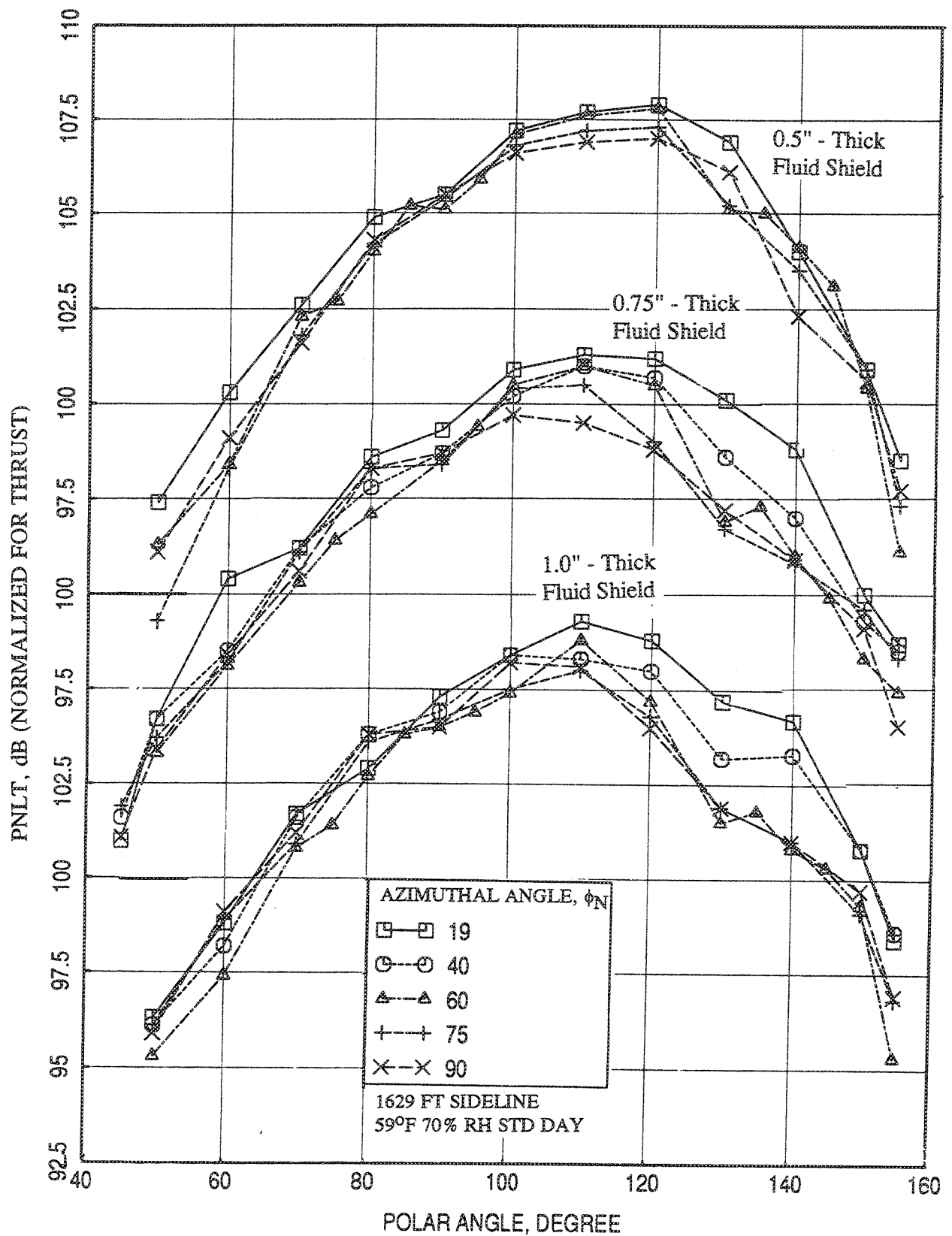


Figure 2.10-22. Comparison of PNLT directivities between azimuthal angles for fluid shield nozzles with different shield thicknesses at static condition at a core jet velocity,  $V_{j,p}=2198$  ft/sec;  $P_{r,p}=2.39$ ,  $P_{r,s}=2.2$ ,  $T_{t,p}=1806^{\circ}\text{R}$ ,  $T_{t,s}=727^{\circ}\text{R}$ .

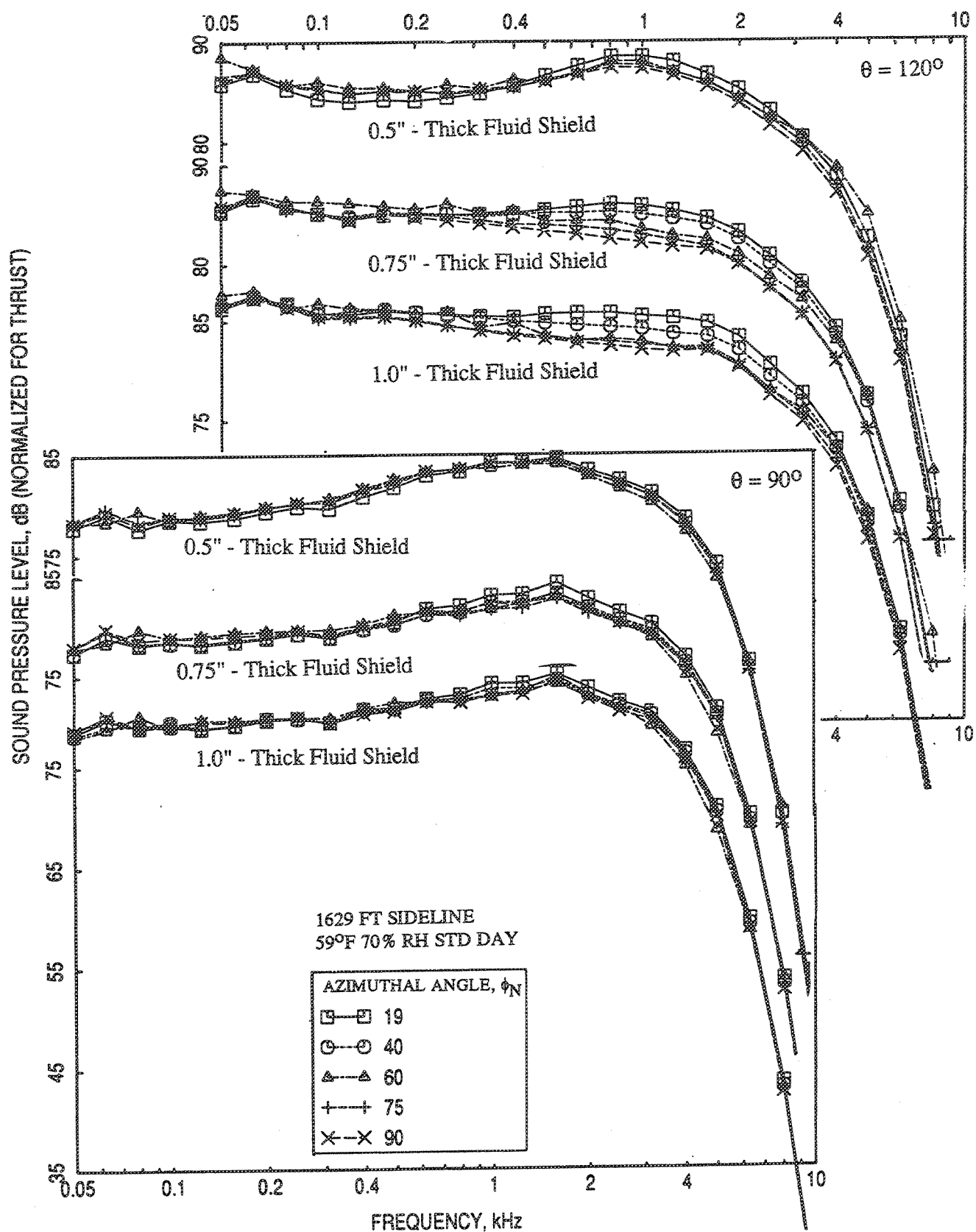


Figure 2.10-23. Comparison of SPL spectra at two polar angles ( $\theta$ ), between azimuthal angles, for fluid shield nozzles with different shield thicknesses at static condition at a core jet velocity,  $V_{j,p}=2198$ ,  $P_{r,p}=2.39$ ,  $P_{r,s}=2.2$ ,  $T_{t,p}=1806^\circ\text{R}$ ,  $T_{t,s}=727^\circ\text{R}$ .

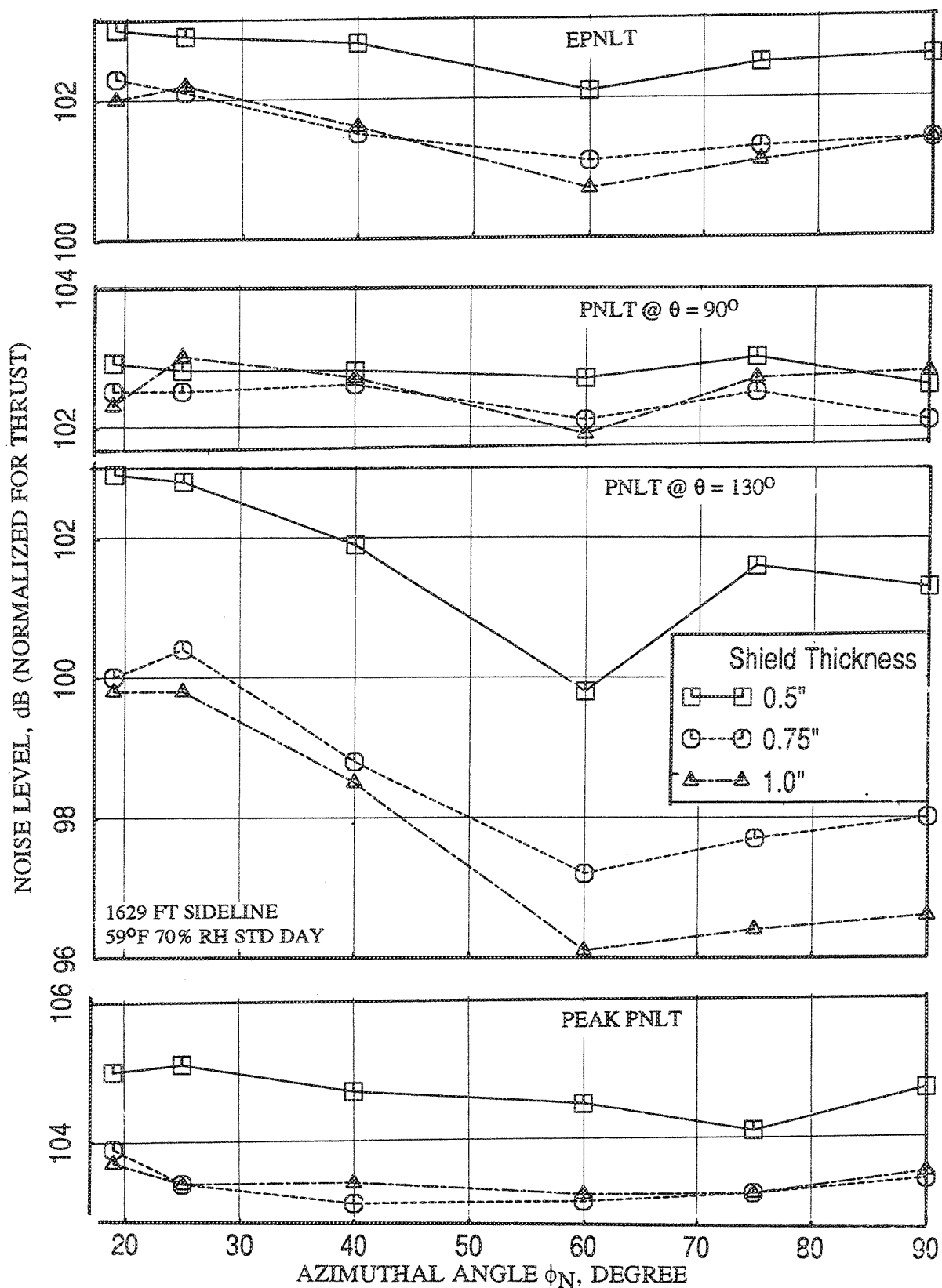


Figure 2.10-24. Comparison of EPNLT, PNLTs at different polar angles ( $\theta$ ), and peak PNLT between the fluid shield nozzles with different shield thicknesses with respect to azimuthal angle with flight simulation ( $M_F=0.32$ ) at a core jet velocity,  $V_{j,p}=2198$  ft/sec;  $P_{r,p}=2.39$ ,  $P_{r,s}=2.2$ ,  $T_{t,p}=1806^\circ\text{R}$ ,  $T_{t,s}=727^\circ\text{R}$ .



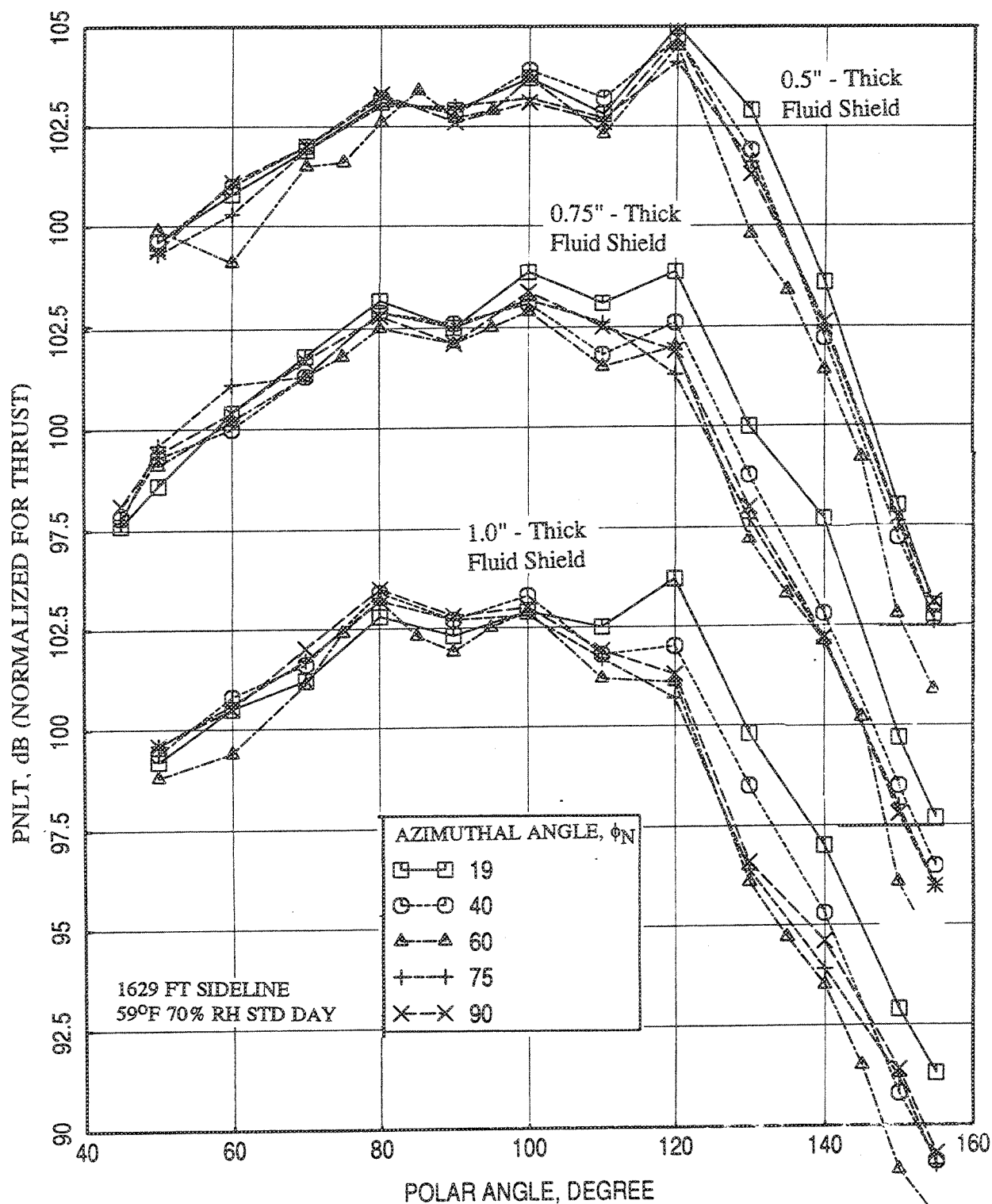


Figure 2.10-25. Comparison of PNLT directivities between azimuthal angles for fluid shield nozzles with different shield thicknesses with flight simulation ( $M_F=0.32$ ) at a core jet velocity,  $V_{j,p}=2193$  ft/sec;  $P_{r,p}=2.39$ ,  $P_{r,s}=2.2$ ,  $T_{t,p}=1806^\circ R$ ,  $T_{t,s}=727^\circ R$ .

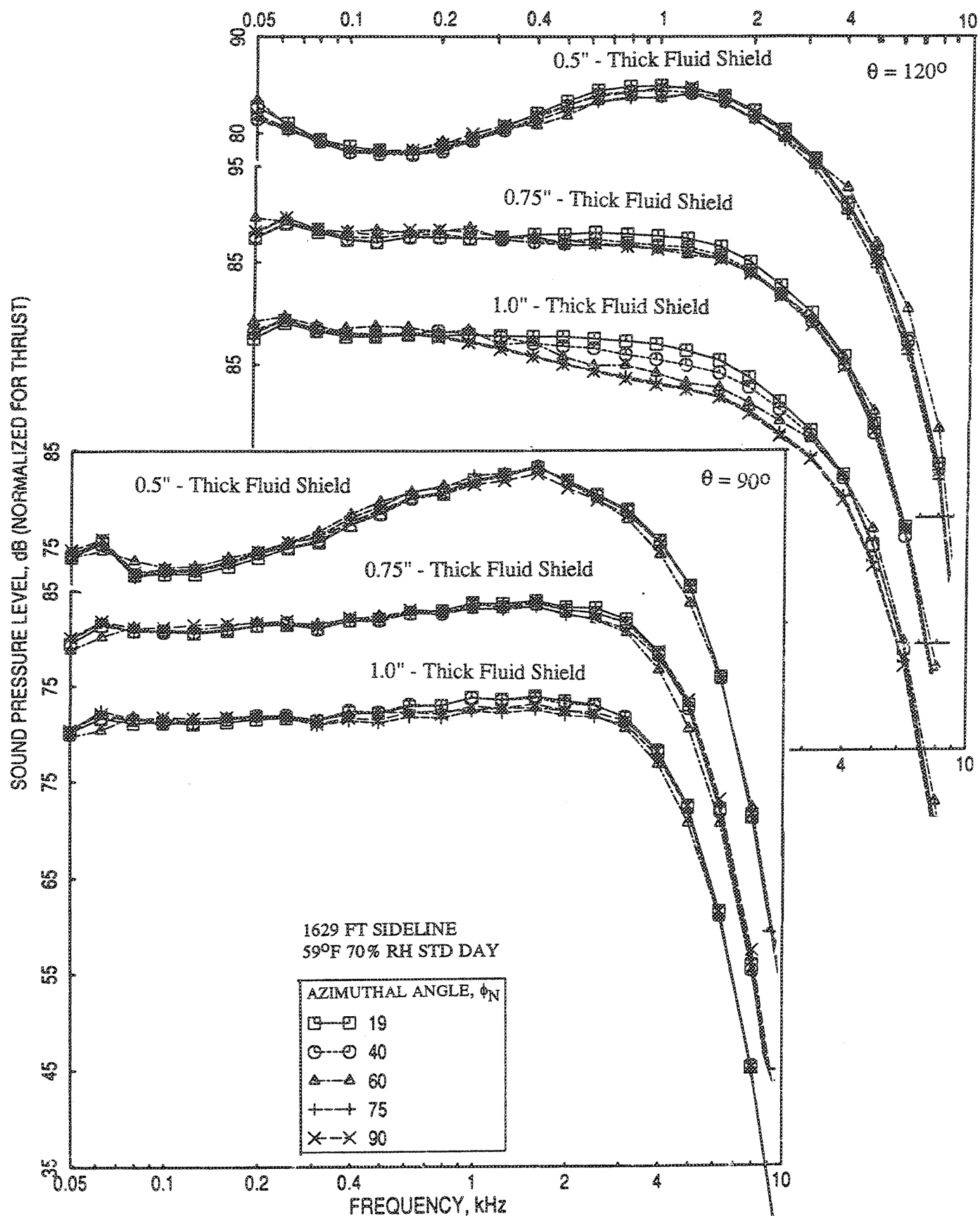


Figure 2.10-26. Comparison of SPL spectra at two polar angles ( $\theta$ ), between azimuthal angles, for fluid shield nozzles with different shield thicknesses with flight simulation ( $M_F=0.32$ ) at a core jet velocity,  $V_{j,p}=2198$ ,  $P_{r,p}=2.39$ ,  $P_{r,s}=2.2$ ,  $T_{t,p}=1806^\circ\text{R}$ ,  $T_{t,s}=727^\circ\text{R}$ .

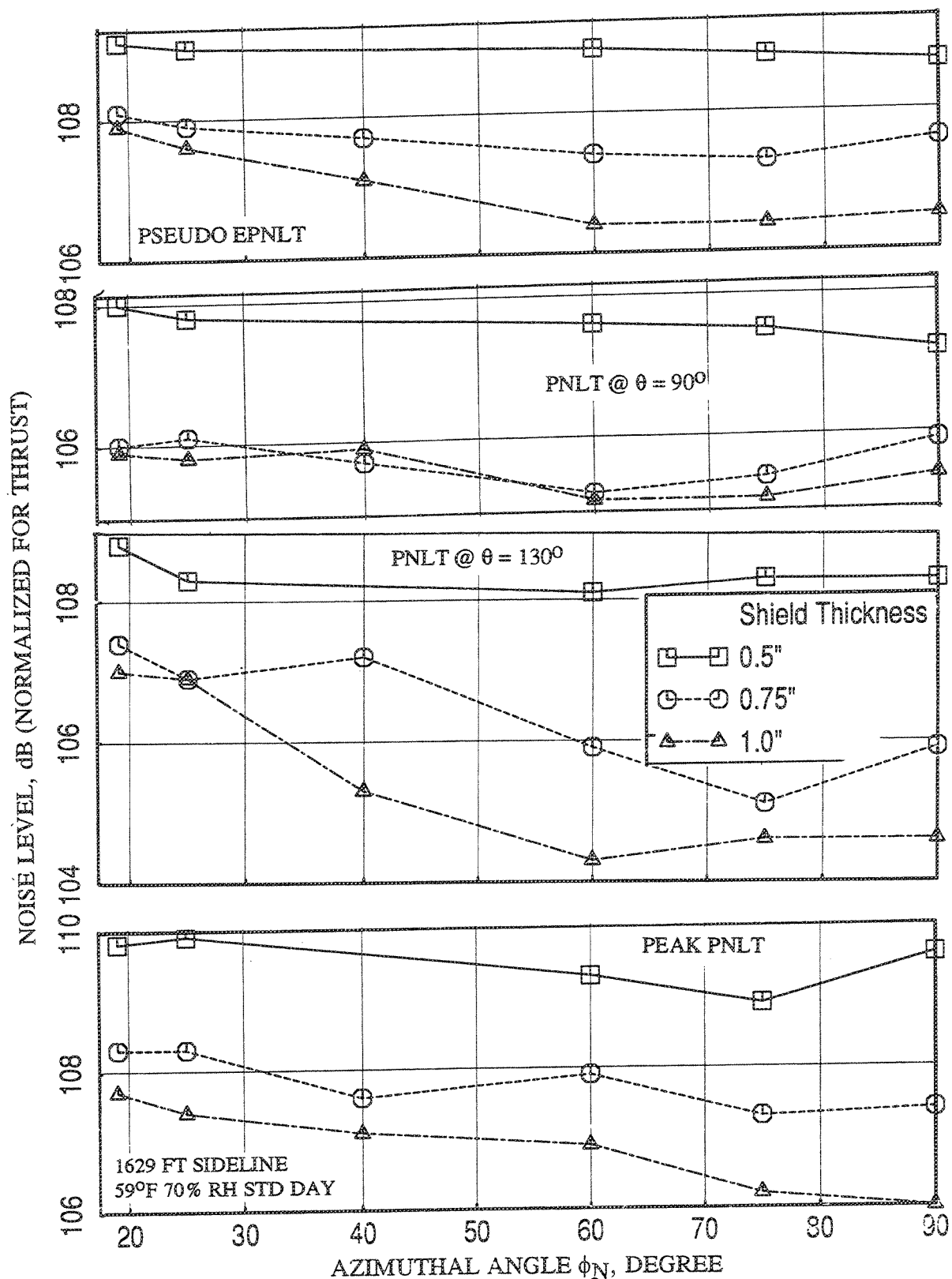


Figure 2.10-27. Comparison of pseudo EPNLT, PNLTs at different polar angles ( $\theta$ ), and peak PNLT between the fluid shield nozzles with different shield thicknesses with respect to azimuthal angle at static condition at a core jet velocity,  $V_{j,p}=2475$ ,  $P_{r,p}=3.19$ ,  $P_{r,s}=2.1.4$ ,  $T_{t,p}=1786^\circ\text{R}$ ,  $T_{t,s}=695^\circ\text{R}$ .

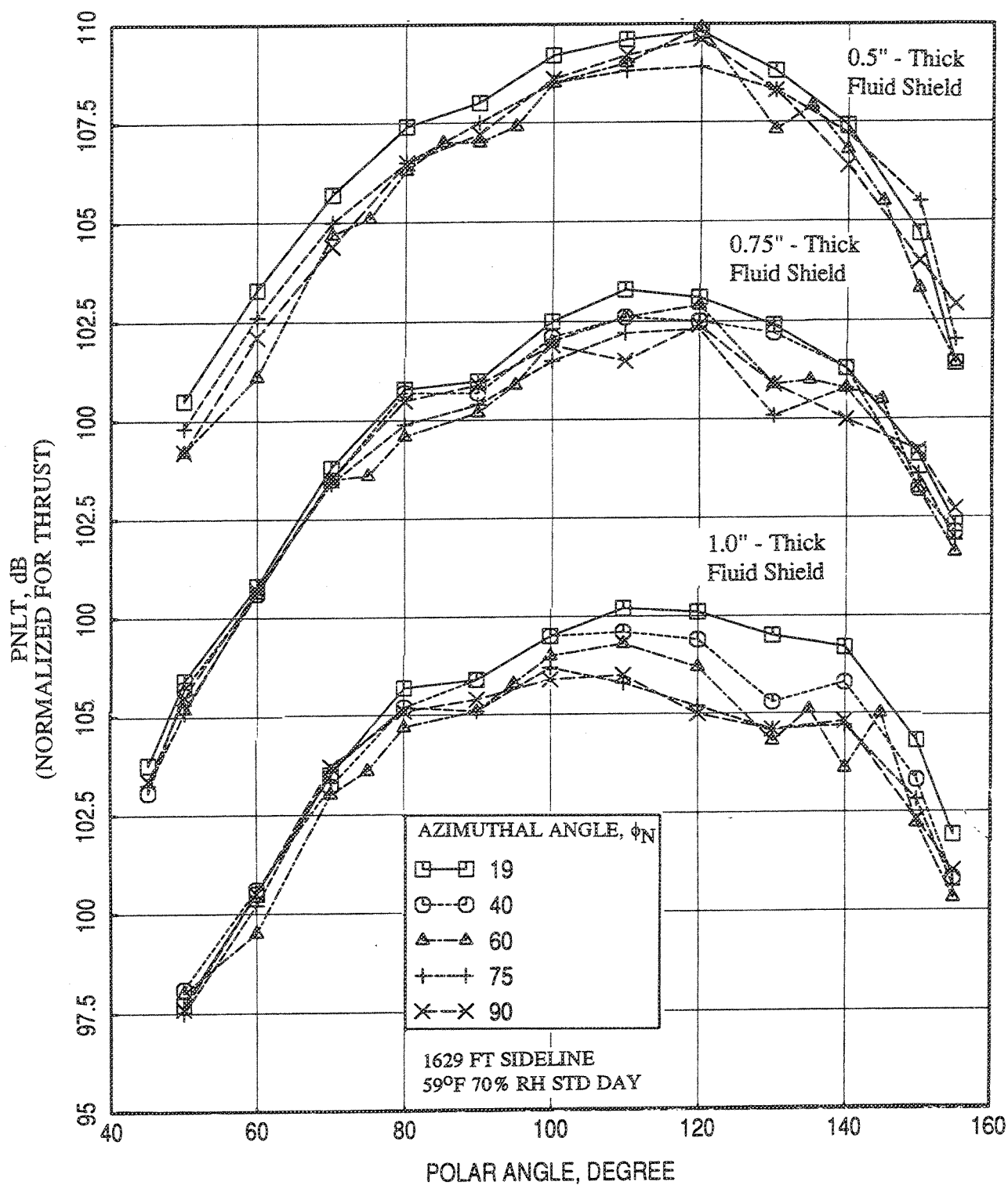


Figure 2.10-28. Comparison of PNLT directivities between azimuthal angles for fluid shield nozzles with different shield thicknesses at static condition at a core jet velocity,  $V_{j,p}=2475$ ,  $P_{r,p}=3.19$ ,  $P_{r,s}=2.1.4$ ,  $T_{t,p}=1786^{\circ}\text{R}$ ,  $T_{t,s}=695^{\circ}\text{R}$ .

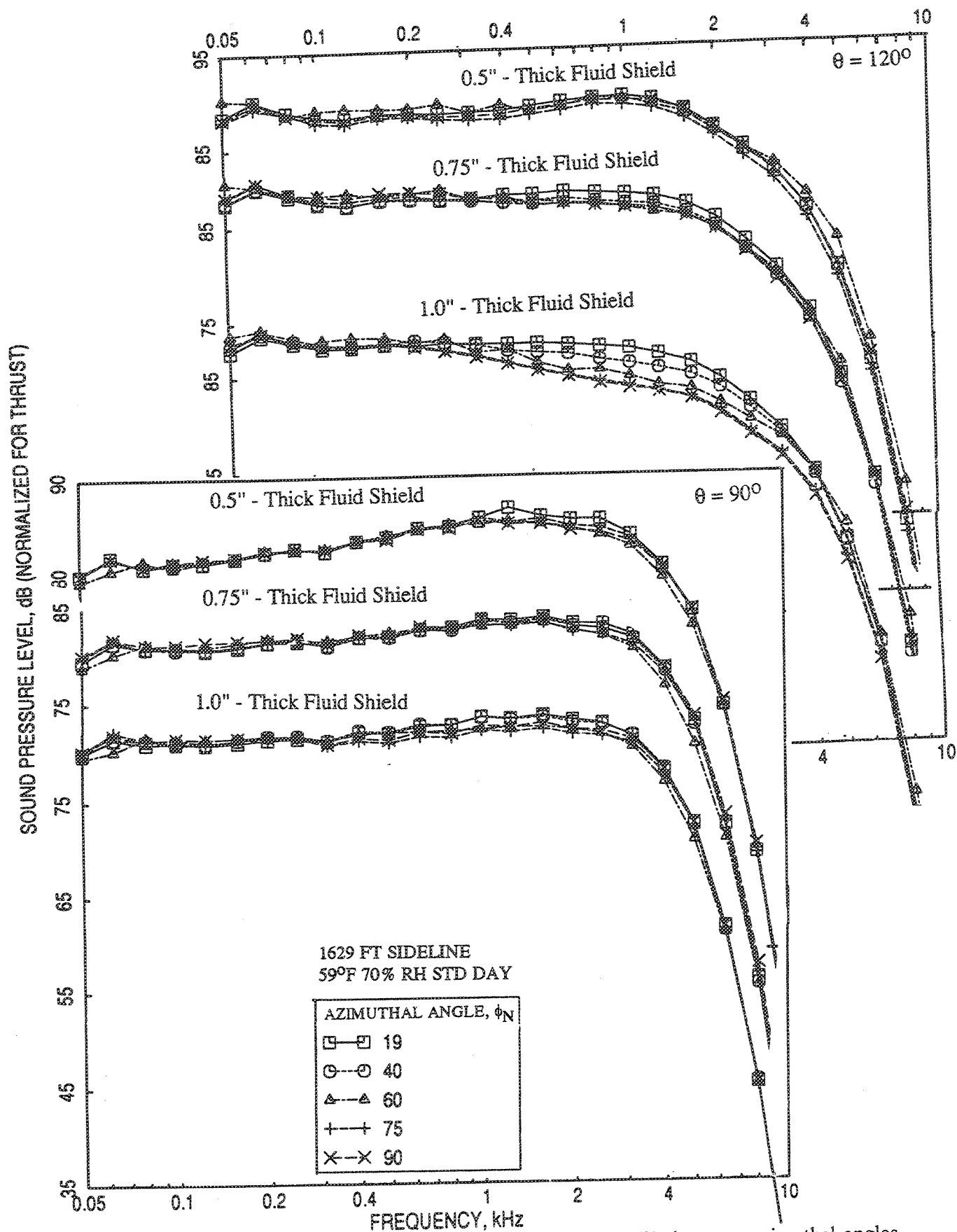


Figure 2.10-29. Comparison of SPL spectra at two polar angles ( $\theta$ ), between azimuthal angles, for fluid shield nozzles with different shield thicknesses at static condition at a core jet velocity,  $V_{j,p}=2475$ ,  $P_{r,p}=3.19$ ,  $P_{r,s}=2.1.4$ ,  $T_{t,p}=1786^\circ\text{R}$ ,  $T_{t,s}=695^\circ\text{R}$ .

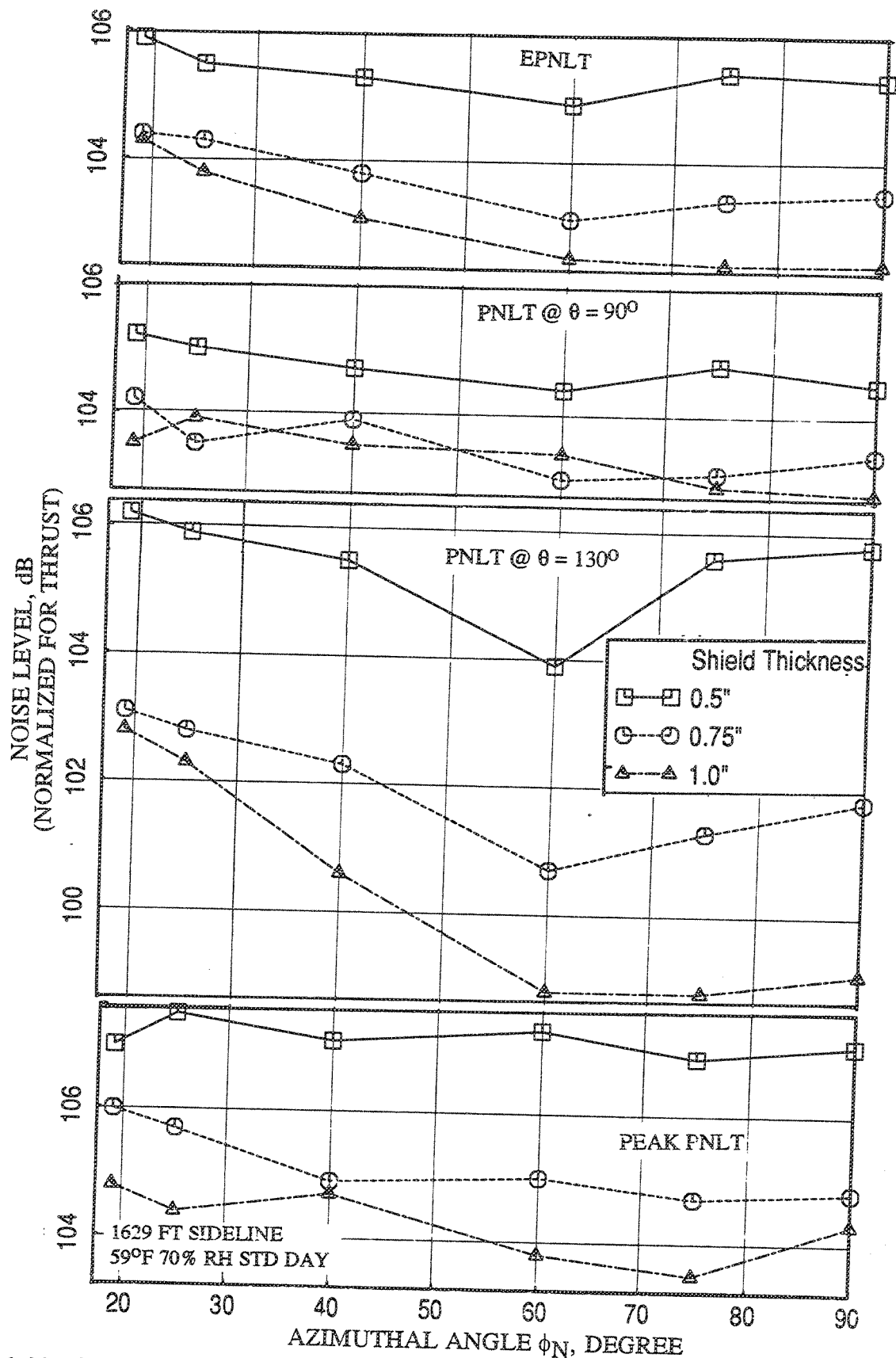


Figure 2.10-30. Comparison of EPNLT, PNLTs at different polar angles ( $\theta$ ), and peak PNLT between the fluid shield nozzles with different shield thicknesses with respect to azimuthal angle with flight simulation ( $M_F=0.32$ ) at a core jet velocity,  $V_{j,p}=2475$ ,  $P_{r,p}=3.19$ ,  $P_{r,s}=2.1.4$ ,  $T_{t,p}=1786^\circ R$ ,  $T_{t,s}=695^\circ R$ .

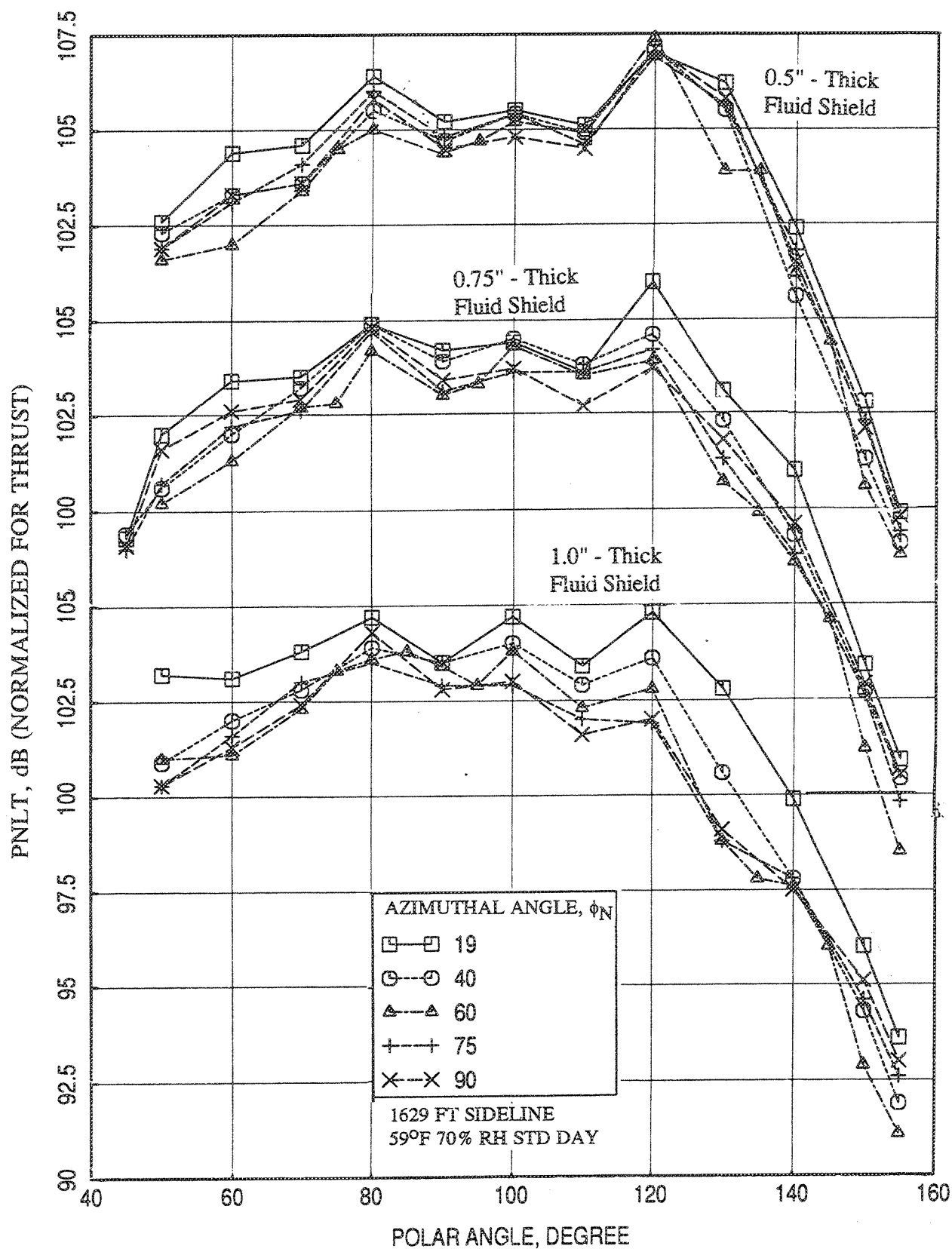


Figure 2.10-31. Comparison of PNL T directivities between azimuthal angles for fluid shield nozzles with different shield thicknesses with flight simulation ( $M_F=0.32$ ) at a core jet velocity,  $V_{j,p}=2475$ ,  $P_{r,p}=3.19$ ,  $P_{r,s}=2.1.4$ ,  $T_{t,p}=1786^\circ R$ ,  $T_{t,s}=695^\circ R$ .

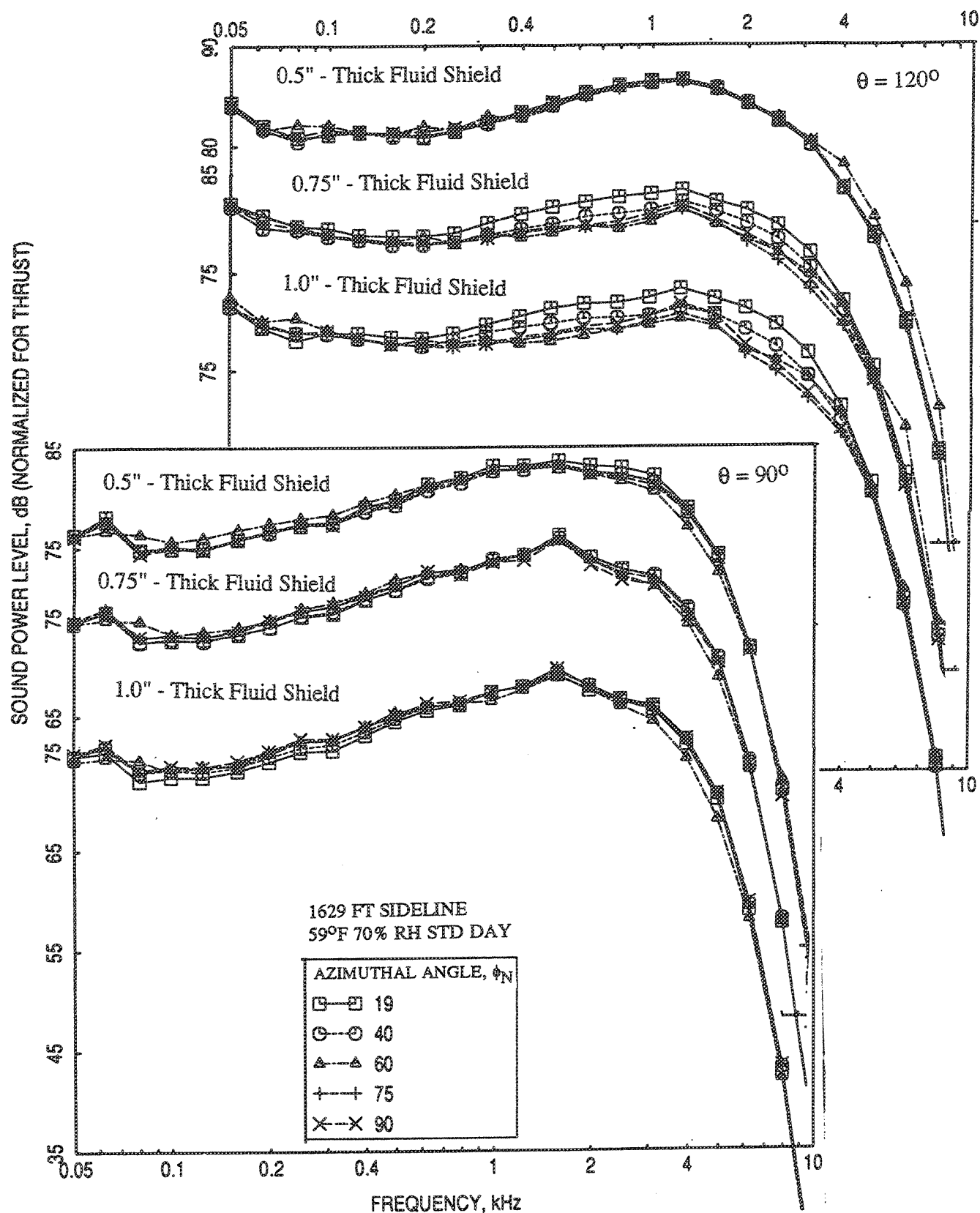


Figure 2.10-32. Comparison of SPL spectra at two polar angles ( $\theta$ ), between azimuthal angles, for fluid shield nozzles with different shield thicknesses with flight simulation ( $M_F=0.32$ ) at a core jet velocity,  $V_{j,p}=2475$ ,  $P_{r,p}=3.19$ ,  $P_{r,s}=2.1.4$ ,  $T_{t,p}=1786^\circ R$ ,  $T_{t,s}=695^\circ R$ .



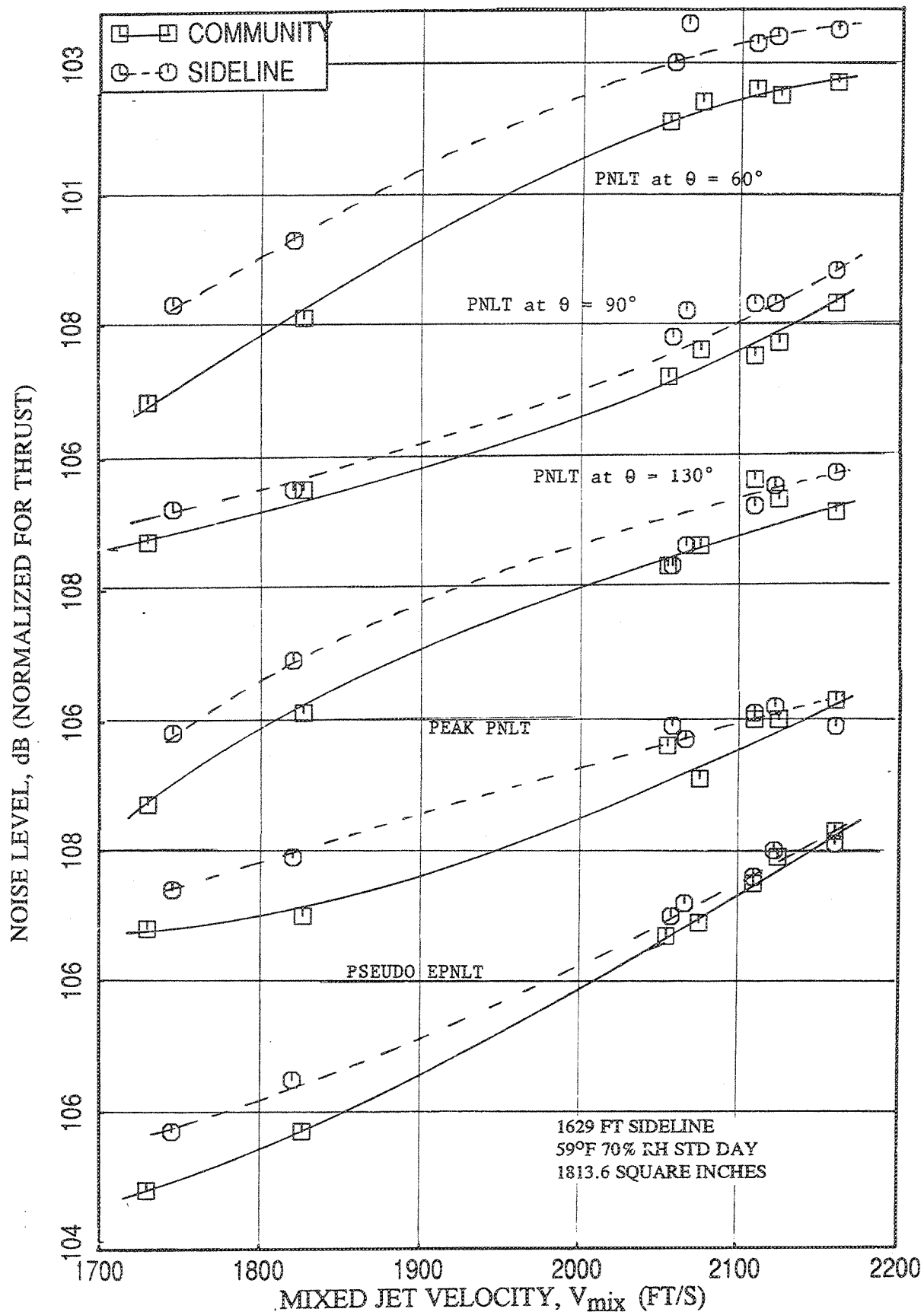


Figure 2.10-33. Comparison of PNLTs at different polar angles ( $\theta$ ), peak PNLT, and pseudo EPNLT between the sideline and community points as a function of jet velocity,  $V_{mix}$  for 0.5"-thick fluid shield nozzle at static condition.

EPNLT for the 0.5"-thick fluid shield nozzle with respect to jet velocity  $V_{mix}$  between community and sideline points. For the entire range of velocity the acoustic levels are slightly higher at the sideline point compared to community point, which indicates that the fluid shield is more effective at the community location. Difference of PNLTs between sideline and community points is higher in the rear arc compared to forward arc. This difference seems to be higher at lower jet velocities. Similar results for 0.75"- and 1.0"-thick fluid shield nozzles are plotted in Figures 2.10-34 and 2.10-35, respectively. All the three fluid shield nozzles show the similar characteristics. However, the difference of noise levels between sideline and community points increases with fluid shield thickness. Maximum of about 2 PNdB at  $\theta=130^\circ$  and about 1 EPNdB between sideline and community points are observed for the 1.0"-thick fluid shield.

**PNLT Directivities and SPL Spectra at  $V_{mix}=1811$  ft/sec :** PNLT directivities comparing between community and sideline points for the three fluid shield nozzles are shown in Figure 2.10-36 at  $V_{mix} = 1811$  ft/sec. Sideline PNLTs are substantially higher in the rear arc compared to community point noise levels. Sound pressure level spectra comparing between community and sideline points for the three fluid shield nozzles at  $V_{mix} = 1811$  ft/sec are plotted in Figures 2.10-37 through 2.10-39. Differences in SPL between sideline and community points are mostly at higher frequencies. These differences increase with increasing fluid shield thickness as well as with polar angle  $\theta$ .

**PNLT Directivities and SPL Spectra at  $V_{mix}=2030$  ft/sec :** PNLT directivities comparing between community and sideline points for the three fluid shield nozzles are shown in Figure 2.10-40 at  $V_{mix} = 2030$  ft/sec. Very little difference in PNdB between sideline and community is observed for 0.5"-thick fluid shield nozzle. However, the difference increases with fluid shield thickness and the sideline PNLTs are substantially higher in the rear arc compared to community point noise levels for 1.0"-thick fluid shield nozzle. Sound pressure level spectra comparing between community and sideline points for the three fluid shield nozzles at  $V_{mix} = 2030$  ft/sec are plotted in Figures 2.10-41 through 2.10-43. Differences in SPL between sideline and community points are negligible for 0.5"-thick fluid shield nozzle for entire frequency range and are substantial for 1.0"-thick fluid shield nozzle at higher frequencies at the rear arc.

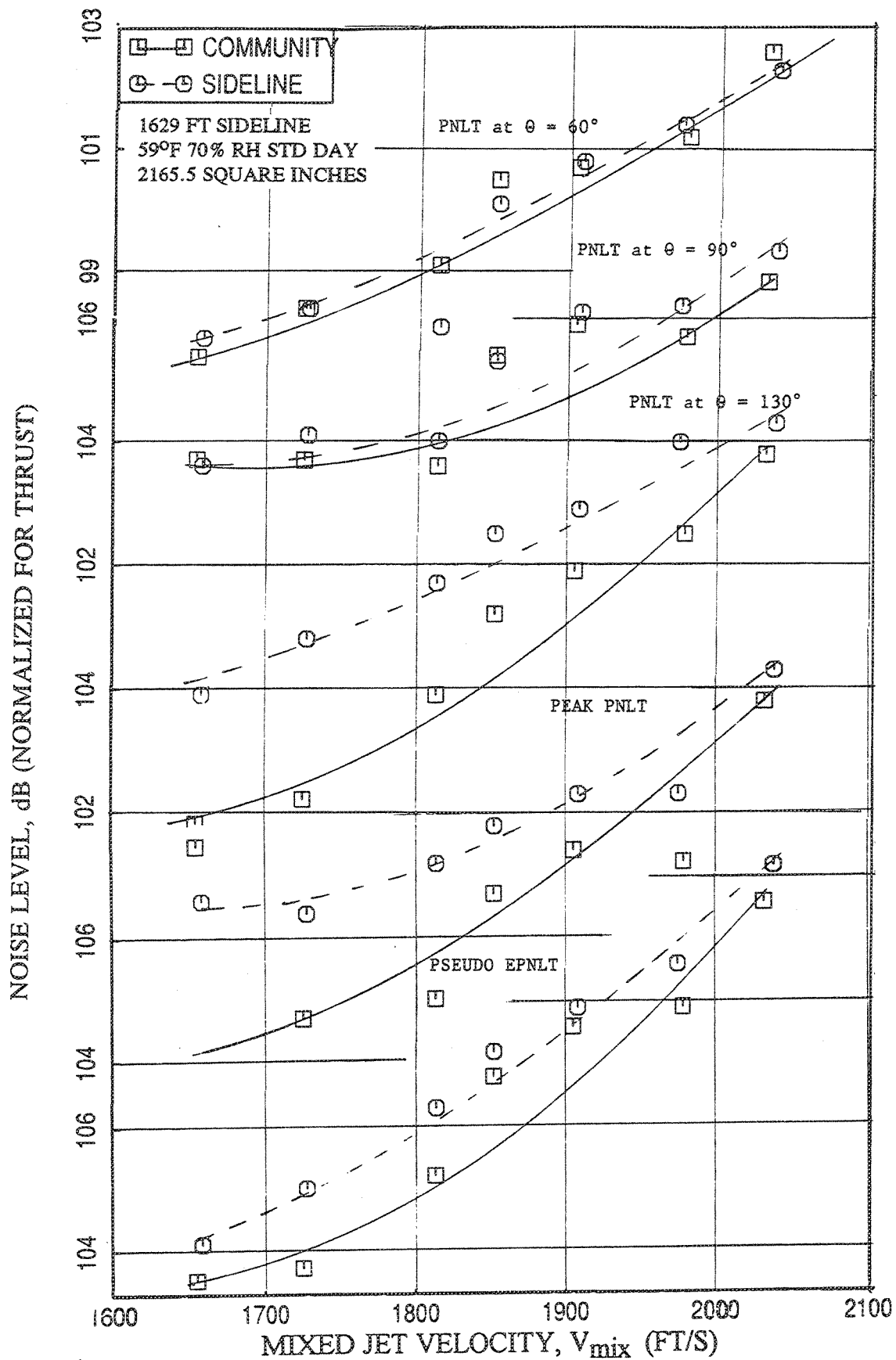


Figure 2.10-34. Comparison of PNLTs at different polar angles ( $\theta$ ), peak PNL, and pseudo EPNLT between the sideline and community points as a function of jet velocity,  $V_{mix}$  for 0.75"-thick fluid shield nozzle at static condition.

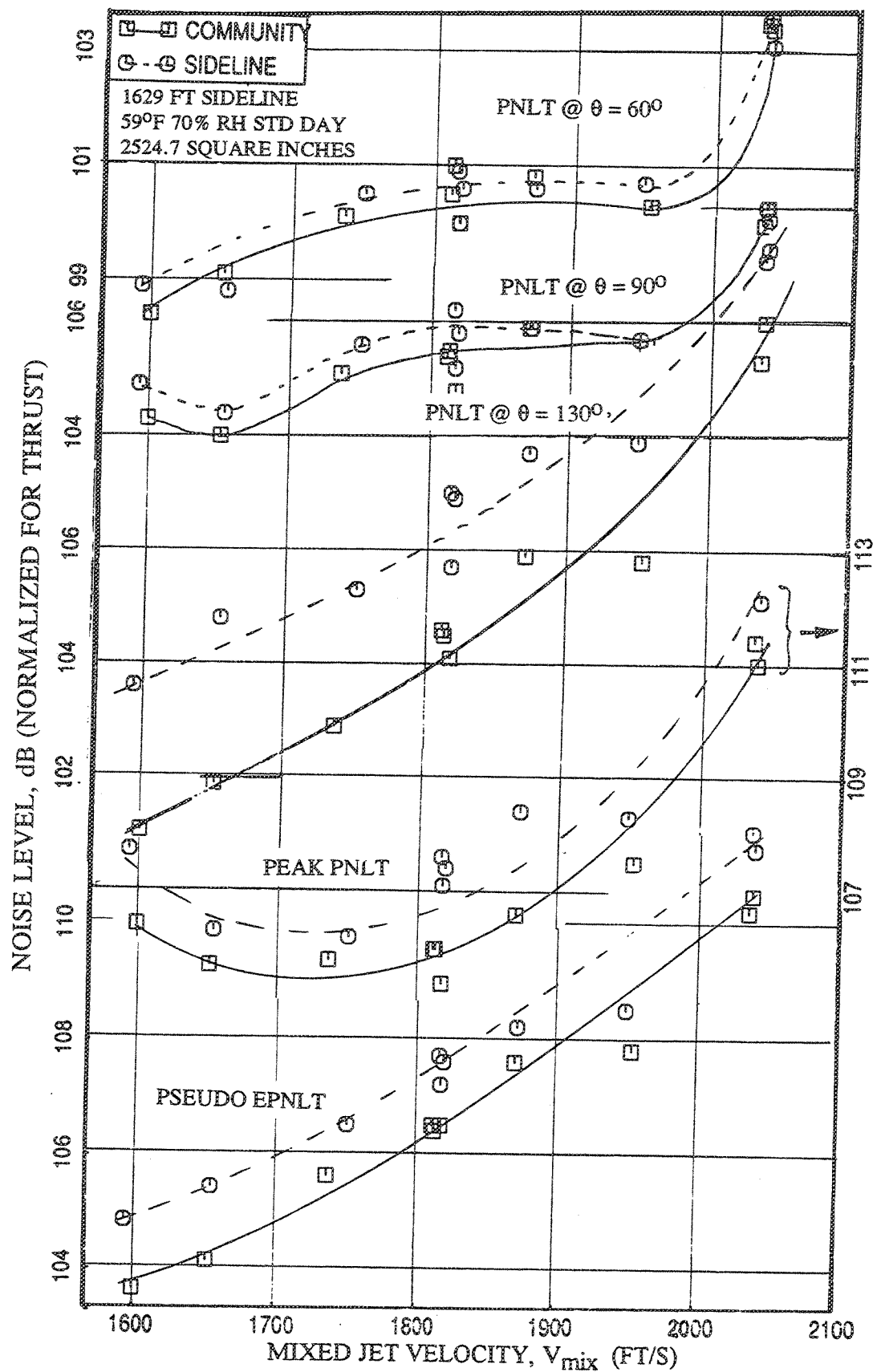


Figure 2.10-35. Comparison of PNLTs at different polar angles ( $\theta$ ), peak PNLT, and pseudo EPNLT between the sideline and community points as a function of jet velocity,  $V_{mix}$  for 1.0"-thick fluid shield nozzle at static condition.

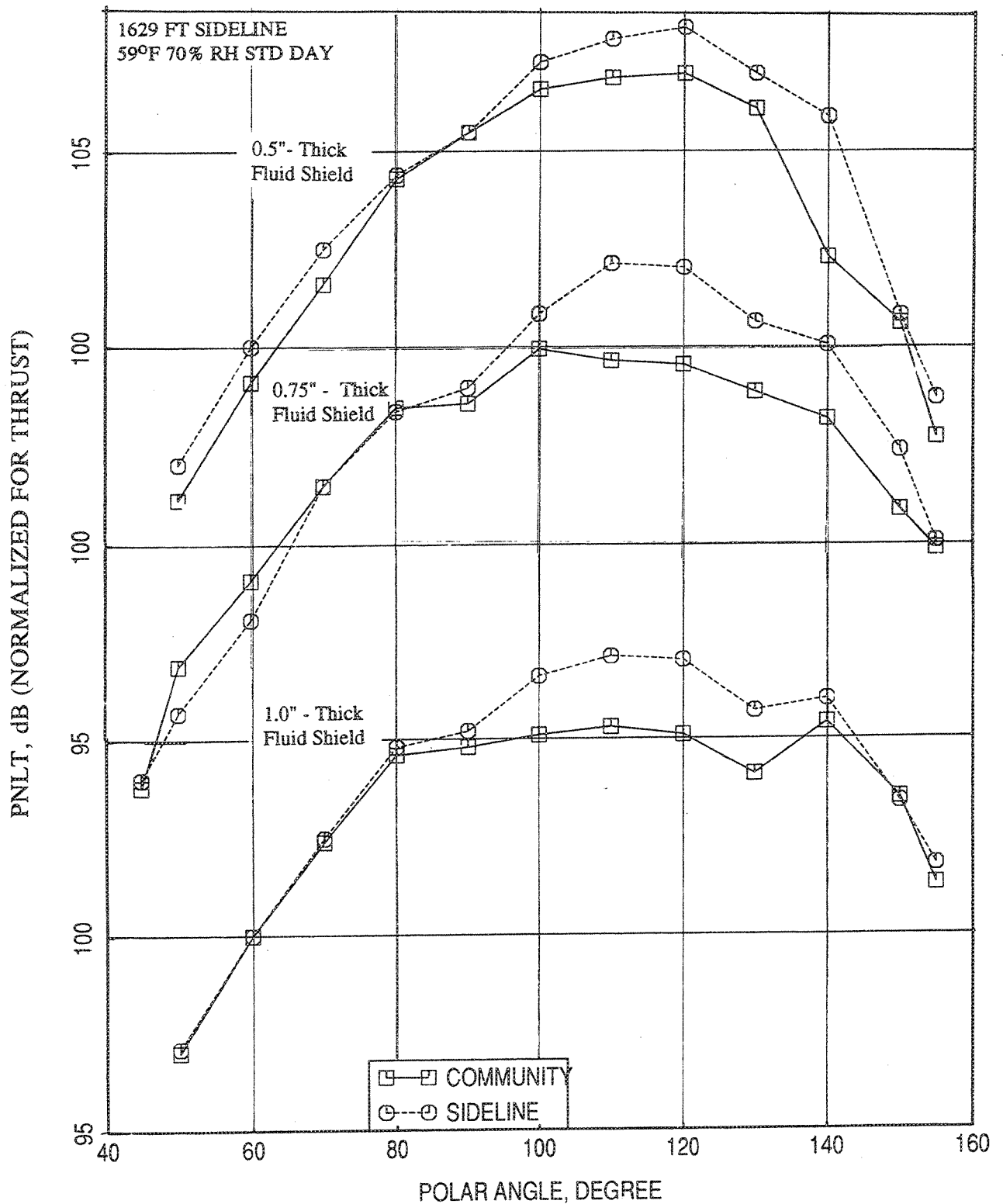


Figure 2.10-36. Comparison of PNL T directivities between the sideline and community points for three fluid shield nozzles at a jet velocity,  $V_{mix}=1811$  ft/sec at static condition.

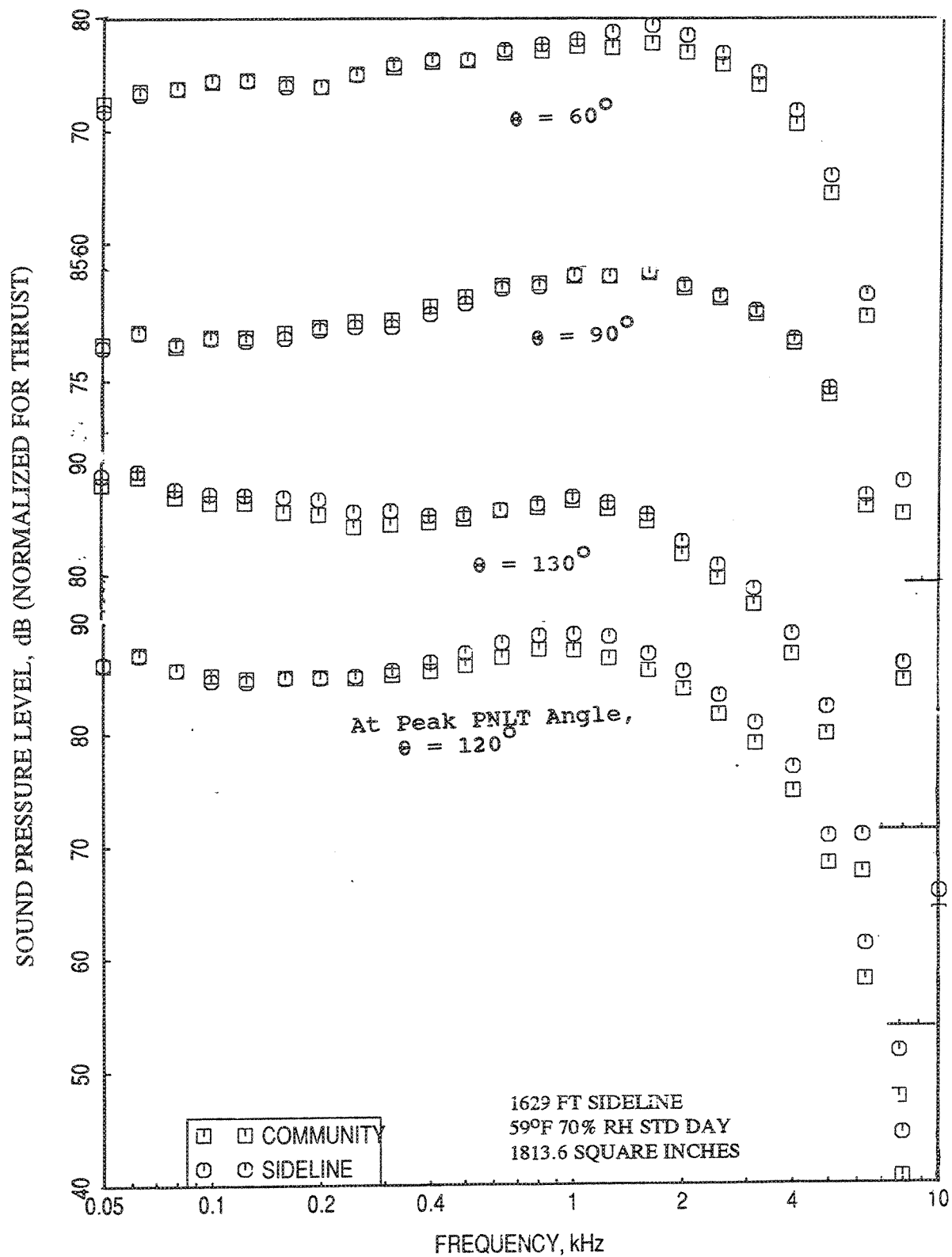


Figure 2.10-37. Comparison of SPL spectra at different polar angles ( $\theta$ ), between the sideline and community points for 0.5"-thick fluid shield nozzle at a jet velocity,  $V_{\text{mix}}=1811$  ft/sec at static condition.

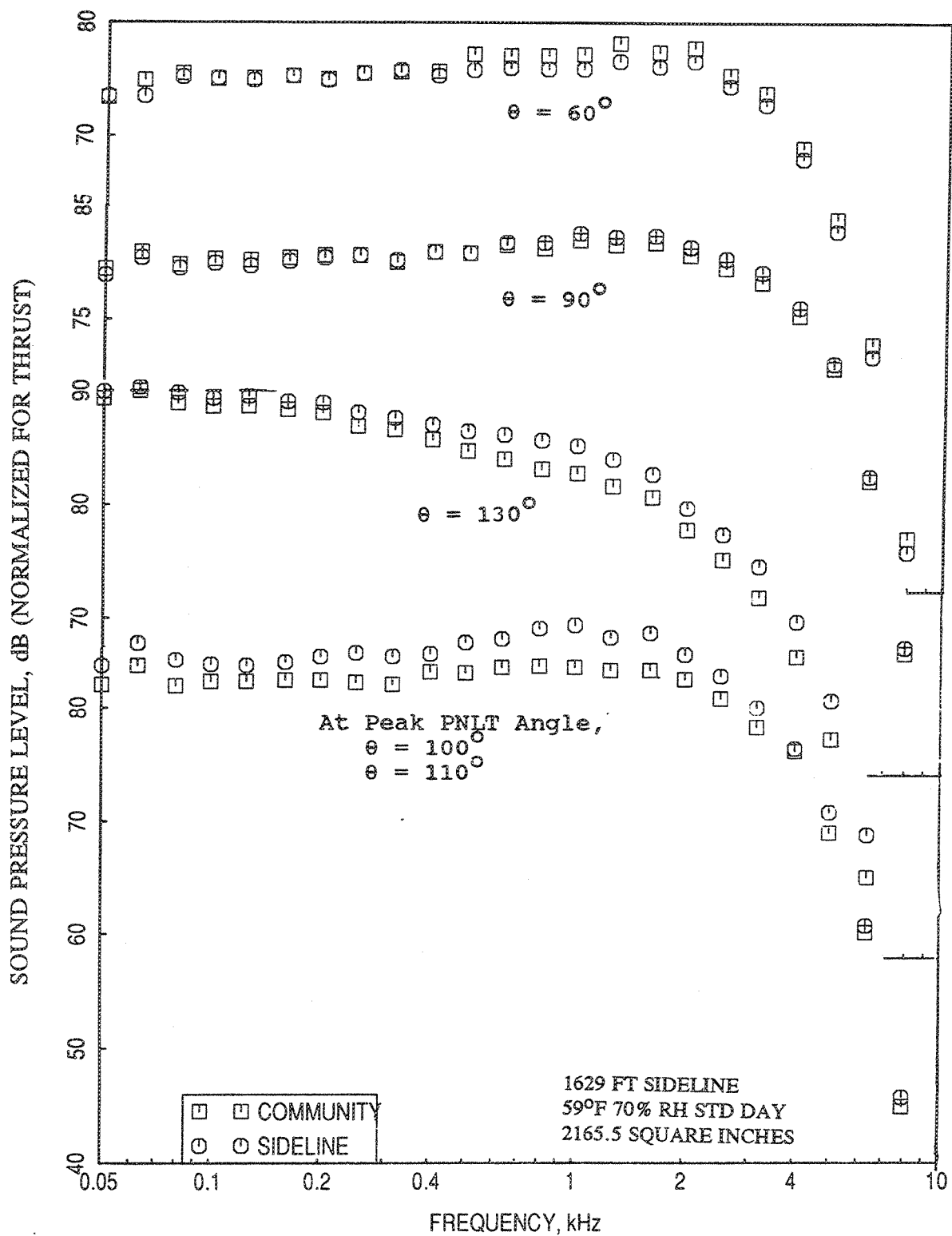


Figure 2.10-38. Comparison of SPL spectra at different polar angles ( $\theta$ ), between the sideline and community points for 0.75"-thick fluid shield nozzle at a jet velocity,  $V_{\text{mix}}=1811$  ft/sec at static condition.

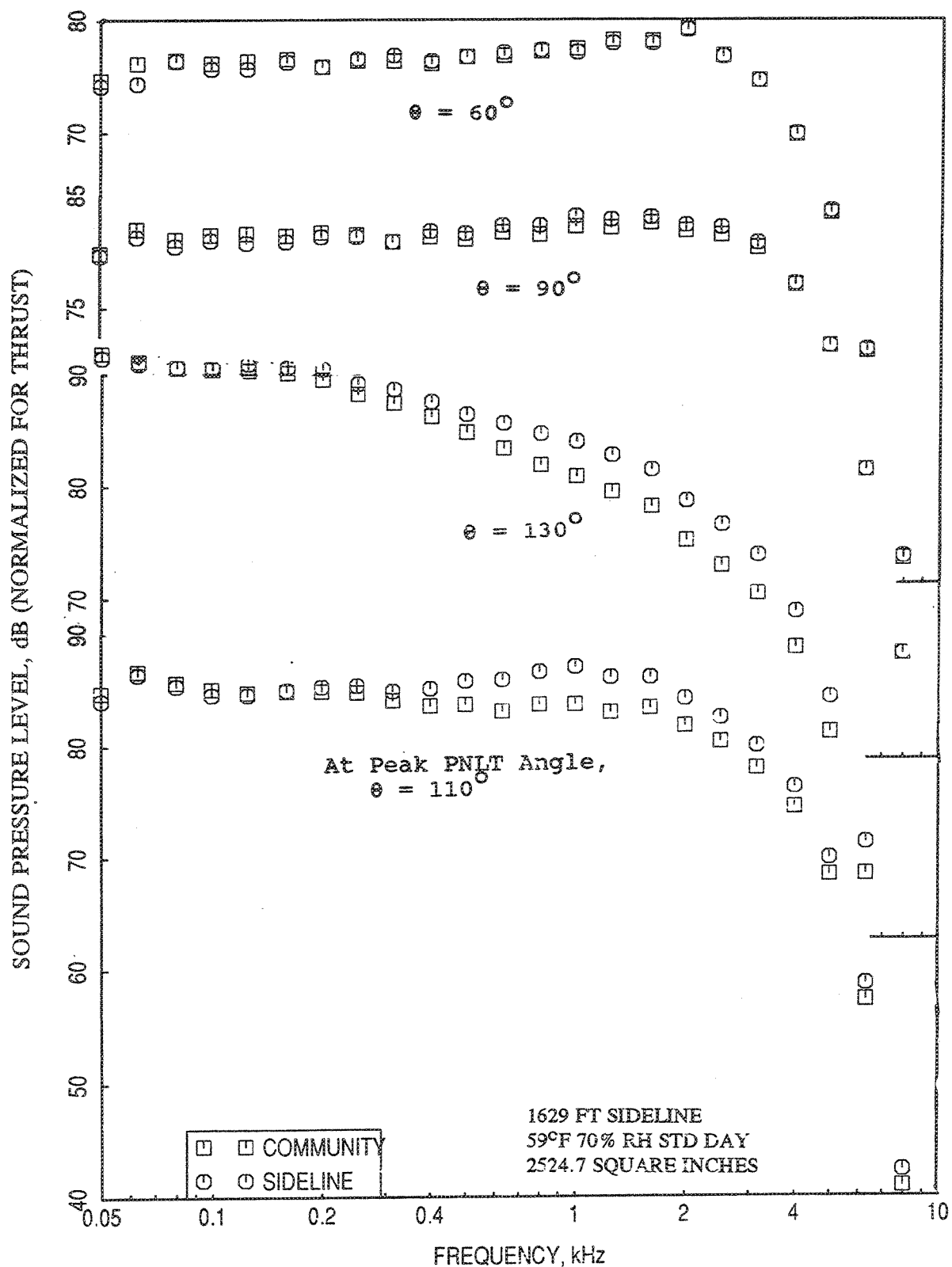


Figure 2.10-39. Comparison of SPL spectra at different polar angles ( $\theta$ ), between the sideline and community points for 1.0"-thick fluid shield nozzle at a jet velocity,  $V_{\text{mix}}=1811$  ft/sec at static condition.



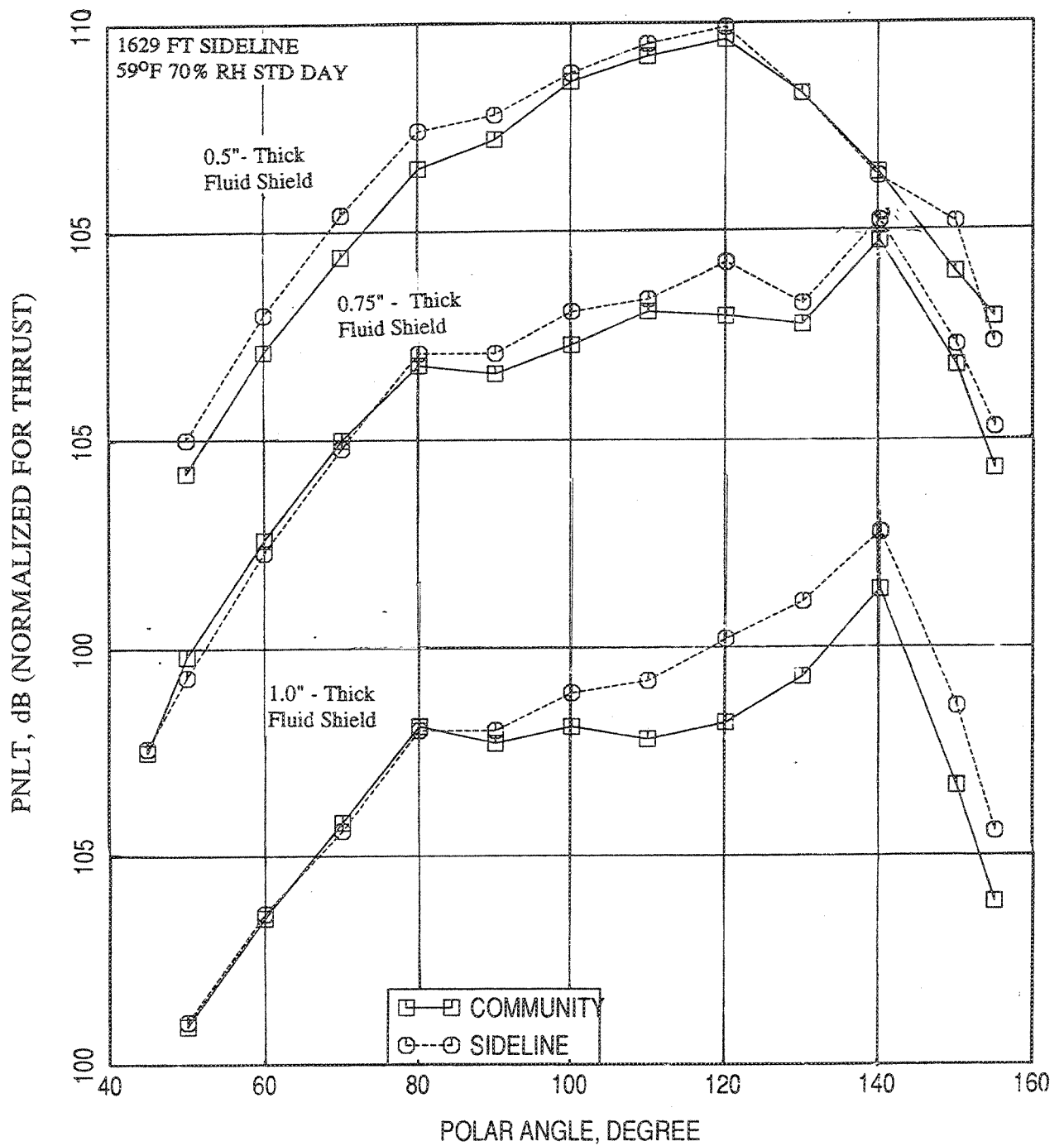


Figure 2.10-40. Comparison of PNL T directivities between the sideline and community points for three fluid shield nozzles at a jet velocity,  $V_{mix} = 2030$  ft/sec at static condition.

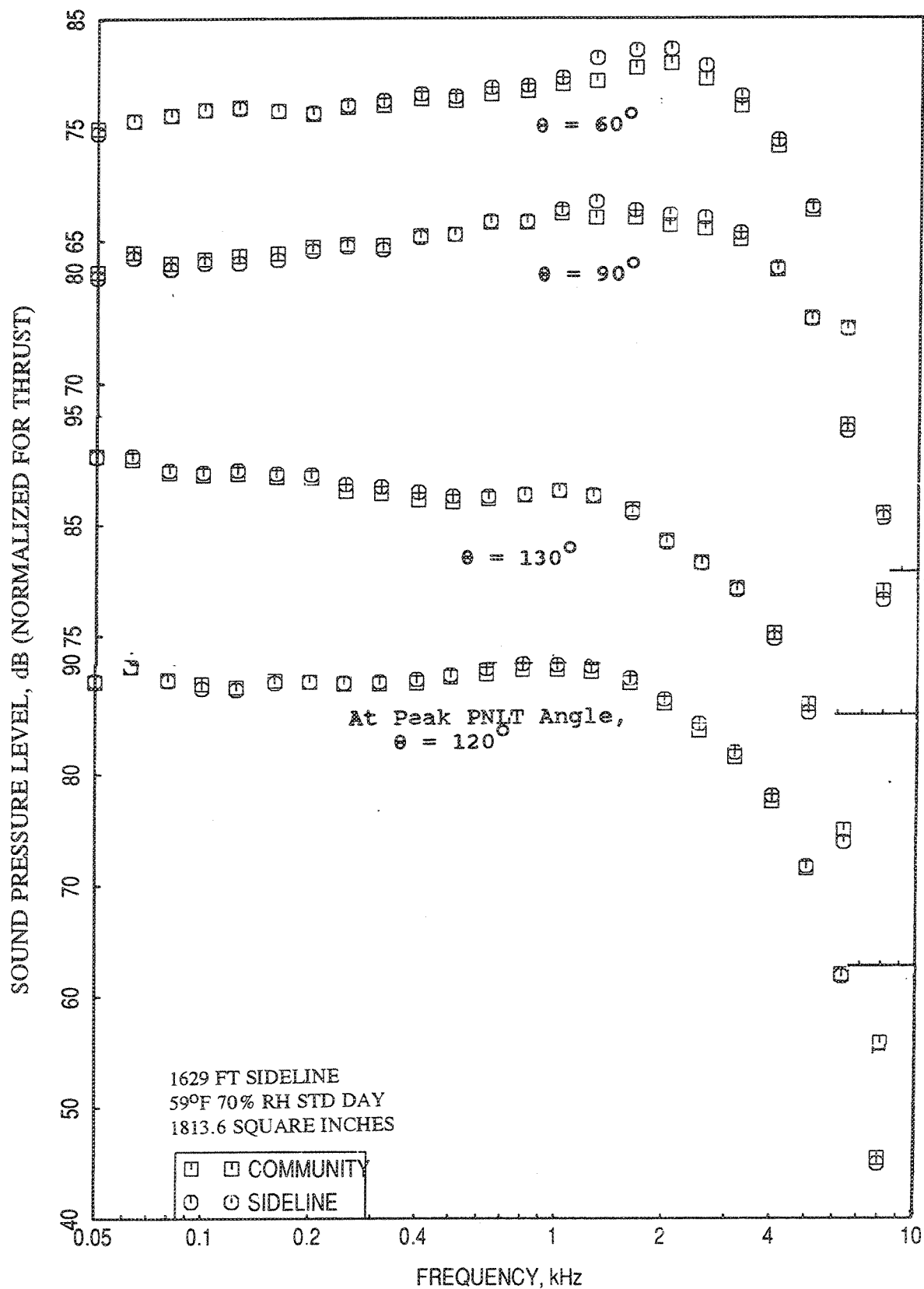


Figure 2.10-41. Comparison of SPL spectra at different polar angles ( $\theta$ ), between the sideline and community points for 0.5"-thick fluid shield nozzle at a jet velocity,  $V_{mix}=2030$  ft/sec at static condition.

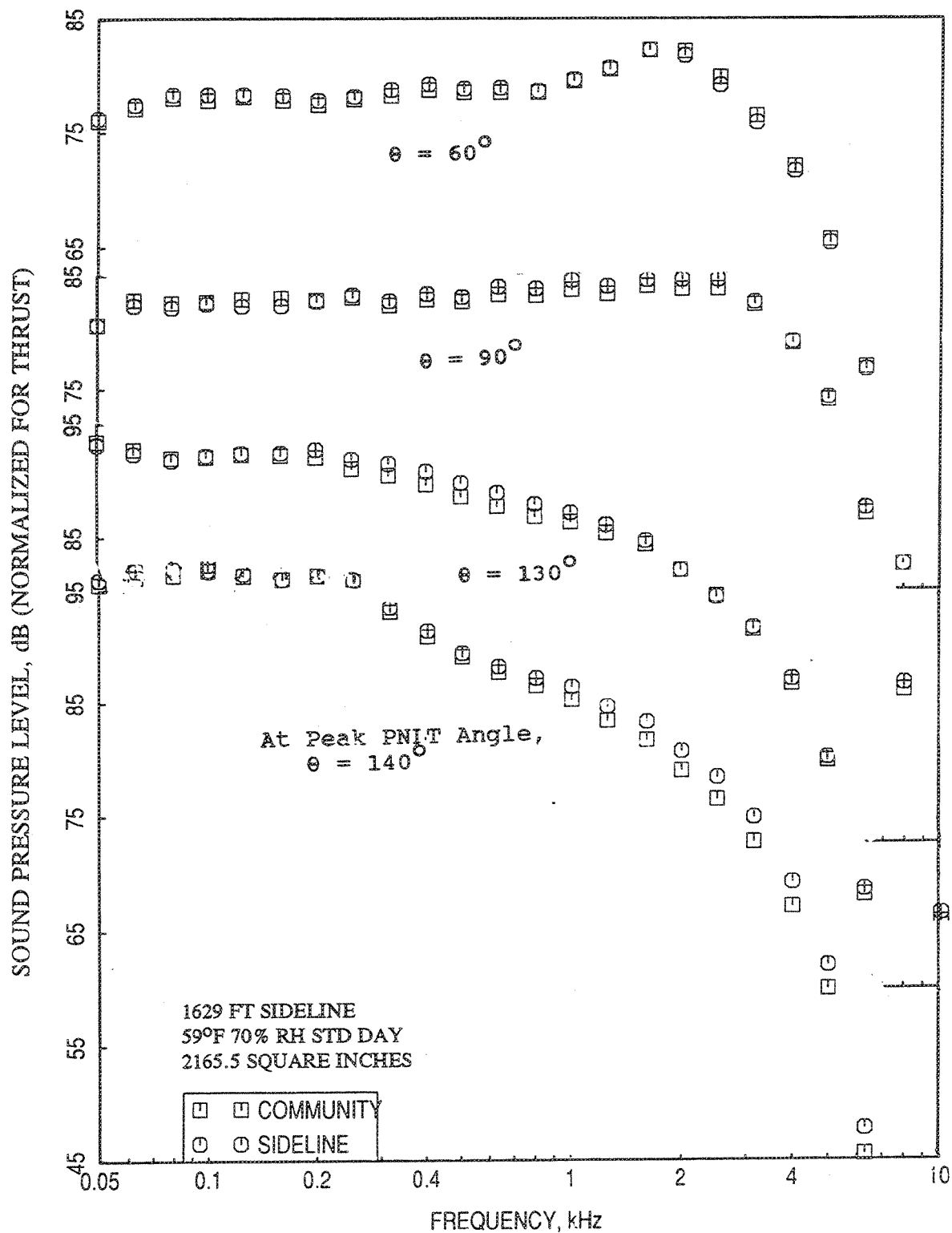


Figure 2.10-42. Comparison of SPL spectra at different polar angles ( $\theta$ ), between the sideline and community points for 0.75"-thick fluid shield nozzle at a jet velocity,  $V_{\text{mix}}=2030$  ft/sec at static condition.

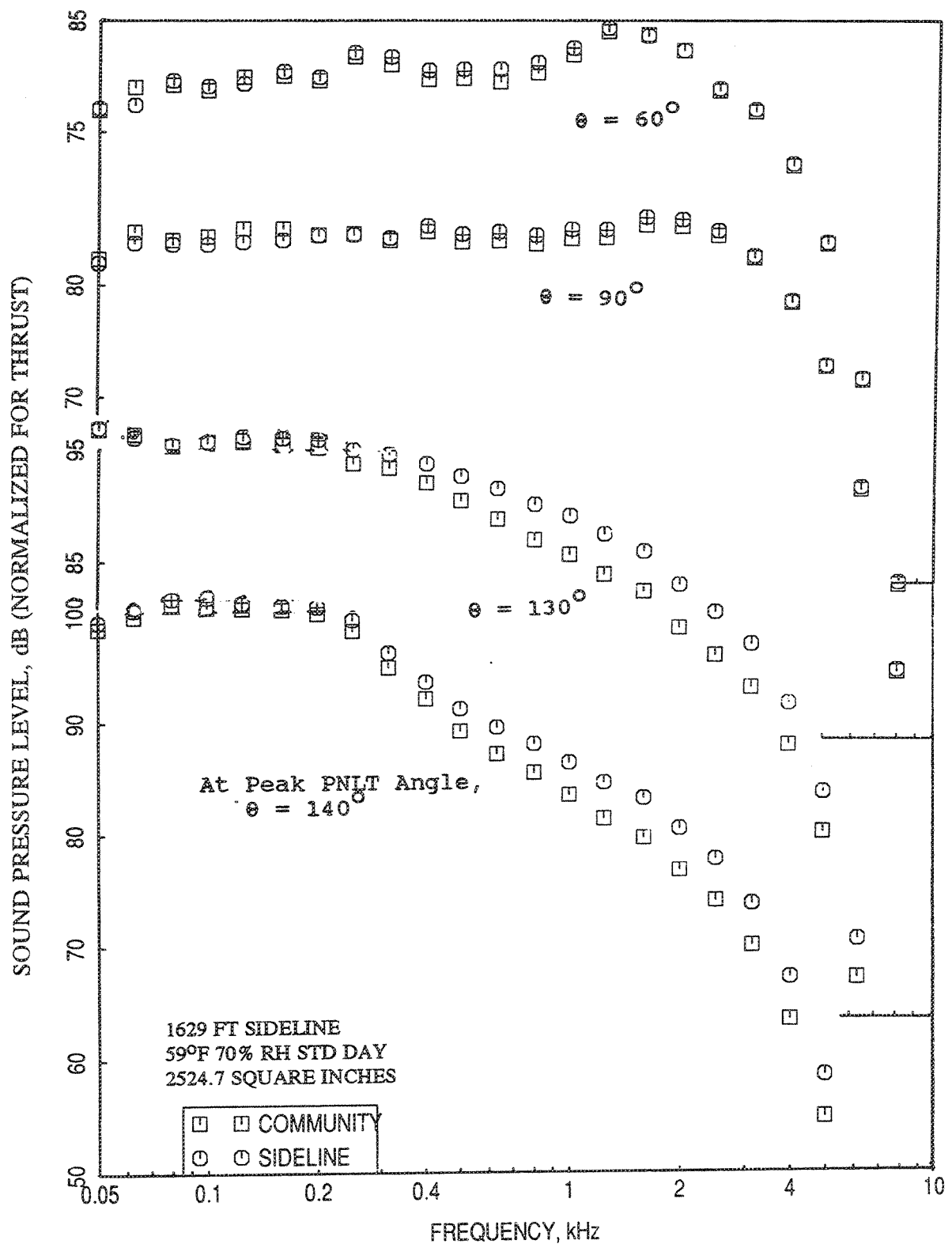


Figure 2.10-43. Comparison of SPL spectra at different polar angles ( $\theta$ ), between the sideline and community points for 1.0"-thick fluid shield nozzle at a jet velocity,  $V_{\text{mix}}=2030$  ft/sec at static condition.

**Flight Simulation Data :** Similar to static case, the data with flight simulation are presented in Figures 2.10-44 through 2.10-54. These results are obtained with a simulated flight Mach number of 0.32. These results show the similar trends as observed with static data.

**Conclusions :** The most important observation is that the azimuthal variation of farfield noise is relatively less dominant. The fluid shield with higher shield thickness is more effective in shielding the noise. Azimuthal noise variation is insignificant with subsonic shield flow. With flight simulation azimuthal noise variation increases compared to the static case. Spectral SPL variation with respect to azimuthal angle is more prominent in the rear arc.

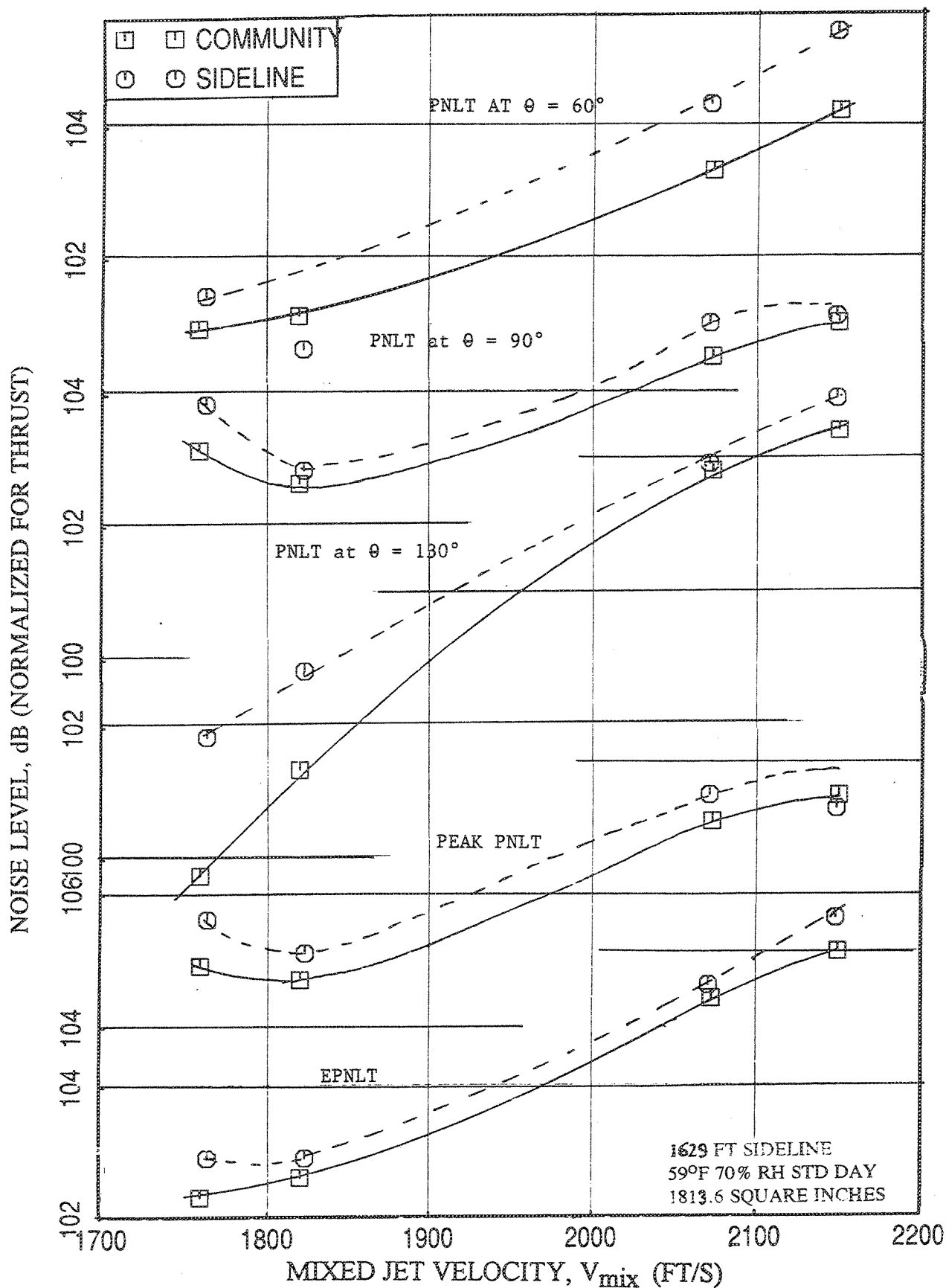


Figure 2.10-44. Comparison of PNLTs at different polar angles ( $\theta$ ), peak PNLT and pseudo EPNLT between the sideline and community points as a function of jet velocity,  $V_{mix}$  for 0.5"-thick fluid shield nozzle with flight simulation ( $M_F=0.32$ ).

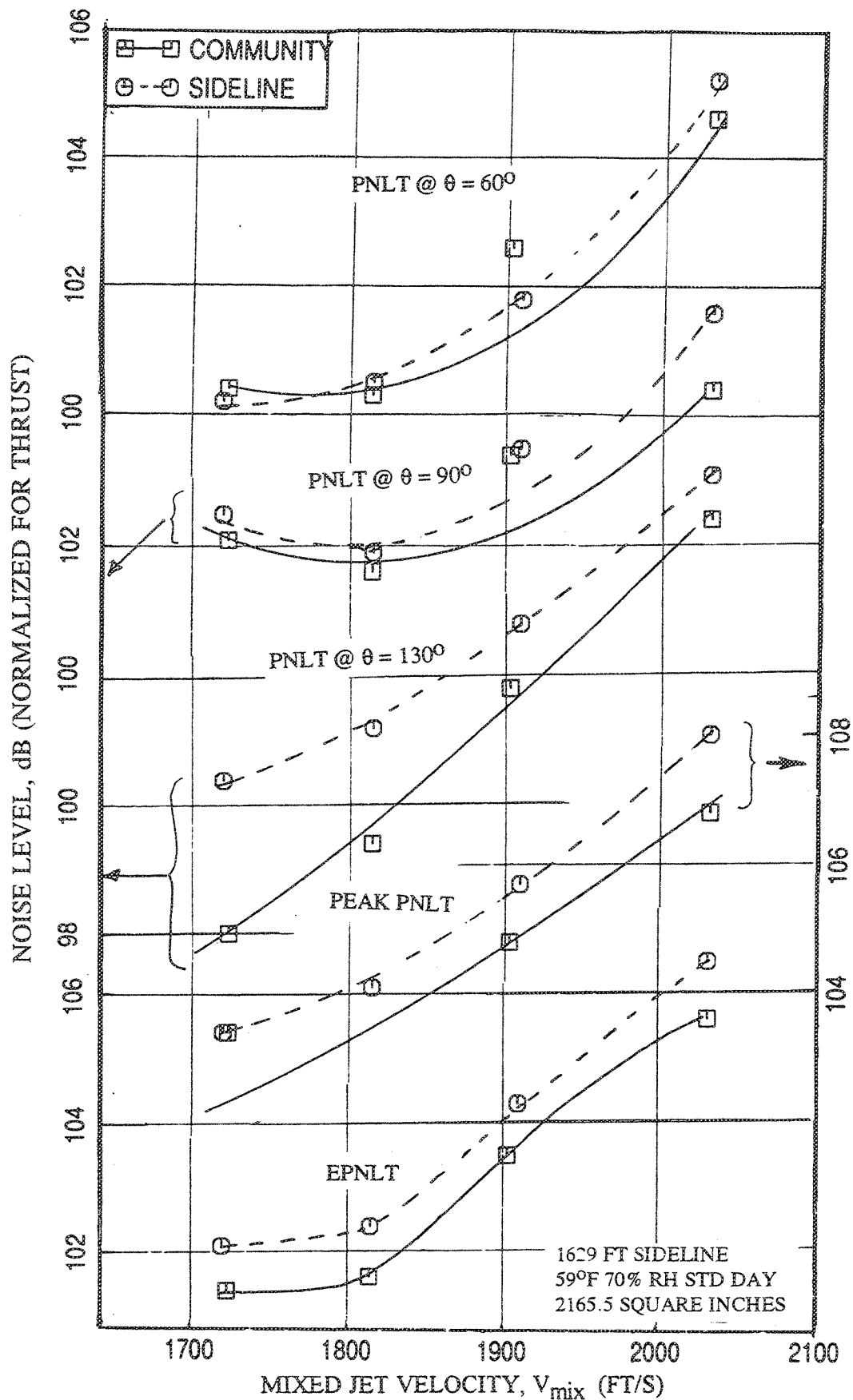


Figure 2.10-45. Comparison of PNLTs at different polar angles ( $\theta$ ), peak PNLT, and pseudo EPNLT between the sideline and community points as a function of jet velocity,  $V_{MIX}$  for 0.75"-thick fluid shield nozzle with flight simulation ( $M_F=0.32$ ).

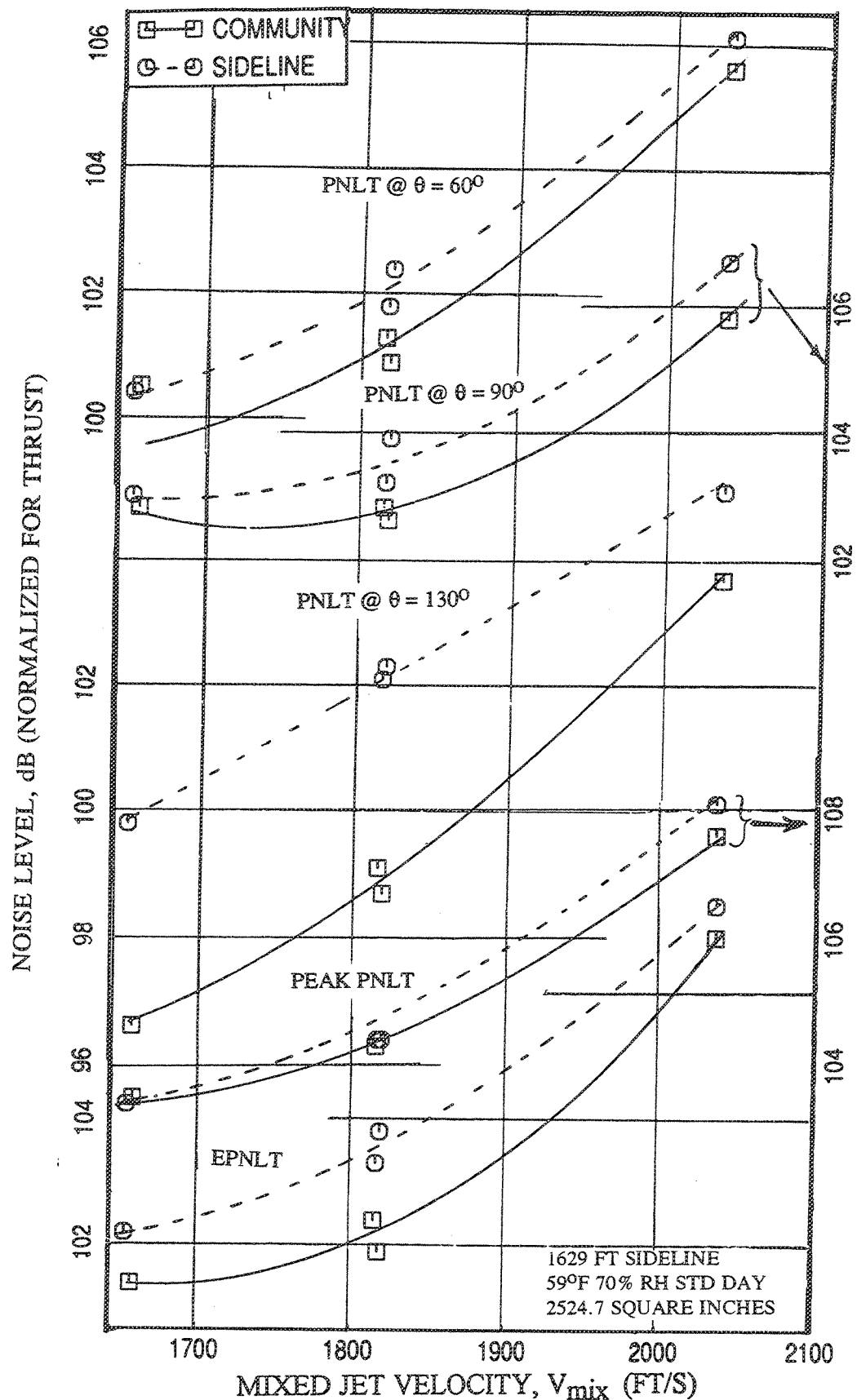


Figure 2.10-46. Comparison of PNLTs at different polar angles ( $\theta$ ), peak PNLT, and pseudo EPNLT between the sideline and community points as a function of jet velocity,  $V_{mix}$  for 1.0"-thick fluid shield nozzle with flight simulation ( $M_F=0.32$ ).



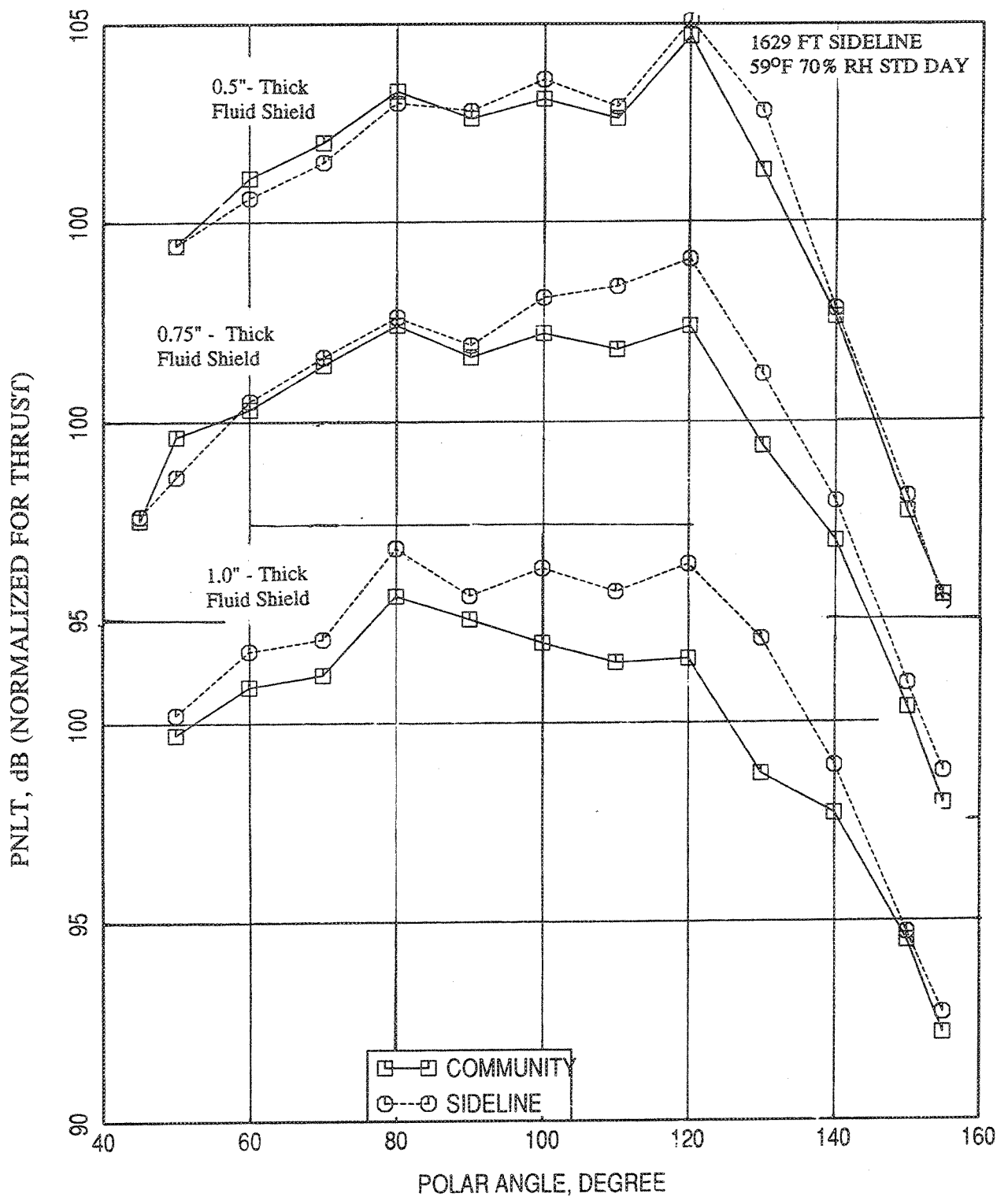


Figure 2.10-47. Comparison of PNLT directivities between the sideline and community points for three fluid shield nozzles at a jet velocity,  $V_{mix} = 1811$  ft/sec with flight simulation ( $M_F=0.32$ ).

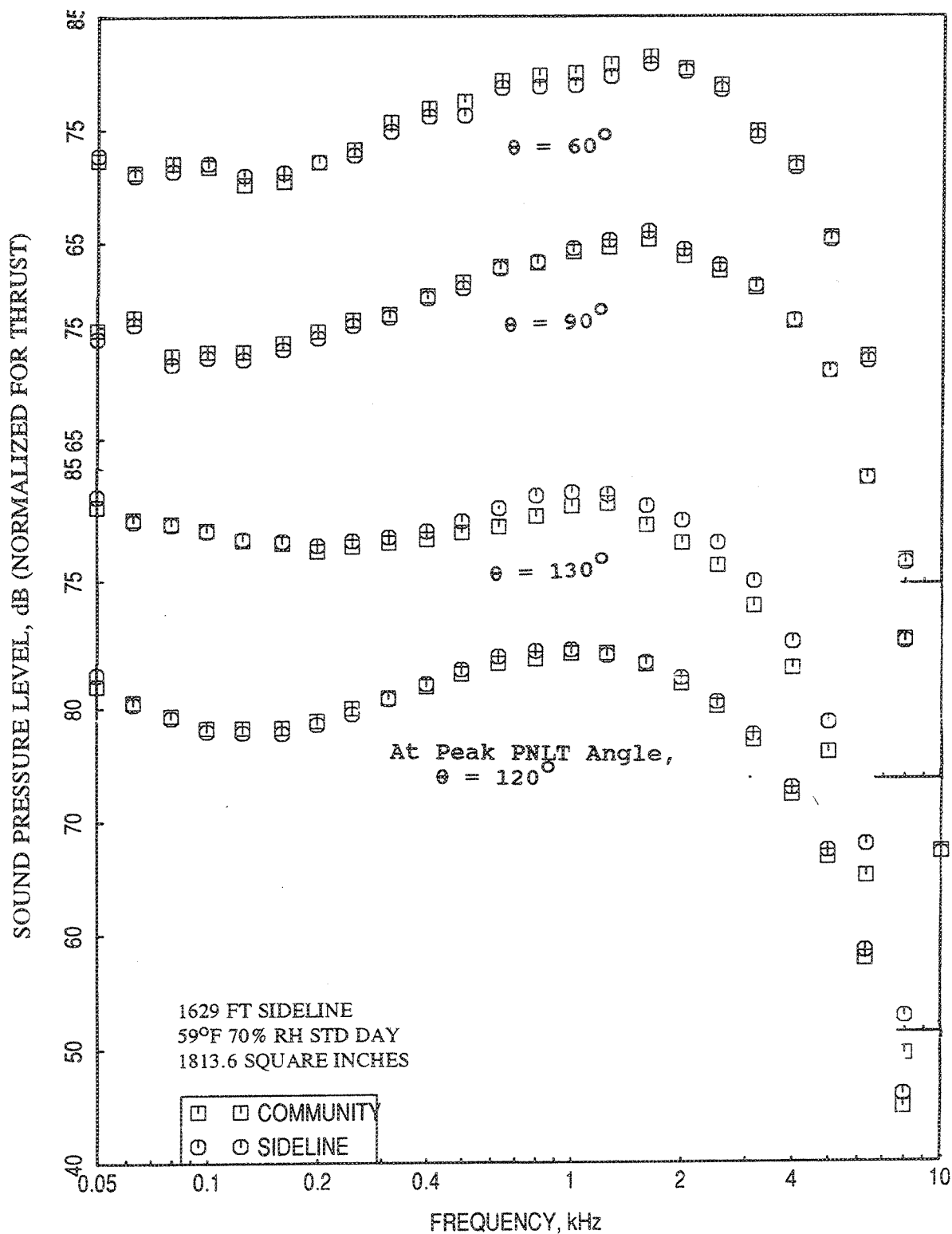


Figure 2.10-48. Comparison of SPL spectra at different polar angles ( $\theta$ ), between the sideline and community points for 0.5"-thick fluid shield nozzle at a jet velocity,  $V_{\text{mix}}=1811$  ft/sec with flight simulation ( $M_F=0.32$ ).

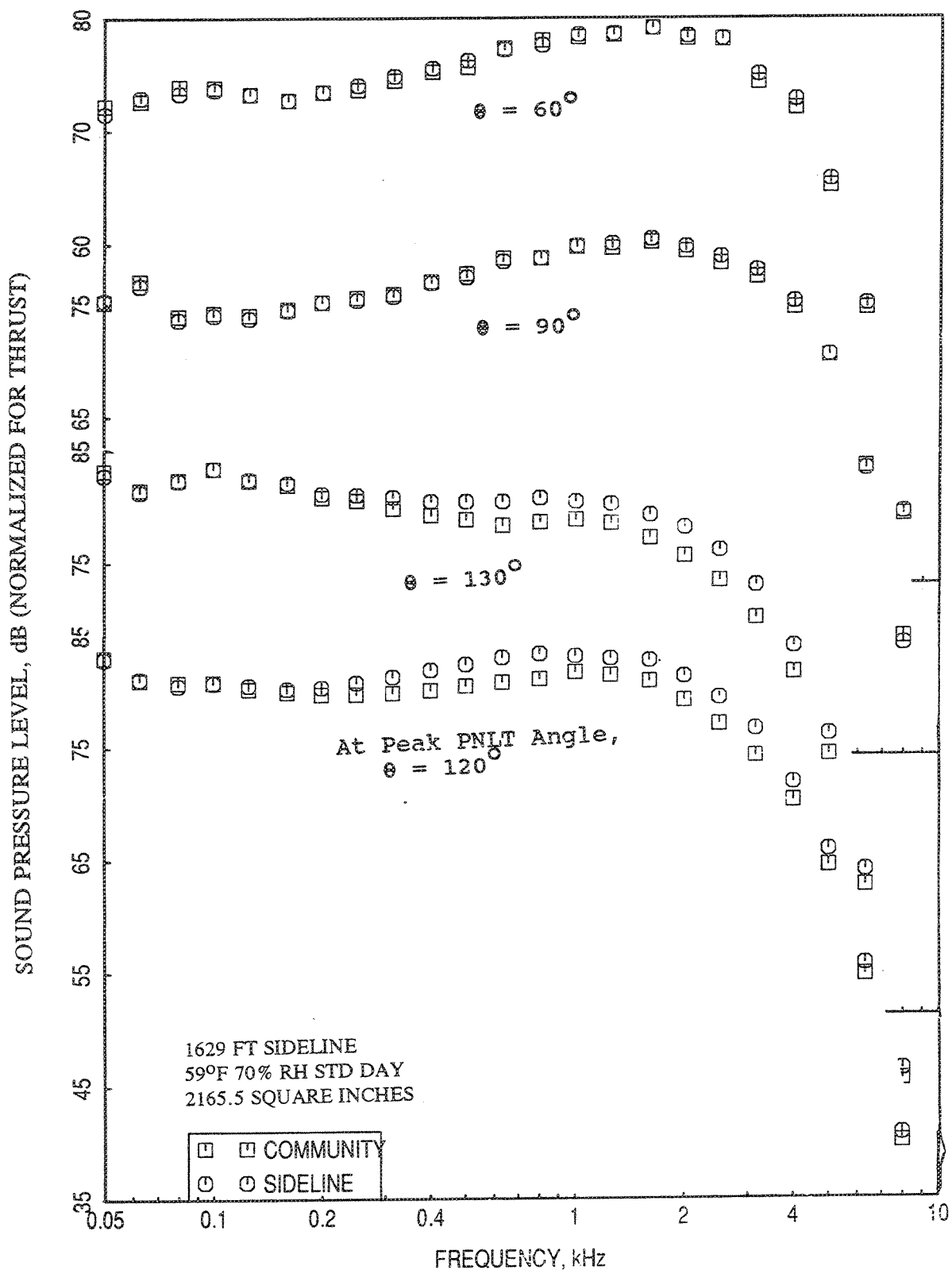


Figure 2.10-49. Comparison of SPL spectra at different polar angles ( $\theta$ ), between the sideline and community points for 0.75"-thick fluid shield nozzle at a jet velocity,  $V_{mix}=1811$  ft/sec with flight simulation ( $M_F=0.32$ ).

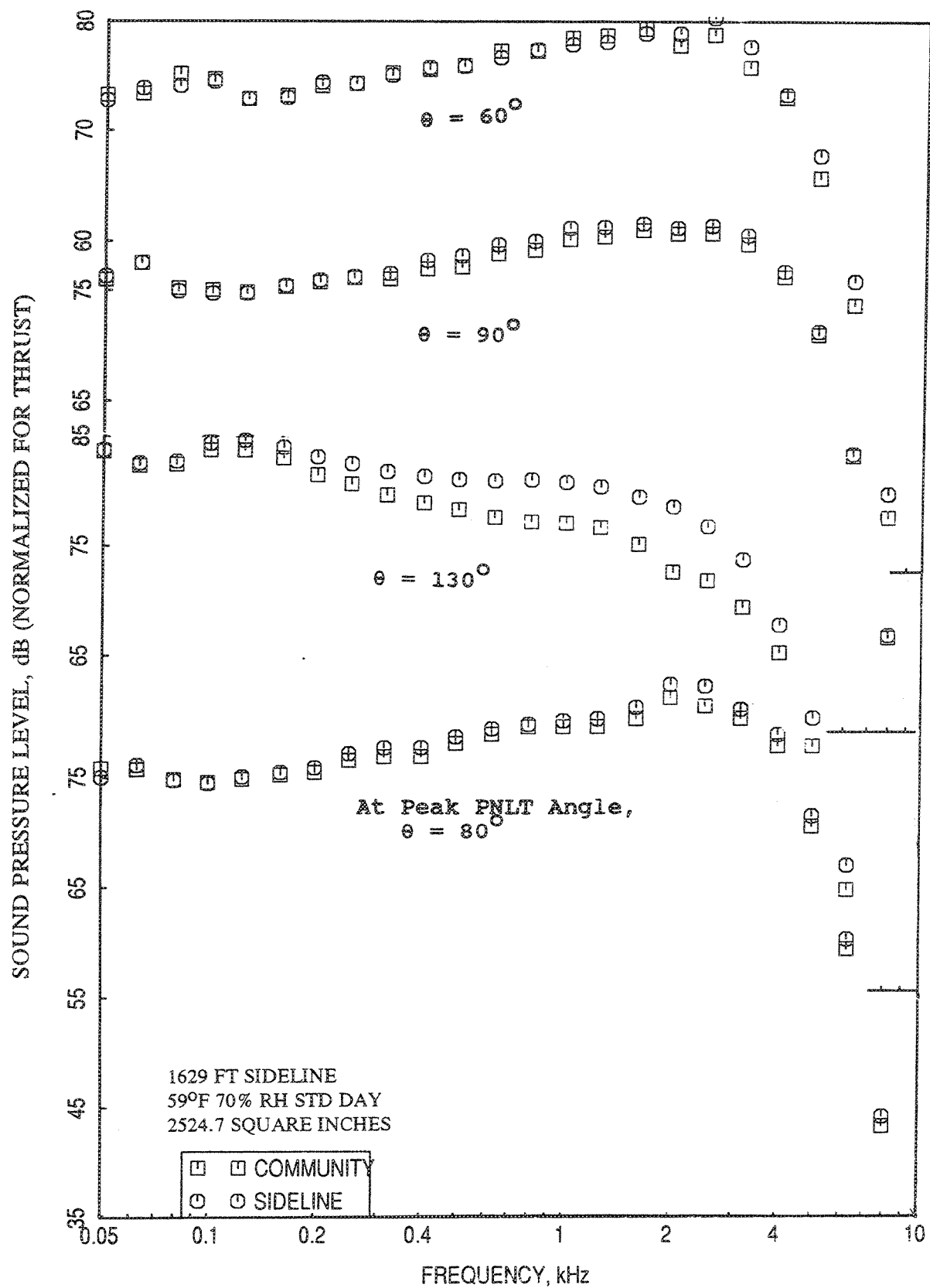


Figure 2.10-50. Comparison of SPL spectra at different polar angles ( $\theta$ ), between the sideline and community points for 1.0"-thick fluid shield nozzle at a jet velocity,  $V_{\text{mix}}=1811$  ft/sec with flight simulation ( $M_F=0.32$ ).

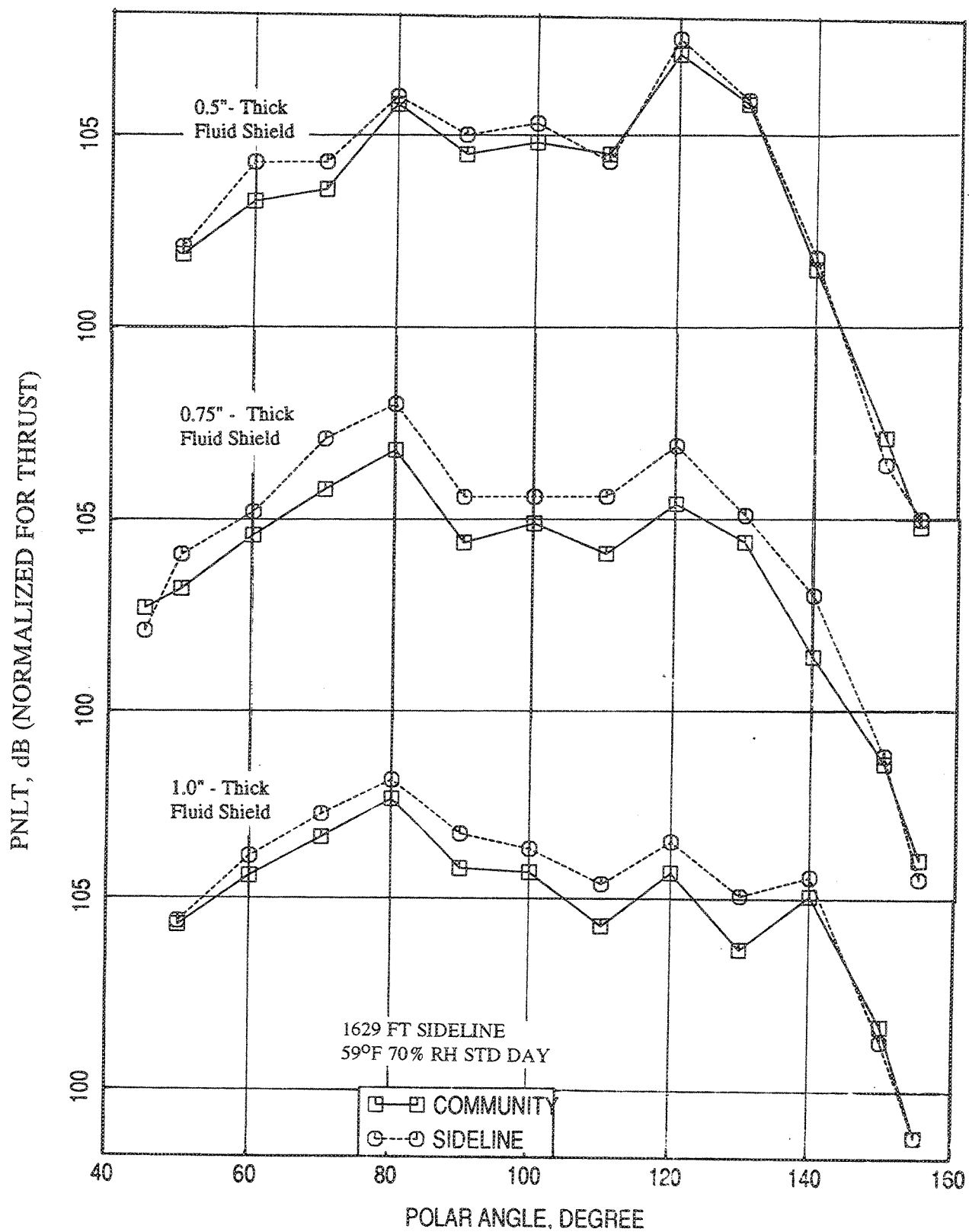


Figure 2.10-51. Comparison of PNLT directivities between the sideline and community points for three fluid shield nozzles at a jet velocity,  $V_{\text{mix}} = 2030$  ft/sec with flight simulation ( $M_F=0.32$ ).

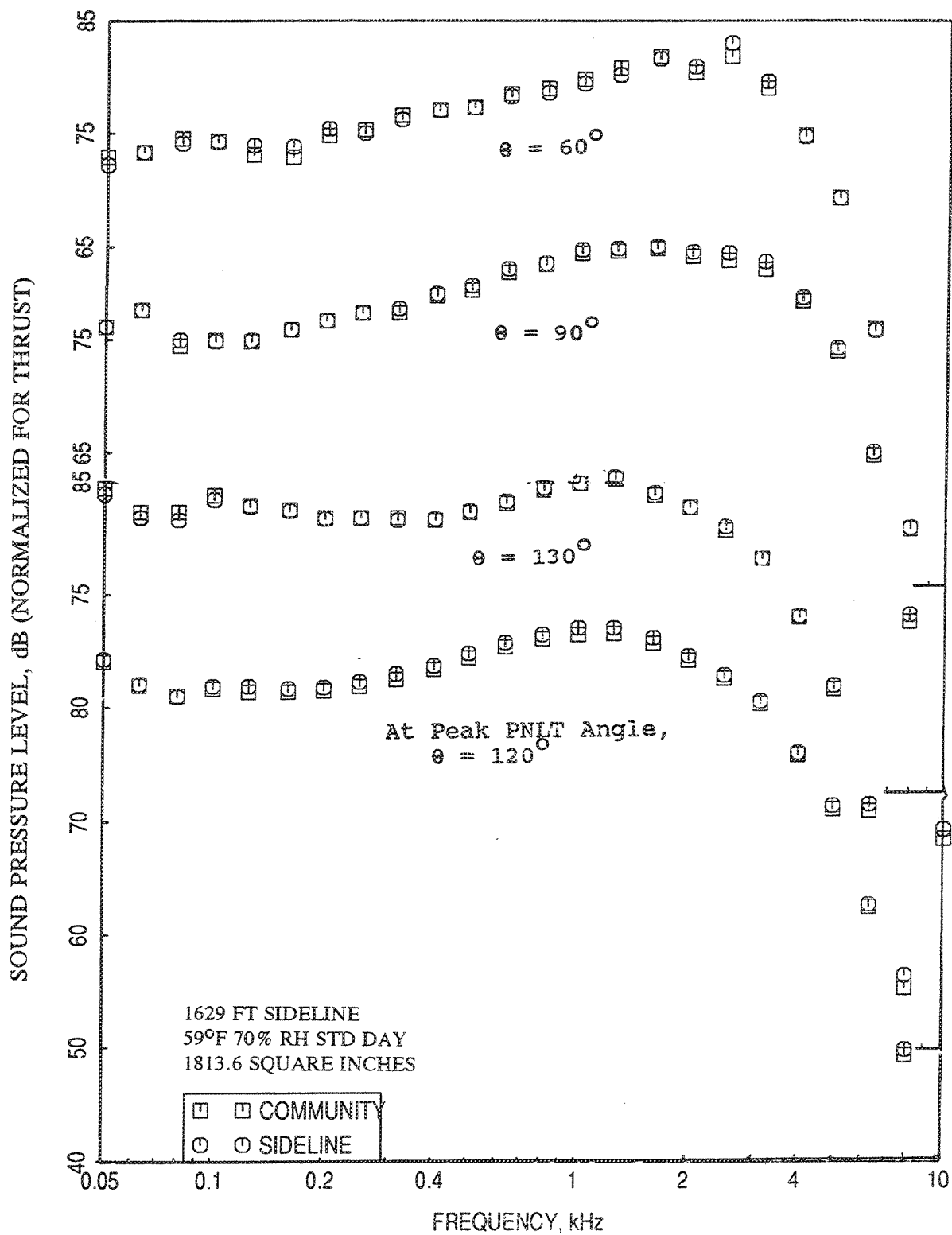


Figure 2.10-52. Comparison of SPL spectra at different polar angles ( $\theta$ ), between the sideline and community points for 0.5"-thick fluid shield nozzle at a jet velocity,  $V_{\text{mix}}=2030$  ft/sec with flight simulation ( $M_F=0.32$ ).

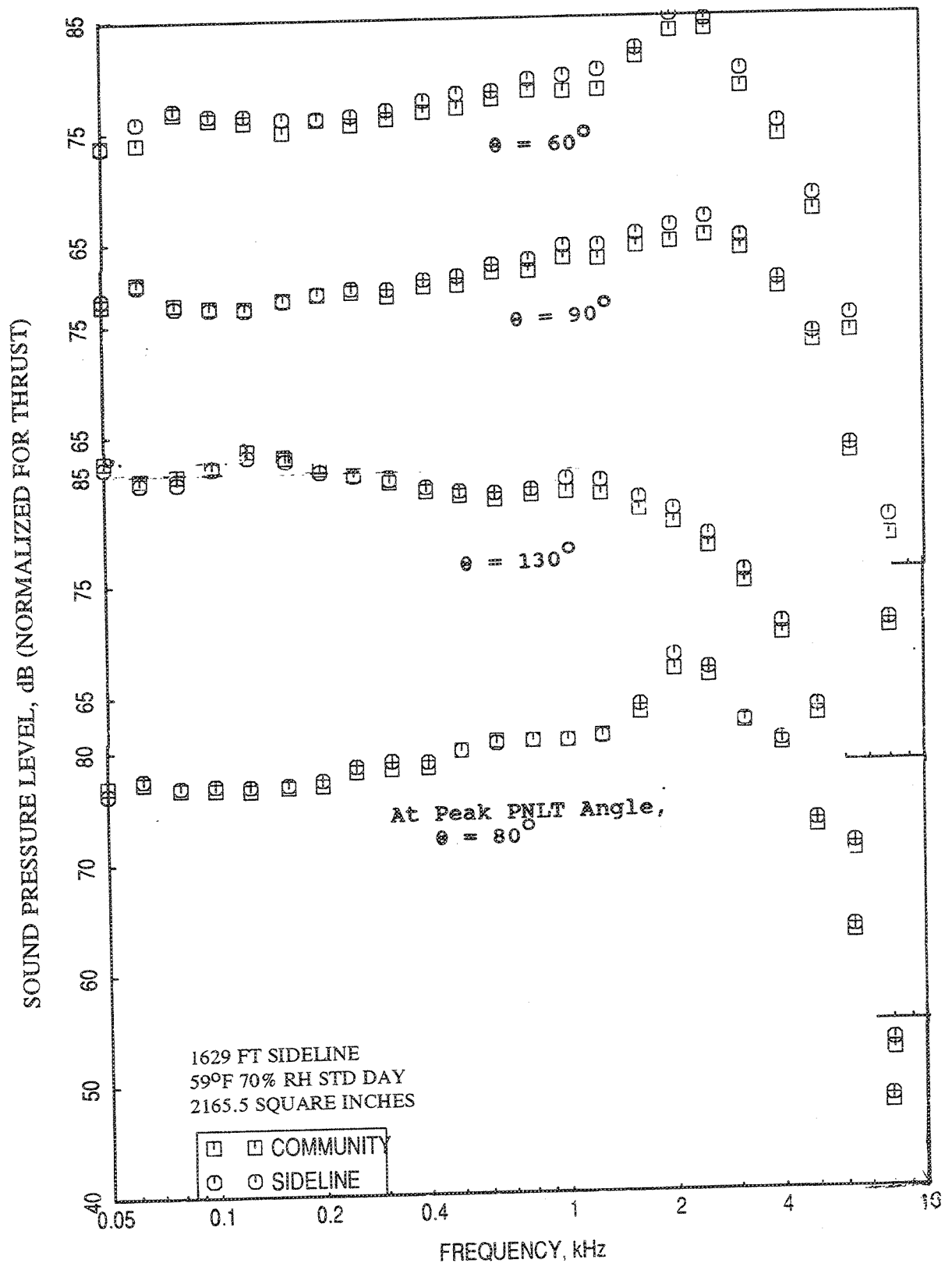


Figure 2.10-53. Comparison of SPL spectra at different polar angles ( $\theta$ ), between the sideline and community points for 0.75"-thick fluid shield nozzle at a jet velocity,  $V_{\text{mix}}=2030$  ft/sec with flight simulation ( $M_F=0.32$ ).

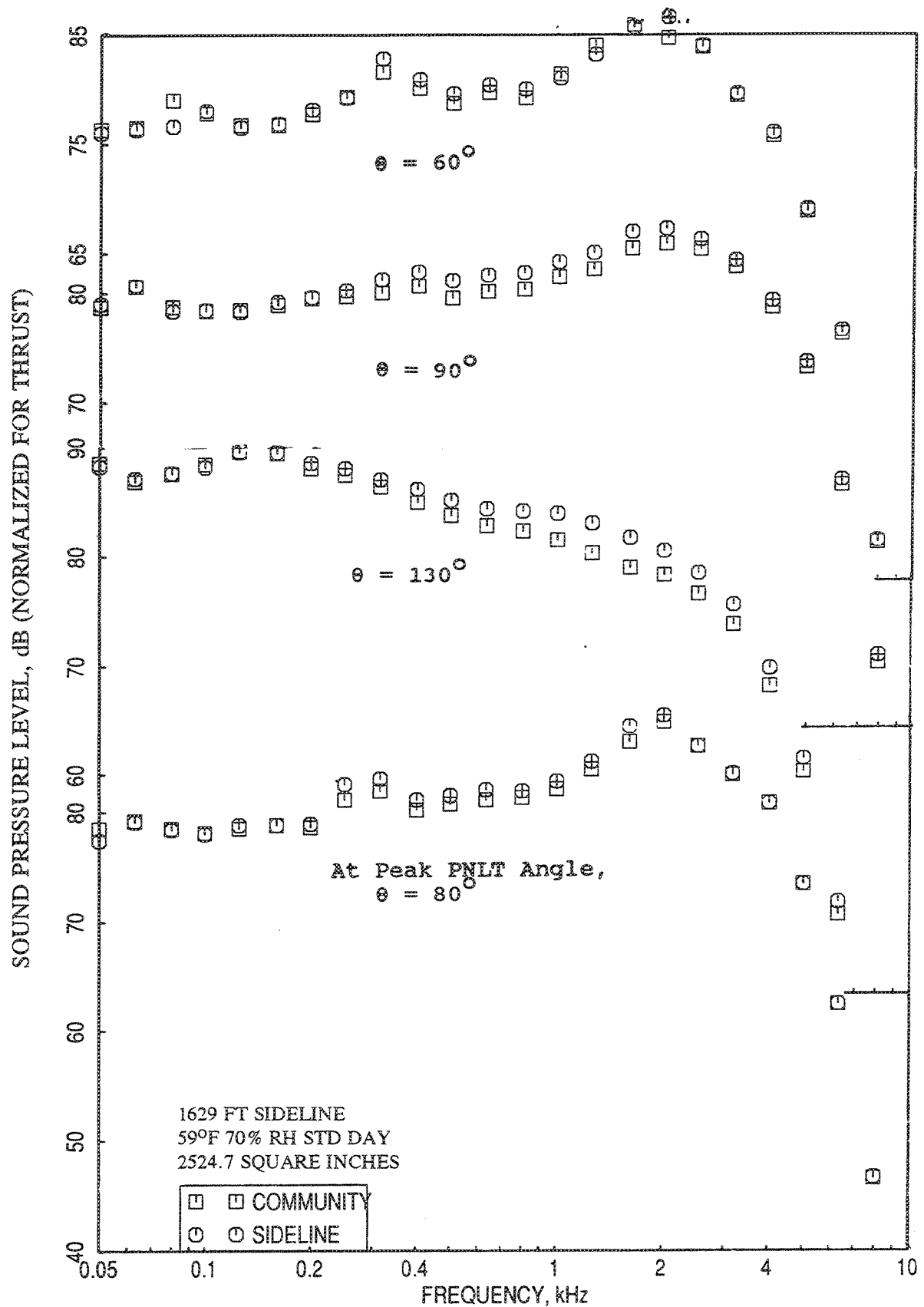


Figure 2.10-54. Comparison of SPL spectra at different polar angles ( $\theta$ ), between the sideline and community points for 1.0"-thick fluid shield nozzle at a jet velocity,  $V_{\text{mix}}=2030$  ft/sec with flight simulation ( $M_F=0.32$ ).



## **2.11 EFFECT OF FLIGHT SIMULATION ON ACOUSTIC CHARACTERISTICS OF FLUID SHIELD NOZZLE CONFIGURATIONS**

It is well known that the noise generated by a jet is considerably effected by flight. Full-scale flight testing is a direct method for obtaining the required levels without using any theory or intermediate steps. However, full-scale flight testing is very expensive and has other problems associated with measurement techniques. Hence, flight simulation on the ground for scale-model nozzle is an attractive alternative to assess the effect of flight on jet noise. For the current program tests were conducted with flight simulation for a Mach number of 0.32 for all the fluid shield nozzle configurations including a single stream conical nozzle and 36-chute suppressor nozzle. For these tests a free-jet is used as a wind tunnel to simulate the effects of flight on model noise sources, with microphones placed outside the free-jet in an anechoic environment. Hence a flight transformation method is utilized to correct the influence of the free-jet shear layer on the transmitted sound, since the shear layer is absent in the flight case. All the results presented in this section are extrapolated to a sideline distance of 1629 feet and are corrected for standard day conditions of 59°F and 70% relative humidity.

### **2.11.1 Single Stream Jets for Convergent Conical and 36-Chute Suppressor Nozzles:**

Before describing the effect of flight on the noise generated by fluid shield nozzle configurations, it is instructive to present some results on the effects of flight on single stream jets for convergent conical nozzle and multi-chute suppressor nozzle. These results are scaled to 1175 square inches.

**Conical Nozzle Results :** Figure 2.11-1 shows the effect of flight on PNLT Levels at various polar angles, peak PNLT, and EPNLT as functions of jet velocity for a 6.54 square inch conical nozzle. Except for forward arc angles the PNLT levels are decreased due to flight at all jet velocities. At subsonic jet velocities the PNLT reduction due to flight is also observed at forward angles. Peak PNLT and EPNLT levels reduce due to flight at all jet velocities. Similar trends are also observed with OASPL at various polar angles, peak OASPL, and OAPWL results with respect to jet velocity, shown in Figure 2.11-2.

PNLT and OASPL directivities for four different jet velocity conditions are shown in Figures 2.11-3 and 2.11-4, respectively. Both PNLT and OASPL levels decrease with

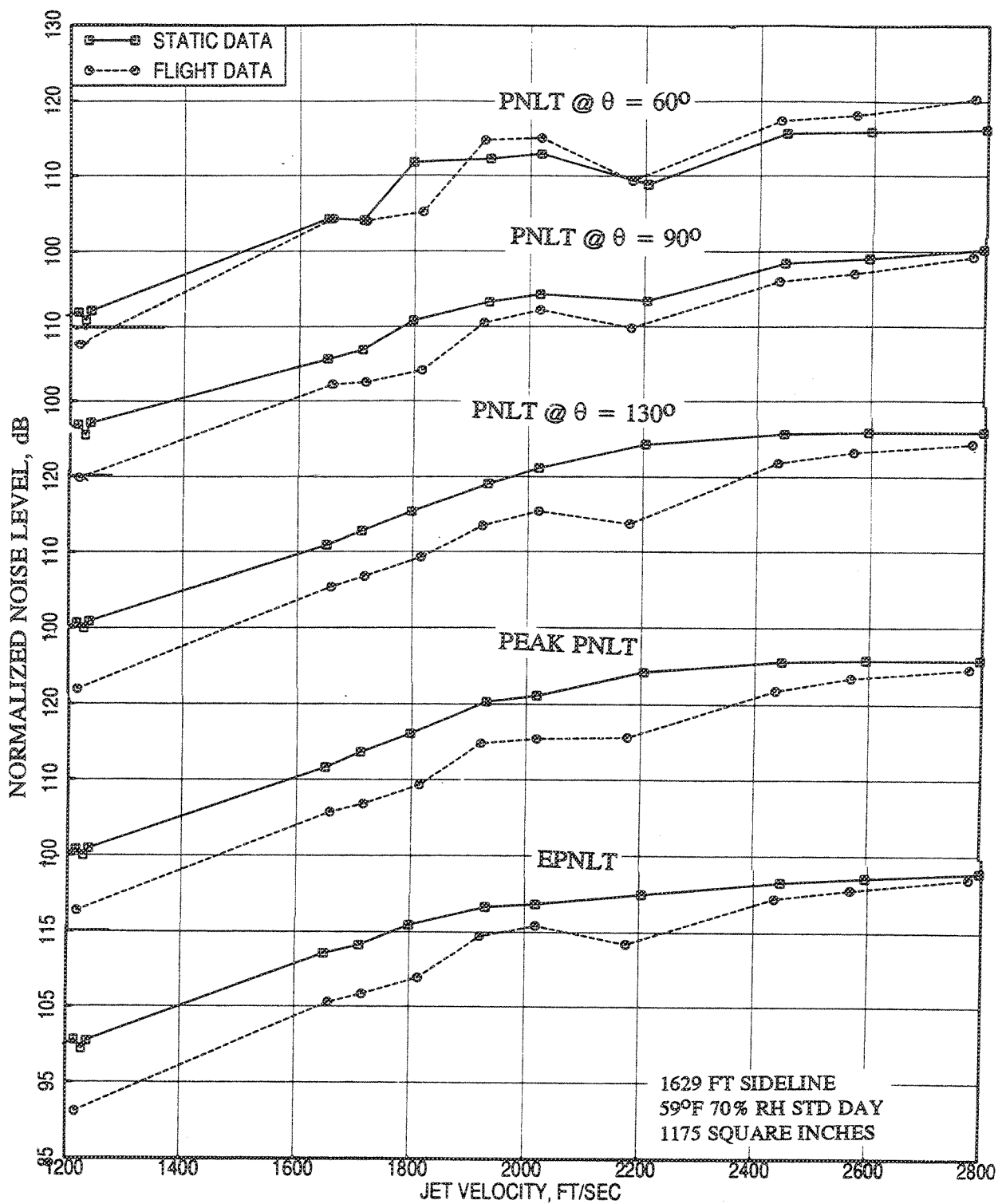


Figure 2.11-1. Effect of flight simulation ( $M_F=0.32$ ) on PNLTs at different polar angles ( $\theta$ ), peak PNLT, and EPNLT as functions of jet velocity,  $V_{j,p}$  for a 6.54 in<sup>2</sup> conical nozzle.

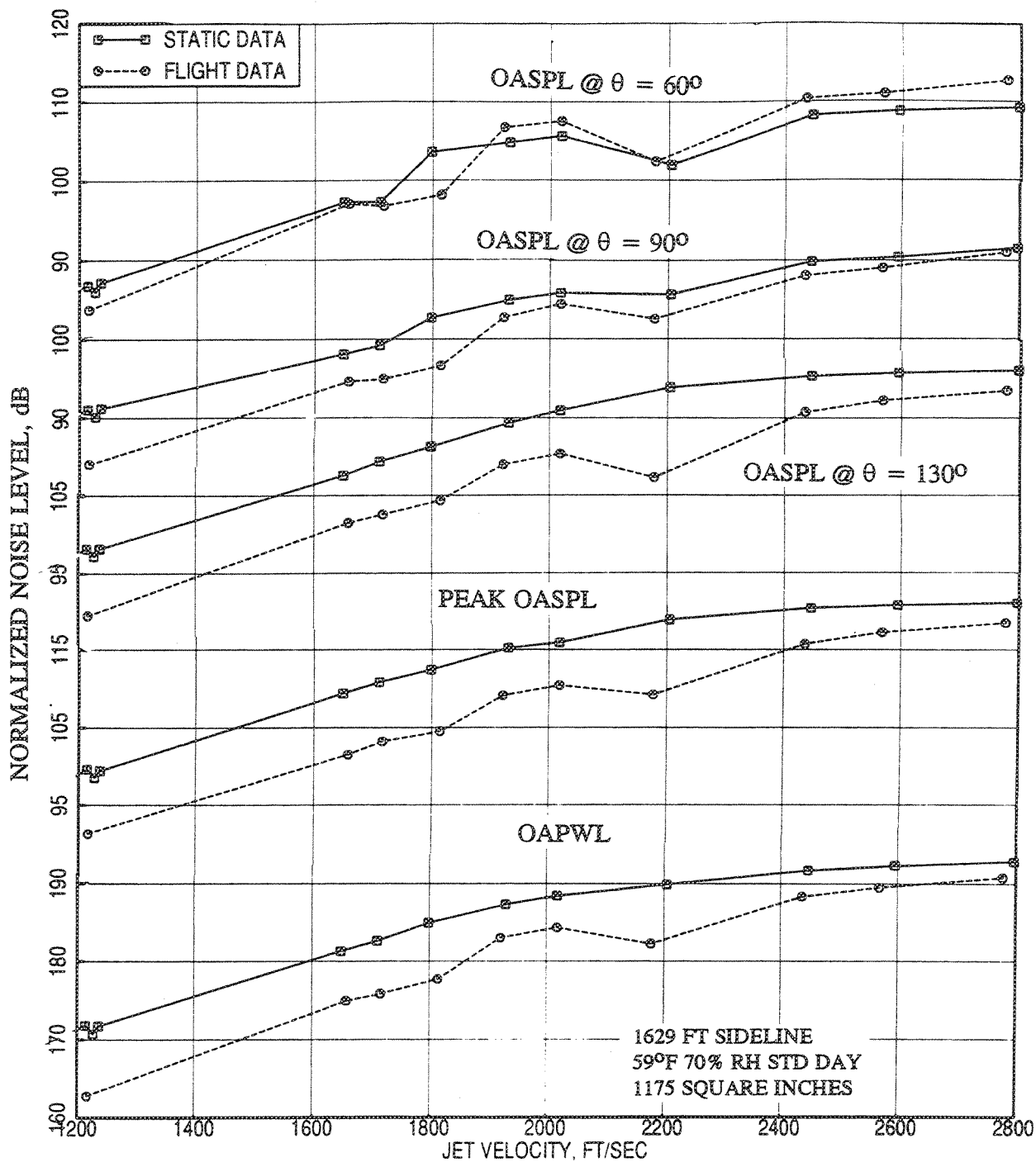


Figure 2.11-2. Effect of flight simulation ( $M_F=0.32$ ) on OASPLs at different polar angles ( $\theta$ ), peak OASPL, and OAPWL as functions of jet velocity,  $V_{j,p}$  for a 6.54 in<sup>2</sup> conical nozzle.

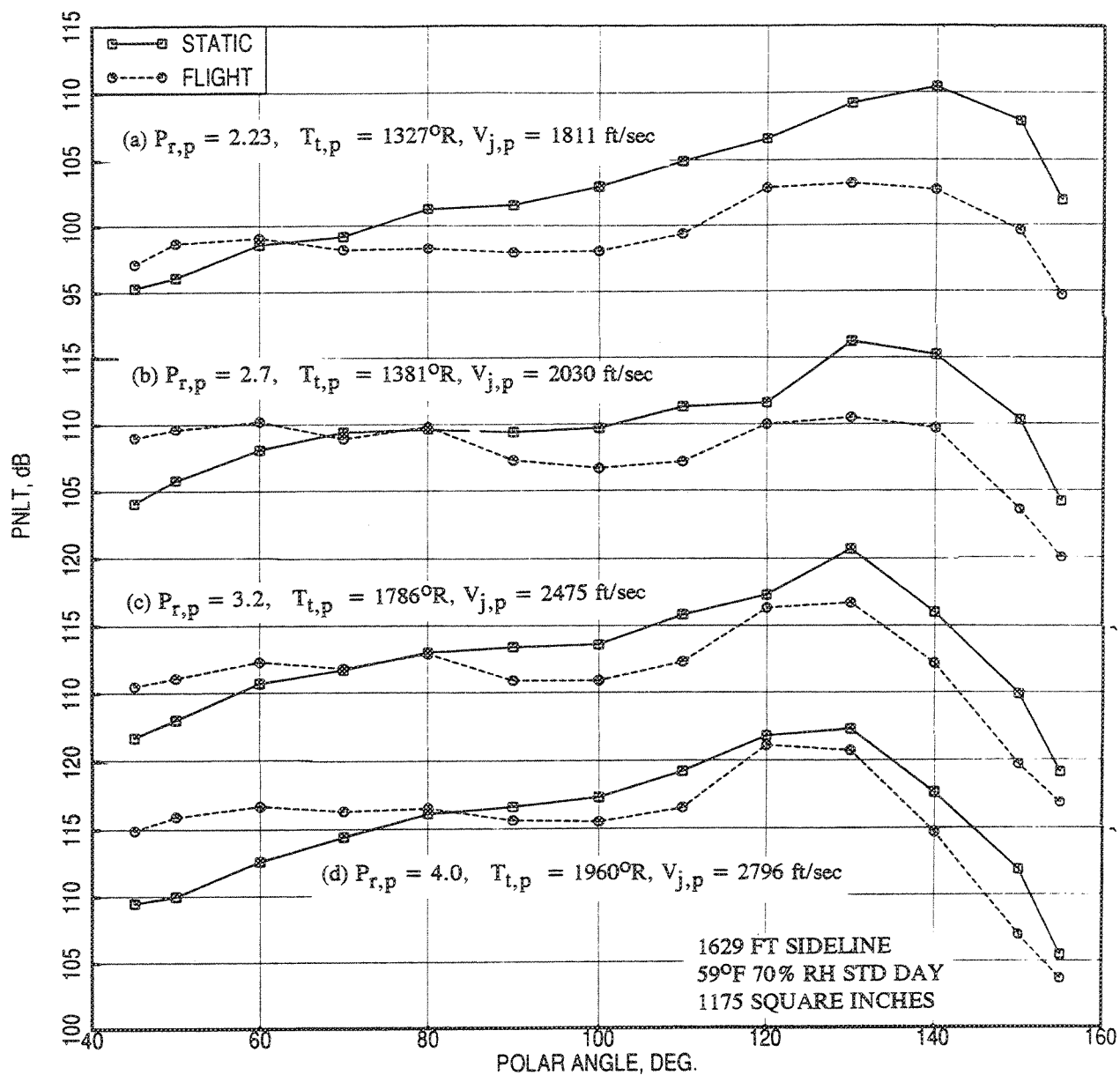


Figure 2.11-3. Effect of flight simulation ( $M_F=0.32$ ) on PNL T directivities at various aerothermodynamic conditions for a 6.54 in<sup>2</sup> conical nozzle.

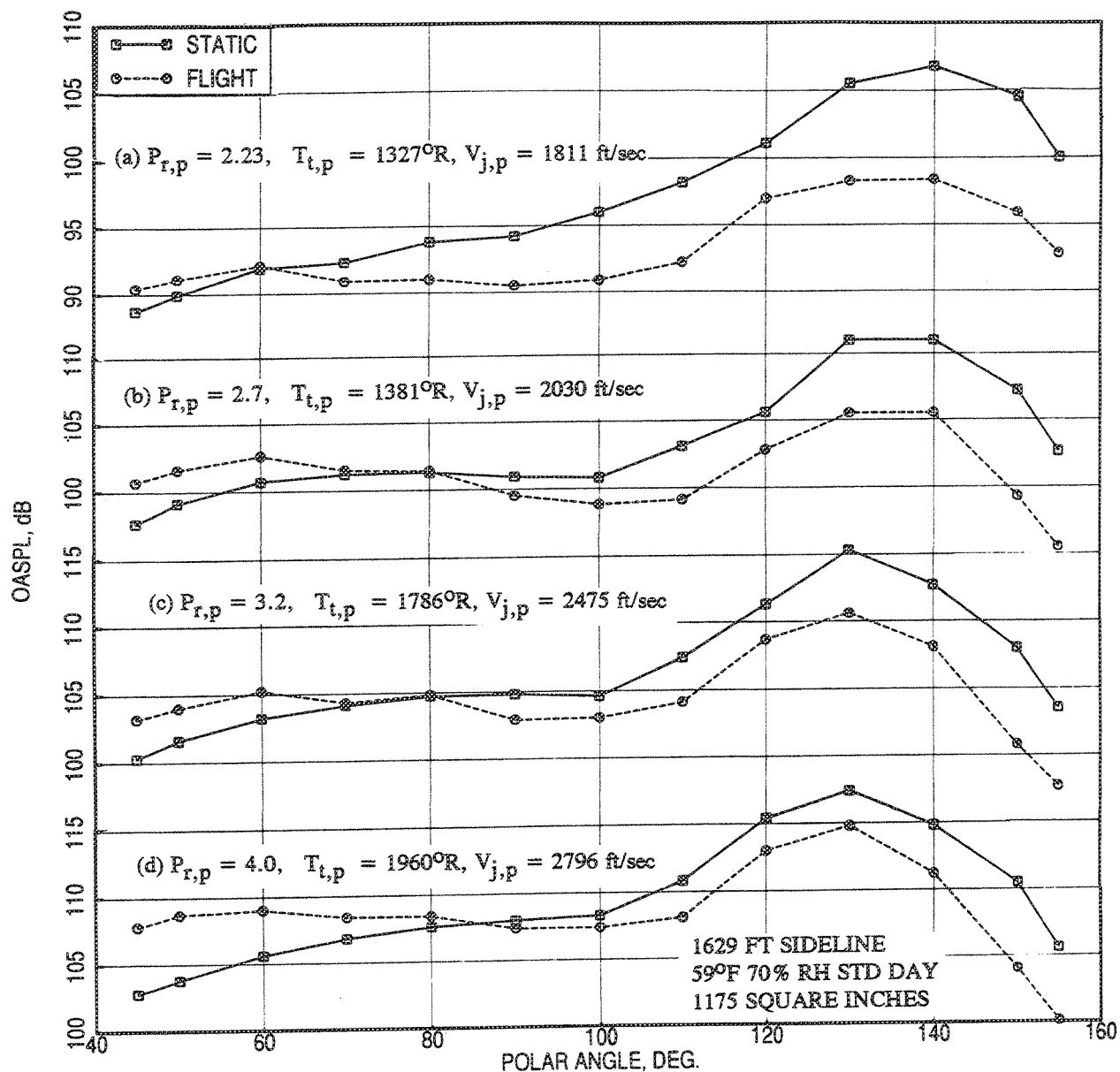


Figure 2.11-4. Effect of flight simulation ( $M_F=0.32$ ) on OASPL directivities at various aerothermodynamic conditions for a 6.54 in<sup>2</sup> conical nozzle.

flight for higher polar angles at all velocity conditions. An increase in levels is observed in the forward arc and the increase is higher for higher velocity conditions. Effect of flight on PWL spectra and SPL spectra at a number of polar angles are shown in Figures 2.11-5 through 2.11-8 for each of the four jet velocity conditions. The PWL levels decrease with flight at all frequencies for all velocity conditions. Similar trend is observed with SPL spectra for higher polar angles. However, the effect of flight diminishes with increasing jet velocity. At lower polar angles the levels decrease with flight at lower frequencies and the trend is reversed at higher frequencies.

The jet noise reduction, observed in Figures 2.11-1 through 2.11-8, is a direct result of a reduction in the shear velocity which correspondingly reduces the turbulence intensities in the jet. Such reduction is obtained at all angles and at all frequencies for subcritical jets without any internal noise and shock noise. For this reason at lower jet velocities noise reduction is observed at all polar angles (see Figures 2.11-1 and 2.11-2). For shock containing jets with no contamination from internal noise, the effect of flight or forward velocity is to provide a noise reduction in the rear arc and a noise increase in the forward arc, which is the case observed at higher jet velocities. These are clearly observed in Figures 2.11-3 through 2.11-8.

**36-Chute Suppressor Nozzle with Porous Plug:** Results similar to those for convergent conical nozzle are shown in Figures 2.11-9 through 2.11-16 for a 36-chute suppressor nozzle with porous plug. For this suppressor the area ratio was 2.5 (SAR) and the internal flow path was convergent. Effect of flight on various acoustic results for the suppressor are qualitatively similar to those of the conical nozzle. Except for forward arc the PNLT levels decrease due to flight at all jet velocities. Peak PNLT and EPNLT levels also reduce due to flight at all jet velocities. At higher velocities the influence of flight on PNLT and EPNLT is small (see Figure 2.11-9). Similar trends are also observed with OASPL at various polar angles, peak OASPL, and OAPWL results with respect to jet velocity, shown in Figure 2.11-10.

PNLT and OASPL levels decrease with flight for higher polar angles at all velocity conditions. An increase in levels is observed in the forward arc and the increase is higher for higher velocity conditions (see Figures 2.11-11 and 2.11-12). Effect of flight on PWL spectra and SPL spectra at a number of polar angles are shown in Figures 2.11-13 through 2.11-16 for each of the four jet velocity conditions. The PWL levels decrease with flight at all lower frequencies for all velocity conditions. Similar trend is observed with SPL spectra for higher polar angles.

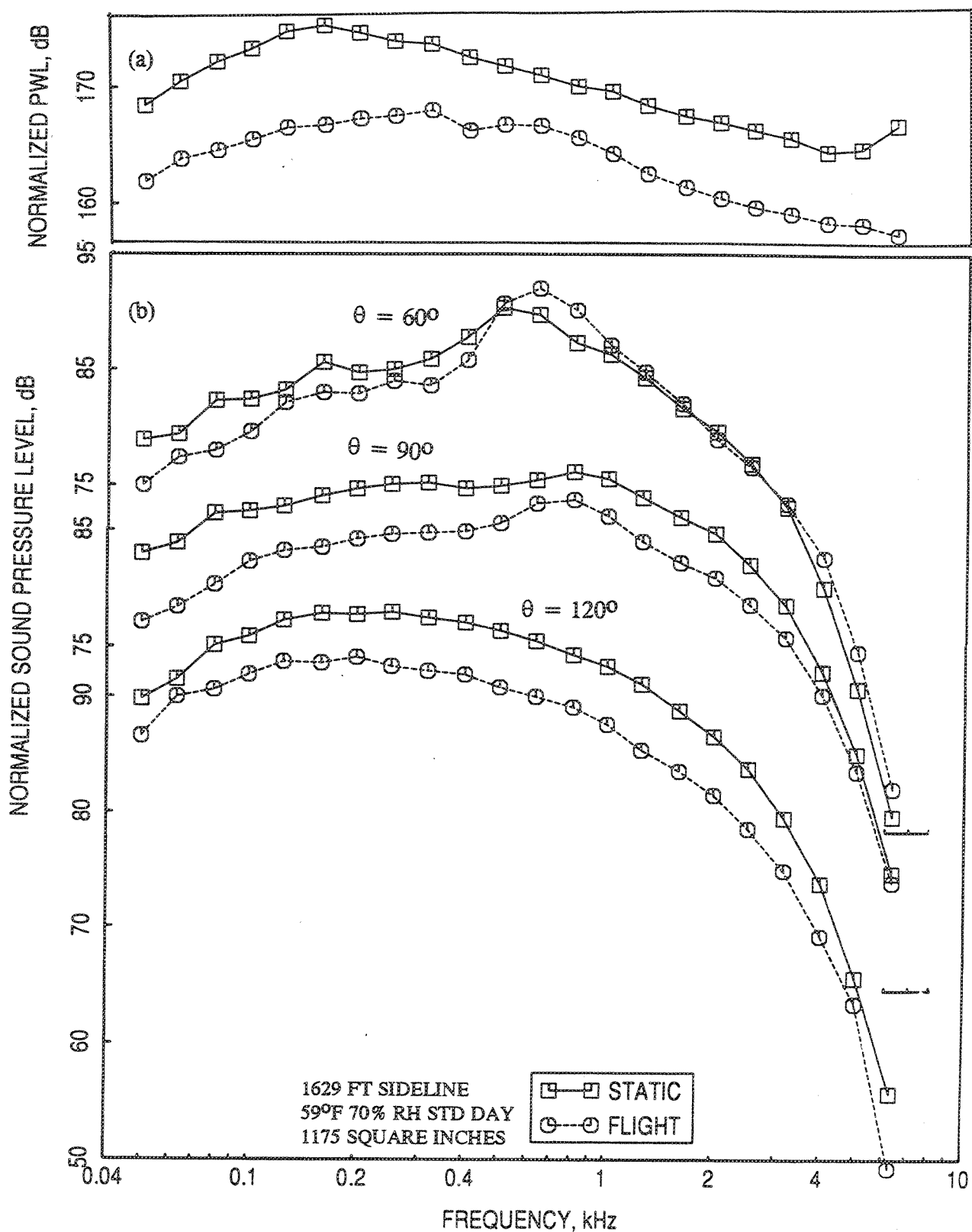


Figure 2.11-5. Effect of flight simulation ( $M_F=0.32$ ) on (a) PWL spectrum and (b) SPL spectra at various polar angles ( $\theta$ ) for a  $6.54 \text{ in}^2$  conical nozzle;  $P_{r,p}=2.23$ .  $T_{t,p}=1327^\circ\text{R}$ ,  $V_{j,p}=1811 \text{ ft/sec}$ .

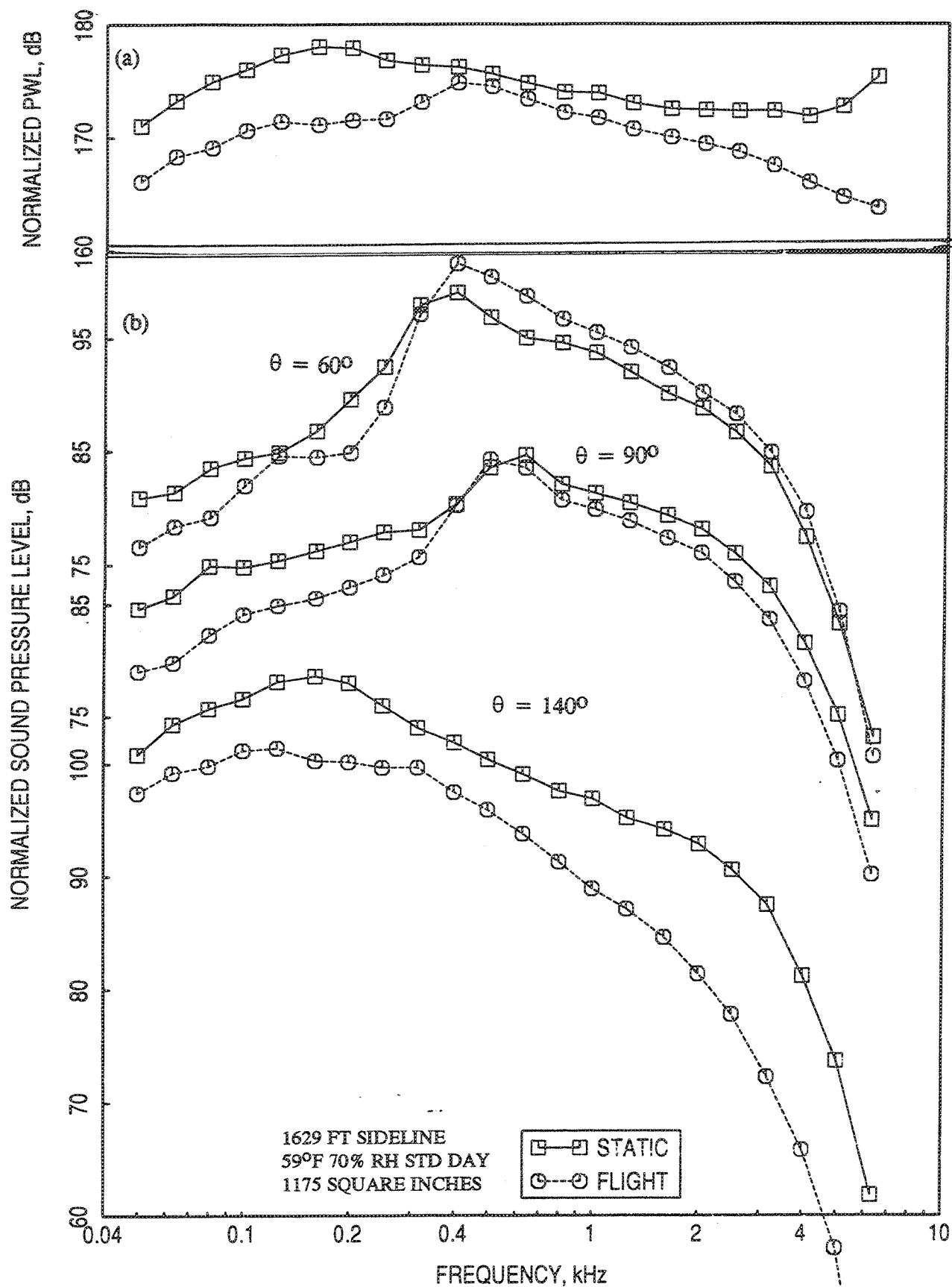


Figure 2.11-6. Effect of flight simulation ( $M_F=0.32$ ) on (a) PWL spectrum and (b) SPL spectra at various polar angles ( $\theta$ ) for a 6.54 in<sup>2</sup> conical nozzle;  $P_{r,p} = 2.7$ ,  $T_{t,p} = 1381^\circ\text{R}$ ,  $V_{j,p} = 2030$  ft/sec.



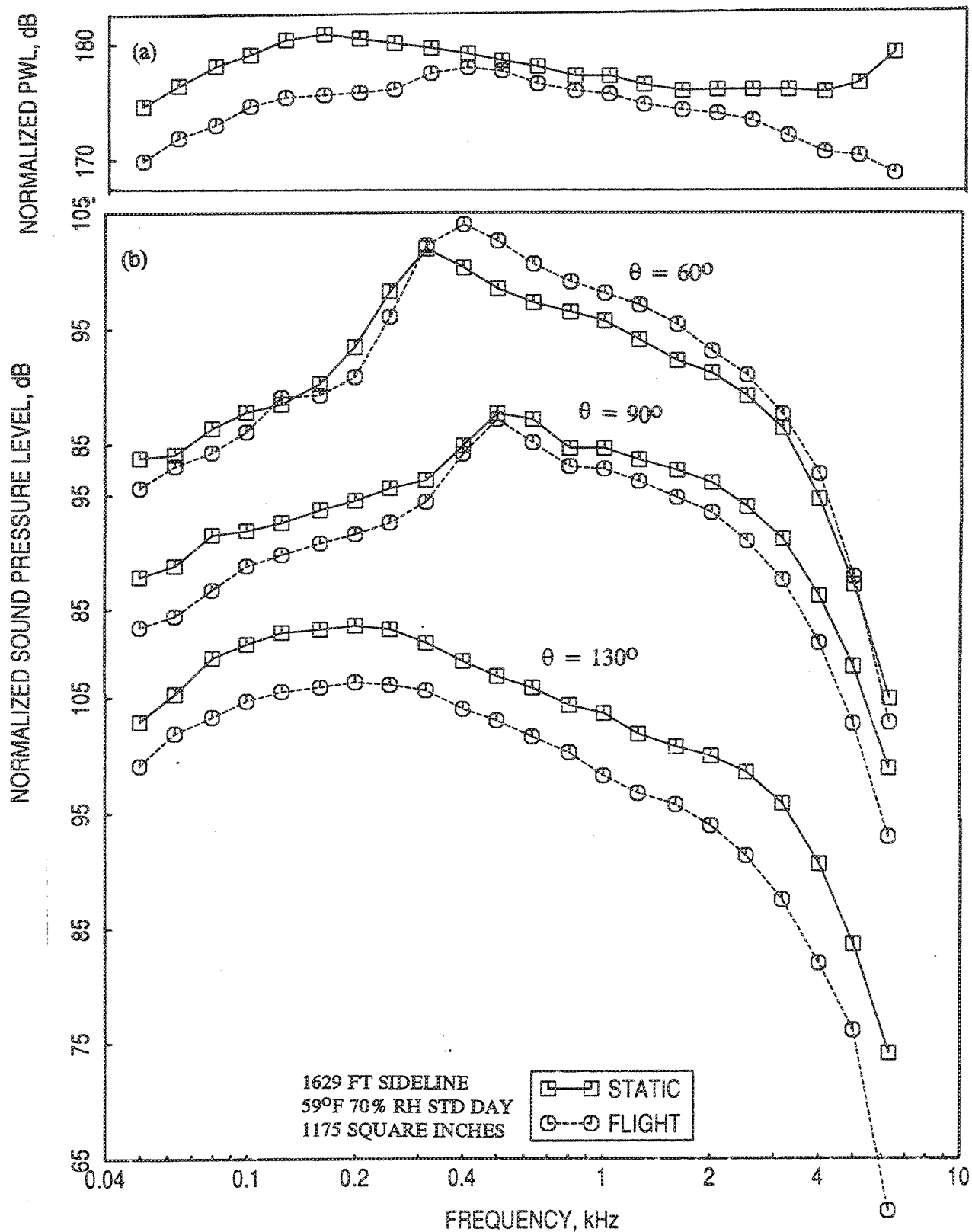


Figure 2.11-7. Effect of flight simulation ( $M_F=0.32$ ) on (a) PWL spectrum and (b) SPL spectra at various polar angles ( $\theta$ ) for a  $6.54 \text{ in}^2$  conical nozzle;  $P_{r,p} = 3.2$ ,  $T_{t,p} = 1786^\circ\text{R}$ ,  $V_{j,p} = 2475 \text{ ft/sec}$ .

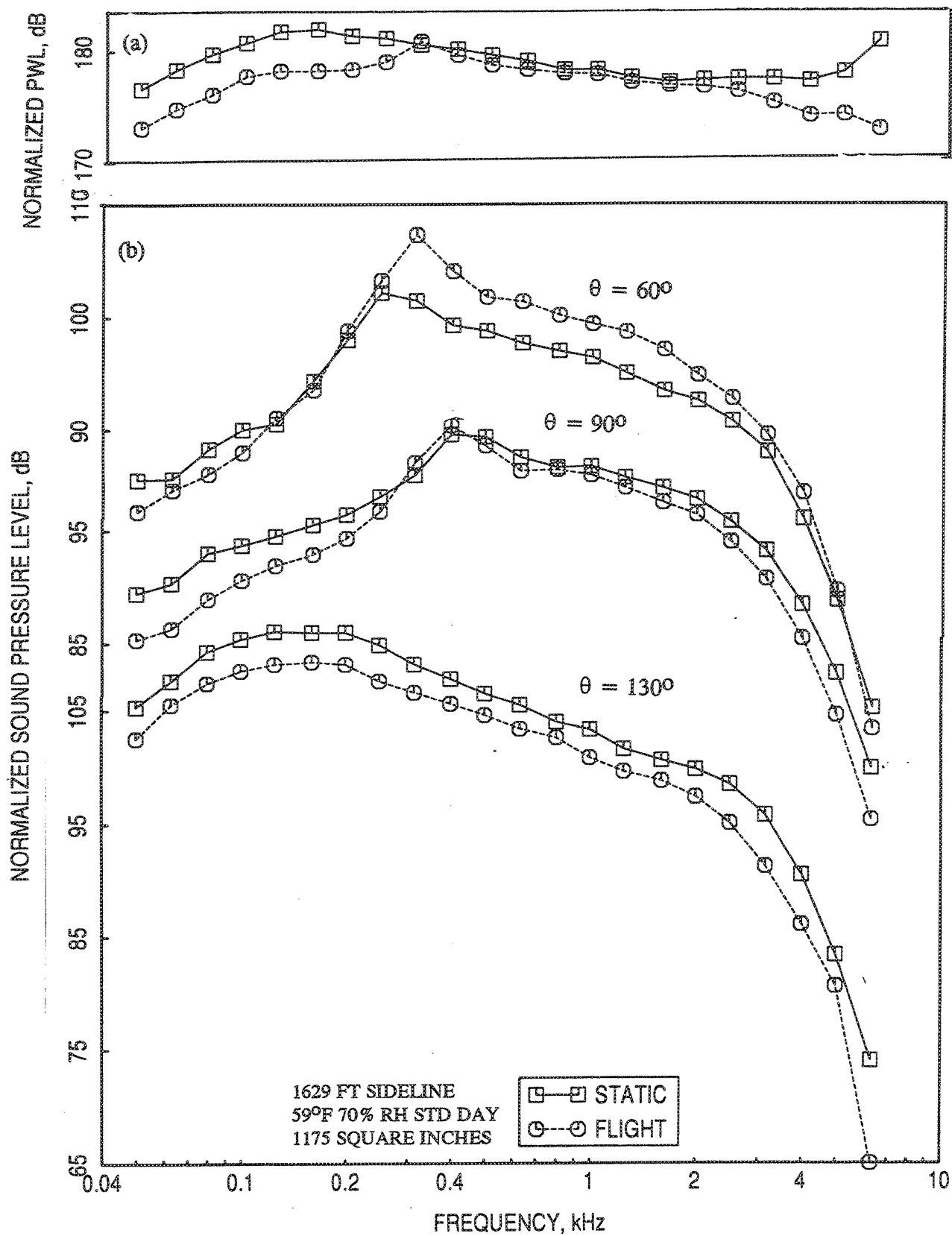


Figure 2.11-8. Effect of flight simulation ( $M_F=0.32$ ) on (a) PWL spectrum and (b) SPL spectra at various polar angles ( $\theta$ ) for a  $6.54 \text{ in}^2$  conical nozzle;  $P_{r,p} = 4.0$ ,  $T_{t,p} = 1960^\circ\text{R}$ ,  $V_{j,p} = 2796 \text{ ft/sec}$ .

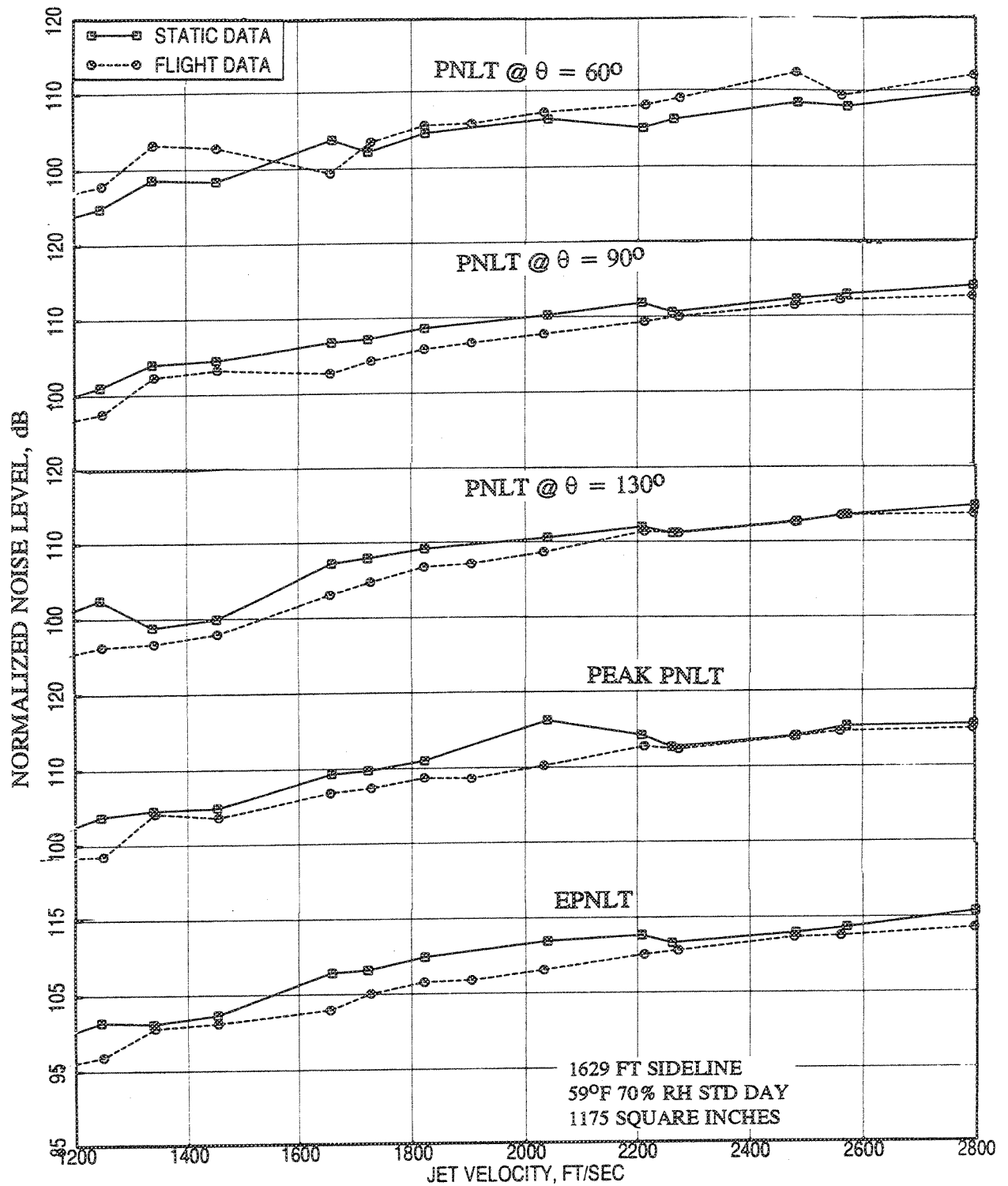


Figure 2.11-9. Effect of flight simulation ( $M_F=0.32$ ) on PNLt's at different polar angles ( $\theta$ ), peak PNLt, and EPNLT as functions of jet velocity,  $V_{j,p}$  for a 36-chute suppressor with porous plug.

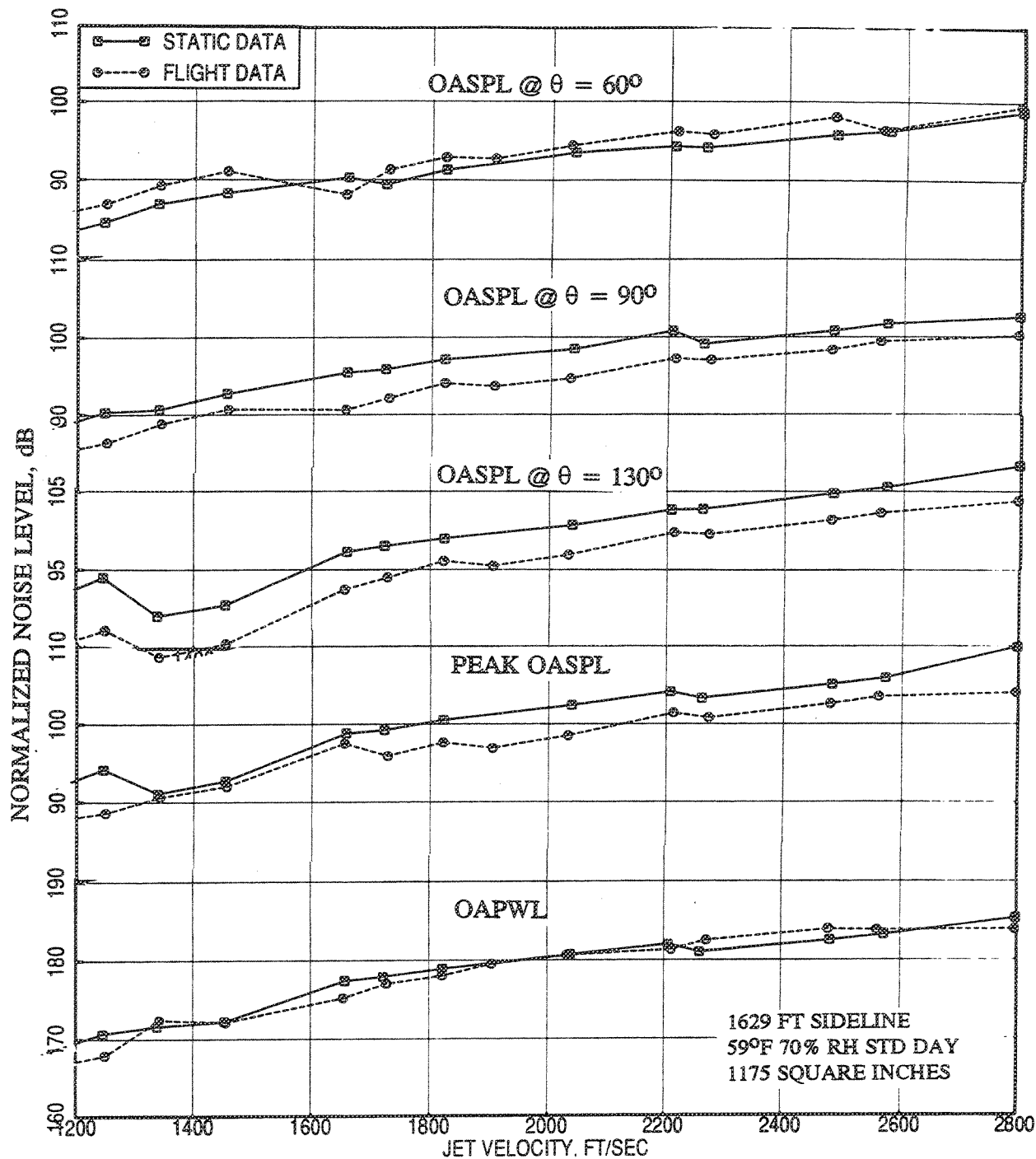


Figure 2.11-10. Effect of flight simulation ( $M_F=0.32$ ) on OASPLs at different polar angles ( $\theta$ ), peak OASPL, and OAPWL as functions of jet velocity,  $V_{j,p}$  for a 36-chute suppressor with porous plug.

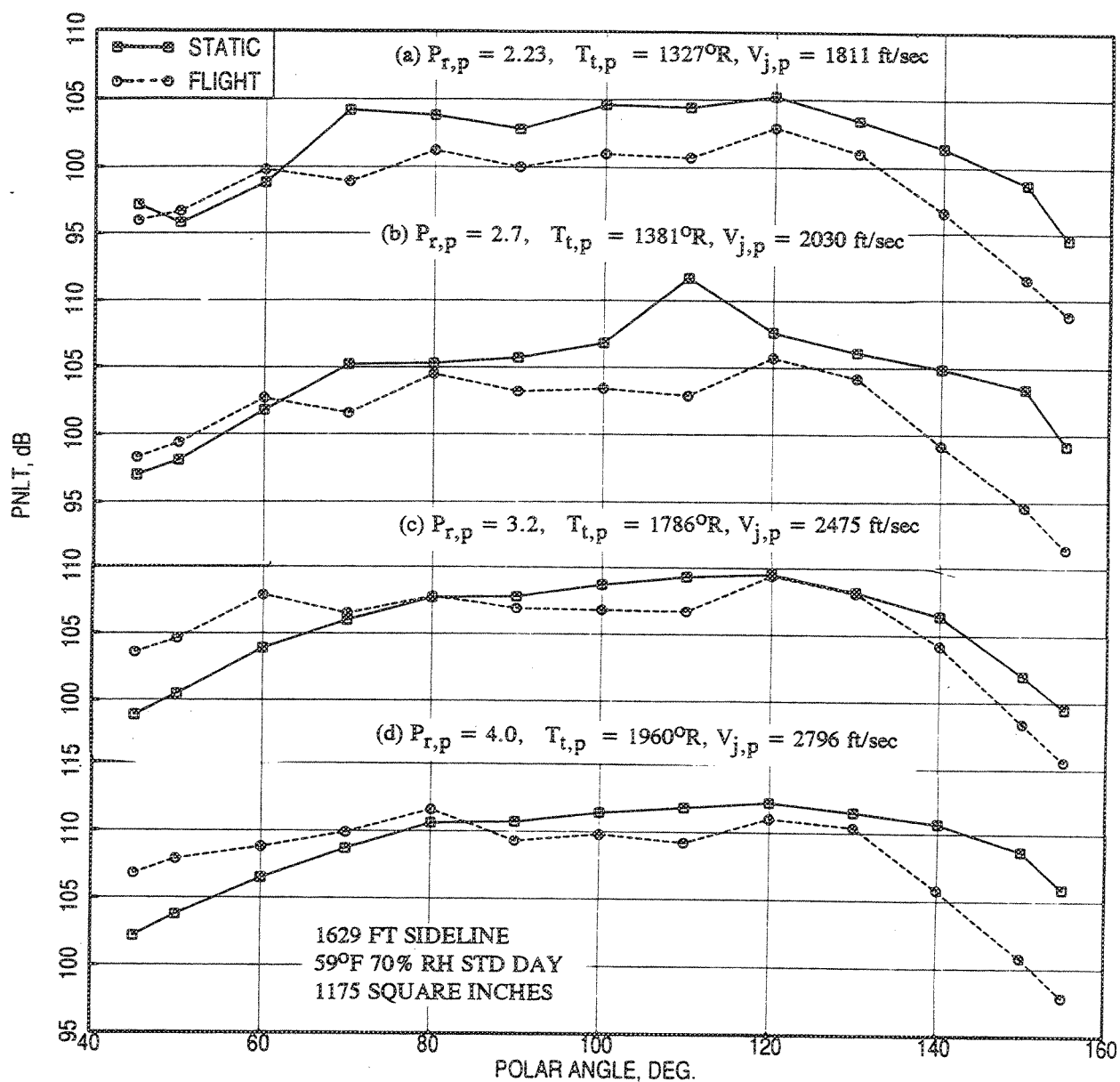


Figure 2.11-11. Effect of flight simulation ( $M_F=0.32$ ) on PNLT directivities at various aerothermodynamic conditions for a 36-chute suppressor with porous plug.

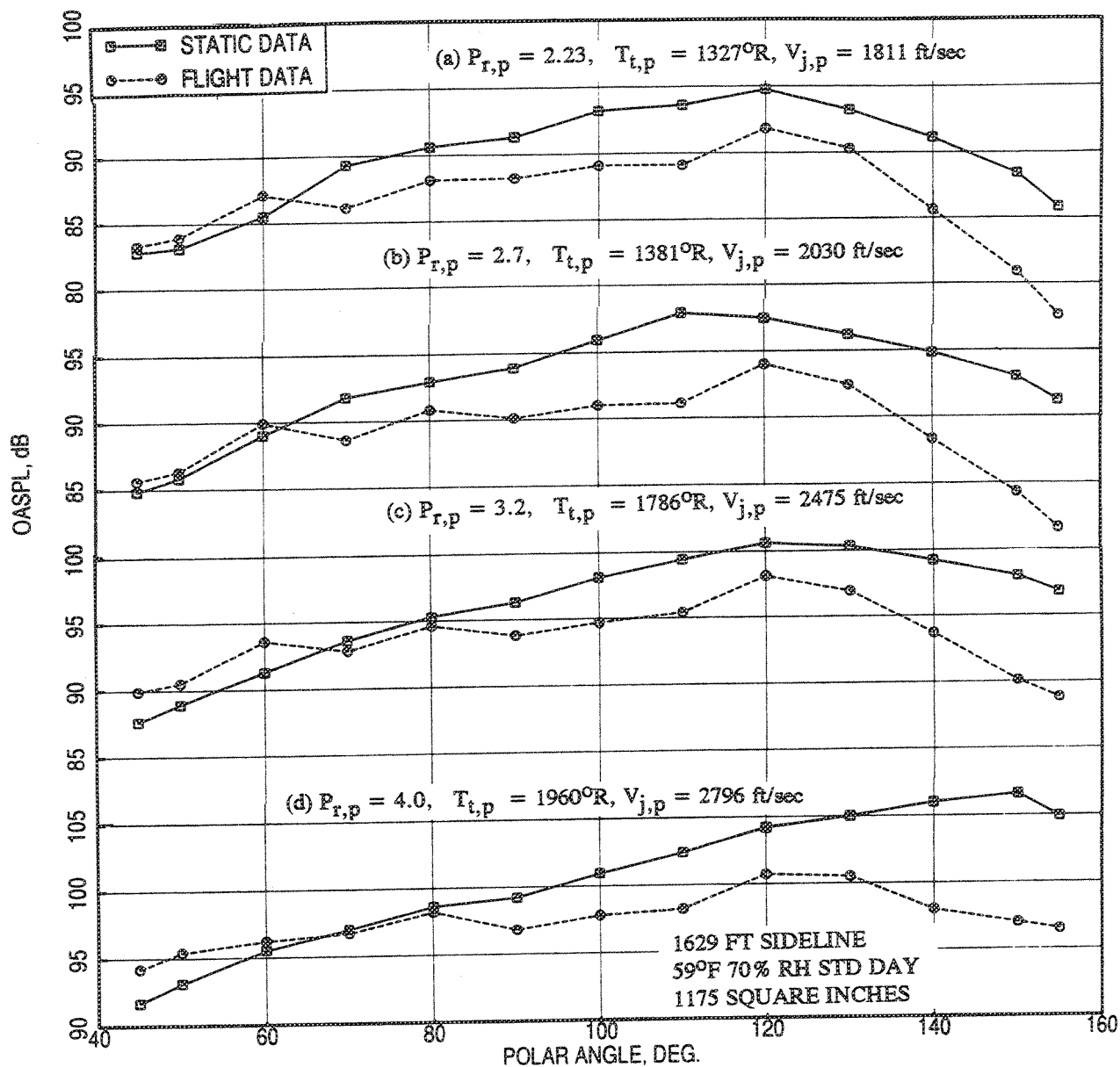


Figure 2.11.12. Effect of flight simulation ( $M_F=0.32$ ) on OASPL directivities at various aerothermodynamic conditions for a 36-chute suppressor with porous plug.

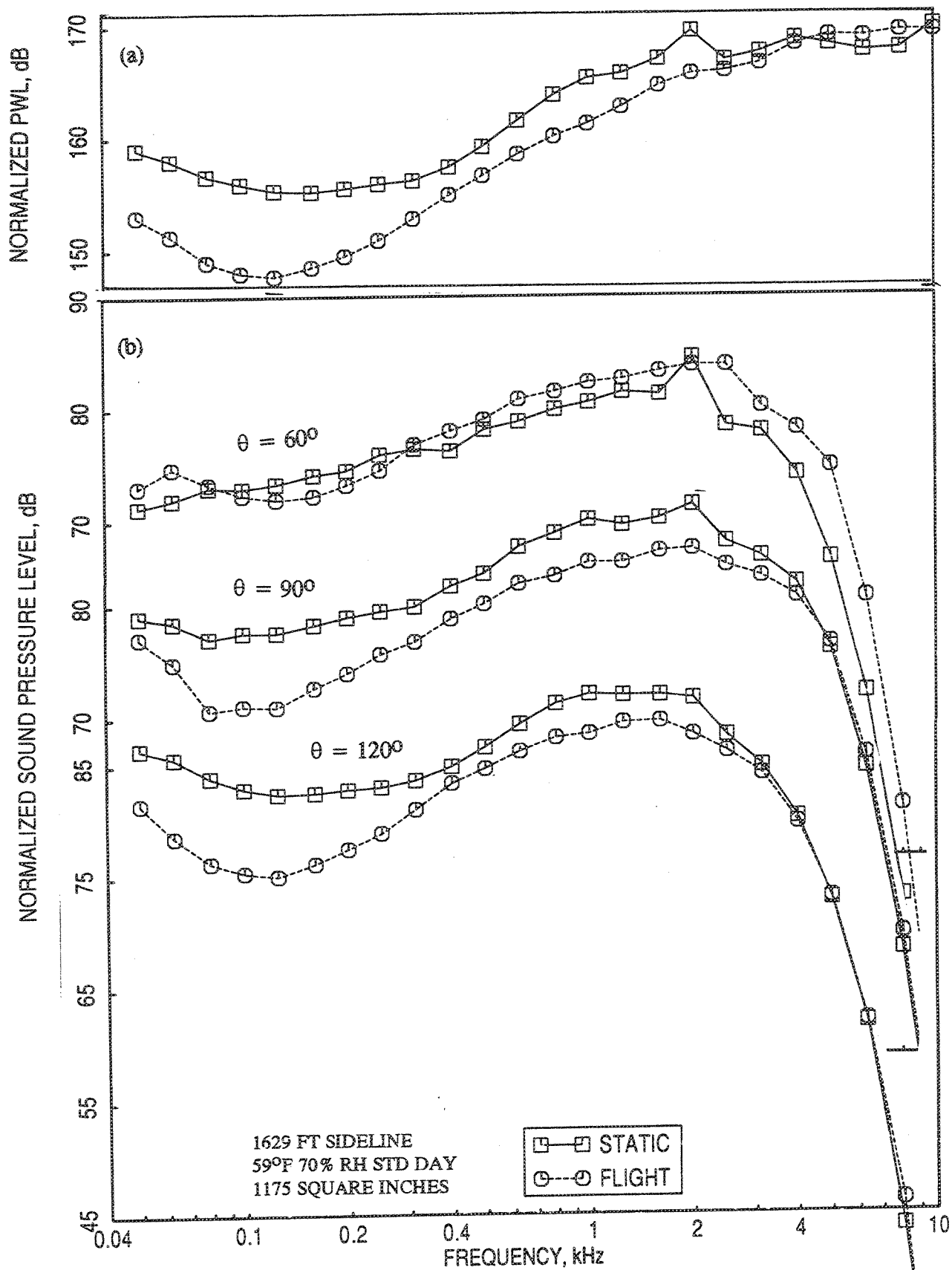


Figure 2.11-13. Effect of flight simulation ( $M_F=0.32$ ) on (a) PWL spectrum and (b) SPL spectra at various polar angles ( $\theta$ ) for a 36-chute suppressor with porous plug;  $P_{r,p}=2.23$ ,  $T_{t,p}=1327^\circ\text{R}$ ,  $V_{j,p}=1811$  ft/sec.

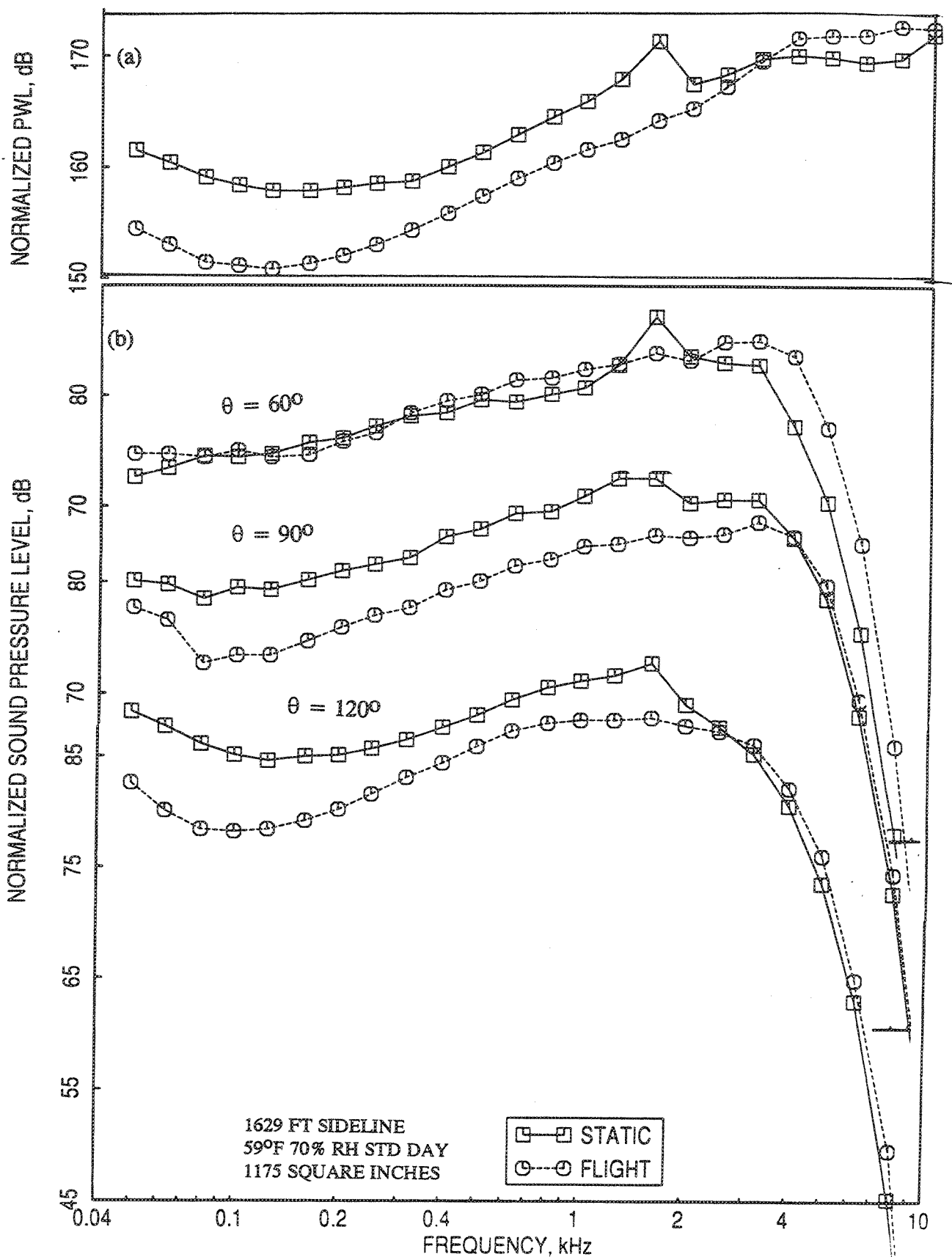


Figure 2.11-14. Effect of flight simulation ( $M_F=0.32$ ) on (a) PWL spectrum and (b) SPL spectra at various polar angles ( $\theta$ ) for a 36-chute suppressor with porous plug;  $P_{r,p} = 2.7$ ,  $T_{t,p} = 1381^\circ\text{R}$ ,  $V_{j,p} = 2030 \text{ ft/sec}$ .



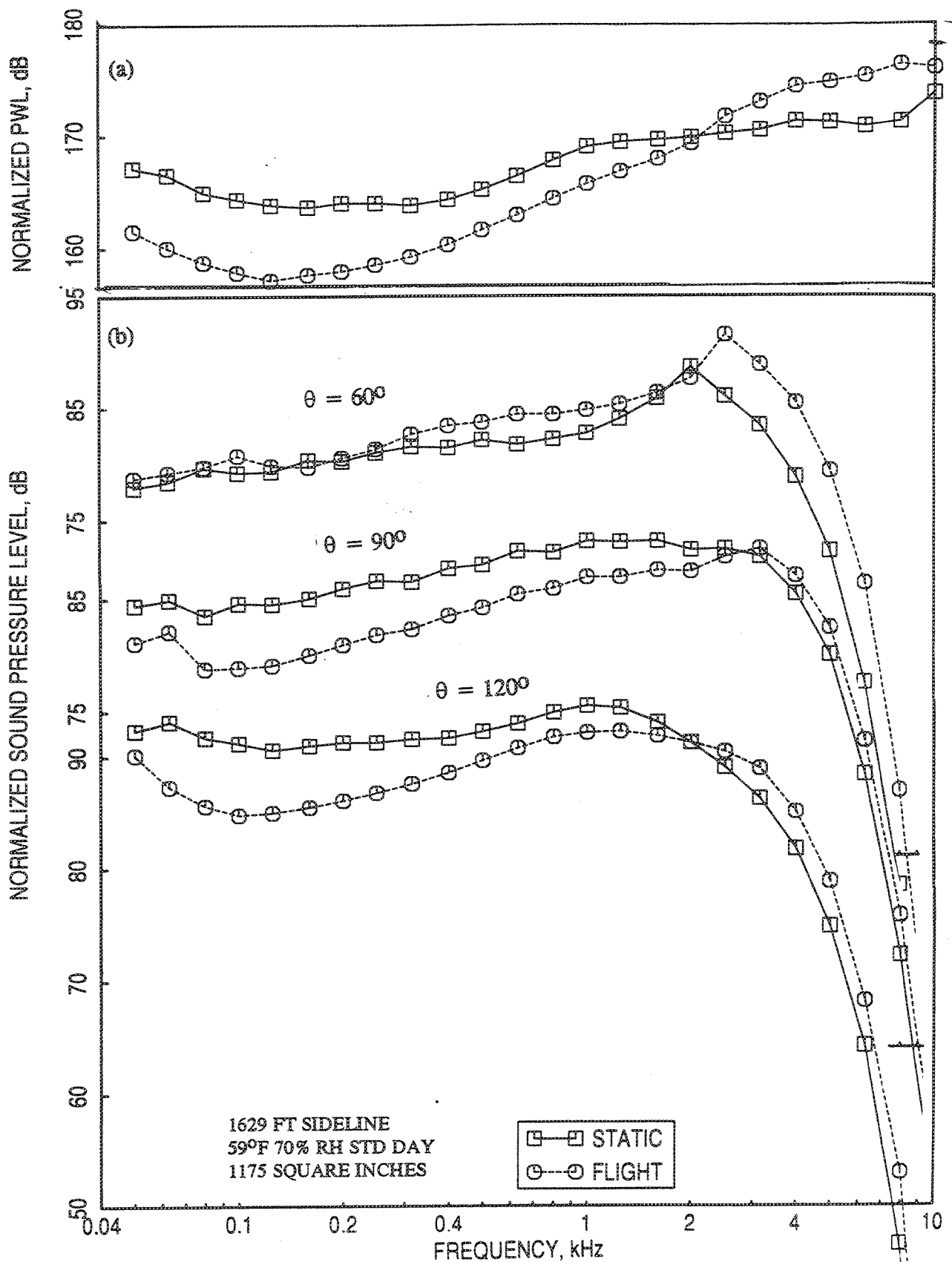


Figure 2.11-15. Effect of flight simulation ( $M_F=0.32$ ) on (a) PWL spectrum and (b) SPL spectra at various polar angles ( $\theta$ ) for a 36-chute suppressor with porous plug;  $P_{r,p} = 3.2$ ,  $T_{t,p} = 1786^\circ\text{R}$ ,  $V_{j,p} = 2475$  ft/sec.

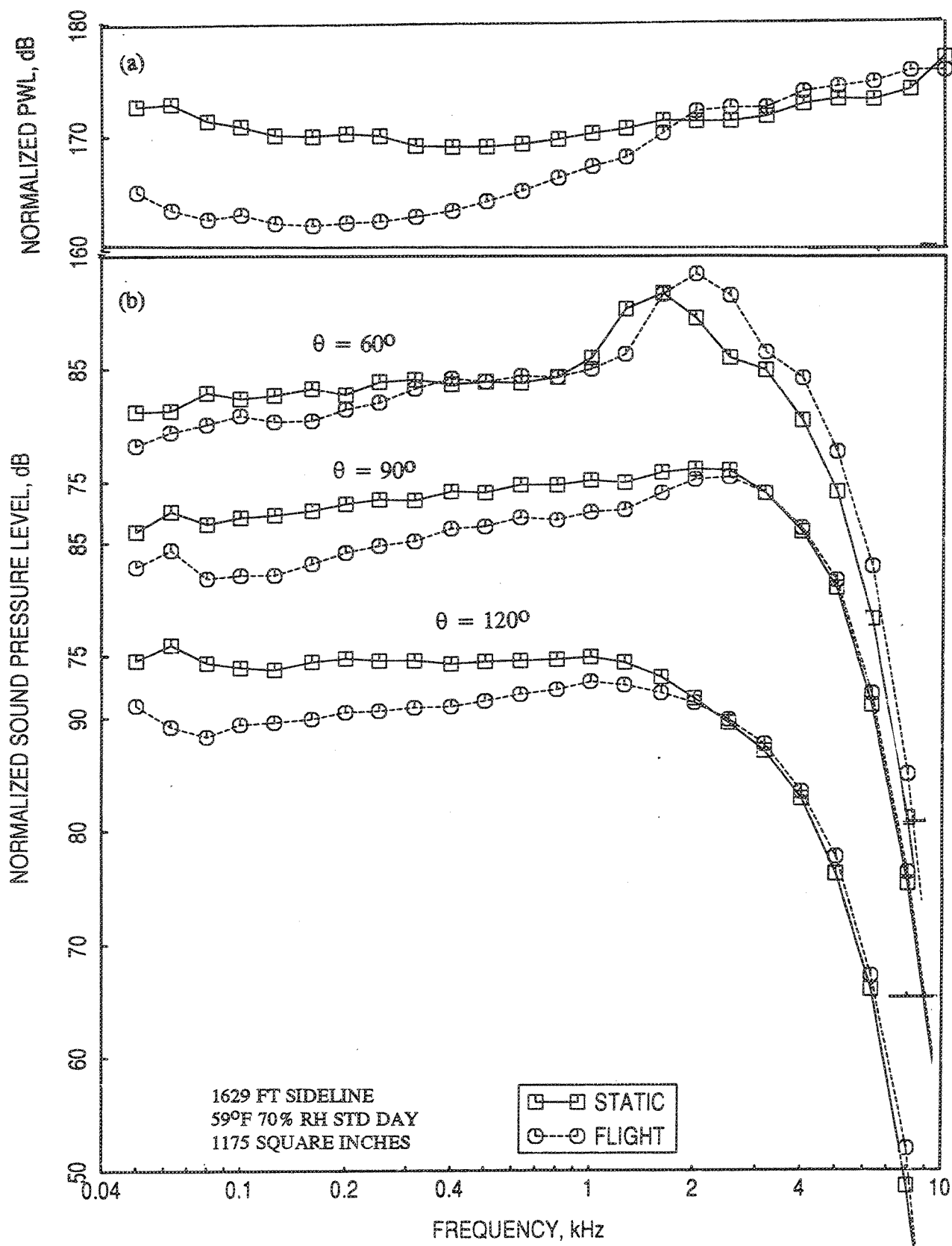


Figure 2.11-16. Effect of flight simulation ( $M_F=0.32$ ) on (a) PWL spectrum and (b) SPL spectra at various polar angles ( $\theta$ ) for a 36-chute suppressor with porous plug;  $P_{r,p} = 4.0$ ,  $T_{t,p} = 1960^\circ R$ ,  $V_{j,p} = 2796$  ft/sec.

**2.11.2 Dual Stream Fluid Shield Nozzle Configurations with Porous Plug :** Effect of flight on acoustic results in terms of EPNLT, PNLT, and SPL at community plane (i.e.,  $\phi=75^\circ$ ) for three fluid shield nozzles of 0.5", 0.75", and 1.0" thick fluid shield configurations with porous plug, scaled to 1813.6, 2165.5, and 2524.7 square inches, respectively, are presented in Figures 2.11-17 through 2.11-27. Figures 2.11-17 through 2.11-19 show the effect of flight on PNLT at various polar angles, peak PNLT, and EPNLT as functions of mass averaged mixed velocity for the three fluid shield nozzles, respectively. For each configuration substantial reduction of PNLT due to flight is observed at higher polar angles. The trend is reversed at lower polar angles. Significant reduction of peak PNLT and EPNLT levels are achieved due to flight at all mixed velocities.

Effect of flight on PNLT directivities and SPL spectra for the three fluid shield configurations are examined for two mixed velocities, namely, 1811 ft/sec (i.e., corresponding to cutback condition) and 2030 ft/sec (corresponding to takeoff condition). Figure 2.11-20 shows the significant noise reduction in terms of PNdB at higher polar angles for the three fluid shield configurations at  $V_{mix}=1811$  ft/sec. At lower angles the trend is reversed. Effect of flight on SPL spectra for each of these three nozzle configurations are shown in Figures 2.11-21 through 2.11-23 for  $V_{mix}=1811$  ft/sec. Similar to conical nozzle results, sound pressure levels reduce significantly at all frequencies at higher polar angles and the reduction at lower polar angles is observed for lower frequencies only. Similar directivity and spectral results for  $V_{mix}=2030$  ft/sec are shown in Figures 2.11-24 through 2.11-27. The effect of flight simulation at  $V_{mix}=2030$  ft/sec is similar to the results of  $V_{mix}=1811$  ft/sec.

In general, the effect of flight on farfield noise is similar for all the nozzle configurations, the conical nozzle, the 36-chute suppressor, and the fluid shield configurations. At the subcritical conditions, the sound field consists of pure jet mixing noise, and hence a reduction with flight simulation is observed at all angles. As the jet becomes supercritical, the shock noise component is dominant in the forward arc, while the jet mixing noise is dominant in the rear arc. Thus, with flight simulation, as the mixing noise component reduces in level at all angles, the shock-associated noise component becomes more prominent in the forward arc, and this leads to smaller noise reductions at smaller polar angles. In fact, at very end of forward arc the noise increases with flight simulation. The shock-associated noise increase with flight velocity is caused by the propagation effects which are present when a stationary sound source is surrounded by a moving fluid or when a sound source is convected in a stationary medium. In addition, the shock noise directivity gets modified by Doppler shift due to flight.

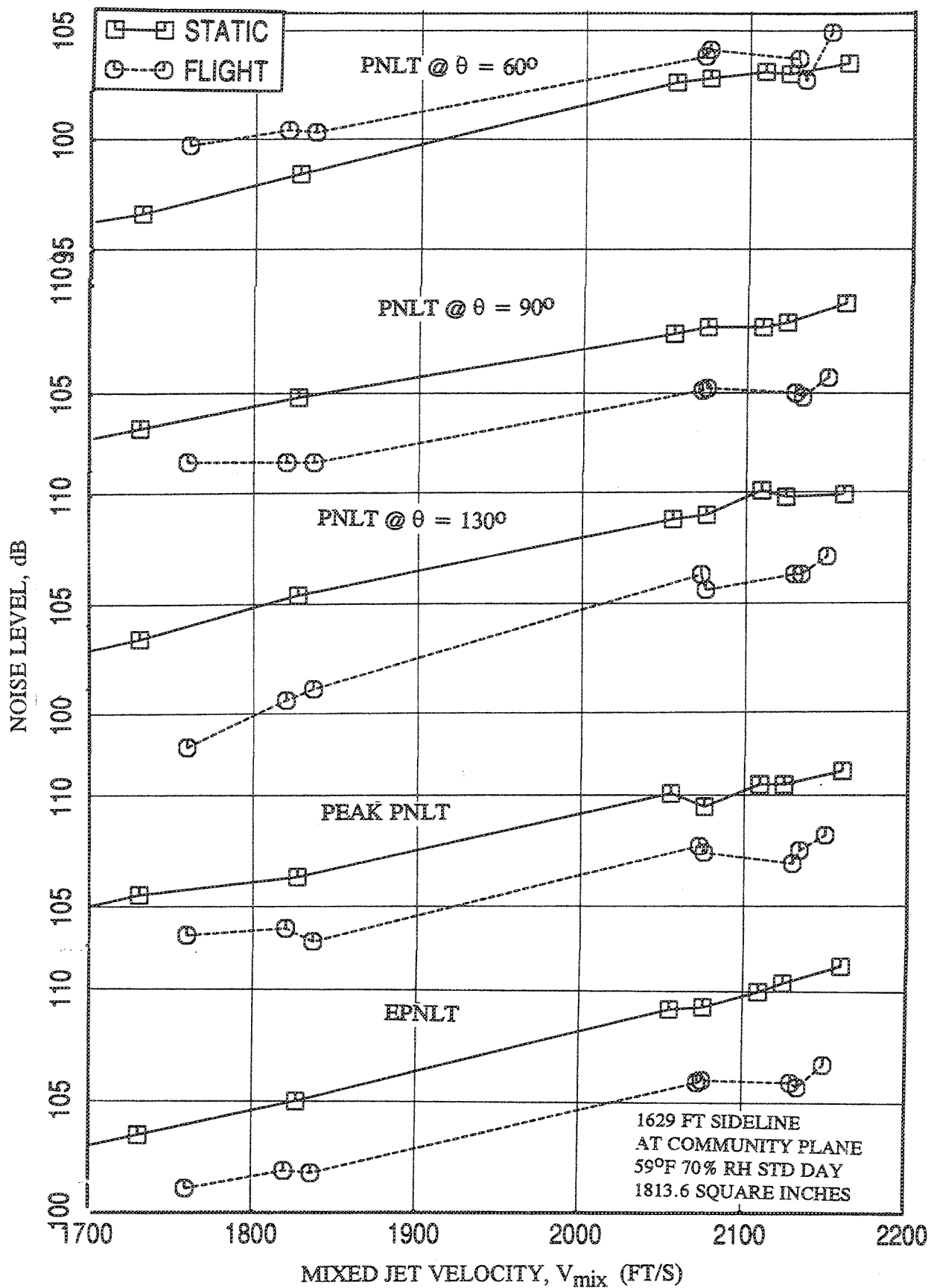


Figure 2.11-17. Effect of flight simulation ( $M_F=0.32$ ) on PNLTs at different polar angles ( $\theta$ ), peak PNLT, and EPNLT as functions of jet velocity,  $V_{mix}$  for 0.5"-thick fluid shield nozzle with porous plug.

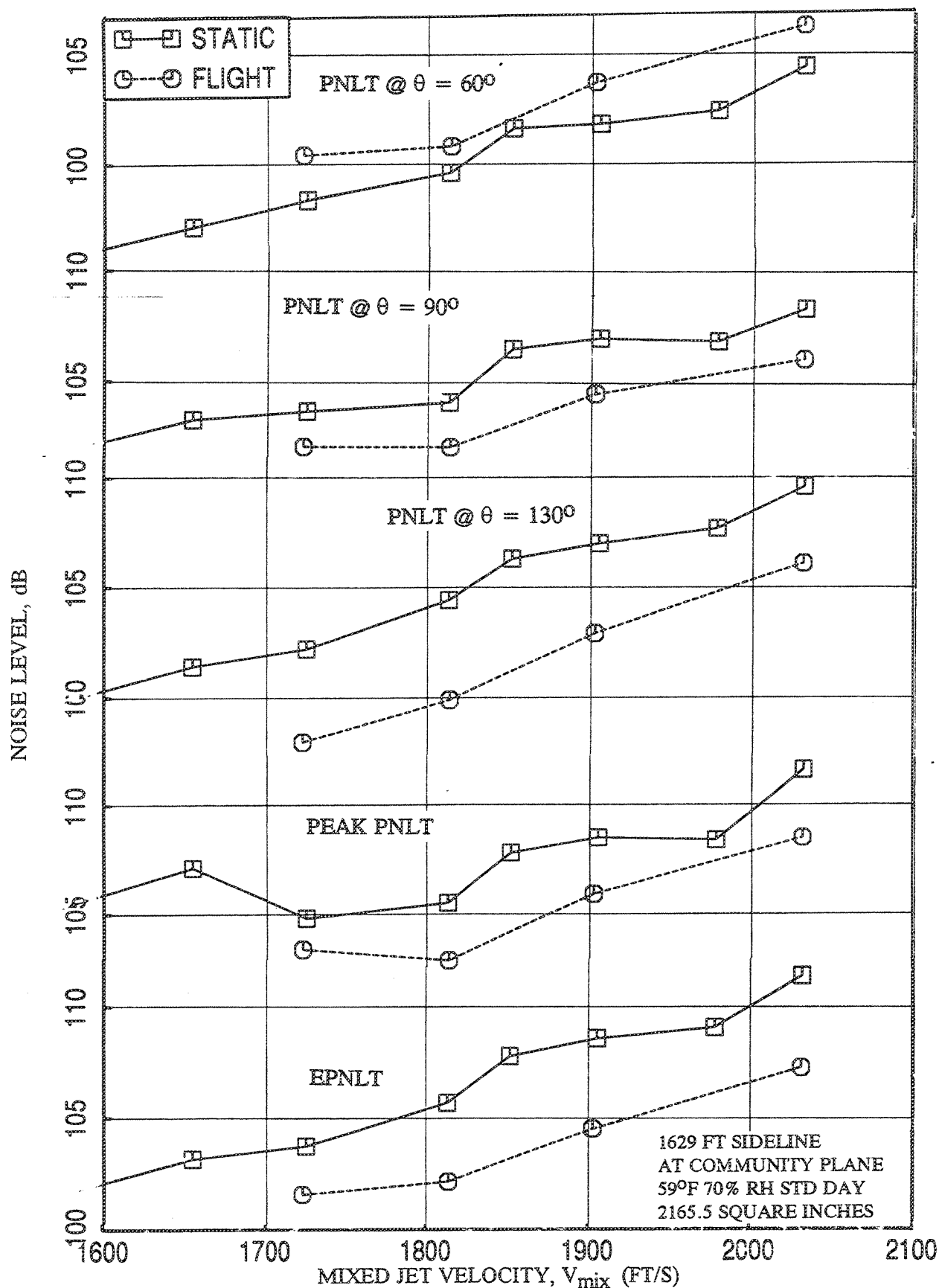


Figure 2.11-18. Effect of flight simulation ( $M_F=0.32$ ) on PNLts at different polar angles ( $\theta$ ), peak PNLt, and EPNLT as functions of jet velocity,  $V_{mix}$  for 0.75"-thick fluid shield nozzle with porous plug.

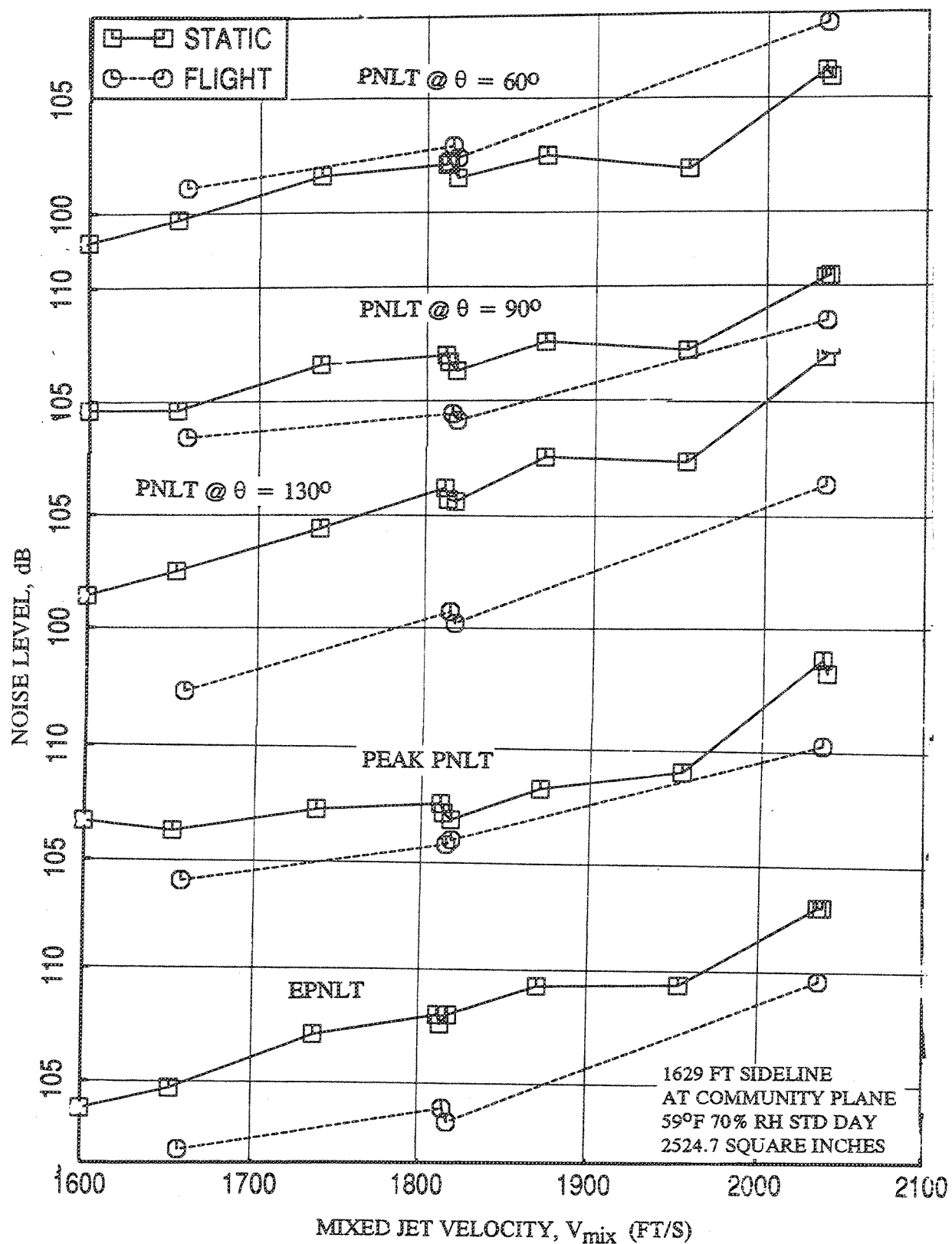


Figure 2.11-19. Effect of flight simulation ( $M_F=0.32$ ) on PNLTs at different polar angles ( $\theta$ ), peak PNLT, and EPNLT as functions of jet velocity,  $V_{mix}$  for 1.0"-thick fluid shield nozzle with porous plug.

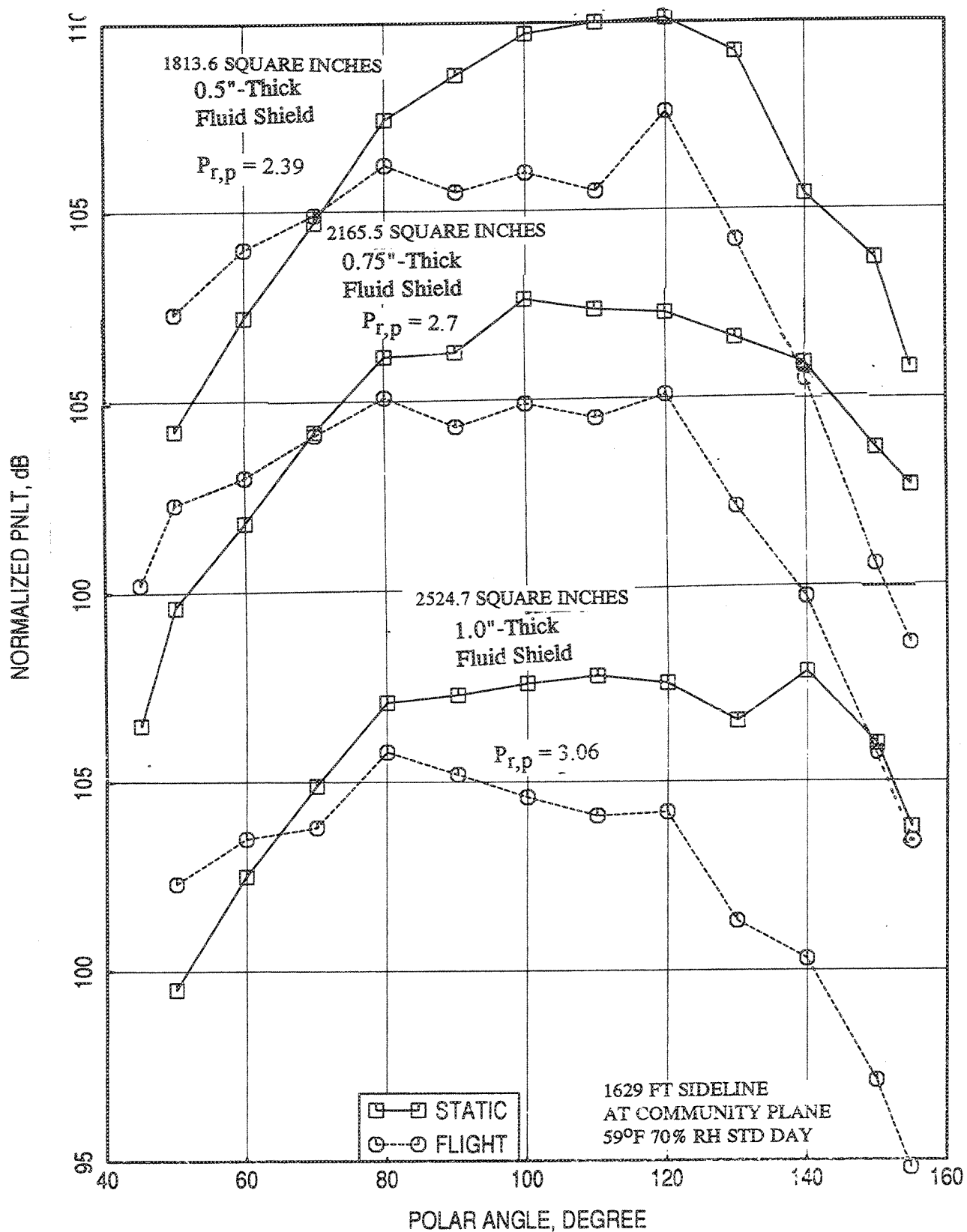


Figure 2.11.20. Effect of flight simulation ( $M_F=0.32$ ) on PNL T directivities for three fluid shield nozzles with porous plug at a jet velocity,  $V_{mix}=1811$  ft/sec,  $T_{t,p} = 1806^\circ R$ ,  $P_{r,s} = 2.2$ ,  $T_{t,s} = 727^\circ R$ .

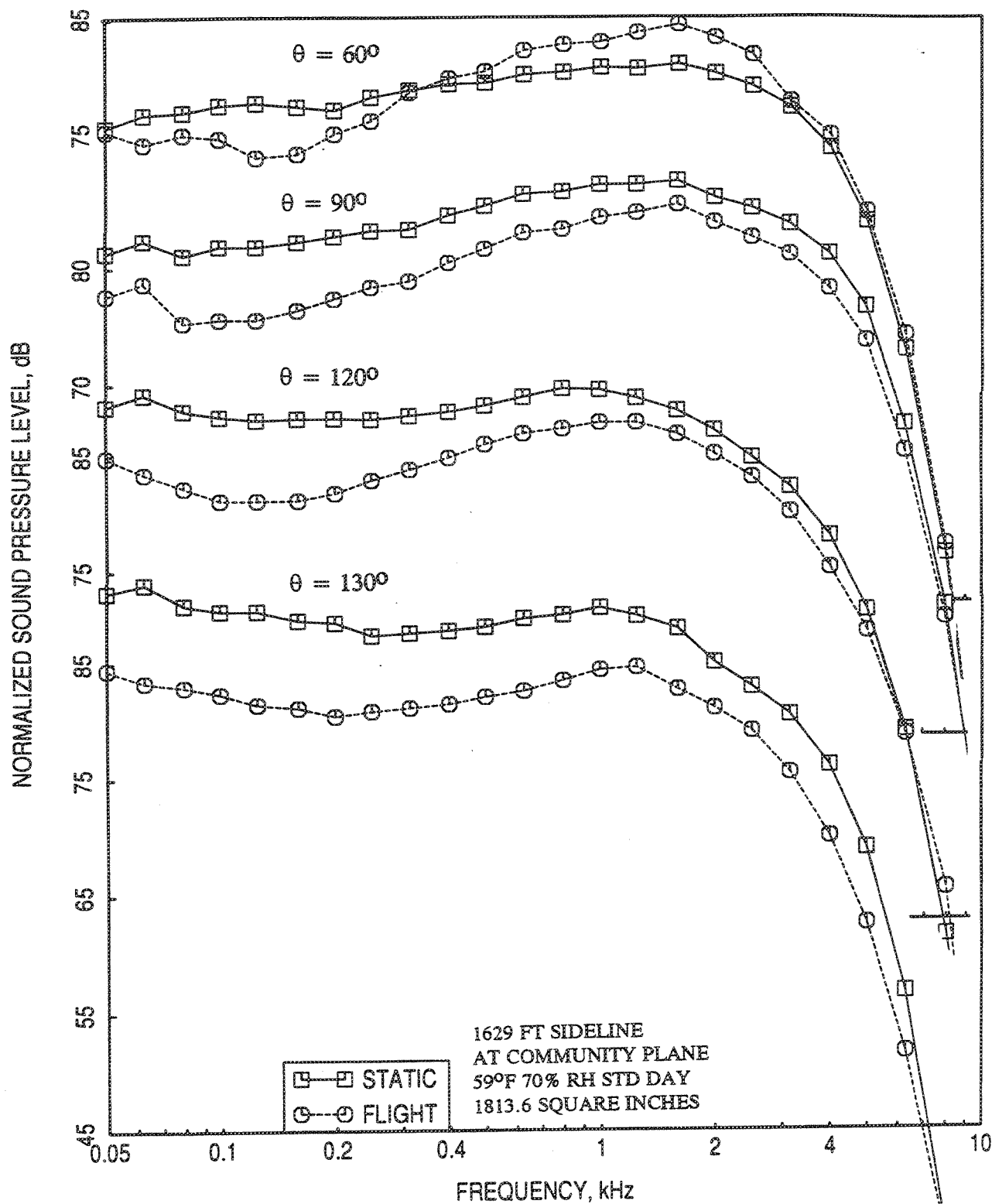


Figure 2.11.21. Effect of flight simulation ( $M_F=0.32$ ) on SPL spectra at different polar angles ( $\theta$ ) for 0.5"-thick fluid shield nozzle with porous plug at a jet velocity,  $V_{mix}=1811$  ft/sec;  $P_{r,p}=2.39$ ,  $T_{t,p}=1806^\circ\text{R}$ ,  $P_{r,s}=2.2$ ,  $T_{t,s}=727^\circ\text{R}$ .



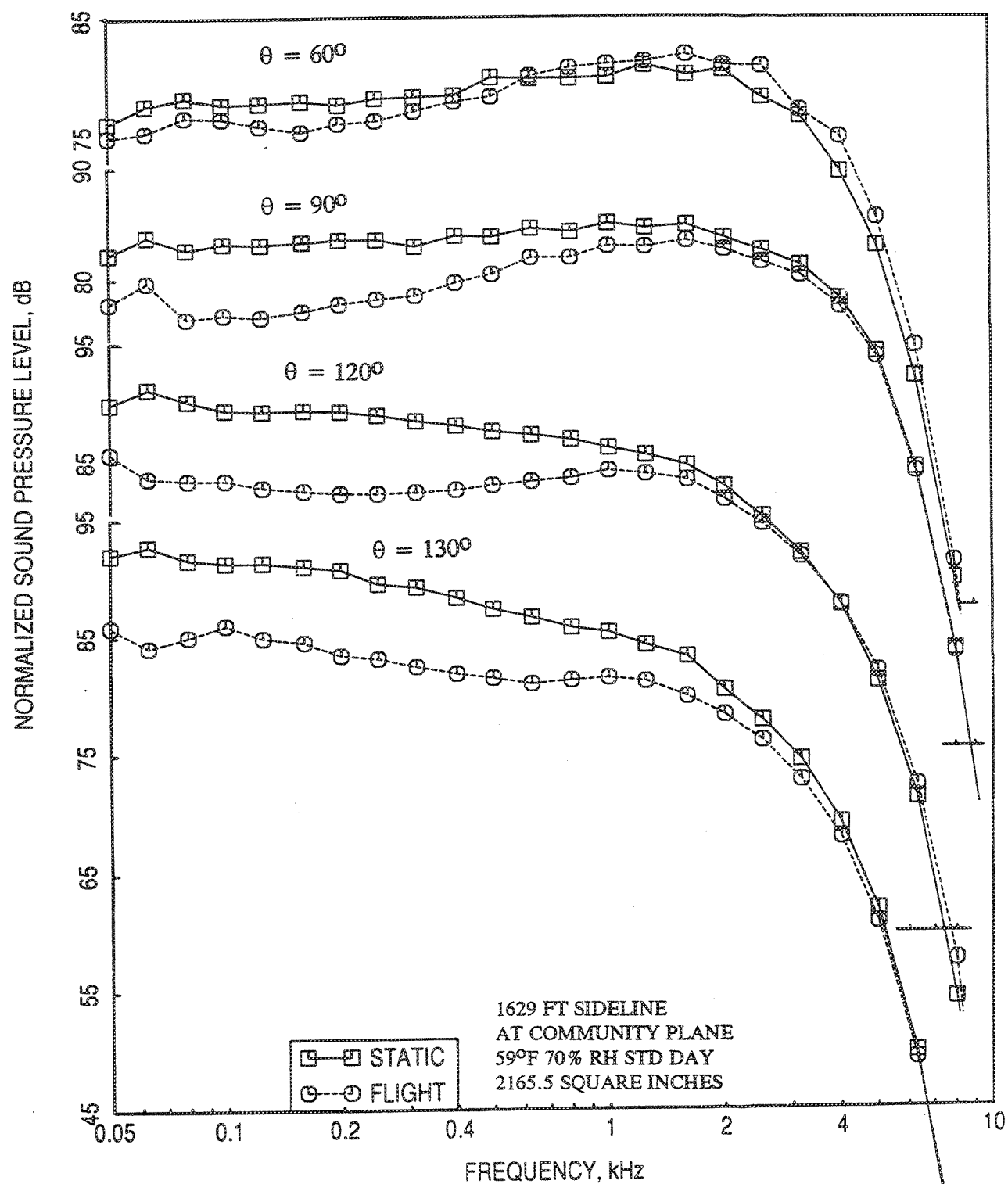


Figure 2.11.22. Effect of flight simulation ( $M_F=0.32$ ) on SPL spectra at different polar angles ( $\theta$ ) for 0.75"-thick fluid shield nozzle with porous plug at a jet velocity,  $V_{mix}=1811$  ft/sec;  $P_{r,p}=2.7$ ,  $T_{t,p}=1806^\circ\text{R}$ ,  $P_{r,s}=2.2$ ,  $T_{t,s}=727^\circ\text{R}$ .

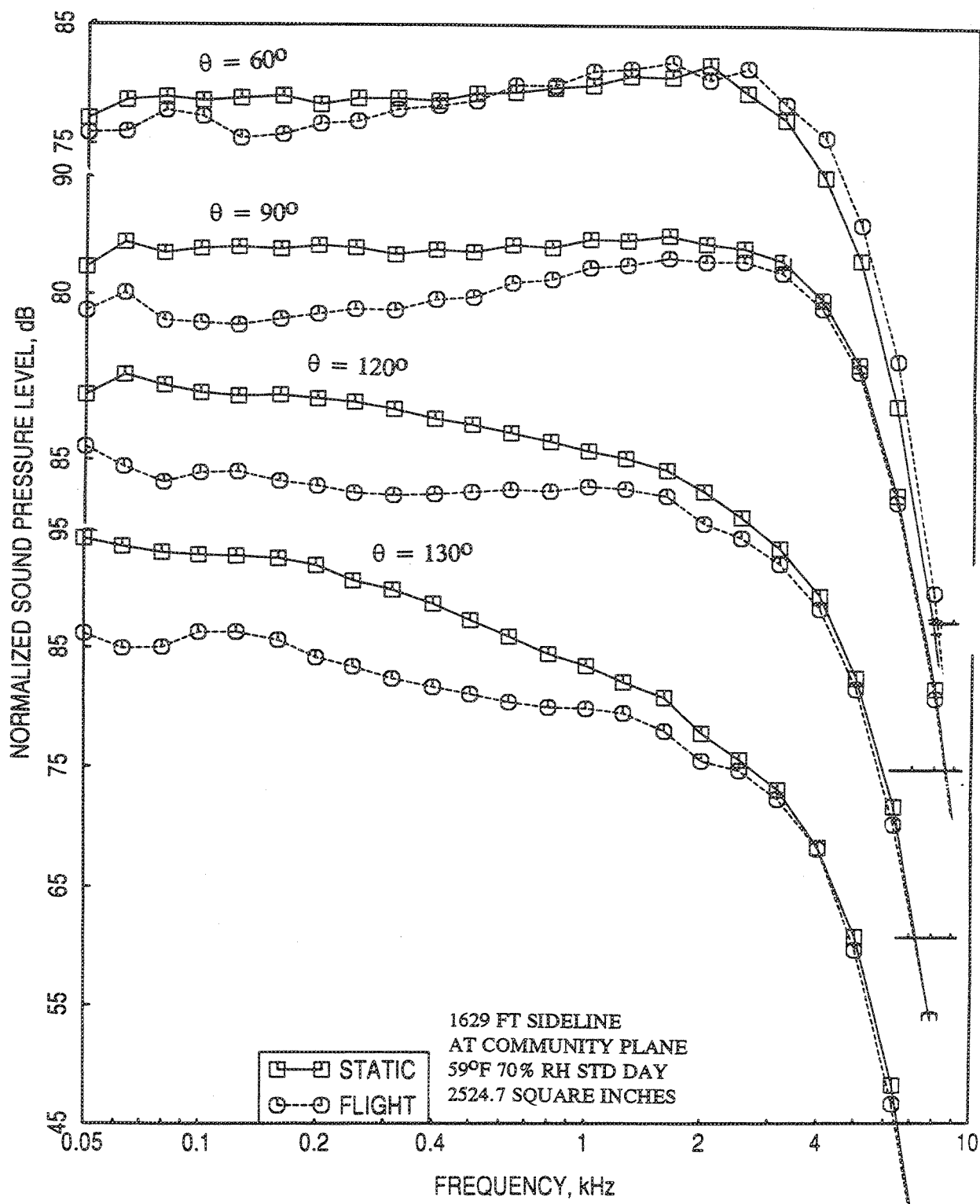


Figure 2.11.23. Effect of flight simulation ( $M_F=0.32$ ) on SPL spectra at different polar angles ( $\theta$ ) for 1.0"-thick fluid shield nozzle with porous plug at a jet velocity,  $V_{mix}=1811$  ft/sec;  $P_{r,p}=3.06$ ,  $T_{t,p}=1806^\circ\text{R}$ ,  $P_{r,s}=2.2$ ,  $T_{t,s}=727^\circ\text{R}$ .

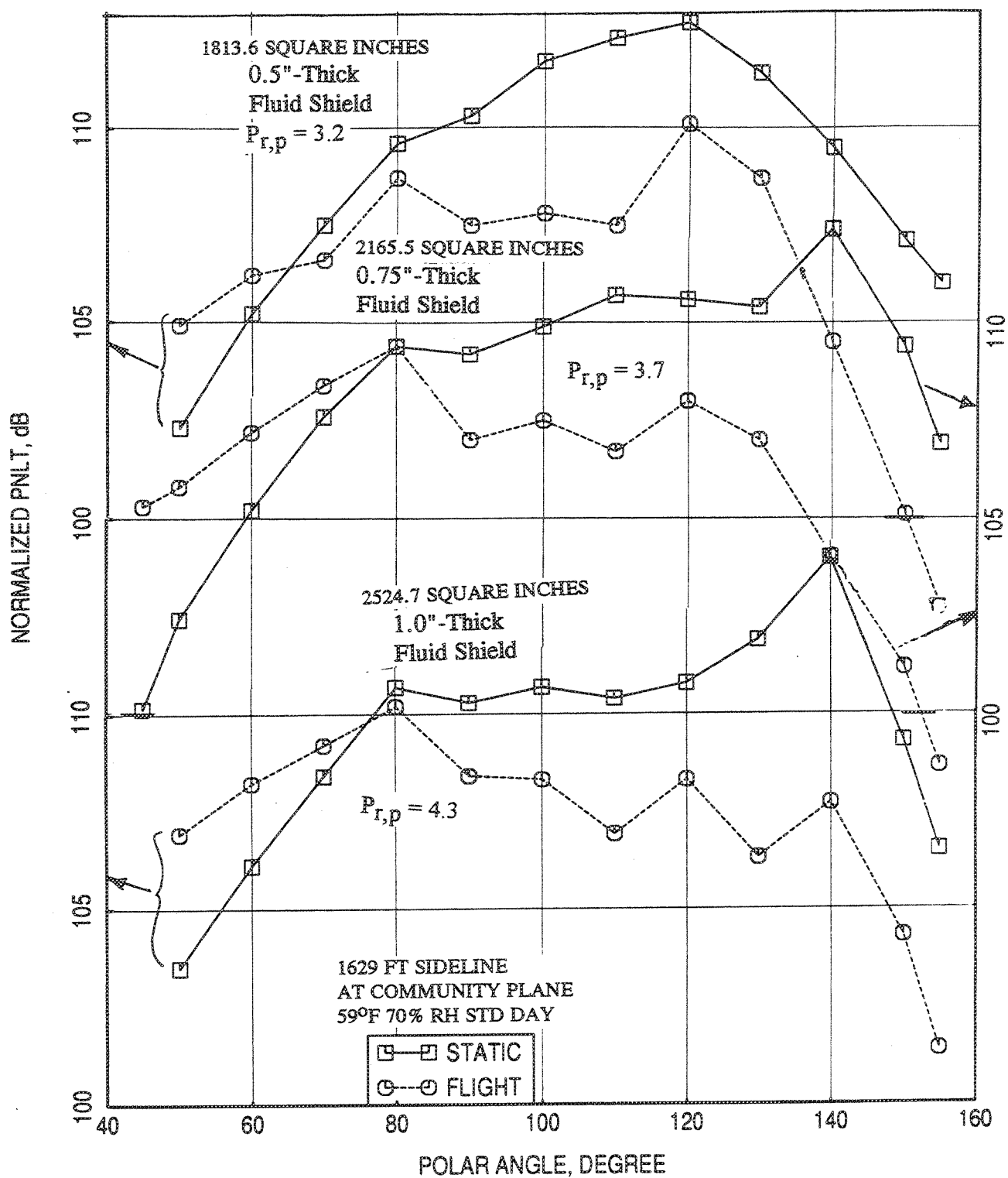


Figure 2.11.24. Effect of flight simulation ( $M_F=0.32$ ) on PNLT directivities for three fluid shield nozzles with porous plug at a jet velocity,  $V_{mix}=2030$  ft/sec,  $T_{t,p} = 1786^\circ R$ ,  $P_{r,s} = 2.14$ ,  $T_{t,s} = 695^\circ R$ .

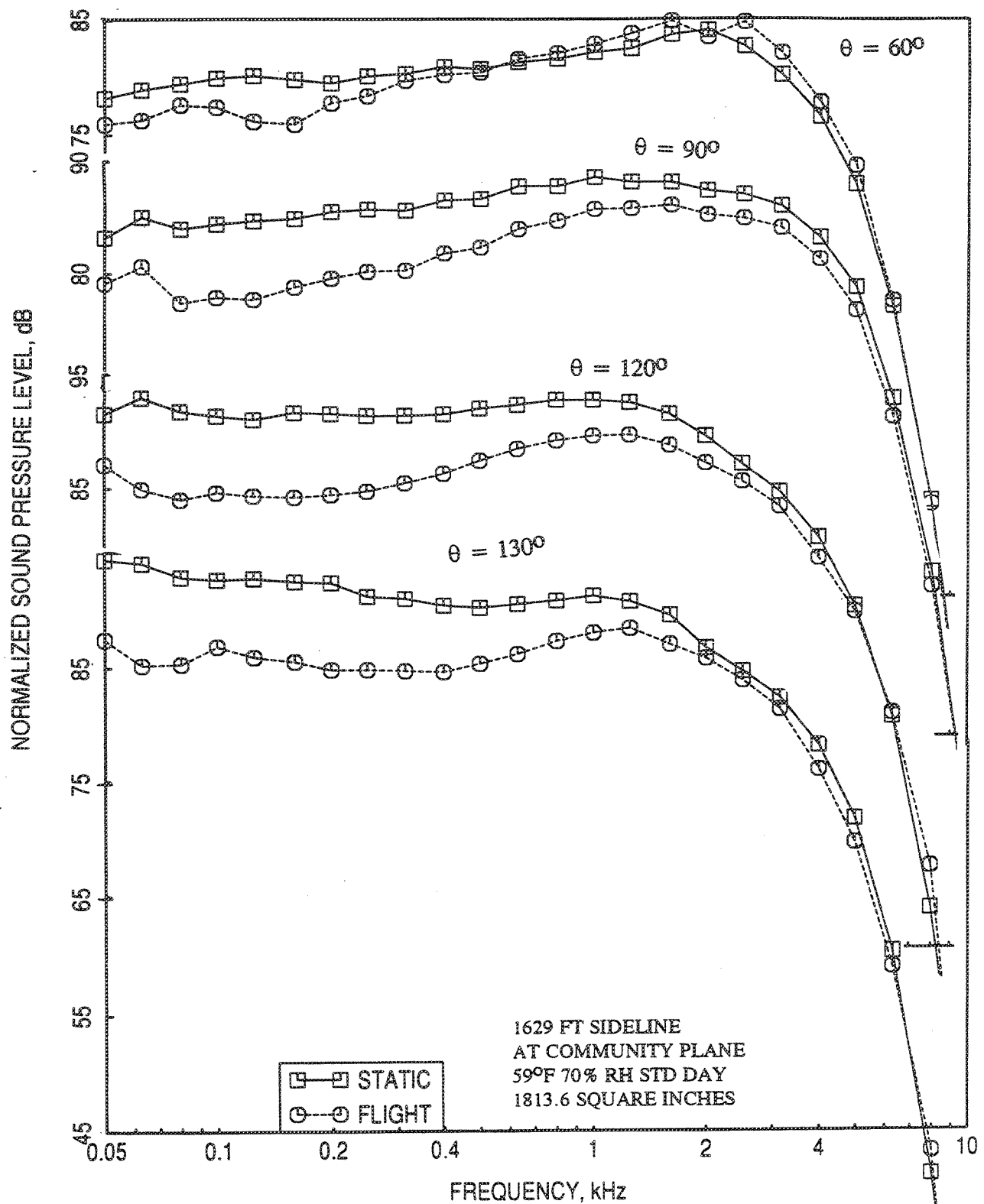


Figure 2.11.25. Effect of flight simulation ( $M_F=0.32$ ) on SPL spectra at different polar angles ( $\theta$ ) for 0.5"-thick fluid shield nozzle with porous plug at a jet velocity,  $V_{mix}=2030$  ft/sec;  $P_{r,p}=3.2$ ,  $T_{t,p}=1786^\circ R$ ,  $P_{r,s}=2.14$ ,  $T_{t,s}=695^\circ R$ .

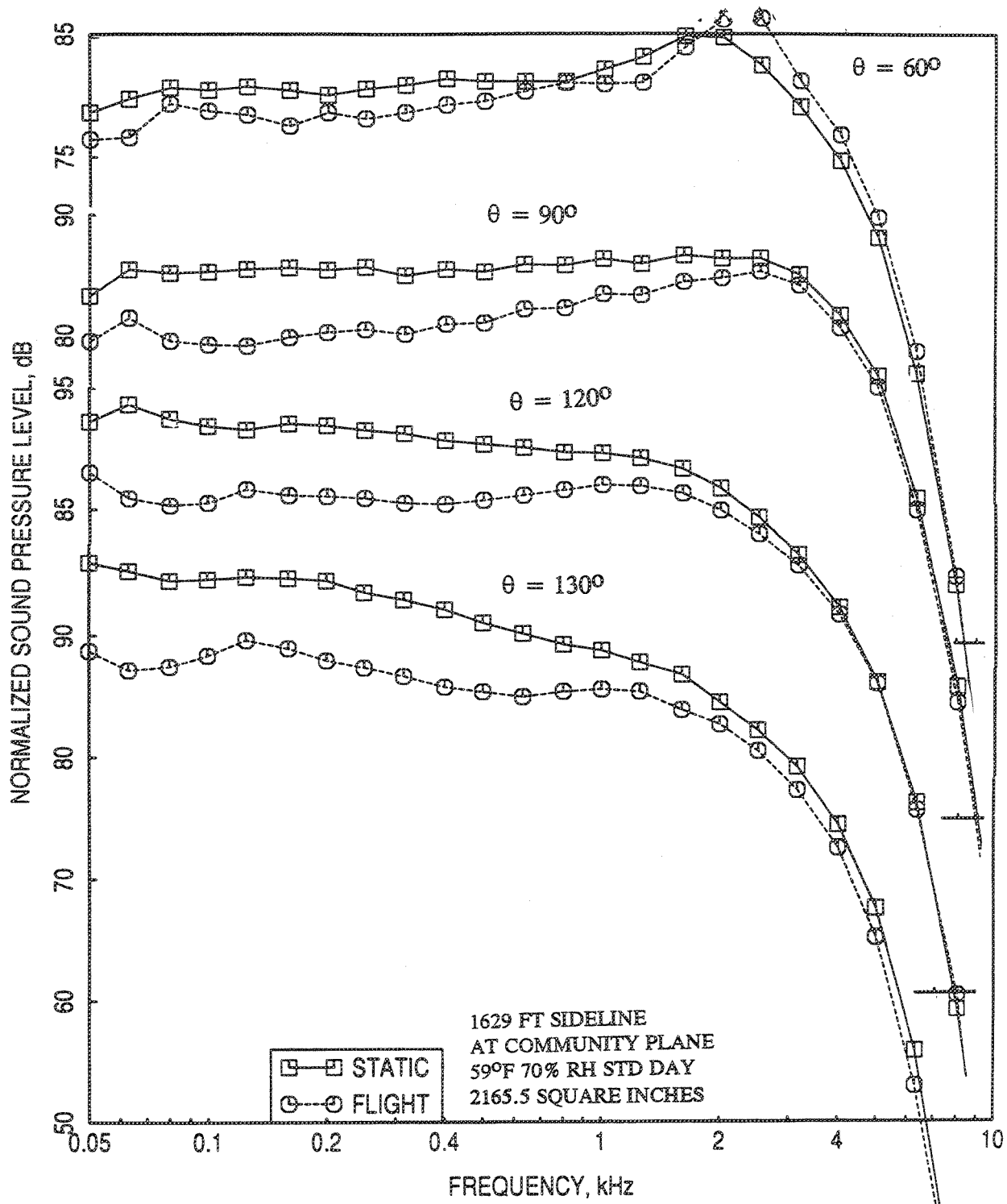


Figure 2.11.26. Effect of flight simulation ( $M_F=0.32$ ) on SPL spectra at different polar angles ( $\theta$ ) for 0.75"-thick fluid shield nozzle with porous plug at a jet velocity,  $V_{mix}=2030$  ft/sec;  $P_{r,p}=3.7$ ,  $T_{t,p}=1786^\circ R$ ,  $P_{r,s}=2.14$ ,  $T_{t,s}=695^\circ R$ .

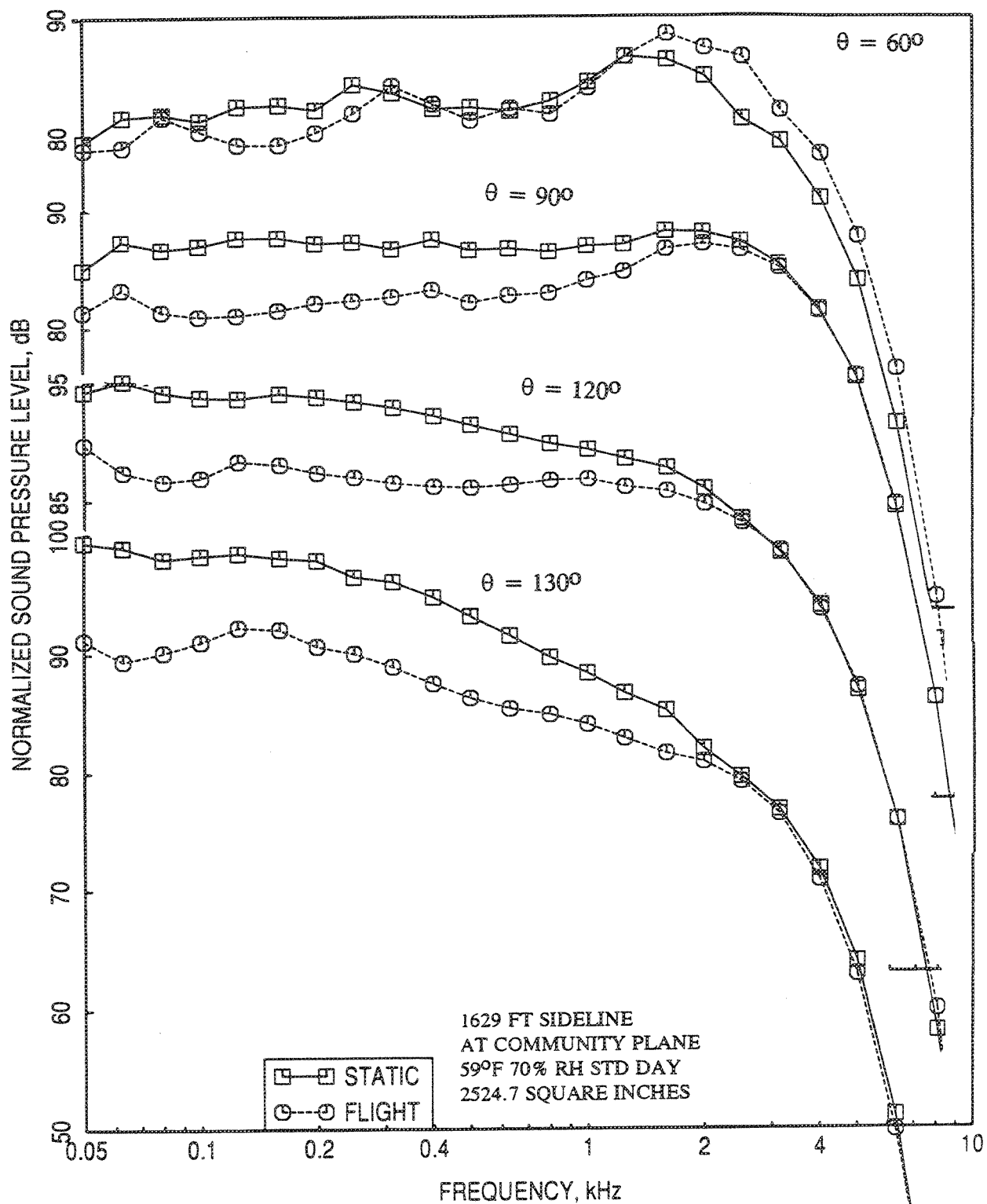


Figure 2.11.27. Effect of flight simulation ( $M_F=0.32$ ) on SPL spectra at different polar angles ( $\theta$ ) for 1.0"-thick fluid shield nozzle with porous plug at a jet velocity,  $V_{mix}=2030$  ft/sec;  $P_{r,p}=4.3$ ,  $T_{t,p}=1786^\circ R$ ,  $P_{r,s}=2.14$ ,  $T_{t,s}=695^\circ R$ .

## 2.12 CONCLUSIONS AND RECOMMENDATIONS

The principle objectives of this investigation are to evaluate the acoustic and aerodynamic characteristics of fluid shield nozzle concept and to assess Far 36, Stage 3 potential for fluid shield nozzle with Flade Cycle. To achieve the above objectives, the following tasks are performed:

1. Acoustic data for nine scale model nozzle configurations are obtained. The effects of simulated flight and geometric and aerothermodynamic flow variables on the acoustic behavior of the fluid shield are determined. The acoustic tests are aimed at studying the effect of (1) shield thickness, (2) wrap angle, (3) mass flow and velocity ratios between secondary and primary streams at fixed mixed velocities, (4) porous plug, and (5) subsonic shield.
2. Shadowgraphic tests to visualize the plume flow on six configurations are conducted to understand the aerodynamic mechanisms of fluid shield nozzles.
3. Static pressure data on suppressor chute surfaces, on shielded and unshielded sides, and on plug surface along hot and cold chute flows are acquired to determine the impact of fluid shield on base drag of the 36-chute suppressor nozzle and the thrust augmentation due to the plug.

The major observations made from the analyses of the measured acoustic, static pressure, and shadowgraphic data and a few recommendations to improve the noise suppression potential of fluid shield concept are as follows :

1. The plume shock structures on the unshielded side are distinctly different from those on the shielded side, as observed in shadowgraphic photographs. On the unshielded side the plume shows vertical and horizontal bright lines, whereas, in the shielded plume, which begins at the shield exit plane, triangular lines are seen on the nozzle surface upstream of the suppressor exit. Close to the suppressor exit plane complex structures are seen compared to rectangular structures of unshielded side. Following this the structures become somewhat rectangular in shape further downstream of the suppressor exit plane. Effectiveness of the porous plug in reducing shock strength is not evident from shadowgraphic pictures, since the complex plume flow prevents the interaction of shocks with the plug.

2. Based on the static pressure distribution on the plug and chutes for the suppressor alone configuration, the effect of nozzle pressure ratio on  $\Delta C_{fg}$  is very little for static cases, however, is significant with flight simulation. In this situation  $(\Delta C_{fg})_{pa}$  (i.e., for the plug) decreases and  $(\Delta C_{fg})_{ca}$  (i.e., for the chutes) increases with respect to nozzle pressure ratio. The combined correction to  $C_{fg}$  is close to zero for static case, but negative with flight simulation. However, with increasing nozzle pressure ratio  $(\Delta C_{fg})_t$  increases and is closer to zero for higher nozzle pressure ratio. The  $(\Delta C_{fg})_t$  is about 0 % and -1.5 % at takeoff for static and with flight simulation, respectively. The corresponding values at cutback are -0.5 % and -2 % respectively. Effect of porous plug on  $\Delta C_{fg}$  is small. For static condition  $\Delta C_{fg}$  is lower for porous plug compared to the rigid plug for entire range of nozzle pressure ratio. However, with flight simulation the difference of  $\Delta C_{fg}$  between rigid and porous plugs is very small and the  $\Delta C_{fg}$  for porous plug is slightly lower compared to rigid plug at higher nozzle pressure ratios. The trend is reversed at lower nozzle pressure ratios.

3. Based on the static pressure distribution on the plug and chutes for the fluid shield configuration, the effect of porous plug on  $\Delta C_{fg}$  is to increase its value at static condition compared to the rigid plug for entire range of mixed nozzle pressure ratio, which is opposite to the trend observed for the suppressor alone configuration. However, with flight simulation the difference of  $\Delta C_{fg}$  between rigid and porous plugs is reduced considerably and the trend is reversed, that the  $\Delta C_{fg}$  for porous plug is slightly lower compared to rigid plug.  $(\Delta C_{fg})_{ca}$  levels drop drastically due to fluid shield nozzle and slight improvement is observed with increasing shield thickness. The combined values (i.e.,  $(\Delta C_{fg})_t$ ) indicate that the  $(\Delta C_{fg})_t$  for 0.5"-thick fluid shield nozzle is about 2 to 3 % lower compared to the suppressor alone configuration. With increasing thickness small reduction of  $(\Delta C_{fg})_t$  is noticed. With flight simulation plug and chute pressure contributions to nozzle  $C_{fg}$  is about 4 to 5 % thrust loss over most of the cycle conditions. This is a significant disadvantage of this shielded-chute combination.

4. Based on the acoustic results, slight noise reduction is achieved due to the porous plug. However, the amount of benefit is much less than what was expected of porous plugs. Shadowgraph results of suppressor indicate insignificant difference in the shock structures between hard wall plug and porous plug configurations. In addition, while the static pressure distributions on plug for suppressor alone configuration indicate some difference between hard wall and porous plugs, similar results for a 0.5"-



thick fluid shield nozzle configuration show even smaller differences between the two plugs.

5. Suppressions of about 8 EPNdB is achieved by the 36-chute suppressor alone configuration with porous plug at takeoff and cutback cycle conditions. While, these noise suppressions are reasonable, higher suppressions would have been helpful in meeting the Noise requirement goals. The measured farfield noise due to the suppressor contains some amount of shock associated noise as evident from acoustic, static pressure, and shadowgraph data. This noise could be reduced by using CD chute designs for takeoff condition. In addition, the chute flow path for this suppressor has relatively higher slope, due to stoability constraint, which might have caused flow separation in the secondary flow and caused noise increase. Improvement on chute suppressor design by optimizing SAR, chute leading edge angle, and chute flow path may contribute some more noise reduction.

6. Substantial noise benefit is obtained due to fluid shields compared to suppressor alone configuration. For the takeoff thrust of about 67 to 69 klbs, with flight simulation, while noise suppression of about 8 EPNdB is achieved by the suppressor alone configuration, additional benefit of about 4 to 8 EPNdB are obtained due to fluid shields of different thicknesses compared to the suppressor alone configuration. Similar noise benefits due to suppressor alone configuration and due to fluid shields are also obtained with respect to core stream velocity. At takeoff condition (i.e., at core velocity of 2475 ft/sec), noise benefit of as high as 8 EPNdB with flight simulation is observed for 0.75" and 1.0" thick shields with respect to the suppressor alone configuration. With respect to FAR 36 Stage 3 noise requirement the best of fluid shield configuration falls short of about 3.5 EPNdB at takeoff with an ideal gross thrust of about 68 klbs. Noise suppression increases with increasing shield thickness until it reaches an optimum value. The trend is reversed by further increase in shield thickness. For the present study 0.75"-thick shield (i.e., about 5.25" for full scale nozzle) seems to be the optimum.

7. Noise level decreases with increasing  $V_F$  and/or  $W_F$ . With respect to shield thickness, minimum  $V_F$  and  $W_F$  for a fixed noise level correspond to the 0.75"-thick shield. The noise characteristics with respect to  $V_F$  and  $W_F$  are of opposing behavior to the  $\Delta C_{fg}$  characteristics, that a lower negative  $(\Delta C_{fg})_t$ , which is desirable for takeoff thrust from performance considerations, occurs at lower velocity and mass flow ratios.

A compromise between acoustic and  $\Delta C_{fg}$  needs to be considered for the application of fluid shield in real engines.

8. Noise levels decrease with respect to increasing fluid shield pressure ratio  $P_{r,s}$ . However, the trend is reversed due to further increase in  $P_{r,s}$ . Normalized PNLT at all angles increases with increasing fluid shield total temperature  $T_{t,s}$  whereas, ideal gross thrust remains more or less same for all the cases. Corresponding normalized SPL spectra also indicate the similar trend at all frequency. Effect  $T_{t,s}$  of is insignificant with flight simulation. It seems beneficial from noise considerations to operate the fluid shield at lower temperature. Noise levels in terms of normalized EPNLT, PNLT, and SPL increase with increasing core stream pressure ratio  $P_{r,p}$  and total temperature  $T_{t,p}$ .

9. Azimuthal variation of farfield noise is relatively less dominant for the fluid shield nozzles. The fluid shield with higher shield thickness is more effective in shielding the noise. Azimuthal noise variation is insignificant with subsonic shield flow. With flight simulation azimuthal noise variation increases compared to the static case.

10. The effect of flight on farfield noise is similar for all the nozzle configurations, the conical nozzle, the 36-chute suppressor, and the fluid shield configurations. At the subcritical conditions, the sound field consists of pure jet mixing noise, and hence a reduction with flight simulation is observed at all angles. As the jet becomes supercritical, the shock noise component is dominant in the forward arc, while the jet mixing noise is dominant in the rear arc. Thus, with flight simulation, as the mixing noise component reduces in level at all angles, the shock-associated noise component becomes more prominent in the forward arc, and this leads to smaller noise reductions at smaller polar angles. In fact, at very end of forward arc the noise increases with flight simulation.

### 3.0 AERO-MIXING TESTS IN AERODYNAMIC RESEARCH LABORATORY FOR TWO DIMENSIONAL FLUID SHIELD SCALE MODEL NOZZLES

Two dimensional fluid-shield scale model nozzles designed and fabricated under APT Task Order No. 4 (Contract NAS3-25951) were tested in GEAE's Aerodynamic Research Laboratory (ARL). The ARL wind-tunnel was operated in a free-jet mode and the nozzle models, which are scaled sector models of the full-scale fluid-shield/suppressor nozzle, were mounted on a sting inside it. Fluid-shield/suppressor nozzles with porous plugs have several low noise features that make them potential candidates for meeting FAR-36, Stage III, noise levels for an HSCT. Hence, an extensive fluid-dynamic and acoustic database is needed to assess their technical aspects, such as, fluid-shield effectiveness, mixing effectiveness, effect of porosity of plug, etc. The aero-mixing tests described here give a physical insight into the mixing characteristics, shock structures and chute/plug pressure distributions for different fluid-shield/suppressor geometries for this nozzle concept. This complements and helps us understand some of the results of the acoustic tests conducted in GEAE's Cell 41 for the round, scaled fluid-shield/suppressor nozzles and reported in the previous section. However, it should be noted that the sub-scale sector models with wedges to be used in the ARL test represent only the 2D "unwrapped" portion of the full-scale round nozzles with axi-symmetric plugs and, hence, can provide only a limited amount of information which can be related to the round nozzles. This test program, nevertheless, gives valuable insight into the development of second generation acoustic nozzles with fluid-shield concept and 2d *rectangular* geometry.

The major objectives of this test were as follows: (i) Provide flow-field diagnostic data on the effect of wedge porosity (shock mitigation) and suppressor/shield geometries (mixing process). (ii) Develop aerodynamic design data base for fluid-shield/suppressor exhaust nozzle concepts. (iii) Provide fluid-dynamic database to be used as reference data in validating CFD and acoustic codes (though, validation was not part of this contract).

A variety of techniques were used to obtain both qualitative and quantitative information regarding the flow-field, namely, shadowgraphs and planar laser sheet (PLS) scanning to visualize the shock-structures and vortices, and laser-velocimetry (LV) to measure two components of mean velocity as well as the turbulent intensity. In the following sub-sections we describe (i) the ARL test facility and data acquisition

procedure (ii) the scale models and the scope of testing (iii) key results from shadowgraphs, LV-data and PLS, and (iv) our conclusions and recommendations.

### 3.1 TEST FACILITY AND DATA ACQUISITION SYSTEMS

#### 3.1.1 Wind Tunnel Facility for Aero-Mixing Tests

**Free-Jet Wind-Tunnel :** The experimental investigation was conducted in the GEAE ARL subsonic wind tunnel. This facility is a single return, continuous flow, ambient wind tunnel. The wind-tunnel was operated as a free-jet with a 2 X 2 feet square section with open throat capable of providing a maximum of approximately 300 ft/s flow without any blockage effect. With the blockage due to the sting and the model the maximum speed was about 225 ft/s which at ambient temperature is Mach number of about 0.2. This flow has controlled temperature and turbulence. Figure 3-1 shows the free-jet wind tunnel layout.

**Model Support System :** The fluid-shield/suppressor nozzle sub-scale sector models were supported in the wind-tunnel by a sting/strut support system (see Figure 3-2). The centerline of the sting was aligned with the test section centerline. The cross-section of the sting is 7.0 inches in diameter and its length is 93.5 inches. The sting has two flow capability with 5.5 lbm/s for each flow. Either of the flow passages can be operated from ambient temperature to 860 degrees Rankine; however, only one flow passage can be heated at a time. For this test program, the inner flow passage provided the hot core flow (at 860 deg. R) and the outer annular passage supplied the fluid-shield flow at ambient temperature. The strut which supports the sting is airfoil shaped (NACA 0012) with approximately 42.0 inch chord in the streamwise direction. The maximum sting plus model blockage was 6.7 % of the cross-sectional area of the test section. Figure 3-3 is a close-up view of the model fluid shield nozzle installed in the wind tunnel.

**Internal Air Supply :** The nozzle core/jet flow is simulated in the model by airflow from a high pressure supply external to the model support system. In the dual-flow mode, a continuous flow of clean, dry, high pressure air at a stagnation temperature of about 860 deg. R enters the inner flow passage of the sting through a supply line in the strut and ambient air is pumped through its outer annular flow passage. Figure 3-4 shows a block diagram of this high pressure air supply system. Both the flow passages then go through a transition to appropriately match the nozzle geometry: the inner round tube slowly transitions into a passage with rectangular cross-section to provide the core flow geometry and the outer annulus simply transitions into a rectangular cross-section on only the top side of the nozzle to provide the fluid-shield geometry.

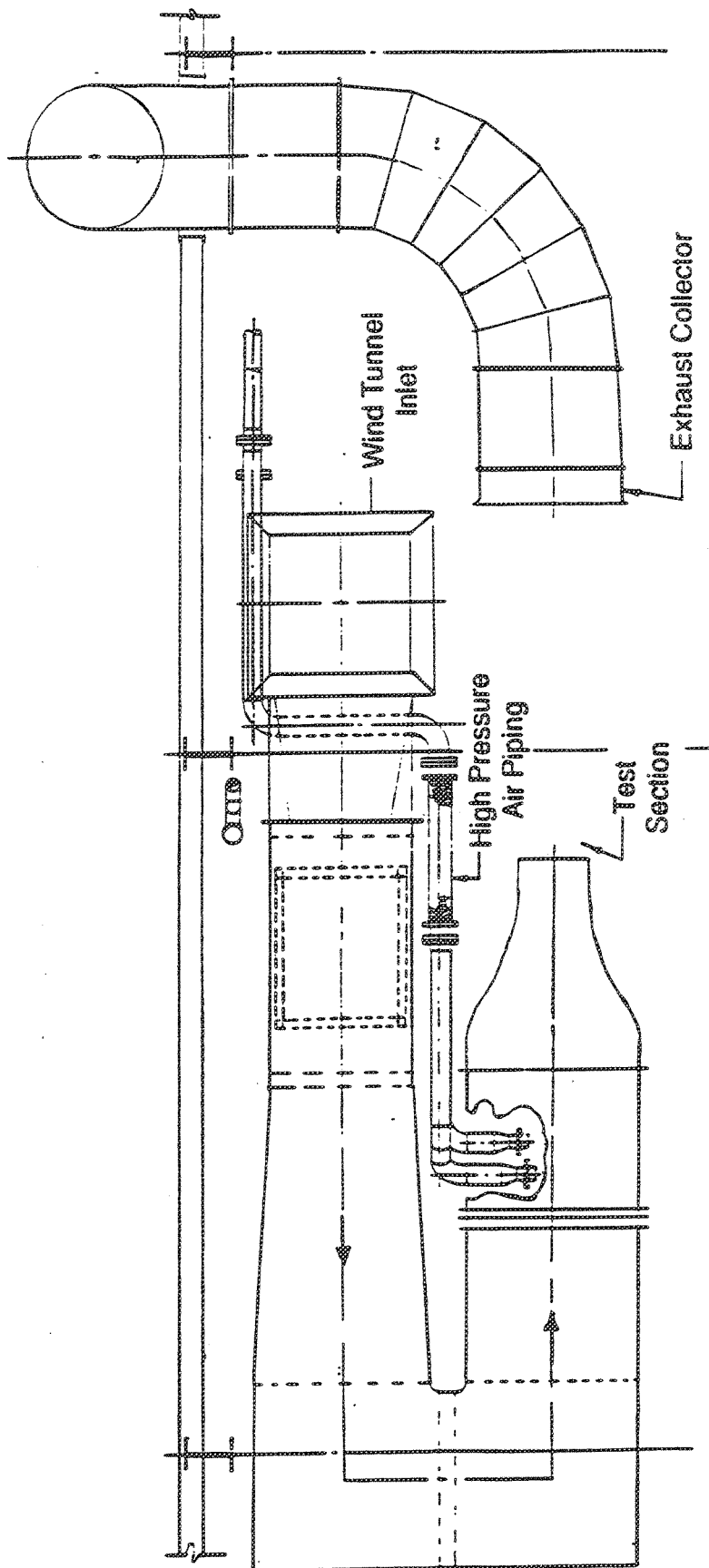


Figure 3-1. Aerodynamic Research Laboratory (ARL) free-jet wind tunnel.

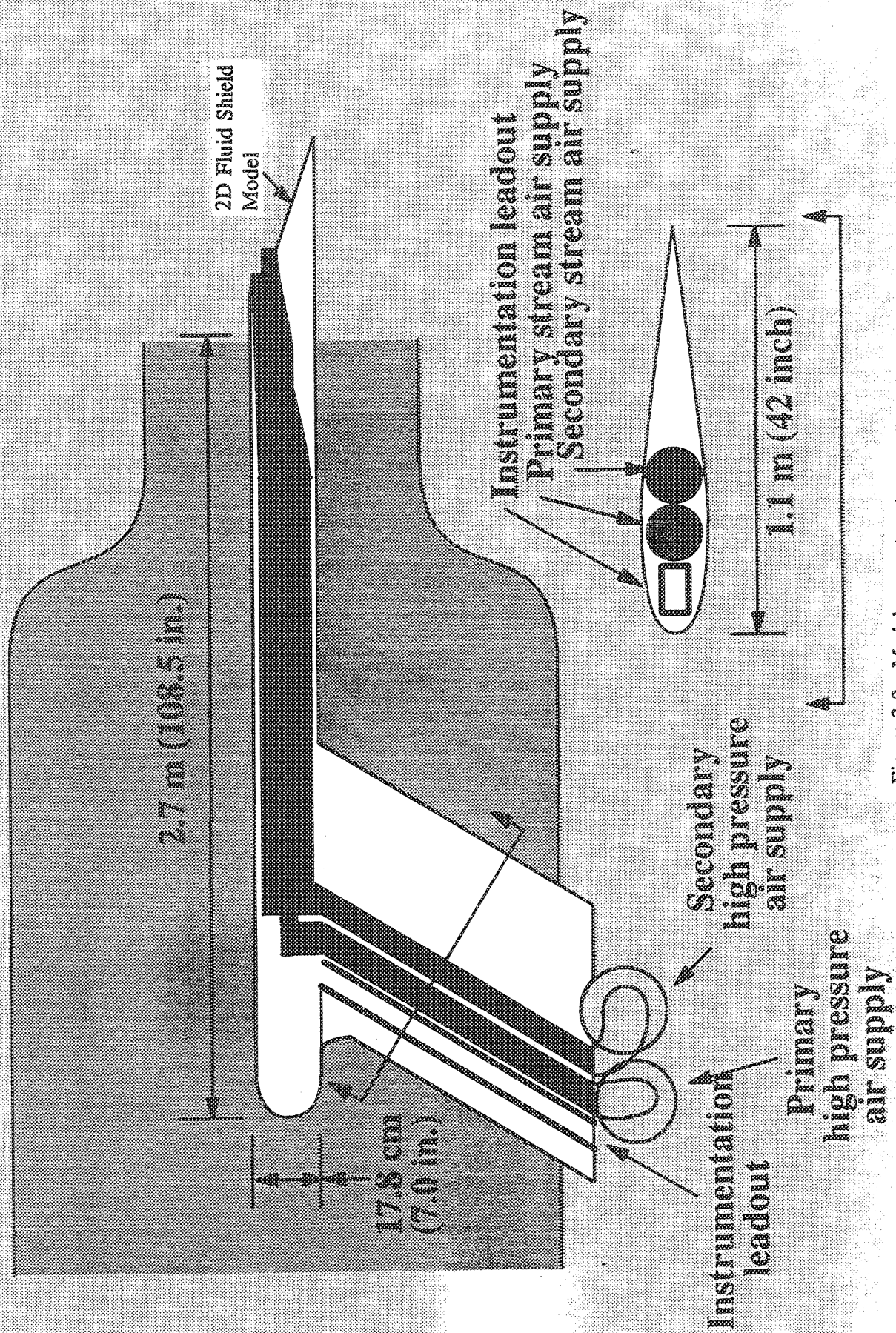


Figure 3-2. Model support system.



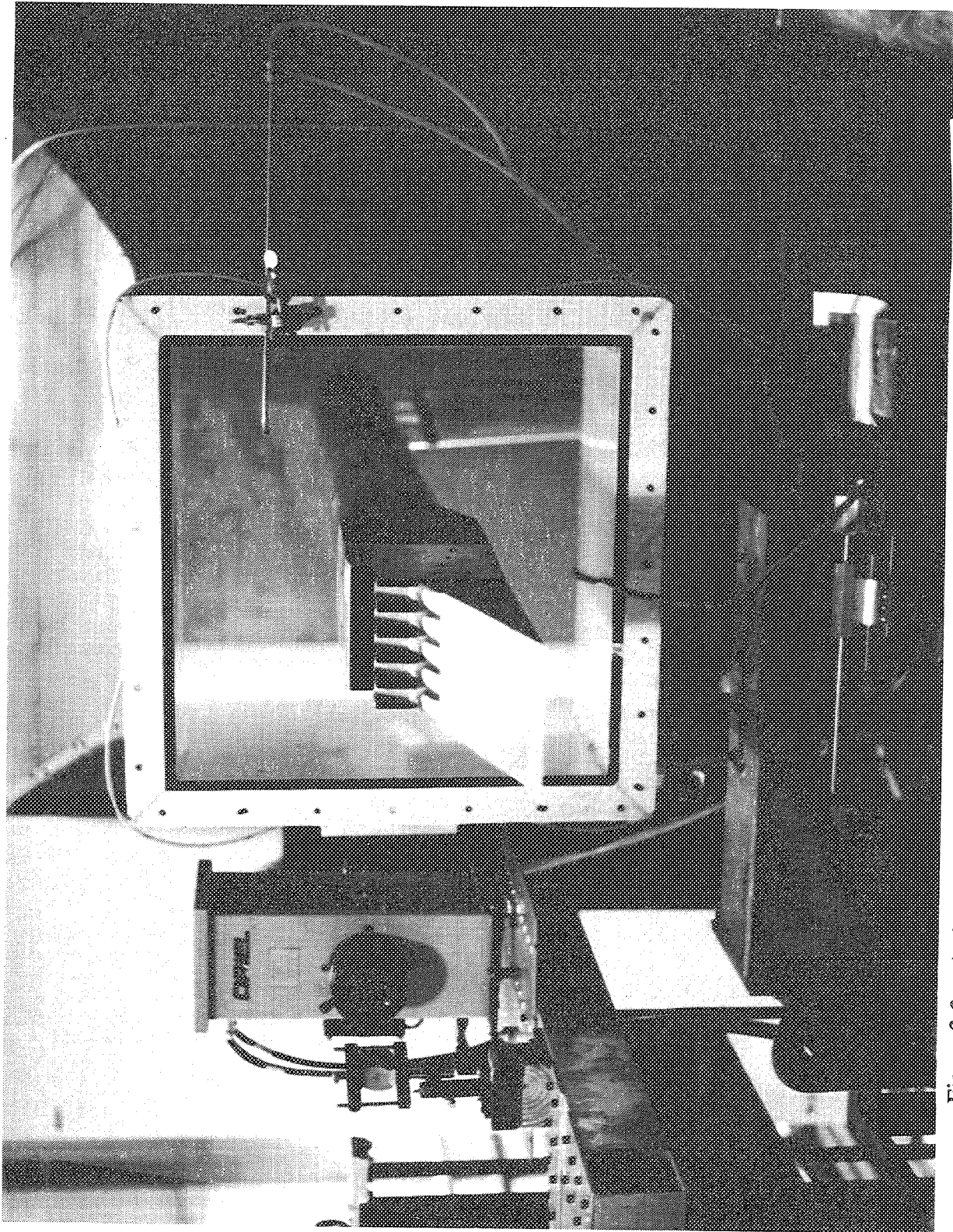


Figure 3-3. A close-up view of the model fluid shield nozzle installed in the wind tunnel.





The details of this internal transition are shown in Figure 3-5. The total and static pressures and the total temperature are measured in the instrumentation section which is just after this transition section. From the instrumentation section the airflow is exhausted through the 2D fluid-shield/suppressor nozzle.

### 3.1.2 Aerodynamic Data Acquisition System

Figure 3-6 shows a diagram of the pressure and temperature acquisition system. All static and total pressures were measured using a pressure acquisition system consisting of three 48 port scanivalve pressure transducers, signal conditioner and analog/digital converter. The pressure signals (data) are supplied to a MICRO VAX II computer system where it can be analyzed (reduced) or down loaded to GEAE's mainframe computer system. Concurrently, a front-end computer with touch-screen application was used for signal and facility control and real time data monitoring and analysis. Temperature data is fed directly to the front-end computer.

### 3.1.3 Shadowgraph System

A sketch of the shadowgraph system is shown in Figure 3-7. Since the light beam needs to pass through the flow, shadowgraphs can be taken for the 2D wedge models only in a vertical plane. A 35 mm camera and a Polaroid camera were used to take still photographs of the shadowgraphs on the screen. The shadowgraph system was mounted on a two-dimensional actuator for axial and vertical (i.e., up and down) movement. Figure 3-8 is a photographic view of the wind tunnel with shadowgraph setup for flow visualization.

### 3.1.4 Laser Velocimetry (LV) System

The Laser Two-Focus (L2F) velocimeter (see Figure 3-9) was used to measure the velocity of the flows non-intrusively. Small particles are always present in the flow or can be injected in the flow through an external source (seeding). These particles scatter light when they pass through the focal volumes formed by two highly focused laser beams inside the fluid. The detection of the scattered light enables one to derive the flow velocity from the time of flight the particles take to move from one beam to another with known separation distance (see Figure 3-9 (b)). This technique is sometimes known as laser transit anemometry or laser transit velocimetry. To obtain

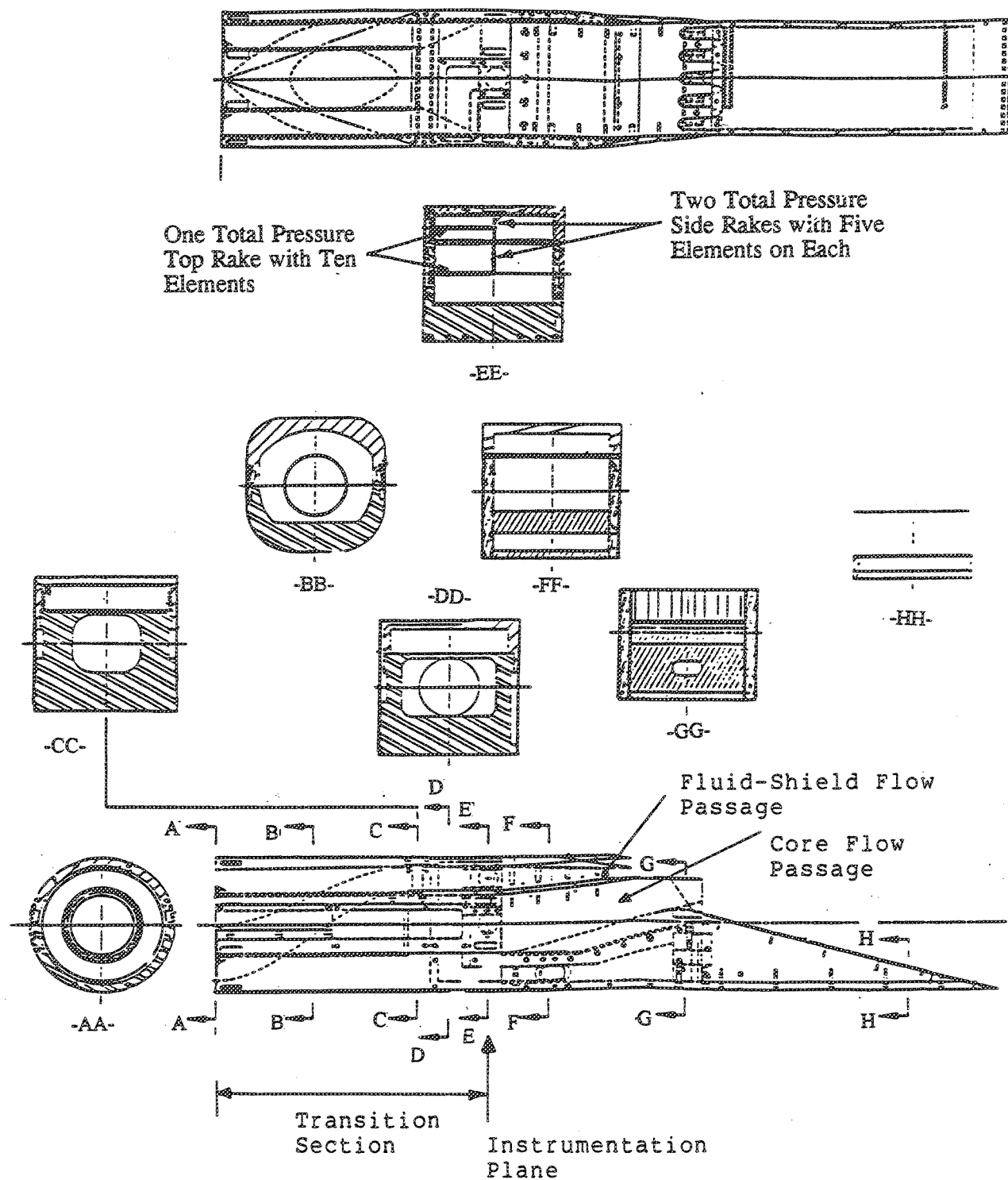


Figure 3-5. Layout of the fluid shield nozzle/sting installation.

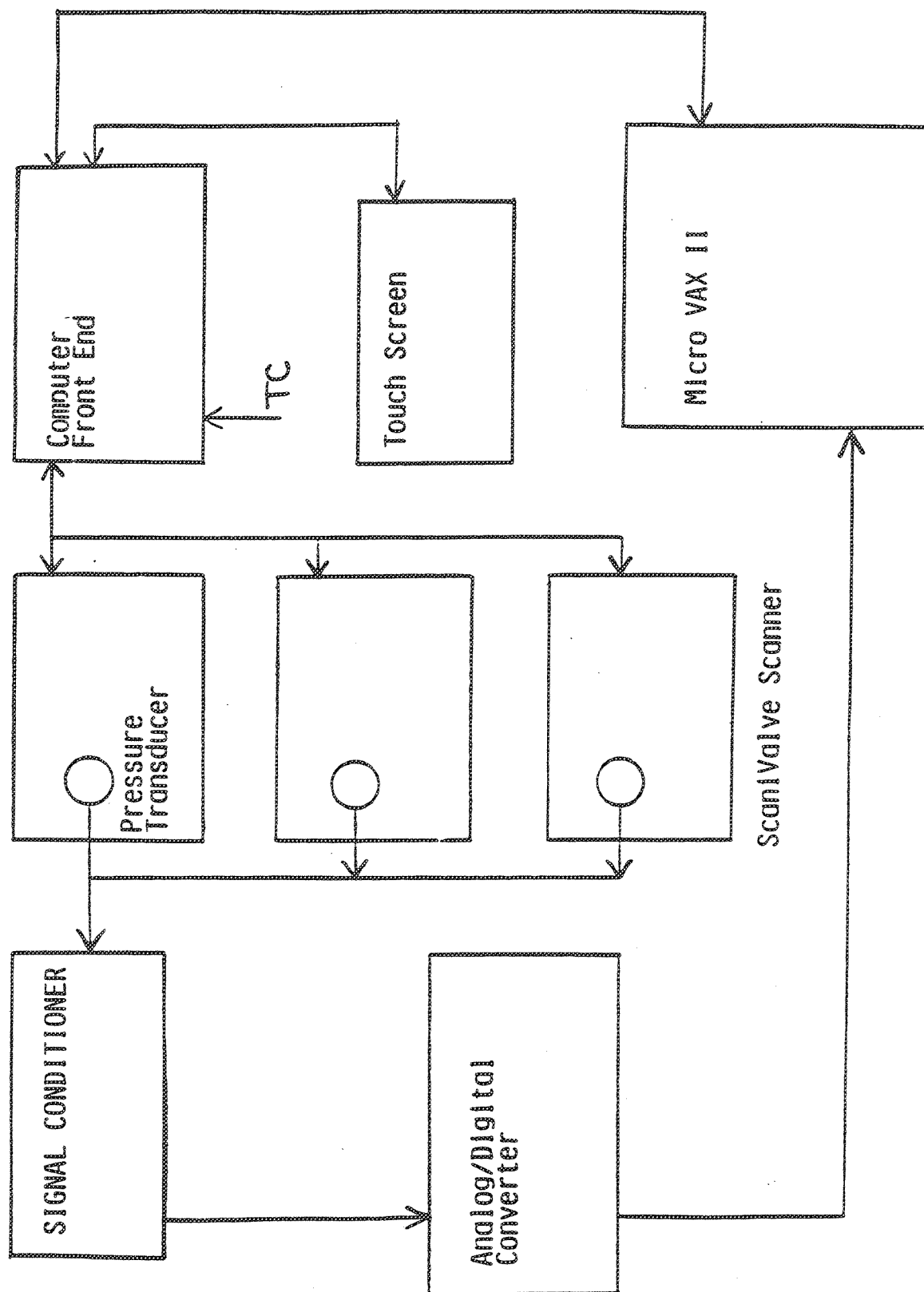


Figure 3-6. Pressure and temperature acquisition system.

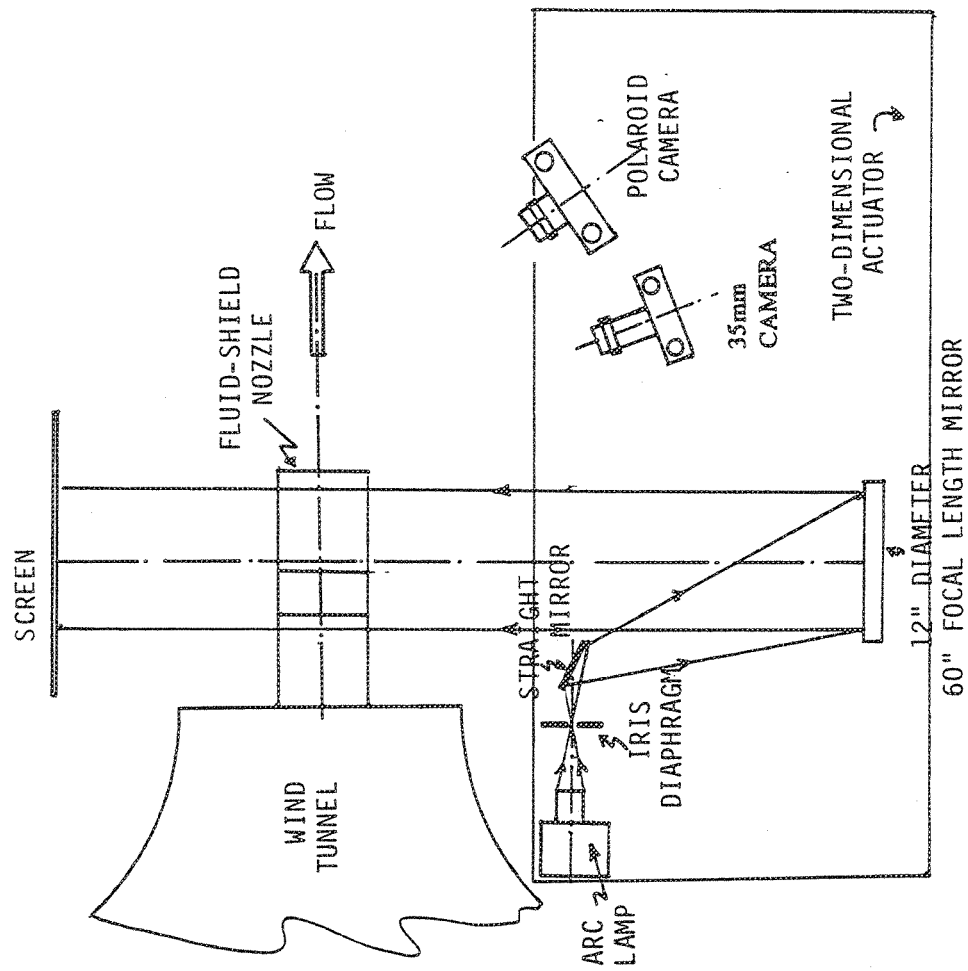


Figure 3-7. Schematic of the shadowgraph set-up (top view).

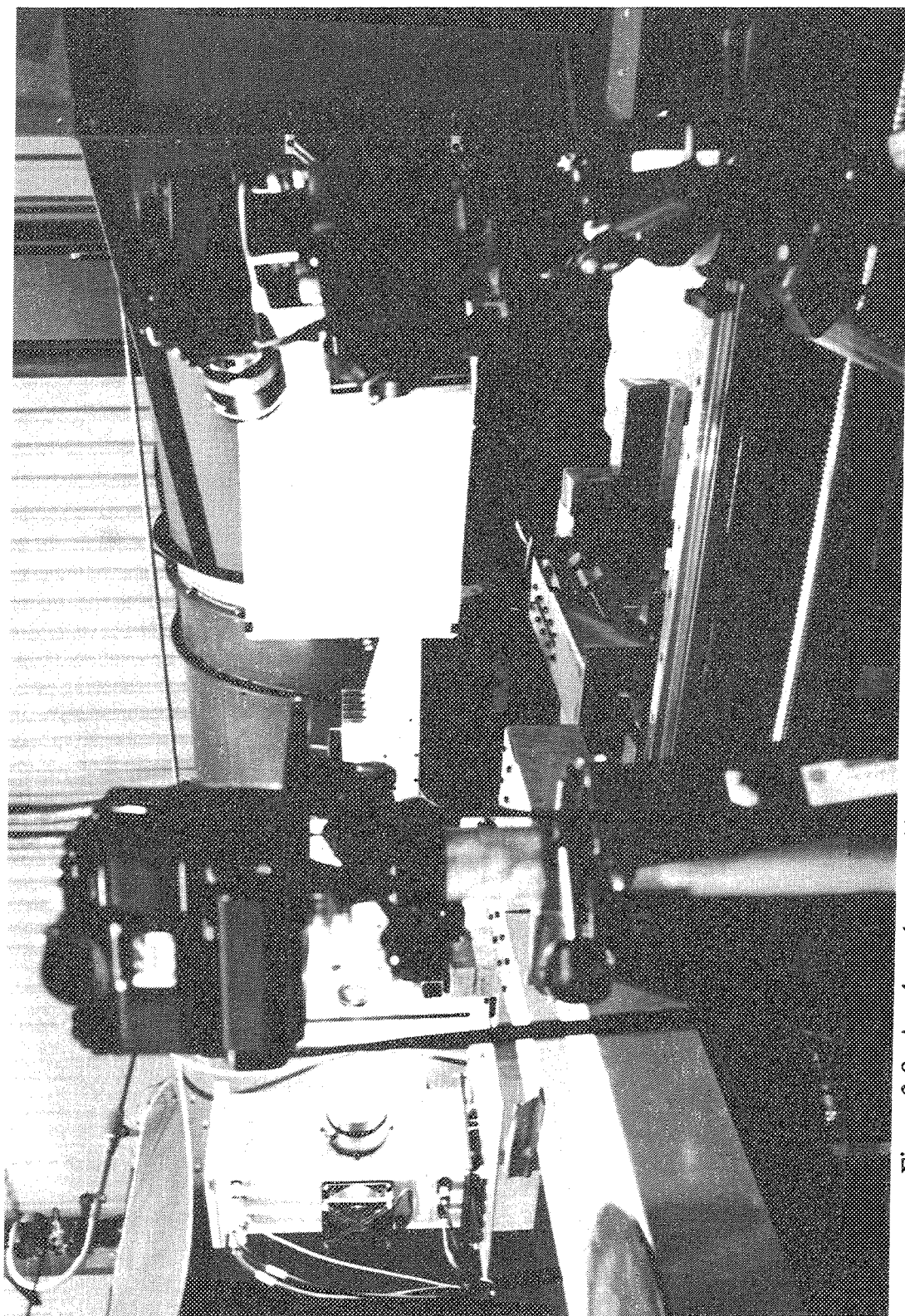
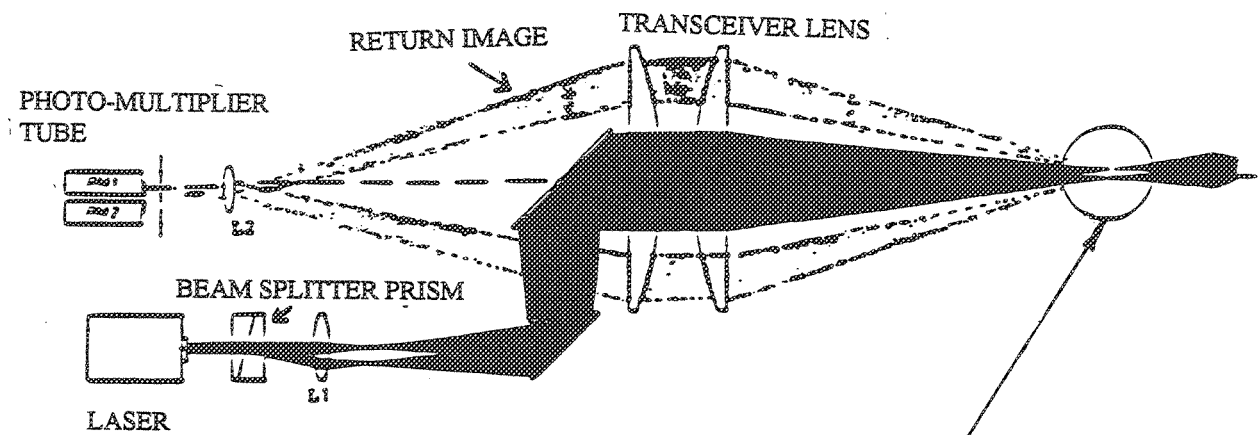
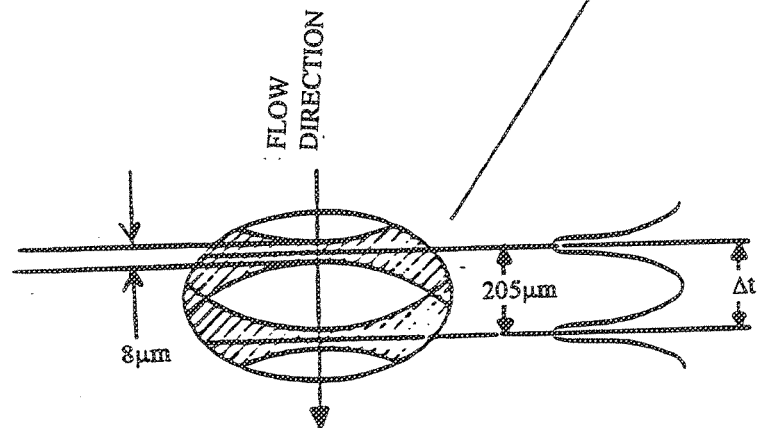


Figure 3-8. Another photographic view of GEAE's ARL subsonic free-jet wind tunnel and the shadowgraph set-up for flow visualization.



(a) Block Diagram of the L2F Optical Transceiver System.



(b) Focal Volumes and Electric Signals

Figure 3-9. Laser two-focus (L2F) velocimeter.

information about the velocity of flow, the time of flight of particles going from one focal volume to the other has to be measured. Figure 3-9 (a) shows schematically how scattered light is imaged onto the photo multiplier tubes. The photo multiplier detects the light quanta and produces an electrical signal. This signal is further amplified and connected to signal conditioning and timing electronics within the laser velocimeter electronic (LVE) cabinet. The L2F system can also give a measure of the turbulent intensity.

### 3.1.5 Planar Laser Sheet (PLS) System

A simplified layout of the planar laser sheet generator is shown in Figure 3-10. The X- and the Z-axis galvanometers are used to obtain one planar laser sheet containing the X-axis, viz., XY -plane or XZ-plane etc. Thus, if a plane transverse to the flow is to be illuminated then it can be obtained by placing the x-axis in the transverse spanwise direction; to obtain a vertical sheet (YZ) of laser-light this set-up was placed at the top of the nozzle. Still colored photographs of the flow visualized by the sheet of laser-light were taken by a 35 mm camera. We also took colored videos with a video camera focused on the laser sheet during the scanning part of this experiment where the location of the laser sheet was varied.



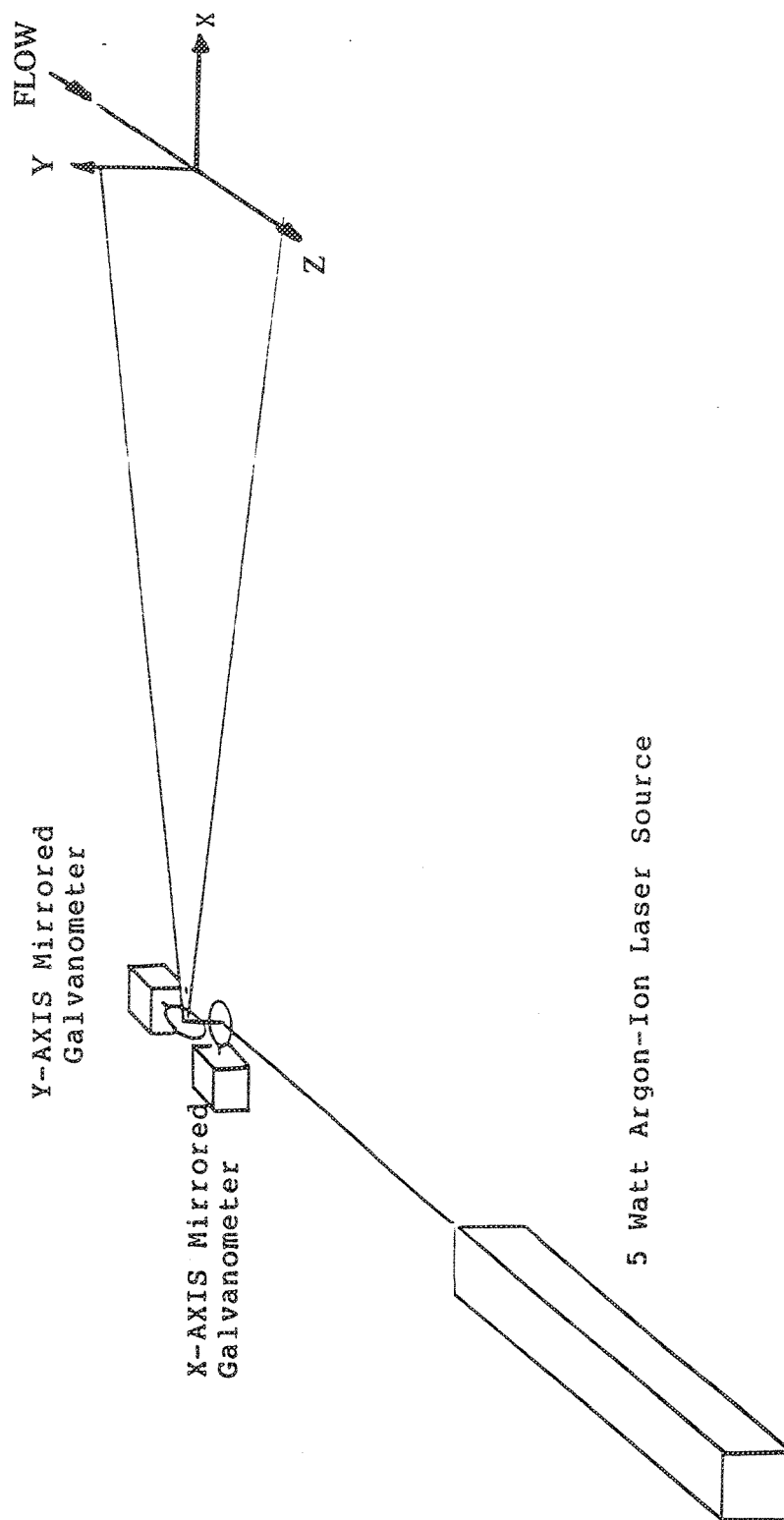


Figure 3-10. Simplified layout of the plane laser sheet generation.



## 3.2 SCALE MODEL NOZZLE DESCRIPTION AND SCOPE OF TESTING

### 3.2.1 Description of Test Nozzle Configurations

The 2D fluid-shield/suppressor nozzles were designed and fabricated under Task Order No. 4 of this contract (NAS3-25951) and represent the take-off flight condition. As mentioned in the introduction, these are sub-scale sector models designed to represent a 2D "unwrapped" portion of the full-scale round fluid-shield/suppressor nozzles. Each sub-scale model has a total of five side-by-side suppressor chutes, a flat fluid-shield on top and a half-wedge below to represent, respectively, the thirty-six suppressor chutes, the partially wrapped fluid-shield and the axi-symmetric plug of the full-scale round nozzle. Figure 3-11 shows a typical 2D scaled nozzle model (with overall dimensions) tested in ARL.

The baseline model configuration in the ARL test is defined to have the same non-dimensional parameters as in the Cell 41 baseline acoustic model and has the following nominal characteristics:

#### (i) Suppressor Chutes:

- \* Core Expansion Ratio (CER) = 1.0 [Convergent Core Flow Nozzle]  
CER is defined as the ratio of core exit area to core throat area
- \* Suppressor Area Ratio (SAR) = 2.5 [SAR is defined as the ratio of the sum of primary and secondary flow areas @ chute exit to the primary flow area @ chute exit.]
- \* Suppressor Chute Depth Ratio (SCD) = 1 [ See Figure 3-12 for definition of SCD.]
- \* Chute Base Angle (CBA.) = 55 deg. [See Figure 3-12 for definition of CBA.]

#### (ii) Fluid-Shield:

- \* Fluid-Shield Thickness ( $t_n$ ) = 0.48 "

#### (iii) Wedge:

- \* Wedge Surface Porosity (WSP) = 10 %
- \* Wedge Angle = 15 deg.

The parametric variations in the suppressor chute models have been selected according to the DOE (Design Of Experiments) technique. A summary of the suppressor chute configurations is given in Table 3.1. Figures 3-13, 3-14 and 3-15 show some of the



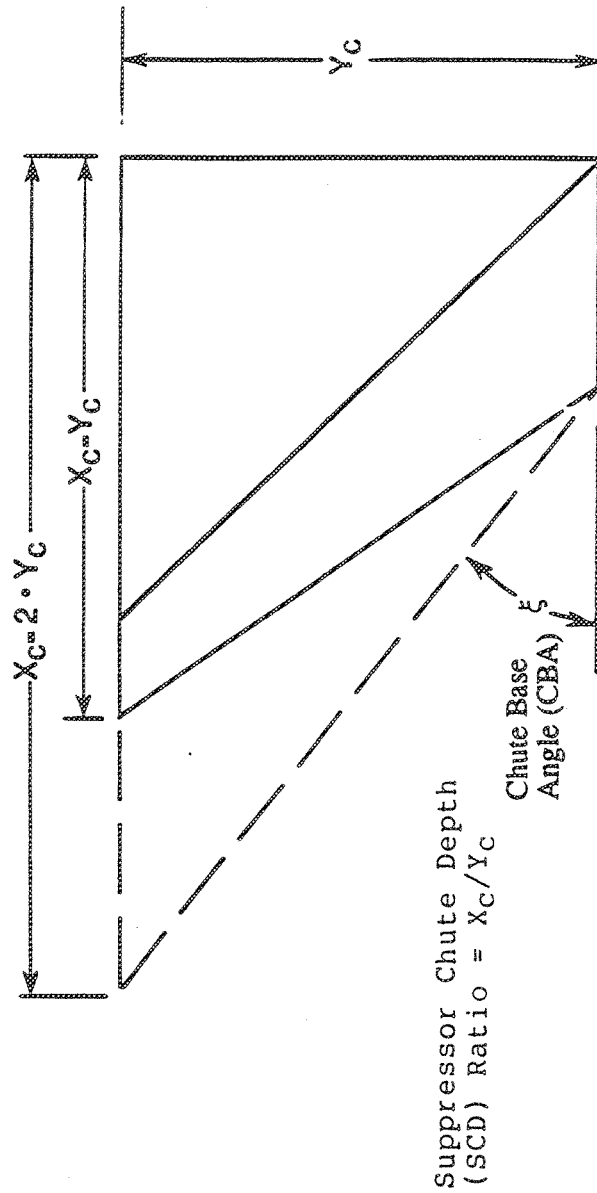


Figure 3-12. Definition of suppressor chute depth ratio (SCD) and chute leading edge angle.

Table 3.1 Suppressor Chute Configuration Summary\*

Chute Model No.	C/CD	CER	SAR	A <sub>g</sub> (in <sup>2</sup> )	SCD	CBA. (degs)
1(Baseline)	C	1.0	2.5	4.01	1	55
2	C	1.0	2.5	4.01	2	30
3	C	1.0	2.9	3.46	1	55
4	C	1.0	2.9	3.46	2	30
5	CD	1.1	2.5	4.01	1	55

\* Abbreviations explained below:

CER = Core Expansion Ratio = Core Exit Area/Core Throat Area

C/CD = Convergent/Convergent-Divergent Nozzle

SAR = Suppressor Area Ratio

= (Primary + Secondary Flow Areas @ Chute Exit)/(Primary Flow Area @ Chute Exit)

A<sub>g</sub> = Core Throat Area

SCD = Suppressor Chute Depth-to-height ratio (see Figure 3-12)

CBA = Chute Base Angle (depends on SCD, see Figure 3-12)

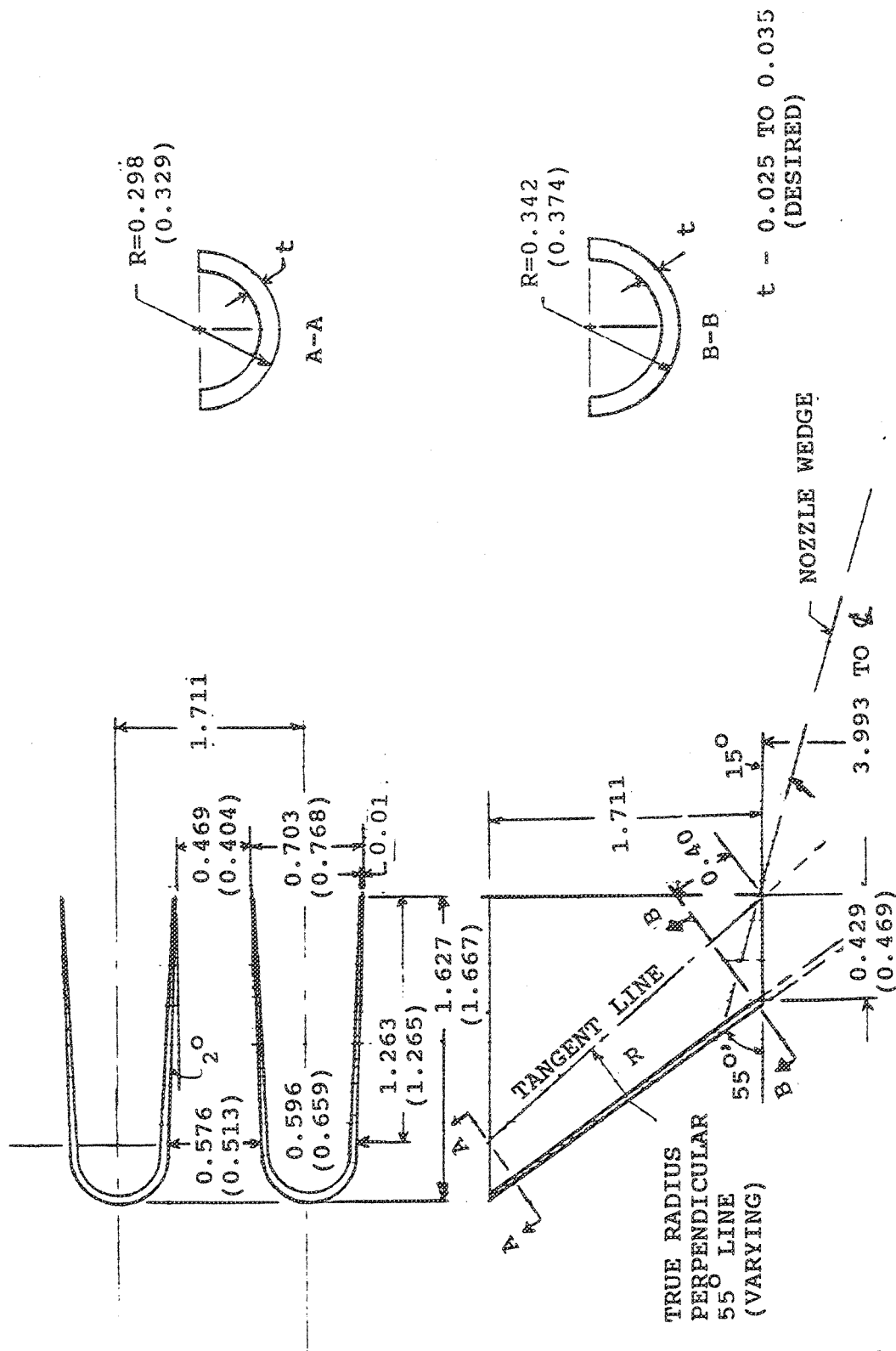


Figure 3-13. Chute design details of the suppressor for aero-mixing fluid shield nozzles; chute depth/height = 1, for SAR = 2.5 (model #1) and 2.9 (model #3, dimensions in parenthesis), all dimensions are in inches.







details of the suppressor chute geometries. As can be inferred from Table 3.1, all models have convergent nozzles, except model # 5 which has a convergent-divergent nozzle. Also all models have  $SAR = 2.5$ , except model # 3 and 4 which have  $SAR = 2.9$ . The reason for selecting these values for  $SAR$  and  $CER$  is that Cell 41 nozzle models have only convergent nozzles, i.e.,  $CER = 1$ , and  $SAR = 2.5$ . A comparison of the available chute geometries, fluid-shield thicknesses and plug porosities in the ARL test and Cell 41 test is given in Table 3.2.

With 5 models of chutes, 2 choices of wedge porosities and 2 choices of fluid-shield thicknesses we have a set of  $(5 \times 2 \times 2) = 20$  possible nozzle configurations. This set of all possible hardware configurations for the test nozzles is given in Table 3.3, where the nomenclature for the test configuration number is also explained. Thus, for example, Test Configuration # 1105 means chute model # 1 (which Table 3.1 says has  $CER = 1.0$ ,  $SAR = 2.5$ ,  $SCD = 1$ ) with 10 % porous wedge and 0.5" of fluid-shield thickness. Note, this is also the baseline model test configuration described above.

**Instrumentation :** Basic model instrumentation consists of i) rakes in the instrumentation section of the model and ii) static pressure taps on the fluid-shield floor, chutes and the wedge. There are four rakes in total in the two flow passages inside the model with each passage having one vertical and one horizontal rake (see Figure 3-4 for rake locations). Each rake has five total pressure probes and one static pressure tap. Further, each horizontal rake has a total temperature probe. These measurements of total and static pressures and total temperature are done inside the instrumentation section of the sting just before the flow reaches the nozzle inlet plane.

In these 2D sectorized nozzle configurations the flow-field in the central portion (both core flow and secondary flow) away from the side-edges was anticipated to simulate the flow-field of the actual round nozzles. Also, the plume flow-field after the 2D wedge ends was not expected to simulate the plume downstream of a conical plug. Hence, the focus of the measurements was in the central portions away from the edges of the wedge.

Each test model configuration is instrumented with static pressure taps in the following locations: 6 on the fluid-shield floor before the chutes begin (3 on the central chute center-line extension and 3 on the neighboring core center-line extension; see Figure 3-16); 10 taps on the chutes (2 on each chute at the same vertical location, one on the

**Table 3.2 Comparison of ARL & Cell 41 Fluid-Shield Nozzle Models  
(Geometrical Parameters)**

Item	ARL	Cell 41
General Geometric Configuration	2D with half wedge	Axi with conical plug
Number of suppressor chutes	5	36
Core Expansion Ratio	1.0 (Conv.) 1.1 (CD)	1.0 (Conv.)
Suppressor Area Ratio( $A_g$ )	2.5 (4.01 in <sup>2</sup> ) 2.9 (3.46 in <sup>2</sup> )	2.5(21.59 in <sup>2</sup> )
Suppressor Chute Depth Ratio	1 2	1
Wedge Surface Porosity	0 % 10 %	0 % 10 %
Fluid-Shield Thickness (Shape/Wrap-around Angle)	0.48"(flat)  0.98"(flat)	0.50"(220 deg) 0.60"(180 deg) 0.75"(220 deg) 1.00"(220 deg)

Table 3.3 Possible Nozzle Test Configurations

CER	SAR	SCD	WSP	$t_n$	Test Config Code No.*
1.0	2.5	1.0	0%	0.5"	1005
1.0	2.5	1.0	0%	1.0"	1010
1.0	2.5	1.0	10%	0.5"	1105 (Baseline)
1.0	2.5	1.0	10%	1.0"	1110
1.0	2.5	2.0	0%	0.5"	2005
1.0	2.5	2.0	0%	1.0"	2010
1.0	2.5	2.0	10%	0.5"	2105
1.0	2.5	2.0	10%	1.0"	2110
1.0	2.9	1.0	0%	0.5"	3005
1.0	2.9	1.0	0%	1.0"	3010
1.0	2.9	1.0	10%	0.5"	3105
1.0	2.9	1.0	10%	1.0"	3110
1.0	2.9	2.0	0%	0.5"	4005
1.0	2.9	2.0	0%	1.0"	4010
1.0	2.9	2.0	10%	0.5"	4105
1.0	2.9	2.0	10%	1.0"	4110
1.1	2.5	1.0	0%	0.5"	5005
1.1	2.5	1.0	0%	1.0"	5010
1.1	2.5	1.0	10%	0.5"	5105
1.1	2.5	1.0	10%	1.0"	5110

\* Nomenclature for Test Configuration Code No. of 4 digits: abcd  
a = Chute Model Number (see Table 3.1)  
b = % Wedge Surface Porosity, WSP/10  
cd = 10 x Nominal Fluid Shield Thickness,  $t_n$  (inch)

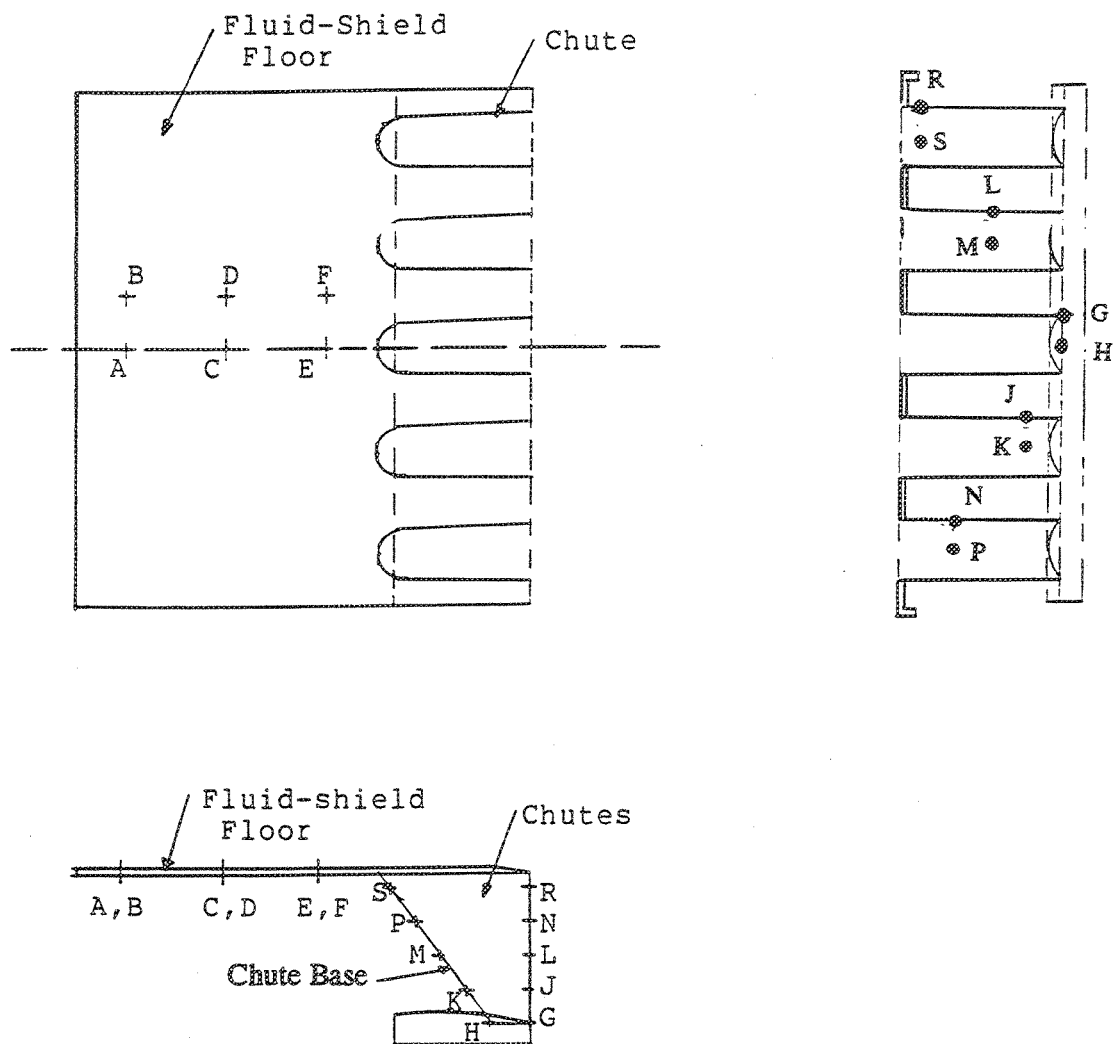


Figure 3-16. Typical static pressure taps on fluid-shield floor and chutes.

leading edge and the other at the trailing edge both facing the secondary flow; each chute has such taps at different vertical locations; see Figure 3-10); 24 taps on the wedge (12 on the chute center-line extension and 12 on the neighboring core center-line extension; see Figure 3-17).

### 3.2.2 Scope of Testing

Each nozzle configuration can be tested under different operating conditions. Having selected constant temperatures for the hot core flow (860 deg R) and the fluid-shield flow (ambient temperature), there are three more flow parameters which can be varied:

- a) The wind-tunnel Mach number,  $M_{wt}$ , to simulate static ( $M_{wt} = 0$ ) or wind-on conditions ( $M_{wt} = 0.2$ ).
- b) The primary or core nozzle pressure ratio ( $P_{r,p}$ ): 2.4 (cut-back cycle) and 3.2 (take-off cycle).
- c) The fluid-shield nozzle pressure ratio ( $P_{r,s}$ ): 0 (no-shield case), 1.6 (sub-sonic), 2.2 (supersonic).

The above choice of  $M_{wt}$ ,  $P_{r,p}$  and  $P_{r,s}$  gives us a combination of  $(2 \times 2 \times 3) = 12$  operating conditions for each nozzle configuration. With regard to budget and time constraints, we tested judiciously only a few nozzle configurations under few operating conditions focused to bring out the major interactions between the geometric parameters and/or operating conditions. The overall strategy was to test certain "must-do" configurations and leave the test matrix sufficiently flexible to accommodate additions and/or deletions depending on the test data gathered up to that point. The test was, hence, carried out in two separate phases: phase 1, where only static pressure measurements and shadowgraphs were found to get a quick assessment of the flow-field, and phase 2, where detailed LV-surveys by using the shadowgraphs for selecting custom-made locations of the LV-traverses for each configuration. Very limited planar laser sheet tests were also done in the end. The final test matrix for which data was obtained is given in Table 3.4. Thus, the effect on the flow field of wedge porosity, shield thickness, chute depth-to-height ratio and the suppressor area ratio can be quantified with these measurements.

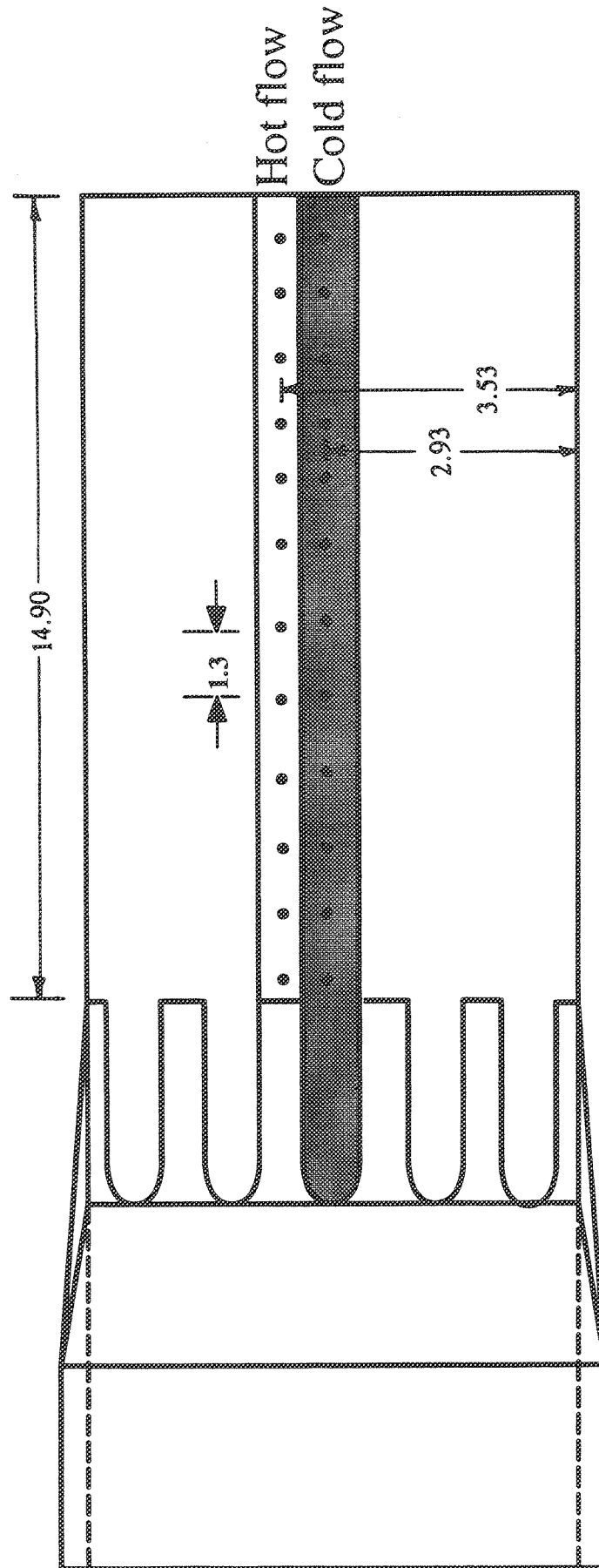


Figure 3-17. Typical static pressure taps on wedge (all dimensions are in inches).

Table 3.4. Test Matrix

Configuration Number	M <sub>wt</sub>	P <sub>r,p</sub>	P <sub>r,s</sub>	Shadowgraph	Laser Velocimetry	Planar Laser Sheet
1005	0.2	3.2	2.2	x		
1100	0.0	3.2	1.0	x		
1105 A	0.0	2.4	1.6	x		
1105 B	0.2	2.4	1.6	x		
1105 C	0.2	2.4	2.2	x		
1105 D	0.0	2.4	2.2	x		
1105 E	0.0	3.2	2.2	x		
1105 F	0.2	3.2	2.2	x	x	
1105 G	0.2	3.2	1.6	x	x	
1105 H	0.0	3.2	1.6	x		
1110	0.2	3.2	2.2	x		
2010	0.2	3.2	2.2	x	x	
2100	0.0	3.2	1.0	x		
2105	0.2	3.2	2.2	x		
3010	0.2	3.2	2.2	x		x
3105	0.2	3.2	2.2	x		
4005	0.2	3.2	2.2	x		
4010	0.2	3.2	2.2	x		x
4110	0.2	3.2	2.2	x	x	
5005	0.2	3.2	2.2	x		
5100 A	0.0	2.2	1.0	x		
5100 B	0.0	3.2	1.0	x		
5105 A	0.2	3.2	2.2	x	x	
5105 B	0.0	3.2	1.6	x		

Configuration # Nomenclature: abcd e

- a = Chute Model Number (see Table 3.1)
- b = % Wedge Surface Porosity, WSP/ 10
- cd = 10 x Nominal Fluid Shield Thickness,  $t_n$  (in.)
- e = Variation in Operating Condition



### 3.3 EXPERIMENTAL RESULTS AND ANALYSIS

In this section, we present and analyze the results obtained from shadowgraphs, LV-data and the planar laser sheet tests for select test points. The shadowgraphs give us a broad perspective of the flow-field, viz. the shock structures and shear layers, and, hence, are presented first for all configurations in section 3.3.1. Its details are analyzed and the flow-field is modeled by using LV-data in section 3.3.2.

#### 3.3.1 Shadowgraph Results

**Baseline Configuration (# 1105 F) :** The baseline configuration (# 1105F) has convergent primary flow passages with suppressor area ratio of 2.5, chute depth equal to its height, 10% porous wedge, primary NPR of 3.2 ( $P_{r,p}$ ), shield NPR of 2.2 ( $P_{r,s}$ ) and wind-tunnel Mach number of 0.2 ( $M_{wt}$ ). Figure 3-18 shows the overall shadowgraph and the static pressure distributions on the wedge and the chute for this configuration. In the pressure plots distances are normalized with the chute height  $Y_C$  (which is 1.710 inches in all configurations) and pressure is normalized with the ambient pressure. Also, in this figure, by chute-base is meant the slanting leading edge of the chute over which the secondary fluid flows.

Broadly speaking we observe (i) complicated shock structures in the main flow over the wedge (ii) some shock-structures in the shield flow which is, indeed, supersonic in this case, and (iii) that these shock-structures for the ARL 2D sector nozzle model are quite different than those for the Cell 41 round fluid-shield model discussed in the previous section.

In particular, notice the following peculiar features in the shadowgraph of Figure 3-18:

- a) main shock-cells going axially rather than parallel to the wedge
- b) shocks coming off the lip and the bottom of the chute although the nozzles for the hot primary flow are convergent and, hence, must be *under expanded*
- c) certain vertical shocks seem to be superimposed in the main flow over the wedge (these are much clearer in certain other configurations)

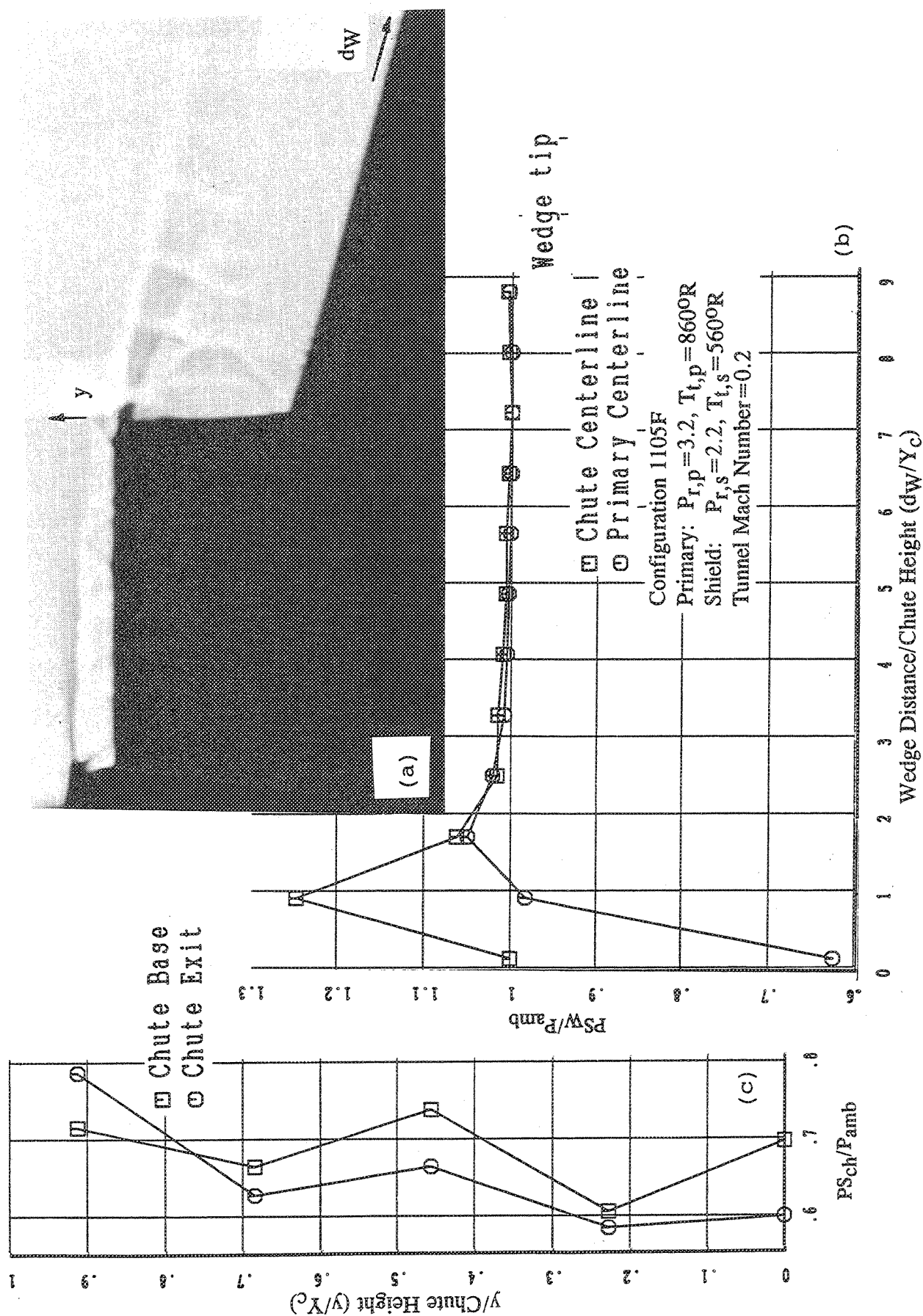


Figure 3-18. (a) Overall shadowgraph and static pressure distributions on (b) the wedge and (c) the chute for the baseline fluid shield model with 10% porous wedge;  $t_n=0.5"$ ,  $SAR=2.5$ ,  $CHR=1.0$ ,  $SCD=1.0$ .

- d) dark thin hairline-like lines protruding from the perforated wedge surface
- e) intersection of the expansion and shock-wave above the chute lip in the shield flow and their non-reflection from the top shear layer, and
- f) changing angles for the shadowgraph lines in the shield-flow, especially, after the chute entrance region.

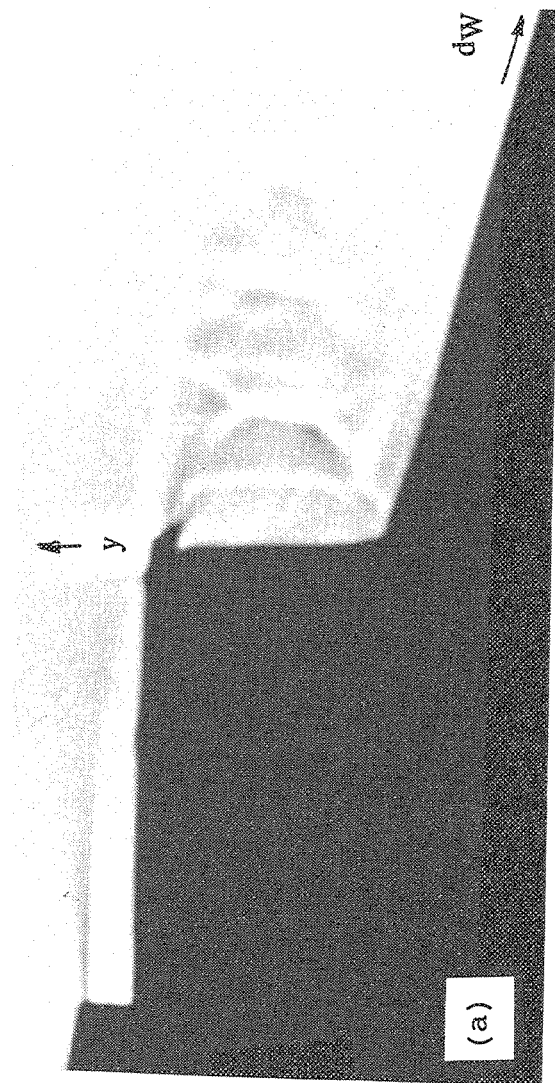
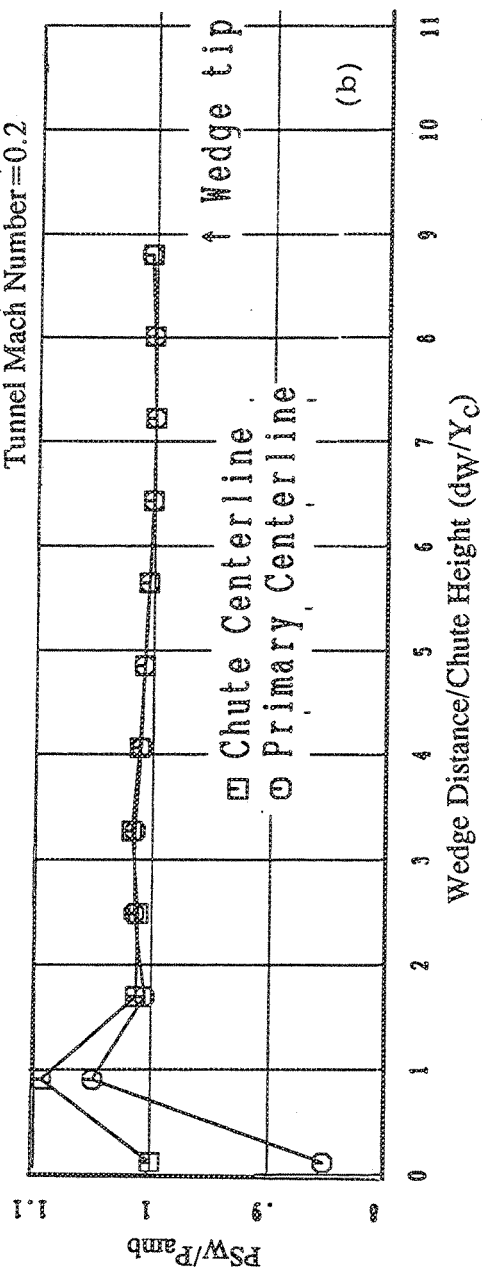
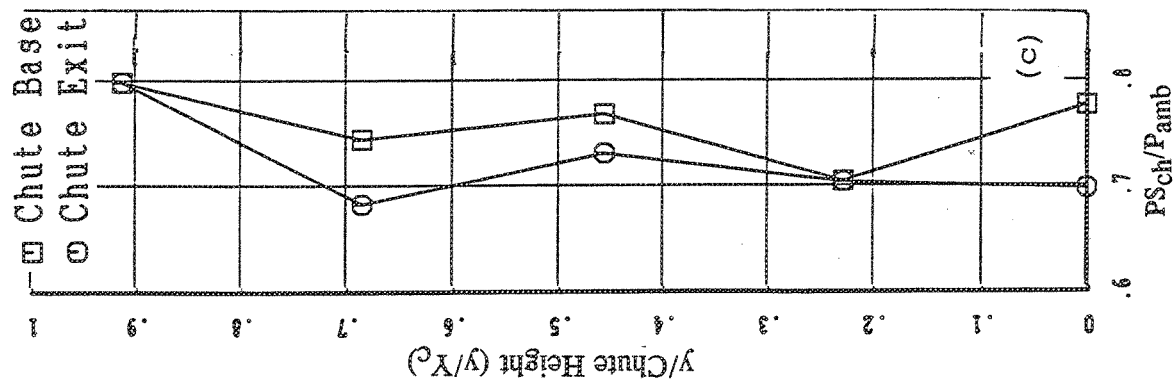
Also note the following features in the pressure distributions of Figure 3-18:

- (a) the pressure jumps at the bottom of the chute on the wedge not only in the primary centerline but also in the chute centerline (secondary-flow centerline); however, note that the p-tap locations are very sparse (order of chute height) compared to the initial variations in shock-structures *within* a chute-height.
- (b) the subsequent *fast* monotonic expansion to ambient pressure downstream of the wedge and subsequent ambient pressure over most of the downstream portion, and
- (c) the static-pressure at the chute exit in the secondary flow is much less than the ambient pressure (60-65 % over two-thirds of the lower height).

The physical origins of these shock-structures are discussed in the next section where detailed LV-data is also presented. We simply note them here so that we can scrutinize and contrast these features in the remaining shadowgraphs and pressure distributions during parametric variations.

**Effect of Nozzle Pressure Ratios (NPR) :** The effect of lowering the shield NPR to 1.6 from the reference value of 2.2, with consequent subsonic shield flow, is shown in Figure 3-19 (configuration # 1105 G). The slower shield flow appears to mix faster with the ambient flow and the wedge shock-structures are more axial and are only slightly altered. The maximum measured pressure values on the wedge have decreased considerably.

The effect of lowering only the primary NPR from 3.2 to 2.4 is captured in Figure 3-20 (config. 1105 C). The shock-cell lengths appear to have decreased although the shield flow structures have remained same. Also the pressure jumps on the wedge have



Configuration 1105G  
 Primary:  $P_{r,p}=3.2$ ,  $T_{t,p}=860^{\circ}\text{R}$   
 Shield:  $P_{r,s}=1.6$ ,  $T_{t,s}=560^{\circ}\text{R}$   
 Tunnel Mach Number=0.2

Figure 3-19. (a) Overall shadowgraph and static pressure distributions on (b) the wedge and (c) the chute for the baseline fluid shield model with 10% porous wedge;  $t_n=0.5$ ,  $SAR=2.5$ ,  $CER=1.0$ ,  $SCD=1.0$ .

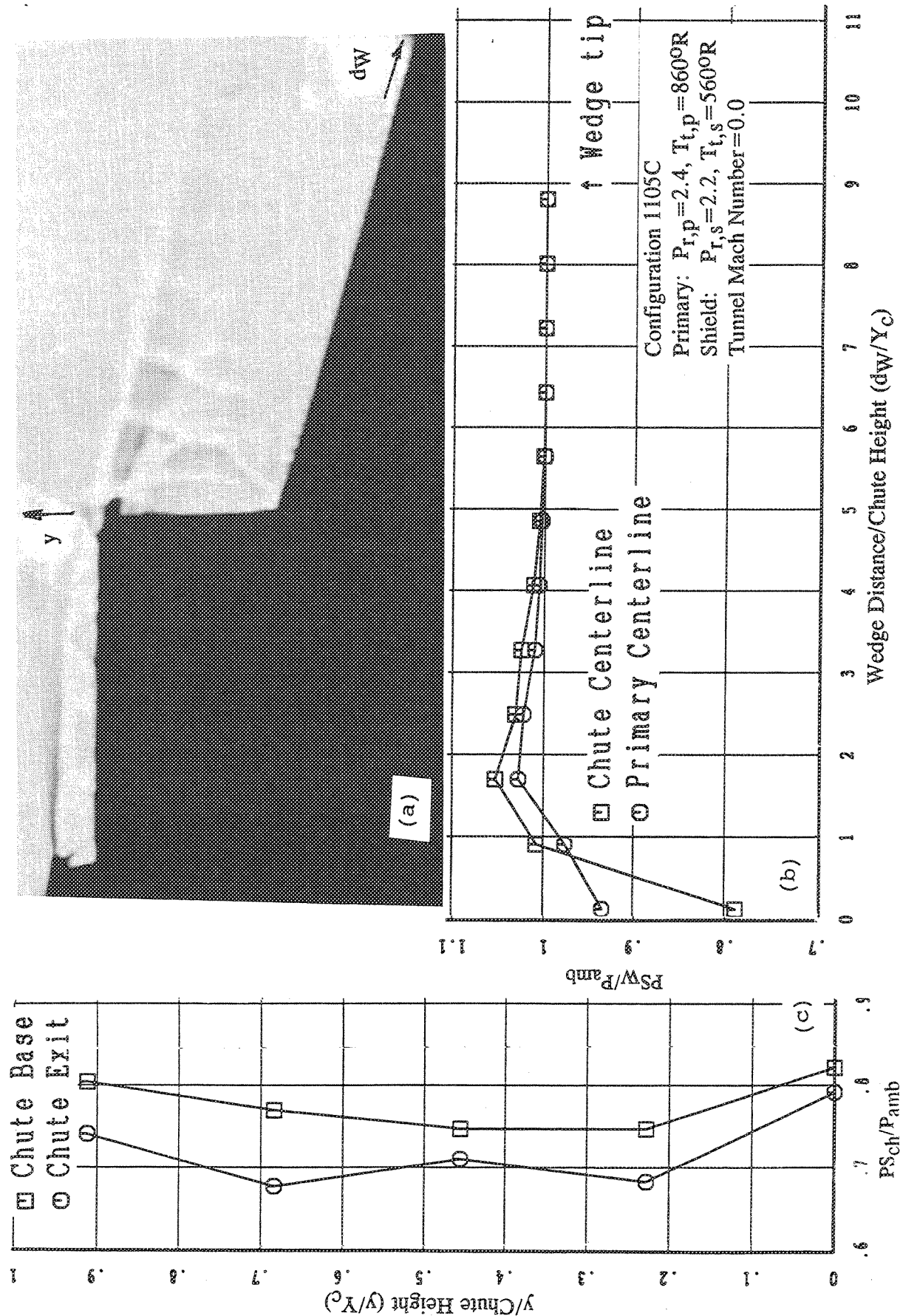


Figure 3-20. (a) Overall shadowgraph and static pressure distributions on (b) the wedge and (c) the chute for the baseline fluid shield model with 10% porous wedge;  $t_\eta=0.5"$ ,  $SAR=2.5$ ,  $CER=1.0$ ,  $SCD=1.0$ .

decreased. The lower portion of the chute-exit appears to have increased static pressure.

Finally, the effect of lowering both the NPR's simultaneously (configuration # 1105 B) is shown in Figure 3-21. With subsonic shield flow and lowered primary jet Mach number the main wedge shock structures and the pressure distributions appear similar to one with same lower primary NPR (compare with Figure 3-20).

**Effect of Wind-Tunnel On/Off :** Figure 3-22 shows the effect of wind-tunnel off (configuration # 1105 E). The shadowgraph does not differ much from the wind-tunnel on condition (see Figure 3-18) and the wedge and chute pressure distributions do show some differences.

For geometric parametric variations we prefer to show the data here with wind-tunnel on condition which is closer to the take-off mode although some configurations were run with wind-tunnel off.

**Effect of Shield Thickness :** Configuration # 1110 has twice the shield thickness as the reference configuration and the corresponding shadowgraph and pressure distributions are shown in Figure 3-23. A close-up is given further in Figure 3-24. These are some of the most crisp shadowgraphs that have been captured in this test. The main shock-cell structure is quite different than the reference case (Figure 3-18) and the shield-flow shows few more shocks downstream of the chute-exit plane. The chute center-line wedge pressure now shows an expansion first rather than compression; but, it further compresses and then re-expands as usual to the ambient pressure.

For this configuration the effect of closing the vent-plugs in the bottom horizontal surface of the wedge is captured in Figures 3-25 and 3-26, and virtually shows no difference with vent-plugs out (compare with Figures 3-23 and 3-24). [These vent plug holes were near the far downstream edge of the wedge where the pressure is already ambient.]

**Effect of Wedge Non-Porosity :** Configuration # 1005 has a non-porous wedge and Figure 3-27 shows the flow-field. Although the shadowgraph shows only slight differences compared to the porous case (Figure 3-18), the wedge pressures show a stronger shock and subsequent strong expansion for the non-porous case at the bottom

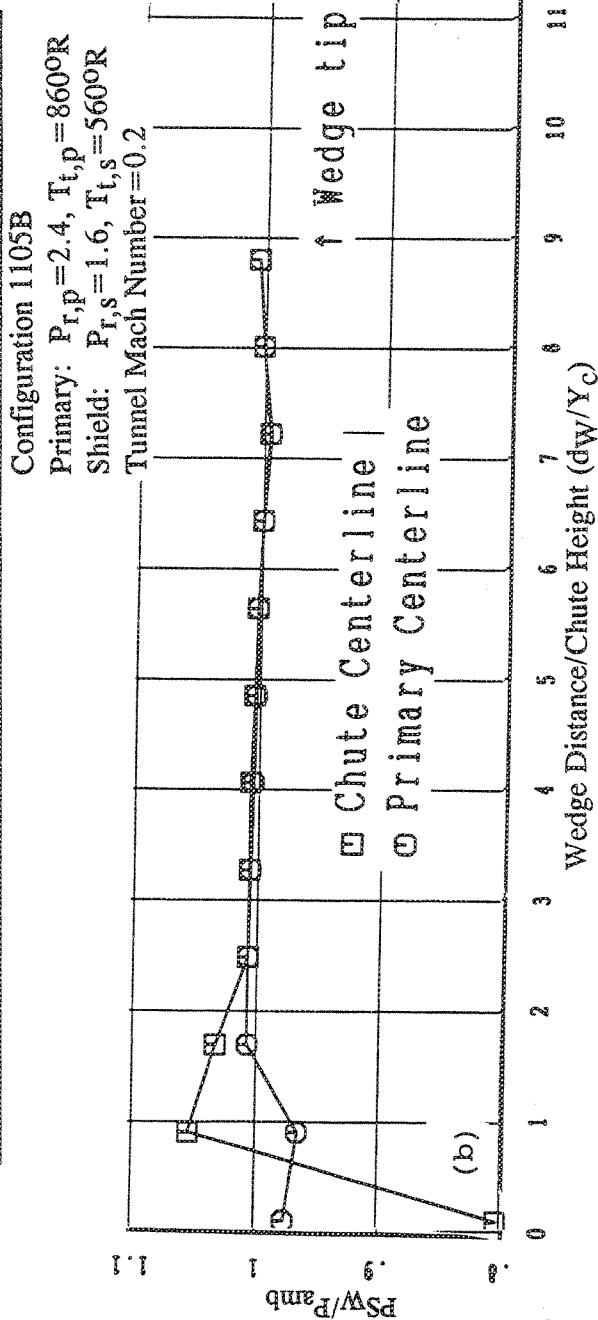
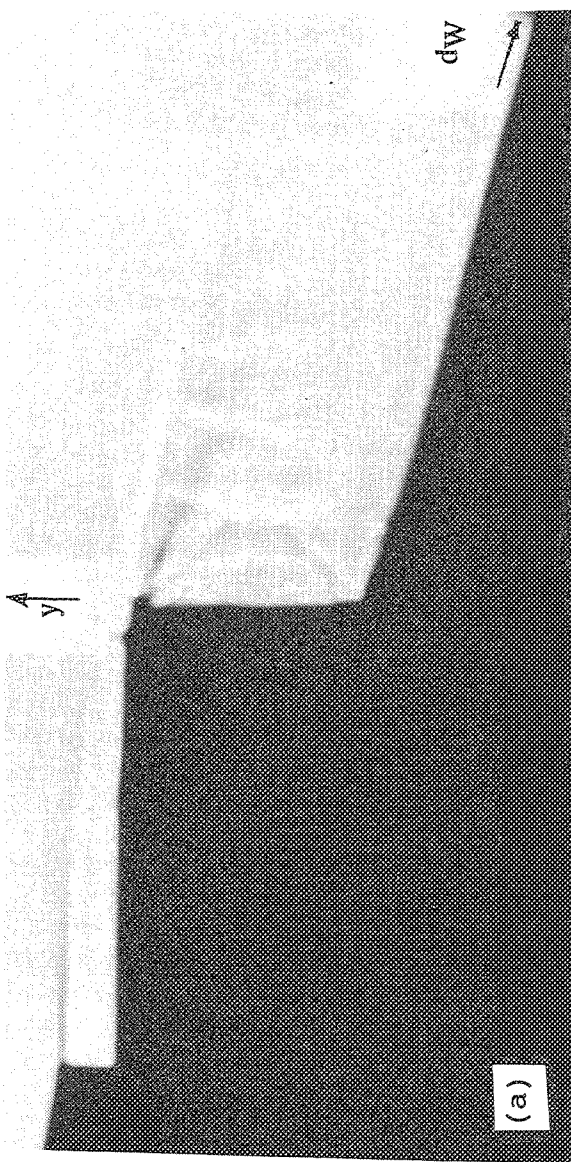
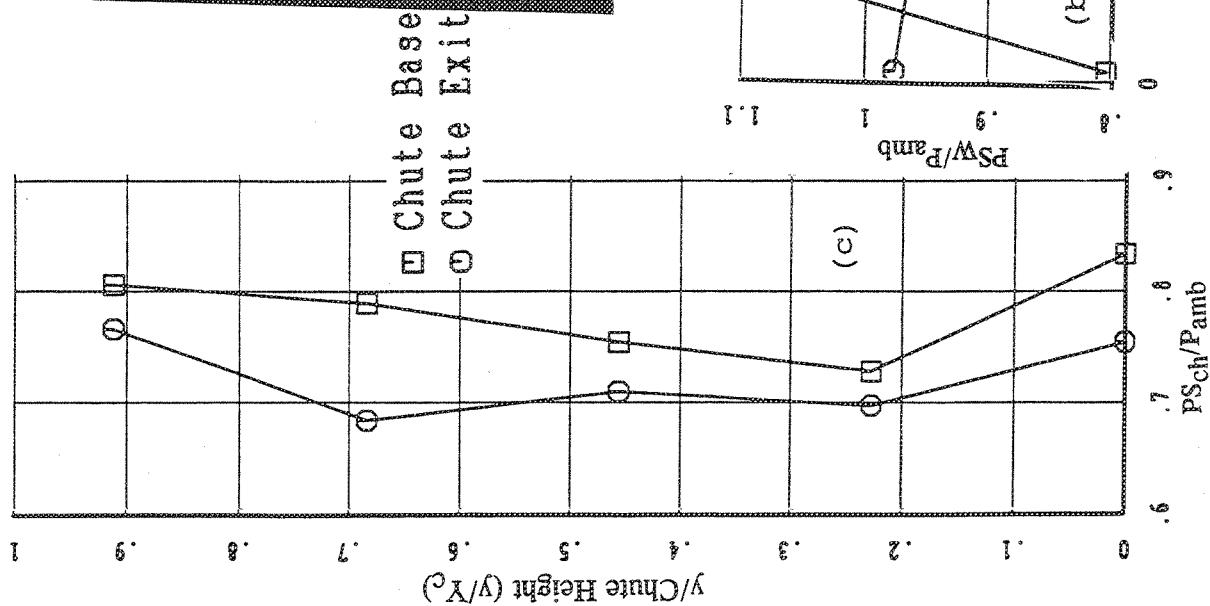


Figure 3-21. (a) Overall shadowgraph and static pressure distributions on (b) the wedge and (c) the chute for the baseline fluid shield model with 10% porous wedge for a subsonic shield;  $t_n=0.5$ ,  $SAR=2.5$ ,  $CER=1.0$ ,  $SCD=1.0$ .

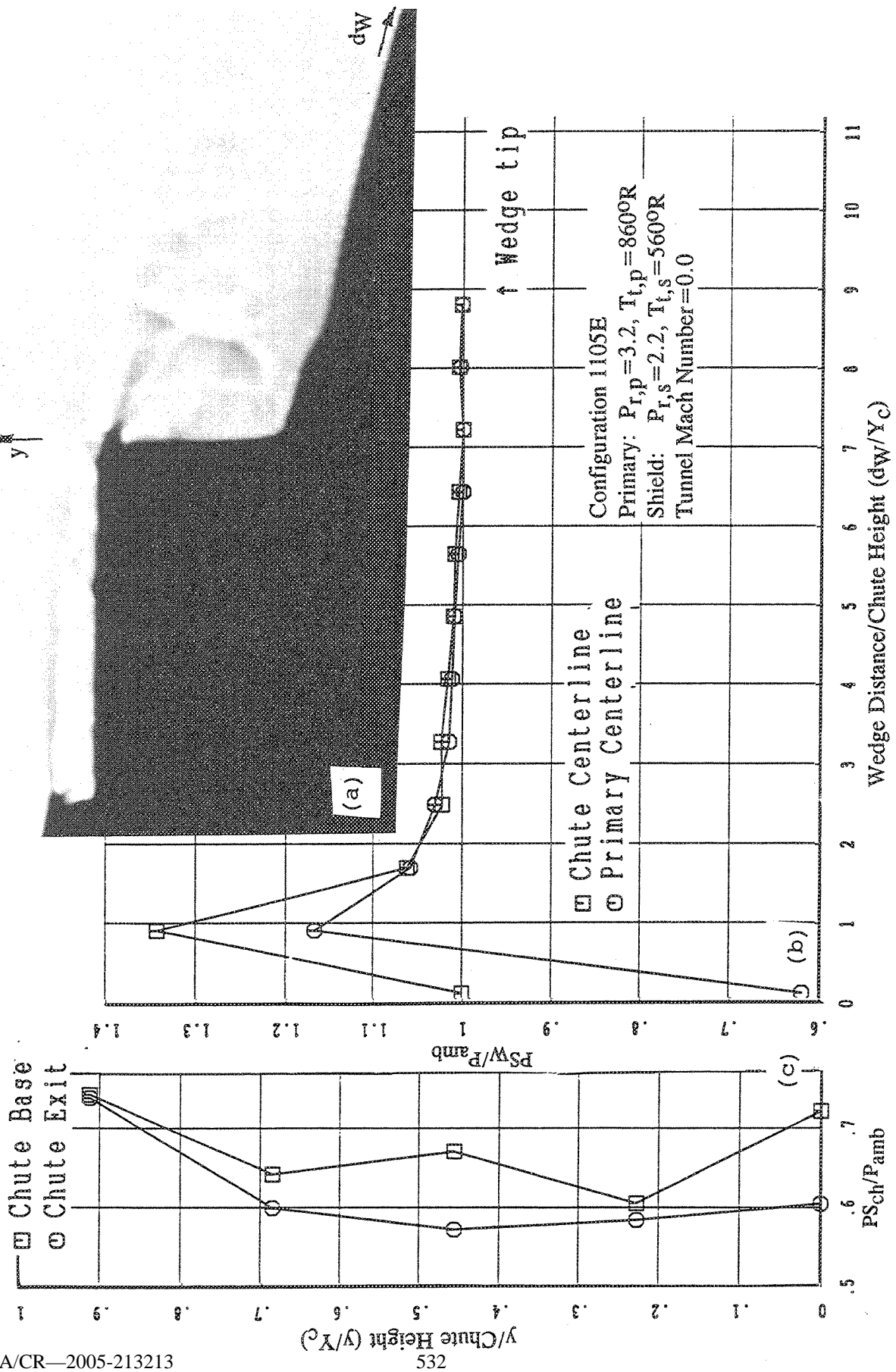


Figure 3-22. (a) Overall shadowgraph and static pressure distributions on (b) the wedge and (c) the chute for the baseline fluid shield model with 10% porous wedge without flight simulation;  $t_n=0.5"$ ,  $SAR=2.5$ ,  $CER=1.0$ ,  $SCD=1.0$ .



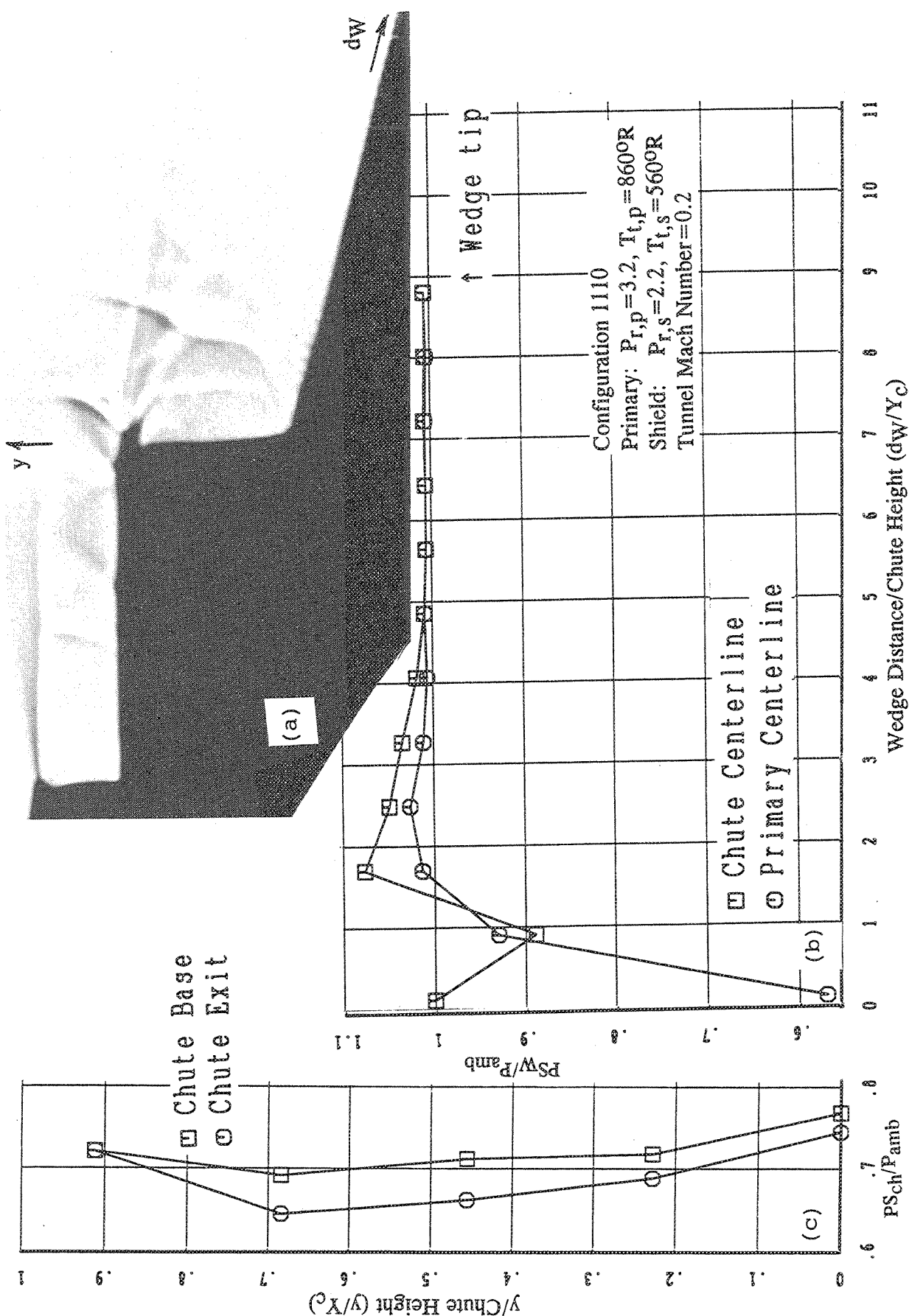


Figure 3-23. (a) Overall shadowgraph and static pressure distributions on (b) the wedge and (c) the chute for the fluid shield model of higher shield thickness ( $t_n=1.0$ ) with 10% porous wedge; SAR=2.5, CER=1.0, SCD=1.0.

Configuration 1110

Primary:  $P_{r,p}=3.2$ ,  $T_{t,p}=860^\circ\text{R}$

Shield:  $P_{r,s}=2.2$ ,  $T_{t,s}=560^\circ\text{R}$

Tunnel Mach Number=0.2

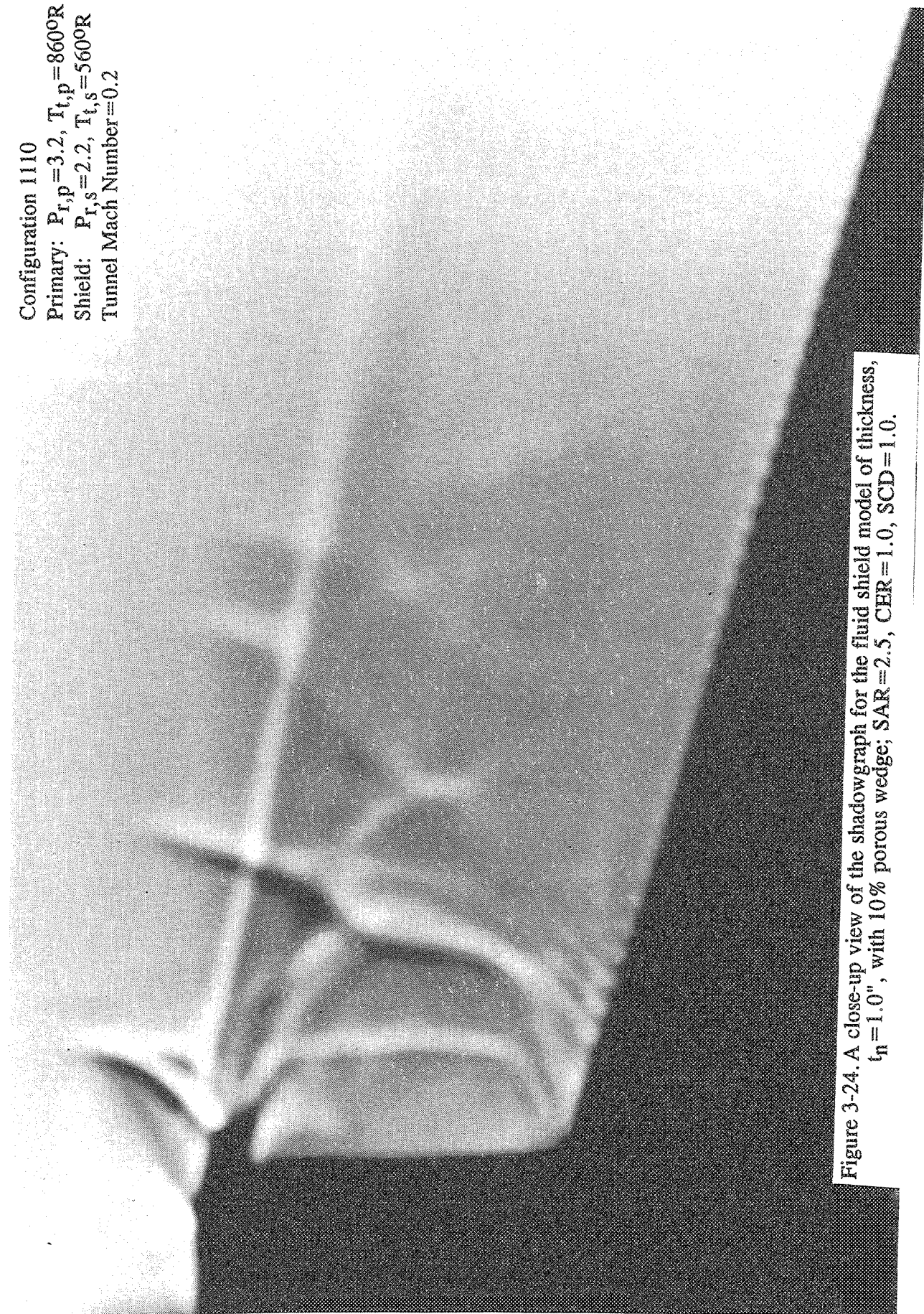


Figure 3-24. A close-up view of the shadowgraph for the fluid shield model of thickness,  $t_n = 1.0''$ , with 10% porous wedge; SAR=2.5, CER=1.0, SCD=1.0.

Configuration 1110 Vent Plug In  
Primary:  $P_{r,p}=3.2$ ,  $T_{t,p}=860^{\circ}\text{R}$   
Shield:  $P_{r,s}=2.2$ ,  $T_{t,s}=560^{\circ}\text{R}$   
Tunnel Mach Number=0.2

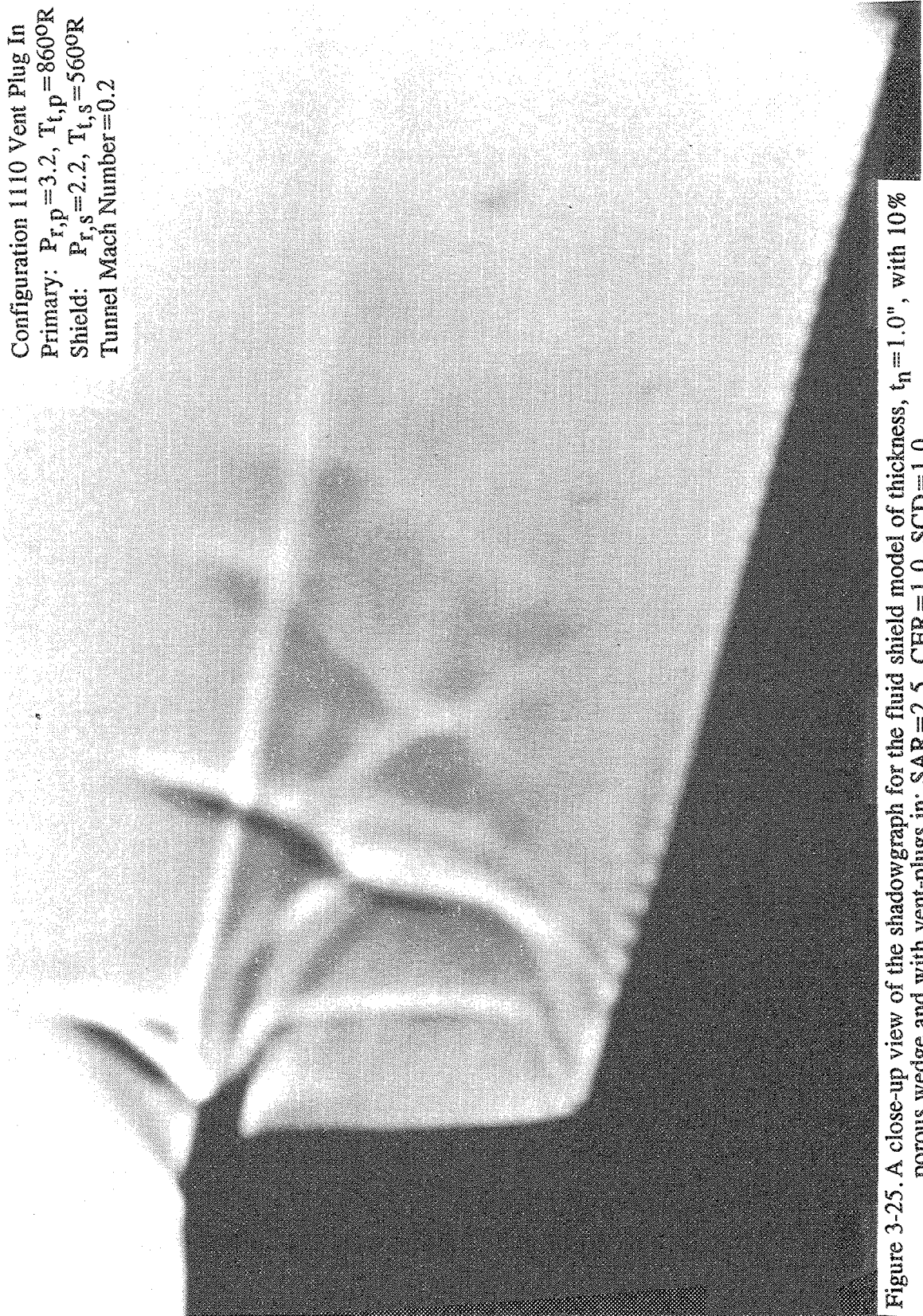


Figure 3-25. A close-up view of the shadowgraph for the fluid shield model of thickness,  $t_{\eta}=1.0"$ , with 10 % porous wedge and with vent-plugs in; SAR=2.5, CER=1.0, SCD=1.0.

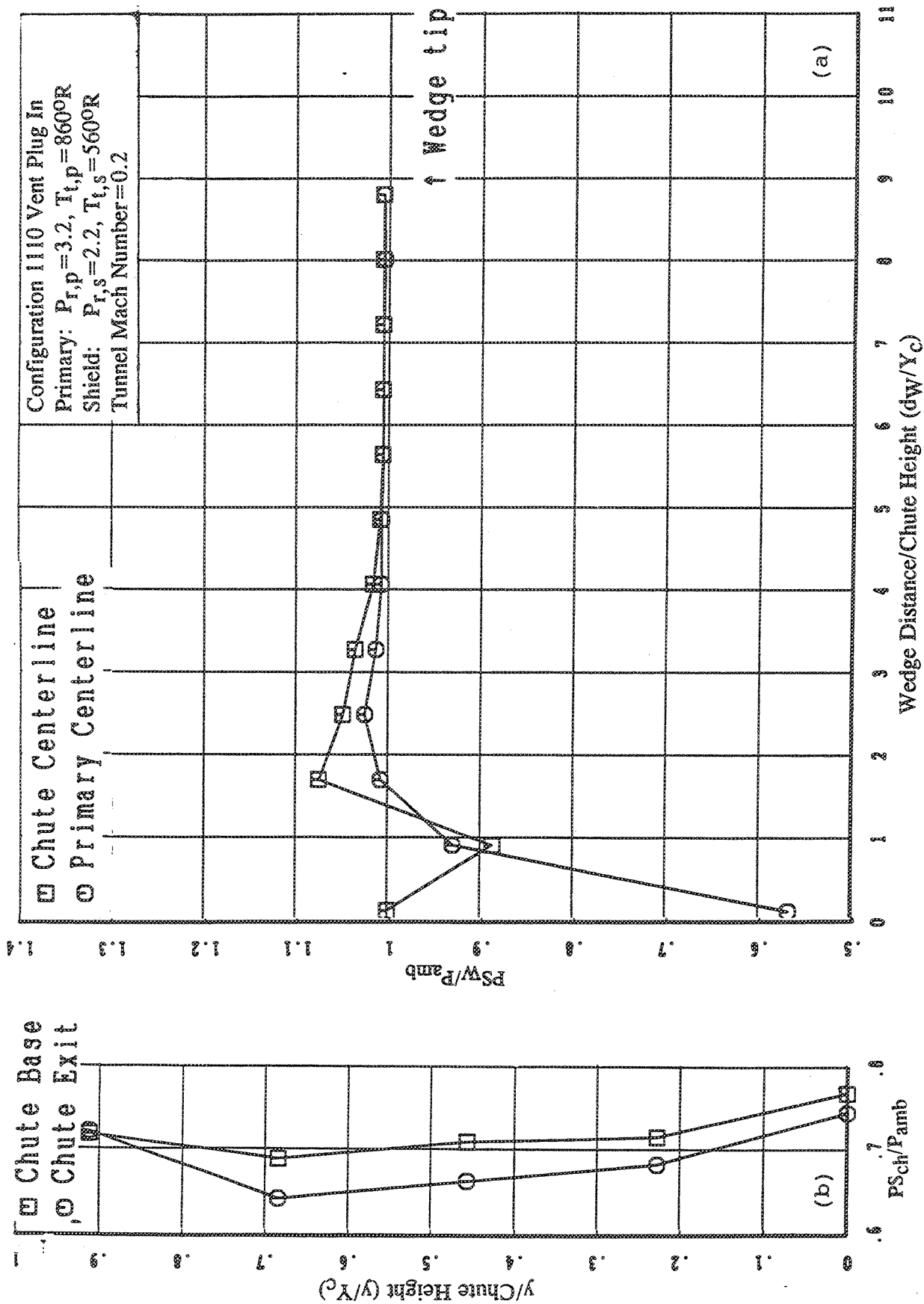


Figure 3-26. Static pressure distributions on (b) the wedge and (c) the chute for the fluid shield model of thickness,  $t_h = 1.0$ " , with 10% porous wedge and with vent-plugs in; SAR = 2.5, CHR = 1.0, SCD = 1.0.



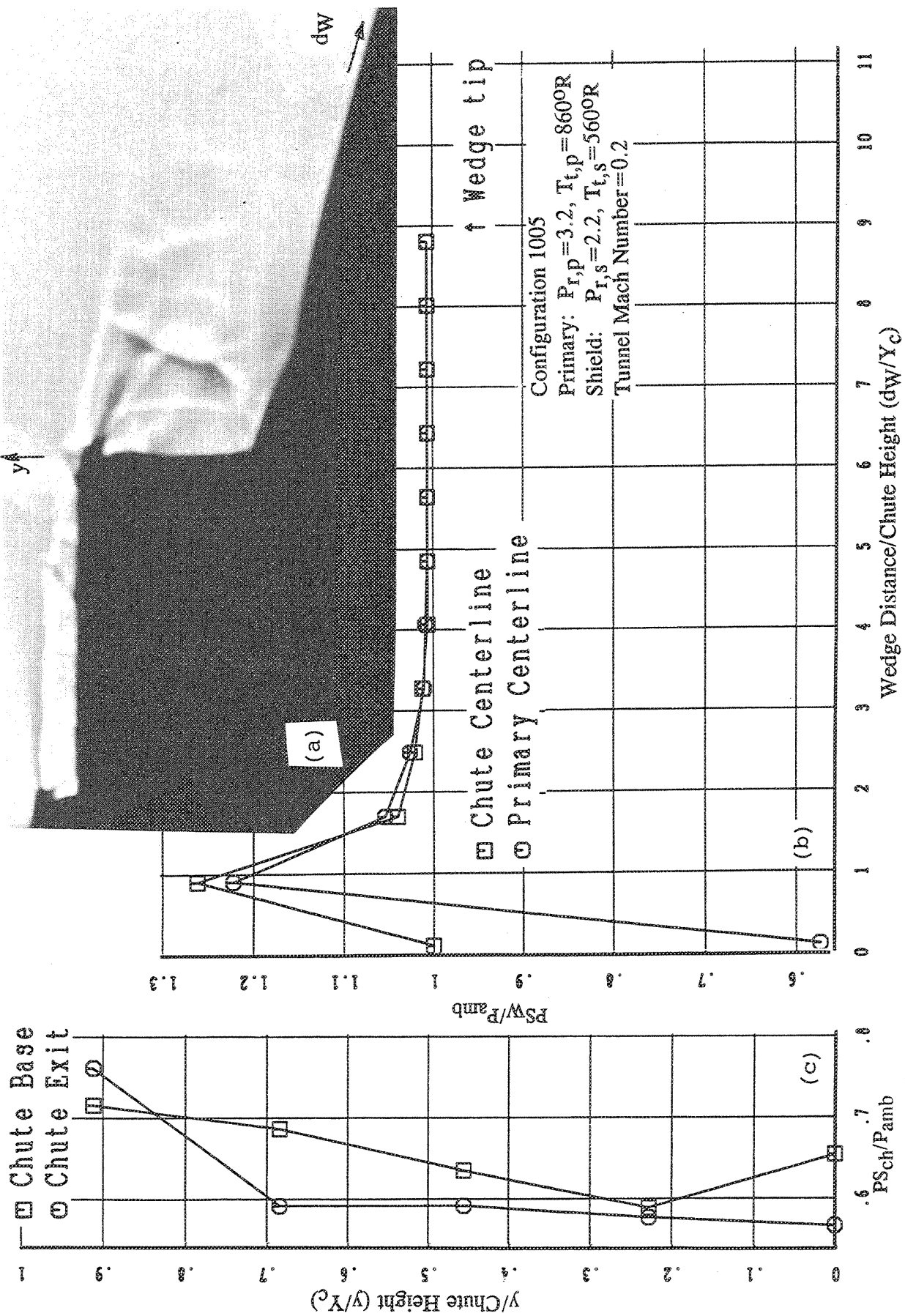


Figure 3-27. (a) Overall shadowgraph and static pressure distributions on (b) the wedge and (c) the chute for the baseline fluid shield model with non-porous wedge;  $t_n=0.5"$ ,  $SAR=2.5$ ,  $CER=1.0$ ,  $SCD=1.0$ .

of the chute for the primary flow. However, as mentioned before, we should be cognizant of the fact that the pressure taps are at large spatial intervals here, whence, we may have missed a stronger peak in the porous case.

**Effect of Suppressor Chute Depth-to-Height (SCD) Ratio :** Doubling this ratio for the half-inch thick shield gives the flow-field for configuration # 2105 as shown in Figure 3-28. Contrast this with Figure 3-18. It appears that the shock-strengths in both the primary flow and the shield flow have been weakened with increase in SCD although more shocks are now visible in the downstream region. Figure 3-29, for the deeper chutes with one-inch thick fluid shield and higher SAR (configuration # 4110), also shows the same differences in the shadowgraph features. The chute exit pressure is more non-uniform. The biggest difference appears to be in the chute pressure distributions which shows a larger range of monotonically increasing pressure at the slant chute leading edge (chute-"base") going from top to bottom (40 - 120 % of ambient pressure).

**Effect of Convergent-Divergent Primary Flowpaths :** Change in the shadowgraphs and pressure distributions due to CD flowpaths is shown in Figure 3-30 (configuration # 5105). The secondary flow over the wedge appears to expand first and then go through the usual cycle of compression and re-expansion. Also, the pressure jump in the primary flow appears less in the CD case.

**Effect of Suppressor Area Ratio (SAR) :** The effect of increasing SAR from 2.5 to 2.9 is shown in Figure 3-31 (configuration # 3105). The shadowgraph has not changed much but the chute and wedge pressure distributions do show some differences.

### 3.3.2 Laser Velocimetry Results & Interpretation

During the conduct of this test program, there were indications through in-house GEAE CFD efforts that the baseline configuration with steeper chute angle (55 degrees) may have largely separated secondary flow to begin with. We, hence, first thoroughly discuss the shallower chute configuration with larger SAR of 2.9 (# 4110) and then analyze the baseline case. The geometric effect of certain parameters is discussed in the end.

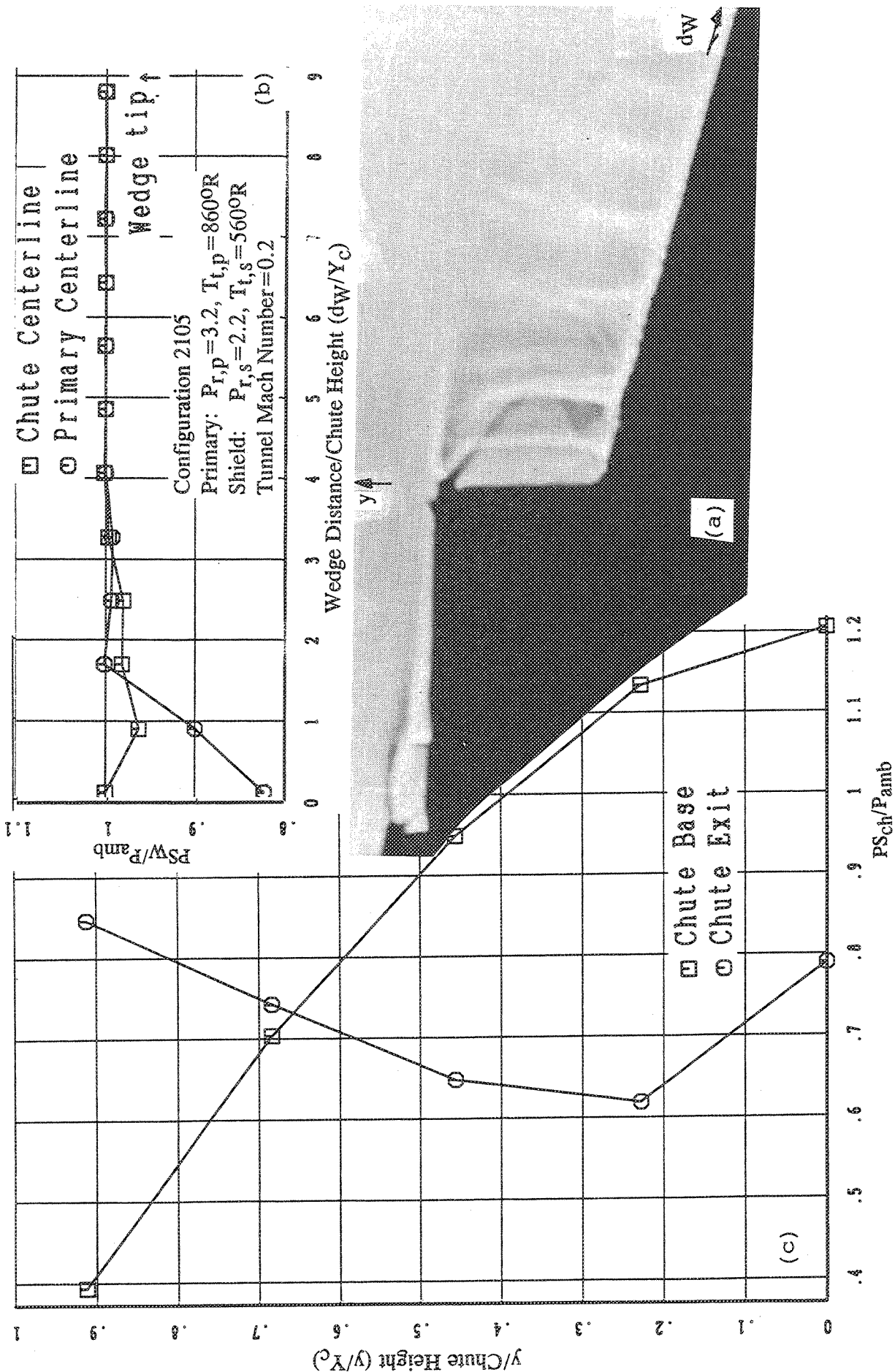


Figure 3-28. (a) Overall shadowgraph and static pressure distributions on (b) the wedge and (c) the chute for the fluid shield model of higher suppressor chute depth-to-height ratio ( $SCD=2$ ) with 10% porous wedge;  $t_w=0.5"$ ,  $SAR=2.5$ ,  $CHR=1.0$ .

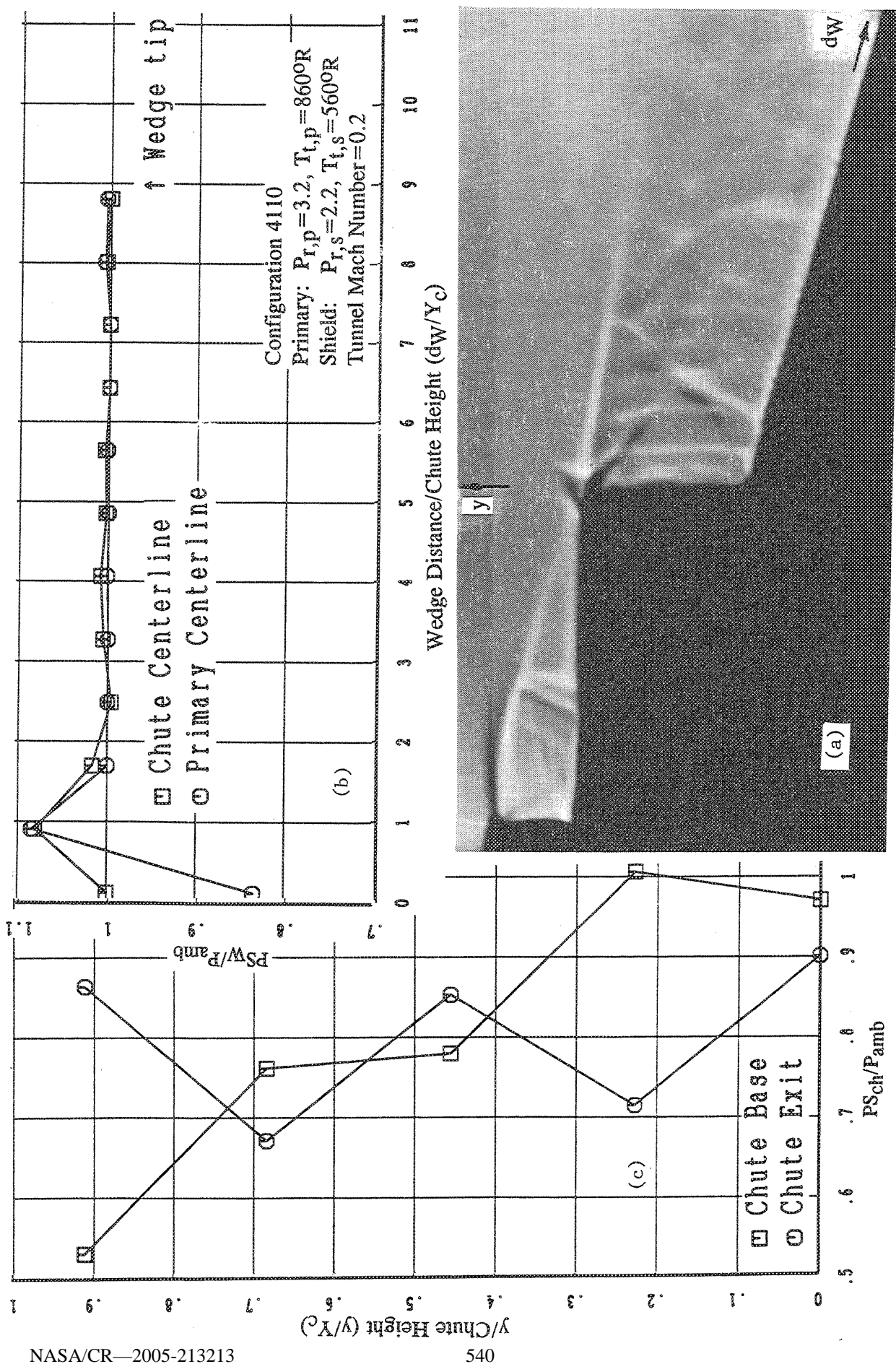


Figure 3-29. (a) Overall shadowgraph and static pressure distributions on (b) the wedge and (c) the chute for the fluid shield model of higher suppressor chute depth-to-height ratio ( $SCD=2$ ), shield thickness ( $t_n=1.0''$ ), and suppressor area ratio ( $SAR=2.9$ ) with 10% porous wedge;  $CHR=1.0$ .



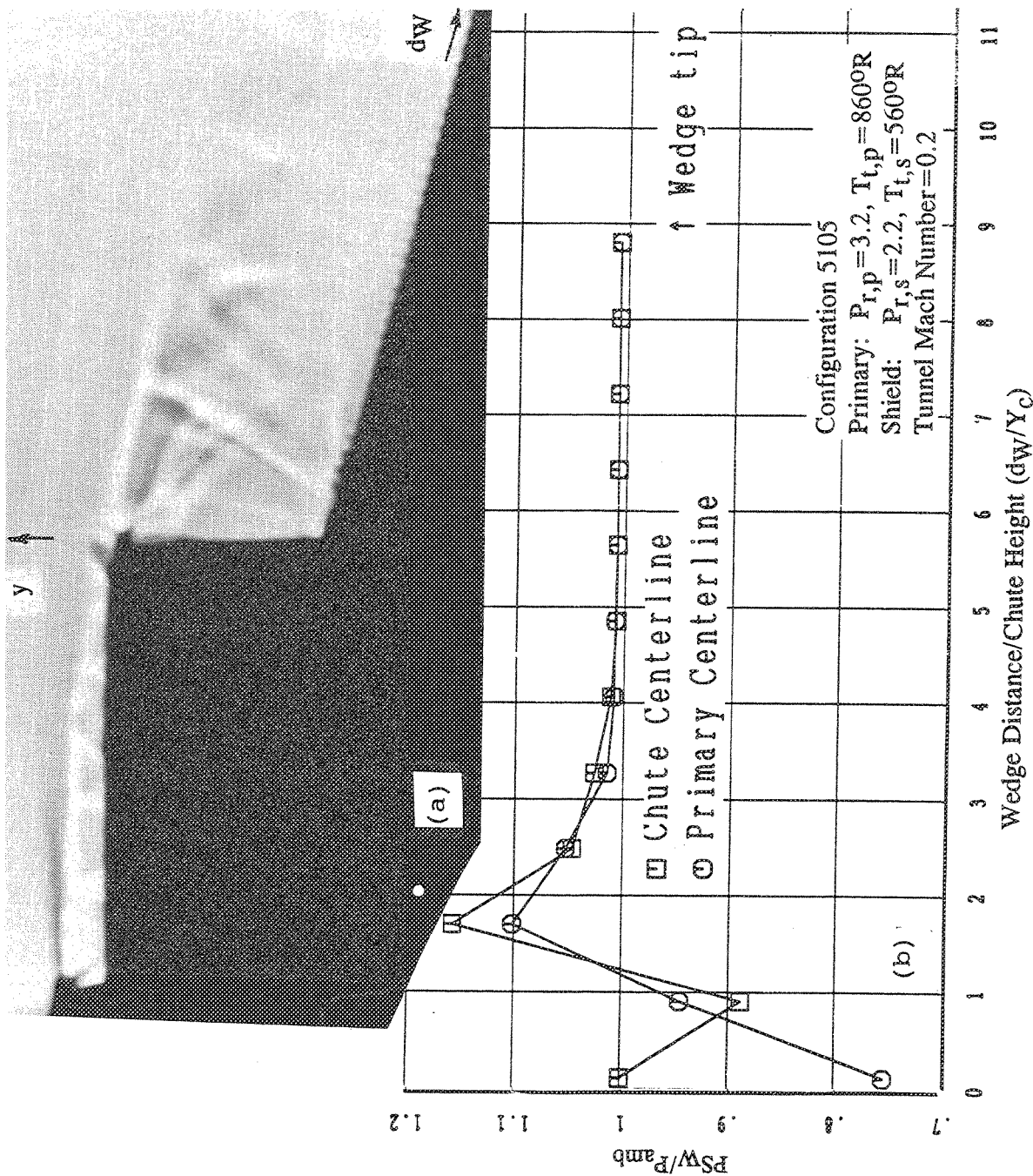
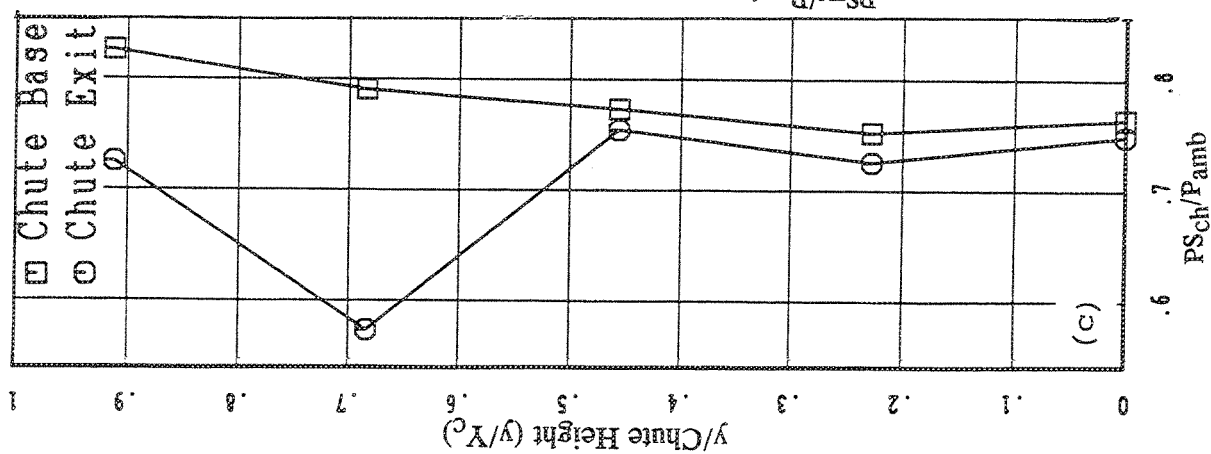


Figure 3-30. (a) Overall shadowgraph and static pressure distributions on (b) the wedge and (c) the chute for the fluid shield model with convergent-divergent chutes and with 10% porous wedge;  $t_\eta=0.5"$ ,  $SAR=2.5$ ,  $CER=1.1$ ,  $SCD=1.0$ .

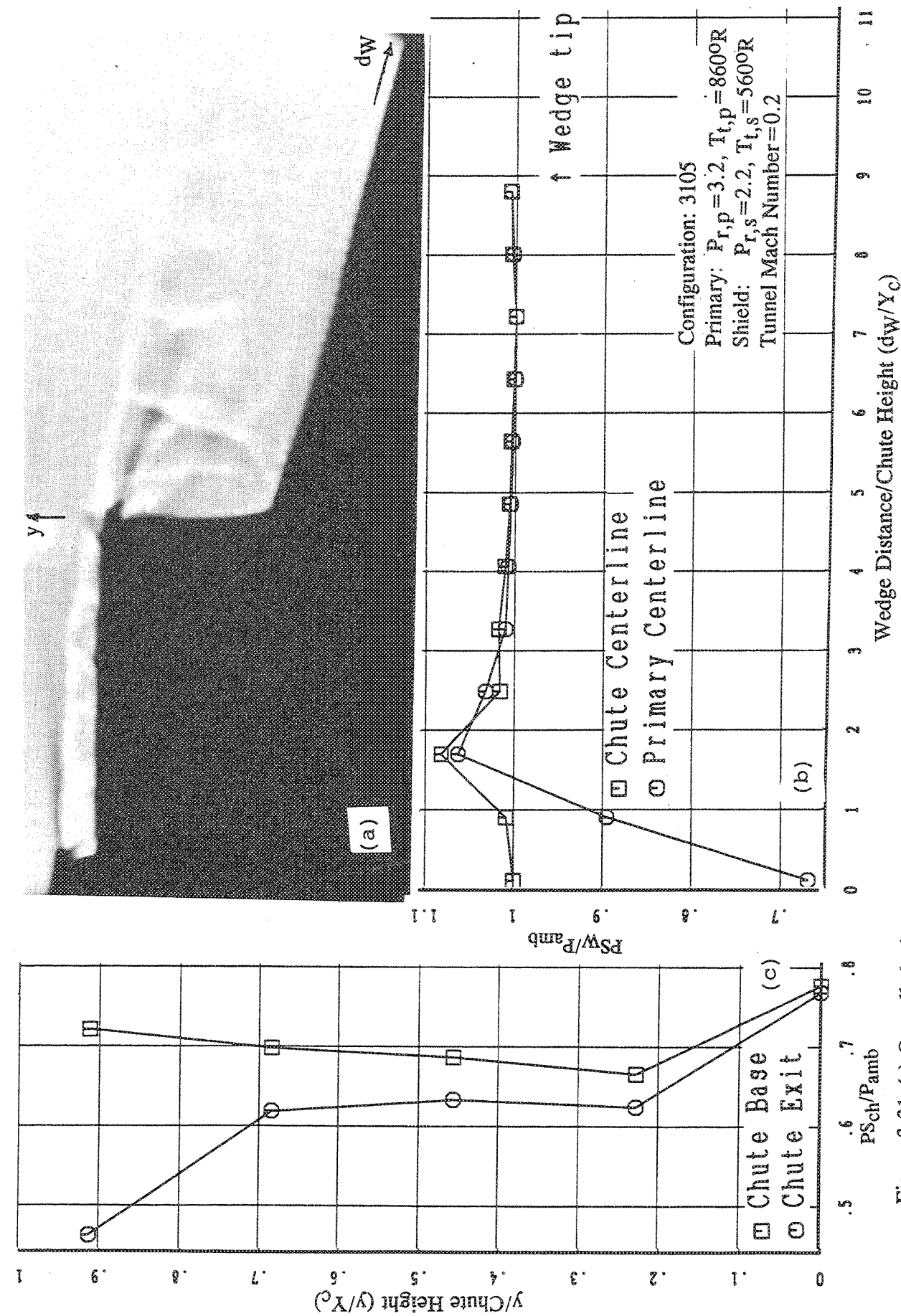


Figure 3-31. (a) Overall shadowgraph and static pressure distributions on (b) the wedge and (c) the chute for the fluid shield model of higher suppressor area ratio ( $SAR=2.9$ ) with 10% porous wedge;  $t_n=0.5"$ ,  $CER=1.0$ ,  $SCD=1.0$ .

### *Shallow Chute Configuration (# 4110) :*

Figure 3-32 shows a close-up of the shadowgraph with some of the dominant visible features labeled for convenience. (J = Jet Border; S = Shield Flow Structures; E = End-Jet Structures; T = Top-Half Structures; B = Bottom-Half Structures; M = Middle Shock). The LV-traverses were tailor-made according to this shadowgraph and the traverse locations are defined in Figure 3-33. Figure 3-34 shows a schematic of some of the dominant features with some of the LV traverses approximately superimposed for better understanding of the LV data to follow.

**Shock Structures on Wedge Surface :** Figure 3-35 shows the mean velocity magnitude and direction along traverse 2 (mid-chute height and parallel to wedge surface) on the primary jet (Plane A) and the end jet (Plane D) centerlines. The mean flow is seen not to be parallel to the traverse lines (mean velocity vector is approximately  $87^\circ$  and the traverse is  $75^\circ$  to the vertical pointing downwards); hence, a streamline is not being traversed. Such mean velocity surveys are, thus, merely spatial distributions of the mean velocity. However, the sharp dips in the mean-velocities for these traverses do signify shocks. If the dip in magnitude is not accompanied by a change in flow angle then the shock must be locally normal to the flow there; however, if it is accompanied by a sharp change in flow angle then the shock must be locally oblique.

For example, the velocity dips in traverse 2 on plane D with almost no corresponding change in flow angles, appears, as in classical 2d shock-cell structure, due to the passage through a *Mach-disk* produced by two coalescing shock waves which themselves are due to the reflection of two expansion waves from the two vertical shear layers originating at the under expanded jet-nozzle boundary intersection. The five dips seem to correspond to the shock-cells defined by the five vertical white stripes E<sub>1</sub>, E<sub>2</sub>, E<sub>3</sub>, etc. in the shadowgraph (also refer to the full shadowgraph (Figure 3-29)). Thus, we conclude that the vertical white stripes parallel to the chute exit edges on the shadowgraph E<sub>1</sub>, E<sub>2</sub>, E<sub>3</sub>, etc. are features of the end-jet shock-cell structures not to be confused with the main central jet shock-cell structures. Other points to note in the end-jet shock structure are the expected decrease in "shock-cell length" as we proceed downstream and the decay of the average centerline velocity due to the growing and convoluting shear layer from the side wall which ultimately consumes the end-jet potential core.

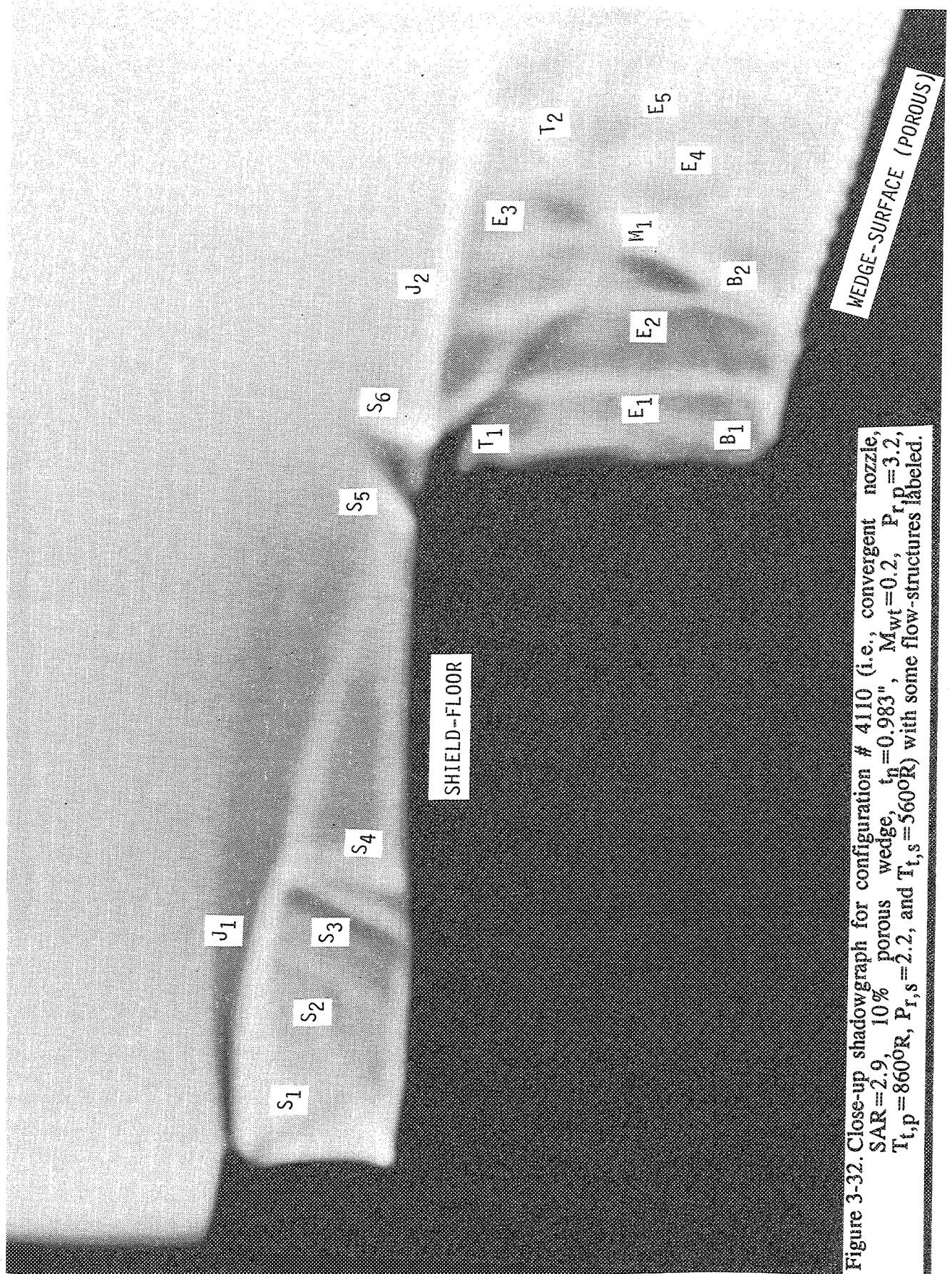
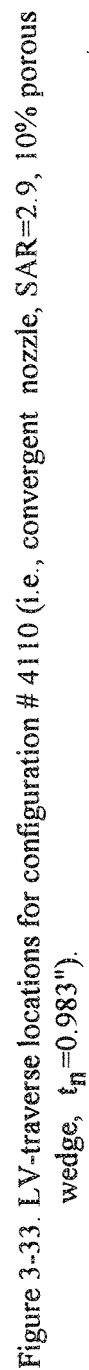


Figure 3-32. Close-up shadowgraph for configuration # 4110 (i.e., convergent nozzle,  $SAR=2.9$ , 10% porous wedge,  $t_n=0.983$ ",  $M_{wt}=0.2$ ,  $Pr_p=3.2$ ,  $T_{t,p}=860^{\circ}R$ ,  $Pr_s=2.2$ , and  $T_{t,s}=560^{\circ}R$ ) with some flow-structures labeled.



# CONFIGURATION 4110

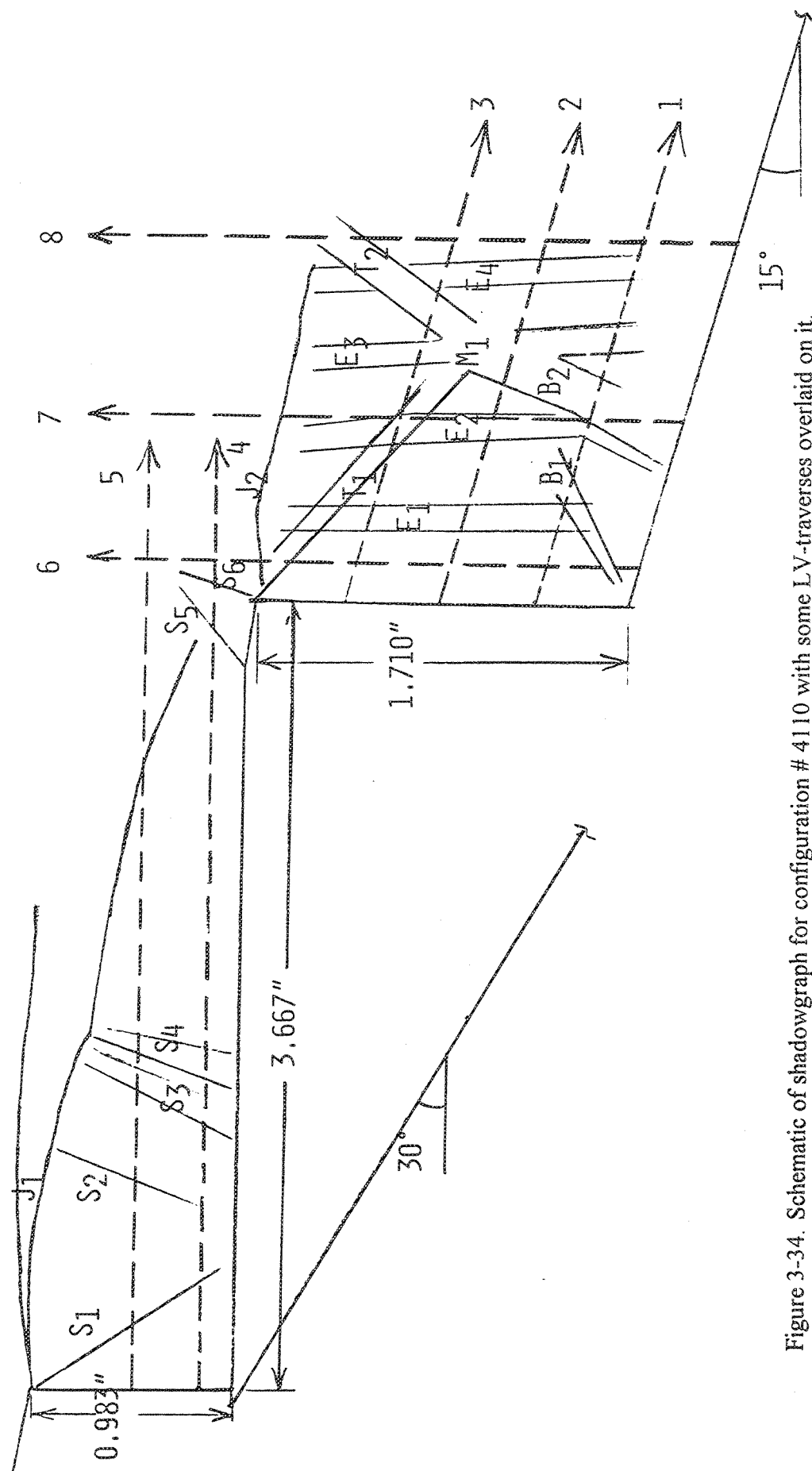


Figure 3-34. Schematic of shadowgraph for configuration #4110 with some LV-traverses overlaid on it.



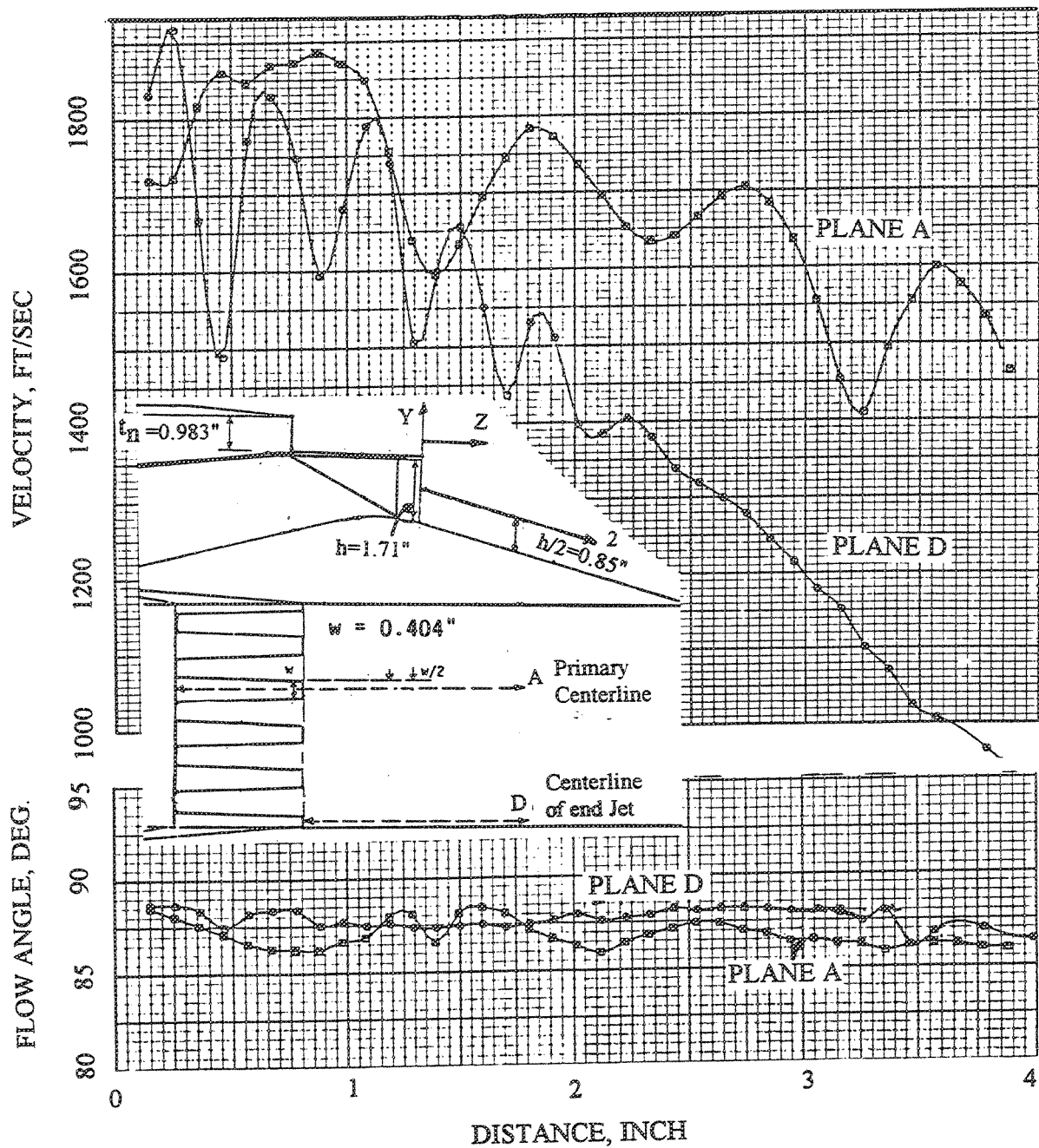


Figure 3-35. Mean velocity distribution for line # 2 in planes A and D (see Figure 3-33) for configuration # 4110 (i.e., convergent nozzle, SAR=2.9, 10% porous wedge,  $t_n=0.983$ ",  $M_{wt}=0.2$ ,  $P_{r,p}=3.2$ ,  $T_{t,p}=860^\circ\text{R}$ ,  $P_{r,s}=2.2$ , and  $T_{t,s}=560^\circ\text{R}$ )

Traverse 2 on plane A (in Figure 3-35), on the other hand, shows a sharp dip in magnitude and also some upward deflection in flow angle at approximately 1.1" corresponding to the location of shock-surface  $M_1$  in the shadowgraph, which appears, hence, slightly oblique to the flow.

Figure 3-36 further compares LV traverses for the primary and the secondary centerlines and the "lip-line" between them (i.e., traverse 2 on planes A, C and B, respectively). The velocity dips at approximately 1.1" immediately show that the shock surface  $M_1$ , at mid-chute height occurs not only in the primary flow but also in the secondary flow region and, hence, the whole span of the nozzle. However, the strength of this shock surface varies in the primary and the secondary flows. It is pertinent to note here that the shield NPR of 2.2 sets a supersonic shield flow which must continue to be supersonic through the chutes at least until it "sees" this shock-surface,  $M_1$ . The sudden dip in magnitude in the "lip-line" traverse on plane B at about 2" and its subsequent proximity to the secondary mean velocity magnitudes marks the protrusion of the growing lip shear layer on the traverse on plane B. However, note that the flow angles on B stay closer to those for the primary flow centerline (i.e., traverse 2 on A). Thus, there must be fairly strong axial vorticity (pointing downstream) near this lip-line which contributes to the mixing process. The dips on line on plane A are also not periodic signifying an axially developing shock-cell structure downstream.

LV-traverses on line 3 in primary flow and secondary flow region (i.e., on planes A and C, respectively, in Figure 3-37) immediately tell us that surface  $T_1$  in Figure 3-32 is a shock surface only in the primary flow and not in the secondary flow (see the dip in the line on plane A at around 0.8" with no corresponding dip there in the line on plane C). On the other hand, surface  $T_2$  (approximately @ 1.4" on #3) appears as velocity dips in the primary as well as the secondary flow paths. It appears as an oblique-shock in the primary whereas, it is fairly normal to the secondary flow as seen from the flow angles at 1.4".

We can use similar reasoning from Figure 3-38 (which shows LV-traverses on planes A (primary) and C (secondary) for line #1) to conclude that surface  $B_2$  in Figure 3-32 (at approximately 0.8" on line #1) is in both the flow regions. The slight differences in the locations of the dips near 0.8" in both the flows imply a corrugated shock-surface  $B_2$ . Immediately downstream on A41101 at approximately 1.25" another shock



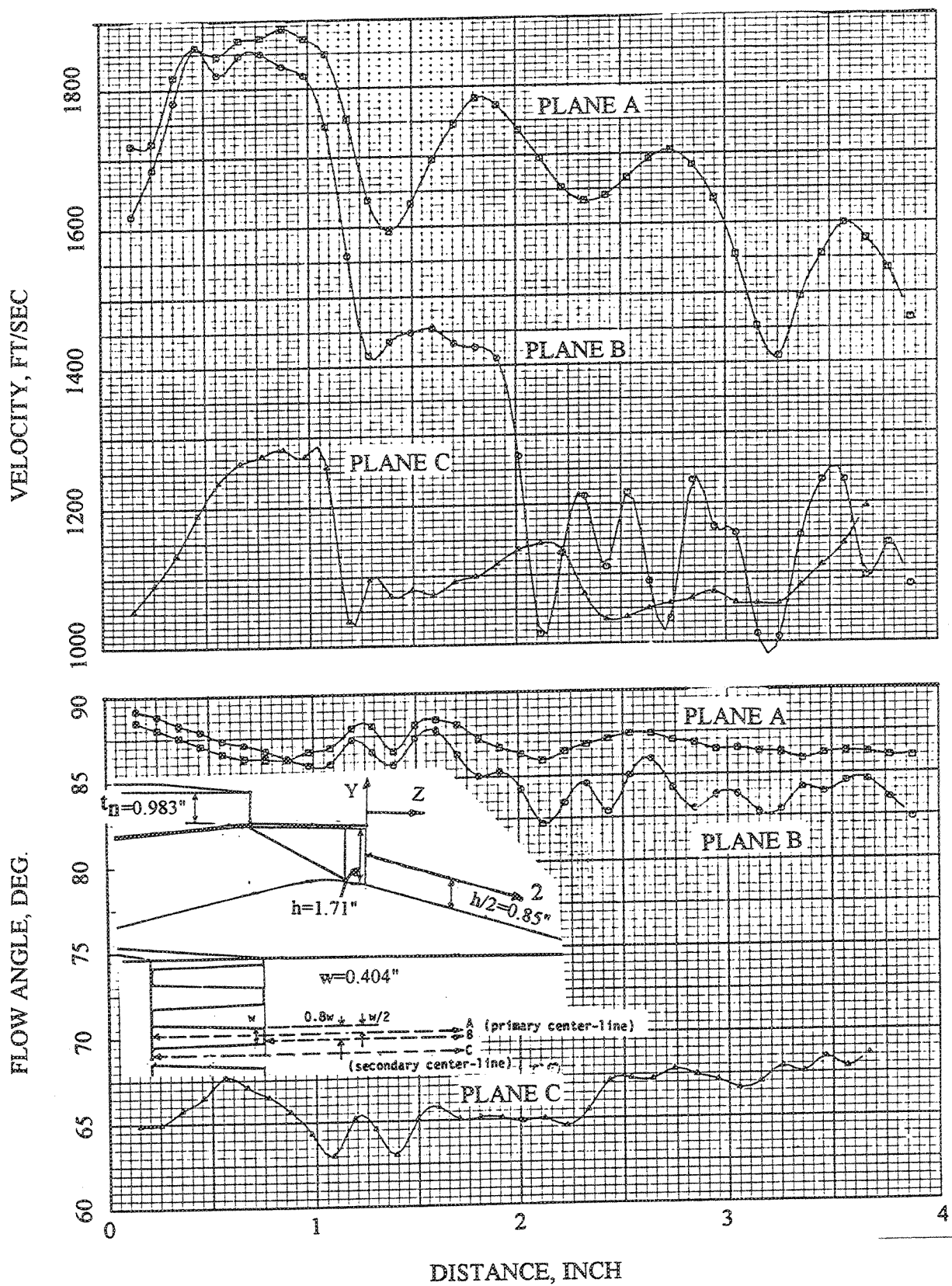


Figure 3-36. Mean velocity distribution for line # 2 in planes A, B and C (see Figure 3-33) for configuration # 4110 (i.e., convergent nozzle, SAR=2.9, 10% porous wedge,  $t_n=0.983"$ ,  $M_{wt}=0.2$ ,  $P_{r,p}=3.2$ ,  $T_{t,p}=860^\circ R$ ,  $P_{r,s}=2.2$ , and  $T_{t,s}=560^\circ R$ ).

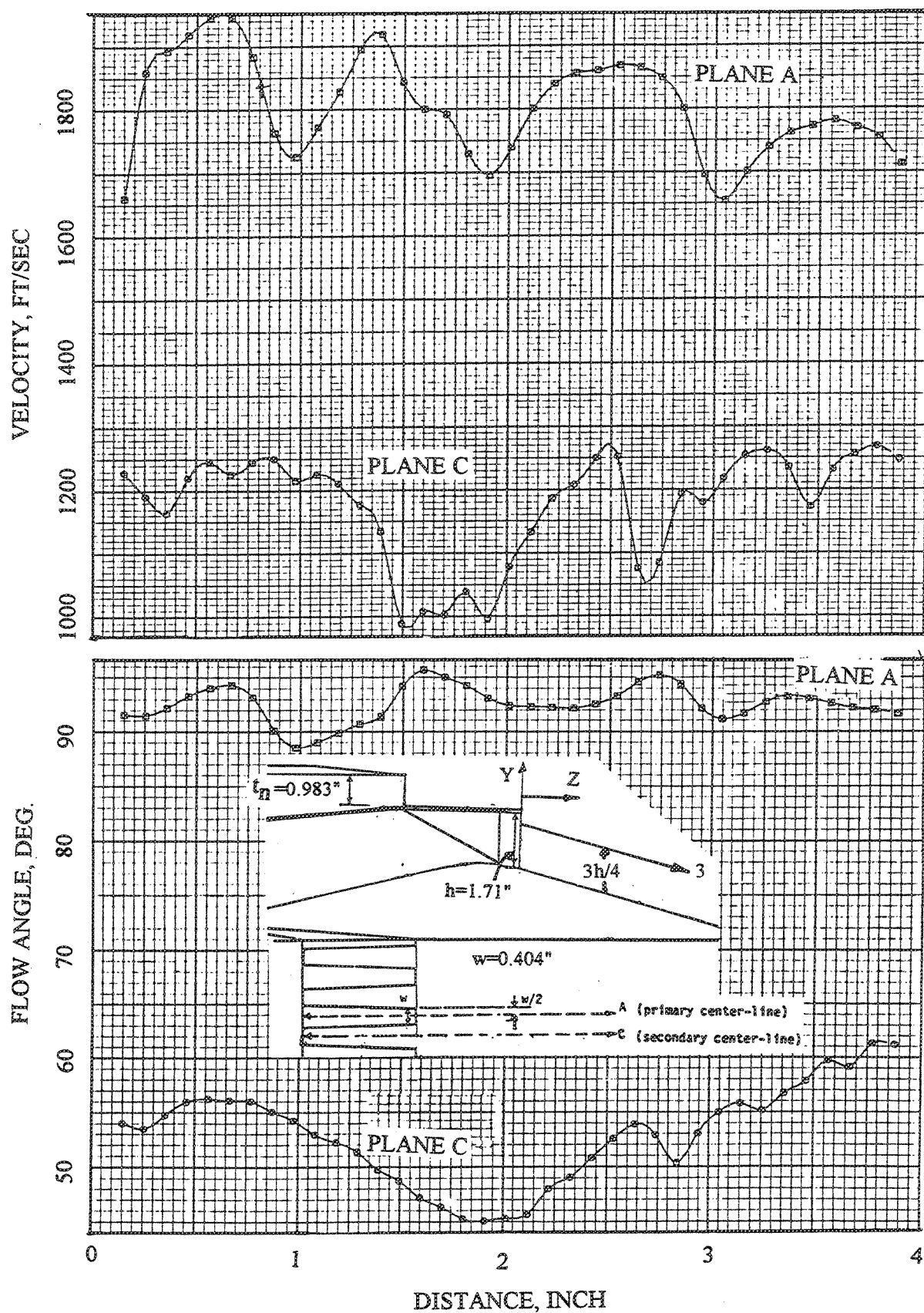


Figure 3-37. Mean velocity distribution for line # 3 in planes A and C (see Figure 3-33) for configuration # 4110 (i.e., convergent nozzle, SAR=2.9, 10% porous wedge,  $t_n=0.983''$ ,  $M_{wt}=0.2$ ,  $P_{r,p}=3.2$ ,  $T_{t,p}=860^\circ\text{R}$ ,  $P_{r,s}=2.2$ , and  $T_{t,s}=560^\circ\text{R}$ ).

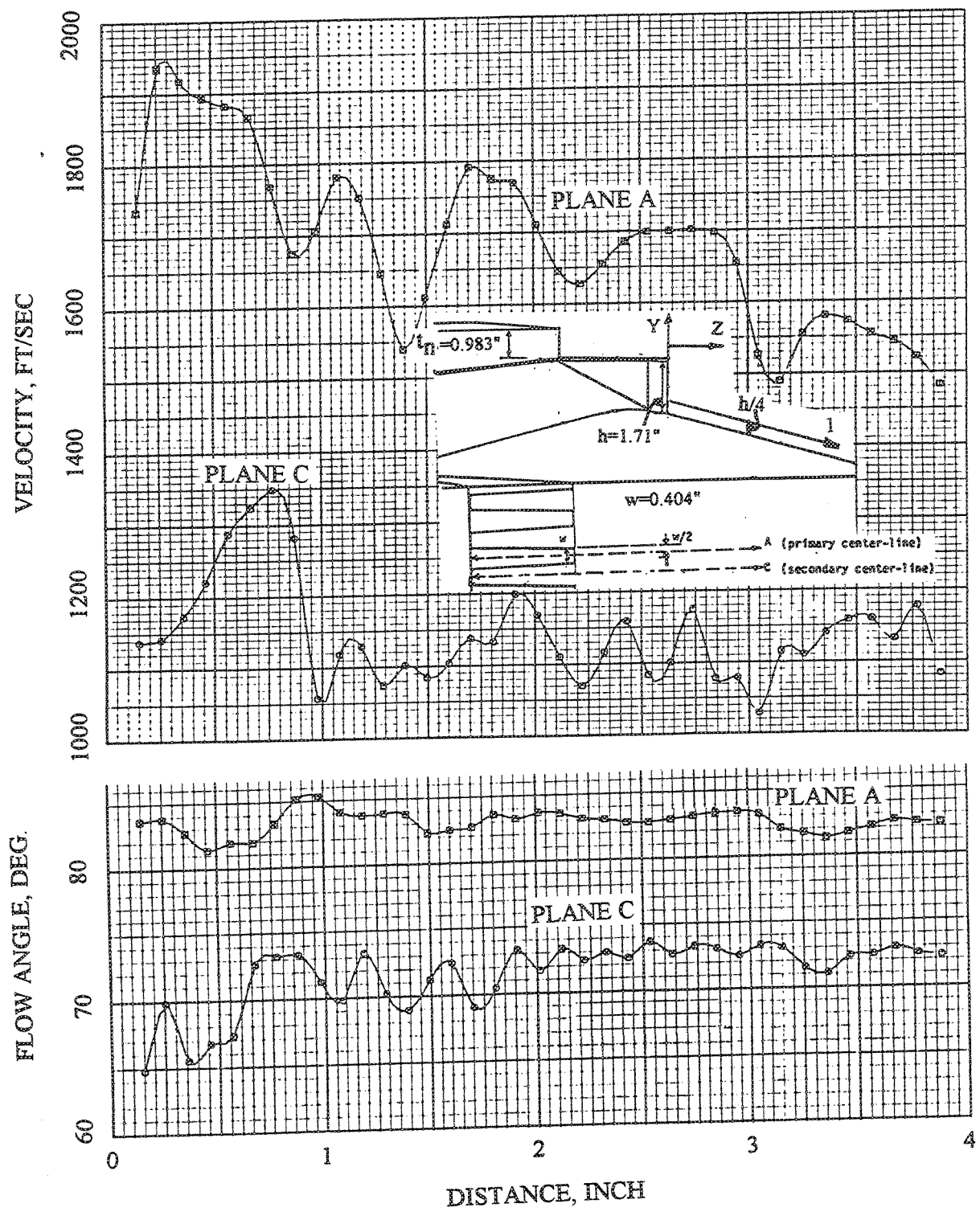


Figure 3-38. Mean velocity distribution for line # 1 in planes A and C (see Figure 3-33) for configuration # 4110 (i.e., convergent nozzle, SAR=2.9, 10% porous wedge,  $t_n=0.983''$ ,  $M_{wt}=0.2$ ,  $P_{r,p}=3.2$ ,  $T_{t,p}=860^\circ R$ ,  $P_{r,s}=2.2$ , and  $T_{t,s}=560^\circ R$ ).

structure exists in the primary flow but it is not so clear in the shadowgraph of Figure 3-32.

Thus, it appears plausible to construct the shape of the dominant shock-cell structures on the wedge surface with the help of both shadowgraphs and LV data.

We show in Figure 3-39 the striking difference in the angularity of mean-velocity vectors in the primary plane, A, and the secondary plane, C, for vertical traverses 6,7,8, and 9 at varying downstream distances. (The vectors are centered on the traverse locations and the horizontal axis in this figure is the top wedge-surface.) Note that the primary flow is divergent between the wedge-surface and a horizontal line through the top chute-lip. The mixing of both the flows with the ambient flow of Mach No. 0.2 is also quantitatively captured in this figure.

The spanwise distribution in the angularity of the flow across the vertical lip shear layer and the two flows on either side (traverses P, Q, R, and S) is captured in Figure 3-40 for mid-chute height and various downstream locations. (The local peaks and troughs appear to be superficial manifestations of the interpolating curve-fitting routine.) As mentioned earlier, the axial vorticity thus generated is enhancing the mixing between the primary flow and the shield-flow passing through the chutes apart from the mixing caused by vertical shear layer vorticity (present due to the difference in horizontal speed components of the primary and the secondary flow). Also note from Figure 3-40, the fairly good similarity of flows between neighboring chutes near the central vertical plane of the nozzle. Thus we can presume that the flow structures are similar from one-chute/one-core passage to the next one, except, as noted before, for those at the end-jets.

**Shield-Flow Shock Structures :** Figures 3-41 and 3-42 show the mean velocity distributions and angles inside the shield flow, respectively, along axial lines 4 and 5 for planes A and C which are coincident with the primary and the chute center lines. Immediately apparent is the shock structure near 1.4" in both planes A and C. These dips seem to correspond to the location of shock-surface  $S_4$  in the shadowgraph (see Figure 3-32). Note that the distortions in the shadowgraph make it difficult to precisely locate the chute-edge or the shield-lip edge so that axial distances cannot be precisely measured and the dips may very well correspond to shock-surface  $S_3$ . However, all evidence seems to be in favor of a further downstream location

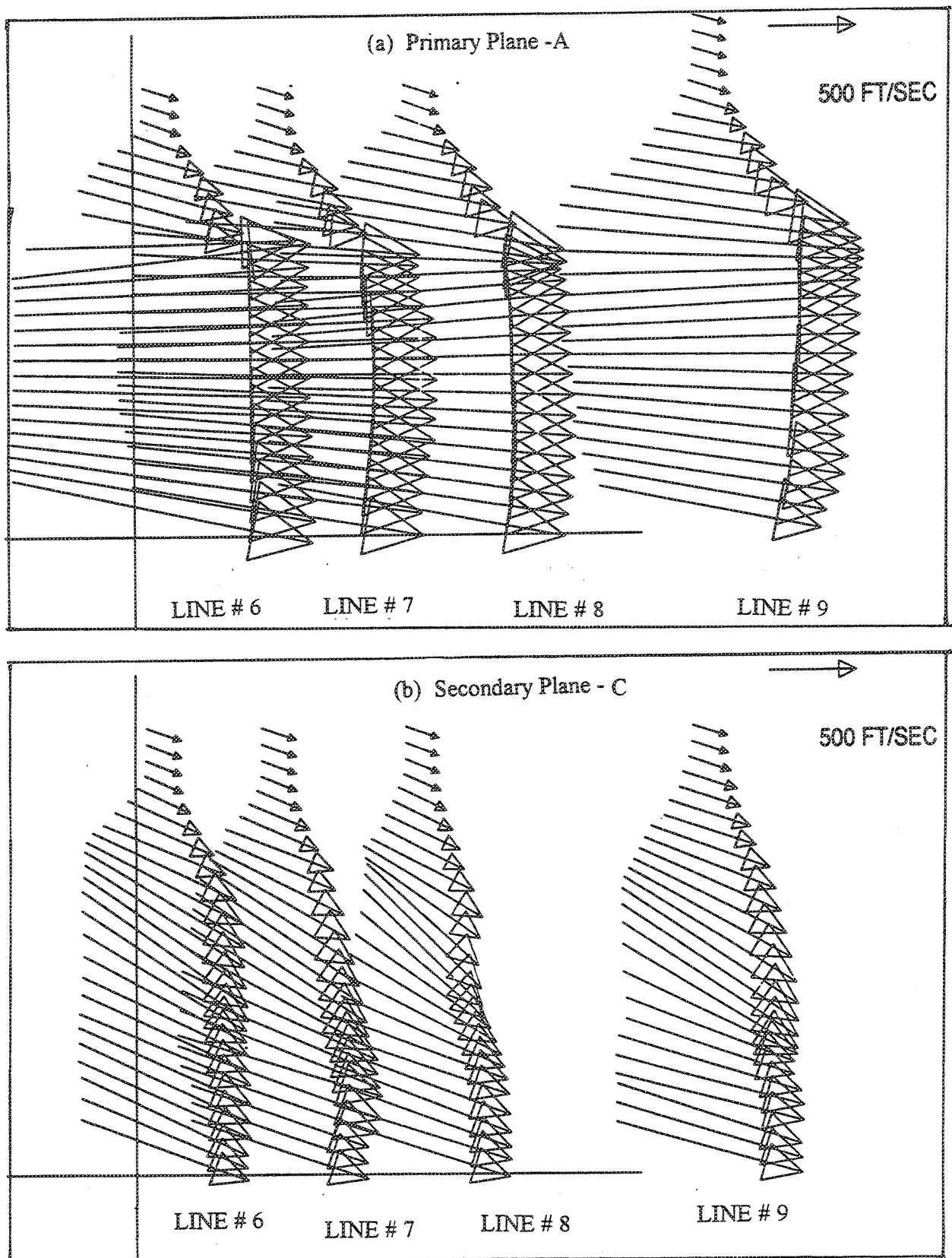


Figure 3-39. Mean velocity vector distributions for vertical line # 6, 7, 8 and 9 in the primary plane and the secondary plane (see Figure 3-33) for configuration # 4110 (i.e., convergent nozzle, SAR=2.9, 10% porous wedge,  $t_n=0.983$ ",  $M_{wt}=0.2$ ,  $P_{r,p}=3.2$ ,  $T_{t,p}=860^\circ\text{R}$ ,  $P_{r,s}=2.2$ , and  $T_{t,s}=560^\circ\text{R}$ ).

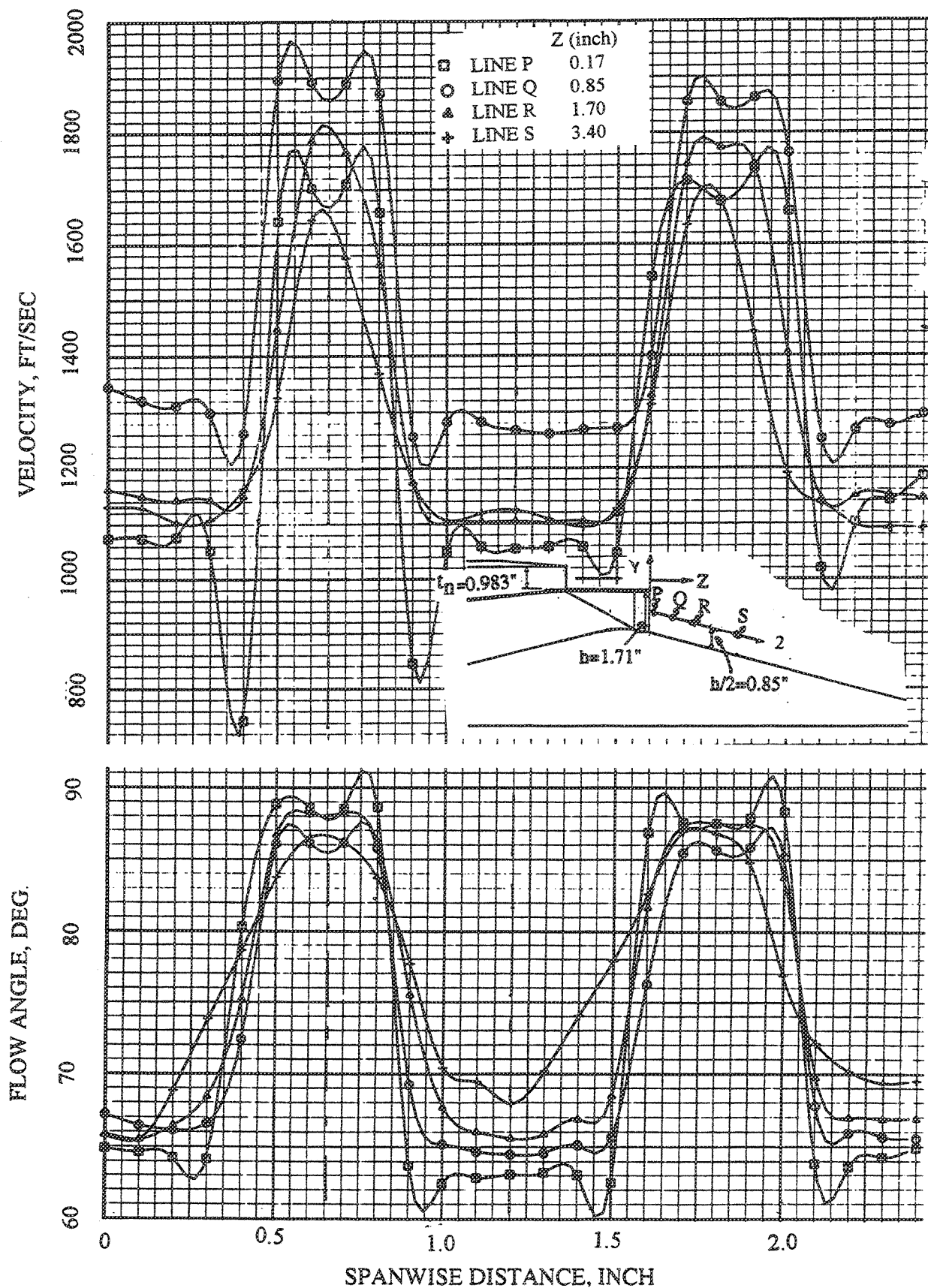


Figure 3-40. Spanwise mean velocity distributions for lines P, Q, R and S in the plane parallel to the wedge containing line # 2 (see Figure 3-33) for configuration # 4110 (i.e., convergent nozzle, SAR=2.9, 10% porous wedge,  $t_n = 0.983''$ ,  $M_{wt}=0.2$ ,  $P_{r,p}=3.2$ ,  $T_{t,p}=860^\circ\text{R}$ ,  $P_{r,s}=2.2$ , and  $T_{t,s}=560^\circ\text{R}$ ).



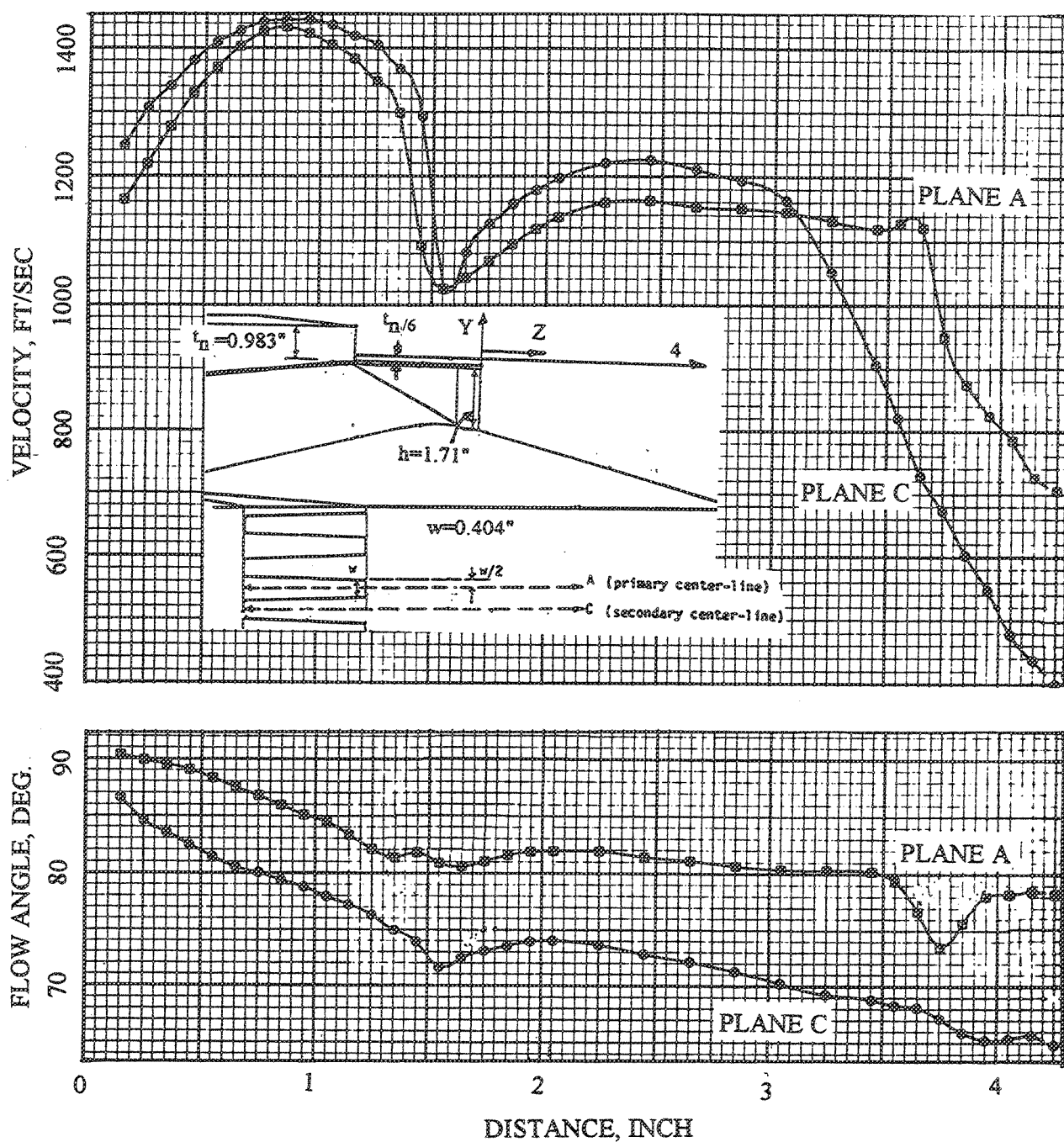


Figure 3-41. Mean velocity distribution in the shield-flow for line # 4 in planes A and C (see Figure 3-33) for configuration # 4110 (i.e., convergent nozzle, SAR=2.9, 10% porous wedge,  $t_n=0.983''$ ,  $M_{wt}=0.2$ ,  $P_{r,p}=3.2$ ,  $T_{t,p}=860^\circ\text{R}$ ,  $P_{r,s}=2.2$ , and  $T_{t,s}=560^\circ\text{R}$ ).

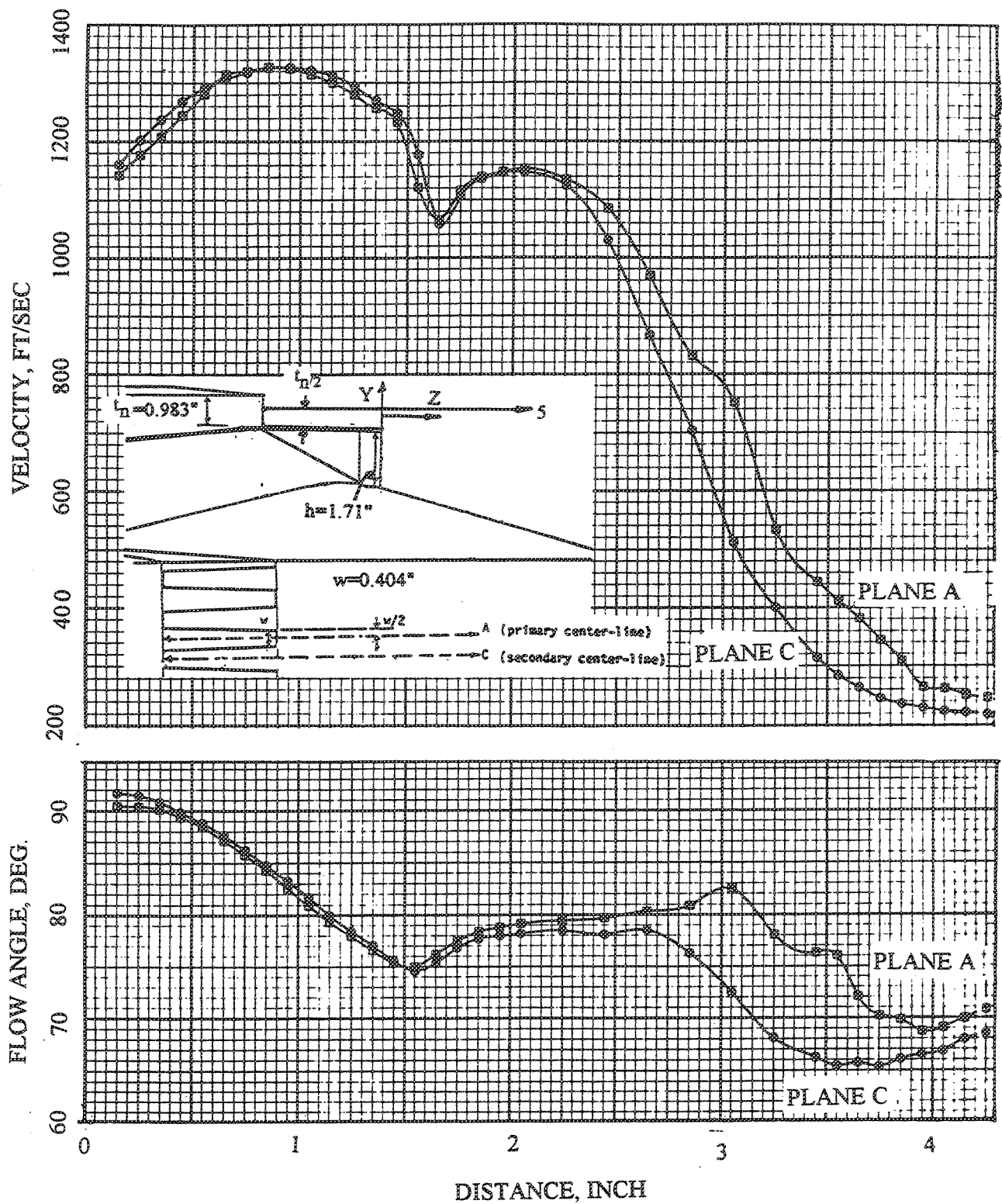


Figure 3-42. Mean velocity distribution in the shield-flow for line # 5 in planes A and C (see Figure 3-33) for configuration # 4110 (i.e., convergent nozzle, SAR=2.9, 10% porous wedge,  $t_n=0.983''$ ,  $M_{wt}=0.2$ ,  $P_{r,p}=3.2$ ,  $T_{t,p}=860^\circ R$ ,  $P_{r,s}=2.2$ , and  $T_{t,s}=560^\circ R$ ).



corresponding to  $S_4$ ; we tentatively think that  $S_3$ , with its sharper contrast corresponds to a similar shock-structure for the end-jet which is closer to the light source. This shock, nevertheless, is stronger near the shield floor than when further away from it (line 4 vs line 5 velocity dip and angular deflection magnitudes at around 1.5"). The decay on line 5 at around 2.25" in Figure 3-42 is due to this line piercing the shear layer or jet border between the top ambient flow and the shield flow starting at the shield-lip. This shear layer is further pulled in towards the shield floor because the shield flow itself is being pulled in downward through the chutes. The downward turning of the flow through the expansion fan,  $S_5$ , and further upward re-deflection through the shock  $S_6$  is clear only from line 4 on plane A (Figure 3-41); whence,  $S_5$  and  $S_6$  must be present only above the shield floor and not inside the chutes, that is, they must be associated with the shape of the shield-floor lip. We will discuss this in some detail later.

Finally, spanwise LV traverses at shield exit plane (see Figure 3-43) have shown fairly periodic mean velocity profiles from one chute centerline to the next, at least for the central chutes. Slight increase in velocities are noted around the chute center-lines due to supersonic expansion inside the chutes. Hence, we can conveniently conclude that the shock structures found above are repeated in other flow passages.

#### Origins of the Shock Structures :

(a) Shock-Structures on the Wedge : Consider the origin of the shock surface  $T_1$  in Figure 3-32 coming off the top chute-lip in the primary core flow. With a convergent core flow path (cross-sectional area for the primary core flow is decreasing up to the chute exit plane) and under-expansion one would "normally" expect the exit flow to expand to the ambient pressure through a centered expansion fan at the top lip. However, this classic text book explanation assumes uniform (parallel) exit velocity distribution. Here, not only do we have a diverging exit velocity distribution (see Figure 3-39(a), traverse 6 on plane A, primary plane) but also a nozzle with multi-dimensional effects - a converging core flow path in the spanwise or horizontal plane but a diverging core flow path in the vertical plane due to the 15-degree top wedge surface. For diverging (non-uniform) under expanded flows in CD nozzles, Courant & Friedrichs (Ref. 29, pp 389-390) offer an explanation for the existence of such lip shocks (which they call "intercepting" shocks) in addition to the usual lip expansion

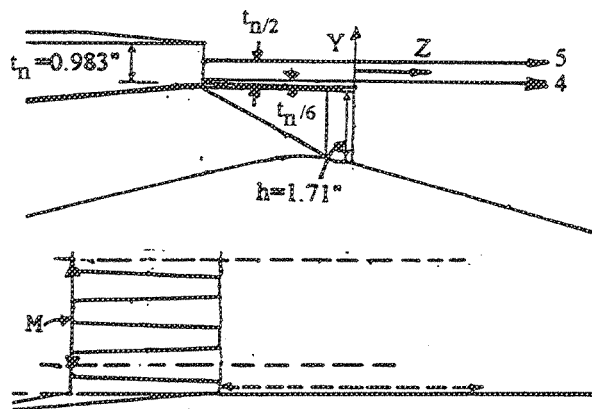
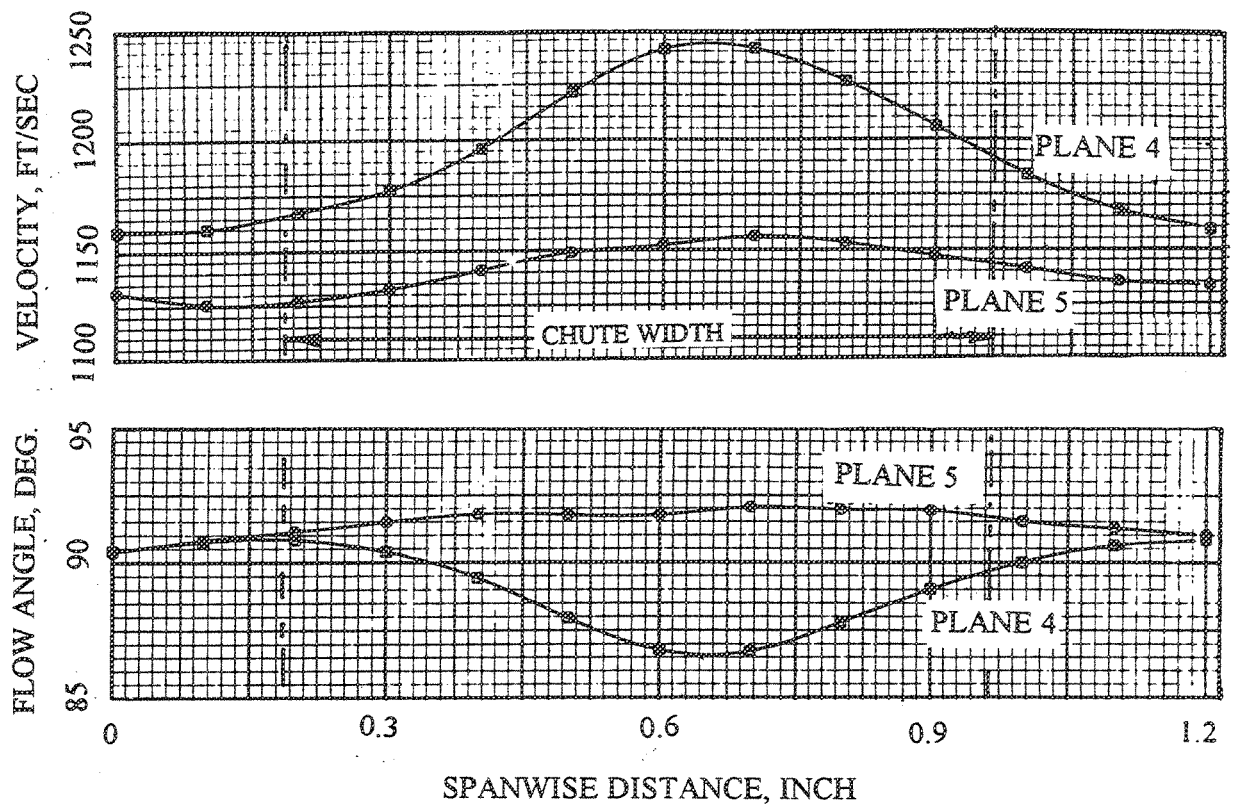


Figure 3-43. Spanwise mean velocity distributions in the shield-flow for line M at different heights (see Figure 3-33) for configuration # 4110 (i.e., convergent nozzle, SAR=2.9, 10% porous wedge,  $t_n=0.983''$ ,  $M_{wt}=0.2$ ,  $P_{r,p}=3.2$ ,  $T_{t,p}=860^{\circ}\text{R}$ ,  $P_{r,s}=2.2$ , and  $T_{t,s}=560^{\circ}\text{R}$ ).

waves. We believe that a similar reasoning may apply in our case and, hence, proceed to explain it further.

Consider supersonic under expanded flow in a 2D-CD nozzle with diverging exit flow (see Figure 3-44). At the top lip the flow can indeed expand through an expansion fan whose strength, hence, must be  $p = P_{\text{exit}} \text{ (primary)} - P \text{ (ambient)}$  thus, the difference in pressure between the leading Mach line and the rear Mach line of this expansion fan, while traveling on a streamline in a "simple" region remains constant and is equal to  $p$ . Now, if the streamline is away from the lip, near the central region of the jet, then due to the divergent nature of the supersonic flow the pressure is still decreasing going from the exit plane to the leading Mach line on this streamline. With a further drop of  $p$  through the expansion fan, hence, the pressure on this streamline is less than  $P_{\text{ambient}}$  when it reaches the rear Mach line. Thus, behind the rear Mach line a pressure gradient is set up from  $P_{\text{ambient}}$  at the lip jet border to some  $p < P_{\text{ambient}}$  in the central region. This gradient curves the jet border concave inwards (as opposed to a straight line jet border in 2D-CD nozzles with uniform exit flow). Now the jet border is a free-streamline on which (according to free streamline theory) the flow speed and temperature must be constant. Consequently, the Mach number on it must also be constant. Hence, the Mach lines originating at the jet border will have constant Mach angles (see Figure 3-45). But since the jet border is concave inwards these Mach lines will intersect each other giving rise to non-unique solutions. In reality, as is well known, this is of course prevented by the formation of a shock wave which is the coalescence of the family of these continuous Mach lines. As can be seen from Figure 3-45, this shock-wave, can start from the lip and the envelope of the Mach lines or the shock-front will be right behind the expansion fan.

One of the features observed in the shadowgraph shown in Figure 3-32 is, indeed, the bulging and inward curving of the jet-border from top-lip as predicted in this reasoning. However, in the fluid-shield nozzle case there are certain differences compared to the 2D-CD case (apart from it being a convergent nozzle) which should be recognized at the outset to assess the applicability of previous reasoning.

- 1) Firstly, for under expansion the pressure in the shield-flow at the top chute-lip,  $P_{\text{lip}}$  (shield flow) is assumed to be lower than  $P_{\text{exit}} \text{ (primary)}$ . Actual measurements have not been made for either of these pressures; only, the total pressure ratios at the primary exit plane and the shield exit plane are known ( $P_t \text{ (primary)} = 3.2 P_{\text{amb}}$  &  $P_t$

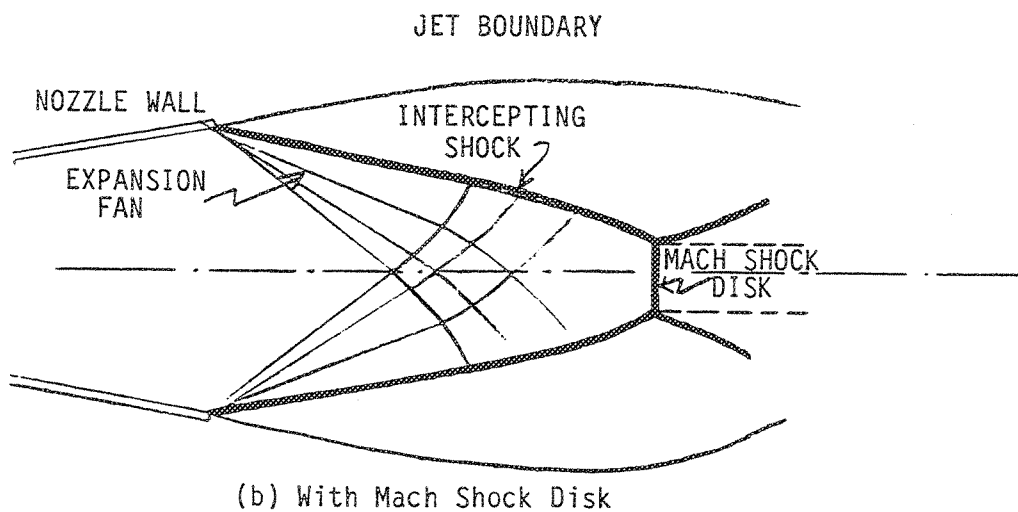
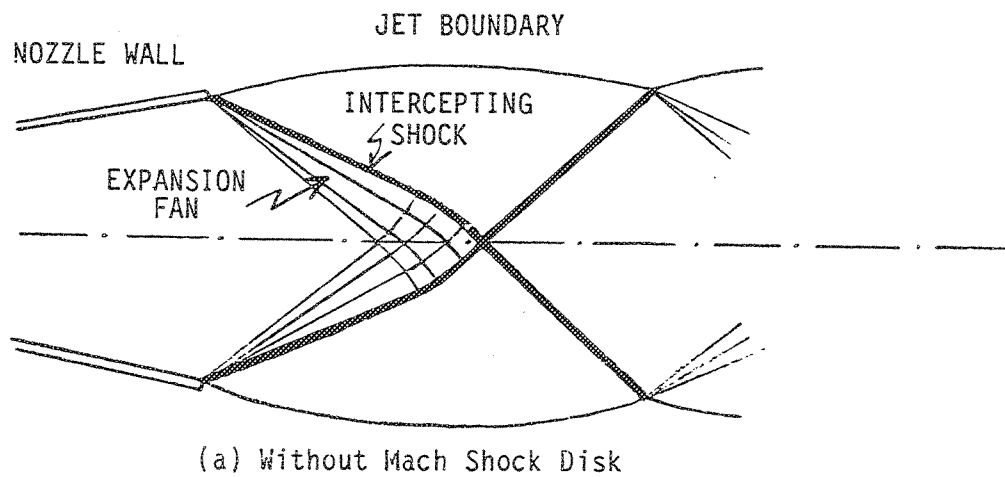


Figure 3-44. Intercepting shock patterns in a diverging jet emitted with a pressure greater than the ambient pressure.

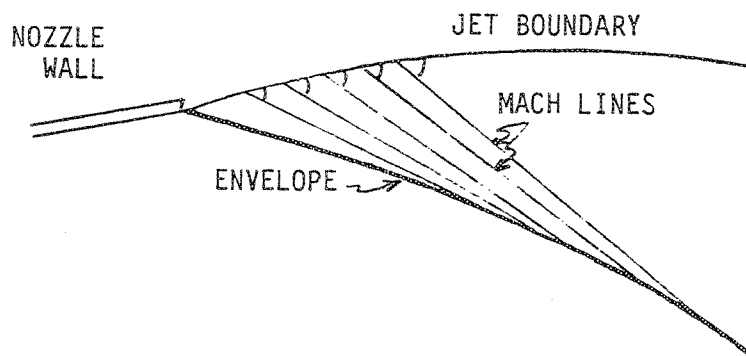


Figure 3-45. Envelope of Mach lines issuing from the jet boundary at equal angles.

(shield) = 2.2 P<sub>amb</sub>). Also the shield flow goes through a series of shocks and expansion waves so that the static pressure at the lip need not be the same as that at the shield exit plane. However, presumably the pressure in the shield-flow downstream of the last lip-shock is close to the static ambient pressure, being equilibrated through the upper shear-layer between the shield-flow and the ambient flow. Thus, using

$$P_{\text{total}}/P_{\text{exit}} = [1 + (\gamma - 1)M_{\text{ex}}^2/2]^{\{(\gamma - 1)/\gamma\}}$$

for  $\gamma = 1.4$ ,  $M_{\text{ex}} = 1$  and  $P_{\text{total}} = 3.2 P_{\text{amb}}$  gives  $P_{\text{exit}} = 1.69 P_{\text{amb}}$ . Hence, with wind-tunnel on at Mach number of 0.2, the previous assumption of  $P_{\text{exit}} (\text{primary}) > P_{\text{lip}}(\text{shield})$  (approximately  $P_{\text{amb}}$ ) seems very plausible.

2) Secondly, for the steeper chute configuration #1 (see Table 3.1 for details) the velocity across the top portion of the primary exit plane is known to be sonic from prior CFD calculations (done during the design phase) and becomes supersonic only close to the wedge-surface. This is also most probably the case for this shallow chute #4. Thus, the sonic-line and, hence, the leading Mach line from the top-lip must be almost vertical near the lip. Further, there are Mach-lines in the supersonic region near the wedge surface which are inclined backwards making some portion of the central jet region "non-simple". However, note from Figure 3-37, line 3 on plane A, that the primary flow velocity in the top portion has two slopes just after exiting and before dipping sharply at the lip-shock. Although the flow is not aligned with the traverse line 3 on plane A, this presumably means that the flow is accelerating faster initially with one value and then with a smaller acceleration value, respectively, before and during its passage through the lip expansion fan until it "sees" the lip-shock. Hence, a key requirement for the previous argument that there ought to exist a pressure gradient from say mid-chute height to outer lip jet-border on the rear Mach-line of the lip expansion fan still appears viable.

We also note here that in the case of dual annular flows in Dosanjh et al (Ref. 30), the lip-shocks in the inner flow were attributed to the pressure in the cavity produced just downstream of the trailing edge of the thick-lip between the two flows. In their case this cavity itself is annular, whereas, in our case this base-cavity can be all around the periphery of the chute trailing edge and the possibility of an independent chute-base pressure inside this cavity arises (not to be confused with the use of the word chute-

base used in previous figures with the shadowgraphs) . However, no effort has been made into finding this cavity pressure. This matter needs to be further looked into.

(b) Shield Flow Shock Structures : In general the origin of shield-flow shocks is similar to those for C-41 nozzle model discussed in the previous section. However, of course, there are certain differences in the ARL model due to different chute configuration (shallower with suppressor depth-to-height ratio of 2 rather than 1) and minor changes in the shield-floor lip geometry. We only discuss the prominent differences in the shock-structures due to these geometric differences.

Up to the shield exit plane the nozzle is convergent and due to the shield NPR of 2.2 the shield-flow is, indeed, under expanded. Hence, the top lip expansion wave exists along the whole span of the shield nozzle as seen in the shadowgraph (Figure 3-32) and as indicated by the initial accelerations of LV-traverse 5 on plane A in Figure 3-42. Also, the outward deflection of the shield jet-border at the lip supports this type of wave.

However, the progression of this flow along the chute center-line and the center-line between the two chutes (on the shield floor) must be different because the chute entrance is right at the shield exit plane for this chute configuration. Thus, the supersonic shield flow inside a chute first has to expand through another expansion fan starting on the bottom at the chute entrance and whose strength is governed by the chute leading edge angle of  $30^\circ$ . This is evidenced as the initial rise in velocity in Figure 3-41 (with downward sloping velocity vectors). The first bulge in the jet-border (see the shadowgraph in Figure 3-32) is also reminiscent of the reflection of this bottom expansion fan from the jet border. However, note that this bulge may also be due to the reflection of another expansion wave originating at the shield-floor due to the previous incident lip expansion wave. With this in mind, the initial shock/expansion wave developments are shown in Figure 3-46 for the two planes - chute center-line and the center-line between two chutes. This figure shows how the oblique shock S4 possibly arises in both these planes and which has been evidenced in the LV-data (Figures 3-41 and 3-42). However, in reality, there are obviously three-dimensional flow effects, such as, spilling of the flow from the shield-floor to the chute in the spanwise direction etc., which are not encompassed in the wave-diagrams of Figure 3-46.

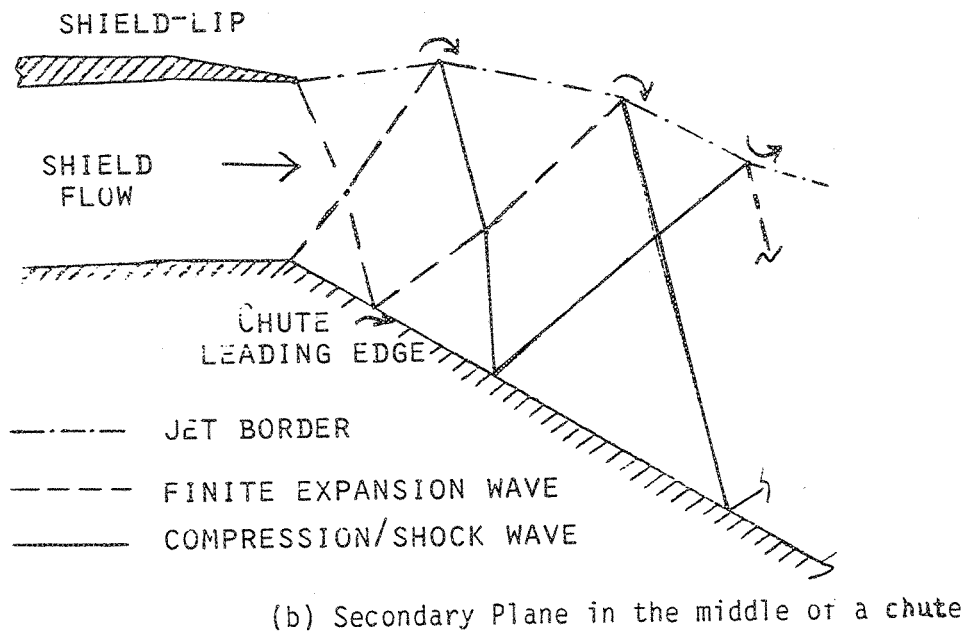
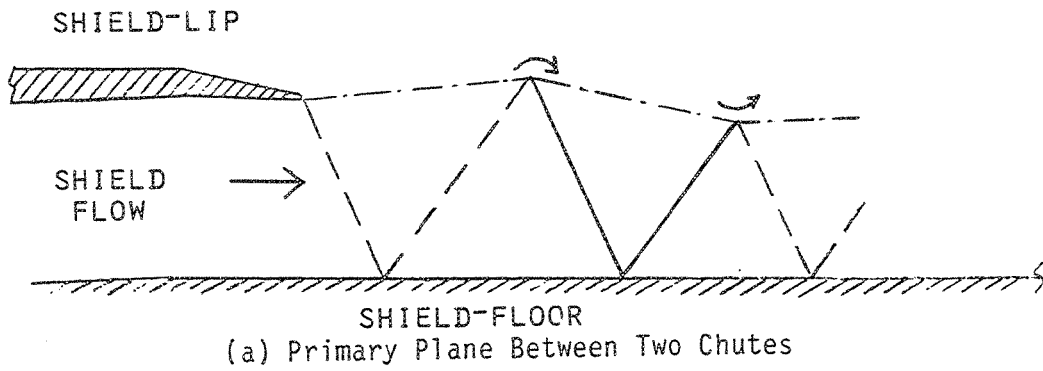


Figure 3-46. Schematic of possible initial wave developments for supersonic shield flow in two vertical planes.

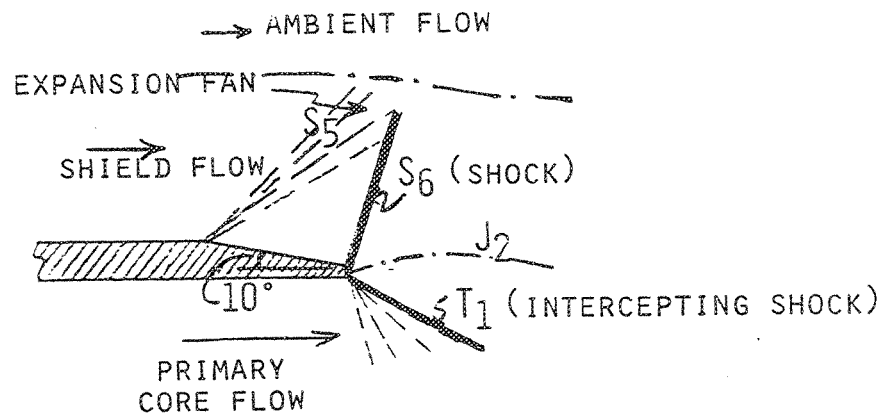


Figure 3-47. Detailed wave diagram near the top chute lip in the primary plane.

Now consider the flow at the shield-floor lip (see Figure 3-32). The expansion fan S5 which is only in plane A is a direct result of the expansion corner of  $10^\circ$  at the shield-floor lip (see Figure 3-47). Further downstream, this supersonic stream has to go through a compression corner because the primary flow underneath is diverging out creating the outward going jet-border; hence, there exists the lip-shock S6 in the shield-flow in the primary plane. It appears both from the shadowgraph and the LV-data that this expansion fan/shock-wave pair originating at the shield-floor lip intersect each other and do not reflect back from the upper jet-border between the shield flow and the ambient flow. Most likely, they simply annihilate each other.

#### *Baseline Configuration ( # 1105 ) :*

Consider the baseline operating condition for this configuration:  $P_{r,p} = 3.2$  and  $P_{r,s} = 2.2$  ( # 1105 F). Figure 3-48 shows the shadowgraph for configuration # 1105F and Figure 3-49 shows the LV-traverse locations tailored to suit the shock features in this shadowgraph. Note that the overall shadowgraph (see Figure 3-18) shows that the shock-cells develop largely axially rather than being parallel to the wedge surface. Hence, the LV-traverses were also selected in the axial direction rather than parallel to the wedge as in the previous configuration # 4110.

Figure 3-50 shows the mean velocity data taken at mid-chute height (i.e., on XZ plane containing # 1) in various vertical planes (i.e., at different X locations along a, e, a, and a) in the secondary flow (central chute) and the primary flow (adjacent jet). Note that the primary flow first accelerates and expands before shocking at  $Z = 1$ " and then repeats it after shocking. The most striking feature is the sudden drop in magnitude around  $Z = 1$ " in both the flows. This corresponds to the location of shock-surface A in the shadowgraph, whence it must be present in both the flows - primary, as well as, secondary. Thus, an overall flat piece of shock-surface A exists along the whole span of the nozzle. The shear-layers shed from the chute side edges will, hence, interact with this shock-surface to contribute to the shock-associated broadband noise.

In order to get an idea about the directions of these mean velocities, we show velocity vector plots in Figure 3-51 for different traverses in the center-lines of primary and secondary flows. The origin of the vector is at the location of the observation point. It brings out the axial evolution of the angular differences in the two flow regions. The primary flow downstream of the chute exit plane in the upper-half region appears fairly



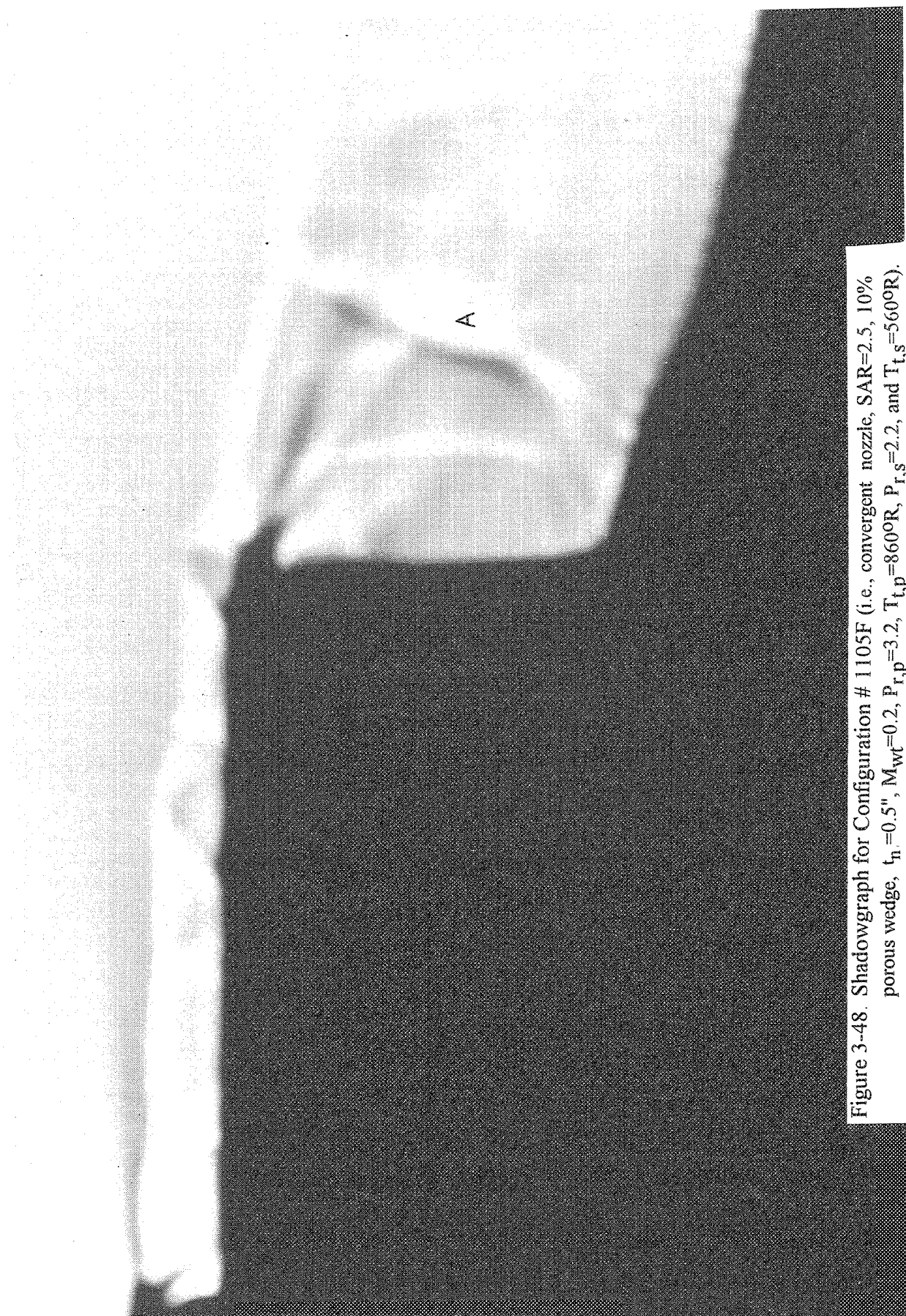


Figure 3-48. Shadowgraph for Configuration # 1105F (i.e., convergent nozzle,  $SAR=2.5$ , 10% porous wedge,  $t_n=0.5"$ ,  $M_{wt}=0.2$ ,  $P_{r,p}=3.2$ ,  $T_{t,p}=860^\circ R$ ,  $P_{r,s}=2.2$ , and  $T_{t,s}=560^\circ R$ ).

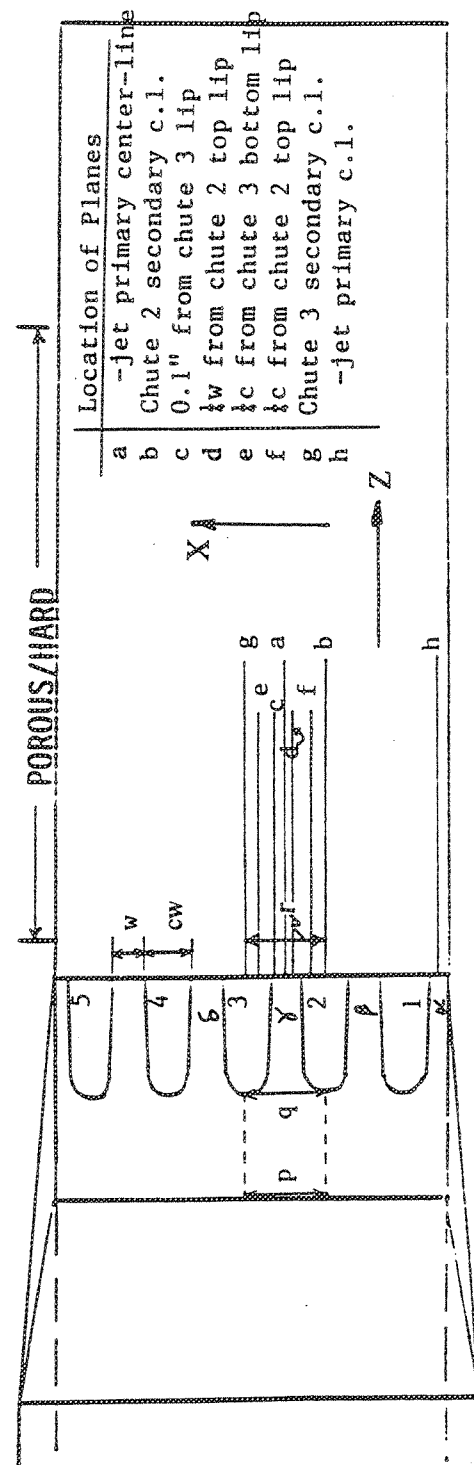
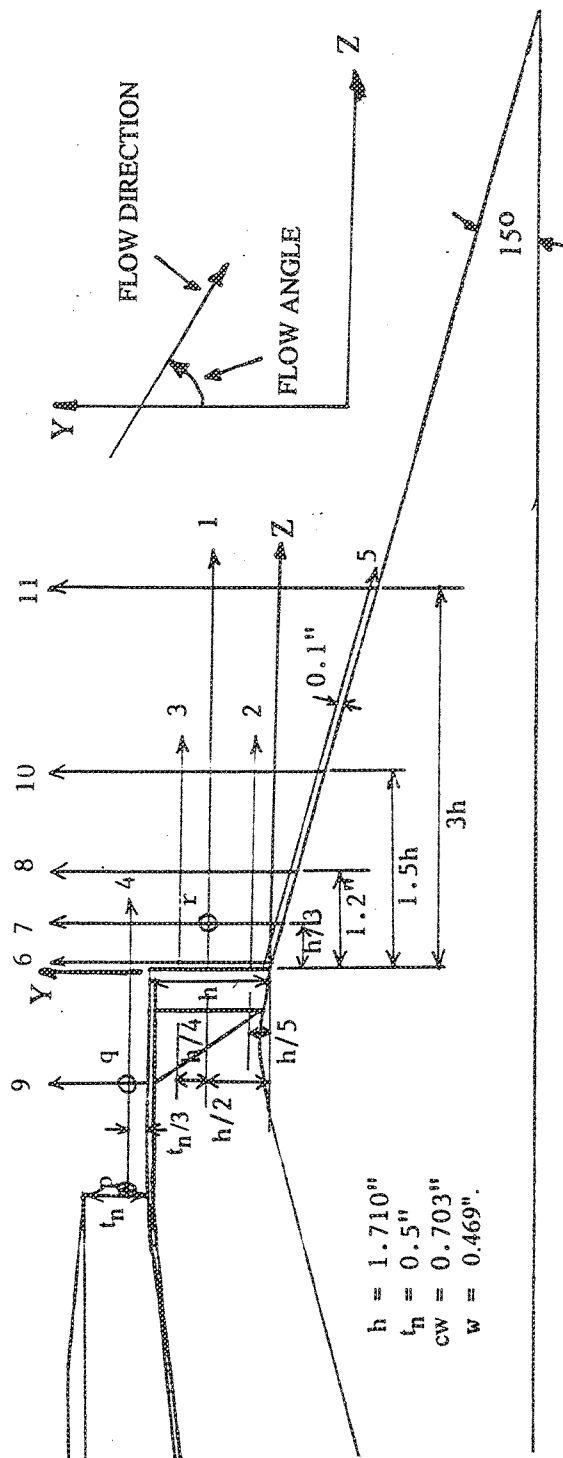


Figure 3-49. LV traverse locations for Configuration # 1105 (i.e., convergent nozzle, SAR=2.5, 10% porous wedge,  $t_n=0.5''$ ).

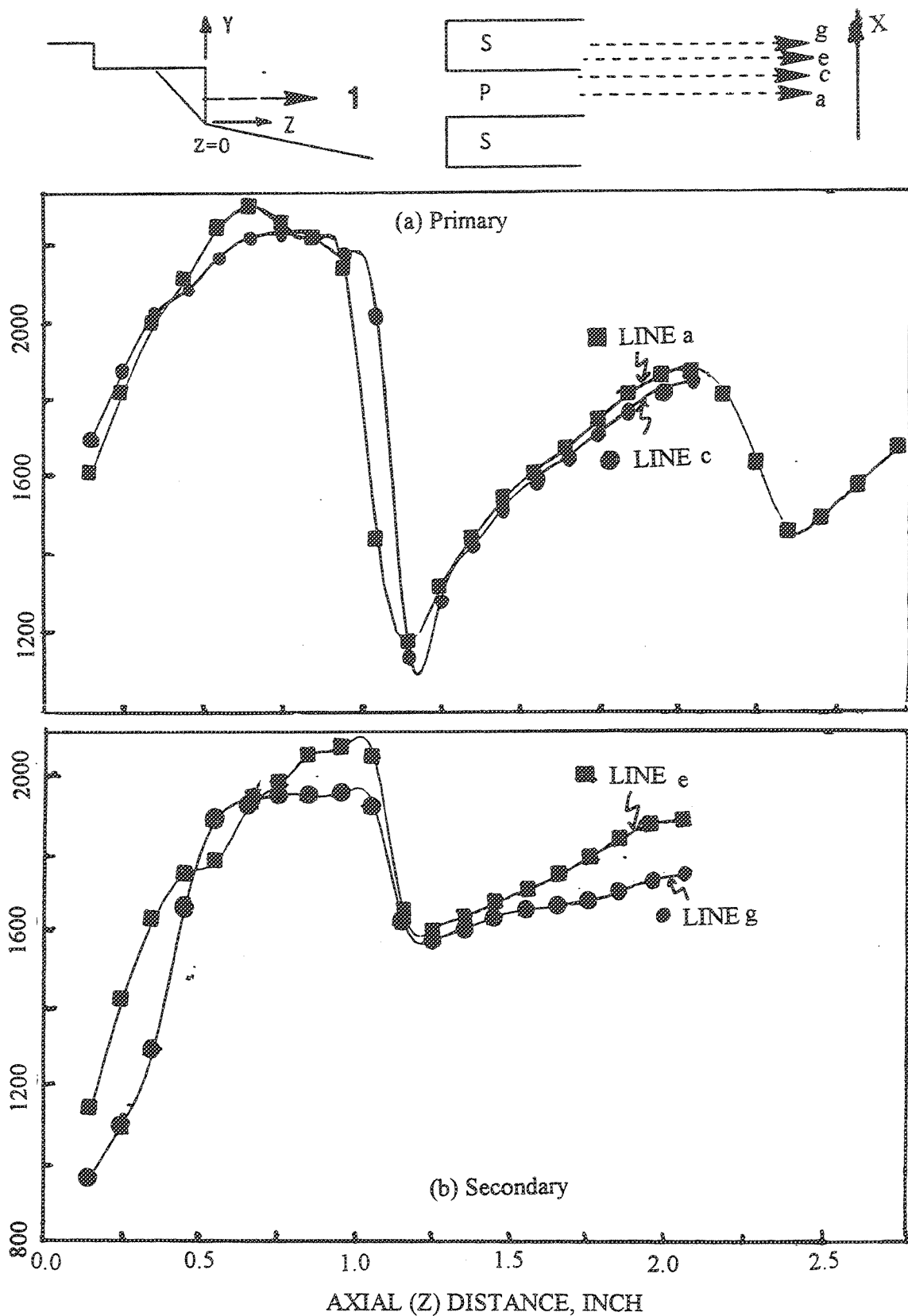


Figure 3-50. Mean velocity LV-data at different spanwise locations on the XZ plane at #1 (see Figure 3-49) for Configuration # 1105F (i.e., convergent nozzle, SAR=2.5, 10% porous wedge,  $t_n=0.5"$ ,  $M_{wt}=0.2$ ,  $P_{r,p}=3.2$ ,  $T_{t,p}=860^\circ\text{R}$ ,  $P_{r,s}=2.2$ , and  $T_{t,s}=560^\circ\text{R}$ ).

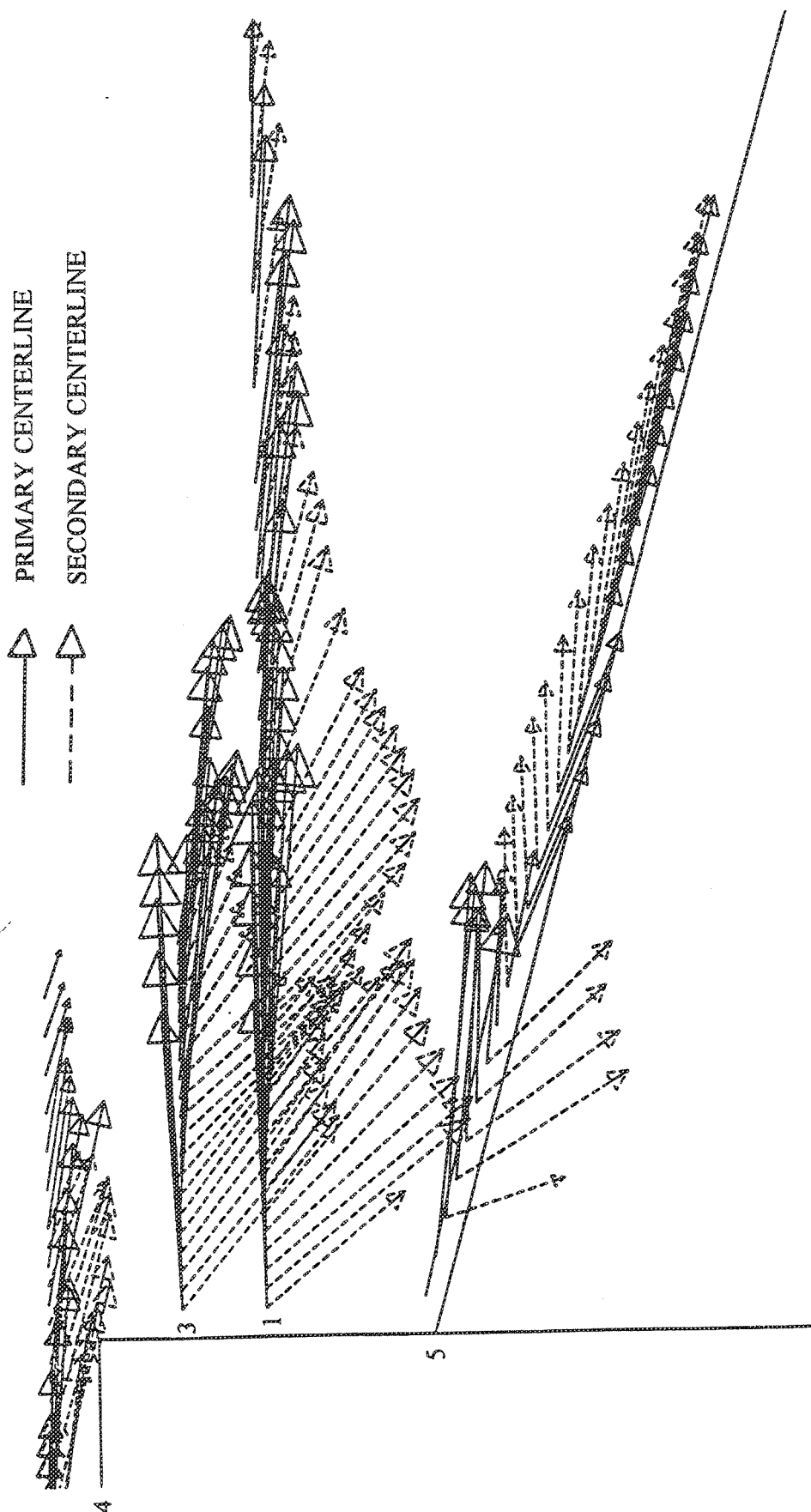


Figure 3-51. Mean velocity vector plots in primary and secondary centerlines (see Figure 3-49) for Configuration # 1105F (i.e., convergent nozzle, SAR=2.5, 10% porous wedge,  $t_n=0.5"$ ,  $M_{wt}=0.2$ ,  $P_{r,p}=3.2$ ,  $T_{t,p}=860^\circ R$ ,  $P_{r,s}=2.2$ , and  $T_{t,s}=560^\circ R$ ).

horizontal; whereas, the secondary flow there is inclined downwards - even steeper than the wedge or the chute angle initially and then gradually becoming axial. This has three immediate implications: (1) Shock A, noted earlier, is nearly normal for the primary flow but is oblique for the secondary flow. (2) The secondary or shield-flow may have separated due to the steep chute angle (55 degs.) right at the chute entrance leading to the steep secondary flow angles. However, note from Figure 3-18, that the chute base and exit pressures are well below ambient (60 - 75 % ambient pressure). (3) The vertical components of these two flows must be generating strong axial vorticity in the shear-layer shed from the side-walls of the chutes. Thus, the mixing between the two supersonic flows will be influenced by not only the vertical vorticity component (arising due to the difference in horizontal velocity components) but also by this axial vorticity component. The axial vorticity will further induce an uplifting of the primary flow and with spanwise spilling of the shield-flow into the chutes strong inverted wing-tip like axial vortices will be shed from the sharp neighboring horizontal edges of adjacent chutes. Also, note the sudden change in angles for both flows near the wedge surface which, perhaps, signifies the rear foot of a lambda shock wave somehow not captured in the shadowgraph.

Figure 3-52 shows the mean velocity vector plots along three vertical traverses in planes a and b. The center of the vector is at the observation point. The diverging velocity vectors in the primary flow are noted once again as in configuration # 4110 where the origin of the oblique lip-shocks for the under expanded "convergent" nozzle was explained using the "intercepting" shock argument. These figures also show quantitatively the velocity profiles in the horizontal shear-layers between (a) the primary and the shield-flow in plane a, and (b) the ambient and the shield-flow in planes a and b. The striking difference in the vertical components of the primary and the secondary flows at the chute exit plane creates axial vorticity which enhances the mixing between them and induces an uplifting tendency in the primary flow which can separate it from the wedge surface. The steep secondary flow angles continue at the downstream station (8) and the latter shift of angle (@ 10) can also be due to three-dimensional swirling effects of the secondary flow bouncing back after impacting the wedge.

Figure 3-53 shows the magnitude and direction of the mean velocity distribution on traverse 4 in the shield flow. It clearly shows the oblique shocks and the expansion waves there through its dips and positive gradients respectively. Generically, these

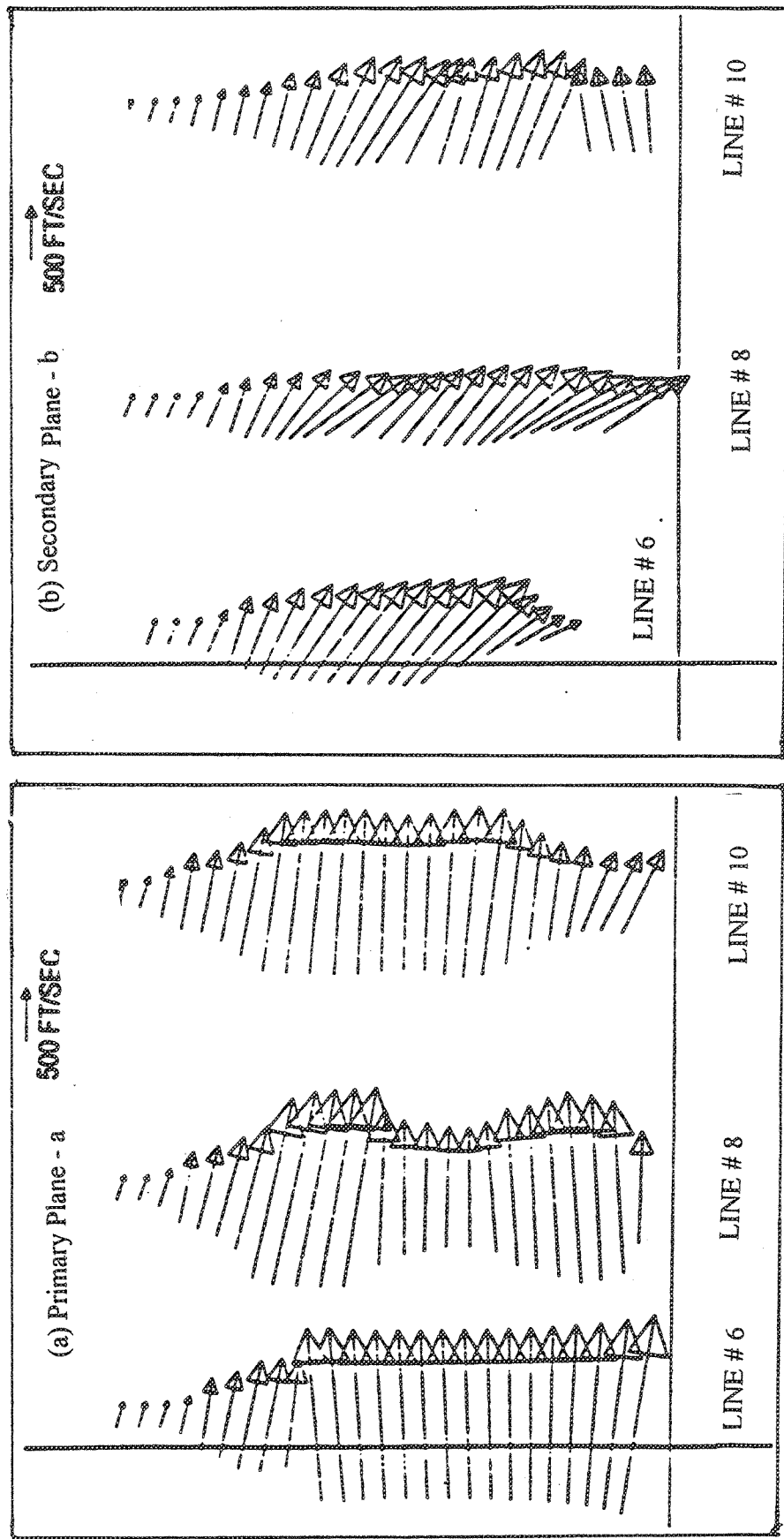
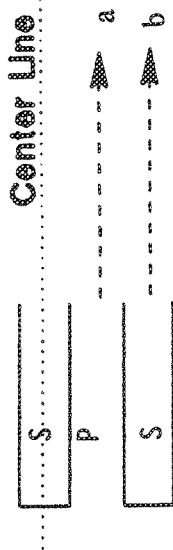
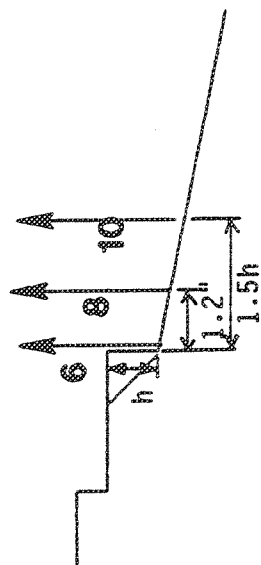


Figure 3-52. Mean velocity vector plots for vertical traverses (see Figure 3-49) for Configuration # 1105F (i.e., convergent nozzle, SAR=2.5, 10% porous wedge,  $t_n=0.5"$ ,  $M_{n,i}=0.2$ ,  $P_{r,p}=3.2$ ,  $T_{t,p}=860^\circ R$ ,  $P_{r,s}=2.2$ , and  $T_{t,s}=560^\circ R$ ).

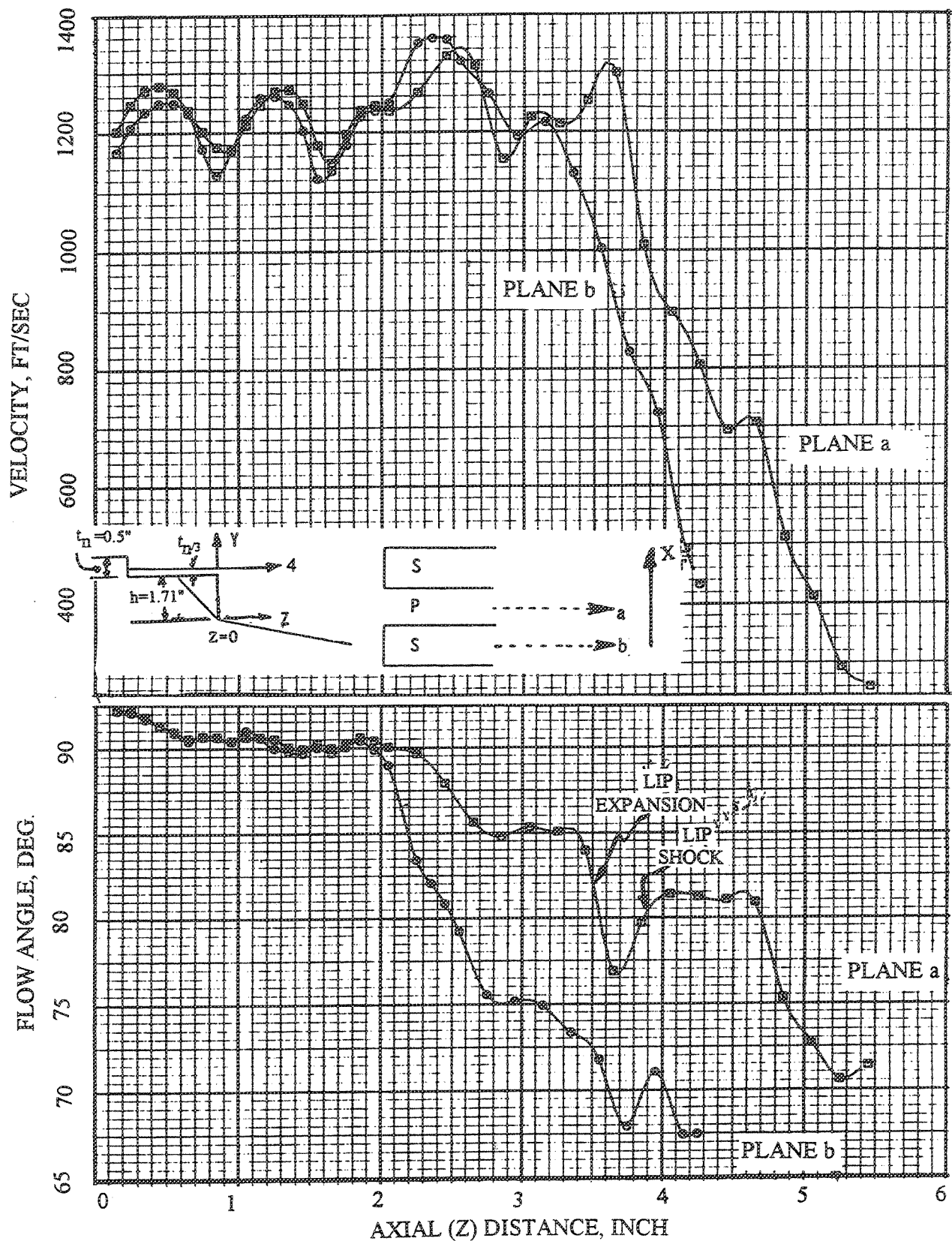


Figure 3-53. Shield-flow LV-data for mean velocities on traverse #4 on planes a and b (see Figure 3-49) of Configuration # 1105F (i.e., convergent nozzle, SAR=2.5, 10% porous wedge.  $t_n=0.5$ ",  $M_{wt}=0.2$ ,  $P_{r,p}=3.2$ ,  $T_{t,p}=860^\circ\text{R}$ ,  $P_{r,s}=2.2$ , and  $T_{t,s}=560^\circ\text{R}$ ).



shield-flow shock-expansion waves seem to follow usual planar shock/expansion reflection laws discussed for configuration # 4110. However, note that in configuration # 1105F the chute entrance is further downstream of the shield-flow nozzle exit plane, unlike configuration # 4110. The dip in angle at 3.5" and the subsequent rise corresponds, respectively, to the expansion-wave originating at the 10 degree chamfered lip of the shield-floor and the lip-shock downstream of it as explained earlier.

**Effect of Subsonic Shield Flow (Configuration # 1105G) :** Figure 3-54 shows a close-up of the shadowgraph for this test condition which has subsonic shield-flow. Also see Figure 3-19 for the pressure distributions. No shock/expansion waves were observed in the shield flow as expected. The shocks on the wedge appear to have some differences from those for configuration # 1105F (see Figure 3-48). We present the comparative LV-data between these two test conditions for traverses 1, 2, 3 and 5 (see Figure 3-49).

Figure 3-55 compares mean velocities in the center-lines of primary flow (a) and secondary flow (g) at mid-chute height (traverse 1). The major shock-surface A at  $Z = 1$ " does not seem to change much in the primary flow. However, in the secondary flow there does not appear to be a shock. The Mach numbers for the secondary flow on traverse g11601 for velocity of 1100 ft/s is approximately sonic ( $M = 1.05$ ) (under the assumption that the total temperature of this flow is the same as that at the shield exit plane which is ambient, 537 deg. R); however, at the location where shock A exists in the primary center-line (@  $Z = 0.95$ " ), the secondary flow velocity of 750 ft/s corresponds to a Mach number of approximately 0.657 which is subsonic. Further, the corresponding flow angles in the secondary flow are highly different and are extremely steep in # 1105G. Most likely this corresponds to a shield-flow that has separated at the 55 degree chute entrance and is further re-circulating downstream.

Figures 3-56 (a) and 3-56 (b) compare the mean velocities for traverse 2 and 3 respectively. The significant differences in the secondary flows are again to be noted. Figure 3-57 compares the velocities for these two conditions for traverse # 5 close to the wedge-surface. Again note the striking difference in the flow angles.

In summary, the above LV-data comparisons tell us the following major effects of lowering the shield nozzle pressure ratio:



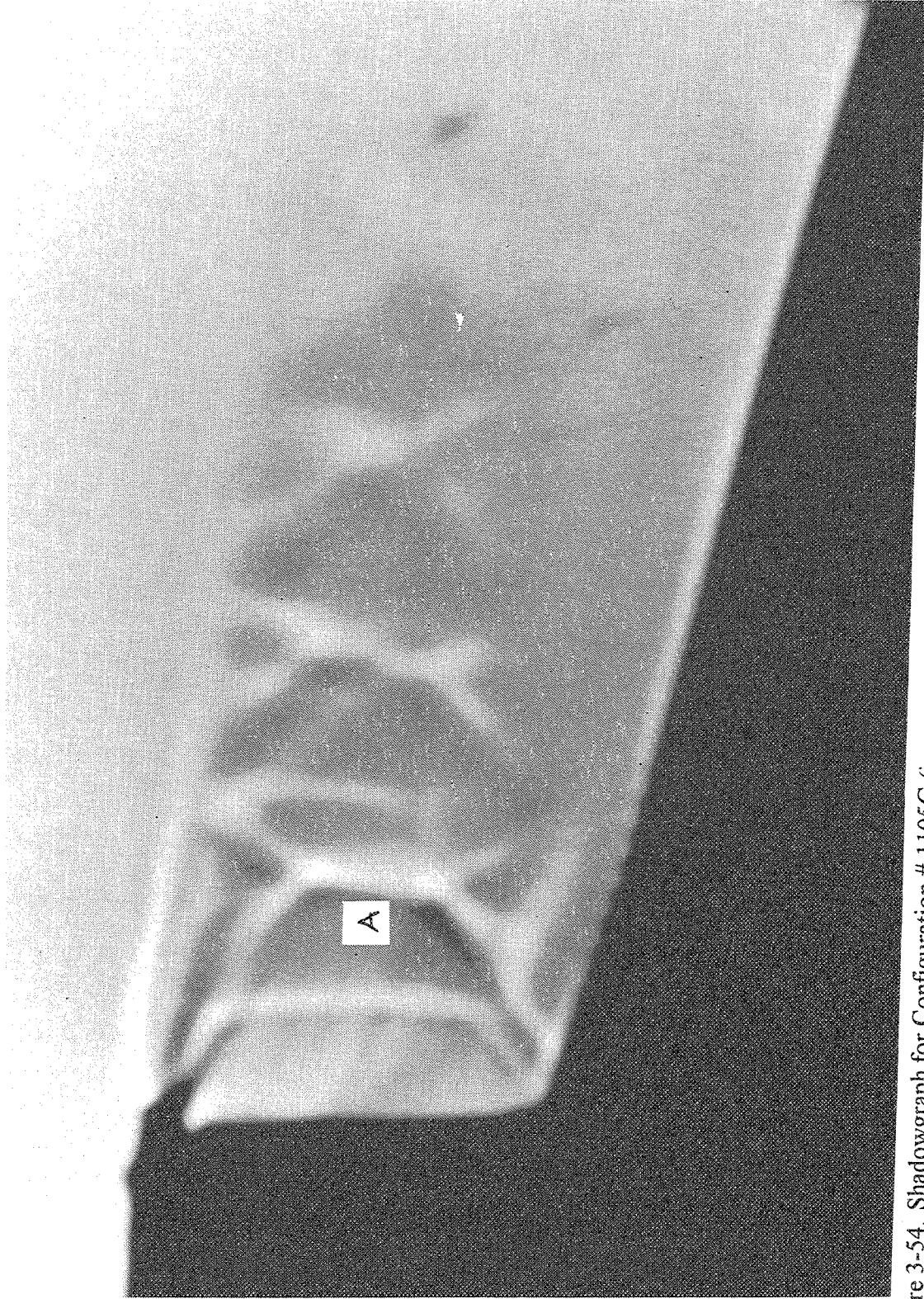


Figure 3-54. Shadowgraph for Configuration # 1105G (i.e., convergent nozzle, SAR=2.5, 10% porous wedge,  $t_n=0.5"$ ,  $M_{wt}=0.2$ ,  $P_{r,p}=3.2$ ,  $T_{t,p}=860^\circ\text{R}$ ,  $P_{r,s}=1.6$ , and  $T_{t,s}=560^\circ\text{R}$ ).

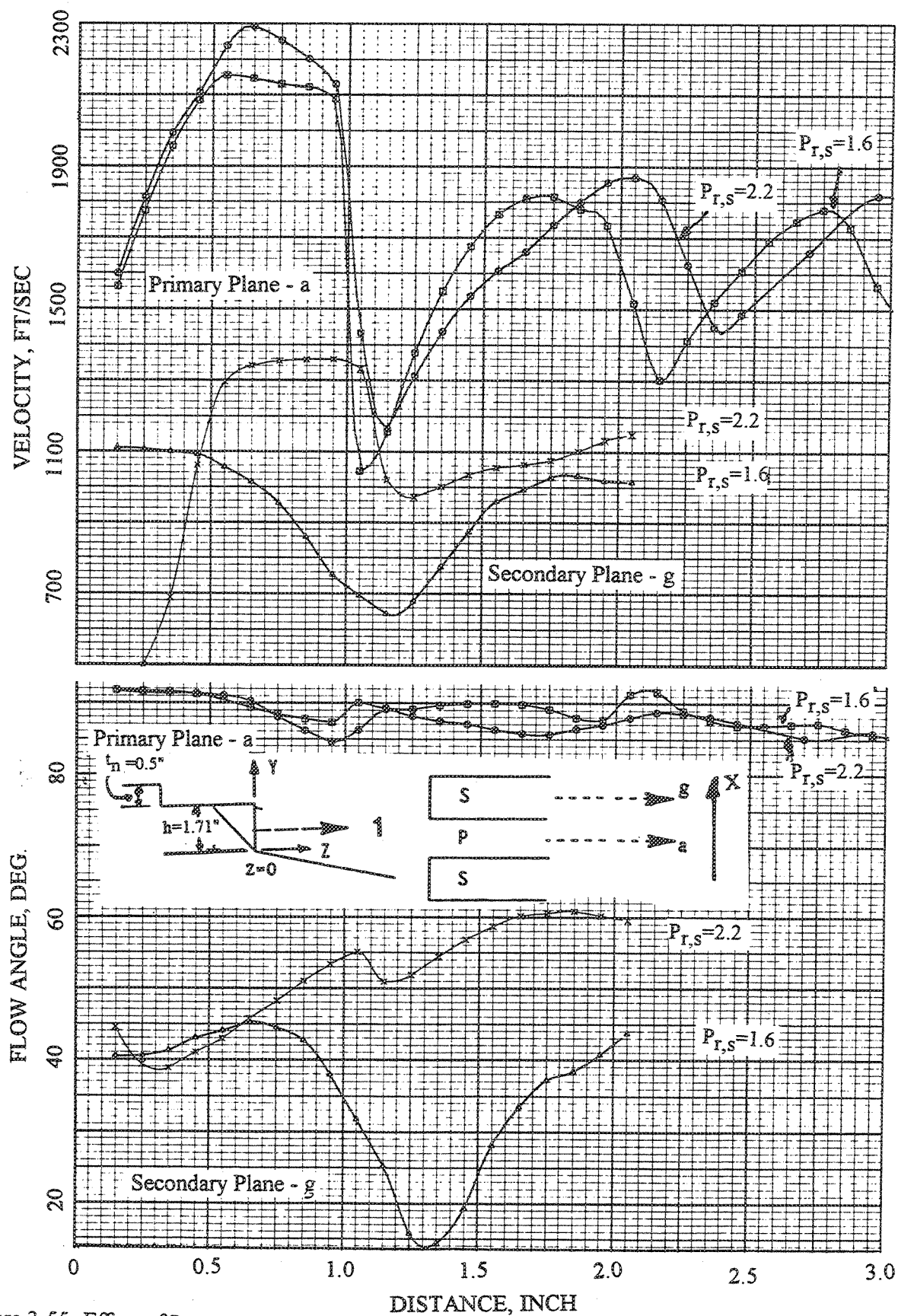


Figure 3-55. Effect of  $P_{r,s}$  on mean velocity distributions at different spanwise locations on the XZ plane at traverse #1 (see Figure 3-49) for Configuration # 1105 (i.e., convergent nozzle, SAR=2.5, 10% porous wedge,  $t_n=0.5"$ ,  $M_{wt}=0.2$ ,  $P_{r,p}=3.2$ ,  $T_{t,p}=860^\circ\text{R}$ , and  $T_{t,s}=560^\circ\text{R}$ ).

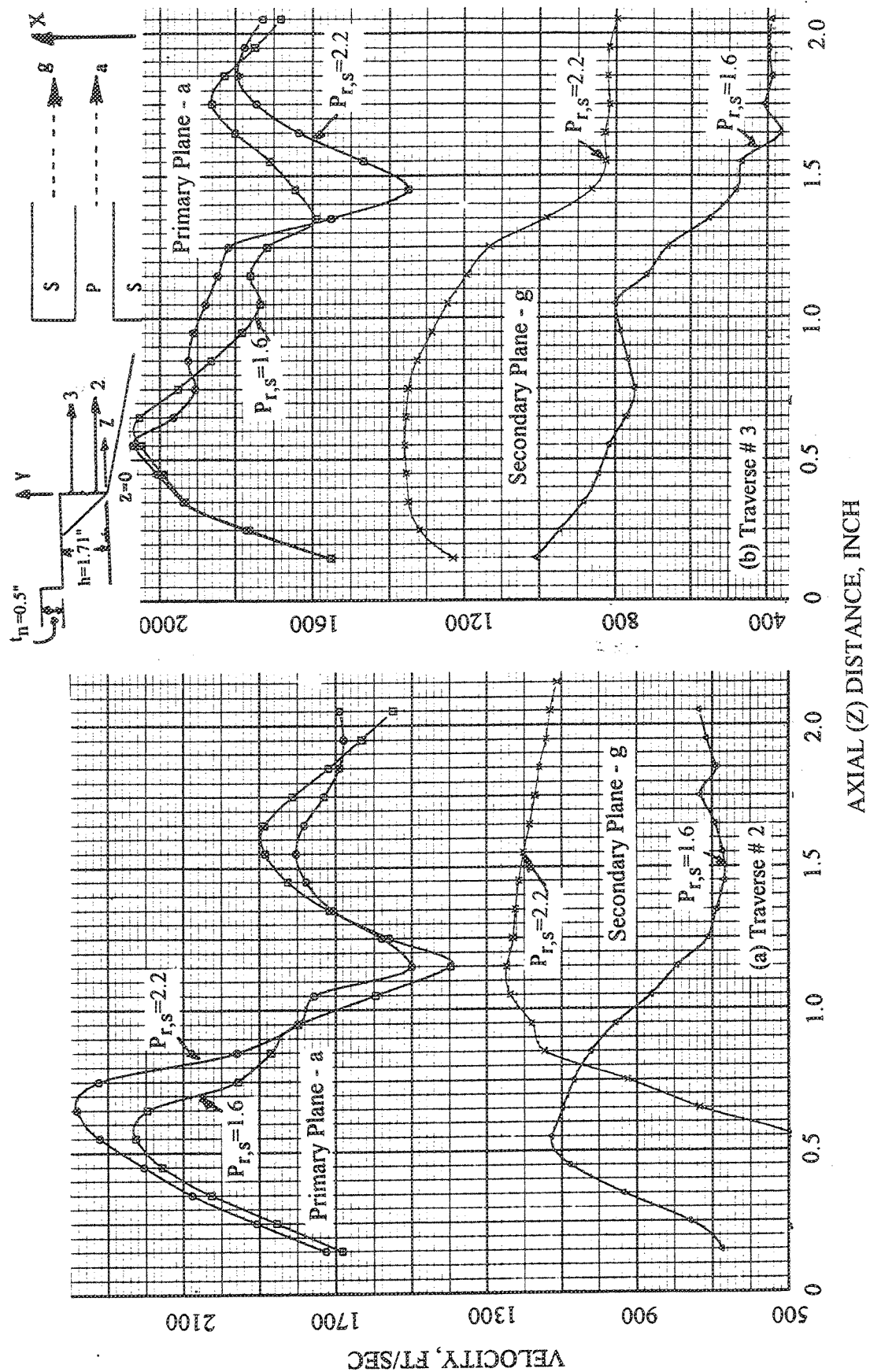


Figure 3-56. Effect of  $Pr,s$  on mean velocity magnitudes at different spanwise locations on the XZ planes at (a) traverse #2 and (b) traverse # 3 (see Figure 3-49) for Configuration # 1105 (i.e., convergent nozzle, SAR=2.5, 10% porous wedge,  $t_n = 0.5"$ ,  $M_{nt} = 0.2$ ,  $Pr,p = 3.2$ ,  $T_{tp} = 860^\circ R$ , and  $T_{ts} = 560^\circ R$ ).

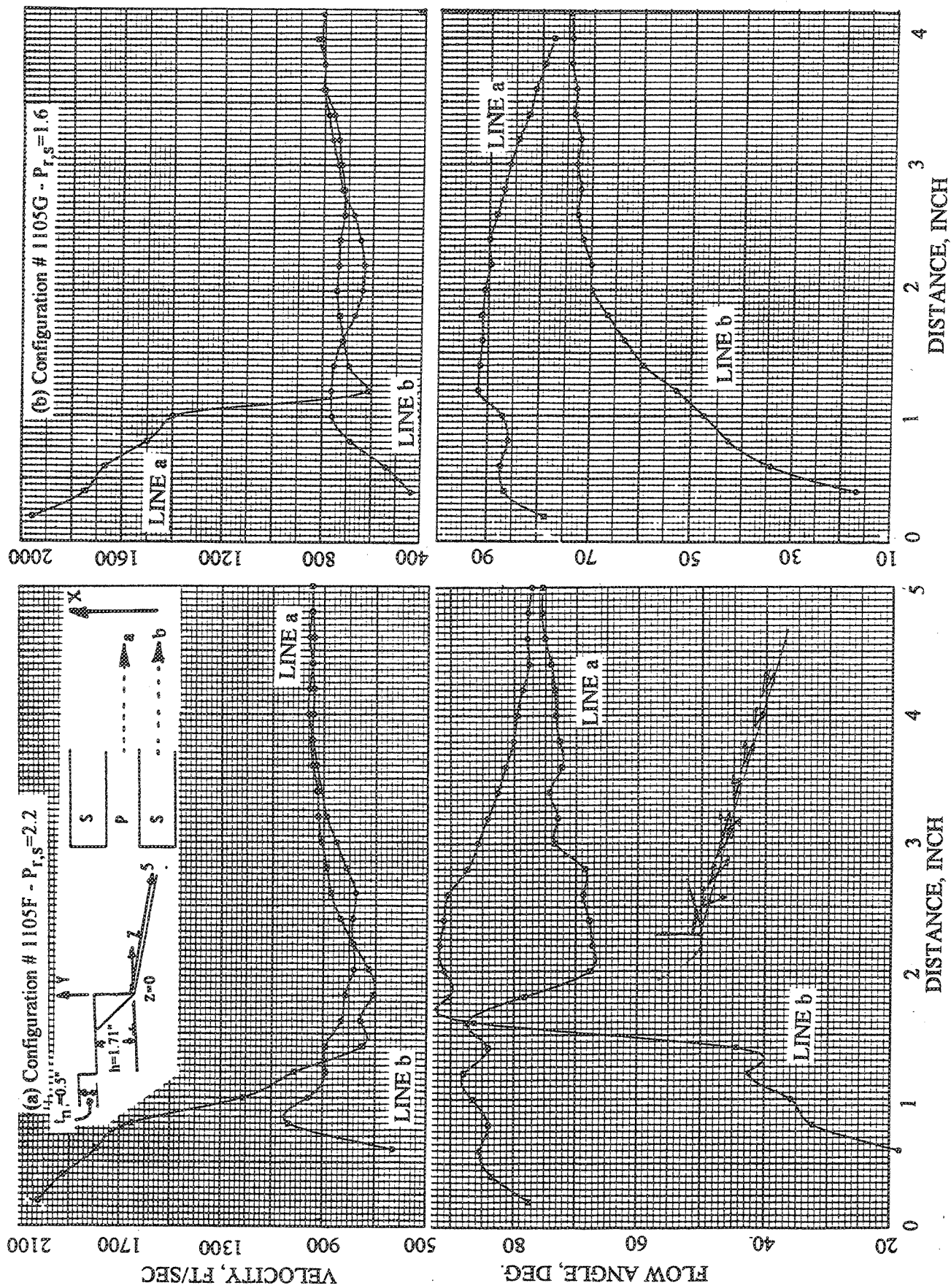


Figure 3-57. Comparison of mean velocities for traverse 5 parallel to wedge surface between primary (at a) and secondary (at b) centerlines for Configurations (a) # 1105F and (b) # 1105G (i.e., convergent nozzle, SAR=2.5, 10% porous wedge,  $t_n=0.5"$ ,  $M_{wt}=0.2$ ,  $P_{r,p}=3.2$ ,  $T_{t,p}=860^\circ R$ , and  $T_{t,s}=560^\circ R$ ).



- 1) The shock-cells develop even more axially, away from the wedge surface. Thus, wedge porosity will affect their strengths even less.
- 2) The dominant shock A is absent from the secondary flow which although sonic at the chute-exit plane is simply subsonic at that location. However, the strength of this dominant shock in the primary flow is almost the same.
- 3) The shock-cell "lengths" contract.
- 4) The shield flow separates at the chute entrance and forms a re-circulating zone further downstream of the chute-exit plane.

*Effect of CD-Core Flow Passages ( # 5105 ) :*

The primary flow-path for # 5105 is convergent-divergent (CD); everything else is similar to configuration # 1105F which has convergent primary flow-paths. Most LV-traverses were done at the same locations as those of #1105 (see Figure 3-49), so that a comparison of the LV-data between them could be made to see the effect of the CD primary flow-path. Some important conclusions follow:

1. Although the shadowgraphs of #5105A and #1105F look considerably different (see Figures 3-30(a) and 3-18(a)), careful examination of the LV-data for #5105A shows that the topology of the shock-structures is similar. For example, the main wedge shock-surface A of #1105F (see Figure 3-48) also exists in #5105, but is simply straightened out at the top and bottom. It is also along the whole span of the nozzle covering both the primary and the secondary flow-paths. Similarly the lip-shocks from the top of the primary chutes also exist in #5105A.
2. The important difference is that with CD primary flow-path, the *strength of this shock A* is considerably *decreased*. (See Figure 3-58 where comparison of LV traverses between configurations # 1105F with convergent core flow path and # 5105A with CD core flow path is made.) For example, the step velocity reductions through this shock at mid-chute height were approximately half of that in #1105F. The downstream shock-trains were also reduced in strength by approximately the same factor. Moreover, the spacing between these shocks (or the "shock-cell spacing") also appears to have decreased.

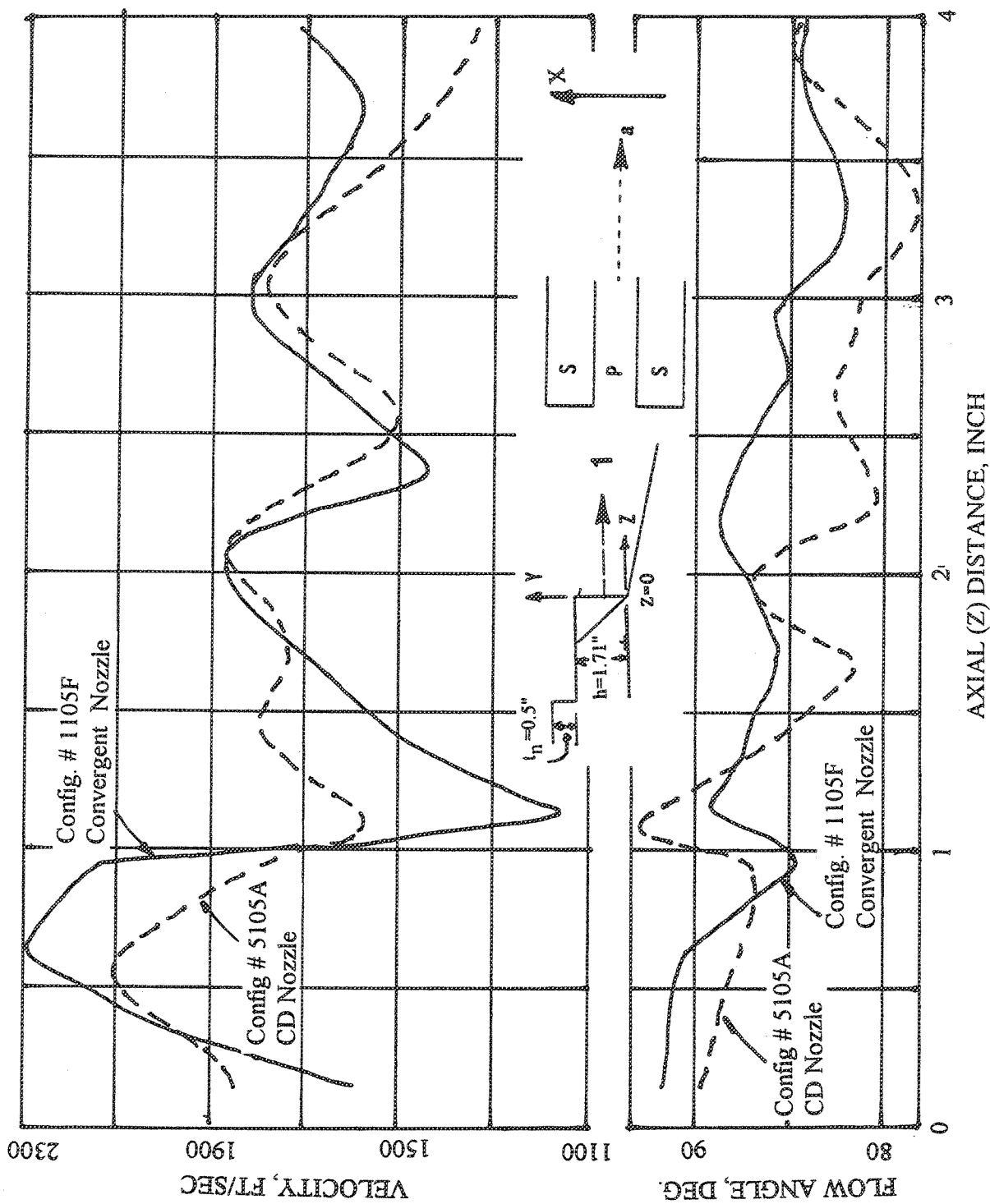


Figure 3-58. Effect of CD core flowpath on mean velocity distribution at primary centerline on an XZ plane at traverse # 1 (see Figure 3-49); SAR=2.5, 10% porous wedge,  $t_n=0.5$ ",  $M_{wt}=0.2$ ,  $P_{r,p}=3.2$ ,  $T_{t,p}=860^\circ\text{R}$ ,  $P_{r,s}=2.2$ , and  $T_{t,s}=560^\circ\text{R}$ .

3. The primary exit velocity at the chutes for CD flow-path is slightly higher than that in the convergent case.
4. Spanwise traverse shows much lower exit velocities at the two side jets compared to the central jets which are quite similar to one another.
5. As in #1105F, the rear foot of a lambda-shock attached to shock A is evident from the LV-data and there seems some evidence that the boundary layer flow is separated just downstream of this rear foot.
6. There is almost no difference in the shield-flow shock/expansion waves as compared to #1105F, as is to be expected.

The weaker wedge shocks imply that with such CD primary flow-paths at least the shock-associated noise can be alleviated considerably.

*Effect of SAR (# 2010) :*

We compare the SAR effect for the shallower chute ( # 2010 with SAR=2.5) with configuration # 4110 (SAR=2.9) in Figure 3-59. The chute model of configuration # 2010 has a gentle leading edge slope of 30 degrees and is similar to configuration # 4110 in this respect. However, #2010 has a suppressor area ratio (SAR) of 2.5 and non-porous wedge as compared to # 4110 which has SAR = 2.9 and 10% porous wedge. Hence, the differences in LV-data should be attributable to these two parameters.

The LV-traverses were similar to those of #4110 in general, except that the primary jet scanned was to the right-side of the nozzle center-line (forward-looking-aft) in # 2010 rather than to its left as in # 4110. Also, spanwise traverses were made only at the exit planes of the shield and the chutes. Some important observations follow.

Table 3-5 summarizes some of the initial shock-surface characteristics in configuration # 2010 and #4110 obtained by traverses in the primary and the secondary flow center-lines parallel and close to the wedge surface (1/4 th chute-height - traverse 1). It reveals that :

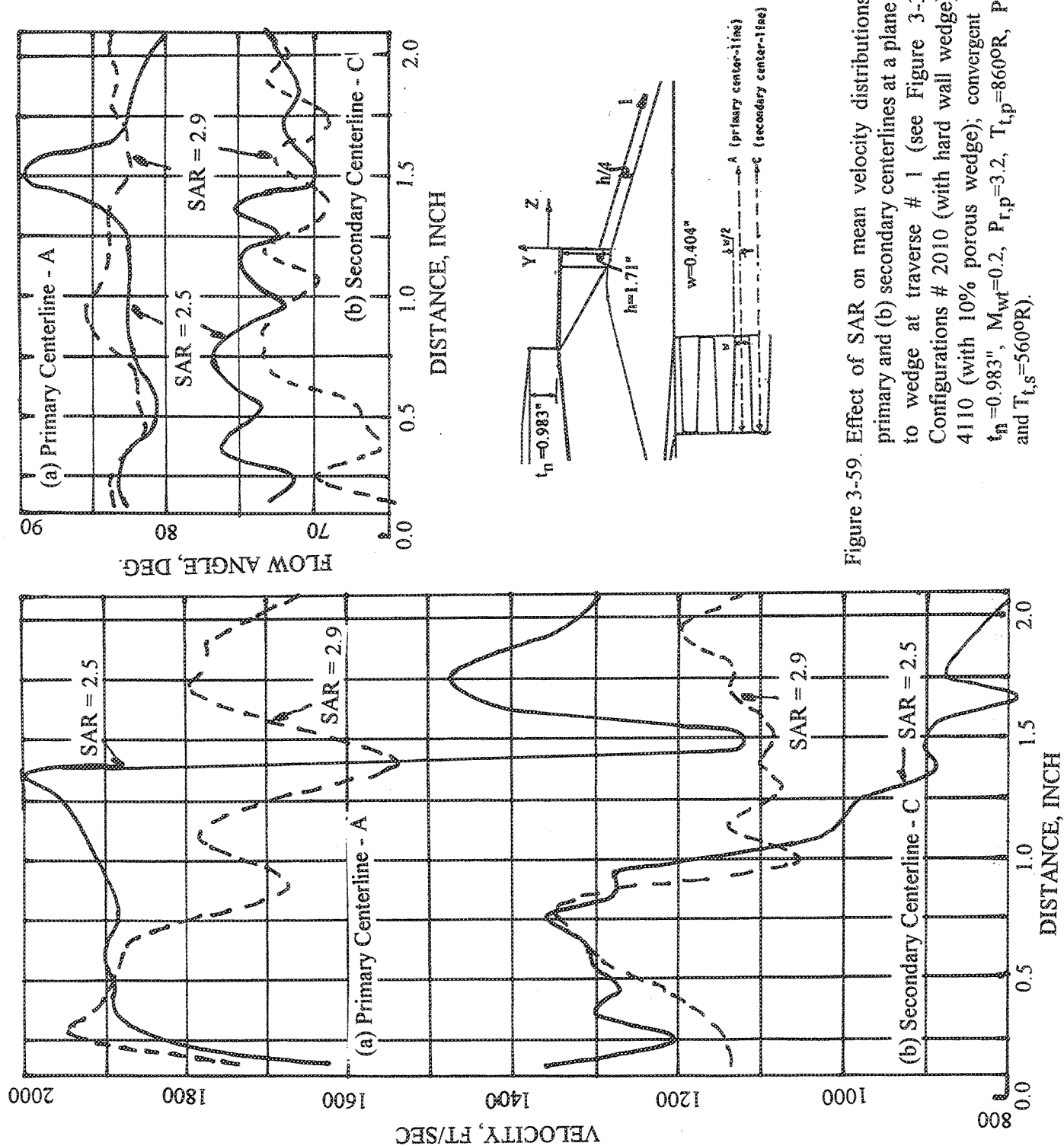


Figure 3-59. Effect of SAR on mean velocity distributions at (a) primary and (b) secondary centerlines at a plane parallel to wedge at traverse # 1 (see Figure 3-33) for Configurations # 2010 (with hard wall wedge) and # 4110 (with 10% porous wedge); convergent nozzle,  $t_n = 0.983$ ",  $M_{wt} = 0.2$ ,  $P_{r,p} = 3.2$ ,  $T_{t,p} = 860^\circ R$ ,  $P_{r,s} = 2.2$ , and  $T_{t,s} = 560^\circ R$ .



**Table 3.5 Effect of SAR on first shock-characteristics in primary and secondary flows (Configurations # 2010 and # 4110)**

Config. #	Primary Flow Shock					Secondary Flow Shock				
	Location		Strength*			Location		Strength*		
	Inches	% h	V1	DV	DV/V1	Inches	% h	V1	DV	DV/V1
2010	1.35	79 %	1950	790	40 %	0.9	53 %	1270	220	17 %
4110	0.75	44 %	1870	200	11 %	0.75	44 %	1350	300	22 %

\* V1, DV in ft/s and shock-strength here is based on DV/V1 for simplicity

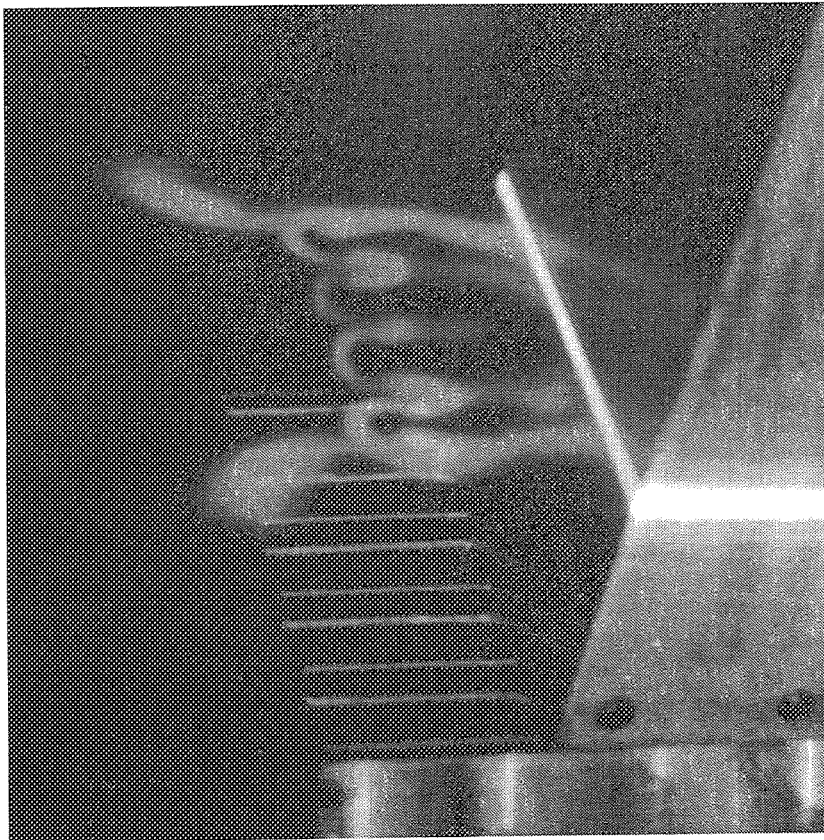
1. In # 2010 the foot of the first shock-surface in the secondary flow is considerably upstream than that in the primary flow unlike that in # 4110 where they were fairly close to each other. In # 2010 neighboring LV-traverses in the two flows reveals that each shock spans the whole width of each flow approximately at the same location. Thus it seems unlikely that these two shock-surfaces are connected by a shock-surface because that connecting shock-piece would then have to be almost parallel to the two flows. However, these two shock-surfaces in the two flows must be connected by a discontinuity surface (like, e.g., a contact surface). Thus in # 2010 there must be a fairly *corrugated* surface of discontinuity spanning the whole nozzle-width, which is comprised of shocks connected by contact surfaces. In # 4110 these shock surfaces were not that far apart in the two streams implying that this shock surface spanned the whole nozzle width and must be only slightly corrugated. This must be due to the fact that the ratios of the width of secondary-to-primary flow at the chute-exit plane are different in the two configurations: # 2010 has 1.5 and # 4110 has 1.9 value for this width ratio.

2. These first shocks in # 2010 are much stronger than the first shocks in # 4110 (if compared on % change in velocity basis). This may be attributable to the effect of porosity in # 4110 on the oblique shocks.

3. The presence of an inverted-V shock or a lambda-shock is not as evident in # 2010 LV-data as it is in # 4110 data and shadowgraph.

### 3.3.3 Planar Laser Sheet (PLS) Results

The edited video cassette of the PLS tests has already been given to NASA. Here we discuss some of the data using still photographs taken during these PLS tests. Examples of spanwise-vertical PLS data for configuration # 3010 are shown in Figures 3-60 and 3-61. In these cases it is the shield-flow that is seeded by steam. The white scattering of light appears to be from steam condensing on the vortex-sheets formed between the primary and the secondary shield flow. In these PLS tests, in general, it turned out that the vortex sheets were better visualized than the shock structures. Hence, a better idea of the mixing between the primary and the secondary flow is obtained. Note the following features:



Aft-looking-forward view

Figure 3-60. Laser-light-sheet visualization in the transverse vertical plane for configuration #3010 with stream seeding in the shield flow at static condition;  $P_{r,p}=3.2$ ,  $P_{r,s}=2.2$ ,  $T_{t,p}=680^{\circ}\text{F}$ , and  $T_{t,s}=480^{\circ}\text{F}$ .

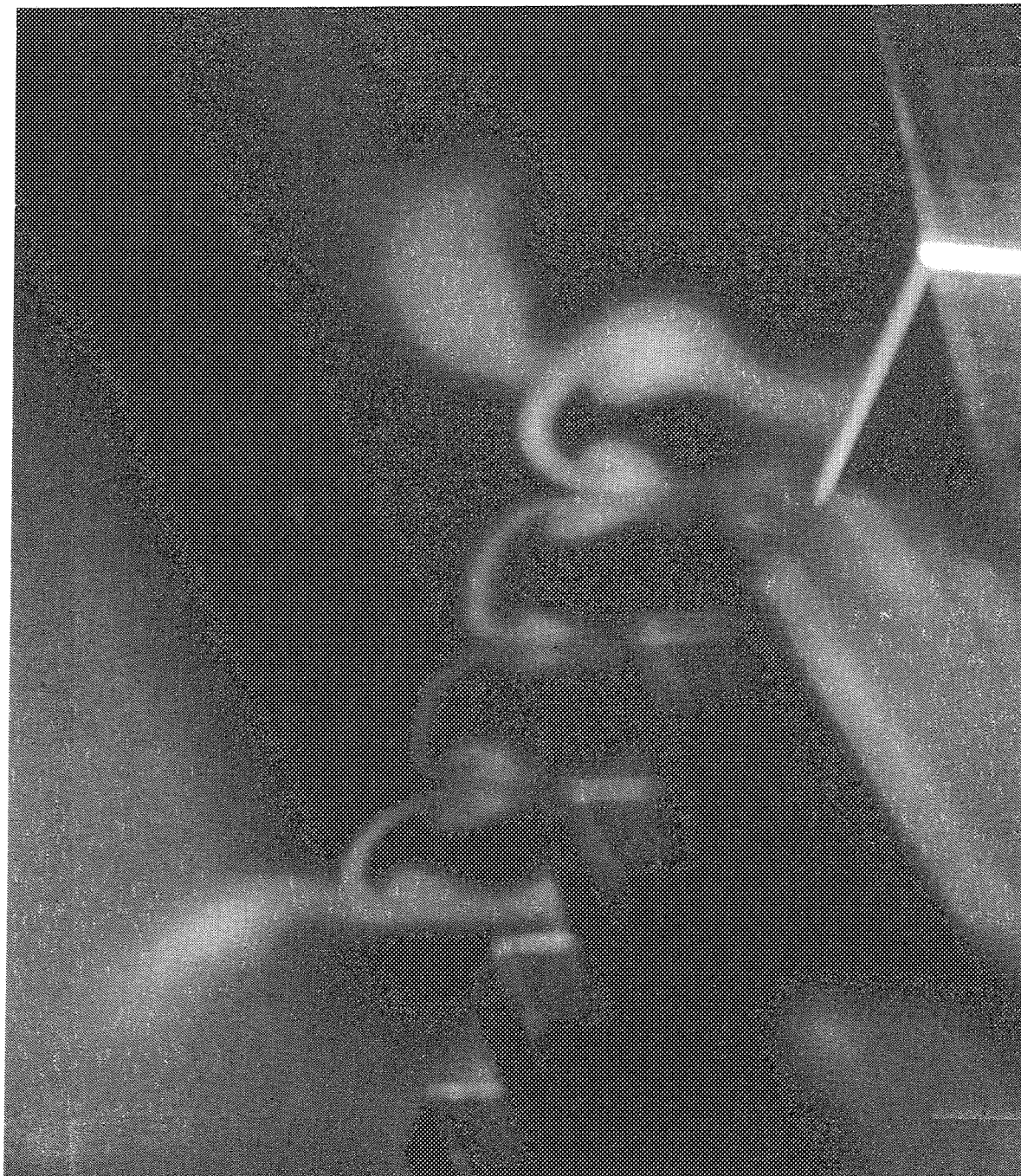


Figure 3-61. Laser-light-sheet visualization in the forward-looking-aft plane for configuration #3010 with stream seeding in the shield flow at static condition,  $P_{r,p}=3.2$ ,  $P_{r,s}=2.2$ ,  $T_{t,p}=68^{\circ}\text{F}$ , and  $T_{t,s}=48^{\circ}\text{F}$ .

1. The mushroom-like vortices appearing in the center of each of the five chutes. A schematic of how the vortex-sheet formed at the edges of the shield-floor is curling, partly due to the spilling of the shield flow in the chutes, is shown in Figure 3-62. The role played by streamwise vorticity due to the difference in vertical velocity components in the primary and the secondary flows is very evident here. Thus it appears that the primary fluid is drawn into the secondary fluid from the *top* of the chutes; whereas, the secondary fluid goes towards the primary flow-path center-lines from the *bottom* of the chutes close to the wedge surface.

2. The inward curling of the vortex-sheets formed at the two side-edges of the nozzle. The streamwise panning by the PLS showed that this curling starts from the shield-exit plane and progresses along the length of the shield-floor. Note that the wind-tunnel flow is off and the Mach number of the shield flow is supersonic at the exit-plane (the shield nozzle pressure ratio is 2.2). These vortex structures are in some sense similar to the familiar wing-tip vortices. The rolling up of this edge vortex sheet shows the other mechanism of mixing - perhaps the more dominant one - between the ambient air and the shield flow besides the usual mixing which causes shear layer thickening in a jet. These edge vortices appear to interact with the two side jets and even at considerable distance downstream do not seem to interact with the central jets. Hence, the original idea of applying the trends obtained from this 2D nozzle test data of central jets to round nozzles still holds.

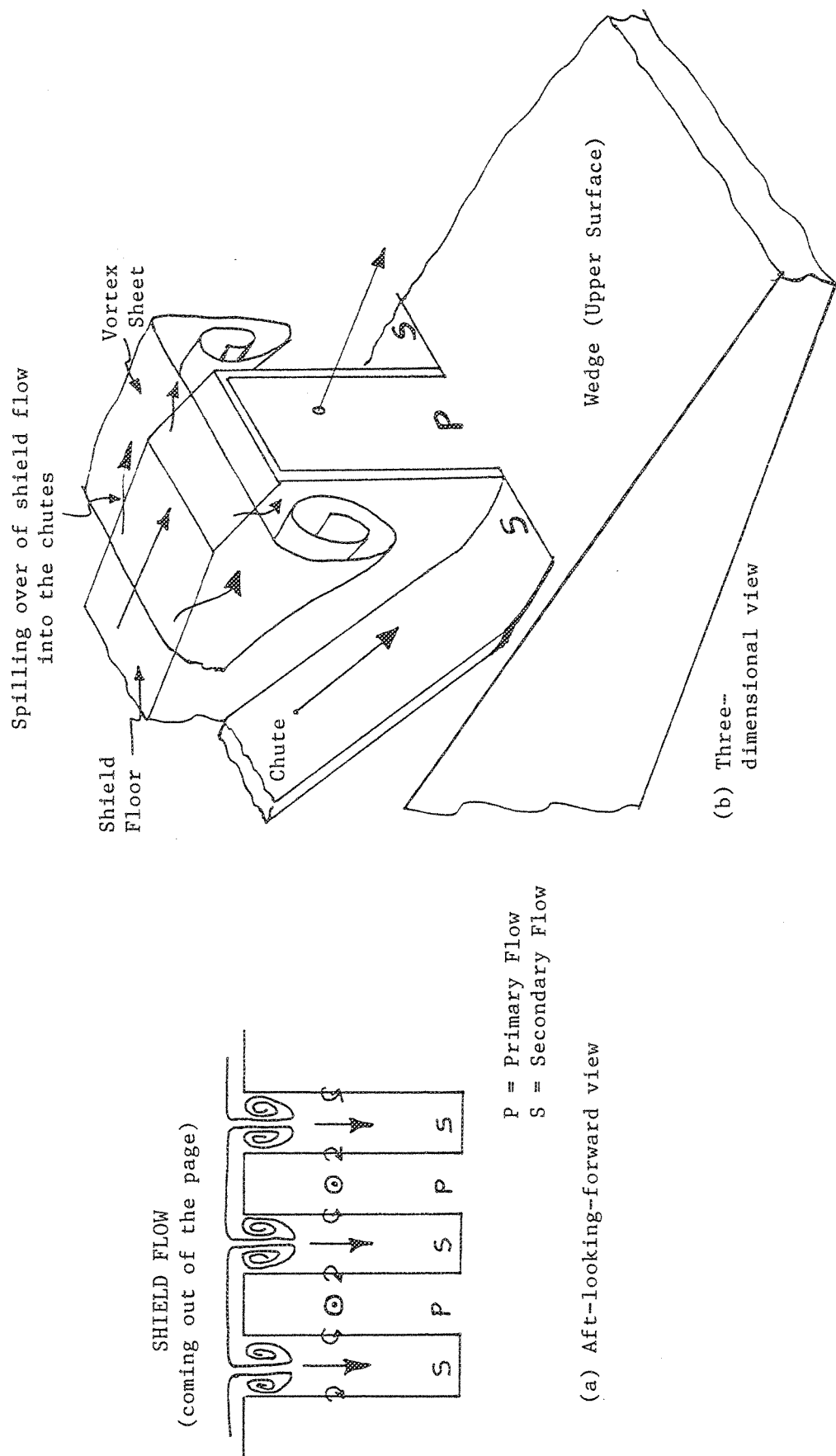


Figure 3-62. Model of vortex-sheet visualization in the laser light sheet (ILS) experiment.

### 3.4 CONCLUSIONS AND RECOMMENDATIONS

#### 3.4.1 Flow-Field Insights

(A) Shield-flow shock-expansion waves are fairly well understood:

expansion waves evolve from the top shield-lip, the chute entrance and the chamfered-edge of the shield-floor lip

reflecting compression waves coalesce into shock-waves, some of which can focus inside the chutes and re-reflect from them

an oblique shock at the shield-floor lip appears to nullify the expansion wave from the chamfered-edge upstream

(B) Gaining better understanding of shock-structures on the wedge:

shock-cells can separate from the wedge-surface rather than hug it

the topology of these shock-surfaces is quite complicated, e.g., a strong Mach-disk-like surface spans the whole width of the nozzle and oblique shocks start from the lips of the primary nozzle although it may be under expanded

(C) Some understanding of the mixing process was attained:

the axial vorticity produced at the vertical chute edges due to the vertical components of the shield-flow and the primary flow provides additional mixing; but it also can uplift the primary flow from the wedge-surface

in a 2d fluid-shield nozzle with wedge on one side there exist strong edge vortices which consume the end-jets very rapidly.

### 3.4.2 Recommendations

1. Since the shield flow itself goes down the suppressor chutes and mixes with the primary flow, rather efficiently due to axial vorticity, not much of it remains further downstream to "shield" the primary flow.
2. The functions of reducing the primary flow speed by mixing with the ambient air and shielding the primary flow by an independent mass of shield-flow needs to be separated by design, not evident in the currently tested configurations. Thus, the shield-flow should not be allowed to go down the chutes; rather, the ambient air should be pulled down independently inside the chutes. This can be implemented by vertically extending the chutes to directly allow only ambient air and extension of the shield-flow exit-plane to the chute-exit plane or further downstream of it.
3. Chute leading edge angle of 55 degrees is too steep and causes strong separation and re-circulation of the secondary flow. Reduction to an angle which allows an unseparated boundary layer inside the chutes for the ambient air (as in (2)) will improve the aerodynamic performance (thrust and pumping) as well as mixing.
4. Although wedge porosity appears to have helped in reducing the strength of the first shock, further reduction in downstream shocks and, hence, shock-associated noise, will be possible if the shock-train "hugs" the wedge surface rather than quickly separate away from it. This can be achieved by (i) reducing the wedge angle or (ii) energizing the turbulent boundary layer at the bottom with axial vorticity or (iii) sucking the boundary layer away from the wedge surface close to the chute exit plane.
5. CD-core flow passages also reduce the shock-strengths and are to be preferred over convergent nozzles from the viewpoint of reducing the shock-associated noise.



## APPENDIX A - LIST OF SYMBOLS

$a$  = Local Speed of Sound ft/sec  
 $A_i$  = Elemental projected area in axial direction for the static pressure  $PS_i$  in sq. inch  
 $A_8$  = Primary stream throat area, sq. inch  
 $A_{98}$  = Fluid shield throat area for takeoff condition, sq. inch  
 $A_J$  = Cross-sectional area of the jet  
 $AMEN$  = Axisymmetric Mixer Ejector Nozzle  
 $a_o$  = Ambient Speed of Sound ft/sec  
 $CBA$  = Chute Base Angle  
 $CER$  = Core Expansion Ratio  
 $C_{fg}$  = Nozzle gross thrust coefficient  
 $D_{eq}$  = Equivalent diameter, in  
 $d_W$  = Slant distance of the wedge from the chute exit plane for 2D models  
 $EPNL$  = Effective Perceived Noise Level based on PNL, dB  
 $EPNLN$  = Normalized Effective Perceived Noise Level based on PNL, dB  
 $EPNLT$  = Effective Tone corrected Perceived Noise Level based on PNLT, dB  
 $EPNLT$  = Effective Tone corrected Perceived Noise Level based on PNLT, dB  
 $EPNLTN$  = Normalized Effective Tone corrected Perceived Noise Level based on PNLT, dB  
 $(FG)_i$  = Ideal gross thrust in lbs  
 $f$  = Frequency, Hz  
 $FLSH$  = Fluid Shield Nozzle  
 $F_{ref}$  = Reference Gross Thrust, 60000 lbs  
 $GEAE$  = General Electric Aircraft Engines  
 $HSCT$  = High Speed Civil Transport  
 $I$  = Noise source intensity  
 $L$  = Plug Length, in  
 $M_c$  = Convection Mach number  
 $M_F$  = Simulated flight Mach number  
 $MGB$  = Noise prediction method by Mani Gliebe and Balsa  
 $M_J$  = Local jet Mach number ( $V_J/a$ )  
 $M_{mix} = V_{mix}/a_o$   
 $MS$  = Noise prediction method by Motsinger and Sieckman  
 $n$  = Jet velocity exponent  
 $NASA$  = National Aeronautics and Space Administration  
 $NF$  = Total normalization factor with respect to thrust and density  
 $\{-10 \log ((FG)_i/F_{ref}) (\rho/\rho_o)^{\omega-1}, dB\}$

$NF_{th}$  = Normalization factor with respect to thrust  $\{-10 \text{ Log } ((FG)_i/F_{ref}), \text{ dB}\}$   
 $NPR$  = Nozzle Pressure Ratio  
 $NRA$  = 2D Mixer-ejector nozzle designed under NASA Research Announcement  
 $OAPWL$  = Overall Sound Power Level, dB  
 $OAPWLN$  = Normalized Overall Sound Power Level, dB  
 $OASPL$  = Overall Sound Pressure Level, dB  
 $OASPLN$  = Normalized Overall Sound Pressure Level, dB  
 $P_{amb}$  = Ambient pressure  
 $PNL$  = Perceived Noise Level, dB  
 $PNLN$  = Normalized Perceived Noise Level, dB  
 $PNLT$  = Tone corrected Perceived Noise Level, dB  
 $PNLTN$  = Normalized Tone corrected Perceived Noise Level, dB  
 $P_{r,p}$  = Primary or core stream nozzle pressure ratio  
 $P_{r,mix}$  = Mixed nozzle pressure ratio  
 $P_{r,s}$  = Secondary or fluid shield stream nozzle pressure ratio  
 $P_R$  = Single stream nozzle pressure ratio (same as  $P_{r,p}$ )  
 $PS_{ch}$  = Static pressure on chute surface  
 $PS_i$  = Static pressure measured by the  $i$ th tap  
 $PS_{pl}$  = Static pressure on plug surface  
 $P_{t,p}$  = Total pressure in primary or core stream  
 $PWL$  = Sound Power Level, dB  
 $PWLN$  = Normalized Sound Power Level, dB  
 $R$  = Radial location of static pressure tap on suppressor chute  
 $R_{Ci}$  = Suppressor inner radius, inch  
 $R_{Co}$  = Suppressor outer radius, inch  
 $RH$  = Relative Humidity, %  
 $SAE$  = Society of Automotive Engineers  
 $SAR$  = Suppressor Area Ratio  
 $SCD$  = Suppressor Chute Depth ratio  
 $SH_{par}$  = Shock Strength Parameter ( $10 \text{ LOG}_{10}[\beta]$ )  
 $SPL$  = Sound Pressure Level, dB  
 $SPLN$  = Normalized Sound Pressure Level, dB  
 $THSH$  = Thermal Shield Nozzle  
 $t_n$  = Shield thickness, in  
 $TOGW$  = Takeoff Gross Weight  
 $T_{t,p}$  = Primary or core stream nozzle total temperature in degree R  
 $T_{t,s}$  = Secondary or fluid shield stream nozzle total temperature in degree R

$T_T$  = Single stream nozzle total temperature in degree R (same as  $T_{t,p}$ )  
 $U_C$  = Convection velocity  
 $V_{j,p}$  = Ideal Nozzle Exhaust Velocity for primary (core) stream ft/sec  
 $V_{j,s}$  = Ideal Nozzle Exhaust Velocity for secondary (flade) stream ft/sec  
 $V_J$  = Ideal Exhaust Velocity for single stream nozzle ft/sec (same as  $V_{j,p}$ ), also jet velocity  
 $V_{mix} = (V_{j,p} \cdot W_p + V_{j,s} \cdot W_s) / (W_p + W_s)$  = Mass averaged mixed velocity  
 $V_{par} = 10 \text{ LOG}_{10}[V_{mix}/a_0]$   
 $V_r = V_{j,s} / V_{j,p}$  = Velocity ratio  
 $W_p$  = Mass Flow Rate for primary stream lbs/sec  
 $W_r = W_s / W_p$  = Mass flow ratio  
 $W_s$  = Mass Flow Rate for secondary stream lbs/sec  
 $X$  = Axial distance for the plug for acoustic models, Also spanwise coordinate for 2D models  
 $Y$  = Vertical coordinate for 2D models at the chute exit plane  
 $y$  = Vertical coordinate for acoustic models  
 $Z$  = Axial distance for the wedge for 2D models, in  
 $\omega$  = Density exponent, 2 for high velocities (Ref. 13)  
 $\theta$  = Angle to Inlet or Polar Angle, degree  
 $\phi$  = Azimuthal angle for traversing microphone array in Cell 41  
 $\psi$  = Azimuthal locations for suppressor instrumentation  
 $\xi$  = Chute Base Angle  
 $\rho$  = Jet density  
 $\gamma$  = Specific heat ratio  
 $\Delta C_{fg}$  = Correction factor to the gross thrust coefficient in % due to the drag or thrust contributions by the relative pressure distributions on plug and chute surfaces  
 $\phi_N$  = Azimuthal angle for fluid shield nozzle  
 $\rho_0$  = Ambient Density of Air  
 $\phi_s$  = Shield wrap angle in degrees.  
 $(\Delta C_{fg})_{ca}$  = average  $\Delta C_{fg}$  for the chutes =  $[\phi_s (\Delta C_{fg})_{cs} + (360 - \phi_s) (\Delta C_{fg})_{cu}] / 360$   
 $(\Delta C_{fg})_{cs}$  =  $\Delta C_{fg}$  for the shielded chutes  
 $(\Delta C_{fg})_{cu}$  =  $\Delta C_{fg}$  for the unshielded chutes  
 $(\Delta C_{fg})_{f-s}$  = Relative  $\Delta C_{fg}$  due to flight simulation =  $[(\Delta C_{fg})^t]_{flight} - [(\Delta C_{fg})^t]_{static}$   
 $(\Delta C_{fg})_{pa}$  = Average  $\Delta C_{fg}$  for the plug  
 $(\Delta C_{fg})_{pc}$  =  $\Delta C_{fg}$  for the plug evaluated by cold flow row data  
 $(\Delta C_{fg})_{ph}$  =  $\Delta C_{fg}$  for the plug evaluated by hot flow row data  
 $(\Delta C_{fg})_t$  = Total  $\Delta C_{fg}$  for the plug and chutes =  $(\Delta C_{fg})_{pa} + (\Delta C_{fg})_{ca}$   
 $B = [M_{mix}^2 - 1]^{1/2}$



## APPENDIX B - TABULATED ACOUSTIC DATA

This appendix contains some acoustic test results in tabular form for conical nozzle, suppressor alone configurations, and the three fluid shield configurations with different thicknesses of same wrap angle of  $220^\circ$ . For each case the actual aerothermodynamic conditions and some acoustic data are presented. The acoustic data includes EPNLT and PNLT at polar angles of 50, 60, 80, 90, 130, and 150 degrees and the maximum (represented by "max") levels. Both normalized (i.e., EPNLTN and PNLTN) and unnormalized values are listed in these tables. All the acoustic data corrected to the standard day conditions of  $59^\circ$  F and 70% relative humidity, extrapolated to 1629' distance and scaled to  $A_8 = 1175$  sq" (i.e., core stream full scale area) for conical nozzle and suppressor alone configurations and to  $A_T$  (i.e., total throat area,  $A_8 + A_{98}$ ), as specified in the data tables, for fluid shield nozzle configurations. Turbulence correction is not applied to the flight simulated data. Following are the definition of the variables used in the data tables:

$P_{r,p}$  = Primary or core stream nozzle pressure ratio

$T_{t,p}$  = Primary or core stream nozzle total temperature in degree R

$W_p$  = Mass Flow Rate for primary stream lbs/sec

$V_{j,p}$  = Ideal nozzle exhaust velocity for primary (core) stream ft/sec

$P_{r,s}$  = Secondary or fluid shield stream nozzle pressure ratio

$T_{t,s}$  = Secondary or fluid shield stream nozzle total temperature in degree R

$W_s$  = Mass flow rate for secondary stream lbs/sec

$V_{j,s}$  = Ideal nozzle exhaust velocity for secondary (flade) stream ft/sec

$V_{mix}$  = Mass average or mixed ideal nozzle exhaust velocity ft/sec

$$= (V_{j,p} \cdot W_p + V_{j,s} \cdot W_s) / (W_p + W_s)$$

$V_r$  = Velocity ratio =  $V_{j,s} / V_{j,p}$

$W_r$  = Mass flow ratio =  $W_s / W_p$

$T_{sr}$  = Static temperature ratio

$V_{par}$  = Velocity parameter =  $10 \text{ LOG}_{10}[V_{mix}/a_o]$

where,  $a_o$  = Ambient Speed of Sound ft/sec

$(FG)_i$  = Ideal gross thrust, klb .

$SH_{par}$  = Shock strength parameter =  $10 \text{ LOG}_{10}[\beta]$

where,  $\beta = [M_{mix}^2 - 1]^{1/2}$  and  $M_{mix} = V_{mix}/a_o$



# CONICAL NOZZLE DATA AT A SIDELINE DISTANCE OF 1629', A8=1175 SQ"

TEST NO	V <sub>j,p</sub> ft/sec	V <sub>par</sub> ft/sec	(FQ) <sub>i</sub> klb	EPNLT	EPNLTN	PNLT	PNLTN	SH <sub>par</sub>	P <sub>r,p</sub>	T <sub>t,p</sub> deg R	W <sub>p</sub> lb/sec										
				50	60	80	90	130	150	max											
STATIC CASE																					
17	873.7	-1.019	16.9	82.2	88.7	75.0	78.3	81.7	81.6	82.4	76.3	83.4	81.4	84.8	88.1	88.0	88.8	82.8	89.8	519.	623.295
18	1214.5	0.411	17.2	92.8	100.6	80.7	84.2	88.4	89.1	92.9	89.9	93.0	88.5	92.0	96.2	96.9	100.7	97.7	100.8	988.	454.402
19	1237.0	0.491	17.4	92.7	100.5	81.2	84.4	88.7	89.3	93.1	89.5	93.1	89.0	92.2	96.5	97.1	100.9	97.3	100.9	1012.	452.516
21	1227.8	0.458	17.4	91.7	99.4	80.3	83.2	87.3	87.8	92.3	88.4	92.3	88.0	90.9	95.0	95.5	100.0	96.1	100.0	997.	455.970
22	1649.2	1.740	30.5	106.6	112.1	96.4	98.8	100.3	100.1	105.4	106.1	106.1	101.9	104.3	105.8	105.6	110.9	111.6	111.6	1131.	594.653
23	1710.7	1.899	30.5	107.4	113.2	96.0	98.3	100.9	101.1	107.0	106.7	107.8	101.8	104.1	106.7	107.4	107.7	115.3	114.0	116.5	572.826
24	1809.0	2.141	31.1	108.7	114.9	96.1	98.6	101.3	101.6	109.2	107.9	110.4	102.2	104.7	107.4	107.7	115.3	114.0	116.5	1337.	552.838
25	1797.5	2.088	36.6	111.3	115.9	105.1	107.1	107.2	106.1	110.7	109.5	111.4	109.8	111.8	111.9	110.8	115.4	114.2	116.1	1182.	655.943
3	1804.5	2.126	36.3	112.9	117.7	104.0	106.3	108.1	107.6	111.8	112.1	114.8	108.7	111.0	112.8	112.3	116.5	116.8	119.5	1182.	647.817
4	1804.5	2.126	36.3	113.3	118.0	104.9	106.7	108.9	107.4	112.0	112.1	115.4	109.6	111.4	113.6	112.1	116.7	116.8	120.1	1182.	647.817
27	1930.8	2.420	38.5	113.4	118.3	105.1	107.4	108.7	108.4	114.1	110.8	115.4	110.0	112.3	113.6	113.3	119.0	115.7	120.3	1302.	641.030
28	2018.9	2.614	40.4	113.8	118.7	105.8	108.1	109.6	109.4	116.2	110.3	116.2	110.7	113.0	114.5	114.3	121.1	115.2	121.1	1379.	643.874
29	2204.7	2.996	34.4	113.1	120.0	99.7	102.0	105.2	106.5	117.4	108.5	117.4	106.6	108.9	112.1	113.4	124.3	115.4	124.3	1809.	502.350
30	2446.2	3.448	49.5	116.6	121.6	108.0	110.7	113.0	113.4	120.7	109.9	120.7	113.0	115.7	118.0	118.4	125.7	114.9	125.7	1787.	650.919
31	2595.5	3.705	51.7	117.0	122.2	108.2	110.7	113.1	113.8	120.7	109.0	120.7	113.4	115.9	118.3	119.0	125.9	114.2	125.9	1960.	640.368
32	2797.6	4.031	70.0	119.3	122.9	110.0	112.6	116.1	116.6	122.3	111.9	122.3	113.6	116.2	119.7	120.2	125.9	115.5	125.9	1960.	804.977

## WITH FLIGHT SIMULATION (M<sub>F</sub>=0.32)

5	1216.5	0.401	16.5	83.3	91.2	78.2	79.8	82.4	81.7	84.0	75.0	84.7	86.2	87.8	90.4	89.7	92.0	83.0	92.7	1.580	1004.	436.713
6	1657.6	1.745	30.4	100.2	105.6	97.6	98.9	98.3	96.8	100.0	95.1	100.3	103.0	104.3	103.7	102.2	105.4	100.5	105.7	-2.77	2.210	1125.
7	1716.1	1.895	30.4	100.9	106.7	96.6	98.3	97.3	96.8	101.1	96.5	101.1	102.3	104.0	103.0	102.5	106.8	102.2	106.8	-2.75	2.210	1205.
8	1814.0	2.136	30.8	102.8	108.9	98.7	99.1	98.3	98.0	103.2	99.6	103.2	104.8	105.2	104.4	104.1	109.3	105.7	109.3	-2.59	2.230	1331.
9	1805.3	2.115	36.7	108.4	113.0	108.9	109.2	107.8	104.7	106.1	100.7	109.2	113.5	113.8	112.4	109.3	110.7	105.3	113.8	-1.48	2.500	1174.
11	1921.3	2.429	38.2	109.4	114.4	108.8	109.8	108.2	105.5	108.5	102.3	109.8	113.8	114.8	113.2	110.5	113.5	107.3	114.8	-1.34	2.540	1308.
12	2018.9	2.644	41.1	110.9	115.8	109.6	110.2	109.8	107.3	110.5	103.6	110.5	114.5	115.1	114.7	112.2	115.4	108.5	115.4	-0.98	2.670	1379.
13	2177.4	2.972	33.5	106.3	113.4	99.9	102.2	102.8	102.6	106.5	102.4	108.4	107.1	109.4	110.0	109.8	113.7	109.6	115.6	-1.99	2.330	1819.
14	2436.2	3.460	49.4	114.4	119.5	111.1	112.3	112.9	110.9	116.7	104.7	116.7	116.2	117.4	118.0	116.0	121.8	109.8	121.8	-0.21	3.050	1790.
15	2568.8	3.690	51.0	115.3	120.6	111.6	112.8	113.0	111.7	117.9	104.9	118.2	116.9	118.1	118.3	117.0	123.2	110.2	123.5	-0.09	3.120	1952.
16	2778.1	4.026	69.8	118.5	122.1	115.9	116.7	116.5	115.6	120.7	107.0	121.1	119.5	120.3	120.1	119.2	124.3	110.6	124.7	0.81	3.980	1942.

# DATA FOR THE SUPPRESSOR ALONE WITH HARD PLUG AT A SIDELINE DISTANCE OF 1629', A8=1175 SQ"

TEST NO	V <sub>i,p</sub> ft/sec	V <sub>par</sub> (FG) <sub>i</sub> kib	EPNLT	EPNLTN	PNLT	PNLTN	50	60	80	90	130	150	max	SH <sub>par</sub>	P <sub>r,p</sub>	T <sub>i,p</sub> deg R	W <sub>p</sub> lb/sec					
STATIC CASE																						
34	711.0	-1.927	10.6	81.9	90.2	74.1	77.7	83.0	83.1	81.6	72.6	84.0	82.3	85.9	91.2	91.3	89.8	80.8	92.2	1.350	512.	481.164
35	888.3	-0.891	17.6	88.8	95.1	80.2	84.2	89.5	89.9	88.7	80.3	90.5	86.5	90.5	95.8	96.2	95.0	86.6	96.8	1.620	510.	635.763
67	1317.8	0.690	50.2	103.1	102.4	98.1	100.9	105.8	105.8	100.4	93.4	105.8	97.5	100.3	105.2	105.2	99.8	92.8	105.2	3.090	525.	1225.700
68	1437.0	1.091	70.6	105.5	103.2	100.3	102.9	107.6	107.7	103.2	96.7	107.7	97.9	100.5	105.2	105.3	100.8	94.3	105.3	4.000	526.	1580.795
36	1241.5	0.563	17.2	95.1	103.0	84.5	88.4	93.8	94.4	95.5	88.2	97.5	92.4	96.3	101.7	102.3	103.4	96.1	105.4	1.610	1007.	446.717
40	1649.9	1.798	29.8	102.8	108.5	93.5	97.7	102.7	102.1	102.2	98.1	104.3	99.2	103.4	108.4	107.8	107.9	103.8	110.0	2.180	1132.	580.673
41	1755.3	2.067	32.0	103.2	108.8	93.5	97.4	102.2	102.8	103.3	97.2	104.9	99.2	103.1	107.8	108.5	109.0	102.8	110.6	2.280	1218.	586.411
42	1805.3	2.180	30.6	103.9	110.2	94.5	97.8	103.1	103.6	103.7	98.3	105.5	100.7	104.0	109.3	109.8	109.9	104.5	111.7	2.220	1325.	545.077
43	1804.9	2.188	36.5	109.6	114.4	100.0	102.4	107.2	107.3	109.2	106.5	109.9	104.8	107.2	112.0	112.1	114.0	111.3	114.7	2.490	1178.	649.763
44	1897.8	2.410	38.2	109.4	114.3	99.8	102.2	106.9	107.4	106.2	107.5	111.6	104.7	107.1	111.8	112.3	111.1	112.4	116.5	2.570	1263.	646.901
45	2025.6	2.689	40.8	107.7	112.6	98.5	101.8	107.1	106.2	105.9	103.5	110.1	103.4	106.7	112.0	111.1	110.8	108.4	115.0	2.690	1379.	648.697
46	2254.1	3.153	45.8	107.4	112.4	99.7	101.5	106.7	106.6	107.2	101.5	108.9	104.7	106.5	111.7	111.6	112.2	106.5	113.9	2.920	1590.	653.785
61	2557.5	3.611	49.0	108.9	114.3	101.2	103.3	107.6	108.0	108.6	103.9	110.3	106.6	108.7	113.0	113.4	114.0	109.3	115.7	3.090	1949.	616.084
60	2435.7	3.446	49.0	108.6	113.6	101.3	103.5	107.7	108.0	108.0	103.5	110.1	106.3	108.5	112.7	113.0	113.0	108.5	115.1	3.090	1772.	647.450
59	2194.5	2.946	33.9	106.7	113.6	98.8	100.1	105.9	106.3	106.4	100.4	108.5	105.7	107.0	112.8	113.2	113.3	107.3	115.4	2.390	1800.	496.698
58	2789.6	3.988	69.1	112.6	116.2	104.1	106.7	111.2	111.5	111.8	109.1	112.7	107.7	110.3	114.8	115.1	115.4	112.7	116.3	4.000	1952.	796.881

## WITH FLIGHT SIMULATION (M<sub>F</sub>=0.32)

47	905.2	-0.818	18.0	86.6	92.7	84.2	86.3	88.6	87.8	85.8	74.3	88.6	90.3	92.4	94.7	93.9	91.9	80.4	94.7	1.639	518.	640.021
48	1313.4	0.777	50.6	102.9	102.4	102.3	104.3	106.8	104.6	98.7	88.4	106.8	101.8	103.8	106.3	104.1	98.2	87.9	106.3	3.122	517.	1238.769
72	1430.4	1.104	71.2	104.1	101.7	102.1	103.9	106.2	105.7	101.2	89.7	106.9	99.7	101.5	103.8	103.3	98.8	87.3	104.5	4.030	518.	1602.419
50	1241.6	0.541	17.3	90.9	98.7	88.1	90.5	92.4	91.5	89.4	77.1	94.3	95.9	98.3	100.2	99.3	97.2	84.9	102.1	1.615	1001.	448.271
62	1660.4	1.804	30.6	98.3	103.8	94.3	95.7	99.1	98.2	97.9	87.6	101.2	99.8	101.2	104.6	103.7	103.4	93.1	106.7	2.205	1132.	593.123
51	1724.4	1.968	30.5	99.7	105.5	95.8	97.0	99.6	99.6	99.6	90.3	102.1	101.6	102.8	105.4	105.4	105.4	96.1	107.9	2.220	1210.	569.260
52	1819.5	2.166	37.2	101.8	106.3	97.3	99.2	101.4	100.8	101.9	91.9	104.1	103.4	103.5	107.7	106.6	106.4	98.0	110.2	2.246	1329.	546.860
63	1813.4	2.101	37.2	101.8	106.3	98.6	99.0	103.2	102.1	101.9	91.4	104.1	103.1	103.5	107.7	106.6	106.4	95.9	108.6	2.510	1180.	660.771
64	1899.4	2.296	38.7	102.9	107.5	98.6	99.6	103.4	102.7	103.1	92.4	105.7	103.2	104.2	108.0	107.3	107.7	97.0	110.3	2.580	1261.	656.351
53	2031.7	2.620	40.8	104.8	109.6	101.8	102.0	105.8	104.7	105.3	96.1	106.1	106.6	106.8	110.6	109.5	110.1	100.9	110.9	2.708	1379.	646.634
54	2262.5	3.087	45.5	106.7	111.6	103.6	103.8	107.4	106.4	106.8	98.4	108.3	108.5	108.7	112.3	111.3	111.7	103.3	113.2	3.225	1599.	646.563
55	2477.7	3.478	51.7	108.7	113.4	106.3	106.9	109.4	108.1	109.1	99.5	110.2	111.0	111.6	114.1	112.8	113.8	104.2	114.9	0.03	1781.	871.961
66	2208.1	2.934	34.8	104.1	110.9	97.8	99.9	103.2	103.3	105.1	95.6	106.7	104.5	106.6	109.9	110.0	111.8	102.3	113.4	2.407	1809.	507.275
56	2561.8	3.614	49.4	108.4	113.8	105.4	105.7	109.0	107.7	109.1	99.7	109.7	110.7	111.0	114.3	113.0	114.4	105.0	115.0	3.110	1946.	620.536
57	2794.0	3.987	69.8	111.1	114.7	107.9	110.3	112.7	110.8	111.7	102.2	112.7	111.4	113.8	116.2	114.3	115.2	105.7	116.2	4.030	1950.	803.351



## DATA FOR THE SUPPRESSOR ALONE WITH POROUS PLUG AT A SIDELINE DISTANCE OF 1629', A8=1175 SQ"

TEST NO	V <sub>i,p</sub> ft/sec	V <sub>par</sub> kib	(FG) <sub>i</sub> kib	EPNLT	EPNLTN	50	60	80	90	PMLT	130	150	max	SH <sub>par</sub>	P <sub>r,p</sub>	T <sub>t,p</sub> deg R	W <sub>p</sub> lb/sec
STATIC CASE																	
490	1245.9	0.463	17.5	93.9	101.5	84.2	87.3	92.6	93.4	94.9	94.9	100.2	101.0	102.5	94.5	103.8	452.909
491	1658.2	1.713	30.5	102.6	107.9	93.2	98.4	102.5	101.5	102.0	98.3	104.0	98.5	103.8	107.8	106.8	592.235
492	939.9	-0.761	17.7	87.8	93.6	80.1	83.0	87.9	88.4	87.9	79.9	89.6	85.8	93.6	94.1	93.6	607.451
493	1339.0	0.772	51.3	102.0	101.3	96.7	99.2	105.2	104.6	99.4	93.1	105.2	96.1	98.6	104.6	98.8	1233.637
494	1453.7	1.120	71.6	104.8	102.4	98.8	100.8	106.5	106.9	102.3	96.9	107.3	96.4	98.4	104.1	104.5	1583.668
503	2797.9	3.935	70.9	112.4	115.7	103.8	106.5	110.6	110.7	111.5	108.7	112.2	107.1	109.8	113.9	114.0	815.845
504	2571.5	3.589	50.4	108.5	113.6	100.2	102.8	107.3	107.7	108.4	103.0	110.1	105.4	108.0	112.5	112.9	630.595
505	2481.5	3.434	52.6	108.4	112.9	100.5	103.9	107.7	107.8	108.2	102.0	109.5	105.0	108.4	112.2	112.3	682.190
506	2208.0	2.923	34.7	105.8	112.6	97.9	98.4	103.7	105.1	105.3	100.2	107.5	104.6	105.1	110.4	111.8	506.257
507	2261.4	3.035	46.0	106.9	111.6	99.1	101.5	105.8	105.9	106.5	101.5	107.9	103.8	106.2	110.5	110.6	654.357
508	2039.2	2.582	41.9	107.4	111.9	98.1	101.8	105.3	105.7	106.1	103.4	111.7	102.6	106.3	109.8	110.2	661.563
509	1902.8	2.277	38.8	109.4	113.9	100.0	101.8	106.7	106.9	106.4	107.7	113.4	104.5	106.3	111.2	111.4	655.971
510	1812.0	2.061	37.1	109.4	113.9	98.8	102.0	106.9	108.0	106.5	107.4	110.4	103.3	106.5	111.4	112.5	657.903
511	1821.9	2.088	31.6	104.1	109.9	95.8	98.8	103.8	102.8	103.4	98.7	105.2	101.6	104.6	109.6	109.2	558.010
512	1722.2	1.852	30.7	102.7	108.2	93.6	96.6	101.4	101.6	102.4	97.4	104.1	99.2	102.2	107.0	107.2	573.509
WITH FLIGHT SIMULATION (M <sub>F</sub> =0.32)																	
495	1455.1	1.108	71.3	103.7	101.3	101.7	105.2	106.0	105.6	100.3	89.0	106.0	99.3	102.8	103.6	103.2	1576.014
496	1342.3	0.749	51.2	101.4	100.7	99.0	103.9	104.9	103.0	97.3	85.7	104.9	98.3	103.2	104.2	102.3	1228.171
497	907.1	-0.957	17.5	85.1	91.6	82.7	85.8	87.0	86.1	83.9	72.8	91.3	89.2	92.3	93.5	92.6	537.
498	1727.7	1.833	30.9	99.6	105.1	95.0	98.0	99.8	98.8	99.3	91.1	101.9	100.5	103.5	105.3	104.3	619.132
499	2272.9	3.020	46.1	105.9	110.6	102.8	104.3	106.1	105.3	106.5	96.4	107.6	107.5	109.0	110.8	110.0	574.875
500	2478.8	3.389	52.4	107.8	112.3	104.6	107.9	107.8	106.9	108.1	98.4	109.4	109.1	112.4	112.3	111.4	651.864
501	2560.4	3.521	50.4	107.5	112.5	103.6	104.4	107.6	107.1	108.5	97.6	109.6	108.6	109.4	112.6	112.1	680.540
502	2796.2	3.904	70.7	110.3	113.5	107.9	108.8	111.6	109.3	110.4	100.8	111.6	111.2	112.1	114.9	112.6	633.534
513	1655.1	1.643	30.4	97.8	103.0	92.2	94.2	98.6	97.5	97.9	87.7	101.6	97.4	99.4	103.8	102.7	813.203
514	1250.1	0.424	17.4	89.3	96.9	85.6	90.3	90.3	89.9	88.6	75.6	90.9	93.2	97.9	97.9	97.5	590.877
515	1821.5	2.051	31.4	100.8	106.6	96.7	99.8	101.2	100.0	101.0	91.5	102.9	102.5	105.6	107.0	105.8	448.879
516	1807.8	2.022	37.0	103.9	108.3	102.8	105.8	103.2	103.3	102.7	92.7	105.8	107.2	110.2	107.6	107.7	555.409
517	1905.1	2.258	39.0	102.3	106.8	99.4	101.3	102.7	102.1	102.7	92.8	104.1	103.9	105.8	107.2	106.6	659.084
518	2032.8	2.540	41.5	103.6	108.1	99.4	102.7	104.5	103.2	104.2	94.6	105.7	103.9	107.2	109.0	107.7	658.524
519	2213.1	2.900	34.8	103.4	110.1	98.0	101.4	102.3	102.6	104.7	94.2	106.0	104.7	108.1	109.0	109.3	656.720
																	505.664

DATA FOR 0.5"-THICK, 220° FLUID SHIELD NOZZLE WITH HARD PLUG AT A SIDELINE DISTANCE OF 1629'  
A8=1175 SQ", A98=638.6 SQ", AT=1813 SQ", AT COMMUNITY POINT AT STATIC CONDITION

TEST NO	P <sub>r,p</sub>	T <sub>t,p</sub> deg R	W <sub>p</sub> lb/sec	V <sub>j,p</sub> ft/sec	P <sub>r,s</sub>	T <sub>t,s</sub> deg R	W <sub>s</sub> lb/sec	V <sub>j,s</sub> ft/sec	V <sub>mix</sub> ft/sec	V <sub>r</sub>	W <sub>r</sub>	T <sub>sr</sub>
74	1.60	515.	625.32	882.	1.29	519.	237.89	662.	821.	0.75	0.38	1.07
75	3.15	513.	1259.47	1313.	1.60	517.	339.40	883.	1222.	0.67	0.27	1.22
81	1.60	1001.	447.75	1230.	1.30	692.	209.48	775.	1085.	0.63	0.47	0.73
82	2.17	1821.	454.51	2095.	2.14	733.	389.09	1312.	1734.	0.63	0.86	0.40
88	2.40	1804.	505.17	2202.	2.18	727.	397.95	1321.	1813.	0.60	0.79	0.41
89	3.18	1790.	672.07	2475.	2.14	715.	393.93	1296.	2039.	0.52	0.59	0.44
116	3.31	1902.	674.94	2590.	2.15	775.	378.48	1353.	2145.	0.52	0.56	0.45
96	3.04	1787.	643.05	2431.	1.29	808.	190.57	826.	2064.	0.34	0.30	0.56
95	3.16	1784.	669.02	2465.	1.60	743.	282.86	1059.	2047.	0.43	0.42	0.49
119	3.19	1782.	672.97	2472.	1.90	770.	335.56	1245.	2064.	0.50	0.50	0.49
115	3.19	1797.	670.03	2482.	2.42	719.	442.39	1389.	2047.	0.56	0.66	0.42
99	2.43	1801.	509.81	2214.	1.30	778.	196.67	822.	1826.	0.37	0.39	0.51
100	2.46	1810.	514.76	2233.	1.60	773.	276.13	1081.	1830.	0.48	0.54	0.47
103	2.43	1800.	509.95	2213.	1.90	728.	345.16	1211.	1808.	0.55	0.68	0.42
104	2.35	1800.	493.17	2176.	2.40	730.	435.40	1393.	1809.	0.64	0.88	0.39
123	3.21	1974.	642.00	2611.	2.13	770.	376.18	1341.	2142.	0.51	0.59	0.43
124	3.19	1492.	738.35	2257.	2.10	740.	378.37	1303.	1934.	0.58	0.51	0.55
127	3.20	1785.	674.48	2477.	2.13	630.	416.06	1213.	1994.	0.49	0.62	0.39
120	3.20	1777.	676.07	2471.	2.13	906.	346.49	1455.	2127.	0.59	0.51	0.56

TEST NO	V <sub>mix</sub> ft/sec	V <sub>par</sub>	(FG) <sub>i</sub> klb	EPNLT	EPNLTN	50	60	80	90	PNLT	130	150	max	SH <sub>par</sub>						
74	821.2	-1.322	22.0	90.6	96.0	83.6	85.7	90.2	91.1	89.1	78.8	91.5	88.9	91.0	95.5	96.4	94.4	84.2	96.8	-9.00
75	1221.8	0.407	60.7	102.5	101.3	95.3	98.0	103.3	103.4	99.0	93.8	103.4	94.0	96.7	102.0	102.1	97.7	92.5	102.1	-1.13
81	1084.9	-0.113	22.2	92.7	95.4	85.4	87.5	92.4	93.3	64.4	84.0	95.4	88.1	90.2	95.1	96.0	67.1	86.7	98.1	-9.00
82	1733.6	1.893	45.5	103.4	107.8	94.1	97.3	103.2	103.8	103.5	97.2	105.5	98.5	101.7	107.6	108.2	107.9	101.6	109.9	-3.74
88	1813.4	2.072	50.9	105.1	108.9	96.7	98.6	104.2	104.7	104.7	98.9	107.0	100.5	102.4	108.0	108.5	108.5	102.7	110.8	-2.59
89	2038.9	2.581	67.6	111.2	113.7	100.6	103.1	107.9	108.5	108.6	105.5	110.0	103.1	105.6	110.4	111.0	111.1	108.0	112.5	-0.91
116	2145.4	2.774	70.2	111.1	113.7	100.7	103.0	107.7	107.9	108.7	106.2	110.9	103.3	105.6	110.3	110.5	111.3	108.8	113.5	-0.70
96	2064.0	2.643	53.5	110.4	114.6	100.4	102.9	107.4	107.8	109.2	103.5	109.6	104.6	107.1	111.6	112.0	113.4	107.7	113.8	-1.61
95	2047.0	2.598	60.6	110.9	114.3	101.1	103.6	108.1	108.5	109.1	104.5	110.2	104.4	106.9	111.4	111.8	112.4	107.8	113.5	-1.27
119	2063.6	2.613	64.7	109.9	112.8	99.9	102.4	107.0	107.5	108.5	103.6	109.9	102.8	105.3	109.9	110.4	111.4	106.3	112.9	-1.00
115	2047.4	2.558	70.8	110.4	112.6	99.7	102.4	107.0	107.5	108.3	105.6	109.9	101.8	104.5	109.1	109.6	110.4	107.7	112.0	-0.73
99	1826.1	2.144	40.1	105.9	111.5	96.2	98.4	104.0	105.3	106.0	100.5	107.8	101.8	104.0	109.6	110.9	111.6	106.1	113.4	-4.38
100	1830.4	2.163	45.0	106.2	111.0	96.9	98.9	104.1	105.4	107.3	99.3	107.8	101.8	103.8	109.0	110.3	112.2	104.2	112.7	-3.46
103	1808.4	2.093	48.1	105.6	109.9	95.8	98.0	103.6	105.2	106.1	99.6	107.3	100.1	102.3	107.9	109.5	110.4	103.9	111.6	-3.00
104	1808.8	2.124	52.2	106.2	109.9	96.3	99.2	104.3	105.4	105.0	99.3	106.5	100.0	102.9	108.0	109.1	108.7	103.0	110.2	-2.38
123	2141.7	2.774	67.8	110.4	113.3	99.5	102.3	106.9	107.1	108.8	105.7	110.3	102.4	105.2	109.8	110.0	111.7	108.6	113.2	-0.87
124	1933.8	2.319	67.1	109.1	111.0	98.7	101.6	105.7	106.2	106.8	102.1	108.3	100.6	103.5	107.6	108.1	108.7	104.0	110.2	-0.83
127	1994.5	2.445	67.6	109.6	111.9	99.2	101.6	106.4	106.9	107.8	103.6	109.8	101.5	103.9	108.7	109.2	110.1	105.9	112.1	-0.98
120	2126.7	2.732	67.6	110.1	112.8	99.1	102.5	106.6	107.3	108.1	105.0	109.8	101.8	105.2	109.3	110.0	110.8	107.7	112.5	-0.75

DATA FOR 0.5"-THICK, 220° FLUID SHIELD NOZZLE WITH HARD PLUG AT A SIDELINE DISTANCE OF 1629'  
A8=1175 SQ", A98=638.6 SQ", A<sub>T</sub>=1813 SQ", AT COMMUNITY POINT WITH FLIGHT SIMULATION (M<sub>F</sub>=0.32)

TEST NO	P <sub>r,p</sub>	T <sub>t,p</sub> deg R	W <sub>p</sub> lb/sec	V <sub>j,p</sub> ft/sec	P <sub>r,s</sub>	T <sub>t,s</sub> deg R	W <sub>s</sub> lb/sec	V <sub>j,s</sub> ft/sec	V <sub>mix</sub> ft/sec	V <sub>r</sub>	W <sub>r</sub>	T <sub>sr</sub>
107	2.44	1807.	511.02	2222.	1.93	724.	351.40	1220.	1814.	0.55	0.69	0.42
108	2.47	1812.	516.97	2239.	1.61	723.	286.72	1048.	1814.	0.47	0.55	0.44
111	2.45	1810.	512.46	2228.	1.93	788.	336.39	1272.	1849.	0.57	0.66	0.46
112	2.38	1790.	501.55	2185.	2.42	729.	439.87	1399.	1818.	0.64	0.88	0.40
130	1.60	536.	612.87	899.	1.30	536.	239.79	687.	839.	0.76	0.39	1.06
132	1.62	1001.	458.89	1242.	1.31	691.	214.75	782.	1095.	0.63	0.47	0.73
137	3.19	526.	1260.40	1336.	1.59	524.	334.29	884.	1241.	0.66	0.27	1.22
138	2.19	1821.	457.77	2104.	2.18	723.	398.42	1316.	1738.	0.63	0.87	0.39
144	2.39	1780.	506.88	2183.	2.19	721.	400.99	1318.	1801.	0.60	0.79	0.41
145	3.20	1786.	676.62	2477.	2.16	693.	403.62	1283.	2031.	0.52	0.60	0.42
151	3.20	1501.	738.34	2266.	2.13	726.	387.85	1303.	1934.	0.57	0.53	0.54
152	3.21	1808.	673.13	2497.	2.40	725.	436.90	1389.	2061.	0.56	0.65	0.43
155	3.22	1800.	676.16	2494.	2.13	898.	348.22	1449.	2138.	0.58	0.51	0.55
156	3.22	1817.	671.60	2504.	1.90	778.	333.64	1251.	2088.	0.50	0.50	0.49
159	3.19	1784.	672.57	2473.	1.61	810.	272.28	1114.	2082.	0.45	0.40	0.54
161	3.21	1777.	679.03	2475.	2.12	616.	418.40	1195.	1987.	0.48	0.62	0.38
162	3.06	1779.	646.95	2433.	1.30	857.	187.93	865.	2080.	0.36	0.29	0.60
165	3.34	1900.	681.23	2596.	2.16	808.	371.98	1384.	2168.	0.53	0.55	0.47
166	3.22	1935.	650.12	2586.	2.15	773.	379.85	1353.	2131.	0.52	0.58	0.44

TEST NO	V <sub>mix</sub> ft/sec	V <sub>par</sub>	(FG) <sub>i</sub> klb	EPNLT	EPNLTN	PNLT	PNLTN	SH <sub>par</sub>		
				50	60	80	90	130	150	max
107	1813.7	2.069	48.6	103.0	107.1	98.3	100.2	102.2	102.7	101.9
108	1814.3	2.054	45.3	103.1	107.7	98.0	99.7	102.5	102.4	103.6
111	1849.1	2.100	48.8	102.9	107.0	97.9	98.8	102.2	102.0	103.3
112	1817.8	2.022	53.2	-12.6	-9.3	0.0	0.0	0.0	0.0	0.0
130	839.5	-1.273	22.2	86.5	91.7	85.9	86.7	89.7	86.4	78.1
132	1095.1	-0.051	22.9	91.0	94.2	88.2	89.5	93.3	92.6	88.4
137	1241.1	0.417	61.5	98.8	97.5	98.0	98.7	101.7	100.2	94.8
138	1737.5	1.834	46.2	101.1	105.2	98.5	100.1	101.7	101.7	98.0
144	1801.3	1.954	50.8	101.7	105.3	98.9	100.4	102.6	101.4	100.1
145	2030.9	2.491	68.2	105.7	108.0	102.3	103.5	106.0	105.1	105.7
151	1934.5	2.272	67.7	105.4	107.2	103.0	104.2	105.6	105.1	104.6
152	2060.9	2.547	71.1	106.5	108.5	103.3	106.1	106.1	105.4	106.3
155	2138.4	2.719	68.1	106.6	109.2	103.2	104.3	106.8	105.6	106.5
156	2088.1	2.604	65.2	106.7	109.4	103.3	106.0	106.1	105.6	106.5
159	2081.6	2.594	61.1	106.7	109.9	103.5	104.6	106.7	106.0	107.2
161	1987.0	2.469	67.8	107.2	109.5	104.8	106.1	108.0	106.9	106.6
162	2079.9	2.623	54.0	106.8	110.9	104.1	105.5	107.3	106.7	106.6
165	2168.3	2.787	71.0	107.2	109.7	103.7	105.2	107.1	106.2	107.3
166	2131.4	2.713	68.2	106.8	109.5	103.1	104.4	107.1	105.9	107.1

DATA FOR 0.5"-THICK, 220° FLUID SHIELD NOZZLE WITH HARD PLUG AT A SIDELINE DISTANCE OF 1629'  
A8=1175 SQ", A98=638.6 SQ", AT=1813 SQ", AT SIDELINE POINT AT STATIC CONDITION

TEST NO	P <sub>r,p</sub>	T <sub>t,p</sub> deg R	W <sub>p</sub> lb/sec	V <sub>j,p</sub> ft/sec	P <sub>r,s</sub>	T <sub>t,s</sub> deg R	W <sub>s</sub> lb/sec	V <sub>j,s</sub> ft/sec	V <sub>mix</sub> ft/sec	V <sub>r</sub>	W <sub>r</sub>	T <sub>sr</sub>
73	1.60	516.	625.08	882.	1.31	522.	245.10	682.	826.	0.77	0.39	1.07
79	3.16	516.	1260.89	1317.	1.60	514.	340.29	881.	1225.	0.67	0.27	1.21
80	1.60	1001.	447.75	1230.	1.30	692.	209.48	775.	1085.	0.63	0.47	0.73
83	2.16	1806.	452.51	2080.	2.15	732.	389.56	1314.	1726.	0.63	0.86	0.40
84	2.39	1810.	502.19	2201.	2.18	730.	397.13	1323.	1813.	0.60	0.79	0.41
93	3.20	1785.	677.29	2477.	2.14	712.	394.76	1293.	2041.	0.52	0.58	0.44
117	3.30	1901.	673.09	2586.	2.14	761.	380.19	1337.	2135.	0.52	0.56	0.44
97	3.06	1787.	647.28	2437.	1.29	790.	192.74	816.	2065.	0.33	0.30	0.55
94	3.17	1793.	669.37	2474.	1.60	736.	284.21	1054.	2051.	0.43	0.42	0.49
118	3.19	1794.	670.61	2480.	1.90	773.	334.90	1248.	2070.	0.50	0.50	0.49
114	3.19	1787.	671.98	2475.	2.41	708.	443.99	1375.	2038.	0.56	0.66	0.42
98	2.43	1796.	510.55	2210.	1.30	778.	196.67	822.	1824.	0.37	0.39	0.51
101	2.47	1798.	517.21	2229.	1.59	769.	273.87	1071.	1828.	0.48	0.53	0.47
102	2.43	1800.	508.54	2213.	1.90	728.	344.21	1211.	1808.	0.55	0.68	0.42
105	2.35	1800.	493.17	2176.	2.40	730.	435.40	1393.	1809.	0.64	0.88	0.39
122	3.21	1952.	645.76	2596.	2.12	774.	373.44	1341.	2136.	0.52	0.58	0.43
125	3.20	1502.	738.09	2267.	2.14	738.	386.11	1316.	1941.	0.58	0.52	0.54
126	3.17	1795.	666.22	2475.	2.14	652.	410.89	1237.	2003.	0.50	0.62	0.40
121	3.21	1778.	677.98	2474.	2.12	907.	344.67	1452.	2130.	0.59	0.51	0.56

TEST NO	V <sub>mix</sub> ft/sec	V <sub>par</sub> ft/sec	(FG) <sub>i</sub> klb	EPNLT	EPNLTN	PNLT	PNLTN	SH <sub>par</sub>												
73	826.0	-1.297	22.3	89.5	94.8	83.0	86.1	90.6	91.1	88.3	91.4	95.9	96.4	94.5	83.9	96.4	-9.00			
79	1224.5	0.425	60.9	101.4	100.1	95.1	97.7	103.2	103.2	98.9	93.4	103.6	93.8	96.4	101.9	101.9	92.2	102.3	-1.11	
80	1084.9	-0.130	22.2	93.4	95.9	84.7	87.6	92.9	94.0	93.2	84.3	96.0	87.2	90.1	95.4	96.5	95.7	86.8	98.5	-9.00
83	1726.0	1.862	45.2	104.4	108.7	95.1	98.3	103.9	104.4	103.3	98.4	106.7	99.4	102.6	108.2	108.7	107.6	102.7	111.0	-3.77
84	1813.3	2.084	50.7	105.9	109.8	96.5	100.2	104.5	105.5	105.9	100.5	107.5	100.3	104.0	108.3	109.3	109.7	104.3	111.3	-2.62
93	2040.8	2.581	68.0	109.6	112.0	100.8	103.7	107.9	108.6	108.8	105.6	109.9	103.3	106.2	110.4	111.1	111.3	108.1	112.4	-0.88
117	2135.3	2.745	69.9	110.1	112.7	100.2	103.1	107.9	108.2	109.9	105.9	110.9	102.8	105.7	110.5	110.8	112.5	108.5	113.5	-0.73
97	2065.3	2.645	53.9	108.6	112.8	100.7	102.9	107.2	107.5	108.2	103.3	109.6	104.8	107.0	111.3	111.6	112.3	107.4	113.7	-1.57
94	2050.7	2.606	60.8	108.9	112.3	101.4	103.2	107.8	108.4	108.4	103.7	110.0	104.7	106.5	111.1	111.7	111.7	107.0	113.3	-1.26
118	2069.7	2.610	64.7	108.9	111.7	99.1	102.5	107.2	107.4	108.4	103.8	110.0	101.9	105.3	110.0	110.3	111.3	106.7	112.8	-1.00
114	2037.5	2.529	70.7	109.6	111.7	99.8	102.3	106.9	107.2	109.1	105.8	110.7	101.9	104.4	109.0	109.3	111.2	107.9	112.8	-0.74
98	1824.2	2.144	40.1	105.9	111.5	96.5	98.7	104.2	105.3	106.0	99.6	107.8	102.1	104.3	109.8	110.9	111.6	105.2	113.4	-4.38
101	1828.4	2.162	45.0	107.1	112.0	98.6	100.6	104.9	105.8	106.9	100.2	110.1	103.5	105.5	109.8	110.7	111.8	105.1	115.0	-3.43
102	1808.4	2.106	47.9	106.1	110.4	96.6	99.3	104.4	105.3	106.5	100.6	107.6	100.9	103.6	108.7	109.6	110.8	104.9	111.9	-3.00
105	1808.8	2.124	52.2	106.1	109.8	96.9	99.6	104.5	105.1	105.7	101.0	107.5	100.6	103.3	108.2	108.8	109.4	104.7	111.2	-2.38
122	2136.0	2.746	67.7	109.5	112.3	99.7	102.2	107.1	107.6	108.6	105.4	110.7	102.5	105.0	109.9	110.4	111.4	108.2	113.5	-0.87
125	1940.6	2.326	67.8	107.8	109.7	99.2	101.8	106.5	106.6	107.1	102.4	108.9	101.1	103.7	108.4	108.5	109.0	104.3	110.8	-0.79
126	2003.0	2.463	67.1	108.7	111.1	99.4	102.0	106.8	107.3	108.0	104.2	110.1	101.8	104.4	109.2	109.7	110.4	106.6	112.5	-0.99
121	2129.8	2.738	67.7	109.7	112.4	99.9	102.6	107.1	107.2	108.8	105.3	110.3	102.6	105.3	109.8	109.9	111.5	108.0	113.0	-0.74

DATA FOR 0.5"-THICK, 220° FLUID SHIELD NOZZLE WITH HARD PLUG AT A SIDELINE DISTANCE OF 1629'  
A8=1175 SQ", A98=638.6 SQ", AT=1813 SQ", AT SIDELINE POINT WITH FLIGHT SIMULATION (MP=0.32)

TEST NO	P <sub>r,p</sub>	T <sub>t,p</sub> deg R	W <sub>p</sub> lb/sec	V <sub>j,p</sub> ft/sec	P <sub>r,s</sub>	T <sub>t,s</sub> deg R	W <sub>s</sub> lb/sec	V <sub>j,s</sub> ft/sec	V <sub>mix</sub> ft/sec	V <sub>r</sub>	W <sub>r</sub>	T <sub>sr</sub>
106	2.44	1803.	511.61	2219.	1.92	724.	350.49	1218.	1812.	0.55	0.69	0.42
109	2.48	1803.	519.79	2237.	1.58	736.	278.00	1040.	1820.	0.46	0.53	0.45
110	2.45	1802.	514.69	2225.	1.30	785.	195.78	825.	1839.	0.37	0.38	0.51
113	2.38	1801.	499.74	2191.	2.41	730.	437.57	1397.	1820.	0.64	0.88	0.40
129	1.61	524.	622.53	893.	1.30	538.	236.25	680.	834.	0.76	0.38	1.09
131	1.60	1000.	453.73	1230.	1.30	693.	212.04	776.	1085.	0.63	0.47	0.73
133	3.18	519.	1281.15	1325.	1.60	537.	337.21	900.	1236.	0.68	0.26	1.26
139	2.16	1846.	449.12	2104.	2.17	726.	395.58	1315.	1735.	0.63	0.88	0.39
140	2.40	1790.	506.03	2191.	2.11	723.	385.79	1292.	1802.	0.59	0.76	0.41
149	3.22	1784.	678.69	2481.	2.16	706.	397.94	1293.	2042.	0.52	0.59	0.43
150	3.20	1510.	736.50	2274.	2.15	820.	367.17	1390.	1980.	0.61	0.50	0.60
153	3.21	1815.	670.11	2500.	2.41	728.	438.18	1395.	2063.	0.56	0.65	0.42
154	3.20	1788.	674.74	2480.	2.14	900.	349.13	1454.	2130.	0.59	0.52	0.55
157	3.20	1823.	668.15	2505.	1.90	757.	338.81	1236.	2078.	0.49	0.51	0.47
158	3.18	1788.	670.73	2475.	1.60	775.	275.11	1080.	2069.	0.44	0.41	0.52
160	3.21	1757.	682.84	2460.	2.13	591.	430.20	1176.	1964.	0.48	0.63	0.37
164	3.33	1922.	676.14	2610.	2.16	804.	372.57	1380.	2173.	0.53	0.55	0.46
167	3.21	1947.	646.02	2592.	2.15	774.	379.60	1354.	2133.	0.52	0.59	0.43
168	3.06	1801.	640.93	2445.	1.31	847.	190.57	866.	2083.	0.35	0.30	0.59

TEST NO	V <sub>mix</sub> ft/sec	V <sub>par</sub> ft/sec	(FG) <sub>i</sub> klb	EPNLT	EPNLTN	50	60	80	90	130	150	max	50	60	80	90	130	150	max	SH <sub>par</sub>	
106	1812.3	2.078	48.6	103.2	107.4	98.6	100.2	102.7	102.7	102.6	92.8	105.8	102.8	104.3	106.8	106.8	106.8	106.8	97.0	110.0	-2.91
109	1819.5	2.058	45.1	103.2	107.8	98.1	99.8	102.3	102.5	103.4	93.5	105.2	102.8	104.5	107.0	107.2	108.1	108.1	98.2	109.8	-3.47
110	1839.3	2.073	40.6	102.9	108.3	98.0	100.0	102.4	102.2	103.3	93.2	105.0	103.3	105.3	107.8	107.5	108.7	108.7	98.5	110.3	-4.15
113	1820.5	2.016	53.0	102.6	105.9	99.0	100.5	102.5	102.2	101.8	91.7	104.6	102.3	103.8	105.8	105.5	105.1	105.1	95.0	107.9	-2.27
129	834.3	-1.300	22.3	87.2	92.5	85.3	87.2	89.7	89.0	85.2	72.8	93.7	90.6	92.5	95.0	94.3	90.5	90.5	78.1	99.0	-9.00
131	1085.0	-0.092	22.5	91.5	94.3	88.6	90.0	93.2	93.0	89.9	76.5	93.2	91.4	92.8	96.0	95.8	92.7	92.7	79.3	96.0	-9.00
133	1236.4	0.425	62.2	99.9	98.6	99.0	100.1	103.7	101.3	94.9	83.7	103.7	97.6	98.7	102.3	99.9	93.5	93.5	82.3	102.3	-1.08
139	1734.7	1.823	45.5	101.0	105.2	97.6	99.5	101.8	101.3	100.2	89.1	102.9	101.8	103.7	106.0	105.5	104.4	104.4	93.3	107.1	-3.75
140	1802.0	1.978	49.9	102.0	105.7	98.9	100.2	102.2	102.2	101.5	91.4	104.3	102.6	103.9	105.9	105.9	105.2	105.2	95.1	108.0	-2.73
149	2042.2	2.507	68.3	106.0	108.3	102.9	103.7	106.2	105.2	105.9	97.7	107.5	105.2	106.0	108.5	107.5	108.2	108.2	100.0	109.8	-0.85
150	1979.8	2.373	67.9	105.6	107.5	102.8	103.6	106.2	105.1	105.5	96.5	107.5	104.7	105.4	108.1	107.0	107.4	107.4	98.4	109.4	-0.74
153	2063.1	2.552	71.1	106.6	108.7	103.1	105.7	106.5	105.5	106.9	98.4	107.7	105.2	107.8	108.6	107.6	109.0	109.0	100.5	109.8	-0.71
154	2130.0	2.702	67.8	106.6	109.3	103.1	104.5	107.0	106.0	106.7	98.2	108.1	105.7	107.1	109.6	108.6	109.3	109.3	100.8	110.7	-0.75
157	2077.9	2.583	65.0	106.6	109.4	103.3	105.2	106.7	106.1	106.8	97.6	108.4	106.1	108.0	109.5	108.9	109.6	109.6	100.4	111.2	-1.00
158	2068.9	2.568	60.8	107.1	110.3	104.6	105.3	106.3	106.1	107.1	98.2	108.9	107.8	108.5	109.5	109.3	110.3	110.3	101.4	112.1	-1.21
160	1963.7	2.418	67.9	107.2	109.4	104.2	106.3	107.5	106.5	107.4	98.1	109.5	106.4	108.5	109.7	108.7	109.6	109.6	100.3	111.7	-0.99
164	2173.3	2.801	70.8	107.4	110.0	103.9	105.2	108.0	106.5	107.6	99.3	108.9	106.5	107.8	110.6	109.1	110.2	110.2	101.9	111.5	-0.65
167	2133.4	2.713	68.0	106.6	109.3	103.1	104.6	106.1	105.5	106.8	98.9	107.9	105.8	107.3	108.8	108.2	109.5	109.5	101.6	110.6	-0.85
168	2083.4	2.610	53.8	106.1	110.2	103.8	104.3	105.6	105.4	106.3	96.9	108.5	107.9	108.4	109.7	109.5	110.4	110.4	101.0	112.6	-1.55

DATA FOR 0.5" THICK, 220° FLUID SHIELD NOZZLE WITH POROUS PLUG AT A SIDELINE DISTANCE OF 1629',  
A8 = 1175 SQ", A98 = 638.6 SQ", A<sub>T</sub> = 1813 SQ", AT COMMUNITY POINT AT STATIC CONDITION

TEST NO	P <sub>r,p</sub>	T <sub>t,p</sub> deg R	W <sub>p</sub> lb/sec	V <sub>j,p</sub> ft/sec	P <sub>r,s</sub>	T <sub>t,s</sub> deg R	W <sub>s</sub> lb/sec	V <sub>j,s</sub> ft/sec	V <sub>mix</sub> ft/sec	V <sub>r</sub>	W <sub>r</sub>	T <sub>sr</sub>
172	1.63	519.	633.32	901.	1.31	524.	242.94	684.	841.	0.76	0.38	1.07
263	3.18	555.	1214.42	1370.	1.60	545.	328.12	907.	1272.	0.66	0.27	1.19
173	1.59	998.	441.65	1221.	1.30	692.	208.00	775.	1078.	0.63	0.47	0.73
188	2.15	1830.	447.32	2089.	2.15	735.	388.71	1317.	1730.	0.63	0.87	0.39
189	2.41	1808.	504.59	2209.	2.19	742.	394.06	1338.	1827.	0.61	0.78	0.41
196	3.18	1810.	665.42	2489.	2.13	732.	385.88	1307.	2055.	0.53	0.58	0.44
266	3.31	1900.	678.12	2588.	2.31	805.	400.59	1435.	2160.	0.55	0.59	0.46
177	3.05	1797.	638.85	2441.	1.30	772.	196.88	819.	2059.	0.34	0.31	0.54
184	3.16	1790.	663.24	2469.	1.61	778.	276.66	1091.	2063.	0.44	0.42	0.51
185	3.20	1804.	670.77	2490.	1.92	771.	338.87	1255.	2076.	0.50	0.51	0.48
264	3.19	1760.	680.16	2456.	2.36	740.	426.99	1391.	2045.	0.57	0.63	0.45
176	2.42	1807.	505.37	2213.	1.30	746.	200.30	805.	1813.	0.36	0.40	0.48
180	2.45	1793.	513.77	2217.	1.59	741.	279.03	1051.	1807.	0.47	0.54	0.46
181	2.42	1799.	506.60	2208.	1.90	731.	343.50	1213.	1806.	0.55	0.68	0.43
195	2.37	1786.	499.39	2176.	2.40	732.	434.80	1395.	1813.	0.64	0.87	0.40
206	3.19	1946.	645.44	2586.	2.14	738.	387.71	1316.	2109.	0.51	0.60	0.41
203	3.19	1502.	738.84	2265.	2.12	764.	377.45	1332.	1949.	0.59	0.51	0.56
202	3.19	1804.	671.45	2487.	2.15	592.	435.06	1182.	1974.	0.48	0.65	0.36
269	3.19	1788.	674.58	2476.	2.14	895.	351.74	1450.	2124.	0.59	0.52	0.55

TEST NO	V <sub>mix</sub> ft/sec	V <sub>par</sub> ft/sec	(FQ) <sub>i</sub> kib	EPNLT	EPNLTN	PNLT	PNLTN	PHLTN	SH <sub>par</sub>											
172	841.0	-1.248	22.9	90.5	95.8	83.0	86.0	90.5	90.7	89.5	78.7	91.3	88.3	91.3	95.8	96.0	94.8	84.0	96.6	-9.00
263	1271.6	0.539	61.0	100.7	99.7	92.5	95.8	101.3	101.7	99.5	94.1	102.7	91.4	94.7	100.2	100.6	98.4	93.0	101.6	-1.08
173	1078.0	-0.178	21.8	93.8	96.1	85.8	88.5	93.1	93.9	92.5	84.4	94.5	88.1	90.8	95.4	96.2	94.8	86.7	96.8	-9.00
188	1730.0	1.859	45.0	103.5	107.9	92.8	96.6	101.8	103.4	103.4	97.5	105.5	97.2	101.0	106.2	107.8	107.8	101.9	109.9	-3.84
189	1826.8	2.100	51.0	106.2	109.9	95.4	98.4	103.6	104.8	105.4	99.9	106.3	99.2	102.2	107.4	108.6	109.2	103.7	110.1	-2.51
196	2055.1	2.595	67.2	110.4	113.0	99.7	102.6	107.0	107.7	108.8	104.5	110.1	102.3	105.2	109.6	110.3	111.4	107.1	112.7	-0.91
266	2160.0	2.924	72.4	112.2	114.9	100.6	103.5	107.9	109.1	109.9	107.2	111.1	103.3	106.2	110.6	111.8	112.6	109.9	113.8	-0.59
177	2058.9	2.661	53.5	109.3	113.5	100.6	103.1	107.0	107.4	108.2	103.7	109.6	104.8	107.3	111.2	111.6	112.4	107.9	113.8	-1.61
184	2063.2	2.641	60.3	110.8	114.2	101.0	103.8	107.9	108.2	109.2	104.6	109.8	104.4	107.2	111.3	111.6	112.6	108.0	113.2	-1.24
185	2075.7	2.675	65.1	110.9	113.9	100.2	102.8	106.7	108.0	109.0	105.0	109.5	103.1	105.7	109.6	110.9	111.9	107.9	112.4	-0.98
264	2045.3	2.705	70.4	112.1	114.6	101.3	103.9	107.8	108.5	110.4	107.0	110.5	103.7	106.3	110.2	110.9	112.8	109.4	112.9	-0.74
176	1813.2	2.105	39.8	105.9	111.5	95.9	98.9	103.5	104.9	106.0	99.9	108.4	101.5	104.5	109.1	110.5	111.6	105.5	114.0	-4.55
180	1807.0	2.077	44.5	106.2	111.0	96.3	99.2	104.1	105.3	106.7	100.7	108.1	101.1	104.0	108.9	110.1	111.5	105.5	112.9	-3.60
181	1805.9	2.075	47.7	105.5	109.8	96.3	99.1	103.5	104.7	105.8	99.4	106.9	100.6	103.4	107.8	109.0	110.1	103.7	111.2	-3.04
195	1812.9	2.055	52.6	105.8	109.2	95.9	98.9	103.3	104.4	104.1	99.0	106.1	99.4	102.4	106.8	107.9	107.6	102.5	109.6	-2.31
206	2109.5	2.758	67.7	111.1	114.0	100.1	103.1	107.5	108.0	110.1	106.3	110.5	103.0	106.0	110.4	110.9	113.0	109.2	113.4	-0.92
203	1949.2	2.444	67.6	109.2	111.3	98.5	101.9	106.6	106.9	107.7	103.2	108.6	100.6	104.0	108.7	109.0	109.8	105.3	110.7	-0.80
202	1974.1	2.499	67.9	110.2	112.6	100.0	102.8	107.2	107.4	107.9	103.5	109.5	102.4	105.2	109.6	109.8	110.3	105.9	111.9	-1.03
269	2124.4	2.852	67.8	111.5	114.4	99.9	103.0	107.8	108.2	109.8	106.3	110.5	102.8	105.9	110.8	111.1	112.8	109.3	113.4	-0.77

DATA FOR 0.5"-THICK, 220° FLUID SHIELD NOZZLE WITH POROUS PLUG AT A SIDELINE DISTANCE OF 1629',  
A8 = 1175 SQ", A98 = 638.6 SQ", A<sub>T</sub> = 1813 SQ", AT COMMUNITY POINT WITH FLIGHT SIMULATION (M<sub>F</sub> = 0.32)

TEST NO	P <sub>r,p</sub>	T <sub>t,p</sub> deg R	W <sub>p</sub> lb/sec	V <sub>j,p</sub> ft/sec	P <sub>r,s</sub>	T <sub>t,s</sub> deg R	W <sub>s</sub> lb/sec	V <sub>j,s</sub> ft/sec	V <sub>mix</sub> ft/sec	V <sub>r</sub>	W <sub>r</sub>	T <sub>sr</sub>
211	1.59	999.	441.73	1221.	1.29	764.	194.14	800.	1093.	0.66	0.44	0.81
212	2.45	1810.	512.23	2230.	1.31	800.	197.27	847.	1845.	0.38	0.39	0.52
213	3.33	1897.	678.95	2592.	2.15	776.	377.97	1355.	2150.	0.52	0.56	0.45
216	3.21	1785.	676.24	2481.	2.41	767.	425.58	1431.	2075.	0.58	0.63	0.46
217	3.22	1785.	676.82	2482.	2.15	764.	380.69	1344.	2073.	0.54	0.56	0.47
224	3.19	1508.	732.40	2270.	2.14	761.	378.87	1337.	1952.	0.59	0.52	0.56
225	3.22	1929.	648.27	2582.	2.15	783.	375.48	1361.	2134.	0.53	0.58	0.44
228	3.22	1780.	676.45	2478.	2.16	897.	351.69	1460.	2130.	0.59	0.52	0.55
229	2.48	1817.	516.01	2247.	1.63	766.	281.73	1093.	1839.	0.49	0.55	0.47
232	2.46	1774.	517.24	2209.	1.89	790.	327.56	1256.	1839.	0.57	0.63	0.47
233	2.40	1795.	501.95	2196.	2.41	750.	429.22	1415.	1836.	0.64	0.86	0.41
236	2.17	1839.	448.56	2106.	2.16	767.	380.55	1350.	1759.	0.64	0.85	0.41
237	2.40	1799.	501.29	2198.	2.20	740.	395.10	1340.	1820.	0.61	0.79	0.41
243	3.21	1784.	674.56	2480.	1.92	805.	330.32	1284.	2087.	0.52	0.49	0.51
244	3.17	1787.	664.32	2469.	1.63	789.	277.98	1110.	2068.	0.45	0.42	0.52
247	3.07	1785.	643.74	2438.	1.32	849.	191.82	876.	2080.	0.36	0.30	0.59
248	3.22	1810.	669.43	2499.	2.16	644.	414.99	1236.	2016.	0.49	0.62	0.39
251	1.62	553.	605.27	923.	1.30	570.	230.07	707.	863.	0.77	0.38	1.10
252	3.18	536.	1230.71	1346.	1.64	532.	340.58	916.	1253.	0.68	0.28	1.20

TEST NO	V <sub>mix</sub> ft/sec	V <sub>par</sub>	(FG) <sub>i</sub> klb	EPNLT	EPNLN	50	60	80	90	130	150	max	PNLTN	80	90	130	150	max	SH <sub>par</sub>	
211	1092.8	-0.200	21.6	89.0	91.2	87.1	88.1	91.3	90.5	85.6	74.9	91.3	89.3	90.3	93.5	92.7	87.8	77.1	93.5	-9.00
212	1845.2	2.075	40.7	100.4	105.7	96.5	98.7	101.9	97.7	96.8	91.6	105.4	101.8	104.0	107.2	103.0	102.1	96.9	110.7	-4.12
213	2149.7	2.726	70.6	106.7	109.2	103.3	104.9	106.9	105.7	107.1	99.2	108.2	105.7	107.3	109.3	108.1	109.5	101.6	110.6	-0.67
216	2075.5	2.574	71.1	106.0	108.0	102.6	104.1	106.2	105.2	105.6	98.6	107.4	104.7	106.2	108.3	107.3	107.7	100.7	109.5	-0.66
217	2072.6	2.560	68.1	105.9	108.3	102.5	103.8	106.3	105.1	106.3	97.7	107.7	104.9	106.2	108.7	107.5	108.7	100.1	110.1	-0.80
224	1951.8	2.283	67.4	103.9	105.7	101.1	102.3	104.7	102.9	103.4	95.8	105.4	102.9	104.1	106.5	104.7	105.2	97.6	107.2	-0.79
225	2134.1	2.679	67.9	105.7	108.3	101.6	102.7	105.5	104.8	106.3	98.4	107.5	104.3	105.3	108.2	107.5	109.0	101.1	110.2	-0.83
228	2129.7	2.682	68.1	105.9	108.5	102.5	103.7	106.0	105.0	106.3	98.5	106.9	104.9	106.1	108.4	107.4	108.7	100.9	109.4	-0.71
229	1839.5	2.045	45.6	102.4	107.0	98.1	98.8	102.0	102.2	103.1	93.3	105.2	102.6	103.3	106.5	106.7	107.6	97.8	109.7	-3.29
232	1839.4	2.045	48.3	101.9	105.9	97.5	98.9	101.9	101.8	102.2	92.1	104.3	101.6	103.0	106.0	105.9	106.3	96.2	108.4	-2.79
233	1836.2	2.034	53.1	101.8	105.2	99.1	100.3	103.1	101.9	101.1	91.9	103.4	102.4	103.6	106.4	105.2	104.4	95.2	106.7	-2.19
236	1759.1	1.851	45.3	101.1	105.3	98.4	99.7	101.8	101.9	98.5	90.3	103.7	102.6	103.9	106.0	106.1	102.7	94.5	107.9	-3.60
237	1819.6	1.998	50.7	101.9	105.5	98.7	100.4	102.6	101.9	100.6	92.0	104.0	102.3	104.0	106.2	105.5	104.2	95.6	107.6	-2.53
243	2086.9	2.601	65.2	106.1	108.8	103.0	103.8	106.3	105.0	106.4	98.1	107.6	105.7	106.5	109.0	107.7	109.1	100.8	110.3	-0.92
244	2068.4	2.563	60.6	106.8	110.1	106.0	104.3	106.5	105.6	106.8	98.3	108.4	109.2	107.5	109.7	108.8	110.0	101.5	111.6	-1.21
247	2079.9	2.583	54.0	106.1	110.1	103.5	103.8	106.8	105.5	106.3	97.3	108.1	107.5	107.8	110.8	109.5	110.3	101.3	112.1	-1.52
248	2015.9	2.447	67.9	106.0	108.3	102.9	104.4	106.5	105.5	106.5	97.4	107.3	105.1	106.6	108.7	107.7	108.7	99.6	109.5	-0.92
251	863.4	-1.236	22.4	87.4	92.5	86.5	88.1	90.2	89.1	83.3	71.9	90.2	91.7	93.3	95.3	94.3	88.5	77.1	95.3	-9.00
252	1252.9	0.389	61.2	97.1	95.7	95.6	96.9	99.8	98.4	93.2	82.9	99.8	94.2	95.5	98.4	97.0	91.8	81.5	98.4	-1.06

DATA FOR 0.5"-THICK, 220° FLUID SHIELD NOZZLE WITH POROUS PLUG AT A SIDELINE DISTANCE OF 1629',  
A8=1175 SQ", A98=638.6 SQ", At=1813 SQ", AT SIDELINE POINT AT STATIC CONDITION

TEST NO	P <sub>r,p</sub>	T <sub>t,p</sub> deg R	W <sub>p</sub> lb/sec	V <sub>j,p</sub> ft/sec	P <sub>r,s</sub>	T <sub>t,s</sub> deg R	W <sub>s</sub> lb/sec	V <sub>j,s</sub> ft/sec	V <sub>mix</sub> ft/sec	V <sub>r</sub>	W <sub>r</sub>	T <sub>sr</sub>
171	1.63	519.	633.32	901.	1.31	524.	242.94	684.	841.	0.76	0.38	1.07
259	3.15	538.	1222.41	1344.	1.60	530.	332.73	895.	1248.	0.67	0.27	1.20
174	1.60	1002.	444.32	1231.	1.30	695.	207.55	777.	1086.	0.63	0.47	0.73
187	2.15	1820.	448.60	2083.	2.15	769.	379.96	1347.	1746.	0.65	0.85	0.41
193	2.41	1810.	504.30	2210.	2.19	729.	397.57	1326.	1820.	0.60	0.79	0.41
197	3.19	1795.	670.42	2481.	2.14	743.	384.80	1321.	2058.	0.53	0.57	0.45
267	3.31	1900.	678.12	2588.	2.31	805.	400.59	1435.	2160.	0.55	0.59	0.46
178	3.04	1797.	636.75	2438.	1.30	817.	191.36	842.	2069.	0.35	0.30	0.57
183	3.13	1784.	658.10	2456.	1.61	765.	279.02	1082.	2047.	0.44	0.42	0.51
186	3.20	1783.	674.88	2475.	1.88	770.	332.02	1236.	2067.	0.50	0.49	0.49
265	3.19	1760.	680.16	2456.	2.36	705.	437.51	1358.	2026.	0.55	0.64	0.43
175	2.42	1795.	507.18	2205.	1.30	726.	203.05	794.	1802.	0.36	0.40	0.47
179	2.45	1802.	512.43	2223.	1.56	731.	273.98	1024.	1805.	0.46	0.53	0.45
182	2.42	1804.	505.86	2211.	1.91	722.	347.46	1210.	1803.	0.55	0.69	0.42
194	2.37	1786.	499.39	2176.	2.39	732.	432.99	1392.	1812.	0.64	0.87	0.40
205	3.19	1946.	645.44	2586.	2.14	738.	387.71	1316.	2109.	0.51	0.60	0.41
204	3.19	1502.	738.84	2265.	2.12	764.	377.45	1332.	1949.	0.59	0.51	0.56
201	3.19	1804.	671.45	2487.	2.15	592.	435.06	1182.	1974.	0.48	0.65	0.36
268	3.19	1782.	675.76	2472.	2.14	895.	351.74	1450.	2122.	0.59	0.52	0.55

TEST NO	V <sub>mix</sub> ft/sec	V <sub>par</sub> ft/sec	(FG) <sub>i</sub> klb	EPNLTN	PNLT	PNLTN	SH <sub>par</sub>													
171	841.0	-1.248	22.9	89.6	90.6	90.9	89.2	78.8	91.6	89.1	91.7	95.9	96.2	94.5	84.1	96.9	-9.00			
259	1247.5	0.456	60.3	101.2	100.1	94.5	97.5	102.6	103.0	99.4	93.9	103.8	93.4	101.5	101.9	98.3	92.8	102.7	-1.13	
174	1086.2	-0.145	22.0	93.2	95.7	85.0	88.2	92.9	93.8	93.2	85.0	95.2	87.5	90.7	95.4	96.3	95.7	87.5	97.7	-9.00
187	1745.6	1.898	45.0	104.4	108.8	95.1	98.1	102.8	103.9	104.6	97.5	106.2	99.5	102.5	107.2	108.3	109.0	101.9	110.6	-3.75
193	1820.3	2.072	51.0	105.8	109.6	96.7	99.6	104.2	104.8	106.2	100.2	107.2	100.4	103.3	107.9	108.5	109.9	103.9	110.9	-2.53
197	2057.9	2.615	67.5	109.5	112.1	100.5	103.5	107.9	108.3	108.8	105.7	110.4	103.1	106.1	110.5	110.9	111.4	108.3	113.0	-0.87
267	2160.0	2.924	72.4	110.9	113.6	101.8	104.3	108.9	109.6	110.5	106.8	110.7	104.5	107.0	111.6	112.3	113.2	109.5	113.4	-0.59
178	2069.3	2.683	53.3	108.3	112.6	100.3	103.0	107.0	107.4	108.3	103.1	109.8	104.6	107.3	111.3	111.4	112.6	107.4	114.1	-1.61
183	2046.7	2.606	59.6	109.8	113.2	101.5	104.0	108.2	108.4	109.8	104.0	111.5	104.9	107.4	111.6	111.8	113.2	107.4	114.9	-1.31
186	2066.6	2.648	64.7	109.6	112.5	101.3	103.9	108.1	108.5	108.9	105.3	110.0	104.2	106.8	111.0	111.4	111.8	108.2	112.9	-1.00
265	2026.1	2.664	70.4	110.3	112.7	99.2	102.6	107.5	108.2	110.1	107.0	110.1	101.6	105.0	109.9	110.6	112.5	109.4	112.5	-0.77
175	1801.7	2.052	39.8	105.7	111.2	96.2	99.1	103.6	104.8	106.0	99.5	107.7	101.7	104.6	109.1	110.3	111.5	105.0	113.2	-4.60
179	1805.3	2.063	44.1	106.6	111.5	98.3	100.1	104.7	105.5	106.4	100.2	108.6	103.1	104.9	109.5	110.3	111.2	105.0	113.4	-3.70
182	1803.4	2.061	47.8	106.1	110.3	96.7	99.5	104.0	105.0	106.2	100.7	107.8	100.9	103.7	108.2	109.2	110.4	104.9	112.0	-3.03
194	1812.3	2.053	52.5	105.8	109.3	96.5	99.4	103.6	104.3	106.6	100.4	107.0	100.0	102.9	107.1	107.8	110.1	103.9	110.5	-2.33
205	2109.5	2.758	67.7	110.1	113.0	101.2	103.8	108.2	108.8	109.7	106.5	110.6	104.1	106.7	111.1	111.7	112.6	109.4	113.5	-0.92
204	1949.2	2.444	67.6	108.6	110.8	100.3	103.0	107.7	107.9	107.9	104.2	109.0	102.4	105.1	109.8	110.0	110.0	106.3	111.1	-0.80
201	1974.1	2.499	67.9	109.3	111.7	100.6	103.3	107.5	107.8	108.6	104.6	109.9	103.0	105.7	109.9	110.2	111.0	107.0	112.3	-1.03
268	2122.0	2.847	67.8	110.5	113.5	101.1	103.9	108.1	108.8	110.0	107.1	110.7	104.0	106.8	111.0	111.7	112.9	110.0	113.6	-0.77



DATA FOR 0.5"-THICK, 220° FLUID SHIELD NOZZLE WITH POROUS PLUG AT A SIDELINE DISTANCE OF 1629',  
A8=1175 SQ", A98=638.6 SQ", A<sub>T</sub>=1813 SQ", AT SIDELINE POINT WITH FLIGHT SIMULATION (M<sub>F</sub>=0.32)

TEST NO	P <sub>r,p</sub>	T <sub>t,p</sub> deg R	W <sub>p</sub> lb/sec	V <sub>j,p</sub> ft/sec	P <sub>r,s</sub>	T <sub>t,s</sub> deg R	W <sub>s</sub> lb/sec	V <sub>j,s</sub> ft/sec	V <sub>mix</sub> ft/sec	V <sub>r</sub>	W <sub>r</sub>	T <sub>sr</sub>
209	2.43	1807.	508.91	2220.	1.30	817.	191.49	842.	1843.	0.38	0.38	0.53
210	1.61	1005.	448.18	1242.	1.31	774.	199.31	829.	1115.	0.67	0.44	0.82
214	3.33	1900.	677.98	2594.	2.16	772.	380.01	1353.	2148.	0.52	0.56	0.45
215	3.23	1791.	679.25	2491.	2.43	773.	427.96	1444.	2086.	0.58	0.63	0.46
221	3.22	1779.	677.54	2478.	2.15	765.	378.94	1342.	2071.	0.54	0.56	0.47
223	3.21	1492.	740.86	2262.	2.15	755.	381.63	1334.	1947.	0.59	0.52	0.56
226	3.22	1936.	647.00	2587.	2.16	781.	377.80	1363.	2136.	0.53	0.58	0.44
227	3.22	1782.	675.63	2479.	2.16	900.	351.26	1462.	2131.	0.59	0.52	0.55
230	2.47	1735.	526.05	2190.	1.62	772.	279.76	1094.	1809.	0.50	0.53	0.49
231	2.46	1791.	514.47	2219.	1.90	789.	329.51	1260.	1845.	0.57	0.64	0.46
234	2.40	1782.	503.22	2187.	2.40	725.	435.51	1390.	1817.	0.64	0.87	0.40
235	2.19	1806.	457.19	2099.	2.16	776.	378.67	1358.	1763.	0.65	0.83	0.42
241	2.41	1801.	503.58	2205.	2.20	735.	396.00	1335.	1822.	0.61	0.79	0.41
242	3.24	1785.	679.40	2488.	1.92	803.	330.04	1280.	2093.	0.51	0.49	0.51
245	3.17	1781.	665.28	2465.	1.63	795.	278.19	1118.	2068.	0.45	0.42	0.53
246	3.07	1782.	643.88	2436.	1.32	862.	192.41	891.	2080.	0.37	0.30	0.60
249	3.22	1788.	674.35	2484.	2.16	635.	418.89	1229.	2003.	0.49	0.62	0.39
250	1.61	569.	592.49	931.	1.29	589.	223.02	710.	870.	0.76	0.38	1.10
257	3.19	533.	1239.99	1345.	1.64	537.	340.01	923.	1254.	0.69	0.27	1.22

TEST NO	V <sub>mix</sub> ft/sec	V <sub>par</sub> ft/sec	(FG) <sub>i</sub> klb	EPNLT	EPNLTN	PNLT	PNLTN	SH <sub>par</sub>												
209	1843.0	2.110	40.1	102.1	107.6	96.3	98.7	101.8	101.5	103.1	92.7	104.9	101.8	104.2	107.3	107.0	108.6	98.2	110.4	-4.26
210	1114.7	-0.122	22.4	88.8	91.5	86.5	87.7	91.2	89.9	86.2	72.9	93.7	89.1	90.3	93.8	92.5	88.8	75.5	96.3	-9.00
214	2148.3	2.723	70.6	107.2	109.6	103.8	106.1	107.9	105.8	107.6	98.9	108.0	106.2	108.5	110.3	108.2	110.0	101.3	110.4	-0.67
215	2086.0	2.596	71.8	105.9	108.0	102.0	103.3	105.6	105.8	106.5	97.8	108.1	104.1	105.4	107.7	107.9	108.6	99.9	110.2	-0.62
221	2070.7	2.548	68.0	106.1	108.4	102.6	104.8	106.5	105.5	106.4	96.9	108.0	104.9	107.2	108.8	107.8	108.8	99.3	110.3	-0.81
223	1946.8	2.272	67.9	104.6	106.3	101.9	103.7	105.8	103.7	104.5	95.5	106.1	103.6	105.4	107.5	105.4	106.2	97.2	107.8	-0.76
226	2136.1	2.683	68.0	105.9	108.5	102.1	103.9	105.4	105.2	106.5	97.8	107.9	104.7	106.5	108.0	107.8	109.1	100.4	110.5	-0.82
227	2131.3	2.685	68.0	106.1	108.6	102.4	103.9	106.2	105.3	106.2	98.0	107.6	104.8	106.3	108.6	107.7	108.6	100.4	110.2	-0.71
230	1809.4	1.974	45.3	102.2	106.6	96.9	99.2	102.4	101.7	102.7	92.4	105.4	101.3	103.6	106.8	106.1	107.1	96.8	109.8	-3.31
231	1844.6	2.057	48.4	102.1	106.2	97.3	98.4	101.8	101.7	102.4	92.3	105.0	101.4	102.5	105.9	105.8	106.5	96.4	109.1	-2.79
234	1816.9	1.988	53.0	102.2	105.4	98.7	100.2	103.0	101.4	101.8	91.8	104.2	101.9	103.4	106.3	104.7	105.1	95.1	107.4	-2.23
235	1763.3	1.858	45.8	101.8	105.9	98.2	100.2	102.5	102.6	100.6	90.4	104.4	102.3	103.4	106.7	106.8	104.8	94.6	108.6	-3.43
241	1822.3	2.001	50.9	102.2	105.8	98.7	99.9	102.3	102.1	102.1	92.4	104.4	102.3	103.5	105.9	105.7	105.7	96.0	108.0	-2.49
242	2092.8	2.618	65.7	106.5	109.2	103.1	104.8	106.9	105.4	107.1	98.0	107.9	105.8	107.5	109.6	108.1	109.8	100.7	110.6	-0.89
245	2067.8	2.561	60.6	106.4	109.6	102.9	104.8	107.7	105.6	106.7	97.1	108.4	106.1	108.0	110.9	108.8	109.9	100.3	111.6	-1.20
246	2080.4	2.588	54.1	105.8	109.8	104.6	103.4	105.5	104.6	106.0	95.9	107.6	108.6	107.4	109.5	108.6	110.0	99.9	111.6	-1.51
249	2003.5	2.420	68.1	106.0	108.2	102.7	103.5	106.3	104.9	106.5	97.0	107.4	104.9	105.7	108.5	107.1	108.7	99.2	109.6	-0.92
250	870.5	-1.200	22.1	87.0	92.0	85.9	87.7	89.7	88.6	83.1	71.5	97.8	90.8	92.6	94.6	93.5	88.0	76.4	102.7	-9.00
257	1253.8	0.393	61.6	98.3	96.9	96.7	98.3	102.0	99.5	93.9	82.4	102.0	95.3	96.9	100.6	98.1	92.5	81.0	100.6	-1.03

DATA FOR 0.75"-THICK, 220° FLUID SHIELD NOZZLE WITH POROUS PLUG AT A SIDELINE DISTANCE OF 1629"  
A8=1175 SQ", A98=990.5 SQ", AT=2165.5 SQ", AT COMMUNITY POINT AT STATIC CONDITION

TEST NO	P <sub>r,p</sub>	T <sub>t,p</sub> deg R	W <sub>p</sub> lb/sec	V <sub>j,p</sub> ft/sec	P <sub>r,s</sub>	T <sub>t,s</sub> deg R	W <sub>s</sub> lb/sec	V <sub>j,s</sub> ft/sec	V <sub>mix</sub> ft/sec	V <sub>r</sub>	W <sub>r</sub>	T <sub>sr</sub>
331	1.60	524.	621.84	891.	1.30	523.	373.35	674.	810.	0.76	0.60	1.06
332	1.61	999.	452.40	1239.	1.29	699.	320.45	773.	1046.	0.62	0.71	0.74
335	2.82	1809.	591.25	2372.	1.30	728.	316.43	795.	1822.	0.34	0.54	0.49
337	2.86	1798.	601.57	2379.	1.60	727.	443.18	1048.	1814.	0.44	0.74	0.47
339	2.79	1800.	587.53	2357.	1.90	725.	538.34	1208.	1808.	0.51	0.92	0.44
340	2.73	1809.	573.40	2342.	2.19	727.	619.65	1324.	1813.	0.57	1.08	0.42
354	3.20	1785.	677.67	2478.	2.13	696.	617.16	1276.	1905.	0.52	0.91	0.43
363	2.42	1803.	507.41	2210.	2.20	728.	619.90	1328.	1725.	0.60	1.22	0.41
364	2.18	1840.	451.65	2110.	2.16	730.	607.79	1316.	1655.	0.62	1.35	0.39
367	3.80	1780.	802.12	2619.	1.92	711.	546.32	1204.	2046.	0.46	0.68	0.47
368	3.79	1772.	801.90	2611.	2.16	696.	622.53	1285.	2032.	0.49	0.78	0.45
372	3.22	1798.	674.26	2492.	2.16	609.	663.79	1202.	1852.	0.48	0.98	0.37
375	3.22	1784.	677.02	2482.	2.15	903.	540.87	1459.	2027.	0.59	0.80	0.56
376	3.23	1512.	740.37	2282.	2.14	718.	606.93	1300.	1840.	0.57	0.82	0.53
379	3.35	1919.	678.05	2613.	2.15	696.	619.08	1283.	1978.	0.49	0.91	0.40
380	3.74	1784.	786.35	2610.	1.60	739.	436.88	1056.	2055.	0.40	0.56	0.52
383	3.59	1785.	754.59	2576.	1.30	807.	298.74	837.	2083.	0.32	0.40	0.59
384	3.21	558.	1222.25	1379.	1.62	607.	489.55	968.	1261.	0.70	0.40	1.32

TEST NO	V <sub>mix</sub> ft/sec	V <sub>par</sub>	(FG) <sub>i</sub> klb	EPNLT	EPNLTN	50	60	80	90	130	150	max	50	60	80	90	130	150	max	SH <sub>par</sub>
331	809.7	-1.384	25.0	88.4	93.1	83.1	85.7	90.3	90.3	87.8	75.8	90.6	87.7	90.3	94.9	94.9	92.4	80.4	95.2	-9.00
332	1045.7	-0.290	25.1	91.0	92.0	84.0	86.9	91.4	92.0	89.5	81.2	93.7	85.0	87.9	92.4	92.4	90.5	82.2	94.7	-9.00
335	1822.4	2.123	51.4	106.7	110.9	97.6	100.9	105.0	105.4	106.9	101.3	108.0	101.8	105.1	109.2	109.6	111.1	105.5	112.2	-3.43
337	1814.2	2.103	58.9	106.9	110.2	97.5	100.6	105.0	105.6	107.2	102.0	108.1	100.8	103.9	108.3	108.9	110.5	105.3	111.4	-2.70
339	1807.9	2.088	63.3	106.2	108.9	96.2	99.6	104.5	105.0	105.3	101.6	106.7	98.9	102.3	107.2	107.7	108.0	104.3	109.4	-2.29
340	1813.1	2.084	67.2	105.7	107.9	97.4	99.6	104.0	104.1	104.4	101.4	105.5	99.6	101.8	106.2	106.3	106.6	103.6	107.7	-1.93
354	1905.1	2.278	76.7	108.6	110.2	99.1	101.8	106.6	107.0	107.0	105.3	108.5	100.7	103.4	108.2	108.6	108.6	106.9	110.1	-1.22
363	1725.3	1.819	60.5	103.7	106.2	95.9	98.4	103.3	103.7	102.2	99.1	104.8	98.5	101.0	105.9	106.3	104.8	101.7	107.3	-2.68
364	1654.6	1.625	54.5	103.1	106.1	94.5	97.2	103.2	103.3	101.4	96.2	107.1	97.5	100.2	106.2	106.3	104.4	99.2	110.1	-3.79
367	2045.8	2.547	85.7	111.7	112.9	101.6	104.3	108.7	108.6	109.9	109.3	110.4	102.8	105.5	109.9	109.8	111.1	110.5	111.6	-0.63
368	2031.7	2.517	89.9	111.4	112.2	101.6	104.4	108.6	108.4	109.6	108.6	111.6	102.4	105.2	109.4	109.2	110.4	109.4	112.4	-0.50
372	1851.9	2.114	77.0	107.8	109.1	98.8	101.6	106.3	106.5	106.3	103.7	107.8	100.1	102.9	107.6	107.8	107.6	105.0	109.1	-1.30
375	2027.4	2.480	76.0	109.1	111.0	98.2	101.5	106.5	106.2	106.9	106.5	107.7	100.0	103.3	108.3	108.0	108.7	108.3	109.5	-0.99
376	1840.0	2.058	77.0	107.0	108.0	98.6	101.8	106.3	105.8	105.1	102.8	106.5	99.6	102.8	107.3	106.8	106.1	103.8	107.5	-1.05
379	1978.2	2.373	79.8	109.1	110.6	99.3	102.4	106.9	106.9	107.7	106.1	108.4	100.8	103.9	108.4	108.4	109.2	107.6	109.9	-1.05
380	2054.8	2.538	78.1	110.7	112.5	101.2	104.0	108.3	108.2	110.2	107.3	110.3	103.0	105.8	110.1	110.0	112.0	109.1	112.1	-0.89
383	2083.0	2.597	68.2	110.2	113.0	100.9	103.8	109.4	108.7	109.8	105.2	110.3	103.6	106.5	112.1	111.4	112.5	107.9	113.0	-1.17
384	1261.4	0.419	67.1	99.3	97.9	92.9	95.8	101.6	101.7	96.5	89.7	101.9	91.5	94.4	100.2	100.3	95.1	88.3	100.5	-1.48

DATA FOR 0.75" THICK, 220° FLUID SHIELD NOZZLE WITH POROUS PLUG AT A SIDELINE DISTANCE OF 1629"  
A8=1175 SQ", A98=990.5 SQ", A<sub>T</sub>=2165.5 SQ", AT SIDELINE POINT AT STATIC CONDITION

TEST NO	P <sub>r,p</sub>	T <sub>t,p</sub> deg R	W <sub>p</sub> lb/sec	V <sub>j,p</sub> ft/sec	P <sub>r,s</sub>	T <sub>t,s</sub> deg R	W <sub>s</sub> lb/sec	V <sub>j,s</sub> ft/sec	V <sub>mix</sub> ft/sec	V <sub>r</sub>	W <sub>r</sub>	T <sub>sr</sub>
330	1.61	523.	625.39	894.	1.30	523.	373.60	673.	811.	0.75	0.60	1.06
333	1.61	1001.	452.02	1240.	1.30	696.	325.40	780.	1047.	0.63	0.72	0.74
334	2.81	1804.	591.43	2368.	1.30	727.	316.70	794.	1819.	0.34	0.54	0.49
336	2.85	1809.	598.61	2384.	1.61	730.	444.19	1053.	1817.	0.44	0.74	0.46
338	2.80	1803.	589.12	2363.	1.90	726.	538.15	1209.	1812.	0.51	0.91	0.44
341	2.73	1804.	574.30	2338.	2.21	728.	623.66	1331.	1814.	0.57	1.09	0.42
358	3.22	1777.	683.50	2478.	2.15	696.	623.24	1284.	1908.	0.52	0.91	0.43
359	2.42	1804.	507.27	2211.	2.21	730.	621.86	1334.	1728.	0.60	1.23	0.41
365	2.19	1832.	455.38	2112.	2.17	730.	610.60	1320.	1658.	0.62	1.34	0.39
366	3.77	1786.	794.39	2618.	1.90	719.	538.72	1203.	2046.	0.46	0.68	0.48
369	3.79	1794.	796.12	2627.	2.15	696.	619.87	1281.	2038.	0.49	0.78	0.44
373	3.22	1808.	672.31	2499.	2.16	606.	664.51	1198.	1852.	0.48	0.99	0.37
374	3.23	1780.	679.07	2480.	2.15	909.	539.31	1464.	2031.	0.59	0.79	0.56
377	3.22	1512.	738.08	2280.	2.15	705.	614.81	1291.	1831.	0.57	0.83	0.52
378	3.34	1909.	677.87	2603.	2.14	699.	613.73	1281.	1975.	0.49	0.91	0.40
381	3.74	1783.	786.58	2609.	1.60	741.	436.29	1058.	2055.	0.41	0.55	0.52
382	3.59	1787.	753.14	2577.	1.30	812.	297.81	839.	2084.	0.33	0.40	0.59
385	3.16	547.	1216.29	1358.	1.60	578.	492.02	932.	1235.	0.69	0.40	1.29

TEST NO	V <sub>mix</sub> ft/sec	V <sub>par</sub> kfb	(FG) <sub>i</sub>	EPNLT	EPNLTN	50	60	80	90	130	150	max	PNLTN	80	90	130	150	max	SH <sub>par</sub>
330	811.3	-1.375	25.2	88.7	93.3	83.0	85.6	90.3	90.4	88.3	76.5	90.8	87.6	90.2	94.9	95.0	92.9	81.1	95.4
333	1047.5	-0.282	25.3	91.5	92.6	83.9	86.9	91.7	92.8	90.5	81.4	94.1	85.0	88.0	92.8	93.9	91.6	82.5	95.2
334	1819.2	2.115	51.3	107.1	111.3	98.5	101.3	105.1	105.7	107.0	102.9	108.4	102.7	105.5	109.3	109.9	111.2	107.1	112.6
336	1817.3	2.111	58.9	106.8	110.1	97.4	100.3	104.4	105.5	105.7	102.3	108.0	100.7	103.6	107.7	108.8	109.0	105.6	111.3
338	1811.9	2.098	63.5	106.7	109.4	97.0	100.0	104.4	105.5	106.6	102.0	107.9	99.7	102.7	107.1	108.2	109.3	104.7	110.6
341	1813.6	2.085	67.5	106.8	109.0	96.2	98.6	103.9	104.5	106.2	102.9	107.7	98.4	100.8	106.1	106.7	108.4	105.1	109.9
358	1908.1	2.285	77.5	109.0	110.5	99.1	101.9	106.9	107.2	108.0	105.4	109.4	100.6	103.4	108.4	108.7	109.5	106.9	110.9
359	1727.7	1.825	60.6	105.1	107.6	96.7	98.5	102.7	104.2	104.8	100.5	106.5	99.2	101.0	105.2	106.7	107.3	103.0	109.0
365	1658.4	1.635	54.9	103.7	106.7	94.4	97.5	102.9	103.2	103.5	97.7	106.2	97.4	100.5	105.9	106.2	106.5	100.7	109.2
366	2046.0	2.547	84.8	112.2	113.5	101.4	104.4	109.0	109.2	110.9	108.7	111.1	102.7	105.7	110.3	110.5	112.2	110.0	112.4
369	2038.0	2.530	89.7	111.9	112.8	101.1	104.1	108.8	108.8	110.1	109.1	112.0	101.9	104.9	109.6	109.6	110.9	109.9	112.8
373	1852.2	2.115	77.0	108.3	109.6	98.7	101.2	105.9	106.4	107.6	104.3	108.9	100.0	102.5	107.2	107.7	108.9	105.6	110.2
374	2030.6	2.515	76.9	110.0	111.9	99.7	102.2	106.7	106.9	109.2	106.6	109.5	101.6	104.1	108.6	108.8	111.1	108.5	111.4
377	1830.6	2.036	77.0	107.7	108.7	99.1	102.1	106.3	106.3	107.0	103.1	107.6	100.0	103.0	107.3	107.3	107.9	104.0	108.5
378	1974.8	2.366	79.3	109.8	111.3	99.7	102.6	106.6	107.4	109.2	105.8	109.5	101.2	104.1	108.1	108.9	110.7	107.3	111.0
381	2055.4	2.539	78.1	111.1	112.9	101.1	104.1	108.7	108.6	110.5	107.3	111.1	102.9	105.9	110.5	110.4	112.3	109.1	112.9
382	2084.3	2.600	68.1	110.1	112.9	101.5	104.2	108.7	108.4	109.5	105.8	110.3	104.3	107.0	111.5	111.2	112.3	108.6	113.1
385	1235.2	0.328	65.6	100.1	98.7	93.0	96.2	101.8	101.9	97.7	90.7	102.6	91.6	94.8	100.4	100.5	96.3	89.3	101.2

TEST NO	P <sub>r,p</sub>	T <sub>t,p</sub> deg R	W <sub>p</sub> lb/sec	V <sub>j,p</sub> ft/sec	P <sub>r,s</sub>	T <sub>t,s</sub> deg R	W <sub>s</sub> lb/sec	V <sub>j,s</sub> ft/sec	V <sub>mix</sub> ft/sec	V <sub>r</sub>	W <sub>r</sub>	T <sub>sr</sub>
AT SIDELINE POINT												
348	2.40	1804.	505.39	2203.	2.21	726.	624.65	1329.	1720.	0.60	1.24	0.40
342	2.74	1801.	577.89	2342.	2.19	725.	621.27	1323.	1814.	0.57	1.08	0.42
349	3.20	1791.	675.71	2481.	2.14	701.	616.72	1283.	1909.	0.52	0.91	0.43
370	3.76	1787.	791.42	2615.	2.14	698.	615.59	1280.	2031.	0.49	0.78	0.45
AT COMMUNITY POINT												
344	2.41	1806.	506.42	2207.	2.20	729.	621.79	1329.	1723.	0.60	1.23	0.41
343	2.73	1804.	575.37	2340.	2.20	727.	622.56	1327.	1814.	0.57	1.08	0.42
353	3.20	1787.	677.35	2479.	2.13	692.	618.51	1272.	1903.	0.51	0.91	0.42
371	3.76	1787.	791.42	2615.	2.14	698.	615.59	1280.	2031.	0.49	0.78	0.45
TEST NO	P <sub>r,p</sub>	T <sub>t,p</sub> deg R	W <sub>p</sub> lb/sec	V <sub>j,p</sub> ft/sec	P <sub>r,s</sub>	T <sub>t,s</sub> deg R	W <sub>s</sub> lb/sec	V <sub>j,s</sub> ft/sec	V <sub>mix</sub> ft/sec	V <sub>r</sub>	W <sub>r</sub>	T <sub>sr</sub>
AT SIDELINE POINT												
348	2.40	1804.	505.39	2203.	2.21	726.	624.65	1329.	1720.	0.60	1.24	0.40
342	2.74	1801.	577.89	2342.	2.19	725.	621.27	1323.	1814.	0.57	1.08	0.42
349	3.20	1791.	675.71	2481.	2.14	701.	616.72	1283.	1909.	0.52	0.91	0.43
370	3.76	1787.	791.42	2615.	2.14	698.	615.59	1280.	2031.	0.49	0.78	0.45
AT COMMUNITY POINT												
344	2.41	1806.	506.42	2207.	2.20	729.	621.79	1329.	1723.	0.60	1.23	0.41
343	2.73	1804.	575.37	2340.	2.20	727.	622.56	1327.	1814.	0.57	1.08	0.42
353	3.20	1787.	677.35	2479.	2.13	692.	618.51	1272.	1903.	0.51	0.91	0.42
371	3.76	1787.	791.42	2615.	2.14	698.	615.59	1280.	2031.	0.49	0.78	0.45
TEST NO	P <sub>r,p</sub>	T <sub>t,p</sub> deg R	W <sub>p</sub> lb/sec	V <sub>j,p</sub> ft/sec	P <sub>r,s</sub>	T <sub>t,s</sub> deg R	W <sub>s</sub> lb/sec	V <sub>j,s</sub> ft/sec	V <sub>mix</sub> ft/sec	V <sub>r</sub>	W <sub>r</sub>	T <sub>sr</sub>
AT SIDELINE POINT												
348	2.40	1804.	505.39	2203.	2.21	726.	624.65	1329.	1720.	0.60	1.24	0.40
342	2.74	1801.	577.89	2342.	2.19	725.	621.27	1323.	1814.	0.57	1.08	0.42
349	3.20	1791.	675.71	2481.	2.14	701.	616.72	1283.	1909.	0.52	0.91	0.43
370	3.76	1787.	791.42	2615.	2.14	698.	615.59	1280.	2031.	0.49	0.78	0.45
AT COMMUNITY POINT												
344	2.41	1806.	506.42	2207.	2.20	729.	621.79	1329.	1723.	0.60	1.23	0.41
343	2.73	1804.	575.37	2340.	2.20	727.	622.56	1327.	1814.	0.57	1.08	0.42
353	3.20	1787.	677.35	2479.	2.13	692.	618.51	1272.	1903.	0.51	0.91	0.42
371	3.76	1787.	791.42	2615.	2.14	698.	615.59	1280.	2031.	0.49	0.78	0.45
TEST NO	P <sub>r,p</sub>	T <sub>t,p</sub> deg R	W <sub>p</sub> lb/sec	V <sub>j,p</sub> ft/sec	P <sub>r,s</sub>	T <sub>t,s</sub> deg R	W <sub>s</sub> lb/sec	V <sub>j,s</sub> ft/sec	V <sub>mix</sub> ft/sec	V <sub>r</sub>	W <sub>r</sub>	T <sub>sr</sub>
AT SIDELINE POINT												
348	2.40	1804.	505.39	2203.	2.21	726.	624.65	1329.	1720.	0.60	1.24	0.40
342	2.74	1801.	577.89	2342.	2.19	725.	621.27	1323.				

AT SIDELINE POINT																				
348	1719.8	1.834	60.4	102.1	104.7	99.0	100.2	102.9	102.5	100.4	92.0	103.4	101.6	102.8	105.5	105.1	103.0	94.6	106.0	-2.73
342	1814.2	2.086	67.6	102.9	105.1	99.1	101.0	103.1	102.4	101.7	93.9	104.6	101.3	103.2	105.3	104.6	103.9	96.1	106.8	-1.90
349	1909.1	2.287	76.7	105.4	107.0	103.0	102.9	106.8	104.6	103.9	97.0	106.8	104.6	104.5	108.4	106.2	105.5	98.6	108.4	-1.21
370	2031.1	2.516	88.8	108.2	109.0	105.8	106.9	109.7	107.3	106.8	100.5	109.7	106.7	107.8	110.6	108.2	107.7	101.4	110.6	-0.55
AT COMMUNITY POINT																				
344	1723.1	1.842	60.4	101.5	104.1	99.4	100.4	102.8	102.1	98.0	90.3	103.4	102.0	103.0	105.4	104.7	100.6	92.9	106.0	-2.72
343	1813.6	2.077	67.5	102.1	104.3	100.1	100.8	102.9	102.1	99.9	93.3	102.9	102.3	103.0	105.1	104.3	102.1	95.5	105.1	-1.90
353	1902.6	2.272	76.6	104.5	106.1	102.7	103.7	105.9	104.5	102.9	96.5	105.9	104.3	105.3	107.5	106.1	104.5	98.1	107.5	-1.23
371	2031.1	2.516	88.8	107.3	108.2	104.9	106.3	108.5	106.1	106.1	100.3	108.5	105.8	107.2	109.4	107.0	107.0	101.2	109.4	-0.55

DATA FOR 1.0"-THICK, 220° FLUID SHIELD NOZZLE WITH POROUS PLUG AT A SIDELINE DISTANCE OF 1629"  
A8=1175 SQ", A98=1349.7 SQ", AT=2524.7 SQ", AT COMMUNITY POINT AT STATIC CONDITION

TEST NO	P <sub>r,p</sub>	T <sub>t,p</sub> deg R	W <sub>p</sub> lb/sec	V <sub>j,p</sub> ft/sec	P <sub>r,s</sub>	T <sub>t,s</sub> deg R	W <sub>s</sub> lb/sec	V <sub>j,s</sub> ft/sec	V <sub>mix</sub> ft/sec	V <sub>r</sub>	W <sub>r</sub>	T <sub>sr</sub>
272	1.61	521.	628.08	893.	1.30	524.	509.31	675.	795.	0.76	0.81	1.07
273	1.61	1008.	451.93	1245.	1.29	703.	435.76	774.	1014.	0.62	0.96	0.74
279	3.18	524.	1260.51	1332.	1.60	521.	716.64	889.	1171.	0.67	0.57	1.21
280	3.21	1781.	679.05	2476.	2.15	693.	848.53	1279.	1811.	0.52	1.25	0.43
286	4.36	1780.	922.24	2726.	2.13	696.	840.21	1277.	2035.	0.47	0.91	0.47
290	4.36	1787.	919.72	2731.	1.91	696.	750.75	1188.	2038.	0.43	0.82	0.48
291	4.31	1782.	911.14	2719.	1.61	701.	616.81	1033.	2038.	0.38	0.68	0.51
294	4.09	1790.	861.80	2685.	1.30	726.	430.24	793.	2055.	0.30	0.50	0.55
295	3.18	1810.	665.50	2488.	1.31	708.	442.77	794.	1811.	0.32	0.67	0.49
298	3.34	1908.	681.09	2603.	2.14	696.	842.38	1279.	1871.	0.49	1.24	0.40
299	3.18	1504.	734.90	2264.	2.12	696.	833.34	1271.	1736.	0.56	1.13	0.51
302	3.22	1790.	678.86	2486.	2.15	908.	738.70	1464.	1953.	0.59	1.09	0.56
303	3.18	1809.	665.70	2487.	1.91	718.	738.72	1206.	1813.	0.48	1.11	0.45
306	3.08	1805.	645.90	2455.	2.21	729.	848.75	1332.	1818.	0.54	1.31	0.43
323	2.40	1800.	504.28	2198.	2.20	727.	847.04	1328.	1652.	0.60	1.68	0.41
324	2.20	1834.	457.32	2117.	2.16	729.	829.73	1315.	1600.	0.62	1.81	0.39
327	3.23	1807.	677.25	2500.	1.60	725.	602.54	1044.	1815.	0.42	0.89	0.48
328	3.22	1788.	679.68	2485.	2.14	574.	927.36	1161.	1721.	0.47	1.36	0.35

TEST NO	V <sub>mix</sub> ft/sec	V <sub>par</sub> par	(FG) <sub>i</sub> klb	EPNLT	EPNLTN	50	60	80	90	PNLT	130	150	max	80	90	130	150	max	SH <sub>par</sub>	
272	795.2	-1.402	28.1	89.4	93.3	82.9	85.3	91.1	92.0	88.5	75.1	92.6	86.8	89.2	95.0	95.9	92.4	79.0	96.5	-9.00
273	1014.1	-0.346	28.0	90.4	90.5	83.8	86.8	92.5	93.4	86.0	77.9	93.6	83.9	86.9	92.6	93.5	86.1	78.0	93.7	-9.00
279	1171.4	0.237	72.0	99.0	97.3	93.3	96.1	101.5	102.1	94.9	88.3	102.3	91.5	94.3	99.7	100.3	93.1	86.5	100.5	-2.00
280	1811.3	2.113	86.0	108.0	108.9	99.2	102.1	106.7	107.0	106.2	103.9	107.6	100.1	103.0	107.6	107.9	107.1	104.8	108.5	-1.44
286	2034.9	2.618	111.5	112.9	112.7	103.6	106.2	110.8	110.4	112.0	109.4	114.1	103.5	106.1	110.7	110.3	111.9	109.3	114.0	-0.28
290	2037.6	2.624	105.8	112.9	113.2	103.0	105.9	110.5	110.5	112.5	110.0	113.5	103.8	106.3	111.0	110.9	113.7	111.4	114.3	-0.68
291	2038.4	2.626	96.8	113.1	114.0	102.9	105.5	110.2	110.1	112.8	110.6	113.5	103.8	106.3	111.0	111.8	113.5	111.7	113.7	-1.02
294	2054.8	2.661	82.5	112.3	114.2	102.2	105.1	109.6	109.9	111.6	109.8	111.8	104.1	107.0	111.5	111.8	113.5	111.7	113.7	-1.02
295	1810.9	2.112	62.4	108.2	111.4	99.3	102.3	107.0	106.8	108.3	103.3	109.0	102.5	105.5	110.2	110.0	111.5	106.5	112.2	-2.98
298	1870.7	2.253	88.6	109.3	110.3	100.3	102.5	107.4	107.6	107.6	105.8	108.3	101.3	103.5	108.4	108.6	108.6	106.8	109.3	-1.33
299	1736.5	1.930	84.6	107.1	107.6	98.9	101.6	107.3	106.6	104.4	103.4	107.3	99.5	102.2	107.9	107.2	105.0	104.0	107.9	-1.40
302	1953.4	2.435	86.1	109.4	110.8	99.8	101.9	106.8	107.2	107.4	106.8	109.1	101.2	103.3	108.2	108.6	108.8	108.2	110.5	-1.21
303	1813.1	2.111	79.1	107.6	109.1	99.3	102.2	106.4	106.7	105.7	104.3	107.2	100.8	103.7	107.9	108.2	107.2	105.8	108.7	-1.84
306	1817.6	2.122	84.4	108.0	109.1	98.5	101.5	106.1	106.3	105.6	105.0	106.9	99.5	102.5	107.1	107.3	106.6	106.0	107.9	-1.51
323	1652.4	1.720	69.4	104.7	106.6	96.5	99.7	104.4	104.6	102.5	100.3	106.3	98.3	101.5	106.2	106.4	104.3	102.1	108.1	-2.87
324	1599.7	1.580	64.0	103.8	106.1	95.5	98.7	104.2	104.6	101.4	98.2	106.7	97.7	100.9	106.4	106.8	103.6	100.4	108.9	-3.76
327	1814.6	2.127	72.2	108.1	110.3	100.4	103.1	106.7	107.2	106.8	103.9	108.5	102.6	105.3	108.9	109.4	109.0	106.1	110.7	-2.31
328	1721.1	1.897	86.0	107.8	108.4	100.2	102.8	106.7	107.5	105.3	103.9	108.2	100.8	103.4	107.3	108.1	105.9	104.5	108.8	-1.64

DATA FOR 1.0"-THICK, 220° FLUID SHIELD NOZZLE WITH POROUS PLUG AT A SIDELINE DISTANCE OF 1629'  
A8=1175 SQ", A98=1349.7 SQ", AT=2524.7 SQ", AT SIDELINE POINT AT STATIC CONDITION

TEST NO	P <sub>r,p</sub>	T <sub>t,p</sub> deg R	W <sub>p</sub> lb/sec	V <sub>j,p</sub> ft/sec	P <sub>r,s</sub>	T <sub>t,s</sub> deg R	W <sub>s</sub> lb/sec	V <sub>j,s</sub> ft/sec	V <sub>mix</sub> ft/sec	V <sub>r</sub>	W <sub>r</sub>	T <sub>sr</sub>
271	1.62	520.	632.62	896.	1.31	528.	515.92	686.	802.	0.77	0.82	1.08
274	1.61	1001.	451.77	1237.	1.30	695.	446.22	782.	1011.	0.63	0.99	0.74
275	3.18	520.	1262.97	1326.	1.60	531.	707.46	895.	1171.	0.68	0.56	1.24
284	3.23	1782.	682.19	2482.	2.14	699.	841.54	1282.	1819.	0.52	1.23	0.43
285	4.35	1779.	921.24	2724.	2.14	700.	838.97	1281.	2036.	0.47	0.91	0.47
289	4.36	1788.	919.87	2732.	1.91	696.	750.36	1187.	2038.	0.43	0.82	0.48
292	4.31	1784.	909.97	2720.	1.61	698.	620.09	1033.	2037.	0.38	0.68	0.51
293	4.09	1780.	865.17	2678.	1.30	726.	428.13	789.	2053.	0.29	0.49	0.55
296	3.16	1816.	661.22	2487.	1.30	728.	430.35	795.	1820.	0.32	0.65	0.50
297	3.35	1901.	684.84	2601.	2.15	696.	845.53	1282.	1872.	0.49	1.23	0.40
300	3.22	1507.	742.67	2276.	2.14	702.	838.37	1284.	1750.	0.56	1.13	0.52
301	3.22	1788.	678.36	2484.	2.14	902.	739.30	1457.	1949.	0.59	1.09	0.55
304	3.18	1809.	666.75	2488.	1.91	721.	737.17	1209.	1816.	0.49	1.11	0.45
305	3.09	1811.	645.80	2461.	2.20	725.	847.81	1326.	1817.	0.54	1.31	0.43
319	2.40	1800.	505.20	2201.	2.21	727.	849.54	1330.	1655.	0.60	1.68	0.41
325	2.18	1838.	453.05	2109.	2.15	727.	828.95	1311.	1593.	0.62	1.83	0.39
326	3.23	1805.	679.32	2501.	1.61	724.	611.13	1055.	1816.	0.42	0.90	0.48
329	3.22	1783.	680.46	2481.	2.14	573.	927.30	1159.	1719.	0.47	1.36	0.35

TEST NO	V <sub>mix</sub> ft/sec	V <sub>par</sub> ft/sec	(FG) <sub>i</sub> klb	EPNLT	PNLT	PNLTN	SH <sub>par</sub> max													
271	802.0	-1.366	28.6	89.8	93.6	84.0	86.7	91.9	92.3	88.4	76.4	92.9	87.8	90.5	95.7	96.1	92.2	80.2	96.7	-9.00
274	1011.0	-0.360	28.2	91.8	91.9	83.9	87.1	92.5	92.9	90.1	81.4	94.8	84.0	87.2	92.6	93.0	90.2	81.5	94.8	-9.00
275	1171.4	0.237	71.7	100.5	98.8	94.4	97.0	103.4	103.0	97.8	90.6	103.4	92.7	95.3	101.7	101.3	96.1	88.9	101.7	-2.03
284	1819.4	2.132	86.2	109.2	110.1	99.6	102.2	106.9	107.4	108.5	104.9	109.0	100.5	103.1	107.8	108.3	109.4	105.8	109.9	-1.42
285	2036.3	2.621	111.4	114.3	114.1	103.7	106.3	110.7	110.7	113.8	111.3	115.5	103.6	106.2	110.6	110.6	113.7	111.2	115.4	-0.28
289	2038.3	2.626	105.8	113.7	114.0	102.9	105.6	110.2	110.3	113.8	110.2	114.6	103.1	105.8	110.4	110.5	114.0	110.4	114.8	-0.43
292	2036.5	2.622	96.8	113.7	114.5	102.8	105.5	110.5	110.5	113.3	111.4	114.2	103.6	106.3	111.3	111.3	114.1	112.2	115.0	-0.68
293	2052.7	2.656	82.5	112.5	114.4	102.9	105.4	109.8	109.9	111.5	109.4	112.0	104.8	107.3	111.7	111.8	113.4	111.3	113.9	-1.01
296	1820.2	2.134	61.8	108.6	111.9	99.8	102.6	107.2	107.3	108.6	103.0	109.6	103.1	105.9	110.5	110.6	111.9	106.3	112.9	-3.01
297	1872.1	2.256	89.0	109.9	110.9	99.4	102.3	107.2	107.6	109.4	106.5	110.1	100.3	103.3	108.1	108.5	110.3	107.4	111.0	-1.30
300	1750.2	1.958	86.0	108.1	108.6	99.4	102.1	106.6	107.2	106.9	104.0	107.8	99.9	102.6	107.1	107.7	107.4	104.5	108.3	-1.31
301	1948.7	2.424	85.9	110.1	111.5	98.7	102.3	106.9	107.3	109.5	106.3	109.9	100.1	103.7	108.3	108.7	110.9	107.7	111.3	-1.22
304	1816.3	2.119	79.3	108.9	110.4	99.5	102.1	106.5	107.4	108.2	105.3	108.8	101.0	103.6	108.0	108.9	109.7	106.8	110.3	-1.83
305	1817.2	2.121	84.4	108.7	109.8	98.6	101.5	106.3	106.7	107.2	104.9	108.6	99.7	102.6	107.4	107.8	108.3	106.0	109.7	-1.51
319	1654.9	1.727	69.7	106.1	107.9	97.1	99.5	104.7	105.1	105.5	101.5	106.9	98.9	101.3	106.5	106.9	107.3	103.3	108.7	-2.83
325	1593.2	1.562	63.5	105.0	107.3	95.9	99.1	103.7	105.1	103.8	99.6	107.9	98.2	101.3	105.9	107.3	106.1	101.8	110.2	-3.88
326	1815.9	2.130	72.8	109.2	111.4	100.1	102.9	106.8	107.6	109.0	105.2	110.0	102.3	105.1	109.0	109.8	111.2	107.4	112.2	-2.26
329	1719.0	1.892	85.9	109.0	109.6	99.3	102.4	107.4	107.6	108.2	105.5	109.6	99.9	103.0	108.0	108.2	108.8	106.1	110.2	-1.65

DATA FOR 1.0"-THICK, 220° FLUID SHIELD NOZZLE WITH POROUS PLUG AT A SIDELINE DISTANCE OF 1629'  
A8=1175 SQ", A98=1349.7 SQ", A<sub>T</sub>=2524.7 SQ", WITH FLIGHT SIMULATION (M<sub>F</sub>=0.32)

TEST NO	P <sub>r,p</sub>	T <sub>t,p</sub> deg R	W <sub>p</sub> lb/sec	V <sub>j,p</sub> ft/sec	P <sub>r,s</sub>	T <sub>t,s</sub> deg R	W <sub>s</sub> lb/sec	V <sub>j,s</sub> ft/sec	V <sub>mix</sub> ft/sec	V <sub>r</sub>	W <sub>r</sub>	T <sub>sr</sub>								
AT SIDELINE POINT																				
288	4.36	521.	1727.71	1466.	2.14	694.	843.39	1276.	1404.	0.87	0.49	1.63								
308	3.09	1805.	648.00	2458.	2.20	725.	846.09	1324.	1816.	0.54	1.31	0.43								
309	3.22	1807.	675.52	2498.	2.14	692.	842.85	1274.	1818.	0.51	1.25	0.42								
318	2.41	1797.	507.04	2201.	2.20	726.	846.47	1326.	1654.	0.60	1.67	0.41								
AT COMMUNITY POINT																				
287	4.35	1789.	918.55	2732.	2.13	695.	840.82	1276.	2036.	0.47	0.92	0.46								
307	3.08	1806.	646.97	2458.	2.20	728.	846.26	1329.	1818.	0.54	1.31	0.43								
313	3.21	1787.	677.77	2482.	2.14	696.	841.59	1278.	1815.	0.52	1.24	0.43								
314	2.41	1806.	505.79	2208.	2.19	729.	843.37	1328.	1658.	0.60	1.67	0.41								
TEST NO	V <sub>mix</sub> ft/sec	V <sub>par</sub> ft/sec	(FG) <sub>i</sub> klb	EPNLT	EPNLTN	50	60	80	90	PNLT	130	150	max	SH <sub>par</sub>						
AT SIDELINE POINT																				
288	2036.0	2.621	111.6	110.1	109.9	107.1	108.8	110.8	109.4	107.8	104.0	110.8	106.9	108.7	110.7	109.3	107.7	103.8	110.7	-0.28
308	1816.1	2.118	84.3	104.8	105.8	101.7	103.3	105.9	104.7	103.6	96.2	105.9	102.8	104.4	107.0	105.8	104.7	97.3	107.0	-1.52
309	1818.4	2.124	85.8	105.3	106.3	102.5	104.0	105.8	105.5	103.9	97.1	106.0	103.4	104.9	106.7	106.4	104.8	98.0	106.9	-1.46
318	1653.7	1.724	69.6	102.8	104.6	99.9	101.0	103.9	103.6	100.4	93.1	104.0	101.7	102.8	105.7	105.4	102.2	94.9	105.8	-2.85
AT COMMUNITY POINT																				
287	2035.9	2.621	111.3	109.6	109.5	107.0	108.3	110.3	108.5	106.4	104.4	110.3	106.9	108.2	110.2	108.4	106.3	104.3	110.2	-0.29
307	1817.9	2.122	84.4	103.3	104.4	101.2	102.4	104.7	104.1	100.2	96.0	106.0	102.3	103.5	105.8	105.2	101.3	97.1	107.1	-1.51
313	1815.1	2.116	85.7	103.9	104.9	101.8	102.9	105.8	104.4	100.7	96.7	105.8	102.7	103.8	106.7	105.3	101.6	97.6	106.7	-1.45
314	1657.7	1.734	69.5	102.0	103.8	100.2	101.1	104.1	103.4	97.2	92.0	104.1	102.0	102.9	105.9	105.2	99.0	93.8	105.9	-2.85





## REFERENCES

1. Salikuddin, M, et al, "Design Report for Fluid Shield Scale Model Nozzle for Acoustic and Aeromixing Experiments", General Electric Technical Information Series Report no. R93-AEB-297, 1993.
2. Majjigi, R. K, et al., "Free Jet Feasibility Study of a Thermal Acoustic Shield Concept for AST/VCE Application - Single Stream Nozzles", NASA CR 3758, 1984.
3. Liepmann, H.W. and Roshko, A., "Elements of Gas Dynamics", Wiley, New York, 1957.
4. Zucrow, M. J. and Hoffman, J. D., "Gas Dynamics, Vol. I", Wiley, New York, 1976.
5. Ben-Dor, G., "Shock Wave Reflection Phenomena", Springer - Verlag, New York, 1991.
6. Tam, C. K. W., "Forward Flight Effects on Broadband Shock Associated Noise of Supersonic Jets", AIAA-89-1088, 1989.
7. Maestrello, L., "An Experimental Study on Porous Plug Jet Noise Suppressor", AIAA-79-0673, 1979.
8. Bauer, A. B., "Jet Noise Suppression by Porous Plug Nozzles", AIAA-81-1993, 1981.
9. Kibens, V. and Wlezien, R. W., "Noise Reduction Mechanisms in Supersonic Jets with Porous Centerbodies", AIAA Journal, 1985.
10. Das, I. S. and Dosanjh, D. S., "Short Conical Solid/Perforated Plug Nozzle as Supersonic Jet Noise Suppressor", Journal of Sound and Vibration, 166, pp. 391-406, 1991.

11. Yamamoto, K., Brausch, J.F., Balsa, T.F., Janardan, B.A., and Knott, P.R., "Experimental Investigation of Shock-Cell Noise Reduction for Single Stream Nozzles in Simulated Flight". NASA CR 3845, 1984.
12. Gliebe, P.R., "Diagnostic Evaluation of Jet Noise Suppression Mechanisms", J. Aircraft, 17 (12), pp. 837-842, 1980.
13. Hoch, R. E., Duponchel, J. P., Cocking, B. J., and Bryce, W. D., "Studies of the Influence of Density on Jet Noise", Journal of Sound and Vibration, 28 (4), pp. 649-668, 1973.
14. Behrens, et al, "High Velocity Jet Noise Source Location and Predictions - Task 1 Supplement - Certification of the General Electric Jet Noise Anechoic Test Facility", GE Contractor Report - FAA-RD-76-79, Ia, 1977.
15. Mani, R., et al, "High Velocity Jet Noise Source Location and Predictions - Task 4 - Development/Evaluation of Techniques for 'In-Flight' Investigation", GE Contractor Report - FAA-RD-76-79, IV, 1977.
16. Ahuja, K. K., Tester, B. J., and Tanna, H. K., "The Free Jet as a Simulator of Forward Velocity Effects on Jet Noise". NASA CR-3056, 1978.
17. Amiet, R. K., "Correlation of Open Jet Wind Tunnel Measurements for Shear Layer Refraction". AIAA Paper No. 75-532, 1975.
18. Amiet, R. K., "Refraction of Sound by Shear Layer Refraction". AIAA Paper No. 77-54, 1977.
19. "Gas Turbine Jet Exhaust Noise Prediction". Prepared by: Gas Turbine Propulsion Subcommittee of SAE Committee A-21, Aircraft Noise, ARP-876C, 1983.
20. Gliebe, P. R., et al., "High Velocity Jet Noise Source Location and Reduction". Final Report Submitted to U. S. Dept. of Transportation, Report No. FAA-RD-76-79, Task III, Vol. I, 1978.

21. Vogt, P. G., Bhutiani, P. K., and Knott, P. R., "Free-Jet Acoustic Investigation of High Radius Ratio Coannular Plug Nozzles", GE Comprehensive Data Report, Volume I, R81AEG212, Contract NAS3-20619, 1981.
22. Janardan, B. A., et. al., "Free-Jet Investigation of Mechanically Suppressed, High-Radius-Ratio Coannular Plug Model Nozzles", Comprehensive Data Report for NASA-GE Contract NAS3-21608, GE TM No. R81AEG484, 1981.
23. Blozy, J. T., et. al., "Acoustic and Aerodynamic Performance Investigation of Inverted Velocity Profile Coannular Plug Nozzles", Comprehensive Data Report for NASA-GE Contract NAS3-19777, GE TM No. R79AEG166, 1979.
24. Vdoviak, J. W., Knott, P. R., and Ebacker, J. J., "Aerodynamic/Acoustic Performance of YJ101/Double Bypass VCE with Coannular Plug Nozzle", Final Report for NASA-GE Contract NAS3-20582, GE TM No. R80AEG369, NASA CR-159869, 1981.
25. Brausch, J. F., Motsinger, R. E., and Hoerst, D. J., "Simulated Flight Acoustic Investigation of Treated Ejector Effectiveness on Advanced Mechanical Suppressors for High Velocity Jet Noise Reduction", NASA CR-4019, 1986.
26. Powell, A., "On the Mechanics of Choked Jet Noise", Proc. Physical Society, B, Vol. LXVI, pp. 1039-1056, 1953.
27. Harper-Bourne, M. and Fisher, M. J., "The Noise From Shock Waves in Supersonic Jets", Noise Mechanisms, AGARD-CP-131, pp. 11-1 - 11-13, 1974.
28. Brown, W. H., et al., "Axisymmetric Mixer/Ejector Nozzle (AMEN) Test Report", GE Technical Information Series, 1993.
29. Courant, R. and Friedrichs, K.O. "Supersonic Flow and Shock Waves." Springer-Verlag, N.Y., 1976.
30. Dosanjh, D. S., Abdel-Hamid, A. N., and Yu, J. C., "Noise Reduction from Interacting Coaxial Supersonic Jet Flows. in Basic Aerodynamic Noise Research," (ed : Schwartz, I. R.), NASA SP-207, pp. 63-101, 1969.

REPORT DOCUMENTATION PAGE			Form Approved OMB No. 0704-0188	
Public reporting burden for this collection of information is estimated to average 1 hour per response, including the time for reviewing instructions, searching existing data sources, gathering and maintaining the data needed, and completing and reviewing the collection of information. Send comments regarding this burden estimate or any other aspect of this collection of information, including suggestions for reducing this burden, to Washington Headquarters Services, Directorate for Information Operations and Reports, 1215 Jefferson Davis Highway, Suite 1204, Arlington, VA 22202-4302, and to the Office of Management and Budget, Paperwork Reduction Project (0704-0188), Washington, DC 20503.				
1. AGENCY USE ONLY (Leave blank)		2. REPORT DATE February 2005		3. REPORT TYPE AND DATES COVERED Final Contractor Report
4. TITLE AND SUBTITLE  Acoustic and Aero-Mixing Experimental Results for Fluid Shield Scale Model Nozzles			5. FUNDING NUMBERS  WBS-22-714-09-46 NAS3-25951	
6. AUTHOR(S)  M. Salikuddin, V.G. Mengle, H.W. Shin, and R.K. Majjigi				
7. PERFORMING ORGANIZATION NAME(S) AND ADDRESS(ES)  General Electric Aircraft Engines One Neumann Way Cincinnati, Ohio 45125-1988			8. PERFORMING ORGANIZATION REPORT NUMBER  E-14721	
9. SPONSORING/MONITORING AGENCY NAME(S) AND ADDRESS(ES)  National Aeronautics and Space Administration Washington, DC 20546-0001			10. SPONSORING/MONITORING AGENCY REPORT NUMBER  NASA CR-2005-213213	
11. SUPPLEMENTARY NOTES  This research was originally published internally as HSR024 in January 2004. Responsible person, Diane Chapman, Ultra-Efficient Engine Technology Program Office, NASA Glenn Research Center, organization code PA, 216-433-2309.				
12a. DISTRIBUTION/AVAILABILITY STATEMENT  Unclassified - Unlimited Subject Categories: 01, 02, 05, and 07  Available electronically at <a href="http://gltrs.grc.nasa.gov">http://gltrs.grc.nasa.gov</a> This publication is available from the NASA Center for AeroSpace Information, 301-621-0390.			12b. DISTRIBUTION CODE	
13. ABSTRACT (Maximum 200 words) The principle objectives of this investigation are to evaluate the acoustic and aerodynamic characteristics of fluid shield nozzle concept and to assess Far 36, Stage 3 potential for fluid shield nozzle with Flade Cycle. Acoustic data for nine scale model nozzle configurations are obtained. The effects of simulated flight and geometric and aerothermodynamic flow variables on the acoustic behavior of the fluid shield are determined. The acoustic tests are aimed at studying the effect of (1) shield thickness, (2) wrap angle, (3) mass flow and velocity ratios between shield and core streams at constant cycle specific thrust (i.e., mixed velocity), (4) porous plug, and (5) subsonic shield. Shadowgraphs of six nozzle configurations are obtained to understand the plume flowfield features. Static pressure data on suppressor chutes in the core stream (shielded and unshielded) sides and on plug surface are acquired to determine the impact of fluid shield on base drag of the 36-chute suppressor nozzle and the thrust augmentation due to the plug, respectively.				
14. SUBJECT TERMS  High speed civil transport; Acoustics; Aerodynamics; Fluid shield nozzle			15. NUMBER OF PAGES 623	
			16. PRICE CODE	
17. SECURITY CLASSIFICATION OF REPORT Unclassified	18. SECURITY CLASSIFICATION OF THIS PAGE Unclassified	19. SECURITY CLASSIFICATION OF ABSTRACT Unclassified	20. LIMITATION OF ABSTRACT	



